

T. Pradeep
Publications 2024

Contents

1. Publications	9-461
2. Editorials	464-472
3. Patents/Technology	474-475
4. Selected media reports	477-489

Journal papers in 2024

Publications from our group

1. Formation and dissociation of dimethyl ether clathrate hydrate in interstellar ice mimics, Bijesh Malla, Gaurav Vishwakarma, Soham Chowdhury, Samir Nayak, Sharma S. R. K. C. Yamijala and Thalappil Pradeep, *J. Phys. Chem. C*, 128 (2024) 2463–2470. (DOI: 10.1021/acs.jpcc.3c07792)
2. Spontaneous α -C-H carboxylation of ketones by gaseous CO₂ at the air-water interface of aqueous microdroplets, Pallab Basuri, Sinchan Mukhopadhyay, K. S. S. V. Prasad Reddy, Keerthana Unni, B. K. Spoorthi, Jenifer Shantha Kumar, Sharma S. R. K. C. Yamijala and Thalappil Pradeep, *Angew. Chem.* 63 (2024) e202403229. (DOI: 10.1002/anie.202403229)
3. Spontaneous weathering of natural minerals in charged water microdroplets forms nanomaterials, B. K. Spoorthi, Koyendrila Debnath, Pallab Basuri, Ankit Nagar, Umesh V. Waghmare and Thalappil Pradeep, *Science*, 384 (2024) 1012–1017. (DOI: 10.1126/science.adl3364)
4. Interfacial growth of large area single-crystalline silver sheets through ambient microdroplets, Depanjan Sarkar, Anirban Som, Keerthana Unni, Sujan Manna, and Thalappil Pradeep, *Small*, (2024) 2400159. (DOI: 10.1002/smll.202400159)
5. Observing atomically precise nanocluster aggregates in solution by mass photometry, Jayoti Roy, Ila Marathe, Vicki Wysocki and Thalappil Pradeep, *Chem. Commun.* 60 (2024) 6655–6658. (DOI: 10.1039/D4CC00363B)
6. Interparticle anti-galvanic reactions of atomically precise silver nanoclusters with plasmonic gold nanoparticles: interfacial control of atomic exchange, Paulami Bose, Jayoti Roy, Vikash Khokhar, Biswajit Mondal, Ganapati Natarajan, Sujan Manna, Vivek Yadav, Anupriya Nyayban, Sharma S. R. K. C. Yamijala, Nonappa and Thalappil Pradeep, *Chem. Mater.* 36 (2024) 7581–7594. (DOI: 10.1021/acs.chemmater.4c00620)
7. Partitioning photochemically formed CO₂ into clathrate hydrate under interstellar conditions, Gaurav Vishwakarma, Bijesh Malla, Rajnish Kumar and Thalappil Pradeep, *Phys. Chem. Chem. Phys.* 26 (2024) 1600–16016. (DOI: 10.1039/D4CP01414F)

8. Extensive polymerization of atomically precise alloy metal clusters during solid state reactions, B. S. Sooraj, Jayoti Roy, Manish Mukherjee, Anagha Jose and Thalappil Pradeep, *Langmuir* 40 (2024) 15244–15251. (DOI: 10.1021/acs.langmuir.4c01737)
9. Cysteine-protected antibacterial spheroids of atomically precise copper clusters for direct and affordable arsenic detection from drinking water, Jenifer Shantha Kumar, Arijit Jana, Jayathraa Raman, Hema Madhuri Veera, Amoghavarsha Ramachandra Kini, Jayoti Roy, Sourav Kanti Jana, Tiju Thomas and Thalappil Pradeep, *ES&T Letters* 11 (2024) 831–837. (DOI: 10.1021/acs.estlett.4c00264)
10. From solution to microstructures in minutes: microdroplet-derived stand-alone TiO₂ surfaces for simultaneous water harvesting and treatment, Keerthana Unni, Jenifer Shantha Kumar, Anirban Som, Depanjan Sarkar, Thalappil Pradeep, *ACS Sustainable Chem. Eng.* 12 (2024) 11957–11967. (DOI: 10.1021/acssuschemeng.4c02806)
11. Multicolor photoluminescence of Cu₁₄ clusters modulated using surface ligands, Arijit Jana, Subrata Duary, Amitabha Das, Amoghavarsha Ramachandra Kini, Swetashree Acharya, Jan Machacek, Biswarup Pathak, Tomas Base and Thalappil Pradeep, *Chem. Sci.* 15 (2024) 13741–13752. (DOI: 10.1039/D4SC01566E)
12. Enhanced electrical output in an electrostatic generator using charged water, Vishal Kumar, Pillalamarri Srikrishnarka, Ramamurthy Nagarajan, and Thalappil Pradeep, *ACS Sustain. Chem. Eng.* 12 (2024) 13106–13115. (DOI: 10.1021/acssuschemeng.4c01860)
13. Nanocluster reaction-driven in-situ transformation of colloidal nanoparticles to mesostructures, Paulami Bose, Pillalamarri Srikrishnarka, Matias Paatelainen, Nonappa, Amoghavarsha Ramachandra Kini, Anirban Som, and Thalappil Pradeep, *Nanoscale* (2024). (DOI: 10.1039/D4NR02820A)
14. Milling-induced ‘Turn-off’ luminescence in copper nanoclusters, Subrata Duary, Arijit Jana, Amitabha Das, Swetashree Acharya, Amoghavarsha Ramachandra Kini, Jayoti Roy, Ajay Poonia, Deepak Patel, Vivek Yadav, Sudhadevi P. K. Antarjanam, Biswarup Pathak, Kumaran Nair Valsala Devi Adarsh and Thalappil Pradeep, *Inorganic Chemistry* 63 (2024) 18727–18737. (DOI: 10.1021/acs.inorgchem.4c02617)
15. Growth of clathrate hydrates in nanoscale ice films observed using electron diffraction and infrared spectroscopy, Bijesh Malla, Ding-Shyue Yang and Thalappil Pradeep, *J. Phys. Chem. Lett.* (2024) (DOI: 10.1021/acs.jpcllett.4c03106)

16. Simulated interstellar photolysis of N₂O ice: selectivity in photoproducts, Bijesh Malla, Soham Chowdhury, Devansh Paliwal, Hanoona K. M., Gaurav Vishwakarma, Rabin Methikkalam and Thalappil Pradeep, *J. Phys. Chem. C.* (2024) (DOI: 10.1021/acs.jpcc.4c06624)
17. Stable dimer intermediates during intercluster reactions of atomically precise nanoclusters, Swetashree Acharya, Jayoti Roy, Diptendu Roy, Biswarup Pathak and Thalappil Pradeep, *J. Phys. Chem. C.* (2024) (Just accepted)

Editorials

1. Managing water, the mother of resources: thoughts on world water day 2024, Thalappil Pradeep, Michael K. C. Tam and Julio F. Serrano, ACS Sustainable Resour. Manage. 1 (2024) 368–369. (DOI: 10.1021/acssusresmgt.4c00096)
2. Reintroducing the INTRODUCTION: how to write a compelling introduction for the ACS sustainable family of journals, Audrey Moores, Jingwen Chen, Bala Subramaniam, Michael KC Tam, Elizabeth J. Biddinger, Dean Brady, Danielle Julie Carrier, Ivet Ferrer, Nicholas Gathergood, Hongxian Han, Ive Hermans, King Kuok Mimi Hii, Bing Joe Hwang, Milad Kamkar, Kevin Leonard, Watson Loh, Say Chye Joachim Loo, Andrew C. Marr, Michael A.R. Meier, Ryuhei Nakamura, Graham N. Newton, Thalappil Pradeep, Kotaro Satoh, Wil V. Srubar III, Ning Yan, Asha James, Mihir Jha, Atal Shivhare, Julio F. Serrano, and Peter Licence, ACS Sustainable Chem. Eng. 12 (2024) 8581–8583. (DOI: 10.1021/acssuschemeng.4c04252)
3. Fireside chat with Man Mohan Sharma: Catalysis for sustainability, Milad Kamkar, Thalappil Pradeep and Julio F. Serrano, ACS Sustainable Resour. Manage. (2024) (DOI: 10.1021/acssusresmgt.4c00502)

Journal papers

Publications from our group

Formation and Dissociation of Dimethyl Ether Clathrate Hydrate in Interstellar Ice Mimics

Bijesh K. Malla, Gaurav Vishwakarma, Soham Chowdhury, Samir Kumar Nayak, Sharma S. R. K. C. Yamijala, and Thalappil Pradeep*

Cite This: *J. Phys. Chem. C* 2024, 128, 2463–2470

Read Online

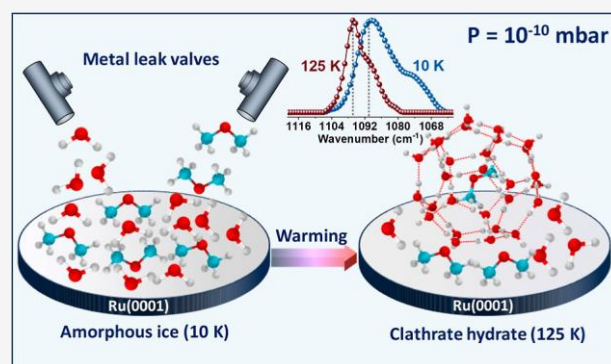
ACCESS

Metrics & More

Article Recommendations

Supporting Information

ABSTRACT: Clathrate hydrates (CHs) are believed to exist within interstellar environments, potentially contributing to the preservation of diverse volatile compounds within icy bodies across the cosmos. In this study, using reflection absorption infrared spectroscopy, we show the formation of dimethyl ether (DME) CH from a vapor-deposited DME–water amorphous ice mixture. Experiments were conducted in an environment mimicking interstellar conditions: ultrahigh vacuum ($P \sim 5 \times 10^{-10}$ mbar) and cryogenic conditions ($T \sim 10$ –150 K). Thermal annealing of the amorphous ice mixture to a higher temperature ($T \sim 125$ K) resulted in the formation of CH. Quantum chemical calculations suggested the formation of 5¹²⁶⁴ cages of structure II CH. Subsequent investigations into the dissociation of DME CH unveiled its transformation into hexagonal ice, requiring a substantial activation energy of 68.04 kJ mol⁻¹. Additionally, confirmation of the formation and dissociation of CH was supported by temperature-programmed desorption mass spectrometry. These results significantly advance our understanding of the existence of CHs under extreme conditions relevant to an interstellar medium.



INTRODUCTION

Clathrate hydrates (CHs) are host–guest crystalline compounds having hydrogen-bonded cages of water with different molecules (mostly gases) encaged within.^{1–3} While the most common CH structures, known as structure I (sI) and structure II (sII), are cubic and formed with small molecules CH₄, CO₂, C₂H₆, O₂, and N₂ within them, large molecules such as 2-methylbutane and cycloheptane form the hexagonal structure H (sH) CH.^{3–6} The formation of this non-stoichiometric crystalline CH is well-known under high-pressure and low-temperature conditions.⁷ However, its existence in ultrahigh vacuum (UHV) under cryogenic conditions was established only recently.^{8,9} Considering the temperature–pressure conditions, it is now clear that they can occur in outer space in addition to icy environments on earth’s sea beds.^{10–12} CHs have garnered significant scientific interest due to their potential implications in energy storage,¹³ climate change,¹⁰ and astrochemistry.^{14,15} Thus, understanding the properties and behavior of CHs is crucial for a wide range of applications.

The formation of CHs in a vacuum at temperatures ranging from 100 to 150 K has been a known phenomenon since the 1990s.^{16,17} However, recent advancements have expanded our understanding of CH formation, particularly in the UHV environment at exceptionally low temperatures. These breakthroughs were achieved by thermal annealing of amorphous

water matrices in the presence of hydrocarbons like CH₄ (at 30 K)¹⁸ and C₂H₆ (at 60 K)¹⁹ for extended durations, leading to the formation of sI CH. Moreover, it has been observed that the dissociation of the CH of carbonyl compounds such as formaldehyde, acetaldehyde, and acetone can catalyze the formation of hexagonal and cubic crystalline ice structures.^{20–22} These findings mark significant progress in our comprehension of CH evolution and hold promise for myriad

applications in materials science, cryogenic chemistry, and astrochemistry. Thus, it is imperative to expand our investigative scope to encompass a broader spectrum of molecules studied under a simulated interstellar medium (ISM).

The simplest ether, dimethyl ether (DME), emerges as a molecule of profound significance, showcasing its relevance in the terrestrial environment and ISM.^{23–25} It is one of the most abundant complex organic molecules detected in space,²⁶ and its presence in interstellar clouds and protostellar environments offer valuable insights into the chemistry of the

Received: November 28, 2023

Revised: January 14, 2024

Accepted: January 16, 2024

Published: February 6, 2024



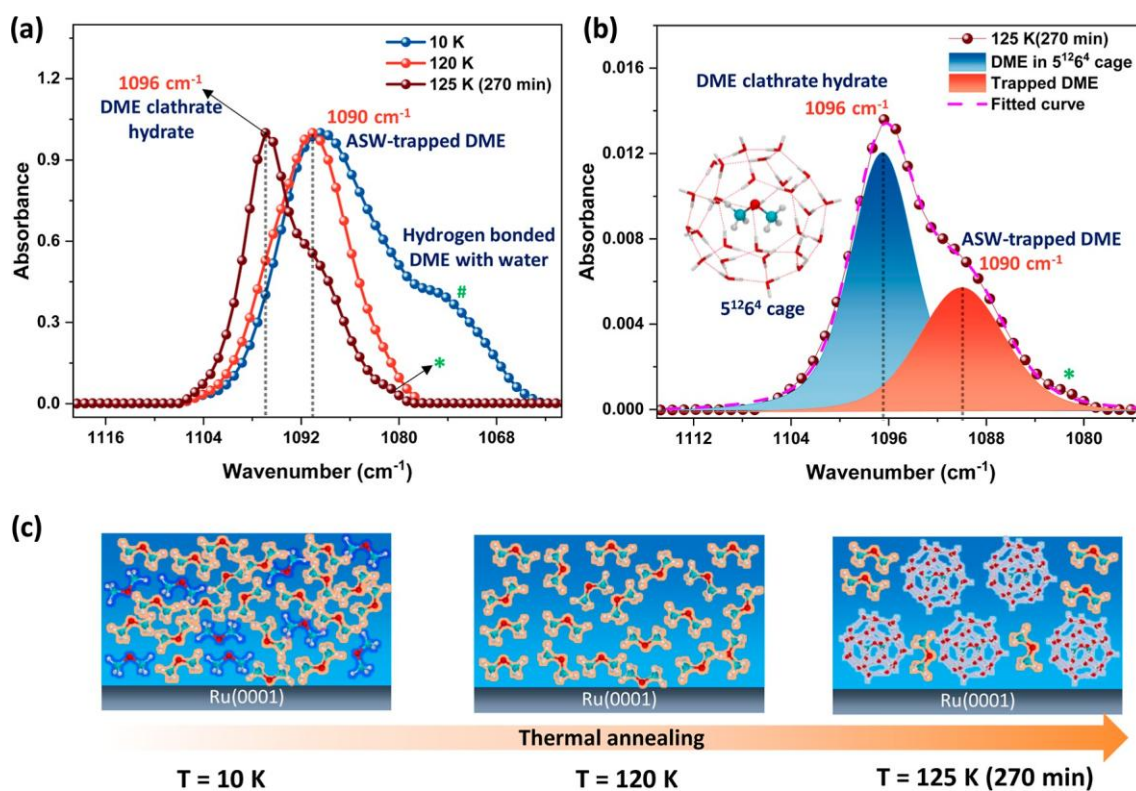


Figure 1. RAIRS study of DME CH. (a) Normalized temperature-dependent RAIR spectra of 300 ML of a DME–H₂O (1:5) ice mixture in the C–O antisymmetric stretching region of DME. (b) IR spectrum after 270 min at 125 K is deconvoluted into two components, shown in blue (peak centered at 1096 cm⁻¹) and red (peak centered at 1090 cm⁻¹) shades. The DFT-optimized structure of DME inside the 5¹²⁶⁴ cage is shown in the inset. The peak labeled as * in the spectrum at 125 K and 270 min is attributed to a very tiny amount of dilutes. The ice mixture was codeposited on the Ru(0001) surface at 10 K and annealed to 125 K with a ramping rate of 2 K min⁻¹. (c) Schematic illustration of DME interaction with water at various temperatures. Blue and orange-colored DME molecules represent the strong and weak hydrogen bonding nature of water molecules, respectively, and engaged DME inside 5¹²⁶⁴ cages is also shown.

cosmos.^{25,27–29} DME is a precursor molecule for forming many organic compounds such as methyl formate, methanol, formaldehyde, methane, and ozone, including those necessary for life.²⁵ On earth, DME has become a clean-burning alternative fuel and aerosol propellant, contributing to sustainable energy solutions.³⁰ Thus, DME plays a dual role as both an eco-friendly fuel source on our planet and a crucial molecule in unraveling the mysteries of the ISM.

DME CH is well-studied in high-pressure systems by nuclear magnetic resonance, X-ray diffraction, and Raman spectroscopy.^{31–33} Buch et al.³⁴ showed the formation of sII DME CH by depositing DME vapor on ice nanocrystals. However, no reports of DME CH under UHV and cryogenic conditions exist. In this study, we investigated the formation of sII DME CH using reflection absorption infrared spectroscopy (RAIRS) and temperature-programmed desorption mass spectrometry (TPD-MS). Further, we elucidated the cage selectivity phenomenon by employing quantum chemical calculations. Through controlled thermal annealing, we induced the transformation of an amorphous DME–water ice mixture into the distinct 5¹²⁶⁴ cage structure of sII CH. Furthermore, we observed that the dissociation of DME CH leads to the formation of stable hexagonal ice (I_h), requiring a substantial activation energy of 68.04 kJ mol⁻¹. This is the first detailed study investigating the formation and evolution of DME CH under simulated ISM conditions.

EXPERIMENTAL SECTION

All experiments were conducted inside a UHV chamber, maintaining a base pressure of $\sim 5 \times 10^{-10}$ mbar. The apparatus is described in detail elsewhere.³⁵ Briefly, this vacuum chamber is equipped with several analytical techniques, including RAIRS, TPD-MS, secondary ion mass spectrometry, low energy ion scattering mass spectrometry, and a VUV lamp. The base pressure of the vacuum chamber is maintained by several turbomolecular pumps, further backed by several oil-free diaphragm pumps. A single crystal Ru(0001) surface 1.5 cm in diameter and 1 mm in thickness was used for our experiments to grow thin ice films. This substrate was securely mounted on a copper holder and positioned at the tip of a closed-cycle helium cryostat. The substrate is also equipped with a 25 Ω resistive heater, allowing precise temperature control in the range of 8 to 1000 K. Temperature measurement was achieved using a K-type thermocouple and a platinum sensor, providing a temperature accuracy of 0.5 K. Before each experiment, Ru(0001) was heated to 400 K repeatedly to ensure cleanliness. It is worth noting that the surface has no effect in this study due to multilayer deposition. Millipore water (H₂O of 18.2 M Ω resistivity) was taken in a vacuum-sealed test tube (with a glass-to-metal seal) and was further purified by several freeze–pump–thaw cycles. DME (99.9%, Sigma-Aldrich) was used without further purification. DME and water were connected to the UHV chamber through separate sample inlet lines. Precise control over the deposition of these two samples was achieved by utilizing all-metal leak

valves. For quantification purposes, we considered that 1.33×10^{-6} mbar exposure for a second equated to 1 monolayer (ML), which in turn was estimated to contain approximately 1.1×10^{15} molecules cm^{-2} , assuming a sticking coefficient of unity.³⁶ To deposit 300 ML of ice consisting of a 1:1 ratio of DME and water mixture, the chamber was backfilled to a total pressure of 5×10^{-7} mbar for 10 min, with DME reaching 2.5×10^{-7} mbar and water pressure also maintained at 2.5×10^{-7} mbar. Different ratios of DME and $\text{H}_2\text{O}/\text{D}_2\text{O}$ (1:5, 1:10, and 1:20) were prepared at 10 K by keeping the total pressure constant and varying the inlet pressure of DME and water accordingly. Throughout the vapor deposition process, mass spectra were continuously recorded to verify both the purity and the ratio of the deposited molecules.

The formation of DME CH was investigated by using both RAIR spectroscopy and TPD mass spectrometry. RAIR spectra were obtained in the $4000\text{--}550$ cm^{-1} range with a spectral resolution of 2 cm^{-1} utilizing a Bruker Vertex 70 FT-IR spectrometer equipped with a liquid nitrogen-cooled mercury cadmium telluride detector. The IR beam path outside the UHV chamber was continuously purged with dry nitrogen to avoid absorption by atmospheric gases. For the TPD-MS experiments, we employed a quadrupole mass spectrometer supplied by Extrel.

COMPUTATIONAL DETAILS

All of the electronic structure calculations were conducted using the Gaussian 09 software package. First, the ground-state geometries of the DME and the CH cages (namely, the 5^{12} , $5^{12}6^2$, and $5^{12}6^4$ cages) were optimized using the density functional theory at the B3LYP/6-311++g(d,p) level of theory.¹⁹ Next, the optimized DME molecule was placed inside the optimized CH cages, and the geometries were reoptimized at the same level of theory. Additionally, we conducted frequency calculations to verify that these geometries are at the minimum of the potential energy surface, and these calculations always yielded nonimaginary frequencies, proving the ground-state nature of these geometries.

RESULTS AND DISCUSSION

The DME CH was created by slow annealing the vapor-deposited amorphous DME–water ice mixture from 10 to 125 K. Three hundred monolayers of DME and water (1:5) ice mixture were codeposited on the Ru(0001) substrate at 10 K, then slowly annealed to 125 K with a ramping rate of 2 K min^{-1} and waited there for 270 min. Figure 1a shows the normalized RAIR spectra of DME at 10, 120, and 125 K (after waiting for 270 min) in the C–O antisymmetric stretching region. The RAIR spectrum at 10 K shows a peak at 1090 cm^{-1} and is accompanied by a broad IR band centered around 1075 cm^{-1} , which is 8 and 23 cm^{-1} red-shifted from the pure amorphous DME peak at 10 K, respectively (the RAIR spectra of pure amorphous DME are shown in Figure S1a). The peaks at 1090 and 1075 cm^{-1} can be attributed to the hydrogen bonding (weak and strong) interaction of DME with water molecules.³⁷ The broad shoulder near 1075 cm^{-1} disappeared with a reduction in the peak intensity at 1090 cm^{-1} when the ice mixture was annealed to 120 K (Figure S2), suggesting the weakening of DME–water hydrogen bonding at higher temperatures and fractional desorption of DME from the ice matrix. Understanding the weakening of hydrogen bonding is facilitated by analyzing the temperature-dependent RAIR

spectra of DME–water (1:1) presented in Figure S3a. This analysis reveals a notable reduction in the intensity of the broad peak (#) and a concurrent increase in the intensity at the 1090 cm^{-1} peak. These changes are observed before the desorption temperature of pure DME (90 K), as illustrated in Figure S6. Further annealing the mixture from 120 to 125 K gives rise to a new peak at 1096 cm^{-1} (Figure S2a), attributed to the DME engaged in CH cages.³⁷ Upon isothermal annealing at 125 K, a gradual decrease in the peak intensity of 1090 cm^{-1} was observed for 180 min; afterward, no further changes until 270 min were observed. This decrease represents the desorption of trapped DME from amorphous solid water (ASW) up to a specific point in time; beyond this point, prolonged waiting does not result in further desorption. By deconvoluting the spectrum at 125 K after 270 min (shown in Figure 1b), we found that 25.3% of the total DME was exclusively engaged in the CH structure, while 15.5% of the total DME was observed to be trapped within the ASW matrix. Additionally, in the C–O symmetric stretching region, a new peak was observed at 928 cm^{-1} upon the formation of CH, which was absent at 10 K (shown in Figure S2b). To investigate the influence of the DME–water ratio on the CH formation fraction, we conducted four temperature-dependent RAIR experiments using different mixtures (1:1, 1:5, 1:10, and 1:20) of DME and water. These various ice mixtures were deposited at 10 K and subsequently subjected to direct annealing at 130 K, with the resulting fraction of DME engaged in CH being calculated and presented in Table S1. Remarkably, the highest observed fraction was 16% for the 1:5 ratio, while the lowest was 6.5% for the 1:20 ratio. It is important to note that the temperature, ratio of host and guest molecules, and annealing time influence CH formation in UHV conditions.^{18,19}

The reported crystal structure of DME CH suggests the formation of sII and a tetragonal structure from an aqueous solution of DME at a temperature of -40 °C.³¹ However, under low-temperature conditions, only sII hydrate was obtained upon vapor deposition of DME on ice nanocrystals.³⁴ DME has a molecular size of 4.1 Å,³⁸ whereas the sII small and large cages have an average cavity radius of 3.91 and 4.73 Å, respectively.⁶ This suggests that DME prefers to form large cages rather than small ones. In the current study, we observed 6 and 12 cm^{-1} blue-shifted peaks in C–O antisymmetric and symmetric stretching regions, respectively, after annealing to 125 K. This same shift was also observed when we performed a temperature-dependent RAIR study, taking H_2O –DME and D_2O –DME ice mixtures at a higher temperature (>130 K) (shown in Figures S3 and S4). Also, sequentially deposited DME and a water–ice mixture showed CH formation above 130 K (Figure S5). A new single peak arises in C–O asymmetric and symmetric stretching, suggesting the formation of single types of cages attributed to the sII large cage. Buch et al.³⁴ showed the formation of DME and H_2S CH where H_2S occupied the small cage, most parts of DME occupied the large cage, and other fractions stayed as adsorbed molecules in the system. The resulting RAIR spectrum we obtained after 270 min at 125 K (Figure 1a) matches the infrared spectrum shown by Buch et al. in their study.³⁴ So, the new peak at 1096 cm^{-1} can be attributed to the large cage ($5^{12}6^4$) of sII CH, and the peak at 1090 cm^{-1} indicates the presence of trapped DME within the ASW matrix.

To further strengthen our claim on the formation of a large cage ($5^{12}6^4$) of sII, we conducted quantum chemical

calculations of DME in various CH cages and computed the infrared spectra of such clathrates. Our simulations yielded significant shifts in the vibrational frequencies after the inclusion of guest molecules into the CH cages, elucidating the diverse structural conformations of CH. Figure 2 shows the

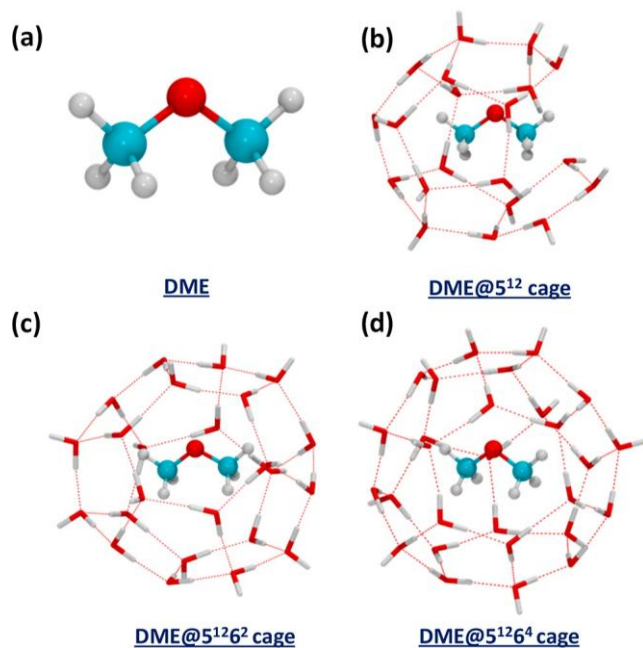


Figure 2. DFT-optimized structures of DME and DME trapped within different CH cages, such as (a) DME, (b) 5^{12} cage, (c) 5^{126^2} cage, and (d) 5^{126^4} cage. Color code used: cyan, C; red, O; and gray, H.

DFT-optimized structures of DME and DME encaged in 5^{12} , 5^{126^2} , and 5^{126^4} cages. It was observed that DME in 5^{126^2} and 5^{126^4} is stable, whereas in the 5^{12} cage, it is unstable, leading to the cage breaking (Figure 2b). The vibrational frequency of

free DME and DME encaged in 5^{126^2} and 5^{126^4} cages in the C–O antisymmetric stretching region is presented in Table S2. It was found that in the case of the 5^{126^2} cage, DME shows a positive shift of 3.05 cm^{-1} , and in the case of the 5^{126^4} , it shows a negative shift of 3.21 cm^{-1} . It is important to note that DME has a molecular size of 4.1 \AA , with the average cavity radius of 5^{126^2} and 5^{126^4} being 4.33 and 4.73 \AA , respectively.⁶ In the case of the 5^{126^2} cage, the larger methyl groups of DME hinder the oxygen atom from approaching the clathrate cage walls,³⁸ resulting in increased steric hindrance and, consequently, a blue shift in frequency. Conversely, the 5^{126^4} cage, with its larger cavity radius, allows for closer proximity between the oxygen atom and the hydrogen atoms of the cage walls, promoting hydrogen bonding and leading to a red shift in the frequency. Experimentally, we observed that pure amorphous DME shows a peak at 1098 cm^{-1} , whereas the DME CH shows a peak at 1096 cm^{-1} , indicating a 2 cm^{-1} redshift. Theoretical calculations reveal that pure DME has a peak at 1090.93 cm^{-1} , whereas DME encaged in the 5^{126^4} cage exhibits a peak at 1187.72 cm^{-1} , corresponding to a 3.2 cm^{-1} redshift. Notably, the experimental shift closely matches the theoretical shift in the 5^{126^4} cage (the large cage of sII). From all of these results, we infer that DME forms the 5^{126^4} cage of sII CH under UHV and cryogenic conditions.

The observation of outgassing patterns within the cometary environment has significantly enhanced our comprehension of various types of ice, such as crystalline ice and CH.¹¹ Here, with the help of TPD-MS, we showed that the DME molecules encaged in the CH cage and a fraction of molecules trapped in the ASW matrix desorb in a molecular volcano (MV) event during the phase transition to crystalline ice.^{39,40} To form DME CH, we vapor-deposited 300 ML of a DME–water (1:5) ice mixture at 10 K, annealed the system to 130 K, and then waited for 2 h to desorb the maximum residual molecules not trapped inside the cages. Subsequently, we cooled the system back to 10 K, annealed the DME CH to 200 K with a ramping rate of 10 K min^{-1} , and collected the mass spectra to measure

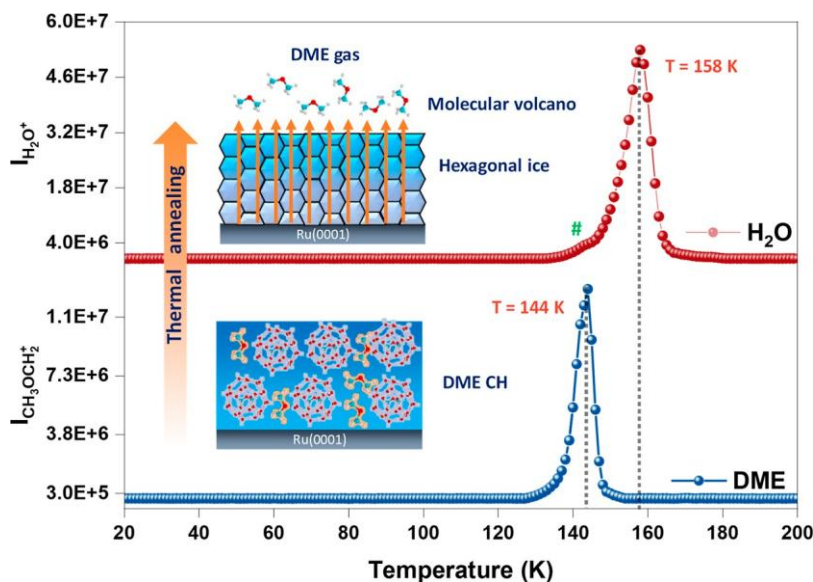


Figure 3. TPD-MS study of DME CH. TPD mass spectra of 300 ML of a DME–H₂O (1:5) ice mixture after hydrate formation. The red spectrum represents the H₂O desorption, and the blue spectrum represents the DME desorption. Mass spectra are plotted between the intensity of H₂O⁺ ($m/z = 18$) and CH₃OCH₂⁺ ($m/z = 45$) with respect to temperature. The peak labeled (#) is attributed to a phase transition from CH to I_h . A schematic illustration of the MV event or transition from DME CH to I_h is shown inside the plot.

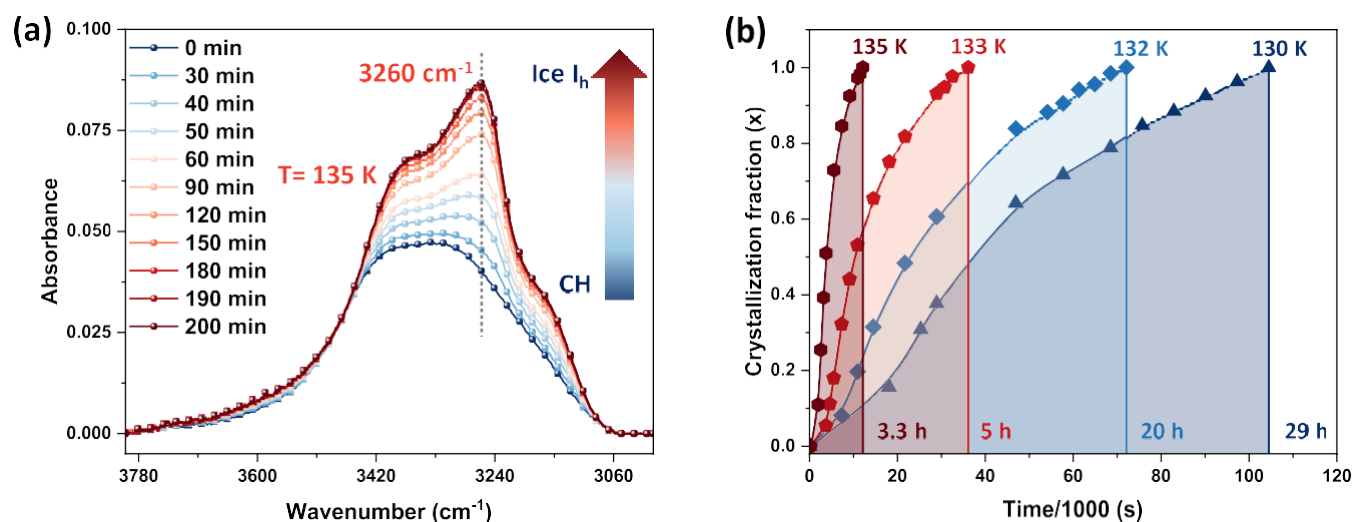


Figure 4. (a) Time-dependent RAIR spectra of 300 ML of the DME–H₂O (1:5) ice mixture at 135 K in the O–H stretching region. The vertical cut at 3260 cm⁻¹ was utilized to determine the crystallization fraction. (b) Crystallization fraction vs time for 300 ML of the DME–H₂O (1:5) mixture at 130, 132, 133, and 135 K. The vertical cut for the crystallization fraction at different temperatures shows the crystallization half-time.

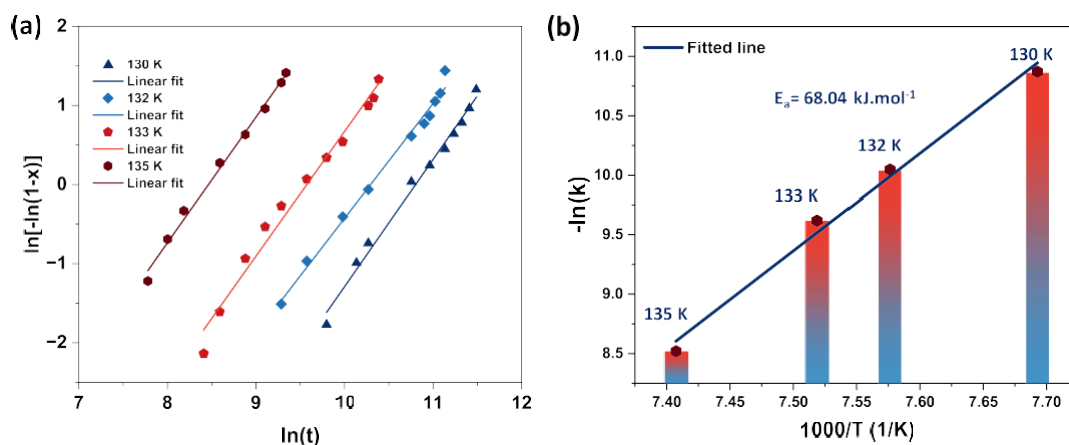


Figure 5. (a) Plot of the linearized form of the Avrami equation for ASW crystallization. Plots of $\ln[-\ln(1-x)]$ versus $\ln(t)$ at different temperatures of 130, 132, 133, and 135 K were evaluated using the O–H stretching bands. The obtained data points were fitted using the Avrami equation. (b) Arrhenius plot of $-\ln(k)$ versus $(1/T)$, achieved from the analysis of the slope and intercept of the linearly fitted lines of the plot (a) for different temperatures. The activation energy (E_a) of ice crystallization was calculated from the slope of the linearly fitted straight line of plot (b).

the intensities at $m/z = 18$ (water) and $m/z = 45$ (DME). In Figure 3, the blue and red spectra represent the mass spectra for DME and water, respectively. The peak at 144 K (in the blue spectrum) is attributed to the MV peak. When the water molecules participating in CH cages turn to I_h along with ASW, all of the cages are broken, resulting in the desorption of molecules at a time showing a sharp MV peak. The phase transition (CH to I_h) peak in the red spectrum is shown by #. The peak at 158 K in the red spectrum represents the sublimation of the water matrix. While pure DME endures in the solid phase up to 93 K (Figure S6), DME in CH form is stable in the solid phase until 144 K in UHV conditions. This suggests the possibility of the presence of DME in the hot core regions of the ISM. A parallel experiment utilizing deuterated water yielded similar results, with the MV peak observed at 147 K for DME and a water desorption peak at 161 K due to the bulkier mass and reduced mobility of deuterated water molecules (shown in Figure S7).

The study of crystallization kinetics, specifically focusing on the transition from CH to I_h, holds significant relevance in

various scientific disciplines, including CH chemistry, physical chemistry, astrochemistry, and planetary science.^{41–44} We conducted isothermal time-dependent RAIRS experiments utilizing a 300 ML DME–water (1:5) film within the temperature range 130–135 K to assess the kinetic parameters of this phase transition. Figure 4a shows the time-dependent data in the O–H stretching region. At 0 min, the spectrum represents the water molecules that participated in the CH phase and the remaining ASW. The 200 min spectrum represents the I_h crystalline feature, comparable to the previous literature.^{45–48} It is well-known that pure amorphous ice converts to I_h at elevated temperatures in UHV.⁴⁷ We have created I_h from pure amorphous water at 140 K and compared it with our results (Figure S8). The crystallization fraction at different temperatures versus time is shown in Figure 4b (calculated from the infrared spectra shown in Figure S9). The absorbance intensity at 3260 cm⁻¹ was used to evaluate the crystallization fraction, $x(t)$ using eq 1.

$$x(t) = \frac{\Delta A(1)}{\Delta A(2)} \quad (1)$$

$\Delta A(1)$ represents the difference between absorbance at a specific time t and one at time 0, and $\Delta A(2)$ is the corresponding value for the difference between the absorbance at time 0 and a completely crystallized film. Thermodynamics of the dissociation of CH and its impact on the crystallization of water ice can be understood from the crystallization fraction. The observed crystallization times indicate a significant difference, with 29 h required at 130 K and only 3.3 h at 135 K. This strongly suggests that higher temperatures facilitate a more rapid dissociation of DME CH, enhancing the crystallization kinetics. To underscore this point further, we conducted a comparative analysis of the crystallization fraction for DME CH and pure water at 130 K, as depicted in Figure S10. Notably, in the case of pure water at 135 K, a considerably extended period of 12 h was necessary for crystallization to occur. This further supports the correlation between the elevated temperature, increased DME CH dissociation, and accelerated crystallization kinetics.

Kinetics parameters and activation energy for the CH to I_h transition were evaluated using the Avrami equation.^{49,50}

$$x(t) = 1 - \exp(-k \cdot t)^n \quad (2)$$

where k is the rate constant, t is the time, and n is a parameter related to the crystallization mechanism.⁵⁰ The variable “ n ” can take values within the range of 1 to 4, and these values are used to predict the nature of the crystallization process.^{51,52} eq 2 can be rearranged in a linear form.

$$\ln(-\ln[1 - x(t)]) = n \ln(t) + n \ln k \quad (3)$$

Figure 5a shows plots of $\ln(-\ln[1 - x(t)])$ versus $\ln(t)$ at different temperatures. The values of n and k at various temperatures were calculated using the slope and intercept of linearly fitted lines and are shown in Table 1. The value

Table 1. Kinetics Parameters Estimated Using the Avrami Equation at Various Temperatures

temperature (K)	130	132	133	135
n	1.60	1.45	1.57	1.58
rate constant (k)	1.9×10^{-5}	4.3×10^{-5}	6.65×10^{-5}	1.9×10^{-4}

obtained for n is found between 1.4 and 1.6, indicating that the nucleation started from CH and amorphous ice interfaces and grew in a polyhedral manner in the side ice matrix.^{21,52,53} The slope of the linearly fitted line of the Arrhenius plot (Figure 5b) was used to determine the activation energy (E_a) of ice crystallization. It was found to be 68.04 kJ mol⁻¹ for the transition from CH to I_h . Our previous studies reported that the activation energy for the desorption-induced ASW to I_h transition is ~52–58 kJ mol⁻¹,^{20,45,46} less than the value from the current study. This suggests that the higher thermodynamic stability of DME CH leads to its slow transformation to I_h .

CONCLUSIONS

Here, we show the formation of sII DME CH in DME–H₂O interstellar ice mimics. A vapor-deposited amorphous DME and water ice mixture was created at 10 K in UHV; its further

annealing to 125 K resulted in a new IR peak at 1096 cm⁻¹, indicating the formation of DME CH. Quantum chemical calculations provided compelling evidence for the creation of the large cage structure (5¹²6⁴) of sII. Additionally, TPD-MS revealed the phenomenon of DME molecules desorbing in a MV event during the transition from CH to crystalline ice. The RAIR study showed that CH resulted in the formation of I_h upon dissociation. The kinetics of crystallization were systematically analyzed using the Avrami equation, revealing a kinetic energy requirement of 68.04 kJ mol⁻¹ for the dissociation and subsequent formation of I_h . These findings provide a comprehensive mechanistic insight into the formation and dissociation of DME CH within interstellar environments, advancing our understanding of complex processes occurring within such celestial settings.

ASSOCIATED CONTENT

Supporting Information

The Supporting Information is available free of charge at <https://pubs.acs.org/doi/10.1021/acs.jpcc.3c07792>.

Temperature- and time-dependent RAIR, TPD-MS spectra of pure DME, and DME–water ice mixtures (PDF)

AUTHOR INFORMATION

Corresponding Author

Thalappil Pradeep – Department of Science and Technology Unit of Nanoscience (DST UNS) and Thematic Unit of Excellence (TUE), Department of Chemistry, Indian Institute of Technology Madras, Chennai 600036, India; Centre of Excellence on Molecular Materials and Functions, Indian Institute of Technology Madras, Chennai 600036, India; International Centre for Clean Water, Chennai 600113, India; orcid.org/0000-0003-3174-534X; Email: pradeep@iitm.ac.in

Authors

Bijesh K. Malla – Department of Science and Technology Unit of Nanoscience (DST UNS) and Thematic Unit of Excellence (TUE), Department of Chemistry, Indian Institute of Technology Madras, Chennai 600036, India
 Gaurav Vishwakarma – Department of Science and Technology Unit of Nanoscience (DST UNS) and Thematic Unit of Excellence (TUE), Department of Chemistry, Indian Institute of Technology Madras, Chennai 600036, India
 Soham Chowdhury – Department of Science and Technology Unit of Nanoscience (DST UNS) and Thematic Unit of Excellence (TUE), Department of Chemistry, Indian Institute of Technology Madras, Chennai 600036, India
 Samir Kumar Nayak – Department of Chemistry, Indian Institute of Technology Madras, Chennai 600036, India
 Sharma S. R. K. C. Yamijala – Department of Chemistry, Centre for Atomistic Modelling and Materials Design, Centre for Quantum Information, Communication, and Computing, and Centre of Excellence on Molecular Materials and Functions, Indian Institute of Technology Madras, Chennai 600036, India; orcid.org/0000-0003-1773-9226

Complete contact information is available at: <https://pubs.acs.org/doi/10.1021/acs.jpcc.3c07792>

Author Contributions

B.K.M. and T.P. designed the experiments, B.K.M., G.V., and S.C. performed the experiments and analyzed the results. T.P. proposed the project and supervised the progress. S.K.N. and S.S.R.K.C.Y. performed the quantum chemical calculations. The manuscript was written with the contributions of all authors.

Notes

The authors declare no competing financial interest.

ACKNOWLEDGMENTS

We acknowledge the Science and Engineering Research Board (SERB), Department of Science and Technology (DST), and the Government of India for their research funding. T.P. acknowledges funding from the Centre of Excellence on Molecular Materials and Functions under the Institution of Eminence scheme of IIT Madras. S.S.R.K.C.Y. acknowledges the financial support of IIT Madras through its new faculty support grants NFSG (IP2021/0972CY/NFSC008973), NFIG (RF2021/0577CY/NFIG 008973), and DST-SERB (SRG/2021/001455). B.K.M. thanks the Council of Scientific and Industrial Research (CSIR) for his research fellowship. G.V. and S.C. thank IITM for their research fellowship. S.K.N. thanks the Prime Minister's Research Fellowship (PMRF) for his research fellowship.

REFERENCES

- (1) Davy, H. VIII. On a Combination of Oxymuriatic Gas and Oxygene Gas. *Philos. Trans. R. Soc. London* 1811, 101, 155–162.
- (2) Sloan, E. D. Fundamental Principles and Applications of Natural Gas Hydrates. *Nature* 2003, 426, 353–359.
- (3) Devlin, J. P. Structure, Spectra, and Mobility of Low-pressure Ices: Ice I, Amorphous Solid Water, and Clathrate Hydrates at T < 150 K. *J. Geophys. Res.: Planets* 2001, 106 (E12), 33333–33349.
- (4) Ratcliffe, C. I. The Development of Clathrate Hydrate Science. *Energy Fuels* 2022, 36 (18), 10412–10429.
- (5) Truong-Lam, H. S.; Seo, S.; Kim, S.; Seo, Y.; Lee, J. D.; Lee, J. D. In Situ Raman Study of the Formation and Dissociation Kinetics of Methane and Methane/Propane Hydrates. *Energy Fuels* 2020, 34 (5), 6288–6297.
- (6) Sloan, E. D.; Koh, C. A.; Koh, C. A. *Clathrate Hydrates of Natural Gases*; CRC Press, 2007.
- (7) Khurana, M.; Yin, Z.; Linga, P. A Review of Clathrate Hydrate Nucleation. *ACS Sustain. Chem. Eng.* 2017, 5 (12), 11176–11203.
- (8) Ghosh, J.; Vishwakarma, G.; Kumar, R.; Pradeep, T. Formation and Transformation of Clathrate Hydrates under Interstellar Conditions. *Acc. Chem. Res.* 2023, 56, 2241–2252.
- (9) Vishwakarma, G.; Malla, B. K.; Reddy, K. S. S. V. P.; Ghosh, J.; Chowdhury, S.; Yamijala, S. S. R. K. C.; Reddy, S. K.; Kumar, R.; Pradeep, T. Induced Migration of CO₂ from Hydrate Cages to Amorphous Solid Water under Ultrahigh Vacuum and Cryogenic Conditions. *J. Phys. Chem. Lett.* 2023, 14, 2823–2829.
- (10) Hester, K. C.; Brewer, P. G. Clathrate Hydrates in Nature. *Ann. Rev. Mar. Sci.* 2009, 1, 303–327.
- (11) Luspay-Kuti, A.; Mousis, O.; Hässig, M.; Fuselier, S. A.; Lunine, J. I.; Marty, B.; Mandt, K. E.; Wurz, P.; Rubin, M. The Presence of Clathrates in Comet 67P/Churyumov-Gerasimenko. *Sci. Adv.* 2016, 2 (4), No. e1501781.
- (12) Mousis, O.; Schmitt, B. Sequestration of Ethane in the Cryovolcanic Subsurface of Titan. *Astrophys. J.* 2008, 677 (1), L67–L70.
- (13) Yin, Z.; Zheng, J.; Kim, H.; Seo, Y.; Linga, P. Hydrates for Cold Energy Storage and Transport: A Review. *Adv. Appl. Energy* 2021, 2, 100022.
- (14) Devlin, J. P. Structure, Spectra, and Mobility of Low-pressure Ices: Ice I, Amorphous Solid Water, and Clathrate Hydrates at T < 150 K. *J. Geophys. Res.: Planets* 2001, 106 (E12), 33333–33349.
- (15) Thomas, C.; Mousis, O.; Picaud, S.; Ballenegger, V. Variability of the Methane Trapping in Martian Subsurface Clathrate Hydrates. *Planet. Space Sci.* 2009, 57 (1), 42–47.
- (16) Blake, D.; Allamandola, L.; Sandford, S.; Hudgins, D.; Freund, F. Clathrate Hydrate Formation in Amorphous Cometary Ice Analogs in Vacuo. *Science* 1991, 254 (5031), 548–551.
- (17) Fleyfel, F.; Devlin, J. P. FT-IR Spectra of 90 K Films of Simple, Mixed, and Double Clathrate Hydrates of Trimethylene Oxide, Methyl Chloride, Carbon Dioxide, Tetrahydrofuran, and Ethylene Oxide Containing Decoupled Water-D₂. *J. Phys. Chem.* 1988, 92 (3), 631–635.
- (18) Ghosh, J.; Methikkalam, R. R. J.; Bhuin, R. G.; Ragupathy, G.; Choudhary, N.; Kumar, R.; Pradeep, T. Clathrate Hydrates in Interstellar Environment. *Proc. Natl. Acad. Sci. U.S.A.* 2019, 116 (5), 1526–1531.
- (19) Malla, B. K.; Vishwakarma, G.; Chowdhury, S.; Selvarajan, P.; Pradeep, T. Formation of Ethane Clathrate Hydrate in Ultrahigh Vacuum by Thermal Annealing. *J. Phys. Chem. C* 2022, 126 (42), 17983–17989.
- (20) Ghosh, J.; Vishwakarma, G.; Das, S.; Pradeep, T. Facile Crystallization of Ice Ih via Formaldehyde Hydrate in Ultrahigh Vacuum under Cryogenic Conditions. *J. Phys. Chem. C* 2021, 125 (8), 4532–4539.
- (21) Vishwakarma, G.; Malla, B. K.; Chowdhury, S.; Khandare, S. P.; Pradeep, T. Existence of Acetaldehyde Clathrate Hydrate and Its Dissociation Leading to Cubic Ice under Ultrahigh Vacuum and Cryogenic Conditions. *J. Phys. Chem. Lett.* 2023, 14, 5328–5334.
- (22) Ghosh, J.; Bhuin, R. G.; Vishwakarma, G.; Pradeep, T. Formation of Cubic Ice via Clathrate Hydrate, Prepared in Ultrahigh Vacuum under Cryogenic Conditions. *J. Phys. Chem. Lett.* 2020, 11 (1), 26–32.
- (23) Semelsberger, T. A.; Borup, R. L.; Greene, H. L. Dimethyl Ether (DME) as an Alternative Fuel. *J. Power Sources* 2006, 156 (2), 497–511.
- (24) Terwisscha Van Scheltinga, J.; Ligterink, N. F. W.; Boogert, A. C. A.; Van Dishoeck, E. F.; Linnartz, H. Infrared Spectra of Complex Organic Molecules in Astronomically Relevant Ice Matrices - I. Acetaldehyde, Ethanol, and Dimethyl Ether. *Astron. Astrophys.* 2018, 611, A35.
- (25) Peeters, Z.; Rodgers, S. D.; Charnley, S. B.; Schriver-Mazzuoli, L.; Schriver, A.; Keane, J. V.; Ehrenfreund, P. Astrochemistry of dimethyl ether. *Astron. Astrophys.* 2006, 445, 197–204.
- (26) Snyder, L. E.; Buhl, D.; Schwartz, P. R.; Clark, F. O.; Johnson, D. R.; Lovas, F. J.; Giguere, P. T. Radio Detection of Interstellar Dimethyl Ether. *Astrophys. J.* 1974, 191, L79.
- (27) Modica, P.; Palumbo, M. E. Formation of Methyl Formate after Cosmic Ion Irradiation of Icy Grain Mantles. *Astron. Astrophys.* 2010, 519 (2), A22.
- (28) Cernuto, A.; Tosi, P.; Martini, L. M.; Pirani, F.; Ascenzi, D. Experimental Investigation of the Reaction of Helium Ions with Dimethyl Ether: Stereodynamics of the Dissociative Charge Exchange Process. *Phys. Chem. Chem. Phys.* 2017, 19 (30), 19554–19565.
- (29) Skouteris, D.; Balucani, N.; Ceccarelli, C.; Faginas Lago, N.; Codella, C.; Falcinelli, S.; Rosi, M. Interstellar Dimethyl Ether Gas-Phase Formation: A Quantum Chemistry and Kinetics Study. *Mon. Not. R. Astron. Soc.* 2019, 482 (3), 3567–3575.
- (30) Matzen, M.; Demirel, Y. Methanol and Dimethyl Ether from Renewable Hydrogen and Carbon Dioxide: Alternative Fuels Production and Life-Cycle Assessment. *J. Clean. Prod.* 2016, 139, 1068–1077.
- (31) Gough, S. R.; Garg, S. K.; Ripmeester, J. A.; Davidson, D. W. Dielectric Relaxation and Nuclear Magnetic Resonance Studies of Two Clathrate Hydrates of Dimethyl Ether. *J. Phys. Chem.* 1977, 81 (23), 2158–2163.

- (32) Huang, P.; Liu, X.; Wada, Y.; Katoh, K.; Arai, M.; Tamura, M. Decomposition and Raman Spectrum of Dimethyl Ether Hydrate. *Fuel* 2013, *105*, 364–367.
- (33) Udachin, K. A.; Ratcliffe, C. I.; Ripmeester, J. A. A Dense and Efficient Clathrate Hydrate Structure with Unusual Cages. *Angew. Chem., Int. Ed.* 2001, *40* (7), 1303–1305.
- (34) Buch, V.; Devlin, J. P.; Monreal, I. A.; Jagoda-Cwiklik, B.; Uras-Aytemiz, N.; Cwiklik, L. Clathrate Hydrates with Hydrogen-Bonding Guests. *Phys. Chem. Chem. Phys.* 2009, *11* (44), 10245–10265.
- (35) Bag, S.; Bhuin, R. G.; Methikkalam, R. R. J.; Pradeep, T.; Kephart, L.; Walker, J.; Kuchta, K.; Martin, D.; Wei, J. Development of Ultralow Energy (1–10 eV) Ion Scattering Spectrometry Coupled with Reflection Absorption Infrared Spectroscopy and Temperature Programmed Desorption for the Investigation of Molecular Solids. *Rev. Sci. Instrum.* 2014, *85* (1), 014103.
- (36) Moon, E. S.; Kang, H.; Oba, Y.; Watanabe, N.; Kouchi, A. Direct Evidence for Ammonium Ion Formation in Ice through Ultraviolet-Induced Acid-Base Reaction of NH_3 With H_3O^+ . *Astrophys. J.* 2010, *713* (2), 906–911.
- (37) Schriver-Mazzuoli, L.; Coanga, J. M.; Schriver, A.; Ehrenfreund, P. Infrared Spectra of $(\text{CH}_3)_2\text{O}$ and $(\text{CH}_3)_2\text{O} + \text{H}_2\text{O}$ at Low Temperature. *Vib. Spectrosc.* 2002, *30* (2), 245–257.
- (38) Kulig, W.; Kubisiak, P.; Cwiklik, L. Steric and Electronic Effects in the Host-Guest Hydrogen Bonding in Clathrate Hydrates. *J. Phys. Chem. A* 2011, *115* (23), 6149–6154.
- (39) May, R. A.; Smith, R. S.; Kay, B. D. The Release of Trapped Gases from Amorphous Solid Water Films. I. “Top-down” Crystallization-Induced Crack Propagation Probed Using the Molecular Volcano. *J. Chem. Phys.* 2013, *138*, 104501.
- (40) Collings, M. P.; Anderson, M. A.; Chen, R.; Dever, J. W.; Viti, S.; Williams, D. A.; McCoustra, M. R. S. A Laboratory Survey of the Thermal Desorption of Astrophysically Relevant Molecules. *Mon. Not. R. Astron. Soc.* 2004, *354*, 1133–1140.
- (41) Cao, H. S. Formation and Crystallization of Low-Density Amorphous Ice. *J. Phys. D Appl. Phys.* 2021, *54* (20), 203002.
- (42) Takeya, S.; Fujihisa, H.; Alavi, S.; Ohmura, R. Thermally Induced Phase Transition of Cubic Structure II Hydrate: Crystal Structures of Tetrahydropyran- CO_2 Binary Hydrate. *J. Phys. Chem. Lett.* 2023, *14* (7), 1885–1891.
- (43) Minissale, M.; Aikawa, Y.; Bergin, E.; Bertin, M.; Brown, W. A.; Cazaux, S.; Charnley, S. B.; Coutens, A.; Cuppen, H. M.; Guzman, V.; et al. Thermal Desorption of Interstellar Ices: A Review on the Controlling Parameters and Their Implications from Snowlines to Chemical Complexity. *ACS Earth Space Chem.* 2022, *6* (3), 597–630.
- (44) Bartels-Rausch, T.; Bergeron, V.; Cartwright, J. H. E.; Escribano, R.; Finney, J. L.; Grothe, H.; Gutiérrez, P. J.; Haapala, J.; Kuhs, W. F.; Pettersson, J. B. C.; et al. Ice Structures, Patterns, and Processes: A View across the Icefields. *Rev. Mod. Phys.* 2012, *84* (2), 885–944.
- (45) Vishwakarma, G.; Malla, B. K.; Methikkalam, R. R. J.; Pradeep, T. Rapid Crystallization of Amorphous Solid Water by Porosity Induction. *Phys. Chem. Chem. Phys.* 2022, *24* (42), 26200–26210.
- (46) Vishwakarma, G.; Ghosh, J.; Pradeep, T. Desorption-Induced Evolution of Cubic and Hexagonal Ices in an Ultrahigh Vacuum and Cryogenic Temperatures. *Phys. Chem. Chem. Phys.* 2021, *23* (41), 24052–24060.
- (47) Watanabe, N.; Kouchi, A. Ice Surface Reactions: A Key to Chemical Evolution in Space. *Prog. Surf. Sci.* 2008, *83* (10–12), 439–489.
- (48) Ghosh, J.; Vishwakarma, G.; Das, S.; Pradeep, T. Facile Crystallization of Ice I_h via Formaldehyde Hydrate in Ultrahigh Vacuum under Cryogenic Conditions. *J. Phys. Chem. C* 2021, *125* (8), 4532–4539.
- (49) Avrami, M. Kinetics of Phase Change. II Transformation-Time Relations for Random Distribution of Nuclei. *J. Chem. Phys.* 1940, *8*, 212–224.
- (50) Harada, K.; Sugimoto, T.; Kato, F.; Watanabe, K.; Matsumoto, Y. Thickness Dependent Homogeneous Crystallization of Ultrathin Amorphous Solid Water Films. *Phys. Chem. Chem. Phys.* 2020, *22* (4), 1963–1973.
- (51) Hage, W.; Hallbrucker, A.; Mayer, E.; Johari, G. P. Crystallization Kinetics of Water below 150 K. *J. Chem. Phys.* 1994, *100* (4), 2743–2747.
- (52) Lee, D. H.; Kang, H. Acid-Promoted Crystallization of Amorphous Solid Water. *J. Phys. Chem. C* 2018, *122* (42), 24164–24170.
- (53) Avrami, M. Kinetics of Phase Change. II Transformation-Time Relations for Random Distribution of Nuclei. *J. Chem. Phys.* 1940, *8* (2), 212–224.

Formation and Dissociation of Dimethyl Ether Clathrate Hydrate in Interstellar Ice Mimics

Bijesh K. Malla¹, Gaurav Vishwakarma¹, Soham Chowdhury¹, Samir Kumar Nayak², Sharma S.

R. K. C. Yamijala^{2,3,4,5} and Thalappil Pradeep^{1,5,6}*

¹Department of Science and Technology Unit of Nanoscience (DST UNS) and Thematic Unit of Excellence (TUE), Department of Chemistry, Indian Institute of Technology Madras, Chennai 600036, India.

²Department of Chemistry, Indian Institute of Technology Madras, Chennai, 600036 India,

³Centre for Atomistic Modelling and Materials Design, Indian Institute of Technology Madras, Chennai 600036, India.

⁴Centre for Quantum Information, Communication, and Computing, Indian Institute of Technology Madras, Chennai 600036, India.

⁵Centre for Molecular Materials and Functions, Indian Institute of Technology Madras, Chennai 600036, India,

⁶International Centre for Clean Water, IITM Research Park, Chennai 600113, India.

This PDF file includes:

Figure S1 to S10 (pages S2-S10)

Table S1, S2 (pages S3, S5)

Supporting information 1:

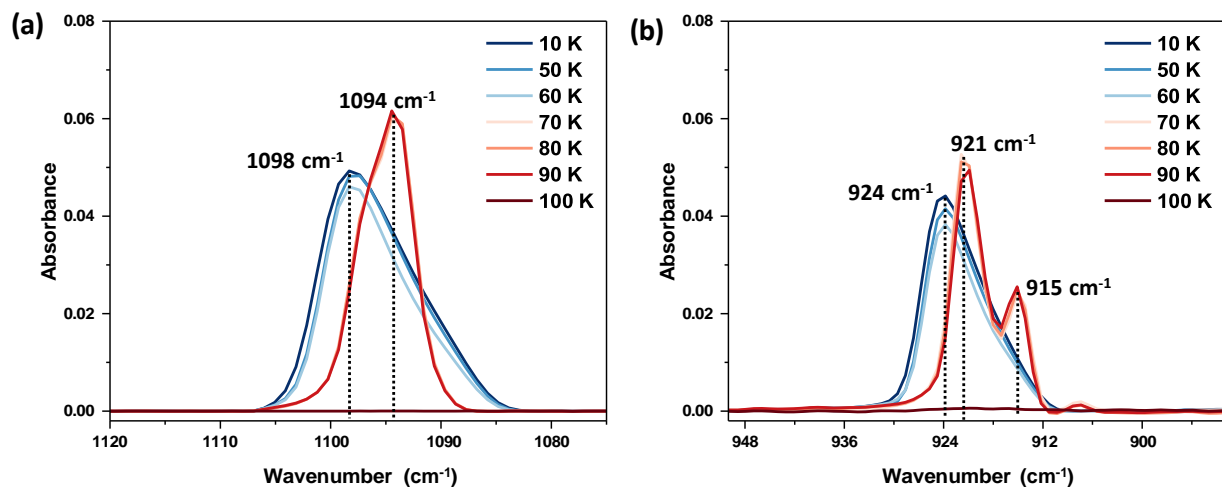


Figure S1. Temperature-dependent RAIR spectra of pure 150 ML DME in (a) C-O antisymmetric stretching region and (b) C-O symmetric stretching region. Pure DME vapor was deposited on Ru(0001) substrate at 10 K and annealed to 100 K with an annealing rate of 2 K min⁻¹. Vapor-deposited DME resulted in amorphous form at 10 K and crystallized above 70 K.

Supporting information 2:

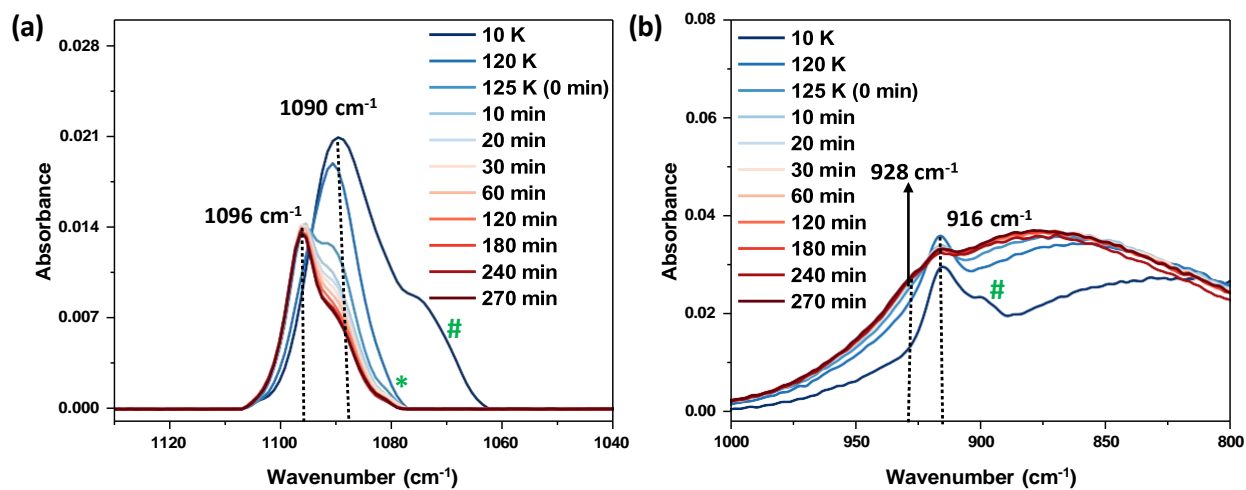


Figure S2. Temperature and time-dependent RAIR spectra of 300 ML of DME-H₂O (1:5) ice mixture in (a) C-O antisymmetric stretching region and (b) C-O symmetric stretching region. DME and water vapor were co-deposited on Ru(0001) substrate at 10 K and annealed to 125 K with an annealing rate of 2 K min⁻¹, then waited there for 270 min.

Supporting information 3:

Table S1. Comparison of the Percentage of DME CH formation from total DME at different ratios of DME-water.

(DME:H₂O) ratio	Percentage of DME CH formation from total DME (%)
1:20	6.5
1:10	8.1
1:5	16
1:1	13

Supporting information 4:

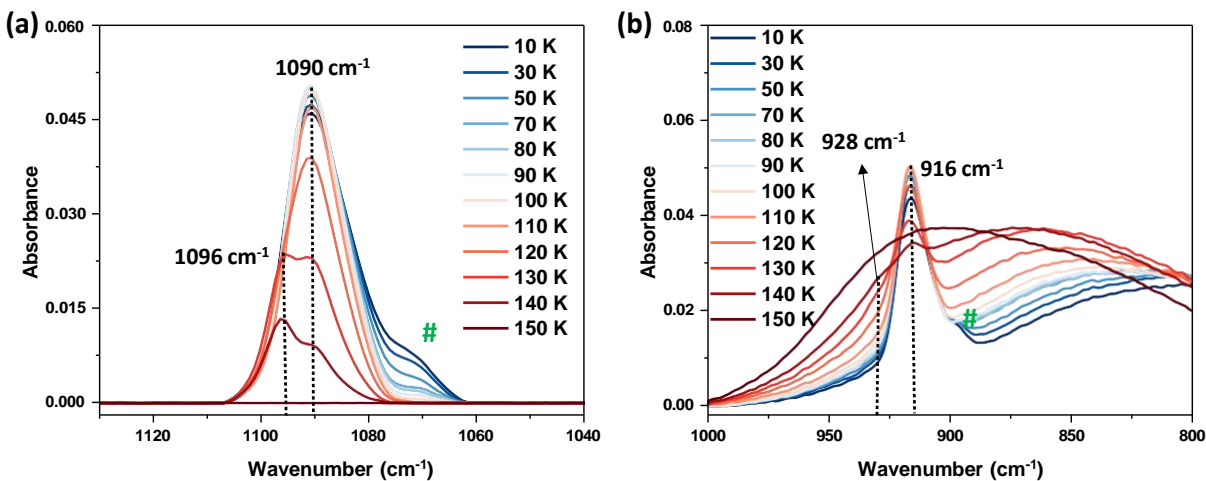


Figure S3. Temperature-dependent RAIR spectra of 300 ML of DME-H₂O (1:1) ice mixture in (a) C-O antisymmetric stretching region and (b) C-O symmetric stretching region. The peak # is attributed to the strong hydrogen bonding interaction of DME and water. DME and water vapor were co-deposited on Ru(0001) substrate at 10 K and annealed to 150 K with an annealing rate of 2 K min⁻¹.

Supporting information 5:

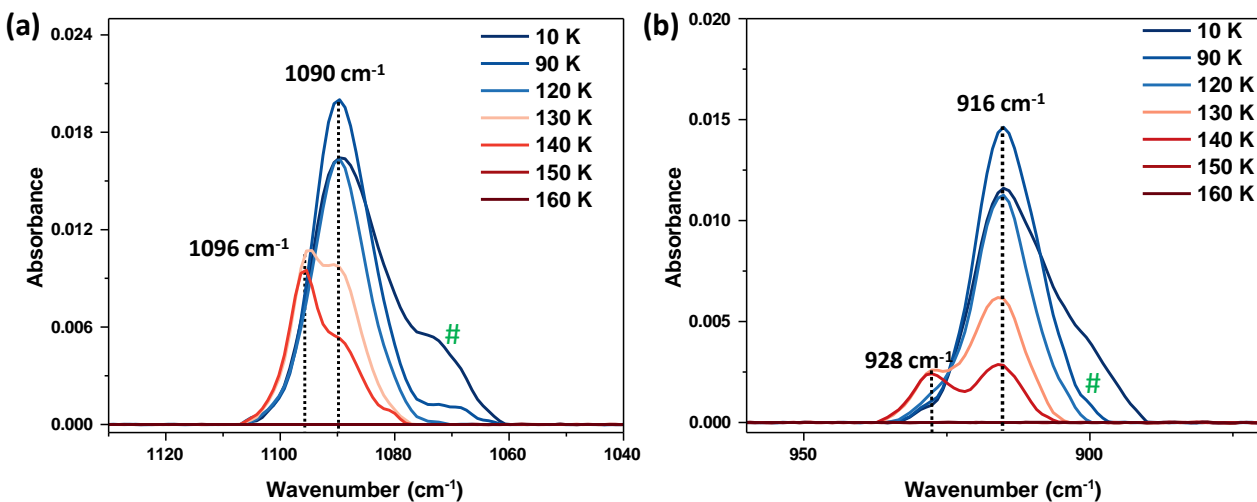


Figure S4. Temperature-dependent RAIR spectra of 300 ML of DME-D₂O (1:1) ice mixture in (a) C-O antisymmetric stretching region and (b) C-O symmetric stretching region. The peak # is attributed to the strong hydrogen bonding interaction of DME and water. DME and water vapor were co-deposited on Ru(0001) substrate at 10 K and annealed to 160 K with an annealing rate of 2 K min⁻¹.

Supporting information 6:

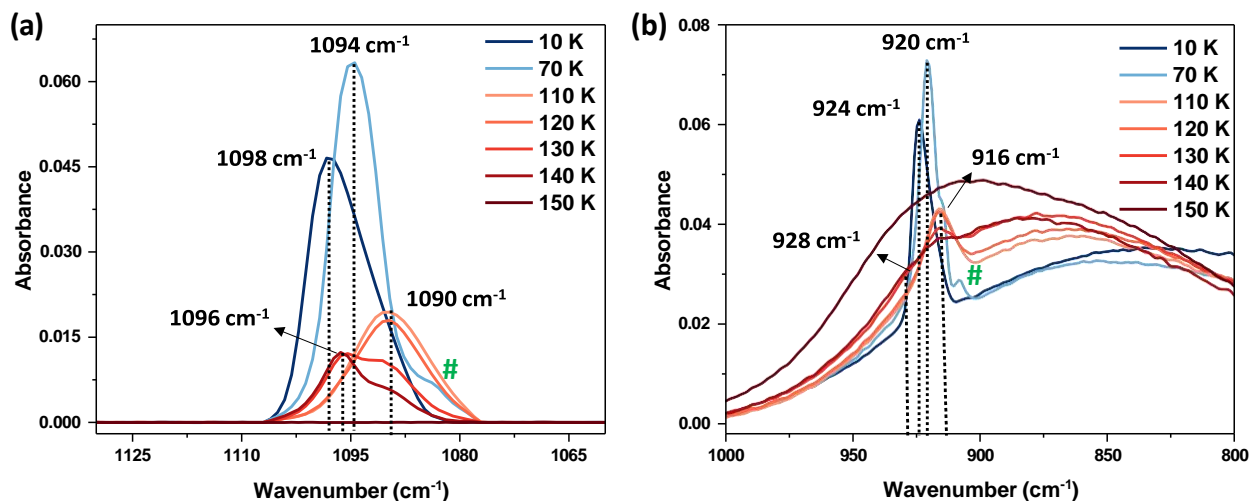


Figure S5. Temperature-dependent RAIR spectra of 300 ML of DME@H₂O (1:1) ice mixture in (a) C-O antisymmetric stretching region and (b) C-O symmetric stretching region. The peak # is attributed to the strong hydrogen bonding interaction of DME and water. DME and water were sequentially deposited on Ru(0001) substrate at 10 K and annealed to 150 K with an annealing rate of 2 K min⁻¹. The sequential deposition was carried out by condensing 150 ML of H₂O ice over the same coverage of DME ice, thus making it a (1:1) mixture.

Supporting information 7:

Table S2. Comparison of the computational and experimental vibrational shifts of DME CH compared to free DME in the C-O antisymmetric region.

System	B3LYP/6-311++g(d,p) Asymmetric stretch		Experimental	
	IR asymmetric stretch (cm ⁻¹)	Shift (cm ⁻¹)	IR asymmetric stretch (cm ⁻¹)	Shift (cm ⁻¹)
DME	1190.93	NA	1098	NA
DME@5 ¹²	NA	NA	NA	NA
DME@5 ¹² 6 ²	1193.98	3.05	NA	NA
DME@5 ¹² 6 ⁴	1187.72	-3.21	1096	-2

Supporting information 8:

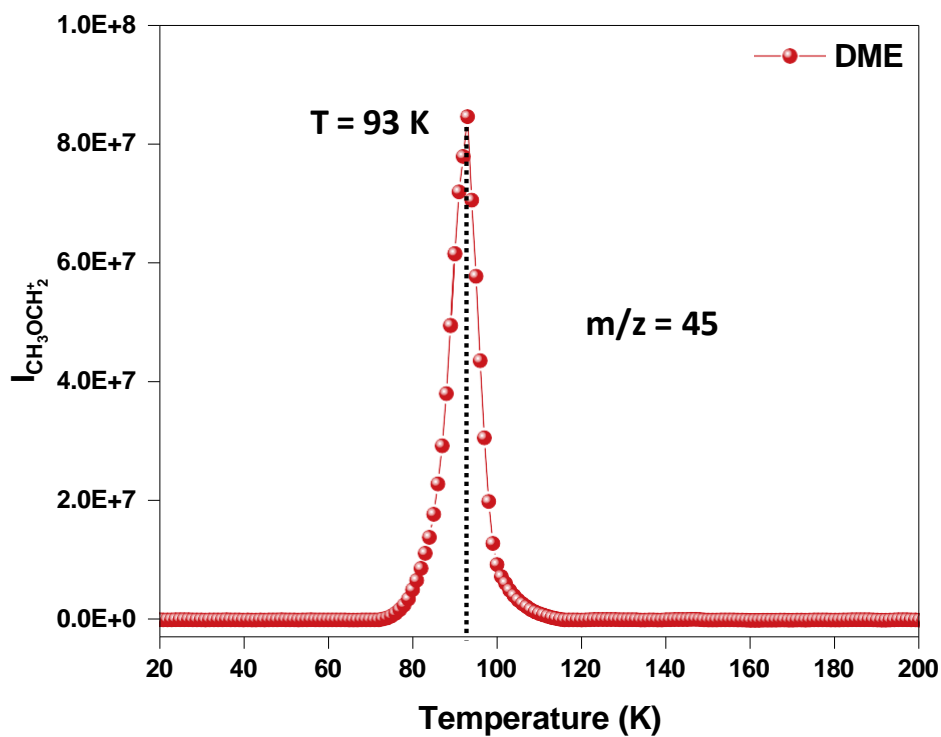


Figure S6. TPD-MS plot of 150 ML of pure DME. The intensity of $\text{CH}_3\text{OCH}_2^+$ ($m/z = 45$) versus the temperature of Ru(0001) substrate is plotted. The peak at 93 K is attributed to the desorption of DME. The pure DME vapor was deposited on Ru(0001) substrate at 10 K and further annealed to 200 K with an annealing rate of 10 K/min.

Supporting information 9:

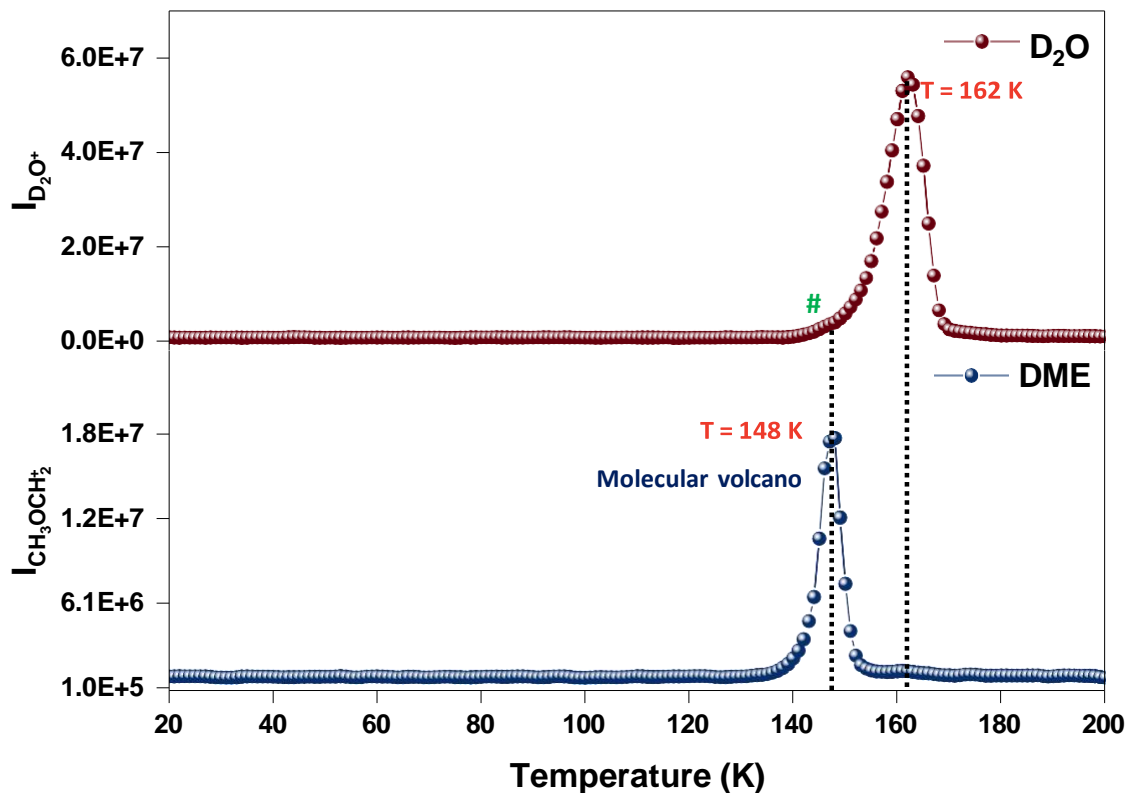


Figure S7. TPD-MS study of deuterated DME clathrate hydrate. TPD mass spectra of 300 ML of DME-D₂O (1:5) ice mixture after hydrate formation. The red spectrum represents the D₂O desorption, and the blue spectrum represents the DME desorption. Mass spectra is plotted for D₂O⁺ (m/z = 18) and CH₃OCH₂⁺ (m/z = 45) with respect to temperature. The peak labeled (#) is attributed to the phase transition from clathrate hydrate to hexagonal ice.

Supporting information 10:

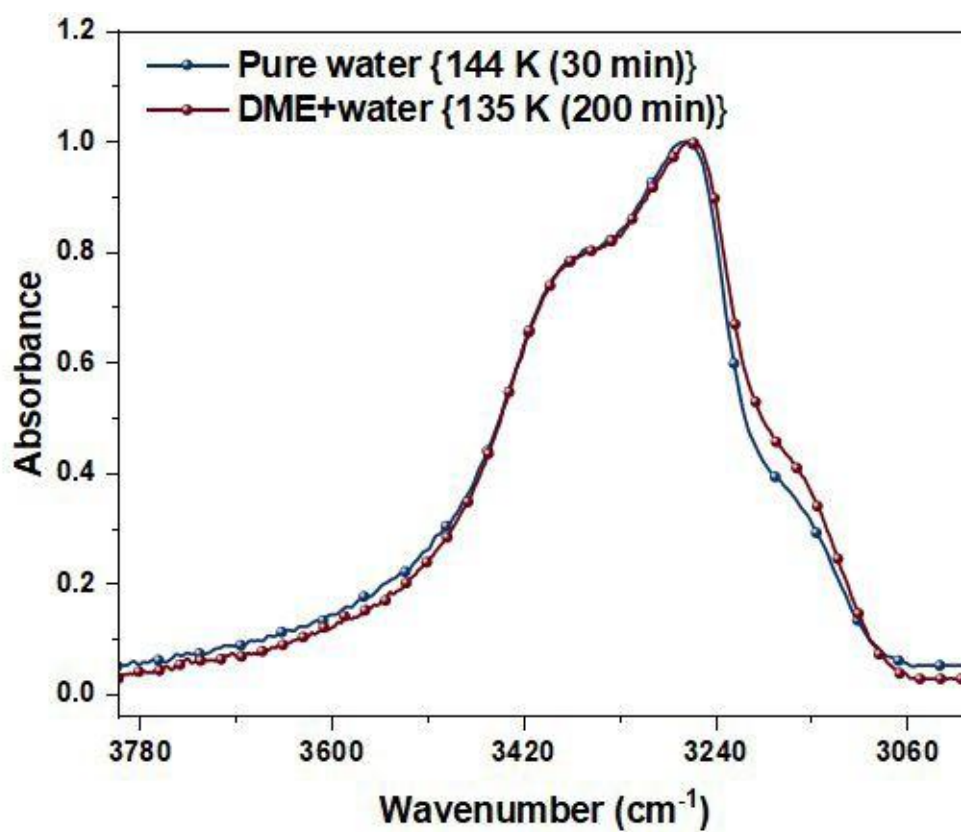


Figure S8. Comparison of the normalized RAIR spectra of hexagonal crystalline ice obtained by thermally annealing pure water at 144 K for 30 min and DME and water ice mixture (1:5) at 135 K for 200 min.

Supporting information 11:

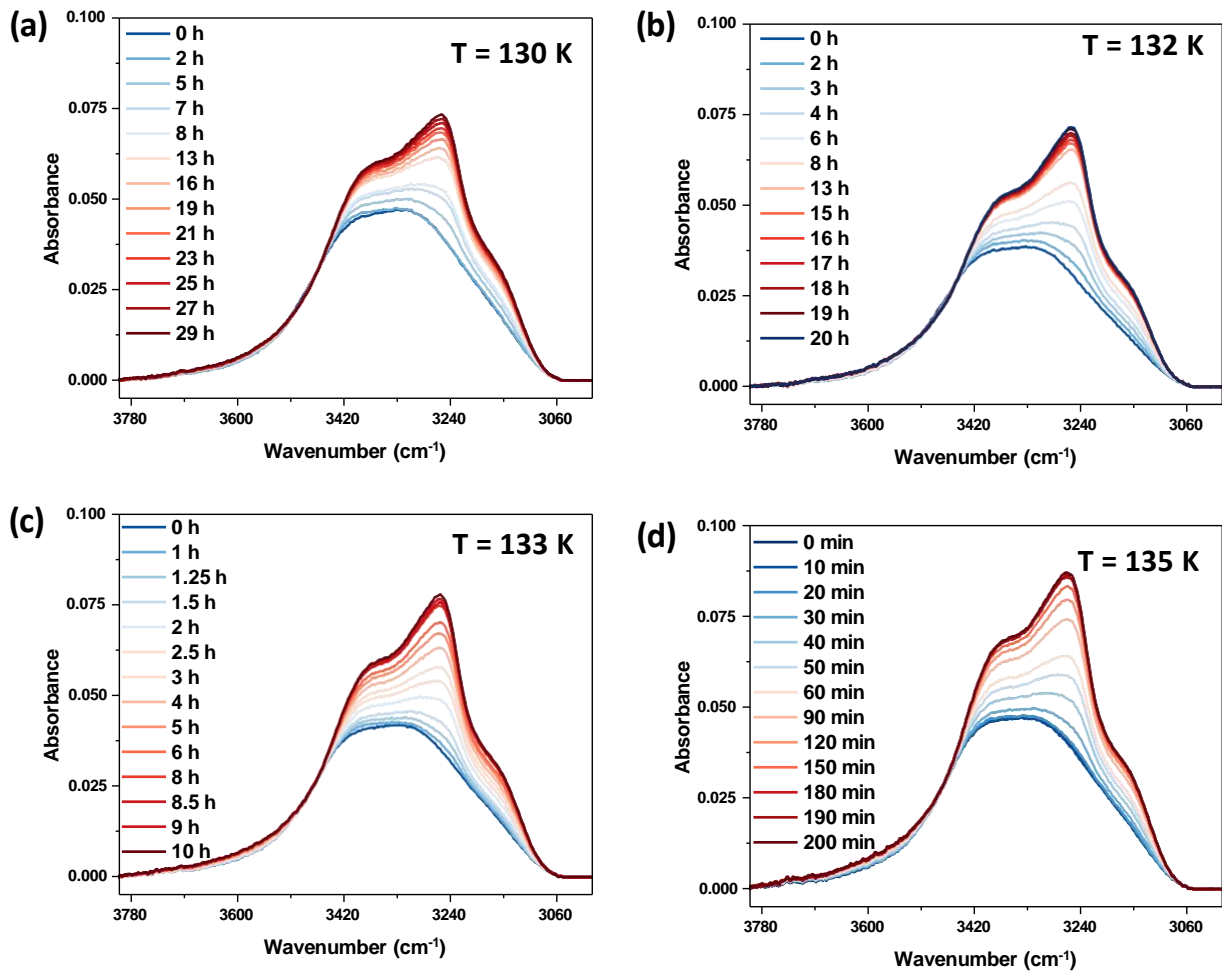


Figure S9. RAIR study of phase transition from amorphous solid water to hexagonal ice through clathrate hydrate dissociation. Isothermal time-dependent RAIR spectra of 300 ML of DME-H₂O (1:5) in the O-H stretching region at (a) 130 K, (b) 132 K, (c) 133 K, and (d) 135 K. DME and water vapor were co-deposited on Ru(0001) substrate at 10 K and annealed at a rate of 2 K min⁻¹ to the set temperatures.

Supporting information 12:

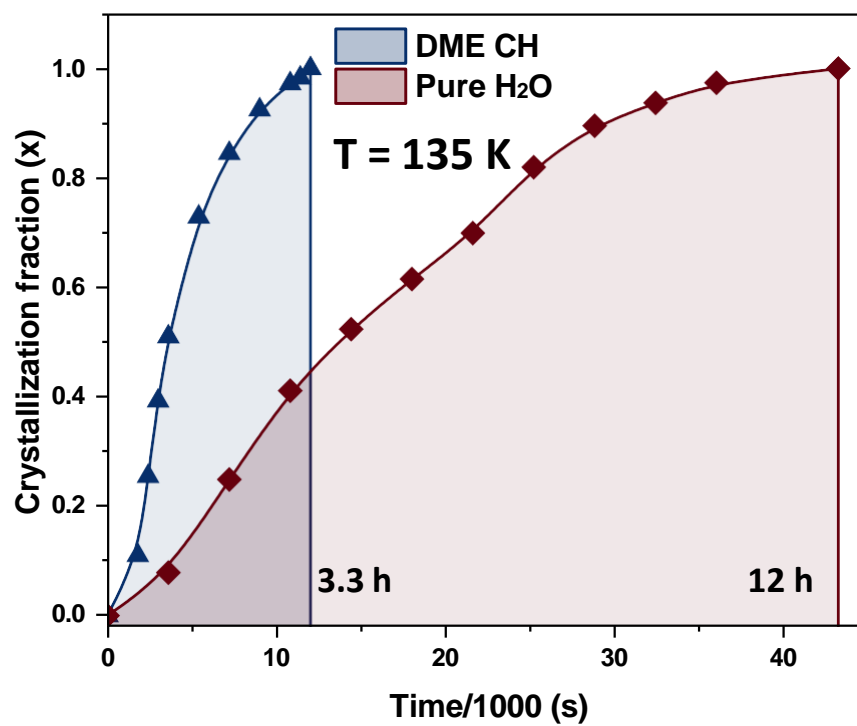


Figure S10. Crystallization fraction vs time for 300 ML of DME-H₂O (1:5) (blue color curve) and 150 ML of pure H₂O ice (brown color curve) at 135 K.

Spontaneous α -C–H Carboxylation of Ketones by Gaseous CO₂ at the Air-water Interface of Aqueous Microdroplets

Pallab Basuri⁺, Sinchan Mukhopadhyay⁺, K. S. S. V. Prasad Reddy, Keerthana Unni, B. K. Spoorthi, Jenifer Shantha Kumar, Sharma S. R. K. C. Yamijala, and Thalappil Pradeep*

Dedicated to Professor C.N.R. Rao on the occasion of his 90th birthday.

Abstract: We present a catalyst-free route for the reduction of carbon dioxide integrated with the formation of a carbon-carbon bond at the air/water interface of negatively charged aqueous microdroplets, at ambient temperature. The reactions proceed through carbanion generation at the α -carbon of a ketone followed by nucleophilic addition to CO₂. Online mass spectrometry reveals that the product is an β -ketoacid. Several factors, such as the concentration of the reagents, pressure of CO₂ gas, and distance traveled by the droplets, control the kinetics of the reaction. Theoretical calculations suggest that water in the microdroplets facilitates this unusual chemistry. Furthermore, such a microdroplet strategy has been extended to seven different ketones. This work demonstrates a green pathway for the reduction of CO₂ to useful carboxylated organic products.

Increasing carbon dioxide emissions in the atmosphere and decreasing forest cover of Earth are some of the biggest concerns of humanity. CO₂ capture and conversion are methods to tackle this problem. Researchers worldwide have come up with several plausible solutions that include capturing CO₂ by advanced materials,^[1] reducing it by electrochemical means,^[2] and converting it to small organic molecules.^[3,4] Among these, a direct chemical reaction

between CO₂ and organic molecules to form fine chemicals is particularly advantageous from an industrial point of view. However, direct nucleophilic addition by a carbanion to the C-center of the chemically inert CO₂ to form a carbon-carbon bond is energetically unfavorable. To overcome this, much attention was given to catalytic processes such as electrochemical^[2,5] and photoelectrochemical^[6,7] reduction of CO₂, photocatalytic artificial photosynthesis,^[8,9] and catalytic reduction.^[10,11] However, most of the processes are complex, energy-consuming, expensive, and environmentally unfriendly in totality. Therefore, we need simple, ecofriendly, and efficient methods to convert CO₂ into value-added products.

Microdroplets are promising platforms for understanding chemical and biological reactions occurring at small volumes, single cells, and at single-molecule levels. They exhibit an extraordinary physicochemical environment in comparison to conventional synthesis in bulk solutions. For example, enormous enhancement in the rate of the reaction,^[12] spontaneous reduction of species,^[13,14] and occurrence of unfavorable reactions,^[15,16,17] are known in microdroplets. Recently, we found that the high acidity of microdroplets protonates carboxylic acids to make them electrophiles to undergo nucleophilic addition-elimination reaction.^[18] Similarly, Huang et al. showed that microdroplets could protonate inert CO₂ (g) at the gas-liquid interface followed by a reaction with aliphatic amines forming a C–N bond.^[19] This reaction shows tremendous acceleration using carbonate and bicarbonate salts.^[26] The Zare group recently found that aqueous microdroplets containing 1,2,3-triazole can efficiently convert CO₂ into formic acid.^[27] They have further demonstrated a reaction between toluene and CO₂ in water microdroplets.^[28] Ge et al. has also demonstrated that the gas-liquid interface of microdroplets significantly accelerates photocatalytic CO₂ reduction reactions.^[29,30]

Here, we utilized the unique environment of microdroplets to achieve CO₂ reduction in-water integrated with C–C bond formation, leading to carboxylation at the α -position of an aliphatic ketone. Online mass spectrometry was performed to characterize the reaction.

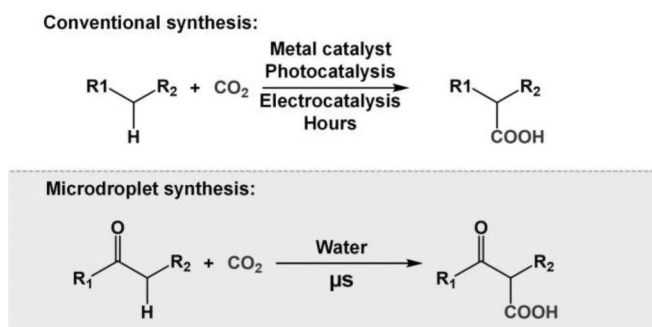
Scheme 1 compares the CO₂ reduction toward C–C coupling performed using the slow conventional bulk synthesis methods^[20–25] with the rapid microdroplet synthesis. Figure 1 shows the results from microdroplet reaction of acetylacetone (AcAc) with CO₂(g). The detailed experimental protocol is presented in Supporting Information 1. The

[*] Dr. P. Basuri, S. Mukhopadhyay, K. Unni, Dr. B. K. Spoorthi, J. Shantha Kumar, Prof. T. Pradeep
 DST Unit of Nanoscience and Thematic Unit of Excellence,
 Department of Chemistry
 Indian Institute of Technology Madras
 600036 Chennai, Tamil Nadu, India
 E-mail: pradeep@iitm.ac.in

Dr. K. S. S. V. P. Reddy
 Department of Chemistry
 Indian Institute of Technology Madras
 600036 Chennai, Tamil Nadu, India

Dr. S. S. R. K. C. Yamijala
 Centre for Atomistic Modelling and Materials Design, Centre for
 Molecular Materials and Functions, Centre for Quantum Informa-
 tion, Communication, and Computing, Department of Chemistry
 Indian Institute of Technology Madras
 600036 Chennai, Tamil Nadu, India

[†] These authors contributed equally to this work



Scheme 1. A comparative study of CO₂ to C–C bond formation using conventional method^[20–25] vs microdroplet method.

reaction was carried out by performing electrospray of AcAc (aq.) in negative ion mode in a nebulized condition at 5 μL/min flow rate and 3 kV spray voltage, as shown in Figure 1a. In N₂-nebulized electrospray ionization, the major species seen was deprotonated AcAc [M–H][–] at *m/z* 99 (Figure 1b), further confirmed by its collision induced dissociation, resulting in a fragmented peak at *m/z* 57 (neutral loss of CH₂CO) as shown in Figure S1a. Strikingly, by changing the nebulization gas from N₂ to CO₂, a product peak at *m/z* 143, [M–H + 44][–], was seen (Figure 1c). The conversion ratio (CR), the ratio between the product and reagent plus product intensities expressed in percentage, i.e., CR (%) = [I_p/(I_p + I_r)] × 100, was 35 %. Tandem mass spectrometry of the product peak at *m/z* 143 gave two major fragmented species corresponding to CO₂ and H₂O losses, and two minor peaks due to CO and C₂H₆ losses, respectively (Figure S1b). MS/MS/MS of the isolated peak at *m/z* 99 again showed a characteristic loss of CH₂CO (Figure S1c) which matched with the MS/MS of AcAc.

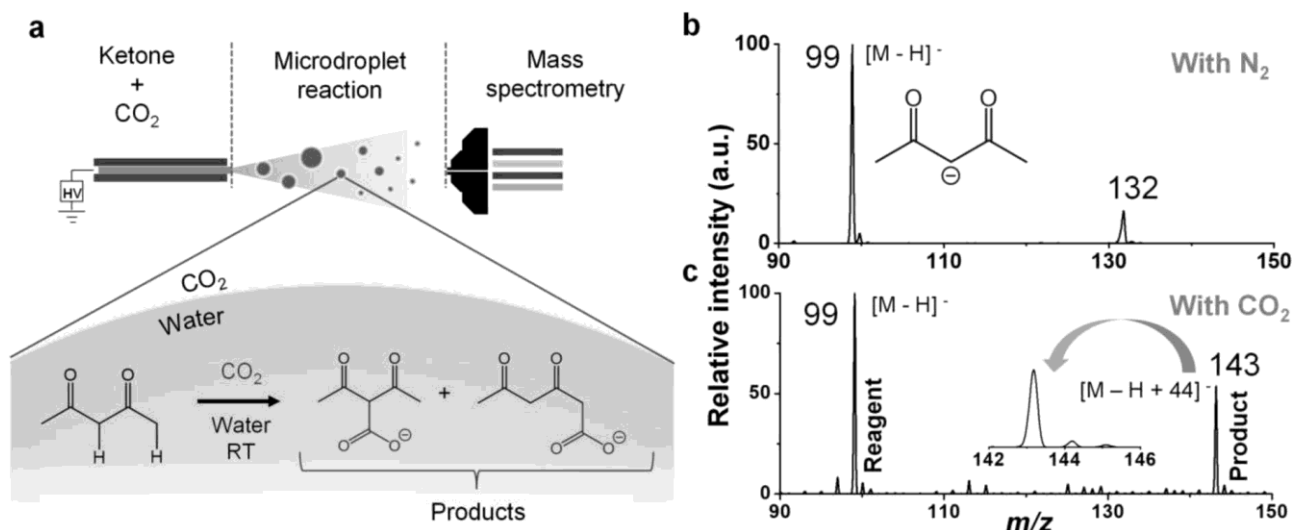


Figure 1. Microdroplet reaction between acetylacetone and CO₂(g). a) Schematic illustration of experimental procedure and scheme of reaction between acetylacetone and CO₂. CO₂ can exist in solution too, in addition to the interface, as it dissolves in water. Mass spectrum of 10 mM acetylacetone in water in b) nitrogen and c) CO₂-nebulized electrospray. Inset of b shows structure of the species detected corresponding to AcAc anion. Inset of c shows the zoomed-in spectrum of the peak at *m/z* 143.

Scheme S1 shows structures of the major fragmented species. The loss of CO₂ requires a moderate collision energy (~40 V) as evident from Figure S2. All of these give us confidence to identify the peak to be a covalently bonded product of a reaction between the ketone and CO₂. Among the two positional isomeric products in Figure 1a, we speculate that the carboxylation reaction occurs at the center position of AcAc, due to the higher acidity of these two protons compared to the protons in the methyl groups. The product peak was further confirmed by performing the droplet reaction with an isotopically labeled reagent (Figure S3). Note that we did not observe any di-carboxylated product, as evident from the MS/MS spectrum of the peak at *m/z* 187 (Figure S4), which arises from the background. We also conducted a bulk reaction by continuous bubbling of CO₂ in a solution of AcAc. A time-dependent ESI MS measurement of the bulk reaction mixture shows no product formation (SI 2 and Figure S5). To rule out any possibility of contamination from the experimental setup, we recorded background spectra that showed complete absence of the reagent or product (Figure S6).

We then performed pressure dependent experiment to evaluate the effect of CO₂ concentration at the droplet interface. Figure S7 shows the CR vs. CO₂ gas pressure plot. To our surprise, we observed a drastic decay of the CR with increasing nebulization gas pressure. With increasing gas pressure, the concentration of CO₂ around the droplet environment cannot be significantly increased. Although, the actual concentration of CO₂ around the droplet is hard to evaluate. We believe that within the lowest pressure regime, the CO₂ concentration around the droplet is significantly higher than it reaches the saturation limit of the reaction. In this case, we suggest that the droplet velocity plays a role in converting into product, hence, high CR.^[28] Similar results

were also observed in the distance experiments, discussed later in this article.

The concentrations of the reactants are indeed an important parameter in controlling the rate of the reaction in such microdroplet chemistry.^[31] We observed a dramatic concentration effect when we varied the concentration of AcAc from 1 μM to 10 mM. Figure S8a displays a stack of mass spectra at different concentrations. We found that the product peak intensity falls exponentially with increasing the reagent concentration, as shown in Figure S8b. At low concentration, most of the AcAc anions are available at the surface to participate in reaction with CO_2 , in contrast to the high concentration where molecules at the droplet core are unreactive, lowering down the overall CR.

The spray potential has been found to have a minimal effect on the conversion ratio (Figure S9a). Upon increasing it from 0 to 1.5 kV, ionization efficiency increases which drives the reaction. Note that at 0 kV, we only observe a noise (Figure S9b). We believe that AcAc ion concentration saturates at 1.5 kV spray potential resulting in a plateau in the potential vs CR plot of the reaction.

We then planned a different approach for the reaction and used $(\text{NH}_4)_2\text{CO}_3$ as a source of CO_2 . By spraying 1 : 30 molar ratio of AcAc: $(\text{NH}_4)_2\text{CO}_3$ in water, we observed a deprotonated species corresponding to carboxylation of

AcAc (Figure S10). We also observed a significant increase in the product peak intensity in this case than in the CO_2 -nebulization experiment. The CR was $\sim 75\%$. We also performed a reaction with CO_2 present in ambient air which resulted in low product yield as compared to that from a gas cylinder (Figure S11).

Contrary to the observation by Cooks et al., where the authors reported C–N bond formation with CO_2 and amine, both in positive and negative ion modes, we found no reaction in the positive ion mode. A peak at m/z 145 was observed at low intensity in the positive ion mode, although the MS/MS spectrum did not show a characteristic neutral loss of CO_2 (Figure S12). We speculate that the mechanism (Figure 2a) of the reaction involves the formation of carbanion nucleophiles in the first place in negatively charged microdroplets. This is due to the high acidity of the enolate proton, which undergoes C–H cleavage to make the carbanion. Such negatively charged species occupy the gas-liquid interface to minimize the electrostatic repulsion and cause nucleophilic attack to the C-center of the CO_2 . For CO_2 nebulized conditions, the microdroplet surface acts as a reaction site, as shown by reaction path 1 (Figure 2a). However, the reaction with ammonium carbonate undergoes via its decomposition to $\text{CO}_2(\text{g})$ which eventually creates micro/nano-bubbles at the interior of the droplet as shown

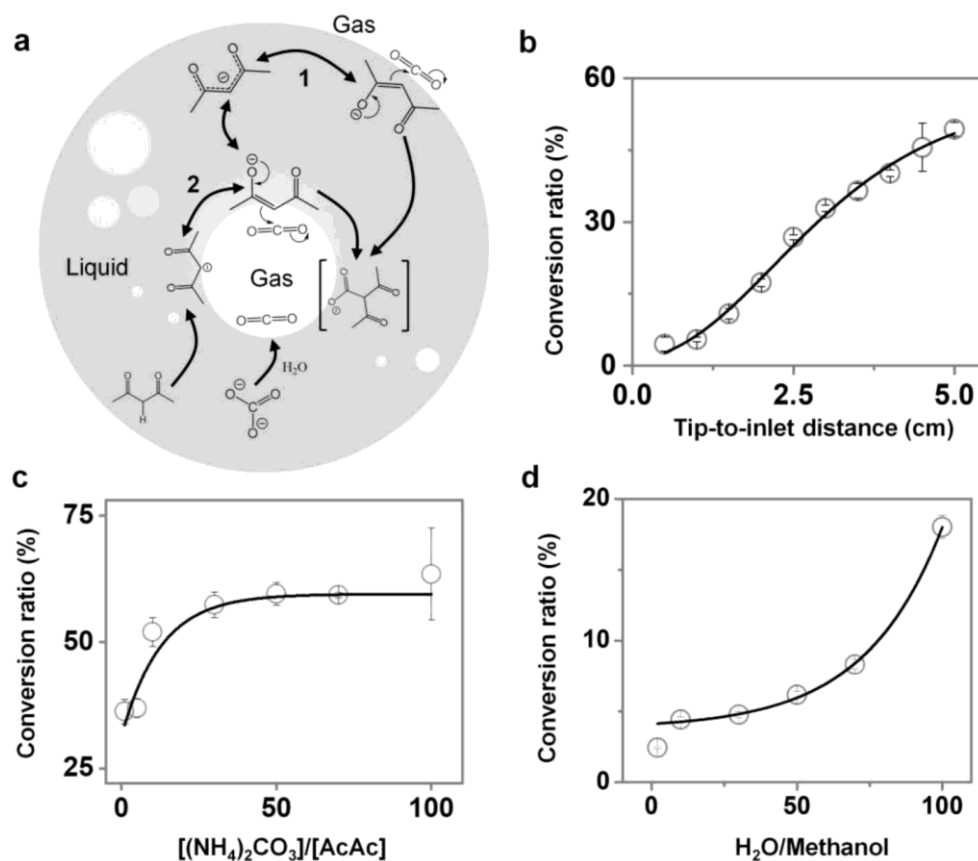


Figure 2. Microdroplet reaction at different conditions. a) In-droplet carboxylation reaction mechanism involving both intrinsic formation of CO_2 from the dissociation of ammonium carbonate and externally nebulized CO_2 . Effect of b) tip-to-inlet distance, c) ratio of ammonium carbonate and acetylacetone and d) ratio of water and methanol on the reaction progression.

in Figure 2a. Gas-liquid interfaces of such micro/nanobubbles serve as a reaction site for this heterogenic interfacial reaction (path 2). Such nanobubbles within microdroplets have been observed previously.^[32] Notably, reaction via dissolved CO₂ in water cannot be overruled both in CO₂ nebulization and with ammonium carbonate. We excluded any electrochemical pathway of the reaction through radical generation by performing a control experiment with the addition of TEMPO which does not affect our reaction (Figure S13).

Tip-to-inlet distance is known to affect microdroplet chemistry by regulating the flight time of the droplets. We observed a dramatic difference in the CR by changing the tip-to-inlet distance. Figure 2b shows a sigmoidal increase of the CR with increasing distance from 0.5 to 5 cm while spraying AcAc with (NH₄)₂CO₃. This suggests that the reaction progression depends highly on the time travelled by the droplet in air. Figure S14 shows a series of mass spectra with varying distances. A similar experiment with CO₂ nebulization was performed (Figure S15). We observed that beyond a distance of 3 cm, the CR decreases which might be due to complete desolvation resulting in the release of the gas phase ion. To account for the droplet size effect, we have conducted a control experiment in which we varied the tip diameter of the emitter while maintaining a constant distance of 1.5 cm. We found that reducing the tip diameter increases the product peak intensity significantly (Figure S16). The smaller the droplets higher the surface area. It proves that the reaction is occurring at the surface of the droplet. This contributes to the enrichment of the reactant molecules at the surface, resulting in an increased conversion ratio.^[33]

Encouraged by the above findings, we performed an experiment by varying the (NH₄)₂CO₃ to AcAc ratio in solution. In Figure 2c we found that the CR rises quickly from 10 to 70 % by increasing the (NH₄)₂CO₃ ratio from 5 to 30 %. After that, it reaches a plateau. Mass spectra of the corresponding ratios are shown in Figure S17. Additionally, we performed imaging experiments of deposited droplets to visualize the number of microbubbles formed (Figure S18a–c). We observed that the number density of microbubbles per droplet increases significantly with increasing the concentration of (NH₄)₂CO₃ (Figure S18d).

We found that the reaction is not supported by organic solvents. To check the effect of organic solvents, we added methanol to the bulk solution. By varying the solvent composition from 0 % to 95 % of H₂O in methanol, we found an increase of CR from 3 to 18 % at a 1 : 1 molar ratio of the ammonium carbonate to AcAc (Figure 2d). Figure S19 shows the mass spectra of the corresponding data points at different solvent compositions. Firstly, we assessed that owing to high dielectric constant, water in the droplet helps in holding the net charges better than the organic contents such as methanol. Which in turn drives the generation of the carbanion to react with CO₂ at the interface. Secondly, we suggest that this could also be regulated by the equilibrium of ammonium carbonate to CO₂ conversion. At higher water concentrations, the equi-

rium shifts to the CO₂ side which helps in generating microbubbles for the reaction to occur.

We further verified our conjecture of reaction through microbubbles by changing the pH of the solution. We observed that lowering the pH of the solution linearly increases the CR of the reaction (Figure S20). We concluded that low pH influences the formation of microbubbles inside microdroplets.

To understand the effect of ionic strength, we conducted an experiment by adding a noninteractive salt, CaCl₂ and compared the results with the results in the absence of it (Figure S21). Interestingly, we observed a significant increment of product peak intensity upon the addition of CaCl₂. The addition of non-interactive salt is known to influence the reaction rate when the reaction proceeds through the formation of a charged species. The increase of product peak intensity upon the addition of CaCl₂ further supports our mechanism that the reaction goes through the formation of the carbanion. The addition of CaCl₂ will induce an increased concentration of Cl ions in the droplet. We assessed that an increased concentration of Cl ions increases the rate of the reaction. Thus, we observed an increased conversion ratio after the addition of CaCl₂.

To gain deeper insights into the reduction mechanism of CO₂ in the presence of AcAc and water, we conducted a series of density functional theory simulations (see computational details for further details) on the complexes of AcAc, CO₂, and H₂O. We examined the role of solvent molecules by varying the number of explicit water molecules in our simulations from one to three and found that the presence of explicit water molecules plays a crucial role in capturing CO₂. The CO₂ reduction reaction begins with the formation of a carbanion complex from AcAc through the keto-enol tautomerism. The Gibbs free energy profiles for the tautomerism with varying numbers of explicit water molecules are shown in Figure 3(a). Complex 1 represents AcAc solvated with three explicit water molecules. The proton transfer (keto-enol tautomerism) within AcAc generates complex 2, and the transition state is represented by TS1/2. In the presence of one explicit water molecule, the activation barrier for the proton transfer is about 34.2 kcal/mol, and it is reduced to 21.47 kcal/mol in presence of three explicit water molecules. The drastic decrement in the activation barrier with an increase in the water molecules is due to the ease of proton transfer in the network of more explicit water molecules. The calculated free energy change ($\sim G$) between the keto and enol tautomer is about 1 kcal/mol, where we find that the keto form is more stable than the enol form. Water, being a polar solvent, slightly stabilizes the keto form with a high dipole moment.^[34–37]

Next, we computed the barriers for CO₂ capture using the enol form (complex 2) in three explicit water molecules. The Gibbs free energy profile for this reaction is shown in Figure 3(b). Here, complex 3 depicts the interaction of CO₂ with complex 2 with some reorientation. The transfer of a proton from complex 3 to the surrounding water molecules is exergonic and stabilizes the formation of carbanion complex 4 by 9.45 kcal/mol. The formation of a C–C bond between carbanion (complex 4) and CO₂ generates the

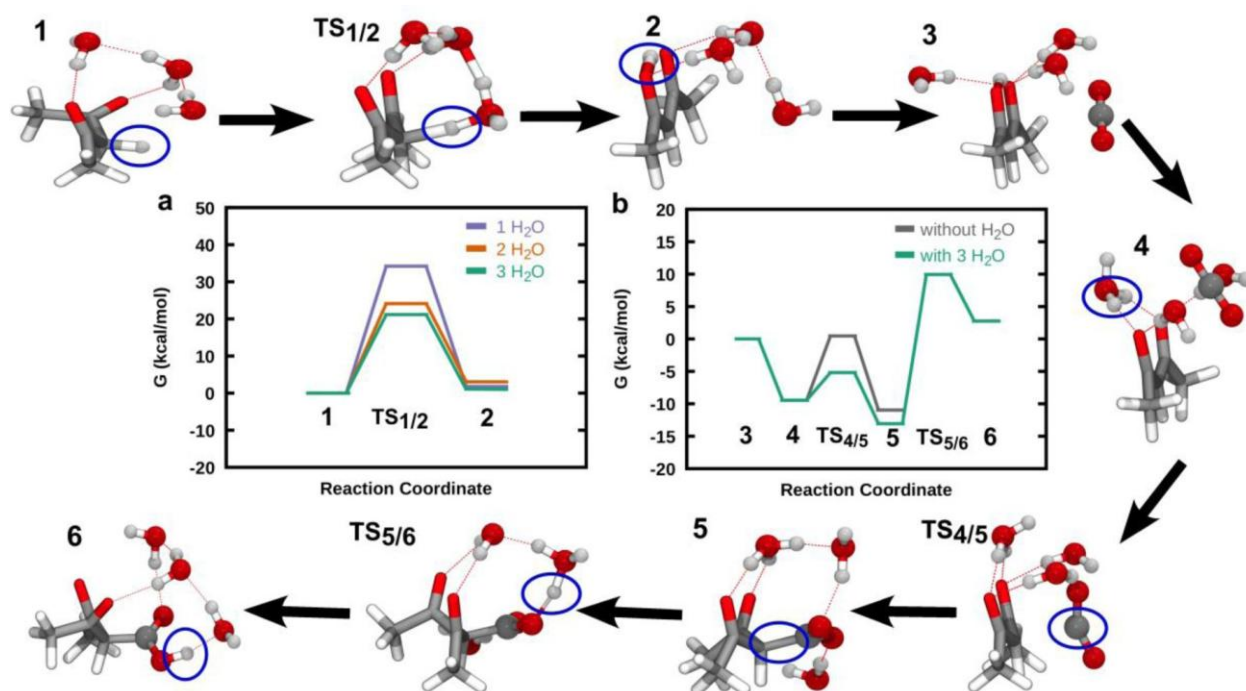


Figure 3. Free energy landscape for CO₂ reduction over AcAc and DFT optimized structures in the presence of three explicit water molecules along the reaction pathway.

carboxylate anion (complex 5). The computed activation barrier for the C–C bond formation is 4.27 kcal/mol. The formation of C–C bond decreases the free energy of the complex 5 to 13.06 kcal/mol. Here, C–C bond length decreases from 3.75 to 1.6 Å. We also calculated the activation barrier of C–C bond formation between the carbanion and CO₂ in the gas phase, which is 8.9 kcal/mol (Figure 3(b)). Hence, we conclude that CO₂ reduction is facilitated by solvated water. Finally, the transfer of proton from the water molecules to the COO group results in the formation of the carboxylic acid (Complex 6). The barrier for this proton transfer (TS5/6) is around 23 kcal/mol. Complex 6 is less stable than complex 5 since holding a proton on the carboxylate anion is less preferred than releasing it into the water (in other words, carboxylic acid prefers to lose a proton in water). We have also observed a similar result with complex 2, where it was stabilized by approximately 7 kcal/mol by releasing the proton to water (see Figure S22).

We calculated the activation barriers for the formation of a C–C bond in both neutral (i.e., representing the core of the droplet) and charged media (representing the surface of the microdroplet) by considering up to three explicit water molecules. As shown in Figure S23, the barriers for the C–C bond formation in the neutral medium is 19.3 kcal/mol when three explicit water molecules are considered (18.60 and 17.60 kcal/mol in the presence of one and two water molecules, respectively). In contrast, the barrier is only 4.27 kcal/mol when the system is negatively charged. Moreover, for the system representing the microdroplet environment, the carboxylate complex formation step (5) is exergonic, whereas the same step is endergonic for the system

representing the bulk environment. Together, these results strongly indicate that the formation of a C–C bond (which is the crucial step in our reaction) is more favorable in microdroplets than in bulk water.

We extended our microdroplet chemistry to several other ketones. These include acetone, 1,1,1-trifluoro-5,5-dimethyl-2,4-hexanedione, benzophenone, acetophenone, dimedone (5,5-dimethylcyclohexane-1,3-dione), and cyclopentane-1,3-dione. Based on the above observations, we decided to perform these reactions with ammonium carbonate with a 1 : 1 ratio of both the reagents in solution. The mass spectrum and the MS/MS of the reagents and the products are presented in Figures S24–29. The CR values of other products range from 0.008 to 28 %, while that for the reaction between 1 : 1 AcAc and (NH₄)₂CO₃ was highest at 33 %. Strikingly, we observed that two of the cyclic diketones, i.e., dimedone and cyclopentane-1,3-dione did not react well. We assessed that the reaction mechanism goes through the formation of carbanion from the enol form of the diketones. In the case of AcAc, the keto-enol equilibrium shifts towards the enol side due to the intermolecular hydrogen bonding through a six-member ring formation (as shown below in Scheme S2a). However, these two cyclic ketones cannot form stable enol due to their ring strain. The Schemes S2b and S2c below show the equilibrium structure of the keto and enol form of the two cyclic diketones. Note that ketones having no α -H do not undergo this reaction (Figure S26). This also supports our reaction mechanism of the formation of carbanion via C–H bond cleavage in charged microdroplets. Our product, β -diketo acid, is known for its instability at room temperature.^[38,39] It was also evident from the ESI MS of the

crude product where we observed low product yield, synthesized upon two-hour deposition and liquid phase extraction from a scaled-up multiplexed electrospray setup (Figure S30).

In summary, we introduced a method of forming C–C bond with chemically inert CO₂ and the α -carbon of ketones, in charged aqueous microdroplets. Ionization of ketone by a C–H cleavage at the α position is the first step of the reaction. Interfacial enrichment of the newly formed carbanion helps in reaction progression via a nucleophilic attack to the C-center of CO₂, which is a key step of the reaction. Our work shows a tremendous possibility to convert environmental CO₂ to useful products. The science discussed here has implications in understanding interfacial chemistry at the gas-liquid phase, the latter in a confined volume, such as in clouds, aerosols, rain droplets, and mist.

Supporting Information

A brief discussion on the experimental procedures, computational details, MS of the reaction by varying gas pressure, distance, concentration, and solvent effect, MS of the bulk reaction, and MS and MS/MS of other reactants and products, presented in Supporting Information. The authors have cited additional references within the Supporting Information.^[40–42]

Acknowledgements

P. B. thanks IIT Madras for research fellowship. S. M., K. U., and B. K. S. thank UGC for their research fellowship. T. P. acknowledges funding from the Centre of Excellence on Molecular Materials and Functions under the Institute of Eminence scheme of IIT Madras. S. S. R. K. C. Y. acknowledges the financial support of IIT Madras through the MPHASIS faculty fellowship and through its new faculty support grants NFSG (IP2021/0972CY/NFSC008973), NFIG (RF2021/0577CY/NFIG008973), and DST-SERB (SRG/2021/001455).

Conflict of Interest

The authors declare no conflict of interest.

Data Availability Statement

The data that support the findings of this study are available in the supplementary material of this article.

Keywords: Carbon dioxide reduction · microdroplet chemistry · air–water interface · mass spectrometry · carbanion

[1] C. Lu, X. Zhang, X. Chen, *Accounts Mater. Res.* **2022**, *3*, 913–921.

- [2] S. Nitopi, E. Bertheussen, S. B. Scott, X. Liu, A. K. Engstfeld, S. Horch, B. Seger, I. E. L. Stephens, K. Chan, C. Hahn, J. K. Nørskov, T. F. Jaramillo, I. Chorkendorff, *Chem. Rev.* **2019**, *119*, 7610–7672.
- [3] Q. Liu, L. Wu, R. Jackstell, M. Beller, *Nat. Commun.* **2015**, *6*, 5933.
- [4] S. Saini, R. S. Das, A. Kumar, S. L. Jain, *ACS Catal.* **2022**, *12*, 4978–4989.
- [5] T. N. Nguyen, M. Salehi, Q. Van Le, A. Seifitokaldani, C. T. Dinh, *ACS Catal.* **2020**, *10*, 10068–10095.
- [6] V. Kumaravel, J. Bartlett, S. C. Pillai, *ACS Energy Lett.* **2020**, *5*, 486–519.
- [7] A. U. Pawar, C. W. Kim, M.-T. Nguyen-Le, Y. S. Kang, *ACS Sustainable Chem. Eng.* **2019**, *7*, 7431–7455.
- [8] J. He, C. Janáky, *ACS Energy Lett.* **2020**, *5*, 1996–2014.
- [9] S. R. Lingampalli, M. M. Ayyub, C. N. R. Rao, *ACS Omega* **2017**, *2*, 2740–2748.
- [10] A. Modak, P. Bhanja, S. Dutta, B. Chowdhury, A. Bhaumik, *Green Chem.* **2020**, *22*, 4002–4033.
- [11] M. D. Porosoff, J. G. Chen, *J. Catal.* **2013**, *301*, 30–37.
- [12] Z. Wei, Y. Li, R. G. Cooks, X. Yan, *Annu. Rev. Phys. Chem.* **2020**, *71*, 31–51.
- [13] J. K. Lee, D. Samanta, H. G. Nam, R. N. Zare, *J. Am. Chem. Soc.* **2019**, *141*, 10585–10589.
- [14] J. K. Lee, D. Samanta, H. G. Nam, R. N. Zare, *Nat. Commun.* **2018**, *9*, 1562.
- [15] I. Nam, J. K. Lee, H. G. Nam, R. N. Zare, *Proc. Nat. Acad. Sci.* **2017**, *114*, 12396 LP–12400.
- [16] I. Nam, H. G. Nam, R. N. Zare, *Proc. Nat. Acad. Sci.* **2018**, *115*, 36 LP–40.
- [17] A. J. Grooms, A. N. Nordmann, A. K. Badu-Tawiah, *Angew. Chem. Int. Ed.* **2023**, *62*, e202311100.
- [18] P. Basuri, L. E. Gonzalez, N. M. Morato, T. Pradeep, R. G. Cooks, *Chem. Sci.* **2020**, *11*, 12686–12694.
- [19] K.-H. Huang, Z. Wei, R. G. Cooks, *Chem. Sci.* **2021**, *12*, 2242–2250.
- [20] T. Fujihara, Y. Tsuji, *Front. Chem.* **2019**, *7*.
- [21] C.-K. Ran, L.-L. Liao, T.-Y. Gao, Y.-Y. Gui, D.-G. Yu, *Curr. Opin. Green Sustain. Chem.* **2021**, *32*, 100525.
- [22] W. Huang, J. Lin, F. Deng, H. Zhong, *Asian J. Org. Chem.* **2022**, *11*, e202200220.
- [23] A. Banerjee, G. R. Dick, T. Yoshino, M. W. Kanan, *Nature* **2016**, *531*, 215–219.
- [24] S. Wang, G. Du, C. Xi, *Org. Biomol. Chem.* **2016**, *14*, 3666–3676.
- [25] J. Luo, I. Larrosa, *ChemSusChem* **2017**, *10*, 3317–3332.
- [26] L. Feng, X. Yin, S. Tan, C. Li, X. Gong, X. Fang, Y. Pan, *Anal. Chem.* **2021**, *93*, 15775–15784.
- [27] X. Song, Y. Meng, R. N. Zare, *J. Am. Chem. Soc.* **2022**, *144*, 16744–16748.
- [28] Y. Meng, E. Gnanamani, R. N. Zare, *J. Am. Chem. Soc.* **2023**, *145*, 7724–7728.
- [29] Q. Ge, Y. Liu, K. Li, L. Xie, X. Ruan, W. Wang, L. Wang, T. Wang, W. You, L. Zhang, *Angew. Chem. Int. Ed.* **2023**, *62*, e202304189.
- [30] Q. Ge, Y. Liu, W. You, W. Wang, K. Li, X. Ruan, L. Xie, T. Wang, L. Zhang, *PNAS Nexus* **2023**, *2*, pgad389.
- [31] C. J. Chen, E. R. Williams, *Chem. Sci.* **2023**, *14*, 4704–4713.
- [32] P. Basuri, A. Chakraborty, T. Ahuja, B. Mondal, J. S. Kumar, T. Pradeep, *Chem. Sci.* **2022**, *13*, 13321–13329.
- [33] B. M. Marsh, K. Iyer, R. G. Cooks, *J. Am. Soc. Mass Spectrom.* **2019**, *30*, 2022–2030.
- [34] P. Roy, S. Biswas, A. Pramanik, P. Sarkar, *Int. J. Res. Soc. Nat. Sci.* **2017**, *2*, 2455–5916.
- [35] J. W. Bunting, J. P. Kanter, R. Nelander, Z. Wu, *Can. J. Chem.* **1995**, *73*, 1305–1311.

- [36] T. Tsukahara, K. Nagaoka, K. Morikawa, K. Mawatari, T. Kitamori, *J. Phys. Chem. B* **2015**, *119*, 14750–14755.
- [37] G. Alagona, C. Ghio, P. I. Nagy, *Phys. Chem. Chem. Phys.* **2010**, *12*, 10173–10188.
- [38] K. J. Pedersen, *J. Am. Chem. Soc.* **1929**, *51*, 2098–2107.
- [39] A. V. Ignatchenko, M. E. Springer, J. D. Walker, W. W. Brennessel, *J. Phys. Chem. C* **2021**, *125*, 3368–3384.
- [40] J.-D. Chai, M. Head-Gordon, *Phys. Chem. Chem. Phys.* **2008**, *10*, 6615–6620.
- [41] M. J. Frisch, G. W. Trucks, H. B. Schlegel, G. E. Scuseria, M. A. Robb, J. R. Cheeseman, G. Scalmani, V. Barone, G. A. Petersson, H. Nakatsuji, *Google Sch. There is no Corresp. Rec. this Ref.* **2020**.
- [42] A. V. Marenich, C. J. Cramer, D. G. Truhlar, *J. Phys. Chem. B* **2009**, *113*, 6378–6396.

Manuscript received: February 15, 2024
Accepted manuscript online: April 5, 2024
Version of record online: May 29, 2024

Supporting Information
©Wiley-VCH 2021
69451 Weinheim, Germany

Spontaneous α -C-H Carboxylation of Ketones by Gaseous CO₂ at the Air-water Interface of Aqueous Microdroplets

Pallab Basuri, Sinchan Mukhopadhyay, K. S. S. V. Prasad Reddy, Keerthana Unni, B. K. Spoorthi, Shantha Kumar Jenifer, S. R. K. C. Yamijala Sharma, and Thalappil Pradeep*

Abstract: We present a catalyst-free route for the reduction of carbon dioxide integrated with the formation of a carbon-carbon bond at the air/water interface of negatively charged aqueous microdroplets, at ambient temperature. The reactions proceed through carbanion generation at the α -carbon of a ketone followed by nucleophilic addition to CO₂. Online mass spectrometry reveals that the product is an α -ketoacid. Several factors, such as the concentration of the reagents, pressure of CO₂ gas, and distance traveled by the droplets, control the kinetics of the reaction. Theoretical calculations suggest that water in the microdroplets facilitates this unusual chemistry. Furthermore, such a microdroplet strategy has been extended to seven different ketones. This work demonstrates a green pathway for the reduction of CO₂ to useful carboxylated organic products.

DOI: 10.1002/anie.2021XXXXX

Table of Contents

Serial No.	Details	Page No
SI 1	Experimental details	3
Figure S1	MS/MS spectra of m/z 99 and 143	4
Scheme S1	Reaction scheme of water loss pathway and De-carboxylation pathway from the product m/z 143	5
Figure S2	Survival Yield calculation	6
Figure S3	Microdroplet carboxylation reaction with deuterated labeled AcAc.	7
Figure S4	Microdroplet carboxylation reaction showing absence of di-carboxylated product	8
SI 2	Bulk reaction and ESI MS measurements	9
Figure S5	Time-dependent ESI MS measurements of the bulk reaction mixtures	10
Figure S6	Background mass spectra were recorded using methanol and water	11
Figure S7	Effect of CO ₂ gas pressure	12
Figure S8	Effect of total reagent concentration in the microdroplet carboxylation reaction	13
Figure S9	Spray voltage variation experiment	14
Figure S10	Microdroplet reaction mass spectrometry of reaction mixture containing 1:30 ratio of AcAc and (NH ₄) ₂ CO ₃ .	15
Figure S11	Microdroplet reaction mass spectrometry between AcAc and CO ₂ using ambient air nebulization	16
Figure S12	Positive ion mode microdroplet reaction mass spectrometry	17
Figure S13	Effect of a radical scavenger on the droplet carboxylation reaction	18
Figure S14	Distance experiments using AcAc and (NH ₄) ₂ CO ₃ reaction mixture	19
Figure S15	Distance experiments using AcAc and CO ₂	20
Figure S16	Electrospray emitter tip diameter variation experiments	21
Figure S17	Microdroplet reaction by varying concentration of AcAc and (NH ₄) ₂ CO ₃	22
Figure S18	Dark field microscopic images of microdroplets	23
Figure S19	Solvent composition dependency of microdroplet reaction	24
Figure S20	Effect of pH on the reagent to product conversion ratio.	25
Figure S21	Effect of ionic strength on our microdroplet carboxylation reaction	26
SI 3	Details of DFT and coordinates for DFT calculation	27
Figure S22	Free energy landscape for Keto-enol transformation over AcAc	34
Figure S23	Free energy landscape for C-C bond formation in neutral and negatively charged microdroplets.	35
Figure S24	Microdroplet reaction with acetone and (NH ₄) ₂ CO ₃	36
Figure S25	Microdroplet reaction with of 1,1,1-trifluoro-5,5-dimethyl-2,4-hexanedione and (NH ₄) ₂ CO ₃	37
Figure S26	Microdroplet reaction with benzophenone and (NH ₄) ₂ CO ₃	38
Figure S27	Microdroplet reaction with acetophenone and (NH ₄) ₂ CO ₃	39
Figure S28	Microdroplet reaction with dimedone and (NH ₄) ₂ CO ₃	40
Figure S29	Microdroplet reaction with cyclopentane-1,3-dione and (NH ₄) ₂ CO ₃	41
Scheme S2	Scheme showing keto-enol tautomerism among a) AcAc, b) cyclopentane-1,3-dione, and c) 5,5-dimethyl-cyclohexane-1,3-dione, respectively	42
Figure S30	ESI MS spectrum of 2 h spray deposited sample after methanol extraction	43

Supporting Information 1:

Sampling and online mass spectrometric measurements:

We prepared 10 mM aqueous solutions for each of the reagents in Millipore water. The solutions were taken in a Hamilton 100 μL syringe and connected to a syringe pump to infuse (at 5 $\mu\text{L}/\text{min}$) through a fused silica capillary (ID = 100 μm ; OD = 300 μm). The capillary and syringe were connected through a union connector. The flow rate of the sample was set to 5 $\mu\text{L}/\text{min}$. The high-voltage power supply was connected to the metallic needle of the syringe. Negative and positive 3-4 kV were applied to generate the charged microdroplets from the tip of the capillary. This home-built ESI setup was held in front of the mass spectrometer inlet at a distance of 1 cm (tip-to-inlet distance). Capillary and tube lens voltages were set to 2 and 20 V, respectively. The capillary temperature was set to 270 $^{\circ}\text{C}$ for most of the experiments. No nebulization gas was applied for most of the experiments. However, the gas pressure experiments were performed by connecting an N_2 source with the ESI source using a stainless-steel union T connector.

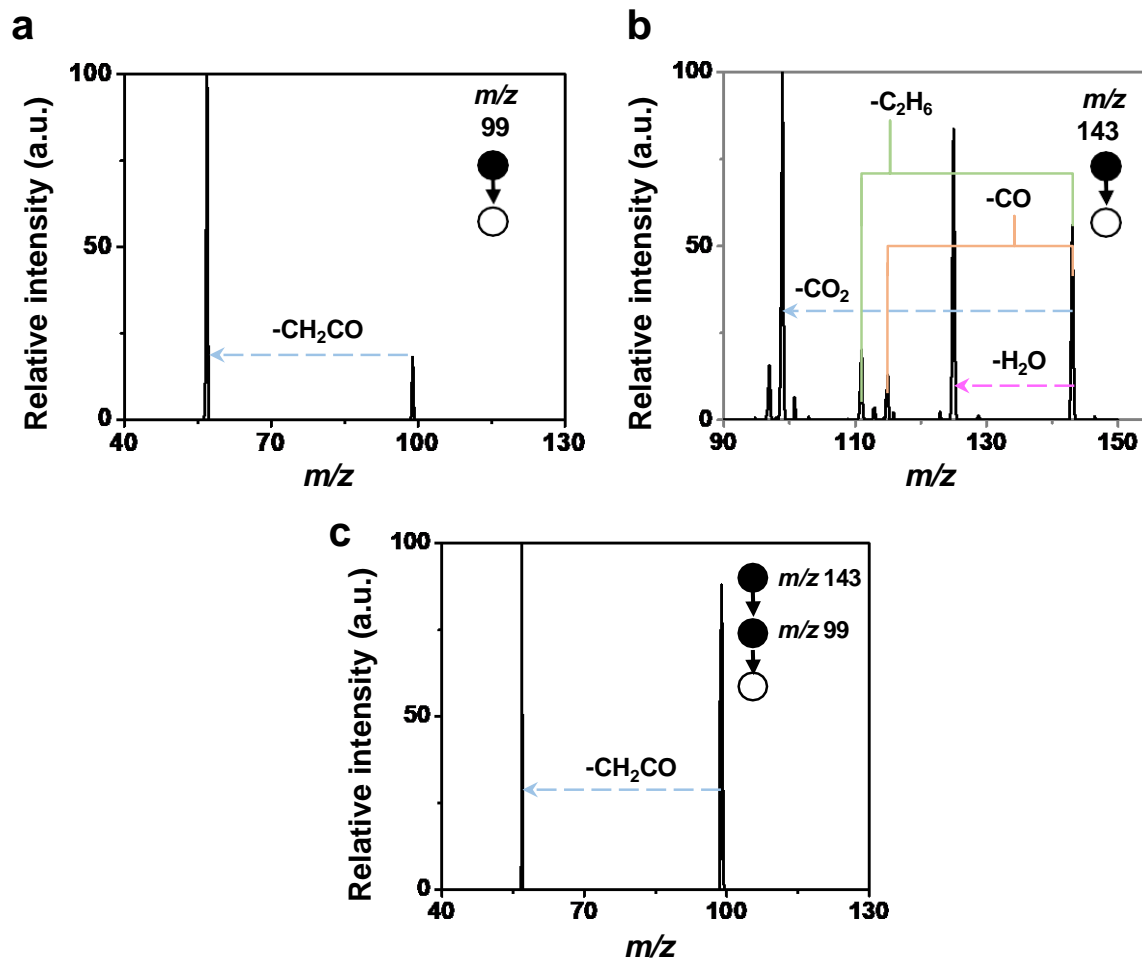
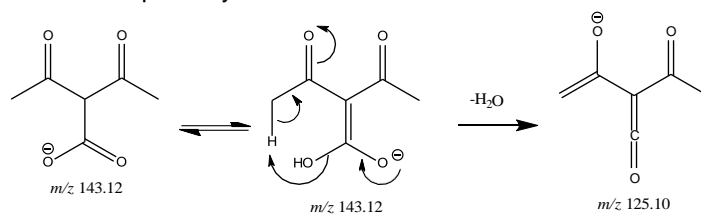
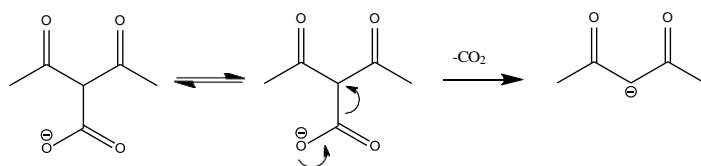


Figure S1. Collision-induced dissociation of the isolated peaks corresponding to the reagent and the product. a) MS/MS spectrum of m/z 99. b) MS/MS spectra of isolated ion of m/z 143 showing a major loss of 44 corresponding to CO_2 . c) MS/MS/MS of the isolated product peak which further supports our assignment.

Water loss pathway



De-carboxylation pathway



Scheme S1. Scheme showing neutral loss of a water and a CO₂ molecule from the isolated product peak during tandem mass spectrometry.

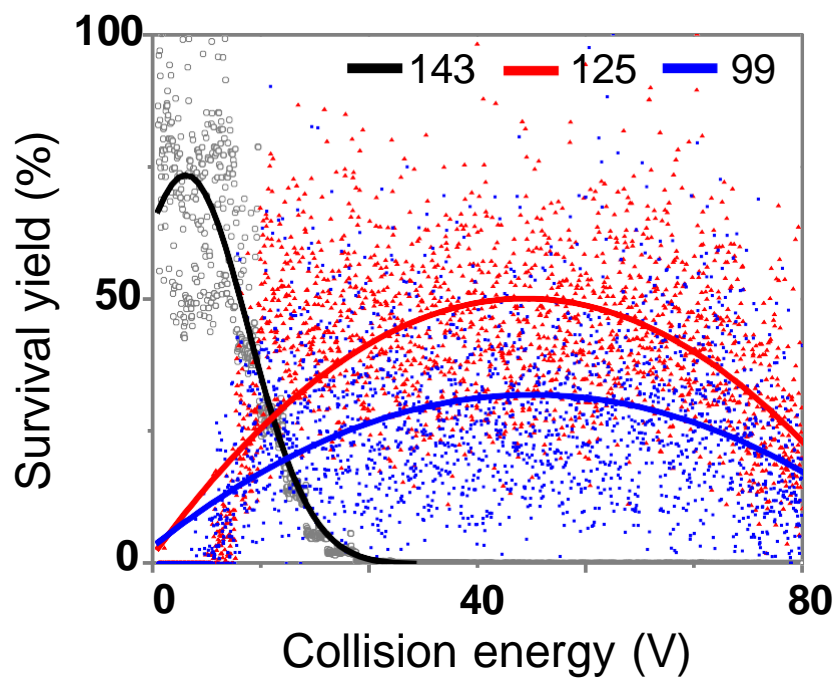


Figure S2. Survival yield plot of the reaction product under high collision energy showing that the C-C bond breaking that leads to a neutral loss of CO₂ from the parent ion takes 40 V collision energy.

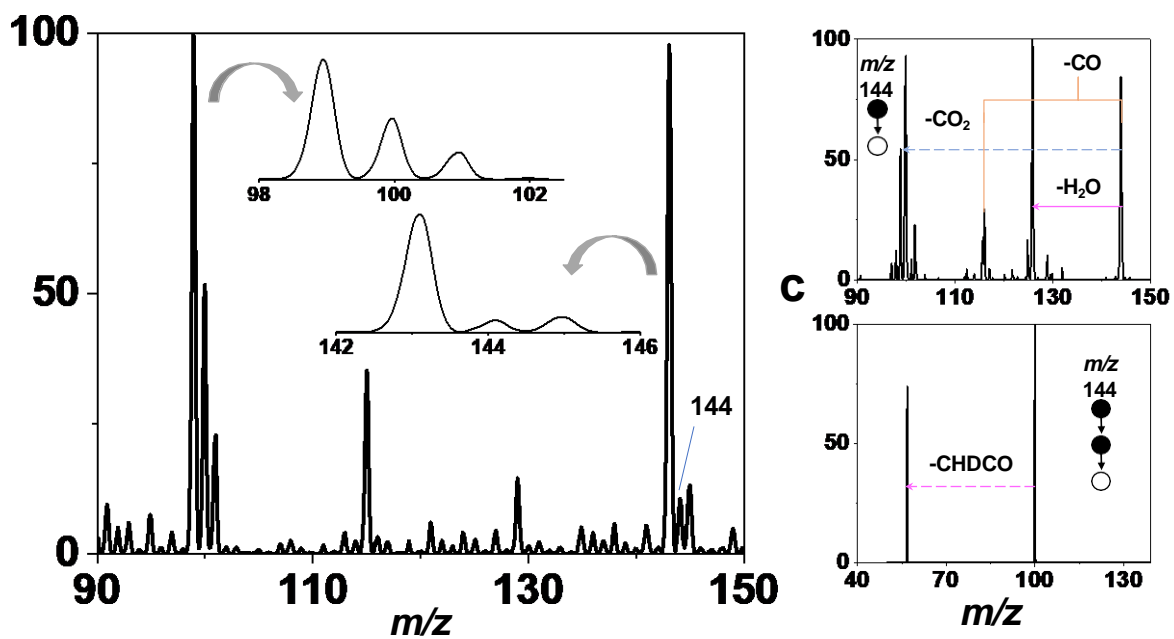


Figure S3. Microdroplet carboxylation of deuterated AcAc. a) Full range mass spectrum showing presence of mono-deuterated AcAc and product peak at m/z 100 and 144, respectively. b and c) MS/MS and MS/MS/MS of the isolated product peak. Peaks at m/z 121 and 131 correspond to background signal.

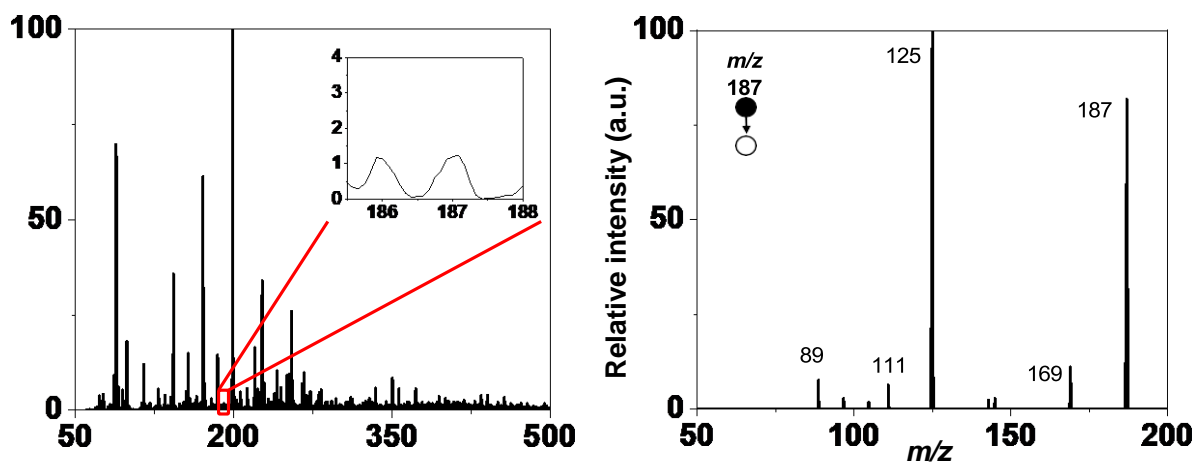


Figure S4. Microdroplet carboxylation reaction showing absence of di-carboxylated product. a) Full range mass spectrum showing absence of di-carboxylated product peak at m/z 187. Small signal in that position corresponds to a background signal which is further confirmed by the MS/MS of the peak (b), showing that the fragmentation pattern is not related to the product.

Supporting Information 2:

Bulk reaction and ESI MS measurements:

A bulk reaction was conducted by continuous bubbling of CO₂ gas from 1 minute up to 30 minutes in an aqueous solution containing 10 mM AcAc. A time-dependent ESI MS measurement was performed in a commercial ESI source with an LTQ-XL mass spectrometer to observe any product formation. We used N₂ as a nebulization gas and -3 kV as spray voltage. Mass spectra as a function of time are shown below where no peak at *m/z* 143 corresponding to product was observed. We only observed the reagent peak at *m/z* 99 as the base peak. All the other peaks at different time intervals are the result of the background signal.

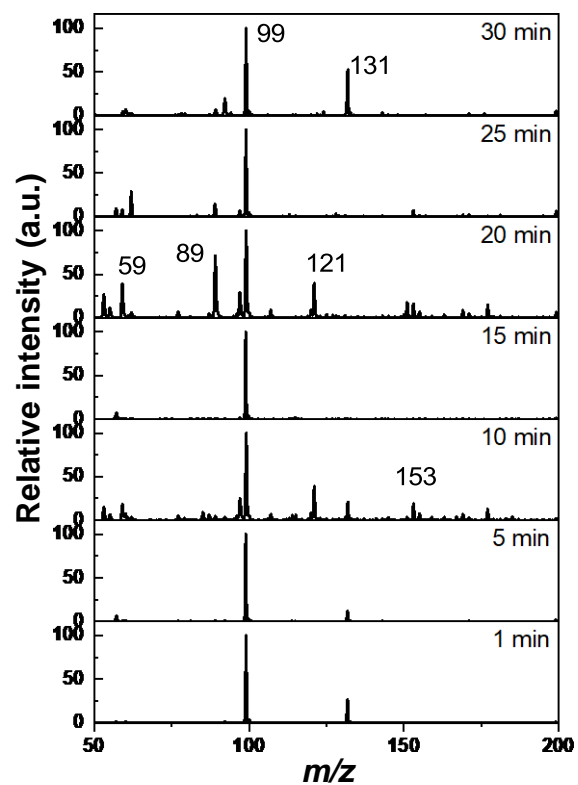


Figure S5. Time-dependent ESI MS measurements of the bulk reaction mixtures. The absence of a peak at m/z 143 shows no product formation in bulk.

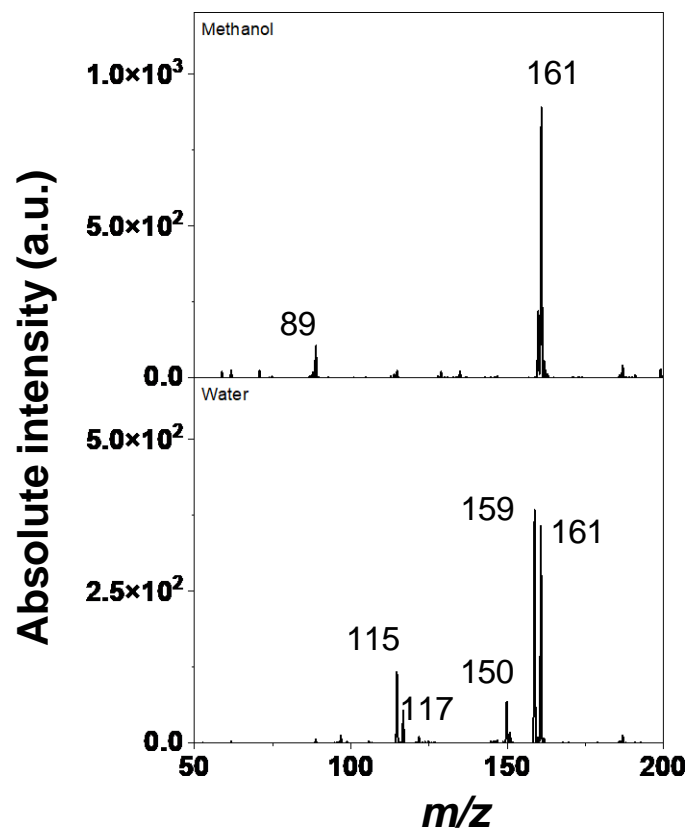


Figure S6. Background mass spectra were recorded using methanol (top) and water (bottom) showing no traces of reagent and product peak at m/z 99 and 143, respectively. Peaks that appeared in the mass spectra are either from solvents or from the instrument.

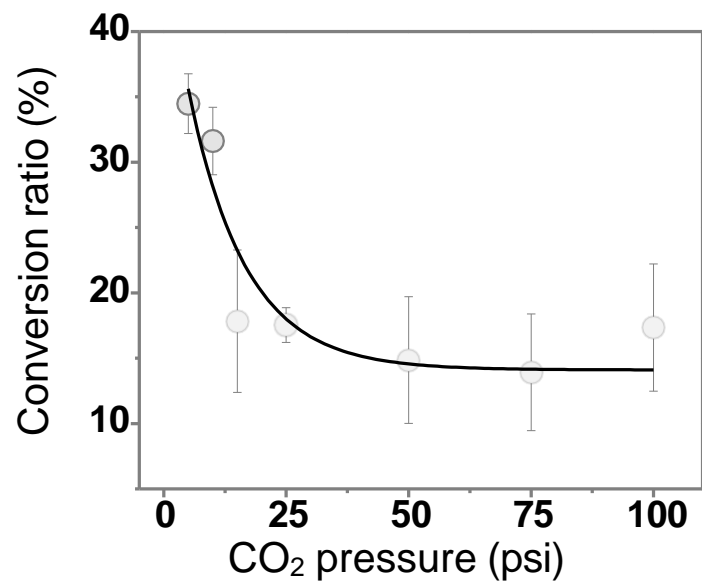
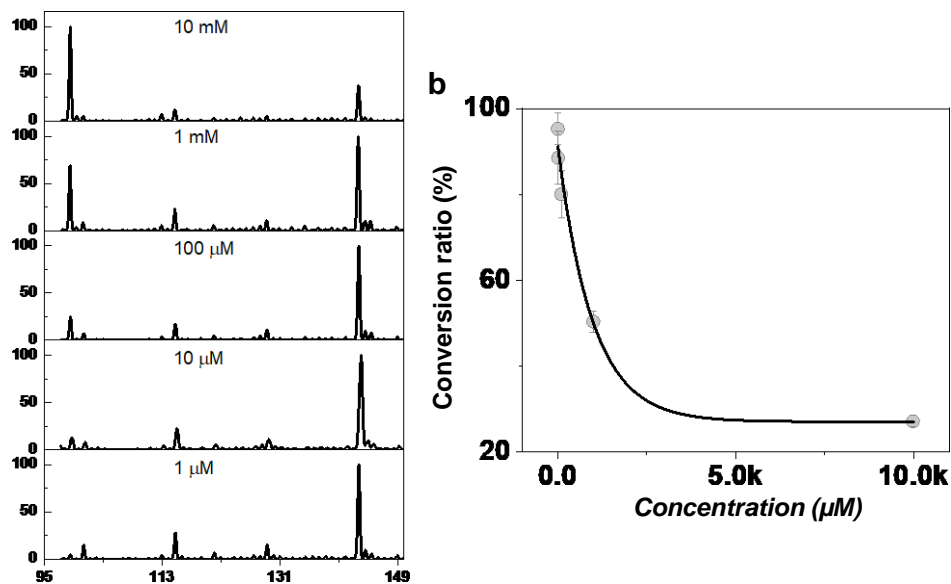


Figure S7. Conversion ratio vs CO₂ gas pressure plot showing that reaction takes place at low CO₂ flow rate which gives enough flight time for the nucleophilic addition reaction.



FigureS8. Effect of total reagent concentration in the microdroplet carboxylation reaction. a) Mass spectra collected at different concentration of AcAc varying from 1 μM to 10 mM, respectively. b) shows the C.R.(%) vs concentration plot where we observed that with increasing concentration, relative intensity of the product peak with respect to the reagent peak, decreases until it reaches a plateau.

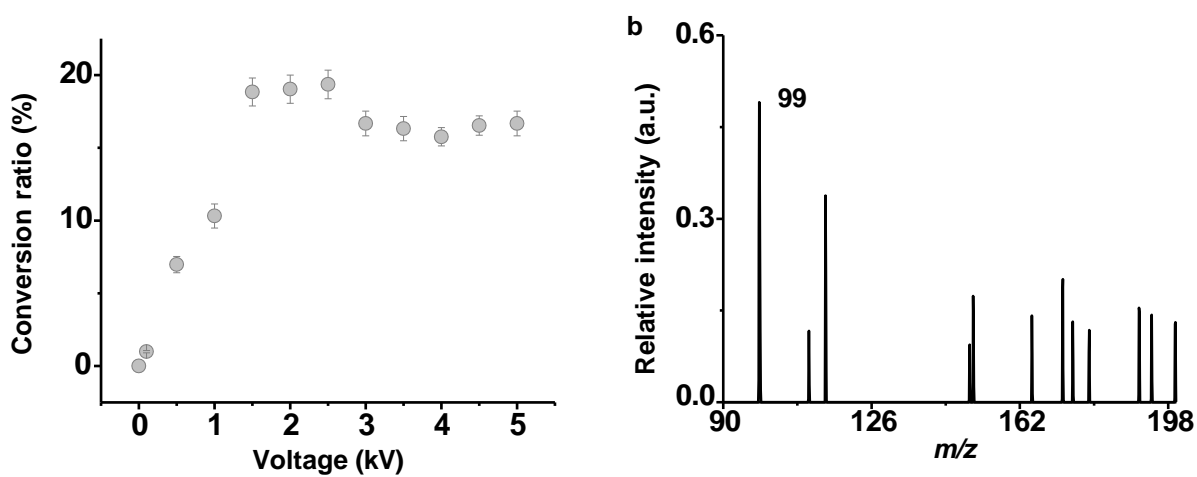


Figure S9. Spray voltage variation experiments a) Effect of spray voltage on the reagent to product conversion ratio of the microdroplet carboxylation reaction. b) Mass spectrum collected at zero applied potential. We observed negligible signal with absolute intensity of 0.6 a.u. A peak at m/z 99 maybe due to in-source gas phase ionization. Absence of product peak at m/z 143 suggests that the reaction does not occur without the application of potential.

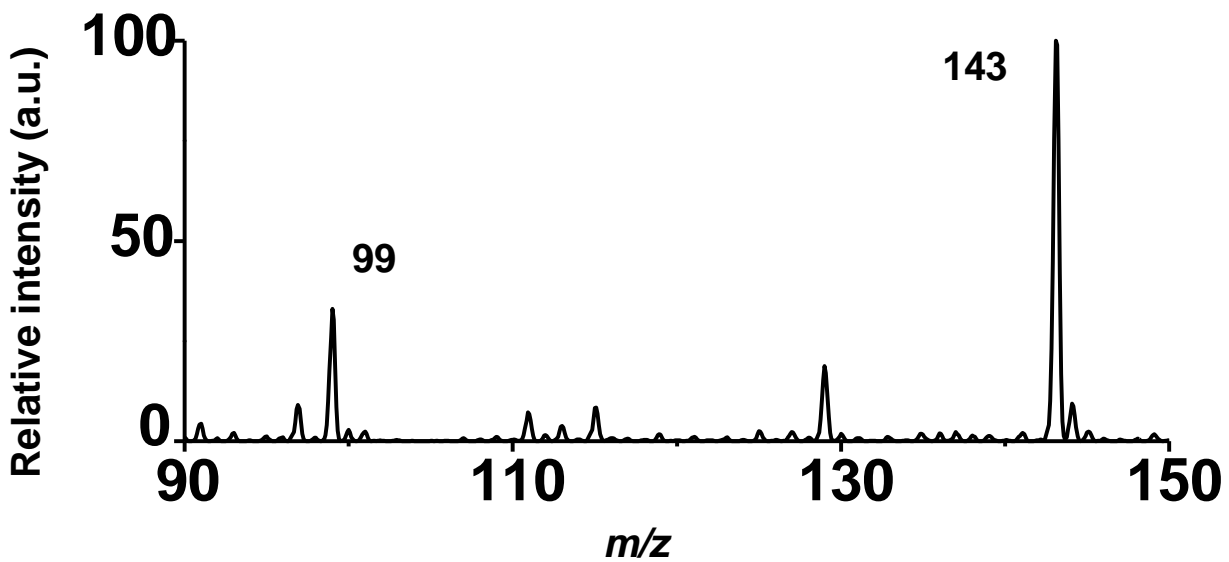


Figure S10. Microdroplet reaction mass spectrometry of reaction mixture containing 1:30 ratio of AcAc and $(\text{NH}_4)_2\text{CO}_3$.

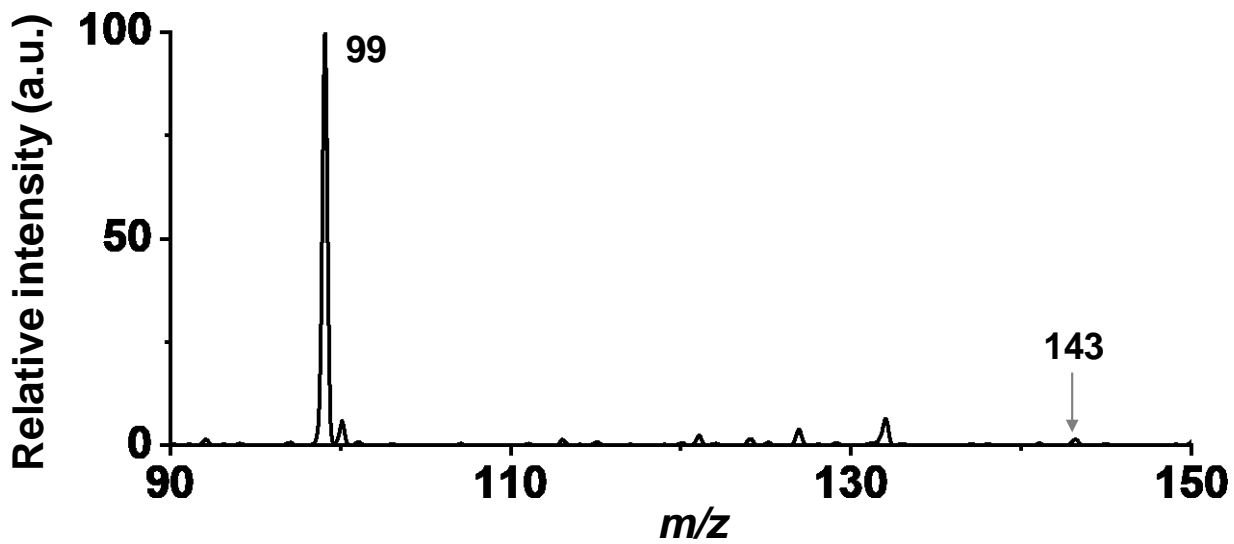


Figure S11. Microdroplet reaction mass spectrometry between AcAc and CO₂ using ambient air nebulization. The experiment was performed using a compressed air cylinder. The CR was 1.4 %.

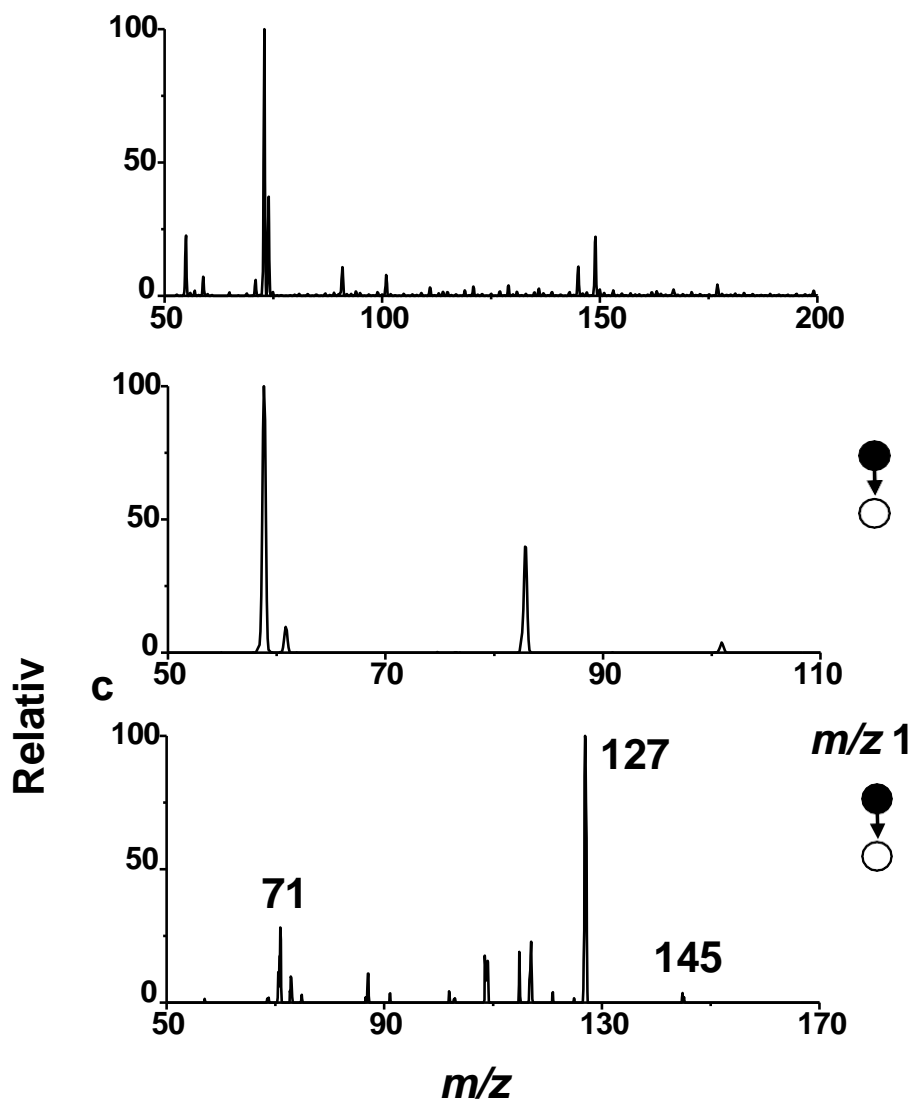


Figure S12. Positive ion mode microdroplet reaction mass spectrometry. a) Mass spectrum of reaction mixture between aqueous AcAc and CO_2 as nebulization gas. b) MS/MS of the reagent peak at m/z 101, showing characteristic loss of CH_2CO and H_2O , respectively. c) MS/MS of the peak at m/z 145, showing a major loss of a water molecule and a loss resulting in a peak at m/z 71. This confirms that the peak at m/z 145 does not correspond to the product.

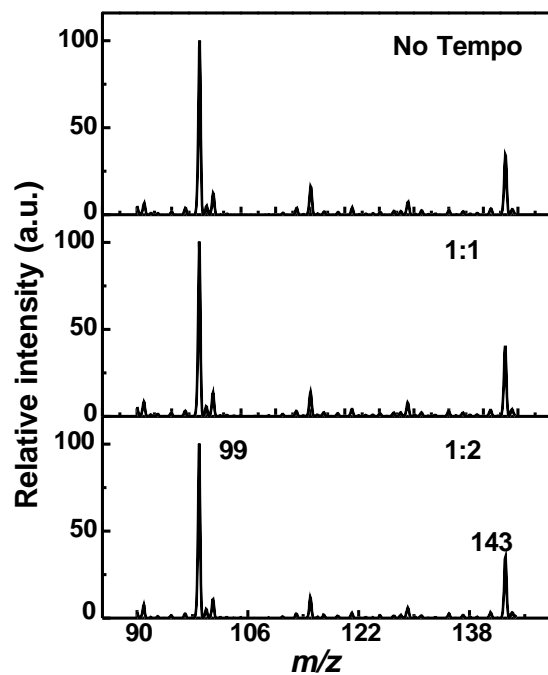


Figure S13. Effect of a radical scavenger i.e., TEMPO on the droplet carboxylation reaction. Mass spectra showing no effect of TEMPO addition with 1:1 and 1:2 ratios of AcAc, confirms that the reaction does not proceed via a radical pathway.

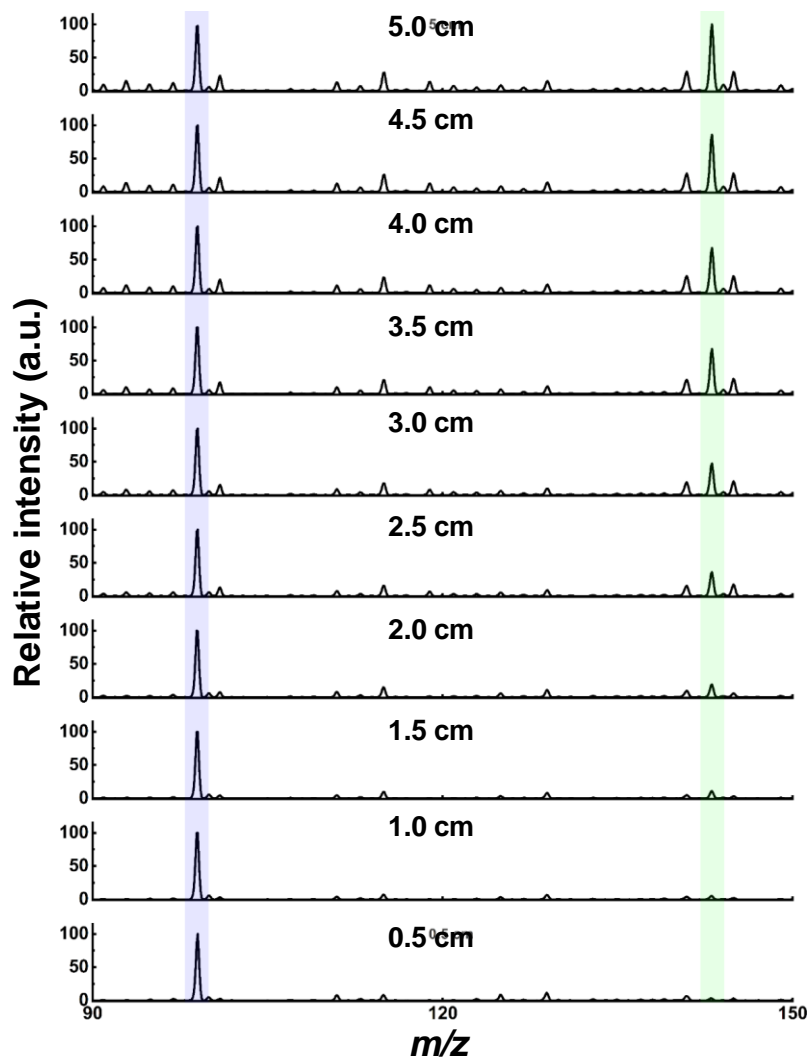


Figure S14. Microdroplet reaction mass spectrometry of reaction between aqueous AcAc and $(\text{NH}_4)_2\text{CO}_3$. Here tip-to-inlet distance is varied from 0.5 cm up to 5 cm. Negative ion mass spectrums are recorded in gradually increasing distance showing the decrease of the substrate (m/z 99) and increase of the product (m/z 143).

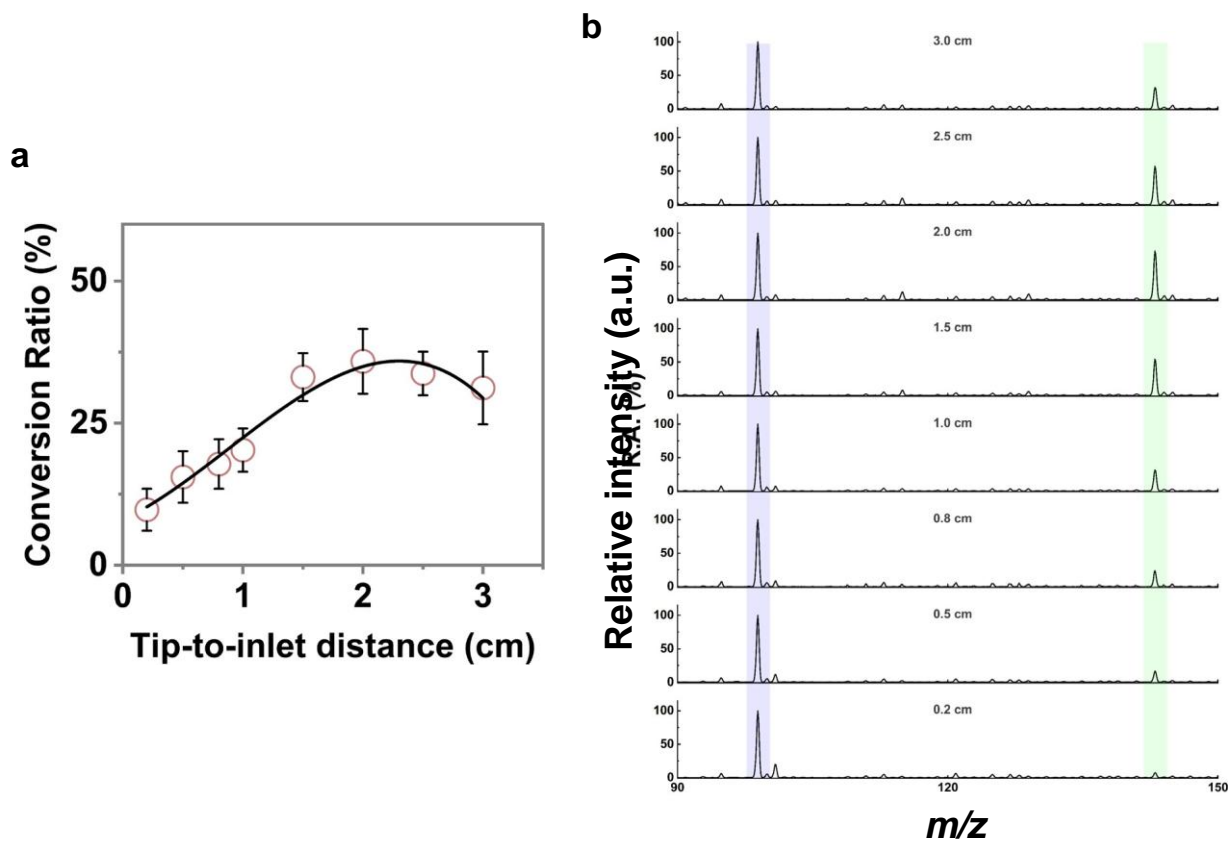


Figure S15. Microdroplet reaction mass spectrometry of reaction between aqueous AcAc and $\text{CO}_2(\text{g})$. Here tip-to-inlet distance varies from 0.2 cm up to 3 cm. a) Change of the conversion ratio of the product ($m/z=143$) vs distance. b) Negative ion mass spectrums are recorded at gradually increasing distances showing the increase of the product (m/z 143).

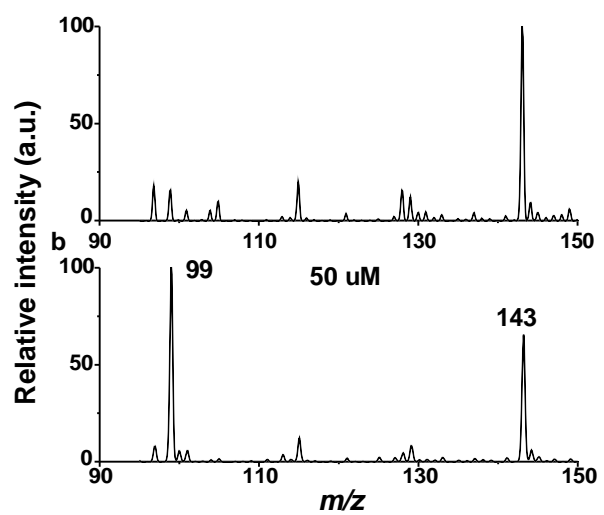


Figure S16. Electrospray emitter tip diameter variation experiments. Online mass spectra collected using two different tip diameter such as a) 15 μm and b) 50 μm , respectively.

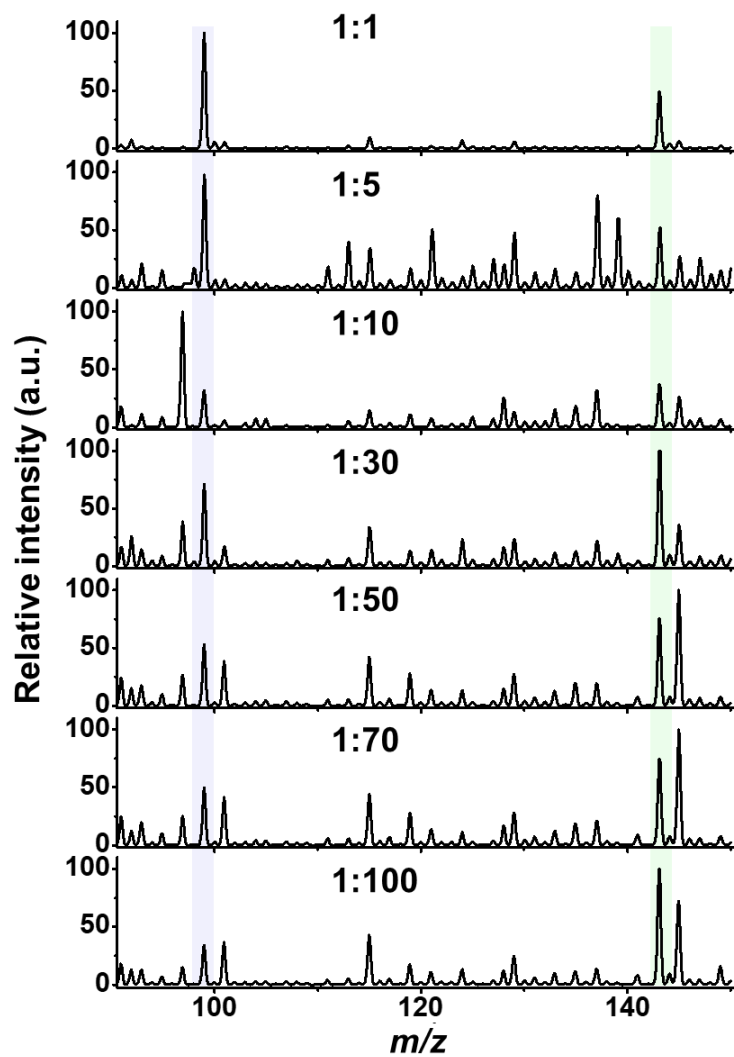


Figure S17. Mass spectra of reaction mixture containing AcAc and $(\text{NH}_4)_2\text{CO}_3$ at varying bulk ratios of both the reagents.

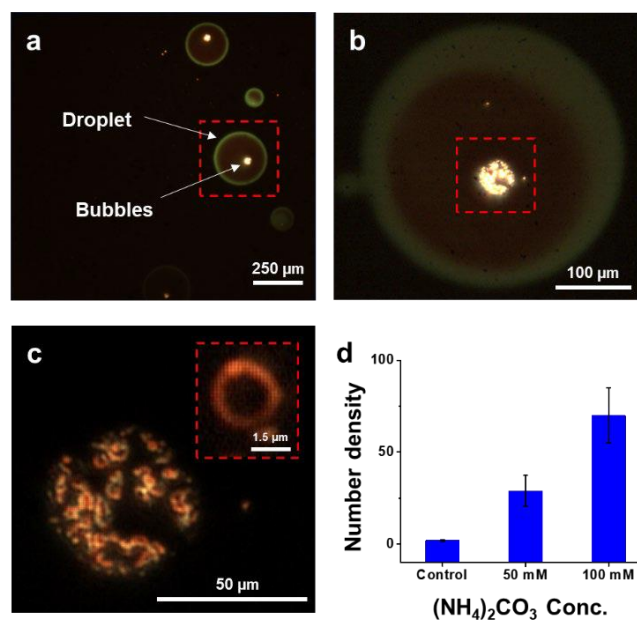


Figure S18. Dark field microscopic images of microdroplets (a) Images of droplet taken on a clean glass slide. (b) Zoomed image of deposited microdroplets shows the aggregated microbubbles inside the microdroplet (indicated in red box), (c) Zoomed image of aggregation of microbubbles inside of the microdroplets, (d) Graph of number density of microbubbles vs $(\text{NH}_4)_2\text{CO}_3$ clearly indicates the increase in number of microbubbles with increase of $(\text{NH}_4)_2\text{CO}_3$ concentration.

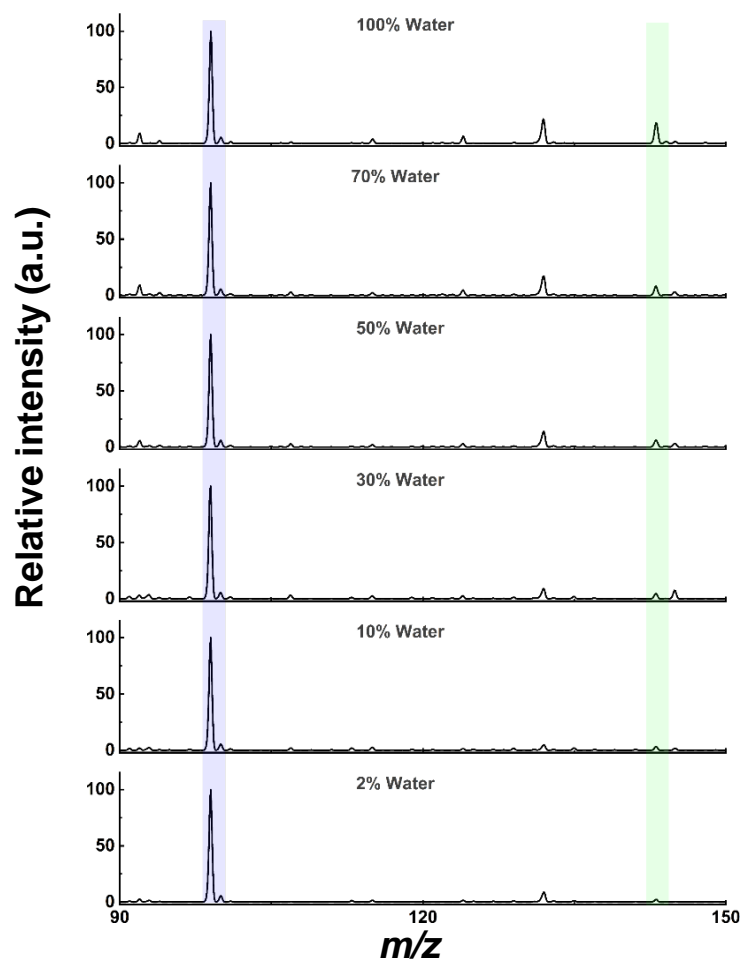


Figure S19. Mass spectrums of the reaction between AcAc and $(\text{NH}_4)_2\text{CO}_3$ for different solvent compositions (water-methanol mixture). The increase of the percentage of water in the methanol (from 2% to 100%) shows a gradual increment of relative abundance of product in the spectrum.

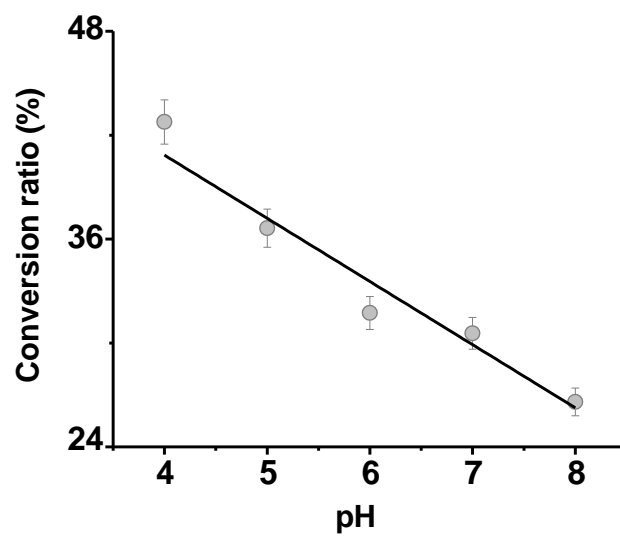


Figure S20. Effect of pH on the reagent to product conversion ratio. Acidic and basic pH solutions were achieved by adding HCl and NaOH, respectively.

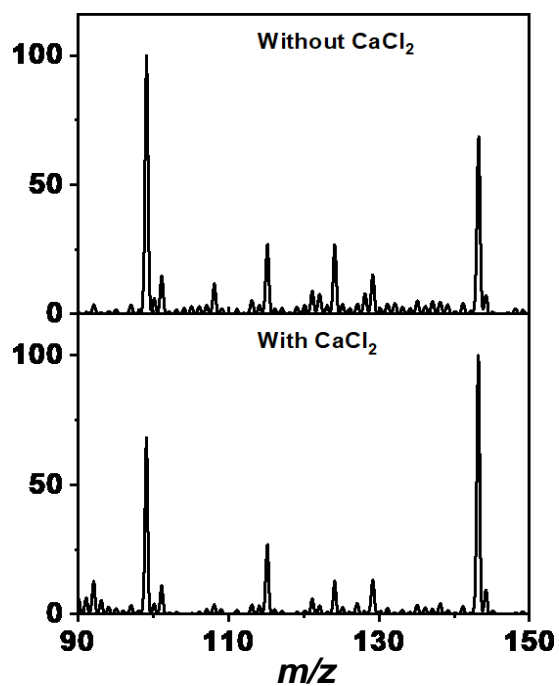


Figure S21. Effect of ionic strength on our microdroplet carboxylation reaction. Ionic strength of the solution was increased by adding a non-interactive salt CaCl₂ in the reaction mixture in equimolar ratio with the reagents having 3 mM final concentration of each reagent.

Supporting information 3

First-principles density functional theory calculations were conducted to understand the reaction mechanism of converting ketones to ketone carboxylates. Specifically, the reaction barrier for the formation of a C-C bond between the ketone and carbon dioxide molecules was examined. To this end, we optimized the geometries of the reactants, products, intermediates, and transition states at the wB97XD/6-31+g(d,p)^[1] level of theory as implemented in the Gaussian16 suite of programs.^[2] Furthermore, vibrational analysis was carried out for all the optimized geometries to confirm the nature of the minimum, i.e., the presence of a single imaginary frequency for transition states, and the absence of imaginary frequencies for intermediates. We included the solvent effects by considering the well-established SMD solvation model, which is a continuum solvation model based on the solute's electron density.^[3] Finally, to include the effects of hydrogen bonding, we have considered up to three explicit water molecules in our simulations. Free energies of all the complexes were computed at 300 K. Optimized cartesian coordinates of all the complexes are given below.

Cartesian coordinates for all the intermediates and transition states optimized using wB97xD/6-31+g(d,p)

Complex 1 (with 1 H₂O)

C	-2.30671500	-1.13201100	-0.38817600
H	-2.26103700	-1.74819700	-1.29060900
H	-2.73499500	-0.16476500	-0.67778900
H	-2.93987900	-1.60019500	0.36633800
C	-0.93227700	-0.88541300	0.15066500
C	0.12277000	-0.49935000	-0.86990500
H	0.35613000	-1.40166300	-1.44671300
C	1.35893800	0.07116300	-0.21208300
C	2.51771300	-0.84166100	0.00780800
H	3.31642500	-0.34327300	0.55769100
H	2.17465900	-1.73060900	0.54863500
H	2.88562500	-1.18611500	-0.96532600
O	-0.66609500	-0.97690200	1.34220700
O	1.37714600	1.24942800	0.13350200
O	-1.09158900	2.66504400	0.06100400
H	-1.76470400	1.98020000	-0.02188200
H	-0.24436300	2.18170100	0.06395100
H	-0.30613000	0.23598300	-1.55785400

Complex TS_{1/2} (with 1 H₂O)

C	-2.54165500	-0.91122200	-0.45655700
H	-2.96840200	-1.67872300	0.19836400
H	-2.33936900	-1.35697500	-1.43247800
H	-3.28775800	-0.11851500	-0.56566400
C	-1.30150300	-0.34447800	0.20267300
C	-0.04286500	-0.64511300	-0.40972700
H	-0.06953800	-1.36299900	-1.22301100
C	1.23964400	-0.38317600	0.16074600
C	2.40844800	-1.20980800	-0.32082700
H	3.30646200	-0.59053900	-0.38880000
H	2.59724800	-1.99748000	0.41809200
H	2.21192300	-1.68902400	-1.28219800
O	-1.45574000	0.34573400	1.24172600
O	1.46147400	0.51803200	1.01733300
O	0.23137500	2.12238800	-0.87844900
H	-0.61190300	2.60517500	-0.81631600
H	0.66610400	2.13329100	0.00536400
H	0.02595200	1.12933300	-1.01608200

Complex 2 (with 1 H₂O)

C	-2.19744200	-1.56155600	-0.30656400
H	-1.88718200	-2.55377600	-0.63928600
H	-2.65699900	-1.04419000	-1.15721500
H	-2.94588700	-1.64267300	0.48452200
C	-1.03594100	-0.73983600	0.16460400
C	0.27689800	-1.02774900	-0.32970100
H	0.41761600	-1.84817800	-1.02189400
C	1.36691200	-0.28663900	0.05128200
C	2.75178600	-0.52729300	-0.43422400
H	3.40700100	-0.73710300	0.41711800
H	2.78508000	-1.36386400	-1.13235300
H	3.12758700	0.37458300	-0.92776800
O	-1.24315900	0.21827400	0.96086700
O	1.26166900	0.72519700	0.90819100
O	-1.03860900	2.61259000	-0.75407800
H	-1.28008800	1.89145200	-0.15337200
H	0.29951300	0.78741100	1.15983100

H	-0.07914000	2.54629600	-0.82180300
---	-------------	------------	-------------

Complex 1 (with 2 H₂O)

C	-2.30671500	-1.13201100	-0.38817600
H	-2.26103700	-1.74819700	-1.29060900
H	-2.73499500	-0.16476500	-0.67778900
H	-2.93987900	-1.60019500	0.36633800
C	-0.93227700	-0.88541300	0.15066500
C	0.12277000	-0.49935000	-0.86990500
H	0.35613000	-1.40166300	-1.44671300
C	1.35893800	0.07116300	-0.21208300
C	2.51771300	-0.84166100	0.00780800
H	3.31642500	-0.34327300	0.55769100
H	2.17465900	-1.73060900	0.54863500
H	2.88562500	-1.18611500	-0.96532600
O	-0.66609500	-0.97690200	1.34220700
O	1.37714600	1.24942800	0.13350200
O	-1.09158900	2.66504400	0.06100400
H	-1.76470400	1.98020000	-0.02188200
H	-0.24436300	2.18170100	0.06395100
H	-0.30613000	0.23598300	-1.55785400

Complex TS_{1/2} (with 2 H₂O)

C	-2.54165500	-0.91122200	-0.45655700
H	-2.96840200	-1.67872300	0.19836400
H	-2.33936900	-1.35697500	-1.43247800
H	-3.28775800	-0.11851500	-0.56566400
C	-1.30150300	-0.34447800	0.20267300
C	-0.04286500	-0.64511300	-0.40972700
H	-0.06953800	-1.36299900	-1.22301100
C	1.23964400	-0.38317600	0.16074600
C	2.40844800	-1.20980800	-0.32082700
H	3.30646200	-0.59053900	-0.38880000
H	2.59724800	-1.99748000	0.41809200
H	2.21192300	-1.68902400	-1.28219800
O	-1.45574000	0.34573400	1.24172600
O	1.46147400	0.51803200	1.01733300
O	0.23137500	2.12238800	-0.87844900
H	-0.61190300	2.60517500	-0.81631600
H	0.66610400	2.13329100	0.00536400
H	0.02595200	1.12933300	-1.01608200

Complex 2 (with 2 H₂O)

C	-2.19744200	-1.56155600	-0.30656400
H	-1.88718200	-2.55377600	-0.63928600
H	-2.65699900	-1.04419000	-1.15721500
H	-2.94588700	-1.64267300	0.48452200
C	-1.03594100	-0.73983600	0.16460400
C	0.27689800	-1.02774900	-0.32970100
H	0.41761600	-1.84817800	-1.02189400
C	1.36691200	-0.28663900	0.05128200
C	2.75178600	-0.52729300	-0.43422400
H	3.40700100	-0.73710300	0.41711800
H	2.78508000	-1.36386400	-1.13235300
H	3.12758700	0.37458300	-0.92776800
O	-1.24315900	0.21827400	0.96086700
O	1.26166900	0.72519700	0.90819100
O	-1.03860900	2.61259000	-0.75407800
H	-1.28008800	1.89145200	-0.15337200
H	0.29951300	0.78741100	1.15983100
H	-0.07914000	2.54629600	-0.82180300

Complex 1 (with 3 H₂O)

C	-2.30671500	-1.13201100	-0.38817600
H	-2.26103700	-1.74819700	-1.29060900
H	-2.73499500	-0.16476500	-0.67778900
H	-2.93987900	-1.60019500	0.36633800
C	-0.93227700	-0.88541300	0.15066500
C	0.12277000	-0.49935000	-0.86990500
H	0.35613000	-1.40166300	-1.44671300
C	1.35893800	0.07116300	-0.21208300
C	2.51771300	-0.84166100	0.00780800
H	3.31642500	-0.34327300	0.55769100
H	2.17465900	-1.73060900	0.54863500
H	2.88562500	-1.18611500	-0.96532600
O	-0.66609500	-0.97690200	1.34220700
O	1.37714600	1.24942800	0.13350200
O	-1.09158900	2.66504400	0.06100400
H	-1.76470400	1.98020000	-0.02188200
H	-0.24436300	2.18170100	0.06395100
H	-0.30613000	0.23598300	-1.55785400

Complex TS_{1/2} (with 3 H₂O)

C	-2.54165500	-0.91122200	-0.45655700
H	-2.96840200	-1.67872300	0.19836400
H	-2.33936900	-1.35697500	-1.43247800
H	-3.28775800	-0.11851500	-0.56566400
C	-1.30150300	-0.34447800	0.20267300
C	-0.04286500	-0.64511300	-0.40972700
H	-0.06953800	-1.36299900	-1.22301100
C	1.23964400	-0.38317600	0.16074600
C	2.40844800	-1.20980800	-0.32082700
H	3.30646200	-0.59053900	-0.38880000
H	2.59724800	-1.99748000	0.41809200
H	2.21192300	-1.68902400	-1.28219800
O	-1.45574000	0.34573400	1.24172600
O	1.46147400	0.51803200	1.01733300
O	0.23137500	2.12238800	-0.87844900
H	-0.61190300	2.60517500	-0.81631600
H	0.66610400	2.13329100	0.00536400
H	0.02595200	1.12933300	-1.01608200

Complex 2 (with 3 H₂O)

C	-2.19744200	-1.56155600	-0.30656400
H	-1.88718200	-2.55377600	-0.63928600
H	-2.65699900	-1.04419000	-1.15721500
H	-2.94588700	-1.64267300	0.48452200
C	-1.03594100	-0.73983600	0.16460400
C	0.27689800	-1.02774900	-0.32970100
H	0.41761600	-1.84817800	-1.02189400
C	1.36691200	-0.28663900	0.05128200
C	2.75178600	-0.52729300	-0.43422400
H	3.40700100	-0.73710300	0.41711800
H	2.78508000	-1.36386400	-1.13235300
H	3.12758700	0.37458300	-0.92776800
O	-1.24315900	0.21827400	0.96086700
O	1.26166900	0.72519700	0.90819100
O	-1.03860900	2.61259000	-0.75407800
H	-1.28008800	1.89145200	-0.15337200
H	0.29951300	0.78741100	1.15983100
H	-0.07914000	2.54629600	-0.82180300

Complex 3 (with 3 H₂O)

C	2.25346900	0.72328500	1.85411900
H	1.71734500	0.96571100	2.77355600
H	2.68072800	1.62430500	1.40976400
H	3.07569700	0.04398800	2.10932200
C	1.37032300	0.02863700	0.86660700
C	0.27425100	-0.76484200	1.33332000
H	0.09631100	-0.85261100	2.39744000
C	-0.58063500	-1.39358500	0.46546600
C	-1.75588600	-2.20126200	0.88226400
H	-1.85432200	-2.22267300	1.96748000
H	-2.66381200	-1.77793900	0.43997600
H	-1.64904600	-3.22295300	0.50409000
O	1.61885400	0.13345500	-0.36842600
O	-0.43024000	-1.30185200	-0.85511200
C	-1.80708800	1.68975700	0.45598500
O	-2.65922400	1.22706900	1.10212800
O	-0.95949100	2.16499300	-0.18604200
O	-2.85046400	-0.13456400	-2.00505700
H	-3.45014200	-0.16803600	-1.25116600
H	-2.03104700	-0.53784200	-1.67808300
H	0.36890000	-0.72882400	-1.01839700
O	2.26357500	2.68228100	-1.36708500
H	1.42255200	3.13866100	-1.25444500
H	2.10620500	1.78957700	-1.00693900
O	2.68259900	-2.52500400	-1.13524000
H	1.80973200	-2.92778900	-1.06029800
H	2.51942100	-1.58653400	-0.96020600

Complex 4 (with 3 H₂O)

C	0	2.49034200	2.07666800	-0.53848700
H	0	2.22111900	3.05177200	-0.94681600
H	0	2.90953900	1.46167600	-1.34291700
H	0	3.26920800	2.19756300	0.22005000
C	0	1.31625700	1.34226700	0.06138100
C	0	0.03012600	1.88179600	-0.15621400
H	0	0.02532400	2.81816000	-0.70269400
C	0	-1.25097300	1.33337100	0.06722600
C	0	-2.43141700	2.04666200	-0.54546300
H	0	-2.81944500	1.42988400	-1.36469100
H	0	-3.22744900	2.14203700	0.19846600
H	0	-2.17680300	3.03088700	-0.94106900
O	0	1.60512600	0.26174500	0.67753700
O	0	-1.52982700	0.25829400	0.69725600
C	0	-0.03572100	-1.82330100	-0.72853100
O	0	-0.02282700	-1.18119500	-1.70075300
O	0	-0.04583900	-2.50478800	0.21647500
O	-1	0.04759600	-0.35784400	2.48007700
H	-1	-0.75622200	-0.19507300	1.93467000
H	-1	0.03798200	-1.29592300	2.77670800
H	-1	0.85077500	-0.20453200	1.93313200
O	0	-3.45940500	-1.38515000	-0.40717900
H	0	-3.81581200	-0.89012600	-1.15284000
H	0	-2.80852600	-0.77854300	0.00286000
O	0	3.38722700	-1.50261400	-0.48915000
H	0	2.79090700	-0.84494200	-0.07554000
H	0	2.93131800	-1.77521200	-1.29289800

Complex TS_{4/5} (with 3 H₂O)

C	0	2.39775200	-1.79099900	-0.58133800
H	0	2.34382000	-2.23545600	0.41652900

H	0	3.36025200	-1.29720800	-0.72081800
H	0	2.30236600	-2.60621500	-1.30717900
C	0	1.27142800	-0.81395900	-0.79255800
C	0	-0.02146500	-1.25348200	-0.33130800
H	0	-0.00207500	-2.28844600	-0.00426000
C	0	-1.34586900	-0.85000900	-0.74441800
C	0	-2.43813200	-1.84667900	-0.45628300
H	0	-3.41700700	-1.37901100	-0.56977800
H	0	-2.35397900	-2.68215300	-1.16014900
H	0	-2.33190000	-2.25762300	0.55182100
O	0	1.55502500	0.29739900	-1.30770700
O	0	-1.67416300	0.23463300	-1.28232300
C	0	0.03695800	-0.34435000	1.59949800
O	0	-0.04177100	0.83470000	1.41550900
O	0	0.13401300	-1.26612500	2.35100000
O	-1	-0.08741600	2.15476100	-1.40267900
H	-1	-0.88794200	1.59377000	-1.34285900
H	-1	-0.08810600	2.78866700	-0.65521500
H	-1	0.70824300	1.58764500	-1.33882800
O	0	-2.93365000	1.71329600	0.88962800
H	0	-2.07296900	1.59142600	1.31222300
H	0	-2.83797400	1.22783700	0.05646400
O	0	3.12839100	1.62055500	0.73902200
H	0	2.74545900	1.20671500	-0.05110600
H	0	2.48435500	1.43317100	1.43198000

Complex 5 (with 3 H₂O)

C	0	2.60458000	0.97642600	1.01280200
H	0	3.31069200	0.58866800	0.26970800
H	0	2.99531900	0.82281400	2.01857000
H	0	2.48259500	2.04539300	0.80492900
C	0	1.29535900	0.28078900	0.83551200
C	0	0.56217900	0.55840700	-0.48021700
H	0	1.32622000	0.78461600	-1.23128000
C	0	-0.32783900	1.79742500	-0.33480500
C	0	-0.05596500	2.93033800	-1.26052800
H	0	-0.75467400	3.75051700	-1.09699800
H	0	0.97621200	3.26726700	-1.11111600
H	0	-0.12267000	2.56619000	-2.29174900
O	0	0.83281300	-0.45864300	1.69590600
O	0	-1.22121300	1.85002200	0.50660600
C	0	-0.23375600	-0.65075200	-1.03679900
O	0	-1.36533100	-0.41581100	-1.53651000
O	0	0.32969000	-1.77142200	-0.99245800
O	-1	-1.82914300	-0.33413300	1.78875800
H	-1	-1.74509400	0.54659800	1.35441800
H	-1	-2.37995100	-0.91145700	1.21170200
H	-1	-0.93670300	-0.73660300	1.88471000
O	0	-3.12616700	-1.75557900	0.09573500
H	0	-2.62893600	-1.39641400	-0.67053600
H	0	-4.03745700	-1.46077700	-0.01945300
O	0	3.01353100	-2.28095000	-0.67270000
H	0	3.31229000	-1.83398600	0.12661900
H	0	2.06137300	-2.05650200	-0.74801400

Complex TS_{5/6} (with 3 H₂O)

C		2.70752400	0.94511200	0.89273800
H		3.38129800	0.57261700	0.11269900
H		3.14064200	0.76695500	1.87705400
H		2.58039100	2.01898900	0.71740700
C		1.39321300	0.24684600	0.75458800

C	0.59461800	0.57371300	-0.50887000
H	1.30397100	0.77731500	-1.31790700
C	-0.24610400	1.83501200	-0.26016100
C	-0.16418300	2.90886800	-1.29030700
H	-0.85099900	3.72445600	-1.06383400
H	0.86726600	3.27839500	-1.32544600
H	-0.38165800	2.48121700	-2.27471300
O	0.96631000	-0.52457600	1.60032800
O	-0.93672100	1.92879500	0.74587200
C	-0.30236000	-0.58229500	-0.97433800
O	-1.49346100	-0.26350200	-1.32651500
O	0.15880800	-1.73395300	-1.00392500
O	-1.89573500	-0.51871100	1.95038800
H	-1.71133500	0.37613200	1.60761700
H	-2.72447600	-1.23292600	0.81076800
H	-1.01095200	-0.92102500	1.93690700
O	-3.05684500	-1.60324900	-0.07733600
H	-2.39994700	-1.06079600	-0.78647100
H	-3.97689500	-1.32761700	-0.20166900
O	2.86178800	-2.38395500	-0.76984000
H	3.13562000	-2.08780300	0.10527200
H	1.91765900	-2.13623200	-0.83135700

Complex 6 (with 3 H₂O)

C	-2.60890200	1.72869900	-1.07581900
H	-1.90278300	2.04612200	-1.84820800
H	-3.02259200	2.59053800	-0.55184800
H	-3.41448600	1.18121900	-1.58009100
C	-1.95608400	0.79109200	-0.11528200
C	-1.08143200	-0.31727100	-0.72105100
H	-1.54112400	-0.66746300	-1.65262400
C	-0.98402700	-1.49684800	0.25062900
C	-2.17428500	-2.39643400	0.31446300
H	-2.11480100	-3.05074900	1.18433000
H	-3.10304900	-1.81970200	0.32676800
H	-2.18194100	-3.00138700	-0.60024900
O	-2.10255100	0.85824900	1.09406400
O	0.02080600	-1.68191000	0.91972800
C	0.29360900	0.23939900	-1.03797300
O	1.03501200	-0.58669400	-1.74230700
O	0.67344700	1.33777000	-0.65365100
O	2.63781000	-0.44280700	1.38735700
H	1.85981400	-0.97652500	1.15605100
H	3.33022800	-0.10010800	-0.23059400
H	2.23555200	0.37718700	1.73295700
O	3.50691500	0.04712900	-1.18865500
H	2.00015500	-0.29444100	-1.69851000
H	4.12454800	-0.64640600	-1.44899000
O	0.96071300	1.72926500	2.14606000
H	0.67370400	1.74217800	1.21743500
H	0.26630000	1.23970100	2.60300200

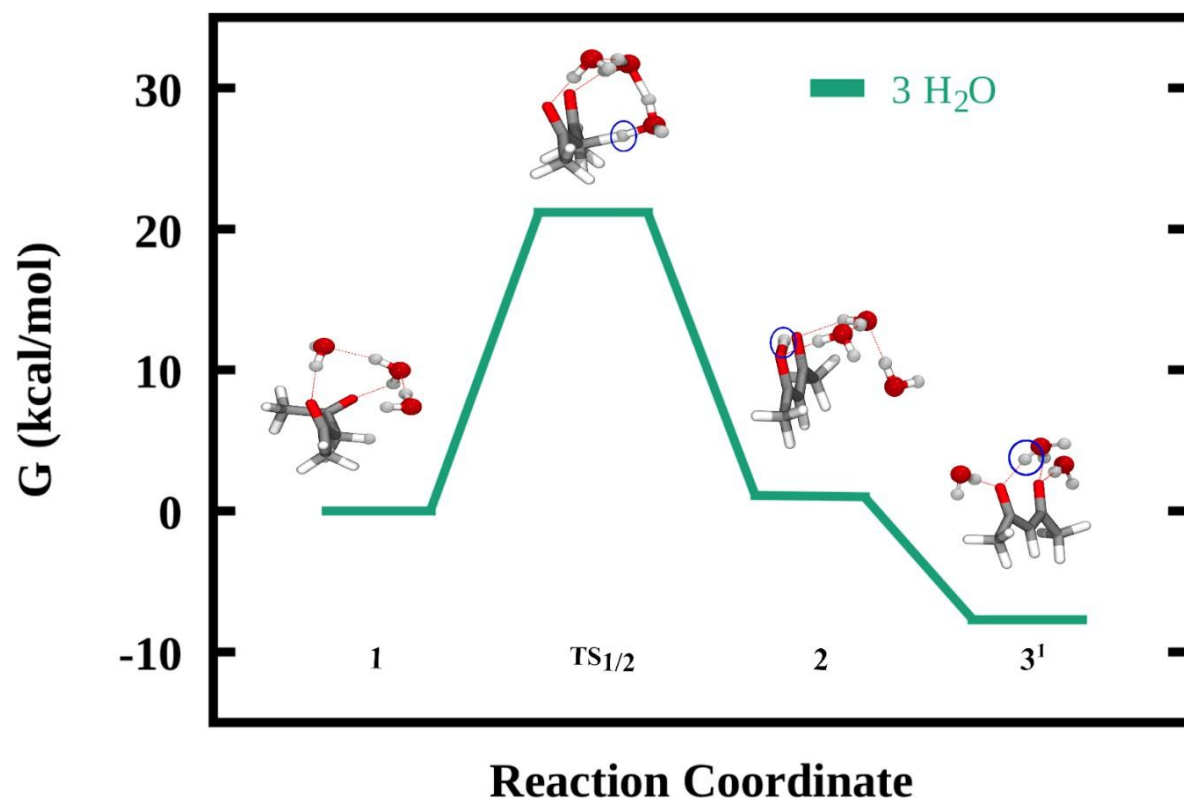


Figure S22. Free energy landscape for keto-enol transformation over AcAc.

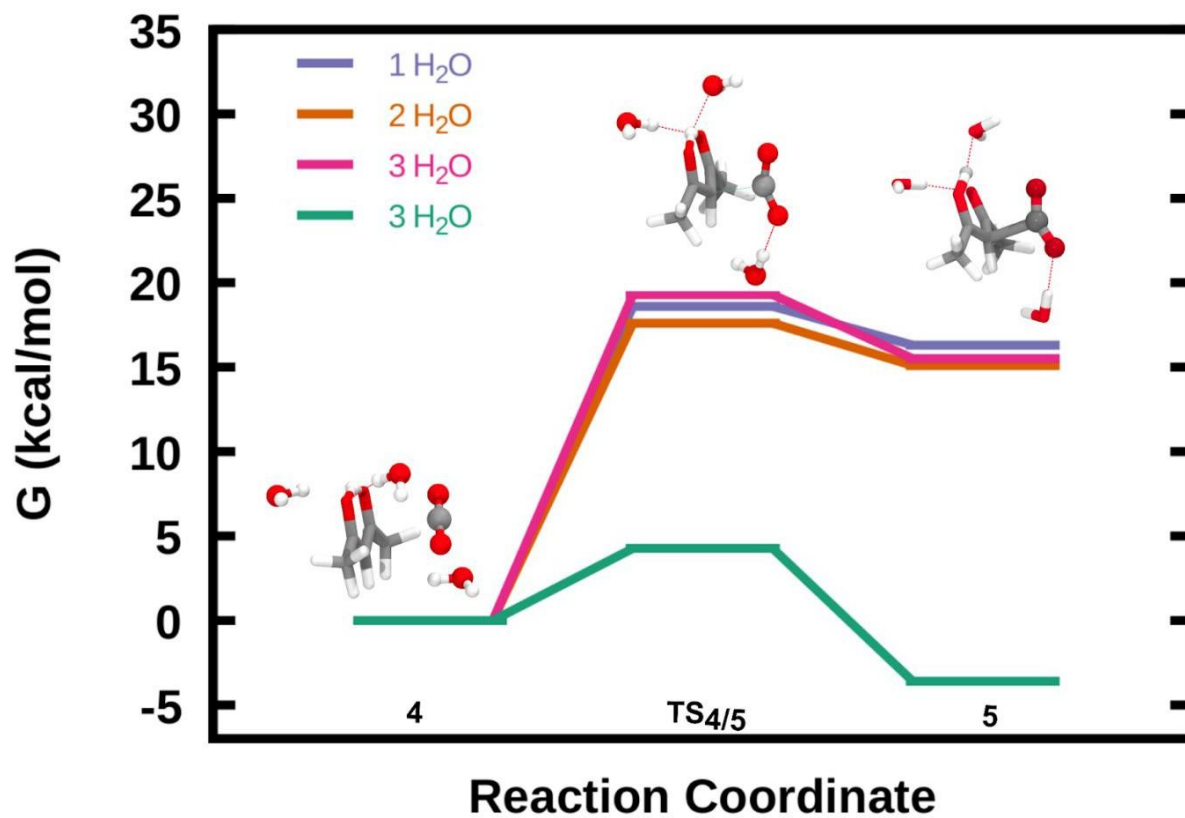


Figure S23: Free energy landscape for C-C bond formation in neutral and negatively charged microdroplets.

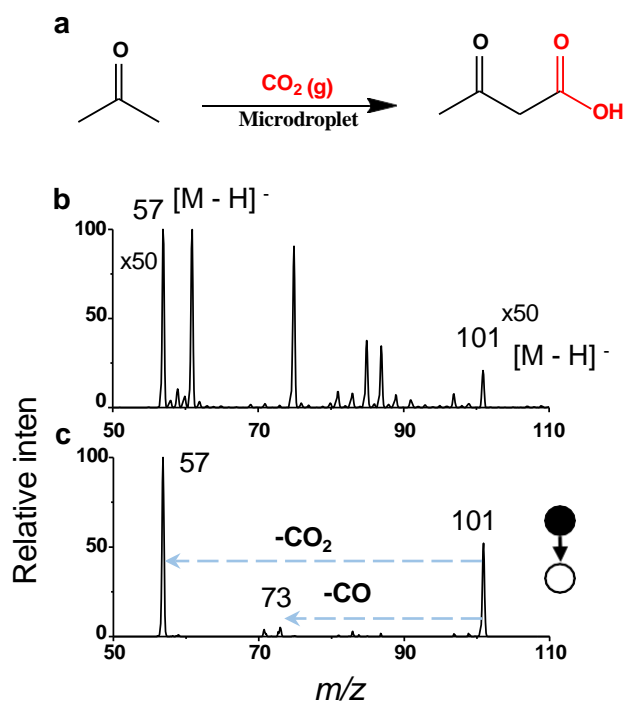


Figure S24. Microdroplet reaction mass spectrometry of reaction mixture containing 1:1 acetone and $(\text{NH}_4)_2\text{CO}_3$ ratio. a) Reaction scheme between acetone and $(\text{NH}_4)_2\text{CO}_3$ b) Negative ion mass spectrum of acetone and $(\text{NH}_4)_2\text{CO}_3$. shows the carboxylated product at m/z 101. The calculated CR is 17%. c) MS/MS spectrum of the product shows neutral losses at 57 and 73, which are CO_2 (m/z 44) and CO (m/z 28) losses, respectively.

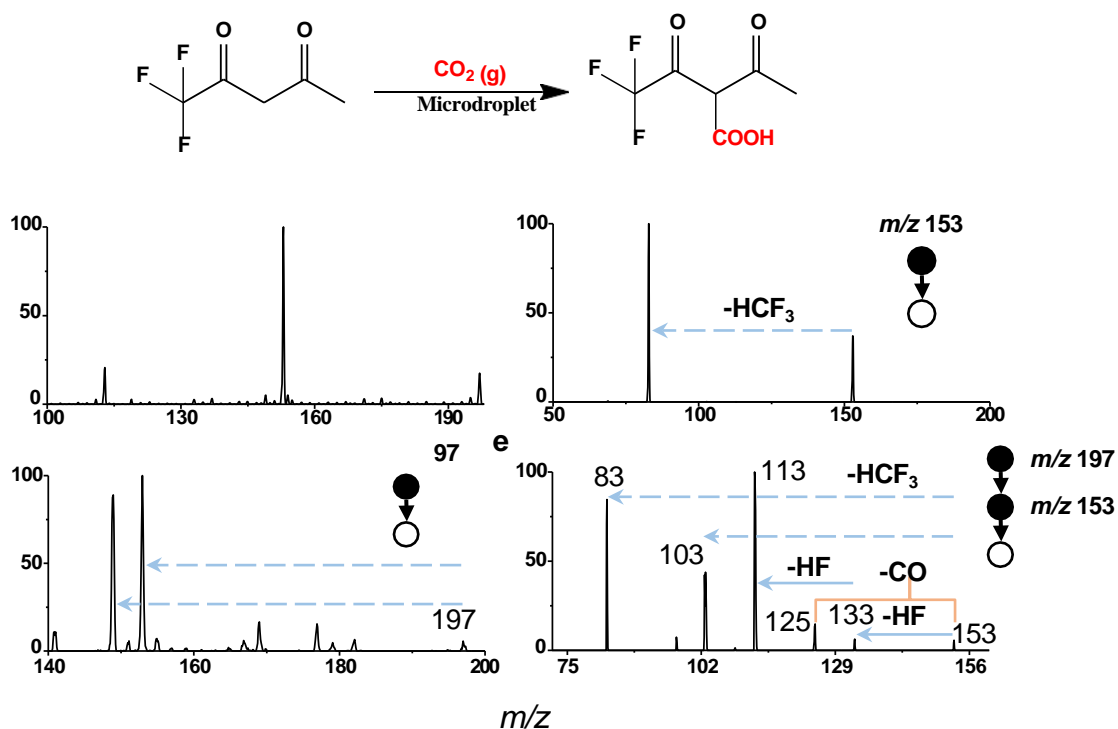


Figure S25. Microdroplet reaction mass spectrometry of reaction mixture containing 1:1 ratio of 1,1,1-trifluoro-5,5-dimethyl-2,4-hexanedione and $(\text{NH}_4)_2\text{CO}_3$. a) Reaction scheme between 1,1,1-trifluoro-5,5-dimethyl-2,4-hexanedione and $(\text{NH}_4)_2\text{CO}_3$. b) Negative ion mass spectrum of 1,1,1-trifluoro-5,5-dimethyl-2,4-hexanedione and $(\text{NH}_4)_2\text{CO}_3$ shows the carboxylated product at $m/z=191$ (the corresponding peak is zoomed to 10 times). The calculated CR is 1.7% c) MS/MS spectrum of the substrate (m/z 153) d) MS/MS spectrum of the product (m/z 197) e) MS/MS/MS spectrum of the product.

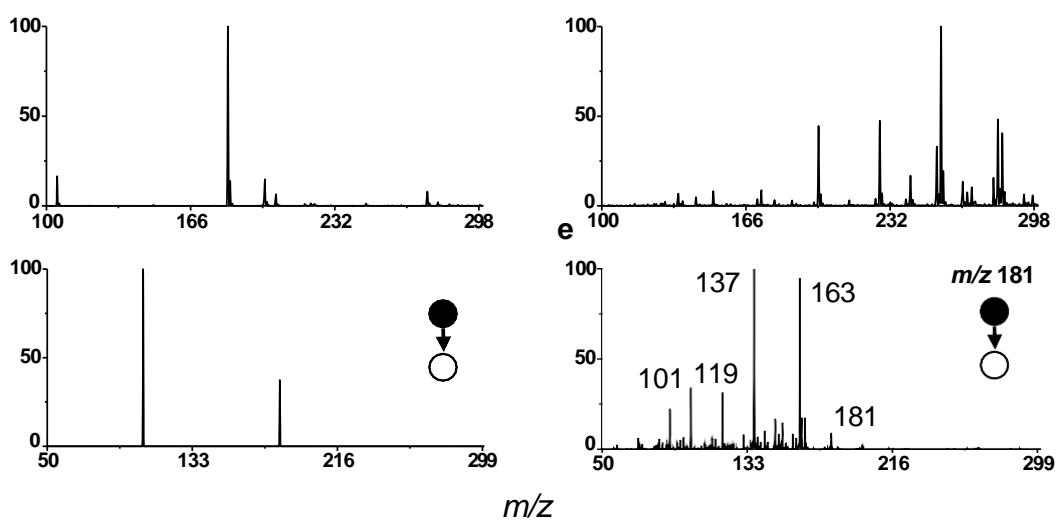
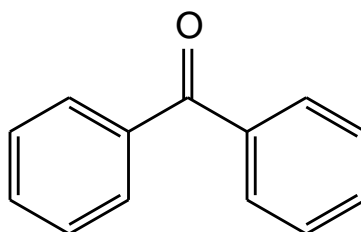


Figure S26. Microdroplet reaction mass spectrometry of reaction mixture containing 1:1 ratio of benzophenone and $(\text{NH}_4)_2\text{CO}_3$. a) Structure of benzophenone shows unavailability of sp^3 C-H. b) Positive ion mass spectrum of benzophenone and $(\text{NH}_4)_2\text{CO}_3$. shows the absence of carboxylated product c) MS/MS spectrum of benzophenone (m/z 183) in positive mode. d) Negative ion mass spectrum of benzophenone and $(\text{NH}_4)_2\text{CO}_3$ shows the absence of the peak for benzophenone itself as it is not ionized in negative mode. e) MS/MS spectrum for the m/z 181 does not correspond to the molecular ion of benzophenone.

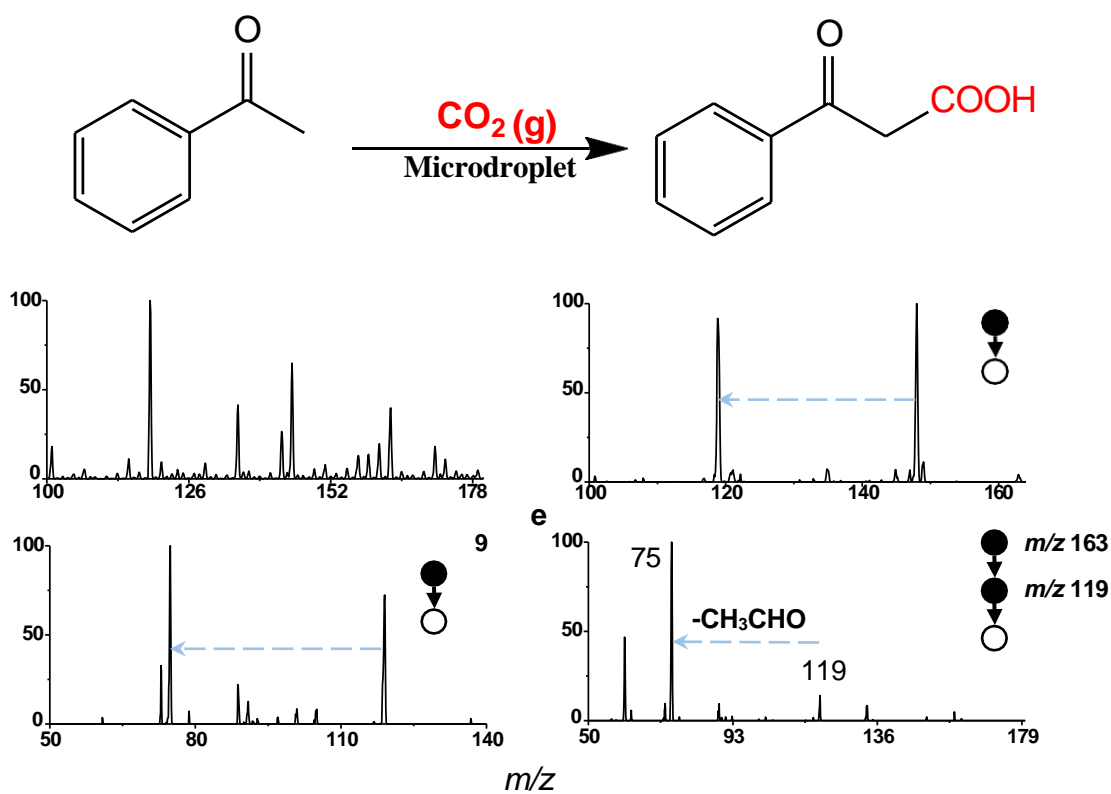


Figure S27. Microdroplet reaction mass spectrometry of reaction mixture containing 1:1 ratio of acetophenone and $(\text{NH}_4)_2\text{CO}_3$. a) Reaction scheme between acetophenone and $(\text{NH}_4)_2\text{CO}_3$. b) Negative ion mass spectrum of acetophenone and $(\text{NH}_4)_2\text{CO}_3$ shows the carboxylated product at m/z 163. The calculated CR is 28% c) MS/MS spectrum of the substrate (m/z 119). d) MS/MS spectrum of the product (m/z 163) e) MS/MS/MS spectrum of the product.

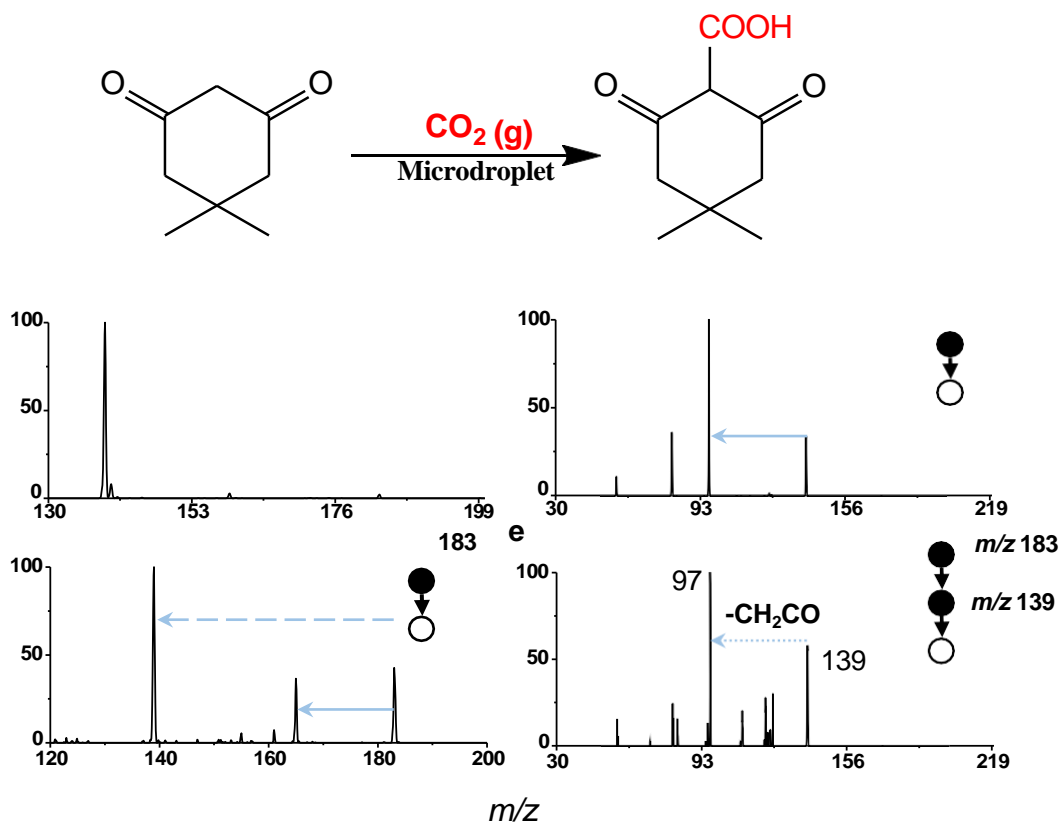


Figure S28. Microdroplet reaction mass spectrometry of reaction mixture containing 1:1 ratio of dimedone (5,5-dimethylcyclohexane-1,3-dione) and $(\text{NH}_4)_2\text{CO}_3$. a) Reaction scheme between dimedone and $(\text{NH}_4)_2\text{CO}_3$ b) Negative ion mass spectrum of dimedone and $(\text{NH}_4)_2\text{CO}_3$ shows the carboxylated product at m/z 183 (corresponding peak is zoomed to 100 times). The calculated CR is 0.02%. c) MS/MS spectrum of the substrate (m/z 139) d) MS/MS spectrum of the product (m/z 183) e) MS/MS/MS spectrum of the product.

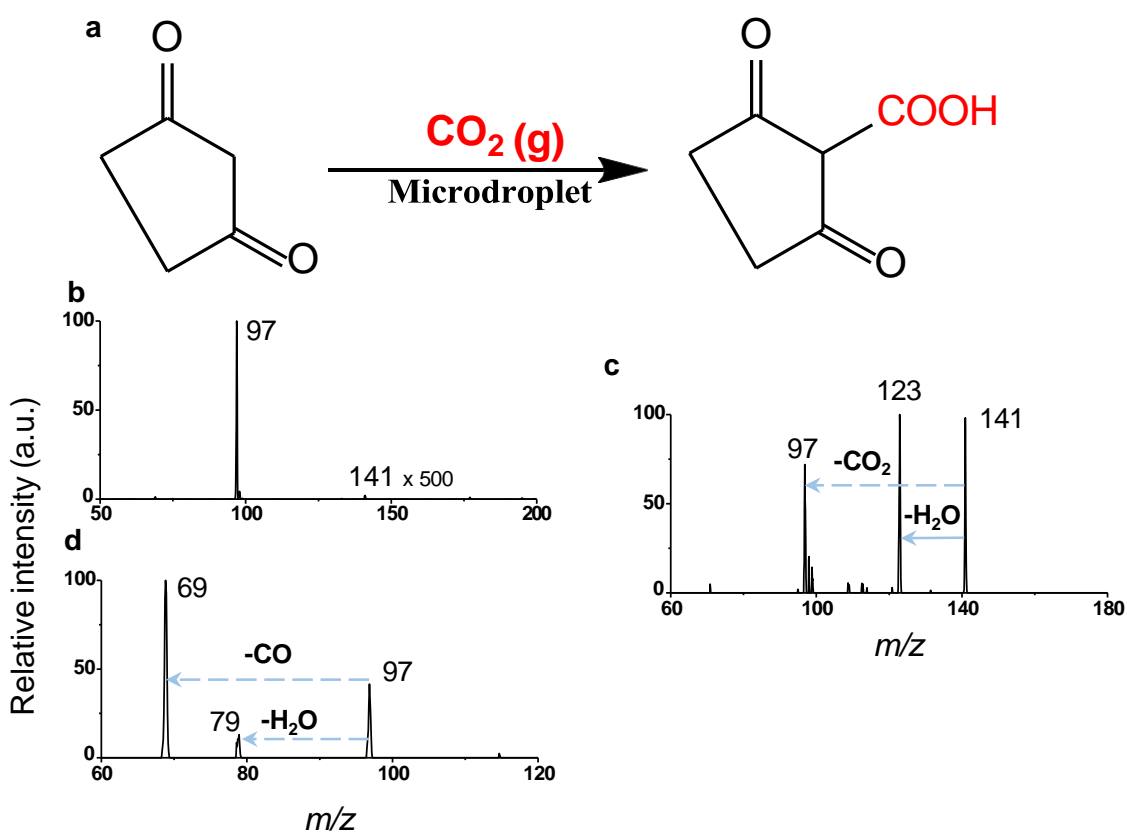
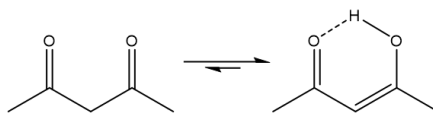


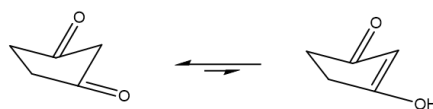
Figure S29. Microdroplet reaction mass spectrometry of reaction mixture containing 1:1 ratio of cyclopentane-1,3-dione and $(\text{NH}_4)_2\text{CO}_3$. a) Reaction scheme between of cyclopentane-1,3-dione and $(\text{NH}_4)_2\text{CO}_3$. b) Negative ion mass spectrum of cyclopentane-1,3-dione and $(\text{NH}_4)_2\text{CO}_3$. shows the carboxylated product at m/z 141 (the corresponding peak is zoomed to 500 times). The calculated CR is 0.008%. c) MS/MS spectrum of the substrate (m/z 139) d) MS/MS spectrum of the product (m/z 141).

Keto-enol tautomerism

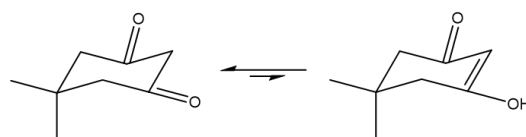
a) Acetylacetone



b) cyclopentane-1,3-dione



c) 5,5-dimethylcyclohexane-1,3-dione



Scheme S2. Scheme showing keto-enol tautomerism among a) AcAc, b) cyclopentane-1,3-dione, and c) 5,5-dimethyl-cyclohexane-1,3-dione, respectively.

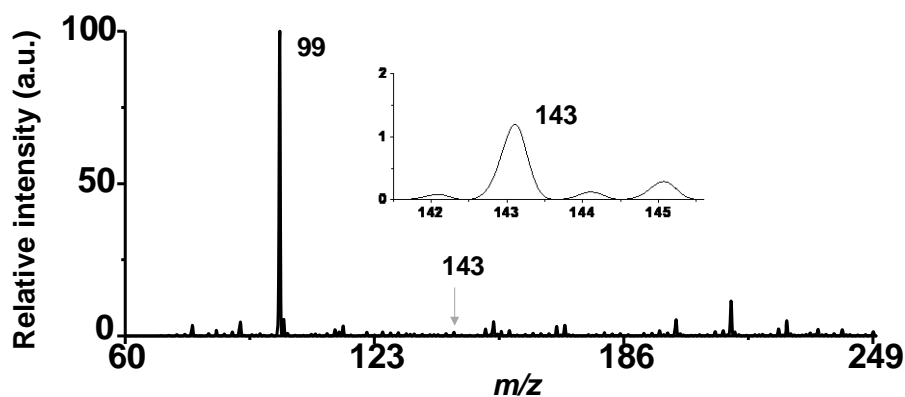


Figure S30. ESI MS spectrum of spray deposited sample after methanol extraction, showing low-intensity product peak. Inset displays a zoomed-in mass spec of the selected mass range showing the peak at m/z 143. This is due to the thermal decomposition of the product during extraction.

References

- [1] J.-D. Chai, M. Head-Gordon, *Phys. Chem. Chem. Phys.* **2008**, *10*, 6615–6620.
- [2] M. J. Frisch, G. W. Trucks, H. B. Schlegel, G. E. Scuseria, M. A. Robb, J. R. Cheeseman, G. Scalmani, V. Barone, G. A. Petersson, H. Nakatsuji, Gaussian 16, Revision C. 01. Gaussian, Inc., Wallingford CT. **2016**.
- [3] A. V. Marenich, C. J. Cramer, D. G. Truhlar, *J. Phys. Chem. B* **2009**, *113*, 6378–6396.

...

Author Contributions

P.B. planned the experiments. P.B., S.M., K.U., and B.K.S. helped in performing the experiments. K.S.S.V.P.R. and Y.S.S.R.K.C. helped with DFT calculations. The first draft of the manuscript was written by P.B. and it was finalized with the help of all the authors. The project was conceived under the guidance of T.P.

NANOPARTICLES

Spontaneous weathering of natural minerals in charged water microdroplets forms nanomaterials

B. K. Spoorthi¹, Koyendril Debnath², Pallab Basuri¹, Ankit Nagar¹, Umesh V. Waghmare², Thalappil Pradeep^{1,3*}

In this work, we show that particles of common minerals break down spontaneously to form nanoparticles in charged water microdroplets within milliseconds. We transformed micron-sized natural minerals like quartz and ruby into 5- to 10-nanometer particles when integrated into aqueous microdroplets generated via electro spray. We deposited the droplets on a substrate, which allowed nanoparticle characterization. We determined through simulations that quartz undergoes proton-induced slip, especially when reduced in size and exposed to an electric field. This leads to particle scission and the formation of silicate fragments, which we confirmed with mass spectrometry. This rapid weathering process may be important for soil formation, given the prevalence of charged aerosols in the atmosphere.

Nanoparticles of minerals exist naturally in soil, and some of them are essential for life (1). Microdroplets have been a topic of interest over the past decade, and the confined environment within them is known to cause chemical synthesis at an accelerated rate, as well as other processes such as the formation of nanoparticles (2). We decided to explore whether natural minerals could disintegrate in microdroplets, through a process opposite to chemical synthesis.

For our experiments, we prepared micron-scale particles of natural quartz (SiO_2) and ruby (Cr-substituted Al_2O_3) for use in an electro spray setup (Fig. 1, A and B). We ground commercial millimeter-sized quartz particles well using a

mortar and pestle and used centrifugation to separate the differently sized particles that formed. We carefully excluded all the particles smaller than 1 mm in size and used particles of 5 to 10 mm that were suspended in water for the experiment (Fig. 1C). Even after ultrasonication to detach any adhered particles, we found some smaller particles attached to a few larger ones (Fig. 1C). These adhering particles had dimensions greater than 100 nm (fig. S1). We took an optical image of the ground quartz powder and an optical microscopic image of the separated particles that we used for electro spray (fig. S2). We electro sprayed a suspension of about 0.1 mg/ml of the separated quartz particles through a capillary

tube that had an inner diameter of 50 mm at a flow rate of 0.5 ml/hour and observed the resulting plume (Fig. 1A). We collected the product of electro spray 1.5 cm away from the spray tip, which resulted in a flight time on the order of 10 ms, consistent with similar experiments (3, 4). The product that was deposited on a transmission electron microscopy (TEM) grid had only 5- to 10-nm-diameter particles (Fig. 1D) throughout the grid. Under higher magnification, particles of different morphologies were observed. The particles showed the (110) plane of quartz (inset of Fig. 1D). Sonication had no effect on the breaking of silica particles. Experimental methods are presented in the supplementary materials, including a video of the electro spray process (movie S1).

To ensure that our initial observations were truly representative of the process, we performed measurements on larger quantities of samples. We built a multinozzle electro spray unit composed of six nozzles. We electro sprayed 1 liter of the suspension that contained 100 mg of the crushed micron-sized particles discontinuously over a month at the optimized conditions (spray voltage and distance) and a 3 ml/hour flow rate, and a deposit

¹Department of Chemistry, Indian Institute of Technology Madras, Chennai 600036, India. ²Theoretical Sciences Unit, Jawaharlal Nehru Centre for Advanced Scientific Research, Bangalore 560064, India. ³International Centre for Clean Water, IIT Madras Research Park, Chennai 600113, India.

*Corresponding author. Email: pradeep@iitm.ac.in

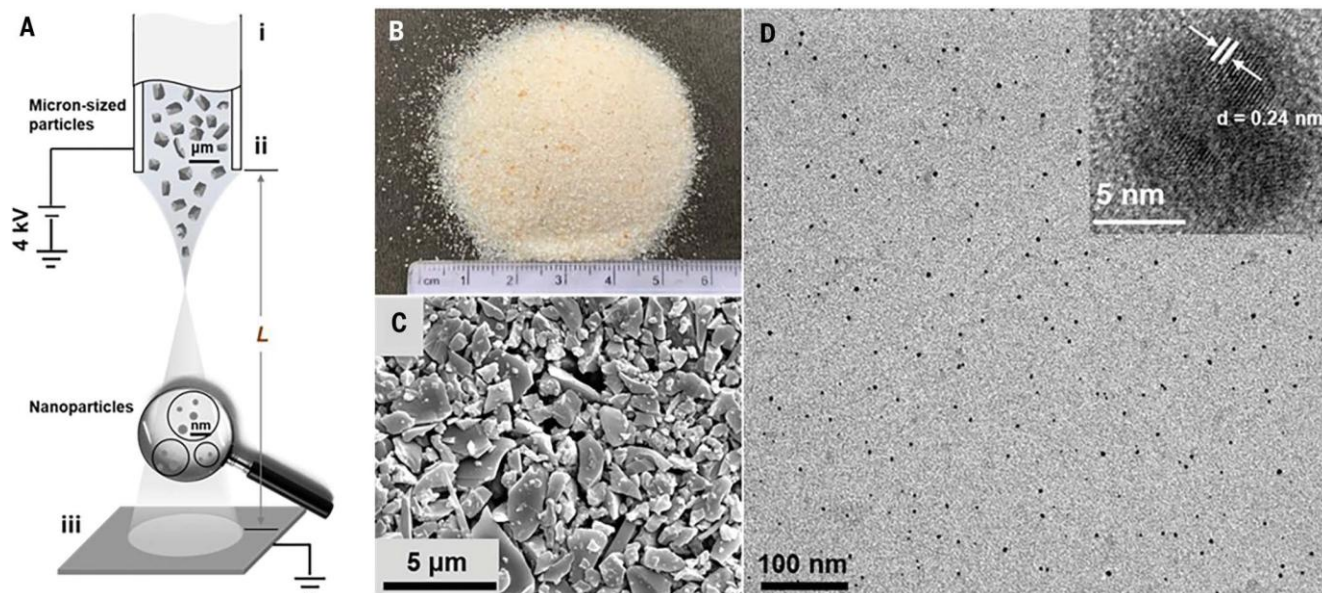


Fig. 1. Process of disintegration of natural quartz in microdroplets. (A) Schematic representation of the disintegration of mineral particles in microdroplets. Setup components include (i) the electro spray emitter, (ii) a spray capillary with a 50-μm inner diameter, and (iii) the conducting substrate at a distance of $L = 1.5$ cm from the tip of the emitter. (B) A photograph of the natural quartz. (C) Field-emission scanning electron microscopy (FESEM) image of

ground and separated natural quartz used for electro spray, showing that the size range of particles is between 1 and 5 μm. A few smaller particles that are naturally adhered to the micron-sized particles remain attached even after ultrasonication. (D) TEM image of natural quartz after electro spray with a high-resolution image of a particle shown in the inset. The plane shown is (110), where d is lattice spacing.

was collected on an aluminum sheet. The electro-spray-deposited particles were strongly adherent to the substrate. We scraped about 60 mg of the powder off the substrate for bulk analysis. This left about 20 mg on the substrate, which we determined gravimetrically. We avoided hard scratching to remove the remaining product on the substrate. This gave us a collection efficiency of ~80% for our electro-spray setup. We made x-ray diffraction measurements of the scraped-off powder using Cu K α radiation to confirm that it was made of quartz (fig. S3) in the form of nanoparticles of ~16-nm average diameter. We calculated the particle size using the Scherrer formula. Independent analysis, the details of which are presented in the supplementary materials, showed the collection yield of electro-spray deposition to be 81%.

We obtained similar experimental results with ruby (Fig. 2, A to C) and fused alumina (Fig. 2, D to F). These experiments show that both natural minerals and their synthetic analogs can be fragmented in charged microdroplets. The synthesis of materials using electro-spray requires optimized conditions (5). For our single-spray experiments, the electro-

spray voltage was 4.0 kV, the tip-to-collector distance was 1.5 cm, and particle loading was 0.1 mg/ml.

Optimized experimental parameters

In the case of silica, below a spray voltage of 2.5 kV, the spray did not occur. From 3.0 kV onward, the spray was uniform. This potential was the threshold at which the electric field breaks the limit of surface tension and forms a plume containing charged microdroplets from the tip of the emitter. The required potential for this varies for different solutions and suspensions. In our experiments, the threshold potential for a stable spray was higher than usual, mainly because we electro-sprayed a fine suspension of quartz. Below 2.5 kV, only micron-sized particles were seen in the outcome. We observed maximum fragmentation at the optimized conditions. Particles fragmented well at 4.5 kV. At 5.5 kV, we even observed finer nanostructures (fig. S4). We characterized the samples before and after electro-spray by Raman spectroscopy (fig. S5) and energy dispersive spectroscopy. We observed fragmentation only with positive applied potential.

Understanding the phenomenon To understand the mechanism of formation of quartz nanoparticles starting from larger particles, we used first-principles density functional theory calculations to determine the effects of reduced size, electric field, and pH on the processes of cleavage and slip in bulk and a (110) terminated slab of SiO₂. The α -SiO₂ structure of quartz belonging to the $P3_21$ (trigonal) space group was used. We chose the (110) plane because it was the one we observed with TEM. Cleavage and slip are two competing processes by which particles can break apart. We define bulk as meaning that the crystal has periodicity along all three directions. We define slab as the breaking of periodicity along the c axis, exposing the (110) surface. Cleavage across the (010) plane was introduced by subjecting the crystal to uniaxial tensile strain localized at a single (010) plane (by increasing the separation along the b direction) to create two separate constituents (Fig. 3A). We estimated the cleavage energy (two times the surface energy) as the difference between the total energy (E_{tot}) of a crystal cleaved along a specific plane and the total energy of the uncleaved relaxed crystal, which is the energy

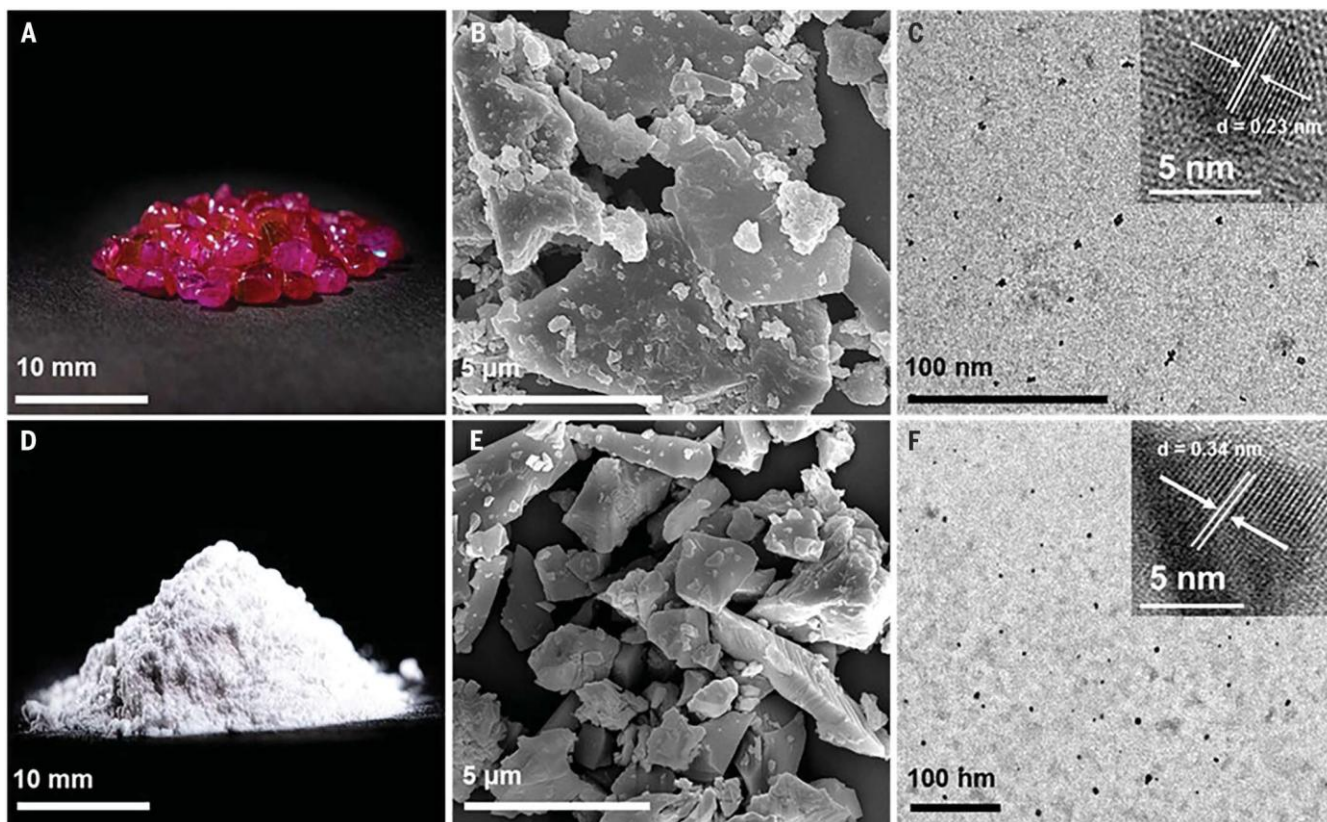


Fig. 2. Process of disintegration of natural and synthetic alumina in microdroplets. (A) Photograph of natural ruby. (B) FESEM image of ground and separated natural ruby before electro-spray. (C) TEM image of natural ruby after electro-spray at optimized conditions. The inset shows a high-resolution image of a particle. The plane marked is (110). (D) Photograph of fused alumina powder. (E) FESEM image of ground and separated fused alumina before electro-spray. (F) TEM image of fused alumina after electro-spray at optimized conditions. The inset shows a high-resolution image of a particle. The plane marked is (012) of α -alumina. In (B) and (E), some smaller particles are observed to be attached to the micron-scale particles naturally.

scale relevant to brittle fracture. During the cleavage of bulk and slab SiO_2 , the energy of cleavage saturates as the separation between surfaces of cleaved parts (Fig. 3B) grows beyond 6 Å. The cleavage energies of the slab are notably lower than that of the bulk, which indicates increased ease in brittle cleavage with reduction in dimension. Consequently, nanocrystals of SiO_2 are more susceptible to fracture than its bulk form. Cleavage of a slab results in the formation of edges in addition to surfaces, and we note surface and edge reconstruction with concave-convex shapes in cleaved slab with lattice constant $b = 10$ Å, where cleavage energy saturates, in contrast to its absence in the cleaved surface of bulk (Fig. 3, C and D).

We examined the competing deformation instability of bulk and slab SiO_2 . This insta-

bility leads to the formation of a stacking fault on the (010) plane, which is achieved with slip localized at a single (010) plane. To accomplish this, we transformed the unit cell vector \vec{b} to yield the generalized stacking fault vector, $\vec{b} \rightarrow \vec{b}_0 + \vec{p} \delta x; 0; z\vec{p}$, where \vec{b} is the periodic cell vector and $x, z \in [0, 1]$ are the fractional coordinates (see Fig. 4A). For better understanding, the formation of slip is illustrated in fig. S6. Stacking faults are locally stable at $(x, z) = (0, 0.5), (0.5, 0),$ and $(0.5, 0.5)$ slip configurations, and their energies relative to the reference structure $(x, z) = (0, 0)$ are used to estimate stacking fault energies (SFEs):

$$\frac{E_{\text{slip}}(\delta x, z\vec{p}) - E_{\text{slip}}(\vec{b}_0; 0\vec{p})}{A}$$

In this equation, $A = ad$, where a is the cell vector and d is the thickness of the slab. Negative SFEs of the (0, 0.5) and (0.5, 0.5) slips in the slab of SiO_2 mean spontaneous formation of extended stacking faults (table S1).

This contrasts with the stacking faults in bulk SiO_2 , which have positive energies as expected, implying formation of finite-sized stacking faulted regions bordered by partial dislocations (table S1). Thus, both the processes (cleavage and stacking fault formation) are energetically more favorable in the slab than in the bulk. The stability (negative SFE) of the stacking fault in the slab is linked with the creation of a step (relaxed structures reveal shear deformations or steps along the b direction) (Fig. 4, B and C) and associated reconstruction blunting the fault edges at the surface. Our results

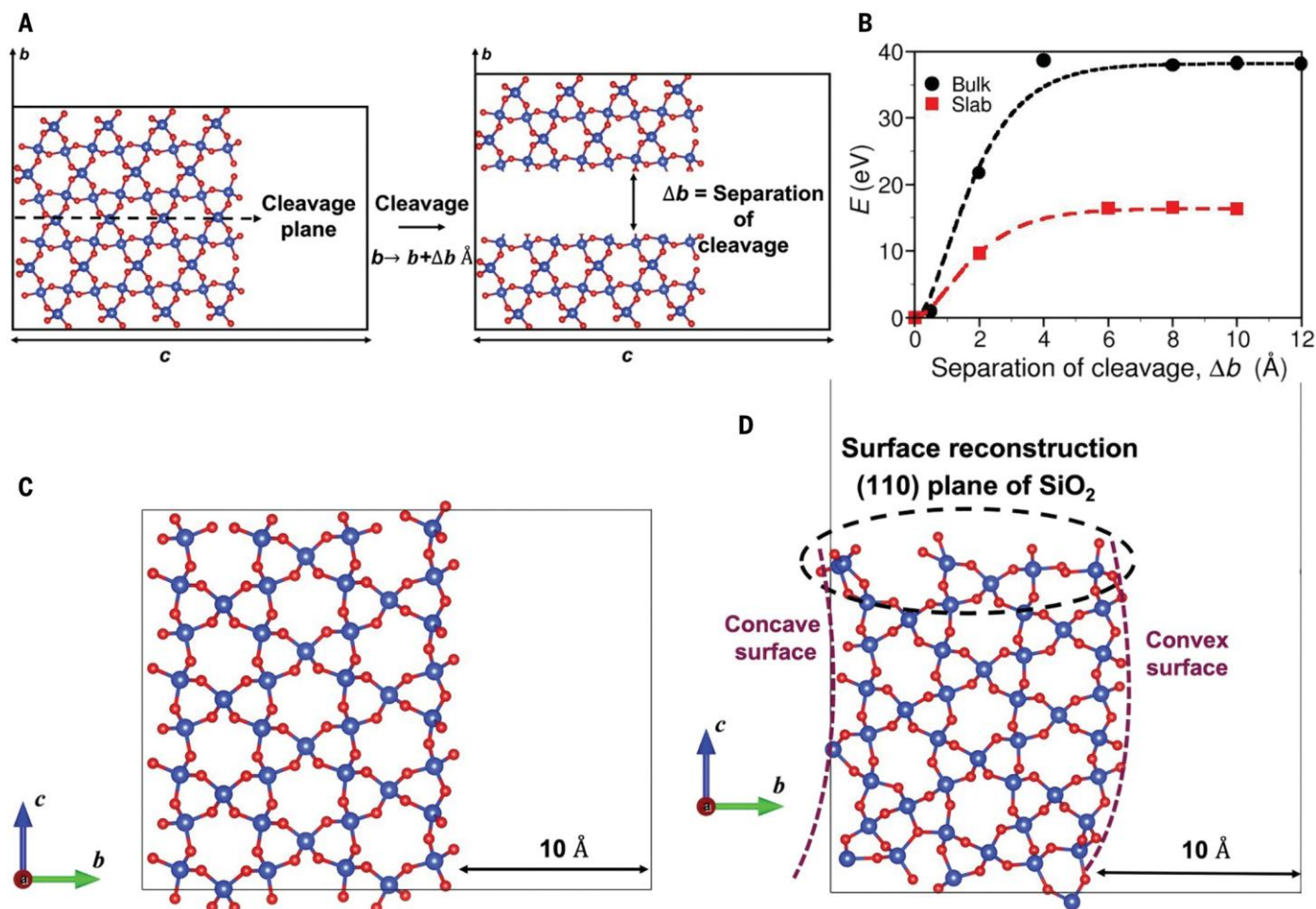


Fig. 3. The process of cleavage and surface reconstruction visualized with first-principles simulations. (A) Schematic of the (110) terminated slab of SiO_2 (left) acted on by uniaxial tensile strain (along the b axis), resulting in two cleaved surfaces (right). The distance, Δb is a measure of separation of the cleaved surfaces, which is composed of vacuum. (B) The relaxed energies of bulk and slab of SiO_2 as a function of separation. The energy surface is constructed using the energy functional form, $E_{\infty} - E_{\infty}(1+x)e^{-x}$, where E_{∞} is the energy of the system in which the cleaved crystals are separated by infinite distance and $x = \Delta b/l$ (where l

is the length scale in this system) for the relaxed structures as a function of separation. The cleavage energies of slab are lower than that of bulk, indicating that nanoscale crystals of SiO_2 are much easier to break than the bulk. (C and D) Optimized structures of the (110) surface of (C) bulk [black data in (B)] and (D) slab SiO_2 [red data in (B)] with a cleavage thickness of 10 Å. We observed concave and convex deformations in the slab. However, no such deformation was seen in the bulk structure. In addition, surface and edge reconstructions were also observed in slab- SiO_2 upon cleavage. Silicon atoms are shown in blue, and oxygen atoms are in red.

show that slip is the primary mechanism that drives the possible formation of nanoparticles in SiO₂.

Our first-principles analysis of the processes of cleavage and slip in bulk and (001) terminated slab (an alternative plane) of SiO₂ revealed that the mechanisms of nanocrystal formation in SiO₂ are not very sensitive to the specific choice of surface (tables S2 and S3). To understand the process of the disintegration of alumina, we simulated the cleavage and slip of a (001) terminated slab of α -Al₂O₃, which has the corundum structure (R3 cspace group) as in silica. The results presented in tables S4 and S5 suggest that its fragmentation to form nanocrystals is indeed driven by the mechanism of slip, similar to silica.

We next investigated the effects of hydrogen (H) atoms on the structure and energies of stacking faults in the (0, 0.5) and (0.5, 0.5) slip configurations. We used H atoms to model protons, which are known to be present in microdroplets, because simulations of a charged system within periodic boundary conditions need to be compensated with opposite charge. Upon addition of a H atom to the structure with slip vector $(x, z) = (0.5, 0.5)$, the SFE remained negative. In addition, an H atom is found to destabilize the (0, 0.5) slip system (table S6). Compared with the (0, 0.5) stacking fault structure without an H atom (fig. S7A), substantial local structural distortions arise with H at the sites near the interacting H atom (fig. S7B). Further, interaction with two H atoms results in the formation of silicate fragments or the chipping away of silicate, suggesting that the H atom facilitates fragmentation of a natural mineral such as quartz in microdroplets (fig. S7C). Application of an electric field, as is typical in electrospray experiments ($E = 10^8$ V/m along the c axis in Fig. 4) improves the stability of (0, 0.5) and (0.5, 0) stacking faults in SiO₂ (table S6).

Our theoretical analysis of mechanical instabilities in bulk and a nanoslab of SiO₂ (cleavage and slip in response to localized uniaxial and shear strains, respectively) suggests that the stacking faults and resulting steps at the surface of SiO₂ may occur in the initial stage of fragmentation into nanoparticles, and the interactions with H atoms and electric field enhance this process, leading to the formation of silicate fragments. Because the cleavage energies decrease substantially with a reduction in dimension, namely, from bulk to slab, we expected fragmentation to follow readily, with possible nucleation at the steps, or the sites of chemical interaction with protons. In addition to the stacking faults and resulting steps, several aspects of the microdroplet environment can drive the fragmentation process. Chemical reaction rate constants can be increased by a factor of more than 10^6 in such confinement (2). Several factors such

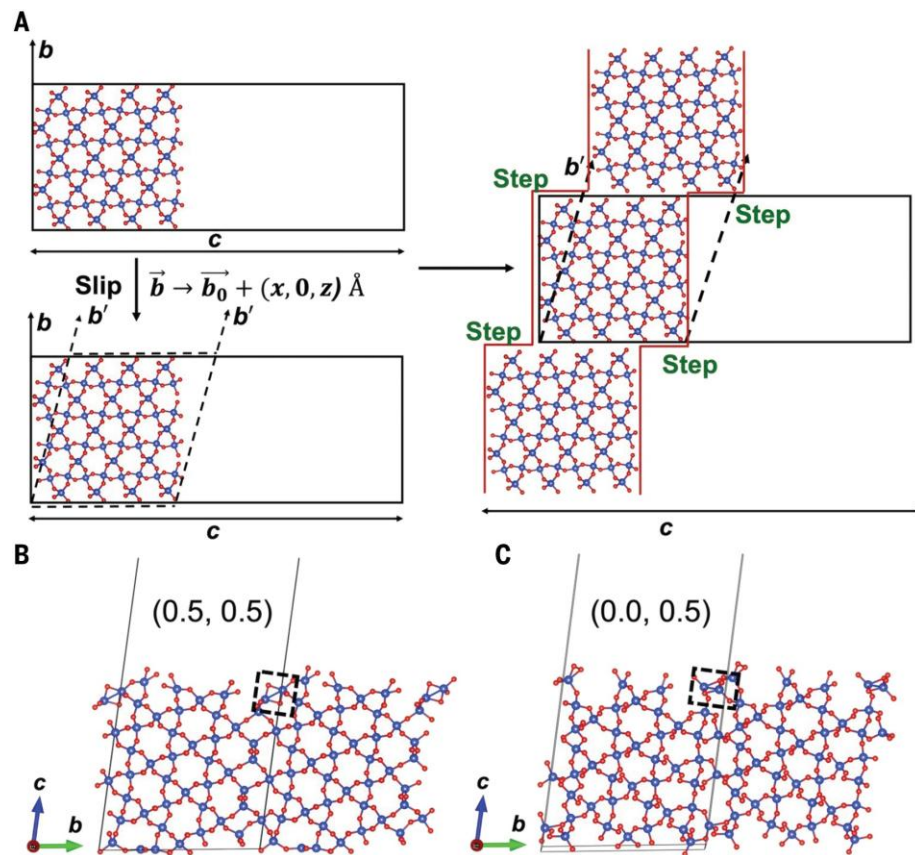


Fig. 4. Stacking fault or slip localized at a (010) plane. (A) Schematic of the (110) terminated slab of SiO₂ acted on by localized shear strain (slip) on (010) plane introduced through a generalized stacking fault vector $\vec{T} = \frac{1}{2} \vec{a} + \vec{b} + \vec{c}$, where \vec{a} and \vec{c} are periodic cell vectors and $(x, z \in [0, 1])$ are the fractional coordinates. (B and C) Relaxed stacking fault structures with (B) $(x, z) = (0.5, 0.5)$ and (C) $(x, z) = (0, 0.5)$. The stacking fault or slip on the (010) plane is introduced by tilting \vec{b} (dashed boxes). Two-unit cells along the b direction are shown for clearer visualization. Silicon atoms are shown in blue, and oxygen atoms are in red.

as pH (6), reactive species such as radicals (7), their surface segregation, strong electric field at the interface (8), and others are likely to contribute additionally to these effects, and some of these may accelerate the process.

Formation of silicates in microdroplets

To test the hypothesis of formation of silicates by microdroplet-induced fragmentation, we electrosprayed 5 mg of silica in 50 ml of water at the optimized conditions on an aluminum substrate. The product was collected, redispersed in water, and centrifuged at 10,000 rpm to remove any larger particles. The upper layer was used for mass spectrometric measurements. In the negative ion mass spectrum of the deposited silica (Fig. 5A), the peaks appeared at mass/charge ratios (m/z) 60.9, 76.9, 94.9, 154.9, and 172.9. This spectrum was compared with that of 200 mM standard sodium silicate solution at pH 8.5 (Fig. 5B). We observed peaks at m/z 60.9, 76.9, 94.9, 154.9, and 172.9 due to $[\text{SiO}_2\text{H}]^-$, $[\text{SiO}_3\text{H}]^-$, $[\text{SiO}_3\text{H}_2\text{O}]^-$, $[\text{Si}_2\text{O}_6\text{H}_3]^-$, and $[\text{Si}_2\text{O}_6\text{H}_3\text{H}_2\text{O}]^-$,

respectively. In addition, we observed peaks at higher masses at m/z 194.9 $[\text{Si}_2\text{O}_6\text{H}_2\text{Na} \cdot \text{H}_2\text{O}]^-$, m/z 212.9 $[\text{Si}_2\text{O}_6\text{H}_2\text{Na} \cdot 2\text{H}_2\text{O}]^-$, and m/z 232.9 $[\text{Si}_3\text{O}_9\text{H}_5]^-$. We did not observe sodium adduct peaks of the standard sodium silicate in the spectrum of deposited silica. Tandem mass spectrometric analysis for sodium silicate (fig. S8) and deposited silica (Fig. 5, C and D) showed the expected features. Two peaks at m/z 94.9 and 172.9 showed the loss of water, confirming the formation of $[\text{SiO}_3\text{H}_2\text{O}]^-$ and $[\text{Si}_2\text{O}_6\text{H}_3 \cdot \text{H}_2\text{O}]^-$ complexes.

Plausible mechanisms

With respect to the energy needed for such processes, our calculations suggest that physical effects in microdroplets are particularly important. Microdroplet convection and shock waves that produce pressures in the megabar range (9) are likely in droplets, which could trigger such effects. We suggest that the observed phenomenon is critically influenced by the following factors: (i) Droplet fission occurs due to Coulomb repulsion. We know from the

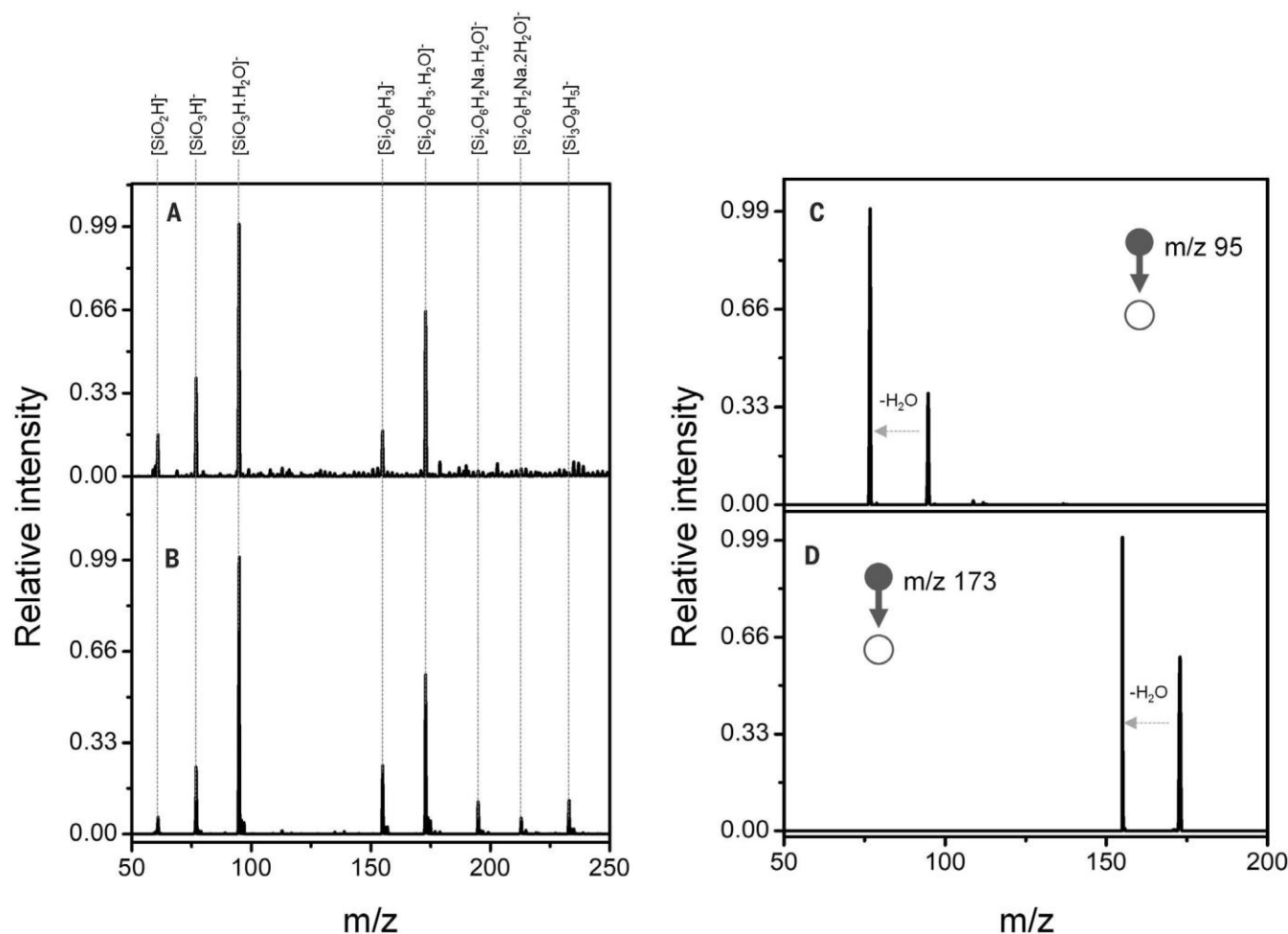


Fig. 5. Mass spectra of silica samples. (A and B) Full-range negative ion mass spectrum of (A) the deposited silica showing the peaks due to silicates compared with that of (B) standard sodium silicate. (C and D) Tandem mass spectra of (C) $[\text{SiO}_3\text{H.H}_2\text{O}]^-$ and (D) $[\text{Si}_2\text{O}_6\text{H}_3.\text{H}_2\text{O}]^-$, showing water loss during fragmentation.

literature that the droplets produced at low flow rates (typically ~ 5 ml/min) have a narrow distribution of sizes, with the most abundant radius in the range of 1.5 μm . Such an electro-spray droplet was shown to have an electric charge of $\sim 10^{-14}$ C, which corresponds to $\sim 60,000$ singly charged ions (10). In our case, the droplet sizes are larger, in the range of approximately tens of micrometers (11); produced at a flow rate of 0.5 ml/hour, that is, 8.3 ml/min; and large enough to accommodate the parent particles. The droplet size reduces along the flight path, which results in the explosion of the droplets. This explosion produces smaller droplets that experience larger stresses (9), leading to the breakage of particles. (ii) Erosion of the quartz particles in the charged droplets and solubility of quartz in water (6 parts per million at 25°C) together bring SiO_2 species into the solution. We tested the possible effect of enhanced acidity in microdroplets on the mineral particles in a separate experiment by electro-spraying pure water on the parent minerals for 4 hours (fig. S9). We saw surface roughening in this experiment, although the changes

are much less pronounced than those shown in Fig. 1. The reactive species at the droplet-air interface may play an important role in these events. (iii) The dissolution and reprecipitation of silica particles may occur in microdroplets. The solubility of quartz in water is influenced by factors such as electrostatic forces, hydration-induced ionization, pH, and Laplace pressure. The interaction between charged silica particles and water droplets is substantial, resulting in the formation of reactive species. We observed the formation of silicate ions during the process (Fig. 5). These ions may reprecipitate under specific conditions. Charged microdroplets can modify surface chemistry, promoting dissolution that leads to nano-sized silica particles. However, these chemical events may occur slowly and therefore may not fully explain the phenomenon of formation of crystalline nanoparticles. (iv) The H_2O radical cation present in the microdroplets (7) can also contribute to the observed phenomenon. To probe this possibility, we analyzed the formation of nanoparticles from silica by simulating it as a charged system. The H_2O radical cation

present in the microdroplets may pull out electrons from silica, and we have simulated the process by removing an electron from the system and adding a compensating jellium background to remove electrostatic divergence of the charged periodic system. Our results confirm that the generalized SFE of slip along the (010) plane is negative [see (0.5, 0.5) slip configuration of the SiO_2 slab in table S7]. (v) The nanoparticles that form may catalyze the fission of microdroplets. This assumption is supported by a study in which it was shown theoretically that nanoparticles actively fragment droplets (12). Accelerated droplet fission further accelerates the particle disintegration. We present a schematic of the fragmentation process in fig. S10.

Atmospheric water droplets, such as clouds and fog, can acquire charges not only because of the ionic species present inside them but also because of contact electrification (13). These charges on naturally occurring droplets cannot be ignored. As we have demonstrated, under the right conditions, electro-sprayed microdroplets can break hard particles, including

complex minerals, and the potential of naturally occurring atmospheric droplets to do the same needs to be explored. If this process does happen, it would be important for weathering and the production of natural nanoparticles (I). Soil forms through rock weathering, a process that involves multiple factors, and it takes 200 to 400 years to yield 1 cm of it, composed of varied particle sizes. Our study highlights the role of charged microdroplets of water in unprecedented weathering, which, to our knowledge, had not yet been explored. Disintegration of minerals makes nascent surfaces, which may participate in catalysis that leads to new chemical transformations in droplets in the presence of reactive species. “Microdroplet showers” composed of nanoparticles and molecules falling on Earth may be of importance to the chemical and biological evolution of the planet.

REFERENCES AND NOTES

- M. F. Hochella Jr. *et al.*, *Science* 363, eaau8299 (2019).
- Z. Wei, Y. Li, R. G. Cooks, X. Yan, *Annu. Rev. Phys. Chem.* 71, 31–51 (2020).
- J. K. Lee, S. Kim, H. G. Nam, R. N. Zare, *Proc. Natl. Acad. Sci. U.S.A.* 112, 3898–3903 (2015).
- A. Wortmann *et al.*, *J. Am. Soc. Mass Spectrom.* 18, 385–393 (2007).
- D. Sarkar *et al.*, *Adv. Mater. Interfaces* 5, 1800667 (2018).
- H. Wei *et al.*, *Proc. Natl. Acad. Sci. U.S.A.* 115, 7272–7277 (2018).
- L. Qiu, N. M. Morato, K.-H. Huang, R. G. Cooks, *Front Chem.* 10, 903774 (2022).
- D. Zhang, X. Yuan, C. Gong, X. Zhang, *J. Am. Chem. Soc.* 144, 16184–16190 (2022).
- M. S. Krivokorytov *et al.*, *Phys. Rev. E* 95, 031101 (2017).
- S. Banerjee, S. Mazumdar, *Int. J. Anal. Chem.* 2012, 282574 (2012).
- P. Basuri *et al.*, *Chem. Sci.* 13, 13321–13329 (2022).
- F. Sicard, J. Toro-Mendoza, A. Striolo, *ACS Nano* 13, 9498–9503 (2019).
- Z. Tang, S. Lin, Z. L. Wang, *Adv. Mater.* 33, e2102886 (2021).

ACKNOWLEDGMENTS

Funding: We acknowledge financial support from the Department of Science and Technology, government of India. We thank M.S.R. Rao for allowing access to his powder x-ray diffraction facility. We thank S. Manna for help with the Raman measurements. B.K.S. thanks the University Grant Commission (UGC) for a research fellowship. P.B. and A.N. thank Indian Institute of Technology (IIT) Madras for their fellowships. K.D. thanks Jawaharlal Nehru Centre for Advanced Scientific Research (JNCASR) for her fellowship. T.P. acknowledges funding from the Centre of Excellence on Molecular Materials and

Functions under the Institution of Eminence Scheme of IIT Madras. T.P. and U.V.W. acknowledge support from JC Bose National Fellowships. Author contributions: T.P. proposed the problem and suggested necessary experiments. B.K.S. performed the synthesis and characterization. K.D. and U.V.W. conducted the computational work. P.B. participated in designing the experimental setup. A.N. performed scanning electron microscopy. T.P. supervised the research. All authors discussed the results and contributed to the writing of the manuscript. Competing interests: T.P., B.K.S., P.B., and A.N. are the authors of two pending patent applications: nos. 202241038282 and PCT/IN2023/050649. The authors declare no other competing interests. Data and materials availability: All relevant data are provided in this paper or the supplementary materials. License information: Copyright © 2024 the authors, some rights reserved; exclusive licensee American Association for the Advancement of Science. No claim to original US government works. <https://www.science.org/about/science-licenses-journal-article-reuse>

SUPPLEMENTARY MATERIALS

[science.org/doi/10.1126/science.adl3364](https://doi.org/10.1126/science.adl3364)
Materials and Methods
Supplementary Text
Figs. S1 to S10
Tables S1 to S7
References (14–17)
Movie S1

Submitted 12 October 2023; accepted 8 April 2024
10.1126/science.adl3364



Supplementary Materials for

Spontaneous weathering of natural minerals in charged water microdroplets forms nanomaterials

B. K. Spoorthi *et al.*

Corresponding author: Thalappil Pradeep, pradeep@iitm.ac.in

Science **384**, 1012 (2024)
DOI: 10.1126/science.adl3364

The PDF file includes:

Materials and Methods
Supplementary Text
Figs. S1 to S10
Tables S1 to S7
References

Other Supplementary Material for this manuscript includes the following:

Movie S1

Materials and Methods

Materials

River sand and natural ruby were purchased from the local market and fused alumina (99+%) was purchased from Sigma-Aldrich. All samples were used without additional purification. Ultrapure water (18.5 M Ω Milli Q) was used for all the experiments. The samples were ground using a laboratory mortar and pestle and suspended in water and centrifuged using a Remi RM-03 plus centrifuge. Prior to centrifugation, the particle suspension was ultrasonicated (Digital ultrasonic cleaner, 40 kHz, 100 W) for 10 min to ensure the separation of particles.

Characterization

Photographs of the initial samples were taken using a digital single-lens reflex (DSLR) camera. Optical images of the micron-sized particles were captured by VH-Z100R Keyence optical microscope. Thermo Scientific Verios G4 UC high-resolution FESEM at 20 kV accelerating voltage was used to study the surface morphology of the micron-sized particles. Energy dispersive spectroscopy (EDS), using FESM confirmed their composition. Thin film of gold was sputtered on the sample to reduce charging. High-resolution TEM images of the nanostructures were taken at an accelerating voltage of 200 kV using a JEOL 3010 instrument. The sizes of the materials were compared by performing thin-film X-ray diffraction using Rigaku SmartLab X-ray diffractometer system with Cu K α radiation ($\lambda = 1.5406 \text{ \AA}$). Raman spectra were recorded using a CRM alpha 300 S spectrometer of Witec, Germany, with an excitation source of 532 nm. The mass spectral data were acquired using a Thermo Scientific LTQ XL mass spectrometer.

Electrospray deposition experiments

A home-built electrospray set-up was used for microdroplet experiments (Fig. 1A). The spray was generated from a Hamilton syringe which was connected to a silica capillary of 50 μm inner diameter through a union connector. The syringe needle was connected to a high voltage power source. A syringe pump controlled the flow rate of the suspension. The substrate was grounded. The experiment was done under ambient conditions (25 $^{\circ}\text{C}$, 50-60% relative humidity). A multi-nozzle set-up was prepared to scale up the method. The components used such as silica capillaries were purchased from Molex, USA. Union connectors and PEEK tubing sleeves were procured from IDEX Health & Science, USA.

Determining the collection yield of the sample

The spray was carried out (as mentioned in the experimental section) at the optimized condition. Initially weight of the bare substrate (aluminum) was taken. Subsequently, the fine suspension of silica was electrosprayed. After the electrospray, the weight of the substrate with the sample was measured. The difference in the weight before and after deposition gives the weight of the silica deposited. The ratio of the sprayed sample with respect to the initial sample gives the collection yield.

Computational details

Our first-principles calculations are based on density functional theory as implemented in QUANTUM ESPRESSO (14), and ultrasoft pseudopotentials to model interactions between valence electrons and the ionic cores. We used a generalized-gradient approximation (GGA) (15) of the exchange-correlation energy with a revised functional PBEsol parameterized by Perdew,

Burke and Ernzerhof (PBE) (16). Electronic wave functions and charge density expansions in plane wave basis sets were truncated at cut-off energies of 30 Ry and 240 Ry respectively. We analyze here bulk and a slab terminated with (110) surfaces of SiO₂, since the TEM images in experiments confirm the (110) surface of quartz or SiO₂. A 1x2x4 supercell is used to model the slab with (110) surfaces by introducing a vacuum layer of 15 Å thickness parallel to the slab separating its adjacent periodic images. Brillouin Zone (BZ) integrations were sampled on uniform 12x12x8 and 2x1x1 meshes of k-points for bulk and slab of SiO₂, respectively. Calculated lattice constants of bulk SiO₂ ($a=4.95$ Å and $c=5.44$ Å) are within the typical GGA errors with respect to their experimental estimates ($a = 4.95$ Å and $c = 5.44$ Å) (17). To simulate responses of the slab to electric field, we add a saw-tooth potential as a function z . Calculations were also performed on the (001) surface of SiO₂ to confirm the conclusion drawn. Similar calculations were conducted on the (001) surface of α -Al₂O₃ (alumina). Additional details are presented in the main text as well as in Tables S2-S5.

Supplementary figures

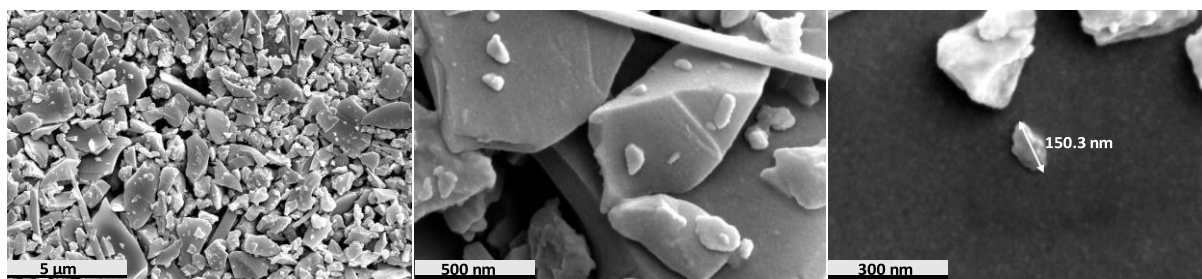


Fig. S1. FESEM images of silica particles before electrospray, at various magnifications, showing that smaller adhering particles are larger than 100s of nm in size.

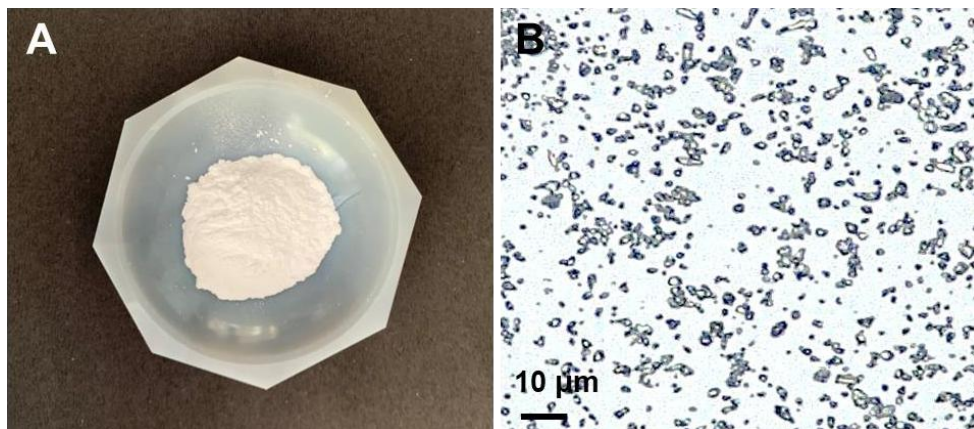


Fig. S2. Images of natural quartz. (A) Photograph of the ground quartz powder used for centrifugation and separation of smaller particles. (B) Optical image of the particles separated by centrifugation and used for electrospray; particles are below 10 μm in size.

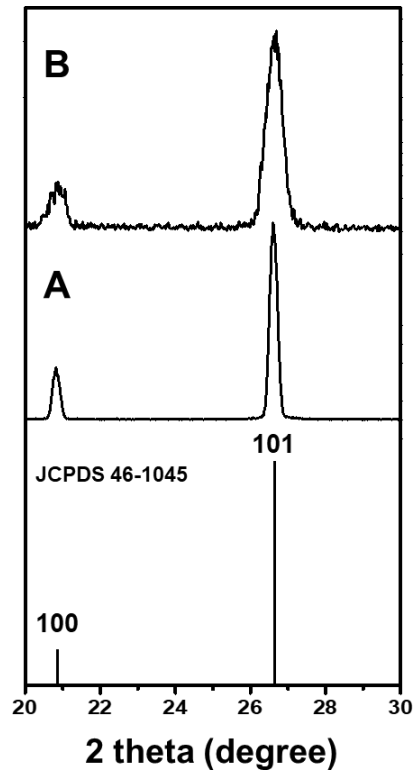


Fig. S3. Detecting nanoparticles in bulk form. XRD of ground natural quartz before (A) and after (B) electro spray deposition, compared with the JCPDS data of quartz. Broadened peaks in (B) indicate the smaller size of the quartz particles.

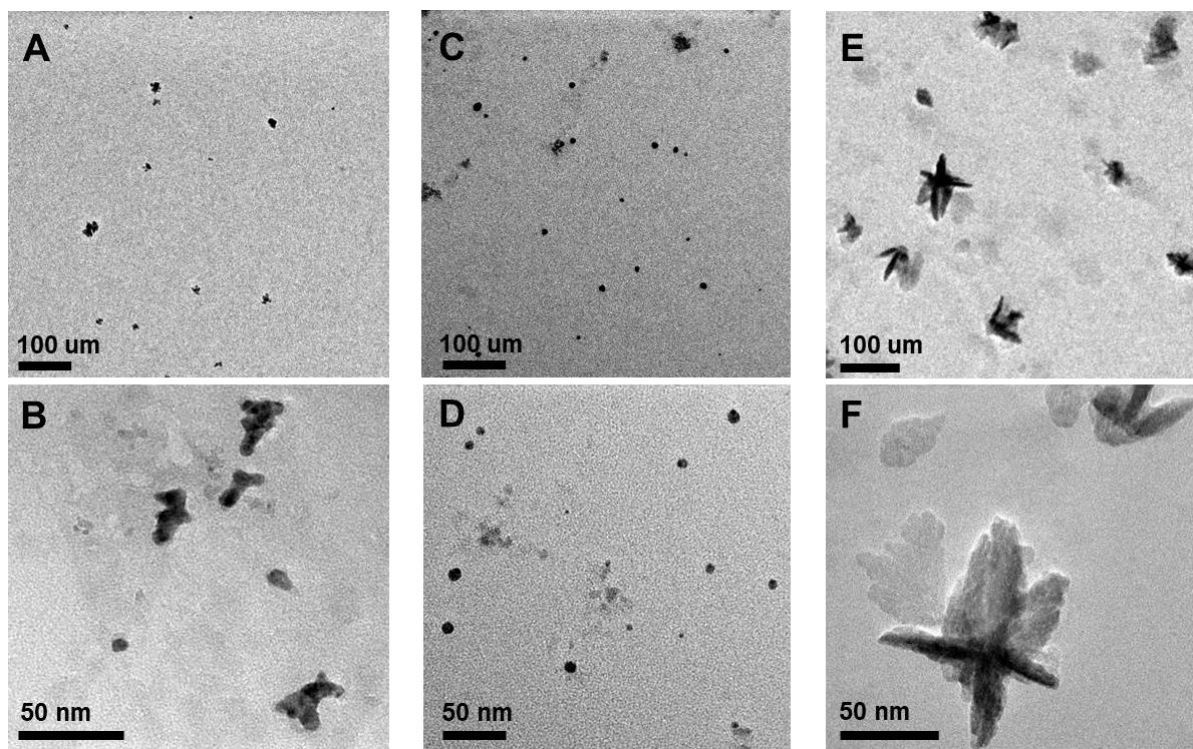


Fig. S4. Effect of spray potential on the particles. HRTEM images of natural quartz at various applied spray potentials (A, B) 3.0 kV where the fragmentation just begins. (C, D) 4.5 kV. (E, F) 5.5 kV.

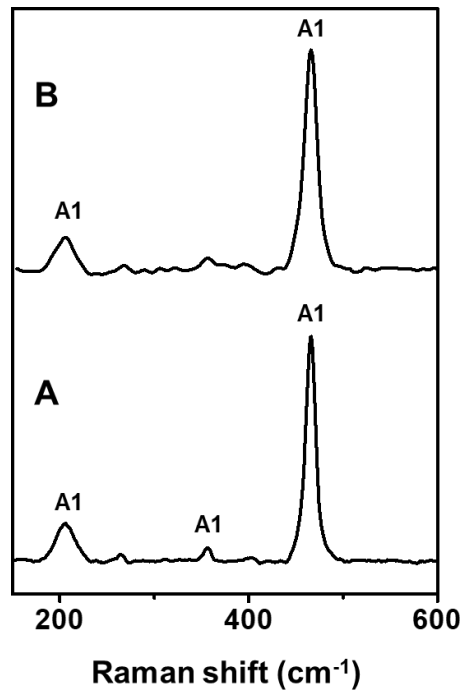


Fig. S5. Raman spectroscopic characterization. Raman spectra showing the characteristic Si-O symmetric stretch (A_1) of natural quartz. (A) Before and (B) after electro spray deposition. Peaks confirm the structural integrity of quartz. The spectra were collected with 532 nm excitation.

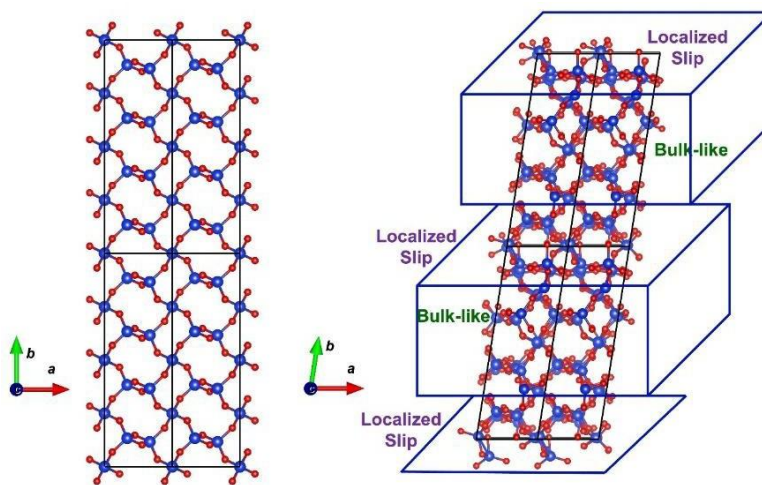


Fig. S6. Illustration of slip. Schematic representation showing ‘no slip’ and ‘slip’ representation of SiO₂. The slip has been introduced in the crystal using the transformation equation as shown in the figure.

Table S1: The generalized SFEs calculated for (110) surface of bulk and slab SiO₂ with (0, 0), (0, 0.5), (0.5, 0) and (0.5, 0.5) slip configurations.

	x	z	Slab	Bulk
SFE (J/m^2)	0.0	0.0	0.0	0.0
	0.5	0.5	-1.21	2.08
	0.5	0.0	1.20	1.65
	0.0	0.5	-0.07	1.73

Table S2: Calculated cleavage energies (in J/m^2) along the (010) direction for the (001) surface of bulk and slab SiO_2 .

Vacuum thickness (\AA)	Bulk	Slab
0	0	0
8	5.84	4.53

Here we have simulated the processes of cleavage and slip in bulk and (001) terminated slab of SiO_2 . We obtained energies of cleavage of bulk and slab of SiO_2 as a function of vacuum thickness, b and find that cleavage energies of the slab are $\sim 20\%$ lower than that of the bulk (see above), supporting our suggestion that breaking of a nanoscale crystal of SiO_2 across (001) surface is easier compared to the bulk.

Table S3: Generalized SFEs calculated for (001) surface of SiO₂ slab with (0, 0), (0, 0.5), (0.5, 0) and (0.5, 0.5) slip configurations.

	x	z	Slab
SFE (J/m^2)	0.0	0.0	0.0
	0.5	0.5	-0.32
	0.5	0.0	0.94
	0.0	0.5	1.13

Here we examine the formation of nanocrystals through nucleation of a stacking fault on (010) plane with slip localized at a single (010) plane, achieved with transformation of the unit cell vector \vec{b} using

$$f = x a + \vec{b} + z c ,$$

where a , \vec{b} and c are the periodic cell vectors, and $(x, z \in [0,1])$ are the fractional coordinates. Negative SFE of (0.5, 0.5) slip on (010) plane in the (001) slab of SiO₂ relative to the reference structure $(x, z) = (0, 0)$ means spontaneous formation of stacking faults (see above), which is similar to what we reported for the (110) surface of SiO₂. We therefore conclude that these mechanisms of nanocrystal formation in SiO₂ are generic and can happen along other surfaces also.

Table S4: Calculated cleavage energies (in J/m^2) along the (010) direction for the (001) surface of bulk and slab of Al_2O_3 .

Vacuum thickness (\AA)	Bulk	Slab
0	0	0
8	7.43	7.30

The simulations of the stable form α - Al_2O_3 (alumina), the corundum structure ($R\bar{3}c$ space group) are presented here. Our estimates of optimized lattice parameters, $a = 5.14 \text{ \AA}$ and $\alpha = 55.35^\circ$ are within the typical GGA errors of their experimental values ($a = 5.13 \text{ \AA}$ and $\alpha = 55.33^\circ$) [14]. Simulation was performed by (a) subjecting the crystal to uniaxial tensile strain localized at a (010) plane, and (b) slip on a (010) plane. We find that cleavage energy of the slab is lower than that of bulk.

Table S5: SFEs of the (010) plane with (0, 0), (0, 0.5), (0.5, 0) and (0.5, 0.5) slip configurations on the (001) surface of neutral and positively charged slab of Al₂O₃.

	x	z	Neutral Slab	Positive Slab
SFE (J/m^2)	0.0	0.0	0.0	0.0
	0.5	0.5	1.86	1.75
	0.5	0.0	2.51	-0.27
	0.0	0.5	1.85	-0.21

Generalized SFEs of four configurations of slip on (010) plane have been tabulated here. Positive SFE in neutral slab of α -Al₂O₃ indicate formation of slip in alumina is not quite favorable. To understand the process of disintegration of alumina in nanoforms, a charged system was simulated by removing an electron and adding a compensating jellium to maintain charge neutrality of the periodic system. The SFEs in charged alumina are negative for the slips at = (0.5, 0.0) and (0.0, 0.5) configurations, supporting spontaneous formation of stacking faults, facilitated by interaction with protons

Table S6. SFEs of (010) direction with (0, 0), (0, 0.5), (0.5, 0) and (0.5, 0.5) slip configurations on the (110) plane of SiO₂ from our DFT-based calculations analyzing the effects of hydrogen atom (H-atom) and electric field ($E = 10^8$ V/m). Our calculations show that SFEs in slab-SiO₂ with (0, 0.5) and (0.5, 0.5) configurations are negative and energetically favorable (marked in bold). The SFEs for bulk remain positive.

SFE (J/m^2)	Slab					
	x	z	w/o H-atom	1 H-atom	2 H-atoms	E
	0.0	0.0	0	0	0	0
	0.5	0.5	-1.21	-0.93	-0.88	-1.20
	0.5	0.0	1.20	1.18	0.90	1.12
	0.0	0.5	-0.07	0.89	-0.83	-0.09

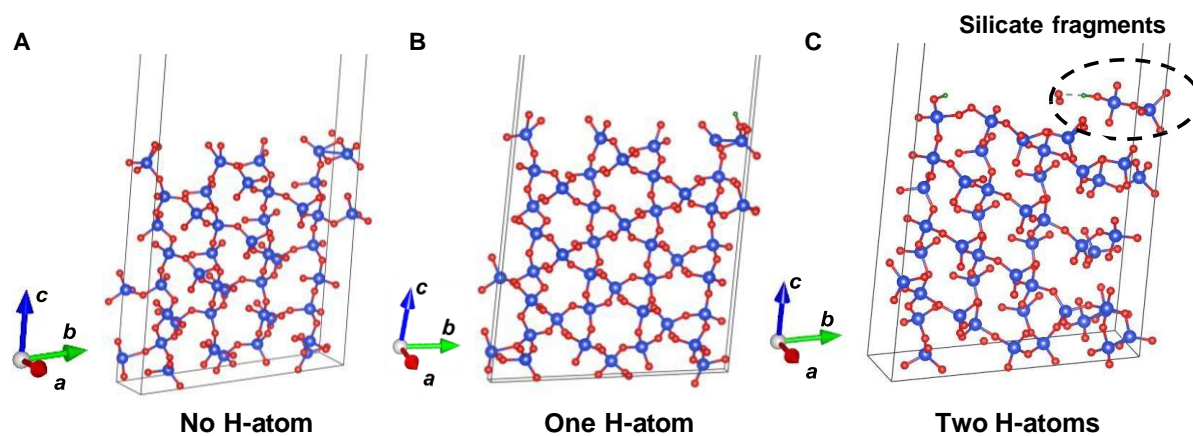


Fig. S7. Silicate formation upon interaction with H atoms. The relaxed stacking fault structures with a slip vector $(x,z) = (0, 0.5)$ (A) without hydrogen atom, (B) with one hydrogen atom and (C) two hydrogen atoms, clearly highlighting surface reconstruction and formation of silicate fragments in $(0, 0.5)$ stacking fault structure with two hydrogen atoms. Silicon atoms are shown in blue, oxygen atoms in red, and hydrogen atoms in green. Hydrogen atoms are shown also with dotted arrows.

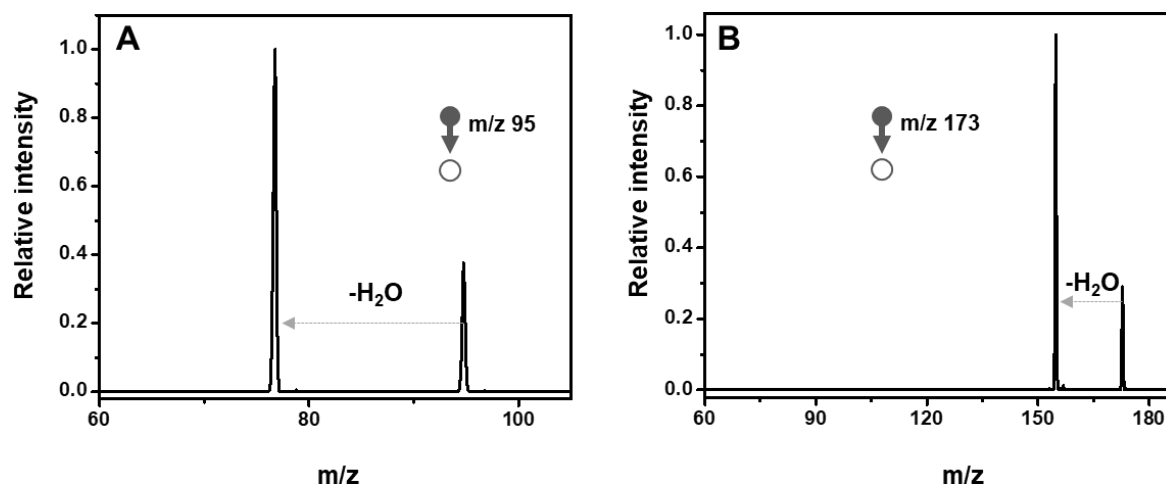


Fig. S8. Confirming the composition of ions in the gas phase. Tandem mass spectra of standard silica solution. (a) and (b) showing the water loss during fragmentation of m/z 95 [$\text{SiO}_3\text{H}\cdot\text{H}_2\text{O}$]⁻ and m/z 173 [$\text{Si}_2\text{O}_6\text{H}_3\cdot\text{H}_2\text{O}$]⁻, respectively.

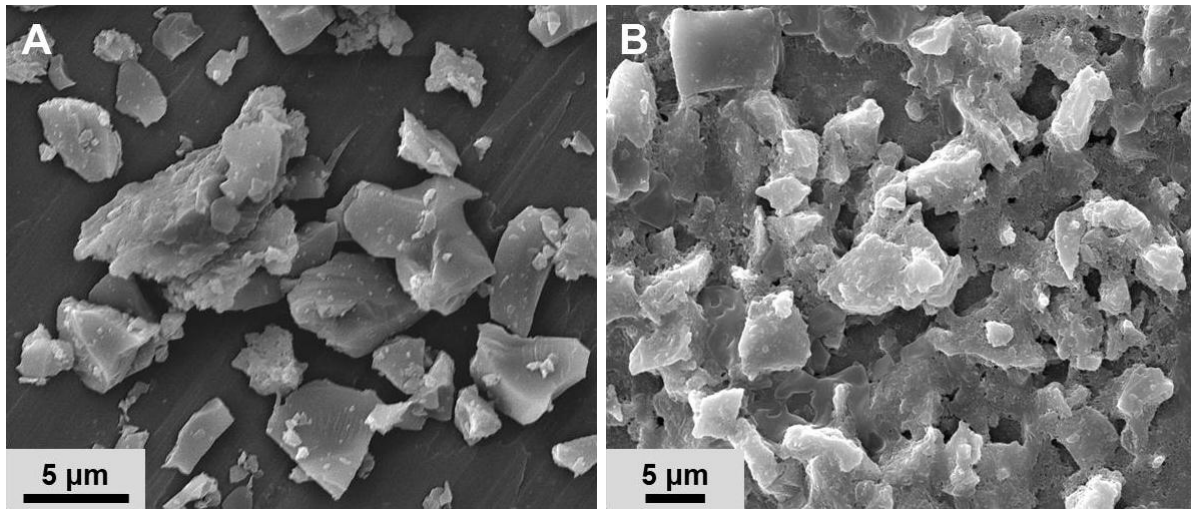


Fig. S9. Effect of charged microdroplets on quartz. FESEM images of natural quartz before (A) and after (B) deposition of charged microdroplets. Pure water was electrospayed under conditions shown in Fig. 1A, onto an aluminum substrate covered with mineral particles for 4 h and the resulting substrate with minerals was analyzed. Increased surface roughness is seen in the product particles.

Table S7: Generalized SFEs calculated for (110) surface of positively charged slab of SiO₂ with slips (0, 0), (0, 0.5), (0.5, 0) and (0.5, 0.5) on the (010) plane.

	x	z	Slab
SFE (J/m^2)	0.0	0.0	0.0
	0.5	0.5	-1.18
	0.5	0.0	0.81
	0.0	0.5	0.03

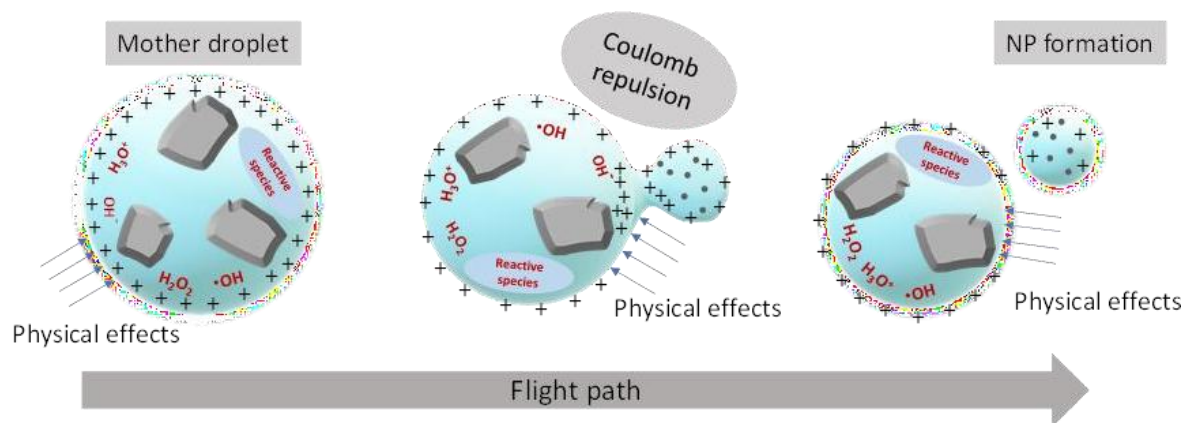


Fig. S10. Illustration of the process. Schematic representation of the mechanism of NP formation.

Movie S1: A detailed video of the experiment demonstrating the spontaneous weathering of natural minerals in charged water microdroplets.

References and Notes

1. M. F. Hochella Jr., D. W. Mogk, J. Ranville, I. C. Allen, G. W. Luther, L. C. Marr, B. P. McGrail, M. Murayama, N. P. Qafoku, K. M. Rosso, N. Sahai, P. A. Schroeder, P. Vikesland, P. Westerhoff, Y. Yang, Natural, incidental, and engineered nanomaterials and their impacts on the Earth system. *Science* **363**, eaau8299 (2019). [doi:10.1126/science.aau8299](https://doi.org/10.1126/science.aau8299) [Medline](#)
2. Z. Wei, Y. Li, R. G. Cooks, X. Yan, Accelerated reaction kinetics in microdroplets: Overview and recent developments. *Annu. Rev. Phys. Chem.* **71**, 31–51 (2020). [doi:10.1146/annurev-physchem-121319-110654](https://doi.org/10.1146/annurev-physchem-121319-110654) [Medline](#)
3. J. K. Lee, S. Kim, H. G. Nam, R. N. Zare, Microdroplet fusion mass spectrometry for fast reaction kinetics. *Proc. Natl. Acad. Sci. U.S.A.* **112**, 3898–3903 (2015). [doi:10.1073/pnas.1503689112](https://doi.org/10.1073/pnas.1503689112) [Medline](#)
4. A. Wortmann, A. Kistler-Momotova, R. Zenobi, M. C. Heine, O. Wilhelm, S. E. Pratsinis, Shrinking droplets in electrospray ionization and their influence on chemical equilibria. *J. Am. Soc. Mass Spectrom.* **18**, 385–393 (2007). [doi:10.1016/j.jasms.2006.10.010](https://doi.org/10.1016/j.jasms.2006.10.010) [Medline](#)
5. D. Sarkar, A. Mahapatra, A. Som, R. Kumar, A. Nagar, A. Baidya, T. Pradeep, Patterned nanobrush nature mimics with unprecedented water-harvesting efficiency. *Adv. Mater. Interfaces* **5**, 1800667 (2018). [doi:10.1002/admi.201800667](https://doi.org/10.1002/admi.201800667)
6. H. Wei, E. P. Vejerano, W. Leng, Q. Huang, M. R. Willner, L. C. Marr, P. J. Vikesland, Aerosol microdroplets exhibit a stable pH gradient. *Proc. Natl. Acad. Sci. U.S.A.* **115**, 7272–7277 (2018). [doi:10.1073/pnas.1720488115](https://doi.org/10.1073/pnas.1720488115) [Medline](#)
7. L. Qiu, N. M. Morato, K.-H. Huang, R. G. Cooks, Spontaneous water radical cation oxidation at double bonds in microdroplets. *Front Chem.* **10**, 903774 (2022). [doi:10.3389/fchem.2022.903774](https://doi.org/10.3389/fchem.2022.903774) [Medline](#)
8. D. Zhang, X. Yuan, C. Gong, X. Zhang, High electric field on water microdroplets catalyzes spontaneous and ultrafast oxidative C-H/N-H cross-coupling. *J. Am. Chem. Soc.* **144**, 16184–16190 (2022). [doi:10.1021/jacs.2c07385](https://doi.org/10.1021/jacs.2c07385) [Medline](#)
9. M. S. Krivokorytov, A. Y. Vinokhodov, Y. V. Sidelnikov, V. M. Krivtsun, V. O. Kompanets, A. A. Lash, K. N. Koshelev, V. V. Medvedev, Cavitation and spallation in liquid metal droplets produced by subpicosecond pulsed laser radiation. *Phys. Rev. E* **95**, 031101 (2017). [doi:10.1103/PhysRevE.95.031101](https://doi.org/10.1103/PhysRevE.95.031101) [Medline](#)
10. S. Banerjee, S. Mazumdar, Electrospray ionization mass spectrometry: A technique to access the information beyond the molecular weight of the analyte. *Int. J. Anal. Chem.* **2012**, 282574 (2012). [doi:10.1155/2012/282574](https://doi.org/10.1155/2012/282574) [Medline](#)
11. P. Basuri, A. Chakraborty, T. Ahuja, B. Mondal, J. S. Kumar, T. Pradeep, Spatial reorganization of analytes in charged aqueous microdroplets. *Chem. Sci.* **13**, 13321–13329 (2022). [doi:10.1039/D2SC04589C](https://doi.org/10.1039/D2SC04589C) [Medline](#)
12. F. Sicard, J. Toro-Mendoza, A. Striolo, Nanoparticles actively fragment armored droplets. *ACS Nano* **13**, 9498–9503 (2019). [doi:10.1021/acs.nano.9b04454](https://doi.org/10.1021/acs.nano.9b04454) [Medline](#)

13. Z. Tang, S. Lin, Z. L. Wang, Quantifying contact-electrification induced charge transfer on a liquid droplet after contacting with a liquid or solid. *Adv. Mater.* **33**, e2102886 (2021). [doi:10.1002/adma.202102886](https://doi.org/10.1002/adma.202102886) [Medline](#)
14. Quantum-ESPRESSO is a community project for high-quality quantum-simulation software based on density-functional theory and is coordinated by P. Giannozzi. See <http://www.quantum-espresso.org> and <http://www.pwscf.org>.
15. X. Hua, X. Chen, W. A. Goddard III, Generalized generalized gradient approximation: An improved density-functional theory for accurate orbital eigenvalues. *Phys. Rev. B Condens. Matter* **55**, 16103–16109 (1997). [doi:10.1103/PhysRevB.55.16103](https://doi.org/10.1103/PhysRevB.55.16103)
16. L. A. Constantin, J. M. Pitarke, J. F. Dobson, A. Garcia-Lekue, J. P. Perdew, High-level correlated approach to the jellium surface energy, without uniform-gas input. *Phys. Rev. Lett.* **100**, 036401 (2008). [doi:10.1103/PhysRevLett.100.036401](https://doi.org/10.1103/PhysRevLett.100.036401) [Medline](#)
17. S. M. Antao, I. Hassan, J. Wang, P. L. Lee, B. H. Toby, State-of-the-art high-resolution powder x-ray diffraction (HRPXRD) illustrated with rietveld structure refinement of quartz, sodalite, tremolite, and meionite. *Can. Mineral.* **46**, 1501 (2008). [doi:10.3749/canmin.46.5.1501](https://doi.org/10.3749/canmin.46.5.1501)

Interfacial Growth of Large Area Single-Crystalline Silver Sheets Through Ambient Microdroplets

Debanjan Sarkar,* Anirban Som, Keerthana Unni, Sujan Manna, and Pradeep Thalappil*

This article is dedicated to Professor Pulickel M. Ajayan.

The creation of micrometer-sized sheets of silver at the air-water interface by direct deposition of electrospray-generated silver ions (Ag^+) on an aqueous dispersion of reduced graphene oxide (RGO), in ambient conditions, is reported. In the process of electrospray deposition (ESD), an electrohydrodynamic flow is created in the aqueous dispersion, and the graphene sheets assemble, forming a thin film at the air-water interface. The deposited Ag^+ coalesce to make single-crystalline Ag sheets on top of this assembled graphene layer. Fast neutralization of Ag^+ forming atomic Ag, combined with their enhanced mobility on graphene surfaces, presumably facilitates the growth of larger Ag clusters. Moreover, restrictions imposed by the interface drive the crystal growth in 2D. By controlling the precursor salt concentration, RGO concentration, deposition time, and ion current, the dimensionality of the Ag sheets can be tuned. These Ag sheets are effective substrates for surface-enhanced Raman spectroscopy (SERS), as demonstrated by the successful detection of methylene blue at nanomolar concentrations.

solvated ions present in a droplet plume undergo reduction to create nanoparticles, which are then deposited onto an electrically grounded surface. This technique offers the advantage of avoiding the use of harsh reducing agents. Notably, recent research from our team has demonstrated the capability of ESD in synthesizing nanomaterials, with the resulting material's dimensional characteristics influenced by the nature of the deposition surface. For example, while ESD of silver and silver-palladium mixture on wire mesh resulted in 1D nanowires,^[6] deposition of palladium on air-water interface formed 2D nanoparticle-nanosheets.^[7]

Interfacial processes have been at the forefront of producing extensive 2D assemblies for many years. In these processes, molecules or particles are confined at the interfaces between liquid and air or between two liquids, allowing them to form

assemblies solely in the 2D plane along the interface. A similar approach has proven successful in the bottom-up synthesis of both inorganic and organic 2D materials.^[8] In these processes, the components undergo reactions at an interface, resulting in the formation of 2D structures.^[9] Taking inspiration from these methods, we attempted the ESD of Ag^+ ions at air-water interfaces. This process led to the creation of Ag nanoparticle-nanosheets (NP-NS), a pseudo-nanosheet where tiny Ag nanoparticles formed through ESD were assembled in a 2D arrangement.^[7] We hypothesized that the restricted mobility of the formed Ag nanoparticles prevents them from merging into genuine 2D structures.

Graphene, a well-known nanomaterial, is famous for its unusual electronic and mechanical properties.^[10–16] Bonding,^[17] transport,^[18] diffusion,^[19,20] and aggregation of metals^[21] on graphene have been extensively studied producing rich science and relevant applications. Extensive research has been conducted to investigate the increased mobility of various metals and metal clusters on graphene surfaces.^[22] According to computational studies, small clusters of gold (Au) and silver (Ag) have a preference for adopting 2D structures on graphene surfaces. Additionally, at higher concentrations, these clusters tend to form islands on the graphene surface.^[23,24] An earlier report from our group showed the coalescence of monolayer-protected Au clusters on graphene surfaces due to their enhanced mobility.^[25]

1. Introduction

Electrospray deposition (ESD) is a method wherein charged droplet sprays are placed onto a surface. Initially employed as a preparative tool in nuclear research,^[1] ESD has progressed into a precise deposition technique applied in various domains. These applications encompass the development of polymer coatings,^[2] the creation of thin conductive ceramic films,^[3] and even the preparation of films involving DNA,^[3] and proteins.^[4] Recently, ambient ESD has emerged as an innovative synthetic method for producing a diverse range of nanomaterials.^[5] In this process,

D. Sarkar, A. Som, K. Unni, S. Manna, P. Thalappil
DST Unit of Nanoscience (DST UNS) and Thematic Unit of Excellence (TUE)

Department of Chemistry
Indian Institute of Technology Madras
Chennai 60036, India

E-mail: debanjan_coe@icsrps.iitm.ac.in; pradeep@iitm.ac.in

D. Sarkar, A. Som, K. Unni, S. Manna, P. Thalappil
Centre of Excellence on Molecular Materials and Functions
Department of Chemistry
Indian Institute of Technology Madras
Chennai 60036, India

 The ORCID identification number(s) for the author(s) of this article can be found under <https://doi.org/10.1002/sml.202400159>

DOI: 10.1002/sml.202400159

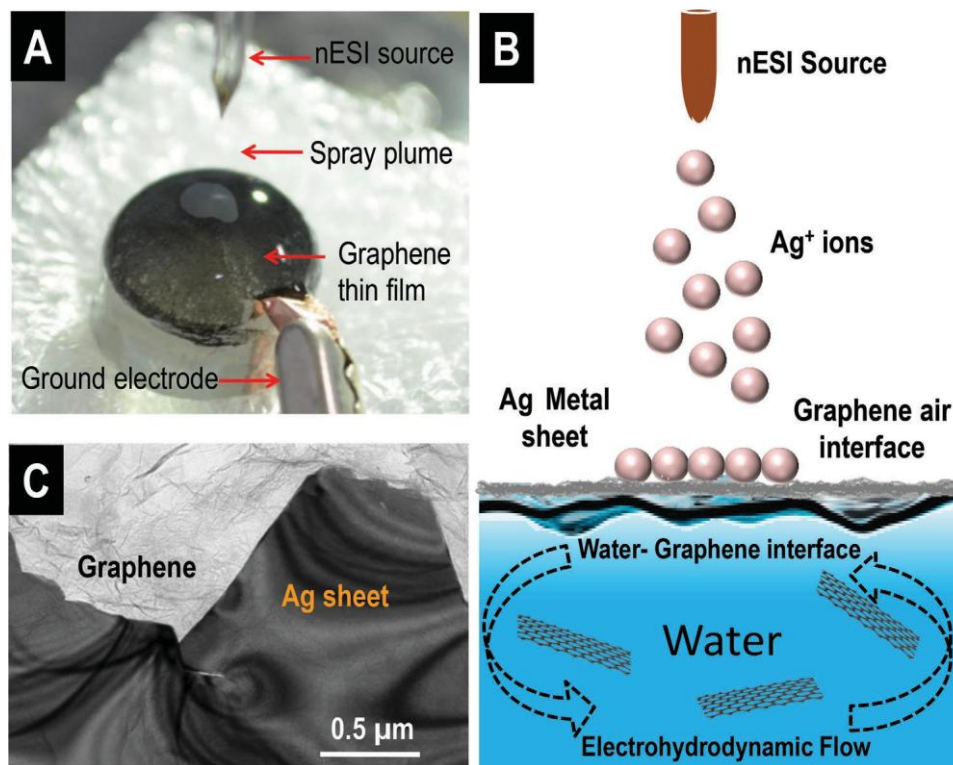


Figure 1. A) Optical micrograph of the electro spray deposition setup, showcasing the formation of a graphene thin film at the air–water interface following ESD onto an aqueous graphene suspension. B) Schematic representation of the ESD process, illustrating the electrohydrodynamic flow within the aqueous RGO suspension, leading to the formation of a thin film at the liquid surface, followed by the deposition of a silver sheet onto the RGO layer, and C) TEM image of the deposited solid silver sheet on the RGO film.

These inspired us to introduce graphene into our ESD synthetic system.

In this work, we successfully achieved the formation of large-area single crystalline silver sheets, measuring hundreds of micrometers in length, on an aqueous suspension of graphene under ambient conditions. Our approach combines several key factors: the ambient ESD method generates tiny silver clusters, the enhanced mobility of these clusters on graphene allows them to coalesce into larger structures, and the presence of an interface restricts their growth in 2D. While various methods exist to fabricate 2D silver sheets with controlled dimensions, such as cathodic arc deposition and magnetron sputtering,^[26–29] they necessitate demanding conditions like high vacuum, elevated temperature, and involvement of specific environments, besides appropriate equipment. Furthermore, these techniques convert existing silver metal into the desired 2D form. In contrast, our straightforward process eliminates the need for specialized chemicals or complex instruments. Instead, it transforms a readily available salt solution into single-crystalline metallic sheets under ambient conditions. This chemical approach with minimum infrastructure offers a significant advantage in terms of simplicity and accessibility. Besides, it extends the scope of ambient synthesis in microdroplets, an active subject area in the context of molecular science.^[30,31] We have extensively characterized these Ag sheets using microscopic and spectroscopic techniques and studied their growth dynamics. The resulting Ag sheets demonstrated excellent SERS activity, making them highly

promising for potential applications in sensing various contaminations.

2. Results and Discussion

2.1. Synthesis of Ag-Sheets using ESD

Figure 1A presents an optical image of the ESD apparatus and the formation of an RGO film on the top of the water surface. Initially, the electro spray deposition of the Ag-salt solution induced an electrohydrodynamic flow that led to the creation of a thin layer of assembled RGO at the air–water interface. As the process continues, the subsequent ESD of Ag^+ ions onto the RGO layer facilitates the neutralization of these ions into Ag atoms, and further, enables the coalescence of Ag atoms to form the desired metal sheets. Formation of the assembled RGO layer is facilitated by ESD-induced electrohydrodynamic motion in the aqueous RGO dispersion. This entire process is schematically presented in **Figure 1B**. In a previous report, we demonstrated a similar electrohydrodynamic flow in pure water to assemble suspended Pd nanoparticles on its surface, leading to the formation of NP–NS.

To establish that the formation of the RGO layer on the water surface was driven by similar forces, control experiments were performed. In such experiments, only DI water was electro-sprayed onto an aqueous suspension of RGO. The assembled RGO film was collected on a glass coverslip (**Figure S1A**,

Supporting Information) and placed on a sheet of paper with letters A, B, & C written using a red marker pen. The letters were clearly visible after placing the RGO-coated cover slip on top of them, indicating the thinness of the film. The RGO layers appear to be closely packed by the electrohydrodynamic flow to form the thin layer, as evidenced by the electrical continuity (Figure S1B, Supporting Information) of the RGO film-coated coverslips. Figure S1C (Supporting Information) schematically depicts the process of RGO assembly at the water surface and the subsequent formation of a metallic Ag sheet on top of it.

In the case of ESD of Ag⁺ ions, a shiny white round spot with a metallic luster was observed just under the sprayer head on the RGO surface after continued deposition for 2 h. This material was collected on various substrates such as transmission electron microscope (TEM) grids, indium tin oxide (ITO)-coated glass slides, and coverslips for further characterization. Electron microscopy analysis confirmed that the shiny spot was indeed composed of Ag metallic sheets. Figure 1C presents a large area TEM image of an Ag sheet formed on RGO. The size of the deposition spot was influenced by the distance between the spray tip and the deposition surface. An optimal distance of 10–15 mm was consistently maintained during all deposition processes.

The air–water interface plays a critical role in the formation of Ag sheets. The RGO suspension's water component not only contributes to the formation of the RGO layer through electrohydrodynamic motion but also facilitates the removal of unwanted organic residues from the Ag salt precursor. Without the air–water interface, no Ag sheet was formed on a dried RGO spot, deposited on an ITO-coated glass slide (Figure S2, Supporting Information). For this experiment, the RGO suspension was subjected to 30 min of bath sonication and then drop-cast onto an ITO-coated glass slide. The RGO was allowed to dry under laboratory conditions before performing a 2-h ESD of AgOAc. To demonstrate the significance of the RGO thin film formed at the air–water interface through electrohydrodynamic flow in the RGO suspension, an additional control experiment was conducted. In it, 1.5 mL of aqueous RGO suspension was placed in a vial and left open in the laboratory environment. After 3 h, a visible film appeared, floating on the surface. This film was then collected onto an ITO-coated slide and allowed to dry. Subsequently, ESD of Ag salt solution was carried out on the dried spot for a duration of 2 h, followed by SEM imaging. Despite the 2-h-long ESD process, no Ag sheets were observed (Figure S3, Supporting Information). In contrast, the electrohydrodynamic flow enables the tighter packing of RGO layers, as evidenced by the electrical continuity measurement depicted in Figure S1 (Supporting Information).

2.2. Characterization of the Synthesized Ag-Sheets

Figure 2A displays a scanning electron microscopy (SEM) image of Ag sheets formed on an ITO-coated glass slide through 5 h of ESD at a spray current of 100–110 nA. The SEM image reveals that the Ag sheets can cover a large area, with individual sheets reaching sizes of up to 30–35 μm. In **Figure 2B**, a higher magnification TEM image of a typical Ag sheet is shown. The presence of graphene layers can be clearly observed underneath the Ag sheet, as indicated by the green arrow. In **Figure 2C,D**, a TEM image of an entire Ag sheet and its corresponding energy-

dispersive X-ray spectroscopy (EDS) mapping are presented, respectively. The inset in **Figure 2D** displays the EDS spectrum collected from the sheet, indicating a composition of 100% Ag. Additionally, the inset in **Figure 2C** shows an X-ray photoelectron spectroscopy (XPS) spectrum of the Ag sheet. This spectrum confirms the presence of Ag 3d_{5/2} at 368.1 eV, providing evidence that the sheets are indeed made of metallic silver.

High-resolution transmission electron microscopy (HRTEM) analysis confirms the crystalline nature of the sheets. **Figure 3A,B** present HRTEM images of the Ag sheet formed on RGO. In **Figure 3A**, the lattice is clearly visible, with interplanar distances corresponding to the Ag(111) plane. The inset of **Figure 3A** displays a fast Fourier transform (FFT) image of the single crystalline Ag sheets, showing the cubic close packing of the lattice. Furthermore, careful imaging at the edges of the sheet reveals the presence of RGO layers surrounding the Ag sheets, as shown in **Figure 3B**. This observation indicates the structural relationship between the Ag sheets and the underlying RGO material.

A thorough investigation using HRTEM was conducted at various locations across the resulting Ag sheet to confirm its single crystalline nature. **Figure S4A–C** (Supporting Information) depicts HRTEM images showing prominent Ag (111) planes, providing evidence that the Ag sheets are indeed single crystalline. X-ray diffraction (XRD) analysis was also conducted to complement the HRTEM findings. For the XRD experiments, the Ag sheets synthesized were placed on a Si-wafer by careful scooping. **Figure 3C** presents the XRD spectrum of the Ag sheets on a Si-wafer substrate. The spectrum reveals solely the peak corresponding to the Ag (111) plane at a 2θ value of 38.23°. **Figure 3D** presents a slow scan spectrum of the Ag (111) region, further confirming the single crystallinity of the Ag sheets formed via ESD. Additionally, the XRD spectrum was collected from the graphene thin film-coated Si-wafer (**Figure S5**, Supporting Information) as a reference.

2.3. Optimizing Parameters for the Formation of Reproducible and Uniform Ag Sheets

We conducted several experiments to optimize the parameters for achieving reproducible and uniform Ag sheets. These experiments are detailed in this section.

2.3.1. Precursor Salt Concentration

Initially, we varied the concentration of the precursor salt (AgOAc in this case) from 2.5 to 10 mM while maintaining a fixed applied potential of 2 kV and a deposition time of 2 h. TEM analysis of the resulting Ag sheets (**Figure S6**, Supporting Information) revealed significant differences in their crystallinity based on the precursor concentration. At a lower concentration of 2.5 mM (**Figure S6A**, Supporting Information), the Ag sheets were only partially single-crystalline, indicating incomplete formation. Increasing the concentration to 5 mM (**Figure S6B**, Supporting Information) led to partial improvement in crystallinity, suggesting a transition toward single-crystallinity but still, the process was incomplete. Utilizing a concentration of 10 mM (**Figure S6C**, Supporting Information) yielded fully single-crystalline Ag sheets

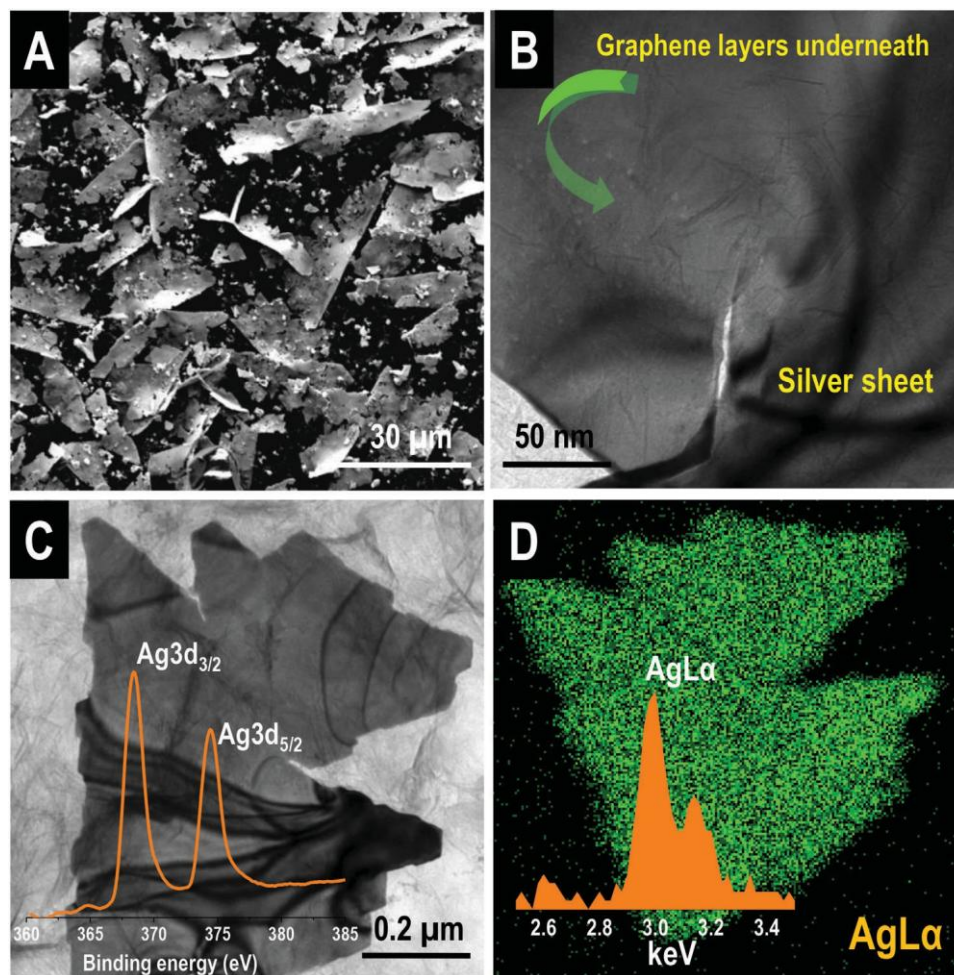


Figure 2. A) SEM image showing Ag sheets synthesized over a large area, B) TEM image of the Ag-sheet revealing its extremely thin nature, with the underlying graphene layers also being observable, C) TEM image showing a large Ag sheet; inset shows an XPS spectrum in the Ag3d region showing that the material is in zero-oxidation state, and D) Energy dispersive spectroscopy (EDS) mapping of the sheet shown in image D; inset of D is the EDS spectrum of the same.

within the 2-h deposition time. This demonstrates the importance of sufficient precursor concentration for achieving complete crystallinity. Based on these findings, we opted for a precursor salt concentration of 10 mm for all the subsequent experiments. Higher concentrations were not explored due to disruptions to the electrospray process caused by high salt content.

2.3.2. RGO Concentration

Upon varying the concentration of RGO in the aqueous suspension, the morphology of the Ag sheets was changed. Figure S7A–C (Supporting Information) showcases TEM images illustrating the Ag sheets formed in an aqueous suspension with different RGO concentrations. At lower RGO concentrations (0.01 wt%), the Ag sheets exhibited a perforated structure. Conversely, an increase in RGO concentration (0.05 wt%) resulted in the formation of solid sheets. This transition is likely attributed to the nonuniform thin film formation (as elaborated earlier, the electrohydrodynamic flow phenomenon leads to the formation of

a thin film of RGO on the water surface) at lower RGO concentrations, with regions displaying defects or cracks in the film. These observations underscore the significance of RGO concentration in influencing the characteristics of the sheets.

2.3.3. Time of Deposition

Similarly, we noted that the nature of the sheets was also dependent on the deposition time. Figure S8 (Supporting Information) shows TEM images of Ag sheets formed after different deposition times. It can be observed that as the deposition time increases, the sheets become more solid in nature, whereas those formed at lower deposition times remain perforated. Furthermore, extending the deposition time beyond the formation of solid sheets leads to an increase in the thickness of the resulting sheets (as depicted in Figure 3E,F). To corroborate this observation, we conducted an experiment utilizing two identical ESD setups to synthesize Ag sheets. One setup was operated for 2 h, while the other was allowed to run for 10 h. Figure S9 (Supporting Information)

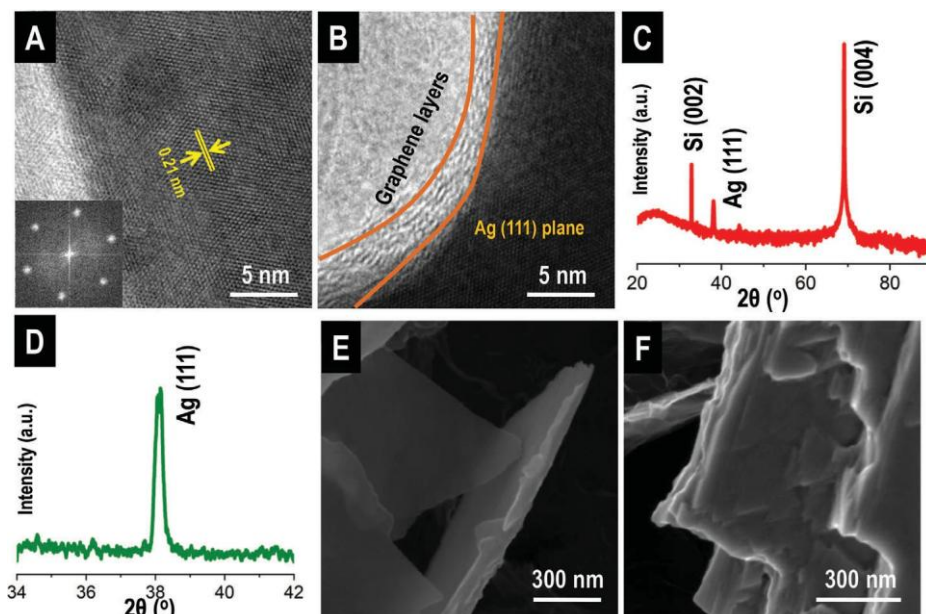


Figure 3. A) HRTEM image of a typical Ag sheet showing Ag (111) plane, these sheets are single crystalline in nature (inset shows the FFT of cubic close packing), B) HRTEM image of an Ag sheet at the edge showing the presence of graphene layers, C) XRD spectrum collected from the as-synthesized Ag sheets, collected over a Si wafer substrate. D) Slow scan XRD spectrum of the Ag (111) region. E) and F) are Field emission scanning electron microscopic (FESEM) images of the Ag sheet showing that these sheets can be very thin or layered in nature depending on the deposition time.

presents FESEM images of the resulting sheets. Notably, the images clearly demonstrate a significant increase in the thickness of the Ag sheets formed during the longer, 10-h deposition process.

2.3.4. Flow Rate, Applied Voltage, and Deposition Rate

It's important to note that another crucial factor influencing the outcome of an ESD process is the deposition rate. A control experiment was performed to investigate the effect of electrospray deposition rate on the synthesized Ag sheets. Two independent experiments were conducted using identical ESD setups except for the deposition rate of the incoming ions. The deposition rate was controlled by monitoring the deposition current using a picoammeter. In one experiment, the current was set at 100 nA (applied voltage 2.0 kV), while 50 nA (applied voltage 1.5 kV) was used in the other. This experiment also demonstrates the effect of flow rate, and different voltages applied for the ESD process as both these parameters are proportional to deposition current. TEM analysis (Figure S10, Supporting Information) of the resulting Ag sheets collected after 1 h of deposition revealed distinct dimensions in the X-Y plane for each deposition current. This data confirms that the Ag sheets initially grow in a 2D fashion and subsequently begin to increase in thickness with extended deposition times. Therefore, careful control of both the deposition time and rate enables precise tailoring of the sheet size, ultimately leading to the creation of a stable, uniform surface for further applications.

2.3.5. Different Precursor Salts

To investigate the influence of the counter anion on Ag sheet formation on graphene, various silver salt precursors were tested.

Ag sheet was formed with all the precursors, including silver acetate, silver perchlorate, and silver nitrate. Figure S11A,B (Supporting Information) present the SEM images of Ag sheets produced using AgClO_4 and AgNO_3 , respectively. These findings reveal that the counter anions have no significant effect on the formation of Ag sheets.

2.4. ESD of Mixtures of Metal Salts

Further, ESD experiments were conducted using mixtures containing different proportions of Ag and Pd precursors to investigate the influence of foreign metal on the Ag sheet formation. In Figure 4A,B, TEM images after ESD of the mixture at two different proportions (Ag: Pd 1:1 and 5:1) are shown. Additionally, EDS mapping was performed to determine the presence of the metals. The data presented indicate that there is minimal or no effect of the foreign atom (Pd in this case) on the Ag sheet formation. The formation of Ag sheets appears to be relatively unaffected by the presence of Pd in the precursor mixture.

2.4.1. Extending the Scope of ESD for Metal Separation

We investigated the potential of ESD on graphene for separating metals by depositing mixed precursor solutions. Our initial experiments focused on noble metals, specifically equimolar mixtures of silver with gold and platinum. As depicted in Figure S12 (Supporting Information), the resulting product exhibited clear separation, despite the initial homogenous precursor mixture. Interestingly, silver formed single-crystalline metallic sheets, while the other metals formed distinct nanoparticle assemblies. We further explored this phenomenon using non-noble metal precursors, including a mixture of silver acetate,

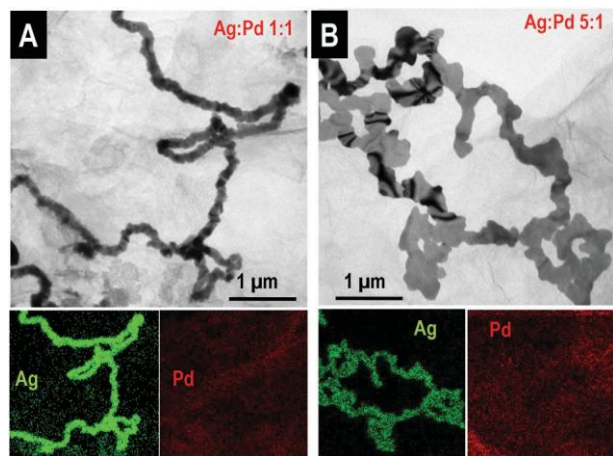


Figure 4. TEM images for ESD of Ag and Pd mixtures: A) Ag: Pd 1:1, and B) Ag: Pd 5:1. Down portions of each figure show EDS maps of the corresponding images.

sodium acetate, and magnesium acetate (representing common hard water contaminants). Figure S13A (Supporting Information) shows an SEM image of the resulting bundle of small Ag sheets. Point EDS analysis (Figure S13B, Supporting Information) confirmed the presence of 100% silver, demonstrating successful separation. Notably, large-area Ag sheets were not observed in this case. This could be attributed to the presence of other metal ions with high mobility occupying the graphene layers, hindering the coalescence of silver. These findings suggest that the ESD method holds promise for effectively separating silver from industrial or mining wastewater. Further research is warranted to explore its applicability to diverse metal-containing waste streams.

2.5. ESD of Other Noble Metals on Air-Water-Graphene Interface

We tested other noble metals to explore the possibility of forming single crystalline sheets using the same technique. In the case of other noble metals (such as Pd, Au, and Pt) on the aqueous suspension of RGO, the formation of 2D structures was not observed; instead, nanoparticles (size 5–10 nm) were formed. Figures S14 and S15 (Supporting Information) show TEM images of the ESD product of Pd and Au, respectively on RGO. This suggests that further optimization of the conditions is necessary to create sheets. This difference in the structures formed is likely to be due to the nature of the softness of the metals. Ag, being relatively soft compared to Au and Pd, allows for more favorable coalescence of atoms, leading to the formation of 2D structures. However, in the case of Au and Pd, the atoms do not coalesce easily, resulting in the formation of nanoparticles instead of 2D structures.

2.6. Surface-Enhanced Raman Spectroscopy (SERS)

Creating a stable and reliable SERS substrate remains a significant challenge due to factors such as nanoparticle aggregation,

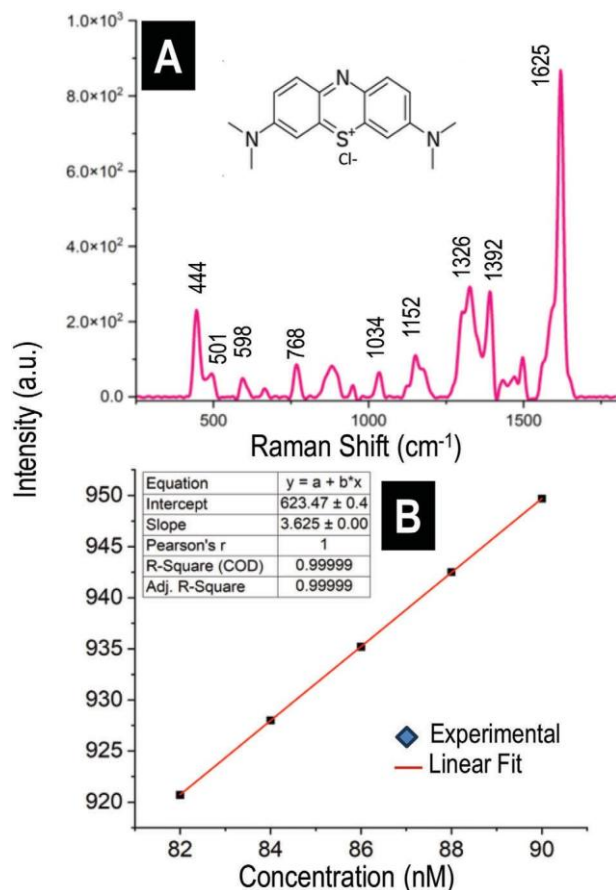


Figure 5. A) Surface-enhanced Raman spectrum of methylene blue, on Ag@RGO surface, B) concentration versus intensity (@1625 cm⁻¹) plot for MB within the concentration range 80–90 nM.

metal oxidation, molecule adsorption/desorption dynamics, substrate instability, and reproducibility.^[32] This is why stable substrates exhibiting robust SERS properties garner significant attention within the scientific community. In this study, we have successfully fabricated a surface comprised of single-crystalline silver sheets deposited on RGO. These metallic sheets exhibit excellent stability and can be reproducibly formed with controlled sizes. The synergistic interaction between silver and RGO endows the fabricated surface with exceptional SERS capabilities.

Here, we tested the SERS property of the ESD-synthesized Ag sheets embedded in graphene, using methylene blue (MB) as a target molecule (Figure 5A). We collected the Raman spectra of various concentrations of MB and constructed a calibration curve to determine the limit of detection. We used the most intense peak for MB at 1625 cm⁻¹ for this purpose (Figure 5B and Figure S16, Supporting Information). By employing linear fitting of the data, we evaluated the theoretical limit of detection with an R² value of 0.99999. Interestingly, we observed acceptable Raman spectra for MB at concentrations as low as 0.08 μM with the Ag sheets. However, the featured peaks were absent for the same sample with RGO as the substrate (Figure S17, Supporting Information). This observation suggests the synergistic effect of RGO and Ag for SERS-based detection.

3. Conclusion

A room temperature process to make large area single crystalline Ag sheets from its salt solution, without any other reagent was demonstrated. Although there are multiple studies on enhanced mobility of atoms on graphene surfaces, experimental proof of it was still a challenge due to limitations in experimental design. Here we demonstrated an ambient method that provides a means to test the fate of metal ions/atoms introduced directly on graphene layers. We report that the formation of metal sheets depends on the concentration of reduced graphene oxide suspension and the nature of the metal. The presence of foreign species, such as Pd atoms does not affect the formation of Ag sheets. The method could be used to separate silver from common contaminants such as alkali and alkaline earth metals from solutions. Due to the SERS property of the metals, the method has potential applicability in various fields, including environmental monitoring and biomedical sensing. Our Ag film could detect methylene blue at nanomolar concentrations. The simplicity and sensitivity of the method make our material an attractive candidate for on-site detection applications.

4. Experimental Section

Materials and Methods: All the chemicals used for the experiments were commercially available and were used without any further purification. Silver acetate (AgOAc) and silver perchlorate (AgClO₄) were purchased from Sigma–Aldrich, India. AgNO₃ was purchased from RANKEM. Reduced graphene oxide (RGO) was chemically synthesized in the laboratory using the modified Hummers' method. Locally available deionized (DI) water was used for making graphene suspension.

Instrumentation: Nanoelectrospray (nESI) emitters were made using a micropipette puller (P-97) purchased from Sutter Instrument, USA. Transmission electron microscopy (TEM) and high-resolution transmission electron microscopy (HRTEM) were performed using an accelerating voltage of 200 kV using a JEOL 3010, 300 kV instrument equipped with a UHR polepiece. A Gatan 794 multiscan CCD camera was used for image acquisition. EDS spectra were collected on the Oxford Semistem system housed on the TEM. Samples were taken onto 300-mesh carbon-coated copper grids (spi Supplies, 3530C-MB) by dipping them into a graphenic suspension after Ag deposition and drying under ambient conditions before examining them in TEM. A field emission scanning electron microscope (FEI Quanta FEG 200, USA) was used to image the Ag sheets. Energy dispersive spectroscopy (EDS) analyses were performed with the same SEM instrument. Some images were collected also with an FEI Quanta 100 instrument having a tungsten filament source. X-ray photoelectron spectroscopic (XPS) measurements were conducted using an Omicron ESCA probe spectrometer with polychromatic MgK α X-rays ($h\nu = 1253.6$ eV). Raman measurements were made using a Confocal Raman micro spectrometer (Witec GmbH, Germany) with 532 and 633 nm laser sources.

Synthesis of Graphene: Reduced graphene oxide (RGO) was synthesized using the modified Hummers' method. 25 mL concentrated sulphuric acid (H₂SO₄), 5 g potassium persulfate (K₂S₂O₈), and 5 g of phosphorus pentoxide (P₂O₅) were mixed in a 250 mL beaker and heated at 90 °C with continuous stirring till all the reagents dissolved in H₂SO₄. Then the temperature of the reaction mixture was brought down to 80 °C, and 6 g of graphite powder was added slowly to it. The temperature of the reaction mixture was maintained at 80 °C for 5 h. Bubbling in the reaction mixture was observed initially, which was subsided with time. After 5 h of heating the reaction mixture was kept for cooling at room temperature. Once it was cooled, it was diluted with 1 L of distilled water and kept undisturbed overnight. The resultant solution was filtered, and the super-

natant was washed thoroughly with water to remove excess acid present in it.

About 230 mL of concentrated H₂SO₄ was taken in a 500 mL beaker and it was maintained at 0–5 °C by keeping it in an ice bath. Then the pre-oxidized graphite was added to the cooled acid with stirring. ≈ 15 g of potassium permanganate (KMnO₄) was carefully added to this mixture. The addition of KMnO₄ was done such that the temperature of the mixture did not go beyond 10 °C. Then this reaction mixture was kept at 35 °C for 2 h. Once the reaction was complete, 1 L of distilled water was added to the mixture very carefully so that the temperature did not go beyond 50 °C. After the addition of water, the mixture was kept for stirring for another 2 h. Afterward, 1.5 L of distilled water and 25 mL of 30% H₂O₂ were added to it. Then it was kept at room temperature for one day. The supernatant was discarded slowly and the remaining solution was centrifuged and repeatedly washed with 10% HCl followed by water. Then the resultant solid was dried in air and 2% (w/v) water dispersion was made, and it was dialyzed for 3 weeks continuously to remove contaminants like salts and acid. After dialysis, the dispersion was diluted to obtain 0.5% (w/v) graphene oxide (GO).

The GO dispersion was then reduced to get RGO. Pre-reduction of GO was done by adding sodium carbonate (5 wt%) and 800 mg of sodium borohydride followed by heating for 1 h. Then the reaction mixture was cooled, centrifuged, and washed with water thoroughly and redispersed. To make a free-standing dispersion of RGO in water, sulfonation was done. For that 20 mg sulfanilic acid and 8 mg sodium nitrite were dissolved in 0.25% NaOH solution followed by the addition of 4 mL 0.1 M HCl. Then the mixture was stirred and kept in an ice bath. After 15 min of stirring, aryl diazonium salt solution was added to 20 mL, 0.5 mg mL⁻¹ RGO dispersion. Then the reaction mixture was kept in an ice bath and stirred for 2 h. After the reaction was complete, it was filtered washed with water repeatedly, and redispersed to obtain 0.05 wt% RGO suspension.

Electrospray Deposition (ESD): Spray emitters for ESD were made using a borosilicate glass capillary of 0.86 mm inner diameter and 1.5 mm outer diameter. The glass capillaries were pulled in such a way that they had an opening of 10–25 μ m at the tip. Each tip underwent quality control through optical microscopy, and any deviation from the desired size range or exhibiting flaws was discarded. This specific size range was chosen based on previous findings, where it was shown to be crucial for achieving long-term stability for ESD.^[6,7,33,34] Selected tips were filled with an aqueous solution (10 mm) of silver acetate (AgOAc) using a microinjector pipette tip. It was then connected to a homemade electrode assembly. A positive voltage in the range 2–2.5 kV was applied through a platinum wire. With the application of the high voltage, a spray plume containing the charged droplets was visible at the tip of the sprayer. This spray plume was directed to an Eppendorf tube containing an aqueous suspension of RGO. To have a stable continuous spray, the liquid was grounded by pasting a copper strip on the inner wall of the vial. The deposition current was maintained at 100–110 nA using a picoammeter. The details are presented in the inset of Figure 1A.

Supporting Information

Supporting Information is available from the Wiley Online Library or from the author.

Acknowledgements

The authors acknowledge DST, Govt. of India, and IIT Madras for research funding. The authors acknowledge Dr. Bivas Saha and Mr. Debmalaya Mukhopadhyay of JNC SAR, Bengaluru for helping in measuring the XRD data.

Conflict of Interest

The authors declare no conflict of interest.

Author Contributions

D.S. was responsible for the conception and design of the work, data collection, data analysis and interpretation, drafting, and editing of the article. A.S. performed TEM measurements, data analysis and interpretation, drafting, and editing of the article. K.U. performed electrospray deposition. S.M. performed Raman measurements. T.P. supervised the study, performed data analysis, interpretation of results, and editing of the article.

Data Availability Statement

The data that support the findings of this study are available from the corresponding author upon reasonable request.

Keywords

ambient ions, electrospray deposition, graphene, microdroplets, SERS, silver sheets

Received: January 8, 2024

Revised: March 26, 2024

Published online:

- [1] G. Siuzdak, T. Hollenbeck, B. Bothner, *J. Mass Spectrom.* **1999**, *34*, 1087.
- [2] M. K. Rahman, T. H. Phung, S. Oh, S. H. Kim, T. N. Ng, K.-S. Kwon, *ACS Appl. Mater. Interfaces.* **2021**, *13*, 18227.
- [3] V. N. Morozov, *Adv. Biochem. Eng. Biotechnol.* **2010**, *119*, 115.
- [4] V. N. Morozov, T. Y. Morozova, *Anal. Chem.* **1999**, *71*, 1415.
- [5] J. Ghosh, R. G. Cooks, *Trends Analyt. Chem.* **2023**, *161*, 117010.
- [6] D. Sarkar, M. K. Mahitha, A. Som, A. Li, M. Wlekinski, R. G. Cooks, T. Pradeep, *Adv. Mater.* **2016**, *28*, 2223.
- [7] D. Sarkar, R. Singh, A. Som, C. K. Manju, M. A. Ganayee, R. Adhikari, T. Pradeep, *J. Phys. Chem. C.* **2018**, *122*, 17777.
- [8] R. Dong, T. Zhang, X. Feng, *Chem. Rev.* **2018**, *118*, 6189.
- [9] H.-S. Jang, B. Seong, X. Zang, H. Lee, J. W. Bae, D.-H. Cho, E. Kao, C. Yang, G. Kang, Y. Liu, H. S. Park, D. Byun, L. Lin, *Adv. Mater. Interfaces.* **2018**, *5*, 1701491.
- [10] Y. Zhang, Y.-W. Tan, H. L. Stormer, P. Kim, *Nat. Plants.* **2005**, *438*, 201.
- [11] A. H. Castro Neto, F. Guinea, N. M. R. Peres, K. S. Novoselov, A. K. Geim, *Rev. Mod. Phys.* **2009**, *81*, 109.
- [12] X. Du, I. Skachko, A. Barker, E. Y. Andrei, *Nat. Nanotechnol.* **2008**, *3*, 491.
- [13] O. C. Compton, S. T. Nguyen, *Small.* **2010**, *6*, 711.
- [14] X. Zhao, Q. Zhang, D. Chen, P. Lu, *Macromolecules.* **2010**, *43*, 2357.
- [15] L.-C. Tang, Y.-J. Wan, D. Yan, Y.-B. Pei, L. Zhao, Y.-B. Li, L.-B. Wu, J.-X. Jiang, G.-Q. Lai, *Carbon.* **2013**, *60*, 16.
- [16] F. Bonaccorso, Z. Sun, T. Hasan, A. C. Ferrari, *Nat. Photonics.* **2010**, *4*, 611.
- [17] W. Zhou, M. D. Kapetanakis, M. P. Prange, S. T. Pantelides, S. J. Pennycook, J.-C. Idrobo, *Phys. Rev. Lett.* **2012**, *109*, 206803/1.
- [18] O. Cretu, A. V. Krashenninnikov, J. A. Rodriguez-Manzo, L. Sun, R. M. Nieminen, F. Banhart, *Phys. Rev. Lett.* **2010**, *105*, 196102/1.
- [19] W. D. Luedtke, U. Landman, *Phys. Rev. Lett.* **1999**, *83*, 1702.
- [20] B. Yoon, W. D. Luedtke, J. Gao, U. Landman, *J. Phys. Chem. B.* **2003**, *107*, 5882.
- [21] C. Zheng, W. Chen, Y. Huang, X. Xiao, X. Ye, *RSC Adv.* **2014**, *4*, 39697.
- [22] B. Wang, B. Yoon, M. Koenig, Y. Fukamori, F. Esch, U. Heiz, U. Landman, *Nano Lett.* **2012**, *12*, 5907.
- [23] S. S. Chae, S. Jang, W. Lee, D. W. Jung, K. H. Lee, J. D. Kim, D. Jeong, H. Chang, J. Y. Hwang, J.-O. Lee, *Small.* **2018**, *14*, 1801529.
- [24] I. Shteplyuk, I. G. Ivanov, N. Pliatsikas, T. Iakimov, S. Lara-Avila, K. H. Kim, N. Ben Sedrine, S. E. Kubatkin, K. Sarakinos, R. Yakimova, *ACS Appl. Nano Mater.* **2021**, *4*, 1282.
- [25] A. Ghosh, T. Pradeep, J. Chakrabarti, *J. Phys. Chem. C.* **2014**, *118*, 13959.
- [26] C. P. Johnson, *Thin Film Process.* **1991**, *11*, 209.
- [27] I. G. Brown, *Annu. Rev. Mater. Res.* **1998**, *28*, 243.
- [28] N. Ghobadi, S. Rezaee, *J Mater Sci Mater Electron.* **2016**, *27*, 8464.
- [29] P. Asanithi, S. Chaiyakun, P. Limsuwan, *J. Nanomater.* **2012**, *2012*, 963609.
- [30] X. Yan, *Int. J. Mass Spectrom.* **2021**, *468*, 116639.
- [31] A. B. Theberge, F. Courtois, Y. Schaerli, M. Fischlechner, C. Abell, F. Hollfelder, W. T. S. Huck, *Angew. Chem., Int. Ed.* **2010**, *49*, 5846.
- [32] J. Prakash, *Int. Rev. Phys. Chem.* **2019**, *38*, 201.
- [33] D. Sarkar, B. Mondal, A. Som, S. J. Ravindran, S. K. Jana, C. K. Manju, T. Pradeep, *Glob. Chall.* **2018**, *2*, 1800052.
- [34] D. Sarkar, A. Som, T. Pradeep, *Anal. Chem.* **2017**, *89*, 11378.

NANO · MICRO
small

Supporting Information

for *Small*, DOI 10.1002/smll.202400159

Interfacial Growth of Large Area Single-Crystalline Silver Sheets Through Ambient Microdroplets

*Depanjan Sarkar**, *Anirban Som*, *Keerthana Unni*, *Sujan Manna* and *Pradeep Thalappil**

Supporting Information

Interfacial Growth of Large Area Single-Crystalline Silver Sheets through Ambient Microdroplets

Debanjan Sarkar*, Anirban Som, Keerthana Unni, Sujan Manna, and Thalappil Pradeep*

*Email: pradeep@iitm.ac.in

*E-mail: depanjansarkar@gmail.com

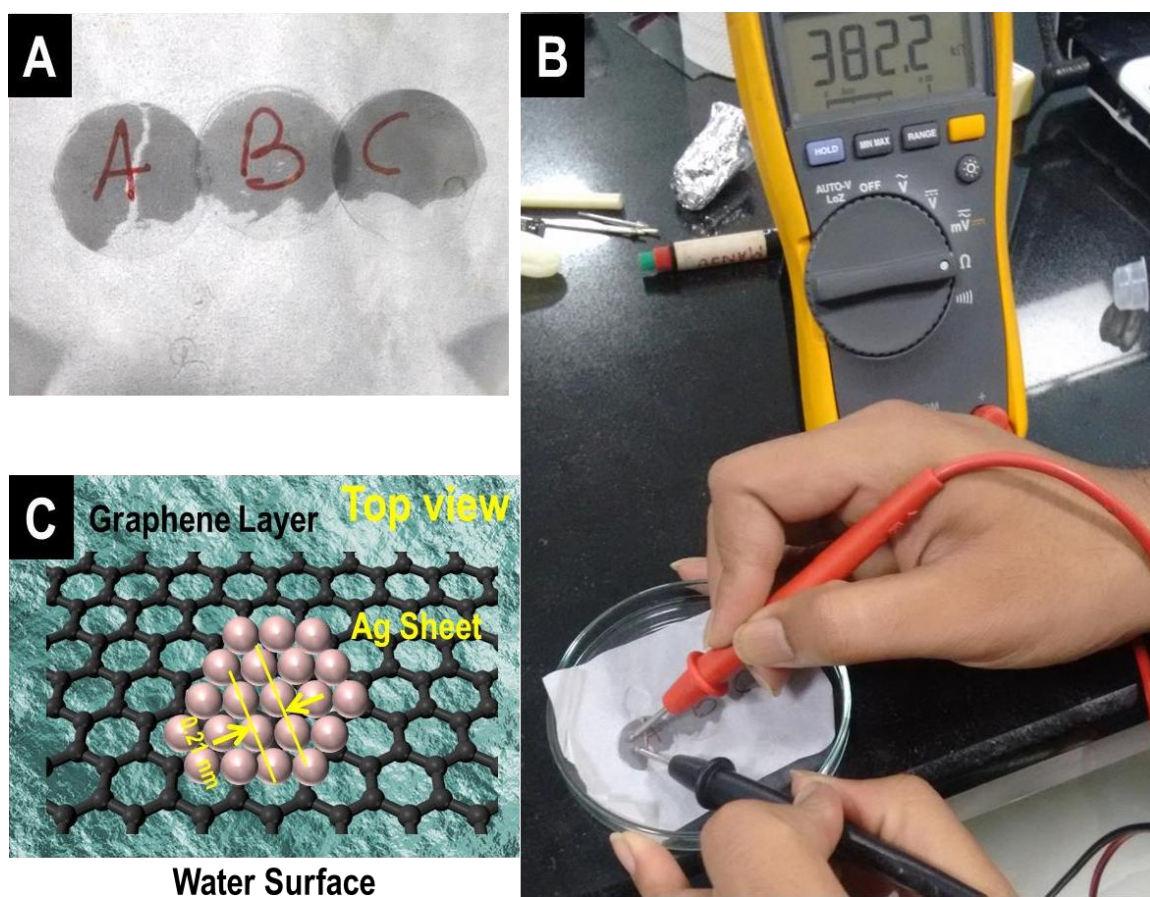


Figure S1. Optical photographs of A) graphene thin films collected on glass cover slips, B) electrical conductivity of the film. C) Schematic representation top view, showing the formation of single crystalline Ag sheet on graphene

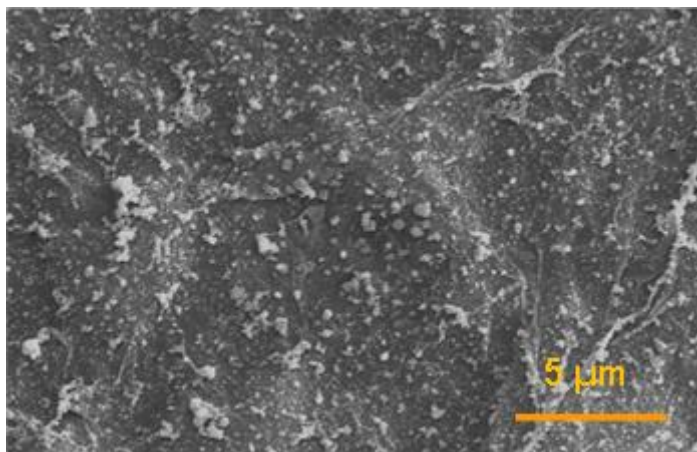


Figure S2. SEM image of ESD of Ag ions on a dried graphene surface.

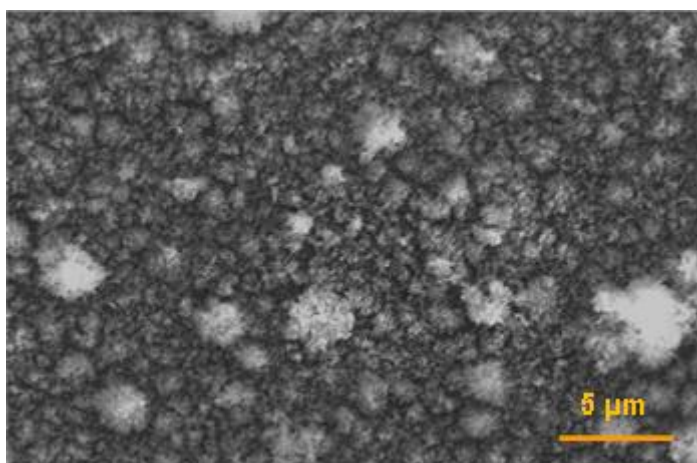


Figure S3. SEM image of ESD of Ag ions on a graphene film formed by evaporation of the solvent.

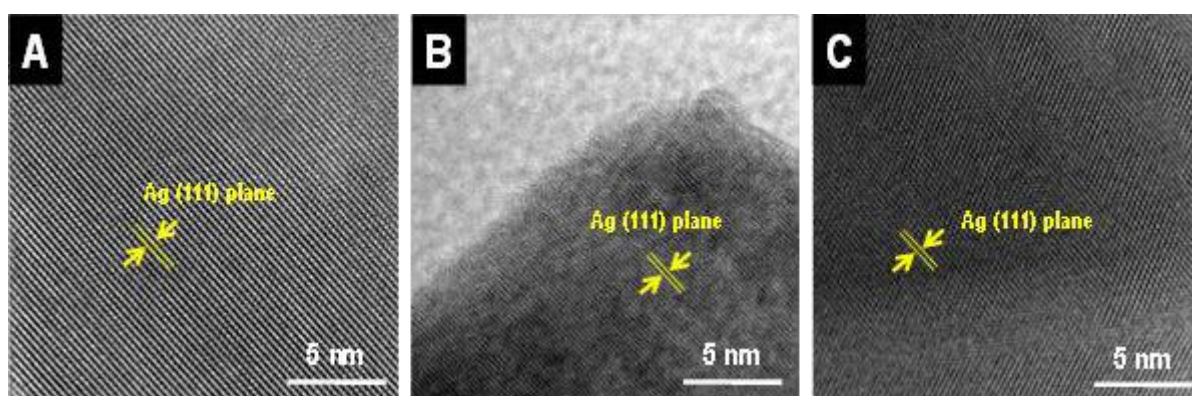


Figure S4. HRTEM images collected from different points of a Ag sheet showing Ag(111) lattice planes.

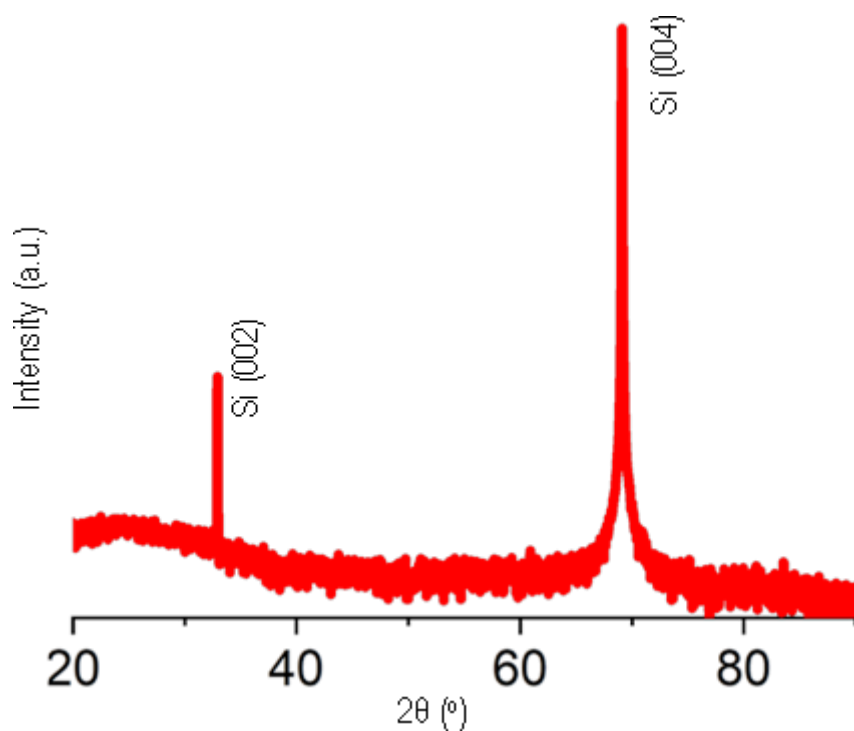


Figure S5. XRD spectrum of the graphene thin film-coated Si-wafer substrate for reference.

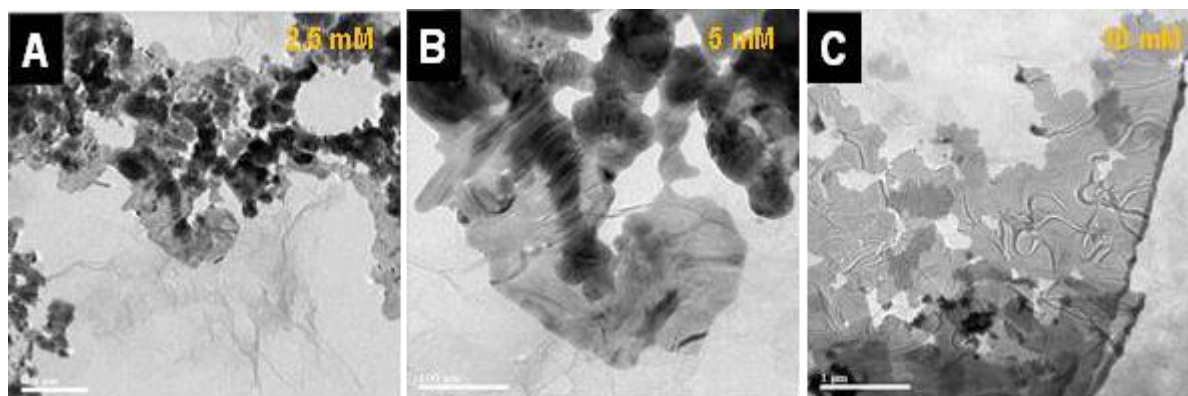


Figure S6. TEM images of Ag sheet synthesized using different precursor concentrations, A) 2.5 mM, B) 5 mM, and C) 10 mM.

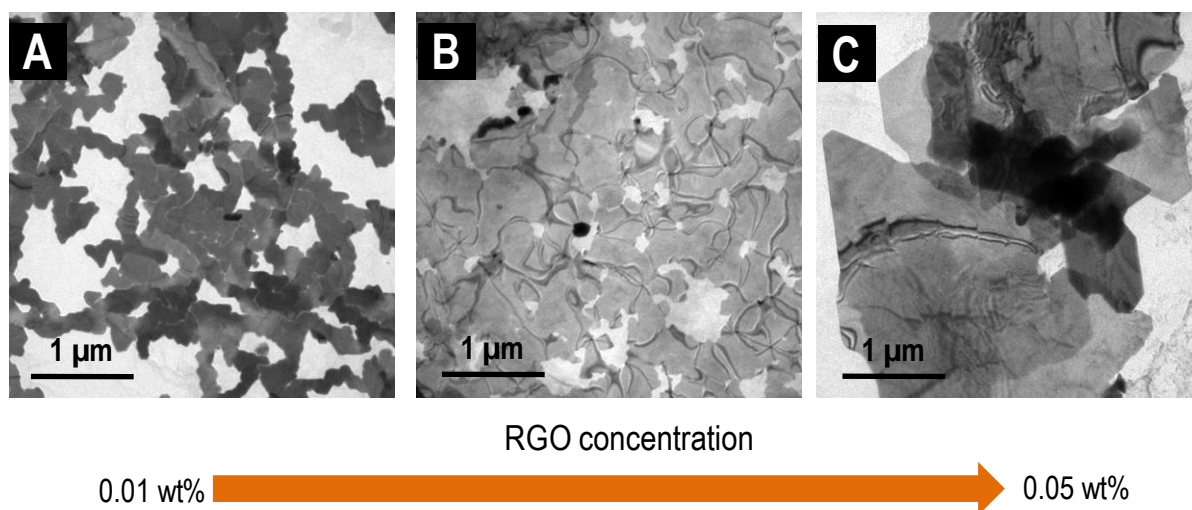


Figure S7. TEM images of Ag sheet formed on RGO. From A) to C) concentration of the RGO suspension increases.

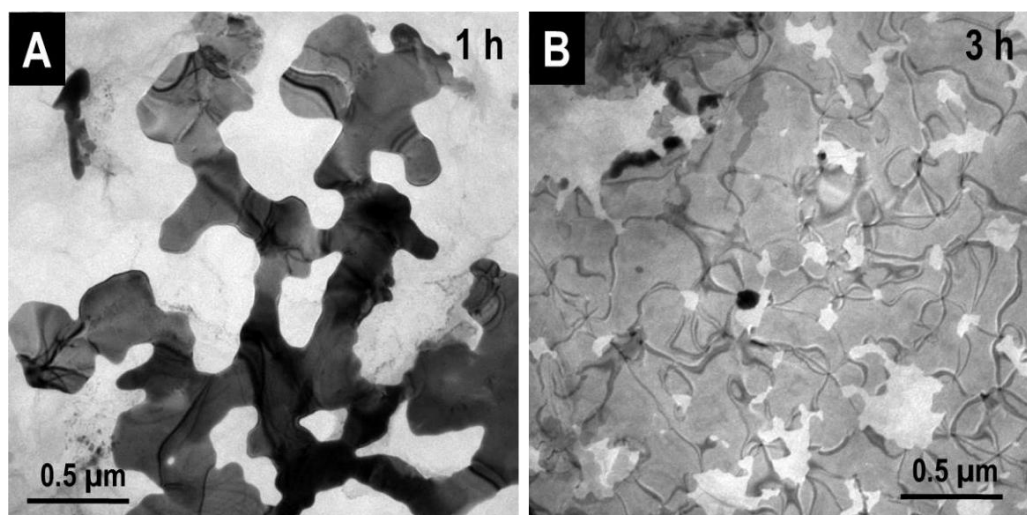


Figure S8. TEM images of the Ag sheet formed on RGO suspension at the different time of deposition.

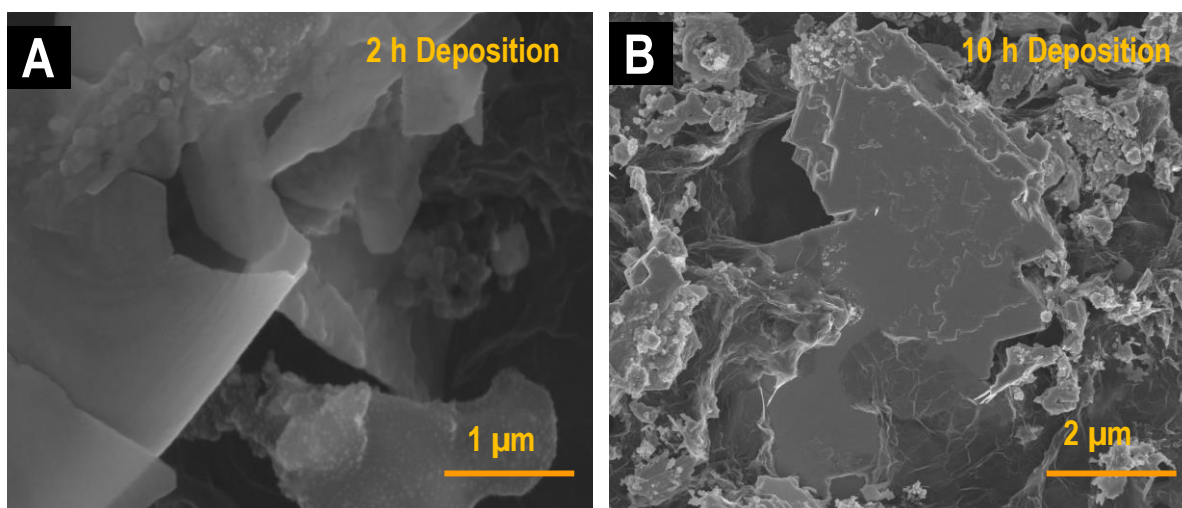


Figure S9. FESEM images of Ag sheets formed after A) 2h deposition, and B) 10 h deposition, showing clear difference in their thickness.

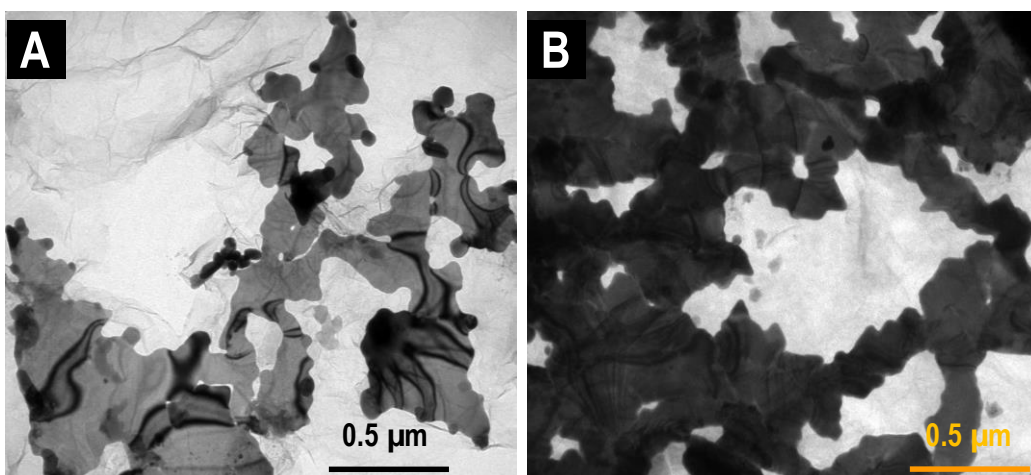


Figure S10. TEM Images of the Ag sheets formed with different deposition currents: A) 50 nA, and B) 100 nA.

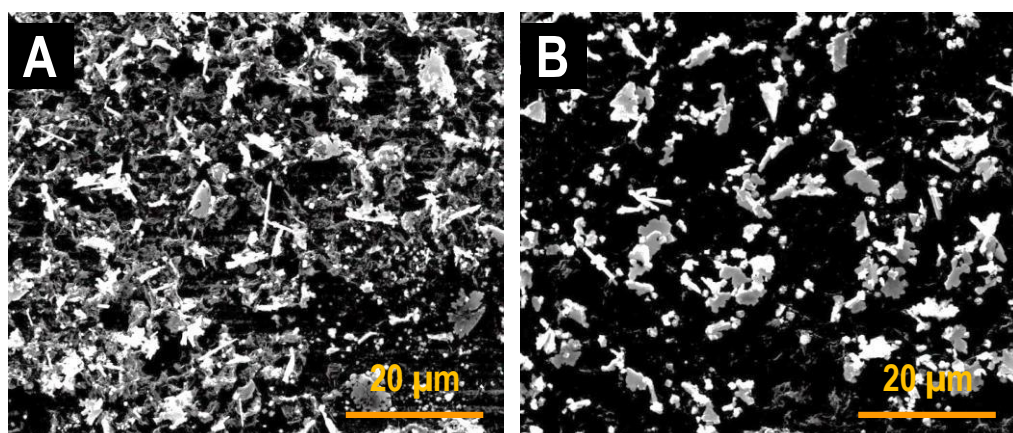


Figure S11. SEM images of Ag sheets synthesized from different precursor salts: A) AgClO_4 , and B) AgNO_3 .

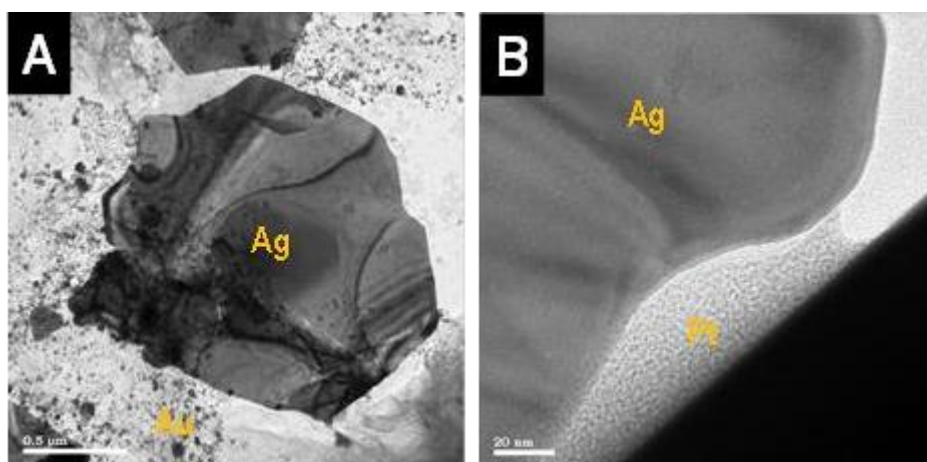


Figure S12. TEM images collected from the ESD samples of mixed precursor of noble metal salts, A) silver-gold, and B) silver-platinum.

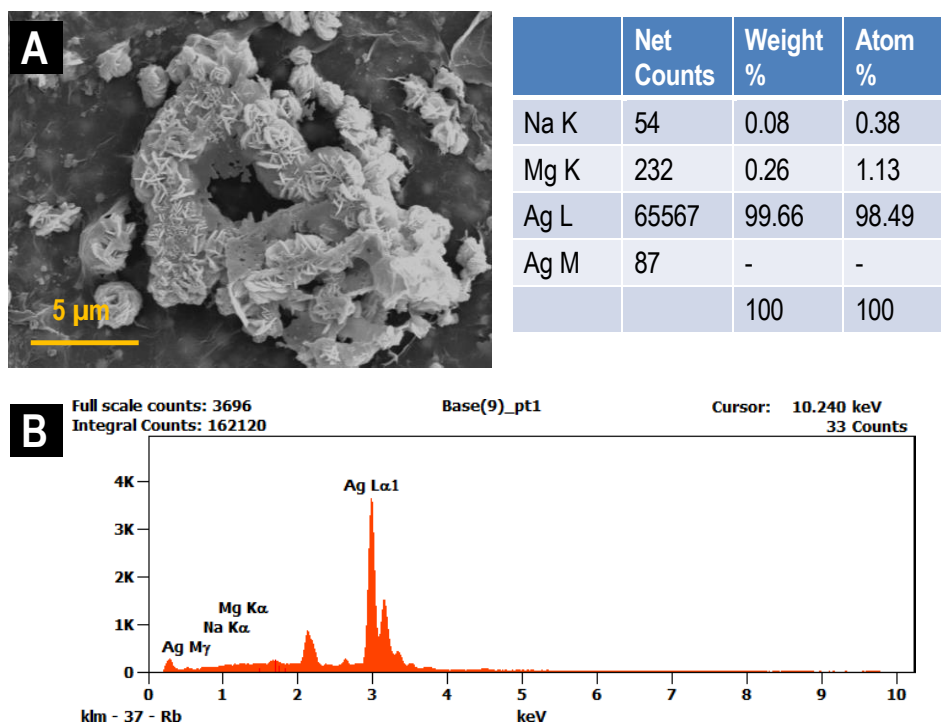


Figure S13. A) SEM image of the Ag sheets formed after ESD of mixed precursor solution of silver acetate, sodium acetate, and magnesium acetate. B) Point EDS spectrum showing that the sheets are made of 100% silver. Atomic percentages are presented in the inset.

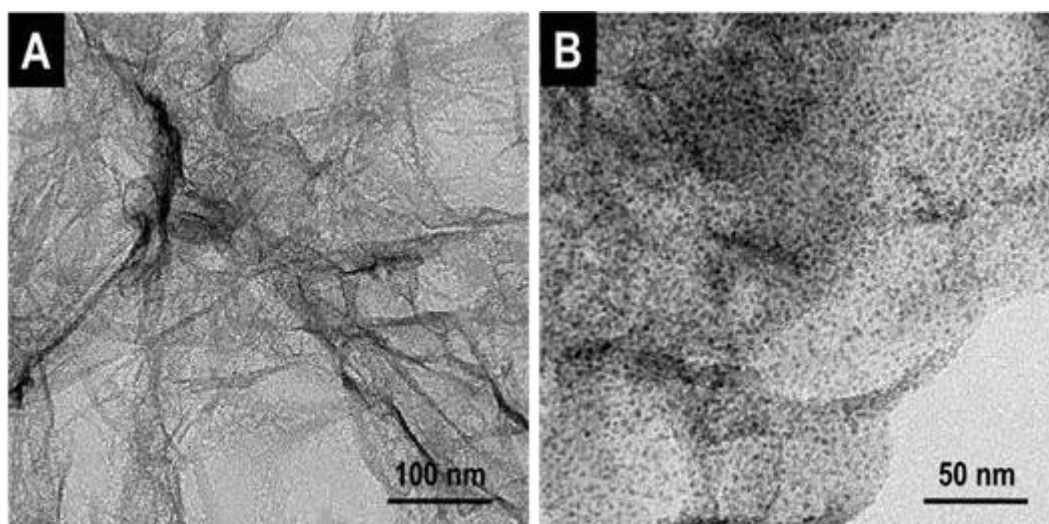


Figure S14. TEM image of Pd nanoparticles formed after ESD of Pd on aqueous suspension of RGO.

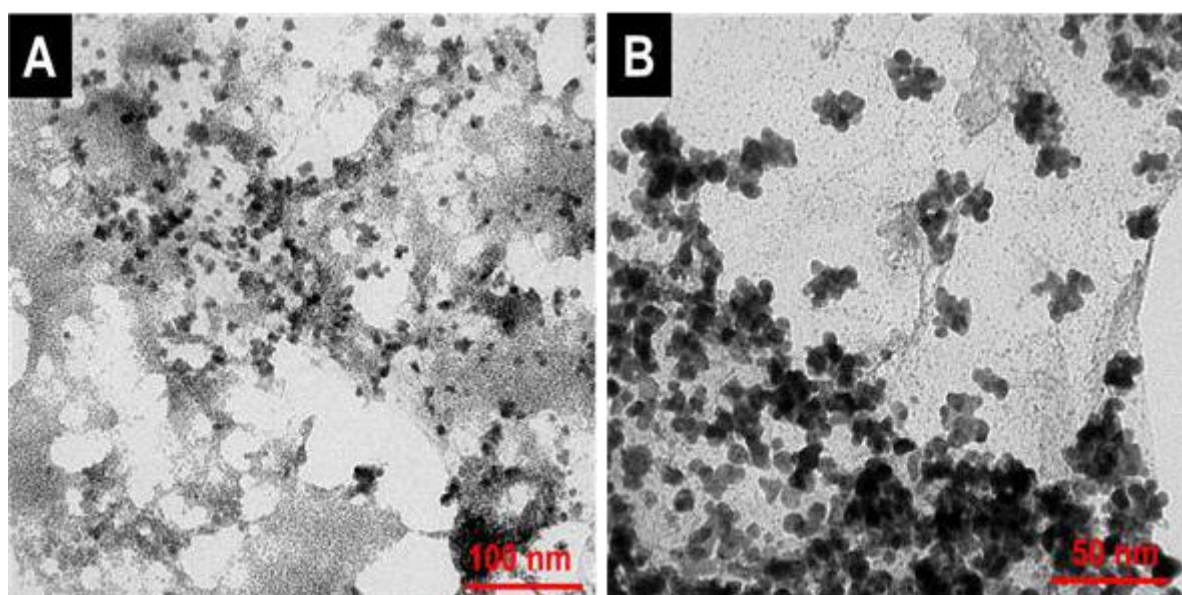


Figure S15. TEM image of Au nanoparticles formed after ESD of Au on aqueous suspension of RGO.

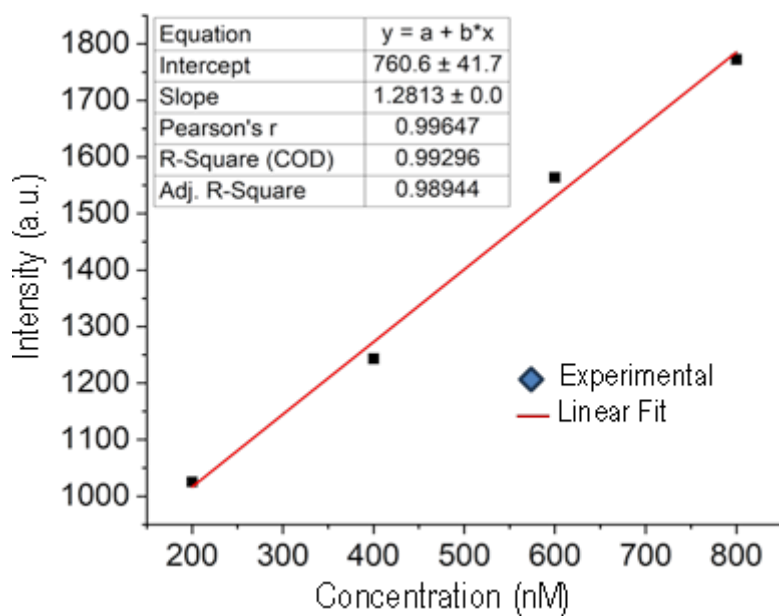


Figure S16. Concentration vs SERS intensity (@1625 cm⁻¹) plot for MB within the concentration range 200-800 nM.

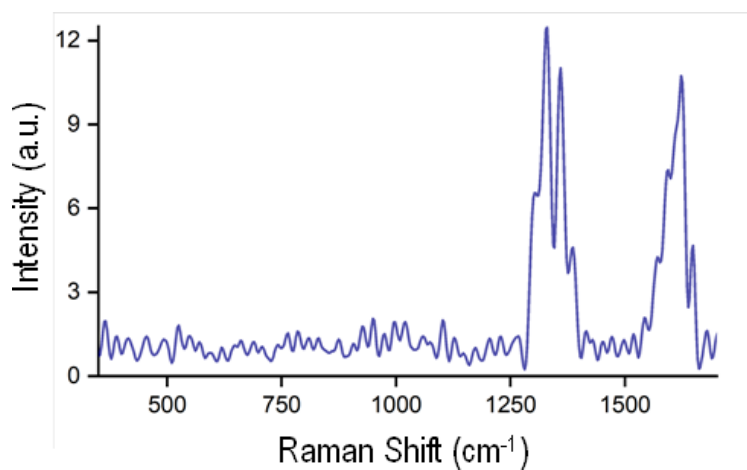


Figure S17. Raman spectrum collected using 0.08 μ M methylene blue on graphene surface.



Observing atomically precise nanocluster aggregates in solution by mass photometry†‡

 Jayoti Roy,^a Ila Marathe,^b Vicki Wysocki^b and Thalappil Pradeep^b  *ac

 Cite this: *Chem. Commun.*, 2024, 60, 6655

 Received 25th January 2024,
 Accepted 15th May 2024

DOI: 10.1039/d4cc00363b

rsc.li/chemcomm

We report the first mass photometric characterization of nanoaggregates of atomically precise nanoclusters (NCs) in solution. The differently-sized nanoaggregates of silver–gold alloy NCs, $[\text{Ag}_{11x}\text{Au}_x(\text{DPPB})_5\text{Cl}_5\text{O}_2]^{2+}$ [$x = 1-5$ and DPPB = 1,4-bis(diphenylphosphino)butane], formed in solution, were examined by mass photometry (MP) with a protein calibration. In addition, we conducted MP studies of varying solvent composition to understand the structural evolution of nanoaggregates. The masses of nanoaggregates were correlated to structures of 15 to 50 nm diameter observed in cryo-electron microscopy.

Atomically precise metal nanoclusters (NCs) belong to an emerging family of materials with potential applications in areas such as energy, environment, and biology.¹⁻³ These NCs, resembling macromolecules, are typically characterized by high-resolution mass spectrometry (MS), single-crystal X-ray diffraction, and other spectroscopic studies.⁴⁻⁶ They undergo structural changes and interact with various molecular entities or with each other in solution.⁷ In such processes, under specific conditions, they form aggregates that are observable by dynamic light scattering (DLS) and related *in situ* spectroscopic/microscopic techniques.⁸⁻¹⁰ Aggregation of NCs is central to building NC-based multi-dimensional materials.^{8,11} Exploring such assemblies of NCs is an emerging area of interest in nanotechnology due to its relevance in deriving tuneable collective properties as well as for exploring novel applications in a wide range of fields.¹²⁻¹⁵ Determining

accurate number of building units in superstructures in the multi-dimensional closed-packed molecular aggregates of NCs is a grand challenge, particularly in solution. However, metal NCs themselves can exhibit a wide range of arrangements, from monomeric species to large multimeric complexes. Consequently, the presence of heterogeneity in complex systems poses a significant challenge for accurately determining the number of building units, especially when ligand-protected NCs form superstructures such as chains, helices, spheres, capsids, and prisms.¹⁶ At the same time, it is a challenge to construct nanoassemblies of precise morphology due to the lack of control of kinetics and assembly dynamics.

Over the years, several techniques have been applied to characterize NC-based multidimensional assemblies and investigate their potential applications in the solid state.¹⁷ Among these techniques, electron microscopy and X-ray scattering have been most relevant to understand their structural integrity.¹⁸ Unfortunately, these techniques have inherent limitations, primarily in determining the number of monomeric units responsible for the formation of such structures. The most efficient way to assess composition of these NC-aggregates is to investigate their masses.¹⁹ The traditional mass analysis technique, mass spectrometry, has focused on measuring ensembles of hundreds or thousands of atoms/molecules in the gas phase by imparting multiple charges on them.²⁰ These methods have been successful in analysing biomolecules, NCs, and NC-based supramolecular-oligomeric small complexes.^{21,22} However, mass spectrometry cannot examine the NC-assembled species directly in solution and consequently their structural evolution.

Here we report the first investigation of the structural evolution of such nanoaggregates in solution using interferometric scattering microscopy (iSCAT), later renamed as mass photometry (MP).²³ MP is an emerging optical technique with a high dynamic mass range, needing only nanomolar concentrations of analyte, and has been used generally for examining biomolecules such as proteins.²³ Earlier, the iSCAT technique has been employed in materials science to accurately infer the

^a DST Unit of Nanoscience (DST UNS) & Thematic Unit of Excellence (TUE), Department of Chemistry, Indian Institute of Technology Madras (IITM), Chennai 600036, India. E-mail: pradeep@iitm.ac.in

^b Department of Chemistry and Biochemistry and Native Mass Spectrometry Guided Structural Biology Center, The Ohio State University, Columbus, Ohio 43210, USA

^c International Centre for Clean Water, 2nd Floor, B-Block, IIT Madras Research Park, Kanagam Road, Taramani, Chennai 600113, India

† Dedicated to Archita Patnaik, a colleague and valued friend, to celebrate her 65th birthday.

‡ Electronic supplementary information (ESI) available. See DOI: <https://doi.org/10.1039/d4cc00363b>

size-distribution of nanoparticles of various sizes without probing their masses.^{24–26} Grant *et al.* employed this method to determine size distributions of gold nanoparticles and compared the results with those obtained from transmission electron microscopy (TEM).²⁵ The iSCAT technique can be demonstrated to have superior accuracy in measuring the particle size distribution of nanoparticles compared to DLS. However, the use of MP for nanoparticle mass determination has remained unexplored. Individual proteins, protein complexes, and their aggregates in the 30 kDa–5 MDa mass range have been examined by this technique, giving new insights into their structural and functional properties; namely, polymerization, host–guest interactions, and self-assembly.^{23,27} These nano-sized nanoparticles are comparable in size to that of many biomolecules such as proteins, antibodies and nucleic acids.²⁸ Thus, MP can be used to study solution-phase aggregation dynamics of NCs, similar to its use in biomolecular interactions. With this objective, we used MP to examine a particular NC system that is known to form precise nanoaggregates in solution.⁸

We used a new series of Ag–Au alloy nanoclusters denoted as $[\text{Ag}_{11y}\text{Au}_x(\text{DPPB})_5\text{Cl}_5\text{O}_2]^{2+}$ [$x = 1–5$]. They are co-protected by 1,4-bis(diphenylphosphino)butane (DPPB) and chloride ligands and exhibit useful photophysical properties.⁸ The unique solvophobic property of this Ag–Au alloy NC leads to the formation of luminescent solution phase self-assemblies. Size-dependent luminescence characteristics of these aggregates and their potential applications have been explored previously.⁸ In this report, we investigated these alloy NCs and their precisely formed nanostructures, by varying the compositions of the solvent system (methanol:water). This investigation was conducted using a Refeyn TwoMP mass photometer (Refeyn Ltd), complemented by cryogenic electron microscopy (cryo-EM).²⁹ Details of the experimental protocol are discussed in the ESI.† To examine the suitability of MP for studying the solution phase self-assembly of atomically precise NCs, we used an equimolar mixture of b-amylose and thyroglobulin with a broad mass range of 50–660 kDa as a standard, in 30% (v/v) methanol solution. A calibration graph ($r^2 = 0.9999$) was obtained from the measurements and the error was estimated to be 5%. Details of the calibration method are described in ESI.† The stability of protein calibrants in 30% (v/v) methanol was confirmed by comparing the same in ammonium acetate (AmAc) solution by MP measurements (see histograms in ESI.†). In Fig. 1, we show the electrospray ionization mass spectrometric (ESI MS) characterization of the parent NC system used in this study. The peaks marked with 1–5 correspond to different NCs with varying number of gold atoms, *i.e.*, $[\text{Ag}_{10}\text{Au}(\text{DPPB})_5\text{Cl}_5\text{O}_2]^{2+}$, $[\text{Ag}_9\text{Au}_2(\text{DPPB})_5\text{Cl}_5\text{O}_2]^{2+}$, $[\text{Ag}_8\text{Au}_3(\text{DPPB})_5\text{Cl}_5\text{O}_2]^{2+}$, $[\text{Ag}_7\text{Au}_4(\text{DPPB})_5\text{Cl}_5\text{O}_2]^{2+}$, and $[\text{Ag}_6\text{Au}_5(\text{DPPB})_5\text{Cl}_5\text{O}_2]^{2+}$, with the same nuclearity ($\text{Ag}_{11y}\text{Au}_x = \text{M}_{11}$, with $x = 1–5$). The position and isotopic distribution of each of these help us to assign the precise composition of the NC (see inset of Fig. 1A(ii)). The well-defined NC aggregates formed with varying solvent compositions was revealed in a previous report by DLS and TEM studies.⁸ As demonstrated, the nature and quantity of the nanoaggregates

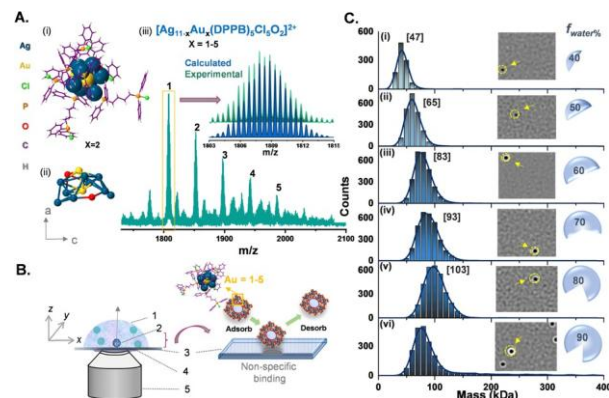


Fig. 1 (A) (i) Calculated structure ($x = 2$), (ii) the metal, $\text{Ag}_{11y}\text{Au}_x$, core ($x = 2$), and (iii) ESI MS of $[\text{Ag}_{11y}\text{Au}_x(\text{DPPB})_5\text{Cl}_5\text{O}_2]^{2+}$ ($x = 1–5$) nanoclusters. In inset, calculated isotopic distribution is stacked with the experimental one. (B) Concept and experimental implementation of MP. Parts in the graphic representation: (1) solvent mixture (sol mix) containing nanoclusters; (2) nanocluster aggregates in solution; (3) glass surface; (4) immersion oil; (5) objective lens. Single-particle landing event on a non-coated cover slide is shown on the right. (C) A stacked plot of the MP histogram of various-sized nanoaggregates with the counts of particle landing events, with varying solvent composition. M_{av} are shown on the spectra as $[\text{xx}]$. The photographs of single-particle binding events on the glass–sol interface during each set of measurements is shown. The corresponding $f_{\text{water}\%}$ of solvent mixture is labelled on each histogram.

are dependent on the solution composition. Specifically, an increase in solution polarity, achieved by increasing the fraction of water (*i.e.*, $f_{\text{water}\%}$), corresponds to an increase in the size of nanoaggregates. To understand the possible intercluster interaction, we tried to predict the structure of NC and its ligand orientation theoretically (see Fig. S1, ESI.†). To measure the mass of each nanoaggregates corresponding to a specific composition, MP experiments were carried out by dropcasting the solution on the pre-treated glass slide (see details in ESI.†), as shown in Fig. 1B. Data for the first set of measurements with NC-aggregates at $f_{40\%}$ solution of the solvent mixture (sol mix) *i.e.*, 40% (v/v) water and 60% (v/v) methanol, are shown in Fig. 1C(i). The nanoaggregates exhibit non-specific binding events on the glass slide during their landing on the substrate, which are captured as microscopic events, as presented in Fig. 1C(i) images. The size distribution resulting from such multiple-binding events was captured and plotted, corresponding to a mass of 47 kDa as determined using protein calibration, at $f_{40\%}$. Several such MP measurements were carried out by increasing $f_{\text{water}\%}$. Upon gradually increasing the water percentage in the sol mix (water%: 50%, 60%, 70%, and 80%), different sets of equimolar NC solutions were prepared, and their mass distributions were measured immediately. The stacked MP histogram presented in Fig. 1C(i)–(vi) are indicative of the average mass distributions (M_{av}) of promptly generated-nanoaggregates across the different sets of NC solutions. It is evident that an increment in the water percentage leads to a systematic increase in M_{av} . It increases from 65 to 83 to 93 to 103 kDa with an increase in water content. This systematic evolution in mass agreed with the previously reported DLS data.⁸ A table containing various percentages of solvents, the corresponding masses of aggregates, and the number of NCs

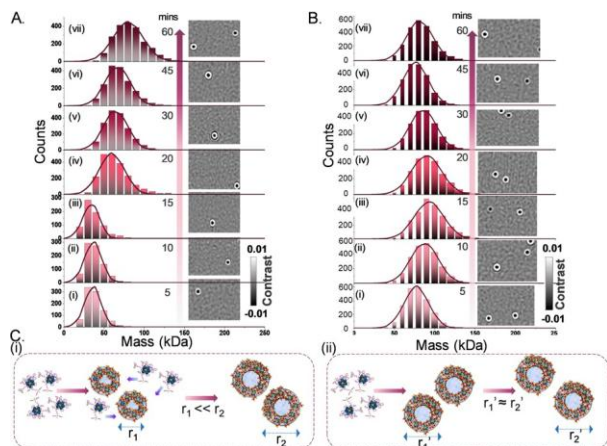


Fig. 2 Stacked plots of the time-dependent mass variation of nanoaggregates with normalized counts of single-particle landing events at (A) $f_{40\%}$ and (B) $f_{80\%}$, respectively, in MP. The time scale of each stack represents the time of data acquisition at a particular sol mix. The photographs of single-particle landing events at the glass–sol mix interface with increasing time are shown as insets with each measurement. (C) Schematic representation of the variation in diameter of nanoassemblies during NC-aggregation at (i) $f_{40\%}$ and (ii) $f_{80\%}$ respectively. r_1 , r_1^0 represent the diameter of the nanoaggregates at the initial stage of growth, and r_2 , r_2^0 represent the same at the final stage.

present in each of them is presented in ESI† (Table S1). Aggregation numbers (N_{NCS}) of 13, 18, 23, 26, 29, and 50 for various solvent compositions corresponding to smaller aggregates, growing aggregates, and bigger aggregates were observed. However, at water% = 90%, the size of nanoaggregates decreases, consistent with the previously reported DLS data (an explanation will be presented later).⁸ As expected, aggregation depends strongly on the input concentration of the NC and the binary solvent composition. In Fig. 2, we show the data obtained at a constant input concentration ($\rho \approx 60$ nM) in two distinct solvent compositions: (i) $f_{40\%}$ which correspond to the formation of the smallest nanoaggregates with $M_{\text{av}} = 47$ kDa, and (ii) $f_{80\%}$ forming the largest nanoaggregates with $M_{\text{av}} = 103$ kDa. Here are two different aggregate dimensions at a given point of growth. A smaller aggregate (*i.e.*, at $f_{40\%}$) grows systematically with time while the larger aggregates remain essentially invariant in time. When the water% is high, *e.g.*, at $f_{80\%}$, individual NCs become unstable in solution, which make them aggregate rapidly. Lower solvent polarity results in a gradual increase in the diameter of the nanoaggregates, whereas higher solvent polarity leads to rapid aggregation, as schematically shown in Fig. 2(C). Fig. 3 illustrates the comparative size-evolution (mass) of nanoaggregates at $f_{40\%}$ and $f_{80\%}$ with changes in solvent polarity, represented as a function of evolution time. The total number of particles non-specifically interacting with the uncoated coverslip during measurements was recorded, and subsequently the mass of a single particle was calculated by spatio-temporal isolation (see ESI† for more details about data processing and mass calculations). In the case of $f_{40\%}$ (Fig. S3, ESI†), time-dependent measurements show a gradual increase in the mass from 39 to 47 kDa (Fig. S3(i)–(iii), ESI†), implying solution phase growth of aggregates during the

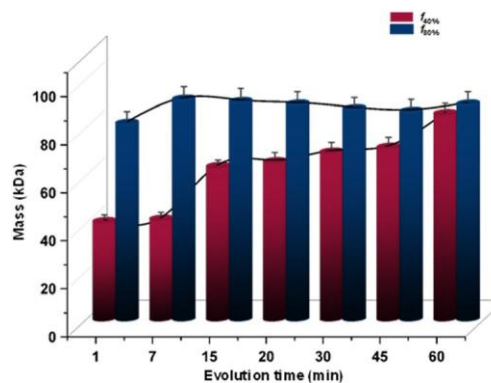


Fig. 3 Time-dependent size-evolution of nanoaggregates.

initial 20 min. After 45 min of incubation, along with simultaneous growth in smaller aggregates (\bullet 100 kDa), larger aggregates (4500 kDa) were also recorded in single particle mass analysis. These two mass distributions are shown in Fig. S3(iv) (ESI†). This phenomenon continued until 60 min of measurement [as shown in Fig. S3(v)(a and b), ESI†]. Similar measurements were performed in the case of $f_{80\%}$. Here, systematic growth of smaller particles in the smaller mass range was absent (see Fig. S3(i)–(iii), ESI†). Moreover, the presence of bigger particles was recorded coherently throughout the entire tracking timeframe, *i.e.*, 5–60 min. The possible N_{NCS} were calculated from the recorded mass (see Fig. S3, ESI†). The evolution of the size and structure of the nanoaggregates was captured first by room-temperature TEM (RT-TEM). Standard time-dependent TEM examination showed that the aggregates were well-defined NCs with a hollow-cage sphere-shaped or vesicle-like structures (as shown in Fig. S5–S7, ESI†). For additional understanding, time dependent RT-TEM micrographs (see S7, ESI† for RT-TEM sample preparation) of $f_{40\%}$ and $f_{80\%}$ were collected. In Fig. S5–S7 (ESI†), time dependent RT-TEM micrographs at $f_{40\%}$ are presented, which in turn reflects that with increasing growth time (*i.e.*, from 0 to 30 to 60 min), there is a gradual increase in M_{av} along with thickening of the wall of the nanoaggregates, corroborating the MP observations (see Table S2, ESI†).

To obtain more precise information about the gradual increase in diameter during solution-phase growth, we employed cryo-EM, as shown in Fig. 4. Detailed cryo-TEM methodology is provided in the ESI.† While RT-TEM images suggest the presence of a hollow-cage morphology within individual nanoaggregates, this feature is less distinct in the cryo-TEM micrographs. This disparity may be attributed to differences in sample preparation methods used in the respective TEM studies. Cryo-TEM micrographs display the size evolution of nanoaggregates over time, revealing sizes of 12.5, 33, and 45 nm at 0, 30, and 60 min of aggregation, respectively. Notably, the trend in gradual increase of diameter derived from cryo-TEM data align well with the MP data. In the case of $f_{80\%}$, cryo-TEM and RT-TEM observations indicate the minimal size evolution of donut-shaped nanoaggregates as a function of growth time (Fig. S5–S11, ESI†). Our data suggest that the aggregates are hollow in nature as we described previously.⁸

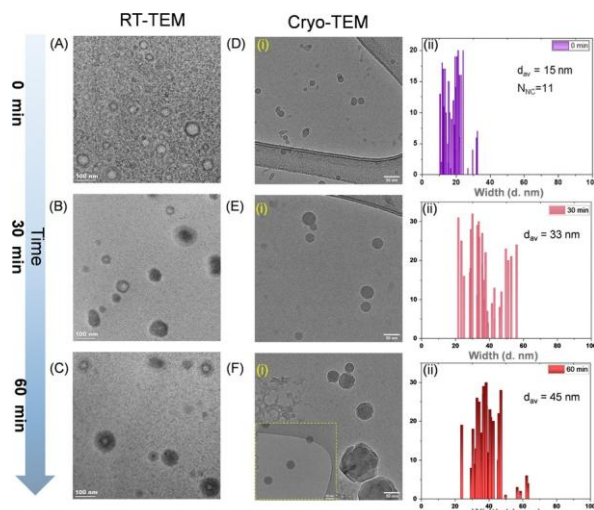


Fig. 4 Time-dependent (A)–(C) RT-TEM (scale bar 100 nm) and (D)–(F)(i) cryo-TEM (scale bar 50 nm) measurements and (ii) the extracted average particle-size distribution with average diameter from cryo-TEM micrographs, all formed at $f_{40\%}$.

As water and methanol are miscible, we believe that the solvent molecules encapsulated within the nanoaggregates also have the same composition as in the bulk. Due to the limited mass accuracy of MP, an exact number of solvent molecules encapsulated in the aggregates is unclear. By assuming a donut-/vesicle-shaped assembly of NCs, we calculated the N_{NC} mathematically from the average radius of the nanoaggregates obtained from the cryo-TEM micrographs. The N_{NC} value, initially (*i.e.*, 0 min incubation) was 12 which is in very good agreement with the mass calculated by MP (see Fig. S3(iv), ESI†). A detailed mechanism of formation of NC-based nanoaggregates and their solution phase evolution are discussed in ESI† (see SI11). To carefully assess the applicability of MP measurements for investigating nanoparticle systems, we tried to correlate the observed MP data with cryo-TEM (see SI12, ESI†).

In conclusion, we presented the first MP studies of atomically precise NC aggregates showing their systematic assembly leading to hollow spheres of precise composition. MP is simple, highly sensitive, intrinsically quantitative, and fast technique in measuring masses of protein complexes. We showed that atomically precise cluster aggregates could be quantified in terms of their N_{NC} in solution. The results could be correlated with cryo-TEM and RT-TEM, which confirmed that the aggregates are hollow spheres. Their solution phase size evolution and dynamics could be observed in real-time (in MP). In conjunction with computational studies, MP makes it possible to propose structures and correlate those with emerging properties such as enhanced luminescence in such aggregates. Our study shows that mass photometry is a new way to explore the properties of nanoparticle assemblies in solution.

Conflicts of interest

There are no conflicts to declare.

Notes and references

- I. Chakraborty and T. Pradeep, *Chem. Rev.*, 2017, 117, 8208–8271.
- S. M. van de Looij, E. R. Hebels, M. Viola, M. Hembury, S. Oliveira and T. Vermonden, *Bioconjugate Chem.*, 2021, 33, 4–23.
- G. Yang, Z. Wang, F. Du, F. Jiang, X. Yuan and J. Y. Ying, *J. Am. Chem. Soc.*, 2023, 145, 11879–11898.
- P. Chakraborty and T. Pradeep, *NPG Asia Mater.*, 2019, 11, 48.
- B. Nieto-Ortega and T. Bu`rgi, *Acc. Chem. Res.*, 2018, 51, 2811–2819.
- J. B. Benedict and P. Coppens, *J. Am. Chem. Soc.*, 2010, 132, 2938–2944.
- P. Chakraborty, A. Nag, A. Chakraborty and T. Pradeep, *Acc. Chem. Res.*, 2019, 52, 2–11.
- M. Jash, A. Jana, A. K. Poonia, E. Khatun, P. Chakraborty, A. Nagar, T. Ahuja, K. V. Adarsh and T. Pradeep, *Chem. Mater.*, 2023, 35, 313–326.
- Y. Pei, P. Wang, Z. Ma and L. Xiong, *Acc. Chem. Res.*, 2018, 52, 23–33.
- L. Yang, H. Cheng, Y. Jiang, T. Huang, J. Bao, Z. Sun, Z. Jiang, J. Ma, F. Sun, Q. Liu, T. Yao, H. Deng, S. Wang, M. Zhu and S. Wei, *Nanoscale*, 2015, 7, 14452–14459.
- M. Sugiuchi, J. Maeba, N. Okubo, M. Iwamura, K. Nozaki and K. Konishi, *J. Am. Chem. Soc.*, 2017, 139, 17731–17734.
- Q. Yao, L. Liu, S. Malola, M. Ge, H. Xu, Z. Wu, T. Chen, Y. Cao, M. F. Matus, A. Pihlajam`aki, Y. Han, H. H`akkinen and J. Xie, *Nat. Chem.*, 2023, 15, 230–239.
- X. Wang, B. Yin, L. Jiang, C. Yang, Y. Liu, G. Zou, S. Chen and M. Zhu, *Science*, 2023, 381, 784–790.
- S. Chen, W. Du, C. Qin, D. Liu, L. Tang, Y. Liu, S. Wang and M. Zhu, *Angew. Chem.*, 2020, 132, 7612–7617.
- T. Li, H. Zhu and Z. Wu, *Nanomaterials*, 2023, 13, 1–23.
- N. Nonappa, *ACS Mater. Au*, 2024, 4(3), 238–257.
- W. A. Dar, A. Jana, K. S. Sugi, G. Paramasivam, M. Bodiuzzaman, E. Khatun, A. Som, A. Mahendranath, A. Chakraborty and T. Pradeep, *Chem. Mater.*, 2022, 34, 4703–4711.
- A. Pinkard, A. M. Champsaur and X. Roy, *Acc. Chem. Res.*, 2018, 51, 919–929.
- S. Basu, H. Fakhouri, C. Moulin, S. Dolai, I. Russier-Antoine, P. F. Brevet, R. Antoine and A. Paul, *Nanoscale*, 2021, 13, 4439–4443.
- M. Kinter, *Anal. Chem.*, 1995, 67, 493–497.
- M. M. Alvarez, J. T. Khoury, T. G. Schaaff, M. N. Shafiqullin, I. Vezmar and R. L. Whetten, *J. Phys. Chem. B*, 1997, 101, 3706–3712.
- V. Liljestr`om, A. Ora, J. Hassinen, H. T. Rekola, N. Nonappa, M. Heilala, V. Hynninen, J. J. Joensuu, R. H. A. Ras, P. T`orm`a, O. Ikkala and M. A. Kostainen, *Nat. Commun.*, 2017, 8, 1–10.
- A. Sonn-Segev, K. Belacic, T. Bodrug, G. Young, R. T. VanderLinden, B. A. Schulman, J. Schimpf, T. Friedrich, P. V. Dip, T. U. Schwartz, B. Bauer, J.-M. Peters, W. B. Struwe, J. L. P. Benesch, N. G. Brown, D. Haselbach and P. Kukura, *Nat. Commun.*, 2020, 11, 1772.
- R. W. Taylor and V. Sandoghdar, *Nano Lett.*, 2019, 19, 4827–4835.
- L. Melo, A. Hui, M. Kowal, E. Boateng, Z. Poursorkh, E. Rocheron, J. Wong, A. Christy and E. Grant, *J. Phys. Chem. B*, 2021, 125, 12466–12475.
- E. D. B. Foley, M. S. Kushwah, G. Young and P. Kukura, *Nat. Methods*, 2021, 18, 1247–1252.
- M. Liebthal, M. S. Kushwah, P. Kukura and K.-J. Dietz, *iScience*, 2021, 24, 103258.
- M. Bamburowicz-Klimkowska, M. Poplawska and I. P. Grudzinski, *J. Nanobiotechnol.*, 2019, 17, 48.
- TwoMP Mass Photometer for Protein Characterization|Refeyn, <https://www.refeyn.com/twomp-mass-photometer>, accessed 18 July 2023.

1 **Electronic Supplementary Information**

2 ***Observing atomically precise nanocluster aggregates in solution by mass***
3 ***photometry***

4 Jayoti Roy,^a Ila Marathe,^b Vicki Wysocki,^b Thalappil Pradeep^{†a,c}

5 ^aDST Unit of Nanoscience (DST UNS) & Thematic Unit of Excellence (TUE), Department of
6 Chemistry, Indian Institute of Technology Madras, Chennai 600036, India.

7 ^bDepartment of Chemistry and Biochemistry and Resource for Native Mass Spectrometry
8 Guided Structural Biology, The Ohio State University, Columbus, Ohio 43210, United States.

9 ^cInternational Centre for Clean Water, 2nd Floor, B-Block, IIT Madras Research Park,
10 Kanagam Road, Taramani, Chennai 600113, India.

11

12 **Table of contents**

Name	Description	Page no.
SI1	Synthesis of nanocluster	S3
SI2	Structure of the nanocluster	S3
SI3	Sample preparation	S4
SI4	MP measurements	S4
SI5	Data processing	S5
SI6	Single particle mass calculation	S5
SI7	The average mass of alloy-nanoclusters	S6
SI8	RT-TEM sample preparation	S7
SI9	Cryo-TEM sample preparation	S7

Table SI1	Aggregation numbers at different solvent mixture	S9
Fig. SI2	MS of calibrants	S9
Fig. SI3	MP spectra at $f_{40\%}$	S10
Fig. SI4	MP spectra at $f_{80\%}$	S11
Fig. SI5	RT-TEM micrographs of $f_{40\%}$ at 5 min	S12
Fig. SI6	RT-TEM micrographs of $f_{40\%}$ at 30 min	S13
Fig. SI7	RT-TEM micrographs of $f_{40\%}$ at 60 min	S14
Fig. SI8	Cryo-TEM micrographs for $f_{80\%}$	S15
Fig. SI9	RT-TEM micrographs of $f_{80\%}$ at 0 mins	S16
Fig. SI10	RT-TEM of $f_{80\%}$ at 30 mins	S16
Fig. SI11	RT-TEM and cryo-TEM comparison of $f_{40\%}$	S17
Table SI2	Comparison between MP and cryo-EM	S18
SI11	Mechanism of aggregation	S18
SI12	Correlation between MP and cryo-EM	S19

1

2

3

4

5

6

7

8

9

1 **SI1. Synthesis and characterization of of phosphine-protected alloy clusters**

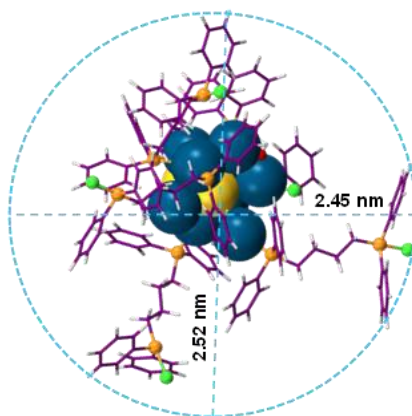
2 We have synthesized diphosphinebutane- and chlorine-co-protected Ag-Au alloy nanoclusters using a
3 single-step co-reduction method. There are only very few reports on phosphine- and halide-protected
4 nanoclusters using a single-step reaction. Here, $\text{Ag}_{11-x}\text{Au}_x$ was synthesized by co-reducing a mixture of
5 silver and gold precursors in the presence of diphosphine ligands in methanol and dichloromethane as
6 co-solvents. About 0.112 mmol AgNO_3 and 0.006 mmol $\text{HAuCl}_4 \cdot 3\text{H}_2\text{O}$ were dissolved in 5 mL of
7 methanol by keeping the total metal ion concentration at 0.118 mmol. To the mixture of Ag and Au
8 precursors, ~ 75 mg of 1,4-bis-(diphenylphosphine)butane (DPPB), dissolved in 9 mL of
9 dichloromethane (DCM), was added with constant stirring. After 20 min of stirring, 35 mg of NaBH_4
10 in 1 mL of ice-cold water was added. The colorless mixture immediately turned brown. After ~ 6-8 h
11 of vigorous stirring in dark, the color of the entire solution turned orange and was kept for aging at 4 C
12 for 24 h. The solution was rotary evaporated and extracted in methanol. During extraction, 10 mL of
13 methanol was introduced to the product and then the solution was centrifuged several times at 8000 rpm
14 for 4-5 min to remove excess DPPB and phosphine complexes as a precipitate. After that, the entire
15 methanol solution was vacuum-dried, and finally, the nanoclusters were cleaned with DCM. The dried
16 alloy nanocluster was dissolved in methanol and used for further characterization.

17 The nanocluster was characterized using positive mode ESI MS measurements. The nanocluster was
18 dissolved in methanol. Waters Synapt G2-Si high-definition mass spectrometer (HDMS) was used to
19 record the ESI MS spectrum. During measurements, capillary voltage was set at 3 kV, and desolvation
20 gas flow was maintained at 450 L h^{-1} . The source and desolvation temperature were maintained at 100
21 and 150 °C.

22 **SI2. Prediction of the structure of the NC**

23 We tried to predict the structure of NC and its ligand orientation theoretically using the Avogadro
24 software package with the universal force field (UFF) method.¹ Furthermore, to optimize the geometry
25 of Ag-Au alloy NCs, we employed a conjugate gradient optimization algorithm with a simple line
26 search technique, and energy convergence of 10^{-6} eV .^{2,3} Fig. 1(A) shows the optimized-NC structure.

1 The $\text{Ag}_{11-x}\text{Au}_x$ core is surrounded by five P of monodentate DPPB ligands, while the remaining terminal
2 P atoms of the DPPB ligands are bound to five Cl atoms. This bonding configuration may be responsible
3 for the aggregation observed in response to changes in the solvent polarity. We also attempted to
4 optimize the NC structure by attaching all phosphorus atoms as bidentate ligands to the $\text{Ag}_{11-x}\text{Au}_x$ core.
5 However, this structural modification did not reach convergence and resulted in complete distortion of
6 the structure. Therefore, we considered that the initial structure, with monodentate P, was the most
7 likely one for this NC. The system shows solvent-dependent aggregation as reported previously.⁴ To
8 calculate the specific volume of the vesicle-like nanoaggregates, we considered the NC to be spherical
9 in nature. Therefore, we used van der Waals diameter in our calculation (see Fig. 1).



15 **Fig. 1** The spherical structure of the NC with its van der Waals diameter (i.e., ~ 2.48 nm).

17 **SI3. Sample preparation for MP characterization**

18 Approximately 15 mg of nanocluster was formed during each set of the synthesis. MP is a label-free
19 single-particle analysis technique. For the MP measurements, 1.35 mg of nanocluster was dissolved
20 in 1 ml of methanol to prepare a working stock (~5 μM).

21 For the MP studies of solvent-induced aggregation with varying water % (i.e., $f_{\text{water}\%}$), 6 sets of
22 reactions were prepared. methanol and water at different ratios were added to each set by keeping the
23 final volume fixed to 100 μL . To each set, 10 μL of stock solution of nanocluster (~500 nM) was
24 added.

1 During each set of MP acquisition, unless otherwise stated 10 μL of solvent mixture was carefully
2 placed in the sample gasket, and then after focusing the object well, 10 μL of 500 nM nanocluster
3 solution was added and mixed well. The final concentration of nanocluster present in the silicone
4 gasket wells was 50 nM (i.e., optimum concentration range for TwoMP).

5

6 **SI4. Mass photometry measurements**

7 Mass photometry is an analytical technique that is used to determine the mass of a sample by
8 measuring the amount of light it scatters during particle landing events on the coverslip. It relies on
9 the relationship between the mass of a particle and its optical properties. This method was already
10 employed to distinguish 24-mer of Apoferritin proteins from Fe^{3+} metal ions containing holoferritin
11 nanocages.⁵ Utilizing MP in such systems opens up new directions to implement this technique in
12 nanomaterials. Instrumental methods used for mass photometric experiments are described below.

13 1) **Measurement, solution preparation, and instrument operation.** For the MP measurements,
14 15 μL of a specific solvent mixture, i.e., 70% water and 30% of methanol, was used to find focus by
15 the objective lens through the ‘Droplet-Dilution Find Focus’ method in AcquireMP (Refeyn) software.
16 This particular solvent mixture was prepared in such a way that the calibrants, as well as the
17 nanocluster aggregates, are stable during the acquisition. After focusing the droplet on top of the glass
18 slide, 5 μL of the NC solutions prepared at different solvent mixture was added to acquire particle
19 landing events on the glass slide. The total solution volume during each measurement was fixed at (15
20 + 5) μL = 20 μL . The data was recorded as a movie by using the same software. Refeyn Two^{MP} mass
21 photometer was used for the study.

22

23 2) **Preparation of glass coverslips.** Glass coverslips (24 \times 50 mm, Thorlabs) were cleaned
24 thoroughly by rinsing alternatively with Milli-Q water and isopropanol for a minimum of 8 times, and
25 then dried using a nitrogen stream and stored in a dry clean place until use. Silicone gaskets (6 cm \times

1 1 cm) were rinsed sequentially with Milli-Q water, isopropanol, and Milli-Q water, dried under a
2 nitrogen stream, and placed on the freshly cleaned coverslips.

3 3) **Mass photometry setup.** All MP measurements were acquired on a Refeyn two^{MP} mass
4 photometer with a $10.8 \times 2.9 \mu\text{m}^2$ field of view.

5 4) **Calibration process.** 1:1 protein mixture, i.e., β -amylase (BA) (10 nM), and thyroglobulin
6 (TGA) (10 nM) were used as calibration mixture in 70% water:30% methanol. These proteins were
7 selected such that the protein mixture can be used to calibrate the mass range of interest (i.e., 50 – 660
8 kDa). Final concentration of each calibrant was 10 nM. We used the same acquisition method for each
9 sample analysis.

10

11 **SI5. Data processing**

12 Dynamic mass photometry movies were processed by treating each frame with a sliding medium
13 background subtraction algorithm with high spatiotemporal resolution using DiscoverMP software. In
14 brief, each frame was divided by its local median, that is, the median of a pre-defined frame interval
15 (here 890 frames) centered around the frame of interest, to calculate the background-subtracted frames,
16 F:

$$17 \quad Fi = \frac{X_i}{X_{i-100:i+100}}$$

18 Where X_i is the current raw frame and $X_{i-100:i+100}$ represents the median pixel values of raw frames, from
19 $i-100$ up to (and including) $i+100$.⁶ Each background-subtracted frame was then additionally treated
20 with a two-dimensional (2D)-median noise filter to remove any large dynamic background sources (for
21 example, fluctuations in illumination, if present). The window size of 890 frames for the sliding median
22 algorithm was chosen during the acquisition of single particle landing events because it was the window
23 size that did not detrimentally affect particle contrast or contrast precision.

24 **SI6. Calculation of single particle mass during particle-landing events on the coverslip**

1 To measure accurate mass for the individual mass of the nanoaggregate of each set of measurements,
2 we selected a particular spherical point spread function (PSF) from a particular ratiometric frame from
3 the entire frames of a measurement. Then we inverted the selection spatially and temporally from the
4 entire acquisition movie. This method enables us to measure the ratiometric contrast, as well as mass/es
5 (in kDa) of individual particle/s accurately per count.⁷⁻⁹

6 We then calculated the kernel density estimate (KDE) plot from the area of each Gaussian distribution.
7 The KDE is calculated as, $a = A\sigma\sqrt{2\pi}$, where a is the area, A is the amplitude and σ is the standard
8 deviation of the fitted Gaussian.

9 Here, the equal binding rate of each nanoaggregates with the coverslip was considered as only Ag-Au
10 alloy nanocluster, i.e., $[\text{Ag}_{11-x}\text{Au}_x(\text{DPPB})_6\text{Cl}_2\text{O}_2]^{2+}$ [x = 0-5] was taken as the precursor for the entire
11 study.

12

13 **SI7. Calculation of the average mass of alloy-NCs**

14 The composition of Au-doped nanocluster used here is $[\text{Ag}_{11-x}\text{Au}_x(\text{DPPB})_5\text{Cl}_5\text{O}_2]^{2+}$ [X = 0-5], where
15 DPPB represents 1,4-bis(diphenylphosphino)butane. In the mass spectrometric study, the Au-undoped
16 and doped nanocluster ionizes at m/z 1808, 1852, 1897, 1942, and 1986 with varying ion intensities.
17 To calculate the approximate number of nanoclusters that are present in the nanoaggregates, the
18 following method is employed –

$$19 \frac{\text{The central mass of nanoaggregates (observed in MS)}}{\text{The average mass of nanocluster (observed in MS)}}$$

20

21

22 The intensity ratio (IR) of five nanoclusters (X = 0-5) = 4119.5:2932.3:2139.2:1583.3:1000.6

23 = 4:3:2:1.6:1

24 Total of IR = 11.6

1 The average mass/charge (m/z) of these Au-undoped and Au-doped nanoclusters =

$$\frac{\sum_i \left(\frac{m}{z} \times z \times \frac{IR_i}{11.6} \right), i = 0 - 5}{z}$$

2

$$= \frac{3670.33}{2}$$

3

$$= 1835.16$$

4

$$= 1835.16$$

5 **SI8. Sample preparation for RT-TEM measurements**

6 During RT-TEM measurements, 3 μ L of NC-solution of binary solvent mixture was dropcasted directly
7 on a regular carbon-coated Cu-grid and kept for drying (\sim 10 min) before inserting the grid for the
8 TEM-imaging.

9 **SI9. Cryo-electron microscopy of nanoaggregates**

10 Cryo-electron microscopy (cryo-EM) was performed using a Thermo Glacios cryo-EM instrument. To
11 prepare the cryo-EM specimens, a 3 μ L droplet of NC-solution was applied to a lacey carbon-coated
12 copper TEM grid. The grid was then rapidly frozen in liquid ethane using the Vitrobot Mark from FEI
13 in Eindhoven, The Netherlands. The freezing conditions involved maintaining a temperature of 4°C
14 with 67% humidity. After vitrification, the grids were either directly transferred to the cryotransfer
15 holder of the microscope or stored in liquid nitrogen until the EM measurements. The imaging took
16 place at a temperature around 90 K. The TEM was operated at an acceleration voltage of 200 kV, and
17 a defocus of the objective lens between 0.5 – 1 μ m was applied to enhance contrast. Cryo-EM
18 micrographs were recorded at various magnifications using a bottom-mounted 4k CMOS camera. The
19 total electron dose in each micrograph was kept below 17 $e^-/\text{\AA}^2$.

20

21

22

1

2

Set	Water (%)	MeOH (%)	Mass (kDa)	No of NCs (Mw = ~3670)
1	40	60	47	13
2	50	50	65	18
3	60	60	83	23
4	70	30	93	26
5	80	20	103	29
6	90	10	84-183	23 - 50

Table SII Calculation of the aggregation number (N_{NCs}) present per nanoaggregate as different solvent mixture.

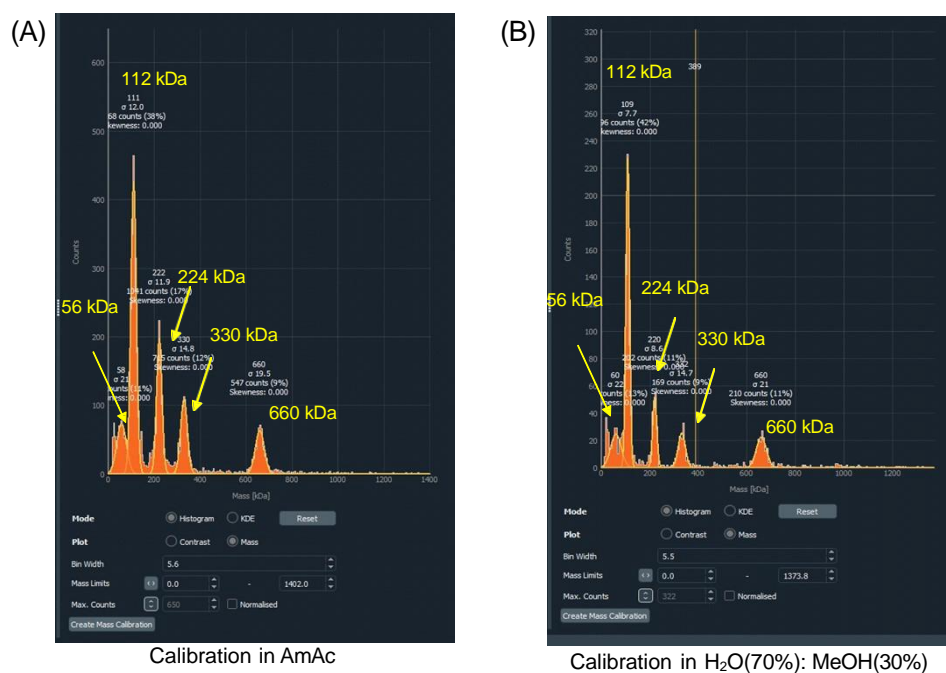


Fig. S12 Histogram of protein calibrants measured in (A) 100 μ M ammonium acetate (AmAc) solution and (B) 70% water and 30% methanol mixture, by MP. Histograms collected from AcquireMP software. The masses of different oligomers are labelled in the histograms.

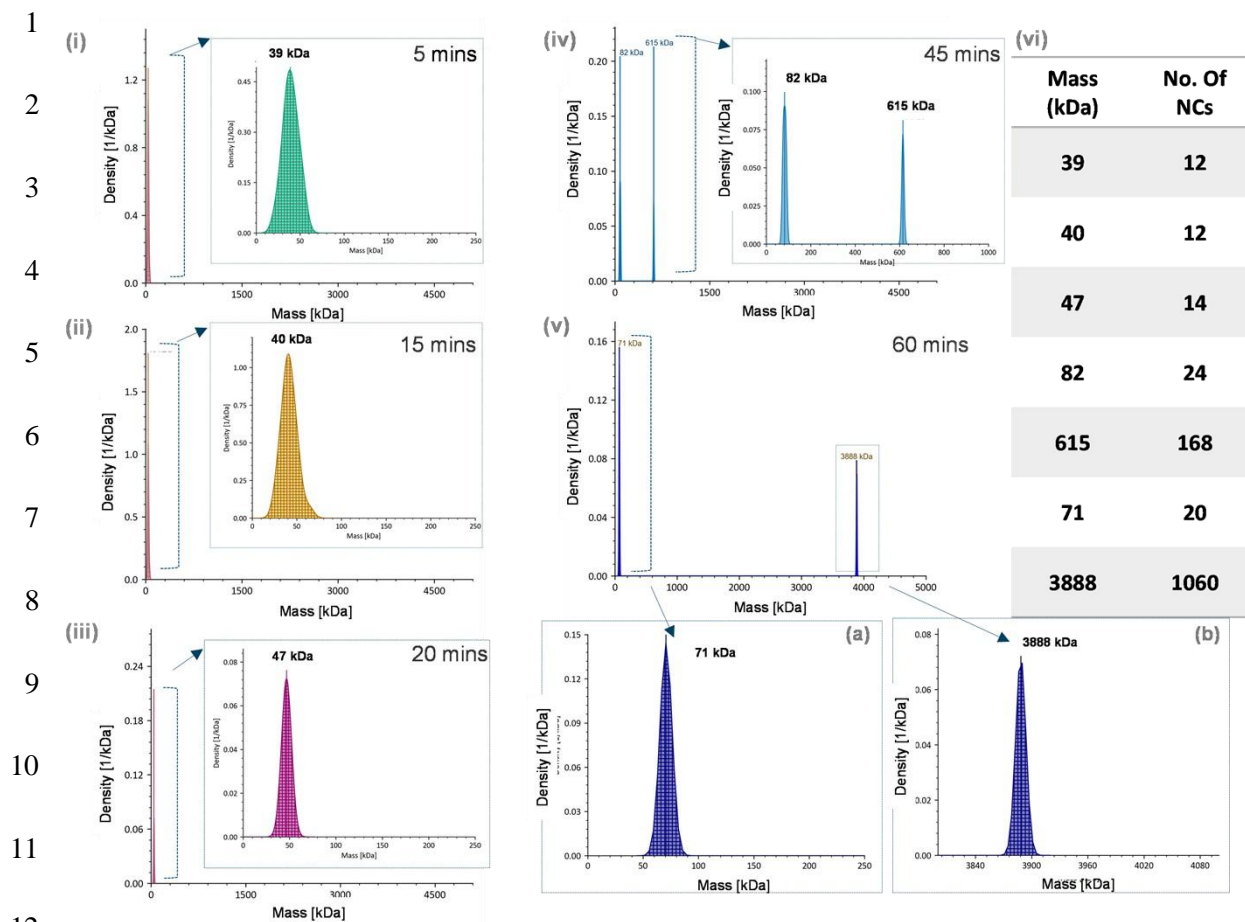
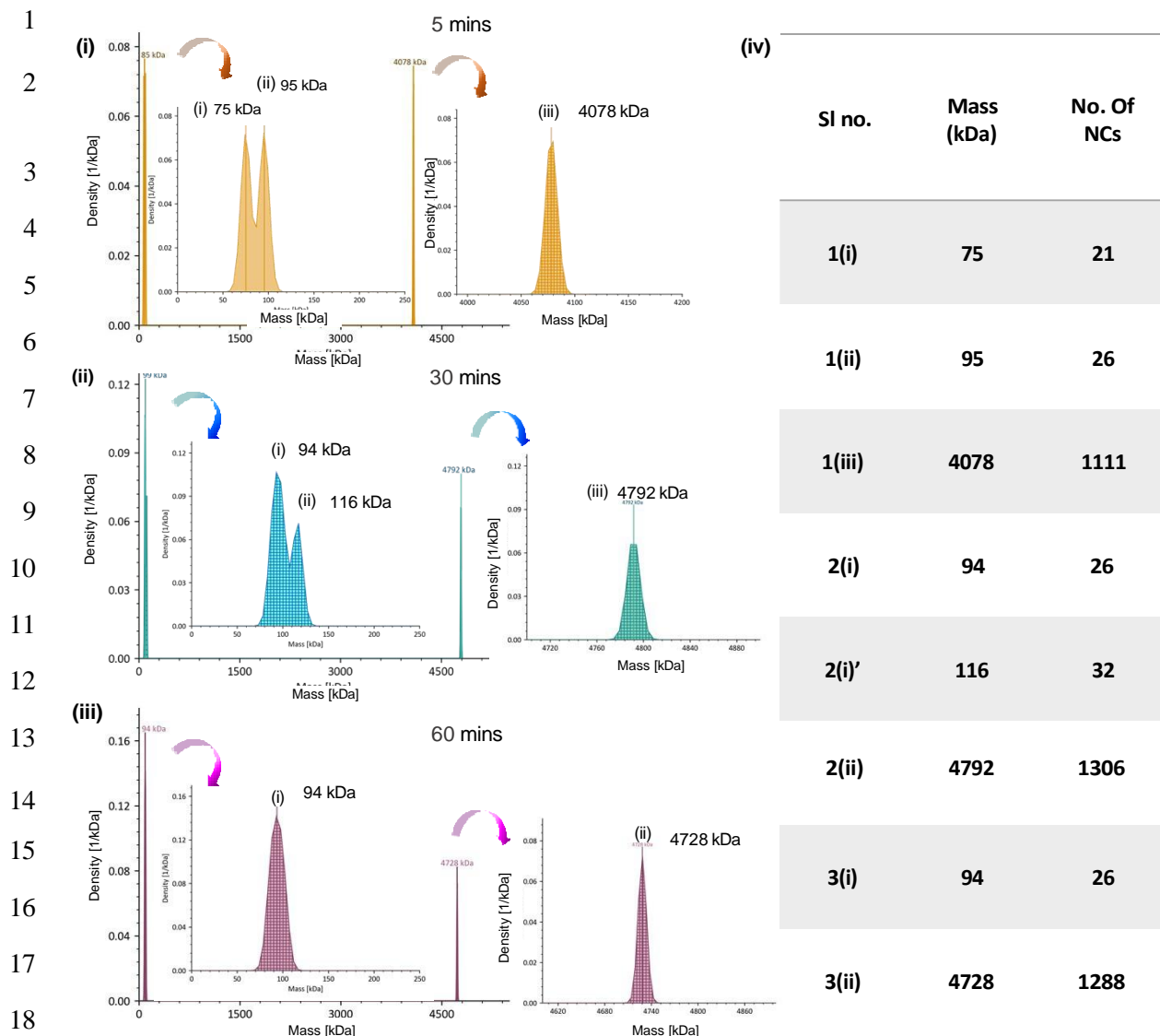


Fig. S13 Spatiotemporal selections of single particle landing event enables determining mass of single nanoaggregate for a particular measurement. (A)(i-v) Time-dependent MP histograms of size-evolution of single particle landing event of nanoaggregates at $f_{40\%}$ in the mass range of 0-5500 kDa. Inset of each histogram shows the expanded mass range labelled with average mass. (vi) Table shows the average number of parent nanocluster present per nanoaggregate.



20 **Fig. S14** Spatiotemporal selections of single particle landing event enables determining mass of single
 21 nanoaggregate for a particular measurement. (A) Time-dependent MP histograms of size-evolution of single
 22 particle landing event of nanoaggregates at $f_{80\%}$ in the mass range of 0-5500 kDa. Inset of each histogram shows
 23 the expanded mass range labelled with average mass. (vi) Table shows the average number of parent nanocluster
 24 present per nanoaggregate.
 25
 26
 27
 28
 29
 30

1

2

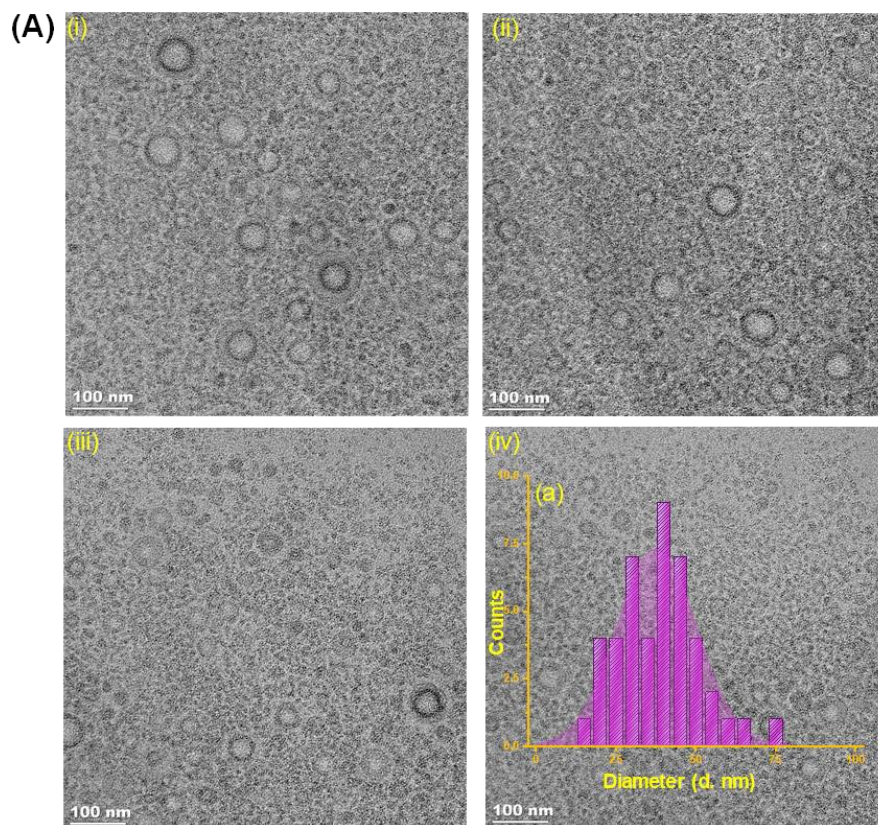


Fig. S15 (A) (i-iv) RT-TEM micrographs of alloy nanocluster-based nanoaggregates of $f_{40\%}$ at 0 min. Inset (a) shows the average particle size distributions observed at 0 min.

1

2

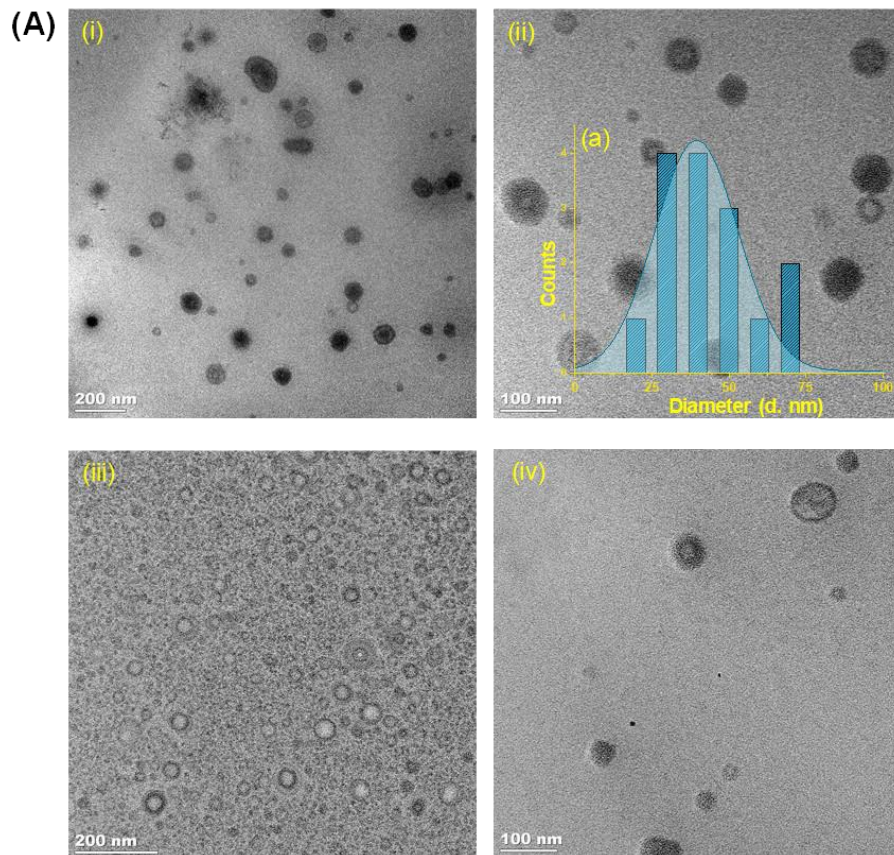


Fig. SI6 (i-iv) RT-TEM micrographs of alloy nanocluster-based nanoaggregates of $f_{40\%}$ at 30 mins. (a) Inset shows average size-distribution of the nanoaggregates as a function of counts after 30 min.

1
2
3
4
5
6
7
8
9
10
11
12
13
14
15
16
17
18
19
20
21
22
23

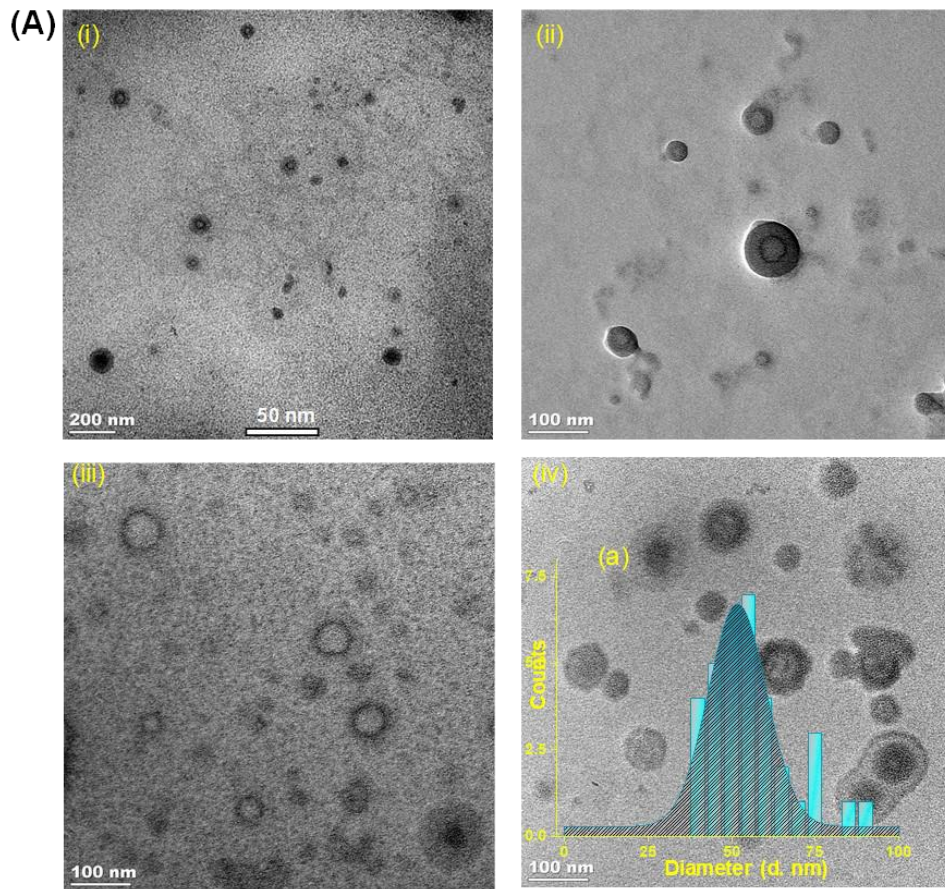


Fig. SI7 (A) (i-iv) RT-TEM micrographs of alloy nanocluster-based nanoaggregates of $f_{40\%}$ at 60 min and inset (a) represents the particle-size distribution.

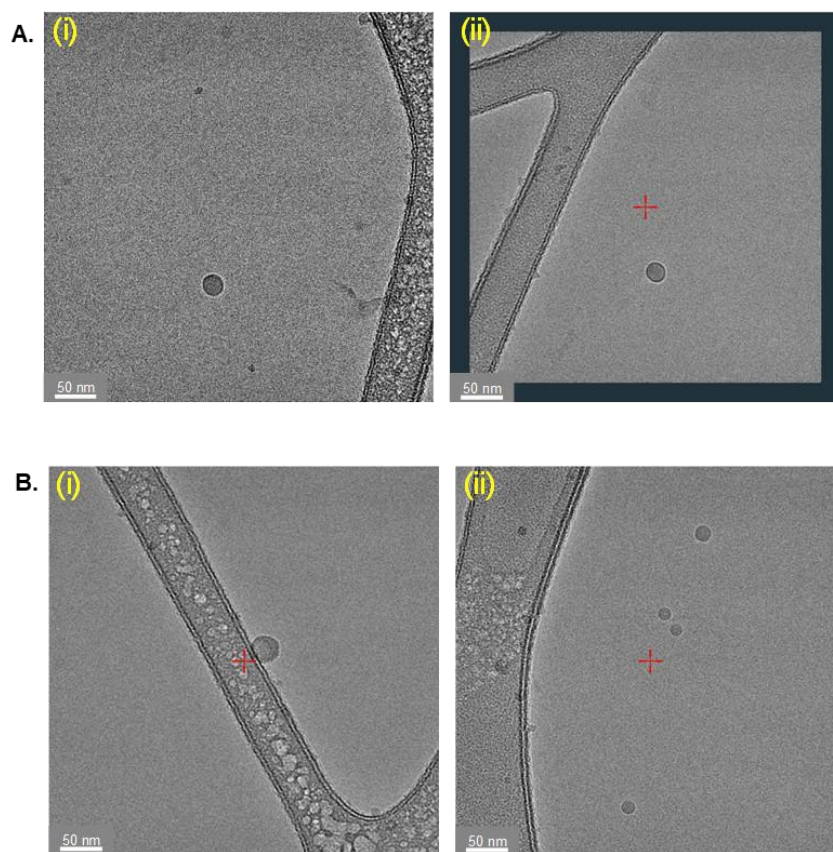
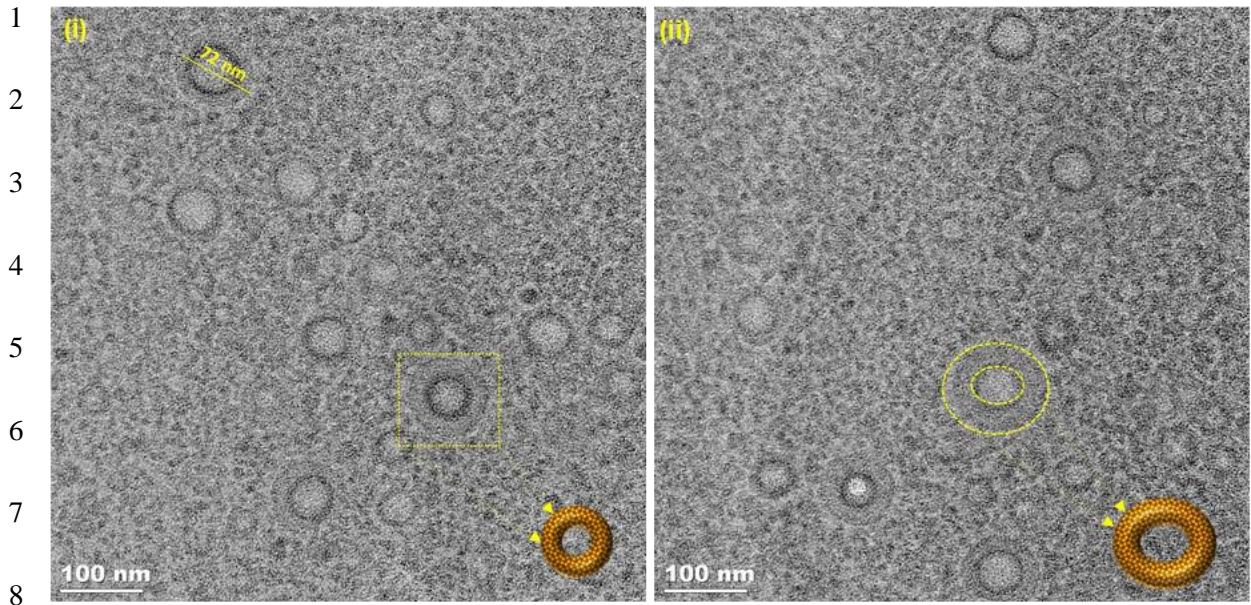


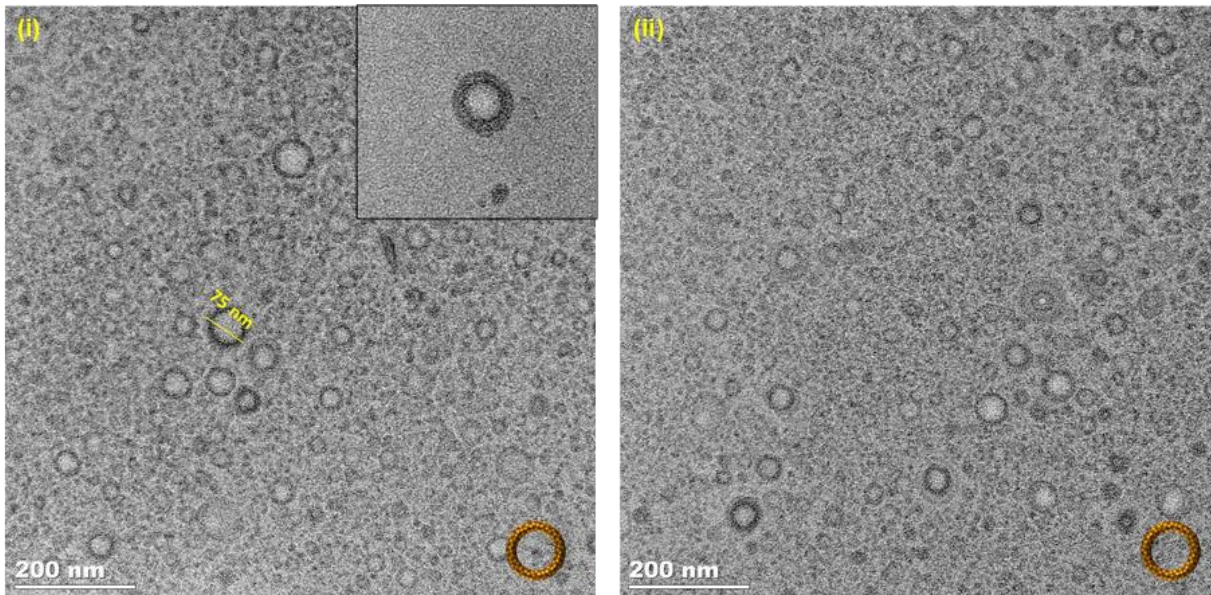
Fig. S18 Cryo-TEM micrographs of $f_{80\%}$ at (A) 0 min, and (B) 30 mins.

- 1
- 2
- 3
- 4
- 5
- 6
- 7
- 8
- 9
- 10
- 11



9 **Fig. SI9** RT-TEM micrographs of alloy nanocluster-based nanoaggregates of $f_{80\%}$ at 0 mins. Inset shows a schematic
10 representation of the donut-shaped nanoaggregates.

11



12 **Fig. SI10** RT-TEM micrographs of alloy nanocluster-based nanoaggregates of $f_{80\%}$ at 30 mins. Inset shows a schematic
13 representation of the donut-shaped nanoaggregates.

14

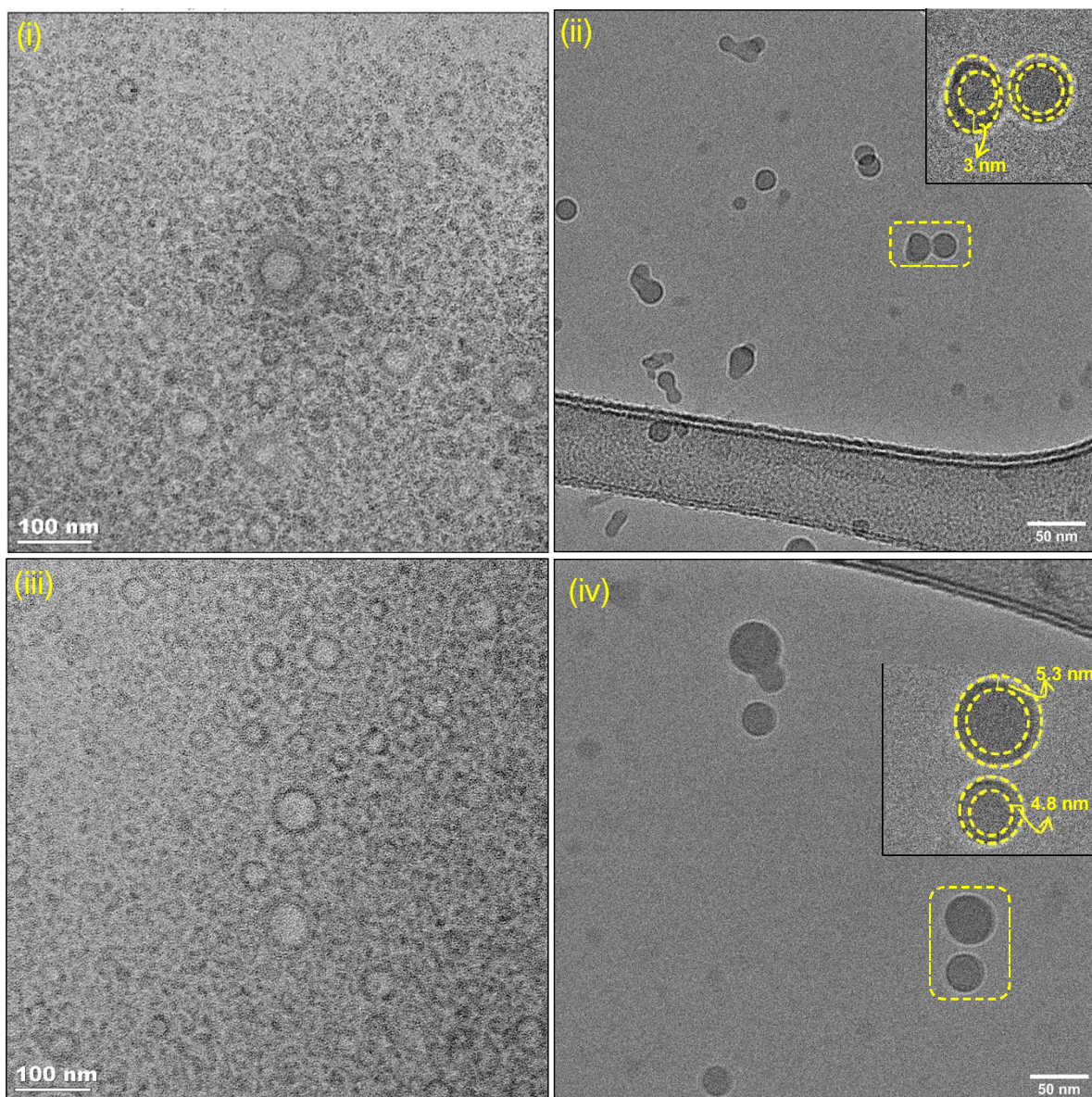


Fig. S111 RT-TEM and cryo-TEM micrographs of nanoaggregates forming at 0 min (i-ii) and at 30 min (iii-iv) of $f_{40\%}$, respectively. Insets of (ii) and (iv) show the expanded view of the vesicle-like structure of nanoaggregate with NC-shell (in nm).

1

2

3

4

5

6

Set	MP				Cryo-TEM				RT-TEM
$f_{water\%}$	Evolution time (min)	Mass (kDa)	Gaussian (σ)	N_{NCS} (Mw of NC = ~3670)	Evolution time (min)	Diameter range (nm)	Avg. radius (nm)	$N_{NCS}/\text{nano aggregate}$	Avg. thickness of the shell (nm)
$f_{40\%}$	0	39	14.4	~11	0	12.5 ± 5	6.25	~12	10.9
$f_{40\%}$	30	70	27.56	~19	30	33 ± 5	16.5	~21	15
$f_{40\%}$	60	86	28.49	~25	60	45 ± 15	22.5	-	16

Table SI2 Comparison of masses (M_{avs}), gaussian (σ), radius, N_{NCS} of nanoaggregates, and thickness of the shell of the nanoaggregate determined at different times of evolution for $f_{40\%}$, from MP, cryo-TEM, and RT-TEM.

1

2 SI11. Possible mechanism of formation and evolution of nanoaggregates

3 The possible mechanism of formation of such hollow spherical superstructures was discussed in the
4 previous report.¹³ The NC is completely soluble in methanol and consists of hydrophilic (Cl) and
5 hydrophobic (DPPB) counterparts in its ligand shell. To understand the details of solution phase self-
6 assembly of NCs encapsulated by DPPB and Cl ligands, we performed a series of time-dependent MP
7 measurements at $f_{40\%}$ and $f_{80\%}$. The self-assembly of NCs and the growth of nanoaggregates with
8 increasing dielectric constant are mainly attributed to π --- π and C-H--- π interactions between DPPB
9 ligands of alloy NCs, as discussed in previous research.¹⁴ Over time, these aggregated assemblies of
10 NCs tend to reach a state of minimum surface energy, resulting in the formation of hollow vesicle-like
11 structures. Each individual vesicle continues to grow within the solution, with the rate of growth being
12 influenced by the polarity of the solvent and the availability of NC monomers in the solution. This
13 growth process continues until the vesicles reach a threshold diameter, beyond which no further growth

1 is discernible. Three major phenomena were observed in terms of mass calculation of such
2 nanoaggregates in solution. First, with increase in water percentage (see Fig. 1C), a greater number of
3 NCs assembled to form nanoaggregates with increased molecular mass. This is in accordance with a
4 previous report where with increase in water, thick-walled nanoaggregates were formed.¹³ Second, at
5 $f_{90\%}$, the overall M_{av} decreased compared to that at $f_{80\%}$. We attribute such phenomena to rapid
6 agglomeration due to a sudden increase in the solvent polarity which effectively reduced the size of the
7 nanoaggregates to retain the spherical morphology. Moreover, it is already known that higher amount
8 of water in a water-methanol binary solvent system causes fast aggregation.¹⁵ Lastly, at a constant
9 water-methanol ratio (i.e., at $f_{40\%}$), initially smaller aggregates were noticed, presumably due to high
10 solubility of NCs in methanol. However, these smaller aggregates grew with time. This is more-likely
11 due to enthalpy driven self-assembly, associated with hydrophobicity of the DPPB ligands (see Fig. 2A
12 and Fig. 3).¹⁴ The growth of nanoaggregates was observed systematically e.g., at $f_{50\%}$, $f_{60\%}$, and $f_{70\%}$.

13

14 **SI12. Correlation between MP and cryo-TEM measurements**

15 We carried out a side-by-side comparison of the MP and cryo-TEM workflows along with the size evolution of
16 nanoaggregates. At $f_{40\%}$, the MP study showed that the average NC, at 1 min of the measurements is ~ 12 (see table
17 in Fig. SI2). In corollary, cryo-TEM measurements at 5 min showed an average particle size-distribution of 12.5
18 ± 5 nm. The average van der Waals diameter of individual NC was ~ 2.48 nm (measured from computationally
19 optimized NC). To calculate the specific volume of the vesicle-like nanoaggregates, we considered the NC to be
20 spherical in nature. Therefore, we used van der Waals diameter in our calculation. Combining RT-TEM and cryo-
21 TEM studies, we confirmed that NCs are aggregating in solution as hollow spheres, as suggested previously.⁴ The
22 density of a nanoaggregate can be estimated by dividing the average mass, as determined by MP, by its average
23 volume, which is derived from cryo-TEM measurements. For instance, at $f_{40\%}$ and after 60 min, the nanoaggregates
24 exhibit an average mass of 86 kDa and a diameter of 45 nm. This results in a calculated density of ~ 0.003 g/cm³.
25 This density is considerably lower than that of bulk water and methanol, which have densities of 1 and 0.792
26 g/cm³, respectively. The deviation could be arising from an under-estimation of the mass by MP or over-estimation
27 of the size by cryo-TEM. Therefore, correlating the findings with more established single molecule mass
28 determination techniques like charge detection mass spectrometry (CDMS) could enhance the

1 measurement accuracy, an area that requires further investigation in future. Such a correlation with
2 CDMS has additional issues as gas phase ions produced by electrospray ionization may lose some or
3 all the solvent molecules or the aggregate ions may be fragmented.

4 **References**

- 5 1 A. K. Rappe, C. J. Casewit, K. S. Colwell, W. A. Goddard III and W. M. Skiff, *Journal of the American*
6 *Chemical Society*, 2002, **114**, 10024–10035.
- 7 2 J. Hafner, *Journal of Computational Chemistry*, 2008, **29**, 2044–2078.
- 8 3 J. P. Perdew, J. A. Chevary, S. H. Vosko, K. A. Jackson, M. R. Pederson, D. J. Singh and C. Fiolhais,
9 *Physical Review B*, 1992, **46**, 6671.
- 10 4 M. Jash, A. Jana, A. K. Poonia, E. Khatun, P. Chakraborty, A. Nagar, T. Ahuja, K. V. Adarsh and T.
11 Pradeep, *Chemistry of Materials*, 2023, **35**, 313–326.
- 12 5 TwoMP Mass Photometer for Protein Characterization | Refeyn, [https://www.refeyn.com/twomp-mass-](https://www.refeyn.com/twomp-mass-photometer)
13 [photometer](https://www.refeyn.com/twomp-mass-photometer), (accessed 18 July 2023).
- 14 6 A. Sonn-Segev, K. Belacic, T. Bodrug, G. Young, R. T. VanderLinden, B. A. Schulman, J. Schimpf, T.
15 Friedrich, P. V. Dip, T. U. Schwartz, B. Bauer, J.-M. Peters, W. B. Struwe, J. L. P. Benesch, N. G.
16 Brown, D. Haselbach and P. Kukura, *Nature Communications*, 2020, **11**, 1772.
- 17 7 S. H. Lai, S. Tamara and A. J. R. Heck, *iScience*, 2021, **24**, 103211.
- 18 8 D. Wu, P. Hwang, T. Li and G. Piszczek, *Gene Therapy* 2021 29:12, 2022, **29**, 691–697.
- 19 9 D. Wu and G. Piszczek, *European Biophysics Journal*, 2021, **50**, 403–409.
- 20 10 H. Fischer, I. Polikarpov and A. F. Craievich, *Protein Science*, 2004, **13**, 2825–2828.
- 21 11 C. Takai, H. Watanabe, T. Asai and M. Fujii, *Colloids and Surfaces A: Physicochemical and*
22 *Engineering Aspects*, 2012, **404**, 101–105.
- 23 12 N. J. Warren, O. O. Mykhaylyk, A. J. Ryan, M. Williams, T. Doussineau, P. Dugourd, R. Antoine, G.
24 Portale and S. P. Armes, *Journal of the American Chemical Society*, 2015, **137**, 1929–1937.
- 25 13 M. Jash, A. Jana, A. K. Poonia, E. Khatun, P. Chakraborty, A. Nagar, T. Ahuja, K. V Adarsh and T.

- 1 Pradeep, *Chemistry of Materials*, 2023, **35**, 313–326.
- 2 14 A. Singh, G. R. Nair, P. Liplap, Y. Gariepy, V. Orsat and V. Raghavan, *Antioxidants*, 2014, **3**, 99–113.
- 3 15 M. P. Kelley, P. Yang, S. B. Clark and A. E. Clark, *Inorganic Chemistry*, 2018, **57**, 10050–10058.
- 4

Interparticle Antigalvanic Reactions of Atomically Precise Silver Nanoclusters with Plasmonic Gold Nanoparticles: Interfacial Control of Atomic Exchange

Published as part of *Chemistry of Materials virtual special issue "C. N. R. Rao at 90"*.

Paulami Bose, Jayoti Roy, Vikash Khokhar, Biswajit Mondal, Ganapati Natarajan, Sujan Manna, Vivek Yadav, Anupriya Nyayban, Sharma S. R. K. C. Yamijala,* Nonappa,* and Thalappil Pradeep*



Cite This: *Chem. Mater.* 2024, 36, 7581–7594



Read Online

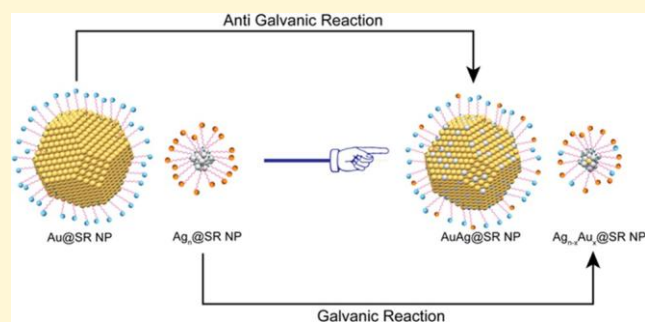
ACCESS

Metrics & More

Article Recommendations

Supporting Information

ABSTRACT: This work demonstrates that antigalvanic reactions (AGRs) between thiol-protected plasmonic gold nanoparticles (NPs) and atomically precise silver nanoclusters (NCs) are an interfacial chemistry-driven phenomenon. We reacted 2,4-dimethylbenzenethiol (DMBT)-protected Au NPs (average diameter of 4.46 ± 0.64 nm) with atomically precise $[\text{Ag}_{25}(\text{DMBT})_{18}]^-$ NC and obtained bimetallic AgAu@DMBT alloy NPs. Systematic investigations with optical absorption spectroscopy, high-resolution transmission/scanning transmission electron microscopy, and elemental mapping revealed the reaction-induced morphological and compositional transformation in NPs. Furthermore, we show that such AGRs get restricted when geometrically rigid interfaces are used. For this, we used 1,3-benzenedithiol (BDT)-protected Au@BDT NPs and $[\text{Ag}_{20}(\text{BDT})_{12}(\text{TPP})_4]^{3-}$ NCs (TPP = triphenylphosphine). Electrospray ionization mass spectrometric (ESI MS) studies revealed that the interparticle reaction proceeds via metal–ligand and/or metal exchange, depending on the interface. Density functional theory (DFT) calculations and molecular docking simulations were used to understand the interactions and reaction energetics leading to favorable events. Interfacial chemistry of this kind might offer a one-pot synthetic strategy to create ultrafine bimetallic NP-based hybrid materials with potential optoelectronic and catalytic applications.



1. INTRODUCTION

Bimetallic nanoparticles (NPs) have attracted significant interest in view of their enhanced catalytic^{1,2} and plasmonic performance.^{3,4} Common synthetic routes to bimetallic NPs include coreduction, thermal breakdown, seed-mediated growth, and galvanic replacement processes.⁵ Classical galvanic reaction (GR), where a noble metal cation is reduced by a less noble ion, is known for its high tunability and efficiency in producing bimetallic NPs.^{6–9} However, the antigalvanic reactions (AGRs), namely, the reduction of metal ions by less reactive (or more noble) metals, were considered impossible. Such a reaction was demonstrated using atomically precise nanoclusters (NCs).^{10,11} Atomically precise metal NCs are classified as molecular materials in view of their precise composition and well-defined electronic structure, physicochemical, and optical properties.^{12–17} The reduction potential of metal NPs decreases as the particle size reduces.^{18–20} Specifically, in the context of ultrasmall ligand-stabilized Au NPs, their oxidation potential becomes notably lower than the reduction potential of a few less noble metal ions.^{21–23} Choi et al. first identified the $[\text{Au}_{24}\text{Ag}(\text{SR})_{18}]^-$, $[\text{Au}_{24}\text{Ag}_2(\text{SR})_{18}]^-$, and

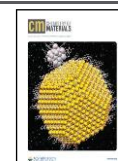
other doped species upon mixing $[\text{Au}_{25}(\text{SR})_{18}]^-$ NC with Ag-thiolate, using mass spectrometry.²⁵ Later, Wu reported reactions of neutral $[\text{Au}_{25}(\text{SR})_{18}]^0$ and other ultrasmall Au and Ag NPs (sized below 3 nm) with metal ions of Ag and Cu.²⁶ $[\text{Au}_{25}(\text{SR})_{18}]^-$ NC was considered a unique candidate for AGR as Ag^+ ions failed to react with 2–3 nm Au NPs.²⁷ Wu et al. reported that the oxidation potential of ligand-free Au NPs was lower than the reduction potential of Ag^+ , leading to the oxidation of gold NP and reduction of Ag^+ , upon mixing the two species.²⁸ Similarly, Jin et al. demonstrated a similar size dependence on the redox potentials of the 11-mercaptoundecanoic acid (MUA)-protected Au particles.²⁹ Pattadar et al. reported a size-dependent AGR reactivity of

Received: March 2, 2024

Revised: May 14, 2024

Accepted: May 16, 2024

Published: May 29, 2024



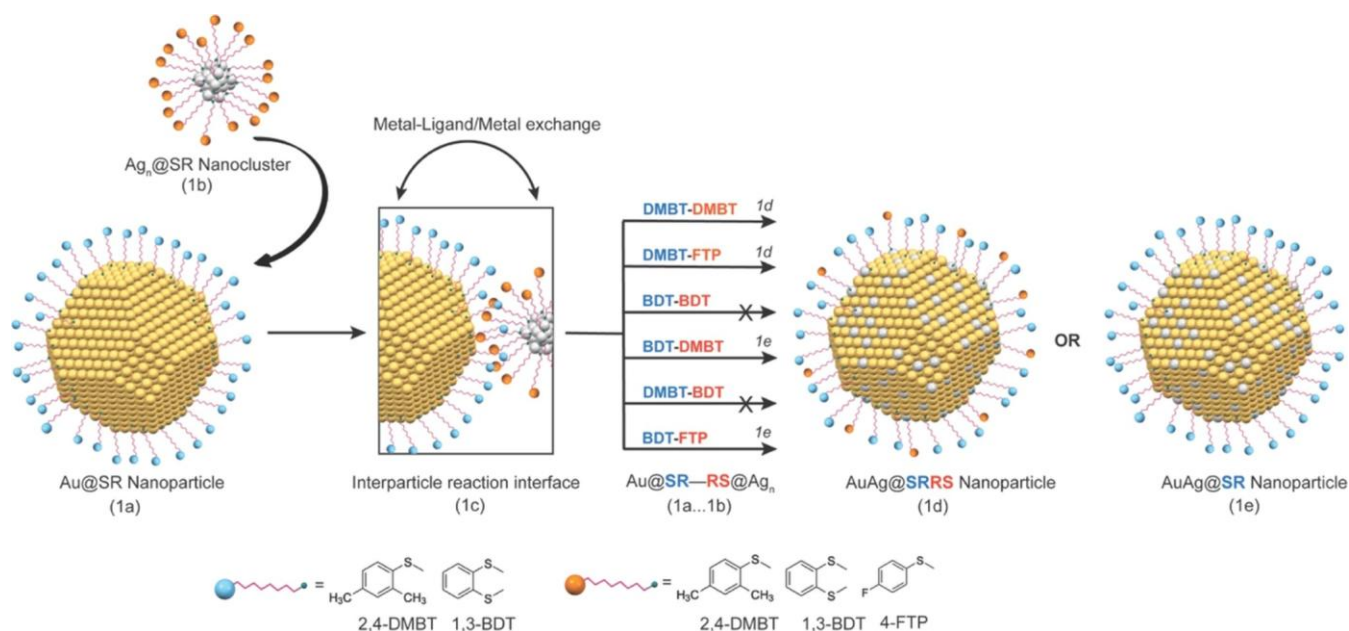


Figure 1. Schematic illustration of the AGRs in Au@SR NP with atomically precise Ag_n@SR NCs via intersystem exchange resulting in bimetallic AuAg@SR NPs. SR corresponds to 2,4-DMBT, 1,3-BDT, and 4-FTP; detailed ligand structures are omitted for clarity. Au@DMBT and Au@BDT NPs are denoted by the label Au@SR. Ag_n@SR refers to [Ag₂₅(DMBT)₁₈]⁻, [Ag₄₄(FTP)₃₀]⁴⁻, [Ag₄₄(FTP)₃₀]³⁻, and [Ag₂₉(BDT)₁₂(TPP)₄]³⁻ NCs. As indicated, Au@BDT–Ag_n@BDT and Au@DMBT–Ag_n@BDT reactions do not occur. Color code: yellow, Au; gray, Ag; green, S; pink/blue/orange, ligand. Note that the atomic dimensions and particle sizes are significantly underestimated to suit the representation.

weakly stabilized and surface-attached Au NPs (diameter ranging between 1 and 4 nm) with Ag⁺ or PtCl₄²⁻ ions.²³ The ligand monolayer on the NC surface plays a prominent role in AGRs.^{16,22–24} Sahu and Prasad reported the solution phase reaction involving Au@DDA (DDA = dodecylamine) and Au@DDT (DDT = dodecanethiol) NPs with Ag⁺ ions, yielding Au@Ag core–shell and monometallic Ag and Au NPs, respectively, at 90 °C.³⁰ The architecture of the resulting NPs was found to be influenced by the nature of ligand binding to the metal NP surface, with excess DDA and DDT ligands facilitating the reduction of Ag⁺ to Ag⁰. Studies also revealed that the heteroatom addition or replacement resulted in alloyed Au NC with either the retention³¹ or an alteration of its original structural framework.³² Ligands facilitate the formation of heterometallic NC frameworks.^{33–35} However, most reports on AGRs are limited to atomically precise ultrasmall NPs with sizes smaller than 3 nm.¹⁰ Considering AGRs from the perspective of interfacial chemistry may help address such processes with plasmonic NPs.³⁶

Atomic exchange during nanocluster–nanoparticle (or interparticle) reactions is a relatively less explored area of study. Ligand-exchange,^{37–45} metal-exchange,^{46–49} and isotopic-exchange^{50–52} reactions of atomically precise metal NCs are well-known.^{13,14,36,53,54} Like molecules, atomically precise metal NCs undergo internanocluster (or intercluster) reactions in solution.^{55–57} Bimetallic and trimetallic NCs have also been prepared using intercluster reactions.^{15,58} Studies on the intercluster reaction mechanism suggest a pathway for the exchange of metal or metal–ligand fragments.⁵⁵ The thiolate monolayer protecting the NC surface is dynamic in nature,^{59,60} and the metal–ligand interface controls the atom transfer in an intercluster reaction.⁶¹ However, most examples of interparticle interactions are purely driven by supramolecular interactions, such as hydrogen-bonding, van der Waals, C–H ··· π, π ··· π, and electrostatic interactions where the reacting

particles retain their intrinsic properties in the superstructures.^{54,62–70} We recently reported the formation of a self-assembled 2D superlattice of monodispersed Ag–Au–alloy NPs by reacting polydispersed Ag NPs with [Au₂₅(SR)₁₈]⁻ NC.⁷¹ As studied using mass spectrometry, the reaction mechanism suggested an interparticle atomic exchange (metal–ligand species), and the metal–ligand interface was crucial for the reaction.⁵⁹ Kazan et al. showed that the thiol acts as a messenger in the metal–atom exchange between the NC and the surface in such reactions.⁷² A later study on the kinetics of isotopic exchanges showed a size dependence when the reacting partner was varied from the nanoscale to bulk metal with an isotopically pure [Ag₂₅(SR)₁₈]⁻ NC.⁵² A recent study showed [Ag₂₅(SR)₁₈]⁻ NC-mediated site-selective etching of anisotropic Au nanotriangles (Au NTs).⁷³ Roy et al. reported [Au₂₅(SR)₁₈]⁻ and CuO NP reaction, which induced the aggregation of Cu-doped NC leading to spherical superstructures.⁷⁴ The feasibility of interparticle reactions and the dynamics at the metal–ligand interface across the gold–silver system of all dimensions is a natural extension of this problem.

Self-assembled colloidal NP-based, also known as supraparticles, hybrid materials are known for their potential catalytic,⁷⁵ optoelectronic,^{76,77} and biological applications.⁷⁸ In reference to our previous and current studies, we presume that modulating the reaction microenvironment (temperature and solvent, for instance) and/or the protecting ligand of NPs could potentially facilitate their assembly into supraparticles, such as superlattices,⁷¹ nanodiscs,⁷⁴ and nanodumbbells.⁶² For example, nanodiscs may find potential applications as nanoflasks for catalysis^{79,80} and selective ion capture.⁸¹ NP superlattices may find prominence in optoelectronic applications, for example, surface-enhanced Raman scattering (SERS)-based sensors,⁸² nanoscale devices,⁸³ and many more possibilities.⁸⁴ In the future, we intend to utilize our concept of

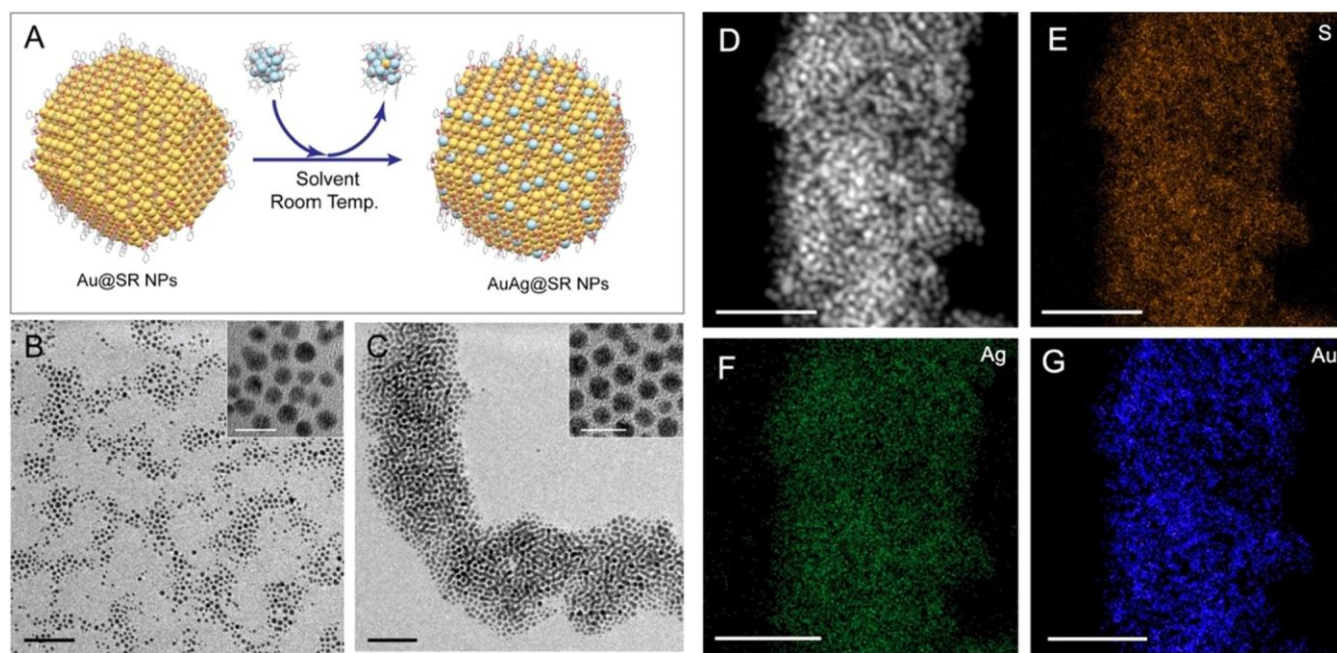


Figure 2. Schematic representation of the interparticle reaction between Au@SR NP and $[\text{Ag}_{25}(\text{SR})_{18}]^{-}$ NC, where SR = 2,4-DMBT (A). TEM images of Au@DMBT NPs before (B) and after (C) the reaction. Dark-field STEM image of the reacted NPs (D) and the corresponding EDS maps of S (E), Ag (F), and Au (G). Scale bars: 50 (B–G) and 10 nm (insets of B and C). Color code in A: yellow, Au; blue, Ag; pink, S; gray, C. H has been omitted for clarity. Note that the ligand structure and anchoring sites are not a true representation of the NP.

interparticle chemistry to develop ultrafine bimetallic NP-based hybrid nanomaterials for such promising optoelectronic and catalytic applications.

Herein, we report the phenomenon of AGR in plasmonic Au NPs by performing interparticle reaction between Au@SR NPs and atomically precise Ag@SR NCs (schematically illustrated in Figure 1). To demonstrate the effect of the metal–ligand (SR–Au···Ag–SR) interface, NPs and NCs protected with monodentate and bidentate thiols, as well as mixed monolayers, were investigated. This work establishes that interparticle reactions are universal across noble metal systems. With the right choice of a particle system, we can now create bimetallic NPs and size-focus them all in one pot, simultaneously. This leads us to propose that atom transfer between NP and NC during interparticle reactions is a potential pathway to AGRs.

2. EXPERIMENTAL SECTION

The materials and methods for the syntheses of NPs, Au@DMBT, and Au@BDT, and the NCs, $[\text{Ag}_{25}(\text{DMBT})_{18}]^{-}$, $[\text{Ag}_{29}(\text{BDT})_{12}(\text{TPP})_4]^{3-}$, and $[\text{PPh}_4]_n[\text{Ag}_{44}(\text{FTP})_{30}]^{-}$ (where, $n = 3, 4$) are included in the Supporting Information (SI 1). Here, the protecting ligands on the particles, such as DMBT, BDT, FTP, and TPP, correspond to 2,4-dimethylbenzenethiol, 1,3-benzenedithiol, 4-fluorothiophenol, and triphenylphosphine, respectively.

2.1. Interparticle Reactions. Initially, a stock solution of NCs (1.0 mg/10 mL) was prepared in the relevant solvent based on its highest solubility. $[\text{Ag}_{25}(\text{DMBT})_{18}]^{-}$ and $[\text{PPh}_4]_n[\text{Ag}_{44}(\text{FTP})_{30}]^{-}$ (where, $n = 3, 4$) NCs were dissolved in DCM. $[\text{Ag}_{29}(\text{BDT})_{12}(\text{TPP})_4]^{3-}$ NC was dissolved in DMF. Then, a solution of Au@DMBT and Au@BDT NPs (5.0 mg/3 mL) was prepared in DCM and DMF, respectively. 0.3 mL of NC was added to the NP solution and allowed to react under rest. The reaction was monitored using high-resolution transmission electron microscopy (HRTEM) and optical absorption spectroscopy. The detailed concentration calculations are presented in the SI. In the subsequent text, this experiment is referred to as reaction@NP.

2.2. Mass Spectral Measurements. We performed electrospray ionization mass spectrometry (ESI MS) using Waters Synapt G2-Si instrument. From the stock solutions, 1 mL of NC and 0.3 mL of NP were mixed, and the reaction mixture was diluted with solvent (DCM or DMF, depending on the particle solubility) while maintaining the total volume at 6 mL. Then, the required volume was taken for time-dependent ESI mass and optical absorption spectral studies. The concentration calculations are presented in the SI. In the subsequent text, these ESI MS measurements are referred to as reaction@NC.

In simple terms, the interparticle reaction (referred to as reaction@NP) requires an excess of Au NPs (for example, $2.50 \mu\text{M}$ Au@DMBT NP reacts with $1.75 \mu\text{M}$ $[\text{Ag}_{25}(\text{DMBT})_{18}]^{-}$ NC), while the mass spectral study (referred to as reaction@NC) necessitates an excess of Ag NC ($3.22 \mu\text{M}$ Au@DMBT NP reacts with $0.12 \mu\text{M}$ $[\text{Ag}_{25}(\text{DMBT})_{18}]^{-}$ NC) to thoroughly comprehend the reaction mechanism (detailed concentration calculations are provided in the Supporting Information, SI 2).

3. RESULTS AND DISCUSSION

3.1. Interparticle Reaction at Structurally and Compositionally Analogous Metal-Monodentate Ligand Interface. Interparticle reaction between a plasmonic Au@DMBT NP and atomically precise $[\text{Ag}_{25}(\text{DMBT})_{18}]^{-}$ NC and the consequent reaction pathway leading to the final product is schematically illustrated in Figure 2A (see the SI for additional data and complete characterization). We prepared Au@DMBT NPs with an average diameter of 4.46 ± 0.64 nm using a modified Brust–Schiffrin method (synthetic procedures in the SI 1). Hereafter, the 2,4-DMBT-capped-Au NPs are referred to as ~ 4.5 nm Au@DMBT NPs. TEM image of the parent Au@DMBT NPs is presented in Figure 2B (further details in the SI, Figure S1). The optical absorption spectrum of Au@DMBT NP has a characteristic localized surface plasmon resonance (LSPR) peak at 520 nm (Figure S1). We utilized the $[\text{Ag}_{25}(\text{DMBT})_{18}]^{-}$ NC synthesized using a reported protocol.⁸⁵ The mass spectrum and optical absorption spectral data of the pure Ag NC are provided in Figure S2. In

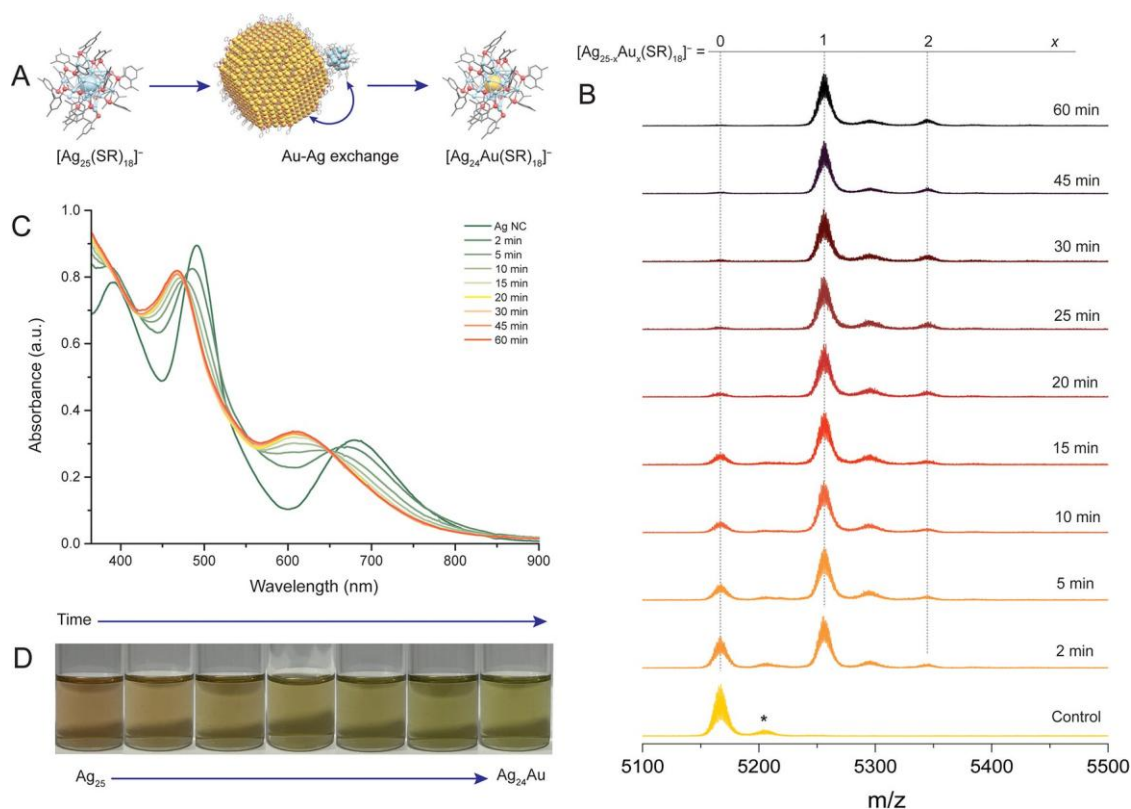


Figure 3. (A) Schematic representation of the metal-exchange pathway as the NC interacts with NP. (B) Time-dependent ESI mass spectra of the interparticle reaction. (C) Corresponding optical absorption spectra of the reaction and (D) resulting change in the color of the solution. The peak labeled * in panel B is due to unidentified contamination. Color code in panel A: yellow, Au; blue, Ag; pink, S; gray, C. H has been omitted for clarity.

the negative ion ESI MS, the $[Ag_{25}(DMBT)_{18}]^-$ NC showed a molecular ion peak centered at m/z 5166, with unidentified contamination at m/z 5204 (refer to the control sample of Figure 3B and full range spectrum in Figure S2A). For our experiment, we mixed known volumes of Au@DMBT NP (2.5 μ M) and $[Ag_{25}(DMBT)_{18}]^-$ NC (1.75 μ M) solutions in DCM at room temperature (refer to the Experimental Section and SI for a description of the calculations of concentrations, SI2). TEM of the reacted Au NPs is presented in Figure 2C (additional data in Figure S3). We estimated the particle size distribution from the most probable diameter of the metallic core of multiple NPs as observed in TEM. The average size of Au@DMBT NPs changes from 4.46 ± 0.64 nm (d -spacing 0.28 nm, fwhm 1.51 nm) to 4.81 ± 0.59 nm (d -spacing 0.27 nm, fwhm 1.40 nm) before and after the reaction, respectively (Figure S4). A slight shift in the distribution toward a lower fwhm value for the reacted Au NPs suggests an onset of size-focusing compared to the parent Au NP.

The effect of alloying on surface plasmon resonance (SPR) in Au and Ag NPs has been studied widely.⁸⁶ Insertion of Ag atoms into a Au NP strongly alters the plasmon resonance and leads to a shift in the peak position depending upon the structure and composition of the alloy NP.^{87,88} The optical spectra of the reaction mixture showed a continuous evolution, indicating spontaneous solution phase dynamics (Figure S5). The system took 30 min to reach equilibrium after particle mixing; visible spectral changes appeared as early as 2 min. Upon reaction with $[Ag_{25}(SR)_{18}]^-$ NC, the reaction mixture exhibited a blue shift of ~ 31 nm in the SPR compared to the parent Au NP, resulting in a modified peak at 488 nm. Such a

change in the spectral feature indicates the insertion of Ag atoms in the parent Au NP. The scanning transmission electron microscopy–energy-dispersive X-ray spectroscopy (STEM–EDS)-based elemental maps of gold (Au M), silver (Ag L), and sulfur (S K) of the reacted NPs are presented in Figure 2D–G. Elemental mapping images of Au–Ag–S showed a uniform distribution across particles, indicating the formation of well-alloyed bimetallic Au–Ag-thiolated hybrid NPs. The EDS spectra collected from various locations on the grid loaded with the reacted NP sample showed a higher Au content compared to Ag (Figure S6).

Our previous work utilized ESI MS to study interparticle reaction mechanisms.^{52,71} Mass spectrometry can track the chemical changes occurring in a Au NC as it reacts with the Au NP, providing mechanistic insight into such reactions. We performed a time-dependent ESI MS of the particle mixture with constant mass spectrometric parameters (refer to the Experimental Section). Such interparticle systems are referred to as reaction@NC in the subsequent text. Figure 3A schematically illustrates that the Au@DMBT NP and $[Ag_{25}(DMBT)_{18}]^-$ NC reactions proceed via a spontaneous intersystem metal-exchange pathway (details on the ratio of particle mixing are in the SI). NP–NC reactions are spontaneous and stoichiometric in nature.^{52,71} Figure 3B shows the time-dependent evolution of the mass spectral features of $[Ag_{25}(DMBT)_{18}]^-$ NC upon interaction with Au NP (full range MS in Figure S7). As the reaction progressed, the peak corresponding to the parent species, $[Ag_{25}(DMBT)_{18}]^-$ NC (m/z 5166), gradually shifted toward a higher mass species, $[Ag_{24}Au(DMBT)_{18}]^-$ NC (m/z 5255),

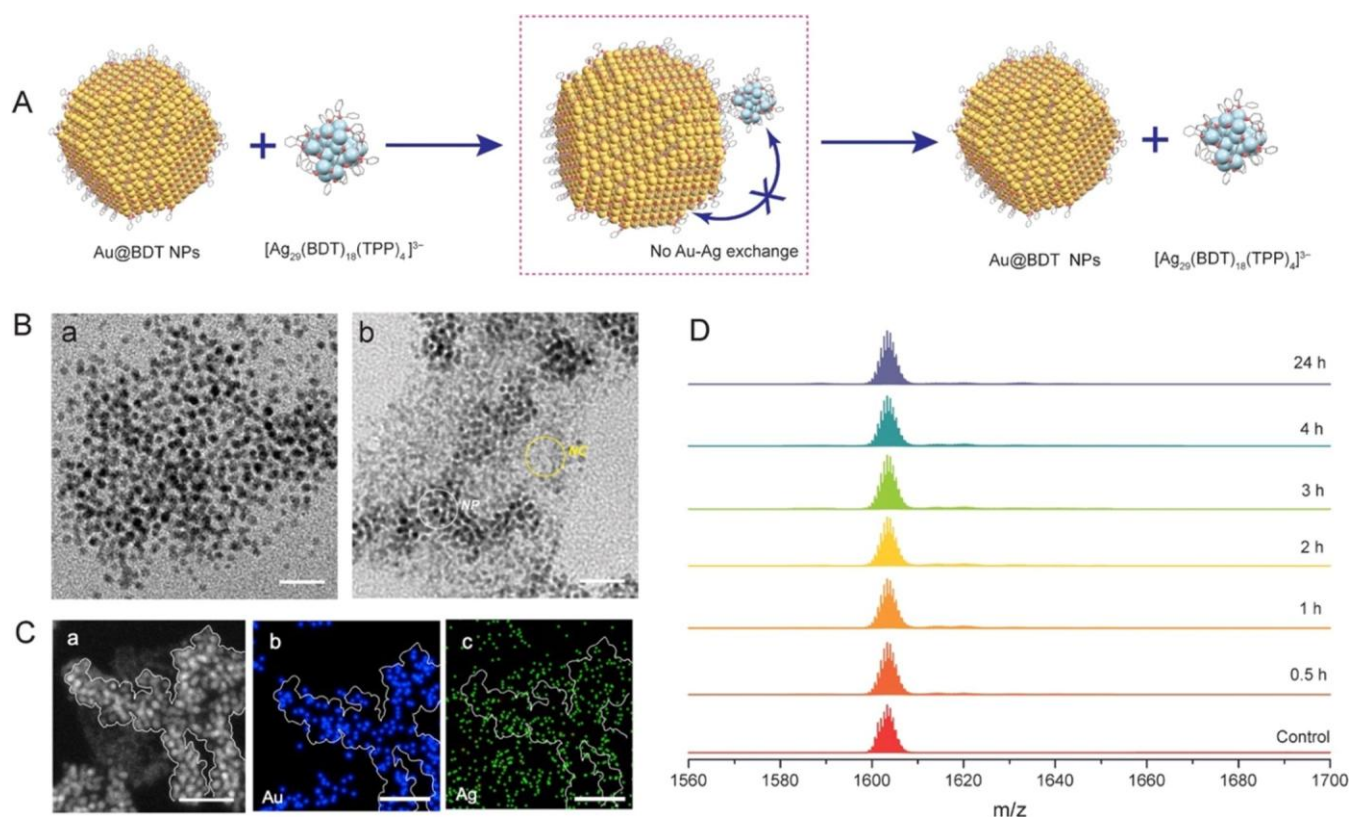


Figure 4. (A) Schematic illustration of a nonreactive 1,3-BDT-protected Au NP and Ag NC interactions. (B) TEM images of the parent Au@BDT NPs (a) and unreacted Au@BDT NPs/[Ag₂₅(BDT)₁₂(TPP)₄]³⁻ NC in the reaction mixture (b). (C) Dark-field STEM image of the reaction mixture (a) and the corresponding EDS maps showing the footprint of elemental Au (b) and Ag (c). (D) Time-dependent ESI mass spectra of the reaction@NC. Scale bar: 20 nm. Color code: yellow, Au; blue, Ag; pink, S; gray, C; H is omitted.

and complete conversion of the former occurred within 30 min. The mass difference with the newly emerged peaks is ~89 Da, which corresponds to a simultaneous Ag (108 Da) loss and Au (197 Da) addition into the [Ag₂₅(DMBT)₁₈]⁻ NC. In addition to the first-doped NC species, [Ag₂₃Au₂(DMBT)₁₈]⁻ NC (m/z 5344) was also observed at a reasonable intensity (isotopic distribution patterns in Figure S8). Similarly, the prominent optical absorption spectral features of [Ag₂₅(DMBT)₁₈]⁻ NC showed a gradual and continuous blue shift as the reaction progressed (Figure 3C). Within 30 min of reaction, the spectral features of the parent NCs evolved into two major features at 470 and 610 nm, resembling the previously reported [Ag₂₄Au(DMBT)₁₈]⁻ NC.⁸⁹ The [Ag₂₅(DMBT)₁₈]⁻ NC reaction with Au@DMBT NP causes a gradual change in the color of the reaction mixture from brown to olive-green with time (Figure 3D). The reacted NC exhibited an ~ 6.8-fold enhancement in photoluminescence compared to the parent [Ag₂₅(DMBT)₁₈]⁻ NC; a similar phenomenon was reported by Bootharaju et al. (Figure S9).⁸⁹

In this section, we correlated the results of the reaction@NP and reaction@NC to propose an overall reaction mechanism for the interparticle reaction between Au NP and Ag NC. Previous ESI MS observations confirm that the NC-NP reaction takes place along a pathway involving atomic exchange between particles. The MS studies of the reacted Au NP indicated that the parent [Ag₂₅(DMBT)₁₈]⁻ NC undergoes complete consumption during the reaction (Figure S10). From the absence of luminescence in the reacted Au NP solution, as seen in the photoluminescence spectra and photographed under UV light, it can be further inferred that the alloying

process via interparticle reaction involves the complete consumption of both the parent [Ag₂₅(DMBT)₁₈]⁻ NC and the intermediate [Ag_{25-x}Au_x(DMBT)₁₈]⁻ NC species (Figure S9). Figure S11 presents TEM images comparing the particle morphologies of the reactants and the products. Therefore, it can be presumed that the smaller NC, upon interaction with the NP, undergoes intersystem atom transfer and eventually gets completely consumed by the larger NPs, resulting in the formation of alloy NPs.

3.2. Interparticle Reaction at Structurally and Compositionally Analogous Metal-Bidentate Ligand Interface. We studied the interparticle reaction by modifying the particle monolayer with a bidentate-capping ligand called 1,3-benzenedithiol (BDT). It is already known that the dithiol-protected NCs show distinctly different chemistry at the metal–ligand interface compared to the monothiolated ones.⁹⁰ Ghosh et al. showed that in the intercluster reactions, dynamics at the metal–ligand interface could be altered with the dithiolates binding to the metal core in a bidentate manner, which, in turn, reduces the flexibility of the interface.⁹¹

The overall reaction for a dithiol-capped particle system, 1,3-BDT-protected plasmonic Au NPs (to be referred to as Au@BDT NPs) and atomically precise [Ag₂₉(BDT)₁₂(TPP)₄]³⁻ NC, is schematically represented in Figure 4A (see the SI for experimental and characterization data). We synthesized the Au@BDT NPs with an average size of 3.70 ± 0.48 nm using a modified Brust–Schiffrin method (TEM image in Figure 4B-a, and further characterization in Figure S12).⁹² The ESI MS of the pure [Ag₂₉(BDT)₁₂(TPP)₄]³⁻ NC shows a molecular ion peak centered at m/z 1603 after the loss of 4 TPP ligands

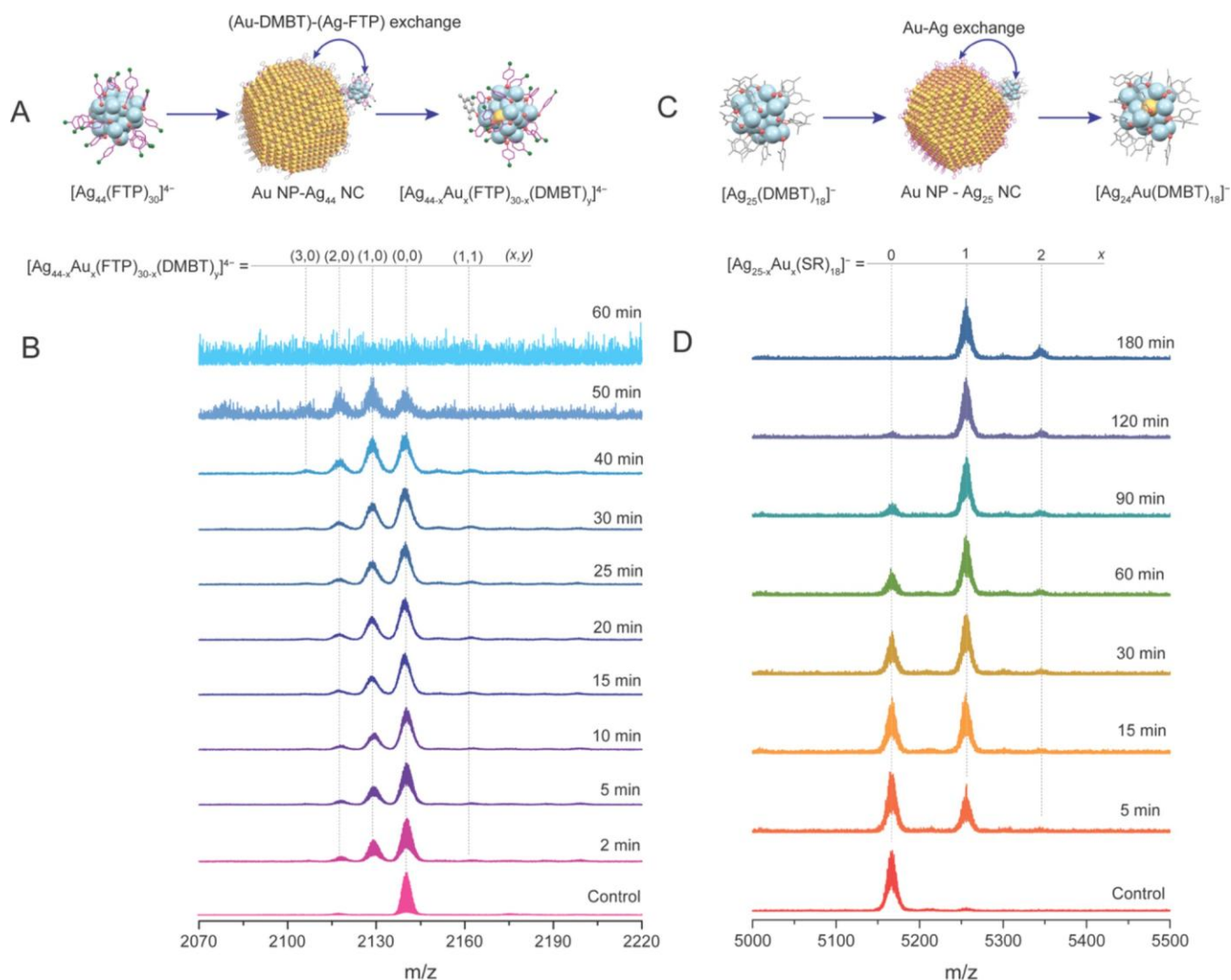


Figure 5. Schematic representation of the interparticle reaction between (A) Au@DMBT NP and $[Ag_{44}(FTP)_{30}]^{4-}$ NC and (B) corresponding time-dependent ESI mass spectra for the reaction@NC. (C) Au@BDT NP and $[Ag_{25}(DMBT)_{18}]^{-}$ NC reaction and (D) corresponding time-dependent ESI mass spectra. Color code: yellow, Au; blue, Ag; pink, S; magenta/gray, C; green, F; H was omitted for clarity.

during electrospray ionization (characterization details in Figure S13).⁹³ For the study of reaction@NP, we mixed known volumes of Au@BDT NP ($4.6 \mu\text{M}$) and $[Ag_{29}(\text{BDT})_{12}(\text{TPP})_4]^{3-}$ NC ($1.55 \mu\text{M}$) solutions in DMF at room temperature (refer to the Experimental Section and concentration calculation in the SI). In Figure 4B-b, the TEM image of the reaction@NP mixture shows an unreacted particle mixture, where the particles with higher and lower contrasts correspond to Au@BDT NPs (highlighted in white) and subnanometer $[Ag_{29}(\text{BDT})_{12}(\text{TPP})_4]^{3-}$ NCs (highlighted in yellow), respectively. The optical absorption spectra of the

constituent particles in the mixture were stable after 24 h of mixing, further confirming that there were no interparticle interactions (Figure S14). A comparative TEM image of the starting materials and the reaction mixture imaged after 30 min and 24 h of mixing are provided in Figure S15. In Figure 4C, the STEM-EDS-based elemental maps show the Au M (Figure 4C-b), and Ag L (Figure 4C-c) translocation across the interparticle reaction mixture (note that the white outline indicates the NP-rich region). The Au M mapping (Figure 4C-b) appears weak in the regions where Au NPs are lesser in concentration. In contrast, the Au-deficit regions showed

higher Ag intensity in the Ag L mapping (Figure 4C-c). Therefore, elemental mapping also indicates that the analyte is composed of unreacted Au and Ag particles. Quantitative STEM-EDS spectra of the Au NP before and after mixing with $[Ag_{29}(\text{BDT})_{12}(\text{TPP})_4]^{3-}$ NC are provided in Figure S16.

We performed the ESI MS experiment to further confirm that the interparticle mixture does not include an atomic exchange between the systems. For the reaction@NC study, we mixed known volumes of Au@BDT NP ($0.23 \mu\text{M}$) and $[Ag_{29}(\text{BDT})_{12}(\text{TPP})_4]^{3-}$ NC ($2.85 \mu\text{M}$) solutions in DMF at room temperature and analyzed the reaction mixture (refer to the Experimental Section and concentration calculation in the SI). All of the mass spectrometric parameters were kept constant during the entire measurement. The MS peak corresponding to $[Ag_{29}(\text{BDT})_{12}]^{3-}$ NC (m/z 1603) remained intact in the reaction mixture even after 24 h. The corresponding optical spectral data given in Figure S17 agrees with the mass spectral observations. Therefore, we conclude that Au@BDT NP and $[Ag_{29}(\text{BDT})_{12}(\text{TPP})_4]^{3-}$ NC are nonreactive, allowing the parent particles to retain their inherent chemical properties. From the above study, we infer

that the introduction of bidentate ligand stabilization into the particle system ultimately inhibits interparticle reactions.

3.3. Role of the Metal–Ligand Interface in an Interparticle Reaction. From the previous discussions, we understand that the monolayers and their nature of bonding to the NP surface are key in controlling their reactivity toward NC.⁷¹ Krishnadas et al. reported the involvement of the metal–ligand (Au–PET–Ag–FTP) fragments in an intercluster reaction between $[\text{Au}_{25}(\text{PET})_{18}]^-$ and $[\text{Ag}_{44}(\text{FTP})_{30}]^{3-}$.⁵⁵ To further investigate the contribution of the ligand in these interparticle (Au NP–Ag NC) events, we have introduced an FTP-protected Ag NC system.

We chose Au@DMBT NP and $[\text{PPh}_4]_n[\text{Ag}_{44}(\text{FTP})_{30}]$ (where, $n = 3, 4$) NC as our particle system where Au-DMBT \cdots Ag-FTP acts as a reacting interface (details in the [Experimental Section](#)). ESI MS and optical absorption spectral data of the $[\text{PPh}_4]_n[\text{Ag}_{44}(\text{FTP})_{30}]$ NC are presented in [Figure S18](#). Using similar experimental conditions as for the DMBT-capped particle system, we conducted both reaction@NP and reaction@NC on the Au@DMBT NP \square $[\text{PPh}_4]_n[\text{Ag}_{44}(\text{FTP})_{30}]$ NC system (refer to the [Experimental Section](#)). The [SI](#) includes microscopic and spectroscopic results for the reaction@NP . As the reaction progressed, the spectral feature corresponding to Au@DMBT NP evolved into an enhanced and blue-shifted SPR at 523 nm in the optical absorption spectra, suggesting a Ag NC-induced chemical change in the parent Au NP ([Figure S19](#)). However, the reaction of Au NP with the $[\text{PPh}_4]_n[\text{Ag}_{44}(\text{FTP})_{30}]$ NC causes a slight increase in their average size, from 4.46 ± 0.64 to 4.72 ± 0.91 nm ([Figure S20](#)). The fwhm values are 1.51 and 1.91 nm, calculated from the size distribution of NPs before and after the reaction, respectively.

[Figure 5A](#) depicts a schematic representation of the mechanistic pathway for the reaction between Au@DMBT NP and $[\text{Ag}_{44}(\text{FTP})_{30}]^{4-}$ NC. As the interparticle reaction progressed, the molecular peak corresponding to the parent species, $[\text{Ag}_{44}(\text{FTP})_{30}]^{4-}$ NC (m/z 2140), shifted gradually toward the species with lower m/z values ([Figure 5B](#)). The $[\text{Ag}_{43}\text{Au}(\text{FTP})_{29}]^{4-}$ NC (m/z 2130) was detected as a major species within 2 min in the reaction. The mass difference with the newly emerged peaks is ~ 10 Da, which corresponds to a Ag–FTP unit (235 Da) loss from the $[\text{Ag}_{44}(\text{FTP})_{30}]^{4-}$ NC and a simultaneous Au (197 Da) addition into it. Along with the first-doped species, $[\text{Ag}_{42}\text{Au}_2(\text{FTP})_{28}]^{4-}$ (m/z 2120) and $[\text{Ag}_{41}\text{Au}_3(\text{FTP})_{27}]^{4-}$ (m/z 2111) NC species were detected in a reasonable intensity. The $[\text{Ag}_{43}\text{Au}(\text{DMBT})(\text{FTP})_{29}]^{4-}$ NC species, as observed at m/z 2164, corresponds to a simultaneous (Ag–FTP) \cdots (Au–DMBT) exchange in the $[\text{Ag}_{44}(\text{FTP})_{30}]^{4-}$ NC (isotopic distributions match in [Figure S21](#)). Noticeable deviations from the parent $[\text{Ag}_{44}(\text{FTP})_{30}]^{4-}$ NC features were observed in the optical spectrum acquired within 2 min of mixing the particles ([Figure S22](#)). Most of the spectral features evolved within 30 min into the reaction, and two major features appeared around 412 and 529 nm, with weaker features around 483 and 643 nm. Moreover, we note that such a blue-shifted spectrum resembles the previously reported Au-doped-Ag₄₄@FTP NC.^{94,95} We carried out the Raman spectral measurements on the reacted Au NP to confirm FTP-DMBT ligand exchange on the NP surface (refer to the [SI](#) for details). As shown in [Figure S23](#), the reacted NP shows distinguishable SERS corresponding to C–X stretching ($191\text{--}282\text{ cm}^{-1}$) and deformation ($775\text{--}877\text{ cm}^{-1}$), ring breathing ($980\text{--}1047\text{ cm}^{-1}$), and C–C stretching (1512--

1681 cm^{-1}) frequencies (wavenumber ranges correspond to the AgAu@DMBT, FTP NP), which are characteristic for halogenated thiophenols.^{96–98} The presence of an electro-negative F atom in the 4-FTP ligand is likely to cause a greater metal–ligand backdonation, leading to a shift in the frequency and relative intensity.⁹⁶ From the foregoing results, we infer that the Ag NC-mediated AGR of Au NPs proceeds via a metal–ligand fragment exchange.

3.4. Interparticle Reaction at a Structurally Complex Metal–Ligand Interface. Next, we studied the Au NP–Ag NC reaction at a geometrically complicated interparticle interface, which included dithiolated and monothiolated NPs to provide a range of geometric/structural rigidity and flexibility, respectively. We chose Au@BDT NP and $[\text{Ag}_{25}(\text{DMBT})_{18}]^-$ NC as our particle system of interest, where Au–BDT \cdots Ag–DMBT acts as a reacting interface (synthesis and characterization in the [SI](#)). Intercluster reactions with BDT-protected metal NCs have been studied extensively in the past. Such reactions usually involve a metal-exchange reaction pathway instead of a metal–ligand exchange.⁹¹ We carried out the reaction@NP and the reaction@NC for the above particle system while keeping the experimental conditions the same as the previous experiments.

The Au@BDT NP and $[\text{Ag}_{25}(\text{DMBT})_{18}]^-$ NC reactions involve an intersystem atom exchange, as schematically represented in [Figure 5C](#). In ESI MS measurement as shown in [Figure 5D](#), we observed a steady shift with time in the molecular peak corresponding to the parent species, $[\text{Ag}_{25}(\text{DMBT})_{18}]^-$ NC (m/z 5166), toward higher mass species, $[\text{Ag}_{24}\text{Au}(\text{DMBT})_{18}]^-$ (m/z 5255) and $[\text{Ag}_{23}\text{Au}_2(\text{DMBT})_{18}]^-$ (m/z 5344) NCs, where the former was a major and the latter was a minor product. However, a slower reaction time (~ 3 h) can be attributed to a hindered interparticle approach because of the geometrically complicated interface compared to the DMBT-capped system (~ 0.5 h) (further discussion in [Section 3.6](#)). Our mass spectral measurements are consistent with the time-dependent optical absorption spectra ([Figure S24](#)). In reaction@NP , the average size of Au@BDT NPs changes after reaction with $[\text{Ag}_{25}(\text{DMBT})_{18}]^-$ NC from 3.70 ± 0.48 nm ([Figure S25A](#)) to 3.17 ± 0.42 nm ([Figure S25B](#)), and the fwhm values are 1.08 and 0.95 nm, respectively. However, unlike the DMBT-capped-interparticle system, we did not observe much change in the overall particle size distribution. The optical absorption spectrum of Au@BDT NPs showed a blue-shifted and enhanced SPR on reaction with $[\text{Ag}_{25}(\text{DMBT})_{18}]^-$ NC, indicating a Ag-doping in Au@BDT NPs ([Figure S26](#)). Therefore, the Au@BDT NP– $[\text{Ag}_{25}(\text{DMBT})_{18}]^-$ NC reaction proceeds via a metal-only exchange, as supported by the data from both the reaction@NP and the reaction@NC .

Next, while maintaining the complexity of the reacting interface (Au–DMBT \cdots Ag–BDT), we studied the particle system with reversed monolayer coverage, such as Au@DMBT NP and $[\text{Ag}_{29}(\text{BDT})_{12}(\text{TPP})_4]^{3-}$ NC. The reaction@NP and reaction@NC for the particle system were performed along a similar line as in the previous one. As for the reaction@NP , TEM images ([Figure S27](#)) and optical spectral data ([Figure S28](#)) suggested that individual particles in the NP–NC mixture remained unreacted in solution for the entire period of measurement. In the time-dependent ESI MS study for the reaction@NC , the $[\text{Ag}_{29}(\text{BDT})_{12}]^{3-}$ NC peak (m/z 1603) remained intact in the solution even after 24 h, also suggesting

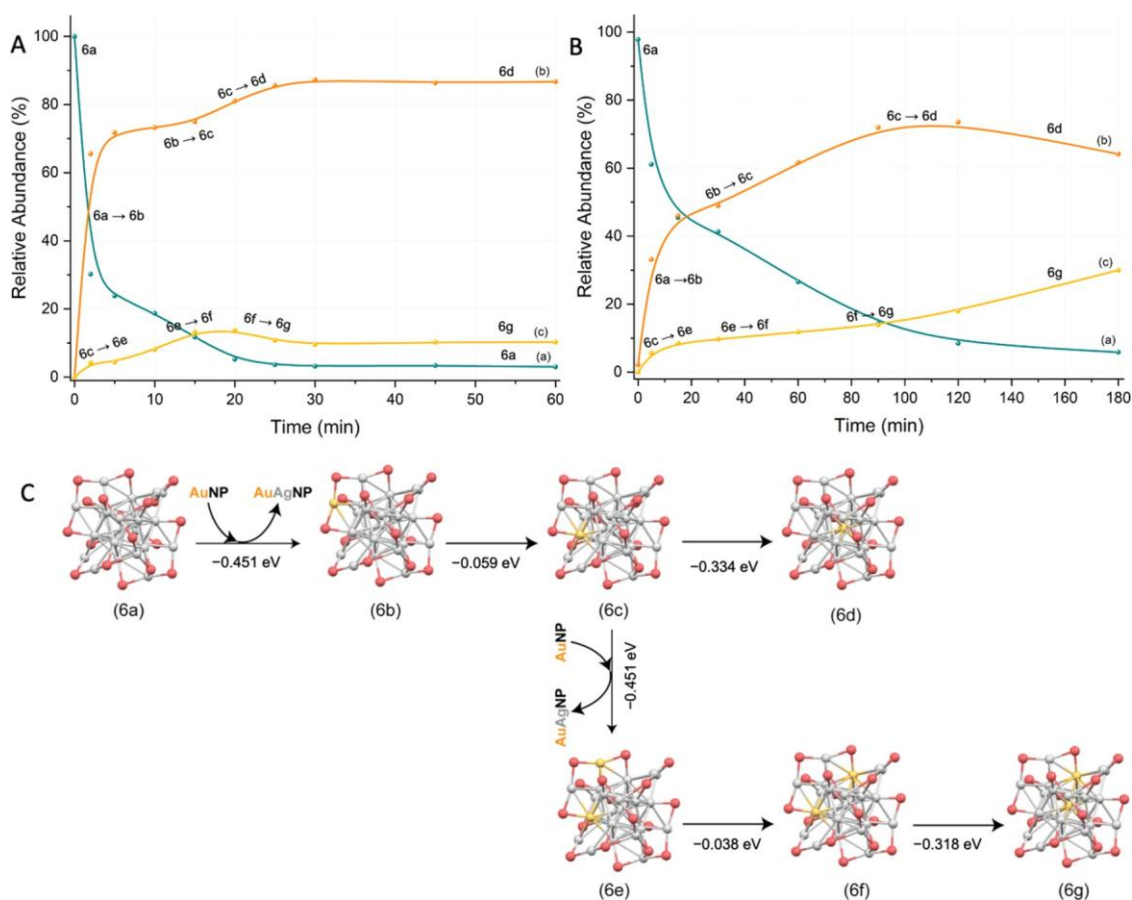


Figure 6. Plot showing the extent of the relative metal exchange (%) as a function of reaction time (in min) for the $[\text{Ag}_{25}(\text{DMBT})_{18}]^{-}$ NC with Au@DMBT (A) and Au@BDT NP (B) interparticle systems. (C) Proposed mechanism of Au-doping in parent $[\text{Ag}_{25}(\text{DMBT})_{18}]^{-}$ NC (a) and the corresponding reaction energies resulting in $[\text{Ag}_{24}\text{Au}(\text{DMBT})_{18}]^{-}$ (b) and $[\text{Ag}_{23}\text{Au}_2(\text{DMBT})_{18}]^{-}$ NCs (c). Color code: yellow, Au; gray, Ag; pink, S. C and H are omitted for simplification.

no reaction with the NP (Figure S29). The corresponding optical spectra agree with the mass spectral observations (Figure S30).

Using Au-BDT···Ag-FTP as a model, we further investigated the absence of ligand participation in NP–NC reactions with a geometrically complex interparticle interface, similar to those observed between Au-BDT···Ag-DMBT. We chose Au@BDT NP and $[\text{PPh}_4]_n[\text{Ag}_{44}(\text{FTP})_{30}]^{-}$ NC as our particle systems where Au-BDT···Ag-FTP acts as a reacting interface (reaction@NC and reaction@NP results are provided in SI, Figure S31). The Au@BDT NP and $[\text{Ag}_{44}(\text{FTP})_{30}]^{-}$ NC reaction proceeds via an interparticle metal-only exchange pathway, as schematically represented in Figure S31A. In ESI MS measurement as shown in Figure S31B, within 5 min of reaction, we observed a rapid shift in the molecular peak corresponding to the parent species, $[\text{Ag}_{44}(\text{FTP})_{30}]^{-}$ NC (m/z 2851), toward lower and higher mass species, $[\text{Ag}_{43}(\text{FTP})_{30}]^{-}$ (m/z 2816) and $[\text{Ag}_{43}\text{Au}(\text{FTP})_{30}]^{-}$ (m/z 2881) NCs, respectively, where the former was a minor product and later was major (isotopic distributions are matched in Figure S31C). No significant mass spectral signals were detected in the MS region associated with $[\text{Ag}_{44}(\text{FTP})_{30}]^{4-}$ NC (m/z 2070–2220) during the reaction. Based on the mass spectral intensity, we presume that $[\text{Ag}_{44}(\text{FTP})_{30}]^{-}$ and $[\text{Ag}_{44}(\text{FTP})_{30}]^{4-}$ NCs upon reaction with Au@BDT NP undergo a Ag loss to form transient $[\text{Ag}_{43}(\text{FTP})_{30}]^{-}$ NC followed by a Ag–Au exchange to form a

stable $[\text{Ag}_{43}\text{Au}(\text{FTP})_{30}]^{-}$ intermediate species. However, determining an accurate interparticle reaction pathway requires additional investigations. Noticeable deviations from the parent $[\text{Ag}_{44}(\text{FTP})_{30}]^{-}$ NC features were observed in the optical spectrum acquired within 5 min of mixing the particles, and the spectrum resembled Au-doped- $\text{Ag}_{44}\text{@FTP}$ NC (Figure S31D).⁹⁵ In the case of reaction@NP, the optical absorption spectrum exhibited a gradual blue shift in SPR of Au@BDT NPs with time, upon reaction with $[\text{Ag}_{44}(\text{FTP})_{30}]^{-}$ NC, indicating Ag-diffusion in the parent Au NP (Figure S31E and schematically illustrated in Figure S31F). The parent Au@BDT NPs were monodispersed in nature and exhibited no assembling tendency (TEM image in Figure S31G-a). Interestingly, the reacted NPs self-assembled in the solution to create sphere-like superstructures; a similar phenomenon was previously reported with Ag- and Cu-doped Au particles (Figure S31H-a).^{71,74} Upon reaction with $[\text{Ag}_{44}(\text{FTP})_{30}]^{-}$ NC, the average size of Au@BDT NPs changed from 3.70 ± 0.48 nm (Figure S31G-b) to 3.01 ± 0.66 nm (Figure S31H-b), and the fwhm values were 1.08 and 1.56 nm, respectively. Unlike the DMBT-capped-interparticle system, the shift in particle size distribution toward a higher fwhm value suggests that the reaction introduced a polydispersity into the Au NPs. From the above discussion, we conclude that the Au@BDT NP– $[\text{Ag}_{44}(\text{FTP})_{30}]^{-}$ NC reaction also proceeds via a metal-only exchange pathway.

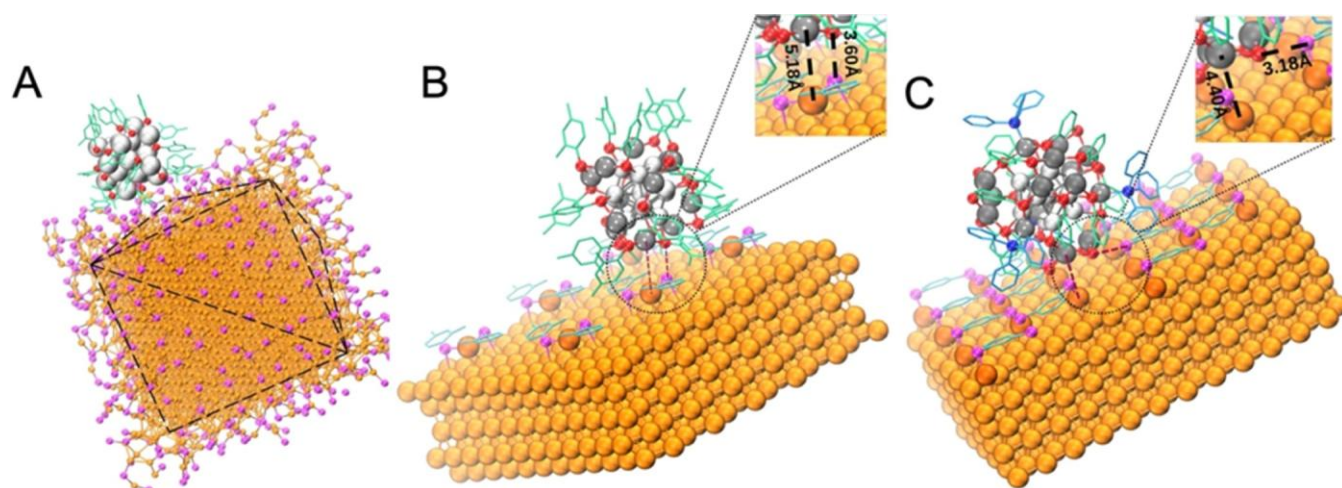


Figure 7. Docking structures of the interactions of (A) $[\text{Ag}_{25}(\text{DMBT})_{18}]^{-}$ NC on SR-protected Au NP, (B) $[\text{Ag}_{25}(\text{DMBT})_{18}]^{-}$ NC on DMBT-monolayered Au(111) surface, and (C) $[\text{Ag}_{29}(\text{BDT})_{12}(\text{TPP})_4]^{3-}$ NC on BDT-monolayered Au(111) surface. Color code: gold, Au; orange, Au_{ad}; gray, Ag NC staple; silver, Ag NC icosahedron; magenta, S of surface ligands; red, S of NC ligands; cyan, C of surface ligands; light green, C of thiolate NC ligands, sky blue, C of TPP ligands; blue, P. H was omitted for clarity.

3.5. Relative Abundance Plots. To better understand the kinetics of atom exchange in an interparticle reaction, we investigated the trend in the abundance (%) of reactant and product NCs as a function of reaction time (Figure 6). In this context, the relative abundance (%) refers to the intensity of an ion of a parent or a product relative to the total parent and product ions at a given time. We assumed that the abundance of the parent NC was 100% at a zero reaction time.

As discussed in the previous section, the Au@DMBT NP and $[\text{Ag}_{25}(\text{DMBT})_{18}]^{-}$ NC reactions proceed via alloy–NC intermediates where $[\text{Ag}_{24}\text{Au}(\text{DMBT})_{18}]^{-}$ and $[\text{Ag}_{23}\text{Au}_2(\text{DMBT})_{18}]^{-}$ NCs were identified as major and minor products, respectively (Figure 3B). Initially, we observed a rapid conversion of the parent $[\text{Ag}_{25}(\text{DMBT})_{18}]^{-}$ NC into its first-doped $[\text{Ag}_{24}\text{Au}(\text{DMBT})_{18}]^{-}$ product, while the second-doped $[\text{Ag}_{23}\text{Au}_2(\text{DMBT})_{18}]^{-}$ product appeared at a much slower rate (Figure 6A). The $[\text{Ag}_{25}(\text{DMBT})_{18}]^{-}$ and $[\text{Ag}_{24}\text{Au}(\text{DMBT})_{18}]^{-}$ NCs have an analogous crystal structure with an M_{13} icosahedron core and six $M_2(\text{SR})_3$ motifs, where M and SR refer to metal and thiolate, respectively. It is reported that doping in $[\text{Ag}_{25}(\text{DMBT})_{18}]^{-}$ to $[\text{Ag}_{24}\text{Au}(\text{DMBT})_{18}]^{-}$ NCs occurs in a nanogymnastic fashion, with metal exchange beginning at the staple and progressing to the Au₁₃ icosahedron core.⁹⁹ The reaction energy (ΔE) values for each step were computed using density functional theory (DFT); further discussion in Section 3.6. The possible explanation for faster $6a \rightarrow 6b$ ($\Delta E = -0.45152$ eV) conversion of the $[\text{Ag}_{25}(\text{DMBT})_{18}]^{-}$ (6a) to highly stable $[\text{Ag}_{24}\text{Au}(\text{DMBT})_{18}]^{-}$ (6b) might be attributed to an interparticle Au–Ag exchange of the surface atoms (Figure 6C). Next, the intrananostructure atomic exchange involves rapid swapping at the staple ($6b \rightarrow 6c$, $\Delta E = -0.05984$ eV) followed by a slower diffusion into the core ($6c \rightarrow 6d$, $\Delta E = -0.33456$ eV) until equilibrium is attained. The interaction between Au@DMBT NP and $[\text{Ag}_{24}\text{Au}(\text{DMBT})_{18}]^{-}$ NC results in the infusion of a second Au-atom, which presumably accounts for the slowest rate of conversion to $[\text{Ag}_{23}\text{Au}_2(\text{DMBT})_{18}]^{-}$ (6g). As per our calculations, the second Au-atom replaces a Ag-atom at the staple position in $\text{Ag}_{24}\text{Au}_m$ ($6c \rightarrow 6e$, $\Delta E = -0.45152$ eV) followed by intrananostructure swapping rearrangements ($6e \rightarrow 6f$, $\Delta E = -0.03808$ eV and $6f \rightarrow 6g$, $\Delta E =$

-0.31824 eV). We believe that the overall interparticle reaction kinematics would be much more complex if the byproducts were also considered.

Similarly, the reaction of Au@BDT NP and $[\text{Ag}_{25}(\text{DMBT})_{18}]^{-}$ NC involves an intersystem metal-only hopping where the $[\text{Ag}_{24}\text{Au}(\text{DMBT})_{18}]^{-}$ and $[\text{Ag}_{23}\text{Au}_2(\text{DMBT})_{18}]^{-}$ NCs were identified as the major and minor products, respectively (Figure 5D). Herein, the $[\text{Ag}_{25}(\text{DMBT})_{18}]^{-}$ to $[\text{Ag}_{24}\text{Au}(\text{DMBT})_{18}]^{-}$ conversion is much slower than the previous one (Figure 6B). The longer reaction time scale may be due to the sterically hindered interparticle interaction at the metal–ligand interface before metal exchange. The mechanism of Au-hopping during the doping reaction presumably takes a similar path, as explained in Figure 6C. We infer that the interparticle reaction time scale depends on the metal–ligand bond and the rigidity of the reaction interface.

3.6. Computational Studies. To understand the driving force and mechanism behind the interparticle reactions, we used the density functional theory (DFT) combined with molecular docking (computational details in S13). Molecular dynamics (MD) simulation of octahedral-shaped Au@SR NPs suggests a surface coverage of Au–SR staples and longer Au–SR chains.¹⁰⁰ Staple and ligand coverage on the facets is heterogeneous, lowest at the vertices where the four faces meet and at the edges between neighboring facets.¹⁰⁰ Lower coverage areas on the NP surface may be sterically more accessible for a facile reaction.

The Ag NC docking on the octahedron Au NP suggests that the Ag NC approaches one of the octahedral facets of the NP and interacts with Au–S staples and chains, ligands, and the bare gold surface of the NP (Figure 7A). To simplify the calculations, we assumed a Au(111) surface with a variable monolayer coverage instead of an octahedral Au NP to interact with Ag NC (detailed discussion on the surface construction in the S14 and Figures S32–S33). Docking interactions of the $[\text{Ag}_{25}(\text{DMBT})_{18}]^{-}$ and $[\text{Ag}_{29}(\text{BDT})_{12}(\text{TPP})_4]^{3-}$ NCs are with 2,4-DMBT (Figure 7B) and 1,3-BDT (Figure 7C)-monolayered Au(111) surfaces at a low ligand and staple coverage, respectively (interatomic distances are highlighted in the inset). A comprehensive analysis of the Ag NC–Au(111)@SR

surface docking interaction at different extents of monolayer coverage in terms of binding energies (BEs) is presented in SI 5 and 6 (Figures S34–S36 and Tables S1 and S2).

We calculated reaction energetics to understand the thermodynamic feasibility of the interparticle reactions. Based on our DFT calculations, the most favorable Au-doping route in $[\text{Ag}_{25}(\text{DMBT})_{18}]^-$ NC is via the $\text{Ag}_2(\text{DMBT})_3$ staple, the Ag_{13} icosahedron, and finally, the icosahedron core (refer to Figure 6C in Section 3.5 and energy values in Tables S3 and S4). In $[\text{Ag}_{23}\text{Au}_2(\text{DMBT})_{18}]^-$ NC, the second Ag-atom preferably occupies the Au_{13} icosahedron position (Figure 6C and energy values in Table S5). Similarly, $[\text{Ag}_{28}\text{Au}(\text{BDT})_{12}(\text{TPP})_4]^{3-}$ NC has its most favorable geometry with Au in the core position (refer to Figure S37 and energy values in Table S6).

Next, we used a 2×1 supercell of the Au(111) surface derived from a (3×4) unit cell to calculate the metallic exchange reaction energies (ΔE) between the Ag NCs and Au(111)@SR surface models (surface description in computation details, SI). Our simulations show that upon reaction, Ag-atom preferably occupies the inner layers of the Au(111) surface instead of the staple or top layer (Figure S38 and ΔE values in Tables S7–S9). Figure S39 shows a comparison of the reaction energies for the NC–surface reactions: (1) $[\text{Ag}_{25}(\text{DMBT})_{18}]^- - \text{Au}(111)\text{@DMBT}$ ($\Delta E = 0.0019$ Ha), (2) $[\text{Ag}_{29}(\text{BDT})_{12}(\text{TPP})_4]^{3-} - \text{Au}(111)\text{@BDT}$ ($\Delta E = 0.0128$ Ha), (3) $[\text{Ag}_{25}(\text{DMBT})_{18}]^- - \text{Au}(111)\text{@BDT}$ ($\Delta E = 0.0038$ Ha), and (4) $[\text{Ag}_{29}(\text{BDT})_{12}(\text{TPP})_4]^{3-} - \text{Au}(111)\text{@DMBT}$ ($\Delta E = 0.0109$ Ha). Reactions (1) and (3) are more feasible than (2) and (4) based on the ΔE values, consistent with our experimental results. However, the calculations suggest that the reactions are slightly endothermic as the optimizations were performed under conditions equivalent to zero temperature. At room temperature, the entropic term ($-T\Delta S$) is expected to further lower the Gibbs free energy so that ΔG becomes negative. This leads to a spontaneous reaction, as observed in our experiments with $[\text{Ag}_{25}(\text{DMBT})_{18}]^-$ NC. Further, the small positive reaction energies for reactions with $[\text{Ag}_{25}(\text{DMBT})_{18}]^-$ NC (reactions 1 and 3) compared to that with $[\text{Ag}_{29}(\text{BDT})_{12}(\text{TPP})_4]^{3-}$ NC (reactions 2 and 4) indicate a low reaction barrier for the former. Therefore, $[\text{Ag}_{25}(\text{DMBT})_{18}]^-$ NC is more reactive toward the Au(111)@SR surface, which is true regardless of the presence of DMBT or BDT monolayers and is consistent with our experimental observations.

Overall, we have found that the $[\text{Ag}_{25}(\text{DMBT})_{18}]^-$ NC binds more strongly to Au(111) monolayer surfaces for low coverages, which are expected to favor the reaction as the surface Au and staple Au and S atoms are sterically more accessible, and that the Ag/Au atomic exchange between the Ag NC and the Au(111)@DMBT is slightly more favorable for $[\text{Ag}_{25}(\text{DMBT})_{18}]^-$ as the reaction energies are smaller. The steric hindrance effects of the slightly larger $[\text{Ag}_{29}(\text{BDT})_{12}(\text{TPP})_4]^{3-}$ NC with bulky TPP groups are likely to be greater, leading to higher energy barriers for the reaction of $[\text{Ag}_{29}(\text{BDT})_{12}(\text{TPP})_4]^{3-}$ compared to $[\text{Ag}_{25}(\text{DMBT})_{18}]^-$, and hence the reaction does not occur. Mechanistically, the calculated reaction energies between different symmetry sites of the NC and surface indicate that the substitution of Ag-atoms into the deeper layers is more feasible, while Au-atoms prefer to occupy the central-atom position and icosahedral sites of the Ag NC.

4. CONCLUSIONS

In summary, we demonstrated AGRs in plasmonic Au NPs with atomically precise Ag NCs where the interparticle metal–ligand interface controls the overall reaction dynamics. Au@DMBT NPs on reaction with $[\text{Ag}_{25}(\text{DMBT})_{18}]^-$ NC resulted in well-alloyed bimetallic NPs. Reaction-driven transformations in the morphology and composition of the Au NPs were studied using HAADF-STEM equipped with EDS. With the introduction of dithiol-induced geometric rigidity at the interface, no reaction was observed for the Au@BDT NP... $[\text{Ag}_{29}(\text{BDT})_{12}(\text{TPP})_4]^{3-}$ NC systems. ESI MS studies confirmed that the reactions involve interparticle metal–ligand and metal-only exchanges in the case of monothiol- and dithiol-capped NPs, respectively. DFT calculation also confirmed that the overall metal-exchange reactions energetically favor the DMBT-capped particle system over the BDT-capped system. Further electrochemical, *in situ* microscopic, and molecular dynamics studies are required to fully comprehend the phenomena behind such reactions. The universality of NP–NC reactions throughout the noble metal system can be further extended to prepare multimetallic alloy particles with controlled size and composition.

ASSOCIATED CONTENT

Supporting Information

The Supporting Information is available free of charge at <https://pubs.acs.org/doi/10.1021/acs.chemmater.4c00620>.

Materials and methods, concentration calculations, UV–vis, ESI MS, TEM, EDS, Raman characterization of particles, and detailed computational analysis of the interparticle reactions (PDF)

AUTHOR INFORMATION

Corresponding Authors

Sharma S. R. K. C. Yamijala – Department of Chemistry, Indian Institute of Technology Madras, Chennai 600036, India; orcid.org/0000-0003-1773-9226; Email: yamijala@iitm.ac.in

Nonappa – Faculty of Engineering and Natural Sciences, Tampere University, FI-33720 Tampere, Finland; orcid.org/0000-0002-6804-4128; Email: nonappa@tuni.fi

Thalappil Pradeep – DST Unit of Nanoscience (DST UNS) and Thematic Unit of Excellence (TUE), Department of Chemistry, Indian Institute of Technology Madras, Chennai 600036, India; International Centre for Clean Water, Chennai 600113, India; orcid.org/0000-0003-3174-534X; Email: pradeep@iitm.ac.in

Authors

Paulami Bose – DST Unit of Nanoscience (DST UNS) and Thematic Unit of Excellence (TUE), Department of Chemistry, Indian Institute of Technology Madras, Chennai 600036, India; Present Address: Faculty of Engineering and Natural Sciences, Tampere University, FI-33720 Tampere, Finland

Jayoti Roy – DST Unit of Nanoscience (DST UNS) and Thematic Unit of Excellence (TUE), Department of Chemistry, Indian Institute of Technology Madras, Chennai 600036, India

Vikash Khokhar – DST Unit of Nanoscience (DST UNS) and Thematic Unit of Excellence (TUE), Department of

Chemistry, Indian Institute of Technology Madras, Chennai 600036, India

Biswajit Mondal – DST Unit of Nanoscience (DST UNS) and Thematic Unit of Excellence (TUE), Department of Chemistry, Indian Institute of Technology Madras, Chennai 600036, India

Ganapati Natarajan – International Centre for Clean Water, Chennai 600113, India

Sujan Manna – DST Unit of Nanoscience (DST UNS) and Thematic Unit of Excellence (TUE), Department of Chemistry, Indian Institute of Technology Madras, Chennai 600036, India

Vivek Yadav – DST Unit of Nanoscience (DST UNS) and Thematic Unit of Excellence (TUE), Department of Chemistry, Indian Institute of Technology Madras, Chennai 600036, India

Anupriya Nyayban – DST Unit of Nanoscience (DST UNS) and Thematic Unit of Excellence (TUE), Department of Chemistry, Indian Institute of Technology Madras, Chennai 600036, India

Complete contact information is available at:

<https://pubs.acs.org/10.1021/acs.chemmater.4c00620>

Author Contributions

P.B. performed the experiments and analyzed the results. J.R. carried out the MS measurements. B.M. and N.N. carried out the EM imaging. V.K., G.N., A.N., and S.S.R.K.C.Y. carried out the calculations. S.M. carried out the Raman measurements. P.B. and V.Y. performed the syntheses. T.P. was the project designer and supervisor, overseeing the progress. Every author made a contribution to the writing of the manuscript.

Notes

The authors declare no competing financial interest.

ACKNOWLEDGMENTS

The authors acknowledge the Department of Science and Technology (DST), Government of India, and the Centre of Excellence program of the Indian Institute of Technology Madras, on the theme of Molecular Materials and Functions, under the Institutions of Eminence of Ministry of Education, India, for supporting their research. The authors also thank the Academy of Finland for project funding (No. 352900), the Photonics Research and Innovation (PREIN) flagship, and the Tampere Microscopy Centre for imaging facilities. The authors are grateful to Anirban Som, Indian Institute of Technology Madras, for his insightful comments that helped to shape the manuscript in its final form. The authors also thank Bhanupriya S. for her technical assistance with the electron microscopic facility at the DST Unit of Nanoscience, Indian Institute of Technology Madras. T.P. thanks the Science and Engineering Research Board (SERB), India, for funding through the SPR/2021/000439 research grant and a JC Bose Fellowship.

DEDICATION

Dedicated to Prof. C. N. R. Rao on the occasion of his 90th birthday.

REFERENCES

- Haldar, K. K.; Kundu, S.; Patra, A. Core-Size-Dependent Catalytic Properties of Bimetallic Au/Ag Core-Shell Nanoparticles. *ACS Appl. Mater. Interfaces* 2014, 6 (24), 21946–21953.
- Gellé, A.; Jin, T.; de la Garza, L.; Price, G. D.; Besteiro, L. V.; Moores, A. Applications of Plasmon-Enhanced Nanocatalysis to Organic Transformations. *Chem. Rev.* 2020, 120 (2), 986–1041.
- Rebello Sousa Dias, M.; Leite, M. S. Alloying: A Platform for Metallic Materials with On-Demand Optical Response. *Acc. Chem. Res.* 2019, 52 (10), 2881–2891.
- Vasicek, T. W.; Kress, P. M.; Jenkins, S. V. Optical Properties of Alloyed Noble Metal Nanoparticles: A Nanotechnology Experiment for Chemistry and Engineering Students. *J. Chem. Educ.* 2020, 97 (10), 3778–3783.
- Gilroy, K. D.; Ruditskiy, A.; Peng, H. C.; Qin, D.; Xia, Y. Bimetallic Nanocrystals: Syntheses, Properties, and Applications. *Chem. Rev.* 2016, 116 (18), 10414–10472.
- Xia, X.; Wang, Y.; Ruditskiy, A.; Xia, Y. 25th Anniversary Article: Galvanic Replacement: A Simple and Versatile Route to Hollow Nanostructures with Tunable and Well-Controlled Properties. *Adv. Mater.* 2013, 25 (44), 6313–6333.
- da Silva, A. G. M.; Rodrigues, T. S.; Haigh, S. J.; Camargo, P. H. C. Galvanic Replacement Reaction: Recent Developments for Engineering Metal Nanostructures towards Catalytic Applications. *Chem. Commun.* 2017, 53 (53), 7135–7148.
- Ha, M.; Kim, J. H.; You, M.; Li, Q.; Fan, C.; Nam, J. M. Multicomponent Plasmonic Nanoparticles: From Heterostructured Nanoparticles to Colloidal Composite Nanostructures. *Chem. Rev.* 2019, 119 (24), 12208–12278.
- Cheng, H.; Wang, C.; Qin, D.; Xia, Y. Galvanic Replacement Synthesis of Metal Nanostructures: Bridging the Gap between Chemical and Electrochemical Approaches. *Acc. Chem. Res.* 2023, 56 (7), 900–909.
- Gan, Z.; Xia, N.; Wu, Z. Discovery, Mechanism, and Application of Antigalvanic Reaction. *Acc. Chem. Res.* 2018, 51 (11), 2774–2783.
- Zhu, M.; Wang, P.; Yan, N.; Chai, X.; He, L.; Zhao, Y.; Xia, N.; Yao, C.; Li, J.; Deng, H.; Zhu, Y.; Pei, Y.; Wu, Z. The Fourth Alloying Mode by Way of Anti-Galvanic Reaction. *Angew. Chem., Int. Ed.* 2018, 57 (17), 4500–4504.
- Murray, R. W. Nanoelectrochemistry: Metal Nanoparticles, Nanoelectrodes, and Nanopores. *Chem. Rev.* 2008, 108 (7), 2688–2720.
- Jin, R.; Zeng, C.; Zhou, M.; Chen, Y. Atomically Precise Colloidal Metal Nanoclusters and Nanoparticles: Fundamentals and Opportunities. *Chem. Rev.* 2016, 116 (18), 10346–10413.
- Chakraborty, I.; Pradeep, T. Atomically Precise Clusters of Noble Metals: Emerging Link between Atoms and Nanoparticles. *Chem. Rev.* 2017, 117 (12), 8208–8271.
- Ghosh, A.; Mohammed, O. F.; Bakr, O. M. Atomic-Level Doping of Metal Clusters. *Acc. Chem. Res.* 2018, 51 (12), 3094–3103.
- Kang, X.; Zhu, M. Tailoring the Photoluminescence of Atomically Precise Nanoclusters. *Chem. Soc. Rev.* 2019, 48 (8), 2422–2457.
- Du, Y.; Sheng, H.; Astruc, D.; Zhu, M. Atomically Precise Noble Metal Nanoclusters as Efficient Catalysts: A Bridge between Structure and Properties. *Chem. Rev.* 2020, 120 (2), 526–622.
- Plieth, W. J. The Work Function of Small Metal Particles and Its Relation to Electrochemical Properties. *Surf. Sci.* 1985, 156, 530–535.
- Bonanni, A.; Pumera, M.; Miyahara, Y. Influence of Gold Nanoparticle Size (2–50 Nm) upon Its Electrochemical Behavior: An Electrochemical Impedance Spectroscopic and Voltammetric Study. *Phys. Chem. Chem. Phys.* 2011, 13 (11), 4980–4986.
- Masitas, R. A.; Zamborini, F. P. Oxidation of Highly Unstable < 4 Nm Diameter Gold Nanoparticles 850 mV Negative of the Bulk Oxidation Potential. *J. Am. Chem. Soc.* 2012, 134 (11), 5014–5017.
- Brainina, Kh. Z.; Galperin, L. G.; Vikulova, EV.; Stozhko, N. Yu.; Murzakaev, AM.; Timoshenkova, OR.; Kotov, YA. Gold Nanoparticles Electrooxidation: Comparison of Theory and Experiment. *J. Solid State Electrochem.* 2011, 15 (5), 1049–1056.
- Pattadar, D. K.; Zamborini, F. P. Size Stability Study of Catalytically Active Sub-2 Nm Diameter Gold Nanoparticles

- Synthesized with Weak Stabilizers. *J. Am. Chem. Soc.* 2018, 140 (43), 14126–14133.
- (23) Pattadar, D. K.; Masitas, R. A.; Stachurski, C. D.; Cliffl, D. E.; Zamborini, F. P. Reversing the Thermodynamics of Galvanic Replacement Reactions by Decreasing the Size of Gold Nanoparticles. *J. Am. Chem. Soc.* 2020, 142 (45), 19268–19277.
- (24) Wu, Z.; Wang, M.; Yang, J.; Zheng, X.; Cai, W.; Meng, G.; Qian, H.; Wang, H.; Jin, R. Well-Defined Nanoclusters as Fluorescent Nanosensors: A Case Study on Au₂₅(SG)₁₈. *Small* 2012, 8 (13), 2028–2035.
- (25) Choi, J.-P.; Fields-Zinna, C. A.; Stiles, R. L.; Balasubramanian, R.; Douglas, A. D.; Crowe, M. C.; Murray, R. W. Reactivity of [Au₂₅(SCH₂CH₂Ph)₁₈]¹⁻ Nanoparticles with Metal Ions. *J. Phys. Chem. C* 2010, 114 (38), 15890–15896.
- (26) Wu, Z. Anti-Galvanic Reduction of Thiolate-Protected Gold and Silver Nanoparticles. *Angew. Chem., Int. Ed.* 2012, 51 (12), 2934–2938.
- (27) Tian, S.; Yao, C.; Liao, L.; Xia, N.; Wu, Z. Ion-Precursor and Ion-Dose Dependent Anti-Galvanic Reduction. *Chem. Commun.* 2015, 51 (59), 11773–11776.
- (28) Wang, M.; Wu, Z.; Chu, Z.; Yang, J.; Yao, C. Chemico-Physical Synthesis of Surfactant- and Ligand-Free Gold Nanoparticles and Their Anti-Galvanic Reduction Property. *Chem. - Asian J.* 2014, 9 (4), 1006–1010.
- (29) Sun, J.; Wu, H.; Jin, Y. Synthesis of Thiolated Ag/Au Bimetallic Nanoclusters Exhibiting an Anti-Galvanic Reduction Mechanism and Composition-Dependent Fluorescence. *Nanoscale* 2014, 6 (10), 5449–5457.
- (30) Sahu, P.; Prasad, B. L. V. Preparation of Ag(Shell)–Au(Core) Nanoparticles by Anti-Galvanic Reactions: Are Capping Agents the “Real Heroes” of Reduction? *Colloids Surf., A* 2015, 478, 30–35.
- (31) Wang, S.; Abroshan, H.; Liu, C.; Luo, T.-Y.; Zhu, M.; Kim, H. J.; Rosi, N. L.; Jin, R. Shuttling Single Metal Atom into and out of a Metal Nanoparticle. *Nat. Commun.* 2017, 8 (1), No. 848.
- (32) Li, Q.; Luo, T.-Y.; Taylor, M. G.; Wang, S.; Zhu, X.; Song, Y.; Mpourmpakis, G.; Rosi, N. L.; Jin, R. Molecular “Surgery” on a 23-Gold-Atom Nanoparticle. *Sci. Adv.* 2017, 3 (5), No. e1603193.
- (33) Wang, Z.; Senanayake, R.; Aikens, C. M.; Chen, W. M.; Tung, C. H.; Sun, D. Gold-Doped Silver Nanocluster [Au₃Ag₃₈(SCH₂Ph)₂₄ × 5]²⁻ (X = Cl or Br). *Nanoscale* 2016, 8 (45), 18905–18911.
- (34) Yang, Y.; Jia, T.; Han, Y.-Z.; Nan, Z.-A.; Yuan, S.-F.; Yang, F.-L.; Sun, D. An All-Alkynyl Protected 74-Nuclei Silver(I)–Copper(I)-Oxo Nanocluster: Oxo-Induced Hierarchical Bimetal Aggregation and Anisotropic Surface Ligand Orientation. *Angew. Chem., Int. Ed.* 2019, 58 (35), 12280–12285.
- (35) Han, B.-L.; Wang, Z.; Gupta, R. K.; Feng, L.; Wang, S.; Kurmoo, M.; Gao, Z.-Y.; Schein, S.; Tung, C.-H.; Sun, D. Precise Implantation of an Archimedean Ag@Cu₁₂ Cuboctahedron into a Platonic Cu₄Bis(Diphenylphosphino)Hexane₆ Tetrahedron. *ACS Nano* 2021, 15 (5), 8733–8741.
- (36) Pradeep, T. *Atomically Precise Metal Nanoclusters*; Elsevier, 2022.
- (37) Knoppe, S.; Bürgi, T. The Fate of Au₂₅(SR)₁₈ Clusters upon Ligand Exchange with Binaphthyl-Dithiol: Interstaple Binding vs. Decomposition. *Phys. Chem. Chem. Phys.* 2013, 15 (38), 15816–15820.
- (38) Niihori, Y.; Kikuchi, Y.; Kato, A.; Matsuzaki, M.; Negishi, Y. Understanding Ligand-Exchange Reactions on Thiolate-Protected Gold Clusters by Probing Isomer Distributions Using Reversed-Phase High-Performance Liquid Chromatography. *ACS Nano* 2015, 9 (9), 9347–9356.
- (39) Huang, Z.; Ishida, Y.; Narita, K.; Yonezawa, T. Kinetics of Cationic-Ligand-Exchange Reactions in Au₂₅ Nanoclusters. *J. Phys. Chem. C* 2018, 122 (31), 18142–18150.
- (40) Zeng, C.; Liu, C.; Pei, Y.; Jin, R. Thiol Ligand-Induced Transformation of Au₃₈(SC₂H₄Ph)₂₄ to Au₃₆(SPh-t-Bu)₂₄. *ACS Nano* 2013, 7 (7), 6138–6145.
- (41) Zeng, C.; Chen, Y.; Das, A.; Jin, R. Transformation Chemistry of Gold Nanoclusters: From One Stable Size to Another. *J. Phys. Chem. Lett.* 2015, 6 (15), 2976–2986.
- (42) Kang, X.; Zhu, M. Transformation of Atomically Precise Nanoclusters by Ligand-Exchange. *Chem. Mater.* 2019, 31 (24), 9939–9969.
- (43) Heinecke, C. L.; Ni, T. W.; Malola, S.; Mäkinen, V.; Wong, O. A.; Häkkinen, H.; Ackerson, C. J. Structural and Theoretical Basis for Ligand Exchange on Thiolate Monolayer Protected Gold Nanoclusters. *J. Am. Chem. Soc.* 2012, 134 (32), 13316–13322.
- (44) Knoppe, S.; Dharmaratne, A. C.; Schreiner, E.; Dass, A.; Bürgi, T. Ligand Exchange Reactions on Au₃₈ and Au₄₀ Clusters: A Combined Circular Dichroism and Mass Spectrometry Study. *J. Am. Chem. Soc.* 2010, 132 (47), 16783–16789.
- (45) Knoppe, S.; Azoulay, R.; Dass, A.; Bürgi, T. In Situ Reaction Monitoring Reveals a Diastereoselective Ligand Exchange Reaction between the Intrinsically Chiral Au₃₈(SR)₂₄ and Chiral Thiols. *J. Am. Chem. Soc.* 2012, 134 (50), 20302–20305.
- (46) Wang, S.; Song, Y.; Jin, S.; Liu, X.; Zhang, J.; Pei, Y.; Meng, X.; Chen, M.; Li, P.; Zhu, M. Metal Exchange Method Using Au₂₅ Nanoclusters as Templates for Alloy Nanoclusters with Atomic Precision. *J. Am. Chem. Soc.* 2015, 137 (12), 4018–4021.
- (47) Niihori, Y.; Hossain, S.; Kumar, B.; Nair, L. V.; Kurashige, W.; Negishi, Y. Perspective: Exchange Reactions in Thiolate-Protected Metal Clusters. *Appl. Mater.* 2017, 5, No. 053201.
- (48) Zhang, B.; Safonova, O. V.; Pollitt, S.; Salassa, G.; Sels, A.; Kazan, R.; Wang, Y.; Ruppel, G.; Barrabés, N.; Bürgi, T. On the Mechanism of Rapid Metal Exchange between Thiolate-Protected Gold and Gold/Silver Clusters: A Time-Resolved in Situ XAFS Study. *Phys. Chem. Chem. Phys.* 2018, 20 (7), 5312–5318.
- (49) Wang, S.; Xiong, L.; Sun, G.; Tang, L.; Zhang, J.; Pei, Y.; Zhu, M. The Mechanism of Metal Exchange in Non-Metallic Nanoclusters. *Nanoscale Adv.* 2020, 2 (2), 664–668.
- (50) Chakraborty, P.; Nag, A.; Natarajan, G.; Bandyopadhyay, N.; Paramasivam, G.; Panwar, M. K.; Chakrabarti, J.; Pradeep, T. Rapid Isotopic Exchange in Nanoparticles. *Sci. Adv.* 2019, 5 (1), No. eaau7555.
- (51) Tang, L.; Kang, X.; Wang, X.; Zhang, X.; Yuan, X.; Wang, S. Dynamic Metal Exchange between a Metalloid Silver Cluster and Silver(I) Thiolate. *Inorg. Chem.* 2021, 60 (5), 3037–3045.
- (52) Chakraborty, P.; Bose, P.; Roy, J.; Nag, A.; Mondal, B.; Chakraborty, A.; Pradeep, T. Isotopic Exchange of Atomically Precise Nanoclusters with Materials of Varying Dimensions: From Nanoscale to Bulk. *J. Phys. Chem. C* 2021, 125 (29), 16110–16117.
- (53) Yao, Q.; Wu, Z.; Liu, Z.; Lin, Y.; Yuan, X.; Xie, J. Molecular Reactivity of Thiolate-Protected Noble Metal Nanoclusters: Synthesis, Self-Assembly, and Applications. *Chem. Sci.* 2021, 12 (1), 99–127.
- (54) Bose, P.; Ramankutty, K. K.; Chakraborty, P.; Khatun, E.; Pradeep, T. A Concise Guide to Chemical Reactions of Atomically Precise Noble Metal Nanoclusters. *Nanoscale* 2024, 16 (4), 1446–1470.
- (55) Krishnadas, K. R.; Ghosh, A.; Baksi, A.; Chakraborty, I.; Natarajan, G.; Pradeep, T. Intercluster Reactions between Au₂₅(SR)₁₈ and Ag₄₄(SR)₃₀. *J. Am. Chem. Soc.* 2016, 138 (1), 140–148.
- (56) Krishnadas, K. R.; Baksi, A.; Ghosh, A.; Natarajan, G.; Pradeep, T. Structure-Conserving Spontaneous Transformations between Nanoparticles. *Nat. Commun.* 2016, 7 (1), No. 13447.
- (57) Krishnadas, K. R.; Baksi, A.; Ghosh, A.; Natarajan, G.; Som, A.; Pradeep, T. Interparticle Reactions: An Emerging Direction in Nanomaterials Chemistry. *Acc. Chem. Res.* 2017, 50 (8), 1988–1996.
- (58) Khatun, E.; Chakraborty, P.; Jacob, B. R.; Paramasivam, G.; Bodiuazzaman, M.; Dar, W. A.; Pradeep, T. Intercluster Reactions Resulting in Silver-Rich Trimetallic Nanoclusters. *Chem. Mater.* 2020, 32 (1), 611–619.
- (59) Salassa, G.; Sels, A.; Mancin, F.; Bürgi, T. Dynamic Nature of Thiolate Monolayer in Au₂₅(SR)₁₈ Nanoclusters. *ACS Nano* 2017, 11 (12), 12609–12614.

- (60) Bürgi, T. Properties of the Gold-Sulphur Interface: From Self-Assembled Monolayers to Clusters. *Nanoscale* 2015, 7 (38), 15553–15567.
- (61) Krishnadas, K. R.; Natarajan, G.; Baksi, A.; Ghosh, A.; Khatun, E.; Pradeep, T. Metal–Ligand Interface in the Chemical Reactions of Ligand-Protected Noble Metal Clusters. *Langmuir* 2019, 35 (35), 11243–11254.
- (62) Som, A.; Samal, A. K.; Udayabhaskararao, T.; Bootharaju, M. S.; Pradeep, T. Manifestation of the Difference in Reactivity of Silver Clusters in Contrast to Its Ions and Nanoparticles: The Growth of Metal Tipped Te Nanowires. *Chem. Mater.* 2014, 26 (10), 3049–3056.
- (63) Nonappa; Lahtinen, T.; Haataja, J. S.; Tero, T.-R.; Häkkinen, H.; Ikkala, O. Template-Free Supracolloidal Self-Assembly of Atomically Precise Gold Nanoclusters: From 2D Colloidal Crystals to Spherical Capsids. *Angew. Chem., Int. Ed.* 2016, 55 (52), 16035–16038.
- (64) Som, A.; Chakraborty, I.; Maark, T. A.; Bhat, S.; Pradeep, T. Cluster-Mediated Crossed Bilayer Precision Assemblies of 1D Nanowires. *Adv. Mater.* 2016, 28 (14), 2827–2833.
- (65) Chakraborty, A.; Fernandez, A. C.; Som, A.; Mondal, B.; Natarajan, G.; Paramasivam, G.; Lahtinen, T.; Häkkinen, H.; Nonappa; Pradeep, T. Atomically Precise Nanocluster Assemblies Encapsulating Plasmonic Gold Nanorods. *Angew. Chem., Int. Ed.* 2018, 57 (22), 6522–6526.
- (66) Chakraborty, P.; Nag, A.; Chakraborty, A.; Pradeep, T. Approaching Materials with Atomic Precision Using Supramolecular Cluster Assemblies. *Acc. Chem. Res.* 2019, 52 (1), 2–11.
- (67) Chakraborty, A.; Dave, H.; Mondal, B.; Nonappa; Khatun, E.; Pradeep, T. Shell-Isolated Assembly of Atomically Precise Nanoclusters on Gold Nanorods for Integrated Plasmonic-Luminescent Nanocomposites. *J. Phys. Chem. B* 2022, 126 (8), 1842–1851.
- (68) Som, A.; Griffo, A.; Chakraborty, I.; Hähl, H.; Mondal, B.; Chakraborty, A.; Jacobs, K.; Laaksonen, P.; Ikkala, O.; Pradeep, T.; Nonappa. Strong and Elastic Membranes via Hydrogen Bonding Directed Self-Assembly of Atomically Precise Nanoclusters. *Small* 2022, 18 (34), No. 2201707.
- (69) Nonappa; Ikkala, O. Hydrogen Bonding Directed Colloidal Self-Assembly of Nanoparticles into 2D Crystals, Capsids, and Supracolloidal Assemblies. *Adv. Funct. Mater.* 2018, 28 (27), No. 1704328.
- (70) Nonappa. Precision Nanoengineering for Functional Self-Assemblies across Length Scales. *Chem. Commun.* 2023, 59, 13800–13819, DOI: 10.1039/D3CC02205F.
- (71) Bose, P.; Chakraborty, P.; Mohanty, J. S.; Nonappa; Ray Chowdhuri, A.; Khatun, E.; Ahuja, T.; Mahendranath, A.; Pradeep, T. Atom Transfer between Precision Nanoclusters and Polydispersed Nanoparticles: A Facile Route for Monodisperse Alloy Nanoparticles and Their Superstructures. *Nanoscale* 2020, 12 (43), 22116–22128.
- (72) Kazan, R.; Muller, U.; Bürgi, T. Doping of Thiolate Protected Gold Clusters through Reaction with Metal Surfaces. *Nanoscale* 2019, 11 (6), 2938–2945.
- (73) Chakraborty, A.; Stanley, M. M.; Mondal, B.; Nonappa; Bodiuzzaman, M.; Chakraborty, P.; Kannan, M. P.; Pradeep, T. Tunable Reactivity of Silver Nanoclusters: A Facile Route to Synthesize a Range of Bimetallic Nanostructures. *Nanoscale* 2023, 15 (6), 2690–2699.
- (74) Roy, J.; Mondal, B.; Vishwakarma, G.; Nonappa; Sridharan, N. V.; Krishnamurthi, P.; Pradeep, T. Dissociative Reactions of [Au₂₅(SR)₁₈][−] at Copper Oxide Nanoparticles and Formation of Aggregated Nanostructures. *Nanoscale* 2023, 15 (18), 8225–8234.
- (75) Hou, K.; Han, J.; Tang, Z. Formation of Supraparticles and Their Application in Catalysis. *ACS Mater. Lett.* 2020, 2 (1), 95–106.
- (76) Talapin, D. V.; Lee, J.-S.; Kovalenko, M. V.; Shevchenko, E. V. Prospects of Colloidal Nanocrystals for Electronic and Optoelectronic Applications. *Chem. Rev.* 2010, 110 (1), 389–458.
- (77) Garcia-Lojo, D.; Núñez-Sánchez, S.; Gómez-Graña, S.; Grzelczak, M.; Pastoriza-Santos, I.; Pérez-Juste, J.; Liz-Marzán, L. M. Plasmonic Supercrystals. *Acc. Chem. Res.* 2019, 52 (7), 1855–1864.
- (78) Chou, L. Y. T.; Zagorovsky, K.; Chan, W. C. W. DNA Assembly of Nanoparticle Superstructures for Controlled Biological Delivery and Elimination. *Nat. Nanotechnol.* 2014, 9 (2), 148–155.
- (79) Zhao, H.; Sen, S.; Udayabhaskararao, T.; Sawczyk, M.; Kucanda, K.; Manna, D.; Kundu, P. K.; Lee, J.-W.; Král, P.; Klajn, R. Reversible Trapping and Reaction Acceleration within Dynamically Self-Assembling Nanoflasks. *Nat. Nanotechnol.* 2016, 11 (1), 82–88.
- (80) Wang, Y.; Zeiri, O.; Raula, M.; Le Ouay, B.; Stellacci, F.; Weinstock, I. A. Host–Guest Chemistry with Water-Soluble Gold Nanoparticle Supraspheres. *Nat. Nanotechnol.* 2017, 12 (2), 170–176.
- (81) Pigliacelli, C.; Maiolo, D.; Nonappa; Haataja, J. S.; Amenitsch, H.; Michelet, C.; Sánchez Moreno, P.; Tirotta, I.; Metrangolo, P.; Baldelli Bombelli, F. Efficient Encapsulation of Fluorinated Drugs in the Confined Space of Water-Dispersible Fluorous Supraparticles. *Angew. Chem., Int. Ed.* 2017, 56 (51), 16186–16190.
- (82) Matricardi, C.; Hanske, C.; Garcia-Pomar, J. L.; Langer, J.; Mihi, A.; Liz-Marzán, L. M. Gold Nanoparticle Plasmonic Superlattices as Surface-Enhanced Raman Spectroscopy Substrates. *ACS Nano* 2018, 12 (8), 8531–8539.
- (83) Cai, J.; Zhang, W.; Xu, L.; Hao, C.; Ma, W.; Sun, M.; Wu, X.; Qin, X.; Colombari, F. M.; de Moura, A. F.; Xu, J.; Silva, M. C.; Carneiro-Neto, E. B.; Gomes, W. R.; Vallée, R. A. L.; Pereira, E. C.; Liu, X.; Xu, C.; Klajn, R.; Kotov, N. A.; Kuang, H. Polarization-Sensitive Optoionic Membranes from Chiral Plasmonic Nanoparticles. *Nat. Nanotechnol.* 2022, 17 (4), 408–416.
- (84) Rao, A.; Roy, S.; Jain, V.; Pillai, P. P. Nanoparticle Self-Assembly: From Design Principles to Complex Matter to Functional Materials. *ACS Appl. Mater. Interfaces* 2023, 15 (21), 25248–25274.
- (85) Joshi, C. P.; Bootharaju, M. S.; Alhilaly, M. J.; Bakr, O. M. [Ag₂₅(SR)₁₈][−]: The “Golden” Silver Nanoparticle. *J. Am. Chem. Soc.* 2015, 137 (36), 11578–11581.
- (86) Cortie, M. B.; McDonagh, A. M. Synthesis and Optical Properties of Hybrid and Alloy Plasmonic Nanoparticles. *Chem. Rev.* 2011, 111 (6), 3713–3735.
- (87) Tokonami, S.; Morita, N.; Takasaki, K.; Toshima, N. Novel Synthesis, Structure, and Oxidation Catalysis of Ag/Au Bimetallic Nanoparticles. *J. Phys. Chem. C* 2010, 114 (23), 10336–10341.
- (88) Mallin, M. P.; Murphy, C. J. Solution-Phase Synthesis of Sub-10 Nm Au–Ag Alloy Nanoparticles. *Nano Lett.* 2002, 2 (11), 1235–1237.
- (89) Bootharaju, M. S.; Joshi, C. P.; Parida, M. R.; Mohammed, O. F.; Bakr, O. M. Templated Atom-Precise Galvanic Synthesis and Structure Elucidation of a [Ag₂₄Au(SR)₁₈][−] Nanocluster. *Angew. Chem., Int. Ed.* 2016, 55 (3), 922–926.
- (90) Bodiuzzaman, M.; Khatun, E.; Sugi, K. S.; Paramasivam, G.; Dar, W. A.; Antharjanam, S.; Pradeep, T. Dithiol-Induced Contraction in Ag₁₄ Clusters and Its Manifestation in Electronic Structures. *J. Phys. Chem. C* 2020, 124 (42), 23426–23432.
- (91) Ghosh, A.; Ghosh, D.; Khatun, E.; Chakraborty, P.; Pradeep, T. Unusual Reactivity of Dithiol Protected Clusters in Comparison to Monothiol Protected Clusters: Studies Using Ag₅₁(BDT)₁₉(TPP)₃ and Ag₂₉(BDT)₁₂(TPP)₄. *Nanoscale* 2017, 9 (3), 1068–1077.
- (92) Brust, M.; Walker, M.; Bethell, D.; Schiffrin, D. J.; Whyman, R. Synthesis of Thiol-Derivatized Gold Nanoparticles in a Two-Phase Liquid–Liquid System. *J. Chem. Soc., Chem. Commun.* 1994, 0 (7), 801–802.
- (93) AbdulHalim, L. G.; Bootharaju, M. S.; Tang, Q.; Del Gobbo, S.; AbdulHalim, R. G.; Eddaoudi, M.; Jiang, D. E.; Bakr, O. M. Ag₂₉(BDT)₁₂(TPP)₄: A Tetravalent Nanocluster. *J. Am. Chem. Soc.* 2015, 137 (37), 11970–11975.
- (94) Krishnadas, K. R.; Baksi, A.; Ghosh, A.; Natarajan, G.; Pradeep, T. Manifestation of Geometric and Electronic Shell Structures of Metal Clusters in Intercluster Reactions. *ACS Nano* 2017, 11 (6), 6015–6023.
- (95) Yang, H.; Wang, Y.; Huang, H.; Gell, L.; Lehtovaara, L.; Malola, S.; Häkkinen, H.; Zheng, N. All-Thiol-Stabilized Ag₄₄ and Au₁₂Ag₃₂

Nanoparticles with Single-Crystal Structures. *Nat. Commun.* 2013, 4 (1), No. 2422.

(96) Emmons, E. D.; Guicheteau, J. A.; Fountain, A. W.; Tripathi, A. Effect of Substituents on Surface Equilibria of Thiophenols and Isoquinolines on Gold Substrates Studied Using Surface-Enhanced Raman Spectroscopy. *Phys. Chem. Chem. Phys.* 2020, 22 (28), 15953–15965.

(97) Varsányi, G.; Láng, L.; Kovner, M. A.; Lempert, K. *Assignment for Vibrational Spectra of Seven Hundred Benzene Derivatives*; Wiley: New York, 1974.

(98) Szafranski, C. A.; Tanner, W.; Laibinis, P. E.; Garrell, R. L. Surface-Enhanced Raman Spectroscopy of Halogenated Aromatic Thiols on Gold Electrodes. *Langmuir* 1998, 14 (13), 3580–3589.

(99) Bootharaju, M. S.; Sinatra, L.; Bakr, O. M. Distinct Metal-Exchange Pathways of Doped Ag₂₅ Nanoclusters. *Nanoscale* 2016, 8 (39), 17333–17339.

(100) Richardi, J.; Fadigas, M. ReaxFF Molecular Dynamics Simulations of Large Gold Nanocrystals. *J. Chem. Theory Comput.* 2022, 18 (4), 2521–2529.

Supporting Information

Interparticle Anti-Galvanic Reactions of Atomically Precise Silver Nanoclusters with Plasmonic Gold Nanoparticles: Interfacial Control of Atomic Exchange

Paulami Bose,^{a†} Jayoti Roy,^a Vikash Khokhar,^a Biswajit Mondal,^a Ganapati Natarajan,^b Sujan Manna,^a Vivek Yadav,^a Anupriya Nyayban,^a Sharma S. R. K. C. Yamijala,^{*c} Nonappa,^{*d} and Thalappil Pradeep ^{*a,b}

^aDST Unit of Nanoscience (DST UNS) and Thematic Unit of Excellence (TUE), Department of Chemistry, Indian Institute of Technology Madras, Chennai 600 036, India.

^bInternational Centre for Clean Water, 2nd Floor, B-Block, IIT Madras Research Park, Kanagam Road, Taramani, Chennai 600113, India.

^cDepartment of Chemistry, Indian Institute of Technology Madras, Chennai 600 036, India.

^{†d}Faculty of Engineering and Natural Sciences, Tampere University, FI-33720, Tampere, Finland.

[†]Present Address

*E-mail: pradeep@iitm.ac.in

Table of Contents

Name	Description	Page No.
SI 1	Experimental section	4-7
SI 2	Concentration calculations	7-11
Figure S1	Characterization of Au@DMBT NP	11
Figure S2	Characterization of [Ag ₂₅ (DMBT) ₁₈] ⁻ NC	12
Figure S3	Morphology of reacted Au@DMBT NPs	12
Figure S4	Particle size distribution of NPs before and after reaction	13
Figure S5	UV-Vis spectra of reaction@NP for Au@DMBT NP and [Ag ₂₅ (DMBT) ₁₈] ⁻ NC system	13
Figure S6	EDS spectrum of reacted NP	14
Figure S7	Full-range ESI mass spectra of the DMBT-capped-NP and NC reaction	14

Figure S8	Isotopic distribution pattern of assigned species for DMBT-DMBT reaction@NC	15
Figure S9	Photoluminescence spectra of reacted $[\text{Ag}_{25}(\text{DMBT})_{18}]^{-}$ NC	15
Figure S10	ESI MS of reaction@NP and @NC mixture	16
Figure S11	Morphological correlation between reactants and the product	16
Figure S12	Characterization of Au@BDT NP	17
Figure S13	Characterization of $[\text{Ag}_{29}(\text{BDT})_{12}(\text{TPP})_4]^{3-}$ NC	17
Figure S14	UV-Vis spectra of reaction@NP for Au@BDT NP and $[\text{Ag}_{29}(\text{BDT})_{12}(\text{TPP})_4]^{3-}$ NC system	18
Figure S15	TEM images of the reaction@NP mixture for BDT-capped NP-NC reaction with time	18
Figure S16	EDS spectra of BDT-capped NP-NC reaction	19
Figure S17	UV-Vis spectra of reaction@NC for Au@BDT NP and $[\text{Ag}_{29}(\text{BDT})_{12}(\text{TPP})_4]^{3-}$ NC system	19
Figure S18	Characterization of $[\text{PPh}_4]_n[\text{Ag}_{44}(\text{FTP})_{30}]$ NC	20
Figure S19	UV-Vis spectra of reaction@NP for Au@DMBT NP and $[\text{Ag}_{44}(\text{FTP})_{30}]^{4-}$ NC system	20
Figure S20	Morphology of Au@DMBT NP before and after reaction with $[\text{Ag}_{44}(\text{FTP})_{30}]^{4-}$ NC system	21
Figure S21	Isotopic distribution pattern of assigned species for DMBT-FTP NC-side reaction	21
Figure S22	UV-Vis spectra of reaction@NC for Au@DMBT NP and $[\text{Ag}_{44}(\text{FTP})_{30}]^{4-}$ NC system	22
Figure S23	Raman studies on reacted Au NP	22
Figure S24	UV-Vis spectra of reaction@NC for Au@BDT NP and $[\text{Ag}_{25}(\text{DMBT})_{18}]^{-}$ NC system	23
Figure S25	Morphology of Au@BDT NP before and after reaction with $[\text{Ag}_{25}(\text{DMBT})_{18}]^{-}$ NC system	23
Figure S26	UV-Vis spectra of reaction@NP for Au@BDT NP and $[\text{Ag}_{25}(\text{DMBT})_{18}]^{-}$ NC system	24
Figure S27	Morphology of Au@DMBT NP before and after reaction with $[\text{Ag}_{29}(\text{BDT})_{12}(\text{TPP})_4]^{3-}$ NC system	24

Figure S28	UV-Vis spectra of reaction@NP for Au@DMBT NP and [Ag ₂₉ (BDT) ₁₂ (TPP) ₄] ³⁻ NC system	25
Figure S29	ESI mass spectra for the reaction@NC for Au@DMBT NP and [Ag ₂₉ (BDT) ₁₂ (TPP) ₄] ³⁻ NC system	25
Figure S30	UV-Vis spectra for the reaction@NC for Au@DMBT NP and [Ag ₂₉ (BDT) ₁₂ (TPP) ₄] ³⁻ NC system	26
Figure S31	Interparticle reaction between Au@BDT NP and [PPh ₄] _n [Ag ₄₄ (FTP) ₃₀] NC	27
SI 3	Computational details	28
SI 4	Au(111)@SR surface construction	29
Figure S32	Surface construction of Au(111)@SR surfaces	29
Figure S33	Ligand orientations at full coverage on Au(111) surface	30
SI 5	Ag NC–Au(111)@SR docking interactions	30
Figure S34	Optimized Au(111)@SR surface with partial ligand coverage	31
SI 6	Ligand coverage calculation	31
Figure S35	Docked NCs on Au(111)@SR with higher coverage monolayers	32
Figure S36	Ag NC docking on optimized Au(111)@SR surfaces	33
Table S1	BE of docked Ag _n (SR) _m NCs on Au(111) surface with higher thiolate coverage	33
Table S2	BE of docked NCs on Au(111)@SR with different numbers of monolayer staples	34
Table S3	DFT calculated energies of parent NCs and Au and Ag atoms	34
Table S4	Isomers of single gold atom substituted [AuAg ₂₄ (DMBT) ₁₈] ⁻	34
Table S5	Isomers of double gold-atom substituted [Au ₂ Ag ₂₃ (DMBT) ₁₈] ⁻	35
Figure S37	Doping pathway of Au atom in [Ag ₂₉ (BDT) ₁₂ (TPP) ₄] ³⁻ NC	35
Table S6	Energies of isomers of single gold atom substituted [AuAg ₂₈ (BDT) ₁₂ (TPP) ₄] ³⁻	35
Figure S38	Optimized Ag-doped Au(111)@SR surfaces	36
SI 7	Energies of DFT-optimized Au(111)@SR surfaces	36
Table S7	Energies of undoped Au(111) monolayer surfaces	36
Table S8	Energies of Ag-alloy isomers of [Au(111)Ag@(DMBT–Au _{ad} –DMBT)] surface with a single Ag atom	36
Table S9	Ag-alloy isomers of the Au(111)Ag@BDT surface	37

Figure S39	Reaction energies for the metallic exchange in Ag NC–Au(111)@SR surface system	37
SI 8	References	38-39

SI 1. Experimental section

Instrumentation. UV-Vis Spectroscopy: The optical absorption spectra were recorded using a Perkin Elmer Lambda 25 instrument with a range of 200 – 1100 nm and a band-pass filter of 1 nm.

HRTEM: High-resolution transmission electron microscopic (HRTEM) imaging was carried out on a JEOL 3010, 300 kV instrument with a UHR polepiece. Energy dispersive analysis (EDS) was performed using an Oxford EDAX connected to the HRTEM. A Gatan 794 multiscan CCD camera was used to capture the images. Samples were prepared by dropcasting the dispersion on carbon-coated copper grids (spi Supplies, 3530C-MB) and dried at ambient conditions.

ESI MS: All the mass spectrometric measurements were carried out in a Waters Synapt G2-Si instrument. The instrument is well equipped with electrospray ionization, and all spectra were measured in the negative ion and resolution mode. The instrument has the capability of measuring ESI MS with high-resolution up to the orders of 50,000 (m/Dm). NaI was used for calibrating the instrument. The measurement conditions were optimized to a capillary voltage of 3 kV, a cone voltage of 20 V, a desolvation gas flow of 400 L/h, a source temperature of 100 °C, a desolvation temperature of 150°C, and a sample infusion rate of 30 mL/h.

HAADF-STEM and EDS mapping: The high-angle annular dark-field scanning transmission electron microscopic imaging was carried out in a JEOL JEM-2800 high-throughput electron microscope equipped with a Schottky-type field emission gun operating at 200 kV with simultaneous bright field (BF) and dark field (DF) STEM imaging modes.

The energy-dispersive X-ray (EDS) spectra and elemental mapping were collected using dual silicon drift detectors.

Raman spectroscopy: Raman measurements were carried out using a WITec GmbH alpha300S confocal Raman equipped with a 532 nm laser as the excitation source. Measurements involved a 20× objective (Plan-Apochromat, Zeiss), 600 grooves/mm grating for 1 s acquisition time. A laser power of ~800 μW was maintained on the sample throughout the measurement.

Materials and methods. Silver nitrate (AgNO_3 , ≥99%), 2-phenylethanethiol (PET, 98%), 2,4-dimethylbenzenethiol (DMBT, 95%), 1,3-benzenedithiol (BDT, 99%), 4-fluorothiophenol (FTP, 98%), triphenylphosphine (TPP, 99%), tetraoctylammonium bromide (TOABr, 98%) and sodium borohydride (NaBH_4 , ≥99%) were purchased from Sigma Aldrich. Tetrachloroauric acid ($\text{HAuCl}_4 \cdot 3\text{H}_2\text{O}$) was prepared from pure gold and aqua regia in the laboratory. All the solvents (dichloromethane, hexane, methanol, and toluene) used were of HPLC grade without further purification. Millipore-produced deionized water (~18.2 MΩ) was used throughout the experiments.

Synthesis of Au@DMBT nanoparticles. The synthesis of 2,4-dimethylbenzenethiol-capped Au nanoparticles, referred to as Au@DMBT NPs, was carried out using a modified Brust-Schiffrin synthesis method.¹ Initially, an aqueous solution of $\text{HAuCl}_4 \cdot 3\text{H}_2\text{O}$ (5.0 mg in 0.5 mL H_2O) was mixed with a solution of tetraoctylammonium bromide (TOABr, 13.4 mg) in 30 mL toluene. The aqueous-organic mixture was vigorously stirred for 15 min, and then 7 μL of 2,4-DMBT was added. Next, 2.0 mg of NaBH_4 in 10 mL of ice-cold water was added dropwise with vigorous stirring as the color of the reaction mixture turned purple. After stirring for nearly an hour, the organic layer was separated, and the size focussing was done with overnight heating at 60 °C. The color of the organic layer changed from purple to wine-red. Further purification was performed by removing the solvent under reduced pressure using a rotary evaporator and washing it with ethanol. Finally, the purified NP was extracted in toluene, dried in a rotary evaporator, and stored in a refrigerator.

The synthesized Au@DMBT NPs were characterized using optical absorption spectroscopy and HRTEM, as presented in Figure S1. From the particle size distribution, the NPs were found to have an average size of 4.46 ± 0.64 nm, referred to as ~ 4.5 nm Au@DMBT NPs. Please note that for particle size calculation, we are referring to the most probable diameter of the metallic core of the particle.

Synthesis of Au@BDT nanoparticles. 1,3-Benzenedithiol-protected Au NPs, referred to as Au@BDT NPs, were synthesized by modifying the typical Brust-Schiffrin synthesis protocol.¹ In a typical synthesis, an aqueous solution of H₂AuCl₄·3H₂O (15.0 mg in 0.5 mL H₂O) was mixed with a solution of TOABr (104.0 mg) in 30 mL toluene. The aqueous-organic mixture was vigorously stirred for 15 min, and then 2 μL of 1,3-BDT was added. Next, 13.6 mg of NaBH₄ in 10 mL of ice-cold water was added in a dropwise manner with vigorous stirring as the reaction mixture turned purple. After an hour, the organic layer was separated, and the size focussing was done with overnight heating at 60 °C. With heating, the organic layer turned to wine-red from purple. For purification, the solvent was rotary evaporated, followed by ethanol wash. Finally, the purified NPs were extracted in toluene, dried in a rotary evaporator, and stored in a refrigerator.

The synthesized Au@BDT NPs were characterized using optical absorption spectroscopy and HRTEM; the data are presented in Figure S11. From the particle size distribution, the NPs were found to have an average size of 3.70 ± 0.48 nm, referred to as ~ 3.7 nm Au@DMBT NPs. Please note, for particle size calculation, we are referring to the most probable diameter of the metallic core of the particle.

Synthesis of [Ag₂₅(DMBT)₁₈]⁻ nanocluster. The NC was synthesized by slightly modifying a previously reported protocol.² First, 38.0 mg of AgNO₃ was dissolved in 2 mL of methanol. To this mixture, 90 μL of 2,4-DMBT was added, which produced an insoluble yellow Ag-thiolate, followed by 17 mL of DCM, and then it was stirred for 15 mins at 0 °C. Afterwards, 0.5 mL of methanolic solution of 6 mg PPh₄Br was added, followed by dropwise addition of 15.0 mg of NaBH₄ in 0.5 mL of ice-cold water. The reaction mixture was further stirred for 7-8 h, followed by overnight aging in the refrigerator. For purification, the crude cluster solution was centrifuged to remove any insoluble impurities, and the collected supernatant was concentrated by rotary evaporation. The precipitate was washed multiple times with methanol. Then, the nanocluster was extracted in DCM and centrifuged again to remove any remaining insoluble impurities. DCM was removed using rotavapor, and the purified NC was obtained in its powdered form.

The purified NC was characterized using optical absorption microscopy, HRTEM, and ESI MS (Figure S2).

Synthesis of [Ag₂₉(BDT)₁₂(TPP)₄]³⁻ nanocluster. The NC was synthesized following a reported method with a slight modification.³ Briefly, 20.0 mg of AgNO₃ was dissolved in a

solvent mixture of 2 mL methanol and 10 mL DCM. To this mixture, 13.5 μL of 1,3-BDT was added and stirred for 15 min. Then, an aqueous solution of 10.5 mg NaBH_4 in 0.5 mL ice-cold water was added dropwise and stirred for another 5 h in dark. Next, the reaction mixture was centrifuged to eliminate insoluble impurities, and the crude cluster was obtained as an orange supernatant. The supernatant was concentrated by rotary evaporation, and the precipitate was washed with methanol. Finally, the purified NC was extracted in DMF.

Optical absorption microscopy, HRTEM, and ESI MS characterization of purified NC solution in DMF confirmed the formation of $[\text{Ag}_{29}(\text{BDT})_{12}(\text{TPP})_4]^{3-}$ (Figure S13).

Synthesis of $[\text{PPh}_4]_n[\text{Ag}_{44}(\text{FTP})_{30}]$ nanocluster. The NC was prepared following a solid-state synthetic route.⁴ In a typical synthesis, 20.0 mg of AgNO_3 and 12.0 mg of PPh_4Br were thoroughly grounded in an agate mortar and pestle for 5 min. Next, 76 μL of 4-FTP was added to the reaction mixture in one shot and further grounded for three more minutes. In the next step, 45.0 mg of NaBH_4 was added and ground until the mixture turned into a brown paste. The mixture was extracted using 7 mL of DCM and left undisturbed at room temperature till the optical absorption spectra showed all the characteristic features of the NC. For the purification, the NC was precipitated with hexane and collected by centrifugation. The precipitate was washed multiple times with hexane, dissolved in DCM, and centrifuged to remove any thiolate impurities. Finally, the purified NC solution was vacuum-dried and stored in the refrigerator. Optical absorption microscopy, HRTEM, and ESI MS characterization of purified NC solution in DCM confirmed the formation of $\text{Ag}_{44}(\text{FTP})_{30}$ (Figure S18). $[\text{Ag}_{44}(\text{FTP})_{30}]^{3-}$ and $[\text{Ag}_{44}(\text{FTP})_{30}]^{4-}$ were the prominent features in the MS of the pure $\text{Ag}_{44}(\text{FTP})_{30}$ NC (Figure S18A).

SI 2. Concentration calculation

(a) $[\text{Ag}_{25}(\text{DMBT})_{18}]^-$ NCs

Molecular weight = 5167

$$\text{Mass of a } [\text{Ag}_{25}(\text{DMBT})_{18}]^- \text{ NC, } m = \frac{5167 \times 10^3}{6.023 \times 10^{23}} = 8.58 \times 10^{-18} \text{ mg}$$

$$\text{Mass of } [\text{Ag}_{25}(\text{DMBT})_{18}]^- \text{ NCs in the stock solution, } W = 1 \frac{\text{mg}}{10 \text{ mL}} = 0.1 \times 10^3 \frac{\text{mg}}{\text{L}}$$

$$\text{Number of particles in the sample, } N = \frac{W}{m} = \frac{0.1 \times 10^3}{8.58 \times 10^{-18}} = 1.16 \times 10^{19} \frac{\text{particles}}{\text{L}}$$

$$\text{Molarity of Au@DMBT NPs in solution, } M_1 = \frac{N}{N_A} = \frac{1.16 \times 10^{19}}{6.023 \times 10^{23}} \text{ M} = 19.3 \mu\text{M}$$

For interparticle reaction (reaction@NP),

0.3 mL (V_1) of Ag_{25} NC from the above solution is diluted to make a 3.3 mL (V_2) solution.

Using the formula, $M_1V_1 = M_2V_2$

$$\text{Molarity of } [\text{Ag}_{25}(\text{DMBT})_{18}]^- \text{ NC, } M_2 = \frac{19.3 \mu\text{M} \times 0.3 \text{ mL}}{3.3 \text{ mL}} = 1.75 \mu\text{M}$$

For ESI MS measurements (reaction@NC),

1 mL (V_1) of $[\text{Ag}_{25}(\text{DMBT})_{18}]^-$ NC from the above solution is diluted to make a 6 mL (V_2) solution.

Using the formula, $M_1V_1 = M_2V_2$

$$\text{Molarity of } [\text{Ag}_{25}(\text{DMBT})_{18}]^- \text{ NC, } M_2 = \frac{19.3 \mu\text{M} \times 1 \text{ mL}}{6 \text{ mL}} = 3.22 \mu\text{M}$$

Size of the metal core of the $[\text{Ag}_{25}(\text{DMBT})_{18}]^-$ NC (from the single crystal XRD) = ~ 1 nm; please note that the metal core diameter as measured in HRTEM (1.9 nm) is slightly overestimated.

$$\text{Surface area of a } \text{Ag}_{25} \text{ NC} = 4\pi R^2 = 3.14 \text{ nm}^2$$

A $[\text{Ag}_{25}(\text{DMBT})_{18}]^-$ NC surface is covered by 18 DMBT ligands.

So, let's assume a DMBT ligand occupies a surface area of 0.17 nm^2 .

$$\text{Mass of 1 DMBT (C}_8\text{H}_9\text{S)} \text{ ligand, } m_{\text{DMBT}} = \frac{137.23 \times 10^3}{6.023 \times 10^{23}} \text{ mg} = 2.28 \times 10^{-19} \text{ mg}$$

(b) Au@DMBT NPs

Average size of Au NP (metal core from HRTEM), $2R = 4.5 \text{ nm}$

$$\text{Volume of a Au NP (sphere), } V = \frac{4}{3}\pi R^3 = 47.69 \text{ nm}^3$$

Let us consider that Au NPs have an fcc structure with a packing fraction of 74%.

$$\text{Net volume of a Au NP, } V_{\text{NP}} = 74\% \text{ of } V = 35.29 \text{ nm}^3$$

Radius of a Au atom, $R_{\text{Au}} = 0.146 \text{ nm}$

$$\text{Volume of a Au atom (sphere), } V_{\text{Au}} = \frac{4}{3}\pi R_{\text{Au}}^3 = 0.013 \text{ nm}^3$$

$$\text{Number of Au atoms per NP, } N_{\text{Au}} = \frac{V_{\text{NP}}}{V_{\text{Au}}} = \sim 2715$$

Mass of a Au atom, $m_{\text{Au}} = 196.96 \text{ u}$

$$\text{Mass of the metal core, } m_{\text{core}} = \frac{N_{\text{Au}} \times m_{\text{Au}}}{N_A} = \frac{2715 \times 196.96 \times 10^3}{6.023 \times 10^{23}} \text{ mg} = 8.88 \times 10^{-16} \text{ mg}$$

The exact ligand coverage over the plasmonic Au NPs is not known. From our calculations on 2,4-DMBT ligand coverage on a $[\text{Ag}_{25}(\text{DMBT})_{18}]^{-}$ NC, we are approximating that 1 DMBT ligand occupies a surface area of $\sim 0.17 \text{ nm}^2$ on a Au NP surface. However, the ligand packing is likely to differ from our approximation.

$$\text{Surface area of Au NP} = 4\pi R^2 = 63.58 \text{ nm}^2$$

$$\text{Number of DMBT ligands per NP, } N_{\text{DMBT}} = \sim 374$$

$$\text{Mass of total ligand coverage, } m_{\text{ligand}} = N_{\text{DMBT}} \times m_{\text{DMBT}} = 8.52 \times 10^{-17} \text{ mg}$$

$$\text{Total mass of a Au@DMBT NP, } m = m_{\text{core}} + m_{\text{ligand}} = 9.73 \times 10^{-16} \text{ mg}$$

For interparticle reaction (reaction@NP),

$$\text{Weight of Au NP (dry weight of the sample), } W = 5 \frac{\text{mg}}{3.3 \text{ mL}} = 1.51 \times 10^3 \frac{\text{mg}}{\text{L}}$$

$$\text{Number of particles in the sample, } N = \frac{W}{m} = \frac{1.51 \times 10^3}{9.73 \times 10^{-16}} = 1.55 \times 10^{18} \frac{\text{particles}}{\text{L}}$$

$$\text{Molarity of Au@DMBT NPs in solution, } M_1 = \frac{N}{N_A} = \frac{1.55 \times 10^{18}}{6.023 \times 10^{23}} \text{ M} = 2.5 \text{ } \mu\text{M}$$

For ESI MS measurements (reaction@NC),

0.3 mL (V_1) of Au NP from the above solution is further diluted to make a 6 mL (V_2) solution.

Using the formula, $M_1 V_1 = M_2 V_2$

$$\text{Particle molarity of Au@DMBT NPs, } M_2 = \frac{2.5 \text{ } \mu\text{M} \times 0.3 \text{ mL}}{6 \text{ mL}} = 0.12 \text{ } \mu\text{M}$$

(c) $[\text{Ag}_{29}(\text{BDT})_{12}(\text{TPP})_4]^{3-}$ NCs

Molecular weight = 5857

$$\text{Mass of a } [\text{Ag}_{29}(\text{BDT})_{12}(\text{TPP})_4]^{3-} \text{ NC, } m = \frac{5857 \times 10^{-3}}{6.023 \times 10^{23}} = 9.72 \times 10^{-18} \text{ mg}$$

$$\text{Mass of } [\text{Ag}_{29}(\text{BDT})_{12}(\text{TPP})_4]^{3-} \text{ NCs in the stock solution, } W = 1 \frac{\text{mg}}{10 \text{ mL}} = 0.1 \times 10^3 \frac{\text{mg}}{\text{L}}$$

$$\text{Number of particles in the sample, } N = \frac{W}{m} = \frac{0.1 \times 10^3}{9.72 \times 10^{-18}} = 1.03 \times 10^{19} \frac{\text{particles}}{\text{L}}$$

$$\text{Molarity of Au@BDT NPs in solution, } M_1 = \frac{N}{N_A} = \frac{1.03 \times 10^{19}}{6.023 \times 10^{23}} \text{ M} = 17.1 \text{ } \mu\text{M}$$

For interparticle reaction (reaction@NP),

0.3 mL (V_1) of $[\text{Ag}_{29}(\text{BDT})_{12}(\text{TPP})_4]^{3-}$ NC from the above solution is diluted to make a 3.3 mL (V_2) solution.

Using the formula, $M_1 V_1 = M_2 V_2$

$$\text{Molarity of } [\text{Ag}_{29}(\text{BDT})_{12}(\text{TPP})_4]^{3-} \text{ NC, } M_2 = \frac{17.1 \text{ } \mu\text{M} \times 0.3 \text{ mL}}{3.3 \text{ mL}} = 1.55 \text{ } \mu\text{M}$$

For ESI MS measurements (reaction@NC),

1 mL (V_1) of $[\text{Ag}_{29}(\text{BDT})_{12}(\text{TPP})_4]^{3-}$ NC from the above solution is diluted to make a 6 mL (V_2) solution.

Using the formula, $M_1V_1 = M_2V_2$

$$\text{Molarity of } [\text{Ag}_{29}(\text{BDT})_{12}(\text{TPP})_4]^{3-} \text{ NC, } M_2 = \frac{17.1 \mu\text{M} \times 1 \text{ mL}}{6 \text{ mL}} = 2.85 \mu\text{M}$$

Size of the metal core of the $[\text{Ag}_{29}(\text{BDT})_{12}(\text{TPP})_4]^{3-}$ NC (from the single crystal XRD) = ~ 1 nm; please note that the metal core diameter as measured in HRTEM (1.7 nm) is slightly overestimated.

$$\text{Surface area of a } [\text{Ag}_{29}(\text{BDT})_{12}(\text{TPP})_4]^{3-} \text{ NC} = 4\pi R^2 = 3.14 \text{ nm}^2$$

A $[\text{Ag}_{29}(\text{BDT})_{12}(\text{TPP})_4]^{3-}$ NC surface is covered by 12 BDT and 4 TPP ligands.

Let's assume that the bidentate and monodentate ligands, i.e, BDT and TPP, contribute 85.7% and 14.3% of the total ligand shell, respectively.

So, 1 BDT ligand occupies a surface area of 0.22 nm².

$$\text{Mass of 1 BDT (C}_6\text{H}_4\text{S}_2\text{)} \text{ ligand, } m_{\text{BDT}} = \frac{140.24 \times 10^3}{6.023 \times 10^{23}} \text{ mg} = 2.32 \times 10^{-19} \text{ mg}$$

(d) Au@BDT NP

Average size of Au NP (metal core from HRTEM), $2R = 3.7 \text{ nm}$

$$\text{Volume of a Au NP (sphere), } V = \frac{4}{3}\pi R^3 = 26.51 \text{ nm}^3$$

Let us consider that Au NPs have an fcc structure with a packing fraction of 74%.

$$\text{Net volume of a Au NP, } V_{\text{NP}} = 74\% \text{ of } V = 19.62 \text{ nm}^3$$

Radius of a Au atom, $R_{\text{Au}} = 0.146 \text{ nm}$

$$\text{Volume of a Au atom (sphere), } V_{\text{Au}} = \frac{4}{3}\pi R_{\text{Au}}^3 = 0.013 \text{ nm}^3$$

$$\text{Number of Au atoms per NP, } N_{\text{Au}} = \frac{V_{\text{NP}}}{V_{\text{Au}}} = \sim 1509$$

Mass of a Au atom, $m_{\text{Au}} = 196.96 \text{ u}$

$$\text{Mass of the metal core, } m_{\text{core}} = \frac{N_{\text{Au}} \times m_{\text{Au}}}{N_A} = \frac{1509 \times 196.96 \times 10^3}{6.023 \times 10^{23}} \text{ mg} = 4.93 \times 10^{-16} \text{ mg}$$

The exact ligand coverage over the plasmonic Au NPs is not known. From our calculations on 1,3-BDT ligand coverage on a $[\text{Ag}_{29}(\text{BDT})_{12}(\text{TPP})_4]^{3-}$ NC, we are approximating that 1 BDT ligand occupies a surface area of ~ 0.22 nm² on a Au NP surface. However, the ligand packing is likely to differ from our approximation.

$$\text{Surface area of Au NP} = 4\pi R^2 = 42.99 \text{ nm}^2$$

Number of BDT ligands per NP, $N_{\text{DMBT}} = \sim 195$

Mass of total ligand coverage, $m_{\text{ligand}} = N_{\text{DMBT}} \times m_{\text{DMBT}} = 4.52 \times 10^{-17} \text{ mg}$

Total mass of a Au@BDT NP, $m = m_{\text{core}} + m_{\text{ligand}} = 5.38 \times 10^{-16} \text{ mg}$

For interparticle reaction (reaction@NP),

Weight of Au NP (dry weight of the sample), $W = 5 \frac{\text{mg}}{3.3 \text{ mL}} = 1.51 \times 10^3 \frac{\text{mg}}{\text{L}}$

Number of particles in the sample, $N = \frac{W}{m} = \frac{1.51 \times 10^3}{5.38 \times 10^{-16}} = 2.81 \times 10^{18} \frac{\text{particles}}{\text{L}}$

Molarity of Au@BDT NPs in solution, $M_1 = \frac{N}{N_A} = \frac{2.81 \times 10^{18}}{6.023 \times 10^{23}} \text{ M} = 4.6 \mu\text{M}$

For ESI MS measurements (reaction@NC),

0.3 mL (V_1) of Au NP from the above solution is further diluted to make a 6 mL (V_2) solution.

Using the formula, $M_1 V_1 = M_2 V_2$

Molarity of Au@BDT NPs, $M_2 = \frac{4.6 \mu\text{M} \times 0.3 \text{ mL}}{6 \text{ mL}} = 0.23 \mu\text{M}$

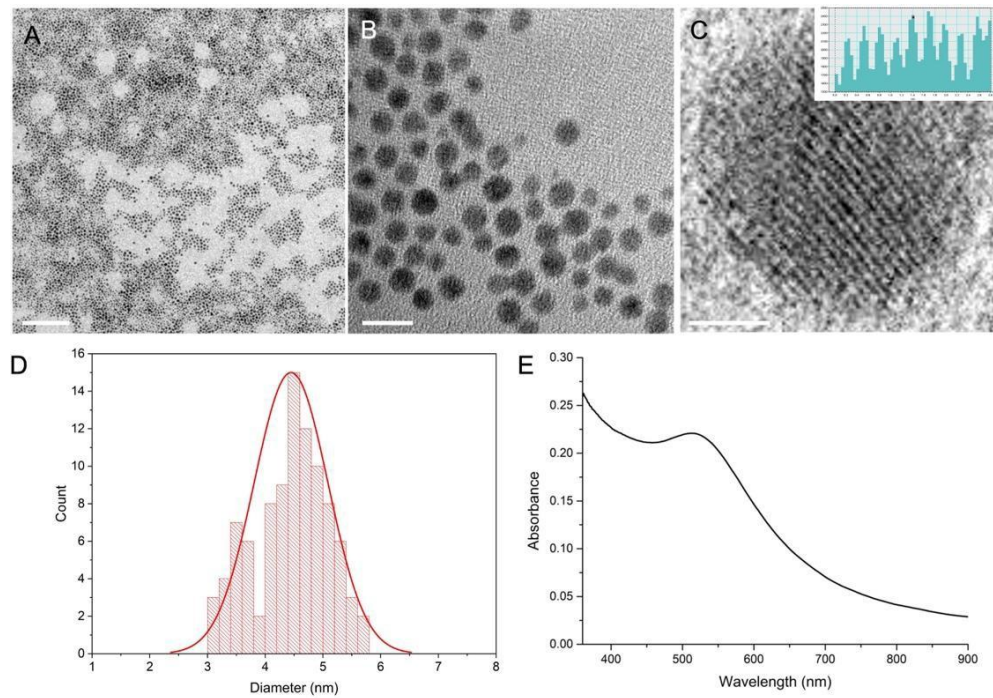


Figure S1. Characterization of Au@DMBT NPs. HRTEM images of Au@DMBT NPs captured at different magnifications (A) 0.1 μm , (B) 10, and (C) 2 nm. Profile of inverse fast Fourier transform (IFFT) in the inset of (C). Corresponding particle size distribution (D), and the optical absorption spectrum (E).

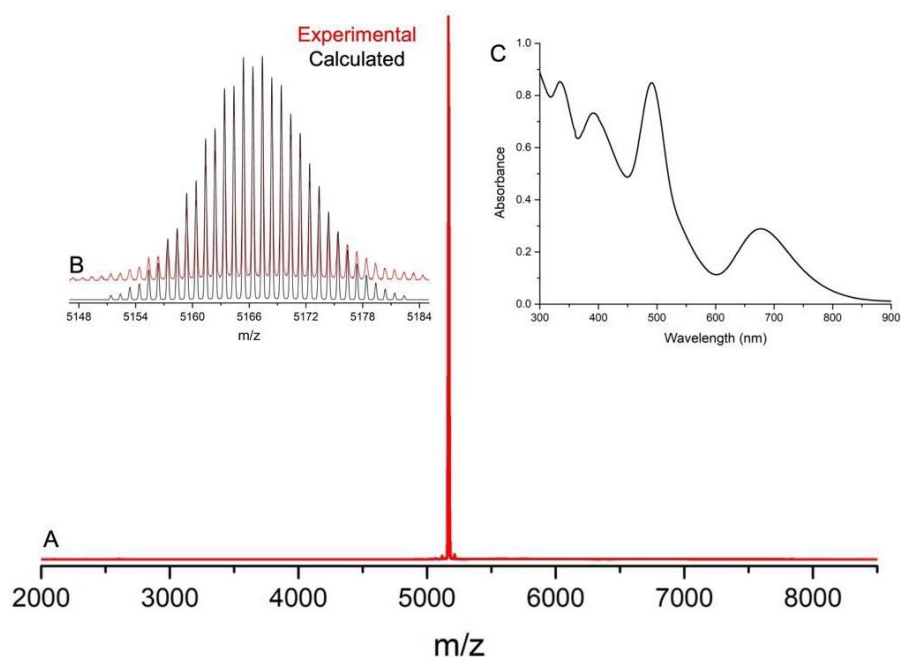


Figure S2. Characterization of $[\text{Ag}_{25}(\text{DMBT})_{18}]^{-}$ NC. (A) ESI MS of the pure NC, (B) comparison of experimental and calculated isotopic distribution pattern, and (C) the optical absorption spectrum. Experimental and calculated spectra are in the red and black trace, respectively.

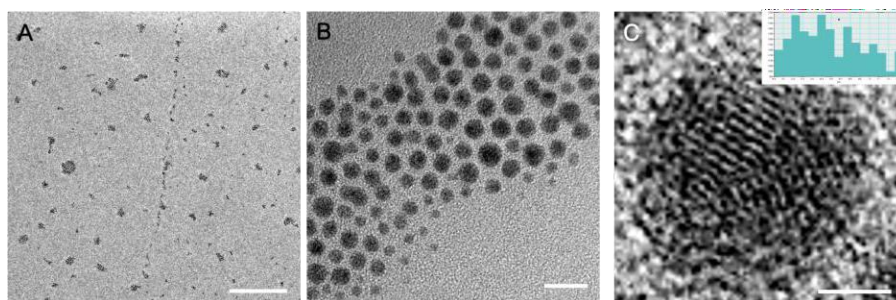


Figure S3. HRTEM images of Au@DMBT NPs after reaction with $[\text{Ag}_{25}(\text{DMBT})_{18}]^{-}$ NC captured at different magnifications (A) 0.2 μm , (B) 10, and (C) 2 nm. Profile of inverse fast Fourier transform (IFFT) in the inset of (C).

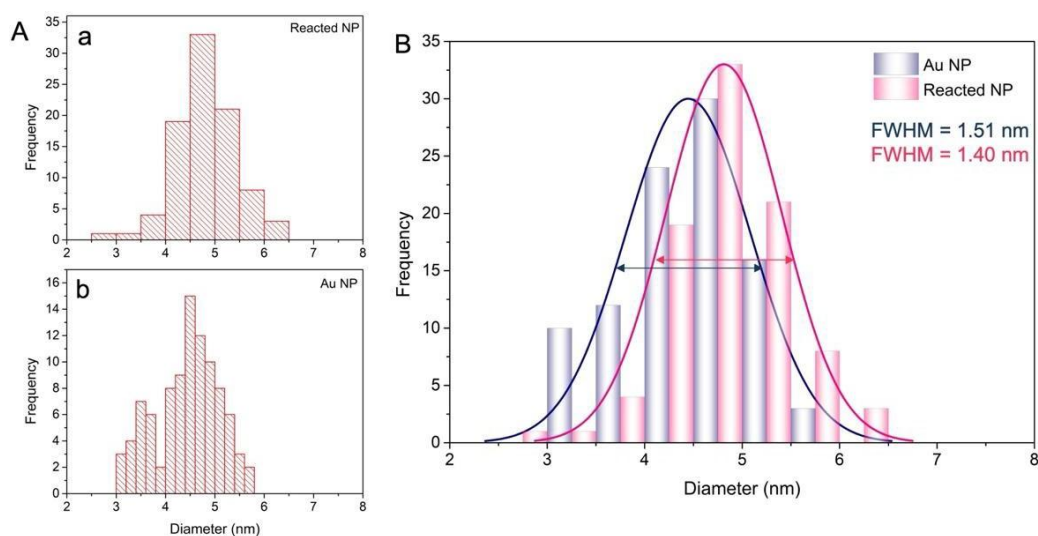


Figure S4. Particle size distribution of Au@DMBT NPs plotted as (A) histogram before (a) and after (b) the reaction. (B) Gaussian fitting of the histograms for fwhm calculation.

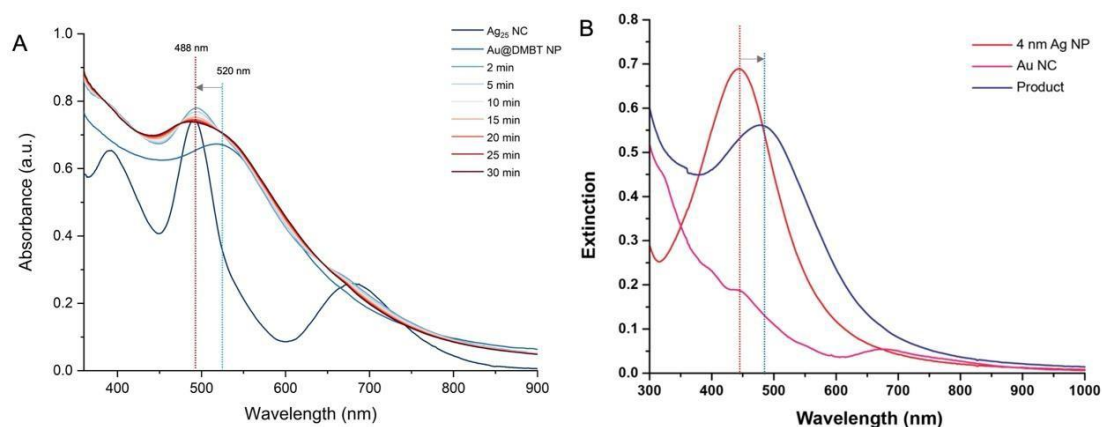


Figure S5. Time-dependent optical absorption spectra of the reaction@NP for Au@DMBT NP and $[\text{Ag}_{25}(\text{DMBT})_{18}]^-$ NC system (A). and (B) Optical absorption spectra of the Ag@PET NPs, $[\text{Au}_{25}(\text{PET})_{18}]^-$ NC, and the doped AgAu@PET NP. The doped NP shows a clear red-shifted SPR, a characteristic feature of bimetallic Au-Ag NPs.⁵ Copyright 2020 Royal Society Publishing Group.

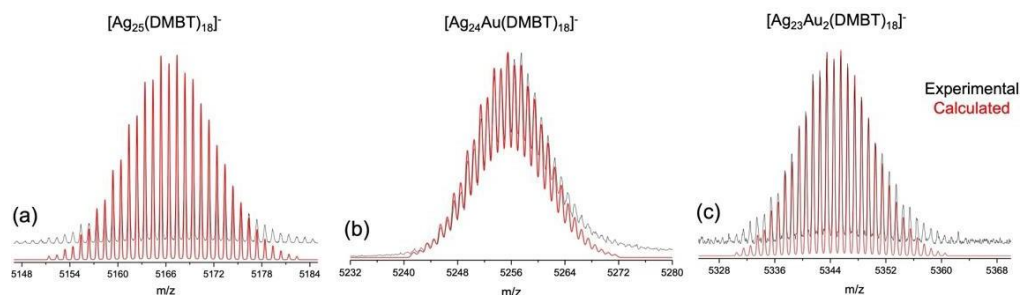


Figure S8. Isotopic distribution pattern for the species detected in the ESI MS experiment for the DMBT-capped NP and NC reaction. Experimental and calculated spectra are in the black and red trace, respectively.

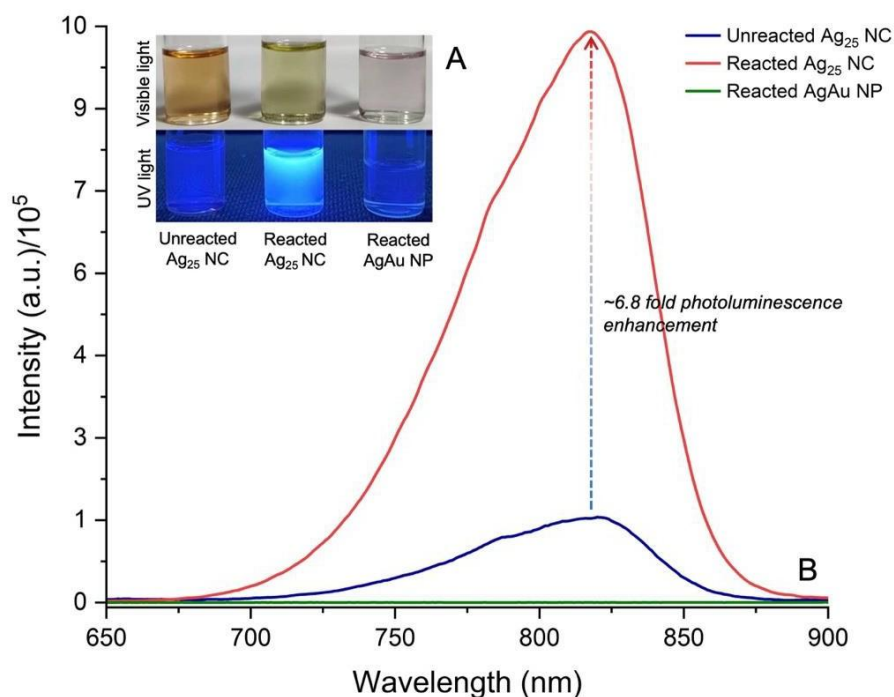


Figure S9. Solutions of $[Ag_{25}(DMBT)_{18}]^-$ NC, photographed under visible and UV light (A) and their corresponding photoluminescence spectra (B), before and after their reaction with Au@DMBT NP, alongside reacted plasmonic AgAu@DMBT NP.

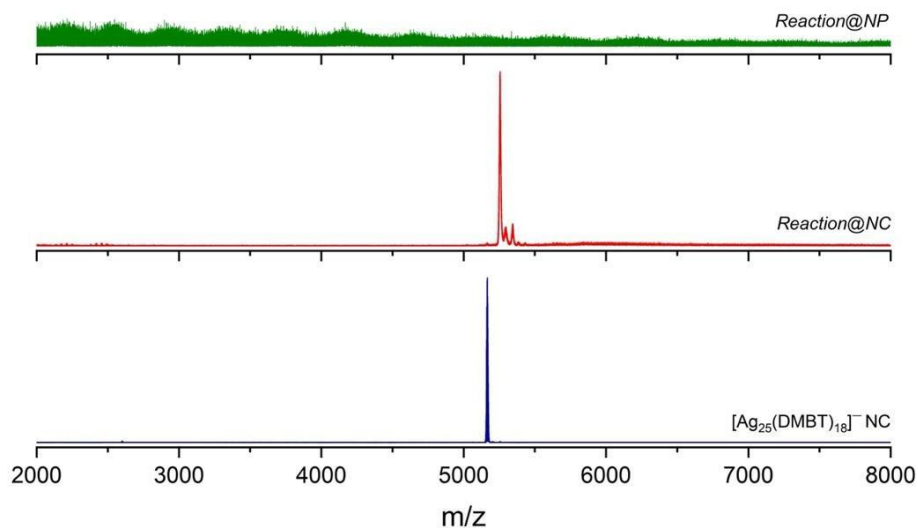


Figure S10. A comparative ESI MS of pure $[\text{Ag}_{25}(\text{DMBT})_{18}]^{-}$ NC and reaction mixture measured after 30 min of reaction@NC and reaction@NP.

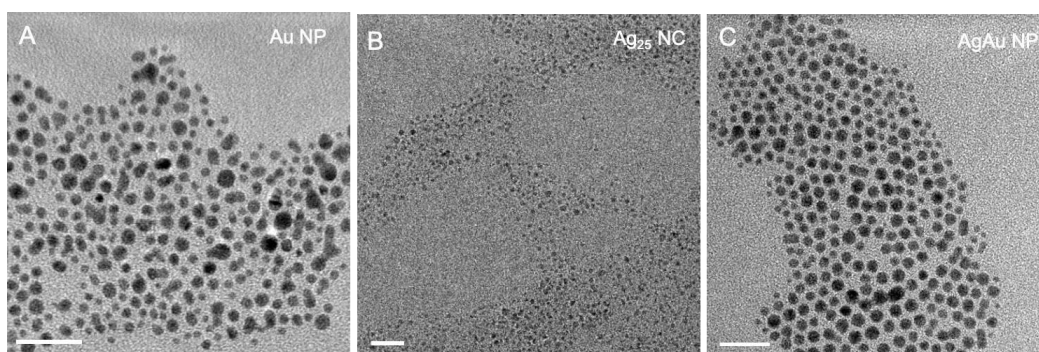


Figure S11. Morphological correlation between reactants and the product. TEM images of reactants, Au@DMBT NP (A) and $[\text{Ag}_{25}(\text{DMBT})_{18}]^{-}$ NC (B), and the product, AgAu@DMBT NP (C). Scale bar: 20 nm.

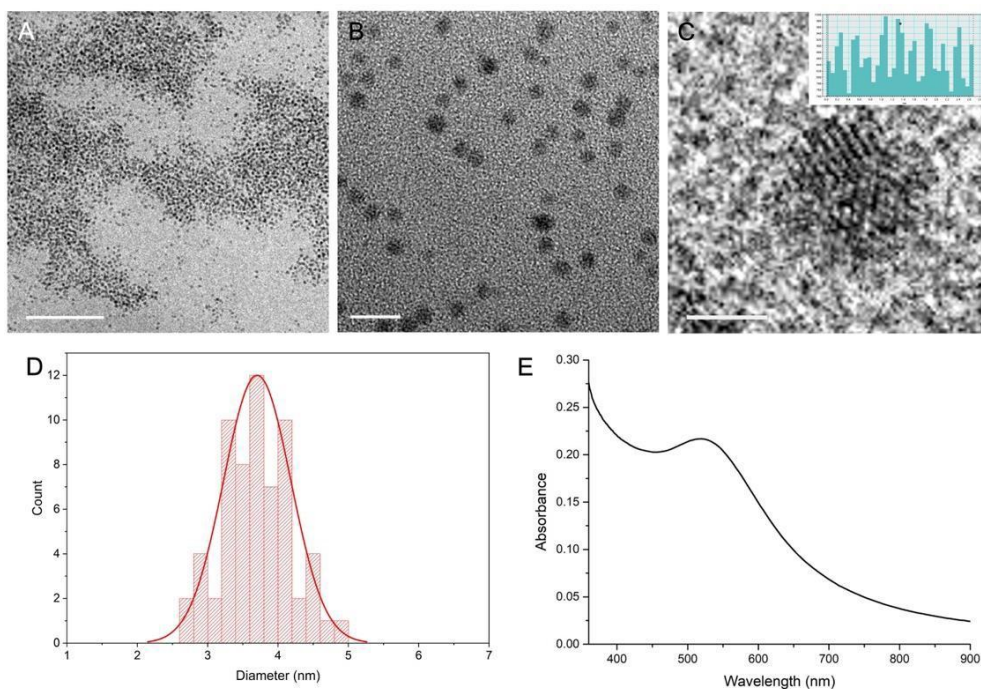


Figure S12. Characterization of Au@BDT NPs. HRTEM images of Au@BDT NPs captured at different magnifications (A) 0.1 μm , (B) 10, and (C) 2 nm. Profile of inverse fast Fourier transform (IFFT) in the inset of (C). Corresponding particle size distribution (D), and the optical absorption spectrum (E).

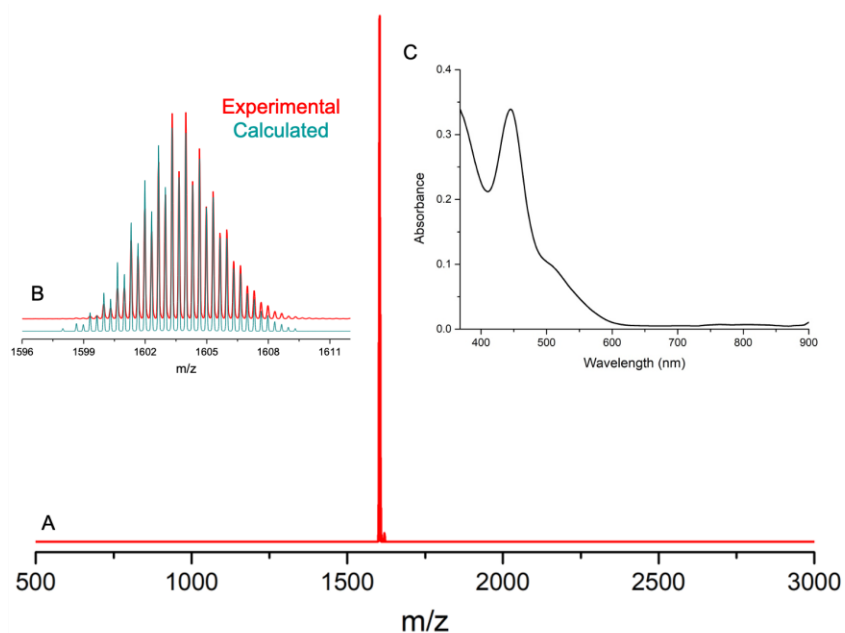


Figure S13. Characterization of $[\text{Ag}_{29}(\text{BDT})_{12}(\text{TPP})_4]^{3-}$ NC. (A) ESI MS of the pure NC after losing 4 TPP ligands, (B) comparison of experimental and calculated isotopic distribution pattern, and (C) the optical absorption spectrum.

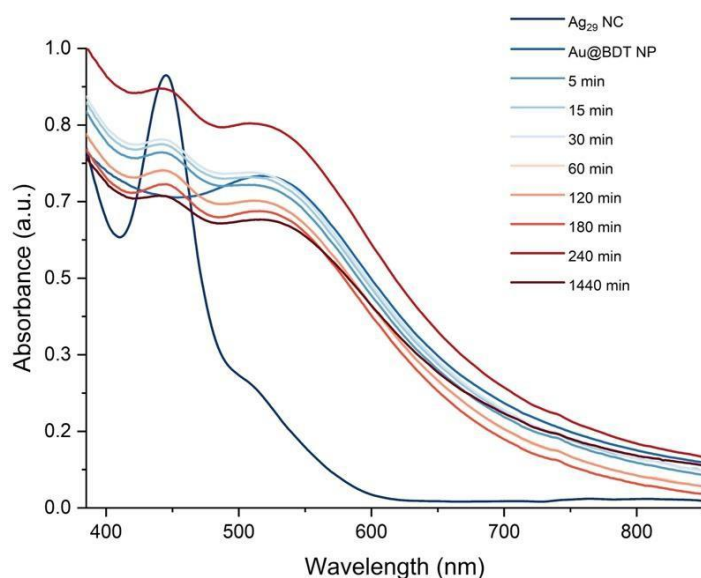


Figure S14. Time-dependent optical absorption spectra of the reaction@NP for Au@BDT NP and $[\text{Ag}_{29}(\text{BDT})_{12}(\text{TPP})_4]^{3-}$ NC reaction. The temporal rise in absorbance is presumably due to aggregation facilitated by non-reactive interparticle interaction, as seen in TEM (Figure S15).

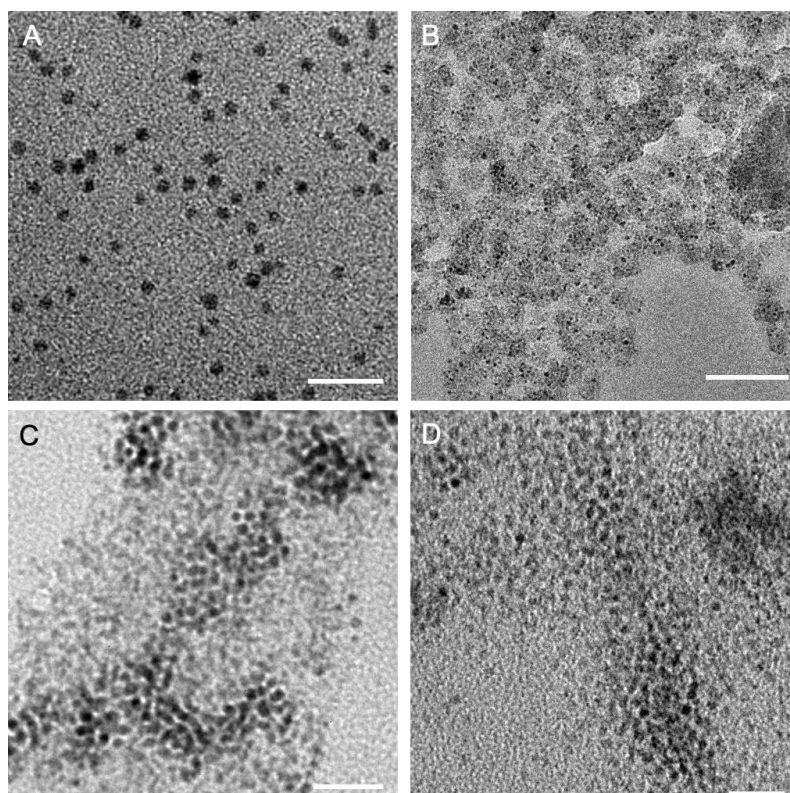


Figure S15. TEM image of the starting materials, (A) Au@BDT NP and (B) $[\text{Ag}_{29}(\text{BDT})_{12}(\text{TPP})_4]^{3-}$ NC, and the reaction mixture imaged after (C) 30 min and (D) 24 h of mixing. For better contrast and to avoid beam-induced damage, the NC was imaged at a lower magnification. Scale bar: (A, C, D) 20, and (B) 100 nm.

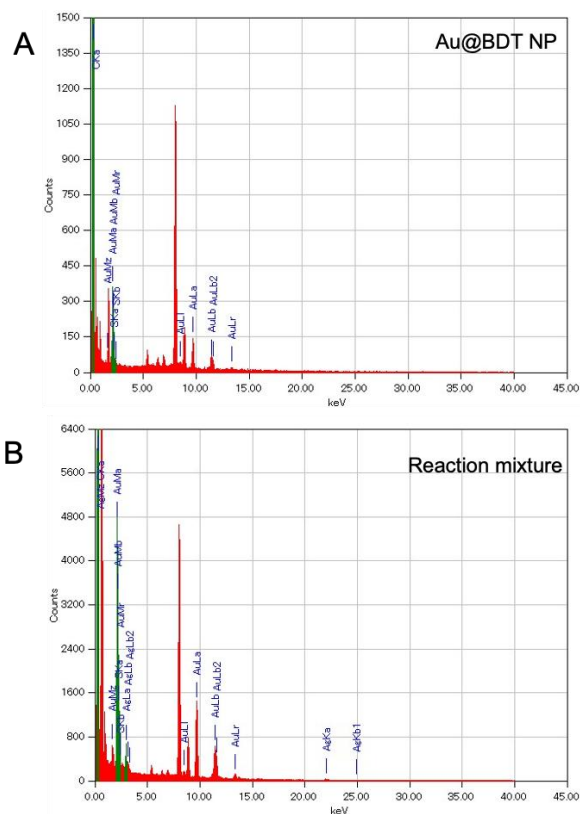


Figure S16. EDS spectra showing the elemental composition of Au@BDT NP (A) before, (B) after mixing with $[\text{Ag}_{29}(\text{BDT})_{12}(\text{TPP})_4]^{3-}$ NC.

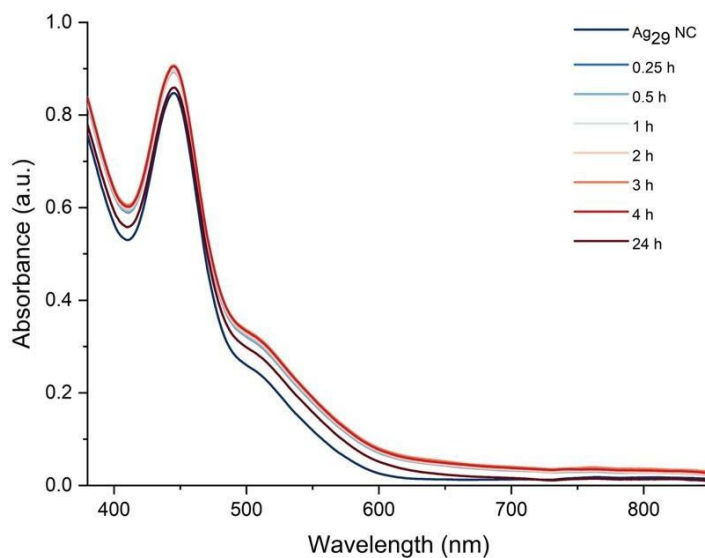


Figure S17. Time-dependent optical absorption spectra of the reaction@NC for Au@BDT NP and $[\text{Ag}_{29}(\text{BDT})_{12}(\text{TPP})_4]^{3-}$ NC system.

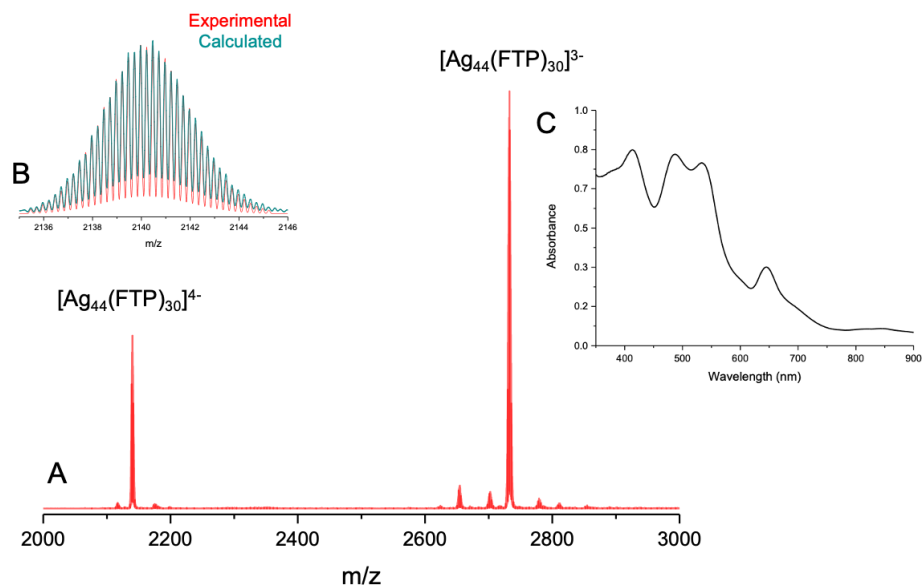


Figure S18. Characterization of pure $[PPh_4]_n[Ag_{44}(FTP)_{30}]$ NC. (A) ESI MS of the pure NC, (B) comparison of experimental and calculated isotopic distribution pattern, and (C) the optical absorption spectrum.

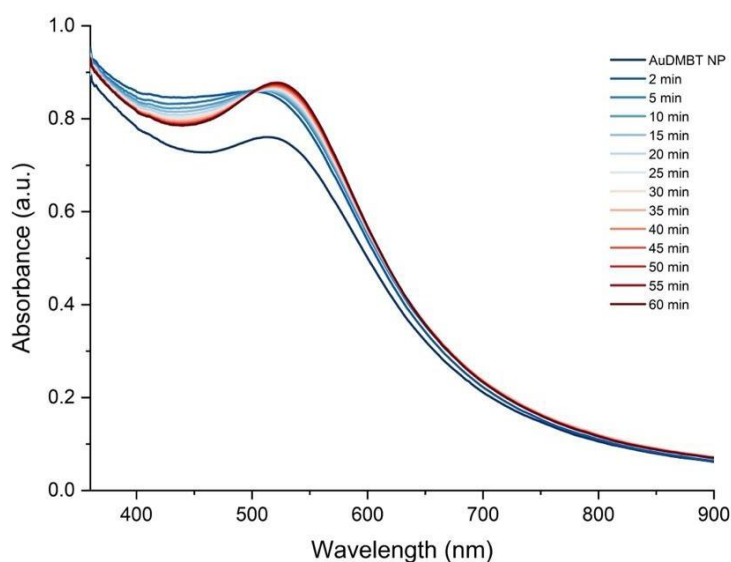


Figure S19. Time-dependent optical absorption spectra of the reaction@NP for Au@DMBT NP and $[Ag_{44}(FTP)_{30}]^{4-}$ NC system.

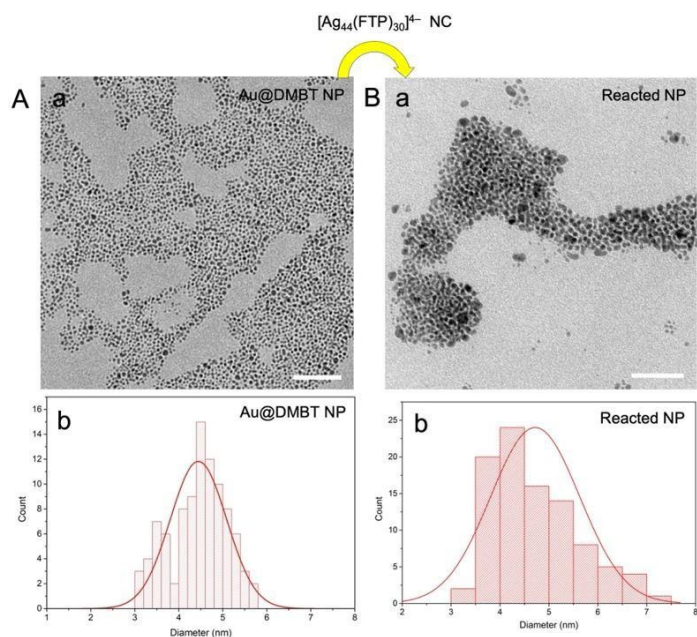


Figure S20. Characterization of reaction@NP for Au@DMBT NP and $[Ag_{44}(FTP)_{30}]^{4-}$ NC system. TEM images (panel-a) and the corresponding particle size distribution (panel-b) of the Au@BDT NPs (A) before and (B) after the reaction. Scale bar: 50 nm.

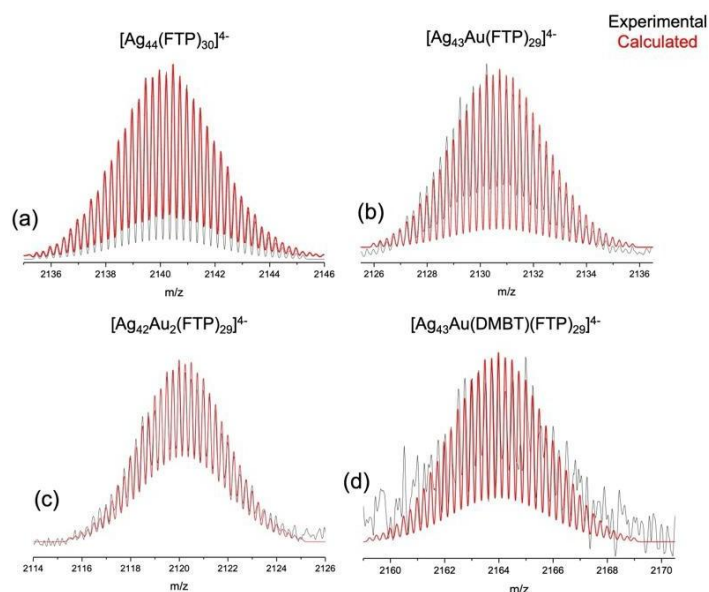


Figure S21. Isotopic distribution pattern for the species detected in the ESI MS experiment for the reaction between Au@DMBT NP and $[Ag_{44}(FTP)_{30}]^{4-}$ NC.

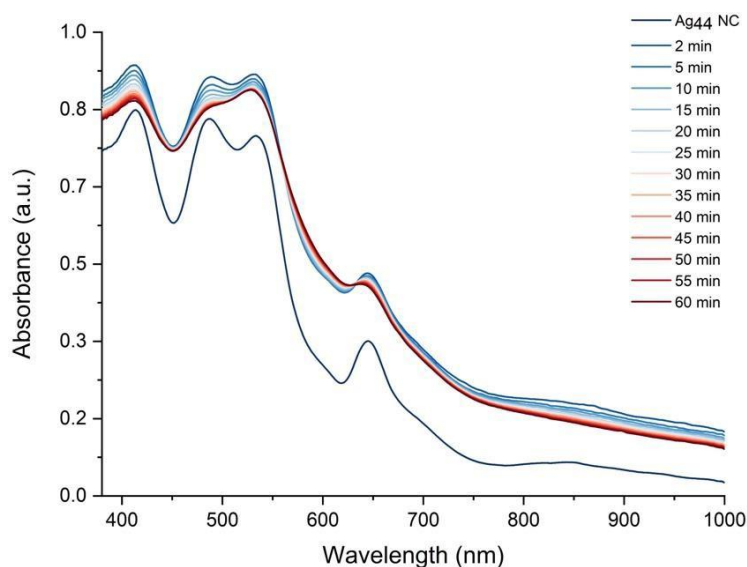


Figure S22. Time-dependent optical absorption spectra of the reaction@NC for Au@DMBT NP and $[\text{Ag}_{44}(\text{FTP})_{30}]^{4-}$ NC system.

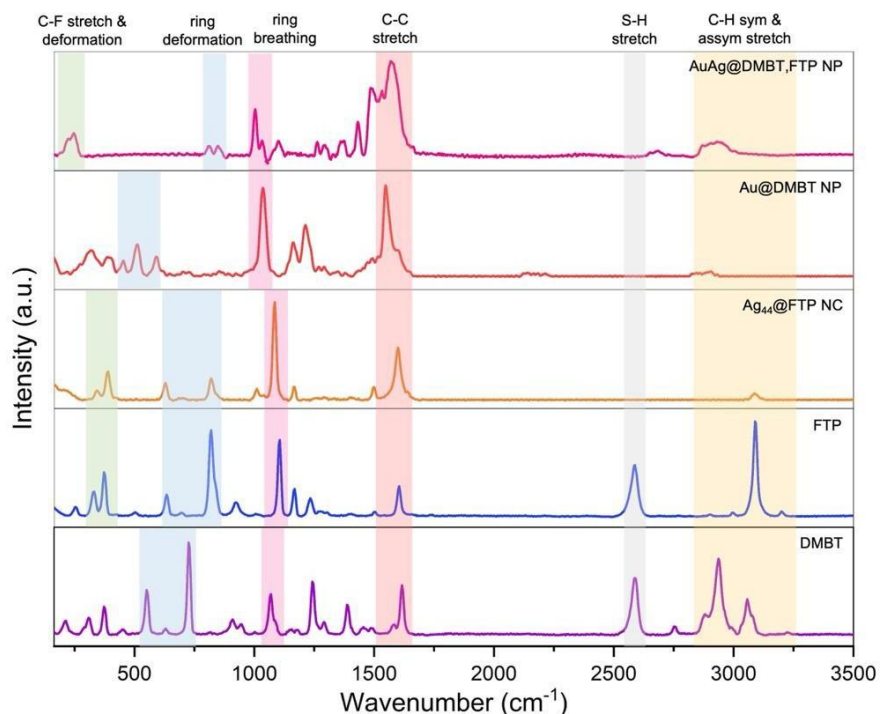


Figure S23. Raman spectra of reacted Au NPs were compared to reactants (Au@DMBT NPs and $[\text{Ag}_{44}(\text{FTP})_{30}]^{4-}$ NC) and referenced with exchanging ligands (4-FTP and 2,4-DMBT).

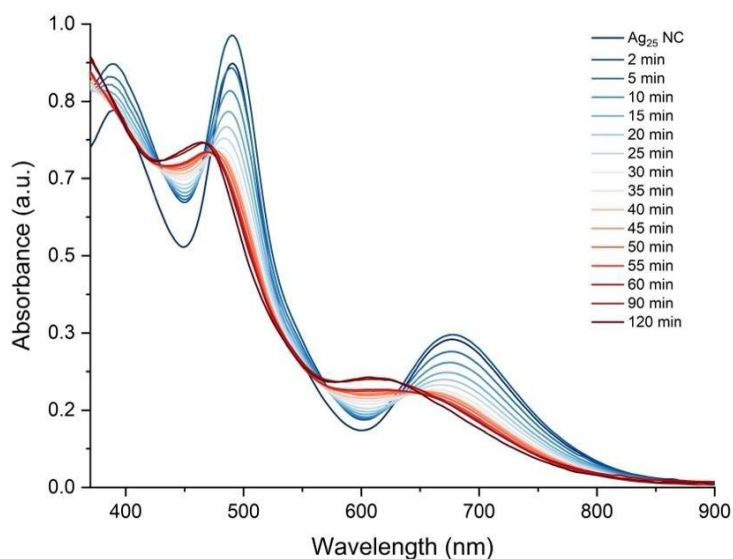


Figure S24. Time-dependent optical absorption spectra of the reaction@NC for Au@BDT NP and $[\text{Ag}_{25}(\text{DMBT})_{18}]^{-}$ NC system.

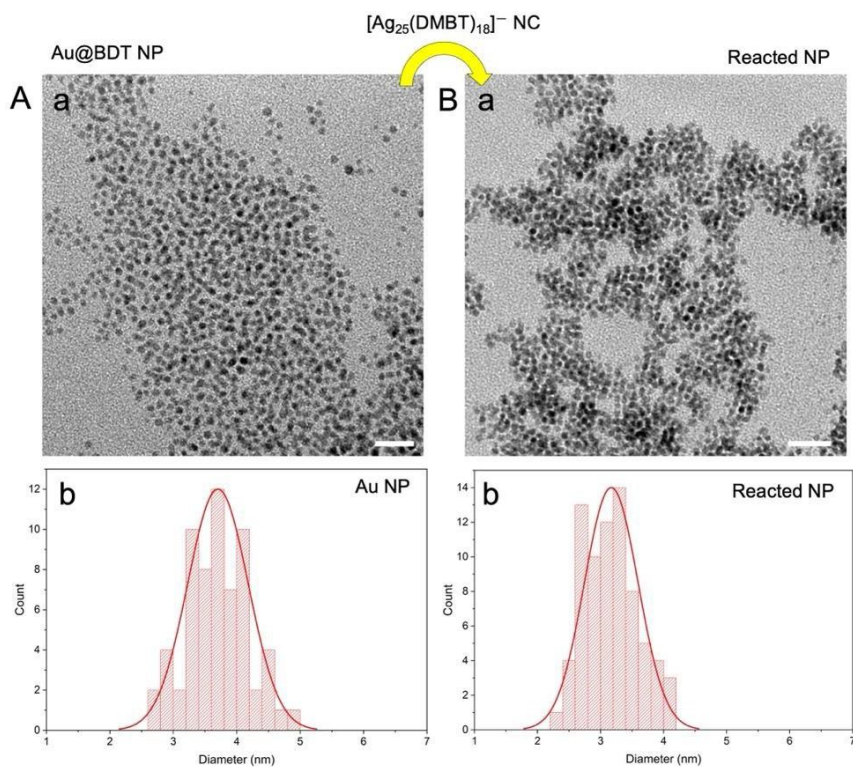


Figure S25. Characterization of reaction@NP for Au@BDT NP and $[\text{Ag}_{25}(\text{DMBT})_{18}]^{-}$ NC system. TEM images (panel-a) and the corresponding particle size distribution (panel-b) of the Au@BDT NPs (A) before and (B) after the reaction. Scale bar: 20 nm.

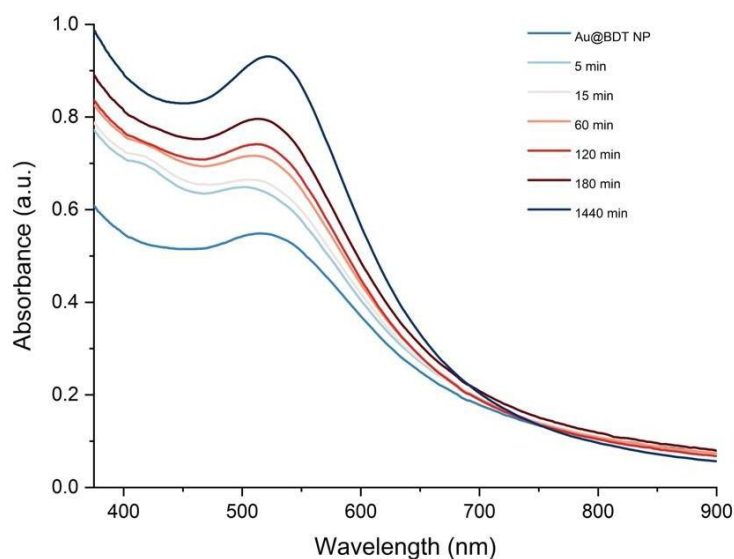


Figure S26. Time-dependent optical absorption spectra of the reaction@NP for Au@BDT NP and $[\text{Ag}_{25}(\text{DMBT})_{18}]^{-}$ NC system.

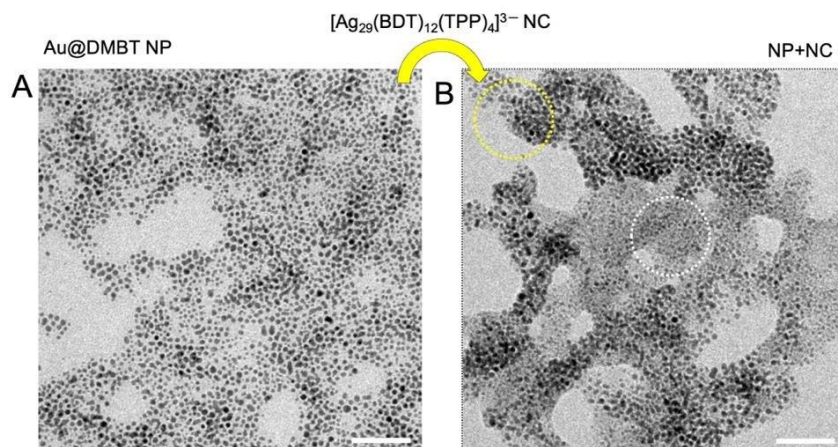


Figure S27. Characterization of reaction@NP for Au@DMBT NP and $[\text{Ag}_{29}(\text{BDT})_{12}(\text{TPP})_4]^{3-}$ NC system. TEM images of the Au@BDT NPs (A) before and (B) after mixing with the NC. The yellow and white encircles correspond to NP- and NC-rich regions, respectively. Scale bar: 50 nm.

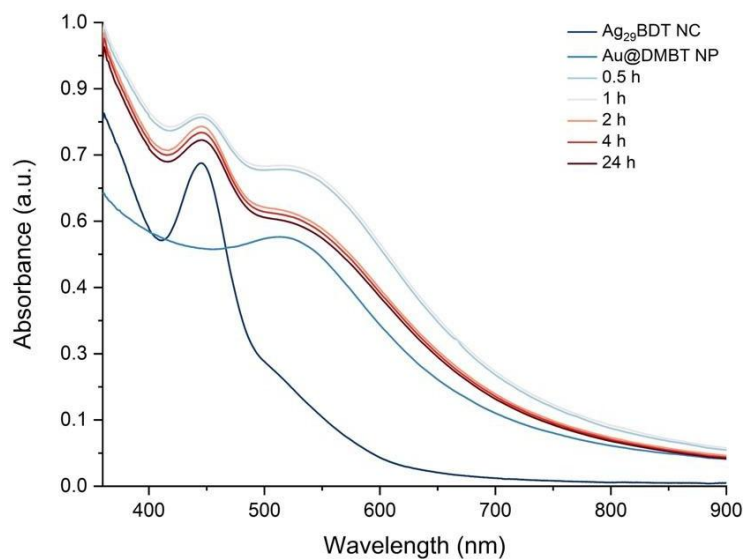


Figure S28. Time-dependent optical absorption spectra of the reaction@NP for Au@DMBT NP and $[\text{Ag}_{29}(\text{BDT})_{12}(\text{TPP})_4]^{3-}$ NC system.

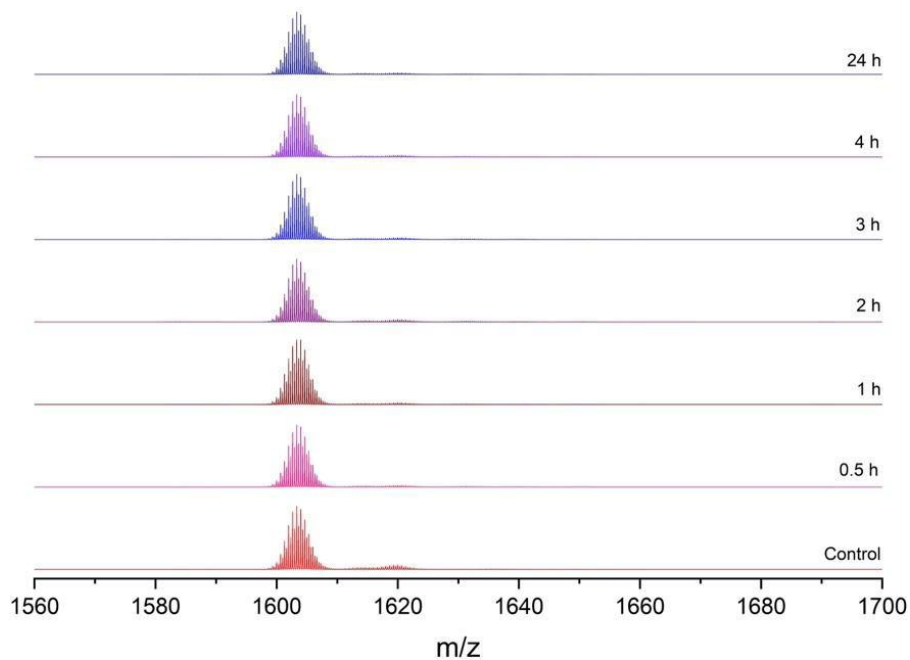


Figure S29. ESI mass spectra for the reaction@NC for Au@DMBT NP and $[\text{Ag}_{29}(\text{BDT})_{12}(\text{TPP})_4]^{3-}$ NC system.

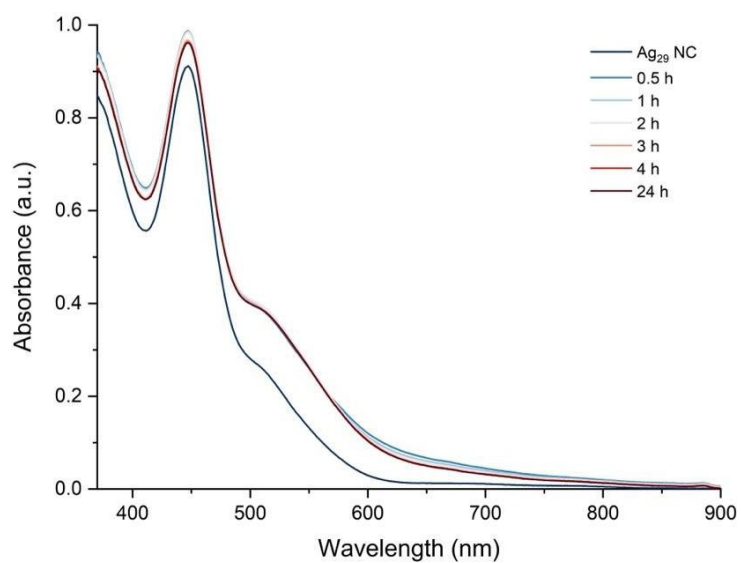


Figure S30. Time-dependent optical absorption spectra of the reaction@NC for Au@DMBT NP and $[\text{Ag}_{29}(\text{BDT})_{12}(\text{TPP})_4]^{3-}$ NC system.

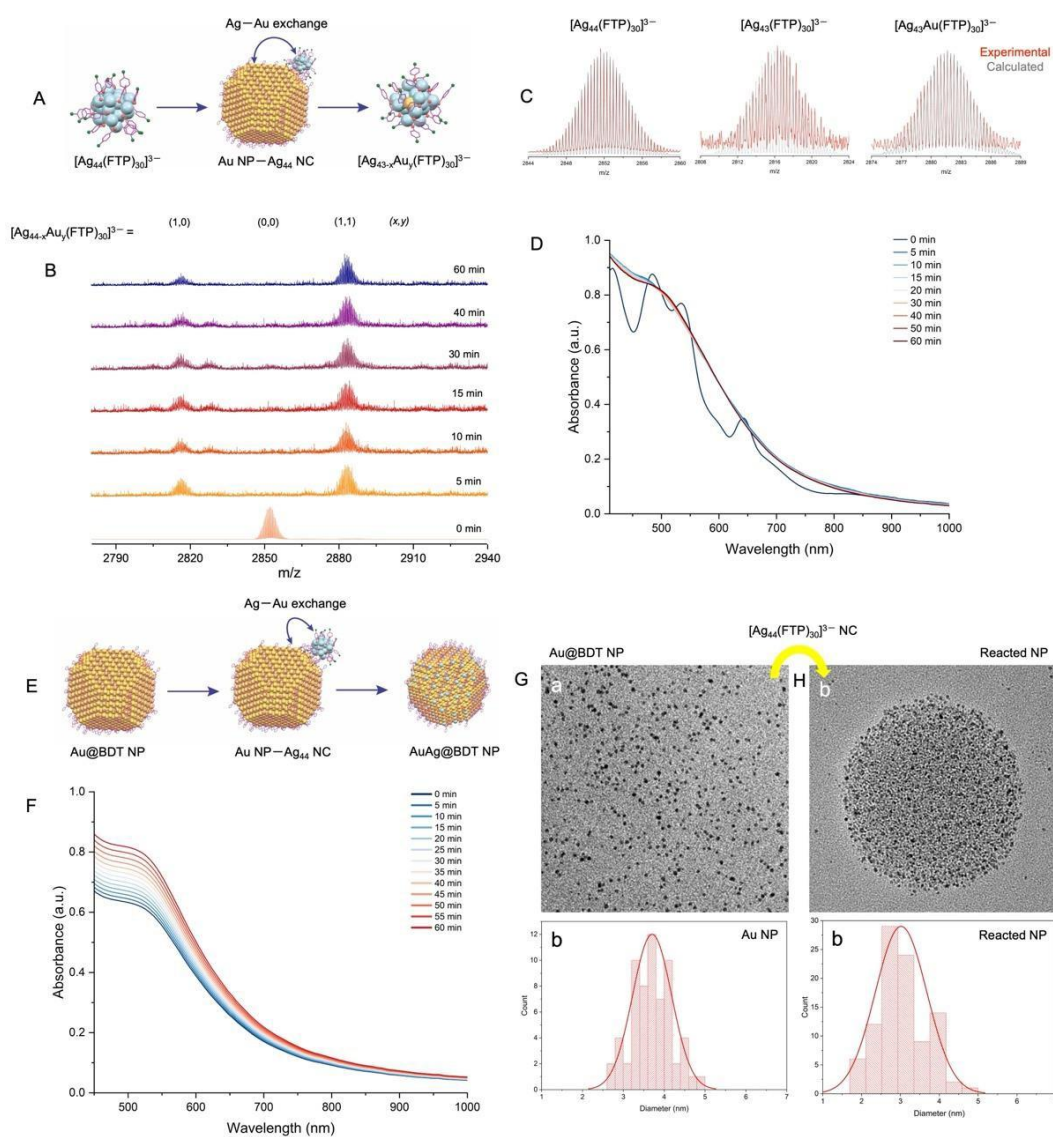


Figure S31. Interparticle reaction between Au@BDT NP and $[Ag_{44}(FTP)_{30}]^{3-}$ NC. For the reaction@NC, (A) the schematic representation of the proposed metal-only exchange pathway as the Ag NC interacts with Au NP, (B) time-dependent ESI MS spectra of the NP-NC reaction, (C) isotopic distribution pattern of the species detected in MS, and (D) the corresponding time-dependent optical absorption spectra of the reaction. For the reaction@NP, (E) the schematic illustration of Au NP – Ag NC reaction mediated Ag-doping of Au@BDT NPs, (F) corresponding time-dependent optical absorption spectra of the reaction, and the TEM images (panel-a) followed by the corresponding particle size distribution (panel-b) of the Au@BDT NPs (G) before and (H) after the reaction. Scale bar: 50 nm. Color code in A and E: Yellow, Au; blue, Ag; pink, S; magenta, C; green, F; H was omitted for clarity.

SI 3. Computational details

We first generated a (3×4×5) surface unit cell for Au(111) from the bulk Au fcc unit cell with lattice parameter 4.078 Å. We used this small (3×4×5) surface unit cell Au(111) slab for the ligand coverage study with DFT using the CP2K program. Two larger-sized slabs were constructed using this slab by repeating it periodically by specified units in the *x*- and *y*-directions: a medium-sized 2×1 Au(111) slab for DFT reaction energetics and a larger 4×3 slab for DFTB and docking studies. We then placed the DMBT and BDT ligands on the surface of the slabs with varying coverages and orientations. Also, the ligand placement in the models was based on different sites. All these slab constructions were done using ASE (Atomic Simulation Environment) scripts, and ligands were placed using the ASE-GUI program.

We optimized both the Ag NC and 5-layered Au(111)@SR (where SR = 2,4-DMBT and 1,3-BDT) structures individually using the CP2K⁶ and the monolayer surfaces only using DFTB+ software packages,⁷ respectively. With the optimized Ag NC and Au(111)@SR structures from DFTB+, we carried out the molecular docking of the Ag NC on the Au(111)@SR surface slab models in a grid box of size 126×126×126 points with point spacing 0.375 Å using AutoDock4 software.⁸ The docking input files were prepared using AutoDockTools. We used three different levels of theory (software packages in brackets): DFT(CP2K), semi-empirical (DFTB+), and classical force-field (Autodock), with a suitable method (program) being chosen depending on the size of the system due to limited computational resources, and a lack of Slater-Koster parameters for Ag-S interactions in the DFTB+ software package. In DFTB+, the LBFGS (Limited-memory Broyden–Fletcher–Goldfarb–Shanno) optimization scheme was used with the parameters set auorgap-1-1; this set was designed to describe the optical excitations of thiolates on gold NCs.^{9–12} D3-dispersion corrections¹³ were used with Becke-Johnson damping.¹⁴ The Broyden charge-mixing scheme was used with Fermi smearing to ensure smooth convergence of the SCF calculation.

To compute the Ag/Au atom-exchange energetics between the Ag NC and monolayer Au(111) surfaces, we used the CP2K software package. The Gaussian Plane Wave (GPW) mixed basis-set method was deployed with the plane-wave cutoff of 500 Ry, and DZVP-MOLOPT-GTH (Double-Zeta Valence Polarize (DZVP) molecular optimized (MOLOPT) Goedecker, Teter,

and Hutter (GTH)) basis sets were used with GTH-PBE potentials for all atom types except Au/Ag, while for the Au/Ag atoms, the DZVP-MOLOPT-SR-GTH (SR denotes shorter range) basis set was used. DFT-D3 dispersion corrections were used of Grimme,¹³ with Fermi-Dirac smearing and Broyden charge mixing. The PBE (Perdew-Burke-Ernzerhof)¹⁵ exchange-correlation functional was used with an SCF convergence of 1×10^{-5} . The BFGS method with a maximum force of 4.5×10^{-4} Hartree/Bohr was used for geometry optimization.

SI 4. Au(111)@SR surface construction

Monomeric DMBT-Au_{ad}-DMBT staples and trimeric Au_{ad}-BDT-Au_{ad}-BDT-Au_{ad} chains are the preferred surface arrangements for the 2,4-DMBT and 1,3-BDT monolayers on Au(111), respectively, where Au_{ad} denotes a Au(111) surface adatom (Figures S32A and B).¹⁶⁻¹⁹ We arranged the 2,4-DMBT or 1,3-BDT ligands and staples on the Au(111) surface in a hexagonal pattern (Figures S32C) with sulfur atoms anchored at different symmetry sites of the surface while varying the ligand orientations and surface coverages (Figures S33). DFT optimization of Au(111) surface with complete (full) ligand (2,4-DMBT or 1,3-BDT) coverage resulted in distorted structures. Therefore, we assumed the Au(111) surface with a lower ligand coverage for these bulky ligands for our subsequent calculations.

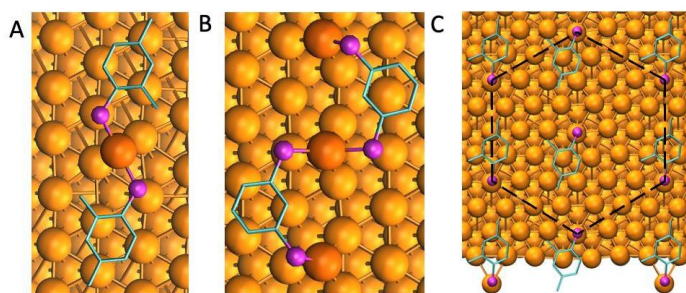


Figure S32. Close-up view of (A) a monomeric DMBT-Au_{ad}-DMBT staple and (B) a trimeric Au_{ad}-BDT-Au_{ad}-BDT-Au_{ad} chain, on Au(111). (C) The hexagonal pattern of the DMBT monolayer on Au(111). The ball-and-stick spheres for the Au adatom are shown in dark orange, the surface Au atoms in gold, the S atoms in magenta, and the C atoms of the ligands shown in stick representation in cyan.

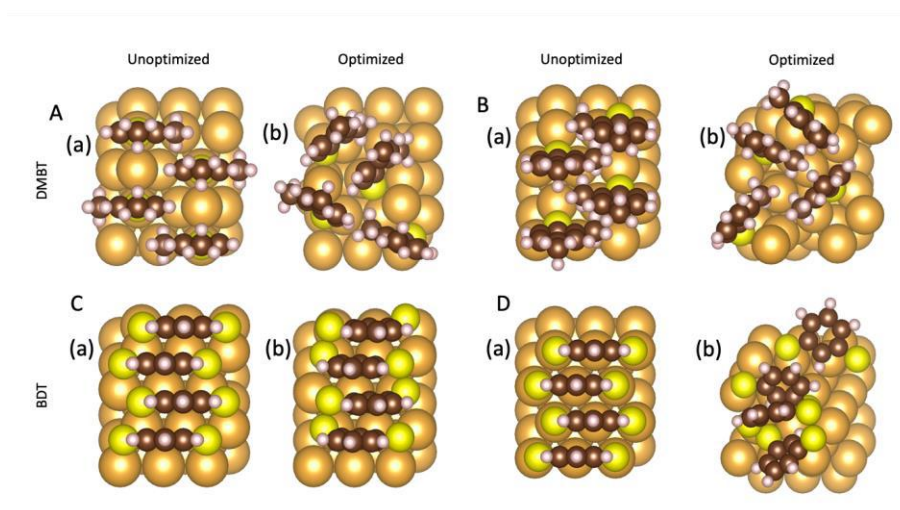


Figure S33. Ligand orientations at full coverage on Au(111) ($3\times 4\times 5$) surface unit cell. Unoptimized (a) and their corresponding optimized (b) structures from DFT calculations with (A) a complete coverage of 2,4-DMBT monolayer attached to Au_{ad} , with ligands perpendicular and (B) a complete coverage of 2,4-DMBT monolayer attached to Au_{ad} with the ligands tilted. (C) a complete coverage of 1,3-BDT monolayer with sulfur atoms attached at hollow sites and (D) a complete coverage of 1,3-BDT monolayer with the sulfur atoms attached at on-top positions. Color code: Gold, Au; yellow, S; brown, C; and white, H.

SI 5. Ag NC–Au(111)@SR docking interactions

We generated six Au(111) surfaces with different ligand and staple coverages and orientations for docking studies (Figure S34 and details in SI 4). Docking interactions of the $[\text{Ag}_{25}(\text{DMBT})_{18}]^{-}$ and $[\text{Ag}_{29}(\text{BDT})_{12}(\text{TPP})_4]^{3-}$ NCs with 2,4-DMBT (Figure 7B) and 1,3-BDT (Figure 7C) monolayered Au(111) surfaces at a low ligand and staple coverage, respectively (interatomic distances are highlighted in the inset). For higher coverage Au(111) surfaces, the docking interactions and orientation of NCs are shown in Figure S35. The docking structures of all six surfaces with the two Ag NCs are provided in Figure S36. Our docking studies revealed that at the lowest ligand coverage, the $[\text{Ag}_{25}(\text{DMBT})_{18}]^{-}$ NC (Binding Energy, BE = -89.39 kcal/mol) interacts more favorably with the Au(111)@SR surface in comparison to $[\text{Ag}_{29}(\text{BDT})_{12}(\text{TPP})_4]^{3-}$ NC (BE = -79.87 kcal/mol). The ligand atoms of Ag_{25} NC are in close contact with the Au(111) surface ligands and staple atoms at lower coverage, giving in a lower BE for $[\text{Ag}_{25}(\text{DMBT})_{18}]^{-}$ with Au(111)@DMBT than Ag_{29} -Au(111)@BDT system. Additionally, docked structures revealed interligand π - π interactions between the stacked

benzene ring of Ag₂₅ and the surface ligand. With the increase in ligand coverage, however, the NC-surface interaction becomes more favorable as a result of an enhanced π - π interaction between the TPP and BDT groups of [Ag₂₉(BDT)₁₂(TPP)₄]³⁻ NC and the BDT monolayer of Au(111) surface. About 12 and 6 ligands are involved in the NC-surface π - π interaction for the Ag₂₅-Au(111)@DMBT and Ag₂₉-Au(111)@BDT system, respectively (BE values in Tables S1 and S2).

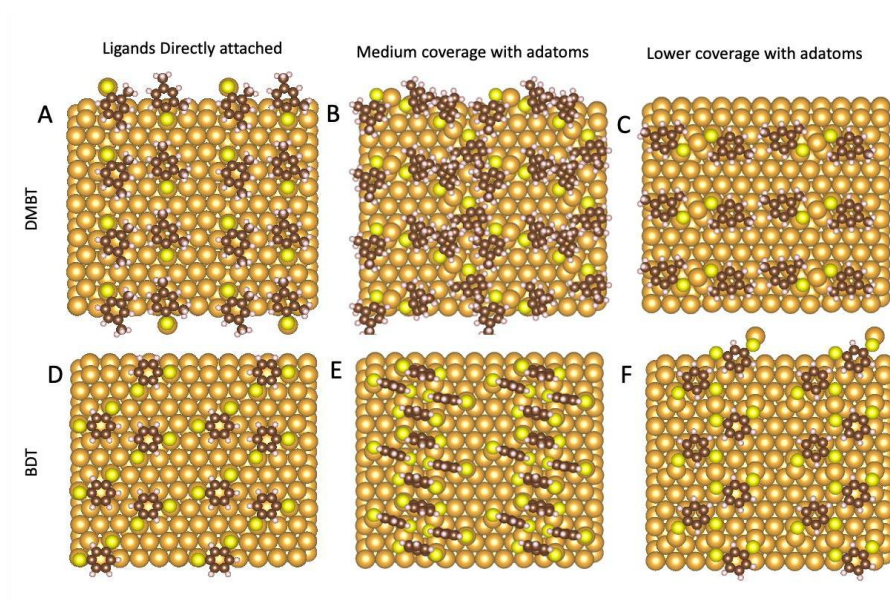


Figure S34. DFTB+-optimized Au(111)@SR with a 4×3 slab of (3×4)-surface unit cells with partial ligand coverage. (A) [Au(111)@(DMBT)₁₂] surface with sulfur atoms of the 2,4-DMBT ligands attached directly to the on-top position of surface Au atoms (21% coverage) and (B) via adatoms at medium (42%) coverage, [Au(111)@(DMBT-Au_{ad}-DMBT)₁₂], and (C) at lower coverage (21%), [Au(111)@(DMBT-Au_{ad}-DMBT)₆]. (D) Au(111) surface with 1,3-BDT ligands attached directly (27% coverage) [Au(111)@(BDT)₁₂], and via ad-atoms with (E) highest coverage (55%), [Au(111)@(Au_{ad}-BDT-Au_{ad}-BDT-Au_{ad})₁₂], and (F) lower coverage (27%) [Au(111)@(Au_{ad}-BDT-Au_{ad}-BDT-Au_{ad})₆]. Color code: Gold, Au; yellow, S; brown, C; and white, H.

SI 6. Ligand coverage calculations

From concentration calculations in SI 2,

Surface area covered by 2,4-DMBT = 0.17 nm²

Surface area covered by 1,3-BDT = 0.22 nm²

Surface area of Au(111) 4×3 slab = 9.63 nm²

Surfaces A to F, as in Figure S34,

1. Surface A - [Au(111)@(DMBT)₁₂]

$$\text{Ligand coverage} = \frac{0.17 \times 12}{9.63} \times 100 \approx 21\%$$

2. Surface B - [Au(111)@(DMBT-Au_{ad}-DMBT)₁₂]

$$\text{Ligand coverage} = \frac{0.17 \times 24}{9.63} \times 100 \approx 42\%$$

3. Surface C - [Au(111)@(DMBT-Au_{ad}-DMBT)₆]

$$\text{Ligand coverage} = \frac{0.17 \times 12}{9.63} \times 100 \approx 21\%$$

4. Surface D - [Au(111)@(BDT)₁₂]

$$\text{Ligand coverage} = \frac{0.22 \times 12}{9.63} \times 100 \approx 27\%$$

5. Surface E - [Au(111)@(Au_{ad}-BDT-Au_{ad}-BDT-Au_{ad})₁₂]

$$\text{Ligand coverage} = \frac{0.22 \times 24}{9.63} \times 100 \approx 55\%$$

6. Surface F - [Au(111)@(Au_{ad}-BDT-Au_{ad}-BDT-Au_{ad})₆]

$$\text{Ligand coverage} = \frac{0.22 \times 12}{9.63} \times 100 \approx 27\%$$

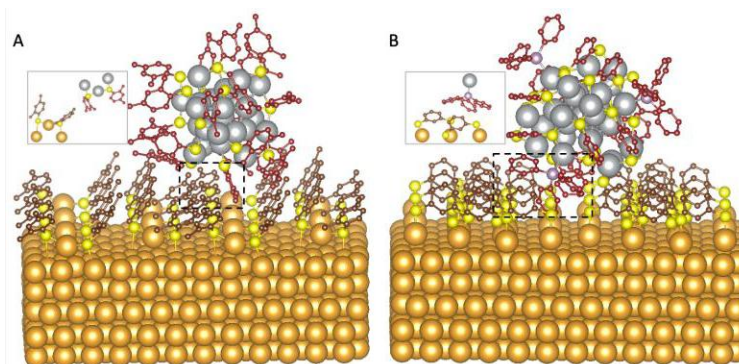


Figure S35. Docked NCs on Au(111)@SR with higher coverage monolayers. (A) [Ag₂₅(DMBT)₁₈]⁻ NC on DMBT-monolayered Au(111) surface, and (B) [Ag₂₉(BDT)₁₂(TPP)₄]³⁻ NC on BDT-monolayered Au(111) surface. Insets show a close-up of

one of the interactions between NC and surface ligands. Color code: Gold, Au; yellow, S; brown, C of surface ligands; gray, Ag; red, C of NC ligands; purple, P of TPP.

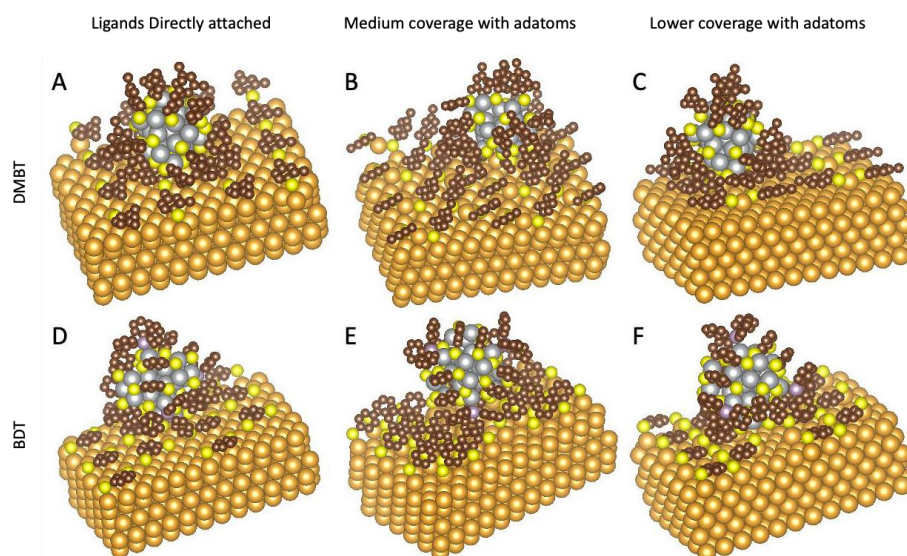


Figure S36. Ag NC docking on optimized Au(111)@SR surfaces, where SR refers to 2,4-DMBT or 1,3-BDT ligands. (A) [Au(111)@(DMBT)₁₂]@Ag₂₅, (B) [Au(111)@(DMBT-Au_{ad}-DMBT)₁₂]@Ag₂₅, and (C) [Au(111)@(DMBT-Au_{ad}-DMBT)₆]@Ag₂₅. Au(111) surface with 1,3-BDT directly attached, (D) [Au(111)@(BDT)₁₂]@Ag₂₉, (E) [Au(111)@(Au_{ad}-BDT-Au_{ad}-BDT-Au_{ad})₁₂]@Ag₂₉, and (F) [Au(111)@(Au_{ad}-BDT-Au_{ad}-BDT-Au_{ad})₆]@Ag₂₉. Color code: Gold, Au; yellow, S; brown, C; gray, Ag; purple, P.

Table S1. BE of docked Ag_n(SR)_m NCs on Au(111) surface with medium thiolate coverage (refer to Figures S34 and S36).

Complex	BE (kCal/mol)
[Au(111)@(DMBT) ₁₂]@Ag ₂₅	-38.75
[Au(111)@(BDT) ₁₂]@Ag ₂₉	-52.62
[Au(111)@(DMBT-Au _{ad} -DMBT) ₁₂]@Ag ₂₅	-11.83
[Au(111)@(Au _{ad} -BDT-Au _{ad} -BDT-Au _{ad}) ₁₂]@Ag ₂₉	-15.59
Au(111)@Ag ₂₅	-83.13
Au(111)@Ag ₂₉	-68.97

Note that, the bare Au(111) surface is represented here as only Au(111).

Table S2. BE of docked NCs on Au(111)@SR with different numbers of monolayer staples (refer to Figure S34 and S36, C and F)

No. of Staples	BE (kcal/mol) [Au(111)@(DMBT-Au _{ad} -DMBT)] @Ag ₂₅	BE (kcal/mol) [Au(111)@(Au _{ad} -BDT-Au _{ad} -BDT-Au _{ad})] @Ag ₂₉
1	-89.39	-79.87
2	-89.48	-78.23
4	-87.19	-80.81
6	-37.64	-45.20

Table S3. DFT calculated energies of parent NCs and Au and Ag atoms

Structure	E ₀ (Ha)
Au	-33.1388
Ag	-36.9305
[Ag ₂₅ (DMBT) ₁₈] ¹⁻	-2025.7609
[Ag ₂₉ (BDT) ₁₂ (TPP) ₄] ³⁻	-2229.1081

Table S4. Isomers of single gold atom substituted [AuAg₂₄(DMBT)₁₈]⁻ NC

Au location	Isomer	Energy (Ha)
Centre of Icosahedron	C	-2022.0003
Icosahedron	I	-2021.9880
Staple	S	-2021.9858

Table S5. Isomers of double gold-atom substituted $[\text{Au}_2\text{Ag}_{23}(\text{DMBT})_{18}]^- \text{NC}$

Au location	Isomer	Energy (Ha)
Icosahedron & Centre of Icosahedron	IC	-2018.2260
Icosahedron & Icosahedron	II	-2018.2143
Icosahedron & Staple	IS	-2018.2129
Staple & Centre of Icosahedron	SC	-2018.2247
Staple & Staple	SS	-2018.2099

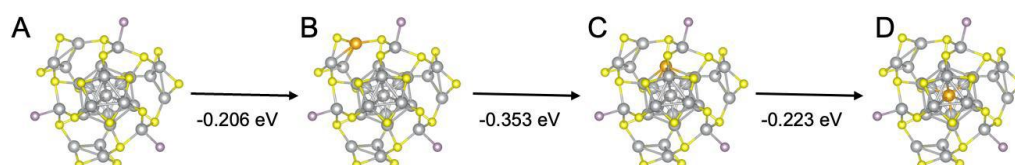


Figure S37. Doping pathway of Au atom in $[\text{Ag}_{29}(\text{BDT})_{12}(\text{TPP})_4]^{3-} \text{NC}$ (A) and reaction energies of intermediate states. The reaction energy is calculated as $\Delta E = E_{\text{Products}} - E_{\text{Reactants}}$. The most favorable Au-doping pathway is from the Ag_3S_3 motif (B) to the Au_{13} icosahedron (C) and finally to the central atom of the core icosahedron position (D). Color code: Gold, Au; yellow, S; gray, Ag; H and C atoms were omitted for clarity.

Table S6. Energies of isomers of single gold atom substituted $[\text{AuAg}_{28}(\text{BDT})_{12}(\text{TPP})_4]^{3-} \text{NC}$

Au location	Isomer	Energy (Ha)
Centre of Icosahedron	C	-2225.3452
Icosahedron	I	-2225.3370
Triangular Ag_3S_3 motif	T	-2225.3240
Bonded to Phosphorus of TPP	P	-2225.3192

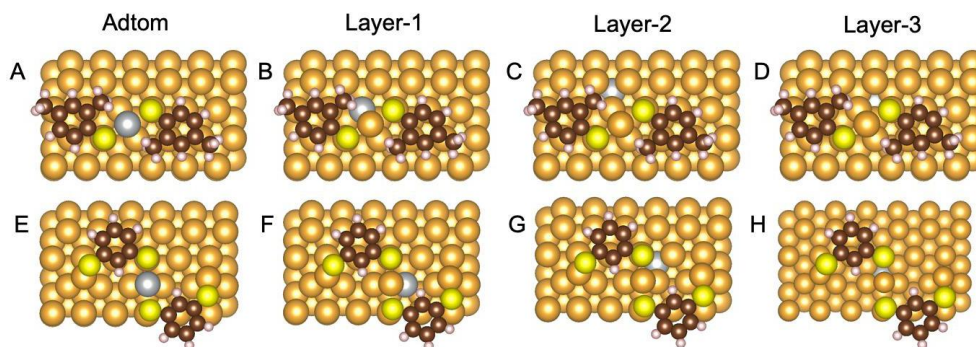


Figure S38. Optimized Ag-doped Au(111) 2×1 slab of the (3×4) surface unit cell of 5-layers with a staple of DMBT/BDT, with Ag-atom at various locations for (A-D) [Au(111)@(DMBT-Au_{ad}-DMBT)] and (E-H) [Au(111)@(Au_{ad}-BDT-Au_{ad}-BDT-Au_{ad})]. Different dopant locations on the Au(111) correspond to staple (A, E), layer-1 (B, F), layer-2 (C, G), and layer-3 (D, H). Color code: Gold, Au; yellow, S; gray, Ag; brown, C; and white, H.

SI 7. Energies of DFT-optimized Au(111)@SR surfaces

Table S7. Energies of undoped Au(111) monolayer surfaces

Structure	E ₀ (Ha)
[Au(111)@(DMBT-Au _{ad} -DMBT)]	-4147.1900
[Au(111)@(Au _{ad} -BDT-Au _{ad} -BDT-Au _{ad})]	-4205.3797

Table S8. Energies of Ag-alloy isomers of [Au(111)Ag@(DMBT-Au_{ad}-DMBT)] surface with a single Ag atom (Figure S38A-D)

Ag location	E (Ha)
Staple	-4150.9632
Layer-1	-4150.9696
Layer-2	-4150.9731
Layer-3	-4150.9720

Table S9. Ag-alloy isomers of the [Au(111)Ag@(Au_{ad}-BDT-Au_{ad}-BDT-Au_{ad})] surface with a single Ag-atom (Figure S38E-H)

Ag location	E (Ha)
Staple	-4209.1510
Layer-1	-4209.1604
Layer-2	-4209.1622
Layer-3	-4209.1617

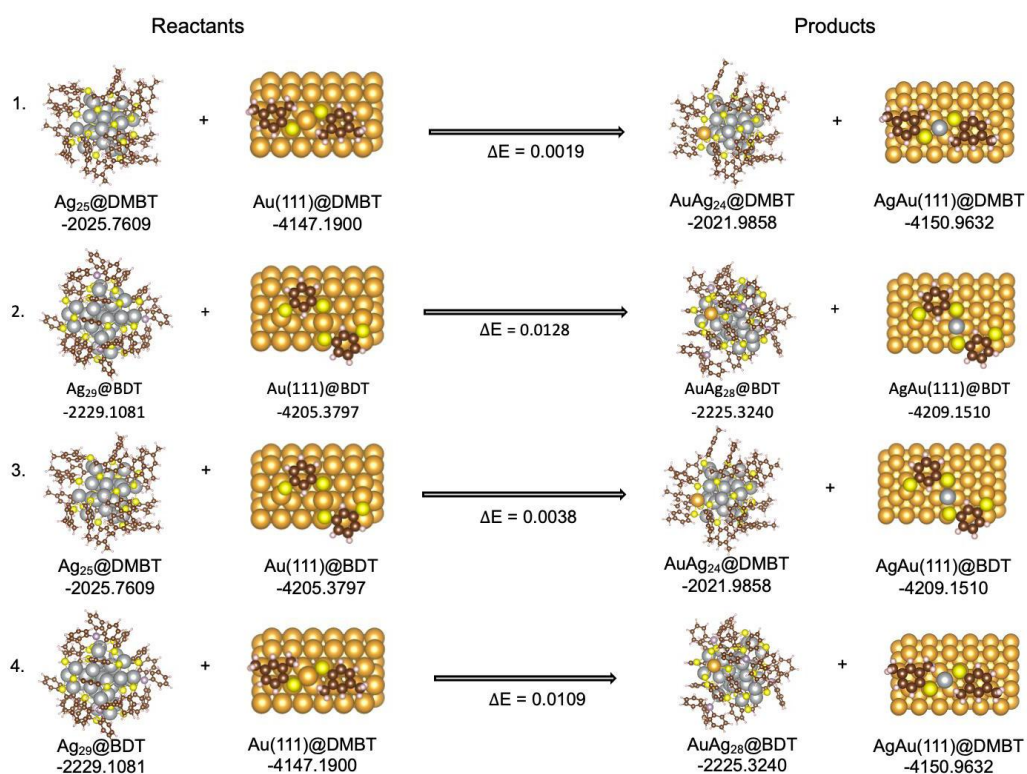


Figure S39. Au-Ag atom-exchange reactions between Ag NC – Au(111) monolayer surface and their reaction energies. The reaction energy is calculated as $\Delta E = E_{\text{Products}} - E_{\text{Reactants}}$. Note that the above surface energies correspond to Au(111) surface, with 2,4-DMBT or 1,3-BDT ligands attached via Au adatoms. All energies are in Hartree (Ha). Color code: Gold, Au; yellow, S; gray, Ag; brown, C; and white, H.

SI 8. References

- (1) Brust, M.; Walker, M.; Bethell, D.; Schiffrin, D. J.; Whyman, R. Synthesis of Thiol-Derivatised Gold Nanoparticles in a Two-Phase Liquid–Liquid System. *J. Chem. Soc. Chem. Commun.* **1994**, No. 7, 801–802.
- (2) Joshi, C. P.; Bootharaju, M. S.; Alhilaly, M. J.; Bakr, O. M. [Ag₂₅(SR)₁₈]⁻: The “Golden” Silver Nanoparticle. *J. Am. Chem. Soc.* **2015**, *137* (36), 11578–11581.
- (3) AbdulHalim, L. G.; Bootharaju, M. S.; Tang, Q.; Del Gobbo, S.; AbdulHalim, R. G.; Eddaoudi, M.; Jiang, D. E.; Bakr, O. M. Ag₂₉(BDT)₁₂(TPP)₄: A Tetravalent Nanocluster. *J. Am. Chem. Soc.* **2015**, *137* (37), 11970–11975.
- (4) Krishnadas, K. R.; Ghosh, A.; Baksi, A.; Chakraborty, I.; Natarajan, G.; Pradeep, T. Intercluster Reactions between Au₂₅(SR)₁₈ and Ag₄₄(SR)₃₀. *J. Am. Chem. Soc.* **2016**, *138* (1), 140–148.
- (5) Bose, P.; Chakraborty, P.; Mohanty, J. S.; Nonappa; Ray Chowdhuri, A.; Khatun, E.; Ahuja, T.; Mahendranath, A.; Pradeep, T. Atom Transfer between Precision Nanoclusters and Polydispersed Nanoparticles: A Facile Route for Monodisperse Alloy Nanoparticles and Their Superstructures. *Nanoscale* **2020**, *12* (43), 22116–22128.
- (6) Kühne, T. D.; Iannuzzi, M.; Del Ben, M.; Rybkin, V. V.; Seewald, P.; Stein, F.; Laino, T.; Khaliullin, R. Z.; Schütt, O.; Schiffmann, F. CP2K: An Electronic Structure and Molecular Dynamics Software Package-Quickstep: Efficient and Accurate Electronic Structure Calculations. *J. Chem. Phys.* **2020**, *152* (19), 194103.
- (7) Hourahine, B.; Aradi, B.; Blum, V.; Bonafé, F.; Buccheri, A.; Camacho, C.; Cevallos, C.; Deshayé, M. Y.; Dumitrică, T.; Dominguez, A.; Ehlert, S.; Elstner, M.; van der Heide, T.; Hermann, J.; Irlé, S.; Kranz, J. J.; Köhler, C.; Kowalczyk, T.; Kubař, T.; Lee, I. S.; Lutsker, V.; Maurer, R. J.; Min, S. K.; Mitchell, I.; Negre, C.; Niehaus, T. A.; Niklasson, A. M. N.; Page, A. J.; Pecchia, A.; Penazzi, G.; Persson, M. P.; Řezáč, J.; Sánchez, C. G.; Sternberg, M.; Stöhr, M.; Stuckenberg, F.; Tkatchenko, A.; Yu, V. W. - z.; Frauenheim, T. DFTB+, a Software Package for Efficient Approximate Density Functional Theory Based Atomistic Simulations. *J. Chem. Phys.* **2020**, *152* (12), 124101.
- (8) Morris, G. M.; Goodsell, D. S.; Halliday, R. S.; Huey, R.; Hart, W. E.; Belew, R. K.; Olson, A. J. Automated Docking Using a Lamarckian Genetic Algorithm and an Empirical Binding Free Energy Function. *J. Comput. Chem.* **1998**, *19* (14), 1639–1662.

- (9) Elstner, M.; Porezag, D.; Jungnickel, G.; Elsner, J.; Haugk, M.; Frauenheim, Th.; Suhai, S.; Seifert, G. Self-Consistent-Charge Density-Functional Tight-Binding Method for Simulations of Complex Materials Properties. *Phys. Rev. B* **1998**, *58* (11), 7260–7268.
- (10) Niehaus, T. A.; Elstner, M.; Frauenheim, Th.; Suhai, S. Application of an Approximate Density-Functional Method to Sulfur Containing Compounds. *J. Mol. Struct. THEOCHEM* **2001**, *541* (1), 185–194.
- (11) Fihey, A.; Hettich, C.; Touzeau, J.; Maurel, F.; Perrier, A.; Köhler, C.; Aradi, B.; Frauenheim, T. SCC-DFTB Parameters for Simulating Hybrid Gold-Thiolates Compounds. *J. Comput. Chem.* **2015**, *36* (27), 2075–2087.
- (12) Vuong, V. Q.; Madrudejos, J. M. L.; Aradi, B.; Sumpter, B. G.; Metha, G. F.; Irle, S. Density-Functional Tight-Binding for Phosphine-Stabilized Nanoscale Gold Clusters. *Chem. Sci.* **2020**, *11* (48), 13113–13128.
- (13) Grimme, S.; Antony, J.; Ehrlich, S.; Krieg, H. A Consistent and Accurate Ab Initio Parametrization of Density Functional Dispersion Correction (DFT-D) for the 94 Elements H-Pu. *J. Chem. Phys.* **2010**, *132* (15), 154104.
- (14) Grimme, S.; Ehrlich, S.; Goerigk, L. Effect of the Damping Function in Dispersion Corrected Density Functional Theory. *J. Comput. Chem.* **2011**, *32* (7), 1456–1465.
- (15) Hammer, B.; Hansen, L. B.; Nørskov, J. K. Improved Adsorption Energetics within Density-Functional Theory Using Revised Perdew-Burke-Ernzerhof Functionals. *Phys. Rev. B* **1999**, *59* (11), 7413–7421.
- (16) Maksymovych, P.; Sorescu, D. C.; Yates, J. T. Gold-Adatom-Mediated Bonding in Self-Assembled Short-Chain Alkanethiolate Species on the Au(111) Surface. *Phys. Rev. Lett.* **2006**, *97* (14), 146103.
- (17) Cossaro, A.; Mazzarello, R.; Rousseau, R.; Casalis, L.; Verdini, A.; Kohlmeyer, A.; Floreano, L.; Scandolo, S.; Morgante, A.; Klein, M. L.; Scoles, G. X-Ray Diffraction and Computation Yield the Structure of Alkanethiols on Gold(111). *Science* **2008**, *321* (5891), 943–946.
- (18) Häkkinen, H. The Gold–Sulfur Interface at the Nanoscale. *Nat. Chem.* **2012**, *4* (6), 443–455.
- (19) Kestell, J.; Abuflaha, R.; Garvey, M.; Tysoe, W. T. Self-Assembled Oligomeric Structures from 1,4-Benzenedithiol on Au(111) and the Formation of Conductive Linkers between Gold Nanoparticles. *J. Phys. Chem. C* **2015**, *119* (40), 23042–23051.


 Cite this: *Phys. Chem. Chem. Phys.*,
2024, 26, 16008

Partitioning photochemically formed CO₂ into clathrate hydrate under interstellar conditions†

 Gaurav Vishwakarma,^a Bijesh K. Malla,^a Rajnish Kumar^{id} *^{bc} and
Thalappil Pradeep^{id} *^{ac}

Clathrate hydrates (CHs), host–guest compounds of water forming hydrogen-bonded cages around guest molecules, are now known to exist under interstellar conditions. Experimental evidence demonstrated that prolonged thermal treatment of a solid mixture of water and CO₂/CH₄ produces CHs at 10–30 K under simulated interstellar conditions. However, in the current study, we show that CO₂ produced photochemically by vacuum ultraviolet irradiation of H₂O–CO mixtures at 10 K and 10^{−10} mbar, gets partitioned into its CH phase and a matrix phase embedded in amorphous ice. The process occurring under simulated interstellar conditions was studied at different temperatures and H₂O–CO compositions. The formation of CO₂ CH and other photoproducts was confirmed using reflection absorption infrared spectroscopy. The UV-induced photodesorption event of CO₂ may provide the mobility required for the formation of CHs, while photoproducts like methanol can stabilize such CH structures. Our study suggests that new species originating during such energetic processing in ice matrices may form CH, potentially altering the chemical composition of astrophysical environments.

 Received 6th April 2024,
Accepted 16th May 2024

DOI: 10.1039/d4cp01414f

rsc.li/pccp

Introduction

Energetic processes, like photoirradiation, are key in shaping the composition of cometary and interstellar ices. Such processes significantly influence the chemical and physical properties of these ices by generating radicals and reactive species.¹

These products can undergo recombination, diffusion, and reactions, potentially forming secondary products and getting trapped within the ice.^{1–3} However, the trapping of photoproducts in clathrate cages during vacuum ultraviolet (VUV) irradiation of interstellar ice analogues has not been observed yet.

Clathrate hydrates (CHs) are inclusion compounds where water hosts and encases guest molecules like CH₄, CO, CO₂, and H₂S within its H-bonded cages.⁴ CHs exist naturally in two structures, sI, and sII, in permafrost and marine sediments under high pressures and low temperatures.^{4,5} However, CHs in interstellar-like environments have also been established

experimentally,^{6–15} and they have stimulated some scientific debate.^{16,17} In one of our previous studies,⁷ we had seen that when an ice mixture containing water and CH₄/CO₂ was subjected to extended annealing at 10–30 K in an ultrahigh vacuum (UHV), CH was formed. This study led to the speculation that photochemically produced molecules might also form CH. Shi *et al.*¹⁸ observed that UV photons caused the trapping of O₂ (in turn, O₃ and H₂O₂) in porous water ice. They demonstrated that irradiation-induced trapping of O₂ in porous water ice is about seven times larger than equilibrium adsorption in the absence of irradiation. Bahr *et al.*¹⁹ also reported the trapping of O₂ and H₂O₂ during the radiolysis of water ice between 40–120 K. Similarly, Fleyfel and Devlin reported the formation of CO₂ CH in a study where they subjected a simple ethylene oxide CH film to electron beam (1.7-MeV) irradiation at 15 K, and heated the resulting ice mixture to 100 K.²⁰ These observations suggest the possibility of the existence of photochemically produced molecules as CH under UHV and cryogenic conditions. However, there have been no studies in this regard.

Recombination, stabilization, and preservation of reactive molecules and free radicals in solid structures require cryogenic temperatures. Consequently, there has been widespread interest in developing methods to stabilize these reactive substances at higher temperatures.²¹ The trapping of such species within CH cages offers a potential solution to this challenge. CH cages may hold such species up to their decomposition temperatures or till the sublimation of ice matrices. Capturing such species, even as they are generated during energetic

^a DST Unit of Nanoscience (DST UNS) and Thematic Unit of Excellence (TUE), Department of Chemistry, Indian Institute of Technology Madras, Chennai 600036, India. E-mail: pradeep@iitm.ac.in

^b Department of Chemical Engineering, Indian Institute of Technology Madras, Chennai 600036, India. E-mail: rajnish@iitm.ac.in

^c International Centre for Clean Water, IIT Madras Research Park, Chennai 600113, India

† Electronic supplementary information (ESI) available: List of photochemical products, temperature and irradiation time-dependent RAIR spectra of pure CO and H₂O–CO films, SIMS spectrum of the irradiated H₂O–CO mixture. See DOI: <https://doi.org/10.1039/d4cp01414f>

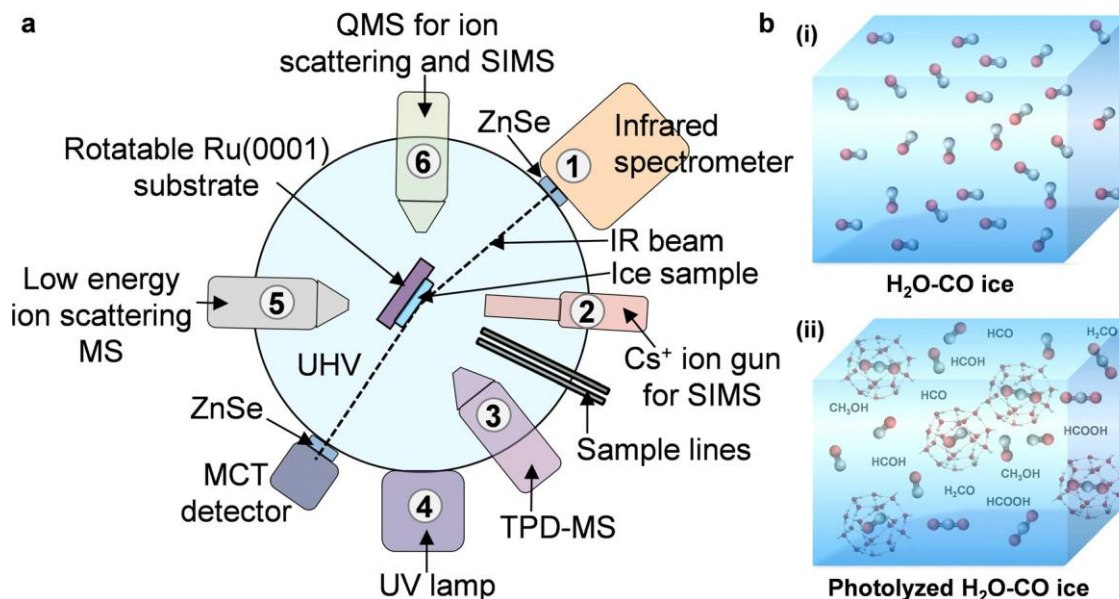


Fig. 1 (a) Schematic of the UHV apparatus. Various tools attached to the UHV chamber are (1) RAIRS setup with ZnSe window and MCT detector, (2) Cs^+ ion gun, (3) TPD-MS setup, (4) UV lamp, (5) low energy ion scattering setup, and (6) quadrupole mass analyzer. The substrate, in the schematic, is oriented for RAIR measurements. (b) Schematic illustration of the composition of $\text{H}_2\text{O-CO}$ mixture (i) before and (ii) after VUV irradiation at 10 K, where the blue cube represents the water matrix.

processes like photon irradiation, holds high significance in planetary science, astrochemistry, and physical chemistry. In cold, dense molecular clouds, H_2O and CO dominate the grain mantles.^{22,23} By mimicking such environments, extensive laboratory studies have been conducted exposing the $\text{H}_2\text{O-CO}$ system to various stimuli (photon, electron, and ion irradiation) to comprehend the formation and evolution of several interstellar molecules. However, the trapping of secondary products during VUV irradiation of $\text{H}_2\text{O-CO}$ ice remains unexplored. The present study investigates the physicochemical fate of photochemically produced CO_2 from an $\text{H}_2\text{O-CO}$ mixture co-deposited at 10 K. The process has been studied at different temperatures and $\text{H}_2\text{O-CO}$ compositions. The evolution of the $\text{H}_2\text{O-CO}$ mixture upon VUV exposure under UHV and cryogenic conditions was monitored by reflection absorption infrared spectroscopy (RAIRS), and temperature-programmed desorption (TPD) mass spectrometry using a custom-built UHV setup, illustrated in Fig. 1a and described in detail elsewhere.²⁴

Experimental methods

Experimental setup

The experimental setup was the same as the one we used to prepare clathrate hydrate (CH) at a cryogenic temperature under ultrahigh vacuum (UHV),^{7,8} and was described in detail elsewhere.²⁴ Briefly, the apparatus consisted of a UHV chamber (with a base pressure $\approx 5 \times 10^{-10}$ mbar), a closed-cycle He cryostat, a gas inlet system, equipped with reflection absorption infrared spectroscopy (RAIRS), temperature-programmed desorption (TPD) mass spectrometry, Cs^+ ion-based secondary ion mass spectrometry (SIMS), low energy ion scattering (LEIS)

mass spectrometry, and an ultraviolet (UV) lamp. The thin ice films were created on cold Ru(0001) substrate. The substrate is mounted at the cold end of the He cryostat and fitted with a precision $x-y-z-y$ sample manipulator that can be reoriented to do various measurements, as shown in Fig. 1a. The substrate temperature could be adjusted using a resistive heater (25 Ω) in the 8–1000 K range and measured by different thermal sensors (K-type thermocouple and a platinum sensor) with a temperature accuracy/uncertainty of 0.5 K. The substrate temperature was controlled by a temperature controller (Lakeshore, Model 336).

Materials and reagents

CO (99.5%) gas was purchased from Rana Industrial Gases & Products and was used without further purification. Millipore water (H_2O of 18.2 M Ω resistivity) was taken in a vacuum-sealed test tube and further purified *via* several freeze–pump–thaw cycles.

Sample preparation

Thin ice films were prepared by vapor deposition on the pre-cooled Ru(0001) substrate at 10 K. The molecular vapor deposition was controlled by two high-precision all-metal leak valves through two inlet lines that were directed to the middle of the substrate. Out of two inlet lines, one was exclusively used for CO and the other for H_2O . The molecular deposition coverage was expressed in monolayers (ML) assuming 1.33×10^{16} molecules cm^{-2} , $s = 1$ ML, estimated to contain $\approx 1.1 \times 10^{15}$ molecules cm^{-2} , as adopted in earlier studies.^{7,8} The purity and ratio of the CO and H_2O ice mixtures were further confirmed during vapor deposition using a residual gas analyzer. Also, the Ru(0001) substrate was repeatedly heated to 400 K prior to each vapor deposition

in order to ensure that the surface was sufficiently clean for the current study. Prior to the current set of experiments, the substrate was polished and annealed at 1000 K.

Determination of the column density (N) and UV lamp flux

We applied the extensively used method²⁵ to estimate the column density of absorbing molecules.

$$N_M = S_M/A_M$$

Where N_M is the column density of molecule M in cm^{-2} , S_M is the integrated area of the specific IR band of molecule M , and A_M is the band strength of the same band in cm^{-1} molecule⁻¹. The values of H_2O column densities in mixed H_2O – CO film were estimated as $N_{\text{H}_2\text{O}} = S_{\text{H}_2\text{O}}/A_{\text{H}_2\text{O}}$, where $S_{\text{H}_2\text{O}}$ was the integrated area of the 1670 cm^{-1} band, $A_{\text{H}_2\text{O}}$ (8×10^{18})²⁵ was the strength of the band absorption. Similarly, the values of CO column densities were estimated as $N_{\text{CO}} = S_{\text{CO}}/A_{\text{CO}}$, where S_{CO} was the integrated area of the 2180 – 2110 cm^{-1} band, A_{CO} (2×10^{17})²⁵ was the strength of the band absorption. In the present work, the ratios of the H_2O – CO mixture were estimated by dividing the column densities of H_2O with CO for each ice sample.

A deuterium lamp (McPherson, Model 634, with MgF_2 window, 30 W) of vacuum ultraviolet (VUV) range, 115–300 nm, was used as the UV light source. The VUV lamp was differentially pumped and attached to the UHV chamber through the MgF_2 window (with a cut-off at 114 nm (10.87 eV)). The UV lamp flux was determined by applying the widely used ozone method ($\text{O}_2 \rightarrow \text{O}_3$ conversion)^{26,27} where solid O_2 was VUV photolyzed at 10 K. The average photon flux reaching the ice sample was estimated to be 6×10^{12} photons $\text{cm}^{-2} \text{ s}^{-1}$.

Experimental protocol

For VUV photoprocessing, the H_2O – CO mixture was prepared by co-depositing H_2O and CO vapors on Ru(0001) at 10 K. The sample preparation method is the same as adopted in our previous studies.^{7,8,13} Briefly, ice films of 100 ML of H_2O and CO were prepared by backfilling the vacuum chamber at a total pressure of 5×10^{-7} mbar for 3 min 20 s, starting from a base vacuum of 5×10^{-10} mbar. For the co-deposition of H_2O and CO in a 1 : 1 ratio, the inlet pressure of H_2O was kept 2.5×10^{-7} mbar and that of CO was 2.5×10^{-7} mbar. Here, the deposition coverages were measured as the product of the dosing time and the chamber pressure of exposure. However, here, the ratio of H_2O to CO in the resulting H_2O – CO mixture was estimated by dividing the column densities of H_2O with CO . Each experiment was carried out in two steps. In the first step, after several heating–cooling cycles, a background RAIR spectrum of the clean substrate was recorded. Then mixed ice composed of H_2O and CO (of desired ratios) was prepared on the Ru(0001) at 10 K. After sample preparation at 10 K, a RAIR spectrum of the unirradiated ice sample was recorded. Then, the substrate was reoriented to expose the as-prepared sample to VUV irradiation. In the second step, the UV lamp was switched on, exposing the sample to VUV radiation for a desired period. After each irradiation, the substrate was again

reoriented to RAIRS configuration to record the IR spectra of the irradiated ice film.

VUV photolysis experiments were performed in two sets, (1) temperature-dependent and (2) H_2O – CO composition-dependent photolysis. In the first set, an H_2O – CO mixture of a fixed composition (H_2O to CO ratio 7.93 : 0.19) was prepared at 10 K and was isothermally irradiated at the corresponding temperatures of 10, 20, and 30 K. For 20 and 30 K experiments, the ice samples were prepared at 10 K and annealed to the set temperatures at an annealing rate of 2 K min^{-1} . In the second set, mixed ice of three different ratios of H_2O – CO (with H_2O to CO ratio = 1.46, 4.09, and 7.72) was prepared and irradiated at 10 K. For both sets of experiments, the ice sample was irradiated for four hours, and RAIR spectra were collected, at 0, 0.5, 1, 1.5, 2, 3, and 4 h.

RAIRS setup

Before and after VUV irradiation of ice samples, RAIR spectra were collected using a Bruker Vertex 70 FT-IR spectrometer in the 4000 – 550 cm^{-1} range with a spectral resolution of 2 cm^{-1} . For a better signal-to-noise ratio, each RAIR spectrum was averaged over 512 scans. During experiments, the IR beam was focused on the ice sample at an incident angle of 80.171° through an infrared transparent ZnSe viewport. The reflected beam from the ice sample was recorded with a liquid nitrogen cooled mercury cadmium telluride (MCT) detector. The IR beam outside the vacuum chamber was purged with dry nitrogen to avoid background noise.

TPD-MS setup

For the TPD-MS experiment, H_2O – CO (1.46) mixture was prepared at 10 K, and the resulting ice sample was exposed to VUV irradiation for 2 h. After irradiation, TPD experiments were performed by rotating the substrate in the TPD configuration. Each TPD experiment was performed at a 30 K min^{-1} heating rate. The thermal desorption profile of CO , CO_2 , and H_2O was recorded by monitoring the $m/z = 28$, 44, and 18, respectively, as a function of substrate temperature.

The TPD module (Extrel CMS) was attached to the vacuum chamber on a 6-inch flange through a Z-axis manipulator. The module consisted of an electron impact source, a mass analyzer, and a detector. The mass analyzer was a quadrupole with 1 to 500 mass range and 1 amu resolution.

SIMS setup

We have conducted ion collision experiments on the H_2O – CO ice surface using Cs^+ of 60 eV kinetic energy produced from a low-energy alkali ion gun (Kimball Physics Inc.). Cs^+ (m/z 133) is a well-known projectile for SIMS. This technique is sensitive only to the first few layers of the surface. The low energy collision of Cs^+ converts the neutral adsorbate species (M) to gas phase ions (CsM^+) by association reaction in a process widely known as reactive ion scattering (RIS). The resulting scattered ions were analyzed using a quadrupole mass analyser. We have used the RIS signal intensities corresponding to the complex of Cs^+ with H_2O ($m/z = 151$ ($\text{Cs}(\text{H}_2\text{O})^+$), $m/z = 169$

(Cs(H₂O)₂⁺, $m/z = 187$ (Cs(H₂O)₃⁺, etc.), with CO { $m/z = 161$ (Cs(CO)⁺, $m/z = 189$ (Cs(CO)₂⁺, $m/z = 217$ (Cs(CO)₃⁺, etc.), and with CO–H₂O complexes { $m/z = 179$ (Cs(CO–H₂O)⁺, $m/z = 197$ (Cs(CO–(H₂O)₂)⁺, $m/z = 207$ (Cs((CO)₂–H₂O)⁺, etc.) to identify the surface structure of H₂O–CO mixture. Here, the signal intensities are directly proportional to the surface population of the molecule (or complex) on the ice surface.

Results and discussion

To begin with, H₂O–CO (1.46) mixture was exposed to VUV irradiation for 2 h at 10 K (details of experimental protocol are given in Experimental method). Full range RAIR spectra collected before and after irradiation are shown in Fig. S1 (ESI†). The photoproducts produced in the process are listed in Table S1 (ESI†). The photochemical products, CO₂, HCO, H₂CO, CH₃OH, and HCOOH, observed in the current work, are consistent with the earlier studies.^{25,28} However, evidence of the formation of CH was observed and discussed for the first time in the current work. A schematic illustration of the composition of the ice mixture before (i) and after (ii) VUV exposure to the H₂O–CO mixture is shown in Fig. 1b. Moreover, in a VUV experiment conducted on pure CO ice, we could not observe any photoproducts with RAIRS (intensity of the CO absorption band does not decrease), as shown in Fig. S2 (ESI†). Literature supports this observation.^{29,30} However, Gerakines *et al.*³¹ observed the formation of CO₂ and other photoproducts through the involvement of excited species, as CO + $h\nu$ → CO*^{*}; CO* + CO → CO₂ + C.

Fig. 2 shows the RAIR spectra for 0 h (black trace) and 2 h (blue trace) VUV irradiation of H₂O–CO (7.72) mixture at 10 K in the CQO antisymmetric stretching region of CO₂ (a) and C = O stretching region of CO (b). In Fig. 2a, at 0 h (without irradiation), the flat line suggests the absence of CO₂ in the H₂O–CO

mixture. However, after 2 h of VUV irradiation, two peaks at 2353 and 2346 cm⁻¹ were observed, which are attributed to CO₂ that exists in amorphous solid water (ASW) pores and CH cages (512 cage of sI),^{4,32} respectively. The assignments are consistent with the previous studies.^{7,14,33,34} Notably, in our present study, we did not detect the IR peak corresponding to CO₂ confined within the large cage (5¹²62) of sI, which would typically occur around 2337 cm⁻¹.³³ It is worth noting that a similar observation has been reported by both Blake *et al.*¹⁴ and Ghosh *et al.*⁷ The CO₂ partitioning in ASW *versus* CH cages has been studied extensively.^{14,15,35} However, significant differences exist between the experimental conditions of the current work and those of the literature. While, the current study observes CO₂ CH formation under UHV at 10 K through VUV irradiation. Previous studies by Blake *et al.* and Netsu *et al.* noted the formation of CO₂ CH at 120 K under high vacuum (HV), with and without CH₃OH, respectively. Similarly, Bauer *et al.* observed its formation at 194 K under HV while warming a CO₂–H₂O amorphous mixture. It should be noted that the vacuum conditions influence both the sublimation temperature and mobility of water and other molecules, which are critical for CH formation.

To further confirm our RAIRS assignments, we heated the photolyzed H₂O–CO ice beyond the desorption temperature of CO₂, around 90 K in a control experiment (Fig. S3, ESI†). The peak at 2353 cm⁻¹ disappeared suggesting the desorption of free CO₂ from water matrix, while the peak at 2346 cm⁻¹ persisted manifesting the trapping of CO₂ in the clathrate cages.⁷ This confirmed that the photochemically produced CO₂ at 10 K is partitioned into the ASW matrix and the CH phase. In the current study, the formation of CH did not lead to a noticeable change in the O–H stretching band (Fig. S1, ESI†). This could be due to the following reasons. We observed in our earlier studies^{9,10,13} that the spectral features of O–H remained broad³⁵ even after CH formation. This may be due to the fact

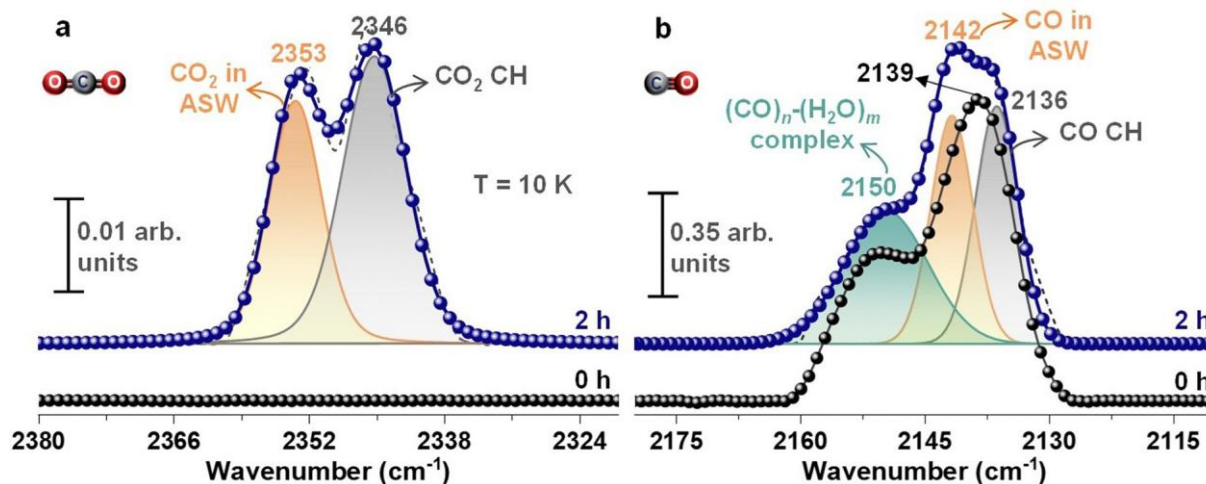


Fig. 2 RAIRS analysis of the formation of CO₂ and CO CH. RAIR spectra before (0 h, black curve) and after VUV irradiation (2 h, blue curve) of 100 ML H₂O–CO (7.72) mixture at 10 K in the (a) CQO antisymmetric stretching region of CO₂, and (b) CQO stretching region of CO. While the peak at 2346 cm⁻¹ in (a) arises due to the formation of CH of CO₂, the peak at 2136 cm⁻¹ in (b) is due to the formation of CH of CO at 10 K. The normalized RAIR spectrum (of 2 h) in (b) was deconvoluted to demonstrate the existence of different CO phases, namely, 2150 cm⁻¹ (CO–H₂O complexes), 2142 cm⁻¹ (pure CO), and 2136 cm⁻¹ (CO CH). For clarity, the spectra in (b) are normalized to 1 in absorbance.

that the CH is distributed in small domains across the ASW matrix, rather than forming an extended crystalline phase under UHV conditions. It should also be noted that UV irradiation causes amorphization of the ordered structure.³⁶

Moreover, in Fig. 2b at 0 h, there are two peaks at ν_{2150} and ν_{2139} cm^{-1} in the CQO stretching region of CO, which are attributed to hydrogen-bonded complexes of CO and H₂O as well as CO in the ASW matrix, respectively.^{37,38} Pure solid CO at 10 K shows an absorption peak at ν_{2142} cm^{-1} (Fig. S2, ESI†). In Fig. 2b, after 2 h of VUV irradiation, three peaks were observed at 2150 (broad), 2142, and 2136 cm^{-1} , which are attributed to CO H₂O complexes, pure CO ice, and CH of CO, respectively.^{37–39} The assignment to 2136 cm^{-1} peak as due to CH of CO is supported by previous infrared analysis.^{38,39} These studies suggested a redshift of ν_{2150} cm^{-1} for the absorption peak of CO within the CH cage, compared to pure CO. Thus, the photolysis of H₂O–CO mixture at 10 K under UHV led to not only the creation of new chemical compounds but also the formation of CH of CO and CO₂ within the ice matrix.

Further, TPD experiments were performed to confirm the formation of CHs of CO and CO₂. It has been shown that the trapped molecules, inside the pores, in CH cages or buried

inside the ASW matrix, desorb during amorphous-to-crystalline ice transition as well as during matrix sublimation.^{7,35,40–42} In our previous studies performed under similar conditions,^{7,11} we have seen an abrupt release of guest molecules, such as CO₂, CH₄, and C₂H₆ trapped in CH cages and from ice matrix during the amorphous-to-crystalline transition, in an event termed as a molecular volcano (MV).⁴³ Fig. 3a shows the desorption of CO ($m/z = 28$), CO₂ ($m/z = 44$), and H₂O ($m/z = 18$) from the photolyzed H₂O–CO (1.46) mixture obtained during 30 K min⁻¹ TPD experiment. The peaks marked *, \$, and # are attributed to the desorption of submonolayer CO, desorption of CO/CO₂ due to the structural transition in the ice matrix during annealing, and co-sublimation of CO/CO₂ along with water, respectively. The peaks at 25 and 38 K for CO (blue trace) correspond to the desorption of multilayer CO, and the desorption of CO that hydrogen bonded with H₂O (CO H₂O complexes), respectively. The peaks at 77 K for CO₂ (green trace) and at 155 K for H₂O (black trace) correspond to the desorption of multilayer CO₂, and sublimation of H₂O matrix, respectively. The inset in Fig. 3a shows a desorption peak at 140 K for CO and CO₂. The peak at 140 K corresponds to MV. Thus, the presence of MV peak for CO and CO₂ in TPD traces suggest the existence of

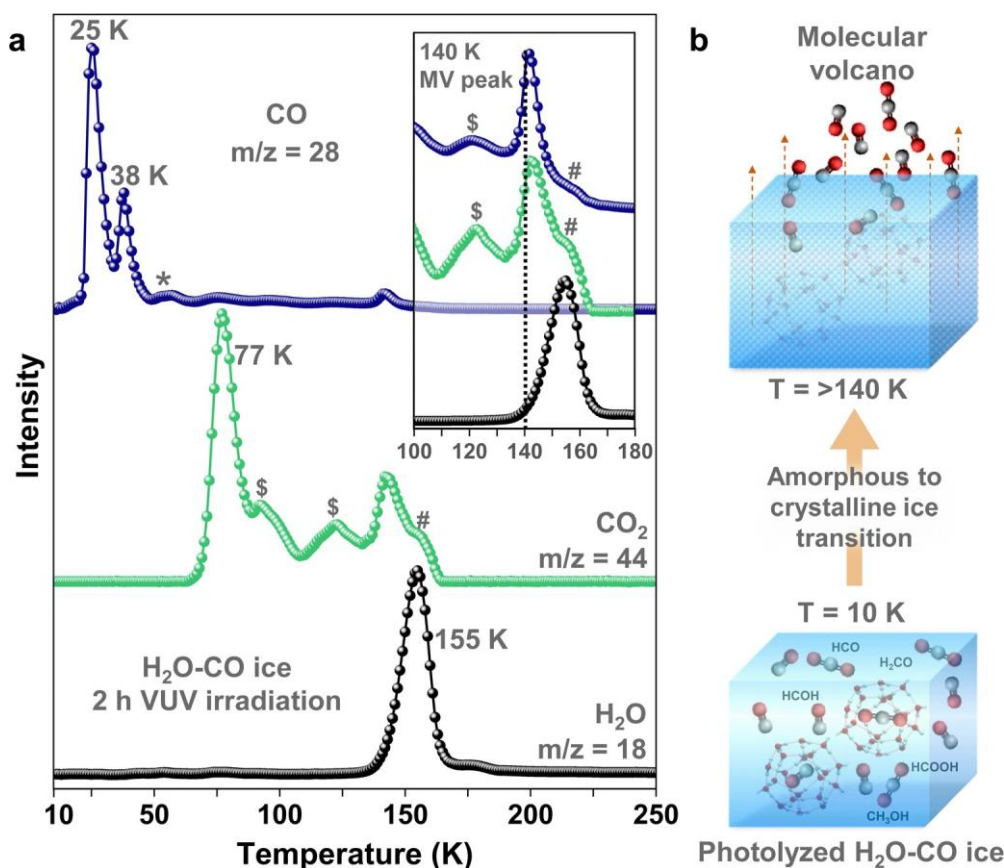


Fig. 3 TPD mass spectrometric analysis of photolyzed H₂O–CO mixture. (a) Desorption of CO, CO₂, and H₂O from photolyzed H₂O–CO mixture during 30 K min⁻¹ TPD experiment. For this, 100 ML of H₂O–CO (1.46) mixture was co-deposited on Ru(0001) substrate at 10 K, and the resulting sample was exposed to VUV irradiation for 2 h. After irradiation, the substrate was annealed at a rate of 30 K min⁻¹ to 250 K. The intensities of the $m/z = 28$ (CO), 44 (CO₂), and 18 (H₂O) were plotted as a function of substrate temperature. (b) Schematic illustration of the MV event during amorphous-to-crystalline ice transition above 140 K. To ensure clarity, only CO and CO₂ desorption events are shown.

their CHs in the ASW matrix.^{7,11,35,40,41} Fig. 3b schematically represents the MV event during the amorphous-to-crystalline transition of H₂O above 140 K. In conclusion, RAIRS (Fig. 2) and TPD-MS (Fig. 3) studies of the photolyzed H₂O–CO mixture confirm the presence of CHs of CO and CO₂ in the ASW matrix.

Furthermore, the extent of photochemically produced CO₂ partitioning at different temperatures and H₂O–CO compositions was examined with RAIRS, and results derived from these experiments are presented in Fig. 4a and b. We examined the effect of temperature by subjecting an H₂O–CO mixture (with an approximately fixed composition, H₂O to CO ratio of 7.93 0.19) to VUV irradiation for 4 h at 10, 20, and 30 K, and analyzed the resulting RAIR spectra. The spectral evolution of the dominant infrared peaks of CO (CQO stretching, 2180–2110 cm⁻¹) and CO₂ (CQO antisymmetric stretching, 2380–2320 cm⁻¹) are shown in Fig. S4a and b (ESI†). The integrated areas of these peaks are plotted as a function of irradiation time and the data are shown in Fig. S4c and d (ESI†). Fig. 4a is derived from Fig. S4d (ESI†) by normalizing the integrated band area of the 2380–2320 cm⁻¹ region (representing total CO₂ produced) with respect to 2346 cm⁻¹ (CO₂ in CH) and 2353 cm⁻¹ (CO₂ in ASW). Here, the area under the curve does not directly correlate with the column density for distinct phases of CO₂. The estimation of column density for the absorption bands at 2353 and 2346 cm⁻¹ was not feasible due to the uncertainty surrounding their respective band strengths. Fig. 4a suggests that the fraction of CO₂ CH

produced at 30 K after 0.5 h of VUV irradiation is larger than that produced at 10 and 20 K. The fraction of CO₂ CH produced at 10 and 20 K is almost equal. Notably, the initial fraction of CO in the H₂O–CO mixture was lower at 30 K, likely due to desorption of CO above 25 K (as shown in Fig. 3a). Further, we have extended our study to monitor the evolution of photochemically produced CH of CO₂ for longer VUV exposure of 4 h. We observed that, as the irradiation time increases (from 0.5 to 4 h), the fraction of CO₂ CH produced get reduced at all temperatures, as marked by the black arrow (Fig. 4a).

Similarly, we examined the effect of the H₂O–CO composition at 10 K using mixtures with different H₂O to CO ratios, 1.46, 4.09, and 7.72. The results derived from RAIRS study are presented in Fig. S5a–d (ESI†). Fig. 4b was derived from Fig. S5d (ESI†), as described above. The results in Fig. 4b indicate that after 0.5 h of irradiation, H₂O–CO mixtures with larger fractions of H₂O produce more CO₂ CH. Nevertheless, similar to Fig. 4a, with increasing irradiation time (from 0.5 to 4 h), the CO₂ trapped in CH decreased for all compositions as marked by the black arrow in Fig. 4b. In conclusion, the combined analysis of Fig. 4a and b revealed interesting trends. Higher temperatures and mixtures with larger H₂O fractions resulted in greater production of CO₂ CH after 0.5 h of photolysis. Moreover, in Fig. 4a and b, the overall decrease in the fraction of CO₂ CH (or increase in the fractions of CO₂ trapped in ASW) with irradiation time (from 0.5 to 4 h) can be attributed to the decomposition of CH structure, possibly by (i) exposure to VUV radiation,

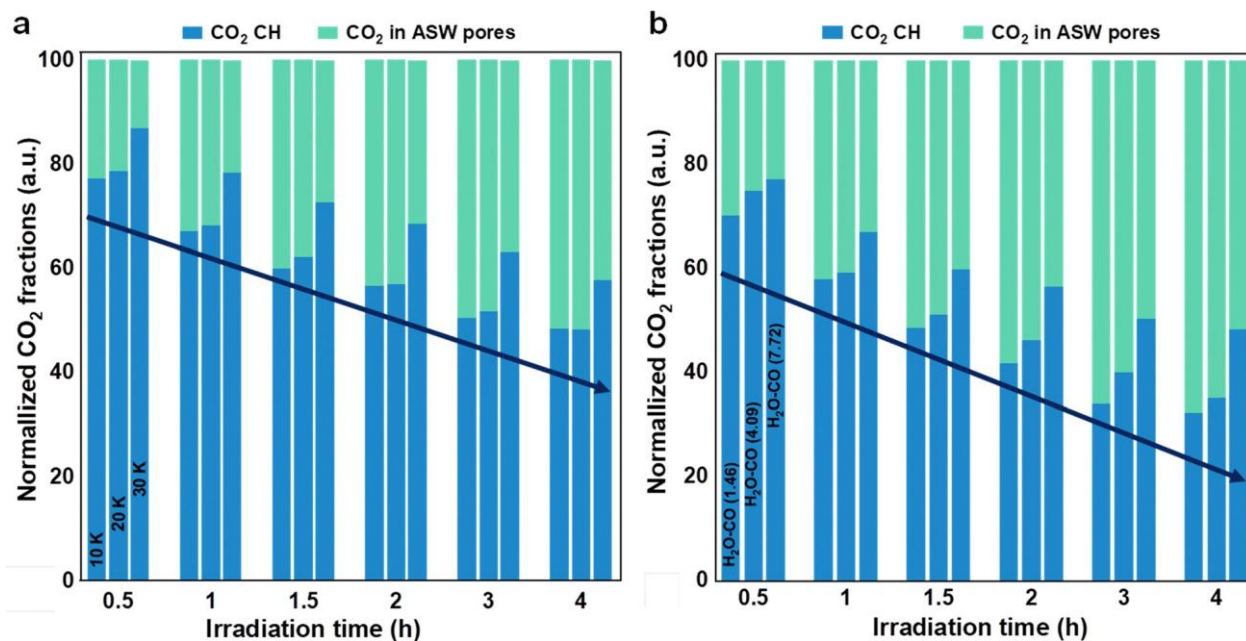


Fig. 4 Trends of photochemically produced CO₂ partitioning at different temperatures and H₂O–CO compositions. (a) Temperature-dependent partitioning of formed CO₂ with respect to VUV irradiation time. For each irradiation time, the first, second, and third columns represent the irradiation temperature, 10, 20, and 30 K, respectively. (b) Composition-dependent partitioning of the formed CO₂ with respect to VUV irradiation time. For each irradiation time, the first, second, and third columns represent the H₂O–CO composition of 1.46, 4.09, and 7.72, respectively. Here, shown is a stacked bar plot of the integrated band area of the photochemically partitioned CO₂ as a function of irradiation time. For this, band areas are derived from RAIRS data (Fig. S3b and S4b, ESI†) by deconvoluting the CQO antisymmetric stretching region of CO₂ (2380–2320 cm⁻¹). The fractions of the CO₂ CH phase, and CO₂ in ASW pores are shown by sky blue, and green, respectively. The decrease in the fraction of CO₂ CH with long VUV exposure time is marked by black arrows in (a) and (b). Fig. 4 has been modified as per the referee's suggestions.

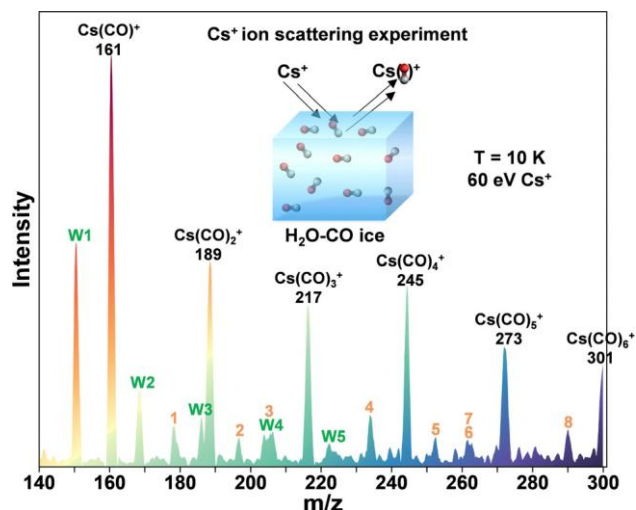


Fig. 5 Cs^+ ion scattering analysis of the surface of unirradiated $\text{H}_2\text{O}-\text{CO}$ (1.46) mixture. The mass spectrum of the unirradiated $\text{H}_2\text{O}-\text{CO}$ mixture was obtained by colliding the sample with 60 eV Cs^+ ions at 10 K. The peaks shown in the mass spectrum correspond to the adducts of Cs^+ ($m/z = 133$) with CO ($m/z = 28$), H_2O ($m/z = 18$), and $\text{CO}-\text{H}_2\text{O}$ complexes. The adducts of $\text{Cs}(\text{CO})_n^+$ are marked in the spectrum. The adducts of $\text{Cs}(\text{H}_2\text{O})_n^+$ are marked by W1–W5, where W1 = $\text{Cs}(\text{H}_2\text{O})_1^+$, and W5 = $\text{Cs}(\text{H}_2\text{O})_5^+$. The adducts of Cs^+ with $\text{CO}-\text{H}_2\text{O}$ complexes are marked as 1 ($m/z = 179$, $(\text{CO}-\text{H}_2\text{O})$), 2 ($m/z = 197$, $\text{CO}(\text{H}_2\text{O})_2$), 3 ($m/z = 207$, $\text{H}_2\text{O}(\text{CO})$), 4 ($m/z = 235$, $\text{H}_2\text{O}(\text{CO})_3$), 5 ($m/z = 253$, $(\text{H}_2\text{O})_2(\text{CO})_3$), 6 ($m/z = 261$, $(\text{CO})_2(\text{H}_2\text{O})_4$), 7 ($m/z = 263$, $\text{H}_2\text{O}(\text{CO})_4$) and 8 ($m/z = 291$, $\text{H}_2\text{O}(\text{CO})_5$). Inset illustrates a schematic representation of the Cs^+ ion scattering experiment.

and (ii) interactions of the photoproducts with H_2O of the CH structure. The CO_2 released after CH decomposition will migrate to the ASW matrix, increasing the CO_2 fraction in the ASW phase.⁸

During VUV irradiation, pure CO ice does not photodissociate (Fig. S2, ESI†). However, when mixed with H_2O , it resulted in several photochemical products^{29,30} as presented in Fig. S1 (ESI†). We considered it important to investigate the structural characteristics of $\text{H}_2\text{O}-\text{CO}$ ice at 10 K using highly surface-sensitive Cs^+ -based secondary ion mass spectrometry.⁴⁴ The result obtained from the Cs^+ ($m/z = 133$) ion scattering experiment, by colliding the unirradiated $\text{H}_2\text{O}-\text{CO}$ ice surface with 60 eV Cs^+ ions at 10 K, is shown in Fig. 5. The result shows that apart from the existence of intra-clusters of H_2O (W1–W5, where W1 = $\text{Cs}(\text{H}_2\text{O})_1^+$, and W5 = $\text{Cs}(\text{H}_2\text{O})_5^+$) and (CO ($\text{Cs}(\text{CO})_1^+$, to $\text{Cs}(\text{CO})_6^+$)) there exist a variety of inter-clusters of CO with H_2O as well, as marked by 1–8. For instance, 1 = $\text{Cs}(\text{CO}-\text{H}_2\text{O})^+$, 2 = $\text{Cs}(\text{CO}(\text{H}_2\text{O})_2)^+$, 3 = $\text{Cs}(\text{H}_2\text{O}(\text{CO})_2)^+$, 4 = $\text{Cs}(\text{H}_2\text{O}(\text{CO})_3)^+$, 5 = $\text{Cs}((\text{H}_2\text{O})_2(\text{CO})_3)^+$, 6 = $\text{Cs}((\text{CO})_2(\text{H}_2\text{O})_4)^+$, 7 = $\text{Cs}(\text{H}_2\text{O}(\text{CO})_4)^+$ and 8 = $\text{Cs}(\text{H}_2\text{O}(\text{CO})_5)^+$. The RAIR spectrum of the unirradiated $\text{H}_2\text{O}-\text{CO}$ mixture presented in Fig. 2b shows a broad peak at $\approx 2150 \text{ cm}^{-1}$ in the CQO stretching of CO . In previous infrared studies,^{37,38,45,46} the peak was assigned to the existence of complex of CO and H_2O , $(\text{CO})_n-(\text{H}_2\text{O})_m$ as 1 : 1 complex. Several other experimental and theoretical simulations have studied the 1 : 1 $\text{CO}-\text{H}_2\text{O}$ complex in detail.^{46–48} However, complexes of $(\text{CO})_n-(\text{H}_2\text{O})_m$ with $n, m \geq 1$ have not been observed yet. In the current work, the complexes of $(\text{CO})_n-(\text{H}_2\text{O})_m$ with varying n

and m have been detected for the first time, at the surface of $\text{H}_2\text{O}-\text{CO}$ mixture at 10 K, owing to the high sensitivity of the ion pickup by Cs^+ ion scattering method. Ishibashi *et al.* revealed that the sensitivity of the Cs^+ -based ion pickup approach in identifying extremely low abundant species on the ice surface is 100 times greater than that of FTIR, even for infrared-active molecules.⁴⁹ Thus, Fig. 5 presents a clear picture of the complexes formed on the surface of mixed $\text{H}_2\text{O}-\text{CO}$ ice at 10 K. Furthermore, experimental and computational investigations are necessary to determine the precise structure and geometry of such $(\text{CO})_n-(\text{H}_2\text{O})_m$ complexes. Additionally, the photoproducts observed by RAIRS were further confirmed by performing Cs^+ ion scattering experiment on photolyzed $\text{H}_2\text{O}-\text{CO}$ mixture as presented in Fig. S6 (ESI†).

While we have known the existence of CHs of stable molecules in the ISM,^{6,7} the present study introduces a new possibility where the reaction products themselves can be incorporated into CH cages. Also, there is a great possibility of conversion of one guest molecule to another inside clathrate cages upon VUV irradiation. This could be a very exciting and unique experiment to be carried out in similar systems. Given that photochemistry can generate a wide range of species, this research presents the potential for various CH phases to exist in the ISM, albeit at potentially low concentrations. Furthermore, it suggests the possibility of enhanced thermodynamic stability for photochemical reaction products, which may serve as an additional factor facilitating the overall reaction. Although the diversity and feasibility of CH phases under astrophysical conditions are already recognized, this study proposes an expanded range and increased feasibility of CHs in the interstellar medium.

Complex organic molecules such as methanol,^{14,50,51} tetrahydrofuran,^{8,12,33} and smaller ethers are known to catalyze/stabilize the formation of mixtures of nonstoichiometric CHs and this aspect has been studied experimentally as well as computationally. Therefore, small amounts of methanol formed upon photoirradiation may catalyze and stabilize the formation of CHs of CO_2 and CO . CHs of many molecules in icy planets, comets, and other extraterrestrial bodies may arise through such photochemical pathways.

Conclusions

This study suggests that the molecules formed during photochemical reactions can be trapped within CH cages even at 10 K under UHV conditions. UV photolysis is known to induce various physicochemical changes in the ice matrix, and in this study, we observed highly unusual and unique events of CH formation. These observations may likely be attributed to three factors: (1) UV light is known to heat the ice upon irradiation, (2) photochemically produced CH_3OH can act as a catalyst for CH formation, as reported in numerous studies, and (3) the photodesorption of CO , CO_2 , and other species can increase the mobility of both the host and the guest molecules, which is essential for CH formation. The impact of temperature and

composition of ice mixture on such processes has been demonstrated. Trapping small molecules, radicals, and reactive species, even as they are generated through photon irradiation, holds direct significance in the context of cometary and interstellar ices. While our experiment proves the confinement of photochemical products in CH cages, the dynamics of various events leading to such cages at 10 K need additional investigations. Photochemical studies of ice mixtures can expand the diversity of CHs in interstellar environments.

Author contributions

T. P. and G. V. designed the research. G. V. and B. K. M. have performed the experiments. T. P. supervised its progress. G. V., B. K. M., R. K., and T. P. have analyzed the results. The first draft of the manuscript was written by G. V. The final version of manuscript was prepared including the contributions of all authors.

Conflicts of interest

The authors declare no competing financial interests.

Acknowledgements

We acknowledge the Science and Engineering Research Board (SERB), Department of Science and Technology (DST), Government of India for research funding. T. P. and R. K. acknowledge funding from the Centre of Excellence on Molecular Materials and Functions under the Institution of Eminence scheme of IIT Madras. G. V. thanks IITM for his research fellowships. B. K. M. thanks the Council of Scientific & Industrial Research (CSIR) for his research fellowship.

References

- R. A. Baragiola, Water ice on outer solar system surfaces: Basic properties and radiation effects, *Planet. Space Sci.*, 2003, 51, 953–961.
- M. S. Westley, R. A. Baragiola, R. E. Johnson and G. A. Barattat, *Nature*, 1995, 373, 405–407.
- R. E. Johnson and T. I. Quickenden, Photolysis and radiolysis of water ice on outer solar system bodies, *J. Geophys. Res.: Planets*, 1997, 102, 10985–10996.
- E. D. Sloan Jr. and C. A. Koh, *Clathrate Hydrates of Natural Gases*, CRC Press, 2007.
- E. D. Sloan, Fundamental principles and applications of natural gas hydrates, *Nature*, 2003, 426, 353–359.
- J. Ghosh, G. Vishwakarma, R. Kumar and T. Pradeep, Formation and Transformation of Clathrate Hydrates under Interstellar Conditions, *Acc. Chem. Res.*, 2023, 56, 2241–2252.
- J. Ghosh, R. R. J. Methikkalam, R. G. Bhuiin, G. Ragupathy, N. Choudhary, R. Kumar and T. Pradeep, Clathrate hydrates in interstellar environment, *Proc. Natl. Acad. Sci. U. S. A.*, 2019, 116, 1526–1531.
- G. Vishwakarma, B. K. Malla, K. S. S. V. P. Reddy, J. Ghosh, S. Chowdhury, S. S. R. K. C. Yamijala, S. K. Reddy, R. Kumar and T. Pradeep, Induced Migration of CO₂ from Hydrate Cages to Amorphous Solid Water under Ultrahigh Vacuum and Cryogenic Conditions, *J. Phys. Chem. Lett.*, 2023, 14, 2823–2829.
- J. Ghosh, R. G. Bhuiin, G. Vishwakarma and T. Pradeep, Formation of Cubic Ice via Clathrate Hydrate, Prepared in Ultrahigh Vacuum under Cryogenic Conditions, *J. Phys. Chem. Lett.*, 2020, 11, 26–32.
- J. Ghosh, G. Vishwakarma, S. Das and T. Pradeep, Facile Crystallization of Ice I_h via Formaldehyde Hydrate in Ultrahigh Vacuum under Cryogenic Conditions, *J. Phys. Chem. C*, 2021, 125, 4532–4539.
- B. K. Malla, G. Vishwakarma, S. Chowdhury, P. Selvarajan and T. Pradeep, Formation of Ethane Clathrate Hydrate in Ultrahigh Vacuum by Thermal Annealing, *J. Phys. Chem. C*, 2022, 126, 17983–17989.
- J. Ghosh, R. G. Bhuiin, G. Ragupathy and T. Pradeep, Spontaneous Formation of Tetrahydrofuran Hydrate in Ultrahigh Vacuum, *J. Phys. Chem. C*, 2019, 123, 16300–16307.
- G. Vishwakarma, B. K. Malla, S. Chowdhury, S. P. Khandare and T. Pradeep, Existence of Acetaldehyde Clathrate Hydrate and Its Dissociation Leading to Cubic Ice under Ultrahigh Vacuum and Cryogenic Conditions, *J. Phys. Chem. Lett.*, 2023, 14, 5328–5334.
- D. Blake, L. Allamandola, S. Sandford, D. Hudgins, D. Blake, L. Allamandola, S. Sandford, D. Hudgins and F. Freund, Clathrate Hydrate Formation in Amorphous Cometary Ice Analogs in Vacuo, *Science*, 1991, 254, 548–551.
- R. P. C. Bauer, A. Ravichandran, J. S. Tse, N. Appathurai, G. King, B. Moreno, S. Desgreniers and R. Sammynaiken, In Situ X-Ray Diffraction Study on Hydrate Formation at Low Temperature in a High Vacuum, *J. Phys. Chem. C*, 2021, 125, 26892–26900.
- M. Choukroun, T. H. Vu and E. C. Fayolle, No compelling evidence for clathrate hydrate formation under interstellar medium conditions over laboratory time scales, *Proc. Natl. Acad. Sci. U. S. A.*, 2019, 116, 14407–14408.
- J. Ghosh, R. R. J. Methikkalam, R. G. Bhuiin, G. Ragupathy, N. Choudhary, R. Kumar and T. Pradeep, *Proc. Natl. Acad. Sci. U. S. A.*, 2019, 116, 14409–14410.
- J. Shi, U. Raut, J. H. Kim, M. Loeffler and R. A. Baragiola, Ultraviolet photon-induced synthesis and trapping of H₂O₂ and O₃ in porous water ice films in the presence of ambient O₂: Implications for extraterrestrial ice, *Astrophys. J., Lett.*, 2011, 738, L3.
- D. A. Bahr, M. Famá, R. A. Vidal and R. A. Baragiola, Radiolysis of water ice in the outer solar system: Sputtering and trapping of radiation products, *J. Geophys. Res.*, 2001, 106, 33285–33290.
- F. Fleyfel and J. P. Devlin, FT-IR spectra of 90 K films of simple, mixed, and double clathrate hydrates of trimethylene oxide, methyl chloride, carbon dioxide, tetrahydrofuran, and ethylene oxide containing decoupled D₂O, *J. Phys. Chem.*, 1988, 92, 631–635.

- 21 P. Goldberg, Free radicals and reactive molecules in clathrate cavities, *Science*, 1963, 142, 378–379.
- 22 A. C. Cheung, D. M. Rank, C. H. Townes, D. D. Thornton and W. J. Welch, Detection of water in interstellar regions by its microwave radiation, *Nature*, 1969, 221, 626–628.
- 23 R. W. Wilson, K. B. Jefferts and A. A. Penzias, Carbon Monoxide in the Orion Nebula, *Astrophys. J.*, 1970, 161, L43.
- 24 S. Bag, R. G. Bhuiin, R. R. J. Methikkalam, T. Pradeep, L. Kephart, J. Walker, K. Kuchta, D. Martin and J. Wei, Development of ultralow energy (1–10 eV) ion scattering spectrometry coupled with reflection absorption infrared spectroscopy and temperature programmed desorption for the investigation of molecular solids, *Rev. Sci. Instrum.*, 2014, 85, 014103.
- 25 L. J. Allamandola, S. A. Sandford and G. J. Valero, Photochemical and thermal evolution of interstellar/precometary ice analogs, *Icarus*, 1988, 76, 225–252.
- 26 A. Schriver, J. M. Coanga, L. Schriver-Mazzuoli and P. Ehrenfreund, FTIR studies of ultraviolet photodissociation at 10 K of dimethyl-ether in argon and nitrogen matrices, in the solid phase and in amorphous water ice, *Chem. Phys. Lett.*, 2004, 386, 377–383.
- 27 G. Leto and G. A. Baratta, Ly- α photon induced amorphization of Ic water ice at 16 Kelvin. Effects and quantitative comparison with ion irradiation, *Astron. Astrophys.*, 2003, 397, 7–13.
- 28 N. Watanabe, O. Mouri, A. Nagaoka, T. Chigai, A. Kouchi and V. Pironello, Laboratory Simulation of Competition between Hydrogenation and Photolysis in the Chemical Evolution of H₂O–CO Ice Mixtures, *Astrophys. J.*, 2007, 668, 1001–1011.
- 29 H. Okabe, *Photochemistry of small molecules*, Wiley, New York, 1978, vol. 431.
- 30 H. Cottin, M. H. Moore and Y. Benilan, Photodestruction of Relevant Interstellar Molecules in Ice Mixtures, *Astrophys. J.*, 2003, 590, 874–881.
- 31 P. A. Gerakines, W. A. Schutte and P. Ehrenfreund, Ultraviolet processing of interstellar ice analogs. I. Pure ices, *Astron. Astrophys.*, 1996, 312, 289–305.
- 32 D. W. Davidson, Y. P. Handa, C. I. Ratcliffe, J. A. Ripmeester, J. S. Tse, J. R. Dahn, F. Lee and L. D. Calvert, Crystallographic Studies of Clathrate Hydrates. Part I, *Mol. Cryst. Liq. Cryst.*, 1986, 141, 141–149.
- 33 F. Fleyfel and J. P. Devlin, Carbon dioxide clathrate hydrate epitaxial growth: spectroscopic evidence for formation of the simple type-II carbon dioxide hydrate, *J. Phys. Chem.*, 1991, 95, 3811–3815.
- 34 R. Kumar, S. Lang, P. Englezos and J. Ripmeester, Application of the ATR-IR Spectroscopic Technique to the Characterization of Hydrates Formed by CO₂, CO₂/H₂ and CO₂/H₂/C₃H₈, *J. Phys. Chem. A*, 2009, 113, 6308–6313.
- 35 R. Netsu and T. Ikeda-Fukazawa, Formation of carbon dioxide clathrate hydrate from amorphous ice with warming, *Chem. Phys. Lett.*, 2019, 716, 22–27.
- 36 A. Kouchi and T. Kuroda, Amorphization of cubic ice by ultraviolet irradiation, *Nature*, 1990, 344, 134–135.
- 37 B. Schmitt, J. M. Greenberg and R. J. A. Grim, The temperature dependence of the CO infrared band strength in CO:H₂O ices, *Astrophys. J.*, 1989, 340, L33–L36.
- 38 E. Dartois, CO clathrate hydrate: Near to mid-IR spectroscopic signatures, *Icarus*, 2011, 212, 950–956.
- 39 L. Cwiklik and J. P. Devlin, Hindering of rotational motion of guest molecules in the Type I clathrate hydrate, *Chem. Phys. Lett.*, 2010, 494, 206–212.
- 40 S. Malyk, G. Kumi, H. Reisler and C. Wittig, Trapping and Release of CO₂ Guest Molecules by Amorphous Ice, *J. Phys. Chem. A*, 2007, 111, 13365–13370.
- 41 A. Bar-Nun, D. Prialnik, D. Laufer and E. Kochavi, Trapping of gases by water ice and implications for icy bodies, *Icarus*, 1985, 63, 317–332.
- 42 G. Natesco and A. Bar-Nun, The Effect of Methanol Clathrate-Hydrate Formation and Other Gas-Trapping Mechanisms on the Structure and Dynamics of Cometary Ices, *Icarus*, 2000, 148, 456–463.
- 43 R. S. Smith, C. Huang, E. K. L. Wong and B. D. Kay, The molecular volcano: Abrupt CCl₄ desorption driven by the crystallization of amorphous solid water, *Phys. Rev. Lett.*, 1997, 79, 909–912.
- 44 Y. Kim, E. S. Moon, S. Shin and H. Kang, Acidic water monolayer on ruthenium(0001), *Angew. Chem., Int. Ed.*, 2012, 51, 12806–12809.
- 45 M. D. Brookes and A. R. W. McKellar, Infrared spectrum of the water-carbon monoxide complex in the CO stretching region, *J. Chem. Phys.*, 1998, 109, 5823–5829.
- 46 A. J. Barclay, A. Van Der Avoird, A. R. W. McKellar and N. Moazzen-Ahmadi, The water-carbon monoxide dimer: New infrared spectra, *ab initio* rovibrational energy level calculations, and an interesting in-termolecular mode, *Phys. Chem. Chem. Phys.*, 2019, 21, 14911–14922.
- 47 D. Yaron, K. I. Peterson, D. Zolanz, W. Klemperer, F. J. Lovas and R. D. Suenram, Water hydrogen bonding: The structure of the water-carbon monoxide complex, *J. Chem. Phys.*, 1990, 92, 7095–7109.
- 48 Y. N. Kalugina, A. Faure, A. Van Der Avoird, K. Walker and F. Lique, Interaction of H₂O with CO: Potential energy surface, bound states and scattering calculations, *Phys. Chem. Chem. Phys.*, 2018, 20, 5469–5477.
- 49 A. Ishibashi, H. Hidaka, Y. Oba, A. Kouchi and N. Watanabe, Efficient Formation Pathway of Methyl Formate: The Role of OH Radicals on Ice Dust, *Astrophys. J., Lett.*, 2021, 921, L13.
- 50 K. Shin, K. A. Udachin, I. L. Moudrakovski, D. M. Leek, S. Alavi, C. I. Ratcliffe and J. A. Ripmeester, Methanol incorporation in clathrate hydrates and the implications for oil and gas pipeline flow assurance and icy planetary bodies, *Proc. Natl. Acad. Sci. U. S. A.*, 2013, 110, 8437–8442.
- 51 J. P. Devlin, Catalytic activity of methanol in all-vapor subsecond clathrate-hydrate formation, *J. Chem. Phys.*, 2014, 140, 164505–164510.

Supplementary Information

Partitioning Photochemically Formed CO₂ into Clathrate Hydrate under Interstellar Conditions

Gaurav Vishwakarma¹, Bijesh K. Malla¹, Rajnish Kumar^{2,3}, and Thalappil Pradeep^{1,3*}*

¹DST Unit of Nanoscience (DST UNS) and Thematic Unit of Excellence (TUE), Department of Chemistry, Indian Institute of Technology Madras, Chennai 600036, India.

²Department of Chemical Engineering, Indian Institute of Technology Madras, Chennai 600036, India.

³International Centre for Clean Water, IIT Madras Research Park, Chennai 600113, India.

Corresponding authors

***Email:** pradeep@iitm.ac.in, rajnish@iitm.ac.in

This pdf file includes:

Fig S1 to S6 (pages S2-S8)

Table S1 (page S3)

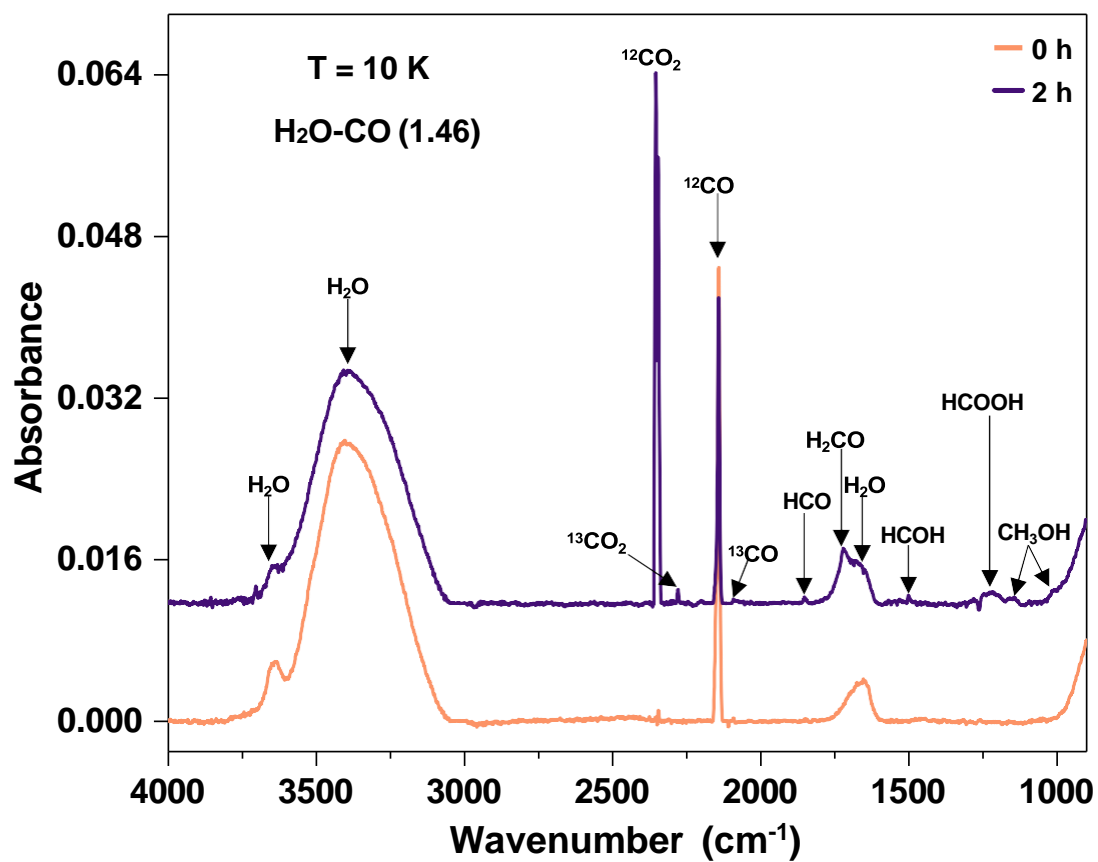


Fig. S1. Full range RAIR spectra of 100 ML $\text{H}_2\text{O-CO}$ (1.46) mixture before and after VUV irradiation at 10 K. The ice mixture was co-deposited on Ru(0001) at 10 K, and the resulting sample was exposed to VUV irradiation for 2 h.

Table S1. Photochemical products obtained during 2 h of VUV irradiation of 100 ML H₂O-CO (1.46) mixture at 10 K

Position (cm⁻¹)	Vibrational Mode	Molecule
~3704	Combination	CO ₂
~3648	OH dangling	H ₂ O
~3400	OH stretch	H ₂ O
2353, 2346	¹² CO stretch	CO ₂
2282, 2278	¹³ CO stretch	¹³ CO ₂
2149, 2141	¹² CO stretch	CO
2092	¹³ CO stretch	¹³ CO
1850	CO stretch	HCO
1721	CO stretch	H ₂ CO
~1650	HOH bending	H ₂ O
1500	H ₂ scissor	H ₂ CO
1219	C-O stretch	HCOOH
1140	CH ₃ rocking	CH ₃ OH
1017	C-O stretch	CH ₃ OH

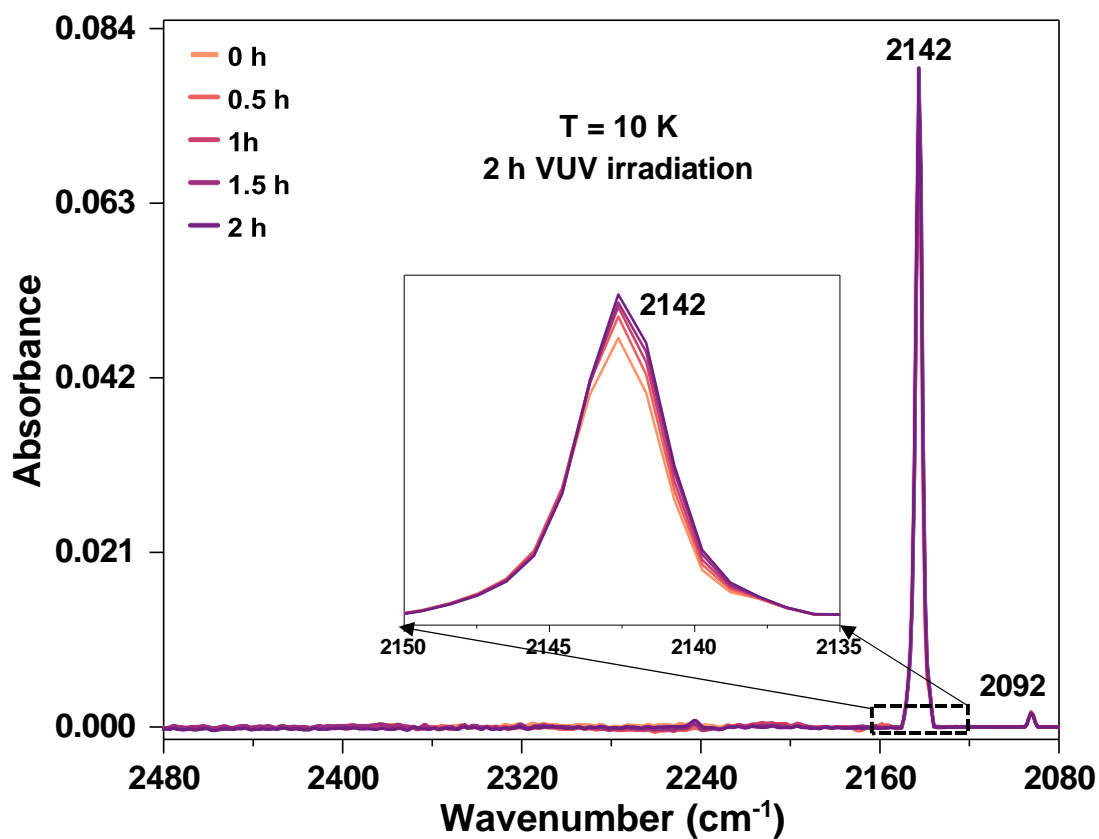


Fig. S2. Irradiation time-dependent RAIR spectra of 50 ML pure CO ice at 10 K in the 2480-2080 cm^{-1} region. Before VUV irradiation, a peak at 2142 cm^{-1} was observed for pure CO ice. During irradiation, we could not observe a decrease in the intensity of the peak at 2142 cm^{-1} ; instead, a very small increase was observed, as presented in inset. This may be due to the background deposition of CO on the ice sample with time or physical changes induced by

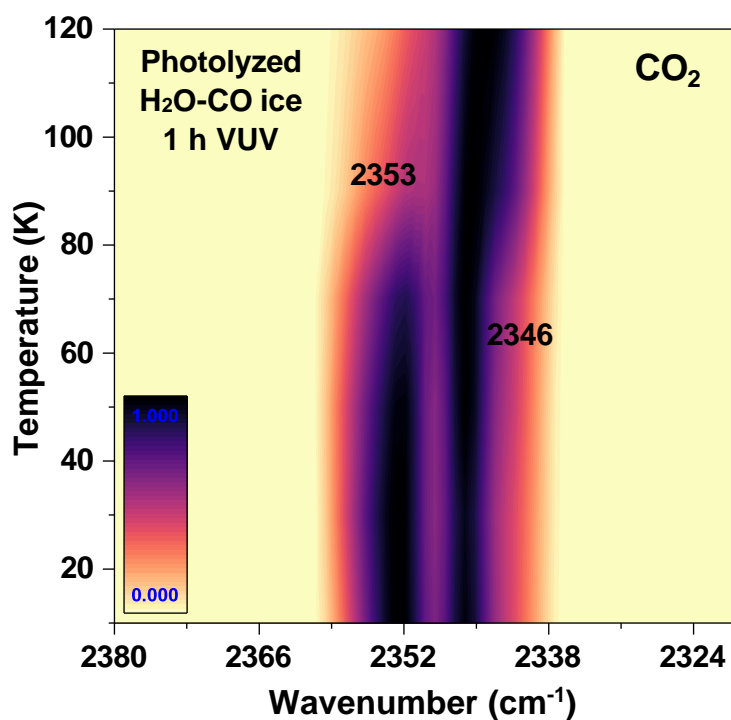


Fig. S3. Temperature-dependent normalized RAIR spectra of photolyzed 50 ML H₂O-CO (~4) ice in the 10–120 K window in the C=O antisymmetric stretching region of CO₂. The ice sample was prepared by co-depositing H₂O and CO vapors on Ru(0001) at 10 K. The as-prepared ice sample was photolyzed by VUV for 1 h. After photolysis at 10 K, the ice sample was heated at a rate of 5 K min⁻¹ to 120 K, and RAIR spectra were collected at regular intervals. When the sample was heated beyond the desorption temperature of CO₂, around 90 K, the peak at 2353 cm⁻¹ disappeared, while the peak at 2346 cm⁻¹ persisted. This confirms our identification of the 2353 cm⁻¹ peak as CO₂ trapped within the water matrix and the 2346 cm⁻¹ peak as CO₂ confined inside the CH cage (5¹² cage of sI).

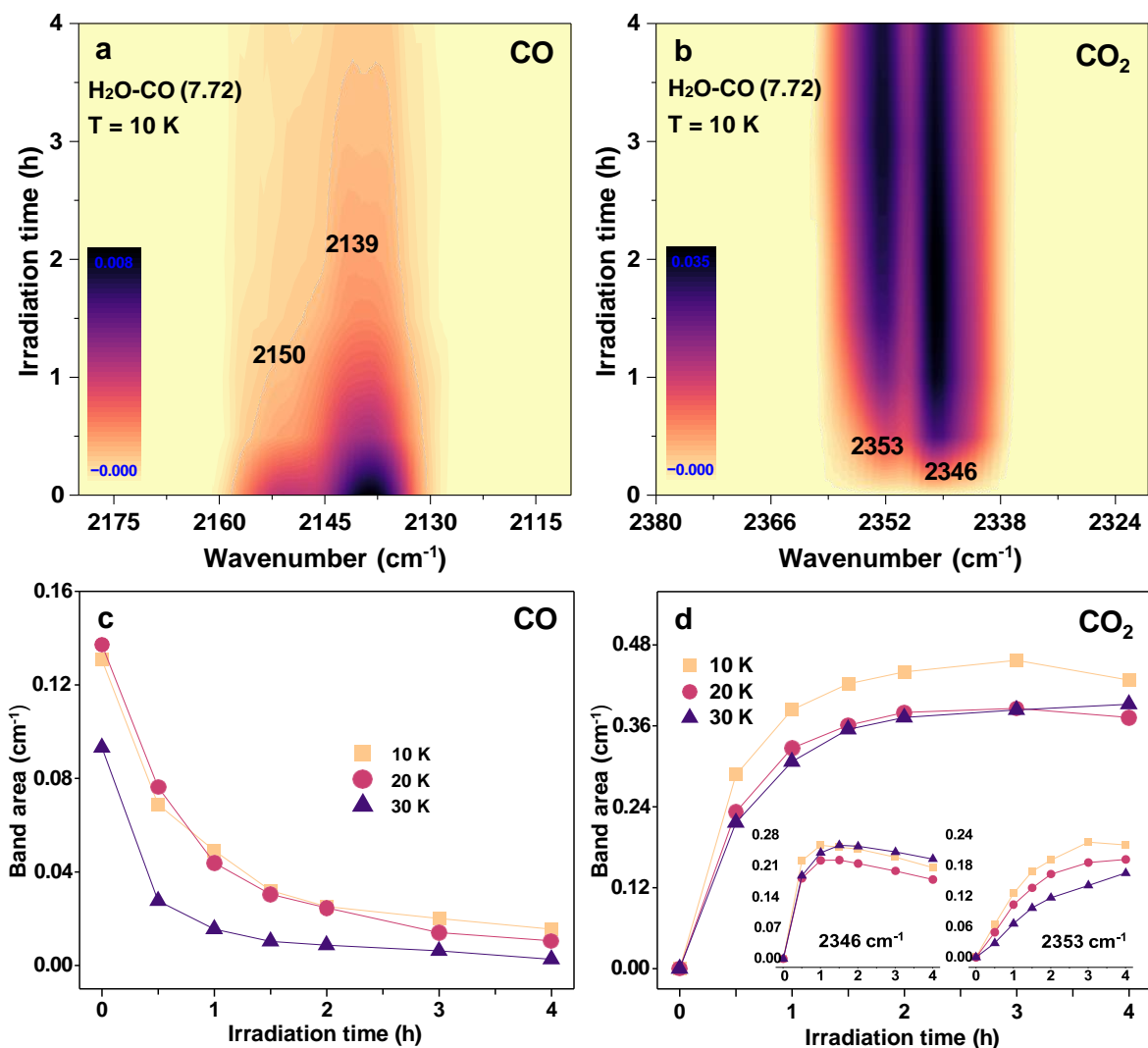


Fig. S4. Irradiation time-dependent RAIR spectra of 100 ML H₂O-CO (7.72) mixture at 10 K in the (a) C=O stretching region of CO and (b) C=O antisymmetric stretching region of CO₂. (c) Evolution of C=O stretching region of CO during VUV irradiation of H₂O-CO mixture. Integrated area of the 2180-2110 cm⁻¹ band was plotted as a function of irradiation time for experiments carried out at 10 (yellow square), 20 (red circle), and 30 K (blue triangle). (d) Evolution of C=O antisymmetric stretching region of CO₂ during VUV irradiation of H₂O-CO mixture. Integrated area of the 2380-2320 cm⁻¹ band was plotted as a function of irradiation time for experiments carried out at 10 (yellow square), 20 (red circle), and 30 K (blue triangle). Inset plots show the evolution of 2346 cm⁻¹ (CO₂ in CH phase) and 2353 cm⁻¹ (CO₂ in ASW phase) bands as a function of irradiation time, derived by deconvoluting the 2380-2320 cm⁻¹ band. In Figs. (c) and (d), lines are only to guide the eye.

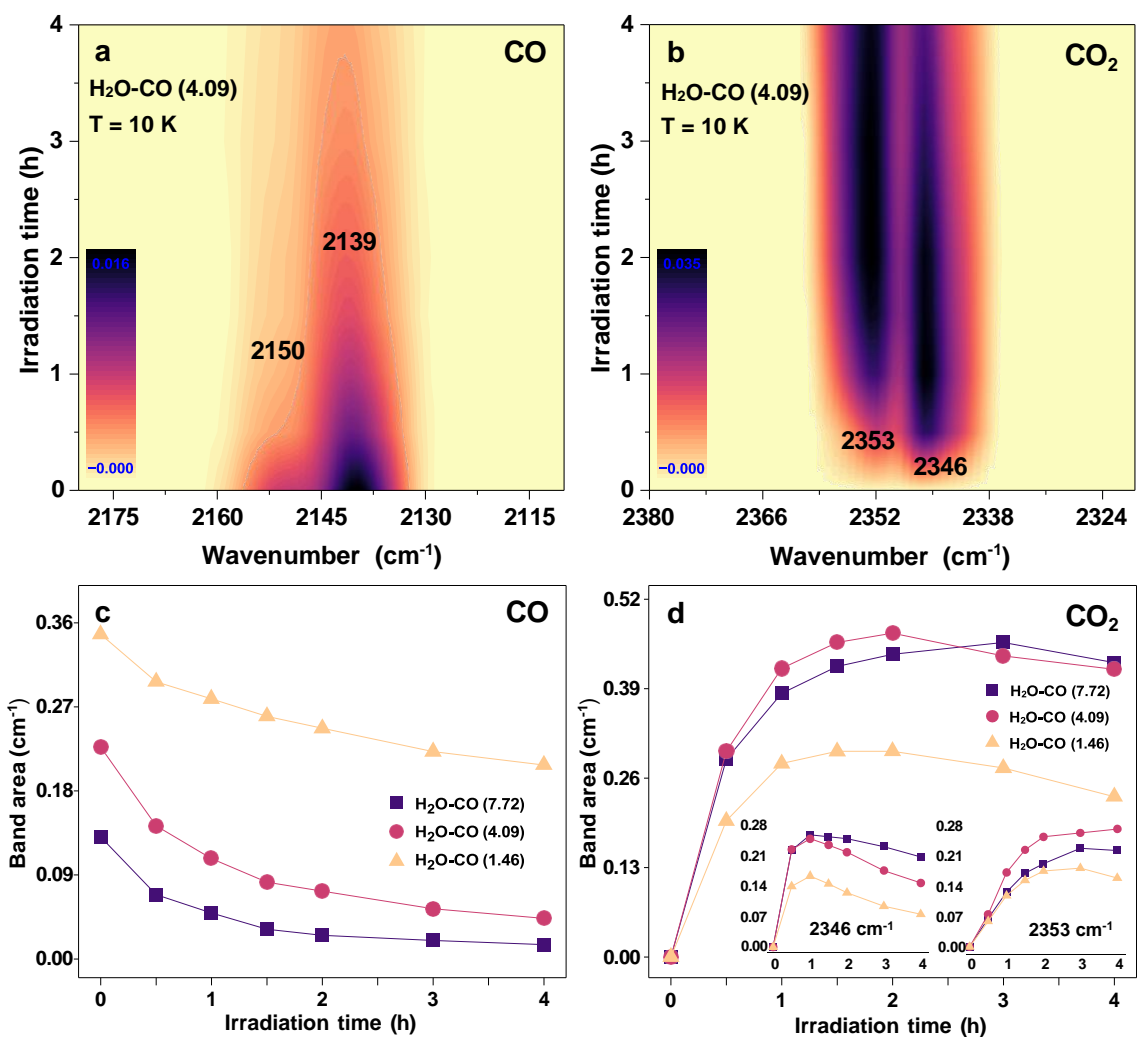


Fig. S5. Irradiation time-dependent RAIR spectra of 100 ML H₂O-CO (4.09) mixture at 10 K in the (a) C=O stretching region of CO and (b) C=O antisymmetric stretching region of CO₂. (c) Evolution of C=O stretching region of CO during VUV irradiation of H₂O-CO mixture. Integrated area of the 2180-2110 cm⁻¹ band was plotted as a function of irradiation time for experiments carried out with ice mixtures having H₂O to CO ratios, 1.46 (yellow triangle), 4.09 (red circle), and 7.72 (blue square). (d) Evolution of C=O antisymmetric stretching region of CO₂ during VUV irradiation of H₂O-CO mixture. Integrated area of the 2380-2320 cm⁻¹ band was plotted as a function of irradiation time for experiments carried out with ice mixtures having H₂O to CO ratios, 1.46 (yellow triangle), 4.09 (red circle), and 7.72 (blue square). Inset plots show the evolution of 2346 cm⁻¹ (CO₂ in CH phase) and 2353 cm⁻¹ (CO₂ in ASW phase) bands as a function of irradiation time, derived by deconvoluting the 2380-2320 cm⁻¹ band. In Figs. (c) and (d), lines are only to guide the eye.

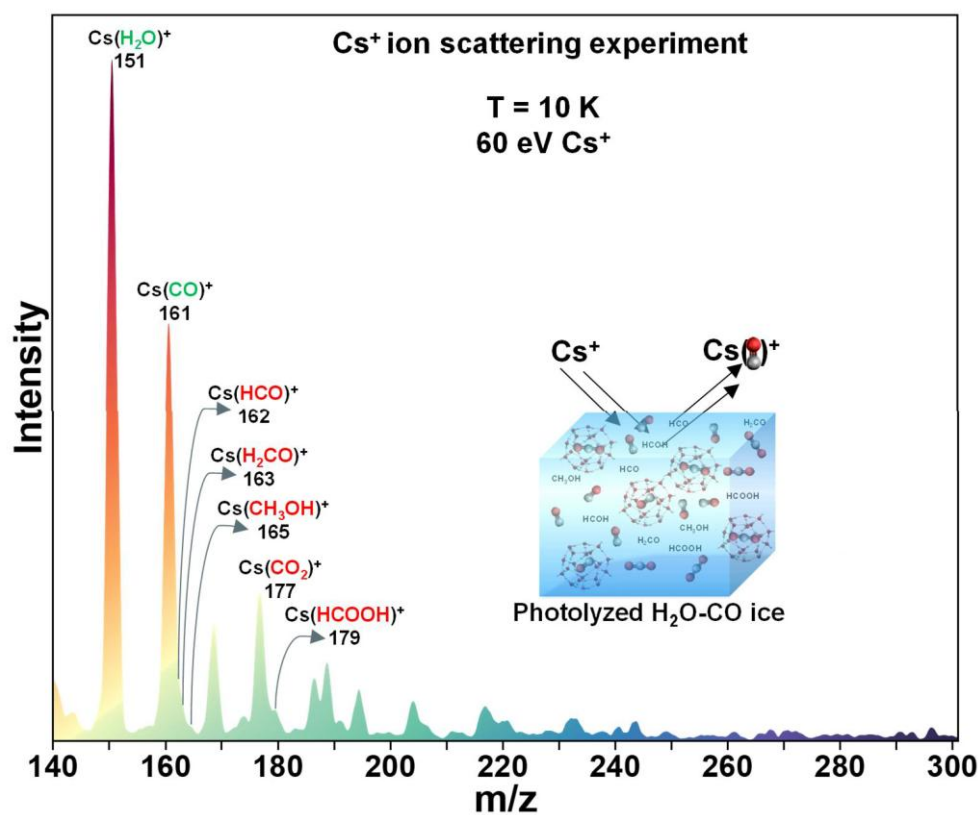


Fig. S6. Surface structure of photolyzed H₂O-CO mixture obtained from Cs⁺ ion scattering experiment. The mass spectrum of the irradiated H₂O-CO mixture was obtained by colliding the sample with 60 eV Cs⁺ ions at 10 K. The peaks marked in the mass spectrum correspond to the adducts of Cs⁺ ($m/z = 133$) with H₂O ($m/z = 151$), CO ($m/z = 161$), HCO ($m/z = 162$), H₂CO ($m/z = 163$), CH₃OH ($m/z = 165$), HCOOH ($m/z = 179$). For clarity, the remaining peaks were not assigned. Inset illustrates a schematic representation of the Cs⁺ ion scattering experiment.

Extensive Polymerization of Atomically Precise Alloy Metal Clusters During Solid-State Reactions

Published as part of *Langmuir virtual special issue* “2023 Pioneers in Applied and Fundamental Interfacial Chemistry: Santanu Bhattacharya”.

B. S. Sooraj,^{||} Jayoti Roy,^{||} Manish Mukherjee, Anagha Jose, and Thalappil Pradeep^{*}



Cite This: *Langmuir* 2024, 40, 15244–15251



Read Online

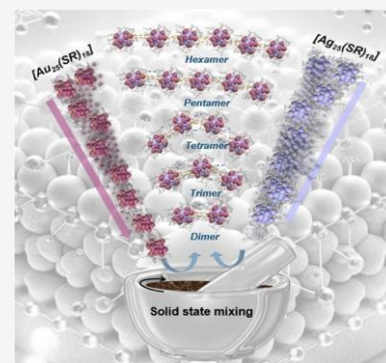
ACCESS

Metrics & More

Article Recommendations

Supporting Information

ABSTRACT: Exploring the reactions between atomically precise metal clusters and the consequences of such reactions has been an exciting field of research during the past decade. Initial studies in the area were on reactions between clusters in the solution phase, which proceed through the formation of dimers of reacting clusters. In the present work, we examine the interaction between two atomically precise clusters, $[\text{Au}_{25}(\text{PET})_{18}]^-$ and $[\text{Ag}_{25}(\text{DMBT})_{18}]^-$, in the solid state, where PET and DMBT are 2-phenylethanethiol and 2,4-dimethylbenzenethiol, respectively. The experiments were performed using different ratios of these two clusters, and it was inferred that the kinetics of the reactions were faster compared with reactions in the solution. The metal exchange between these two clusters, due to their interactions in the solid state, leads to the formation of dimers, trimers, tetramers, and polymers of atomically precise alloy metal clusters. We observed polymer entities up to hexamers, which were observed for the first time. Control experiments revealed that metal exchange is a key factor leading to polymerization. Our work points to a new approach for synthesizing polymers of atomically precise alloy metal clusters.



INTRODUCTION

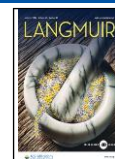
Atomically precise metal clusters are a class of molecules that are well-known for their diverse properties.^{1–8} Their structural integrity, composition, and electronic confinement make them promising candidates for various applications.^{9–12} Over the past decade, exploring the reactions between atomically precise metal clusters has evolved as a new research area of interest. These reactions in the solution phase and in the gas phase have been probed using mass spectrometry.^{13–16} In such reactions, the exchange of metal atoms and ligands occurs, while maintaining the nuclearity of individual clusters.^{17–20} Neumaier et al. have reported the kinetics of the reaction between the clusters $[\text{Au}_{25}(\text{PET})_{18}]^-$ and $[\text{Ag}_{25}(\text{DMBT})_{18}]^-$ in the solution.²¹ This study has identified the formation of dimer species arising from cluster monomers in the course of the evolution of reactions and their existence points to important mechanistic details of the exchange processes.²¹

Supramolecular interactions between metal clusters have been utilized for the bottom-up fabrication of nanomaterials.^{22–28} Directed self-assembly of clusters results in the formation of polymers of atomically precise clusters.^{29–36} However, controlled self-assembly of clusters has been challenging, and Yuan et al. introduced a solvent-mediated approach for precisely synthesizing polymers of clusters.³⁷ In this work, we show that clusters can also interact with each other in the solid state, resulting in the exchange of metal

atoms, which was not studied previously. In the solid state, the concentration of clusters is higher, favoring the adhesion between the clusters and consequently the metal atom exchange interactions, which could result in the formation of polymers of alloy metal clusters.

Specifically, we studied the polymerization that occurred due to metal atom exchange between $[\text{Au}_{25}(\text{PET})_{18}]^-$ and $[\text{Ag}_{25}(\text{DMBT})_{18}]^-$. We performed an experiment in which the powders of these two clusters were mixed in the solid state at various concentrations and times. Mass spectrometric analysis revealed the existence of species up to hexamers, which existed in the beginning. However, while performing mass spectrometry, the dilution in solution breaks the polymer, and eventually monomers exist in the solution. Time-dependent mass spectral analysis inferred that the kinetics of polymerization are faster in the solid state than in solution. The reaction studied using different ratios of the two clusters concluded that higher ratios of $[\text{Au}_{25}(\text{PET})_{18}]^-$ enhanced metal exchange and favored polymerization. Insights from this

Received: May 9, 2024
 Revised: June 19, 2024
 Accepted: June 20, 2024
 Published: June 26, 2024



work proposed a new pathway for developing self-assembled polymers of atomically precise alloy metal clusters by utilizing intercluster reactions in the solid state.

EXPERIMENTAL SECTION

Materials. All the materials were commercially available. Silver nitrate (AgNO_3), 2-phenylethanethiol (PET), 2,4-dimethylbenzenethiol (DMBT), tetraoctylammonium bromide (TOABr), tetraphenylphosphonium bromide (PPh_4Br), and sodium borohydride (NaBH_4) were purchased from Sigma-Aldrich. All the solvents, methanol, ethanol, acetone, chloroform, tetrahydrofuran, and dichloromethane, were purchased from Rankem. All solvents and chemicals were used as such without further purification.

Synthesis of $[\text{Au}_{25}(\text{PET})_{18}]^-$. The $[\text{Au}_{25}(\text{PET})_{18}]^-$ cluster was synthesized using the procedure reported previously.^{16,38} The starting material, $\text{HAuCl}_4 \cdot 3\text{H}_2\text{O}$, was synthesized in the lab by following the method presented in the Supporting Information. A quantity of 40 mg of $\text{HAuCl}_4 \cdot 3\text{H}_2\text{O}$ (0.1 mmol) was taken in 7.5 mL of tetrahydrofuran. Then, 66.5 mg (0.116 mmol) of TOABr was added with continuous stirring. The solution changed from yellow to orange due to complexation. After 15 min of stirring, 68 μL of PET ($\text{C}_8\text{H}_9\text{SH}$) (0.53 mmol) was added. Gradually, the solution turned colorless. After 2 h of vigorous stirring, 40 mg of NaBH_4 (1 mmol) dissolved in 2 mL of ice-cold water was added rapidly. The stirring was continued for 8 h, and a reddish-brown solution was obtained as a crude product. After that, the reaction mixture was dried, and the black particles were collected. They were suspended in methanol, and the mixture was centrifuged at 5000 rpm for 3 min to collect all of the black precipitate completely. This was also done to remove any insoluble byproducts. The precipitate was washed 5 times with methanol to remove excess thiol. Then, the cluster was dissolved in 8 mL of dichloromethane and centrifuged at 10000 rpm for 5 min. The supernatant was collected and dried, and again, it was dissolved in acetone and centrifuged at 10000 rpm for 5 min. The acetone soluble fraction was collected, which is the required $[\text{Au}_{25}(\text{PET})_{18}]^-$.

Synthesis of $[\text{Ag}_{25}(\text{DMBT})_{18}]^-$. The $[\text{Ag}_{25}(\text{DMBT})_{18}]^-$ cluster was synthesized by modifying the reported procedure.³⁹ Exactly 38 mg of AgNO_3 (0.22 mmol) was dissolved in a mixture of 2 mL of methanol and 17 mL of dichloromethane. Into this solution, 90 μL of DMBT ($\text{C}_8\text{H}_9\text{SH}$) (0.66 mmol) was added, which formed a yellow-colored suspension, and it was kept for stirring at 0 °C. After 20 min, a freshly prepared PPh_4Br (~6 mg, 0.014 mmol) solution in methanol (0.5 mL) was added with continued stirring. After 5 min, NaBH_4 (~15 mg, ~0.4 mmol) in 0.5 mL of ice-cold water was added. The color of the reaction mixture changed gradually from light yellow to dark brown. The solution was allowed to stir for 10 h and aged for 24 h in a freezer. The reaction mixture was centrifuged for purification of the cluster, and the supernatant was collected and concentrated to 5 mL. Excess methanol was added to the concentrated solution to precipitate the products. The obtained precipitate was washed multiple times (~5) with methanol. The precipitate was then dissolved in dichloromethane and centrifuged, and the supernatant was collected. The supernatant was dried, and the pure cluster was obtained in powder form.

Mixing of Clusters in the Solid State. The powders of both clusters $[\text{Au}_{25}(\text{PET})_{18}]^-$ and $[\text{Ag}_{25}(\text{DMBT})_{18}]^-$ were measured according to their molar ratio. Then, these clusters were mixed and ground using a mortar and pestle, in the laboratory environment. The clusters were mixed and ground for different time intervals (30 s, 1, 3, and 5 min), and the spectra were collected in each case. The ground mixture was dissolved in cold acetonitrile and held at -10 °C to minimize the solution phase contribution to the reaction. The sample was injected into the mass spectrometer within 30 s (retention time in solution), and the mass spectrum was acquired immediately. The entire mass spectral measurement, from sample preparation to data acquisition, was completed in 2 min. The same mixture was also analyzed using solid-state optical absorption measurements. In the further text, the reaction time corresponds to the grinding time of the two clusters.

RESULTS AND DISCUSSION

The clusters $[\text{Au}_{25}(\text{PET})_{18}]^-$ and $[\text{Ag}_{25}(\text{DMBT})_{18}]^-$ were chosen selectively based on their previous solution phase studies. Both clusters were synthesized as discussed in the Experimental Section. In the following text, the clusters $[\text{Au}_{25}(\text{PET})_{18}]^-$ and $[\text{Ag}_{25}(\text{DMBT})_{18}]^-$ will be represented as $\text{Au}_{25}(\text{SR})_{18}$ and $\text{Ag}_{25}(\text{SR})_{18}$, respectively. The protecting ligands of $\text{Au}_{25}(\text{SR})_{18}$ and $\text{Ag}_{25}(\text{SR})_{18}$ are 2-phenylethanethiol (PET) and 2,4-dimethylbenzenethiol (DMBT), respectively. These ligands were chosen due to their same molar masses (138 Da), which avoid complications due to ligand exchange between clusters in the course of metal exchange. Both clusters were synthesized and were further characterized by UV-vis absorption spectroscopy and electrospray ionization mass spectrometry (ESI-MS). The optical absorption spectra of both clusters exhibited their characteristic peaks, confirming their identity (Figure S1). The characteristic features of $\text{Au}_{25}(\text{SR})_{18}$ were observed at 450 and 690 nm, whereas the characteristic peaks of $\text{Ag}_{25}(\text{SR})_{18}$ were at 465, 495, 530, and 650 nm.⁴⁰ The ESI-MS of both clusters showed their characteristic peaks, with isotopic distribution matching the theoretical pattern (Figure S2). The peak of $\text{Au}_{25}(\text{SR})_{18}$ was at m/z 7393 with a charge of 1-, whereas the peak of $\text{Ag}_{25}(\text{SR})_{18}$ was at m/z 5167 with a charge of 1-. The clusters were mixed for different time intervals in powder form using a mortar and pestle, followed by ESI-MS measurements (Figure S4). The experiments were performed with different molar ratios of the $\text{Au}_{25}(\text{SR})_{18}$ and $\text{Ag}_{25}(\text{SR})_{18}$ clusters. The sample injection into the mass spectrometer was done quickly, within 1 min, to reduce the effect of solvent, and the data were collected within 2 min.

The mass spectrum obtained from the 1:1 molar ratio of $\text{Ag}_{25}(\text{SR})_{18} : \text{Au}_{25}(\text{SR})_{18}$, after mixing them for different time intervals, is presented in Figure 1a. In the mass spectrum, which was collected after 1 min of solid-state mixing, the characteristic features of $\text{Au}_{25}(\text{SR})_{18}$ and $\text{Ag}_{25}(\text{SR})_{18}$ were not observed. A new set of peaks was observed between m/z 5400 to 6000, and the zoomed-in spectra of this region are shown in Figure 1b. Each of the peaks in the isotopic distribution is separated by a m/z of less than 1, showing that these are highly charged species. The peaks observed in Figure 1b have monomer, dimer, and tetramer species, with 1-, 2-, and 4-charges, respectively. The mass separation between these peaks indicates a Au-Ag exchange between the two clusters. More detailed isotopically resolved spectra are not presented to confirm the exchange, although these have been presented in earlier reports.²¹ Exchange between the ligands is not evident from the mass spectrum since the molecular masses of PET and DMBT ligands are the same. The monomeric metal-exchanged species were assigned as $\text{Ag}_{22}\text{Au}_3(\text{SR})_{18}$ (m/z 5434), $\text{Ag}_{21}\text{Au}_4(\text{SR})_{18}$ (m/z 5523), $\text{Ag}_{20}\text{Au}_5(\text{SR})_{18}$ (5612), $\text{Ag}_{19}\text{Au}_6(\text{SR})_{18}$ (m/z 5701), $\text{Ag}_{18}\text{Au}_7(\text{SR})_{18}$ (m/z 5790), $\text{Ag}_{17}\text{Au}_8(\text{SR})_{18}$ (m/z 5879), $\text{Ag}_{16}\text{Au}_9(\text{SR})_{18}$ (m/z 5968), and $\text{Ag}_{15}\text{Au}_{10}(\text{SR})_{18}$ (m/z 6058) (nuclearity is always 25). Furthermore, the dimer species were identified as $\text{Ag}_{43}\text{Au}_7(\text{SR})_{36}$ (m/z 5479), $\text{Ag}_{41}\text{Au}_9(\text{SR})_{36}$ (m/z 5568), $\text{Ag}_{39}\text{Au}_{11}(\text{SR})_{36}$ (m/z 5657), $\text{Ag}_{37}\text{Au}_{13}(\text{SR})_{36}$ (m/z 5746), $\text{Ag}_{35}\text{Au}_{15}(\text{SR})_{36}$ (m/z 5835), and $\text{Ag}_{33}\text{Au}_{17}(\text{SR})_{36}$ (m/z 5925) (nuclearity is always 50). All of the dimer species observed were formed between metal-exchanged species. Notably, we have not observed the dimer formed between the pure parent clusters, $\text{Ag}_{25}(\text{SR})_{18}$ and $\text{Au}_{25}(\text{SR})_{18}$, which were present in the

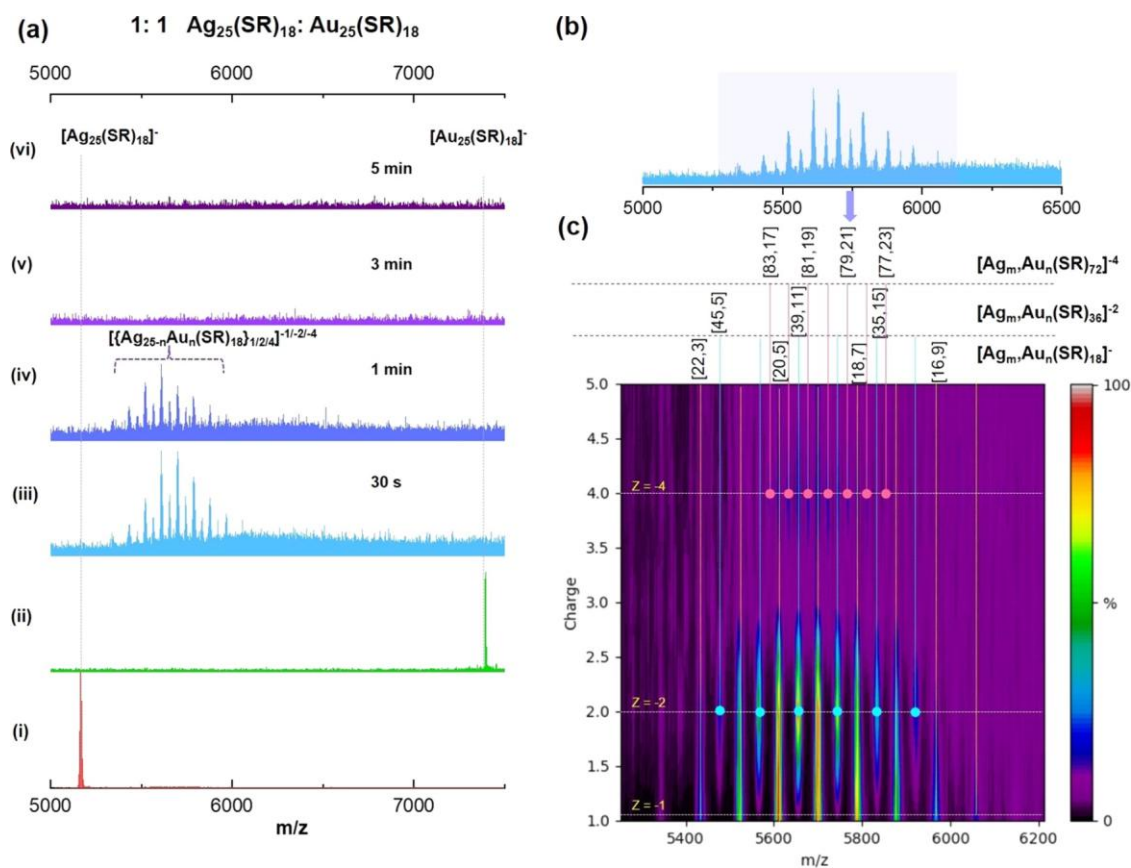


Figure 1. (a) ESI-MS of $\text{Ag}_{25}(\text{SR})_{18}$, $\text{Au}_{25}(\text{SR})_{18}$, and the time-dependent MS of the 1:1 mixture of $\text{Ag}_{25}(\text{SR})_{18}:\text{Au}_{25}(\text{SR})_{18}$ clusters measured after grinding the mixture. (b) Zoomed-in view of the mass spectrum collected after grinding the mixture for 1 min. (c) Heat map of the mass spectrum collected after grinding the mixture for 1 min (the compositions of various polymer species observed and their charge states marked).

previous report of solution phase intercluster reaction.²¹ The tetramer peaks observed were due to $\text{Ag}_{83}\text{Au}_{17}(\text{SR})_{72}$ (m/z 5545), $\text{Ag}_{81}\text{Au}_{19}(\text{SR})_{72}$ (m/z 5590), $\text{Ag}_{79}\text{Au}_{21}(\text{SR})_{72}$ (m/z 5634), and $\text{Ag}_{77}\text{Au}_{23}(\text{SR})_{72}$ (m/z 5679) (nuclearity is always 100). The same peaks were observed in the mass spectrum collected after 3 min of solid-state grinding, but their intensities started to decrease with time. After 5 min of mixing, all of the peaks disappeared due to the degradation of clusters, presumably in the solution. The degraded products mostly consisted of metal thiolates and their exchanged species, which were assigned as $\text{Ag}_5(\text{SR})_6$, $\text{AuAg}_4(\text{SR})_6$, $\text{Au}_2\text{Ag}_3(\text{SR})_6$, and $\text{Au}_3\text{Ag}_2(\text{SR})_6$ (Figure S15).

We have performed the same experiment using different molar ratios, 1:1, 1:3, 3:1, 1:5, and 5:1 of $\text{Ag}_{25}(\text{SR})_{18}$ and $\text{Au}_{25}(\text{SR})_{18}$. The mass spectrum obtained for various molar ratios of the clusters after 1 min of solid-state mixing is presented in Figure 2a. As shown in Figure 1, the ratio 1:1 of $\text{Ag}_{25}(\text{SR})_{18}:\text{Au}_{25}(\text{SR})_{18}$ produced monomers, dimers, and tetramers of the exchanged species. In the mass spectra of 1:3 $\text{Ag}_{25}(\text{SR})_{18}:\text{Au}_{25}(\text{SR})_{18}$, the peaks for the parent clusters were observed. In the range of m/z 7250–7400, monomeric Ag exchanged peaks of $\text{Au}_{25}(\text{SR})_{18}$ clusters were observed, while in the range of m/z 5200–5700, monomeric Au-exchanged peaks of $\text{Ag}_{25}(\text{SR})_{18}$ were identified. The dimer peaks were also observed, but they were mainly concentrated in the range of m/z 7000, indicating that the contribution of Au atoms is more on the dimer, which accounts for the higher molar ratio of $\text{Au}_{25}(\text{SR})_{18}$. The time-dependent mass spectra of 1:3 $\text{Ag}_{25}(\text{SR})_{18}:\text{Au}_{25}(\text{SR})_{18}$ show that metal exchange is

happening within 30 s, and with an increase in time, the intensity of peaks decreases (Figure S3), indicating faster kinetics of the reaction. From the low-intensity peaks, we observed the presence of trimer species (3-), and their compositions were assigned as $\text{Ag}_6\text{Au}_{69}(\text{SR})_{54}$ (m/z 7216), $\text{Ag}_3\text{Au}_{72}(\text{SR})_{54}$ (m/z 7305), and $\text{Au}_{75}(\text{SR})_{54}$ (m/z 7393). To further understand the low-intensity peaks, we made a heat map plot of the mass spectra (Figure S4), and surprisingly, we found the tetramers and pentamers of parent clusters $\text{Ag}_{25}(\text{SR})_{18}$ and $\text{Au}_{25}(\text{SR})_{18}$ (Figure S11). Similarly, in the mass spectra of the ratio 3:1 $\text{Ag}_{25}(\text{SR})_{18}:\text{Au}_{25}(\text{SR})_{18}$ also, the peaks for the parent clusters were observed. Time-dependent mass spectra (Figure S5) show that in the initial 1 min, only monomeric Au-exchanged peaks of $\text{Ag}_{25}(\text{SR})_{18}$ clusters were formed in the range of m/z 5200–5500. However, with increase in time to 3 min, we observed excessive metal exchange between the clusters, and peaks were observed in the range of m/z 5800–6800 (Table S3). Furthermore, in the same range, we observed dimers, trimers, and tetramers of the metal-exchanged species (Figure S6 and Table S3). Besides that, at m/z 6324, a hexamer species $[\text{Ag}_{72}\text{Au}_{78}(\text{SR})_{108}]^{6-}$ was found with the monomeric unit $[\text{Ag}_{12}\text{Au}_{13}(\text{SR})_{18}]^{-}$, which was not previously reported (Figure S12). The mass spectral analysis showed that the kinetics of polymerization is slower in 3:1, compared to 1:3 $\text{Ag}_{25}(\text{SR})_{18}$ and $\text{Au}_{25}(\text{SR})_{18}$. Thus, we conclude that a higher ratio of $\text{Au}_{25}(\text{SR})_{18}$ favors polymerization.

The time-dependent mass spectra of 1:5 $\text{Ag}_{25}(\text{SR})_{18}:\text{Au}_{25}(\text{SR})_{18}$ showed that the parent cluster peak

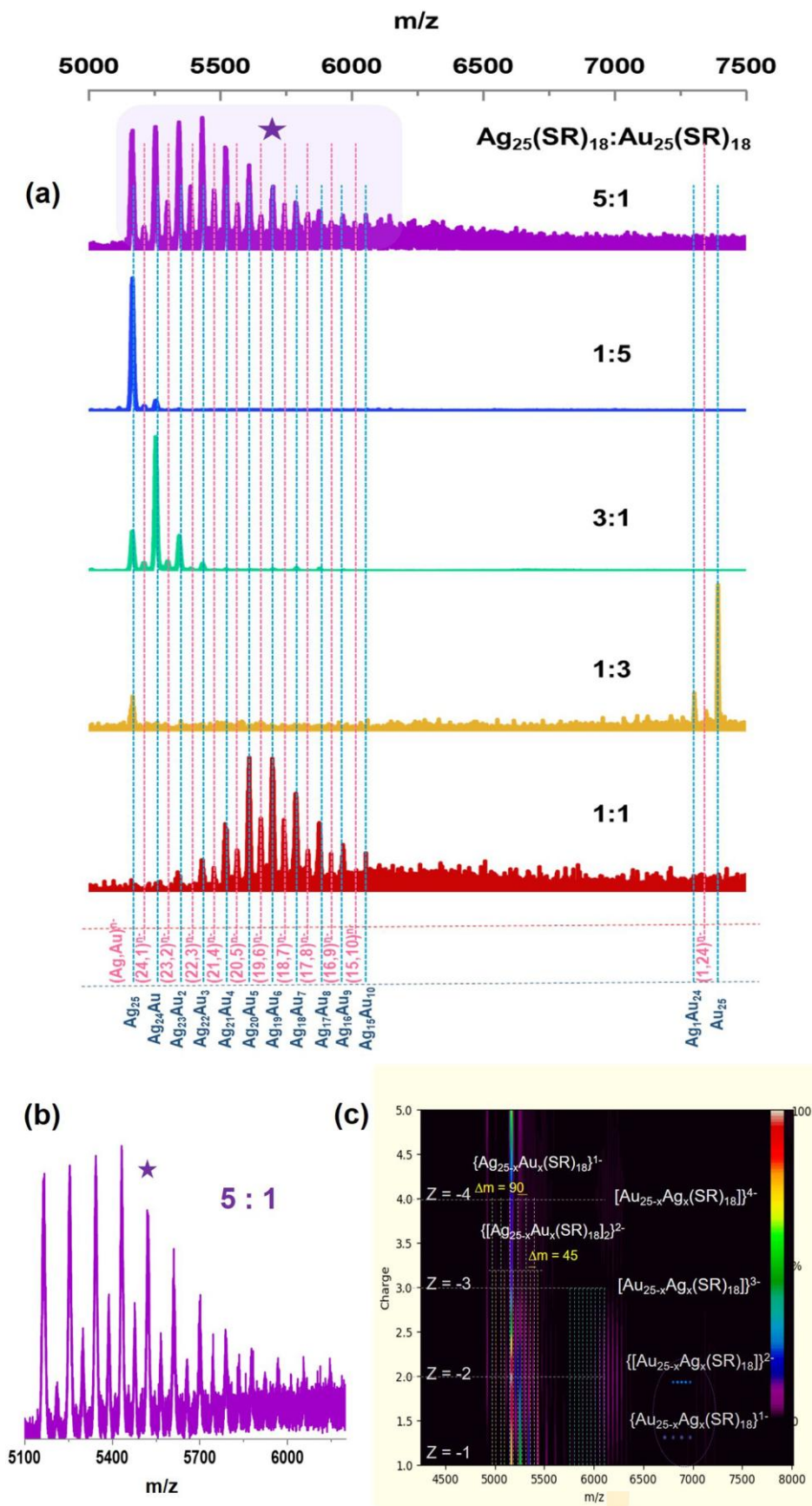


Figure 2. (a) ESI-MS, after 1 min of grinding, of a mixture of $\text{Ag}_{25}(\text{SR})_{18}$ and $\text{Au}_{25}(\text{SR})_{18}$ at various molar ratios. (b) Zoomed-in mass spectrum for the ratio 5:1 of $\text{Ag}_{25}(\text{SR})_{18}:\text{Au}_{25}(\text{SR})_{18}$. (c) Heat map plot for the ratio 5:1 of $\text{Ag}_{25}(\text{SR})_{18}:\text{Au}_{25}(\text{SR})_{18}$ (the compositions of various polymer species observed and their charge states are marked).

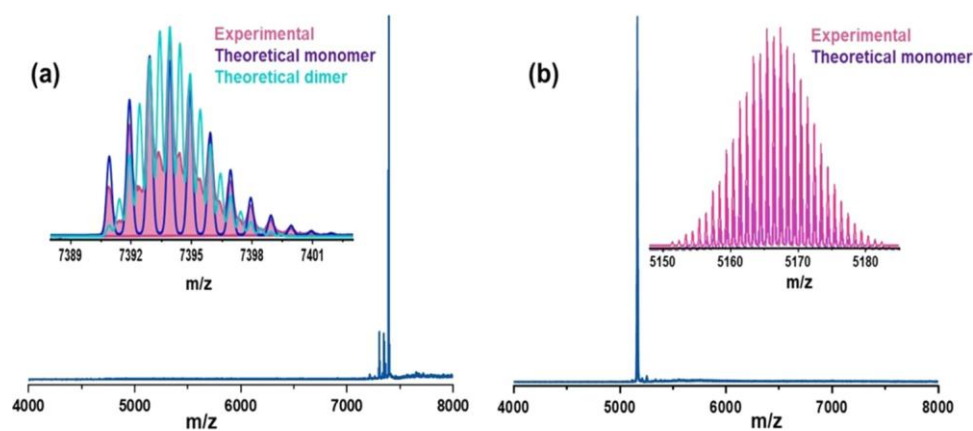


Figure 3. ESI-MS of (a) $\text{Au}_{25}(\text{SR})_{18}$ and (b) $\text{Ag}_{25}(\text{SR})_{18}$ measured after solid-state grinding. The inset shows the matching of the experimental and theoretical isotopic distributions. Dimers and trimers are marked in the inset of (a), and such species are not there in (b). Intensities of the theoretical monomer and dimer peaks were not matched with the experimental spectrum to make sure that the peaks were clearly visible.

of $\text{Au}_{25}(\text{SR})_{18}$ was absent, even though the concentration was higher (Figure S7). Near m/z 5200, Au-exchanged peaks of $\text{Ag}_{25}(\text{SR})_{18}$ were observed along with the less intense peaks around m/z 6000. The kinetics of the reaction were fast such that the peak intensity of the polymer species diminished rapidly. The heat map plot shows that low-intensity peaks around m/z 6000 consist of dimers, trimers, and tetramers (Figure S8), and their composition is presented in detail in Table S4. However, in the time-dependent mass spectra of 5:1 $\text{Ag}_{25}(\text{SR})_{18}:\text{Au}_{25}(\text{SR})_{18}$, the parent cluster peak of $\text{Ag}_{25}(\text{SR})_{18}$ alone was present (Figure S9). Furthermore, the peaks of Au-exchanged species of $\text{Ag}_{25}(\text{SR})_{18}$ were present, along with their dimer, trimer, and tetramer species (Figure S10). The polymer peaks were mainly concentrated near the range of m/z 5200–6000, attributed to the higher amount of $\text{Ag}_{25}(\text{SR})_{18}$ present. The compositions of different polymer species formed are presented in Table S5. We observed from further analysis of the mass spectra that in the presence of higher amount of $\text{Ag}_{25}(\text{SR})_{18}$, the polymers are concentrated toward lower m/z , whereas for higher amount of $\text{Au}_{25}(\text{SR})_{18}$, they are found toward higher m/z values.

Metal atom exchange between the clusters is key for polymerization, which is evident from the mass spectrometry studies, and the polymeric species were formed by alloys. The analysis of mass spectra inferred that the presence of higher ratios of $\text{Au}_{25}(\text{SR})_{18}$ favors the polymerization more compared to $\text{Ag}_{25}(\text{SR})_{18}$, which is evident from the mass spectra of 1:1, 1:3, and 1:5 mixtures (Figure 2). To further explore this, we separately took both $\text{Au}_{25}(\text{SR})_{18}$ and $\text{Ag}_{25}(\text{SR})_{18}$ clusters in powder form, ground them separately using a mortar and pestle, and measured their mass spectra. This was done to understand the response of each cluster toward solid-state mixing. For $\text{Au}_{25}(\text{SR})_{18}$, we observed dimers and trimers in the mass spectrum as seen before,⁴¹ whereas for $\text{Ag}_{25}(\text{SR})_{18}$, only monomers were present (Figure 3). This hinted at the tendency of $\text{Au}_{25}(\text{SR})_{18}$ to form polymers, which corroborates our experimental results. The cluster $\text{Ag}_{25}(\text{SR})_{18}$ alone could not form any polymer due to grinding, which further confirms that metal exchange between the two clusters is the driving force for polymerization.

We performed solid-state optical absorption measurements to confirm that interaction between clusters in the solid state is responsible for metal exchange and polymerization. We have taken equimolar amounts of clusters $\text{Au}_{25}(\text{SR})_{18}$ and

$\text{Ag}_{25}(\text{SR})_{18}$ in the powder form, mixed them for different time intervals, and their corresponding absorption spectra were measured. The absorption spectra of individual clusters and the mixture at various time intervals are shown in Figure S13. The absorption spectra of parent clusters $\text{Au}_{25}(\text{SR})_{18}$ and $\text{Ag}_{25}(\text{SR})_{18}$ in the solid state measurements have shown some differences in the peaks compared to their solution phase data (Figure S1), which could be attributed to solvent effects. After mixing the clusters, the spectral features exhibited a notable shift in the peak positions compared to those of the parent clusters. However, the spectra collected at different time intervals of mixing did not show any prominent difference with respect to time. This suggests that the interaction between the clusters in the solid state is very fast and is completed within a few minutes, which matches well with the mass spectral analysis. The intensity of the absorption peaks also did not decrease even after 45 min of spectral measurement, indicating the stability of the cluster polymers in the solid state. We have also measured the time-dependent UV-vis absorption spectra of the ground mixture of clusters dissolved in cold acetonitrile at a time interval of 30 s and up to 2 min (Figure S14). These control experiments confirmed that the reaction is not very rapid upon dissolution in acetonitrile and that the effect of solvent was minimal on the mass spectral analysis.

The previous report on the solution phase reaction of $\text{Au}_{25}(\text{SR})_{18}$ and $\text{Ag}_{25}(\text{SR})_{18}$ showed that the dimer forms only after 3 min, and metal exchange happens later.²¹ However, in the case of solid-state interaction, the reaction was more rapid than that in solution, and the whole reaction was completed within 5 min. In solution, the molecules will be far apart and have fewer chances of coming together, which is attributed to their slower kinetics. In solid-state mixing, the molecules are closer, which favors strong adhesion, and metal exchange happens between $\text{Au}_{25}(\text{SR})_{18}$ and $\text{Ag}_{25}(\text{SR})_{18}$ within the time scale of polymerization. The exchange efficiency of the two clusters $\text{Ag}_{25}(\text{SR})_{18}$ and $\text{Au}_{25}(\text{SR})_{18}$ in the solid state was nearly 100%. Time-dependent mass spectral analysis shows that initially, dimer species were forming, which further interacted with adjacent monomers or dimers to form oligomers. The polymeric species we have observed constitute both homopolymers and heteropolymers. Homopolymers have high-intensity peaks in the mass spectrum due to the overlap of the peaks of different species at the same m/z value. However, for heteropolymers, the peak intensities were found to be

weaker. In the case of $\text{Ag}_{25}(\text{SR})_{18}:\text{Au}_{25}(\text{SR})_{18}$ ratio of 3:1, we observed an unprecedented hexamer species, and the theoretical agreement of the peak is shown in Figure S12.

The plausible mechanism for the polymerization of clusters can be (i) ligand–ligand interactions ($\pi \cdots \pi$, $\text{C}-\text{H} \cdots \pi$) and (ii) attractive van der Waals forces between the metal atoms and sulfur atoms in the staples of the interacting clusters. The aurophilic interactions⁴² would also play a role, as is evident from the increased tendency of polymerization in the presence of more $\text{Au}_{25}(\text{SR})_{18}$. A schematic representation of these interactions and the formation of polymers of metal clusters is shown in Figure 4. The negative charge on the cluster is

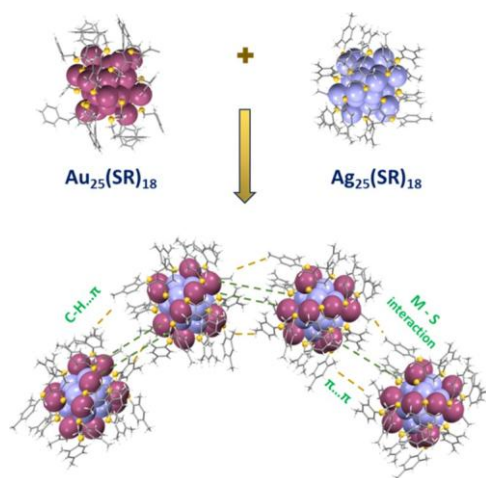


Figure 4. Schematic representation that demonstrates the formation of alloy cluster polymer from the parent clusters and interactions within the polymer.

delocalized throughout, electrostatic repulsion did not prevent intercluster interactions, as reported previously.¹⁵ The counterions of $\text{Au}_{25}(\text{SR})_{18}$ and $\text{Ag}_{25}(\text{SR})_{18}$ are tetraoctylammonium (TOA^+) and tetraphenylphosphonium (Ph_4P^+), respectively, which are smaller compared to the size of metal clusters. Thus, the interference of counterions will be minimal during interaction between the clusters. The presence of $\text{Au}_{25}(\text{SR})_{18}$ and its metal exchange with $\text{Ag}_{25}(\text{SR})_{18}$ are crucial in the polymerization of clusters, which was evident from mass spectrometric observations. The grinding of the clusters also has a crucial role in the formation of alloy cluster polymers, since it promotes the interaction between clusters by providing energy. The mechanical energy from grinding provides the kinetic energy for the clusters to react with each other. As shown in Figure 3, the solid-state grinding of $\text{Ag}_{25}(\text{SR})_{18}$ alone does not form polymers, implying that metal exchange between the clusters is the driving force for polymerization. Thus, intercluster reactions turn out to be a plausible strategy for synthesizing polymers of atomically precise alloy metal clusters.

CONCLUSIONS

In conclusion, we report the polymerization of atomically precise metal clusters due to metal exchange in the solid state. The interaction between electronically stable and geometrically robust metal clusters $[\text{Au}_{25}(\text{PET})_{18}]^-$ and $[\text{Ag}_{25}(\text{DMBT})_{18}]^-$ in the solid state produced dimers (2-), trimers (3-), tetramers (4-), pentamers (5-), and hexamers (6-), which were not reported earlier. This interaction can synthesize controlled

polymers of bimetallic Ag–Au clusters with the desired number of monomeric units by optimizing the ratios of the reactant clusters. The kinetics of the reaction are faster compared to the already known solution phase studies, and the metal exchange between the clusters favors the polymerization. We observed that higher ratios of $\text{Au}_{25}(\text{SR})_{18}$ have faster kinetics for polymerization than higher ratios of $\text{Ag}_{25}(\text{SR})_{18}$. Mass spectrometry revealed the existence of polymers up to hexamers with a 6- charge, but other higher oligomers could also be present, which were not observed due to their weak intensities. Extension of this study using other metal clusters would provide more insights into the mechanism and help generalize this approach to synthesize polymers of atomically precise alloy metal clusters.

ASSOCIATED CONTENT

Supporting Information

The Supporting Information is available free of charge at <https://pubs.acs.org/doi/10.1021/acs.langmuir.4c01737>.

ESI mass spectra, UV–vis absorption spectra, and heat map plots (PDF)

AUTHOR INFORMATION

Corresponding Author

Thalappil Pradeep – Department of Chemistry, DST Unit of Nanoscience (DST UNS) and Thematic Unit of Excellence (TUE), Indian Institute of Technology Madras, Chennai 600036, India; International Centre for Clean Water, Chennai 600113, India; orcid.org/0000-0003-3174-534X; Email: pradeep@iitm.ac.in

Authors

B. S. Sooraj – Department of Chemistry, DST Unit of Nanoscience (DST UNS) and Thematic Unit of Excellence (TUE), Indian Institute of Technology Madras, Chennai 600036, India; orcid.org/0000-0002-6963-6491

Jayoti Roy – Department of Chemistry, DST Unit of Nanoscience (DST UNS) and Thematic Unit of Excellence (TUE), Indian Institute of Technology Madras, Chennai 600036, India

Manish Mukherjee – Department of Chemistry, DST Unit of Nanoscience (DST UNS) and Thematic Unit of Excellence (TUE), Indian Institute of Technology Madras, Chennai 600036, India; Department of Chemistry, Indian Institute of Science Education and Research Kolkata, Kolkata 741246, India

Anagha Jose – Department of Chemistry, DST Unit of Nanoscience (DST UNS) and Thematic Unit of Excellence (TUE), Indian Institute of Technology Madras, Chennai 600036, India

Complete contact information is available at: <https://pubs.acs.org/10.1021/acs.langmuir.4c01737>

Author Contributions

||B.S.S. and J.R. contributed equally to this work. B.S.S. performed the synthesis, characterization, and other experimental studies. J.R. performed the mass spectrometry studies. M.M. and A.J. performed the synthesis and characterization of clusters. B.S.S. wrote the first draft with inputs from J.R. T.P. has conceptualized the work, directed the progress, and edited the final version of the manuscript. All authors have approved the final version of the manuscript.

Notes

The authors declare no competing financial interest.

ACKNOWLEDGMENTS

B.S.S. thanks the Council of Scientific & Industrial Research (CSIR) for the SPM research fellowship. J.R. thanks IIT Madras for a research fellowship. M.M. thanks Kishore Vaigyanik Protsahan Yojana (KVPY) programme and IISER Kolkata for funding. A.J. thanks MHRD for the Prime Minister's Research Fellowship (PMRF). T.P. thanks the Science and Engineering Research Board (SERB), India, for funding through the research grant SPR/2021/000439 and through a JC Bose Fellowship. T.P. also acknowledges funding from the Centre of Excellence on Molecular Materials and Functions under the Institution of Eminence scheme of IIT Madras. We thank the Department of Science and Technology, Government of India, for continuous support of our research program.

DEDICATION

This article is dedicated to Prof. Santanu Bhattacharya on the occasion of his 65th birthday.

REFERENCES

- (1) Jin, R.; Zeng, C.; Zhou, M.; Chen, Y. Atomically Precise Colloidal Metal Nanoclusters and Nanoparticles: Fundamentals and Opportunities. *Chem. Rev.* 2016, *116* (18), 10346–10413.
- (2) Lu, Y.; Chen, W. Sub-Nanometre Sized Metal Clusters: From Synthetic Challenges to the Unique Property Discoveries. *Chem. Soc. Rev.* 2012, *41* (9), 3594–3623.
- (3) Jin, R. Quantum Sized, Thiolate-Protected Gold Nanoclusters. *Nanoscale* 2010, *2* (3), 343–362.
- (4) Templeton, A. C.; Wuelfing, W. P.; Murray, R. W. Monolayer-Protected Cluster Molecules. *Acc. Chem. Res.* 2000, *33* (1), 27–36.
- (5) Ferrando, R.; Jellinek, J.; Johnston, R. L. Nanoalloys: From Theory to Applications of Alloy Clusters and Nanoparticles. *Chem. Rev.* 2008, *108*, 845–910.
- (6) Chakraborty, I.; Pradeep, T. Atomically Precise Clusters of Noble Metals: Emerging Link between Atoms and Nanoparticles. *Chem. Rev.* 2017, *117* (12), 8208–8271.
- (7) Li, S.; Li, N. N.; Dong, X. Y.; Zang, S. Q.; Mak, T. C. W. Chemical Flexibility of Atomically Precise Metal Clusters. *Chem. Rev.* 2024, *124*, 7262.
- (8) Zou, X.; Kang, X.; Zhu, M. Recent Developments in the Investigation of Driving Forces for Transforming Coinage Metal Nanoclusters. *Chem. Soc. Rev.* 2023, *52* (17), 5892–5967.
- (9) Zhu, M.; Aikens, C. M.; Hendrich, M. P.; Gupta, R.; Qian, H.; Schatz, G. C.; Jin, R. Reversible Switching of Magnetism in Thiolate-Protected Au₂₅ Superatoms. *J. Am. Chem. Soc.* 2009, *131* (7), 2490–2492.
- (10) Wang, X.; Zhao, L.; Li, X.; Liu, Y.; Wang, Y.; Yao, Q.; Xie, J.; Xue, Q.; Yan, Z.; Yuan, X.; Xing, W. Atomic-Precision Pt₆ Nanoclusters for Enhanced Hydrogen Electro-Oxidation. *Nat. Commun.* 2022, *13* (1), No. 1596.
- (11) Jin, R. Atomically Precise Metal Nanoclusters: Stable Sizes and Optical Properties. *Nanoscale* 2015, *7* (5), 1549–1565.
- (12) Jose, A.; Jana, A.; Gupte, T.; Nair, A. S.; Unni, K.; Nagar, A.; Kini, A. R.; Spoorthi, B. K.; Jana, S. K.; Pathak, B.; Pradeep, T. Vertically Aligned Nanoplates of Atomically Precise Co₆S₈ Cluster for Practical Arsenic Sensing. *ACS Mater. Lett.* 2023, *5* (3), 893–899.
- (13) Wang, S.; Song, Y.; Jin, S.; Liu, X.; Zhang, J.; Pei, Y.; Meng, X.; Chen, M.; Li, P.; Zhu, M. Metal Exchange Method Using Au₂₅ Nanoclusters as Templates for Alloy Nanoclusters with Atomic Precision. *J. Am. Chem. Soc.* 2015, *137* (12), 4018–4021.
- (14) Baksi, A.; Schneider, E. K.; Weis, P.; Krishnadas, K. R.; Ghosh, D.; Hahn, H.; Pradeep, T.; Kappes, M. M. Nanogymnastics:

Visualization of Intercluster Reactions by High-Resolution Trapped Ion Mobility Mass Spectrometry. *J. Phys. Chem. C* 2019, *123* (46), 28477–28485.

(15) Krishnadas, K. R.; Ghosh, A.; Baksi, A.; Chakraborty, I.; Natarajan, G.; Pradeep, T. Intercluster Reactions between Au₂₅(SR)₁₈ and Ag₄₄(SR)₃₀. *J. Am. Chem. Soc.* 2016, *138* (1), 140–148.

(16) Krishnadas, K. R.; Baksi, A.; Ghosh, A.; Natarajan, G.; Pradeep, T. Manifestation of Geometric and Electronic Shell Structures of Metal Clusters in Intercluster Reactions. *ACS Nano* 2017, *11* (6), 6015–6023.

(17) Huang, B.; Pei, Y. On the Mechanism of Inter-Cluster Alloying Reactions: Two-Stage Metal Exchange of [Au₂₅(PET)₁₈]⁻ and [Ag₂₅(DMBT)₁₈]⁻ Clusters. *J. Mater. Chem. A* 2020, *8* (20), 10242–10251.

(18) Zhang, B.; Salassa, G.; Bürgi, T. Silver Migration between Au₃₈(SC₂H₄Ph)₂₄ and Doped Ag_xAu_{38-x}(SC₂H₄Ph)₂₄ Nanoclusters. *Chem. Commun.* 2016, *52* (59), 9205–9207.

(19) Krishnadas, K. R.; Baksi, A.; Ghosh, A.; Natarajan, G.; Pradeep, T. Structure-Conserving Spontaneous Transformations between Nanoparticles. *Nat. Commun.* 2016, *7*, No. 13447.

(20) Krishnadas, K. R.; Baksi, A.; Ghosh, A.; Natarajan, G.; Som, A.; Pradeep, T. Interparticle Reactions: An Emerging Direction in Nanomaterials Chemistry. *Acc. Chem. Res.* 2017, *50* (8), 1988–1996.

(21) Neumaier, M.; Baksi, A.; Weis, P.; Schneider, E. K.; Chakraborty, P.; Hahn, H.; Pradeep, T.; Kappes, M. M. Kinetics of Intercluster Reactions between Atomically Precise Noble Metal Clusters [Ag₂₅(DMBT)₁₈]⁻ and [Au₂₅(PET)₁₈]⁻ in Room Temperature Solutions. *J. Am. Chem. Soc.* 2021, *143* (18), 6969–6980.

(22) De Nardi, M.; Antonello, S.; Jiang, D. E.; Pan, F.; Rissanen, K.; Ruzzi, M.; Venzo, A.; Zoleo, A.; Maran, F. Gold Nanowired: A Linear (Au₂₅)_n Polymer from Au₂₅ Molecular Clusters. *ACS Nano* 2014, *8* (8), 8505–8512.

(23) Qiao, Y.; Zou, J.; Fei, W.; Fan, W.; You, Q.; Zhao, Y.; Li, M. B.; Wu, Z. Building Block Metal Nanocluster-Based Growth in 1D Direction. *Small* 2023, *20* (9), No. 2305556.

(24) Lahtinen, T.; Hulkko, E.; Sokolowska, K.; Tero, T. R.; Saarnio, V.; Lindgren, J.; Pettersson, M.; Häkkinen, H.; Lehtovaara, L. Covalently Linked Multimers of Gold Nanoclusters Au₁₀₂(pMBA)₄₄ and Au₋₂₅₀(pMBA)_n. *Nanoscale* 2016, *8* (44), 18665–18674.

(25) Lei, Z.; Li, J. J.; Nan, Z. A.; Jiang, Z. G.; Wang, Q. M. Cluster From Cluster: A Quantitative Approach to Magic Gold Nanoclusters [Au₂₅(SR)₁₈]⁻. *Angew. Chem., Int. Ed.* 2021, *60* (26), 14415–14419.

(26) Ito, E.; Takano, S.; Nakamura, T.; Tsukuda, T. Controlled Dimerization and Bonding Scheme of Icosahedral M@Au₁₂ (M = Pd, Pt) Superatoms. *Angew. Chem., Int. Ed.* 2021, *60* (2), 645–649.

(27) Dainese, T.; Antonello, S.; Bogialli, S.; Fei, W.; Venzo, A.; Maran, F. Gold Fusion: From Au₂₅(SR)₁₈ to Au₃₈(SR)₂₄, the Most Unexpected Transformation of a Very Stable Nanocluster. *ACS Nano* 2018, *12* (7), 7057–7066.

(28) Tang, L.; Kang, X.; Wang, S.; Zhu, M. Light-Induced Size-Growth of Atomically Precise Nanoclusters. *Langmuir* 2019, *35* (38), 12350–12355.

(29) Liu, X.; Saranya, G.; Huang, X.; Cheng, X.; Wang, R.; Chen, M.; Zhang, C.; Li, T.; Zhu, Y. Ag₂Au₅₀(PET)₃₆ Nanocluster: Dimeric Assembly of Au₂₅(PET)₁₈ Enabled by Silver Atoms. *Angew. Chem., Int. Ed.* 2020, *59* (33), 13941–13946.

(30) Alhilaly, M. J.; Huang, R. W.; Naphade, R.; Alamer, B.; Hedhili, M. N.; Emwas, A. H.; Maity, P.; Yin, J.; Shkurenko, A.; Mohammed, O. F.; Eddaoudi, M.; Bakr, O. M. Assembly of Atomically Precise Silver Nanoclusters into Nanocluster-Based Frameworks. *J. Am. Chem. Soc.* 2019, *141* (24), 9585–9592.

(31) Wang, Z. Y.; Wang, M. Q.; Li, Y. L.; Luo, P.; Jia, T. T.; Huang, R. W.; Zang, S. Q.; Mak, T. C. W. Atomically Precise Site-Specific Tailoring and Directional Assembly of Superatomic Silver Nanoclusters. *J. Am. Chem. Soc.* 2018, *140* (3), 1069–1076.

(32) Liu, Y.; Yao, D.; Zhang, H. Self-Assembly Driven Aggregation-Induced Emission of Copper Nanoclusters: A Novel Technology for Lighting. *ACS Appl. Mater. Interfaces* 2018, *10* (15), 12071–12080.

- (33) Liu, J.; Tian, Y.; Ai, L.; Wu, Z.; Yao, D.; Liu, Y.; Yang, B.; Zhang, H. Self-Assembly of Au Nanoclusters into Helical Ribbons by Manipulating the Flexibility of Capping Ligands. *Langmuir* 2020, *36* (48), 14614–14622.
- (34) Fu, J.; Miao, Y.; Zhang, D.; Zhang, Y.; Meng, L.; Ni, X.; Shen, J.; Qi, W. Polymer-Enabled Assembly of Au Nanoclusters with Luminescence Enhancement and Macroscopic Chirality. *Langmuir* 2023, *39* (37), 13316–13324.
- (35) Wang, Y. X.; Li, A. J.; Wang, H. L.; Liu, W.; Kang, J.; Lu, J.; Lu, S. Y.; Yang, Y.; Liu, K.; Yang, B. In Situ Seed-Mediated Growth of Polymer-Grafted Gold Nanoparticles. *Langmuir* 2020, *36* (3), 789–795.
- (36) Kauscher, U.; Penders, J.; Nagelkerke, A.; Holme, M. N.; Nele, V.; Massi, L.; Gopal, S.; Whittaker, T. E.; Stevens, M. M. Gold Nanocluster Extracellular Vesicle Supraparticles: Self-Assembled Nanostructures for Three-Dimensional Uptake Visualization. *Langmuir* 2020, *36* (14), 3912–3923.
- (37) Yuan, P.; Zhang, R.; Selenius, E.; Ruan, P.; Yao, Y.; Zhou, Y.; Malola, S.; Häkkinen, H.; Teo, B. K.; Cao, Y.; Zheng, N. Solvent-Mediated Assembly of Atom-Precise Gold–Silver Nanoclusters to Semiconducting One-Dimensional Materials. *Nat. Commun.* 2020, *11* (1), No. 2229.
- (38) Heaven, M. W.; Dass, A.; White, P. S.; Holt, K. M.; Murray, R. W. Crystal Structure of the Gold Nanoparticle $[\text{N}(\text{C}_8\text{H}_{17})_4]\text{[Au}_{25}(\text{SCH}_2\text{CH}_2\text{Ph})_{18}]$. *J. Am. Chem. Soc.* 2008, *130* (12), 3754–3755.
- (39) Joshi, C. P.; Bootharaju, M. S.; Alhilaly, M. J.; Bakr, O. M. $[\text{Ag}_{25}(\text{SR})_{18}]^-$: The “Golden” Silver Nanoparticle Silver Nanoparticle. *J. Am. Chem. Soc.* 2015, *137* (36), 11578–11581.
- (40) Sooraj, B. N. S.; Pradeep, T. Optical Properties of Metal Clusters. In *Atomically Precise Metal Nanoclusters*; Elsevier, 2023; pp 83–101.
- (41) Baksi, A.; Chakraborty, P.; Bhat, S.; Natarajan, G.; Pradeep, T. $[\text{Au}_{25}(\text{SR})_{18}]_2^{2-}$: A Noble Metal Cluster Dimer in the Gas Phase. *Chem. Commun.* 2016, *52* (54), 8397–8400.
- (42) Schmidbaur, H.; Schier, A. Auophilic Interactions as a Subject of Current Research: An up-Date. *Chem. Soc. Rev.* 2012, *41* (1), 370–412.

Supporting Information

Extensive Polymerization of Atomically Precise Alloy Metal Clusters During Solid State Reactions

B. S. Sooraj,^{†,||} Jayoti Roy,^{†,||} Manish Mukherjee,^{†,‡} Anagha Jose,[†] and Thalappil Pradeep*^{†,§}

[†]Department of Chemistry, DST Unit of Nanoscience (DST UNS) and Thematic Unit of Excellence (TUE), Indian Institute of Technology Madras, Chennai 600036, India. E-mail: pradeep@iitm.ac.in

[‡]Department of Chemistry, Indian Institute of Science Education and Research Kolkata, Kolkata 741246, India.

[§]International Centre for Clean Water, Chennai 600113, India.

^{||}These authors contributed equally.

Table of contents

Title	Description	Page no
1.	Experimental section	3
2.	Instrumentation	3
Figure S1	UV-Vis absorption spectrum of (a) [Au ₂₅ (PET) ₁₈] ⁻ , and (b) [Ag ₂₅ (DMBT) ₁₈] ⁻ cluster	4
Figure S2	ESI-MS of (a) [Au ₂₅ (PET) ₁₈] ⁻ , and (b) [Ag ₂₅ (DMBT) ₁₈] ⁻ cluster	4

Figure S3	Time-dependent electrospray ionization mass spectra (ESI MS), after grinding 1:3 mixture of $\text{Ag}_{25}(\text{SR})_{18}$: $\text{Au}_{25}(\text{SR})_{18}$, in solid state	5
Figure S4	Heat map plot obtained from the mass spectra of grinding 1:3 mixture of $\text{Ag}_{25}(\text{SR})_{18}$: $\text{Au}_{25}(\text{SR})_{18}$, in solid state	5
Figure S5	Time-dependent electrospray ionization mass spectra (ESI MS), after grinding 3:1 mixture of $\text{Ag}_{25}(\text{SR})_{18}$: $\text{Au}_{25}(\text{SR})_{18}$, in solid state	6
Figure S6	Heat map plot obtained from the mass spectra of grinding 3:1 mixture of $\text{Ag}_{25}(\text{SR})_{18}$: $\text{Au}_{25}(\text{SR})_{18}$, in solid state	6
Figure S7	Time-dependent electrospray ionization mass spectra (ESI MS), after grinding 1:5 mixture of $\text{Ag}_{25}(\text{SR})_{18}$: $\text{Au}_{25}(\text{SR})_{18}$, in solid state	7
Figure S8	Heat map plot obtained from the mass spectra of grinding 1:5 mixture of $\text{Ag}_{25}(\text{SR})_{18}$: $\text{Au}_{25}(\text{SR})_{18}$, in solid state	7
Figure S9	Time-dependent electrospray ionization mass spectra (ESI MS), after grinding 5:1 mixture of $\text{Ag}_{25}(\text{SR})_{18}$: $\text{Au}_{25}(\text{SR})_{18}$, in solid state	8
Figure S10	Heat map plot obtained from the mass spectra of grinding 5:13 mixture of $\text{Ag}_{25}(\text{SR})_{18}$: $\text{Au}_{25}(\text{SR})_{18}$, in solid state	8
Figure S11	ESI-MS showing various homopolymers of $\text{Au}_{25}(\text{SR})_{18}$ at m/z 7393, and $\text{Ag}_{25}(\text{SR})_{18}$ at m/z 5167	9
Figure S12	ESI-MS of the hexamer species $[\text{Ag}_{72}\text{Au}_{78}(\text{SR})_{108}]^{6-}$, along with its theoretical fitting	9
Figure S13	Solid state UV-Vis absorption spectra of mixing of clusters	10
Figure S14	The time-dependent UV-Vis absorption spectra measured by dissolving the ground mixture in cold acetonitrile	10
Figure S15	The degradation peaks after the reaction, for different ratios of $\text{Ag}_{25}(\text{SR})_{18}$ and $\text{Au}_{25}(\text{SR})_{18}$	11
Table S1	The detailed information of all the polymeric species observed in mass spectrometry studies of 1:1 $\text{Ag}_{25}(\text{SR})_{18}$: $\text{Au}_{25}(\text{SR})_{18}$	11
Table S2	The detailed information of all the polymeric species observed in mass spectrometry studies of 1:3 $\text{Ag}_{25}(\text{SR})_{18}$: $\text{Au}_{25}(\text{SR})_{18}$	12
Table S3	The detailed information of all the polymeric species observed in mass spectrometry studies of 3:1 $\text{Ag}_{25}(\text{SR})_{18}$: $\text{Au}_{25}(\text{SR})_{18}$	12
Table S4	The detailed information of all the polymeric species observed in mass spectrometry studies of 1:5 $\text{Ag}_{25}(\text{SR})_{18}$: $\text{Au}_{25}(\text{SR})_{18}$	13
Table S5	The detailed information of all the polymeric species observed in mass spectrometry studies of 5:1 $\text{Ag}_{25}(\text{SR})_{18}$: $\text{Au}_{25}(\text{SR})_{18}$	14

1. Experimental section

Synthesis of $\text{HAuCl}_4 \cdot 3\text{H}_2\text{O}$

A 24 karat gold coin, weighing 2 g, was taken in a round bottom flask and added 10 ml of conc. HCl into it. Then it was heated at 60°C for 5 minutes. Into the hot solution, 4 ml of conc. HNO_3 was added dropwise, and bubble formation was observed. Continue the addition of HNO_3 until the bubbles are not formed. The solution was heated until the gold dissolves completely. After the complete dissolution of gold, the solution was cooled down to room temperature. Then it is further cooled at 0°C for 24 h, to precipitate out the impurities. The precipitate were removed by filtration, and 5 ml of distilled water was added to the filtrate. Further the filtrate was kept for slow evaporation, in presence of the drying agent phosphorus pentoxide, to get the crystalline product $\text{HAuCl}_4 \cdot 3\text{H}_2\text{O}$.

2. Instrumentation

UV-Vis absorption spectra of the cluster in their respective solution were optimized using a PerkinElmer Lambda 25 spectrophotometer in the 200–1100 nm wavelength range. The slit width used for the measurement is 1 nm.

Mass spectra of all the clusters were measured using Waters Synapt G2Si HDMS instrument. The instrument is equipped with an electrospray ionization source, mass selected ion trap, ion mobility cells, and time of flight mass analyzer. All MS measurements were acquired in the negative ion mode. An optimized operating conditions such as flow rate 15-20 $\mu\text{L}/\text{min}$, capillary voltage 2-3 kV, cone voltage 20 V, source offset 10 V, desolvation gas flow 400 L/min and source temperature 80-100 °C were used for the measurements.

The interaction between the clusters lead to the formation of multiple polymeric species as observed in ESI-MS (see **Figure 1, 2**), making it difficult to assign charge states in the case of metal-exchanged alloy clusters and their polymeric entities, especially when isotopic resolution

is lacking and charge states overlap within complex mass spectra. Experimentally acquired ESI MS spectra were analyzed using UniDec software to address these challenges.¹ This approach allowed for a clearer visualization of the relative intensities of cluster ions, including the less intense polymer ions, in a 'Heat map' plot, and helped to reduce mass uncertainty in the spectrum.

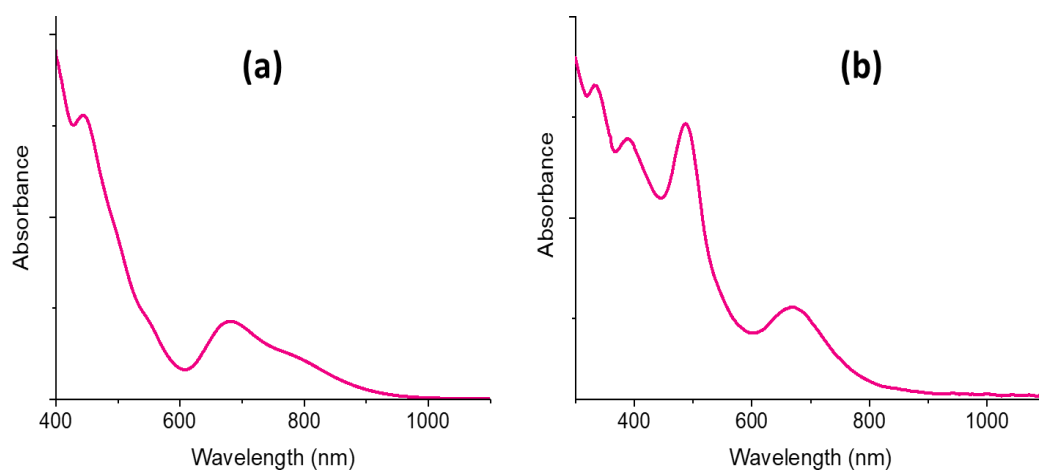


Figure S1. UV-Vis absorption spectra of (a) $[\text{Au}_{25}(\text{PET})_{18}]^{-}$, and (b) $[\text{Ag}_{25}(\text{DMBT})_{18}]^{-}$ clusters in acetonitrile solvent.

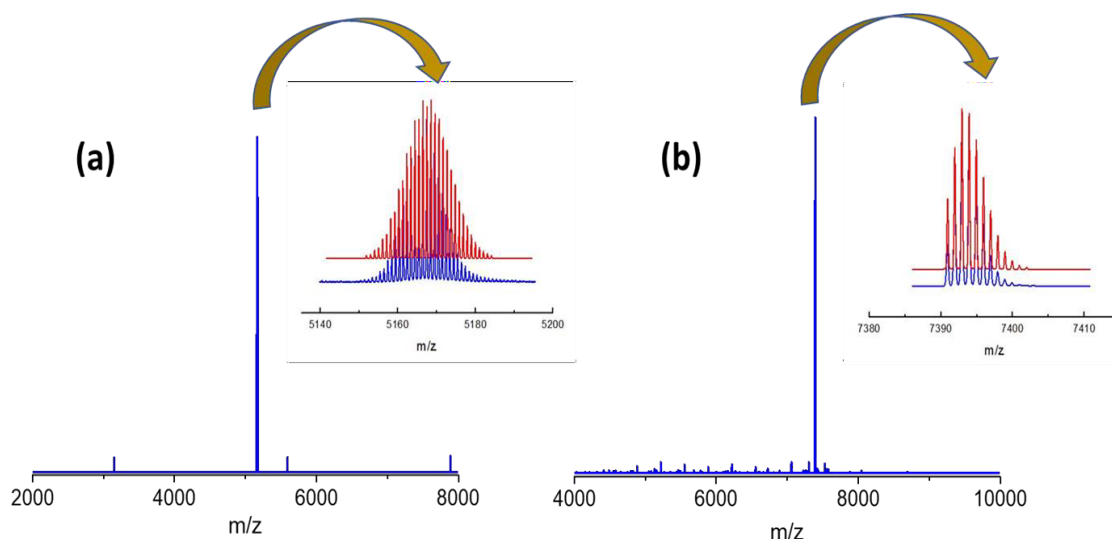


Figure S2. ESI-MS of (a) $[\text{Ag}_{25}(\text{DMBT})_{18}]^{-}$, and (b) $[\text{Au}_{25}(\text{PET})_{18}]^{-}$ cluster, measured in acetonitrile solvent.

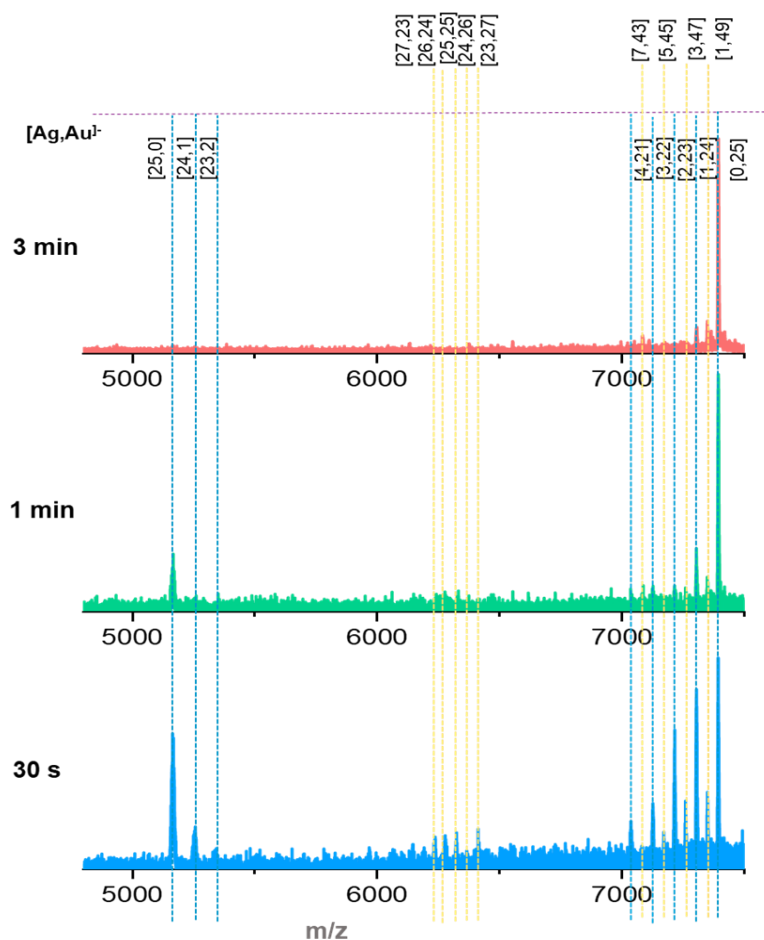


Figure S3. Time-dependent ESI-MS, after grinding 1:3 mixture of $\text{Ag}_{25}(\text{SR})_{18}:\text{Au}_{25}(\text{SR})_{18}$, in the solid state.

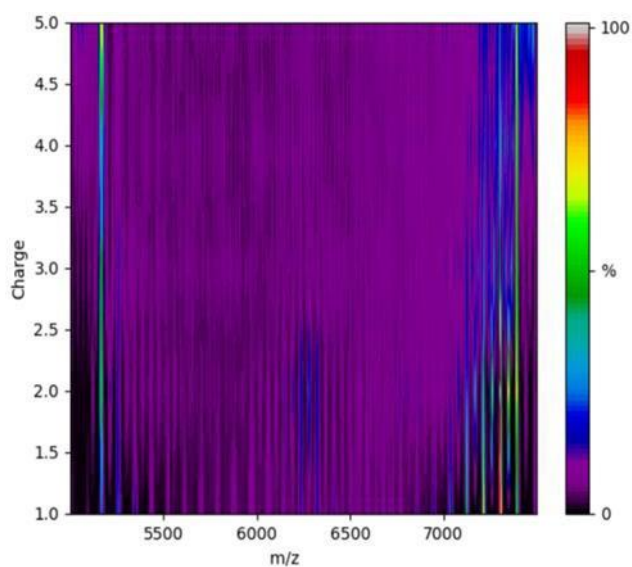


Figure S4. Heat map plot obtained from the mass spectra of grinding 1:3 mixture of $\text{Ag}_{25}(\text{SR})_{18}:\text{Au}_{25}(\text{SR})_{18}$, in the solid state.

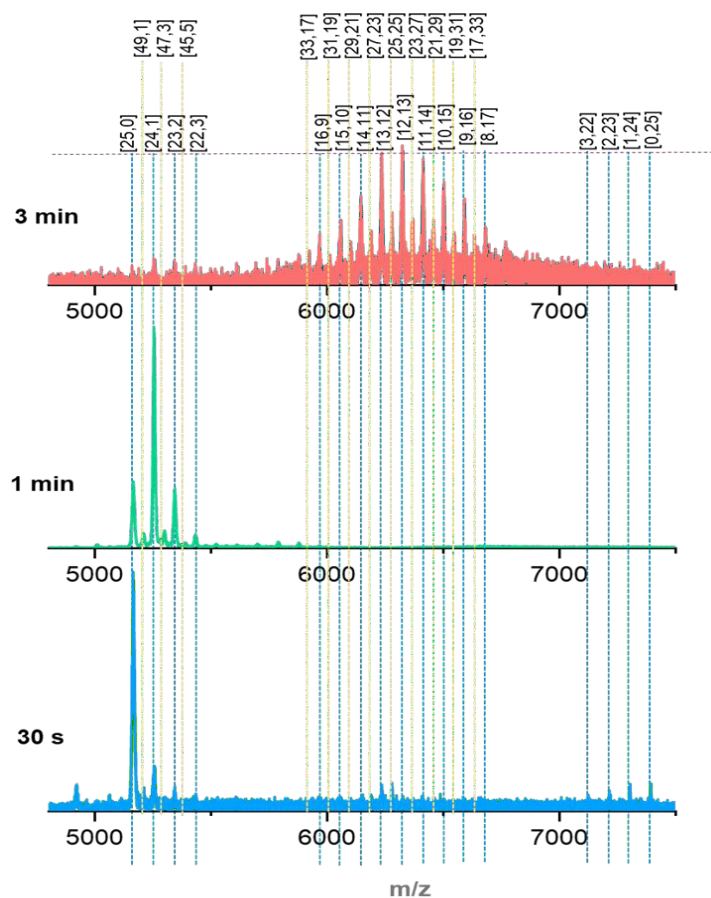


Figure S5. Time-dependent ESI-MS, after grinding 3:1 mixture of $\text{Ag}_{25}(\text{SR})_{18}:\text{Au}_{25}(\text{SR})_{18}$, in the solid state.

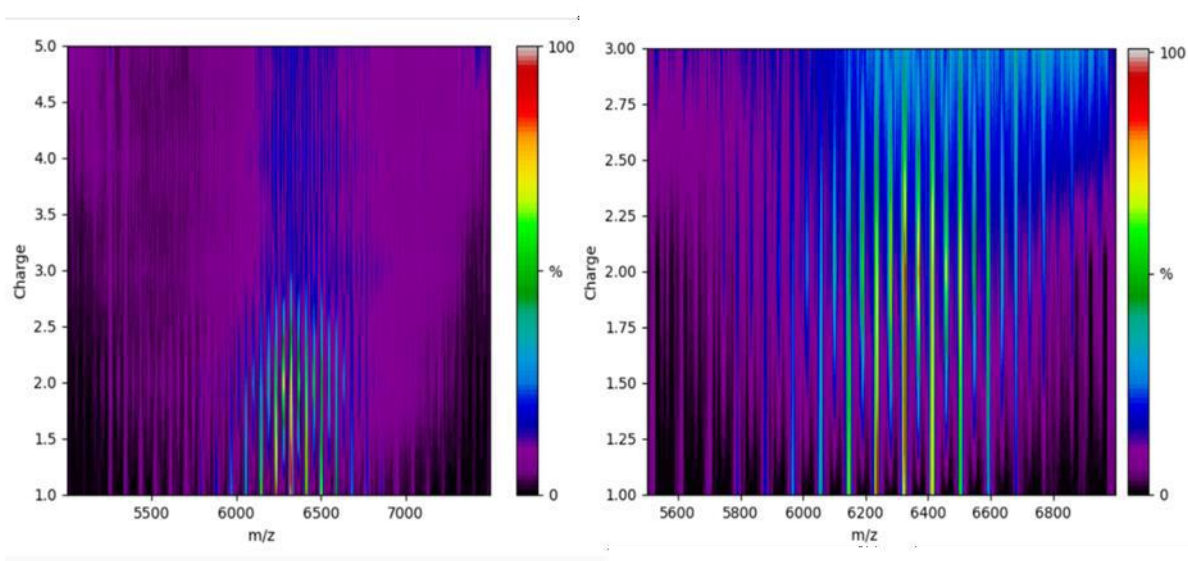


Figure S6. Heat map plot obtained from the mass spectra of grinding 3:1 mixture of $\text{Ag}_{25}(\text{SR})_{18}:\text{Au}_{25}(\text{SR})_{18}$, in the solid state.

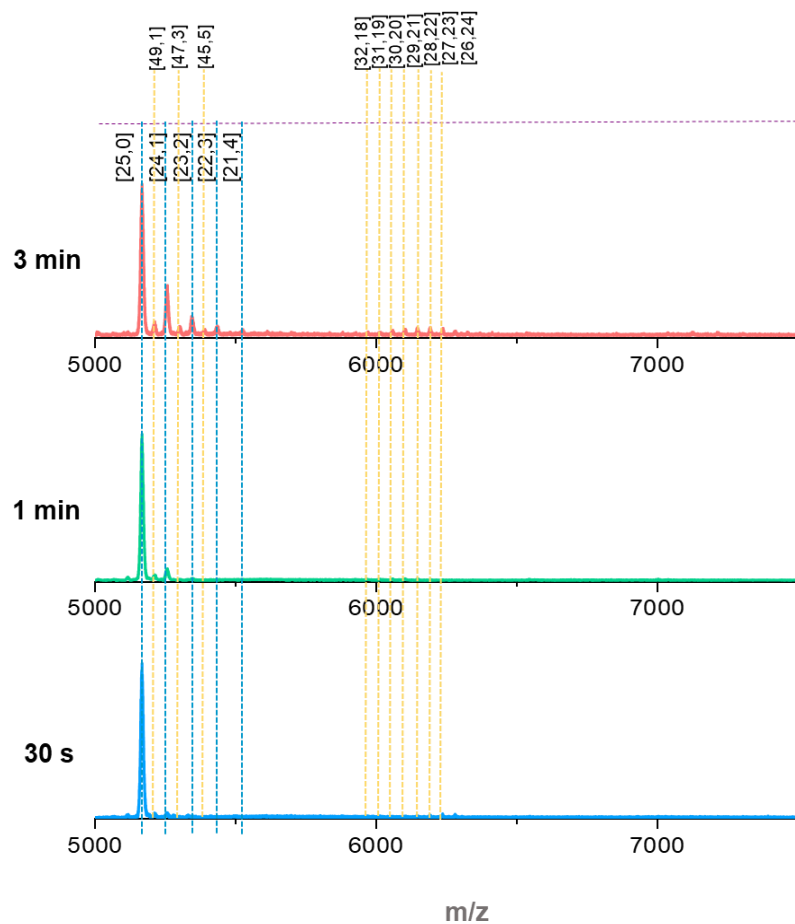


Figure S7. Time-dependent ESI-MS, after grinding 1:5 mixture of $\text{Ag}_{25}(\text{SR})_{18}:\text{Au}_{25}(\text{SR})_{18}$, in the solid state.

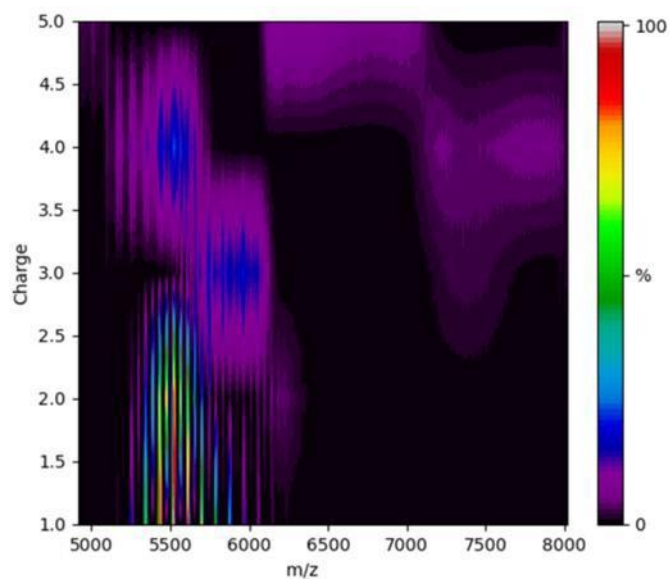


Figure S8. Heat map plot obtained from the mass spectra of grinding 1:5 mixture of $\text{Ag}_{25}(\text{SR})_{18}:\text{Au}_{25}(\text{SR})_{18}$, in the solid state.

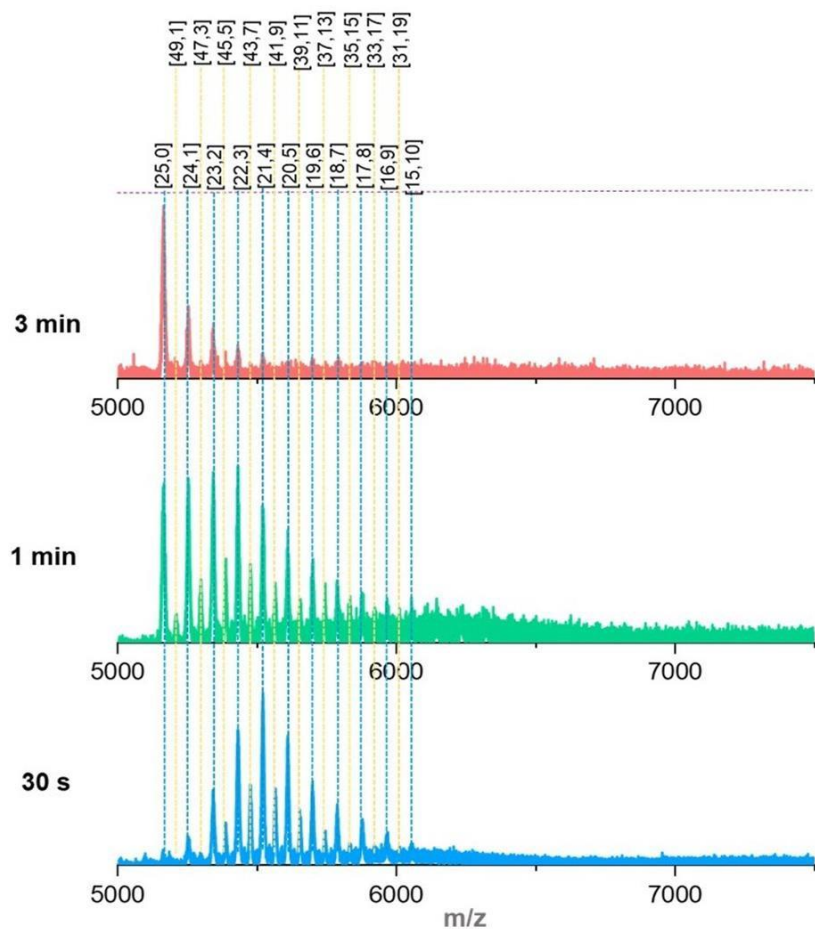


Figure S9. Time-dependent ESI-MS, after grinding a 5:1 mixture of $\text{Ag}_{25}(\text{SR})_{18}:\text{Au}_{25}(\text{SR})_{18}$ in the solid state.

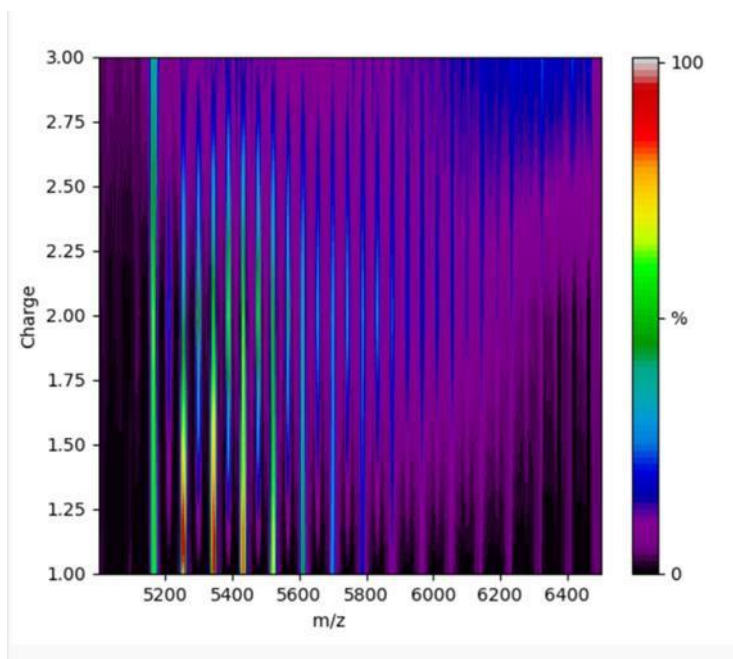


Figure S10. Heat map plot obtained from the mass spectra, of grinding 5:1 mixture of $\text{Ag}_{25}(\text{SR})_{18}:\text{Au}_{25}(\text{SR})_{18}$, in the solid state.

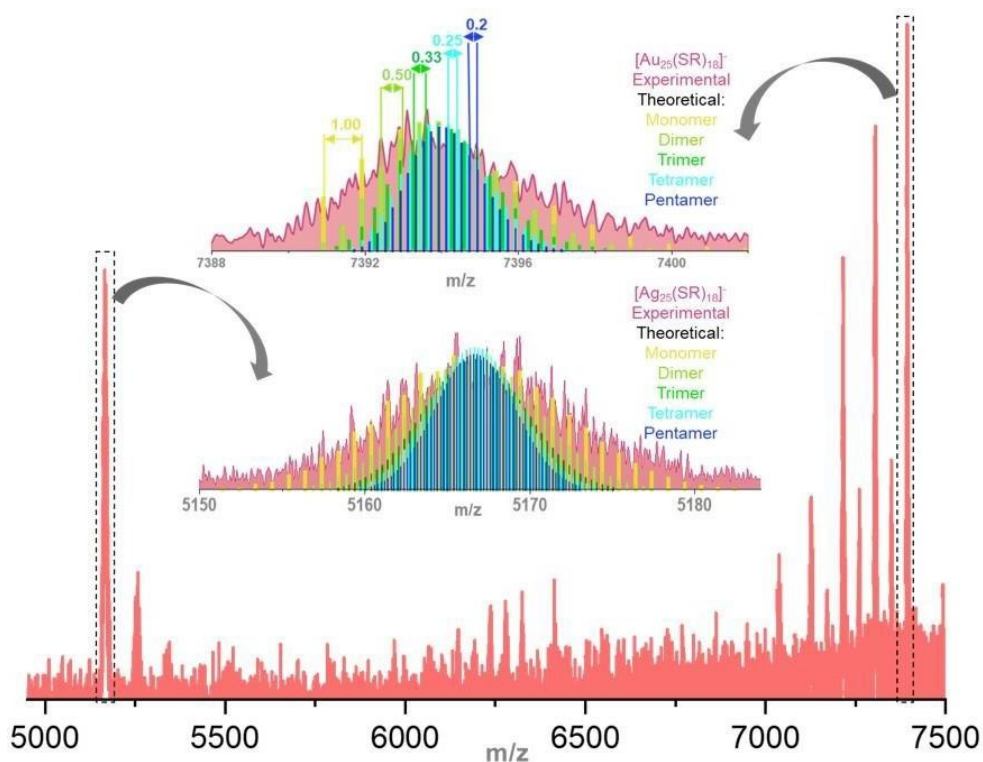


Figure S11. ESI-MS showing various homopolymers of $\text{Au}_{25}(\text{SR})_{18}$ at m/z 7393, i.e., $[\text{Au}_{125}(\text{SR})_{90}]^{5-}$, $[\text{Au}_{100}(\text{SR})_{72}]^{4-}$, $[\text{Au}_{75}(\text{SR})_{54}]^{3-}$, and $[\text{Au}_{50}(\text{SR})_{25}]^{2-}$, and $\text{Ag}_{25}(\text{SR})_{18}$ at m/z 5167, i.e., $[\text{Ag}_{125}(\text{SR})_{90}]^{5-}$, $[\text{Ag}_{100}(\text{SR})_{72}]^{4-}$, $[\text{Ag}_{75}(\text{SR})_{54}]^{3-}$, and $[\text{Ag}_{50}(\text{SR})_{25}]^{2-}$.

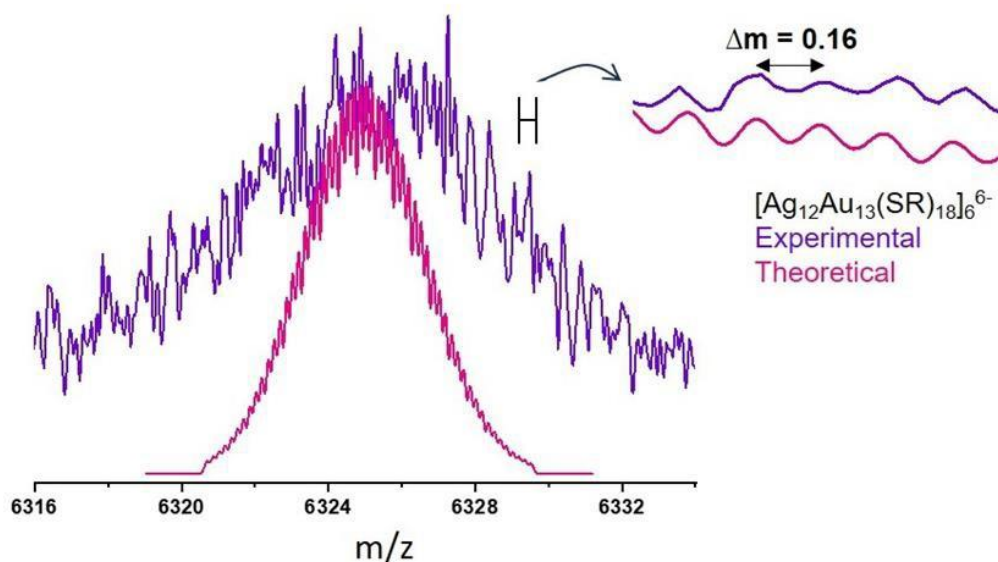


Figure S12. ESI-MS of the hexamer species $[\text{Ag}_{72}\text{Au}_{78}(\text{SR})_{108}]^{6-}$, along with its theoretical fitting. The instrumental resolution was poor at high mas range to clearly resolve all the peaks.

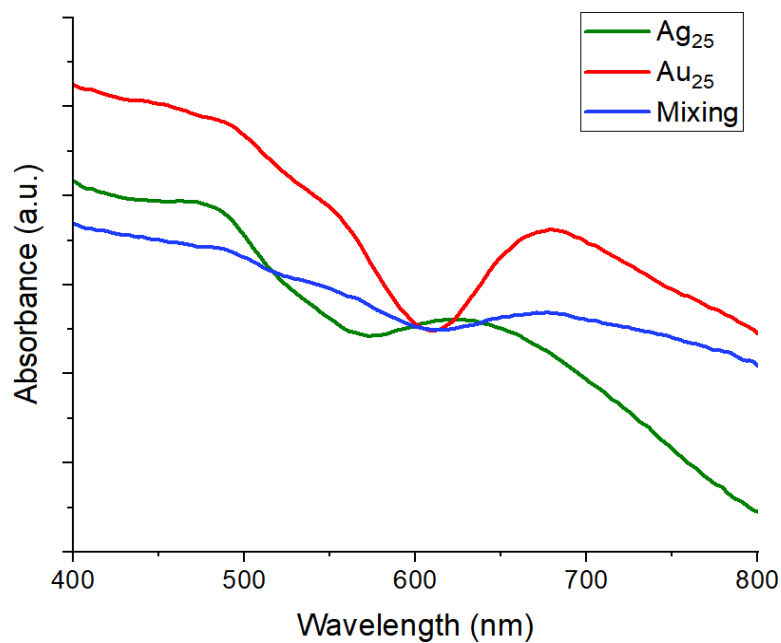


Figure S13. Solid state UV-Vis absorption spectra upon mixing the clusters in the solid state. Due to the limitation of the instrument, we could not measure the spectra above 800 nm.

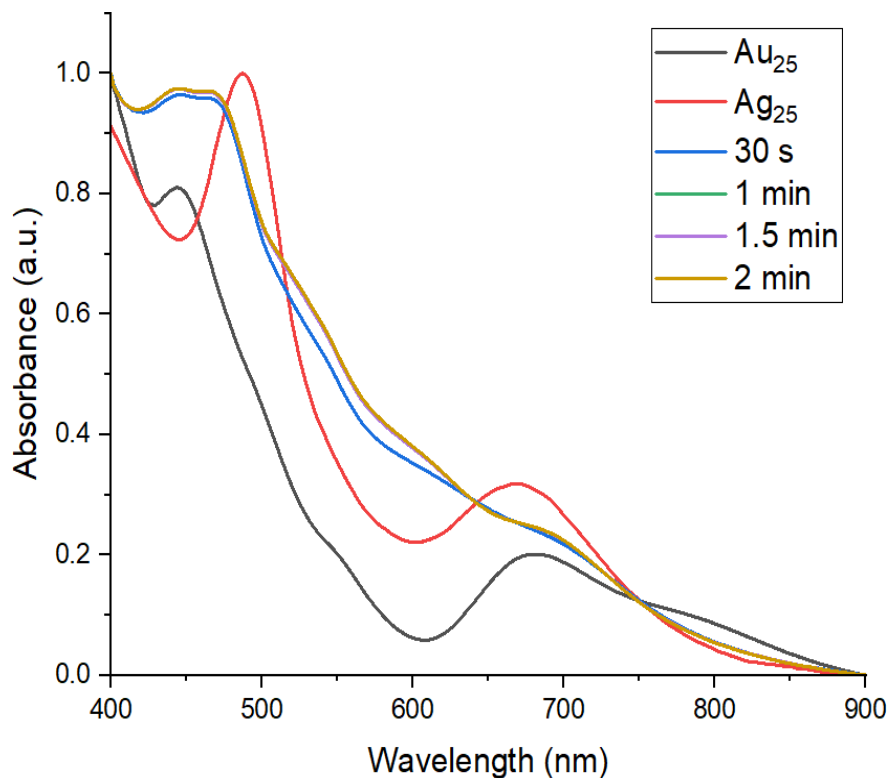


Figure S14. The time-dependent UV-Vis absorption spectra measured by dissolving the ground mixture in cold acetonitrile.

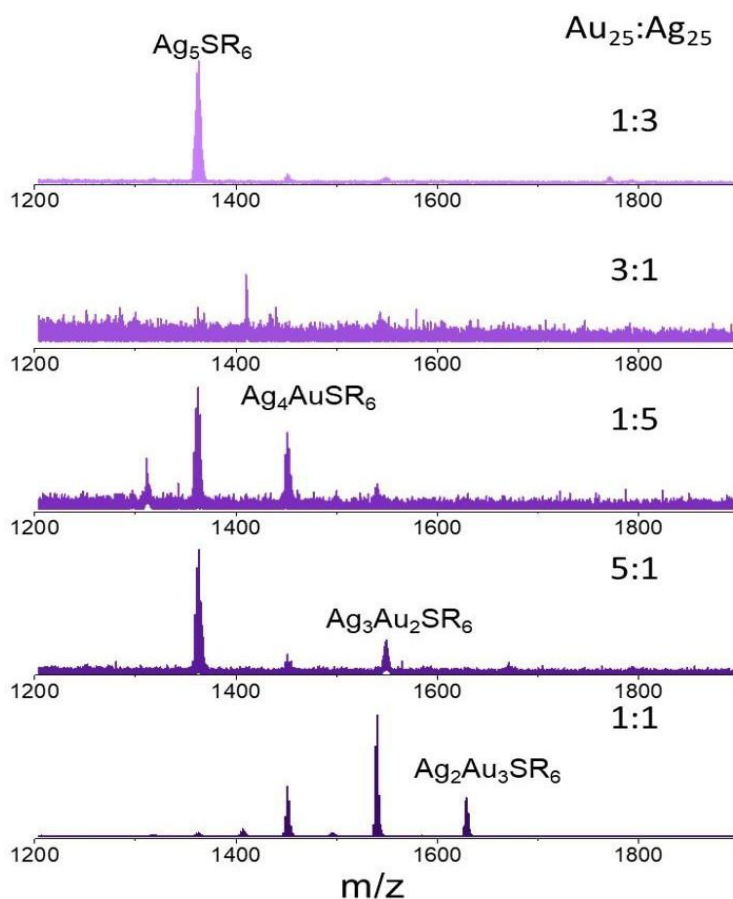


Figure S15. The degradation peaks after the reaction, for different ratios of $\text{Ag}_{25}(\text{SR})_{18}$ and $\text{Au}_{25}(\text{SR})_{18}$.

Table S1. The detailed information of all the polymeric species observed in mass spectrometry studies of 1:1 $\text{Ag}_{25}(\text{SR})_{18}:\text{Au}_{25}(\text{SR})_{18}$.

m/z	Monomers	m/z	Dimers	m/z	Trimers	m/z	Tetramers
7393	$\text{Au}_{25}(\text{SR})_{18}$	7350	$\text{AgAu}_{24}(\text{SR})_{18} + \text{Au}_{25}(\text{SR})_{18}$			5545	$\text{Ag}_{83}\text{Au}_{17}(\text{SR})_{72}$
7305	$\text{AgAu}_{24}(\text{SR})_{18}$	7308	$2[\text{AgAu}_{24}(\text{SR})_{18}]$			5590	$\text{Ag}_{81}\text{Au}_{19}(\text{SR})_{72}$
7216	$\text{Ag}_2\text{Au}_{23}(\text{SR})_{18}$	7260	$\text{AgAu}_{24}(\text{SR})_{18} + \text{Ag}_2\text{Au}_{23}(\text{SR})_{18}$			5634	$\text{Ag}_{79}\text{Au}_{21}(\text{SR})_{72}$
7127	$\text{Ag}_3\text{Au}_{22}(\text{SR})_{18}$	7172	$\text{Ag}_3\text{Au}_{22}(\text{SR})_{18} + \text{Ag}_2\text{Au}_{23}(\text{SR})_{18}$			5679	$\text{Ag}_{77}\text{Au}_{23}(\text{SR})_{72}$

Table S2. The detailed information of all the polymeric species observed in mass spectrometry studies of 1:3 Ag₂₅(SR)₁₈: Au₂₅(SR)₁₈.

m/z	Monomers	m/z	Dimers	m/z	Trimers	m/z	Tetramers
5167	Ag ₂₅ (SR) ₁₈	6280	Au ₂₅ Ag ₂₅ (SR) ₃₆	5167	3[Ag ₂₅ (SR) ₁₈]	5167	4[Ag ₂₅ (SR) ₁₈]
5256	AuAg ₂₄ (SR) ₁₈	6235	Au ₂₄ Ag ₂₆ (SR) ₃₆	7216	3[Ag ₂ Au ₂₃ (SR) ₁₈]	7393	4[Au ₂₅ (SR) ₁₈]
5345	Au ₂ Ag ₂₃ (SR) ₁₈	6324	Au ₂₆ Ag ₂₄ (SR) ₃₆	7305	3[AgAu ₂₄ (SR) ₁₈]		
5434	Au ₃ Ag ₂₂ (SR) ₁₈	6189	Au ₂₃ Ag ₂₇ (SR) ₃₆	7393	3[Au ₂₅ (SR) ₁₈]		
5702	Au ₆ Ag ₁₉ (SR) ₁₈	6144	Au ₂₂ Ag ₂₈ (SR) ₃₆				
5792	Au ₇ Ag ₁₈ (SR) ₁₈	6100	Au ₂₁ Ag ₂₉ (SR) ₃₆				
5970	Au ₉ Ag ₁₆ (SR) ₁₈	6369	Au ₂₇ Ag ₂₃ (SR) ₃₆				
		6414	Au ₂₈ Ag ₂₂ (SR) ₃₆				
		6459	Au ₂₉ Ag ₂₁ (SR) ₃₆				

Table S3. The detailed information of all the polymeric species observed in mass spectrometry studies of 3:1 Ag₂₅(SR)₁₈: Au₂₅(SR)₁₈.

m/z	Monomers	m/z	Dimers	m/z	Trimers	m/z	Tetramers
6324	Ag ₁₂ Au ₁₃ (SR) ₁₈	6324	2[Ag ₁₂ Au ₁₃ (SR) ₁₈]	6324	3[Ag ₁₂ Au ₁₃ (SR) ₁₈]	6324	4[Ag ₁₂ Au ₁₃ (SR) ₁₈]
6413	Ag ₁₁ Au ₁₄ (SR) ₁₈	6370	Ag ₁₂ Au ₁₃ (SR) ₁₈ + Ag ₁₁ Au ₁₄ (SR) ₁₈	6413	3[Ag ₁₁ Au ₁₄ (SR) ₁₈]	6347	3[Ag ₁₂ Au ₁₃ (SR) ₁₈] + Ag ₁₁ Au ₁₄ (SR) ₁₈
6504	Ag ₁₀ Au ₁₅ (SR) ₁₈	6413	Ag ₁₁ Au ₁₄ (SR) ₁₈ + Ag ₁₁ Au ₁₄ (SR) ₁₈	6264	2[Ag ₁₃ Au ₁₂ (SR) ₁₈] + Ag ₁₂ Au ₁₃ (SR) ₁₈	6390	3[Ag ₁₁ Au ₁₄ (SR) ₁₈] + Ag ₁₂ Au ₁₃ (SR) ₁₈
6593	Ag ₉ Au ₁₆ (SR) ₁₈	6459	Ag ₁₁ Au ₁₄ (SR) ₁₈ + Ag ₁₀ Au ₁₅ (SR) ₁₈	6354	2[Ag ₁₂ Au ₁₃ (SR) ₁₈] + Ag ₁₁ Au ₁₄ (SR) ₁₈	6436	3[Ag ₁₁ Au ₁₄ (SR) ₁₈] + Ag ₁₀ Au ₁₅ (SR) ₁₈
6683	Ag ₈ Au ₁₇ (SR) ₁₈	6549	Ag ₁₀ Au ₁₅ (SR) ₁₈ + Ag ₉ Au ₁₆ (SR) ₁₈	6384	2[Ag ₁₁ Au ₁₄ (SR) ₁₈] + Ag ₁₂ Au ₁₃ (SR) ₁₈	6480	3[Ag ₁₀ Au ₁₅ (SR) ₁₈] + Ag ₁₁ Au ₁₄ (SR) ₁₈
6771	Ag ₇ Au ₁₈ (SR) ₁₈	6638	Ag ₉ Au ₁₆ (SR) ₁₈ + Ag ₈ Au ₁₇ (SR) ₁₈	6472	2[Ag ₁₀ Au ₁₅ (SR) ₁₈] + Ag ₁₁ Au ₁₄ (SR) ₁₈	6256	3[Ag ₁₃ Au ₁₂ (SR) ₁₈] + Ag ₁₂ Au ₁₃ (SR) ₁₈
6860	Ag ₆ Au ₁₉ (SR) ₁₈	6683	Ag ₈ Au ₁₇ (SR) ₁₈ + Ag ₈ Au ₁₇ (SR) ₁₈	6530	2[Ag ₁₀ Au ₁₅ (SR) ₁₈] + Ag ₉ Au ₁₆ (SR) ₁₈	6213	3[Ag ₁₃ Au ₁₂ (SR) ₁₈] + Ag ₁₄ Au ₁₁ (SR) ₁₈
6145	Ag ₁₄ Au ₁₁ (SR) ₁₈	6771	Ag ₇ Au ₁₈ (SR) ₁₈ + Ag ₇ Au ₁₈ (SR) ₁₈	6204	2[Ag ₁₃ Au ₁₂ (SR) ₁₈] + Ag ₁₄ Au ₁₁ (SR) ₁₈	6168	3[Ag ₁₄ Au ₁₁ (SR) ₁₈] + Ag ₁₃ Au ₁₂ (SR) ₁₈
6234	Ag ₁₃ Au ₁₂ (SR) ₁₈	6817	Ag ₆ Au ₁₉ (SR) ₁₈ + Ag ₇ Au ₁₈ (SR) ₁₈	6176	2[Ag ₁₄ Au ₁₁ (SR) ₁₈] + Ag ₁₃ Au ₁₂ (SR) ₁₈	6123	3[Ag ₁₄ Au ₁₁ (SR) ₁₈] + Ag ₁₅ Au ₁₀ (SR) ₁₈
6056	Ag ₁₅ Au ₁₀ (SR) ₁₈	6861	Ag ₆ Au ₁₉ (SR) ₁₈ + Ag ₆ Au ₁₉ (SR) ₁₈	6114	2[Ag ₁₄ Au ₁₁ (SR) ₁₈] + Ag ₁₅ Au ₁₀ (SR) ₁₈	6079	3[Ag ₁₅ Au ₁₀ (SR) ₁₈] + Ag ₁₄ Au ₁₁ (SR) ₁₈
5967	Ag ₁₆ Au ₉ (SR) ₁₈	6145	Ag ₁₄ Au ₁₁ (SR) ₁₈ + Ag ₁₄ Au ₁₁ (SR) ₁₈				
5878	Ag ₁₇ Au ₈ (SR) ₁₈	6189	Ag ₁₄ Au ₁₁ (SR) ₁₈ + Ag ₁₃ Au ₁₂ (SR) ₁₈				

5790	$\text{Ag}_{18}\text{Au}_7(\text{SR})_{18}$	6234	$\text{Ag}_{13}\text{Au}_{12}(\text{SR})_{18} + \text{Ag}_{13}\text{Au}_{12}(\text{SR})_{18}$				
		6279	$\text{Ag}_{13}\text{Au}_{12}(\text{SR})_{18} + \text{Ag}_{12}\text{Au}_{13}(\text{SR})_{18}$				
		6324	$\text{Ag}_{12}\text{Au}_{13}(\text{SR})_{18} + \text{Ag}_{12}\text{Au}_{13}(\text{SR})_{18}$				
		6102	$\text{Ag}_{14}\text{Au}_{11}(\text{SR})_{18} + \text{Ag}_{15}\text{Au}_{10}(\text{SR})_{18}$				
		6011	$\text{Ag}_{15}\text{Au}_{10}(\text{SR})_{18} + \text{Ag}_{16}\text{Au}_9(\text{SR})_{18}$				
		5967	$\text{Ag}_{16}\text{Au}_9(\text{SR})_{18} + \text{Ag}_{16}\text{Au}_9(\text{SR})_{18}$				
		5922	$\text{Ag}_{16}\text{Au}_9(\text{SR})_{18} + \text{Ag}_{17}\text{Au}_8(\text{SR})_{18}$				
		5878	$\text{Ag}_{17}\text{Au}_8(\text{SR})_{18} + \text{Ag}_{17}\text{Au}_8(\text{SR})_{18}$				
		5833	$\text{Ag}_{18}\text{Au}_7(\text{SR})_{18} + \text{Ag}_{17}\text{Au}_8(\text{SR})_{18}$				
		5790	$2[\text{Ag}_{18}\text{Au}_7(\text{SR})_{18}]$				

Table S4. The detailed information of all the polymeric species observed in mass spectrometry studies of 1:5 $\text{Ag}_{25}(\text{SR})_{18}$: $\text{Au}_{25}(\text{SR})_{18}$.

m/z	Monomers	m/z	Dimers	m/z	Trimers	m/z	Tetramers
5167	$\text{Ag}_{25}(\text{SR})_{18}$	5212	$\text{AuAg}_{49}(\text{SR})_{36}$	5227	$\text{AuAg}_{49}(\text{SR})_{36} + \text{AuAg}_{24}(\text{SR})_{18}$	5278	$3[\text{AuAg}_{24}(\text{SR})_{18}] + [\text{Au}_2\text{Ag}_{23}(\text{SR})_{18}]$
5256	$\text{AuAg}_{24}(\text{SR})_{18}$	5300	$\text{Au}_3\text{Ag}_{47}(\text{SR})_{36}$			5323	$3[\text{Au}_2\text{Ag}_{23}(\text{SR})_{18}] + [\text{AuAg}_{24}(\text{SR})_{18}]$
5345	$\text{Au}_2\text{Ag}_{23}(\text{SR})_{18}$	5390	$\text{Au}_5\text{Ag}_{45}(\text{SR})_{36}$			5367	$3[\text{Au}_2\text{Ag}_{23}(\text{SR})_{18}] + [\text{Au}_3\text{Ag}_{22}(\text{SR})_{18}]$
5434	$\text{Au}_3\text{Ag}_{22}(\text{SR})_{18}$	5480	$\text{Au}_7\text{Ag}_{43}(\text{SR})_{36}$			5412	$3[\text{Au}_3\text{Ag}_{22}(\text{SR})_{18}] + [\text{Au}_2\text{Ag}_{23}(\text{SR})_{18}]$
5523	$\text{Au}_4\text{Ag}_{21}(\text{SR})_{18}$	5968	$\text{Au}_{18}\text{Ag}_{32}(\text{SR})_{36}$			5501	$3[\text{Au}_4\text{Ag}_{21}(\text{SR})_{18}] + [\text{Au}_3\text{Ag}_{22}(\text{SR})_{18}]$
5612	$\text{Au}_5\text{Ag}_{20}(\text{SR})_{18}$	6013	$\text{Au}_{19}\text{Ag}_{31}(\text{SR})_{36}$			6080	$\text{Au}_{21}\text{Ag}_{29}(\text{SR})_{36} + \text{Au}_{20}\text{Ag}_{30}(\text{SR})_{36}$
		6058	$\text{Au}_{20}\text{Ag}_{30}(\text{SR})_{36}$			6125	$\text{Au}_{21}\text{Ag}_{29}(\text{SR})_{36} + \text{Au}_{22}\text{Ag}_{28}(\text{SR})_{36}$
		6102	$\text{Au}_{21}\text{Ag}_{29}(\text{SR})_{36}$			6169	$\text{Au}_{22}\text{Ag}_{28}(\text{SR})_{36} + \text{Au}_{23}\text{Ag}_{27}(\text{SR})_{36}$
		6147	$\text{Au}_{22}\text{Ag}_{28}(\text{SR})_{36}$			6213	$\text{Au}_{23}\text{Ag}_{27}(\text{SR})_{36} + \text{Au}_{24}\text{Ag}_{26}(\text{SR})_{36}$
		6191	$\text{Au}_{23}\text{Ag}_{27}(\text{SR})_{36}$			6258	$\text{Au}_{25}\text{Ag}_{25}(\text{SR})_{36} +$

							$\text{Au}_{24}\text{Ag}_{26}(\text{SR})_{36}$
		6236	$\text{Au}_{24}\text{Ag}_{26}(\text{SR})_{36}$			6303	$\text{Au}_{25}\text{Ag}_{25}(\text{SR})_{36} + \text{Au}_{26}\text{Ag}_{24}(\text{SR})_{36}$
		6280	$\text{Au}_{25}\text{Ag}_{25}(\text{SR})_{36}$				
		6325	$\text{Au}_{26}\text{Ag}_{24}(\text{SR})_{36}$				
		6369	$\text{Au}_{27}\text{Ag}_{23}(\text{SR})_{36}$				

Table S5. The detailed information of all the polymeric species observed in mass spectrometry studies of 5:1 $\text{Ag}_{25}(\text{SR})_{18}$: $\text{Au}_{25}(\text{SR})_{18}$.

m/z	Monomers	m/z	Dimers	m/z	Trimers	m/z	Tetramers
5167	$\text{Ag}_{25}(\text{SR})_{18}$	5211	$\text{Ag}_{25}(\text{SR})_{18} + \text{AuAg}_{24}(\text{SR})_{18}$	5285	$[\text{AuAg}_{24}(\text{SR})_{18}] + [\text{Au}_3\text{Ag}_{47}(\text{SR})_{36}]$	5322	$[\text{Au}_3\text{Ag}_{47}(\text{SR})_{36}] + [\text{Au}_4\text{Ag}_{46}(\text{SR})_{36}]$
5256	$\text{AuAg}_{24}(\text{SR})_{18}$	5300	$\text{AuAg}_{24}(\text{SR})_{18} + \text{Au}_2\text{Ag}_{23}(\text{SR})_{18}$	5344	$[\text{Au}_3\text{Ag}_{22}(\text{SR})_{18}] + [\text{Au}_3\text{Ag}_{47}(\text{SR})_{36}]$	5410	$[\text{Au}_5\text{Ag}_{45}(\text{SR})_{36}] + [\text{Au}_6\text{Ag}_{44}(\text{SR})_{36}]$
5344	$\text{Au}_2\text{Ag}_{23}(\text{SR})_{18}$	5388	$\text{Au}_2\text{Ag}_{23}(\text{SR})_{18} + \text{Au}_3\text{Ag}_{22}(\text{SR})_{18}$	5373	$[\text{Au}_2\text{Ag}_{23}(\text{SR})_{18}] + [\text{Au}_5\text{Ag}_{45}(\text{SR})_{36}]$		
5432	$\text{Au}_3\text{Ag}_{22}(\text{SR})_{18}$	5477	$\text{Au}_3\text{Ag}_{22}(\text{SR})_{18} + \text{Au}_4\text{Ag}_{21}(\text{SR})_{18}$	5432	$[\text{Au}_4\text{Ag}_{21}(\text{SR})_{18}] + [\text{Au}_5\text{Ag}_{45}(\text{SR})_{36}]$		
5521	$\text{Au}_4\text{Ag}_{21}(\text{SR})_{18}$	5566	$\text{Au}_4\text{Ag}_{21}(\text{SR})_{18} + \text{Au}_5\text{Ag}_{20}(\text{SR})_{18}$	5489	$[\text{Au}_4\text{Ag}_{21}(\text{SR})_{18}] + [\text{Au}_7\text{Ag}_{43}(\text{SR})_{36}]$		
5610	$\text{Au}_5\text{Ag}_{20}(\text{SR})_{18}$	5656	$\text{Au}_5\text{Ag}_{20}(\text{SR})_{18} + \text{Au}_6\text{Ag}_{19}(\text{SR})_{18}$	5521	$[\text{Au}_5\text{Ag}_{20}(\text{SR})_{18}] + [\text{Au}_7\text{Ag}_{43}(\text{SR})_{36}]$		
5699	$\text{Au}_6\text{Ag}_{19}(\text{SR})_{18}$	5745	$\text{Au}_6\text{Ag}_{19}(\text{SR})_{18} + \text{Au}_7\text{Ag}_{18}(\text{SR})_{18}$	5582	$[\text{Au}_5\text{Ag}_{20}(\text{SR})_{18}] + [\text{Au}_9\text{Ag}_{41}(\text{SR})_{36}]$		
5788	$\text{Au}_7\text{Ag}_{18}(\text{SR})_{18}$	5833	$\text{Au}_7\text{Ag}_{18}(\text{SR})_{18} + \text{Au}_8\text{Ag}_{17}(\text{SR})_{18}$				
5877	$\text{Au}_8\text{Ag}_{17}(\text{SR})_{18}$	5922	$\text{Au}_8\text{Ag}_{17}(\text{SR})_{18} + \text{Au}_9\text{Ag}_{16}(\text{SR})_{18}$				
6055	$\text{Au}_{10}\text{Ag}_{15}(\text{SR})_{18}$	6011	$\text{Au}_9\text{Ag}_{16}(\text{SR})_{18} + \text{Au}_{10}\text{Ag}_{15}(\text{SR})_{18}$				
6144	$\text{Au}_{11}\text{Ag}_{14}(\text{SR})_{18}$						
6233	$\text{Au}_{12}\text{Ag}_{13}(\text{SR})_{18}$						
6322	$\text{Au}_{13}\text{Ag}_{12}(\text{SR})_{18}$						

References

- (1) Marty, M. T.; Baldwin, A. J.; Marklund, E. G.; Hochberg, G. K. A.; Benesch, J. L. P.; Robinson, C. V. Bayesian Deconvolution of Mass and Ion Mobility Spectra: From Binary Interactions to Polydisperse Ensembles. *Anal. Chem.* **2015**, *87* (8), 4370–4376. <https://doi.org/10.1021/acs.analchem.5b00140>.

Cysteine-Protected Antibacterial Spheroids of Atomically Precise Copper Clusters for Direct and Affordable Arsenic Detection from Drinking Water

Jenifer Shantha Kumar, Arijit Jana, Jayathraa Raman, Hema Madhuri Veera, Amoghavarsha Ramachandra Kini, Jayoti Roy, Saurav Kanti Jana, Tiju Thomas, and Thalappil Pradeep*



Cite This: *Environ. Sci. Technol. Lett.* 2024, 11, 831–837



Read Online

ACCESS

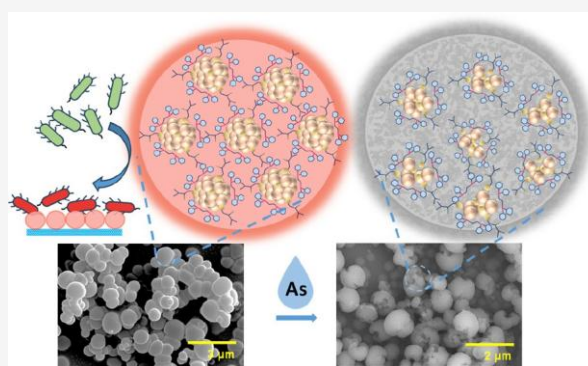
Metrics & More

Article Recommendations

* Supporting Information

ABSTRACT: Rapid and naked-eye detection of water-borne contaminants using molecularly precise nanomaterials has emerged as a promising strategy to reduce the impact of chemical pollution. This study presents a luminescence-based arsenic (*As*) sensor, eliminating the need for sample preparation. Incorporating red-emitting spheroidal cluster-assembled superstructures (CASs), comprised of Cu_{17} nanoclusters (Cu_{17}NCs), coprotected by L-cysteine (L-Cys) and 1,2-bis(diphenylphosphino) ethane (DPPE) ligands, the sensor exhibits notable sensitivity toward arsenite (As^{3+}) and (As^{5+}) ions. A detection limit of 1 ppb in tap water was achieved through luminescence-based quenching. Remarkably, it demonstrates selective detection of *As* amidst common interfering metal ions such as Cd^{2+} , Hg^{2+} , Fe^{3+} , Pb^{2+} , Cu^{2+} , and Cr^{3+} . A sensor disc made of CASs coated on nonwoven polypropylene (PP) mats has been devised for practical field applications. Electron microscopy reveals disrupted morphology of the spheroids due to *As* interaction. Moreover, the CASs exhibit significant antibacterial efficacy against Gram-negative *Escherichia coli* and Gram-positive *Staphylococcus aureus* and antibiofilm properties against *Bacillus subtilis*. This research highlights the effectiveness of atomically precise clusters for a practical application with direct societal relevance.

KEYWORDS: Nanocluster assembly, Cu_{17} nanoclusters, Red luminescence, Arsenic, Sensing, Antibacterial, Antibiofilm



1. INTRODUCTION

One-third of the human population is deprived of access to safe drinking water.¹ Contaminants in water include metal ions and microorganisms, such as bacteria, fungi, protozoa and viruses. Arsenic (*As*) is one of the most hazardous heavy metals (although semimetal technically) prevalent in diverse water sources, which is identified as the largest mass poisoning in the history of humanity.^{2,3} Most regulating agencies have fixed the *As* limit at 10 ppb in drinking water.^{4,5} Quantifying *As* at ppb levels using portable, solid-state sensors has also been challenging.⁶ Lack of an efficient sensing system which is selective, affordable, and easy to handle, particularly in the field, persists.⁷ Also, it is crucial to develop sensing systems capable of detecting both ionic states, considering that inorganic *As* exists as arsenite (As^{3+}) and arsenate (As^{5+}) ions. As^{3+} is predominant in water at reducing conditions such as groundwater, whereas As^{5+} is present in surface waters.⁸ Recently, several promising heavy metal sensing systems based on nanoclusters (NCs) have been developed.^{9–11} NCs are a new class of atomically confined materials carrying fewer atoms than nanoparticles and consequently have a higher surface-to-volume ratio with interesting chemical and photophysical

properties.^{9–13} To date, gold and silver are the preferred NCs due to their facile synthesis, wide range of photophysical properties and stability in ambient conditions.¹⁴ Copper NCs (CuNCs) are nonprecious metal alternatives, more economically viable than NCs of gold, silver, and platinum, exhibiting many versatile applications and are highly biocompatible.^{9,14} They are more readily available and have fascinating optical properties.¹⁴ CuNCs -based luminescence sensors have advantages, such as enhanced quantum yield and tunable excited states.¹⁵ Affordability in the field is an important criterion, especially in resource-limited situations. Aggregation-induced emission (AIE) often observed in CuNCs enhances the emission brightness, structural stability, and sensitivity of CuNCs -assembled solids.^{16,17} Some reports on metal NCs based sensors for *As* detection are available, explicitly involving

Received: April 5, 2024
Revised: June 23, 2024
Accepted: June 25, 2024
Published: June 28, 2024



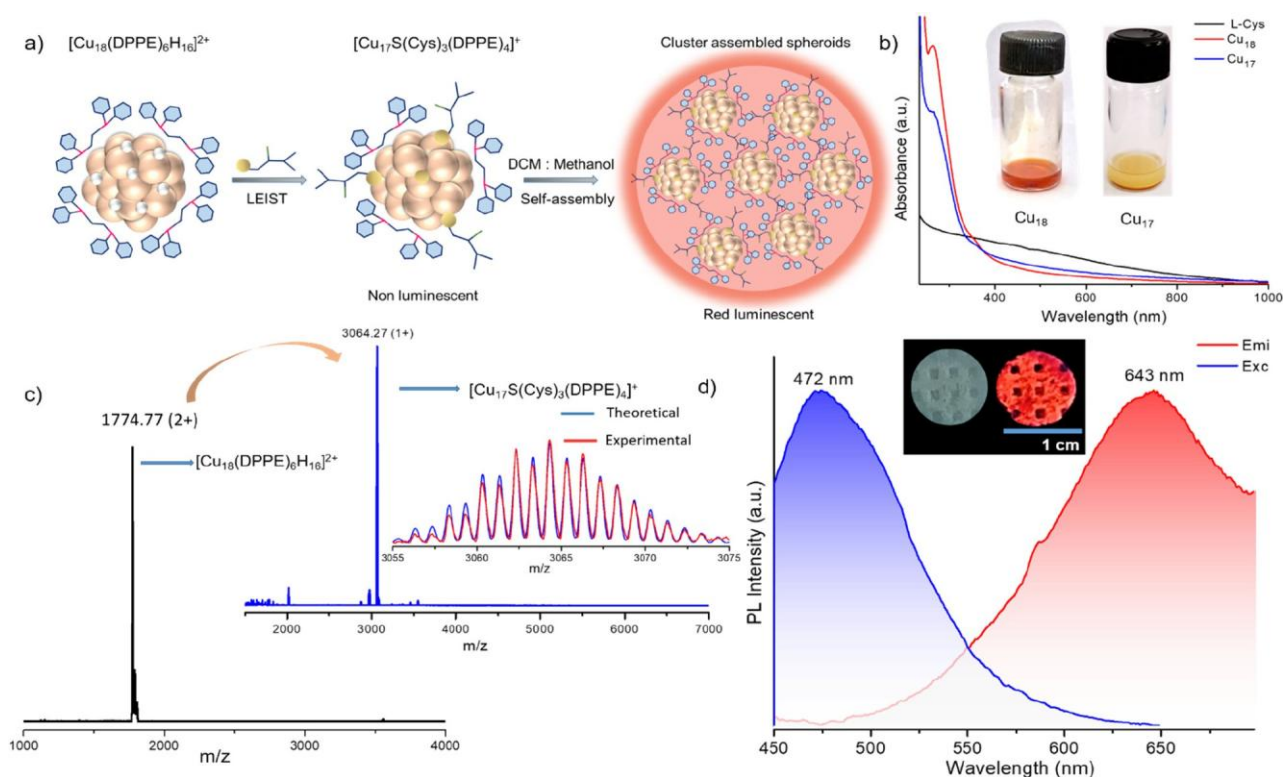


Figure 1. (a) Schematic representation of the synthesis of L-Cys and DPPE-protected Cu_{17} NCs and the self-assembly of the cluster in DCM:methanol (1:1, v/v) solvent mixture. (b) Comparative UV-vis absorption spectra of L-Cys, Cu_{18} , and Cu_{17} NCs. Inset shows the photographs of the respective clusters. (c) Full range ESI MS spectrum of the Cu_{18} NCs and the Cu_{17} NCs in positive ion mode. The inset matches the isotopic distribution of the experimental (blue) and theoretical (red) spectra of Cu_{17} NCs. (d) Photoluminescence excitation and emission spectra of Cu_{17} NCs covered on a PP disc. The inset shows the photograph of the CASs coated on PP mats under daylight (left) and UV light (right).

electrochemical^{18,19} and luminescence^{20,21} responses. A recent report from our group demonstrated that cobalt NCs-assembled plates detect As^{3+} in water electrochemically, with high sensitivity and selectivity.¹⁹ However, luminescence sensors generally offer higher sensitivity toward the analytes over other techniques.²² Luminescent gold and silver NCs have been demonstrated to show selective detection of As at levels far below the permissible limits.^{20,21} To our knowledge, there is no report of CuNCs for As sensing.²³ In this study, we present a sensor composed of red-emitting cluster-assembled superstructures (CASs) of Cu_{17} NCs, which can detect both As^{3+} and As^{5+} ions in tap water at the ppb level with high selectivity. CASs showed disrupted morphology upon exposure to As and subsequent change in emission, forming the basis of sensing.

Besides heavy metal ions, microbial organisms cause immediate and severe health issues worldwide. The Centres for Disease Control and Prevention has expressed that the world is entering a “postantibiotic era”, where mortality will be primarily due to resistant-bacterial diseases.^{24,25} With challenges faced in disinfection, NCs are emerging as novel antimicrobials. Silver²⁶ and CuNCs possess high antibacterial activity.²⁷ Very few studies on CASs are available.^{27,28} The CASs reported here exhibit excellent antibacterial activity against Gram-negative and Gram-positive bacteria in water, showcasing their potential applications as broad-spectrum of antibacterial coatings. They also exhibit biofilm resistance.

2. METHODS AND MATERIALS

Materials and Reagents. Copper iodide (CuI), sodium borohydride (NaBH_4 , 98%) and L-cysteine (L-Cys) were procured from Sigma-Aldrich chemicals. DPPE was supplied by Rankem Chemicals. Solvent-grade dichloromethane (DCM), acetonitrile and methanol (99.5%) were purchased from Finar, India. Sodium arsenite and sodium arsenate were purchased from Aldrich Chemicals. Nutrient agar (NA) and Luria-Bertani (LB) Broth were purchased from Himedia.

Experimental Procedures. The Cu_{17} NCs were synthesized from Cu_{18} NCs using the (Ligand-exchange-induced structural transformation) LEIST method (Figure 1a).²⁹ Details of the syntheses of Cu_{18} and Cu_{17} NCs are furnished in Text S1 and S2, respectively. The sensing experiments are discussed in Text S3.

Details of the antibacterial experiments and analytical methods used in this work are presented in Texts S4 and S5, respectively.

3. RESULTS AND DISCUSSION

Arsenic Sensing Ability of Cu_{17} NCs CASs. The synthesis of the Cu_{17} NCs through a ligand exchange reaction starting from Cu_{18} NCs is schematically shown in Figure 1a and characterization of the Cu_{17} NCs is discussed in Text S6 and Figures 1b-d, Figures S1–3. To create the As-sensing films, Cu_{17} NCs solution was drop-cast onto nonwoven Polypropylene (PP) discs and left to dry at room temperature. The inset of Figure 1d displays photographs of Cu_{17} NCs coating on PP discs under daylight and UV light. Bright red luminescence was

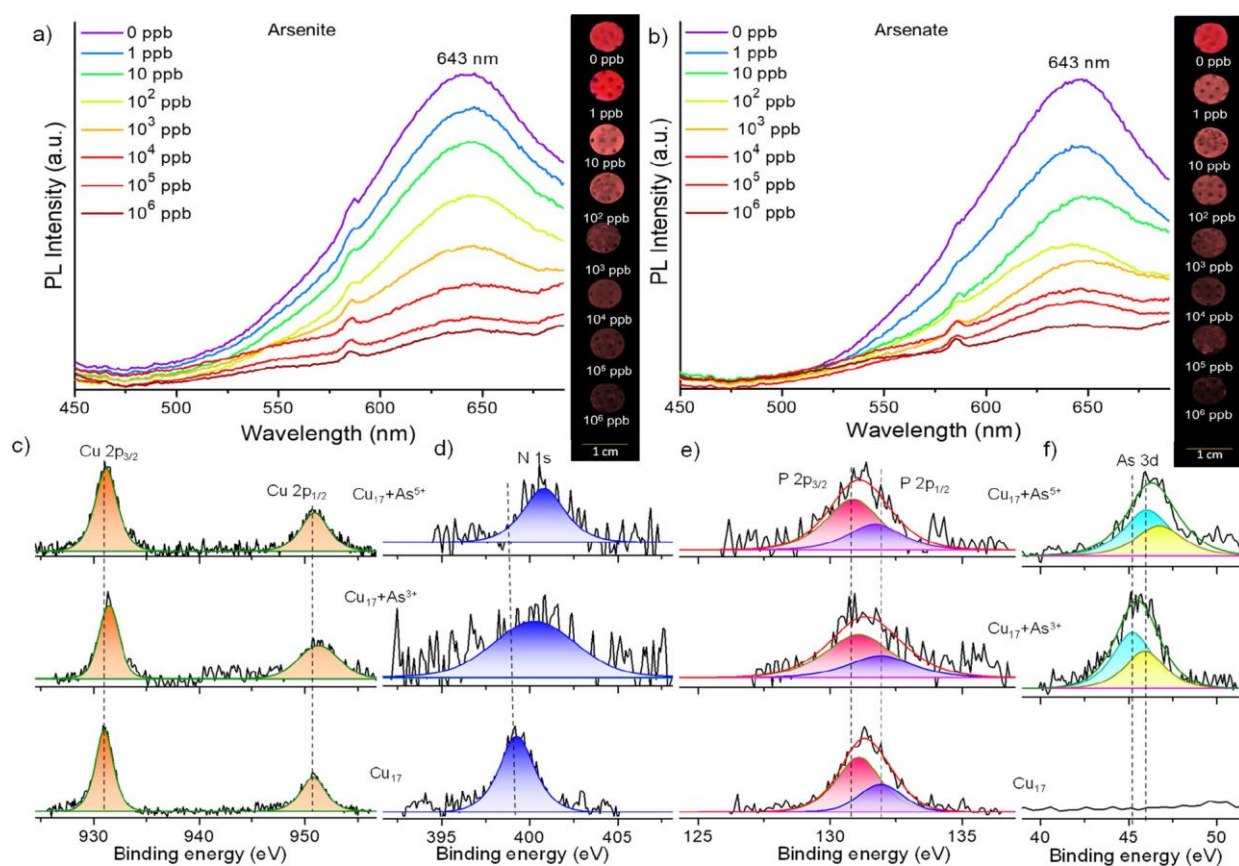


Figure 2. Comparative PL spectra with increasing concentrations of (a) As^{3+} and (b) As^{5+} ions showing the gradual quenching of PL intensity of the PP disc coated with Cu_{17} NCs. Correlative XPS spectra of Cu_{17} NCs having (c) Cu 2p, (d) N 1s, (e) P 2p, and (f) As 3d regions.

observed for the coatings under UV light, which was weak in the NCs solution. Upon investigating the Cu_{17} NCs coatings through a photoluminescence (PL) spectrophotometer, an emission maximum at 643 nm was observed with an excitation at 472 nm (Figure 1d). The spectral maximum of Cu_{17} NCs in DCM: Methanol (1:1) solution is blue-shifted (613 nm) compared to the coating (Figure S4). The emission intensity was also observed to be lower in solution. This indicated the AIE enhancement in the coatings compared to the as-prepared NCs.

The Cu_{17} NCs coating exhibited sensitivity to As, displaying a quenching of the red luminescence upon exposure to As^{3+} or As^{5+} in water (insets of Figures 2a and 2b). The sensor demonstrated the ability to detect both the analytes down to 1 ppb, starting from 10^6 ppb (Figures 2a and b). The correlation coefficient values are $R^2 = 0.98$ and 0.99 for As^{3+} and As^{5+} , respectively (Figures S5 a and b). The performance of Cu_{17} NCs in As sensing has been compared in Table S1 with the existing reports, and the sensors' affordability is discussed in Text S6.

To further investigate the sensing ability toward As X-ray photoelectron spectroscopy (XPS) analysis was performed on the NCs exposed to As^{3+} and As^{5+} ions. Before and after exposure to As, the NCs were loaded onto clean XPS stubs. The recorded survey spectrum displayed all the elements in the Cu_{17} NCs (Figure S6a). Detailed scans reveal peaks corresponding to Cu 2p_{3/2} and Cu 2p_{1/2} at 932.9 and 952.8 eV, respectively, indicating zero oxidation state of Cu in the NCs (Figure 2c).³⁰ Upon interaction with As^{3+} and As^{5+} , Cu 2p_{3/2} peak shifted toward lower binding energy (931.3 and 931.1 eV,

respectively), indicating oxidation of Cu. Similar shifts were observed in the Cu 2p_{1/2} peak upon exposure to As^{3+} and As^{5+} (from 952.8 to 951.3 and 950.9 eV, respectively), along with substantial broadening, confirming oxidation. Peaks of N 1s, P 2p_{3/2} and P 2p_{1/2} showed broadening, indicating their involvement in As sensing (Figures 2d and 2e). Figure 2f shows the presence of As in the cluster after adding As^{3+} and As^{5+} , compared to the Cu_{17} NCs. Sulfur exhibits a similar effect on adding As, wherein it undergoes oxidation (Figure S6b). Oxygen 1s region shows slight shifts, confirming the impact of As on oxygen present in the protecting ligands in the NCs (Figure S6c). Previous reports on As-specific sensing systems highlighted the role of amino groups in binding with As.^{31,32} XPS data confirmed the interaction of both the ligands, DPPE and L-Cys, to As. This comprehensive investigation revealed that exposure to As alters the Cu core and ligands of the NCs.

Furthermore, Fourier-transform infrared (FTIR) analysis was conducted to elucidate the binding interaction between As and Cu_{17} NCs. The FT-IR spectrum of the NCs revealed a set of vibrational features at 1574 and 1617 cm^{-1} corresponding to the stretching and bending vibrations of C=O and NH₂ groups, respectively, of the L-Cys ligand.³³ These peaks exhibit decreased intensity and broadening following interaction with As^{3+} (Figure S7a) or As^{5+} ions (Figure S7b). The peak at 1724 cm^{-1} , corresponding to the C=O stretching mode, similarly displays a declining intensity trend, confirming the interaction with As. Additionally, a decrease in intensity was observed for C–O at 1190 and 1250 cm^{-1} upon exposure to As. Powder X-ray diffraction (PXRD) of the Cu_{17} NCs before and after interaction with As^{3+} reveals significant shifts in the diffraction

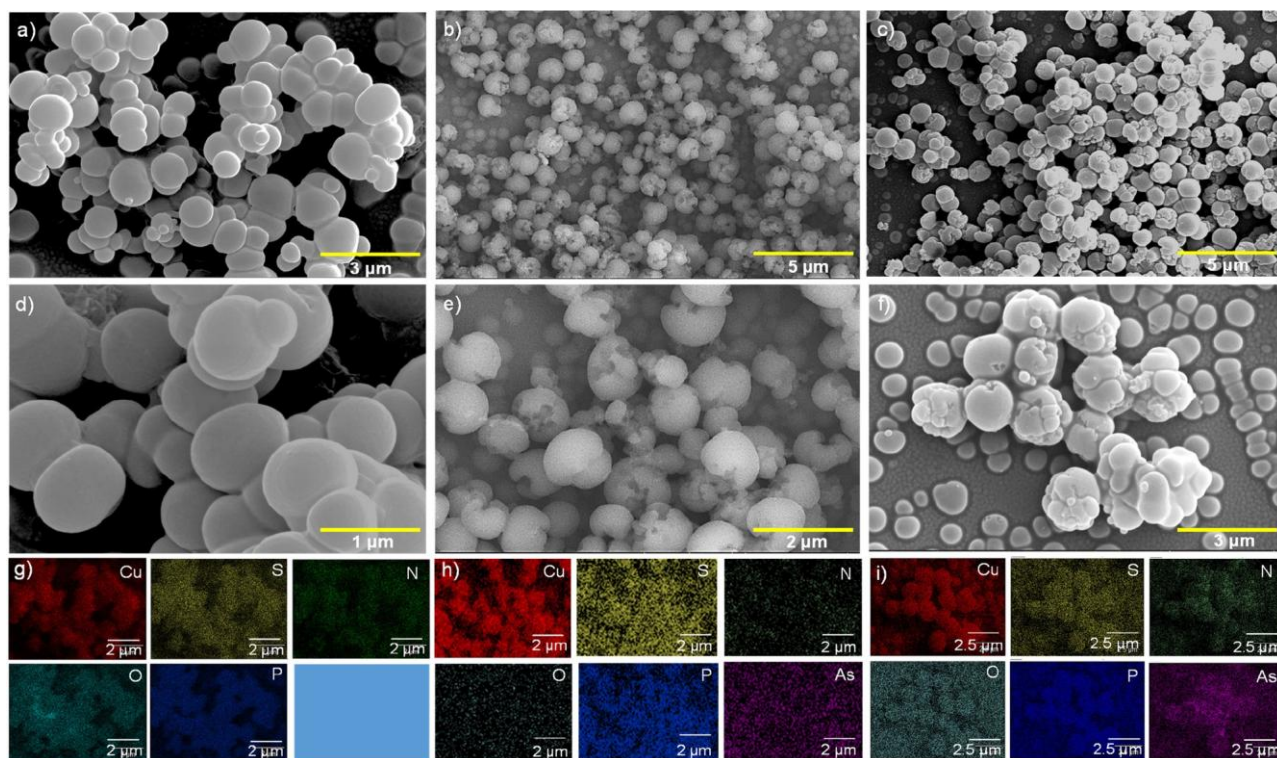


Figure 3. Morphological evolution induced by the As exposure to the CASs spheroids. FESEM micrographs showed (a) as prepared CASs and their disruption induced by the presence of (b) As^{3+} and (c) As^{5+} . Enlarged FESEM images show (d) smooth CASs and disrupted spheres after the exposure of (e) As^{3+} and (f) As^{5+} . EDS elemental maps of (g) untreated CASs spheres and after the exposure to (h) As^{3+} and (i) As^{5+} .

peaks and a notable decrease in intensity, particularly at 2θ values of 8.3° , 9.76° and 28° (Figure S8). While these peaks cannot be assigned in greater detail in the absence of the crystal structure, the observed peak shift and intensity reduction suggest a discernible alteration in the microcrystalline nature of $Cu_{17}NCs$.³⁰

Impact of As on the Morphology of CASs. The formation of CuNC aggregates induced by solvophobic effect was monitored through dynamic light scattering (DLS) studies. The maximum aggregate size reached was ~ 500 nm after 90 min of methanol addition to CuNCs solution in DCM (Figures S9a and b). Several reports exist on the prompt formation of aggregation-induced superstructures in CuNCs.^{17,34,35} Time-dependent PL studies showed a maxima intensity at 643 nm due to the formation of aggregates after 120 min of LEIST reaction. (Figures S10a and b). Examining through field emission scanning electron microscope (FESEM), the CuNCs were observed to be self-assembled into a stable film composed of CASs, as shown in Figure 3a. Figure 3d provides a zoomed-in view of CASs. Nearly uniform spheroidal structures of approximately 500 nm were observed in the $Cu_{17}NCs$ coating. These superstructures form due to the solvent interactions leading to aggregation, resulting in AIE in several systems. Similar solvent-induced aggregation has been reported by Jash et al. in forming superstructures of phosphine-protected Au–Ag alloy NCs.³⁶

Upon exposure to 100 ppb of As, morphological changes were induced in the CASs, disrupting their shape. This alteration occurred after exposure to both As^{3+} (Figure 3b and zoomed-in view in Figure 3e) and As^{5+} (Figure 3c and zoomed-in view in Figure 3f). Energy-dispersive spectroscopy (EDS) maps of the CASs before (Figure 3g) and after adding

As^{3+} (Figure 3h) and As^{5+} (Figure 3i) were recorded to confirm the composition of CASs and their interaction with As. The EDS maps illustrate the spatial distribution of Cu, S, O, N, P, and As elements. Cu of the cluster core was observed along with S, O, N and P present on the L-Cys and DPPE ligands. The spread of As on the disrupted CASs after exposure is evident from the EDS maps in Figures 3h and 3i.

Selectivity toward As. The CASs were found to be selective toward As, while they were unaffected by interfering heavy metal ions commonly present in contaminated water samples. The CASs were individually exposed to 100 ppb of Mn^{2+} , Cu^{2+} , Hg^{2+} , Pb^{2+} , Fe^{2+} , Cr^{2+} , Cd^{2+} , As^{3+} and As^{5+} in Milli-Q water. Photoluminescence (PL) was recorded after the exposure to individual ions of 100 ppb concentration (Figure S11a). The CASs exhibited emission quenching in the presence of As^{3+} and As^{5+} , as observed in Figure S11b. On the other hand, emission intensities remained constant when exposed to the interfering ions. The integrity of the microstructures in the presence of the interfering ions, such as Cr^{3+} , Fe^{2+} and Hg^{2+} , was examined through FESEM studies. The results, depicted in Figures S11c–f, revealed that the spheroidal morphology remained unaffected. A similar study on interfering ions involved tap water spiked with 100 ppb of Zn^{2+} , Pb^{2+} , Hg^{2+} , Cu^{2+} , Cd^{2+} , As^{3+} and As^{5+} . The recorded PL spectra showed that the emission intensity remained unaltered in the presence of the interfering ions, while quenching occurred solely in the presence of As, as shown in Figure S12. Additionally, Figure S12 displays photographs of the CASs-coated PP discs under UV light, captured after exposure to tap water containing ions of interest. This sensor interacts strongly with phosphate ions, but does not respond toward organic triphenyl arsine (TPA). (Figure S13). Phosphate removal

agents will facilitate the practical application of the sensor in field samples.

Antibacterial and Antibiofilm Activity. The impact of CASs on both Gram-positive *Bacillus subtilis* and Gram-negative *Escherichia coli* was investigated. After interaction with the CASs coating, the number of viable bacterial cells was determined through colony counting (Figures S14a-d). The CASs-coated PP discs showed high bactericidal efficiency against *E. coli* and *B. subtilis* cells. The antibacterial activities observed against *E. coli* MTCC 443, *E. coli* MTCC 739, and *B. subtilis* were 97.8%, 98% and 95%, respectively (Figures S14e-g). At the same time, bare PP discs and PP discs coated with CuI, L-Cys, and solvent (methanol and DCM in 1:1 ratio) had significantly less or no effect on the bacteria. Environmental scanning electron microscope (ESEM) analysis was performed to understand the impact of CASs on bacterial cells. *E. coli* MTCC 443 cells exposed to CASs coating for 1 h (Figure S14h and zoomed in view in Figure S14i) showed cell membrane damage in comparison to control cells (Figure S14j and zoomed in view in Figure S14k) The cells exposed to CASs formed ghost cells as their contents appear to be released. Cell membrane damage was observed on the Gram-positive bacteria – *Staphylococcus aureus* and *B. subtilis* also (Figures S15 and S16, respectively). Several mechanisms have been reported for the antibacterial properties of NCs.³⁷ The thiolated ligand metal interface of the NCs induces higher antibacterial activity than free thiols, as they are prone to oxidation and tend to lose their stability.²⁷

Coatings with cationic charges possess antibacterial effect on bacteria by electrostatic binding to the cell envelope, damaging the cells.³⁸ As discussed previously (Text S6), electrospray ionization mass spectrometry (ESI MS) analysis of the Cu₁₇NCs revealed their cationic nature, which could contribute to the net positive charge on the CASs surface. This was further analyzed through electrochemical impedance spectroscopy (EIS). We applied Mott–Schottky (M-S) analysis at the interface of the CASs-coated glassy carbon electrode (GCE) and the electrolyte (Figure S17a). The inverse square capacitance ($1/C_{sc}^2$) plot of CASs-coated film decreases with increasing potential.^{39,40} From Figure S17b, it is evident that there is a sharp decrease of $1/C_{sc}^2$ value with an increase of the potential from –

1 to +0.8 V, and the negative slope of the plot indicates that the coating is positively charged. However, the bare GCE shows a positive slope, indicating its negative charge. The extent of cell damage on the Gram-positive bacteria is lesser than that of *E. coli*, which carry a higher negative charge on the membrane of *E. coli*.^{41,42}

Further, the antibiofilm-forming ability of the CASs was investigated using Gram-positive *B. subtilis* through ESEM. The bacteria formed biofilms on blank PP discs after 4 days (Figure S16a). On the other hand, biofilm was absent on CASs-coated PP discs (Figure S16b). The cell membrane damage inhibits anchoring of the cells to surfaces, preventing growth and the formation of biofilm-supporting extracellular matrices.

Such antibacterial and antibiofilm activity of CASs can also be attributed to their unique morphology. Nanostructures in the range of 500 nm prevent the growth of bacteria through size-induced effects.^{43–45} This explains the adverse impact on *E. coli* cells and *B. subtilis* compared to *S. aureus*, whose cells are smaller and show comparatively lesser cell membrane damage under ESEM. Heckmann et al., in their experiments on nanostructures⁴⁵ showed that nanopillar arrays of polydime-

thylsiloxane possess bactericidal activity on *E. coli*, while *S. aureus* was repelled but not killed. Thus, it is evident that besides the surface charge and chemical composition, the morphology of the CASs plays a significant role in the antibacterial activity.

IMPLICATIONS

We present a novel application of CASs composed of Cu₁₇NCs exhibiting distinctive red luminescence as highly selective sensors for As in water. The sensitivity is extremely promising as it reaches one ppb. The CASs displayed remarkable specificity and selectivity toward As in water, showcasing their potential as efficient and affordable sensors for ensuring water safety on a global scale. In an era marked by increasing concerns about antibacterial resistance, our study also introduces a promising avenue for applying CASs systems as antibacterial surface coatings. These coatings exhibit a broad spectrum of killing efficiency attributed to the positive surface charge on the clusters, thiol functionalization, and nano-spherical structures. This unique combination contributes to their antibacterial efficacy and positions them as excellent antibiofilm platforms. While our findings represent a pioneering observation, suggesting the potential of Cu₁₇ superstructures for detecting ultratrace levels of As and their application in antibacterial and antibiofilm-forming coatings, there is a need for additional studies on the temporal stability and applications in diverse conditions. We estimate that one water quality analysis using such a paper sensor would cost ~ US \$ 0.01 per test. Future research endeavors are essential to unravel the full spectrum of possibilities and refine the applications of CASs in addressing critical issues related to water safety and antibacterial resistance.

ASSOCIATED CONTENT

Supporting Information

The Supporting Information is available free of charge at <https://pubs.acs.org/doi/10.1021/acs.estlett.4c00264>.

More details regarding the methodology, characterization of nanoclusters (mass spectrometry and thermal stability analysis), photoluminescence measurements, electron microscopy, and relevant references (PDF)

AUTHOR INFORMATION

Corresponding Author

Thalappil Pradeep – Department of Chemistry, DST Unit of Nanoscience (DST UNS) and Thematic Unit of Excellence (TUE), Indian Institute of Technology Madras, Chennai 600036, India; orcid.org/0000-0003-3174-534X; Email: pradeep@iitm.ac.in

Authors

Jenifer Shantha Kumar – Department of Chemistry, DST Unit of Nanoscience (DST UNS) and Thematic Unit of Excellence (TUE) and Department of Metallurgical and Materials Engineering, Indian Institute of Technology Madras, Chennai 600036, India; orcid.org/0009-0003-7502-7005

Arijit Jana – Department of Chemistry, DST Unit of Nanoscience (DST UNS) and Thematic Unit of Excellence (TUE), Indian Institute of Technology Madras, Chennai 600036, India

Jayathraa Raman – Department of Chemistry, DST Unit of Nanoscience (DST UNS) and Thematic Unit of Excellence (TUE), Indian Institute of Technology Madras, Chennai 600036, India

Hema Madhuri Veera – Department of Chemistry, DST Unit of Nanoscience (DST UNS) and Thematic Unit of Excellence (TUE), Indian Institute of Technology Madras, Chennai 600036, India

Amoghavarsha Ramachandra Kini – Department of Chemistry, DST Unit of Nanoscience (DST UNS) and Thematic Unit of Excellence (TUE), Indian Institute of Technology Madras, Chennai 600036, India

Jayoti Roy – Department of Chemistry, DST Unit of Nanoscience (DST UNS) and Thematic Unit of Excellence (TUE), Indian Institute of Technology Madras, Chennai 600036, India

Saurav Kanti Jana – Department of Chemistry, DST Unit of Nanoscience (DST UNS) and Thematic Unit of Excellence (TUE), Indian Institute of Technology Madras, Chennai 600036, India; orcid.org/0000-0001-5772-7022

Tiju Thomas – Department of Metallurgical and Materials Engineering, Indian Institute of Technology Madras, Chennai 600036, India

Complete contact information is available at: <https://pubs.acs.org/10.1021/acs.estlett.4c00264>

Notes

The authors declare no competing financial interest.

ACKNOWLEDGMENTS

The authors would like to acknowledge the Department of Science and Technology (DST), Government of India, for constantly supporting our research program. We have also utilized the funding from the project on the Centre of Excellence on Molecular Materials and Functions as part of the Institutes of Eminence scheme of IIT Madras. We thank the Science and Engineering Research Board (SERB) for the SUPRA (Scientific and Useful Profound Research Advancement) project Atomically Precise Materials for Sustainable Water and Energy Harvesting (SPR/2021/000439). J.S.K. thanks the Ministry of Human Resource Development, Government of India, for the senior research fellowship. J. Raman and H. M. Veera, from the Department of Biotechnology, Vel Tech High Tech Dr Rangarajan Dr Sakunthala Engineering College, Chennai 600062, India, had their internships with TP during the course of this work.

REFERENCES

- (1) World Health Organization. <https://www.who.int/news/item/18-06-2019-1-in-3-people-globally-do-not-have-access-to-safe-drinking-water-unicef-who> (accessed Apr 3, 2024).
- (2) Litter, M. I. Chemistry and Occurrence of Arsenic in Water. *Arsenic in Plants* 2022, 25–48.
- (3) German, M. S.; Watkins, T. A.; Chowdhury, M.; Chatterjee, P.; Rahman, M.; Seingheng, H.; SenGupta, A. K. Evidence of Economically Sustainable Village-Scale Microenterprises for Arsenic Remediation in Developing Countries. *Environ. Sci. Technol.* 2019, 53 (3), 1078–1086.
- (4) Mukherjee, S.; Gupte, T.; Jenifer, S. K.; Thomas, T.; Pradeep, T. Arsenic in Water: Fundamentals of Measurement and Remediation. *Encyclopedia of Water*. 2019, 1–11.
- (5) Kumar, A. A.; Som, A.; Longo, P.; Sudhakar, C.; Bhui, R. G.; Gupta, S. S.; Anshup; Sankar, M. U.; Chaudhary, A.; Kumar, R.; Pradeep, T. Confined Metastable 2-Line Ferrihydrite for Affordable Point-of-Use Arsenic-Free Drinking Water. *Adv. Mater.* 2017, 29 (7), No. 1604260.
- (6) Babar, N. U. A.; Joya, K. S.; Tayyab, M. A.; Ashiq, M. N.; Sohail, M. Highly Sensitive and Selective Detection of Arsenic Using Electrogenerated Nanotextured Gold Assemblage. *ACS Omega* 2019, 4 (9), 13645–13657.
- (7) Bhanjana, G.; Dilbaghi, N.; Chaudhary, S.; Kim, K.-H.; Kumar, S. Robust and Direct Electrochemical Sensing of Arsenic Using Zirconia Nanocubes. *Analyst* 2016, 141 (13), 4211–4218.
- (8) Mukherjee, S.; Gupte, T.; Jenifer, S. K.; Thomas, T.; Pradeep, T. Arsenic in Water: Speciation, Sources, Distribution, and Toxicology. *Encyclopedia of Water* 2019, 1–17.
- (9) Goswami, N.; Giri, A.; Bootharaju, M. S.; Xavier, P. L.; Pradeep, T.; Pal, S. K. Copper Quantum Clusters in Protein Matrix: Potential Sensor of Pb²⁺ Ion. *Anal. Chem.* 2011, 83 (24), 9676–9680.
- (10) Nagar, A.; Pradeep, T. Clean Water through Nanotechnology: Needs, Gaps, and Fulfillment. *ACS Nano* 2020, 14 (6), 6420–6435.
- (11) Pradeep, T. Atomically Precise Clusters of Noble Metals: An Introduction. In *Atomically Precise Metal Nanoclusters*; Pradeep, T., Ed.; Elsevier, 2023; pp 1–5. DOI: 10.1016/B978-0-323-90879-5.00008-1.
- (12) Jana, A.; Kini, A. R.; Pradeep, T. Atomically Precise Clusters: Chemical Evolution of Molecular Matter at the Nanoscale. *AsiaChem. Mag.* 2023, 3 (1), 56–65.
- (13) Chakraborty, I.; Pradeep, T. Atomically Precise Clusters of Noble Metals: Emerging Link between Atoms and Nanoparticles. *Chem. Rev.* 2017, 117 (12), 8208–8271.
- (14) Lin, Y.-S.; Lin, Y.-F.; Nain, A.; Huang, Y.-F.; Chang, H.-T. A Critical Review of Copper Nanoclusters for Monitoring of Water Quality. *Sensors and Actuators Reports* 2021, 3, No. 100026.
- (15) Baghdasaryan, A.; Bürgi, T. Copper Nanoclusters: Designed Synthesis, Structural Diversity, and Multiplatform Applications. *Nanoscale* 2021, 13 (13), 6283–6340.
- (16) Zhou, C.; Wang, M.; Yao, Q.; Zhou, Y.; Hou, C.; Xia, J.; Wang, Z.; Chen, J.; Xie, J. Ligand-Dependent Aggregation-Enhanced Photoacoustic of Atomically Precise Metal Nanocluster. *Aggregate* 2023, 5 (1), No. e401.
- (17) Chen, P.-C.; Li, Y.-C.; Ma, J.-Y.; Huang, J.-Y.; Chen, C.-F.; Chang, H.-T. Size-Tunable Copper Nanocluster Aggregates and Their Application in Hydrogen Sulfide Sensing on Paper-Based Devices. *Sci. Rep.* 2016, 6 (1), 24882.
- (18) Xiao, X.-Y.; Song, Z.-Y.; Li, P.-H.; Chen, S.-H.; Li, L.-N.; Yang, M.; Lin, C.-H.; Huang, X.-J. Au₂₅ Nanoclusters Exhibit Superhigh Catalytic Activity in Electrochemical Detection of As(III). *Anal. Chem.* 2021, 93 (41), 14014–14023.
- (19) Jose, A.; Jana, A.; Gupte, T.; Nair, A. S.; Unni, K.; Nagar, A.; Kini, A. R.; Spoorthi, B. K.; Jana, S. K.; Pathak, B.; Pradeep, T. Vertically Aligned Nanoplates of Atomically Precise Co₆S₈ Cluster for Practical Arsenic Sensing. *ACS Mater. Lett.* 2023, 5 (3), 893–899.
- (20) Nain, A.; Tseng, Y.-T.; Lin, Y.-S.; Wei, S.-C.; Mandal, R. P.; Unnikrishnan, B.; Huang, C.-C.; Tseng, F.-G.; Chang, H.-T. Tuning the Photoluminescence of Metal Nanoclusters for Selective Detection of Multiple Heavy Metal Ions. *Sensors Actuators B Chem.* 2020, 321, No. 128539.
- (21) Roy, S.; Palui, G.; Banerjee, A. The As-Prepared Gold Cluster-Based Fluorescent Sensor for the Selective Detection of As(III) Ions in Aqueous Solution. *Nanoscale* 2012, 4 (8), 2734–2740.
- (22) Qian, S.; Wang, Z.; Zuo, Z.; Wang, X.; Wang, Q.; Yuan, X. Engineering Luminescent Metal Nanoclusters for Sensing Applications. *Coord. Chem. Rev.* 2022, 451, No. 214268.
- (23) Yuan, L.; Liang, M.; Hummel, M.; Shao, C.; Lu, S. Rational Design Copper Nanocluster-Based Fluorescent Sensors towards Heavy Metal Ions: A Review. *Chemosensors*. 2023, 11, 159–162.
- (24) Antibiotic resistance threats in the united states 2019. <https://www.cdc.gov/drugresistance/pdf/threats-report/2019-ar-threats-report-508.pdf> (accessed Apr 3, 2024).
- (25) Kannan, U.; Pullangott, G.; Singh, S. P.; Maliyekkal, S. M. 5 - Nanoscale Silver Enabled Drinking Water Disinfection System; Hussain,

C. M., Nassar, N. N., Eds.; Elsevier, 2023; pp 127–166. DOI: 10.1016/B978-0-12-823874-5.00010-3.

(26) Chakraborty, I.; Udayabhasakarao, T.; Deepesh, G. K.; Pradeep, T. Sunlight Mediated Synthesis and Antibacterial Properties of Monolayer Protected Silver Clusters. *J. Mater. Chem. B* 2013, 1 (33), 4059–4064.

(27) Nain, A.; Tseng, Y.-T.; Wei, S.-C.; Periasamy, A. P.; Huang, C.-C.; Tseng, F.-G.; Chang, H.-T. Capping 1,3-Propanedithiol to Boost the Antibacterial Activity of Protein-Templated Copper Nanoclusters. *J. Hazard. Mater.* 2020, 389, No. 121821.

(28) Raffi, M.; Mehrwan, S.; Bhatti, T. M.; Akhter, J. I.; Hameed, A.; Yawar, W.; ul Hasan, M. M. Investigations into the Antibacterial Behavior of Copper Nanoparticles against Escherichia Coli. *Ann. Microbiol.* 2010, 60 (1), 75–80.

(29) Li, J.; Ma, H. Z.; Reid, G. E.; Edwards, A. J.; Hong, Y.; White, J. M.; Mulder, R. J.; O'Hair, R. A. J. Synthesis and X-Ray Crystallographic Characterisation of Frustum-Shaped Ligated [Cu₁₈H₁₆(DPPE)₆]²⁺ and [Cu₁₆H₁₄(DPPA)₆]²⁺ Nanoclusters and Studies on Their H₂ Evolution Reactions. *Chem. – A Eur. J.* 2018, 24 (9), 2070–2074.

(30) Jana, A.; Spoorthi, B. K.; Nair, A. S.; Nagar, A.; Pathak, B.; Base, T.; Pradeep, T. A Luminescent Cu₄ Cluster Film Grown by Electrospray Deposition: A Nitroaromatic Vapour Sensor. *Nanoscale* 2023, 15 (18), 8141–8147.

(31) Kumar, S.; Bhanjana, G.; Dilbaghi, N.; Kumar, R.; Umar, A. Fabrication and Characterization of Highly Sensitive and Selective Arsenic Sensor Based on Ultra-Thin Graphene Oxide Nanosheets. *Sensors Actuators B Chem.* 2016, 227, 29–34.

(32) Yang, M.; Jiang, T.-J.; Wang, Y.; Liu, J.-H.; Li, L.-N.; Chen, X.; Huang, X.-J. Enhanced Electrochemical Sensing Arsenic(III) with Excellent Anti-Interference Using Amino-Functionalized Graphene Oxide Decorated Gold Microelectrode: XPS and XANES Evidence. *Sensors Actuators B Chem.* 2017, 245, 230–237.

(33) Vaishnav, S. K.; Korram, J.; Pradhan, P.; Chandraker, K.; Nagwanshi, R.; Ghosh, K. K.; Satnami, M. L. Green Luminescent CdTe Quantum Dot Based Fluorescence Nano-Sensor for Sensitive Detection of Arsenic (III). *J. Fluoresc.* 2017, 27 (3), 781–789.

(34) Zheng, X.; Chen, Q.; Zhang, Z.; Wang, Z.; Gong, Z. An Aggregation-Induced Emission Copper Nanoclusters Fluorescence Probe for the Sensitive Detection of Tetracycline. *Microchem. J.* 2022, 180, No. 107570.

(35) Jia, X.; Li, J.; Wang, E. Cu Nanoclusters with Aggregation Induced Emission Enhancement. *Small* 2013, 9 (22), 3873–3879.

(36) Jash, M.; Jana, A.; Poonia, A. K.; Khatun, E.; Chakraborty, P.; Nagar, A.; Ahuja, T.; Adarsh, K. V.; Pradeep, T. Phosphine-Protected Atomically Precise Silver–Gold Alloy Nanoclusters and Their Luminescent Superstructures. *Chem. Mater.* 2023, 35 (1), 313–326.

(37) Li, D.; Kumari, B.; Makabenta, J. M.; Tao, B.; Qian, K.; Mei, X.; Rotello, V. M. Development of Coinage Metal Nanoclusters as Antimicrobials to Combat Bacterial Infections. *J. Mater. Chem. B* 2020, 8 (41), 9466–9480.

(38) Li, Y.; Qu, S.; Xue, Y.; Zhang, L.; Shang, L. Cationic Antibacterial Metal Nanoclusters with Traceable Capability for Fluorescent Imaging the Nano–Bio Interactions. *Nano Res.* 2023, 16 (1), 999–1008.

(39) Jana, S. K.; Banerjee, S.; Bayan, S.; Inta, H. R.; Mahalingam, V. Rectification and Amplification of Ionic Current in Planar Graphene/Graphene-Oxide Junctions: An Electrochemical Diode and Transistor. *J. Phys. Chem. C* 2018, 122 (21), 11378–11384.

(40) Jana, S. K.; Chaudhari, K.; Islam, M. R.; Natarajan, G.; Ahuja, T.; Som, A.; Paramasivam, G.; Raghavendra, A.; Sudhakar, C.; Pradeep, T. Selective and Practical Graphene-Based Arsenite Sensor at 10 Ppb. *ACS Appl. Nano Mater.* 2022, 5 (8), 11876–11888.

(41) Chai, S.; Zhou, L.; Chi, Y.; Chen, L.; Pei, S.; Chen, B. Enhanced Antibacterial Activity with Increasing P Doping Ratio in CQDs. *RSC Adv.* 2022, 12 (43), 27709–27715.

(42) Ahimou, F.; Denis, F. A.; Touhami, A.; Dufrêne, Y. F. Probing Microbial Cell Surface Charges by Atomic Force Microscopy. *Langmuir* 2002, 18 (25), 9937–9941.

(43) Fadeeva, E.; Truong, V. K.; Stiesch, M.; Chichkov, B. N.; Crawford, R. J.; Wang, J.; Ivanova, E. P. Bacterial Retention on Superhydrophobic Titanium Surfaces Fabricated by Femtosecond Laser Ablation. *Langmuir* 2011, 27 (6), 3012–3019.

(44) Francesko, A.; Fernandes, M. M.; Ivanova, K.; Amorim, S.; Reis, R. L.; Pashkuleva, I.; Mendoza, E.; Pfeifer, A.; Heinze, T.; Tzanov, T. Bacteria-Responsive Multilayer Coatings Comprising Polycationic Nanospheres for Bacteria Biofilm Prevention on Urinary Catheters. *Acta Biomater.* 2016, 33, 203–212.

(45) Heckmann, T. S.; Schiffman, J. D. Spatially Organized Nanopillar Arrays Dissimilarly Affect the Antifouling and Antibacterial Activities of Escherichia Coli and Staphylococcus Aureus. *ACS Appl. Nano Mater.* 2020, 3 (2), 977–984.

Supporting Information for

Cysteine-Protected Antibacterial Spheroids of Atomically Precise Copper Clusters for Direct and Affordable Arsenic Detection from Drinking Water

*Jenifer Shantha Kumar^{†‡}, Arijit Jana[†], Jayathraa Raman^{†‡}, Hema Madhuri Veera^{†‡},
Amoghavarsha Ramachandra Kini[†], Jayoti Roy[†], Saurav Kanti Jana[†], Tiju Thomas[‡], and
Thalappil Pradeep^{†*}*

[†]Department of Chemistry, DST Unit of Nanoscience (DST UNS) and Thematic Unit of Excellence (TUE), Indian Institute of Technology Madras, Chennai 600036, India.

*E-mail: pradeep@iitm.ac.in

[‡]Department of Metallurgical and Materials Engineering, Indian Institute of Technology Madras, Chennai 600036, India

This supporting information is a 26 page document, including the table of contents, 5 sections of experimental descriptions, 2 sections of discussions, 17 figures, 1 table and this cover page.

Table of contents

Items	Description	Page No.
Text S1	Synthesis of Cu ₁₈ NCs	3
Text S2	Synthesis of Cu ₁₇ NCs	3
Text S3	Sensing experiments	3
Text S4	Antibacterial activity	3
Text S5	Analytical methods	4
Text S6	Characterization of Cu ₁₇ NCs	7
Text S7	Increased affordability of the As sensor	8
Figure S1	Mass spectrum of Cu ₁₈ NCs	9
Figure S2	Mass spectra of Cu ₁₆ and Cu ₁₇ NCs	10
Figure S3	TGA and DTA analysis of CASs	10
Figure S4	PL spectra of Cu ₁₇ NCs in solution and coating	11
Figure S5	Linearity plot of arsenic detection	11
Table S1	Comparison of the Cu ₁₇ NCs-based sensor's performance	12
Figure S6	XPS survey spectrum of Cu ₁₇ NCs and selected spectra in the S 2p and O 1s regions	14
Figure S7	FTIR analysis of Cu ₁₇ NCs	15
Figure S8	PXRD analysis of Cu ₁₇ NCs	16
Figure S9	DLS analysis of Cu ₁₇ NCs	17
Figure S10	PL plot of AIE enhancement	17
Figure S11	Selectivity towards arsenic	18
Figure S12	Selectivity towards arsenic in tap water	19
Figure S13	Effect of organic and inorganic arsenic	20
Figure S14	Antibacterial effect of CASs	21
Figure S15	ESEM images of <i>Staphylococcus aureus</i>	22
Figure S16	ESEM images of <i>Bacillus subtilis</i>	22
Figure S17	Electrochemical impedance spectroscopy of CASs	23
References		23

Text S1. Synthesis of Cu₁₈ Nanoclusters. Cu₁₈ Nanoclusters (NCs) were prepared according to the method reported by Li *et al.*¹ The CuI precursor (95 mg, 0.49 mM) was mixed with 0.03 mM (120 mg) of 1,2-bis-(diphenylphosphino) ethane (DPPE) under an argon environment. 15 ml of acetonitrile was added to it. After 30 min of stirring, the resulting mixture formed a white dispersion, which was reduced using 187 mg (320 mM) of dry NaBH₄. The reaction was allowed to be continuously stirred at 600 rpm for 5 h. An orange-colored precipitate was formed, which was washed several times with acetonitrile and methanol. The extracted orange residue was dissolved in 4 ml dichloromethane (DCM) for further synthesis. UV-Vis and Electrospray ionization mass spectrometry (ESI MS) studies confirmed the formation of Cu₁₈NCs with a relative yield of 70-75% in terms of Cu precursors.

Text S2. Synthesis of Cu₁₇ NCs. Here, 4 ml of purified Cu₁₈NCs in DCM from S1 was taken in a fresh glass bottle, and 50 mg of L-cysteine (L-Cys) dissolved in methanol (2 ml) was added slowly in an inert condition to the Cu₁₈ NCs. The reaction was allowed to proceed for 2.5 h at 22 °C with 400 rpm stirring. Cluster-assembled-superstructures (CASs) were formed rapidly by mixing (DCM) and methanol solvents (1:1, v/v). The CASs were washed several times with methanol to remove excess reagents.

Test S3. Sensing experiments. The purified Cu₁₇NCs of equal volume were used to drop cast on non-woven polypropylene (PP) discs (1 cm diameter) to observe the solid-state emission. Arsenite (As³⁺) and arsenate (As⁵⁺) solutions of various concentrations were prepared separately from their sodium salts in MilliQ water, and the pH was adjusted to 7.5. The interfering metal ion solutions were prepared similarly with CdCl₂, HgCl₂, FeCl₃, PbCl₂, CuCl₂ and CrCl₃ dissolved in water, and the pH was adjusted to 7. Sodium phosphate was used to prepare the phosphate solutions of various concentrations. The contaminated water was allowed to interact with PP discs for 10 minutes.

Test S4. Antibacterial activity. The antibacterial activity of Cu₁₇NCs was studied against gram-negative bacteria *E. coli* (MTCC 443) and *E. coli* (MTCC 739) and gram-positive bacteria *B. subtilis* (ATCC 21331) and *S. aureus* (MTCC 740). The stock cultures of the bacteria were revived in fresh Luria Bertani (LB) Broth. Freshly cultured bacteria were grown from the revived culture in LB Broth to a cell density of $\sim 10^8$ CFU/ml, and the O.D.₆₀₀ values were used to check the growth. The bacteria were diluted to $\sim 10^2$ CFU/ml and drop-casted on sterile PP discs of 1 cm diameter and allowed to interact for 1 h. Following this, PP discs were inverted on the nutrient agar (NA) surface to transfer the bacterial cells from them. Similarly, this was done with sterilized PP discs coated with CuI/solvent (methanol and DCM in 1:1 ratio)/L-Cys/CASs. In short, the bacterial cells were allowed to interact with the coated PP discs for 1 hour and transferred onto freshly prepared NA plates through inversion. The NA plates were then incubated at 37 °C for 24 hours to allow the live cells to grow into colonies. The plate colony counting method was adapted to determine the number of viable cells. The experiments were carried out similarly for *E. coli* (MTCC 443), *E. coli* (MTCC 739), and gram-positive bacteria *B. subtilis* (ATCC 21331) to understand their effect on the bacterial cells. All the experiments were performed in triplicates.

Further, the antibacterial effect was investigated through Environmental Scanning Electron Microscopy (ESEM) imaging. The bacteria were drop cast on the cluster-coated PP discs. The bacterial cells were carefully collected from the discs by washing them with PBS. The collected cells were dehydrated through a graded ethanol treatment (20, 40, 60, 80, 95, 100% ethanol in water) for 10 minutes of exposure in each concentration. The dehydrated cells were subject to gold-sputtering and imaging. The antibiofilm property was investigated by allowing *B. subtilis* cells to grow on the cluster-coated silicon for three days at 37 °C. The grown cells from the sheets were collected with gentle washing and drop cast on stubs for ESEM imaging.

Text S5. Analytical methods

UV-vis spectroscopy

A PerkinElmer Lambda 365 spectrometer was utilized to record absorption spectra in the cluster solutions within the 200-800 nm wavelength range, employing standard quartz cuvettes with a 1 cm optical width.

Mass spectrometry

ESI MS measurements of the parent NCs and ligand-exchanged products were analyzed by a Waters Synapt G2Si high-definition mass spectrometer. The instrument is equipped with an ESI source, step wave ion transfer cell, and quadrupole mass filter. The instrument's ion mobility cell was kept off during the studies. All measurements were recorded in the positive ion mode, and the following optimized parameters were employed during analysis: capillary voltage – 2.75 kV, sampling cone – 0 V, source offset – 0 V, source temperature – 100 °C, desolvation temperature – 150 °C. In addition, the desolvation gas flow was – 400 L/h, the nebulizer gas flow was 2.5 bar, and the ion energy was – 0.2.

Dynamic Light Scattering

Dynamic Light Scattering (DLS) analysis was conducted using a Malvern Zetasizer ZSP device featuring a 633 nm (He-Ne) laser source.

Photoluminescence study

The Horiba Jobin Yvon Nanolog was utilized to measure the photoluminescence (PL) spectra. All emission spectra were corrected and expressed in relative photon flux units to account for the wavelength-dependent response of the spectrometer and detector.

X-ray photoelectron spectroscopy

The X-ray photoelectron spectroscopy (XPS) was carried out in the Omicron ESCA probe TPD instrument. Aluminium source was used to generate non-monochromatic X-rays from a dual anode source with an X-ray power of 300 W. The survey scan was done from 0 to 1100 eV with a pass energy of 50 eV and a step size of 0.5 eV to identify all the elements present in the sample. Detailed scans were done for all the elements of interest with a pass energy of 20 eV and a step size of 0.1 eV to get better resolution for the peaks.

Infrared spectroscopy

The Perkin Elmer Fourier-transform infrared (FTIR) spectrometer was employed for sample measurements. 2.0 mg of NCs were mixed with 20 mg of dry potassium bromide to prepare the pellet.

Powder X-ray diffraction

Powder X-ray diffraction (PXRD) measurements were conducted using a D8 Advance instrument manufactured by Bruker. A Cu K α X-ray source with an energy of 8047.8 eV was utilized. For all PXRD measurements, the sample was drop-cast onto a glass slide, resembling a thin film.

FESEM imaging

The field emission scanning electron microscopy (FESEM) measurements of the CASs were carried out using a FEI Quanta FESEM operated in high vacuum mode with an operating voltage of 30 kV. The same instrument was used to record Energy-dispersive spectroscopy (EDS) spectra and perform elemental imaging.

ESEM imaging

The bacterial samples were analyzed in ESEM under extended low vacuum mode using a FEI QUANTA-200 SEM. The voltage of the electron gun was set at 10 kV for the imaging.

TGA/DTA measurements

Thermogravimetric analysis (TGA) and Differential thermal analysis (DTA) of about 3.5 mg of cluster sample in an alumina crucible were performed using a NETZSCH STA 449 F3 Jupiter instrument equipped with the Proteus-6.1.0 software. Both the measurements were performed under a nitrogen atmosphere at a flow rate of 20 ml/min in the temperature range of 30 to 700 °C with a heating rate of 10 °C/min.

Surface charge measurement

The surface charge of the cluster film was measured by electrochemical impedance spectroscopy (EIS). With this aim, the freshly prepared CASs were coated on a glassy carbon electrode (GCE) and allowed to dry at room temperature. This was used as a working electrode, Pt was the counter electrode, and Ag/AgCl was the reference electrode during the EIS measurement. EIS was carried out using Biologic instrument (SP200) at a frequency of 1kHz. During measurement, a DC potential was varied between -1.2 to 0.8 V. We carried out all measurements at 1 kHz of an input AC signal (20 mV), and the DC potential applied to the cluster-coated film was varied from -1 to +0.8 V. Cluster film was coated on GCE. The GCE was appropriately cleaned with aluminium slurry prior to the cluster coating on it. For control, we performed EIS using bare and cluster-coated GCE in 0.5 M of NaCl.

Text S6. Characterization of Cu₁₇NCs. The synthesis of Cu₁₇ and Cu₁₈NCs was confirmed by UV-vis spectroscopy (Figure 1b) and mass spectrometry. The UV-vis spectra of both NCs show an increase in intensity from 250 nm to 360 nm, originating from the d→sp transition in CuNCs.^{1,2} L-Cys does not show any absorption features in the UV-vis spectra.³ Photographs of

as-synthesized Cu₁₈ and Cu₁₇NCs are presented in the inset of Figure 1b, showing that the color of the solution changes from red to orange (Inset of Figure 1b) as the Ligand exchange induced structural transformation (LEIST) reaction proceeds (Figure 1a). Molecular composition of the clusters was investigated using high-resolution ESI MS studies. ESI MS spectrum of the precursor Cu₁₈NCs shows a peak at m/z 1775 corresponding to the [Cu₁₈(DPPE)₆H₁₆]²⁺ form (Figure 1c), while the singly charged peak at m/z 3550 was also present in the spectrum (shown in Figure S1). The inset of Figure S1 shows that the mass spectra match well with the simulated spectra. The ESI MS spectrum agreed well with the previous reports.^{1,4} Cu₁₇NCs show an intense peak at m/z 3064.27 with a monpositive charge state, showing the composition of the clusters to be [Cu₁₇S(L-Cys)₃(DPPE)₄]⁺ (Figure 1c). The inset shows that the spectrum matches with the simulated one. Other compositions present in the system are [Cu₁₆(DPPE)₄(L-Cys)₃H₂]⁺ (m/z 2972.5), originating from the loss of 1 Cu atom and [Cu₁₇DPPE₆(L-Cys)₅]⁺ (m/z 2020) with S loss (Figure S2). These have been matched to the corresponding theoretical mass spectra. TGA and DTA were performed on Cu₁₇NCs in the solid state. There were no observed mass losses up to 150 °C (Figure S3). The first 6% loss in mass at 153 °C could be attributed to the loss of DPPE, while the subsequent mass loss at 192 °C is due to the loss of L-Cys and DPPE ligands. This shows that the Cu₁₇NCs possess superior thermal stability in the solid state.

Text S7. Increased affordability of the As sensor. The sensing discs have been developed using CuNCs, which are much more affordable than their nanoparticle counterparts and common noble metal (Au, Ag) NCs.⁵⁻⁷ As mentioned in the earlier literature, a sensor composed of non-noble metal-based NCs can reduce the cost per test several times.^{8,9} Thus, it is evident that one of the primary reasons for the increased affordability of our system is the use of copper and the corresponding raw materials. Arsenic detection through Cu₁₇NCs can be performed without preconcentration, additional reagents, and sample processing, which

enables rapid measurements. The PP mat-based sensing discs are easy to carry and are stable at room temperature. PP discs were chosen as the substrate for sensing films over a Whatman filter paper and printing paper as they did not absorb water quickly, allowing ions to interact effectively with the Cu₁₇NCs coating.

From a practical perspective, the amount of Cu₁₇NCs in each sensing disc is approximately 950 ng. The Cu₁₇NCs were synthesized at room temperature and with less energy consumption than traditional synthetic processes, reducing production costs. With the cost of the reagents, PP mat, and other consumables for performing the test, the price of the materials per test is estimated to be \$0.01.

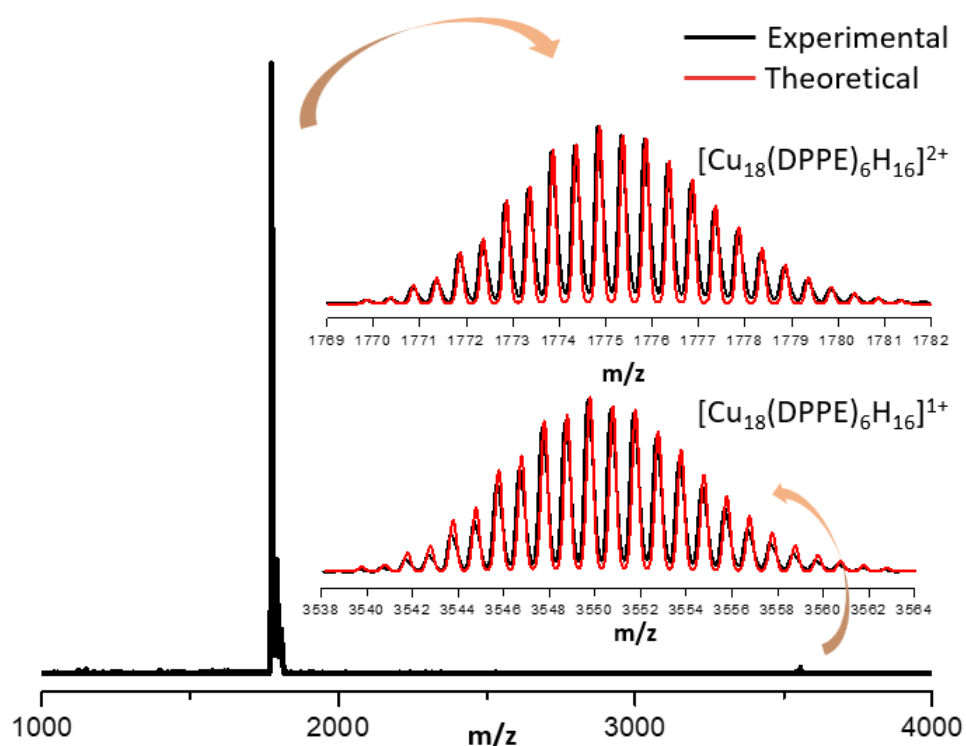


Figure S1. Full range ESI MS spectrum of Cu₁₈NCs. The inset presents the expanded theoretical MS spectra matched with the recorded MS spectra of the doubly (top) and singly (bottom) charged species of Cu₁₈NCs.

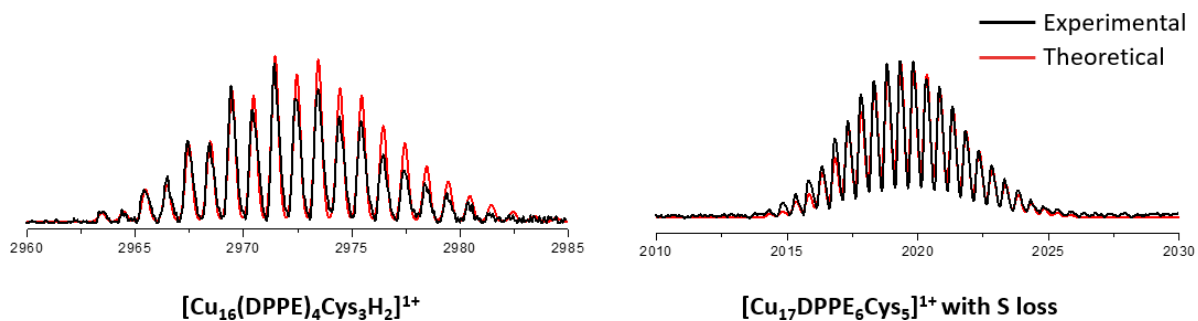


Figure S2. Isotopically resolved peaks of the ESI MS features of Cu₁₆NCs (left) and Cu₁₇NCs with one S loss species (right) matched with the theoretical MS spectra.

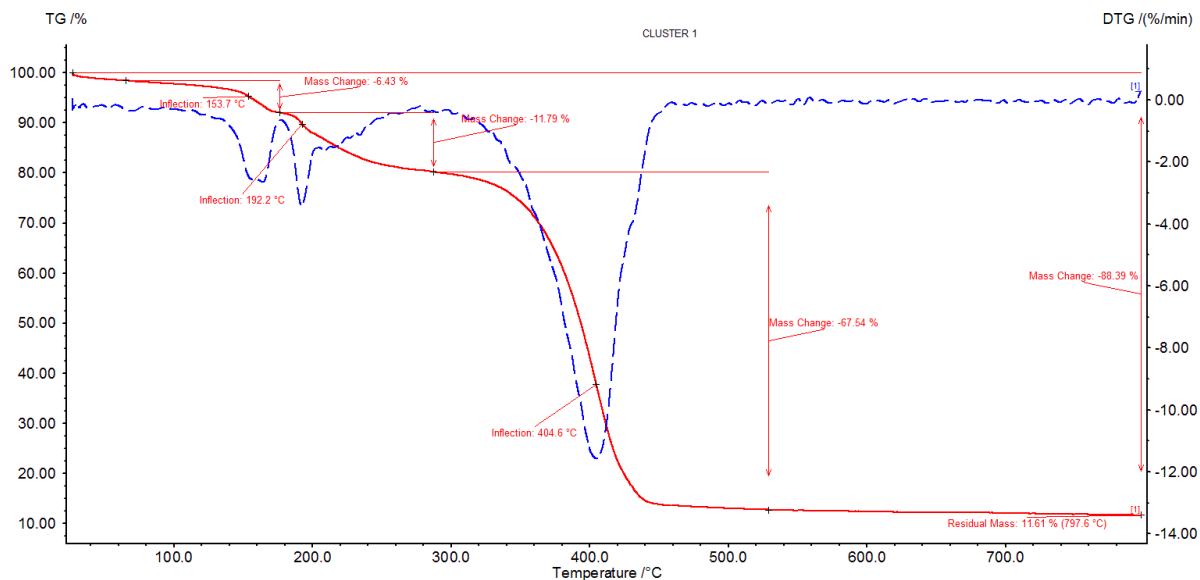


Figure S3. TGA and DTA plots of Cu₁₇NCs CASs.

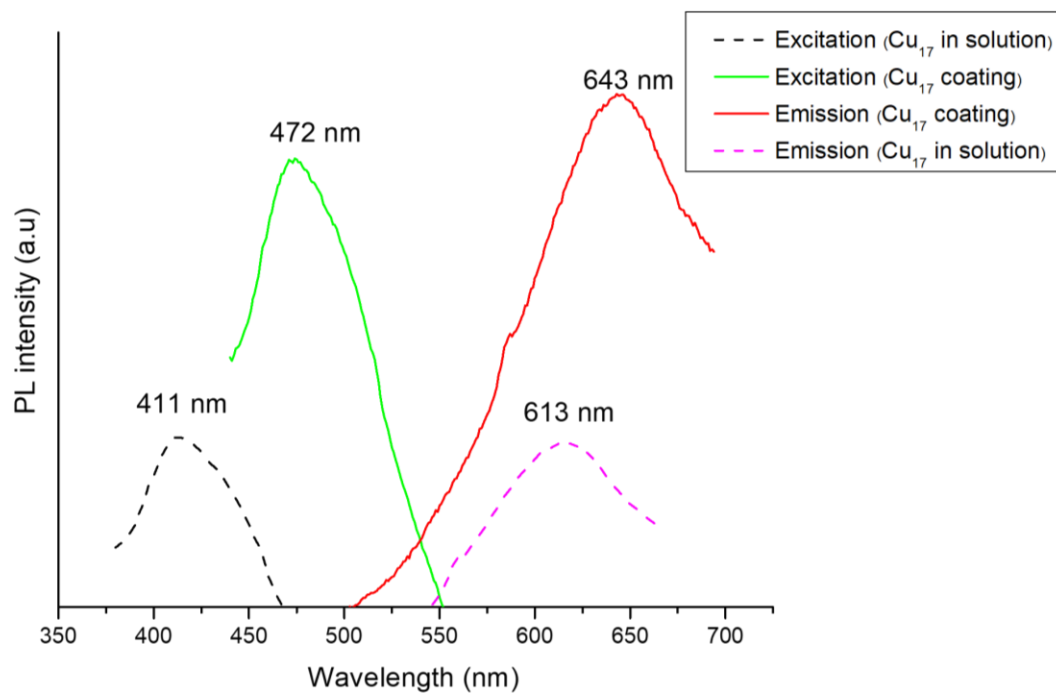


Figure S4. PL excitation and emission spectra of Cu₁₇NCs in solution and after the coatings of CASs on PP discs.

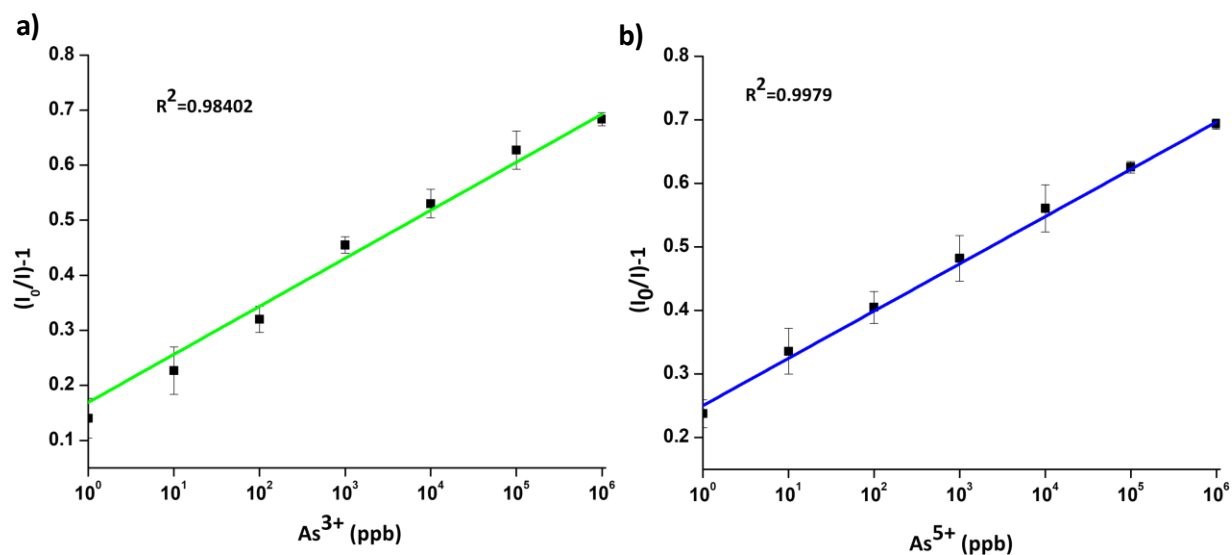


Figure S5. Linear regression plots of luminescence sensing with Cu₁₇NCs for a) As³⁺ and b) As⁵⁺.

Table S1. Comparison of the salient features of Cu₁₇NCs with As sensors reported recently and those available commercially.

Sensor	LOD in ppb	Linear range	Selectivity	Response time	Stability	Cost	Portability & usage	Ref
Cu ₁₇ NCs	1	1-10 ³ ppm	Highly selective to As ³⁺ and As ⁵⁺	10 min	Stable at room temperature	~\$0.01	Solid state sensor with portability	-
Cobalt NCs	0.66	0-100	Highly selective to As ³⁺	~3-5 min	Stable at room temperature	\$1	Electrochemical sensor with liquid buffers	9
Cysteine protected AuNCs	4	-	Highly selective to As ³⁺	-	Stable at room temperature	Added cost due to Gold	Liquid phase	10
Electrogenerated Nanotextured Gold Assemblage	0.1	0.1-9	Highly selective to As ³⁺	5 min	Stable at room temperature	Costly due to Gold usage	Electrochemistry performed in liquid medium	11
chlorin e6	1.37	0-400 ppm	As ⁵⁺ But susceptible to Cu	-	Stable at room temperature Light-sensitive Chlorin e6 used	High due to Chlorin e6 usage	Liquid medium	12
Nanocomposite-modified electrochemical sensor	9	0-2 ppm	Highly selective to As ⁵⁺	>10 min on average	Stable at room temperature	-	Liquid medium employed Preconcentration needed	13
Commercial tests								
HACH, Arsenic test kit, USA	10	0-500	As ³⁺ and As ⁵⁺	30-35 min	Stable at room temperature	\$1.67	Portable	14
Ascel® Arsenic Test Kit	<10	0-1000	As ³⁺ and As ⁵⁺	7 min	Stable at room temperature	\$2.99	Portable, Involves generation of arsine gas, the most toxic form of As	15
Arsenator® Digital Arsenic Test Kit, Wagtech WTD, Palintest Ltd, United Kingdom	2	0-100	As ³⁺ and As ⁵⁺	20 min	Stable at room temperature	\$ 4.59	Portable	16
QUANTOFIX® Arsenic Sensitive Semi-quantitative test strips. MACHEREY-NAGEL GmbH & Co. KG, Düren, Germany, Product No. 91345	5	0-500	As ³⁺ and As ⁵⁺	10 min	Stable at room temperature	\$ 1.01	Portable	17

Quick™ Arsenic Test Kit, Industrial test systems, Inc., USA Part Number: 481396	5	0–>500	As ³⁺ and As ⁵⁺	12 min	Stable at room temperature	\$ 1.78	Portable	18
Merckoquant® Arsenic (Merck Germany, Product No. 1.17927.0001)	10	0–500	As ³⁺ and As ⁵⁺	20 min	Stable at room temperature	\$ 2	Portable	19

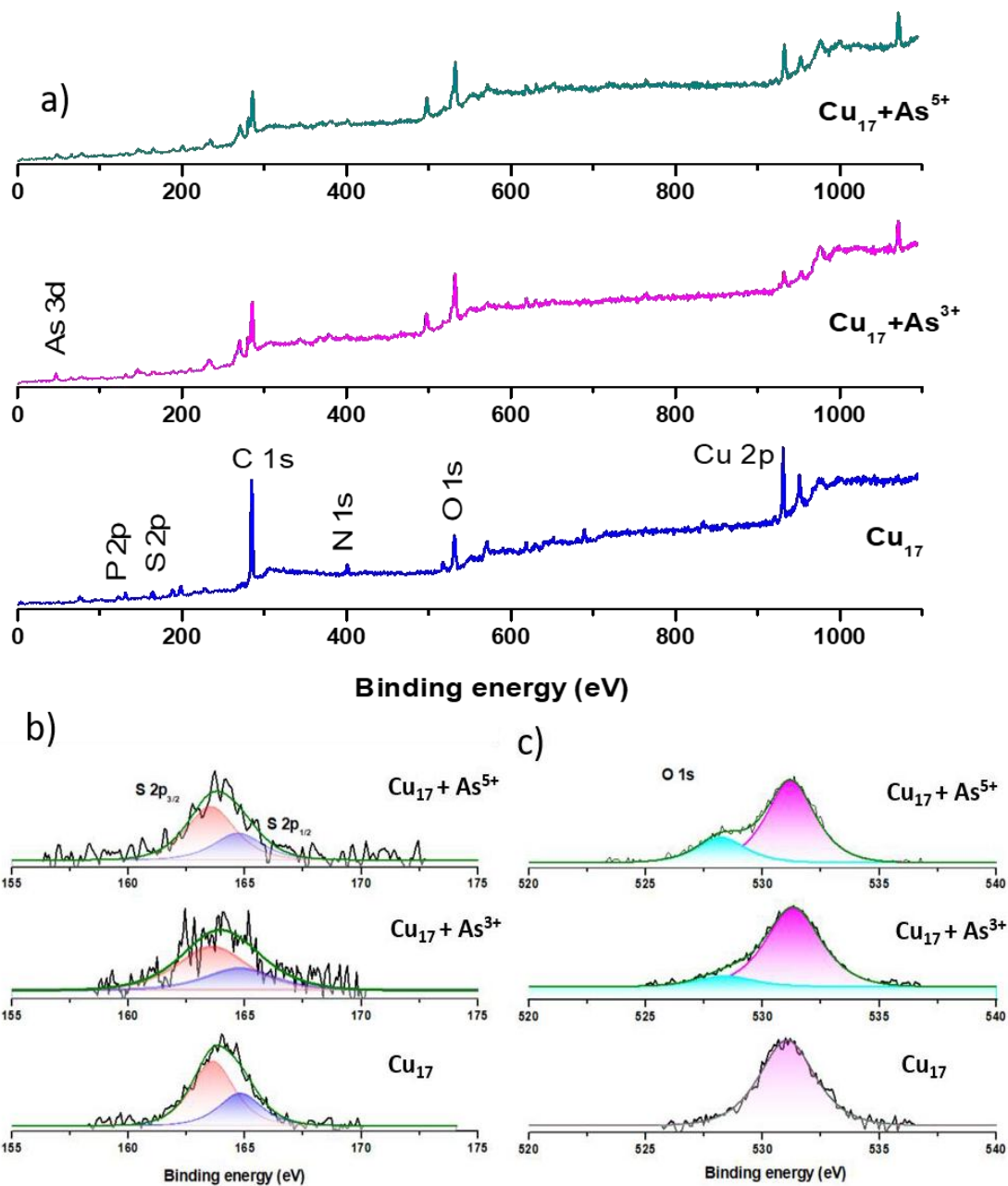


Figure S6. a) XPS survey spectra of pure Cu_{17}NCs and that with As^{3+} and As^{5+} , b) selected XPS spectra in the S 2p and c) O 1s regions.

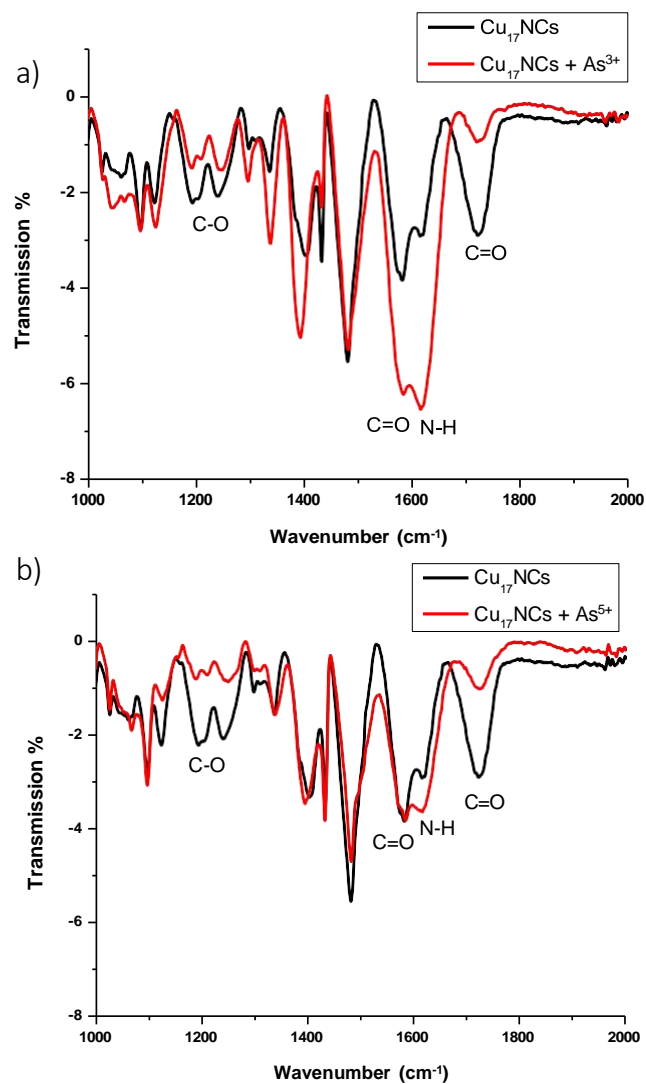


Figure S7. FTIR spectra of Cu₁₇NCs before and after exposure to a) As³⁺ and b) As⁵⁺.

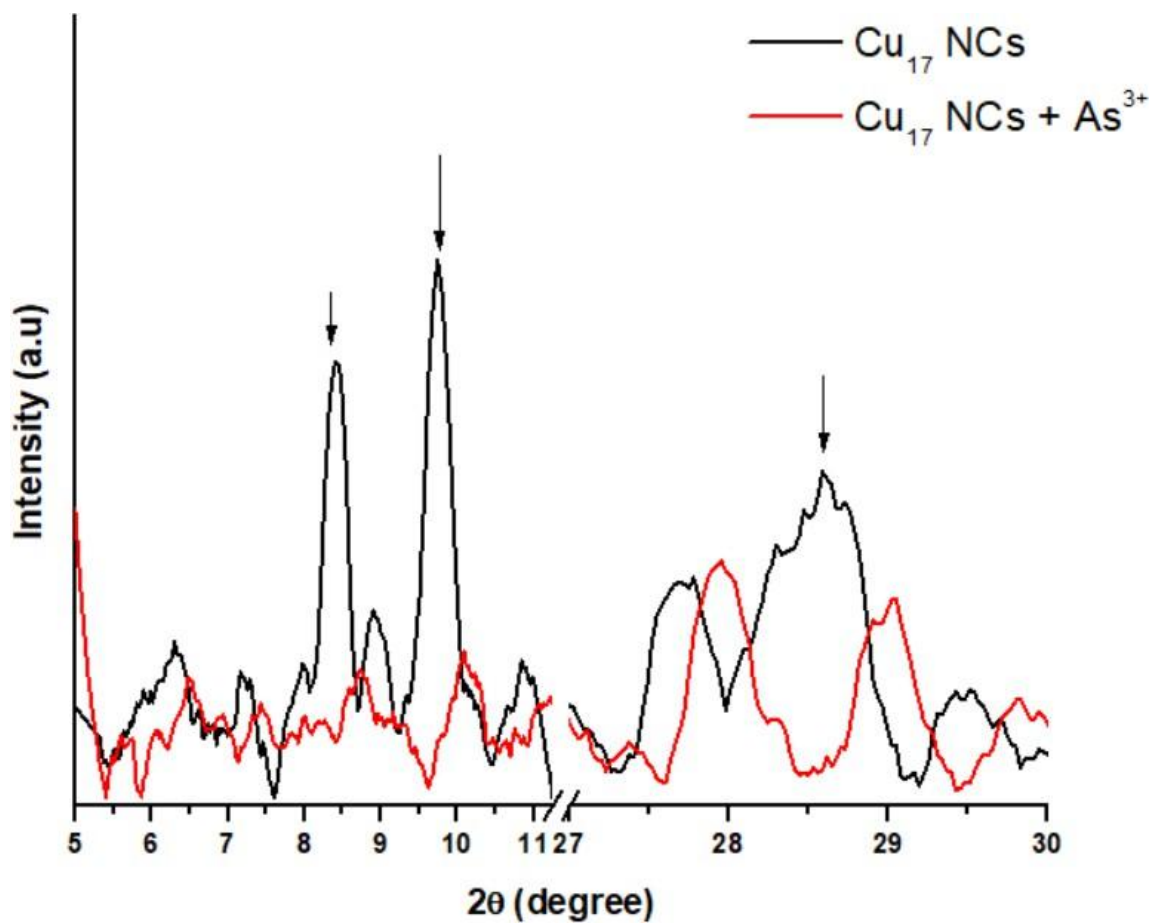


Figure S8. Comparative PXRD spectra of Cu₁₇NCs and Cu₁₇NCs after the exposure to As³⁺.

The arrows indicate the peaks showing significant intensity changes.

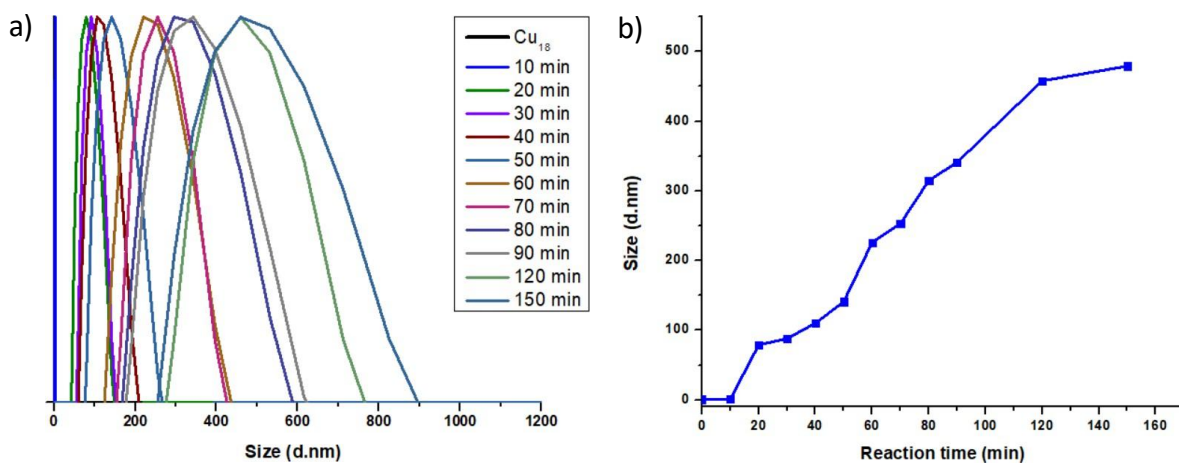


Figure S9. a) Time-dependent DLS spectra of the conversion of Cu₁₈NCs into CASs composed of Cu₁₇NCs after adding L-Cys dissolved in methanol. b) Variation of the size of the CASs plotted against time.

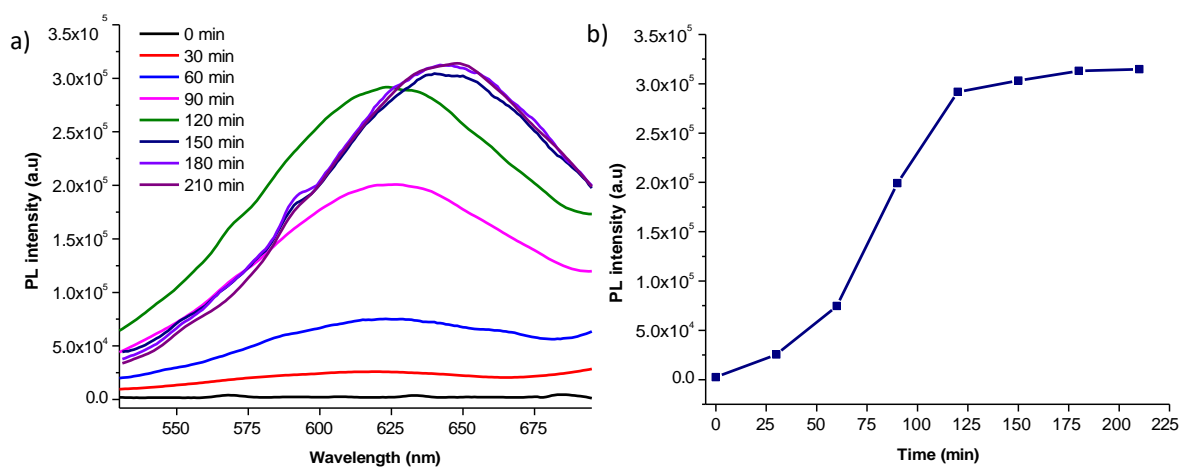


Figure S10. a) Time-dependent PL plot of Cu₁₇NCs during synthesis. b) Luminescence intensity vs time plot at 643 nm.

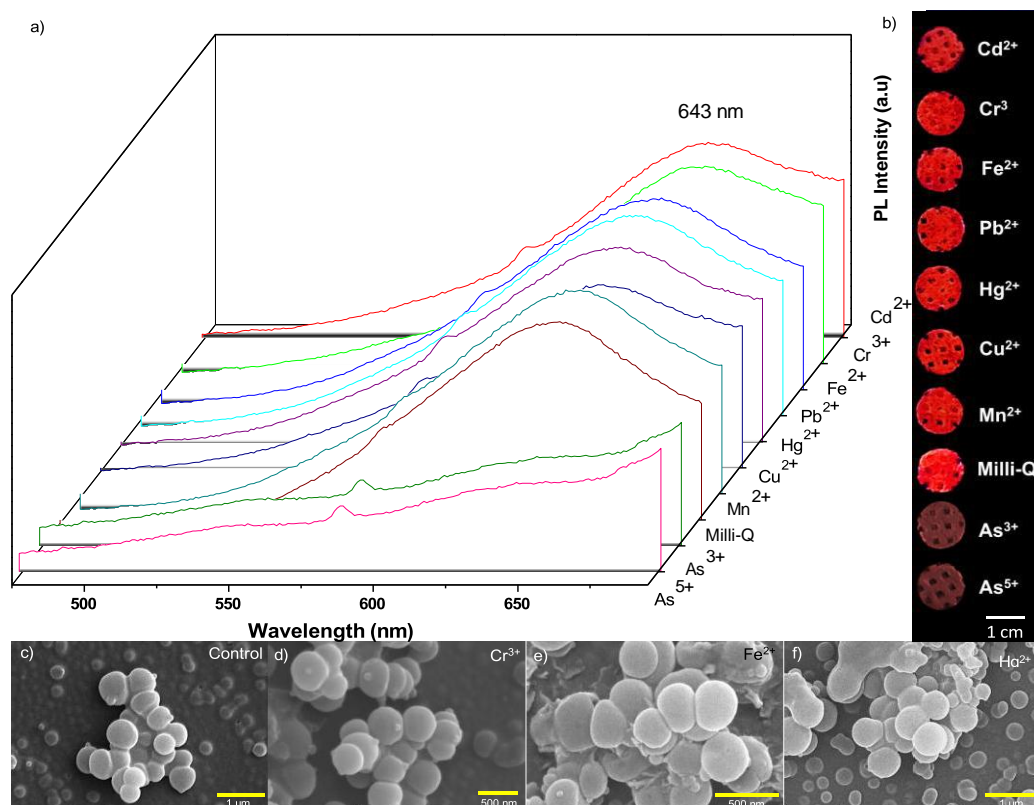


Figure S11. a) Comparative PL spectra showing emission quenching by the exposure of As^{3+} and As^{5+} ions compared to other water-soluble interfering ions. Excitation was at 472 nm. b) Photographs of CASs sensors under 365 nm UV light show the emission quenching only by As^{3+} and As^{5+} . c) FESEM micrographs of CASs and CASs exposed to d) Cr^{3+} , e) Fe^{2+} and f) Hg^{2+} ions. No disruption of the structure was observed for these ions.

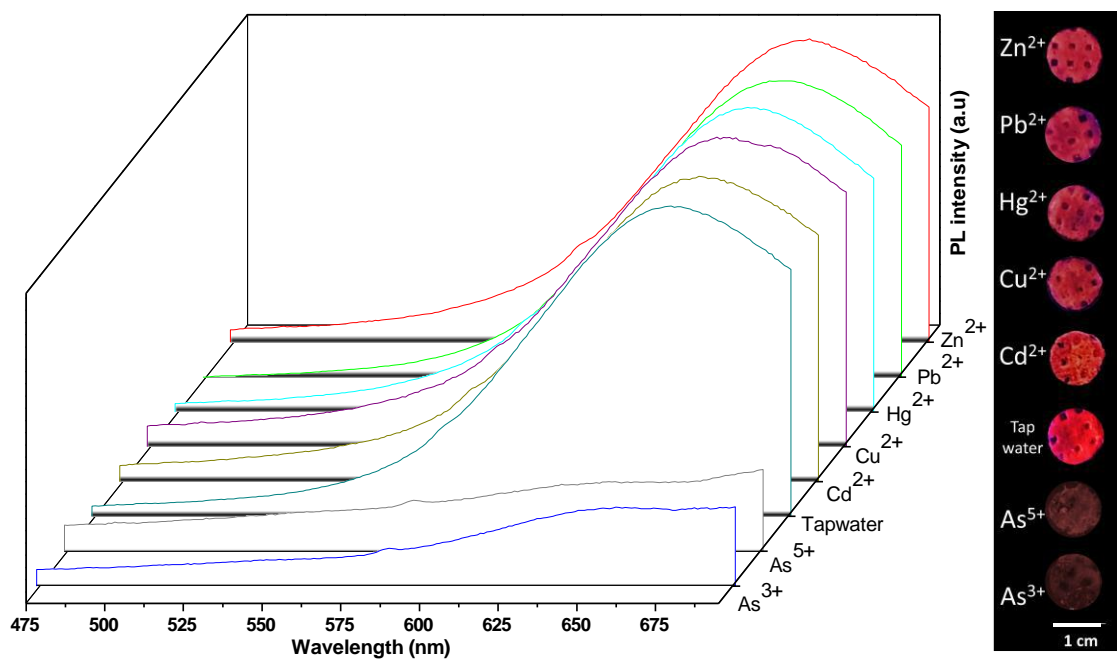


Figure S12. Stacked PL spectra of PP discs containing Cu_{17} spheroids after exposure to the tap water samples spiked with As^{3+} , As^{5+} and interfering ions. Excitation was at 472 nm. The figure on the right shows the photographs (under 365 nm UV light) of the sensing platform after exposure to contaminated tap water.

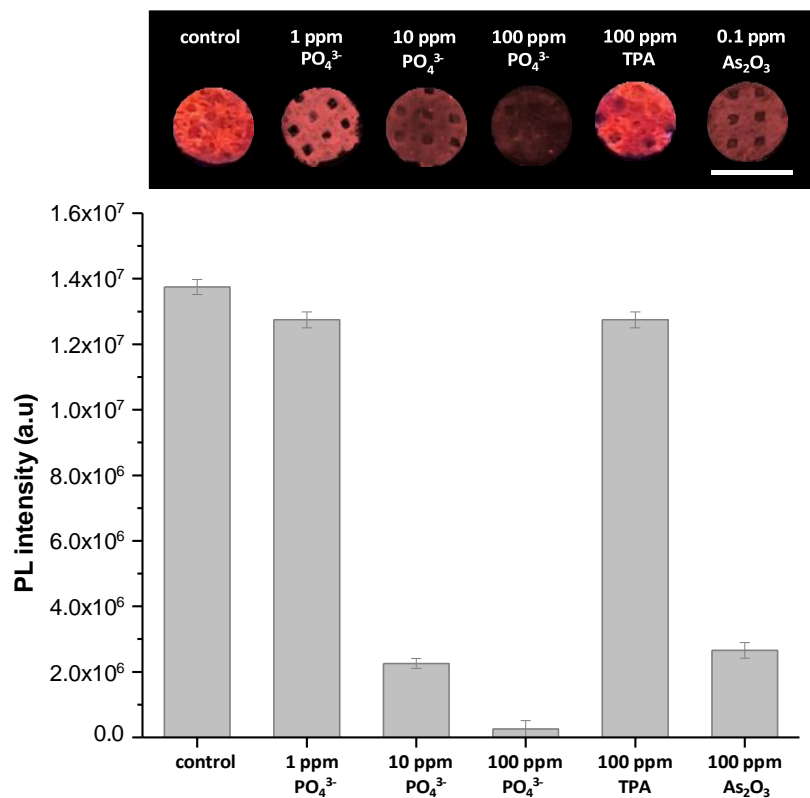


Figure S13. Bar graph showing the effect of phosphates (PO_4^{3-}), triphenyl arsine (TPA) and arsenic trioxide (As_2O_3) on the sensor discs. The inset shows the photographs of the discs under UV light. Phosphate at 10 ppm or higher concentrations can significantly affect the luminescence. 100 ppm of TPA does not affect the emission, while 0.1 ppm of As_2O_3 quenches the emission of the NCs. The scale bar is 1 cm.

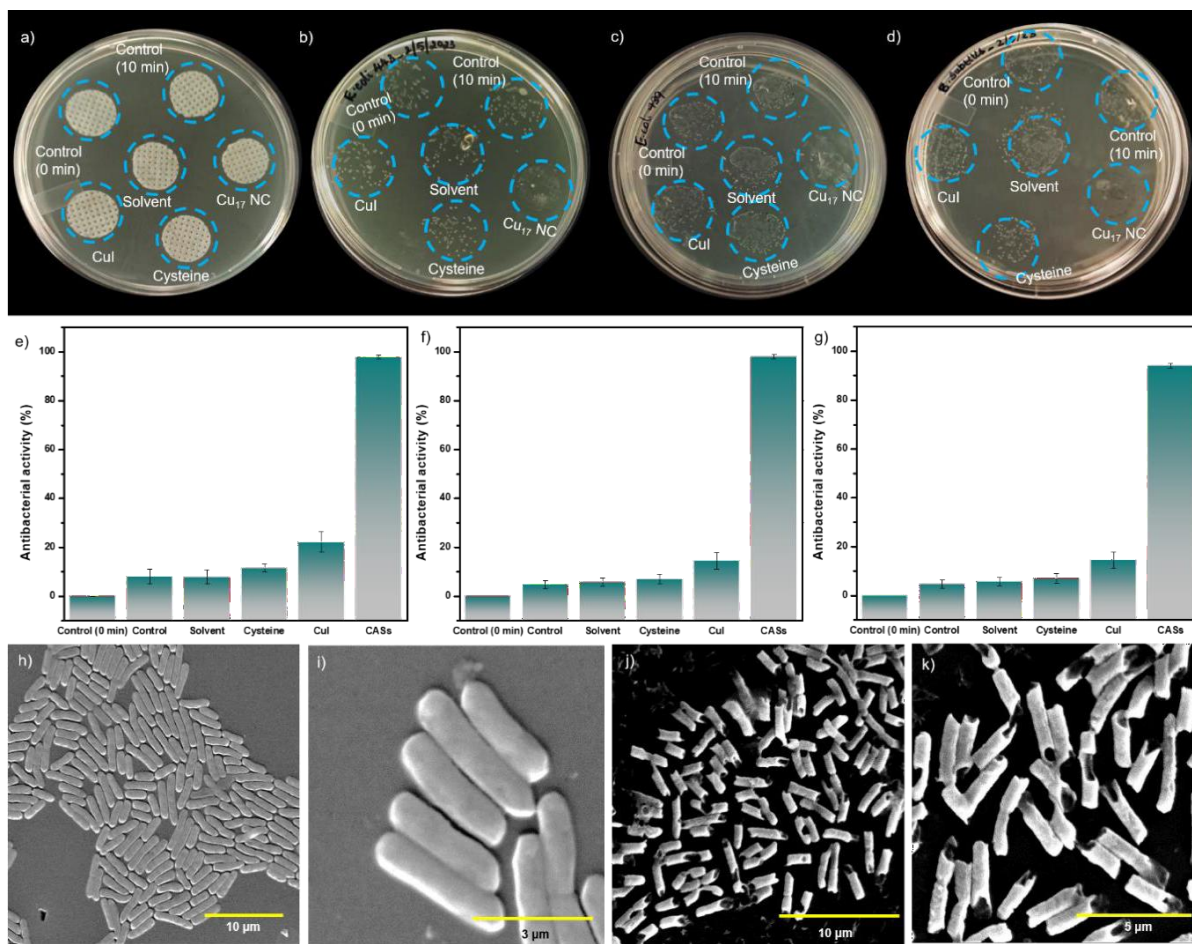


Figure S14. Nutrient agar plates showing a) PP discs placed on the plate with bacteria before incubation. Nutrient agar plates incubated at 32 °C for 24 hours show antibacterial activity against b) *E. coli* MTCC 443, c) *E. coli* MTCC 739, and d) *B. subtilis* after 1 h of exposure. Antibacterial activity plots of e) *E. coli* MTCC 443, f) *E. coli* MTCC 739 and g) *B. subtilis*, determined through colony counting method, performed with triplicates. ESEM images of *E. coli* MTCC 443 h) before and j) after the exposure to CASs. i) and k) show the zoomed-in view of the unaffected and affected cell membranes.

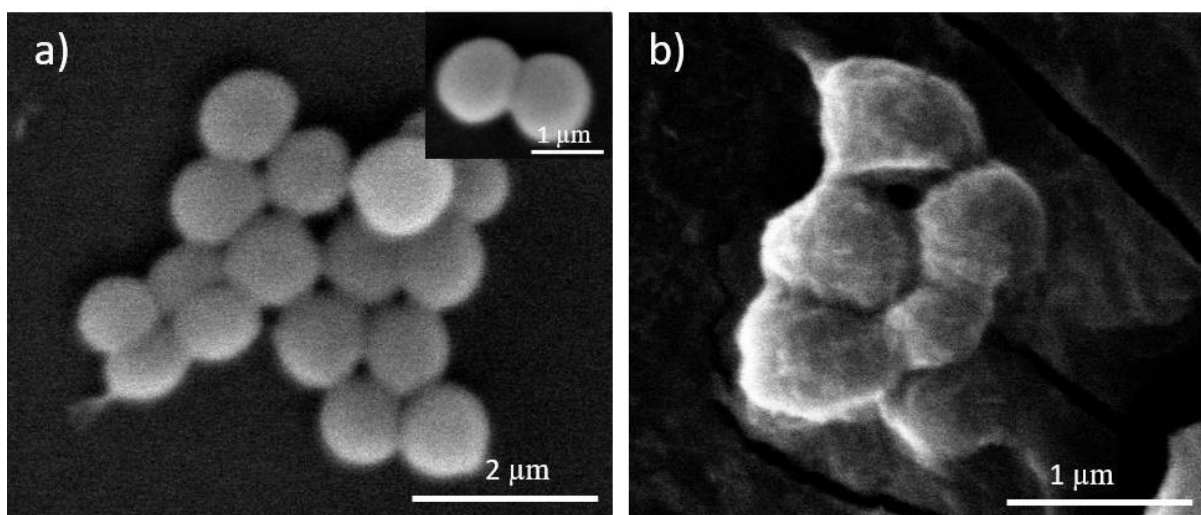


Figure S15. Antibacterial activity of CASs against *Staphylococcus aureus*. ESEM images of *S. aureus* a) control and b) cells interacted with CASs (right). Inset of a) shows the control cells in zoomed-in view.

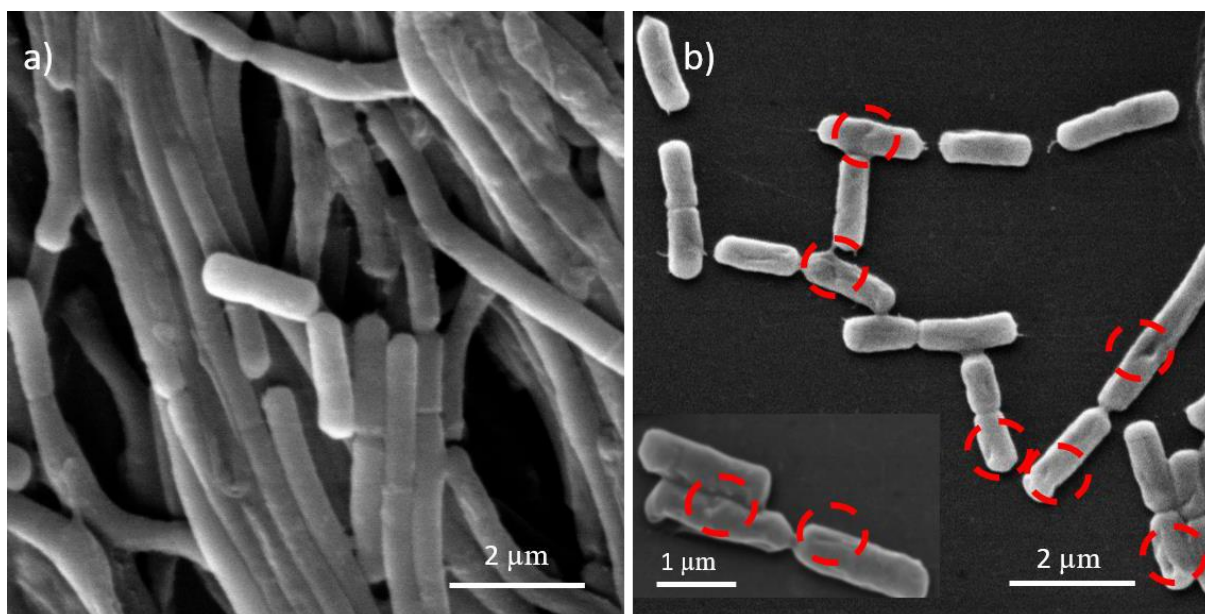


Figure S16. Antibiofilm activity of CASs against *B. subtilis*. ESEM images of a) *B. subtilis* control and b) cells interacted with CASs showing cell membrane damage (red dashed circles) (inset shows the zoomed-in view of the damaged cell membrane).

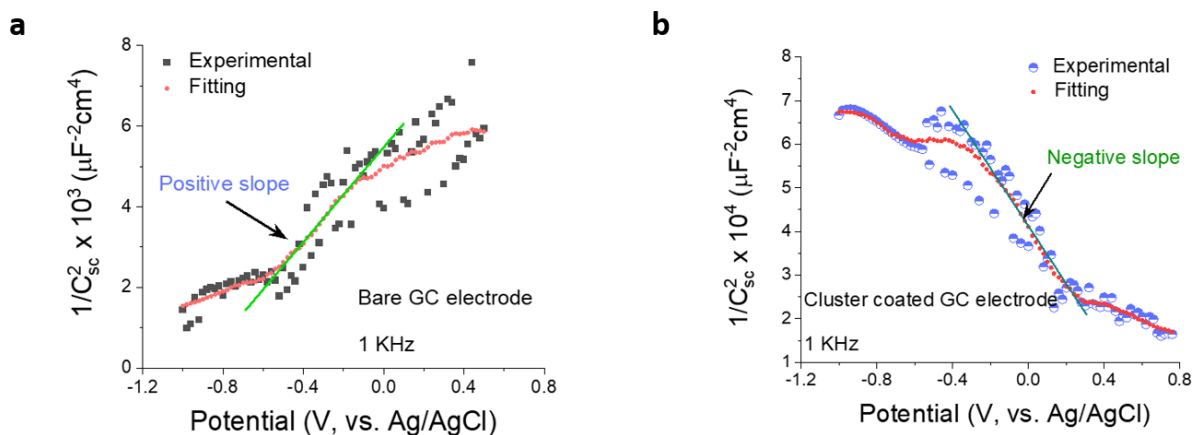


Figure S17. Electrochemical impedance spectroscopy measurement of CASs coating. a) The EIS plot of bare GCE and b) Cu₁₇NCs coated GCE (right). The experiment was carried out in NaCl.

Note:

‡J. Raman and H. M. Veera, from the Department of Biotechnology, Vel Tech High Tech Dr Rangarajan Dr Sakunthala Engineering College, Chennai 600062, India, were having their internships with TP during the course of this work.

Reference:

- (1) Li, J.; Ma, H. Z.; Reid, G. E.; Edwards, A. J.; Hong, Y.; White, J. M.; Mulder, R. J.; O’Hair, R. A. J. Synthesis and X-Ray Crystallographic Characterisation of Frustum-Shaped Ligated [Cu₁₈H₁₆(DPPE)₆]²⁺ and [Cu₁₆H₁₄(DPPA)₆]²⁺ Nanoclusters and Studies on Their H₂ Evolution Reactions. *Chem. – A Eur. J.* **2018**, *24* (9), 2070–2074. <https://doi.org/10.1002/chem.201705448>.
- (2) Jia, X.; Li, J.; Wang, E. Cu Nanoclusters with Aggregation Induced Emission Enhancement. *Small* **2013**, *9* (22), 3873–3879. <https://doi.org/10.1002/smll.201300896>.
- (3) Farrag, M.; Das, M. K.; Moody, M.; Samy El-Shall, M. Ligand-Protected Ultrasmall

- Pd Nanoclusters Supported on Metal Oxide Surfaces for CO Oxidation: Does the Ligand Activate or Passivate the Pd Nanocatalyst? *ChemPhysChem* **2021**, *22* (3), 312–322. <https://doi.org/10.1002/cphc.202000656>.
- (4) Jana, A.; Jash, M.; Dar, W. A.; Roy, J.; Chakraborty, P.; Paramasivam, G.; Lebedkin, S.; Kirakci, K.; Manna, S.; Antharjanam, S.; Machacek, J.; Kucerakova, M.; Ghosh, S.; Lang, K.; Kappes, M. M.; Base, T.; Pradeep, T. Carborane-Thiol Protected Copper Nanoclusters: Stimuli-Responsive Materials with Tunable Phosphorescence. *Chem. Sci.* **2023**, *14* (6), 1613–1626. <https://doi.org/10.1039/D2SC06578A>.
- (5) Jeong, Y.; Yoon, J. Recent Progress on Fluorescent Chemosensors for Metal Ions. *Inorganica Chim. Acta* **2012**, *381*, 2–14. <https://doi.org/10.1016/j.ica.2011.09.011>.
- (6) Baghdasaryan, A.; Bürgi, T. Copper Nanoclusters: Designed Synthesis, Structural Diversity, and Multiplatform Applications. *Nanoscale* **2021**, *13* (13), 6283–6340. <https://doi.org/10.1039/D0NR08489A>.
- (7) Sahu, B.; Kurrey, R.; Deb, M. K.; Shrivastava, K.; Karbhal, I.; Khalkho, B. R. A Simple and Cost-Effective Paper-Based and Colorimetric Dual-Mode Detection of Arsenic(III) and Lead(II) Based on Glucose-Functionalized Gold Nanoparticles. *RSC Adv.* **2021**, *11* (34), 20769–20780. <https://doi.org/10.1039/D1RA02929K>.
- (8) Yuan, X.; Zhu, M. Recent Advances in Atomically Precise Metal Nanoclusters for Electrocatalytic Applications. *Inorg. Chem. Front.* **2023**, *10* (14), 3995–4007. <https://doi.org/10.1039/D3QI00656E>.
- (9) Jose, A.; Jana, A.; Gupte, T.; Nair, A. S.; Unni, K.; Nagar, A.; Kini, A. R.; Spoorthi, B. K.; Jana, S. K.; Pathak, B.; Pradeep, T. Vertically Aligned Nanoplates of Atomically Precise Co₆S₈ Cluster for Practical Arsenic Sensing. *ACS Mater. Lett.* **2023**, *5* (3), 893–899. <https://doi.org/10.1021/acsmaterialslett.3c00085>.

- (10) Roy, S.; Palui, G.; Banerjee, A. The As-Prepared Gold Cluster-Based Fluorescent Sensor for the Selective Detection of As^{III} Ions in Aqueous Solution. *Nanoscale* **2012**, *4* (8), 2734–2740. <https://doi.org/10.1039/C2NR11786J>.
- (11) Babar, N. U. A.; Joya, K. S.; Tayyab, M. A.; Ashiq, M. N.; Sohail, M. Highly Sensitive and Selective Detection of Arsenic Using Electrogenerated Nanotextured Gold Assemblage. *ACS Omega* **2019**, *4* (9), 13645–13657. <https://doi.org/10.1021/acsomega.9b00807>.
- (12) Luo, M.-L.; Chen, G.-Y.; Wang, J.-L.; Chai, T.-Q.; Qian, Z.-M.; Li, W.-J.; Yang, F.-Q. Detection of Arsenic(V) by Fluorescence Sensing Based on Chlorin E6-Copper Ion. *Molecules*. 2024. <https://doi.org/10.3390/molecules29051015>.
- (13) Hamid Kargari, S.; Ahour, F.; Mahmoudian, M. An Electrochemical Sensor for the Detection of Arsenic Using Nanocomposite-Modified Electrode. *Sci. Rep.* **2023**, *13* (1), 8816. <https://doi.org/10.1038/s41598-023-36103-6>.
- (14) HACH Low Range Arsenic Test Kit <https://www.hach.com/p-arsenic-low-range-test-kit/2800000>.
- (15) Ascel® Arsenic Test Kit - 50-Tests <https://sensafe.com/ascel-arsenic-50-tests/>.
- (16) Digital Arsenic Test Kit <https://www.palintest.com/products/arsenator/>.
- (17) Semi-quantitative test strips QUANTOFIX EZ Arsenic Sensitive PP <https://www.mn-net.com/semi-quantitative-test-strips-quantofix-ez-arsenic-sensitive-pp-91345.2>.
- (18) Quick™ Arsenic for Water, Soil, and Wood Test Kit <https://sensafe.com/481396/>.
- (19) MQuant® Arsenic Test https://www.merckmillipore.com/IN/en/product/Arsenic-Test,MDA_CHEM-117927.

From Solution to Microstructures in Minutes: Microdroplet-Derived Stand-Alone TiO₂ Surfaces for Simultaneous Water Harvesting and Treatment

Keerthana Unni, Jenifer Shantha Kumar, Anirban Som, Depanjan Sarkar,* and Thalappil Pradeep*

Cite This: *ACS Sustainable Chem. Eng.* 2024, 12, 11957–11967

Read Online

ACCESS



Metrics & More



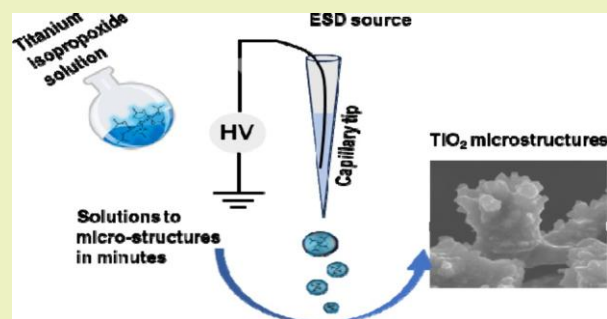
Article Recommendations



Supporting Information

ABSTRACT: We present a straightforward and eco-friendly method to transform a titanium tetraisopropoxide (TTIP) solution into superhydrophobic TiO₂ microstructures by ambient microdroplet deposition. At lower temperatures the micropillars of amorphous TiO₂ act as nucleation sites for condensing humidity to form droplets. However, the microstructures facilitate efficient water runoff despite TiO₂'s hydrophilic character by a combination of surface hydrophobicity and gravity. Additionally, the photocatalytic TiO₂ surface resists biofilm formation and degrades the contaminants, offering long-term collection of safe water and its purification, which has been demonstrated with examples. We demonstrate that the microdroplet-based methodology developed for the conversion of solution into microdroplets can also be applied to other metal oxides, including CuO and ZnO, highlighting the universality of the process.

KEYWORDS: *Electrospray deposition, Ambient microdroplets, Microstructures, TiO₂, Atmospheric water harvesting, Photocatalysis, Antibacterial property, Titanium tetraisopropoxide*



INTRODUCTION

Microdroplets have emerged as a powerful medium for rapid synthesis of molecules^{1–8} and materials.^{9–18} Such methods are sustainable means of synthesis as they require minimum reagents and minimal or no activating agents such as acids, catalysts, etc., are used.⁵ Electrospray deposition (ESD) of microdroplets is a powerful way of creating nanostructures for diverse applications.^{13,19} This paper explores the use of microdroplets to address one of humanity's most important problems, namely clean water, using microdroplet-derived nanostructures.

As the world's population grows and living standards improve, clean water is becoming a major challenge for sustainable development. Safe drinking water is a fundamental human right, yet millions lack its access, leading to devastating health consequences. Additionally, industries and agriculture are highly dependent on water resources, and shortages can lead to economic recession and food insecurity.²⁰ Equally alarming is the contamination of water sources, rendering even existing water supplies unsuitable for consumption.^{21–29} Tackling the global water crisis requires a comprehensive strategy that includes efficient conservation, responsible management, development of innovative purification and desalination technologies and appropriate investment.^{30–36} Establishing alternative water sources is a crucial aspect of making clean water accessible to all.³⁷ Atmospheric water capture (AWC) has emerged as a potential solution to provide clean water to regions

with scant natural water resources.^{38–48} This is primarily because, at any specific time, the Earth's atmosphere holds an astonishing 37.5 million billion gallons of water in the vapor form,⁴⁹ and an effective, cost-efficient device capable of capturing a portion of this could contribute to addressing the water crisis.

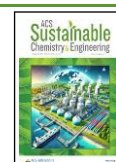
Microstructured surfaces have emerged as an important innovation in water harvesting.^{19,50–53} These surfaces are meticulously designed with tiny, engineered structures that effectively capture and channel water droplets, making them particularly adept at harvesting water from the atmosphere. We had reported the creation of biomimicked hydrophilic–hydrophobic patterned microstructured surfaces with unprecedented water harvesting efficiency.¹⁹ By exploiting principles of condensation and wettability, microstructured surfaces encourage water vapor to condense into droplets, which are then rapidly transported and collected for various purposes, from potable water supplies to irrigation. Over the past decade, there has been renewed interest in developing microstructured

Received: April 3, 2024

Revised: July 8, 2024

Accepted: July 8, 2024

Published: July 18, 2024



surfaces for water harvesting.^{54–56} However, many existing fabrication methods use complex instrumentation such as atom bombardment and electron beam lithography.^{57–59} In addition to their complex fabrication procedures, these surfaces encounter challenges related to extended usage for various reasons, such as substrate material leaching, contamination by volatile organic compounds, dyes, and biofilm formation. Recent research has demonstrated that TiO₂, owing to its photocatalytic properties, can serve as a material for creating surfaces for AWC capable of both water harvesting and contamination removal simultaneously. However, these substrates typically utilize TiO₂-embedded polymers, which can suffer from leaching issues. Thus, there is a pressing need to develop TiO₂ surfaces with microstructures that do not rely on supporting chemicals for effective AWC and treatment.⁶⁰

ESD offers an accessible and practical means of fabricating microstructured surfaces for efficient water harvesting. Another vital consideration in the development of effective water harvesting surfaces is the ability to ensure long-term reusability with acceptable efficiency.⁶⁰ Several factors come into play when assessing a surface's suitability for extended use, with surface stability under varying conditions being an aspect of paramount importance. One significant challenge lies in preserving the surface's stability when exposed to a range of environmental factors and potential contaminants from the atmosphere, which can diminish its capacity to provide clean water effectively. Additionally, the formation of biofilms on these surfaces can act as a hindrance to their extended use. Addressing these issues is pivotal for creating water harvesting surfaces with sustained efficiency and long-term reusability.

Here, we introduce an innovative, environment friendly, and straightforward approach for seamlessly transforming a titanium isopropoxide solution into extensive microstructures of titanium dioxide (TiO₂) under standard atmospheric conditions. These microstructures were deliberately designed in such a way that they collectively induce superhydrophobicity on the surface, allowing water to roll off effortlessly despite TiO₂'s intrinsic hydrophilic nature.⁶¹ When the surface was cooled, the hydrophilic micropillars made of TiO₂ served as nucleation sites for water droplets. Subsequently, the combined influence of the surface's hydrophobic nature and the force of gravity allowed for the easy roll-off of the water droplets. Furthermore, TiO₂ has photocatalytic properties,⁶² rendering it self-cleaning and resistant to biofilm formation when exposed to sunlight. This quality ensures prolonged safe use of the surface while also enabling the degradation of contaminants such as organic dyes and drug molecules, offering a means to purify the collected water, if ambient contaminants are present. Consequently, this engineered surface demonstrates an exceptional ability to independently collect and purify water from the atmosphere simultaneously. This approach was expanded to include other metal oxides, demonstrating its universality in creating microstructures from corresponding solutions within min.

MATERIALS AND METHODS

Materials Used. TTIP, copper acetate monohydrate, zinc acetate dihydrate, rhodamine 6G, methylene blue, rhodamine B, and ibuprofen were purchased from Sigma-Aldrich, India. Indium tin oxide glass slides were bought from Toshniwal Brothers (SR) Pvt. Ltd., India. Stainless steel (SS) mesh was acquired from eBay and was used as the surface to grow the microstructures. Copper TEM grids were sourced from SPI Supplies. Micropipette puller (P-97) and glass capillaries for nanoelectrospray (nESI) were purchased from Sutter Instrument, USA. Milli-Q water was used for all the experiments. Nutrient agar (NA) and

Luria–Bertani (LB) Broth for bacteria culture were purchased from HiMedia.

Instrumentation. Morphologies of microstructures formed using electrospray deposition were analyzed using a Thermo Scientific Verios G4 UC High-Resolution Field Emission Scanning Electron Microscope (HR-FESEM). Prior to imaging, samples were given a gold coating. Energy-dispersive spectroscopy (EDS) was used to analyze the microstructure composition. The static contact angle of the surfaces was measured using the GBX Digidrop contact angle meter. High-Resolution Transmission Electron Microscopy (HR-TEM) measurements were performed using a JEOL 3010 instrument. Thermo Scientific LTQ – XL mass spectrometer was used for analyzing the photocatalysis products. Keyence VHX-950F was used to capture the images of water harvesting experiments. Olympus IX83 inverted fluorescence microscope was used to evaluate the antibacterial activity of TiO₂ microstructures.

Electrospray Deposition. Homemade nanoelectrospray emitters were fabricated using glass capillaries with outer diameters (ODs) of 1.5 mm and inner diameters (IDs) of 0.86 mm. The micropipette puller settings were meticulously optimized to produce pulled tips with openings ranging from 30 to 40 μm. Each tip was thoroughly examined under an optical microscope, and any tips that deviated from the specified dimensions or with defects were discarded. The glass emitter tips were carefully filled with the desired precursor solutions using Eppendorf pipet tips. Subsequently, a platinum (Pt) wire (purchased from Sigma-Aldrich) with a diameter of 0.1 mm was employed to establish electrical connectivity. The nESI assembly was then connected to an external high-voltage source powered by a variable DC power supply (purchased from Sunmach Equipment) using a copper alligator clip. Upon applying a potential of 1–1.30 kV, a spray plume consisting of charged microdroplets was seen emanating from the tip of the emitter. This spray plume was directed toward a grounded electrode composed of a SS mesh of 74 μm mesh-size positioned on an ITO glass slide for neutralization and collection of the generated ions. The distance between the collector surface and the nESI emitter was 8–10 mm. All the parameters, like the distance and voltage, were optimized using trial and error method.

Fabrication of Microstructures Using Electrospray Deposition (ESD) of Microdroplets. First a homogeneous solution of the desired precursor in dry ethanol was prepared. It was then subjected to ESD, where the spray was deposited onto a dedicated SS mesh positioned on a grounded ITO plate. The duration of the ESD process varied from 60 to 120 min depending on the specific objectives of the experiment. Finally, the SS mesh underwent a low-temperature annealing step (100–120 °C) for an hour in a hot air oven, completing the transformation.

Water Harvesting Using Hydrophobic–Hydrophilic TiO₂ Microstructures. To investigate the water capture capabilities of the ESD-synthesized TiO₂ microstructure surfaces, a 1 cm × 1 cm SS mesh with the desired size of microstructures was prepared. This surface was then mounted on a Peltier cooler and brought to temperatures below the dew point for video observation ([Video S1, Supporting Information](#)). Two experiments were conducted: one with the bare SS mesh as a control and another with the sample, TiO₂ microstructure-coating. This allowed us to directly compare the efficiency of the fabricated material for atmospheric water capture. In both the experiments, the surface under examination was carefully attached to the Peltier cooler using silver paste to ensure efficient heat transfer. The entire setup was placed on the viewing stage of a Keyence VHX-950F digital microscope within a controlled environment maintained at 50% relative humidity and 25 °C temperature (dew point ≈13.8 °C). The surface was illuminated for clear microscopic observation. Time-lapse optical microscopy was performed to monitor the nucleation and growth of water droplets on the bare SS mesh and the TiO₂ microstructured surface under the above-mentioned laboratory conditions. There was no separate airflow to the substrate. The temperature of the condensing surface was 12 °C and it was measured using a thermocouple.

Photocatalytic Application Using the Microstructures. To examine the photocatalytic activity of ESD-fabricated TiO₂ micro-

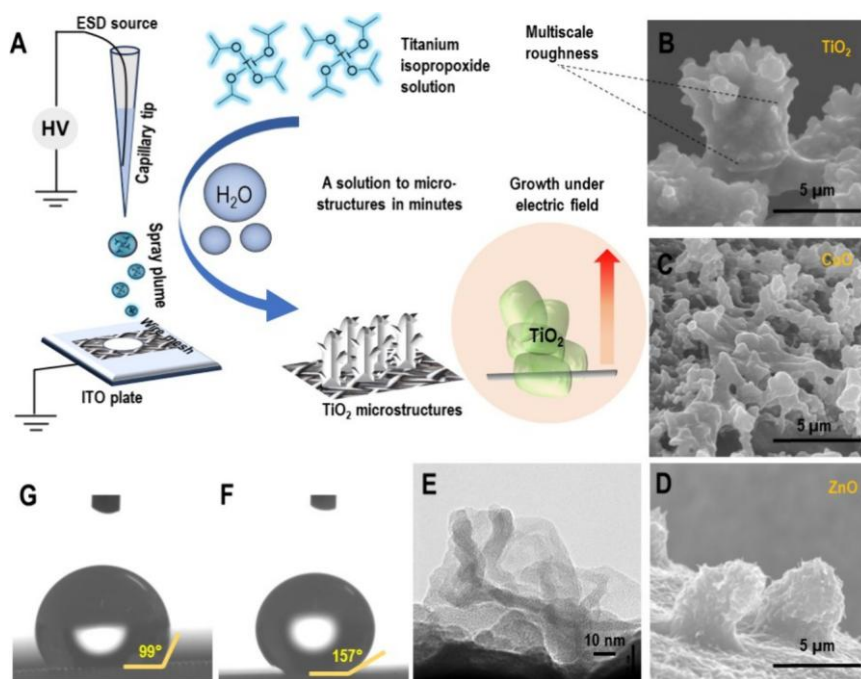


Figure 1. (A) Schematic representation of the ESD fabrication setup used for the microdroplet synthesis of microstructures under ambient conditions. SEM images of (B) TiO_2 , (C) CuO and (D) ZnO microstructures. (E) TEM image of TiO_2 microstructure. Contact angle of water on (F) TiO_2 microstructures, and (G) normal SS wire mesh.

structures, degradation of recalcitrant molecules and dyes was studied using the surface. In all our photocatalytic experiments, natural sunlight was used as the light source, and the samples were exposed to direct sunlight for a specific duration. In the case of ibuprofen, the solution was prepared, and the microstructured surface was immersed in the solution for 30 min. Ibuprofen is a persistent anti-inflammatory drug. Following adsorption, the contaminated surface was exposed to sunlight for 3 h, followed by washing with the desired solvent for extraction of the degradation products for further analysis. Similarly, a mixture of rhodamine 6G, rhodamine B, and methylene blue dyes was prepared. The microstructured surface was then dipped in the solution, and the dried surface was kept under sunlight for 3 h, followed by optical photography.

Antibacterial Activity of the TiO_2 Microstructures. The antibacterial and antiadhesion properties of the TiO_2 microstructured surfaces were assessed using *Escherichia coli* MTCC 443. For all the experiments, fresh cultures of *E. coli* were prepared by reviving the glycerol stock culture stored at -80°C in Luria–Bertani (LB) broth, followed by incubation at 37°C with shaking at 120 rpm. The revived culture was then introduced into freshly prepared LB broth to achieve a concentration of 10^5 CFU/mL. For antiadhesion investigations, the cells were centrifuged at 3000 rpm and rinsed twice with 0.2 M sterile phosphate-buffered saline (PBS, pH 7.5). Subsequently, the cells were suspended in sterile PBS and applied onto various surfaces: a bare SS wire mesh (sample 1), a SS wire mesh coated with TTIP (5 mM) (sample 2), and a TiO_2 microstructured surface (sample 3). After 1 h interaction period with the surfaces at 37°C , they were rinsed with sterilized PBS to eliminate unadhered cells. The samples were then shaken at 100 rpm in sterile PBS for 1 h to collect the adhered cells. Colony counting was employed to determine the number of cells adhered to the surfaces by inoculating the collected cells onto freshly prepared nutrient agar (NA) plates, followed by incubation at 37°C for 24 h.

The resistance to bacterial proliferation was examined by incubating *E. coli* culture at a concentration of 10^3 CFU/mL in LB broth on the surfaces at 37°C for 1 day with gentle agitation. The surfaces were subsequently rinsed with PBS to remove suspended and unadhered cells. The cells grown on the surfaces were retrieved with PBS through gentle agitation for 1 h. This cell suspension was then plated onto NA

plates and incubated under standard conditions, followed by colony counting. The antibacterial efficacy against *E. coli* was evaluated by loading the surfaces with a bacterial suspension of 10^4 CFU/mL and allowing interaction for 1 h under sunlight in static conditions. Control samples were kept in darkness to assess the influence of sunlight. The bacterial suspension on the wire mesh was collected by successive washings with PBS and plated onto freshly prepared NA plates for colony counting after 24 h of incubation at 37°C . Live/dead staining was performed using the BacLight™ Live/Dead viability kit, with a stain prepared by mixing SYTO 9 and propidium iodide dyes in PBS in a 1:1 ratio to visualize the *E. coli* cells under a fluorescence microscope.

The suitability of the TiO_2 coating as an antibacterial surface over repeated cycles of bacterial exposure was investigated to assess its longevity. This involved repeating the antibacterial studies for 5 cycles on the same sample surface. All experiments were conducted in triplicate for each sample.

RESULTS AND DISCUSSION

From Solution to Microstructures. Figure 1A presents a schematic diagram of the custom-built nESI source employed for ESD to make the TiO_2 microstructures. The left-hand portion of the figure illustrates the electrical connections, the nESI tip, and the platinum wire facilitating contact with the precursor solution. TTIP ($\text{C}_{12}\text{H}_{28}\text{O}_4\text{Ti}$), readily available as an inorganic complex, served as the precursor for constructing the TiO_2 microstructures. This complex readily dissolves in polar solvents like ethanol (EtOH) and isopropyl alcohol (IPA) but undergoes instant hydrolysis and condensation to form TiO_2 in the presence of water. Therefore, utilizing pure and anhydrous solvents is crucial for our experiments. Otherwise, TTIP reacts with even trace amounts of moisture present in the solvent, leading to premature formation of TiO_2 and clogging of the nESI tip. Initial ESD experiments were conducted using a 10 mM solution of TTIP in EtOH. Later we reduced the concentration of TTIP, using 5 mM solution for all the experiments. A clear precursor solution was loaded into a $\sim 30\ \mu\text{m}$ nESI tip and connected to the electrospray source. High voltage (1.5–2 kV)

was applied to the solution formed a Taylor cone, followed by a stable spray of charged microdroplets containing dissolved precursor ions. These droplets were directed toward a SS wire mesh as described in the experimental section. As deposition progressed, a white spot gradually grew in diameter, becoming more prominent with longer deposition times. This spot was characterized using electron microscopy, revealing pillar-like structures upon closer inspection. Figure 1B showcases an FESEM image of one such pillar formed after 90 min of deposition. Surprisingly, EDS analysis of the same pillar identified it as composed of TiO₂. Figure S1 presents the EDS spectrum, highlighting the atomic percentages of titanium and oxygen. The next paragraph delves deeper into the mystery, dissecting the surprising journey from a solution of C₁₂H₂₈O₄Ti to TiO₂, within minutes, and its subsequent orientation to form the pillars with dimensions of tens of micrometers.

Based on the ion evaporation model (IEM) of electro spray, we know that the molecules within charged microdroplets exhibit a tendency to migrate toward the droplet's periphery.⁶³ We hypothesize that this behavior plays a crucial role in our microstructure formation. The high propensity of TTIP to undergo hydrolysis and form TiO₂ combined with the IEM forms the foundation of this process. We propose the following sequence of events during the flight path of the charged droplets:

1. As the charged microdroplets travel through air, TTIP molecules migrate toward the periphery of the droplet sphere.
2. These TTIP molecules at the periphery react with atmospheric moisture, forming TiO₂.

This process is schematically depicted in Figure 1A. Beyond converting the precursor to TiO₂, the arrangement of these molecules into microscale structures is paramount to the fabrication process (Figure 1A, bottom portion). First, powerful electrostatic forces act as the driving force, helping the assembly. Second, charged microdroplets containing TiO₂ particles and solvated ions of the unreacted portion of the precursor are deposited on the surface. Subsequent solvent evaporation induces spatial reorganization, leaving behind neutralized TiO₂ deposits contributing to the pillar-like structure. Finally, the observed rough edges can be attributed to two factors: head-on accumulation of incoming material and their orthogonal association, leading to the formation of pillars. The SS wire mesh plays a crucial role in this process. The applied potential difference generates a strong electric field within the gap of the wire mesh, guiding the incoming microdroplets. This field, calculated as 1.5×10^5 V/m for a 1500 V potential difference, effectively attracts and "harpoons" the charged microdroplets into the high-field region near the mesh. Here, they are deposited and neutralized. The deposited TiO₂ particles, now in the nanometre range, significantly alters the electric field experienced by the incoming microdroplets. To test this hypothesis, we conducted a control experiment with a 2 min fixed deposition time, followed by TEM imaging of the sample. Figure S2 shows a TEM image of a TiO₂ structure formed on the TEM grid, with its dimensions in the range of 20–30 nm. The field strength is calculated to be 1.89×10^{11} V/m for a 10 nm particle attached to the mesh. This enhanced field, radiating outward from the deposited particles, creates a strong, attractive force for the next set of charged microdroplets, driven by the Coulombic interaction. Notably, at these elevated fields, especially after initial growth, field emission may play a role in droplet neutralization. Furthermore, the deposited material itself

becomes a point of even higher electric field, further attracting and guiding the assembly of incoming microdroplets, ultimately promoting the growth of elongated microstructures. The SS wire mesh is essential to create the structures. In its absence, on a standard ITO plate as substrate, the elongated microstructure was not seen (Figure S3).

Characterization of the Microstructures and Their Superhydrophobic Property. TEM was performed on the fabricated TiO₂ microstructures to investigate their crystalline nature. For this, ESD was performed on a copper TEM grid without carbon coating. Figure 1E shows a TEM image of a representative TiO₂ pillar. A closer investigation revealed that these pillars are made of amorphous TiO₂. Following an investigation of individual TiO₂ micropillars, their collective behavior as a surface was assessed. Notably, despite the intrinsic hydrophilicity of TiO₂, exhibited by its widespread utilization as a hydrophilic coating material, the surface fabricated via ESD unexpectedly displayed superhydrophobic characteristics. This phenomenon is particularly intriguing as the collective architecture of the micropillars seemingly negates the inherent hydrophilicity of the individual components, resulting in a surface with a significantly higher water contact angle (157°, Figure 1F) compared to a standard stainless-steel mesh (99°, Figure 1G). The reason behind the superhydrophobic character of the surface can be attributed to the following two reasons: (i) Air trapping: microstructures trap air pockets between the consecutive pillars. These air pockets create a barrier between the water and the solid surface, minimizing the direct contact area and reducing the attractive forces between water molecules and the surface.⁶⁴ (ii) Hierarchical Texture: ESD fabricated TiO₂ surfaces exhibit multiscale roughness, as evident from the FESEM image shown in Figure 1B, where each pillar has microstructures with even smaller features within. This hierarchical texture amplifies air trapping and contact angle effects, leading to even stronger hydrophobicity.⁶⁵ Water droplet roll-off experiments were carried out on the TiO₂ microstructures as well as on the SS mesh and the data were captured using a Keyence microscope (Figures S4 and S5).

Extending the Methodology to Other Metal Oxides.

We tested the feasibility of generalizing this methodology for the fabrication of microstructures for multiple metal oxides. Figures 1C and 1D show FESEM images of microstructures created from ESD deposition of copper(II) acetate monohydrate (Cu(CO₂CH₃)₂·H₂O), and zinc acetate dihydrate (Zn(CH₃COO)₂·2H₂O). Ethanolic solutions of 5 mM concentration each were used for ESD. We used ethanolic solutions instead of aqueous solutions for our experiments due to significantly faster electro spray times. This difference was primarily attributed to the solvents' surface tension. Ethanol, with its lower surface tension (21.6 mN/m at 20 °C compared to 72.8 mN/m for water), allows for easier droplet formation and faster electro spray, significantly reducing the fabrication time. Figure S6 shows the large area FESEM images of the fabricated surface, proving that it can be created over a significantly large area. EDS analysis confirms the microstructures' composition, identifying them as CuO (Figure S6A) and ZnO (Figure S6B), respectively. Both surfaces, made of copper and zinc oxide, showed hydrophobic properties when tested. Our findings extend the reach of ambient ESD beyond typical materials, demonstrating its prowess in fabricating superhydrophobic microstructures of vastly different metal oxides. The contact angle measurements of the CuO and ZnO microstructures were

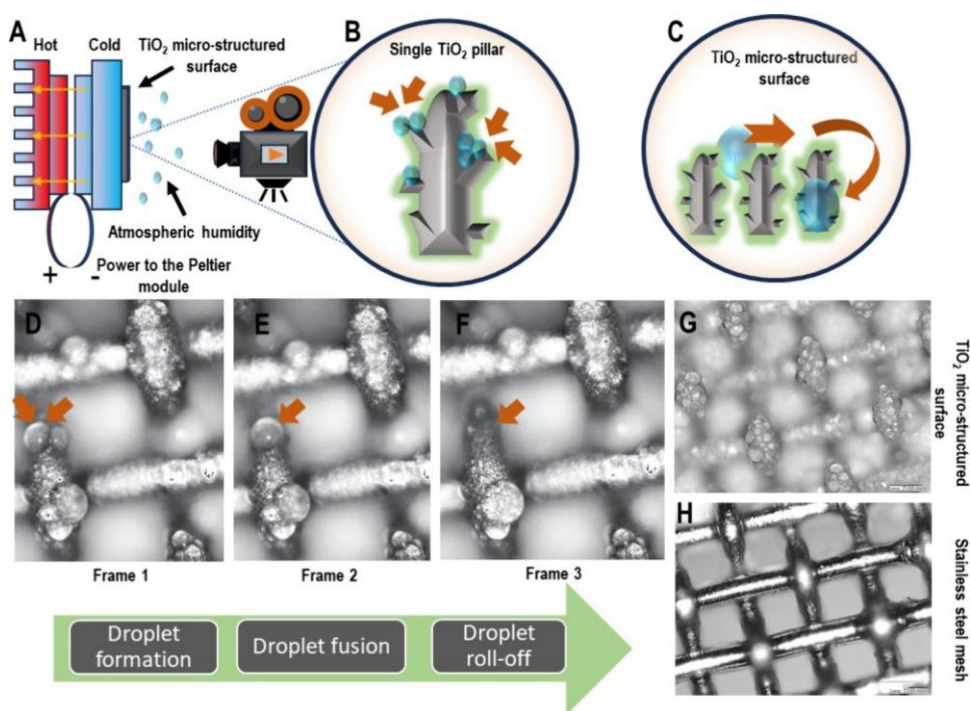


Figure 2. (A) Experimental setup for water harvesting. Schematic representation of (B) droplet formation, and (C) droplet roll-off on a single TiO_2 microstructure. Microscopic image of water harvesting, where the red arrow indicates the successive events of (D) droplet formation, (E) droplet fusion, and (F) droplet roll-off, on TiO_2 microstructures. Comparison between water harvesting efficiency of (G) TiO_2 microstructured surface and (H) stainless steel mesh, upon exposure to the environment, keeping all parameters the same. Details of the experiment are presented in the main text.

157° (Figure S7). This versatility paves the way for exploring a rich materials landscape.

Controlling Parameters for the Dimensions of the Microstructures. The size, shape, and performance of the fabricated microstructures can be finely tuned by adjusting specific parameters within the ESD process. However, maintaining certain parameters is critical for ensuring the generation of reproducible hydrophobic surfaces. This section describes the key fabrication parameters and their influence on the final product.

Deposition Time. The impact of deposition time was investigated by varying the ESD duration from 30 min to 2 h (Figure S8). FESEM images reveal a clear trend; longer deposition times leading to taller vertically growing structures.

Deposition Rate. To optimize microstructure morphology, the ESD deposition rate was monitored via measurements of the deposition current. A current range of 10–12 nA produced ideal microstructures with sharp, multilayered edges. Higher currents resulted in increased deposition of unreacted precursors, leading to rounded edges and significantly reduced water repellency (Figure S9). This highlights the importance of controlling the deposition rate for achieving optimal surface wettability.

Tip Size. For ESD fabrication of TiO_2 microstructures, tip size plays a crucial role in ensuring smooth process flow and minimizing unreacted precursors. All the experiments were performed using the tip size of 25–30 μm . The size of each tip was measured using an optical microscope before proceeding with the ESD process. Figure S10 shows a representative optical image of one such tip. Any tip that did not match the optimum size window was discarded.

Distance between the Spray Tip and the SS Wire Mesh. Electrostatic field strength, governed by the distance between the spray tip and the SS wire mesh, is a critical factor

influencing the stacking of the incoming droplets. To achieve uniform microstructures, we optimized this distance to 8–10 mm. While a closer distance would generate a stronger field, it could lead to inadequate solvent evaporation, creating solvent bridges that disrupt the fabrication process.

Atmospheric Water Capture Using TiO_2 Microstructures. Unexpected transformation of an intrinsically hydrophilic material into a superhydrophobic one, achieved through ESD prompted us to explore its possible use in atmospheric water capture (AWC). This interest stemmed from a biomimetic perspective; nature provides numerous examples of highly efficient AWC strategies often relying on intricate hydrophilic–hydrophobic surface patterns.^{51,66} A prime example is the *Opuntia microdasys*, where minute barbs on its conical spines effectively condense water droplets, while the spine's curvature acts as a natural microfluidic channel, guiding the condensate toward the base through a combination of hydrophilic and hydrophobic regions.⁶⁷ On the other hand, the Namib desert beetle (*Stenocara gracilipes*) utilizes hydrophilic–hydrophobic patterns on its wings to both collect water and, subsequently, transport it to other parts of its body.⁵¹ These observations served as a strong motivator to explore the AWC potential of our ESD-fabricated superhydrophobic surface. For our experiments, a $\sim 100 \text{ mm}^2$ circular area of TiO_2 microstructures, fabricated via ESD on a 1 cm^2 stainless steel mesh, served as the AWC surface. This mesh was secured onto a Peltier cooler using silver paste for efficient thermal contact. AWC experiments were conducted in an air-conditioned room ($\sim 25^\circ \text{C}$, 50% RH) with the surface temperature maintained at 10°C , slightly below the dew point (13.8°C). No external humidifiers or mist generators were employed. The collection surface and cooling module were positioned vertically on a Keyence microscope stage for video recording. Figure 2A schematically illustrates the experimental

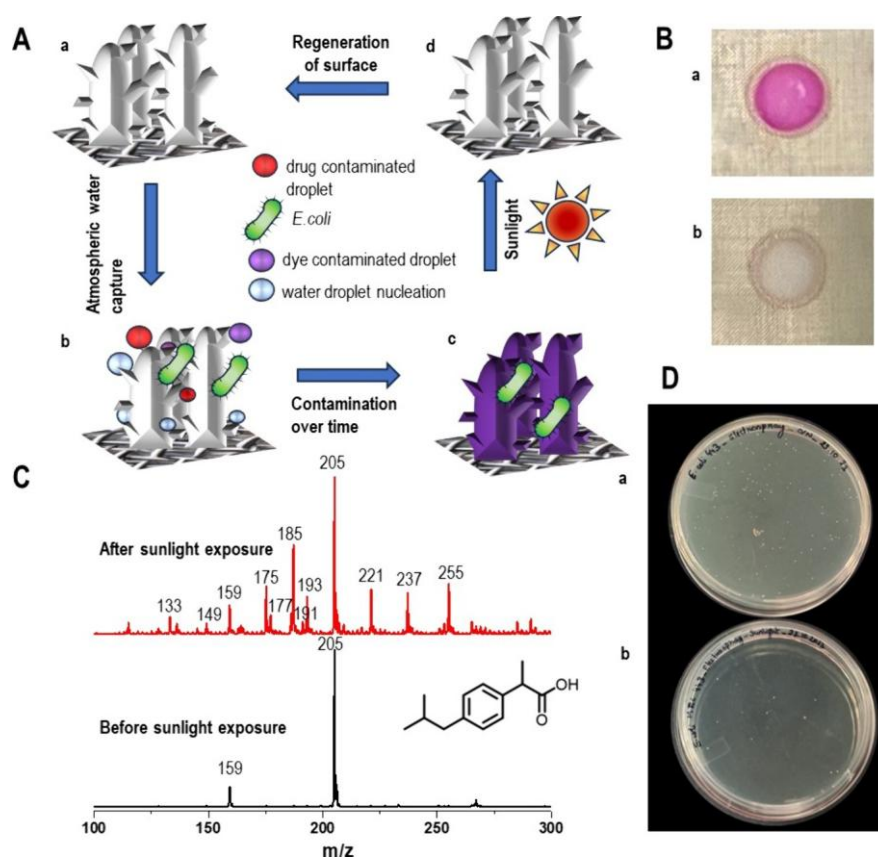


Figure 3. (A) Schematic representation of atmospheric water capture and self-cleaning property of TiO₂ microstructures: (a) TiO₂ microstructures; (b) TiO₂ microstructures during atmospheric water harvesting; (c) contaminated microstructures over time; (d) regenerated TiO₂ microstructures upon sunlight exposure. (B) Optical images of the TiO₂ microstructure surface on a SS wire mesh (a) after dye adsorption and (b) after sunlight exposure. (C) Mass spectra of ibuprofen collected from the solution after washing the drug-adsorbed TiO₂; the black and red traces are before and after sunlight exposure. (D) Optical images of *E. coli* colonies on TiO₂ microstructures (a) before and (b) after sunlight exposure.

setup of AWC. Surfaces with varying microstructures created by ESD for 1, 1.5, and 2 h were investigated for their AWC performance (Figure S11). Notably, while all surfaces exhibited water nucleation, the 1.5 h fabricated surface demonstrated superior water roll-off, a crucial factor for efficient AWC. Therefore, this optimized surface was chosen for further experiments due to its enhanced water collection and release capabilities. The AWC process on the fabricated TiO₂ microstructures can be conceptualized in three key stages:

1. **Nucleation:** The intricate nanoscale edges of the intrinsically hydrophilic TiO₂ structures readily initiate water droplet formation due to their ability to lower the free energy barrier for nucleation. This function can be likened to the minute barbs on a cactus spine, promoting water droplet condensation on the surface.
2. **Coalescence:** Once nucleated droplets reach a critical size, they begin to coalesce with each other due to intermolecular forces, forming larger and heavier droplets.
3. **Roll-off:** When the combined weight of a coalesced droplet overcomes the pinning force exerted by the underlying surface texture and exceeds the adhesive forces, the superhydrophobic nature of the microstructured surface facilitates its effortless roll off. This can be envisioned as a “critical weight threshold” being surpassed, triggered by the combined effect of superhydrophobicity and gravity.

Figures 2B and 2C schematically illustrate the three stages of the AWC process. Figures 2D–F present corresponding optical images, captured from video recordings from the microscope, showcasing a specific region (indicated by the red arrow) where all three stages (nucleation, coalescence, and roll-off) can be sequentially observed. For a dynamic visualization, please refer to Supporting Video S1, which presents a real-time video recording of the AWC process. To elucidate the role of the TiO₂ microstructures in water nucleation, a control experiment was performed using a bare stainless-steel mesh under identical AWC conditions. As evident from Figures 2G and 2H, the TiO₂ microstructured surface exhibited significantly enhanced water nucleation compared to the minimal condensation observed on the bare mesh. Figure S12 shows FESEM images of the surface after keeping the surface underwater for 1 h.

The AWC efficiency for the TiO₂ microstructures (created by 90 min of deposition) was calculated based on the droplets generated on a measured area within a fixed time (90 s). Figure S13 shows the reference image used for the efficiency calculation. From this image, a rectangular area measuring 130.3 μm in length and 34.1 μm in width was selected, and the number of droplets within this area (seven, in this case) was counted, indicated by black crosses in Figure S13. The diameter of a single droplet was then measured; a smaller droplet with a diameter of 17.7 μm was chosen to avoid overestimation. Larger droplets were intentionally excluded from consideration as they resulted from the coalescence of smaller droplets. The volume of water in each droplet was calculated, assuming it to be a

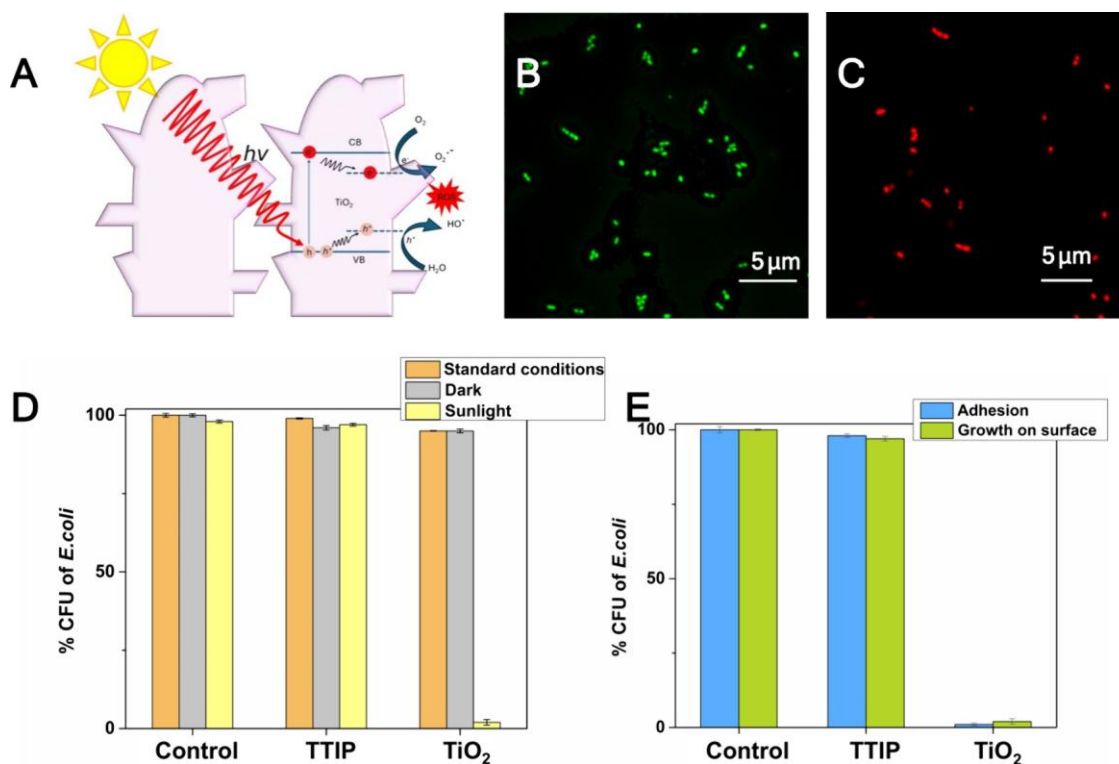


Figure 4. (A) Schematic representation of the mechanism of ROS formation on the microstructures due to photocatalytic activation of TiO₂. Fluorescence microscopy image of (B) *E. coli* control cells and (C) cells exposed to sunlight on TiO₂ surface. (D) Viability of *E. coli* cells on SS mesh, TTIP drop casted surface, and TiO₂ microstructure; experiments were done under standard conditions in the dark as well as in the presence of sunlight. (E) Bar diagram shows the reduction in the growth and adhesion in the *E. coli* cells exposed to TiO₂ surface compared with control cells and TTIP.

hemisphere. This process was repeated in several other areas, and the values were averaged and converted into units of L m⁻² day⁻¹. We estimate that the TiO₂ microstructured surface demonstrated a water capture efficiency of ~40 L m⁻² day⁻¹.

Photocatalytic Self-Cleaning of TiO₂ Microstructures for Prolonged AWC. Degradation of Organic Molecules.

Figure 3A schematically illustrates self-cleaning mechanism of the fabricated TiO₂ microstructures. Initially, the clean surface captures atmospheric water vapor (3Aa, 3Ab), leading to potential contamination due to the different contaminants present in the atmosphere. But in our case, the sunlight exposure triggers a regenerative process (3Ad) because of the photocatalytic activity of TiO₂. To assess this self-cleaning capability, photocatalytic degradation of various pollutants was investigated. A mixture of dyes (rhodamine 6G, rhodamine B, methylene blue) was adsorbed onto the surface and exposed to sunlight for 3 h. Remarkably, no visible trace of dye remained (Figures 3Ba, 3Bb show before and after sunlight exposure, respectively), highlighting the effectiveness of TiO₂ microstructures for both self-cleaning and degrading diverse organic pollutants. Similarly, ibuprofen served as a model drug to test the effect. A 10 mM solution (1:9 methanol: water) was prepared and the microstructure surface was immersed for 30 min. Following adsorption, the surface was exposed to sunlight for 3 h. Subsequent washing and mass spectrometry analysis revealed significant degradation of ibuprofen (Figures 3C and S14, the black and red traces demonstrate before and after sunlight exposure). The decrease in the intensity of *m/z* 205 peak suggests breakdown via the OH radical-induced pathway, further evidenced by the appearance of additional peaks signifying the addition of OH groups (*m/z* 221, 237, 255 (H₂O adduct of *m/z* 237)). The peaks at lower mass ranges are

peaks due to further degradation of the hydroxylated products. The degradation products and corresponding *m/z* values are mentioned in the Table S1. Although these peaks may be attributed to species of higher toxicity than the parent molecules, they are short-lived intermediates of the entire degradation pathway and the final degradation product may be harmless. Control experiments proved that in the absence of TiO₂ there was no degradation of the drug molecule. TiO₂ typically has a large band gap (>3.2 eV), which means it can only absorb UV light and not visible light, limiting its photocatalytic activity under sunlight. However, we speculate that the following factors may have contributed to the photocatalytic activity of the TiO₂ microstructures under sunlight. Size and surface area: The microstructures created using ambient microdroplet deposition had a high surface area-to-volume ratio, which increased the availability of active sites for photocatalytic reactions.^{68,69} Enhanced light absorption: The curvatures and micronano-metre-sized grooves (evident from Figure 1B) of microstructures led to light scattering and multiple reflections within the structures, enhancing the absorption of sunlight, including the UV component. Doping and defects: As mentioned

previously, the synthesized TiO₂ was amorphous, implying it may have oxygen defects. Oxygen defects are common in amorphous materials due to their lack of long-range crystalline order. These oxygen vacancies create defect states within the band gap, effectively reducing the band gap energy. This reduction probably allowed the TiO₂ microstructures to absorb visible light, extending its photocatalytic activity beyond the UV region. Increased surface reactivity: The presence of oxygen defects increased the number of active sites on the surface of amorphous TiO₂. These active sites facilitated the adsorption

and activation of reactant molecules, leading to higher photocatalytic activity.

Antibacterial Property of the TiO₂ Microstructures. Water harvesting surfaces face challenges posed by bacterial growth, impacting long-term efficacy. This study assessed the antibacterial activity of ESD-fabricated TiO₂ microstructures under sunlight using *E. coli* bacteria. Significant bacterial killing was observed on sunlight-exposed TiO₂ sample (Figure 3Db), contrasting with the absence of such activity in the samples maintained in the dark (Figure 3Da). Control experiments (Figure S15A) with blank wire mesh and TTIP coated (by drop casting method) mesh under light and dark conditions reinforced these findings. This confirms the effectiveness of sunlight-exposed TiO₂ surfaces in eliminating bacteria.

Literature provides a framework for understanding the degradation and antibacterial properties of TiO₂.⁷¹ Under sunlight, the TiO₂ microstructure undergoes photoexcitation. An electron leaps from the valence band (VB) to the conduction band (CB), creating a hole in the VB. These energetic electron-hole pairs migrate to the surface. Here, they interact with adsorbed water and oxygen, generating highly reactive oxygen species (ROS) like hydroxyl radicals ($\cdot\text{OH}$) and superoxide radicals ($\text{O}_2^{\cdot-}$). Figure 4A schematically represents the mechanism of ROS generation on the TiO₂ microstructures upon photoexcitation. Ultimately, the generated ROS are responsible for the degradation and antibacterial properties of TiO₂.

Previous studies have established the enhanced antibacterial properties of TiO₂ under sunlight. Subsequent experiments were conducted to test and quantify the antibacterial efficacy of the ESD-fabricated surfaces. Fluorescence imaging of *E. coli* cells was carried out to assess antibacterial activity. Figure 4B presents a fluorescence image of *E. coli* cells drop-casted on a SS wire mesh and exposed to sunlight. The presence of green emission indicates live bacterial cells in the absence of TiO₂. Conversely, Figure 4C shows cells after exposure to sunlight with TiO₂ microstructures. The red-stained cells indicate dead bacteria proving the antibacterial effect of TiO₂.⁷² Evaluation of the antibacterial activity revealed a viability of 2% in bacterial cells exposed to sunlight with TiO₂ compared to 97% in cells treated with TTIP and the control group (refer to Figure 4D). Control experiments were conducted under standard conditions and in the absence of sunlight to confirm the role of TiO₂ structures in *E. coli* eradication. The antibacterial efficacy of TiO₂ persisted even after subjecting it to five cycles of loading with 10⁴ CFU/mL of *E. coli* cells and exposure to sunlight (refer to Figure S15B). This was contrasted with bacterial cells incubated on wire mesh kept in the dark and another control group exposed to sunlight. The high antibacterial activity may also be attributed to the surface roughness of the microstructures. Literature suggests that nanometer-scale structures with high aspect ratios do not facilitate the growth of *E. coli* cells.⁷³

The presence of a hydrophobic surface significantly hampered *E. coli* growth, with only 2% of viable cells detected after 24 h of incubation under standard conditions. In contrast, drop casted surfaces facilitated bacterial growth and exhibited adherence. Notably, TiO₂ surfaces demonstrated notable resistance to bacterial attachment, attributed to their high hydrophobicity and ROS production, showcasing their efficacy in inhibiting bacterial biofilm formation.

The self-cleaning property was evaluated using *E. coli* cells, where TiO₂ surfaces loaded with these cells were subjected to gentle washing. Colony counting on nutrient agar plates

revealed that TiO₂ microstructures effectively deterred *E. coli* adhesion in water, with only 1% adherence observed, contrasting starkly with wire mesh, which retained 98% of bacterial cells postwashing (refer to Figure 4E).

Sustainability of the ESD Technique. Creation of nanomicro structures on surfaces using conventional techniques like, electron lithography, chemical vapor deposition, physical vapor deposition, cathodic arc deposition, magnetron sputtering, etc., requires specific conditions like, high-temperature, high-vacuum, definite gas environments, etc. These requirements eventually add up to the carbon footprint of the synthesis method. In contrast, ESD serves as a sustainable solution by promoting direct conversion of a precursor solution to microstructures by a feasible room-temperature technique with minimal use of chemicals and energy. In this report, we present a technique that converts TTIP, a precursor solution of Ti to TiO₂ microstructures within minutes at room temperature. These microstructures can be utilized as a standalone surface for atmospheric water capture and treatment to address one of the sustainable development goals.

CONCLUSIONS

This study presents a novel, eco-friendly, and convenient method for producing extensive TiO₂ microstructures directly from a TTIP solution under ambient conditions. These specially designed microstructures, collectively offer great super hydrophobicity allowing water droplets to roll-off efficiently despite TiO₂'s inherent hydrophilic nature, enabling efficient atmospheric water harvesting. Under sunlight, the photocatalytic properties of TiO₂ activate breaking down of contaminants like organic dyes and drugs, resulting in an essentially self-cleaning surface for sustainable water collection. Sunlight also generates ROS that prevent bacterial growth and biofilm formation, addressing a key challenge for long-term use. This unique combined capability allows for the independent collection and purification of water from the atmosphere, offering a promising solution for water scarcity challenges. Additionally, the approach's versatility was demonstrated by successfully creating microstructures from other metal oxide solutions, highlighting its potential for broader applications.

ASSOCIATED CONTENT

Supporting Information

The Supporting Information is available free of charge at <https://pubs.acs.org/doi/10.1021/acssuschemeng.4c02806>.

Video S1 of water capture in TiO₂ microstructure (MP4)

FESEM image and EDS spectra of TiO₂ microstructures; TEM image of TiO₂ structure formed after 2 min of deposition; FESEM image of deposited TiO₂ on an ITO plate; a water droplet roll-off experiment on TiO₂ microstructure surface; a water droplet adhesion experiment on TiO₂ microstructures and SS wire mesh; FESEM images and EDS spectra of CuO and ZnO microstructures; contact angles of CuO-coated SS mesh and ZnO-coated mesh; time-dependent FESEM images of TiO₂ microstructures; FESEM image of TiO₂ structures at higher deposition rate; optical image of a nESI tip; atmospheric water harvesting on TiO₂ microstructures; FESEM of surface immersed in water; optical image of TiO₂ microstructures during the AWC experiment; mass spectrum for ibuprofen degradation; bacterial activity;

ibuprofen degradation products and m/z of the corresponding ions (PDF)

AUTHOR INFORMATION

Corresponding Authors

Depanjan Sarkar – DST Unit of Nanoscience and Thematic Unit of Excellence, Department of Chemistry, Indian Institute of Technology Madras, Chennai 600036, India; Centre of Excellence on Molecular Materials and Functions, Department of Chemistry, Indian Institute of Technology Madras, Chennai 600036, India; International Centre for Clean Water, Indian Institute of Technology Madras Research Park, Chennai 600013, India; Email: depanjansarkar@gmail.com

Thalappil Pradeep – DST Unit of Nanoscience and Thematic Unit of Excellence, Department of Chemistry, Indian Institute of Technology Madras, Chennai 600036, India; Centre of Excellence on Molecular Materials and Functions, Department of Chemistry, Indian Institute of Technology Madras, Chennai 600036, India; International Centre for Clean Water, Indian Institute of Technology Madras Research Park, Chennai 600013, India; orcid.org/0000-0003-3174-534X; Email: pradeep@iitm.ac.in

Authors

Keerthana Unni – DST Unit of Nanoscience and Thematic Unit of Excellence, Department of Chemistry, Indian Institute of Technology Madras, Chennai 600036, India; Centre of Excellence on Molecular Materials and Functions, Department of Chemistry, Indian Institute of Technology Madras, Chennai 600036, India; International Centre for Clean Water, Indian Institute of Technology Madras Research Park, Chennai 600013, India

Jenifer Shantha Kumar – DST Unit of Nanoscience and Thematic Unit of Excellence, Department of Chemistry, Indian Institute of Technology Madras, Chennai 600036, India; Centre of Excellence on Molecular Materials and Functions, Department of Chemistry, Indian Institute of Technology Madras, Chennai 600036, India; International Centre for Clean Water, Indian Institute of Technology Madras Research Park, Chennai 600013, India; orcid.org/0009-0003-7502-7005

Anirban Som – DST Unit of Nanoscience and Thematic Unit of Excellence, Department of Chemistry, Indian Institute of Technology Madras, Chennai 600036, India; Centre of Excellence on Molecular Materials and Functions, Department of Chemistry, Indian Institute of Technology Madras, Chennai 600036, India; International Centre for Clean Water, Indian Institute of Technology Madras Research Park, Chennai 600013, India; orcid.org/0000-0002-6646-679X

Complete contact information is available at:

<https://pubs.acs.org/10.1021/acssuschemeng.4c02806>

Author Contributions

K.U.: design of the work, data collection, data analysis and interpretation, drafting and editing of the article. J.S.K.: microbiology and fluorescence microscopy experiments. A.S.: TEM measurements, data analysis, and interpretation. D.S.: conception and design of work, supervision of data analysis, interpretation of results, drafting and editing of the article. T.P.: conception and design of work, supervision of data analysis, interpretation of results, and writing of the final version of the article.

Notes

The authors declare no competing financial interest.

ACKNOWLEDGMENTS

We acknowledge the Science and Engineering Research Board (SERB), Department of Science and Technology (DST), and the Government of India for their research funding. T.P. acknowledges the financial support of SERB SUPRA (Grant SPR/2021/000439). D.S. acknowledges the Centre of Excellence on Molecular Materials and Functions under the Institution of Eminence Scheme of IIT Madras. K.U. thanks the University Grants Commission (UGC), Government of India, for her fellowship. J.S.K. thanks IIT Madras for research fellowship. We acknowledge Prof. Pijush Ghosh and Amit Kumar for helping us conduct the contact angle measurements.

ABBREVIATIONS

TTIP, titanium tetraisopropoxide; AWC, atmospheric water harvesting; VB, valence band; CB, conduction band; ROS, reactive oxygen species; ESD, electrospray deposition; SS, stainless steel; LB, Luria–Bertani; PBS, phosphate buffered saline; NA, nutrient agar; IPA, isopropyl alcohol; ITO, indium tin oxide

REFERENCES

- (1) Wei, Z.; Li, Y.; Cooks, R. G.; Yan, X. Accelerated Reaction Kinetics in Microdroplets: Overview and Recent Developments. *Annu. Rev. Phys. Chem.* 2020, 71 (1), 31–51.
- (2) Girod, M.; Moyano, E.; Campbell, I.; Cooks, R. G. Accelerated Bimolecular Reactions in Microdroplets Studied by Desorption Electrospray Ionization Mass Spectrometry. *Chem. Sci.* 2011, 2 (3), 501–510.
- (3) Sahota, N.; AbuSalim, D. I.; Wang, M. L.; Brown, C. J.; Zhang, Z.; El-Baba, T. J.; Cook, S. P.; Clemmer, D. E. A Microdroplet-Accelerated Biginelli Reaction: Mechanisms and Separation of Isomers Using IMS-MS. *Chem. Sci.* 2019, 10 (18), 4822–4827.
- (4) Mehrgardi, M. A.; Mofidfar, M.; Zare, R. N. Sprayed Water Microdroplets Are Able to Generate Hydrogen Peroxide Spontaneously. *J. Am. Chem. Soc.* 2022, 144 (17), 7606–7609.
- (5) Lee, J. K.; Samanta, D.; Nam, H. G.; Zare, R. N. Micrometer-Sized Water Droplets Induce Spontaneous Reduction. *J. Am. Chem. Soc.* 2019, 141 (27), 10585–10589.
- (6) Meng, Y.; Gnanamani, E.; Zare, R. N. Catalyst-Free Decarboxylative Amination of Carboxylic Acids in Water Microdroplets. *J. Am. Chem. Soc.* 2023, 145 (1), 32–36.
- (7) Meng, Y.; Gnanamani, E.; Zare, R. N. One-Step Formation of Pharmaceuticals Having a Phenylacetic Acid Core Using Water Microdroplets. *J. Am. Chem. Soc.* 2023, 145 (14), 7724–7728.
- (8) Meng, Y.; Zare, R. N.; Gnanamani, E. One-Step, Catalyst-Free Formation of Phenol from Benzoic Acid Using Water Microdroplets. *J. Am. Chem. Soc.* 2023, 145 (35), 19202–19206.
- (9) Li, A.; Luo, Q.; Park, S. J.; Cooks, R. G. Synthesis and Catalytic Reactions of Nanoparticles Formed by Electrospray Ionization of Coinage Metals. *Angew. Chemie - Int. Ed.* 2014, 53 (12), 3147–3150.
- (10) Li, A.; Baird, Z.; Bag, S.; Sarkar, D.; Prabhath, A.; Pradeep, T.; Cooks, R. G. Cooks. Using Ambient Ion Beams to Write Nanostructured Patterns for Surface Enhanced Raman Spectroscopy. *Angew. Chem., Int. Ed.* 2014, 53 (46), 12528–12531.
- (11) Ghosh, J.; Cooks, R. G. Mass Spectrometry in Materials Synthesis. *TrAC - Trends Anal. Chem.* 2023, 161, No. 117010.
- (12) Lee, J. K.; Samanta, D.; Nam, H. G.; Zare, R. N. Spontaneous Formation of Gold Nanostructures in Aqueous Microdroplets. *Nat. Commun.* 2018, 9 (1), 1562.
- (13) Sarkar, D.; Mahitha, M. K.; Som, A.; Li, A.; Wlekinski, M.; Cooks, R. G.; Pradeep, T. Metallic Nanobrushes Made Using Ambient Droplet Sprays. *Adv. Mater.* 2016, 28 (11), 2223–2228.

- (14) Fang, H.; Wang, D.; Yuan, L.; Wu, X.; Guo, H.; Chen, H.; Huang, K.; Feng, S. Electric-Field-Induced Assembly of Ag Nanoparticles on a CuO Nanowire Using Ambient Electro Spray Ionization. *New J. Chem.* 2017, 41 (8), 2878–2882.
- (15) Sarkar, D.; Mondal, B.; Som, A.; Ravindran, S. J.; Jana, S. K.; Manju, C. K.; Pradeep, T. Holey MoS₂ Nanosheets with Photocatalytic Metal Rich Edges by Ambient Electro spray Deposition for Solar Water Disinfection. *Glob. Challenges* 2018, 2 (12), No. 1800052.
- (16) Satyabola, D.; Ahuja, T.; Bose, S.; Mondal, B.; Srikrishnarka, P.; Kannan, M. P.; Spoorthi, B. K.; Pradeep, T. Transformation of Nanodiamonds to Onion-like Carbons by Ambient Electro spray Deposition. *J. Phys. Chem. C* 2021, 125 (20), 10998–11006.
- (17) Bose, S.; Chatterjee, A.; Jenifer, S. K.; Mondal, B.; Srikrishnarka, P.; Ghosh, D.; Chowdhuri, A. R.; Kannan, M. P.; Elchuri, S. V.; Pradeep, T. Molecular Materials through Microdroplets: Synthesis of Protein-Protected Luminescent Clusters of Noble Metals. *ACS Sustain. Chem. Eng.* 2021, 9 (12), 4554–4563.
- (18) Zhang, H.; Liu, Z.; Li, H.; Fu, Z.; Zhang, G.; Zhang, H.; Wang, G.; Zhang, Y. PdFe Alloy Nanoparticles Supported on Nitrogen-Doped Carbon Nanotubes for Electro catalytic Upcycling of Poly(ethylene terephthalate) Plastics into Formate Coupled with Hydrogen Evolution. *J. Mater. Chem. A* 2024, 12, 15984–15995.
- (19) Sarkar, D.; Mahapatra, A.; Som, A.; Kumar, R.; Nagar, A.; Baidya, A.; Pradeep, T. Patterned Nanobrush Nature Mimics with Unprecedented Water-Harvesting Efficiency. *Adv. Mater. Interfaces* 2018, 5 (19), 1–7.
- (20) Michalak, A. M.; Xia, J.; Brdjanovic, D.; Mbiyozo, A.-N.; Sedlak, D.; Pradeep, T.; Lall, U.; Rao, N.; Gupta, J. The Frontiers of Water and Sanitation. *Nat. Water* 2023, 1 (1), 10–18.
- (21) Williams, P.; Benton, L.; Warmerdam, J.; Sheehan, P. Comparative Risk Analysis of Six Volatile Organic Compounds in California Drinking Water. *Environ. Sci. Technol.* 2002, 36 (22), 4721–4728.
- (22) Ahuja, S. Overview: Current Status of Environmental Research on Water Contaminants. In *Contaminants in Our Water: Identification and Remediation Methods*; ACS Symposium Series, 1352; American Chemical Society, 2020; pp 1–11, DOI: 10.1021/bk-2020-1352.ch001.
- (23) Wu, L.; Qiu, X.-W.; Wang, T.; Tao, K.; Bao, L.-J.; Zeng, E. Y. Water Quality and Organic Pollution with Health Risk Assessment in China: A Short Review. *ACS ES&T Water* 2022, 2 (8), 1279–1288.
- (24) Magnuson, M. L.; Allgeier, S. C.; Koch, B.; De Leon, R.; Hunsinger, R. Responding to Water Contamination Threats. *Environ. Sci. Technol.* 2005, 39 (7), 153A–159A.
- (25) Shah, A.; Arjunan, A.; Baroutaji, A.; Zakharova, J. A Review of Physicochemical and Biological Contaminants in Drinking Water and Their Impacts on Human Health. *Water Sci. Eng.* 2023, 16 (4), 333–344.
- (26) Schwarzenbach, R. P.; Egli, T.; Hofstetter, T. B.; von Gunten, U.; Wehrli, B. Global Water Pollution and Human Health. *Annu. Rev. Environ. Resour.* 2010, 35 (1), 109–136.
- (27) Lin, L.; Yang, H.; Xu, X. Effects of Water Pollution on Human Health and Disease Heterogeneity: A Review. *Front. Environ. Sci.* 2022, 10, 880246.
- (28) Kumar, R.; Qureshi, M.; Vishwakarma, D. K.; Al-Ansari, N.; Kuriqi, A.; Elbeltagi, A.; Saraswat, A. A Review on Emerging Water Contaminants and the Application of Sustainable Removal Technologies. *Case Stud. Chem. Environ. Eng.* 2022, 6, No. 100219.
- (29) Bashir, I.; Lone, F. A.; Bhat, R. A.; Mir, S. A.; Dar, Z. A.; Dar, S. A. Concerns and Threats of Contamination on Aquatic Ecosystems. *Bioremediation and Biotechnology: Sustainable Approaches to Pollution Degradation* 2020, 1–26.
- (30) Nagar, A.; Pradeep, T. Clean Water through Nanotechnology: Needs, Gaps, and Fulfillment. *ACS Nano* 2020, 14 (6), 6420–6435.
- (31) He, C.; Liu, Z.; Wu, J.; Pan, X.; Fang, Z.; Li, J.; Bryan, B. A. Future Global Urban Water Scarcity and Potential Solutions. *Nat. Commun.* 2021, 12 (1), 1–11.
- (32) Shemer, H.; Wald, S.; Semiat, R. Challenges and Solutions for Global Water Scarcity. *Membranes (Basel)* 2023, 13 (6), 612.
- (33) Reddy, S. M. W.; McDonald, R. I.; Maas, A. S.; Rogers, A.; Girvetz, E. H.; North, J.; Molnar, J.; Finley, T.; Leathers, G.; L. DiMuro, J. Finding Solutions to Water Scarcity: Incorporating Ecosystem Service Values into Business Planning at The Dow Chemical Company's Freeport, TX Facility. *Ecosyst. Serv.* 2015, 12, 94–107.
- (34) Ahuja, S. Overview of Global Water Challenges and Solutions. In *Water Challenges and Solutions on a Global Scale*; ACS Symposium Series, 1206; American Chemical Society, 2015; p 1, DOI: 10.1021/bk-2015-1206.ch001.
- (35) Zhao, L.; Du, C.; Zhou, C.; Sun, S.; Jia, Y.; Yuan, J.; Song, G.; Zhou, X.; Zhao, Q.; Yang, S. Structurally Ordered AgNPs@C₃N₄/GO Membranes toward Solar-Driven Freshwater Generation. *ACS Sustain. Chem. Eng.* 2020, 8 (11), 4362–4370.
- (36) Kim, J. F.; Park, A.; Kim, S.-J.; Lee, P.; Cho, Y.; Park, H.; Nam, S.; Park, Y. Harnessing Clean Water from Power Plant Emissions Using Membrane Condenser Technology. *ACS Sustain. Chem. Eng.* 2018, 6 (5), 6425–6433.
- (37) Ndeketya, A.; Dundu, M. Alternative Water Sources as a Pragmatic Approach to Improving Water Security. *Resour. Conserv. Recycl. Adv.* 2022, 13, No. 200071.
- (38) Liu, X.; Beysens, D.; Bourouina, T. Water Harvesting from Air: Current Passive Approaches and Outlook. *ACS Mater. Lett.* 2022, 4 (5), 1003–1024.
- (39) Hu, Y.; Fang, Z.; Wan, X.; Ma, X.; Wang, Y.; Dong, M.; Ye, Z.; Peng, X. Ferrocene Dicarboxylic Acid Ligand-Exchanged Hollow MIL-101(Cr) Nanospheres for Solar-Driven Atmospheric Water Harvesting. *ACS Sustain. Chem. Eng.* 2022, 10 (19), 6446–6455.
- (40) Bagi, S.; Wright, A. M.; Oppenheim, J.; Dinca, M.; Román-Leshkov, Y. Accelerated Synthesis of a Ni₂Cl₂(BTDD) Metal–Organic Framework in a Continuous Flow Reactor for Atmospheric Water Capture. *ACS Sustain. Chem. Eng.* 2021, 9 (11), 3996–4003.
- (41) Wu, M.; Zhou, Y.; Aleid, S.; Tang, X.; Zhao, Y.; Li, R.; Wang, P. Recyclable and Degradable Biomass-Based Water Vapor Sorbents for Efficient Atmospheric Water Harvesting. *ACS Sustain. Chem. Eng.* 2024, 12 (3), 1255–1264.
- (42) Salehi, A. A.; Ghannadi-Maragheh, M.; Torab-Mostaedi, M.; Torkaman, R.; Asadollahzadeh, M. A Review on the Water-Energy Nexus for Drinking Water Production from Humid Air. *Renew. Sustain. Energy Rev.* 2020, 120, No. 109627.
- (43) Ahrestani, Z.; Sadeghzadeh, S.; Motejadded Emrooz, H. B. An Overview of Atmospheric Water Harvesting Methods, the Inevitable Path of the Future in Water Supply. *RSC Adv.* 2023, 13 (15), 10273–10307.
- (44) Zhou, X.; Lu, H.; Zhao, F.; Yu, G. Atmospheric Water Harvesting: A Review of Material and Structural Designs. *ACS Mater. Lett.* 2020, 2 (7), 671–684.
- (45) Feng, A.; Akther, N.; Duan, X.; Peng, S.; Onggowarsito, C.; Mao, S.; Fu, Q.; Kolev, S. D. Recent Development of Atmospheric Water Harvesting Materials: A Review. *ACS Mater. Au* 2022, 2 (5), 576–595.
- (46) Wang, B.; Zhou, X.; Guo, Z.; Liu, W. Recent Advances in Atmosphere Water Harvesting: Design Principle, Materials, Devices, and Applications. *Nano Today* 2021, 40, No. 101283.
- (47) Feng, A.; Mao, S.; Onggowarsito, C.; Naidu, G.; Li, W.; Fu, Q. Tillandsia-Inspired Composite Materials for Atmospheric Water Harvesting. *ACS Sustain. Chem. Eng.* 2023, 11 (15), 5819–5825.
- (48) Li, Z.; Tang, L.; Wang, H.; Singh, S. C.; Wei, X.; Yang, Z.; Guo, C. Nature-Inspired Surface Engineering for Efficient Atmospheric Water Harvesting. *ACS Sustain. Chem. Eng.* 2023, 11 (30), 11019–11031.
- (49) USGS. Atmosphere and the Water Cycle. 2019, <https://www.usgs.gov/special-topics/water-science-school/science/atmosphere-and-water-cycle>.
- (50) Shi, Y.; Ilic, O.; Atwater, H. A.; Greer, J. R. All-Day Fresh Water Harvesting by Microstructured Hydrogel Membranes. *Nat. Commun.* 2021, 12 (1), 2797.
- (51) Zhang, F.; Guo, Z. Bioinspired Materials for Water-Harvesting: Focusing on Microstructure Designs and the Improvement of Sustainability. *Mater. Adv.* 2020, 1 (8), 2592–2613.

(52) Zhang, Y.; Wang, T.; Wu, M.; Wei, W. Durable Superhydrophobic Surface with Hierarchical Microstructures for Efficient Water Collection. *Surf. Coat. Technol.* 2021, 419, No. 127279.

(53) Guo, Y.; Yu, G. Materials Innovation for Global Water Sustainability. *ACS Mater. Lett.* 2022, 4 (4), 713–714.

(54) Zhang, S.; Huang, J.; Chen, Z.; Lai, Y. Bioinspired Special Wettability Surfaces: From Fundamental Research to Water Harvesting Applications. *Small* 2017, 13 (3), No. 1602992.

(55) Lu, H.; Shi, W.; Guo, Y.; Guan, W.; Lei, C.; Yu, G. Materials Engineering for Atmospheric Water Harvesting: Progress and Perspectives. *Adv. Mater.* 2022, 34 (12), No. 2110079.

(56) Chen, Y.; Zheng, Y. Bioinspired Micro-/Nanostructure Fibers with a Water Collecting Property. *Nanoscale* 2014, 6 (14), 7703–7714.

(57) Zuo, Y.; Zheng, L.; Zhao, C.; Liu, H. Micro-/Nanostructured Interface for Liquid Manipulation and Its Applications. *Small* 2020, 16 (9), No. 1903849.

(58) Ras, R. H. A.; Tian, X.; Chang, B.; Timonen, J. V. I. Droplet Manipulation on Liquid-Repellent Surfaces. In *Non-wettable Surfaces: Theory, Preparation, and Applications*; Ras, R. H. A., Marmur, A., Eds.; The Royal Society of Chemistry, 2016; pp 368–384; DOI: 10.1039/9781782623953-00368.

(59) Cao, M.; Ju, J.; Li, K.; Dou, S.; Liu, K.; Jiang, L. Facile and Large-Scale Fabrication of a Cactus-Inspired Continuous Fog Collector. *Adv. Funct. Mater.* 2014, 24 (21), 3235–3240.

(60) Ghosh, R.; Baut, A.; Belleri, G.; Kappl, M.; Butt, H.-J.; Schutzius, T. M. Photocatalytically Reactive Surfaces for Simultaneous Water Harvesting and Treatment. *Nat. Sustain.* 2023, 6 (12), 1663–1672.

(61) Wang, R.; Hashimoto, K.; Fujishima, A.; Chikuni, M.; Kojima, E.; Kitamura, A.; Shimohigoshi, M.; Watanabe, T. Light-Induced Amphiphilic Surfaces. *Nature* 1997, 388, 431–432.

(62) Fujishima, A.; Honda, K. Electrochemical Photolysis of Water at a Semiconductor Electrode. *Nature* 1972, 238 (672), 37–38.

(63) Konermann, L.; Ahadi, E.; Rodriguez, A. D.; Vahidi, S. Unraveling the Mechanism of Electrospray Ionization. *Anal. Chem.* 2013, 85 (1), 2–9.

(64) Parvate, S.; Dixit, P.; Chattopadhyay, S. Superhydrophobic Surfaces: Insights from Theory and Experiment. *J. Phys. Chem. B* 2020, 124 (8), 1323–1360.

(65) Yoon, Y.; Kim, D.; Lee, J. B. Hierarchical Micro/Nano Structures for Super-Hydrophobic Surfaces and Super-Lyophobic Surface against Liquid Metal. *Micro Nano Syst. Lett.* 2014, 2 (1), 1–18.

(66) Zhan, D.; Guo, Z. Overview of the Design of Bionic Fine Hierarchical Structures for Fog Collection. *Mater. Horizons* 2023, 10 (11), 4827–4856.

(67) Gurera, D.; Bhushan, B. Passive Water Harvesting by Desert Plants and Animals: Lessons from Nature. *Philos. Trans. R. Soc. A Math. Phys. Eng. Sci.* 2020, 378 (2167), 20190444.

(68) Zhao, T.; Zhao, Y.; Jiang, L. Nano-/microstructure improved photocatalytic activities of semiconductors. *Philosophical Transactions of the Royal Society A: Mathematical, Physical and Engineering Sciences* 2013, 371 (2000), No. 20120303.

(69) Kamat, P. V. TiO₂ Nanostructures: Recent Physical Chemistry Advances. *J. Phys. Chem. C* 2012, 116 (22), 11849–11851.

(70) Pham, H. H.; Wang, L. W. Oxygen Vacancy and Hole Conduction in Amorphous TiO₂. *Phys. Chem. Chem. Phys.* 2015, 17 (1), 541–550.

(71) Yu, J. C.; Ho, W.; Lin, J.; Yip, H.; Wong, P. K. Photocatalytic Activity, Antibacterial Effect, and Photoinduced Hydrophilicity of TiO₂ Films Coated on a Stainless Steel Substrate. *Environ. Sci. Technol.* 2003, 37 (10), 2296–2301.

(72) Lorenzetti, M.; Dogša, I.; Stošicki, T.; Stopar, D.; Kalin, M.; Kobe, S.; Novak, S. The Influence of Surface Modification on Bacterial Adhesion to Titanium-Based Substrates. *ACS Appl. Mater. Interfaces* 2015, 7 (3), 1644–1651.

(73) Gonzalez Arellano, D. L.; Kolewe, K. W.; Champagne, V. K.; Kurtz, I. S.; Burnett, E. K.; Zakashansky, J. A.; Arisoy, F. D.; Briseno, A. L.; Schiffman, J. D. Gecko-Inspired Biocidal Organic Nanocrystals Initiated from a Pencil-Drawn Graphite Template. *Sci. Rep.* 2018, 8 (11618), 1–8.

Supporting Information for

From Solution to Microstructures in Minutes: Microdroplet-Derived Stand-alone TiO₂ Surfaces for Simultaneous Water Harvesting and Treatment

Keerthana Unni, Jenifer Shantha Kumar, Anirban Som, Depanjan Sarkar, and Thalappil Pradeep**

DST Unit of Nanoscience (DST UNS) and Thematic Unit of Excellence (TUE), Department of Chemistry, Indian Institute of Technology Madras, Chennai – 600036, India.

Centre of Excellence on Molecular Materials and Functions, Department of Chemistry, Indian Institute of Technology Madras, Chennai – 600036, India.

International Centre for Clean Water, Indian Institute of Technology Madras Research Park, Chennai, 600013.

Supporting Information Content

Total number of pages-10

Total number of figures-15

Total number of tables-1

Table of Contents

Sl. No	Title	Page no
Figure S1	FESEM image and EDS spectrum of TiO ₂ microstructures	S2
Figure S2	TEM image of TiO ₂ structure formed after two minutes of deposition.	S3
Figure S3	FESEM image of deposited TiO ₂ on an ITO plate	S3
Figure S4	A water droplet roll-off experiment on TiO ₂ microstructure surface	S3
Figure S5	A water droplet adhesion experiment on TiO ₂ microstructures and SS wire mesh	S4
Figure S6	FESEM images and EDS spectra of CuO and ZnO microstructures	S4
Figure S7	The contact angles of CuO-coated SS mesh and ZnO-coated mesh	S4

Figure S8	Time-dependent FESEM images of TiO ₂ microstructures	S5
Figure S9	FESEM image of TiO ₂ structures at higher deposition rate	S6
Figure S10	Optical image of a nESI tip	S6
Figure S11	Atmospheric water harvesting on TiO ₂ microstructures	S7
Figure S12	FESEM of surface immersed in water	S7
Figure S13	Optical image of TiO ₂ microstructures during the AWC experiment.	S8
Figure S14	Mass spectrum for ibuprofen degradation	S8
Figure S15	Bacterial activity	S9
Table S1	Ibuprofen degradation products and m/z of the corresponding ions	S9
Video S1	Video of water capture in TiO ₂ microstructure	AVI file is attached

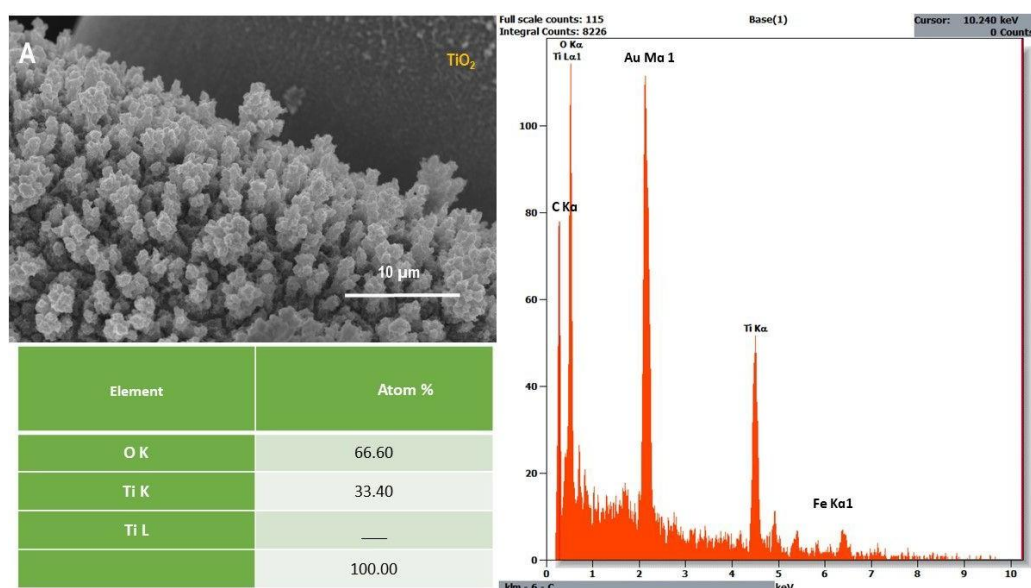


Figure S1. FESEM image and EDS spectrum of TiO₂ microstructures. The EDS-derived atomic percentages are presented in the table. The carbon peaks in the EDS spectra are attributed to carbon tape used to fix the sample on the SEM stub, with some contribution possibly from the organic counterpart of the precursors deposited during ESD. The Fe peak is attributed to the stainless-steel wire mesh.

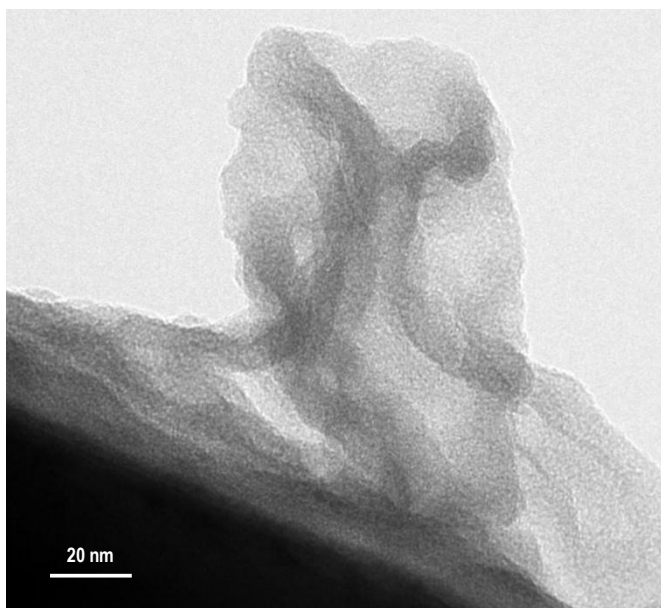


Figure S2. TEM image of TiO₂ structures formed after two minutes of deposition time.

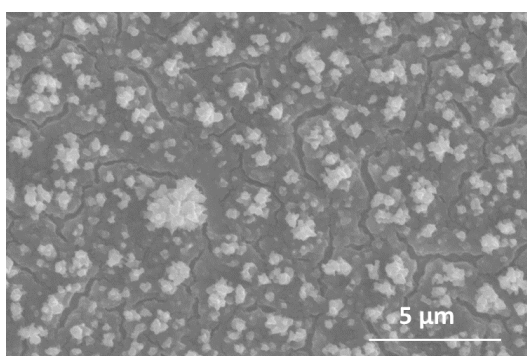


Figure S3. FESEM image of deposited TiO₂ on an ITO plate.



Figure S4. A water droplet roll-off experiment on TiO₂ microstructure surface.

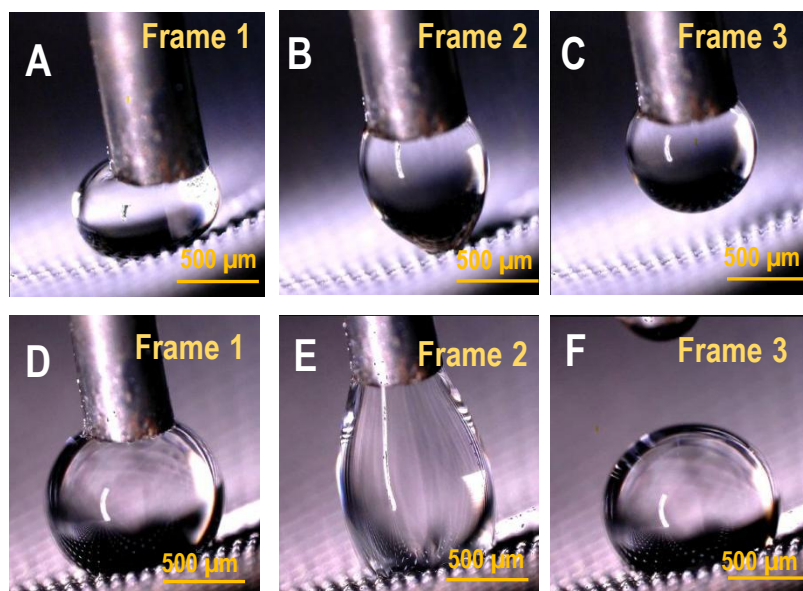


Figure S5. A water droplet adhesion experiment on (A-C) TiO₂ microstructure surface and on (D-F) SS wire mesh showing the superhydrophobicity of the TiO₂ structures.

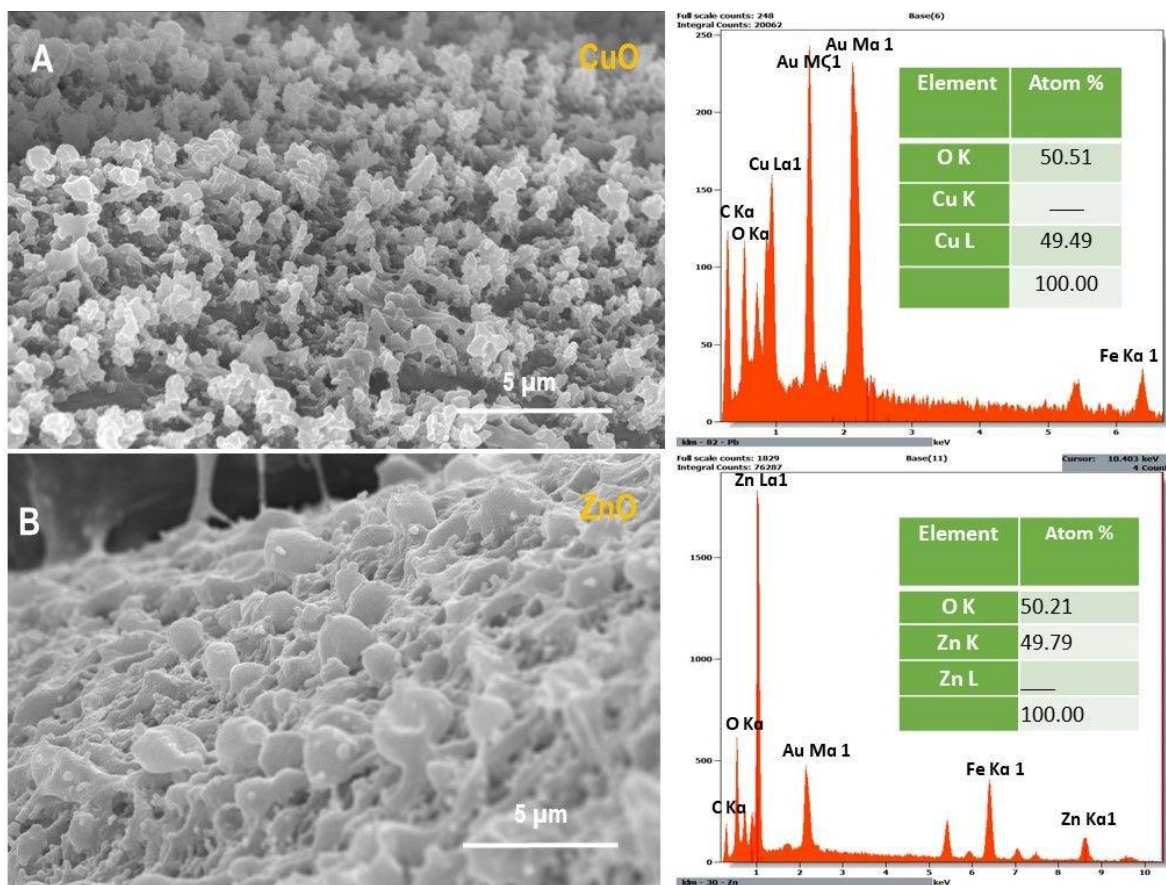


Figure S6. FESEM images and EDS spectra of A) CuO and B) ZnO microstructures. Elemental percentages are presented as insets.

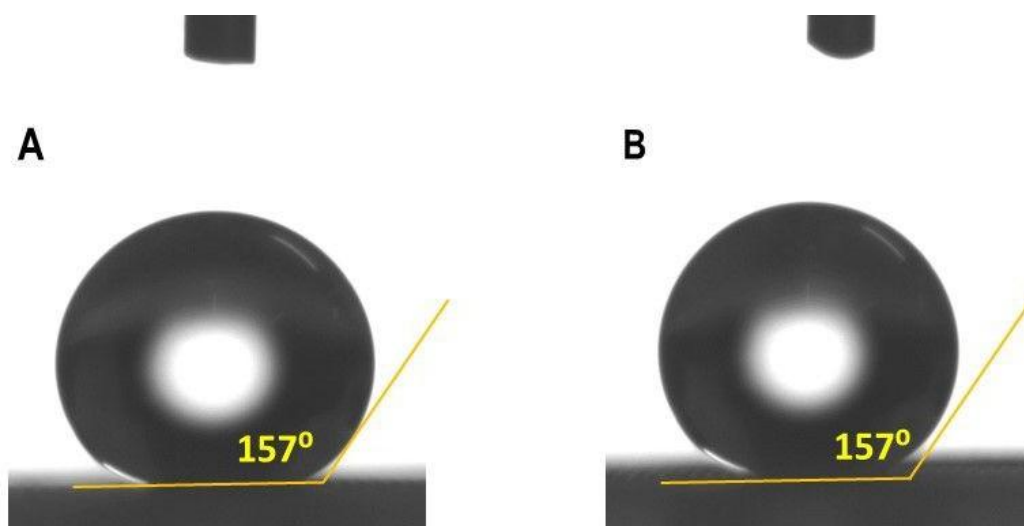


Figure S7. The contact angles of A) CuO-coated SS mesh and B) ZnO-coated SS mesh.

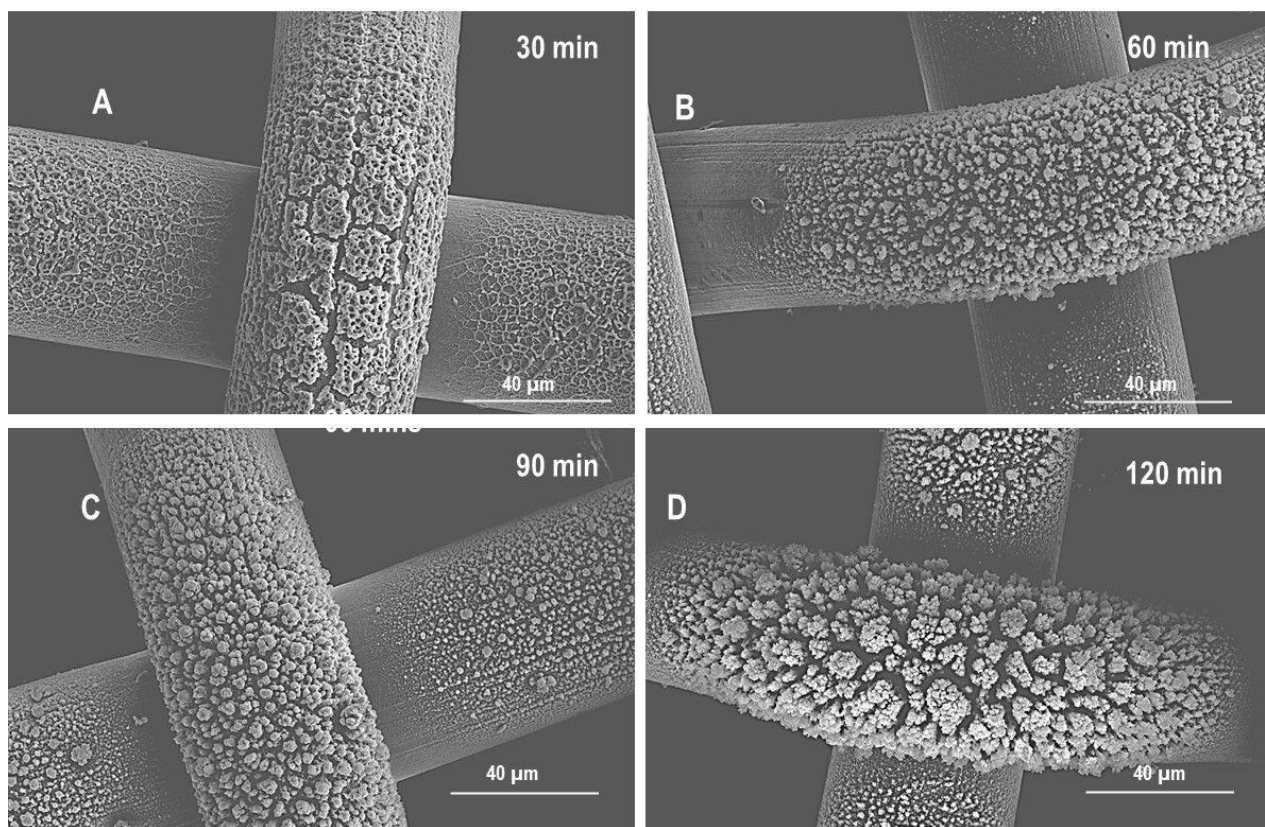


Figure S8. FESEM images of TiO₂ microstructures after ESD of A) 30 min, B) 60 min, C) 90 min, and D) 120 min at a junction of a wire-mesh.

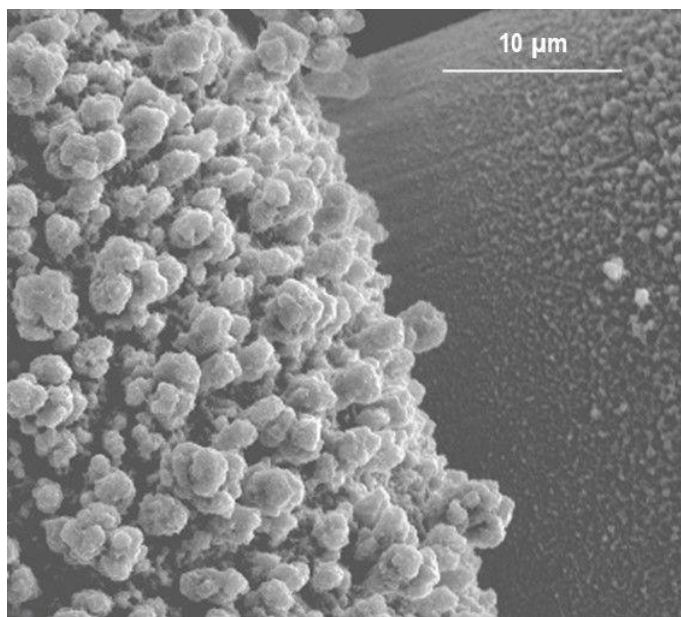


Figure S9. FESEM images of TiO₂ microstructures at higher deposition rate.

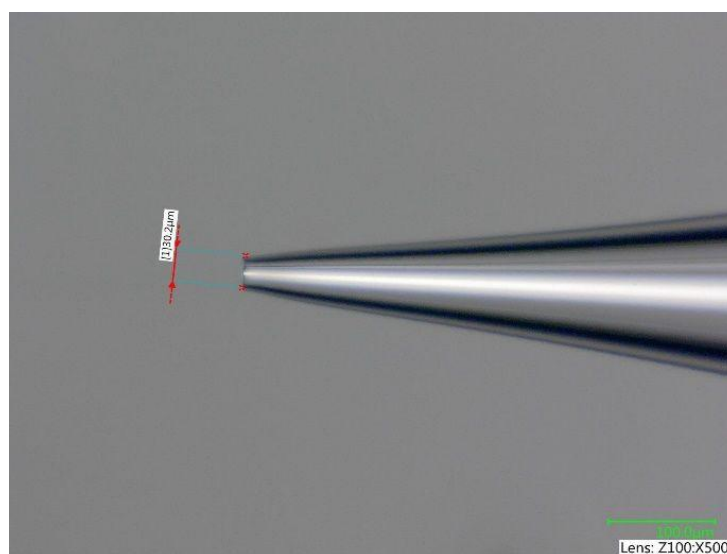


Figure S10. Optical image of a nESI tip (30 μm).

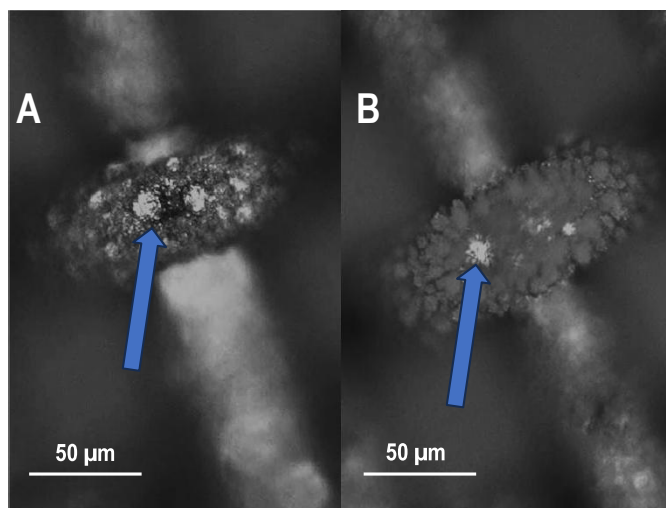


Figure S11. Atmospheric water harvesting on the TiO₂ microstructure, A) water nucleation on 1 h electro sprayed surface and B) water nucleation on 2 h electro sprayed surface.

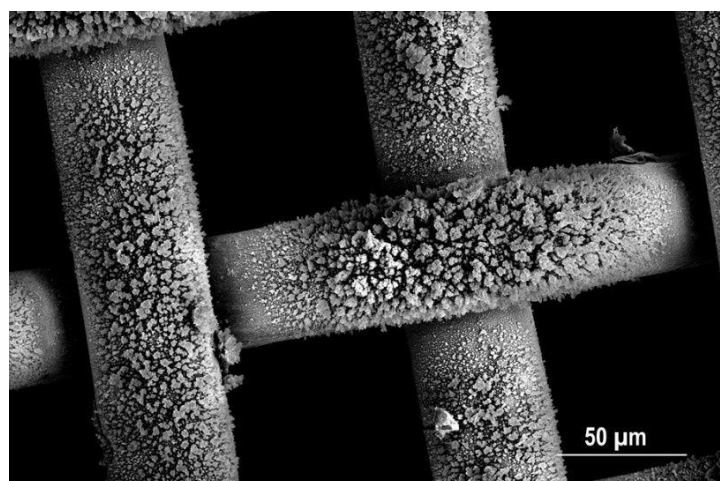


Figure S12. FESEM of the surface immersed in water for 1 h.

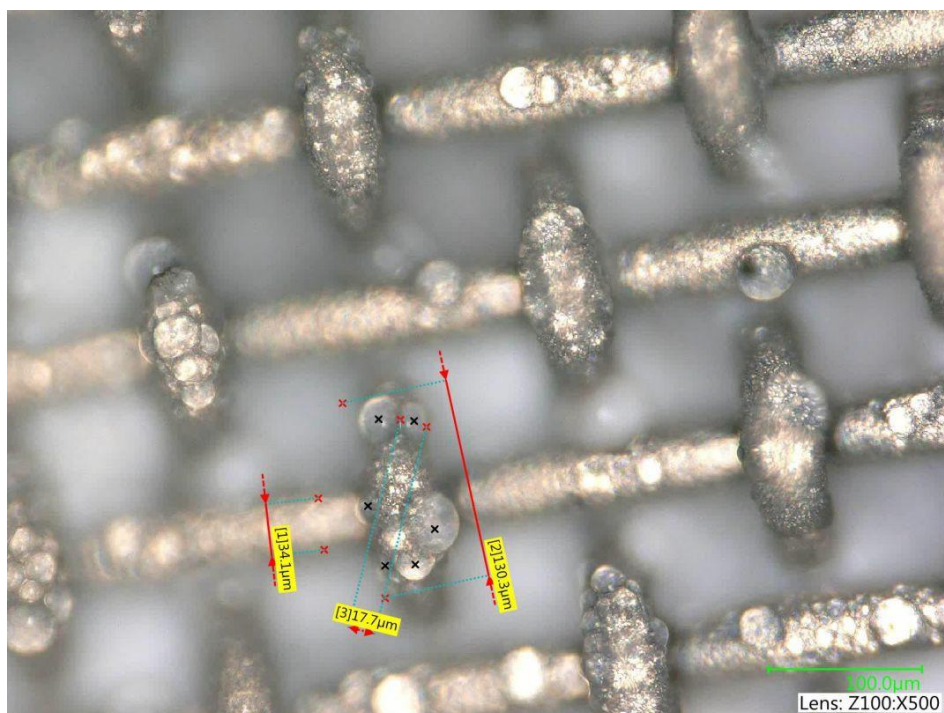


Figure S13. Optical image of TiO₂ microstructures during the AWC experiment. The length measurements indicate the area that was considered for calculating the AWC efficiency.

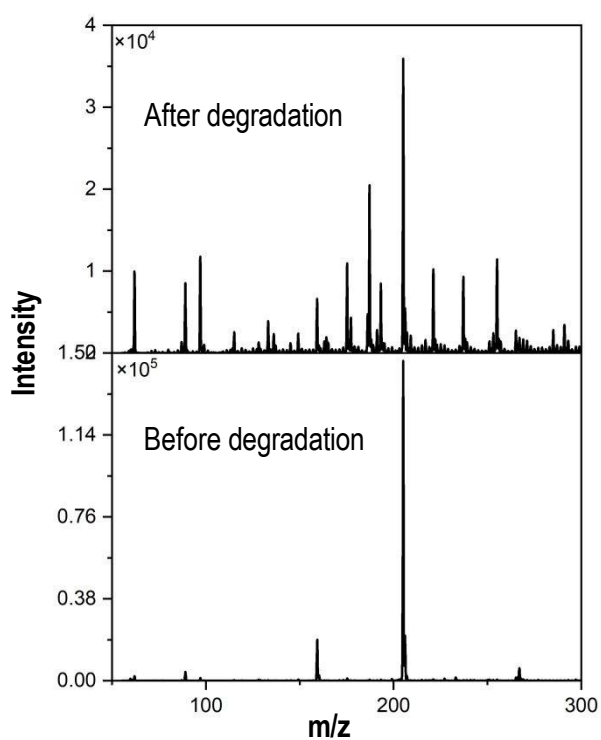


Figure S14. Mass spectrum showing photocatalytic degradation of ibuprofen on TiO₂ surface.

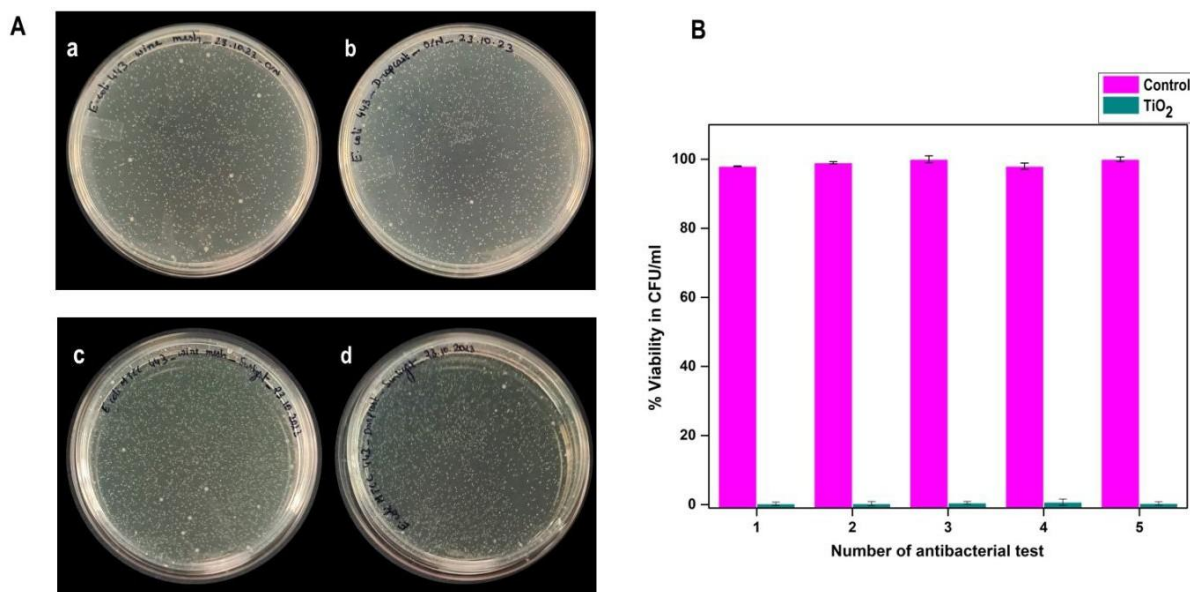
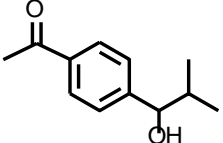
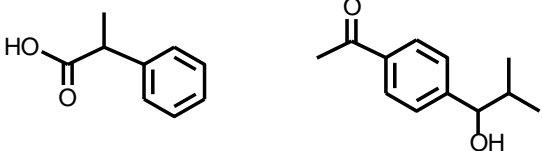
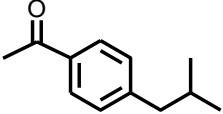
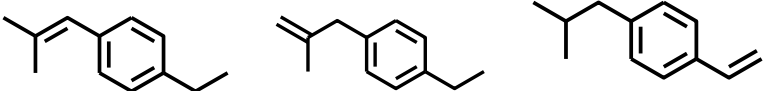
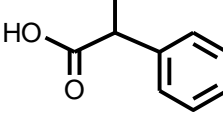
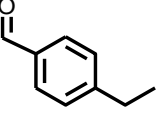


Figure S15. A) Growth of *E.coli* colonies on a) SS mesh, b) drop casted TTIP on an SS mesh, c) SS mesh after sunlight exposure, d) drop casted TTIP on SS mesh after sunlight exposure. B) Bar diagram showing the retained antibacterial activity of the TiO₂ surface after 5 repeated cycles of exposure of *E.coli* bacteria.

Table S1. Ibuprofen degradation products and m/z of the corresponding negative ions.

m/z of negative ions	Structures of degraded product molecules
255	Water adducts of <i>m/z</i> 237
237	
221	
193	

S9

191	
177	
175	
159	
149	
133	

Video S1 is available separately as an AVI file.

Cite this: *Chem. Sci.*, 2024, 15, 13741

All publication charges for this article have been paid for by the Royal Society of Chemistry

Multicolor photoluminescence of Cu₁₄ clusters modulated using surface ligands†‡

Arijit Jana,^a Subrata Duary,^a Amitabha Das,^b Amoghavarsha Ramachandra Kini,^a Swetashree Acharya,^a Jan Machacek,^c Biswarup Pathak,^b *^b Tomas Base^c *^c and Thalappil Pradeep^b *^a

Copper nanoclusters exhibit unique structural features and their molecular assembly results in diverse photoluminescence properties. In this study, we present ligand-dependent multicolor luminescence observed in a Cu₁₄ cluster, primarily protected by *ortho*-carborane-9,12-dithiol (*o*-CBDT), featuring an octahedral Cu₆ inner kernel enveloped by eight isolated copper atoms. The outer layer of the metal kernel consists of six bidentate *o*-CBDT ligands, in which carborane backbones are connected through m₃-sulphide linkages. The initially prepared Cu₁₄ cluster, solely protected by six *o*-CBDT ligands, did not crystallize in its native form. However, in the presence of *N,N*-dimethylformamide (DMF), the cluster crystallized along with six DMF molecules. Single-crystal X-ray diffraction (SCXRD) revealed that the DMF molecules were directly coordinated to six of the eight capping Cu atoms, while oxygen atoms were bound to the two remaining Cu apices in antipodal positions. Efficient tailoring of the cluster surface with DMF shifted its luminescence from yellow to bright red. Luminescence decay profiles showed fluorescence emission for these clusters, originating from the singlet states. Additionally, we synthesized microcrystalline fibers with a one-dimensional assembly of DMF-appended Cu₁₄ clusters and bidentate DPPE linkers. These fibers exhibited bright greenish-yellow phosphorescence emission, originating from the triplet state, indicating the drastic surface tailoring effect of secondary ligands. Theoretical calculations provided insights into the electronic energy levels and associated electronic transitions for these clusters. This work demonstrated dynamic tuning of the emissive excited states of copper nanoclusters through the efficient engineering of ligands.

Received 6th March 2024
Accepted 19th July 2024

DOI: 10.1039/d4sc01566e
rsc.li/chemical-science

Introduction

Atomically precise nanoclusters of transition metals, especially copper, are an emerging class of quantum materials with multicolor luminescence characteristics.^{1–3} Based on their structure-specific optical emission characteristics, these ultra-small copper clusters have great potential in the areas of bio-imaging,^{4,5} X-ray scintillation devices,^{6,7} molecular recognition,^{8,9} optoelectronic devices^{10,11} and photo-assisted catalytic

transformation reactions.¹² Small copper clusters (nuclearity below 15) usually show strong visible luminescence, whereas medium and large clusters (nuclearity greater than 15) exhibit weak emission in the near-infrared (NIR) region and some of them are non-emissive.^{13–15} Such variability in emission properties can be assigned to the size confinement effect, surface defects, and structural isomerization, as well as to the contribution of Cu d orbitals. For example, various notable reports of ultrasmall copper clusters, *i.e.*, Cu₄,¹⁶ Cu₆,¹⁷ Cu₈,¹⁸ Cu₁₂,¹⁹ Cu₁₃²⁰ and Cu₁₄,²¹ emit light with high quantum yields. There is a report of Cu₁₅ NCs with weak NIR emission characteristics in the crystalline state.²² On the other hand, large copper clusters, *i.e.*, Cu₂₀,²³ Cu₂₅,²⁴ Cu₃₆,²⁵ Cu₅₀,²⁶ Cu₅₃,²⁷ Cu₆₁²⁸ and Cu₈₁,²⁹ protected by various phosphine and thiol ligands are reported to exhibit no emission at all. The structural investigation of such clusters is essential to understand their excited state electronic relaxation behavior. We note that the family of copper clusters is less explored in comparison to gold and silver analogues due to a number of factors including slow-reducing nature, lower half-cell potential (0.52 V) of Cu^I/Cu⁰, and higher reactivity under ambient conditions.³⁰ Sometimes,

^aDST Unit of Nanoscience (DST UNS), Thematic Unit of Excellence (TUE), Department of Chemistry, Indian Institute of Technology, Madras, Chennai 600036, India. E-mail: pradeep@iitm.ac.in

^bDepartment of Chemistry, Indian Institute of Technology Indore, Indore 453552, India. E-mail: biswarup@iiti.ac.in

^cDepartment of Syntheses, Institute of Inorganic Chemistry, The Czech Academy of Sciences, 1001 Husinec – Rez, 25068, Czech Republic. E-mail: tbase@iic.cas.cz

† This article is dedicated to Professor Ashok Kumar Mishra, a valued friend and colleague, to celebrate his 65th birthday.

‡ Electronic supplementary information (ESI) available: Instrumentation and additional experimental and theoretical results. CCDC 2337402. For ESI and crystallographic data in CIF or other electronic format see DOI: <https://doi.org/10.1039/d4sc01566e>



spontaneous self-aggregation of clusters results in amorphous, insoluble aggregates with a lower tendency for crystallization. As a result, the synthesis and crystallization of new copper clusters with tunable optical properties represents an unexplored research area of atomically precise nanomaterials.

Surface ligands are essential not only for the structural stability of the clusters but also for tuning their electronic properties. Various ligands such as phosphines,³¹ selenols,³² thiols,³³ carbenes,³⁴ amidinates,³⁵ alkynyls³⁶ and mixed ligands^{37,38} have been used for stabilizing different metal clusters. Solvent molecules and secondary ligand-assisted modulation of the optical absorption and emission features have also been observed in various metal NCs.^{39,40} For example, the Ag₂₉ nanocluster shows multifold emission enhancement by the surface modification of diphosphine ligands and external solvent conjugated counter ions.^{41,42} Theoretical studies verified the surface-sensitive electronic nature of metal clusters. In this regard, using bulky carborane-thiol ligands with 3D aromaticity within their nearly icosahedral molecular framework reduces the reactivity associated with the metal core of the cluster and modulates its optical properties. A handful of copper clusters, such as Cu₄,⁴³ Cu₁₄,⁴⁴ Cu₁₆,²¹ and Cu₁₇,⁴⁵ stabilized with carborane thiols, have been synthesized and their structure-specific luminescence properties have been reported. However, secondary ligand-assisted luminescence tuning is less known for carborane-thiol protected nanoclusters. As a result, ligand-specific luminescence tailoring of carborane-thiol protected copper clusters is a growing area of research with exciting opportunities.

Cluster-assembled framework solids (CAFSs) are a new class of materials in which, clusters act as nodes for the framework. These materials are similar to well-known metal-organic frameworks (MOFs).⁴⁶ Although there are several reports of gold, silver, copper and their alloy clusters, only a few CAFS materials have been synthesized to date.^{47–49} Most of them are composed of silver clusters as nodes with multidentate pyridines, such as pyrazine,⁵⁰ 4,4'-bipyridine,⁵¹ 4,4'-azopyridine,⁵² benzene-1,3,5-tricarboxylic acid tris-pyridin-4-ylamide,⁵³ 5,10,15,20-tetra(4-pyridyl)porphyrin,⁵⁴ 1,1,2,2-tetrakis(4-(pyridin-4-yl)phenyl)-ethene,⁵⁵ etc., as linkers. The strongly coordinating nitrogen atoms of the aromatic pyridine rings promote coordination with open metal centers. Such framework solids retain the functional properties of the metal clusters and exhibit enhanced thermal, catalytic and optical stabilities compared to the parent clusters. In the present work, we have introduced a bidentate diphosphine molecule, which can be used as an alternative linker for synthesizing framework solids of copper clusters.

In this work, we have synthesized an *ortho*-carborane-9,12-dithiol (*o*-CBDT)-protected Cu₁₄ cluster using the ligand exchange reaction. This cluster (abbreviated as Cu₁₄) was crystallized with six DMF molecules (abbreviated as Cu₁₄-DMF). High-resolution mass spectrometric analyses confirmed the formation of clusters, bare as well as solvated with DMF. A comparison of the Cu₁₄ cluster with the respective DMF-solvated cluster showed a significant change in optical emission properties. In the presence of DPPE as a linker, the red emissive Cu₁₄-DMF clusters grow into microcrystalline \square bers

(abbreviated as Cu₁₄- \square ber) upon a one-dimensional framework assembly of the cluster and linkers with bright yellowish-green emission. The binding of the secondary ligands to the core-shell type Cu₁₄ cluster results either in clusters separated (zero-dimensional) or linked into a \square ber (one-dimensional framework) with characteristic tunable emission properties. This study showcases multiple optical emissive states of clusters that are precisely altered by tuning the surface ligands.

Results and discussion

Synthesis of the Cu₁₄ cluster and its surface tailoring using DMFs

The Cu₁₄ cluster was synthesized using the ligand exchange reaction of the *o*-CBDT ligand with the [Cu₁₈(DPPE)₆H₁₆] cluster, protected by DPPE and hydride ligands [DPPE = 1,2-bis(diphenylphosphino)ethane]. The details of the synthesis are shown in the Experimental section. At the end of an overnight reaction, the Cu₁₄ cluster was formed, resulting in a yellow-colored solution. The UV-vis absorption spectrum of the Cu₁₄ cluster (measured in dichloromethane (DCM) solution) showed no characteristic absorption peak. Instead, a broad absorption band, slightly below 450 nm was observed (shown in Fig. 1b). After dissolving the Cu₁₄ cluster in a DCM : DMF (1 : 1 v/v) mixture of solvents, two weak UV-vis absorption bands at 366 and 418 nm appeared. Similar absorption features were also observed by dissolving the Cu₁₄ cluster in DMF. Such variation of the absorption features suggests DMF-assisted transformation of these clusters at the molecular level. The molecular composition of clusters before and after DMF addition was analyzed using high-resolution electrospray ionization mass spectrometry (HR-ESI-MS). A Waters Synapt G2Si HDMS instrument with a nano-ESI source coupled with a time-of-flight mass analyzer was used for the measurement. The details of the MS instrumentation and sample preparation are shown in the ESI.† The positive ion mode ESI-MS spectrum of the Cu₁₄ cluster shows one major peak at *m/z* 2127.74 in the positive (1+) charge state (Fig. 1c), which was assigned to the molecular composition, [Cu₁₄(S₂C₂B₁₀H₁₀)₆]⁺. The isotopic distribution of the experimental spectrum matches well with the theoretical one (shown as an inset of Fig. 1c). To gain additional insight, tandem MS-MS fragmentation studies by varying the collision energy (CE) of the selected molecular ion (at *m/z* 2127.74) were performed (data are shown in Fig. S1†). Up to a CE of 70 eV, no fragmentation of the selected molecular ion peak was observed. Increasing the CE from 75 to 150 eV resulted in the appearance of new fragmented peaks at *m/z* 2064.06, 1461.39, 1397.49, 1286.26, 1223.30, 1112.78 and 1048.98. These peaks were assigned to [Cu₁₃(S₂C₂B₁₀H₁₀)₆]⁺, [Cu₁₀(S₂C₂B₁₀H₁₀)₄]⁺, [Cu₉(S₂C₂B₁₀H₁₀)₄]⁺, [Cu₁₀S(S₂C₂B₁₀H₁₀)₃]⁺, [Cu₉S(S₂C₂B₁₀H₁₀)₃]⁺, [Cu₁₀S₂(S₂C₂B₁₀H₁₀)₂]⁺ and [Cu₉S₂(S₂C₂B₁₀H₁₀)₂]⁺, respectively. Systematic losses of fragments consisting of Cu accompanied by mono- and dithiolate-carborane fragments further confirmed the molecular composition of the Cu₁₄ cluster. Systematic fragmentation of surface ligands and metal-thiolate motifs by applying CE was in agreement with our earlier studies of carborane thiol-protected silver and copper clusters.^{43,56,57}



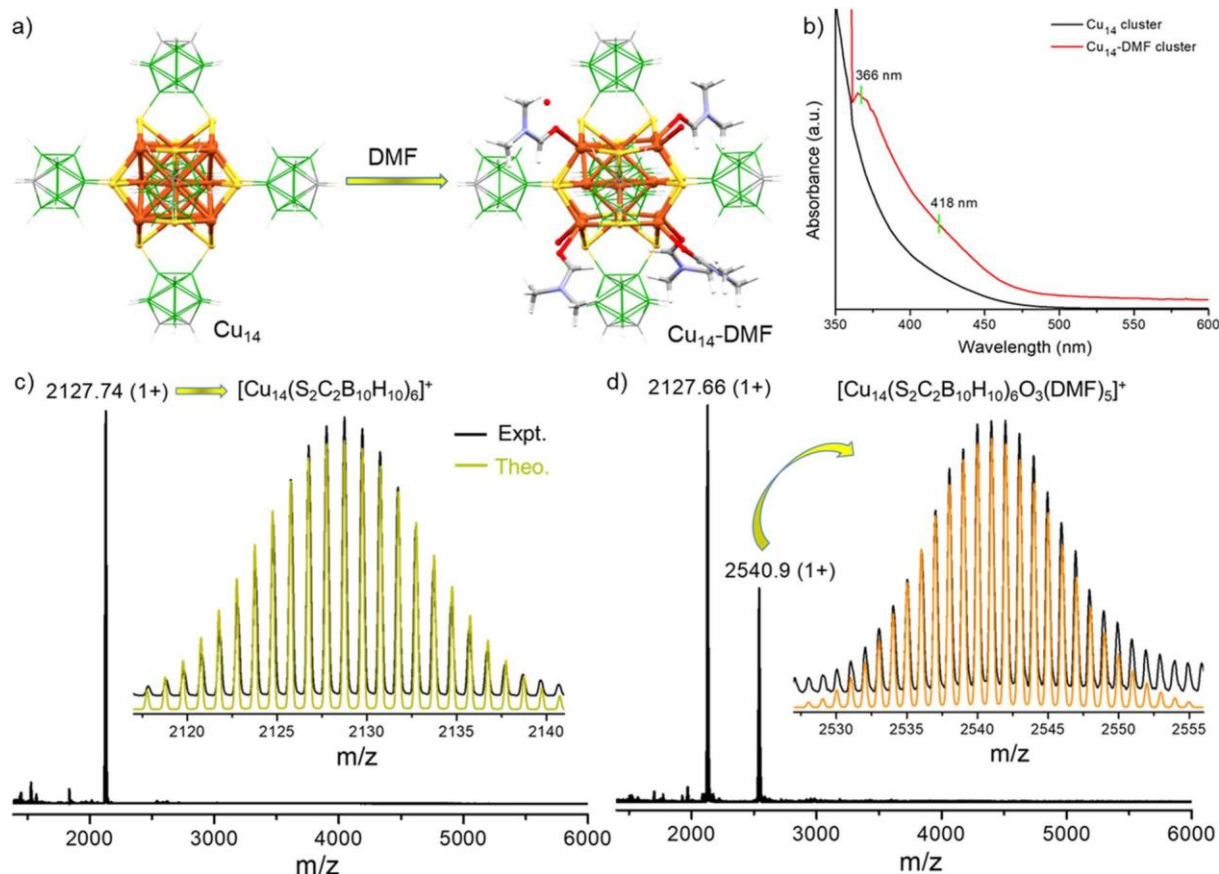


Fig. 1 (a) Schematic representation shows the attachment of DMF molecules to the outer shell of the as-synthesized Cu_{14} cluster. Color code: orange, copper; yellow, sulfur; green, boron; grey, carbon; red, oxygen; blue, nitrogen; white, hydrogen. (b) Comparative UV-vis absorption spectra of both clusters. Positive ion-mode ESI-MS spectrum of (c) as-synthesized Cu_{14} without any DMFs (cluster dissolved in DCM or acetonitrile for MS studies) and (d) with five DMFs and three oxygens (after the addition of DMF to the solution). Inset shows exact matching of the isotopic distribution of the experimental peak with the simulated pattern.

Additionally, we have investigated the mass spectrum of the Cu_{14} cluster after adding a small amount (0.5–0.75 ml) of DMF. The positive ion mode ESI-MS spectrum shows two prominent peaks at m/z 2127.66 and 2540.9 in the positive (1+) charge state (Fig. 1d). Along with the original $[\text{Cu}_{14}(\text{S}_2\text{C}_2\text{B}_{10}\text{H}_{10})_6]^+$ (m/z 2127.66) peak, the appearance of the new peak at m/z 2540.9 indicates the binding of five DMFs and three oxygen with the parent Cu_{14} cluster. The isotopic distribution of the experimental spectrum matches well with the theoretically simulated one (shown as an inset of Fig. 1d).

The collision energy dependent MS-MS fragmentation (at a CE of 15 eV) of the selected peak at m/z 2540.9 (Fig. S2†) shows the appearance of a new peak at m/z 2127.32 and this mass loss of 413.24 units corresponds to the loss of all five molecules of DMFs and three oxygen atoms from the cluster. Along with this primary peak, another secondary overlapped peak (at m/z 2143.26) appeared at a CE of 60 eV, manifesting the formation of $[\text{Cu}_{14}(\text{S}_2\text{C}_2\text{B}_{10}\text{H}_{10})_6\text{O}]^+$ species. Three minor peaks (appeared at the increased CE of 100 eV) at m/z 1921.16, 1857.36 and 1461.43 match well with the species of $[\text{Cu}_{14}(\text{S}_2\text{C}_2\text{B}_{10}\text{H}_{10})_5]^+$, $[\text{Cu}_{13}(\text{S}_2\text{C}_2\text{B}_{10}\text{H}_{10})_5]^+$ and $[\text{Cu}_{10}(\text{S}_2\text{C}_2\text{B}_{10}\text{H}_{10})_4]^+$, respectively. These three peaks indicate the

fragmentation of kernel metal atoms and surface bound *o*-CBDT ligands. Altogether, mass spectrometric studies verified the formation of DMF and oxygen bound clusters from the parent Cu_{14} cluster.

Structure of the Cu_{14} -DMF cluster

The as-prepared Cu_{14} cluster did not crystallize from its DCM solution. However, it formed yellow cube-like crystals at room temperature (25 °C) from a DCM : DMF (1 : 1, v/v) mixture. The optical microscopy images of these cuboidal crystals are shown in Fig. S3.† The surface topography of the same crystals under different magnifications (by FESEM studies) is shown in Fig. S4.† Single crystal X-ray diffraction of a suitable crystal revealed that the nanocluster crystallized in a trigonal crystal system with the space group of $R\bar{3}m$. Crystallographic data are summarized in more detail in Tables S1–S4.† The total molecular structure of the cluster, including six *o*-CBDT, two oxygen and six DMF, is shown in Fig. 2b and d. Although the as-prepared cluster did not have any DMFs, the addition of this solvent enhanced the crystallization tendency of the clusters by facilitating short contact interactions. The EDS elemental spectrum showed 6.34 atomic% of nitrogen and also proved the



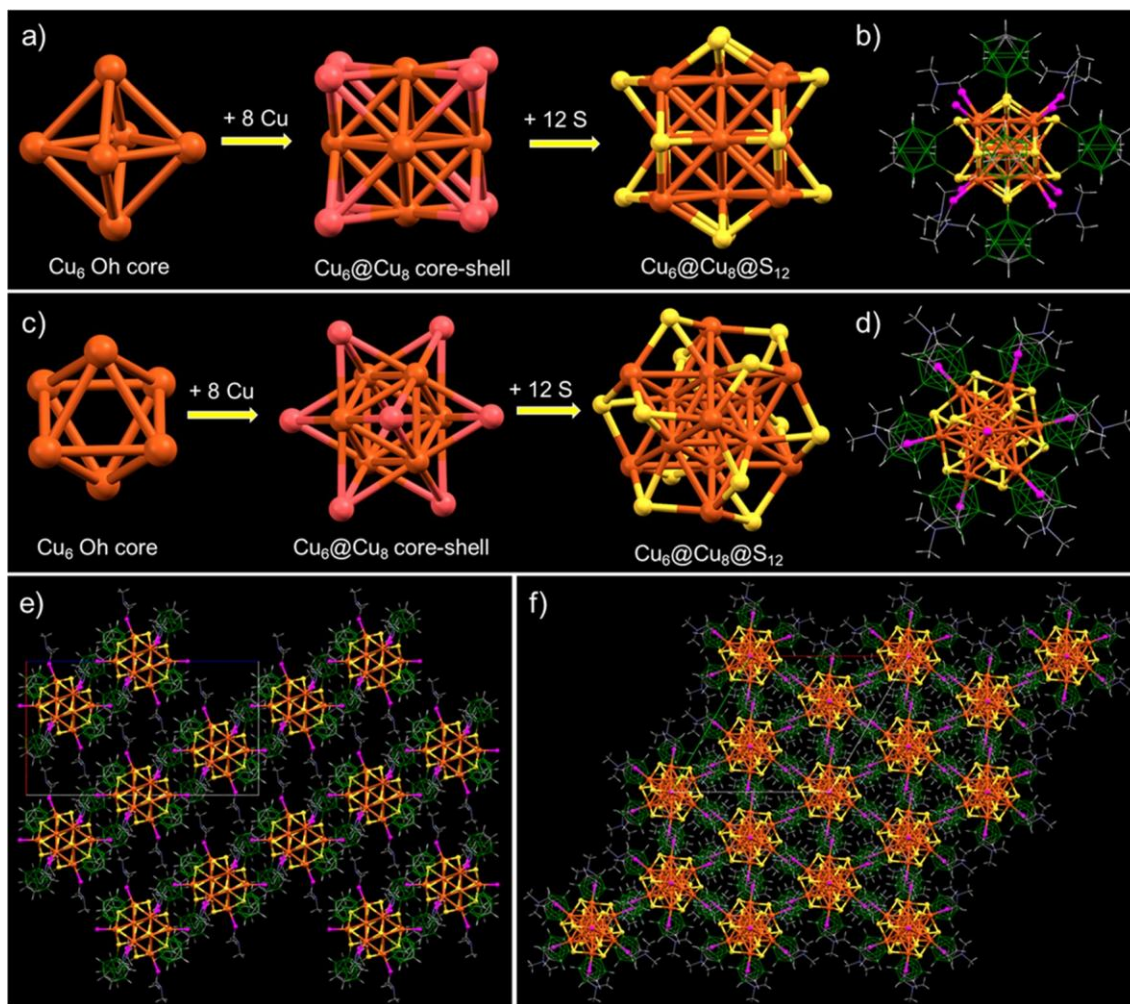


Fig. 2 (a and c) Structural anatomy of the Cu_{14} -DMF cluster with an octahedral Cu_6 inner kernel encapsulated by eight Cu atoms resulting in a $\text{Cu}_6@Cu_8$ octacapped-octahedral core-shell geometry. Copper sulphide ($\text{Cu}_{14}\text{S}_{12}$) framework structure, viewed from two different orientations. (b and d) The full molecular structure of the Cu_{14} nanocluster with six primary *ortho*-carborane-9,12-dithiol ligands and secondary DMF molecules. Supramolecular packing of the same nanocluster viewed along (e). (b and f) *c* crystallographic orientations. Color code: orange and crimson red = copper, yellow = sulfur, magenta = oxygen, green = boron, grey = carbon, blue = nitrogen, and white = hydrogen.

presence of nitrogen in the crystal (shown in Fig. S5†). It is noteworthy that no counter ions were detected in the unit cell of this cationic cluster. This absence is attributed to the lack of intense diffraction peaks at higher angles for these crystals. However, the negative ion mode ESI-MS spectrum of dissolved single crystals revealed an intense peak at m/z 126.9, indicating that iodide serves as a counter ion for the cluster (see Fig. S6†). The powder X-ray diffraction (PXRD) spectrum of Cu_{14} -DMF showed good agreement with the simulated spectrum obtained from SCXRD data, indicating the phase purity of the sample (see Fig. S7†). The primary diffraction peaks are centered at 2θ values of 6.02° , 7.99° , 9.05° , 10.88° , and 12.85° , corresponding to (101), (2-10), (003), (20-1), and (2-13) lattice planes, respectively.

To gain deeper insights into the atomic structure, the framework of the cluster was analyzed in detail. The cluster has an octahedral Cu_6 inner kernel with an average Cu–Cu distance of 2.65 \AA (shown in Fig. 2a and c). The inner kernel is further

surrounded by eight copper atoms, positioned above the trigonal faces of the inner Cu_6 octahedron. The interatomic Cu–Cu distances of these capping Cu atoms from the octahedral inner kernel Cu atoms range from 2.65 to 2.75 \AA and the distance from the centroid of the Cu_3 face of the inner octahedron to the capped Cu atoms connected to the oxygen of DMF is 2.19 \AA , while that to the Cu atoms bound to a free oxygen is 2.29 \AA (shown in Fig. S8†). This observation indicates that the two Cu atoms connected to free oxygens are further away than the other six Cu atoms capping the triangular faces of the kernel. Six bidentate *o*-CBDT ligands are connected to the outer portion of the core–shell region, where each S is m_3 bridging three Cu atoms, one from the Cu_6 inner kernel and two from the Cu_8 outer shell. The Cu–S distance is 2.31 – 2.36 \AA . A similar type of core–shell structural geometry was earlier reported for Ag_{14} clusters.^{58,59}

The complete molecular structure of the cluster (shown in Fig. 2b and d) demonstrated that six carborane ligands are



situated above the faces of the cube formed by the eight outer Cu atoms of the cluster, where the distances between the centroids of the carboranes are 12.49–12.78 Å (shown in Fig. S9†). Along with these carboranes, six DMF molecules and two oxygen atoms are connected to the eight outer copper atoms, with the DMF at the apices of a trigonal antiprism and the oxygen substituted copper atoms capping its bases (shown in Fig. 2d). The interatomic distance between the two bare oxygens is 11.37 Å (shown in Fig. S10†).

We have analyzed the solid-state packing of the Cu₁₄–DMF cluster and examined various intercluster interactions responsible for their solid-state packing. This trigonal crystal system is packed as slanted layers of clusters (along the *b* crystallographic axis), with an average interlayer spacing of 14.9 Å (shown in Fig. 2e). Alternatively, it resembles hexagonal packing along the *c* crystallographic axis, with each cluster tightly packed alongside six neighboring cluster units, as illustrated in Fig. 2f. Careful observations of the intermolecular non-van der Waals interactions reveal that all three types of major interactions, namely CH/O, CH/B and CH/HB, are centered on the methyl C–H end of the DMF molecules (Fig. 3a and b). The average bond lengths of CH/O, CH/B and CH/HB interactions are 2.81, 3.04 and 2.19 Å, respectively (Fig. 3c). Our failure to obtain crystals of Cu₁₄ without the additional DMF may be linked to the lack of opportunities for such intermolecular interactions.

Additional characterization of Cu₁₄ and Cu₁₄–DMF clusters

Infrared (IR) spectroscopy further verified the binding of the ligands present in these clusters. The IR vibrational bands at

2595 and 2612 cm⁻¹ (for Cu₁₄) and 2594 and 2616 cm⁻¹ (for Cu₁₄–DMF) were assigned to the B–H stretching vibrations and those at 3056 cm⁻¹ (both for Cu₁₄ and Cu₁₄–DMF) were assigned to the C–H vibrations of the carborane ligands (shown in Fig. S11†). The broad appearance of the vibrational bands for these clusters in comparison to the free *o*-CBDT ligand is probably due to the prominent ligand-centered intercluster interactions, as similar broadening of vibrational bands has been reported for alcoholic species dominated by strong hydrogen bonding interactions.⁶⁰ The vibrational bands at 1190, 1102, 980 and 871 cm⁻¹ (for Cu₁₄ and Cu₁₄–DMF) are assigned to various B–B–B and B–B–C bending modes, while the band at 731 cm⁻¹ (for both Cu₁₄ and Cu₁₄–DMF) is related to the carborane cage breathing mode of the ligand.

X-ray photoelectron spectroscopy (XPS) analysis was performed to understand the chemical environments of the constituent elements present in the cluster. The XPS survey spectrum shows the presence of the expected elements Cu, S, B and C in both clusters (Fig. S12†). The selected spectral regions of Cu 2p_{3/2} and 2p_{1/2} at 932.5 and 952.4 eV, respectively, pointed out the presence of mixed Cu⁰ and Cu^I oxidation states, which were observed in previous studies of copper clusters too.^{61,62} The spectral analysis of the Cu LMM region revealed a single peak at ~570 eV for both Cu₁₄ and Cu₁₄–DMF clusters, indicating a similar oxidation state for copper in both clusters (see Fig. S13†).^{63,64} Spectral fittings of the C 1s region showed one major peak at 284.8 for both clusters, and a minor peak at 286.7 was observed for the Cu₁₄–DMF cluster, due to the presence of DMF ligands. Thermogravimetric analysis (TGA) was conducted to investigate the thermal stability of these clusters. The results

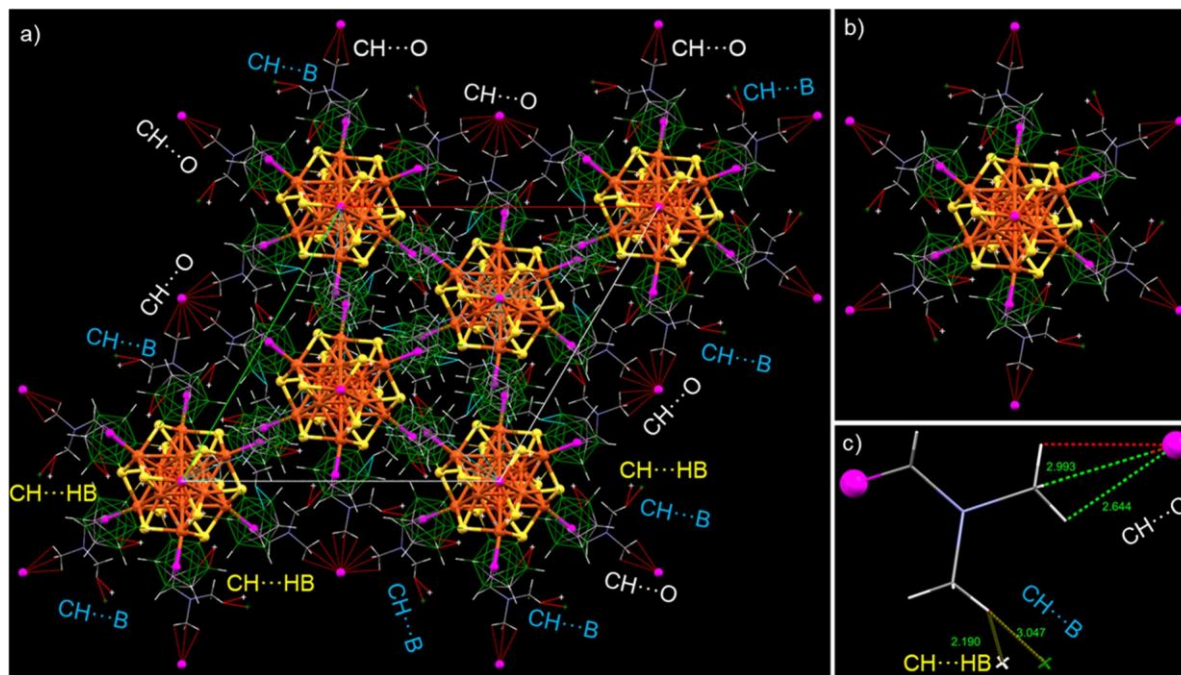


Fig. 3 (a) Different types of intermolecular non-van der Waals interactions of a unit cell of the Cu₁₄–DMF cluster. (b) Expanded view of the same interactions of a single cluster. The methyl groups of the secondary DMFs heavily interact with neighboring clusters through these interactions. (c) The CH/O, CH/B and CH/HB interactions of DMF with marked distances.



(shown in Fig. S14 and S15†) revealed a weight loss of 13.47% at 113.2 °C for Cu₁₄ and 16.10% at 119.3 °C for Cu₁₄-DMF. The mass reduction in both cases can be attributed to the detachment of *o*-CBDT ligands or their fragments from the Cu₁₄ cluster, whereas Cu₁₄-DMF exhibited additional loss of DMF molecules too. Therefore, the overall mass loss upon heating up to 400 °C for Cu₁₄-DMF (~46%) exceeds that of the Cu₁₄ cluster (~31%) for ~15%, which corresponds to approximately 6 molecules of DMF.

Luminescence modulation of Cu₁₄ by surface tailoring of DMF

We examined the photoluminescence properties of both Cu₁₄ and Cu₁₄-DMF clusters. The as-prepared Cu₁₄ cluster has yellow luminescence both in solid and solution states. However, the Cu₁₄ cluster tailored with DMF shows bright red luminescence in solution in both states (shown in the inset of Fig. 4a). Photoluminescence emission measurements show that the Cu₁₄ cluster (in DCM solution) has an emission maximum at 599 nm upon photoexcitation at 400 nm (Fig. 4a). Excitation spectra are

shown in Fig. S16.† We have observed significant emission enhancement (~10 times) of the cluster upon its solidification by keeping the emission maxima at the same wavelength, *i.e.*, at 599 nm.

The addition of DMF showed ~15-fold emission enhancement with a 50 nm red shift of the emission band from 599 to 649 nm. The Cu₁₄-DMF cluster shows 3-fold enhanced emission upon solidification, keeping the emission band at the same position. We estimated the relative quantum yield (RQY) of these clusters and found it to be approximately ~10% and ~23% for Cu₁₄ and Cu₁₄-DMF clusters, respectively, in the solid state and ~4.6% and ~15.05% in their respective solutions. The variation of luminescence upon self-aggregation, the chemical binding of secondary ligands and the effect of external stimuli such as temperature and pressure have been observed for other copper clusters before.^{65–67} Luminescence decay measurements show a fast decay lifetime of 0.33 ns for the Cu₁₄ cluster in solution, which increases to 5.54 ns upon solidification (Fig. S17a and b†). The Cu₁₄-DMF cluster exhibits an emissive lifetime of 0.3 ns in DMF solution and 3.7 ns in the solid state

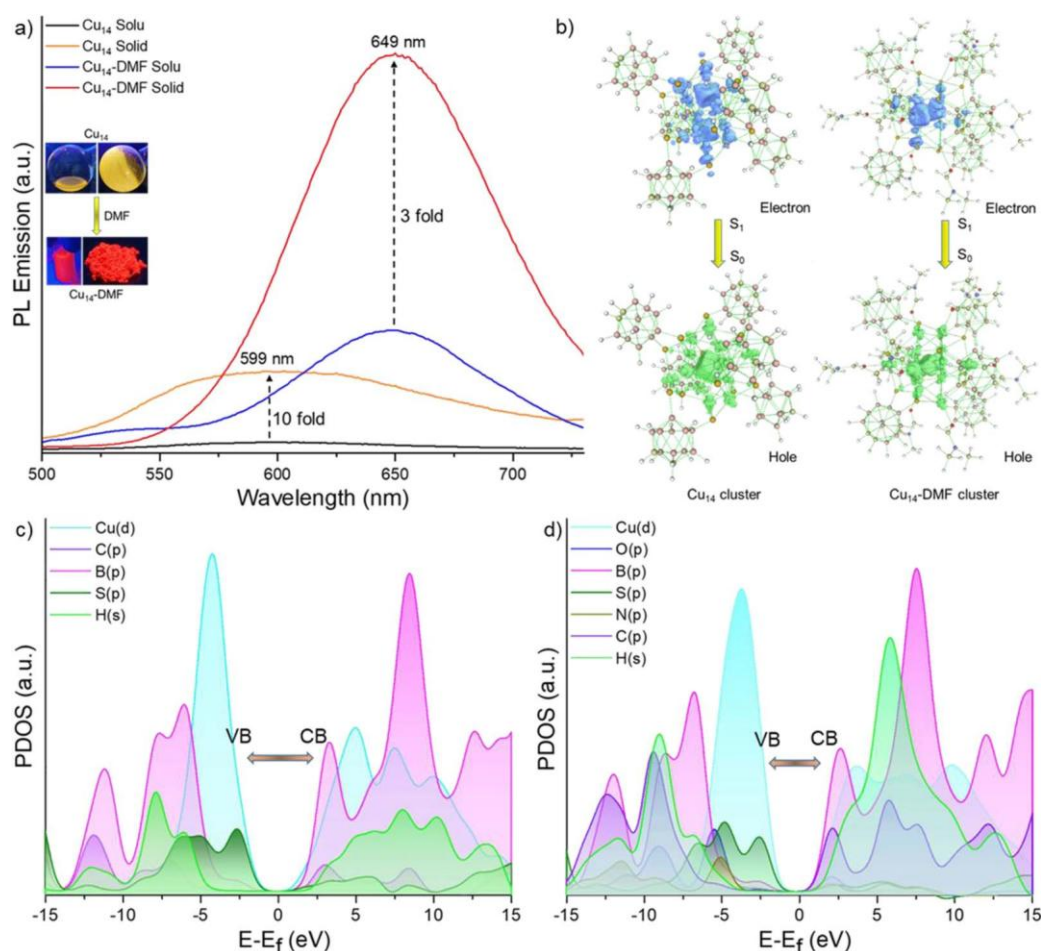


Fig. 4 (a) Photoluminescence emission spectra of Cu₁₄ and Cu₁₄-DMF clusters in solution and solid states. Surface functionalization of the Cu₁₄ nanocluster with DMF results in enhanced emission with the emission maximum red shifted from yellow to red. Inset shows the photograph of the respective clusters under 365 nm UV light. Distribution of holes and electrons in the natural transition orbitals (NTOs) for the emissive relaxation, *i.e.*, S₁/S₀ of (b) Cu₁₄ and Cu₁₄-DMF clusters. PDOS plot of the (c) Cu₁₄ and (d) Cu₁₄-DMF clusters, where VB = valence band and CB = conduction band.



(Fig. S17c and d†). These rapid excited state decay profiles suggest that the fluorescence emission for both clusters originates from their singlet excited states. Oxygen sensitivity experiments (shown in Fig. S18†) showed no significant emission quenching after oxygen bubbling, which further verified the presence of a singlet excited state for both clusters.

Theoretical understanding of electronic energy levels

Density functional theory (DFT) and time-dependent DFT calculations were conducted using the Gaussian 09 package to understand the electronic structures and associated optical absorption and emission spectra for these clusters.⁶⁸ The calculated UV-vis absorption spectrum of the Cu₁₄-DMF cluster shows two absorption bands at 320 and 417 nm, which are in good agreement with the weakly resolved experimental absorption bands (Fig. S19a†). These absorption peaks at 320 and 417 nm are attributed to the electronic transitions from HOMO-15 to LUMO+9 and HOMO to LUMO+17 levels, respectively (where the HOMO is the highest occupied molecular orbital and the LUMO is the lowest unoccupied molecular orbital). The electron density maps of these molecular orbitals show that HOMO-15 and HOMO are kernel centered and LUMO+9 and LUMO+17 are delocalized towards the peripheral ligand shell (Fig. S19b†). Therefore, electronic absorption occurred from the core to the ligand states. These excitations of electrons are from the d and p-core orbitals of Cu and S, respectively, to the p-orbitals of C and B in the ligand part. These observations are further supported by the quantitative Kohn-Sham orbital analysis (Fig. S20†). For the Cu₁₄-DMF cluster, the LUMO state exhibits a greater contribution from DMF, indicating the significant role of DMF in influencing the electronic properties of the cluster (Fig. S20†). The electron density maps of the frontier molecular orbitals, *i.e.*, the HOMO and LUMO of these clusters, are shown in Fig. S21.†

To understand the origin of the fluorescence of Cu₁₄ and Cu₁₄-DMF clusters, we have systematically studied the low-lying singlet excited states of the clusters. Initially, the excited state S₁ geometry of both clusters was optimized. On the basis of the optimized geometry of the S₁ states, the vertical emission bands for the S₁ / S₀ transition have been calculated to be at 615 nm and 647 nm with an oscillator strength of 1.1×10^{-3} and 1.3×10^{-3} for Cu₁₄ and Cu₁₄-DMF clusters, respectively. These values closely align with the experimental results. Natural transition orbital (NTO) analysis (Fig. 4b) revealed that the distribution of holes is localized in the Cu₆ inner kernel and Cu₆@Cu₈ core-shell regions and electrons are diffused towards the outer Cu₈-S₁₂ motifs and metal-ligand interfacial region of the cluster, primarily involving Cu-d orbitals for the hole and S-p orbitals for the electron. So, the electronic population of the inner copper-sulphide region of these clusters is predominantly responsible for their emissive states. Additionally, the projected density of states (PDOS) analysis (Fig. 4c and d) indicated that the valence band edges of both clusters are dominated by Cu-d and S-p orbitals. On the other hand, the conduction band edge experiences a minor contribution from the C-p orbitals of DMF in the Cu₁₄-DMF cluster. Such a contribution leads to the

stabilization of the conduction band in the Cu₁₄-DMF cluster compared to the Cu₁₄ cluster. This results in a reduced overall emissive band gap for the Cu₁₄-DMF cluster.

DPPE-assisted 1D framework assembly of the Cu₁₄-DMF cluster

Interestingly, we have observed a drastic luminescence shift from red (for Cu₁₄-DMF) to greenish-yellow by adding DPPE to the Cu₁₄-DMF cluster. The photographic images of the resulting fibers under UV light are shown in Fig. 5a. The details of the synthesis of the fibers are given in the Experimental section. These microfibers emit bright green light (maximum at 561 nm) in a solution of DCM and DMF (shown in Fig. 5b). The luminescence decay profile (Fig. S22†) shows an average lifetime of 26.2 ms for the green emitting Cu₁₄ fibers, which suggests phosphorescence emission, originating from the triplet excited state. The quenching of the emission intensity upon oxygen exposure and subsequent emission enhancement by nitrogen exposure further corroborated the presence of a triplet excited state for this framework solid (shown in Fig. S23†). Similar type PL studies by oxygen exposition were performed to confirm the existence of triplet excited states for gold and silver clusters.^{69,70} Upon evaporation of the solvents (both DCM and DMF), these green emitting microfibers turned into bright yellow emitters (emission maximum of 580 nm), with an average lifetime of 55.6 ms (Fig. 5c and S22†). So, the emissive excited state of these Cu₁₄ fibers depends on surface-adsorbed solvent molecules and this luminescence regenerates upon exposure to DCM vapors. This interconversion is reversible for several cycles of DCM exposure. Both the green and yellow emitting fibers exhibit a higher RQY (~40%) compared to the Cu₁₄ and Cu₁₄-DMF clusters. The enhanced phosphorescence emission of Cu₁₄ fibers could result from enhanced charge transfer between the linker and the cluster. The optical microscopy images (shown in Fig. 5d) of the dried fibers showed various needle-shaped fibers with a length of 65 ± 20 nm. FESEM imaging provides additional insights into the surface morphology of these microfibers with a width of 150 ± 50 nm (Fig. 5e). The powder X-ray diffraction study (shown in Fig. 5f) showed the appearance of sharp diffraction peaks, which reveal the microcrystalline nature of these fibers. A similar type of microcrystalline nature was reported for other cluster-assembled framework solids.^{47,50}

The EDS elemental mapping (shown in Fig. 5h-k) shows the presence of Cu, S, B and P in the microcrystalline solids. The IR spectrum of the Cu₁₄ fibers showed (Fig. S24†) the presence of characteristic vibrational peaks for carborane ligands and DPPE linkers. In addition to the cage breathing modes at 692 and 729 cm⁻¹ and the B-B-B and B-B-C bending modes at 1178, 1099, and 980 cm⁻¹, we have detected B-H and C-H vibrational peaks at 2588 and 3056 cm⁻¹, respectively, which confirm the presence of carboranes in the Cu₁₄ fibers. The presence of DPPE linkers in the CAFS is indicated by the appearance of a moderate vibrational peak at 484 cm⁻¹ (out-of-plane ring deformation of the Cu-DPPE framework) and an intense peak at 513 cm⁻¹ (in-plane ring deformation of the Cu-DPPE framework).⁷¹ These vibrational features are also observed in the IR spectrum of free



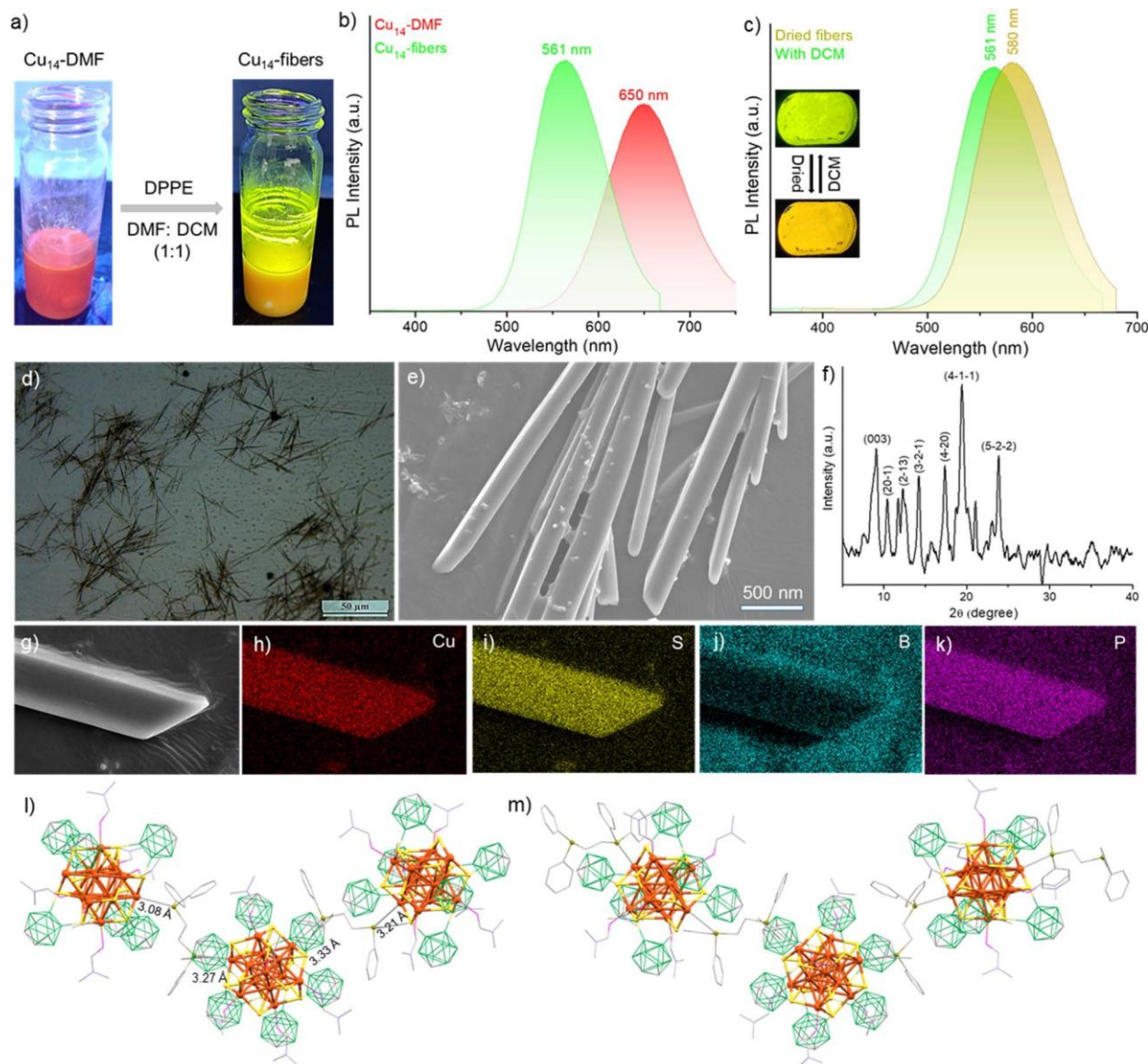


Fig. 5 (a) Photographs of the reaction bottle under a 365 nm UV lamp showing DPPE-assisted formation of Cu_{14} microfibers. (b) Comparative photoluminescence spectra before and after the formation of microfibers. (c) PL spectra of microfibers upon their interactions with DCM. (d) Optical and (e) FESEM micrographs of the as-prepared microfibers. (f) The powder X-ray diffraction pattern demonstrating the crystallinity of these fibers. (g) FESEM micrograph and (h–k) respective elemental mapping of a single fiber. (l and m) DFT optimized one-dimensional assembly of Cu_{14} -DMF clusters with DPPE linkers. P/Cu coordination distances are marked here. Hydrogens are removed for clarity.

DPPE (see Fig. S25†). Along with these peaks, the deformation of the P–CH₂ mode at 1402 cm⁻¹ and the stretching modes of P–(C₆H₅) at 1102 cm⁻¹ in the Cu_{14} -DMF fibers confirm the binding of DPPE.⁷¹ We also noted slight variations at 1434 and 1485 cm⁻¹ in the vibrational features associated with the C–H deformation and stretching modes of DPPE, attributable to its binding in the Cu_{14} fibers. XPS studies further verified the presence of DPPE linkers in these microfibers, without disturbing the electronic environments of Cu, S and B (shown in Fig. S26†). TGA measurements show enhanced thermal stability (up to ~370 °C) for the Cu_{14} fibers in comparison to the Cu_{14} -DMF cluster (~120 °C) (shown in Fig. S27†). A similar type of enhanced stability was observed for CAFSS of structurally

related Ag clusters.⁷² To verify the stability of the cluster, we have dissolved the microfibers in DMF by heating them at 60 °C for 3 h. Green emitting fibers formed a red emitting solution after heat treatment in DMF (shown in Fig. S28†). The extracted solution shows a similar bright red emission (maximum at 650 nm) with a characteristic emission of the Cu_{14} -DMF cluster.

Mass spectrometric studies further verified the presence of Cu_{14} clusters in the fibers. The ESI-MS spectrum in the positive ion mode shows three major peaks at m/z 891.32, 859.65 and 398.51 in the lower mass region (shown in Fig. S29a†). These peaks are assigned to $[\text{Cu}_4\text{S}(\text{S}_2\text{C}_2\text{B}_{10}\text{H}_{10})(\text{DPPE})]^+$, $[\text{Cu}_4(\text{S}_2\text{C}_2\text{B}_{10}\text{H}_{10})(\text{DPPE})]^+$ and $[\text{DPPE}]^+$, respectively. Along with these peaks, there are some minor peaks at m/z 3043.74, 2589.15 and



2127.83, corresponding to $[\text{Cu}_{14}(\text{S}_2\text{C}_2\text{B}_{10}\text{H}_{10})_6(\text{DMF})_6\text{O}(\text{DPPE})\text{Cu}]^+$, $[\text{Cu}_{14}(\text{S}_2\text{C}_2\text{B}_{10}\text{H}_{10})_6(\text{DPPE})\text{Cu}]^+$ and $[\text{Cu}_{14}(\text{S}_2\text{C}_2\text{B}_{10}\text{H}_{10})_6]^+$, respectively (Fig. S29b†). The ESI-MS spectrum in negative ion mode shows different monoanionic peaks at m/z 1313.87, 1052.07, 933.56, 791.11 and 653.62, corresponding to $[\text{Cu}_3\text{S}(\text{S}_2\text{C}_2\text{B}_{10}\text{H}_{10})_3(\text{DPPE})(\text{DMF})]^-$, $[\text{Cu}_2\text{S}_4(\text{DPPE})_2]^-$, $[\text{Cu}_2\text{S}_4(\text{S}_2\text{C}_2\text{B}_{10}\text{H}_{10})(\text{DPPE})(\text{DMF})]^-$, $[\text{Cu}_3\text{S}_4(\text{DPPE})(\text{DMF})]^-$ and $[\text{Cu}_2\text{S}_4(\text{DPPE})]^-$, respectively (Fig. S30†). The appearance of these fragmented peaks suggested DPPE-assisted polymerization of the cluster.

Theoretical calculations were performed to understand the favorable binding of DPPE linkers for this framework solid. We investigate two possible configurations, each entailing the substitution of either one DMF molecule or one bare oxygen atom with a DPPE molecule. Moreover, we examine four distinct arrangements involving the replacement of substituents (DMF and oxygen) with DPPE, namely: (a) two DMF molecules positioned opposite each other, (b) two DMF molecules situated nearby, (c) one DMF molecule and one bare oxygen atom and (d) two bare oxygen atoms positioned opposite each other. The structural representation of these configurations is presented in Fig. S31†. The comparative relative reaction energy changes (DE) (Fig. S32†) show that bare oxygen substitution (DE : -1.56 eV) is more favorable than DMF substitution (DE : -0.22 eV), in place of the mono-DPPE linker. In a similar fashion, the substitution of two opposite bare oxygens is found to be most feasible (DE : -3.16 eV) among other replacement configurations considered for two DPPE linkers. So, the assembly of the Cu_{14} -DMF cluster with DPPE linkers through the bare oxygen sites resulted in a one dimensional framework solid. Two copper atoms bonded with the bare oxygen are connected to the bidentate DPPE ligand through Cu-P linkages with an average distance of 3.2 \AA , resulting in this 1D CAFS. The structural representation of the 1D framework solid is shown in Fig. 51 and m.

Conclusions

In summary, we have successfully synthesized a yellow-emitting Cu_{14} cluster protected by *ortho*-carborane-9,12-dithiol ligands through the LEIST reaction of a Cu_{18} cluster. Mass spectrometric studies confirmed the presence of six carborane-thiol ligands in the shell of the synthesized Cu_{14} cluster. X-ray-suitable single crystals were grown using DMF-assisted crystallization. The structure has a $\text{Cu}_6@ \text{Cu}_8$ core-shell geometry with six carborane-thiol ligands positioned over the cubical faces of the Cu_8 outer shell of the cluster. The crystallization was facilitated by intermolecular interactions involving six DMF molecules connected to the outer Cu_8 shell. The surface modification played a crucial role in tuning the luminescence properties of the cluster, transforming its emission from yellow to red. Furthermore, we extended our study to the synthesis of one-dimensional microcrystalline fibers, utilizing the cluster as a node and DPPE as a convenient linker. These assembled superstructures exhibited luminescence tuning from red to greenish-yellow. Notably, the emission characteristics of these

fibers were further modulated upon DCM adsorption. This investigation highlights the fascinating impact of surface tailoring on the luminescence features of copper clusters through the introduction of secondary ligands. In conclusion, our work showcases the site-specific modification of primary and secondary ligands on the outer shell of the cluster, leading to the development of a novel class of atomically precise materials with tunable luminescence. We envision that multi-dentate phosphine ligands can increase the possibility of the formation of higher order cluster assembled framework solids.

Experimental section

Chemicals

Copper iodide (CuI) and 1,2-bis(diphenylphosphine)ethane (DPPE) were purchased from Sigma-Aldrich and Spectrochem Chemicals, respectively. *Ortho*-carborane-9,12-dithiol (*o*-CBDT) was synthesized by following the previous literature,⁷³ starting from *ortho*-carborane, which was purchased from Katchem s.r.o. (Czech Republic). HPLC-grade solvents such as, dichloromethane (DCM), chloroform (CHCl_3), *n*-hexane, *N,N*-dimethyl formamide (DMF), acetone, acetonitrile and methanol (99.5%) were purchased from Rankem Chemicals and Finar, India. Milli-Q water was used for cluster synthesis and purification. All the chemicals were commercially available and used as such without additional purification.

Synthesis of the $[\text{Cu}_{18}(\text{DPPE})_6\text{H}_{16}]$ nanocluster

The Cu_{18} cluster was synthesized using a modified synthetic protocol from the literature.⁷⁴ In brief, 95 mg (0.49 mM) of CuI was mixed with 120 mg (0.03 mM) of DPPE under argon and then 15 ml of acetonitrile (as received) was added to it. After 30 min of additional stirring, the as-formed white complexes were reduced by directly adding 180–185 mg of dry NaBH_4 powder. After another hour of stirring at room temperature, an orange-colored precipitate was formed, which indicated the formation of the crude product. The final product was collected as an orange solid by centrifugation and further washed three times using 5 ml of acetonitrile and methanol each in succession, to remove excess starting reagents. Finally, the solid product, Cu_{18} , was dissolved in DCM and used for further reactions. The UV-vis and ESI-MS spectra (shown in Fig. S33†) confirmed the formation of the cluster. The yield was calculated to be 70–75% relative to the copper precursor.

Synthesis of Cu_{14} and Cu_{14} -DMF nanoclusters

The Cu_{14} nanocluster was synthesized through a ligand exchange reaction starting from the polyhydrido Cu_{18} cluster. In brief, the Cu_{18} cluster (~ 35 mg) was dissolved in 7 ml of DCM at room temperature and reacted with 25 mg of *o*-CBDT ligand. After 3 hours of stirring, the resulting yellowish solution with characteristic yellow emission indicated the formation of the Cu_{14} cluster. The solvent was evaporated to dryness under reduced pressure and the solid crude product was purified by washing and decanting with methanol (3×4 ml). Finally, the product dissolved in DCM was used for further studies. The



yield of the Cu₁₄ cluster is 45–50% relative to that of Cu₁₈. After overnight size stabilization at 4 °C, the Cu₁₄ cluster was converted to the Cu₁₄–DMF cluster by adding DMF (3 ml) to the DCM (3 ml) solution of the cluster. A highly concentrated solution (~30 mg ml⁻¹) in a DCM : DMF mixture (1 : 1 v/v) was used for crystallization. After 15 days, yellowish cuboid crystals were formed.

Synthesis of Cu₁₄–DMF fibers

The Cu₁₄–DMF fibers originate from the Cu₁₄–DMF cluster. Initially, 30 mg of Cu₁₄–DMF cluster was dissolved in a solution of DMF and DCM (1 : 1, v/v). After stirring for 30 minutes, 8.5 mg of DPPE was added to the solution. Subsequently, with an additional 2–3 hours of stirring, Cu₁₄ fibers began to form within the reaction vessel. Following a further 0.5–1 hour of stirring, yellowish fibers were collected *via* centrifugation (1000 rpm for 3 minutes) and washed with DCM (2–3 times). The microcrystalline fibers were dried at 30 °C by casting them onto filter paper. The addition of excess DPPE to the as-synthesized Cu₁₄ cluster (in DCM solution) did not result in the formation of fibers. The yield of the fibers is approximately 65%.

Data availability

All data needed to evaluate the conclusions in the paper are present in the paper and/or the ESI.†

Author contributions

A. J. conceived and planned the project, with input from T. P. He conducted the synthesis of the cluster and conducted the majority of the experimental studies. S. D. assisted A. J. during the synthesis and scale-up of the clusters. A. D. conducted theoretical calculations under the guidance of B. P. A. R. K. conducted XPS and SEM studies. S. A. conducted mass spectrometric studies. J. M. and T. B. synthesized and characterized the carborane-thiol utilized in the research. The initial draft of the manuscript was written by A. J., with all authors contributing to its finalization. T. P., T. B. and B. P. supervised the project and finalized the manuscript.

Conflicts of interest

There are no conflicts to declare.

Acknowledgements

The authors acknowledge the support of the Department of Science and Technology (DST), Govt. of India and the Ministry of Education, Youth and Sports (MEYS) of Czech Republic for their financial support to the bilateral research projects, DST/INT/Czech/P-16/2020 and LTAIN19152, respectively. The authors would like to thank Dr Sudhadevi Antharjanam and Sophisticated Analytical Instrumental Facility, Indian Institute of Technology Madras (SAIF-IITM) for single crystal XRD, lifetime and thermogravimetric measurements. A. J. acknowledges

financial support from IIT Madras. T. P. acknowledges funding from the Centre of Excellence on Molecular Materials and Functions under the Institute of Eminence Scheme of IIT Madras.

References

- 1 R. Jin, C. Zeng, M. Zhou and Y. Chen, *Chem. Rev.*, 2016, 116, 10346–10413.
- 2 I. Chakraborty and T. Pradeep, *Chem. Rev.*, 2017, 117, 8208–8271.
- 3 X. Liu and D. Astruc, *Coord. Chem. Rev.*, 2018, 359, 112–126.
- 4 Y. An, Y. Ren, M. Bick, A. Dudek, E. Hong-Wang Waworuntu, J. Tang, J. Chen and B. Chang, *Biosens. Bioelectron.*, 2020, 154, 112078.
- 5 H. Ao, H. Feng, S. Pan, Z. Bao, Z. Li, J. Chen and Z. Qian, *ACS Appl. Nano Mater.*, 2018, 1, 5673–5681.
- 6 J. Qiu and X. Liu, *Light: Sci. Appl.*, 2023, 12, 12–14.
- 7 K. Kirakci, K. Fejfarov'a, J. Martin'c'ik, M. Nikl and K. Lang, *Inorg. Chem.*, 2017, 56, 4609–4614.
- 8 S. Shahsavari, S. Hadian-Ghazvini, F. H. Saboor, I. M. Oskouie, M. Hasany, A. Simchi and A. L. Rogach, *Mater. Chem. Front.*, 2019, 3, 2326–2356.
- 9 A. Jana, B. K. Spoorthi, A. S. Nair, A. Nagar, B. Pathak, T. Base and T. Pradeep, *Nanoscale*, 2023, 15, 8141–8147.
- 10 L. Ai, W. Jiang, Z. Liu, J. Liu, Y. Gao, H. Zou, Z. Wu, Z. Wang, Y. Liu, H. Zhang and B. Yang, *Nanoscale*, 2017, 9, 12618–12627.
- 11 G. Smolentsev, C. J. Milne, A. Guda, K. Haldrup, J. Szlachetko, N. Azzaroli, C. Cirelli, G. Knopp, R. Bohinc, S. Menzi, G. Pamplidis, D. Gashi, M. Beck, A. Mozzanica, D. James, C. Bacellar, G. F. Mancini, A. Tereshchenko, V. Shapovalov, W. M. Kwiatek, J. Czaplak-Masza'ak, A. Cannizzo, M. Gazzetto, M. Sander, M. Levantino, V. Kabanova, E. Rychagova, S. Ketkov, M. Olaru, J. Beckmann and M. Vogt, *Nat. Commun.*, 2020, 11, 1–9.
- 12 A. Sagadevan, A. Ghosh, P. Maity, O. F. Mohammed, O. M. Bakr and M. Rueping, *J. Am. Chem. Soc.*, 2022, 144, 12052–12061.
- 13 B. Huitorel, H. El Moll, R. Utrera-Melero, M. Cordier, A. Fargues, A. Garcia, F. Massuyeau, C. Martineau-Corcoss, F. Fayon, A. Rakhmatullin, S. Kahlal, J. Y. Saillard, T. Gacoin and S. Perruchas, *Inorg. Chem.*, 2018, 57, 4328–4339.
- 14 K. K. Chakraborty, J.-H. Liao, S. Kahlal, Y.-C. Liu, M.-H. Chiang, J.-Y. Saillard and C. W. Liu, *Angew. Chem., Int. Ed.*, 2016, 55, 14704–14708.
- 15 P. C. Ford, E. Cariati and J. Bourassa, *Chem. Rev.*, 1999, 99, 3625–3647.
- 16 B. Huitorel, H. El Moll, M. Cordier, A. Fargues, A. Garcia, F. Massuyeau, C. Martineau-Corcoss, T. Gacoin and S. Perruchas, *Inorg. Chem.*, 2017, 56, 12379–12388.
- 17 H. Wu, R. Anumula, G. N. Andrew and Z. Luo, *Nanoscale*, 2023, 15, 4137–4142.
- 18 P. P. Sun, B. L. Han, H. G. Li, C. K. Zhang, X. Xin, J. M. Dou, Z. Y. Gao and D. Sun, *Angew. Chem., Int. Ed.*, 2022, 61, 1–7.
- 19 X. Liu and K. L. Huang, *Inorg. Chem.*, 2009, 48, 8653–8655.



- 20 X. Lin, J. Tang, C. Zhu, L. Wang, Y. Yang, R. Wu, H. Fan, C. Liu and J. Huang, *Chem. Sci.*, 2023, 14, 994–1002.
- 21 J. H. Huang, L. Y. Liu, Z. Y. Wang, S. Q. Zang and T. C. W. Mak, *ACS Nano*, 2022, 16, 18789–18794.
- 22 S. Nematullov, R. W. Huang, J. Yin, A. Shkurenko, C. Dong, A. Ghosh, B. Alamer, R. Naphade, M. N. Hedhili, P. Maity, M. Eddaoudi, O. F. Mohammed and O. M. Bakr, *Small*, 2021, 17, 1–6.
- 23 A. W. Cook, Z. R. Jones, G. Wu, S. L. Scott and T. W. Hayton, *J. Am. Chem. Soc.*, 2018, 140, 394–400.
- 24 T.-A. D. Nguyen, Z. R. Jones, B. R. Goldsmith, W. R. Buratto, G. Wu, S. L. Scott and T. W. Hayton, *J. Am. Chem. Soc.*, 2015, 137, 13319–13324.
- 25 C. Dong, R. W. Huang, C. Chen, J. Chen, S. Nematullov, X. Guo, A. Ghosh, B. Alamer, M. N. Hedhili, T. T. Isimjan, Y. Han, O. F. Mohammed and O. M. Bakr, *J. Am. Chem. Soc.*, 2021, 143, 11026–11035.
- 26 C. Xu, Y. Jin, H. Fang, H. Zheng, J. C. Carozza, Y. Pan, P.-J. Wei, Z. Zhang, Z. Wei, Z. Zhou and H. Han, *J. Am. Chem. Soc.*, 2023, 145, 25673–25685.
- 27 P. Yuan, R. Chen, X. Zhang, F. Chen, J. Yan, C. Sun, D. Ou, J. Peng, S. Lin, Z. Tang, B. K. Teo, L. S. Zheng and N. Zheng, *Angew. Chem., Int. Ed.*, 2019, 58, 835–839.
- 28 A. Ghosh, R. W. Huang, B. Alamer, E. Abou-Hamad, M. N. Hedhili, O. F. Mohammed and O. M. Bakr, *ACS Mater. Lett.*, 2019, 1, 297–302.
- 29 R. W. Huang, J. Yin, C. Dong, A. Ghosh, M. J. Alhilaly, X. Dong, M. N. Hedhili, E. Abou-Hamad, B. Alamer, S. Nematullov, Y. Han, O. F. Mohammed and O. M. Bakr, *J. Am. Chem. Soc.*, 2020, 142, 8696–8705.
- 30 Z. Luo, A. W. Castleman and S. N. Khanna, *Chem. Rev.*, 2016, 116, 14456–14492.
- 31 S. F. Yuan, H. W. Luyang, Z. Lei, X. K. Wan, J. J. Li and Q. M. Wang, *Chem. Commun.*, 2021, 57, 4315–4318.
- 32 F. Ke, Y. Song, H. Li, C. Zhou, Y. Du and M. Zhu, *Dalton Trans.*, 2019, 48, 13921–13924.
- 33 Z. Wu, J. Liu, Y. Gao, H. Liu, T. Li, H. Zou, Z. Wang, K. Zhang, Y. Wang, H. Zhang and B. Yang, *J. Am. Chem. Soc.*, 2015, 137, 12906–12913.
- 34 X. H. Ma, J. Li, P. Luo, J. H. Hu, Z. Han, X. Y. Dong, G. Xie and S. Q. Zang, *Nat. Commun.*, 2023, 14, 1–11.
- 35 C. Y. Liu, S. F. Yuan, S. Wang, Z. J. Guan, D. en Jiang and Q. M. Wang, *Nat. Commun.*, 2022, 13, 1–8.
- 36 L. M. Zhang and T. C. W. Mak, *J. Am. Chem. Soc.*, 2016, 138, 2909–2912.
- 37 C. Xu, X. Y. Yi, T. K. Duan, Q. Chen and Q. F. Zhang, *Polyhedron*, 2011, 30, 2637–2643.
- 38 O. Fuhr, S. Dehnen and D. Fenske, *Chem. Soc. Rev.*, 2013, 42, 1871–1906.
- 39 W. Ishii, Y. Okayasu, Y. Kobayashi, R. Tanaka, S. Katao, Y. Nishikawa, T. Kawai and T. Nakashima, *J. Am. Chem. Soc.*, 2023, 145, 11236–11244.
- 40 Y. Zeng, S. Havenridge, M. Gharib, A. Baksi, K. L. D. M. Weerawardene, A. R. Ziefuß, C. Strelow, C. Rehbock, A. Mews, S. Barcikowski, M. M. Kappes, W. J. Parak, C. M. Aikens and I. Chakraborty, *J. Am. Chem. Soc.*, 2021, 143, 9405–9414.
- 41 E. Khatun, A. Ghosh, P. Chakraborty, P. Singh, M. Bodiuzzaman, G. Paramasivam, G. Natarajan, J. Ghosh, S. K. Pal and T. Pradeep, *Nanoscale*, 2018, 10, 20033–20042.
- 42 X. Kang, X. Wei, P. Xiang, X. Tian, Z. Zuo, F. Song, S. Wang and M. Zhu, *Chem. Sci.*, 2020, 11, 4808–4816.
- 43 A. Jana, M. Jash, W. A. Dar, J. Roy, P. Chakraborty, G. Paramasivam, S. Lebedkin, K. Kirakci, S. Manna, S. Antharjanam, J. Machacek, M. Kucerakova, S. Ghosh, K. Lang, M. M. Kappes, T. Base and T. Pradeep, *Chem. Sci.*, 2023, 14, 1613–1626.
- 44 Y. L. Li, J. Wang, P. Luo, X. H. Ma, X. Y. Dong, Z. Y. Wang, C. X. Du, S. Q. Zang and T. C. W. Mak, *Adv. Sci.*, 2019, 6, 6–11.
- 45 Y. Li, Z. Wang, X. Ma, P. Luo, C. Du and S. Zang, *Nanoscale*, 2019, 11, 5151–5157.
- 46 A. Ebina, S. Hossain, H. Horihata, S. Ozaki, S. Kato, T. Kawawaki and Y. Negishi, *Nanomaterials*, 2020, 10, 1–48.
- 47 R. W. Huang, Y. S. Wei, X. Y. Dong, X. H. Wu, C. X. Du, S. Q. Zang and T. C. W. Mak, *Nat. Chem.*, 2017, 9, 689–697.
- 48 M. J. Alhilaly, R. W. Huang, R. Naphade, B. Alamer, M. N. Hedhili, A. H. Emwas, P. Maity, J. Yin, A. Shkurenko, O. F. Mohammed, M. Eddaoudi and O. M. Bakr, *J. Am. Chem. Soc.*, 2019, 141, 9585–9592.
- 49 X. Y. Dong, H. L. Huang, J. Y. Wang, H. Y. Li and S. Q. Zang, *Chem. Mater.*, 2018, 30, 2160–2167.
- 50 W. A. Dar, A. Jana, K. S. Sugi, G. Paramasivam, M. Bodiuzzaman, E. Khatun, A. Som, A. Mahendranath, A. Chakraborty and T. Pradeep, *Chem. Mater.*, 2022, 34, 4703–4711.
- 51 X. Y. Dong, Y. Si, J. Sen Yang, C. Zhang, Z. Han, P. Luo, Z. Y. Wang, S. Q. Zang and T. C. W. Mak, *Nat. Commun.*, 2020, 11, 1–9.
- 52 A. K. Das, S. Biswas, A. Kayal, A. C. Reber, S. Bhandary, D. Chopra, J. Mitra, S. N. Khanna and S. Mandal, *Nano Lett.*, 2023, 23, 8923–8931.
- 53 R. Nakatani, S. Biswas, T. Irie, J. Sakai, D. Hirayama, T. Kawawaki, Y. Niihori, S. Das and Y. Negishi, *Nanoscale*, 2023, 15, 16299–16306.
- 54 M. Zhao, S. Huang, Q. Fu, W. Li, R. Guo, Q. Yao, F. Wang, P. Cui, C.-H. Tung and D. Sun, *Angew. Chem., Int. Ed.*, 2020, 59, 20031–20036.
- 55 X. H. Wu, P. Luo, Z. Wei, Y. Y. Li, R. W. Huang, X. Y. Dong, K. Li, S. Q. Zang and B. Z. Tang, *Adv. Sci.*, 2018, 6, 1–7.
- 56 A. Jana, M. Jash, A. K. Poonia, G. Paramasivam, M. R. Islam, P. Chakraborty, S. Antharjanam, J. Machacek, S. Ghosh, K. N. V. D. Adarsh, T. Base and T. Pradeep, *ACS Nano*, 2021, 15, 15781–15793.
- 57 A. Jana, P. M. Unnikrishnan, A. K. Poonia, J. Roy, M. Jash, G. Paramasivam, J. Machacek, K. N. V. D. Adarsh, T. Base and T. Pradeep, *Inorg. Chem.*, 2022, 61, 8593–8603.
- 58 G. Deng, B. K. Teo and N. Zheng, *J. Am. Chem. Soc.*, 2021, 143, 10214–10220.
- 59 X. Q. Liang, Y. Z. Li, Z. Wang, S. S. Zhang, Y. C. Liu, Z. Z. Cao, L. Feng, Z. Y. Gao, Q. W. Xue, C. H. Tung and D. Sun, *Nat. Commun.*, 2021, 12, 1–10.



- 60 E. Drougkas, M. Bache, X. Liang, N. von Solms and G. M. Kontogeorgis, *J. Mol. Liq.*, 2023, 391, 123279.
- 61 A. K. Das, S. Biswas, V. S. Wani, A. S. Nair, B. Pathak and S. Mandal, *Chem. Sci.*, 2022, 13, 7616–7625.
- 62 W. Wei, Y. Lu, W. Chen and S. Chen, *J. Am. Chem. Soc.*, 2011, 133, 2060–2063.
- 63 M. Shima, K. Tsutsumi, A. Tanaka, H. Onodera and M. Tanemura, *Surf. Interface Anal.*, 2018, 50, 1187–1190.
- 64 W. F. Banholzer and M. C. Burrell, *Surf. Sci.*, 1986, 176, 125–133.
- 65 Y. Shi, J. Ma, A. Feng, Z. Wang and A. R. Rogach, *Aggregate*, 2021, 2, 1–15.
- 66 S. Kolay, S. Maity, D. Bain, S. Chakraborty and A. Patra, *Nanoscale Adv.*, 2021, 3, 5570–5575.
- 67 Q. Benito, X. F. Le Goff, S. Maron, A. Fargues, A. Garcia, C. Martineau, F. Taulelle, S. Kahlal, T. Gacoin, J. P. Boilot and S. Perruchas, *J. Am. Chem. Soc.*, 2014, 136, 11311–11320.
- 68 M. J. Frisch, G. W. Trucks, H. B. Schlegel, G. E. Scuseria, M. A. Robb, J. R. Cheeseman, G. Scalmani, V. Barone, B. Mennucci, G. A. Petersson, *et al.*, *Gaussian 09, Revision B.01*, Gaussian Inc., Wallingford, CT, 2009.
- 69 M. Agrachev, W. Fei, S. Antonello, S. Bonacchi, T. Dainese, A. Zoleo, M. Ruzzi and F. Maran, *Chem. Sci.*, 2020, 11, 3427–3440.
- 70 C. Zhu, J. Xin, J. Li, H. Li, X. Kang, Y. Pei and M. Zhu, *Angew. Chem., Int. Ed.*, 2022, 61, 1–6.
- 71 A. M. F. Benial, V. Ramakrishnan and R. Murugesan, *Spectrochim. Acta, Part A*, 2002, 58, 1703–1712.
- 72 Z. Wang, M. Wang, Y. Li, P. Luo, T. Jia, R. Huang, S. Zang and T. C. W. Mak, *J. Am. Chem. Soc.*, 2018, 140, 1069–1076.
- 73 (a) J. Plešek and S. Hermanek, *Collect. Czech. Chem. Commun.*, 1981, 46, 687–692; (b) J. Plešek, Z. Janoušek and S. Hermanek, *Collect. Czech. Chem. Commun.*, 1978, 43, 1332–1338.
- 74 J. Li, H. Z. Ma, G. E. Reid, A. J. Edwards, Y. Hong, J. M. White, R. J. Mulder and R. A. J. O'Hair, *Chem.–Eur. J.*, 2018, 24, 2070–2074.



Supporting Information

Multicolor Photoluminescence of Cu₁₄ Cluster Modulated by Surface Ligands

Arijit Jana^a, Subrata Duary^a, Amitabha Das^b, Amoghavarsha Ramachandra Kini^a, Swetashree Acharya^a, Jan Machacek^c, Biswarup Pathak^{b*}, Tomas Base^{c*} and Thalappil Pradeep^{a*}

^aDST Unit of Nanoscience (DST UNS) and Thematic Unit of Excellence (TUE), Department of Chemistry, Indian Institute of Technology, Madras, Chennai – 600036, India

^bDepartment of Chemistry, Indian Institute of Technology Indore, Indore 453552, India

^cDepartment of Syntheses, Institute of Inorganic Chemistry, The Czech Academy of Sciences, 1001 Husinec – Rez, 25068, Czech Republic

* pradeep@iitm.ac.in, tbase@ic.acs.cz, biswarup@iiti.ac.in

Table of content

Sl. No	Content	Page no
	Instrumentation	2-5
Table S1	Crystal data and structure refinement for Cu ₁₄ -DMF cluster	6
Table S2	Atomic coordinates and equivalent isotropic displacement parameters for Cu ₁₄ -DMF cluster	7
Table S3	Anisotropic displacement parameters for Cu ₁₄ -DMF cluster	8
Table S4	Hydrogen coordinates and isotropic displacement parameters for Cu ₁₄ -DMF cluster	9
Fig. S1	Collision energy dependent MSMS fragmentation pattern of the selected molecular ion peak of Cu ₁₄ cluster	10
Fig. S2	Collision energy dependent MSMS fragmentation pattern of the selected molecular ion peak of Cu ₁₄ -DMF cluster	11
Fig. S3	Optical microscopic images of Cu ₁₄ -DMF crystals	12
Fig. S4	FESEM micrographs of cuboidal Cu ₁₄ -DMF crystals at different magnifications	12
Fig. S5	EDS spectral profile and elemental mapping of Cu ₁₄ -DMF crystals	13
Fig. S6	Negative ion mode ESI mass spectrum of the Cu ₁₄ -DMF crystals	13
Fig. S7	Comparative PXRD pattern of Cu ₁₄ -DMF	14
Fig. S8	Structural skeleton of the [Cu ₁₄ O ₂ (DMF) ₆] skeleton with marked interatomic distances	15
Fig. S9	Distances between the two opposite centroids of the carborane ligands of the Cu ₁₄ -DMF cluster	15
Fig. S10	Interatomic distances between two free oxygens present in the Cu ₁₄ -DMF cluster	16
Fig. S11	Comparative IR spectra of <i>ortho</i> -carborane 9,12-dithiol ligand, Cu ₁₄ and Cu ₁₄ -DMF clusters	16
Fig. S12	Comparative XPS spectra of Cu ₁₄ and Cu ₁₄ -DMF clusters	17
Fig. S13	Comparative Cu LMM Auger spectra of Cu ₁₄ and Cu ₁₄ -DMF clusters	18
Fig. S14	Thermogravimetric (TG) and differential analysis (DTA) traces of Cu ₁₄ cluster	18

Fig. S15	TG and DTA traces of Cu ₁₄ -DMF cluster	19
Fig. S16	Photoluminescence excitation spectra of Cu ₁₄ and Cu ₁₄ -DMF clusters	19
Fig. S17	Luminescence decay profile of as prepared Cu ₁₄ cluster and Cu ₁₄ -DMF cluster in solution and solid state	20
Fig. S18	PL emission spectra of Cu ₁₄ and Cu ₁₄ -DMF clusters upon oxygen exposure in their respective solution	20
Fig. S19	Comparative UV-vis absorption spectrum of Cu ₁₄ -DMF cluster shows the matching of the experimental and simulated spectrum	21
Fig. S20	Kohn-Sham electronic energy level diagram for Cu ₁₄ -DMF cluster	21
Fig. S21	Frontier molecular orbitals of Cu ₁₄ and Cu ₁₄ -DMF clusters	22
Fig. S22	Luminescence decay profiles of green and yellow emitting Cu ₁₄ -fibers at room temperature	23
Fig. S23	Oxygen sensitivity PL studies of green emitting Cu ₁₄ -fibers	23
Fig. S24	Comparative IR spectra of Cu ₁₄ -DMF cluster and Cu ₁₄ -fibers	24
Fig. S25	Comparative IR spectra of free DPPE and Cu ₁₄ -fibers	25
Fig. S26	Comparative XPS spectra of Cu ₁₄ -DMF and Cu ₁₄ -fibers	26
Fig. S27	TG and DTG analysis of Cu ₁₄ -fibers	26
Fig. S28	Photographs of the Cu ₁₄ -fibers under UV light and after its dissolution in DMF. PL emission profile of the fiber, and the extracted DMF solution	27
Fig. S29	Positive ion mode ESI-MS spectrum of Cu ₁₄ -fibers after dissolving them in DMF	27
Fig. S30	Negative ion mode ESI-MS spectrum of Cu ₁₄ -fibers after dissolving them in DMF	28
Fig. S31	Optimized structural models of most probable bindings of DPPE linkers with the Cu ₁₄ -DMF cluster	28
Fig. S32	A comparative energy profile of the probable binding of DPPE linkers at the various position of the Cu ₁₄ -DMF cluster	29
Fig. S33	Characterization of the of Cu ₁₈ nanocluster through UV-vis absorption and mass spectrometric studies	29
	References	30

Instrumentation

a) UV-vis absorption spectroscopy

UV-vis absorption spectra were measured in the wavelength range of 1100-200 nm using Perkin Elmer Lambda 365 UV-vis spectrometer, equipped with a bandpass filter of 1 nm. The scan rate of spectral acquisition is 100 nm/min.

b) Mass spectrometry

Mass spectra of the clusters were measured by Waters Synapt G2Si HDMS instrument. The instrument is equipped with a nano-electrospray ionization source, mass selected ion trap, ion mobility cells, and time of flight mass analyzer. Optimized operating conditions such as flow rate 10-15 $\mu\text{L}/\text{min}$, capillary voltage 2-3 kV, cone voltage 20 V, source offset 10 V, desolvation gas flow 400 L/min, source temperature 100 °C and desolvation temperature 150 °C were used for the measurements. Collision-induced dissociation (CID) studies were performed upon colliding the selected molecular ion with argon gas inside the trap cell of the instrument. Gradually increasing the collision energy (CE 0 to 200 for Cu_{14} and CE 0 to 100 for $\text{Cu}_{14}\text{-DMF}$) leads to the fragmentation of the species. All the measurements used low concentrations ($\sim 1 \mu\text{g}/\text{ml}$) of cluster samples.

c) Photoluminescence spectroscopy

Photoluminescence spectra were measured using Horiba Jobin Yvon Nanolog spectrometers by applying 3 nm bandpass filter having a resolution bandwidth of 5 nm. The Nanolog instrument has a 450 W Xenon-arc lamp source, double monochromator with gratings, associated reflective optics, and CCD detector. Samples dissolved in the respective solvents were placed inside the 1 cm quartz cuvette to measure the spectrum.

Calculation of the relative quantum yield

We used our previously synthesized $\text{Cu}_4\text{-ICBT}$ cluster (which has an emission maximum at 595 nm with an absolute quantum yield (QY) of 18% at room temperature) as a standard.¹ The relative quantum yield (RQY) of these Cu_{14} clusters was calculated using the following equation.

$$\text{RQY-sample} = \text{QY-std} * \text{Exc.-std} * \text{Area (PL-sample)} / \text{Exc.-sample} * \text{Area (PL-std)}$$

$$\text{RQY Cu}_{14}\text{-solid} = 10.04 \pm 2.1 \% ; \text{RQY Cu}_{14}\text{-DMF solid} = 23.14 \pm 1.5 \%$$

$$\text{RQY Cu}_{14}\text{-solution} = 4.6 \pm 1.2 \% ; \text{RQY Cu}_{14}\text{-DMF solution} = 15.05 \pm 2.0 \%$$

$$\text{RQY Cu}_{14}\text{-fiber (green)} = 39.23 \pm 1.3 \% ; \text{RQY Cu}_{14}\text{-fiber (yellow)} = 41.71 \pm 1.1 \%$$

d) Optical microscopy

Optical microscopic images in transmission mode were collected using a LEICA optical microscope equipped with LAS V4.8 software. Polarization of the crystals were checked using an optical polarizer.

e) Scanning electron microscope

Scanning electron microscopic (SEM) images are recorded using a Verios G4 UC, Thermo Scientific field emission scanning electron microscope (FESEM). After transferring the sample on the carbon tape, gold sputtering was performed to increase the conductivity of the sample. All the FESEM images were collected in high vacuum at an operating voltage of 10-15 kV. Energy dispersive analysis of X-ray (EDAX) was performed using the same instrument.

f) Infrared spectroscopy

FT-IR spectra were measured in the transmission mode using a JASCO-4100 FT-IR spectrometer after preparing potassium bromide (KBr) pellets of the respective samples.

g) X-ray photoelectron spectroscopy

X-ray photoelectron spectroscopy (XPS) was performed using an Omicron Nanotechnology ESCA probe TPD spectrometer, equipped with polychromatic dual Mg K α ($h\nu = 1253.6$ eV) and Al K α ($h\nu = 1486.6$ eV) X-ray source. Clusters were drop casted onto the XPS grid for the measurements. Binding energy of the spectral regions of different elements were calibrated with respect to C 1s (285.0 eV).

h) Thermogravimetric analysis

Thermogravimetric measurements in the temperature range of 25 to 800 °C were measured using a NETZSCH STA 449 F3 Jupiter instrument equipped with Proteus-6.1.0 software. About 3-4 mg of crystalline sample was loaded in an alumina crucible for the measurement. Nitrogen and argon were used as protective environments. Thermal flow rate of the measurement was 10 °C/min.

i) TCSPC measurement

Time resolved PL lifetime measurements were performed using Horiba DeltaFlex time-correlated single photon count (TCSPC) spectrometer equipped with Horiba Delta diode 405 nm laser. Resulted emissive photons were collected using Horiba PPD-850 detector. The triexponential fittings of the decay curve was performed by deconvolution procedure of DAS6 (v. 6.8, Horiba Jobin Yvon) software.

j) Single crystal X-ray diffraction

Single crystal X-ray diffraction (SC-XRD) data collection was performed with Bruker D8 VENTURE single crystal X-ray diffractometer equipped with monochromatic Mo K α ($\lambda =$

0.71073 Å) or Cu K α ($\lambda = 1.54178$ Å) radiations and PHOTON 100 CMOS detector. The data collection was performed at 200-296 K based on the requirement of the specific crystals. The automatic cell determination routine, with 24 frames at two different orientations of the detector was employed to collect reflections for unit cell determination. Further, intensity data for structure determination were collected through an optimized strategy which gave an average 4-fold redundancy. The program APEX3-S SAINT (Bruker, 2016) was used for integrating the frames, followed by a multi-scan absorption correction using the program SADABS (Bruker, 2016). The structure was solved by SHELXT-2014 (Sheldrick, 2014) and refined by full-matrix least squares techniques using SHELXL-2018, (Sheldrick, 2018) software package. Hydrogens on all carbon and boron atoms were fixed at calculated positions and refined by rigid body constrains with C-H or B-H = 1.10 Å. Sometimes different restraints (DFIX, SIMU, ISOR, DELU, etc.) were applied to their bond distances and thermal parameters (U_{ij}) values during refinement to maintain sensible molecular geometry as well as reasonable anisotropic displacement parameter (ADP) values. Moreover, FLAT restraint was needed to be applied for atoms in the phenyl ring to lie in a common plane.

k) Powder X-ray diffraction

Powder XRD measurements were performed using a D8 Advance Bruker, using Cu K α as the X-ray source (25 kV). Thin samples of clusters were placed on a clean glass slide for measurements.

l) Computational details

Molecular level Density Functional Theory (DFT) calculations were conducted using the Gaussian 09 D.01 program.² The Becke's three-parameter hybrid exchange functional and Lee-Yang-Parr's (B3LYP) correlation functional were implemented in conjunction with the Pople's 6-31G* basis set for non-metal elements and LANL2DZ-ECP (effective core potential) for Cu atoms.³⁻⁶ For the TD-DFT calculations, 500 singlet-to-singlet excitation energies were considered. Structural optimization was performed for the S₀ and S₁ states of both the clusters. The wavefunction for the hole and electron pair distribution analysis of clusters were calculated using the UB3LYP functional. The Kohn-Sham orbital analysis and hole and electron pair distribution analysis were performed using Multiwfn.⁷

Table S1. Crystal data and structure refinement for Cu₁₄-DMF cluster

Identification code	Arijit-Cu ₁₄	
Empirical formula	C ₃₀ H ₁₀₂ B ₆₀ Cu ₁₄ N ₆ O ₈ S ₁₂	
Formula weight	2598.05	
Temperature	297(2) K	
Wavelength	0.71073 Å	
Crystal system	Trigonal	
Space group	R -3:H	
Unit cell dimensions	a = 19.5323(4) Å	α = 90°
	b = 19.5323(4) Å	β = 90°
	c = 29.2601(6) Å	γ = 120°
Volume	9667.5(4) Å ³	
Z	3	
Density (calculated)	1.339 mg/m ³	
Absorption coefficient	2.485 mm ⁻¹	
F(000)	3858	
Crystal size	0.260 x 0.250 x 0.200 mm ³	
Theta range for data collection	3.262 to 25.000°	
Index ranges	-23 ≤ h ≤ 23, -23 ≤ k ≤ 23, -34 ≤ l ≤ 34	
Reflections collected	48536	
Independent reflections	3786 [R(int) = 0.1415]	
Completeness to theta = 25.000°	99.6 %	
Absorption correction	Semi-empirical from equivalents	
Max. and min. transmission	0.4708 and 0.1730	
Refinement method	Full-matrix least-squares on F ²	
Data / restraints / parameters	3786 / 219 / 242	
Goodness-of-fit on F ²	1.040	
Final R indices [I > 2σ(I)]	R1 = 0.0560, wR2 = 0.1588	
R indices (all data)	R1 = 0.0850, wR2 = 0.1835	
Extinction coefficient	n/a	
Largest diff. peak and hole	1.028 and -0.657 e.Å ⁻³	

Table S2. Atomic coordinates ($\times 10^4$) and equivalent isotropic displacement parameters ($\text{\AA}^2 \times 10^3$) for Cu_{14} -DMF cluster. $U(\text{eq})$ is defined as one third of the trace of the orthogonalized U^{ij} tensor.

	x	y	z	$U(\text{eq})$
Cu(1)	4841(1)	2431(1)	7961(1)	51(1)
Cu(2)	6229(1)	3797(1)	7959(1)	43(1)
Cu(3)	6667	3333	7174(1)	57(1)
O(1)	6667	3333	6390(4)	133(4)
O(2)	3542(14)	1600(20)	7655(14)	276(10)
N(1)	2367(17)	1460(20)	7526(14)	237(9)
C(3)	2798(19)	1110(20)	7738(17)	261(9)
C(4)	2530(30)	2200(20)	7743(17)	272(16)
C(5)	1512(19)	900(30)	7466(17)	241(15)
N(1')	2437(15)	1279(19)	7420(11)	230(8)
O(2')	3547(12)	2080(20)	7701(11)	298(10)
C(3')	2807(16)	1860(20)	7802(11)	250(9)
C(4')	3025(19)	1460(20)	7066(10)	234(12)
C(5')	1653(15)	1030(20)	7309(12)	233(12)
C(1)	5050(4)	5584(4)	7002(2)	66(2)
B(3)	5077(4)	5351(4)	7568(3)	59(2)
S(1)	5424(1)	3206(1)	7321(1)	45(1)
S(2)	6361(1)	5057(1)	8073(1)	44(1)
B(10)	5290(4)	4078(4)	7216(2)	48(2)
B(7)	4667(4)	4300(4)	7568(3)	51(2)
B(8)	5731(4)	4949(4)	7567(2)	47(2)
B(2)	5946(5)	5784(4)	7209(3)	59(2)
B(9)	6085(4)	5003(4)	6996(2)	53(2)
B(1)	5645(5)	5418(5)	6641(3)	73(2)
C(2)	4637(4)	4782(4)	6688(2)	67(2)
B(4)	4253(5)	4731(5)	7216(3)	73(2)
B(6)	4374(4)	3949(5)	6997(3)	58(2)
B(5)	5243(5)	4385(5)	6644(3)	58(2)

Table S3. Anisotropic displacement parameters ($\text{\AA}^2 \times 10^3$) for Cu₁₄-DMF cluster. The anisotropic displacement factor exponent takes the form: $-2\pi^2[h^2a^{*2}U^{11} + \dots + 2hka^*b^*U^{12}]$

	U ¹¹	U ²²	U ³³	U ²³	U ¹³	U ¹²
Cu(1)	51(1)	53(1)	51(1)	1(1)	2(1)	27(1)
Cu(2)	46(1)	43(1)	44(1)	-2(1)	-5(1)	23(1)
Cu(3)	54(1)	54(1)	63(1)	0	0	27(1)
O(1)	153(7)	153(7)	93(8)	0	0	76(3)
O(2)	279(12)	253(13)	278(12)	-26(11)	-20(11)	121(10)
N(1)	246(12)	237(12)	241(12)	-4(10)	-48(10)	130(10)
C(3)	266(12)	253(12)	266(12)	-15(10)	-21(10)	131(9)
C(4)	280(20)	260(20)	260(20)	13(19)	-44(19)	114(18)
C(5)	270(20)	220(20)	170(20)	3(18)	-114(17)	72(17)
N(1')	242(11)	236(11)	239(12)	-9(10)	-46(10)	140(9)
O(2')	296(13)	278(13)	290(12)	-10(11)	-23(11)	122(10)
C(3')	255(11)	247(12)	260(11)	-10(10)	-27(10)	134(9)
C(4')	255(19)	221(18)	250(20)	4(17)	-47(17)	137(15)
C(5')	279(19)	178(17)	160(18)	4(15)	-145(15)	53(15)
C(1)	72(4)	65(4)	73(5)	9(4)	-13(4)	41(4)
B(3)	61(4)	55(4)	67(5)	2(4)	-6(4)	34(4)
S(1)	47(1)	44(1)	43(1)	-2(1)	-3(1)	23(1)
S(2)	45(1)	43(1)	43(1)	0(1)	-1(1)	22(1)
B(10)	45(4)	46(4)	51(4)	3(3)	-2(3)	22(3)
B(7)	48(4)	53(4)	54(4)	0(3)	-6(3)	27(3)
B(8)	51(4)	45(4)	49(4)	3(3)	-4(3)	27(3)
B(2)	58(4)	52(4)	63(5)	8(4)	-7(4)	25(4)
B(9)	55(4)	49(4)	53(4)	10(3)	-3(3)	24(3)
B(1)	82(6)	69(5)	65(5)	17(4)	-3(4)	36(5)
C(2)	73(4)	66(4)	64(4)	5(3)	-15(4)	37(4)
B(4)	66(5)	84(6)	85(6)	3(5)	-12(4)	49(5)
B(6)	52(4)	55(4)	65(5)	4(4)	-9(4)	26(4)
B(5)	65(5)	62(5)	48(4)	3(3)	-8(3)	33(4)

Table S4. Hydrogen coordinates ($\times 10^4$) and isotropic displacement parameters ($\text{\AA}^2 \times 10^3$) for the Cu_{14} -DMF cluster.

	x	y	z	U(eq)
H(3)	2586	637	7900	313
H(4A)	2235	2405	7591	408
H(4B)	2381	2108	8059	408
H(4C)	3086	2577	7720	408
H(5A)	1272	1177	7325	361
H(5B)	1435	472	7275	361
H(5C)	1272	706	7759	361
H(3')	2588	2008	8035	300
H(4'1)	3528	1617	7206	350
H(4'2)	2870	994	6883	350
H(4'3)	3064	1876	6877	350
H(5'1)	1353	941	7585	349
H(5'2)	1630	1430	7130	349
H(5'3)	1435	548	7137	349
H(1)	4968	6089	6924	80
H(2)	5021	5670	7862	70
H(2A)	4350	3937	7866	62
H(4)	6443	6381	7275	71
H(5)	6678	5093	6928	64
H(6)	5943	5774	6337	87
H(7)	4263	4733	6394	80
H(8)	3665	4656	7282	88
H(9)	3866	3362	6921	69
H(10)	5291	4077	6341	69

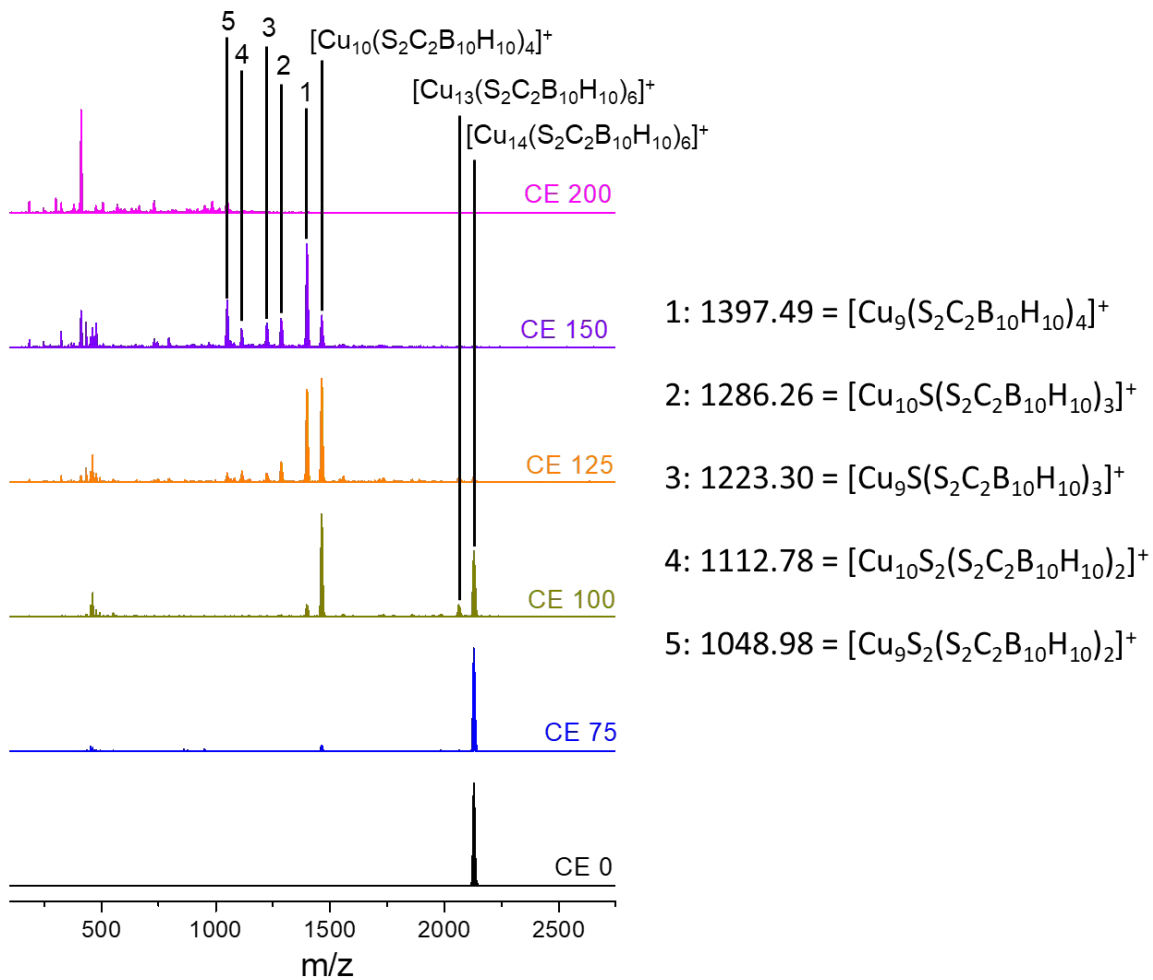


Fig. S1 Collision energy dependent MSMS fragmentation patterns of the selected molecular ion peak (at m/z 2127.74) of the Cu_{14} cluster. Losses of metal kernels and surface ligands from the parent cluster were observed at higher CE.

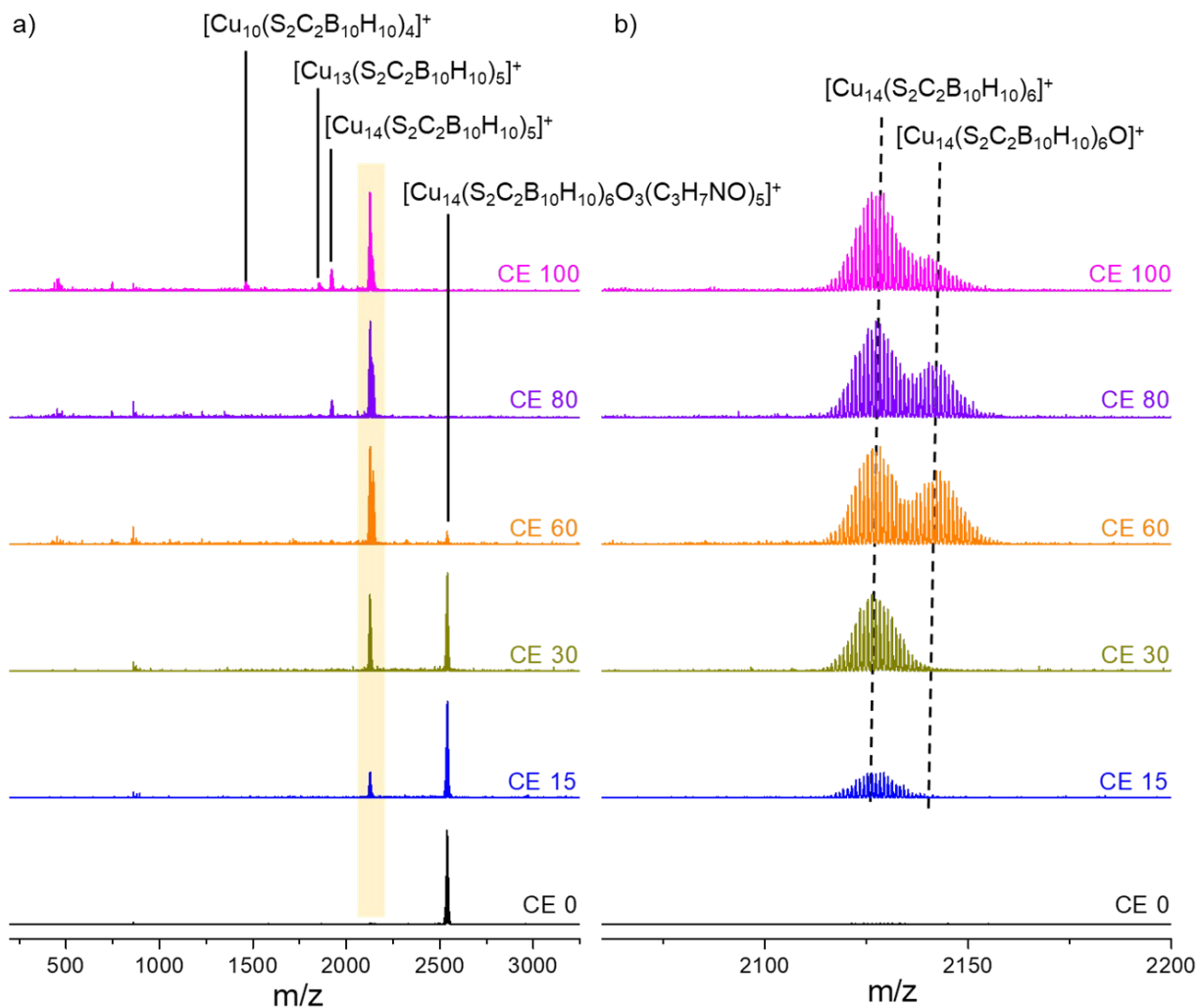


Fig. S2 a) Collision energy dependent MSMS fragmentation patterns of the selected molecular ion peak (at m/z 2540.9) of the Cu_{14} -DMF cluster. Losses of metal kernels and surface ligands were observed from the parent cluster at higher CE. b) Expanded view of the highlighted region.

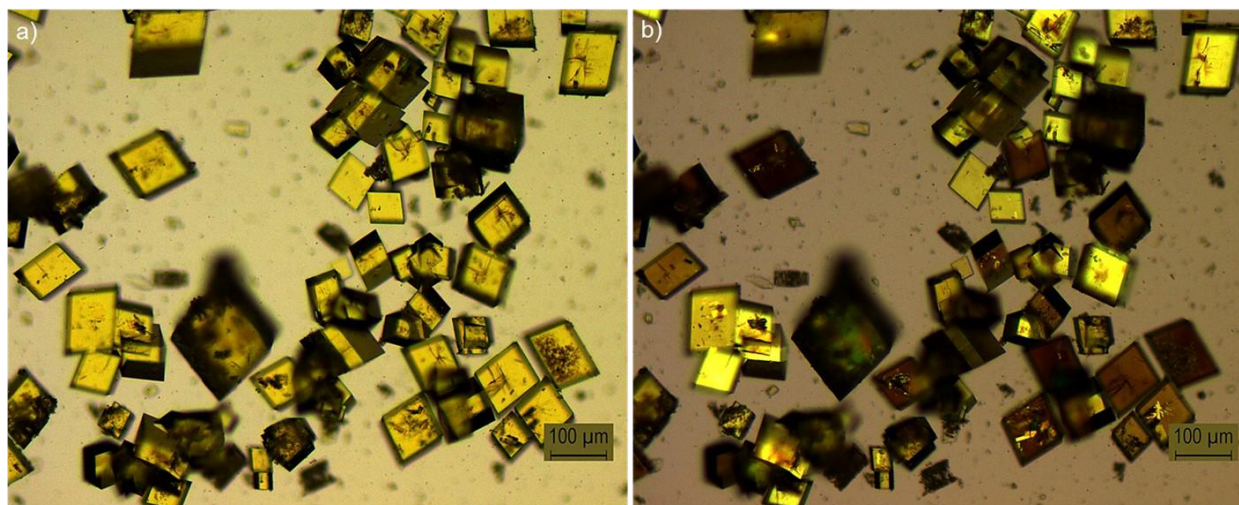


Fig. S3 Optical microscopic images of cuboidal shaped Cu₁₄-DMF crystals a) without polarizer and b) with polarizer.

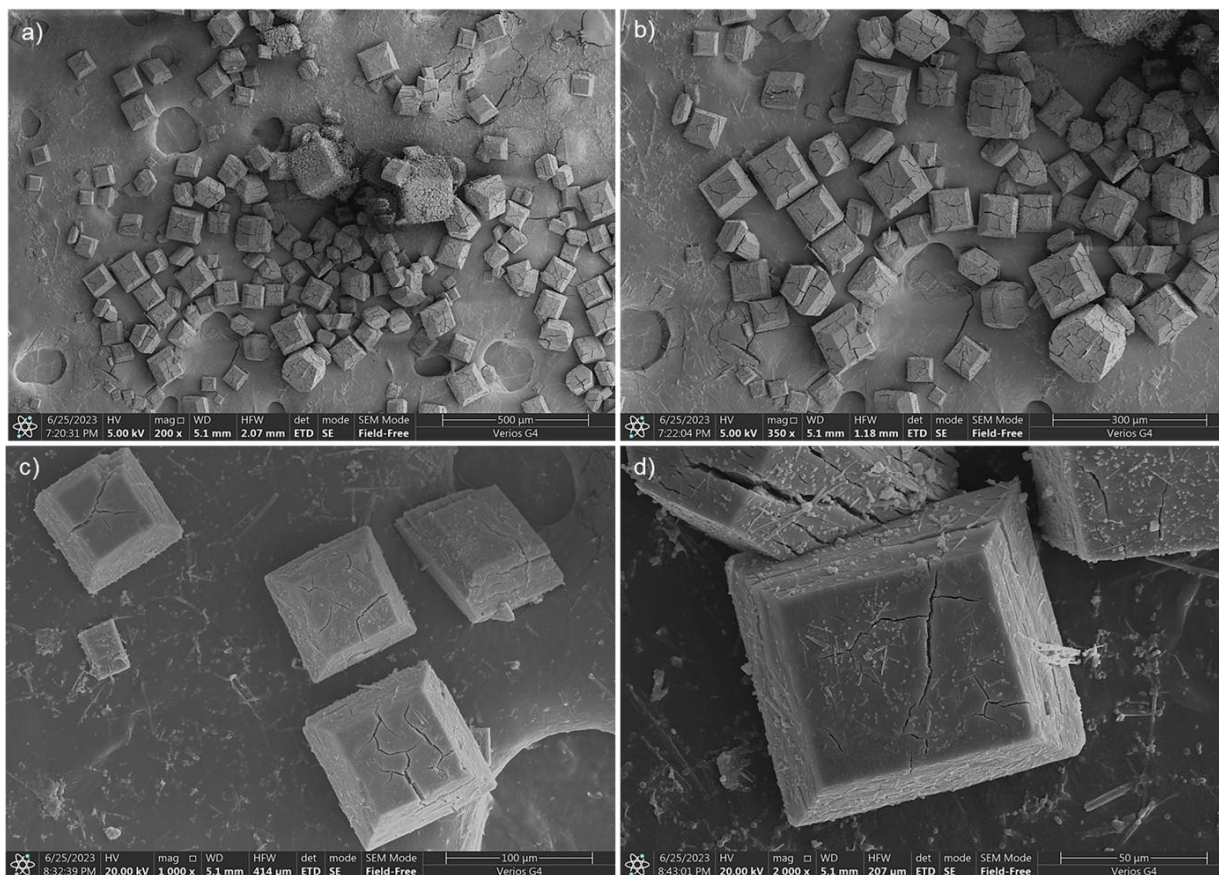


Fig. S4 a-d) Field emission scanning electron micrograph (FESEM) of cuboidal Cu₁₄-DMF crystals at different magnifications. The appearance of the cracks in the crystals is due to the effect of solvent drying.

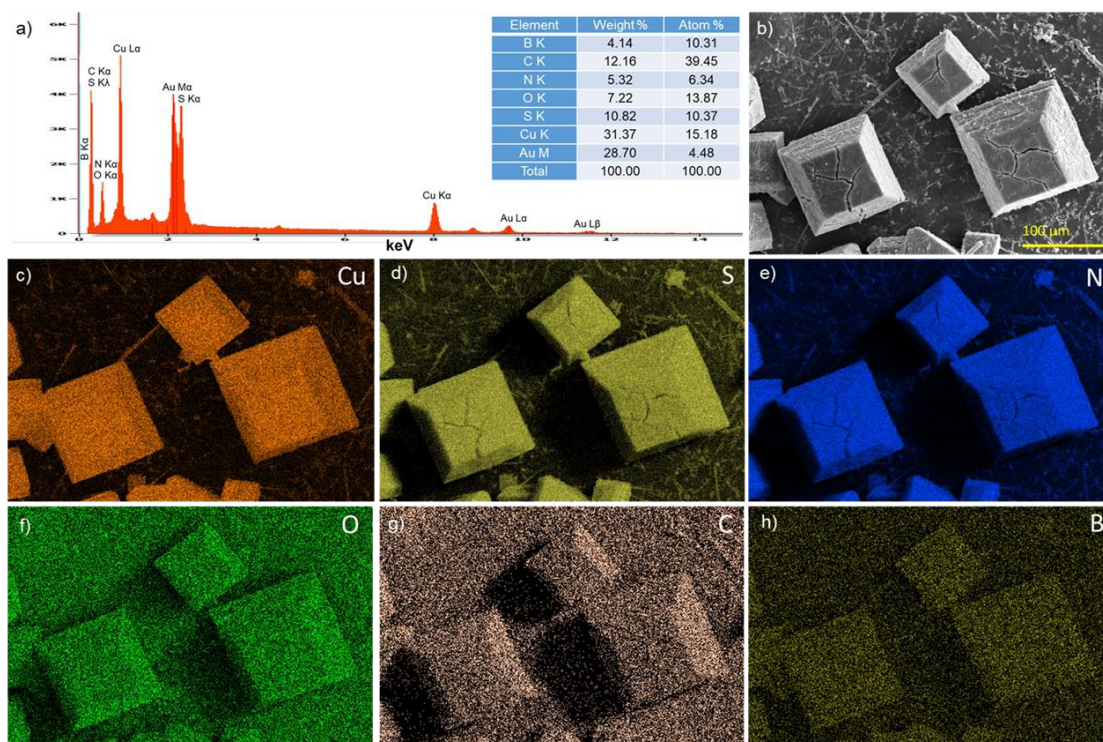


Fig. S5 a) The EDS spectral profile of Cu_{14} -DMF crystals. Inset shows the atomic weight % of various elements present in the crystal. b) FESEM micrograph of the selected crystals used for elemental mapping. c-h) Elemental mapping of the respective elements present in the crystal.

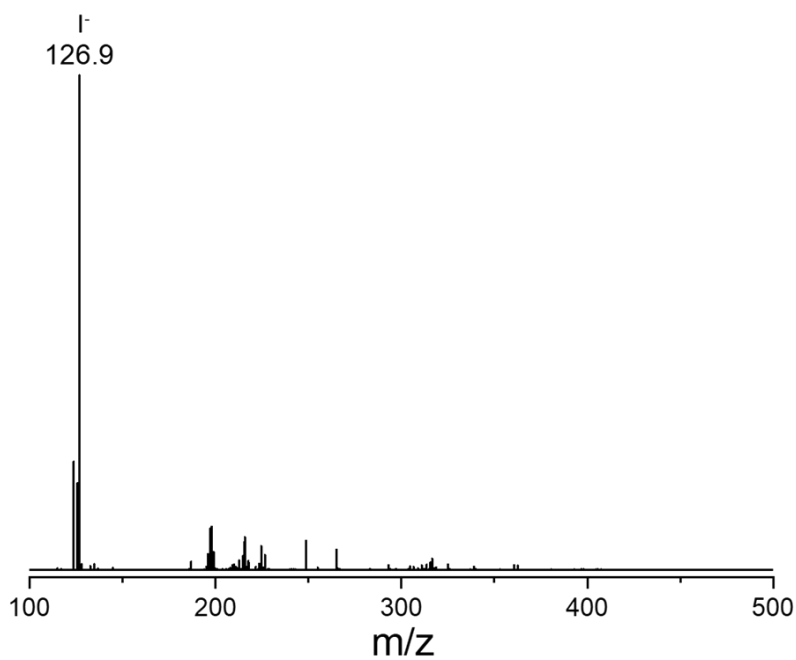


Fig. S6 Negative ion mode ESI mass spectrum of the Cu_{14} -DMF crystals, obtained by dissolving a few crystals in DMF.

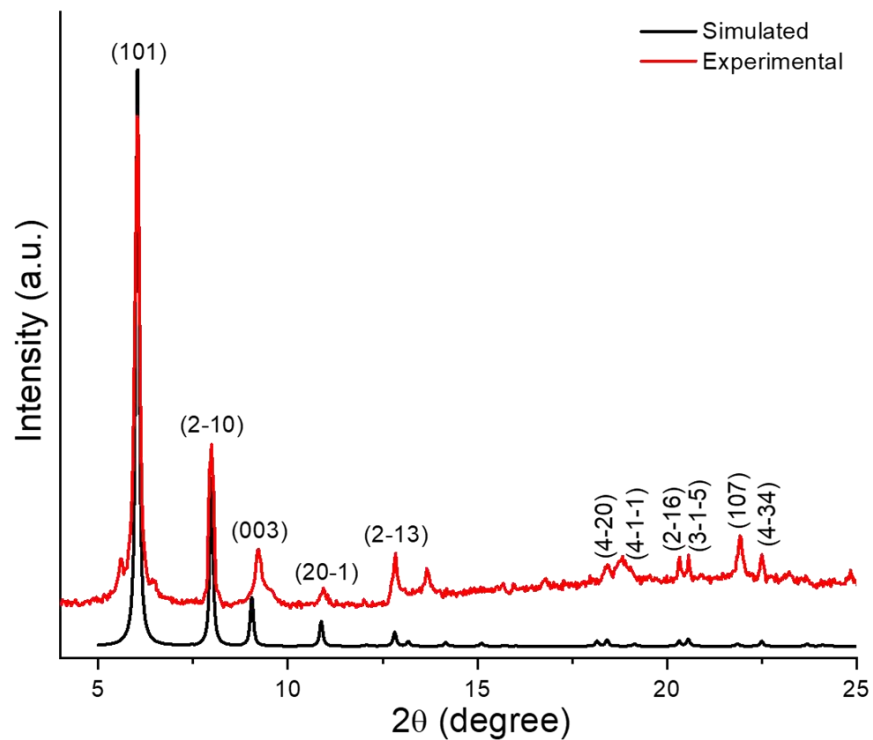


Fig. S7 Comparative PXRD pattern of Cu₁₄-DMF alongside the simulated spectrum derived from single crystal X-ray diffraction.

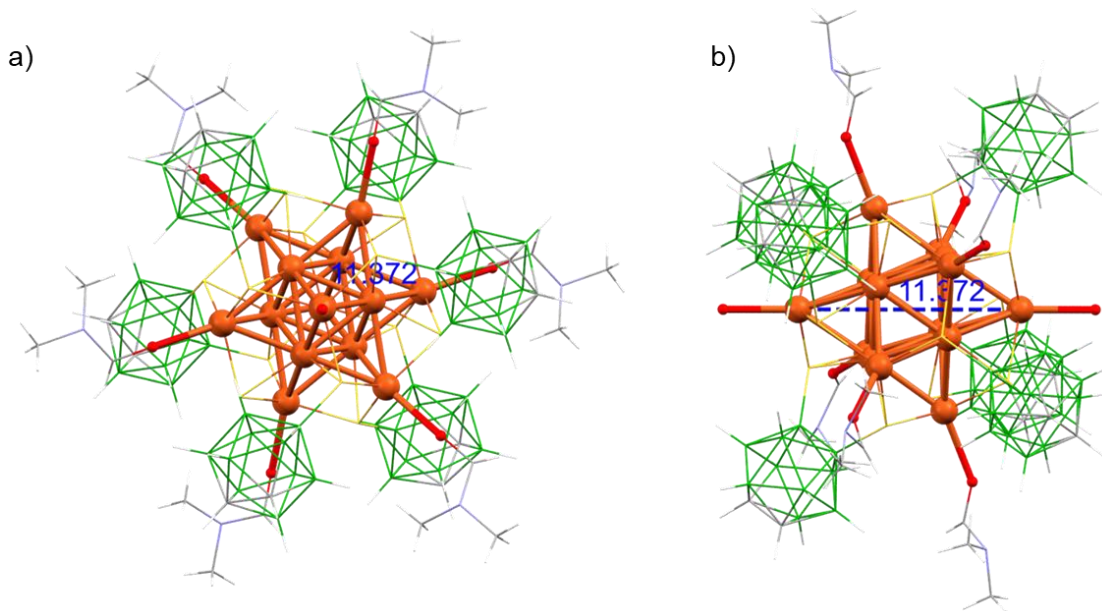


Fig. S10 Interatomic distances between two free oxygens present in the Cu_{14} -DMF cluster. a) Top view and b) side view of the cluster.

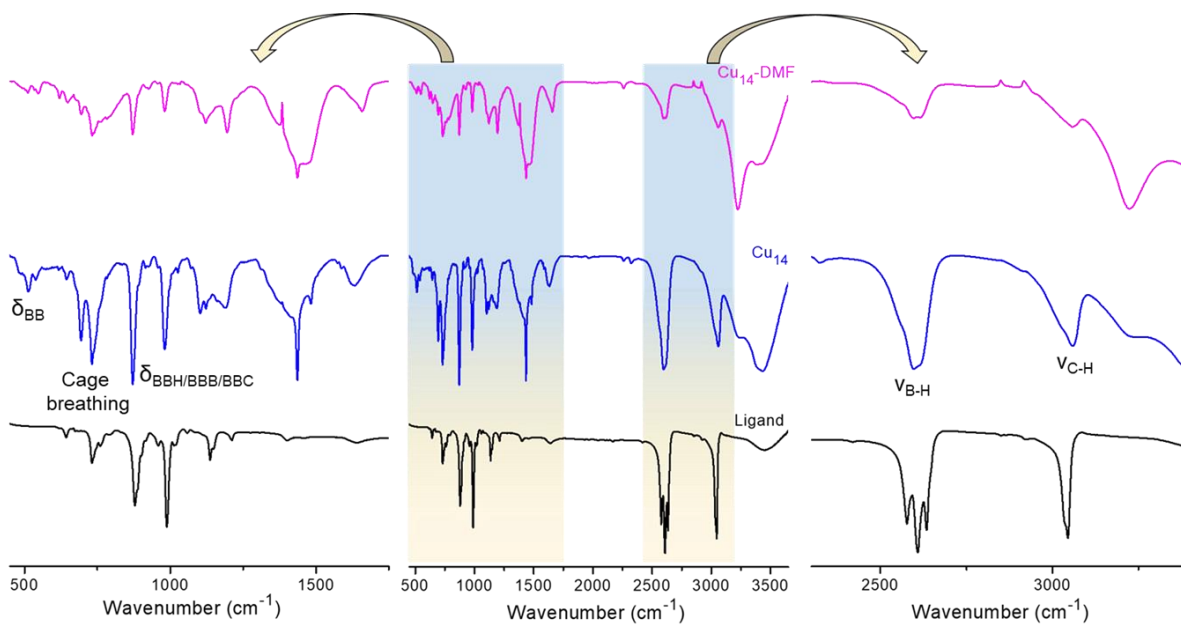


Fig. S11 Comparative IR spectra of *ortho*-carborane 9,12-dithiol ligand, Cu_{14} and Cu_{14} -DMF clusters. Expanded views of the highlighted regions with respective assignments are shown.

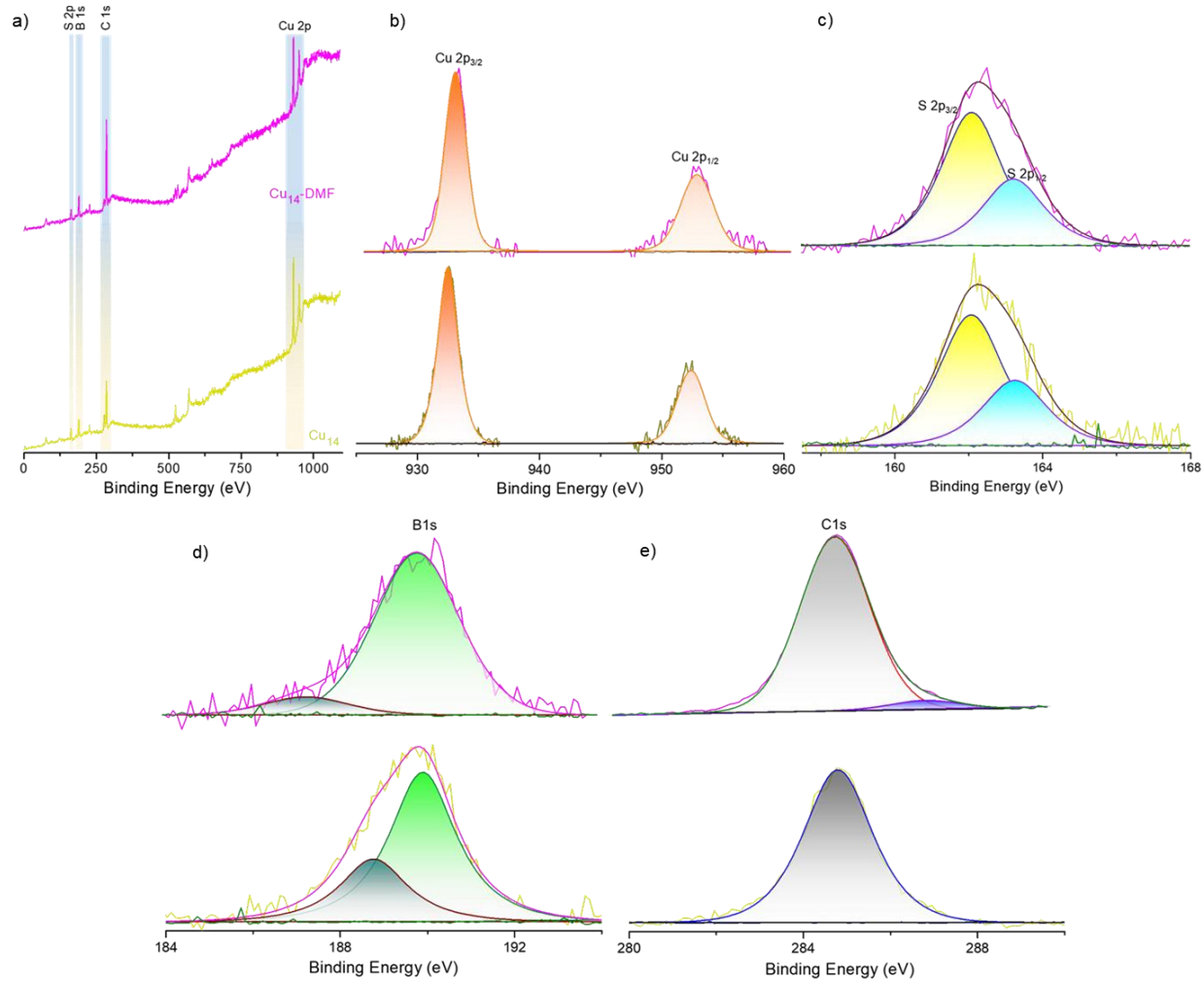


Fig. S12 Comparative XPS spectra of Cu_{14} and Cu_{14} -DMF clusters. a) Survey spectra and selected spectral fittings of b) Cu 2p, c) S 2p, d) B 1s, and e) C 1s regions. Color code of the spectrum: brown line: Cu_{14} and pink line: Cu_{14} -DMF.

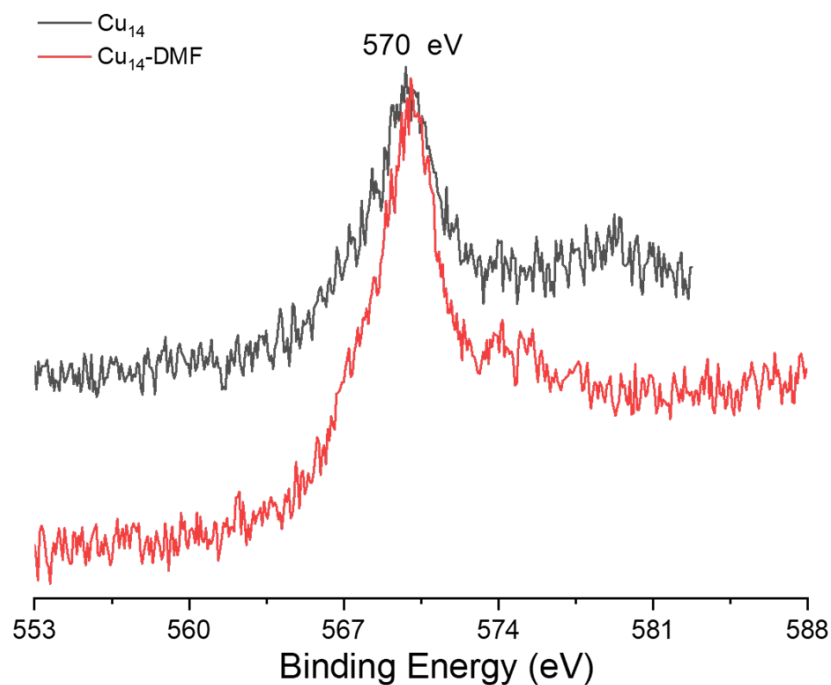


Fig. S13 Comparative Cu LMM Auger spectra of Cu_{14} and Cu_{14} -DMF clusters.

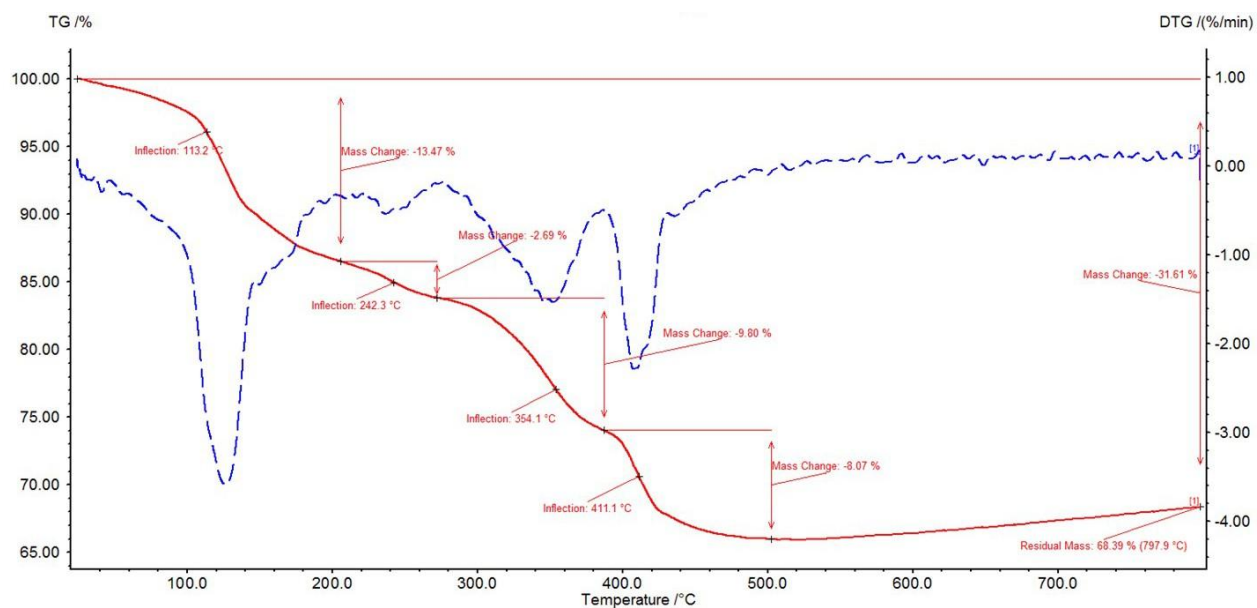


Fig. S14 Thermogravimetric (TG) and differential TG analysis of Cu_{14} cluster under nitrogen atmosphere at a flow rate of 20 ml/min. The heating gradient was 10 K/ min.

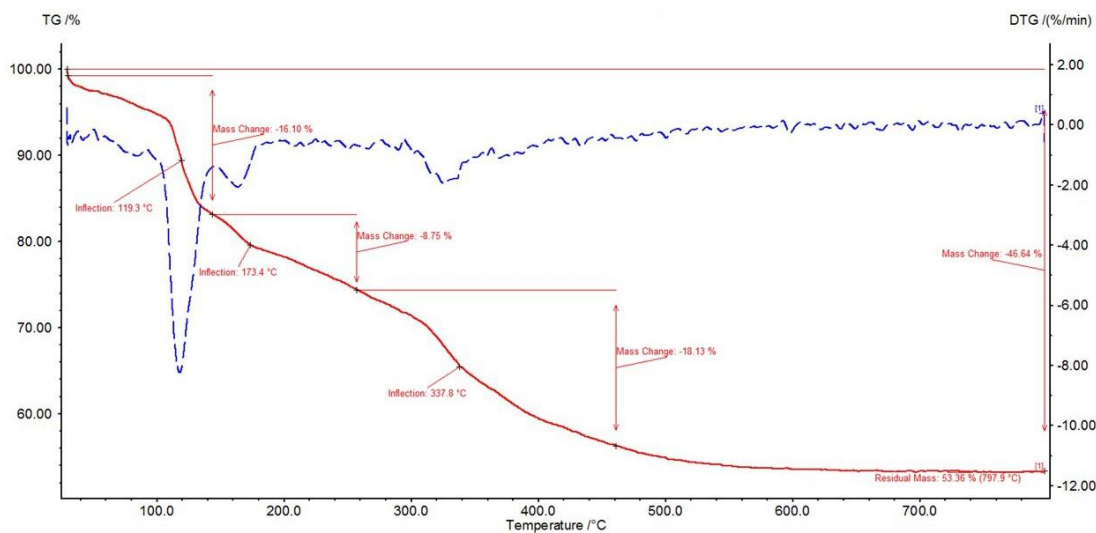


Fig. S15 Thermogravimetric (TG) and differential TG analysis of Cu_{14} -DMF cluster under nitrogen atmosphere at a flow rate of 20 ml/min. The heating gradient was 10 K/min.

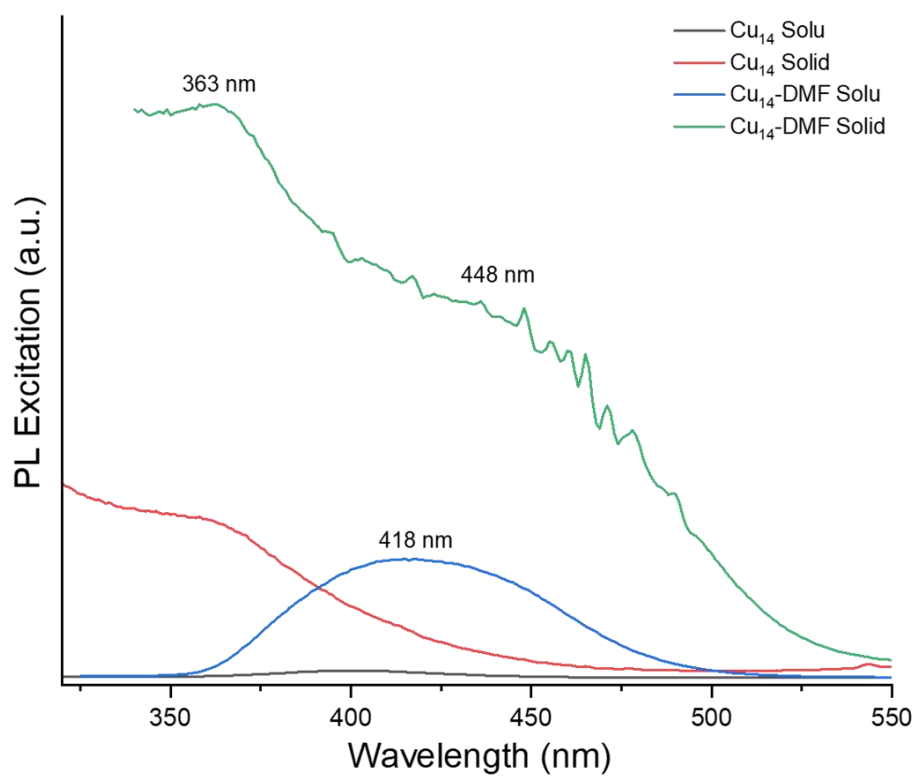


Fig. S16 Photoluminescence excitation spectra of Cu_{14} and Cu_{14} -DMF clusters in their respective states.

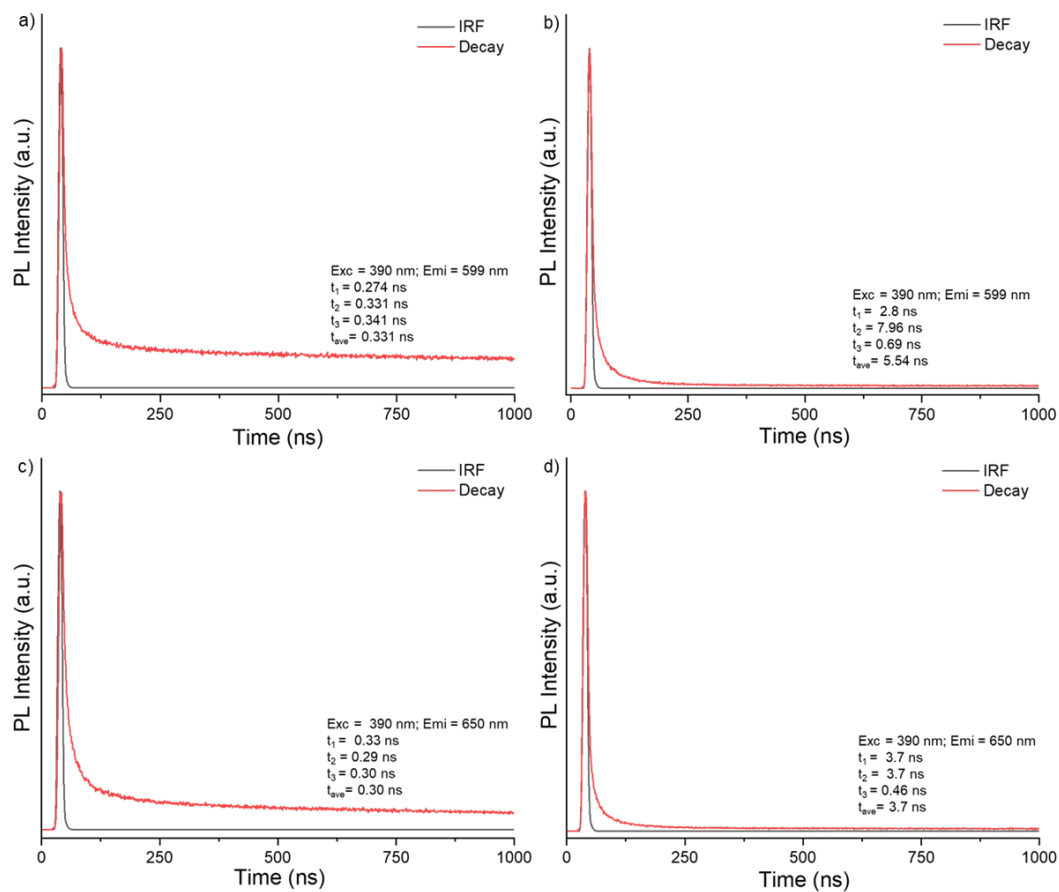


Fig. S17 Luminescence decay profiles and respective decay times of as prepared Cu_{14} cluster in a) DCM solution and b) solid state and Cu_{14} -DMF cluster in c) DMF solution and d) solid state.

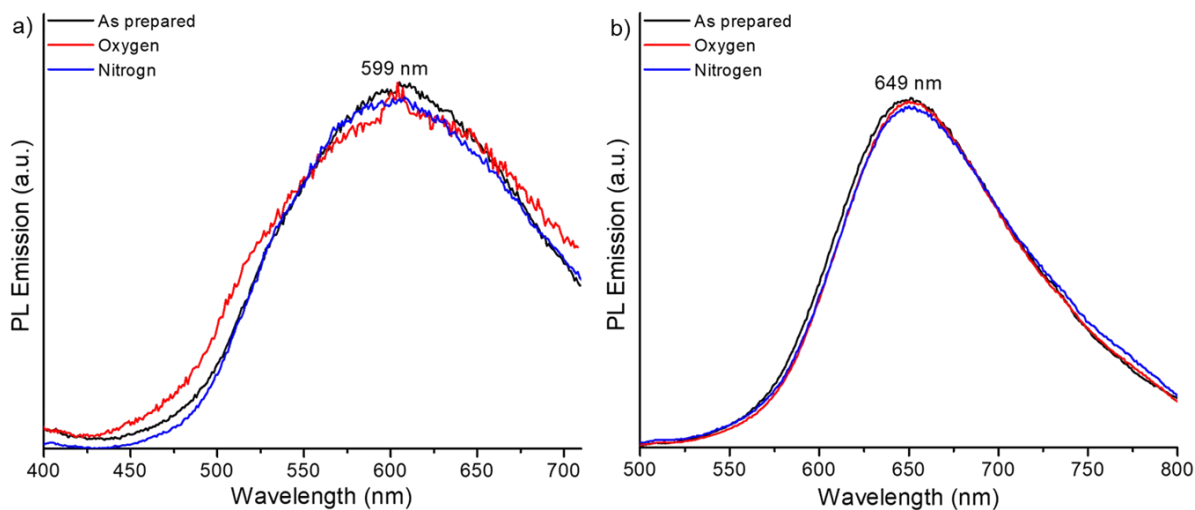


Fig. S18 PL emission spectra of a) Cu_{14} and b) Cu_{14} -DMF in their respective solutions showed no change in their emission intensity upon oxygen exposure.

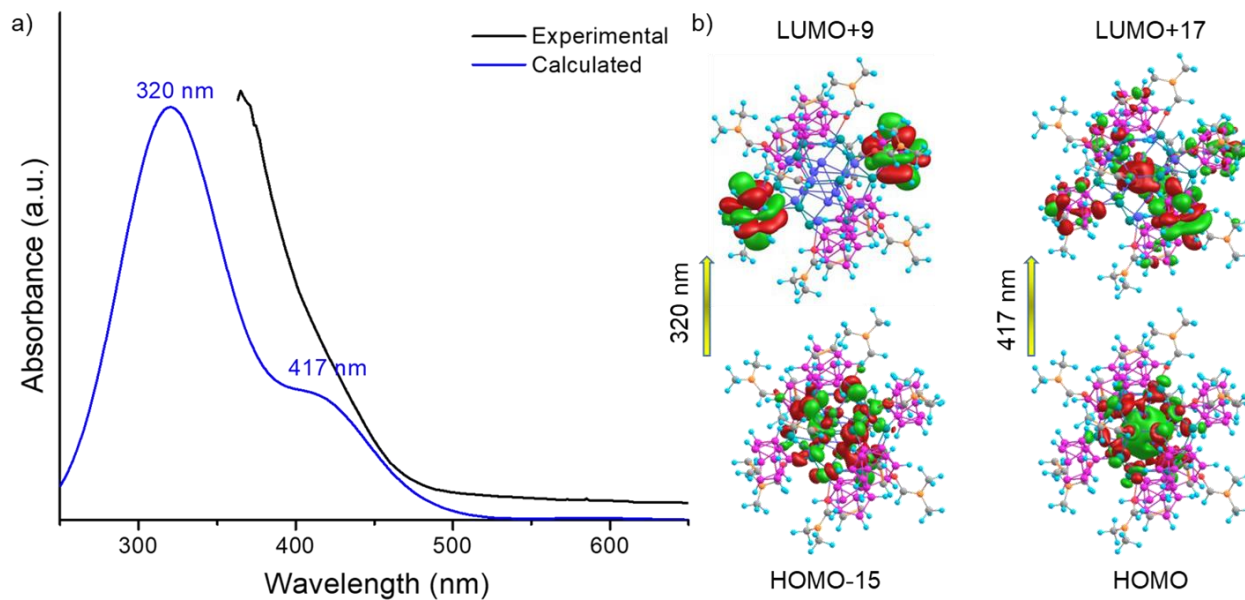


Fig. S19 a) Comparative UV-vis absorption spectrum of Cu_{14} -DMF cluster shows the matching of the experimental and simulated spectrum. b) Molecular orbitals associated with the respective absorption features.

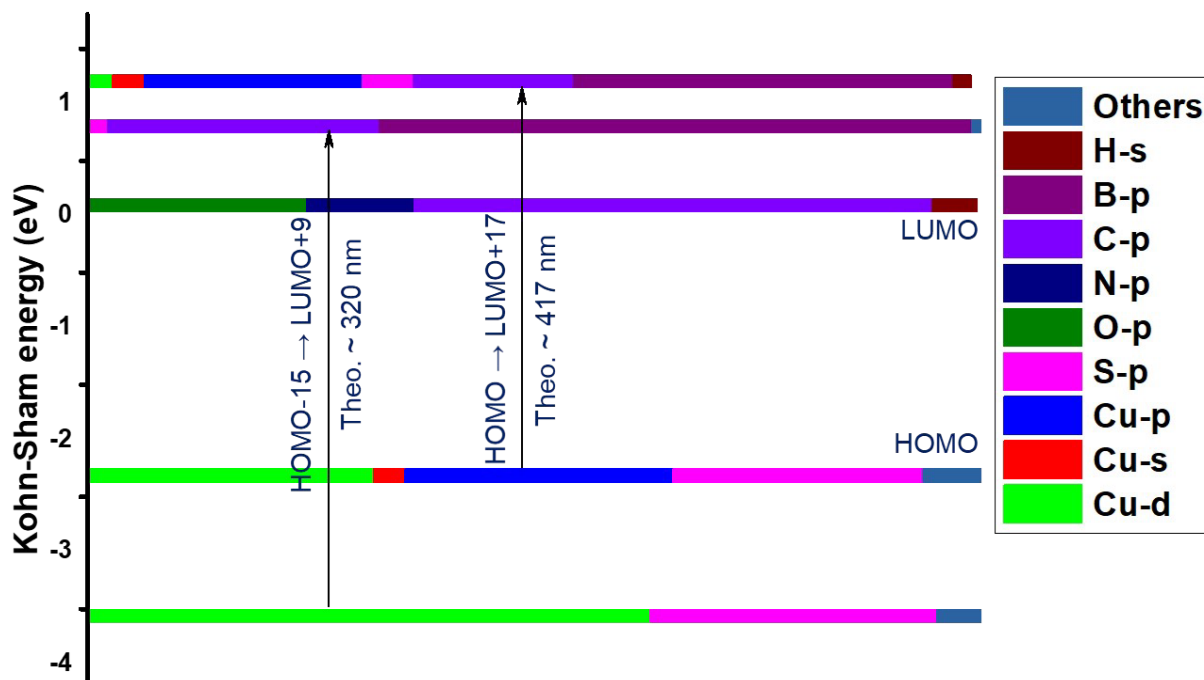
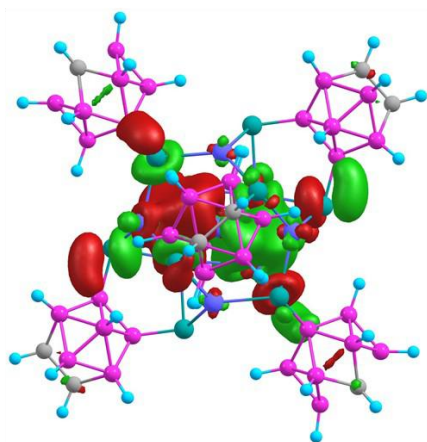


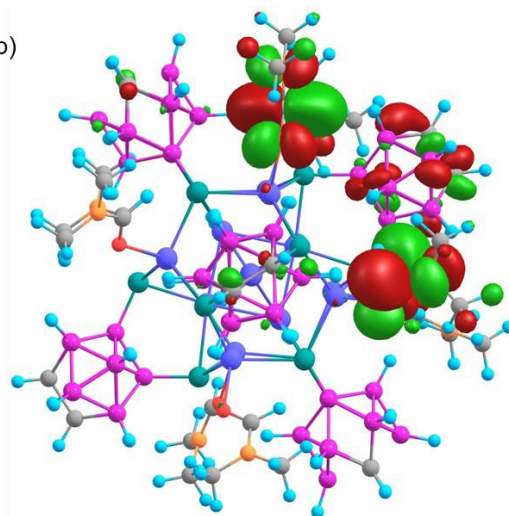
Fig. S20 Kohn-Sham electronic energy level diagram for Cu_{14} -DMF cluster. Electronic transitions of the optical absorption features are marked here.

a)

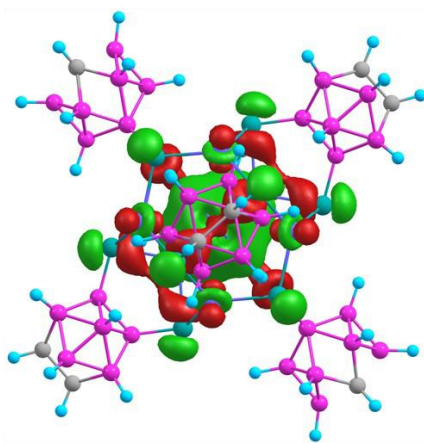


LUMO

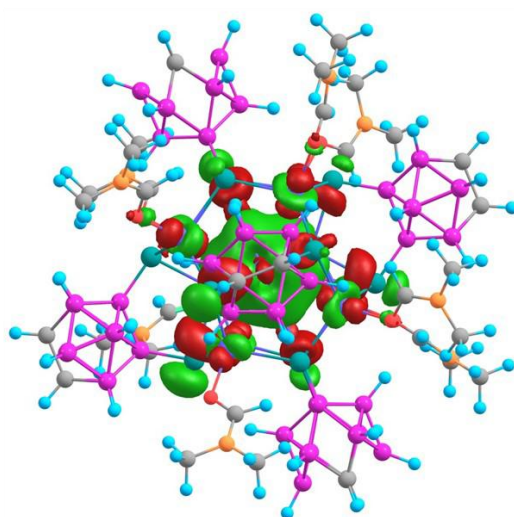
b)



LUMO



HOMO



HOMO

Fig. S21 Frontier molecular orbitals of a) Cu_{14} and b) Cu_{14} -DMF clusters.

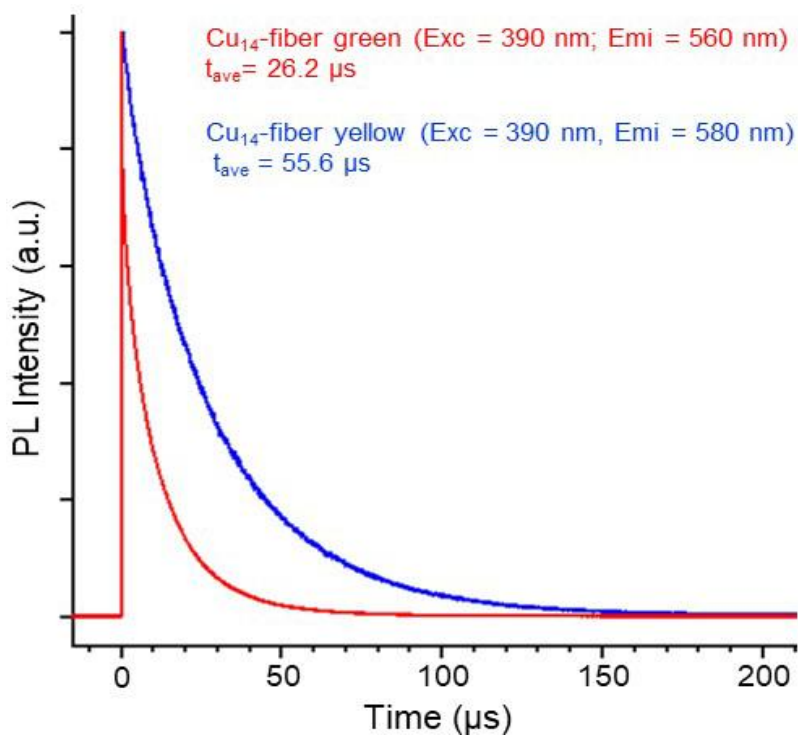


Fig. S22 Luminescence decay profiles of green and yellow emitting Cu₁₄-fibers at room temperature.

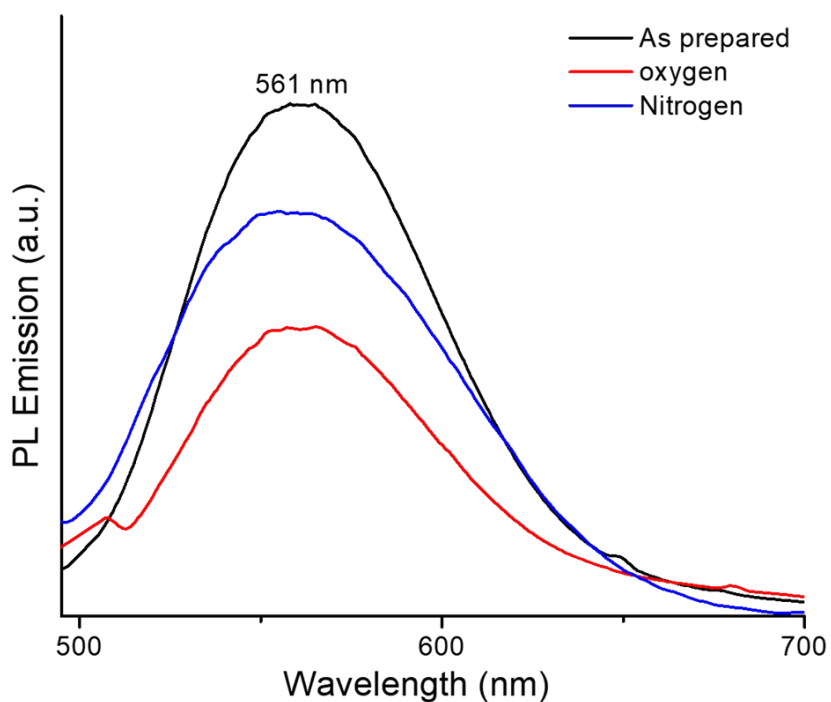


Fig. S23 Comparative PL studies were conducted on green emitting Cu₁₄-fibers, both pre- and post-exposure to oxygen gas. Subsequently, nitrogen was introduced after the oxygen exposure. Excitation was at 400 nm.

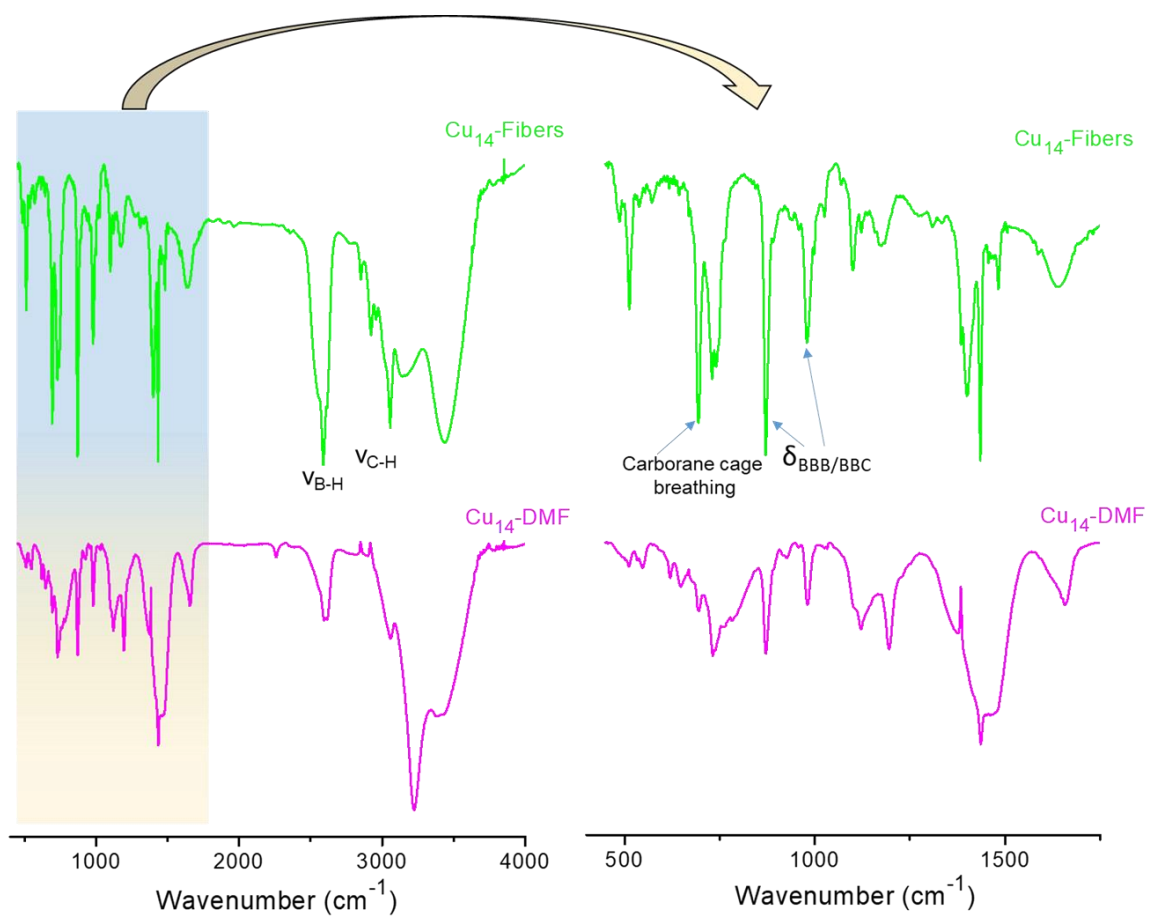


Fig. S24 Comparative IR spectra of Cu_{14} -DMF cluster and Cu_{14} -fibers.

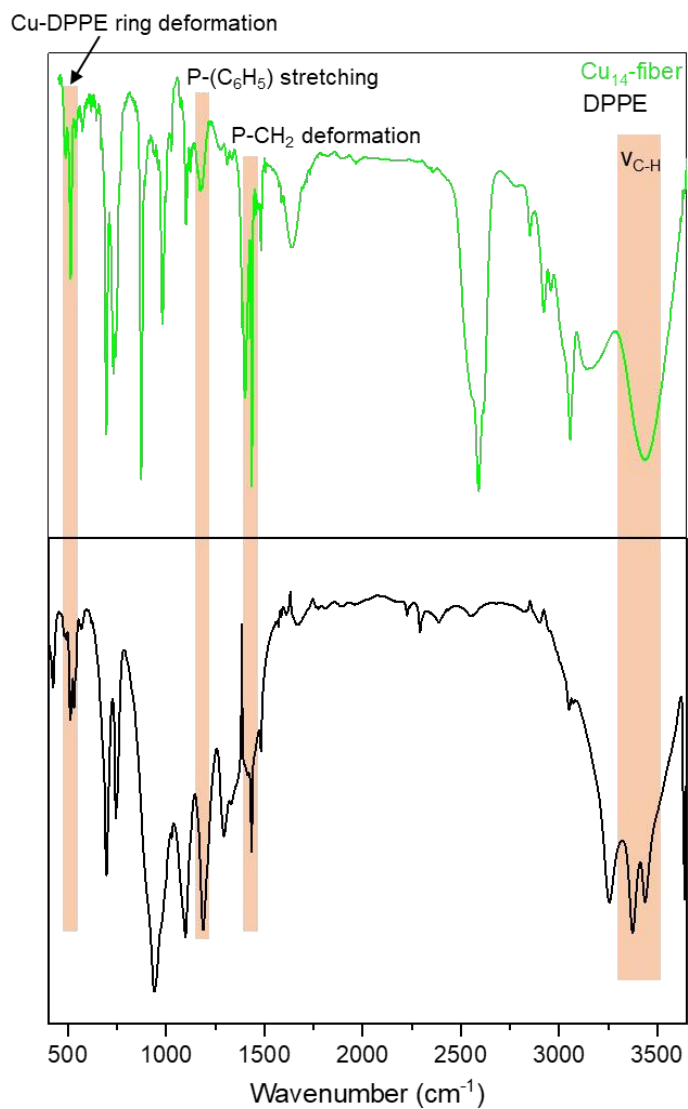


Fig. S25 Comparative IR spectra of free DPPE and Cu_{14} -fibers. Minor variations in the highlighted peak positions indicate the binding of DPPE to the cluster.

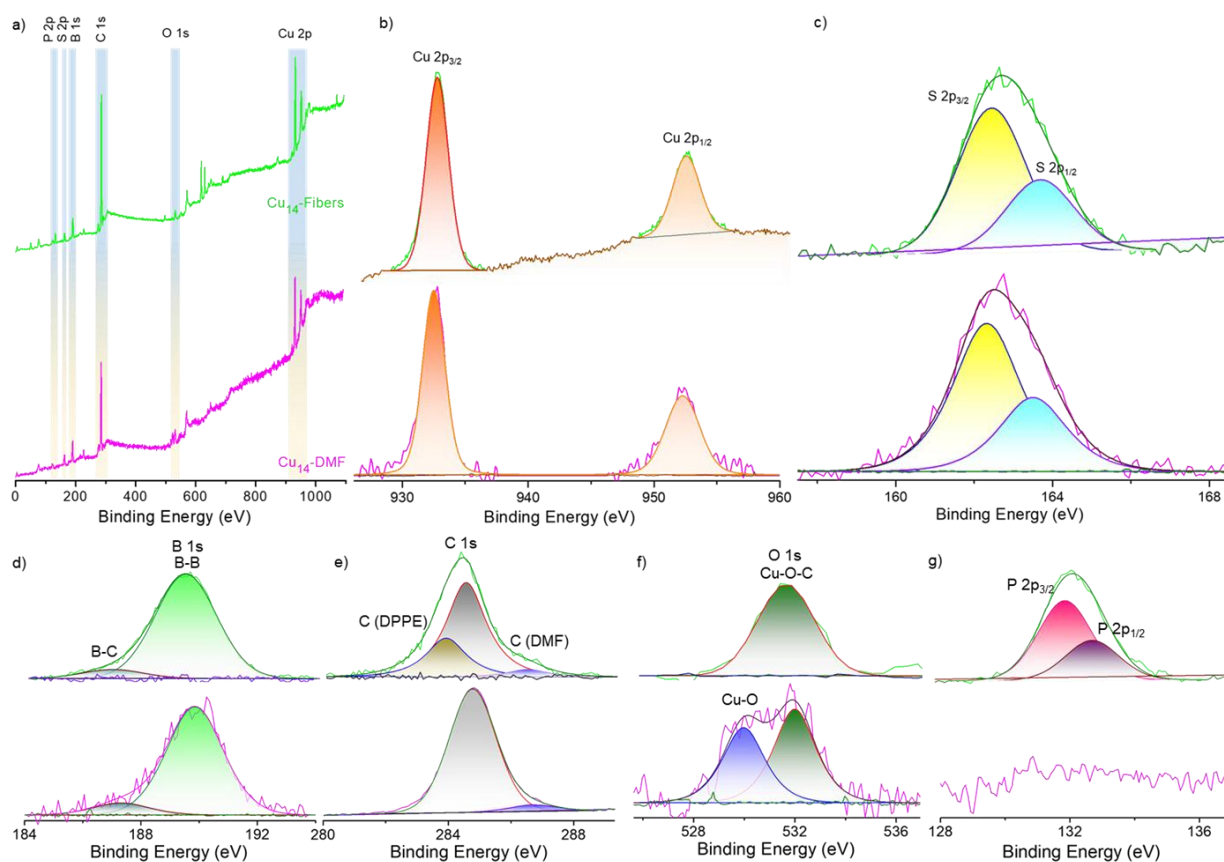


Fig. S26 Comparative XPS a) survey spectra of Cu₁₄-DMF and Cu₁₄-fibers. Selected area spectral fittings of b) Cu 2p, c) S 2p, d) B 1s, e) C 1s, f) O 1s, g) P 2p regions. Color code: green line = Cu₁₄-fibers, pink = Cu₁₄-DMF.

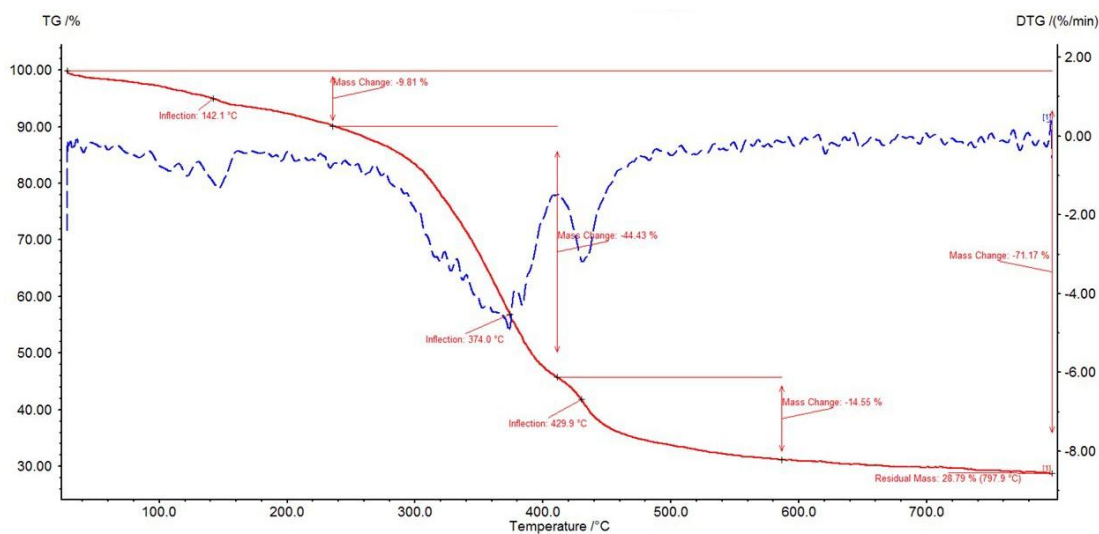


Fig. S27 Thermogravimetric (TG) and differential TG analysis of Cu₁₄-fibers under nitrogen atmosphere at a flow rate of 20 ml/min. The heating rate was 10 K/ min.

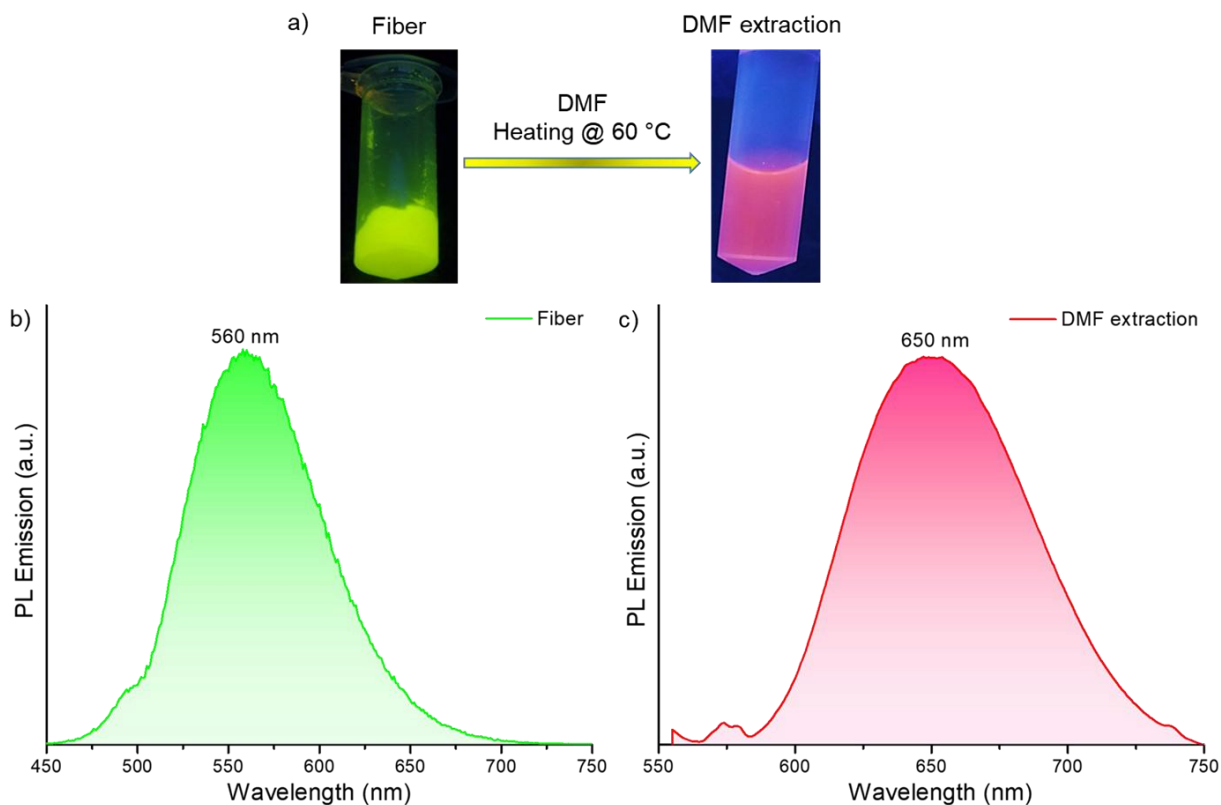


Fig. S28 a) Photographs of the Cu_{14} -fibers under UV light and after its extraction in DMF. PL emission profiles of the b) fiber, and c) the extracted DMF solution.

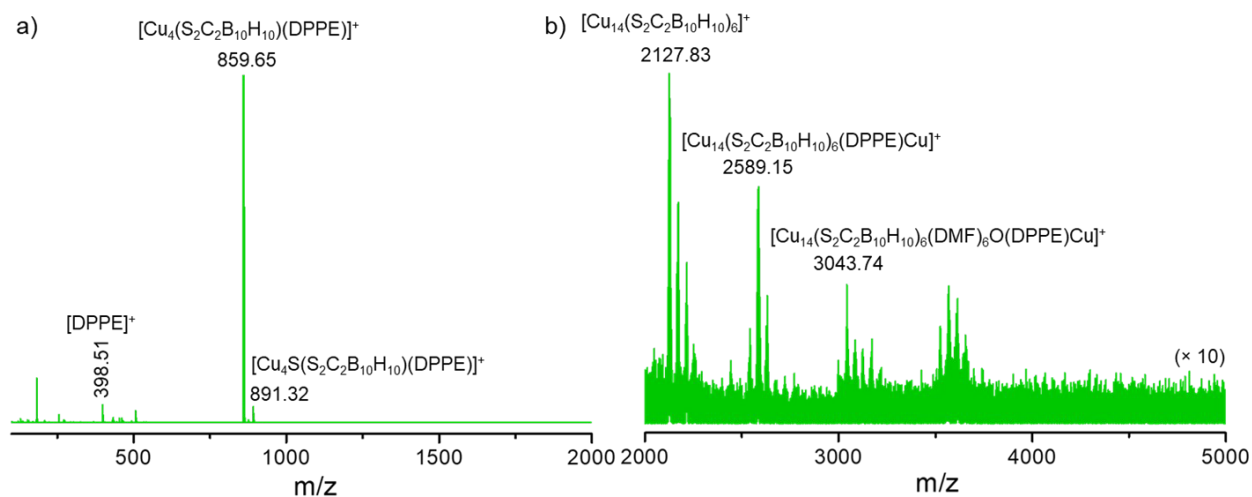


Fig. S29 Positive ion mode ESI-MS spectrum of Cu_{14} -fibers after dissolving them in DMF. a) Mass range of m/z 100-2000 and b) expanded view of the spectrum in the mass range of m/z 2000-5000. Peaks of interest are marked here.

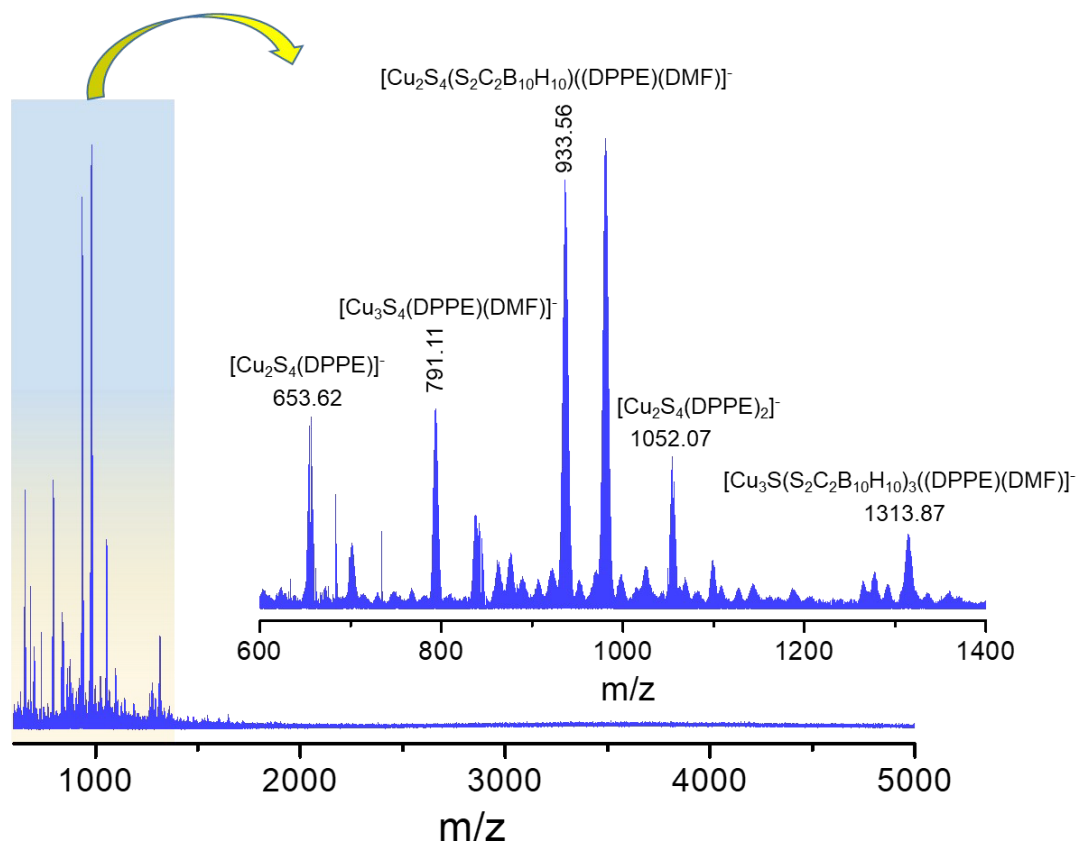


Fig. S30 Full range negative ion mode ESI-MS spectrum of Cu_{14} -fibers after dissolving them in DMF. Inset shows an expanded view of the spectrum along with the respective peaks are marked here. Appearance of DPPE attached Cu peaks indicate the 1D assembly of DPPE linkers with the clusters.

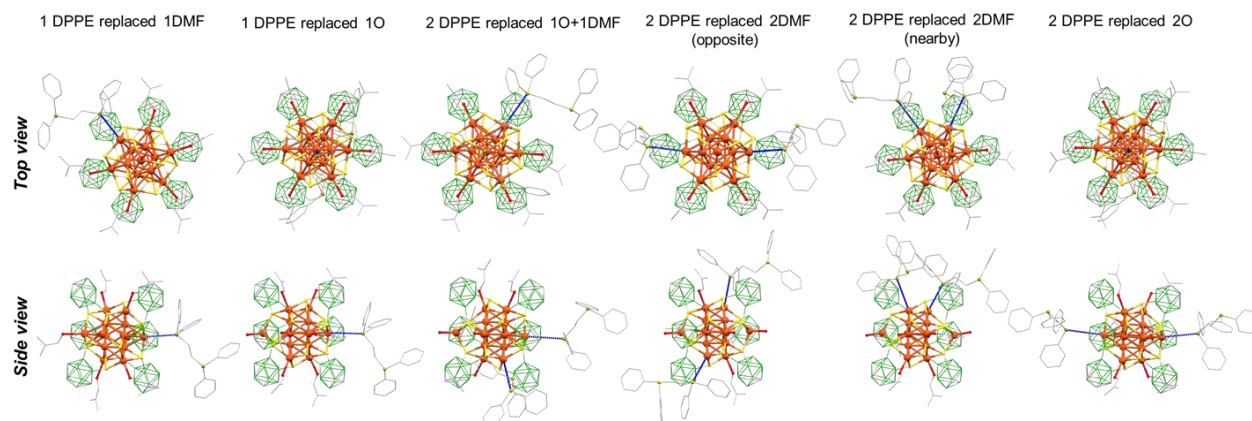


Fig. S31 Optimized structural models of most probable bindings of DPPE linkers with the Cu_{14} -DMF cluster. Hydrogen atoms are removed for clarity. Color codes: orange = copper, yellow = sulfur, green = boron, grey = carbon, red = oxygen and brown = phosphorus.

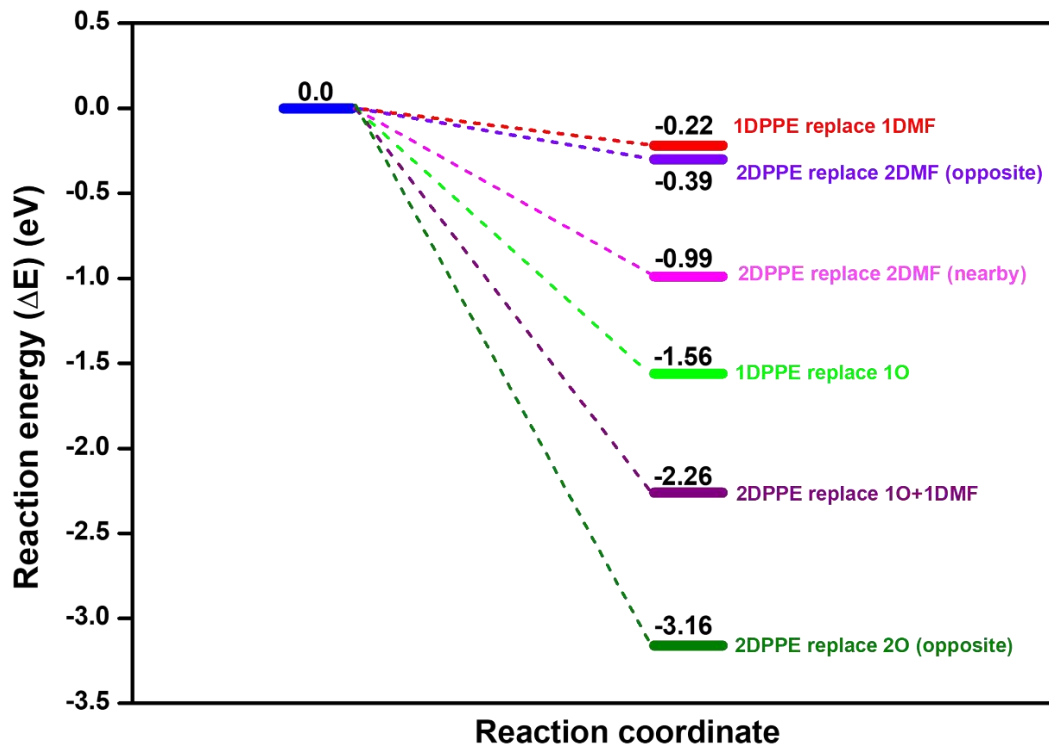


Fig. S32 A comparative energy profile of the probable binding of DPPE linkers at various positions of the Cu_{14} -DMF cluster.

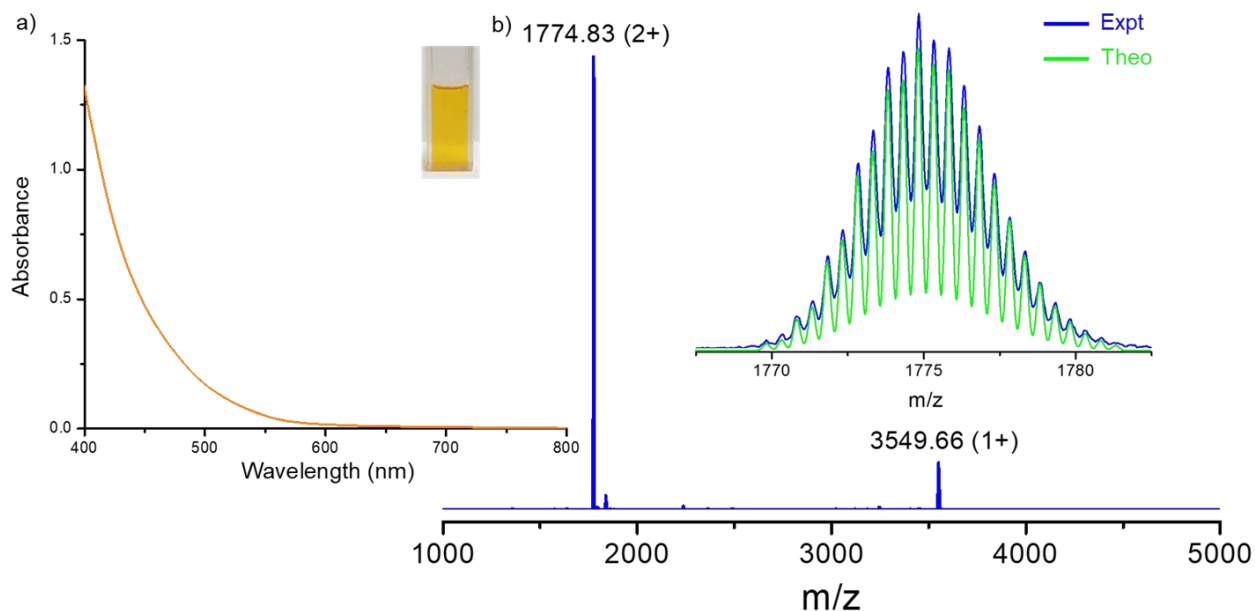


Fig. S33 a) UV-vis absorption spectrum of $[\text{Cu}_{18}(\text{DPPE})_6\text{H}_{16}]$ nanocluster. Inset shows the photographic image of the cluster in DCM. b) Full range mass spectrum of the Cu_{18} cluster in positive ion mode shows the presence of di- (at m/z 1774.83) and mono- cationic (at m/z 3549.66) species for the cluster. Inset shows

the exact matching of the isotopic distributions of the experimental and theoretical spectra for the 2+ charge state species.

References

1. A. Jana, M. Jash, W. A. Dar, J. Roy, P. Chakraborty, G. Paramasivam, S. Lebedkin, K. Kirakci, S. Manna, S. Antharjanam, J. Machacek, M. Kucerakova, S. Ghosh, K. Lang, M. M. Kappes, T. Base and T. Pradeep, *Chem. Sci.*, 2023, **14**, 1613–1626.
2. Frisch, M. J.; Trucks, G. W.; Schlegel, H. B.; Scuseria, G. E.; Robb, M. A.; Cheeseman, J. R.; Scalmani, G.; Barone, V.; Mennucci, B.; Petersson, G. A. et al. Gaussian 09, Revision B.01; Gaussian Inc.: Wallingford, CT, **2009**.
3. A. D. Becke, *Phys. Rev. A: At., Mol., Opt. Phys.*, 1988, **38**, 3098–3100.
4. A. D. Becke, *J. Chem. Phys.*, 1993, **98**, 1372–1377.
5. W. J. Hehre, R. Ditchfield and J. A. Pople, *J. Chem. Phys.*, 1972, **56**, 2257–2261.
6. P. C. Hariharan and J. A. Pople, *Theor. Chim. Acta*, 1973, **28**, 213–222.
7. T. Lu and F. Chen, *J. Comput. Chem.*, 2012, **33**, 580–592.

Enhanced Electrical Output in an Electrostatic Generator Using Charged Water

Vishal Kumar, Pillalamarri Srikrishnarka, Ramamurthy Nagarajan,* and Thalappil Pradeep*

Cite This: *ACS Sustainable Chem. Eng.* 2024, 12, 13106–13115

Read Online

ACCESS\$

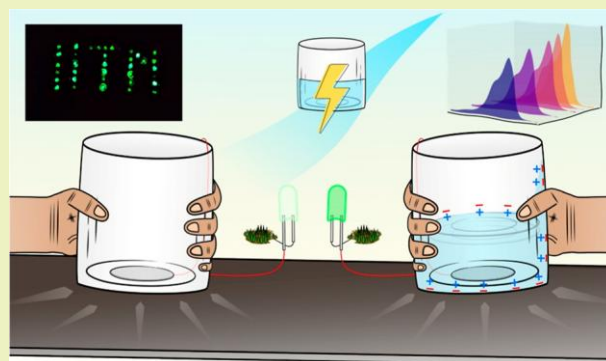
Metrics & More

Article Recommendations

Supporting Information

ABSTRACT: Electrostatic charging of water, particularly at the water–hydrophobic interface, continues to perplex researchers despite centuries of work. Recent advancements in energy harvesting, materials synthesis, and sensing employing electrohydrodynamic processes have generated renewed interest in the electrostatic charging of water. This work aims to understand the charging of water from an energy-harvesting perspective. We used a single-electrode electrostatic generator initially to demonstrate enhancement of the electric output with the addition of water. Through several control measurements, we established that the enhancement was a result of the electrostatic charging of water. The role of electrode wettability and pH on the electric output was studied. The effect of pH on the charging of water was correlated with the output voltage. The system was extended to a double-electrode electrostatic generator (DE-EG) to expand the applicability of the technique and increase the output. Using the DE-EG, we demonstrated the influence of an electric field on the charging of water. The electricity thus produced was used to power multiple light-emitting diodes. Furthermore, the technique was employed to treat wastewater containing a dye using a 3D-printed linear actuator. The insights presented are useful in enhancing the performance of water-based EGs and could help to better understand various electrohydrodynamic processes.

KEYWORDS: triboelectricity, energy harvesting, triboelectric generator, water charging, streaming electrification



INTRODUCTION

The Kelvin water dropper¹ and Leyden jar² are a few examples of early electrostatic generators (EGs) wherein water was used to store electric charge and produce electricity.³ In such systems, the charging of water is driven by an external field, which pushes the charge into the water through electrostatic induction. Unlike induced charging, in contact charging, which is a more prevalent form of charging two surfaces when brought in contact and separated, develops an electrostatic charge. Much like solids, liquids in contact with other materials also develop static charge. Streaming or flow electrification refers to electrostatic charging at a liquid–solid interface because of flow.⁴ It can further be extended to an air–liquid⁵ interface, as in the case of aerosols, or a liquid–liquid interface, as in the case of emulsions.⁶ The phenomenon has been known for many decades^{7,8} and is still a topic of active investigation.^{9,10} For example, the flow of hydrocarbons in petroleum pipelines causes accumulation of charge, leading to electric discharges causing explosion.^{8,11} Though the streaming electrification of hydrocarbons has been known and studied, the contact electrification of water became prominent only after the advent of the semiconductor chip industry. Previously, electrostatic charging with water was considered

highly unlikely owing to its million-fold higher conductivity compared to hydrocarbons.⁸

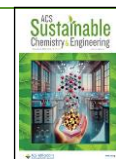
Electrostatic charging at the water–hydrophobic interface has been a subject of discussion for a long time. Studies on electrostatic charging at the water–hydrophobic interface have shown that water gets positively charged,^{10,12} and the hydrophobic surface (generally, a polymer) gets negatively charged.^{7,13} Burgo et al. studied charging of water when passed through tubes of different types of materials: glass, polymers, and metals. In the study, water always acquired a positive charge irrespective of the materials it was in contact with, except for the case where it was flown through air, where it acquired negative charge.¹⁰ A number of charging mechanisms based on experimental and theoretical findings have been put forward. Most of these mechanisms are based on ion(s) adsorption at the solid–liquid interface, though they differ in the types of ions and mechanism of adsorption. The charging

Received: March 2, 2024

Revised: August 3, 2024

Accepted: August 5, 2024

Published: August 16, 2024



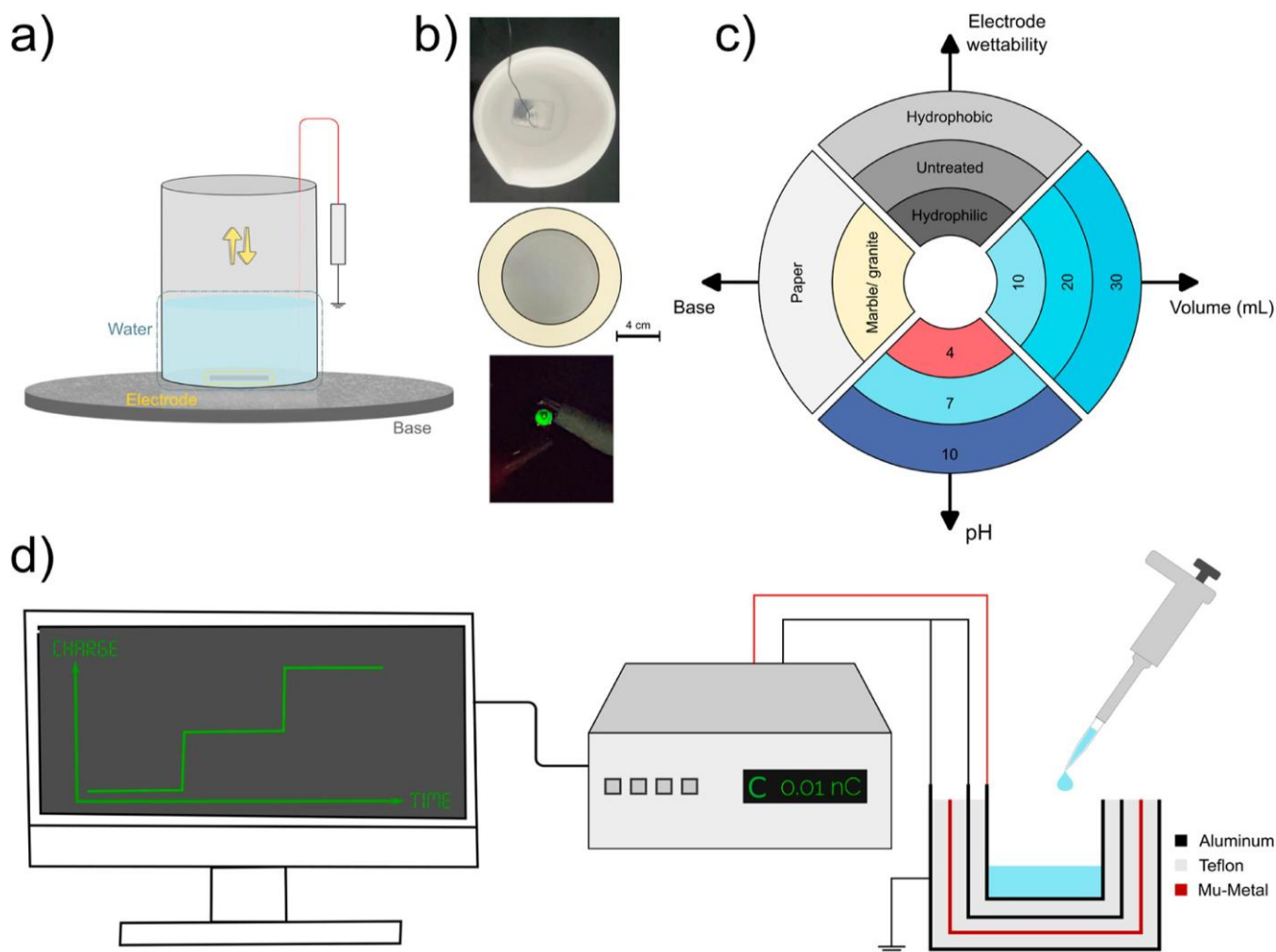


Figure 1. Illustration showing (a) tapping of the PTFE beaker containing water, (b) photograph of the setup □top: PTFE beaker with an electrode attached on the granite slab, middle: back of the beaker, and bottom: powering an LED using the SE-EG, (c) changes made to the EG □volume of water, pH, electrode wettability, and contacting surface, and (d) schematic of charge measurement setup with the Faraday cup, and materials used for its construction are listed on the right.

at the water–hydrophobic interface is attributed to the formation of a double layer, leading to adsorption of OH^- ions at the hydrophobic surface. This excess of OH^- ions on a hydrophobic surface makes it negatively charged and leaves the water with an excess of H^+ ions, making it positively charged.^{5,7} Kudin and Car modeled in detail the behavior of hydroxide and hydronium ions at the water–hydrophobic interface.⁹ They observed that the hydronium ion clusters tend to occupy surface and subsurface regions, whereas the hydroxide ions prefer the surface layer. This preferential occupation of hydroxide ions could explain the negative charge acquired by hydrophobic polymeric surfaces like polytetrafluoroethylene (PTFE) in contact with water. Some claim that the observed electrophoretic mobility may not arise from the adsorption of ions but because of the anisotropic distribution of water molecules at the water–hydrophobic interface. The water droplets in oils have positively charged H atom sticking toward the oil.⁶ Others attribute the charging to concoctions of ions present in the water, prominently the presence of carbonate (CO_3^{2-}) and bicarbonate (HCO_3^-) anions from dissolution of atmospheric CO_2 .¹⁴ The presence of H^+ and OH^- ions could not alone account for the calculated negative charge measured through interfacial tension or the zeta-potential at the

hydrophobic surface.^{14,15} The charging of water droplets has also been observed to change physicochemical properties such as surface tension.¹⁶ Furthermore, recent studies have pointed out a correlation between the charging of droplets and viscosity, which is a surface tension-dependent quantity. This implies that charging is dependent on surface tension, but at the same time these parameters are altered by charging.¹⁷

The advent of the triboelectric (nano)generator (TG/TENG) has generated a renewed interest in the electrostatic charging of water.^{18–21} Two types of liquid–solid-based TG exist. One is droplet-based, which utilizes continuous impingement of droplets on hydrophobic surfaces; such systems are useful for energy harvesting from rainwater.^{22,23} The other is continuous flow-based, in which water is continuously pumped through an open tubular structure; such systems are useful for energy harvesting from running water bodies such as rivers, seas, or flow through pipes.²⁴ In both categories, water is passed on a hydrophobic surface, which causes triboelectric charging at the water–hydrophobic interface. The hydrophobic surface becomes negatively charged, and water becomes positively charged. Such liquid–solid-based TGs have several advantages over the solid–solid type in conventional TGs, such as reduced friction, better contact, and

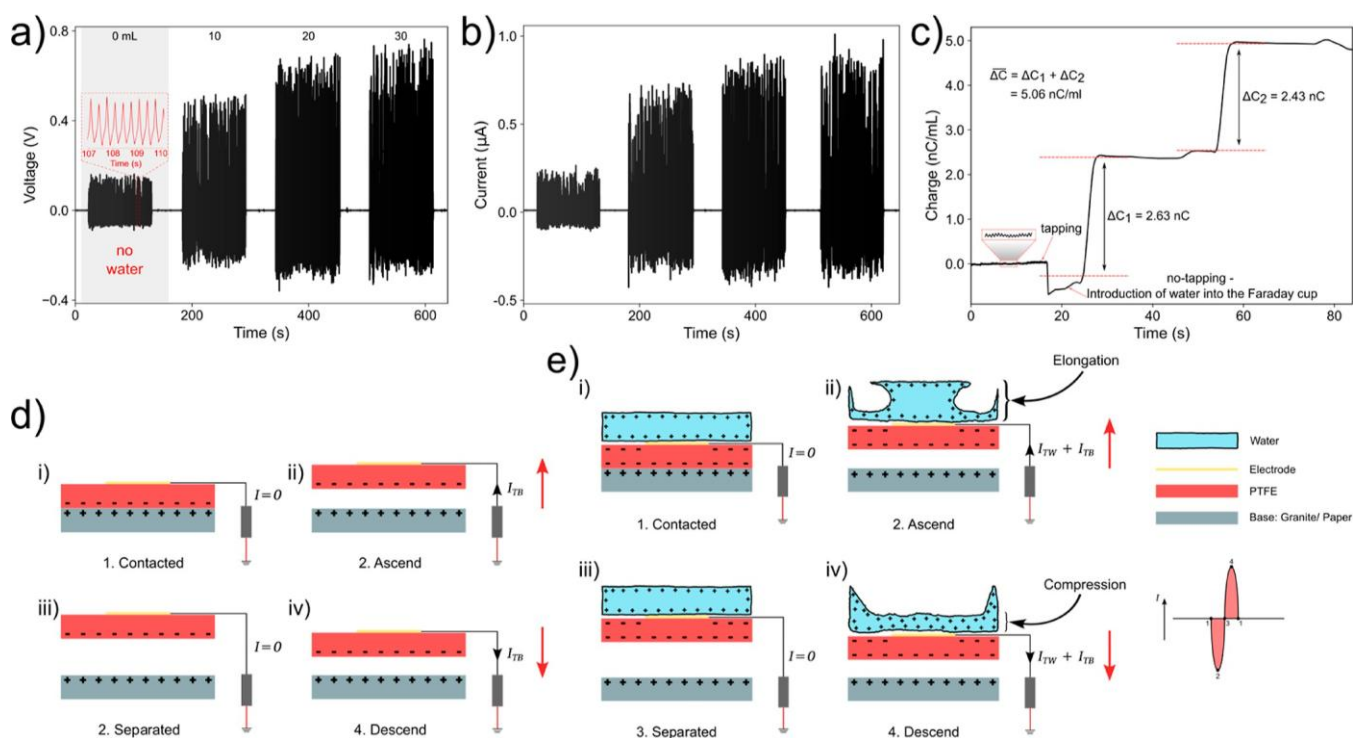


Figure 2. (a) Output voltage of the SE-EG at different volumes of water, and the inset shows the zoomed-in view of the voltage profile at 0 mL, (b) current with sequential addition of water in steps of 10 mL, (c) charge of water when tapped on the granite slab, (d,e) working mechanism of the SE-EG without and with water, respectively.

efficient heat transfer. The solid–solid type TG suffers from heating due to continuous rubbing and poor heat transfer of insulators, while the water-based TG has better heat dissipation.²⁴

Previous studies have discussed using water as a component in TGs/TENGs. However, the enhancement caused by the addition of water and the factors affecting it have hardly been discussed. These setups require water to start with and therefore lack distinction between those with and without the application of water. Furthermore, since the water-based TG operates under wet conditions, it becomes imperative to understand the effect of wetting properties of the electrode on the output performance.

In this article, we looked at the enhancement in the electric output (both voltage and current) by adding water and its subsequent charging in a PTFE beaker. We started with a simple setup that can harvest mechanical energy to produce electricity. As we progressively added water, a jump in the electric output was observed. By focusing on the energy harvesting aspect of charged water, we studied the effect of electrode wettability and pH on the output voltage. Furthermore, the effect of the electric field on the charging of water and its effect on output voltage have been studied. Additionally, through powering multiple light-emitting diodes (LEDs) with the setup, we have demonstrated the capacity of the process to drive low-power devices. The technique was further expanded for the treatment of dye-containing water by using a 3D-printed linear actuator (LA).

MATERIALS AND METHODS

Materials. Methylene blue (MB) was purchased from SRL. Sodium hydroxide (NaOH) pellets, sodium chloride (NaCl), and hydrochloric acid (HCl), were purchased from Rankem. An Al tape was purchased from the local market. A 200 mL PTFE beaker was

purchased from a local market. The beaker has an outer diameter of 6.8 cm, height of 8.8 cm, thickness of 0.24 cm, and a weight of 127 g. All measurements were performed in a temperature range of 23 ± 1.5 °C and humidity range of $51 \pm 2\%$ RH. The humidity was controlled using a OriginO60 Dehumidifier. The tapping force was calculated using an Arduino powered force sensing resistor sensor. However, the electrostatically charged PTFE beaker surface interfered with force measurement, making the accurate force measurement difficult.

Instrumentation. The UV–vis spectra were recorded by using a PerkinElmer Lambda 365 UV–vis spectrophotometer. The electrodes' morphology was studied using a Thermo Scientific Verios G4 UC SEM. The contact angle was measured using a GBX Digidrop contact angle meter with a $10 \mu\text{L}$ water droplet. The charge, current, and voltage measurements were performed by using a Keithley 6514 electrometer.

Design and Fabrication of the Faraday Cup. An in-house Faraday cup was designed and fabricated to accurately measure charges at the subnano Coulomb level. The design employed a two-level grounding scheme to protect the system against the external electrostatic field. Mu-metal shielding was introduced to protect against the magnetic field. To avoid electric contact, PTFE was used as a separator between metals. For charge measurement, the test material was introduced into the Faraday cup. To obtain the charge reading, the Faraday cup was connected to an electrometer. For data acquisition, Keithley ExceLINX software, which is an Add-in to Microsoft Excel, was used. The electrometer, Keithley 6514, was interfaced with the computer using an IEEE-488 USB to GPIB interface, Keithley KUSB-488B.

Linear Actuator. To perform continuous tapping for a long duration for dye-degradation experiments, a 3D-printed LA was developed. The modeling of the LA was done in FreeCAD and printed in a Flashforge Dreamer 3D-printer. The linear rail was driven using a servo motor (SG90) and controlled using a microcontroller, Xiao SAMD21. The programming was done in the Arduino IDE.

Preparation of the Electrode. The fabrication of hydrophilic (philic-) and hydrophobic (phobic-) Al electrodes were done by

modifying a previously described²⁵ method for the preparation of philic- and phobic-Cu surfaces.

Hydrophilic Aluminum. To make philic-Al, the metal tapes were dipped in 1 M aq. sol. NaOH for 14–17 min. Before dipping, the tapes were cut to the right size, and the adhesive side was kept well protected by sealing the back side with Teflon tape.

Hydrophobic Aluminum. The NaOH-treated philic-Al tapes were submerged in a 6 mM ethanol solution of stearic acid for 2 min and then kept for drying. Once dried, the process was repeated twice for a superior hydrophobic coating.

RESULTS AND DISCUSSION

Figure 1 illustrates the overall design of the experimental setup. Inside a PTFE beaker, aluminum tape (length = 3.5 cm, width = 2.5 cm, thickness = 30 μm) with conductive adhesive was stuck to the bottom. This Al tape acts as an electrode. While the electrode was pasting, a metal wire was attached to the tape on the adhesive side. For the measurement, a load was connected between the electrode and the ground, as shown in Figure 1a,b. When the beaker was tapped on a surface, here on a granite slab, the system acts like a single-electrode electrostatic (or a triboelectric) generator (SE-EG) and produces electricity. Since the bottom of the beaker had a ring-shaped protrusion (OD = 6.8 cm, ID = 4.8 cm) along its periphery, the actual contact area, ca. 18 cm^2 , was much smaller than the cross-sectional area of the beaker, as shown in Figure 1b. In order to characterize the system in detail, various parameters were varied systematically, as shown in Figure 1c. This includes measuring the output voltage with the change in volume of water added, pH of water, electrode wettability, and base material upon which the beaker was tapped. For the charge measurement, an in-house-developed Faraday cup was connected to the electrometer. Figure 1d shows a schematic of the charge measurement system. The power generation parameters (voltage and current) from the device are listed in Figure 2. Figure 2a,b shows the voltage and current profile when the beaker was tapped constantly on the granite slab. The inset in Figure 2a shows a zoomed-in view of the voltage waveform generated by the SE-EG at base voltage (0 mL). The beaker was tapped with a hand at a frequency of 3 Hz, as shown in Figure S1. The observed tapping height was 2.5–3 cm and tapping force was 2.5–2.7 N. Interestingly, when water was added sequentially into the beaker, both the voltage and the current showed an increase by more than 3 times (Figure 2a,b). This increase in electric output by addition can be attributed to the contact charging of water with PTFE, as shown by us previously¹² and by others.²⁶ The system was observed to be current-limiting, as the output current remains unchanged when measured across resistors ranging from 100 Ω to 1 $\text{M}\Omega$, while the voltage scales following Ohm's law with the increase in resistance. To uniformly compare different systems, we used 1 $\text{M}\Omega$ as a standard to measure the output voltage and current across all of the setups.

Figure 2c shows the charge measurement with normal water (pH 7) as a result of tapping on granite. Here, 20 mL of water was placed in a PTFE beaker and tapped for 15 s for contact charging. From this, 500 μL of water was collected using a custom-made PTFE pipette and transferred to the Faraday cup connected to the electrometer. This was to keep the nature of the contacting materials the same throughout the measurement. The value obtained was scaled to obtain the charge per mL of the liquid. The measurement was continued with fresh 500 μL , in steps.

Mechanism. The SE-EG without added water is essentially a typical TG in vertical contact-separation mode,^{27,28} whose working mechanism is shown in Figure 2d. The repeated contact between PTFE and granite causes charging. The periodic tapping motion between two charged surfaces generates an oscillating electric field. This changing electric field induces a change in the electric potential at the electrode surface. This leads to the push and pull of the electrons across the load, causing a current, I_{TB} , to flow. The cycle consists of four distinct phases. During contact, Figure 2d(i), and separation, Figure 2d(iii), positions, the negatively charged PTFE surface reverses its direction and comes to a temporary halt. Hence, there is no change in the induced electric field on the electrode and, consequently, zero I_{TB} . As the PTFE surface ascends, Figure 2d(ii), it moves away from the positively charged base, reducing the pull on electrons and causing them to be pushed away from the electrode. This increases the induced charge and drives I_{TB} toward the electrode. Conversely, during descent, Figure 2d(iv), the PTFE surface approaches the positively charged base, decreasing the induced charge on the electrode. This causes the electrons to move toward the electrode and hence the current, I_{TB} , away from it. The behavior is akin to how a charged object, when approaching a neutral gold leaf electroscope, induces a charge separation within the electroscope through electrostatic induction, causing its leaves to move apart. For instance, if a negatively charged object is near the electroscope, it repels the electrons. These electrons move away from the cap and accumulate on the gold leaves, making the cap positively charged and the leaves negatively charged. As a result, the leaves repel each other and spread apart. When the charged object is removed, the charge redistributes evenly throughout the electroscope, causing the leaves to collapse.^{2,29,30} Interestingly, if an oppositely charged object (in this case, positively charged) is brought near the negatively charged electroscope, it attracts some of the excess electrons. This decreases the induced negative charge on the leaves, decreasing their repulsion and causing reduced separation between the gold leaves.

With water added, as shown in Figure 2e, the rapid oscillation of the beaker over a small distance in a short period of time causes the sloshing of water.³¹ The combination of sloshing, as captured and explained in detail by Constantin et al.,³¹ and charging of water at the water–hydrophobic interface, as discussed previously, leads to the observed enhancement in the electric output. When the positively charged water in the beaker is stationary, as shown in Figure 2e(i), the negatively charged PTFE surface pushes electrons away from the electrode, while both the positively charged water and the positively charged base pull electrons toward it. As a result, the induced charge on the electrode (or the number of electrons pushed away) is less than it would be without water being present. When the beaker accelerates upward, as depicted in Figure 2e(ii), the water moves away from the base due to the rapid acceleration. This upward movement of the positively charged water increases the induced charge on the electrode by reducing the pull on the electrons, allowing the negatively charged PTFE to push more electrons away. The outward electron movement creates an inward current flow toward the electrode, adding excess current (I_{TW}) to the base current (I_{TB} , which occurs without water). During the beaker's downward descent, the water's inertia causes it to maintain its upward acceleration, lagging

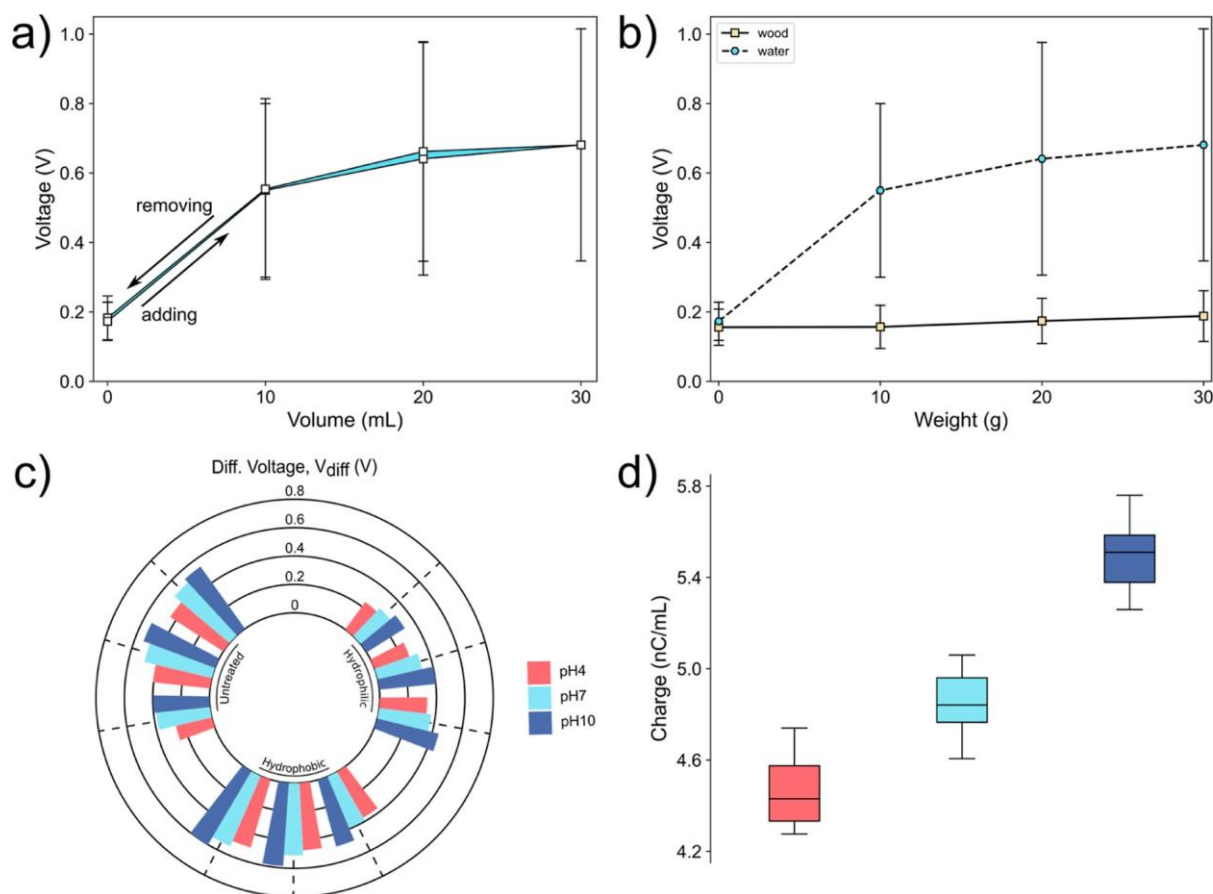


Figure 3. (a) Cyclic testing showing the role of water addition on peak voltage, (b) effect of weight on voltage output, (c) differential voltage, V_{diff} , at different pH for electrodes with different wettability, and (d) charge of water at different pH.

behind and eventually crashing against the beaker's base, forming a valley. This compression brings the positively charged water closer to the electrode, pulling electrons toward it and causing the current to flow away from the electrode, as shown in Figure 2e(iii). As the beaker reaches the top of its ascent and begins to reverse direction, it momentarily halts, resulting in no current flow, as illustrated in Figure 2e(iv). This cycle of movement creates a compound effect of water sloshing and charging within the PTFE beaker. The alternating current flows generated by these movements result in an enhanced electric output, demonstrating how mechanical motion can be converted into electrical energy through this triboelectric system.

Factors Affecting the Electric Output of the SE-EG. Cyclic Test and Effect of Weight. To test whether the increase in the output was indeed a result of the addition of water, we performed a cyclic test, in which we sequentially added water from 0 to 30 mL and then reduced it from 30 to 0 mL in steps of 10 mL and recorded the voltage in each step. The system traced back to almost the same values as shown in Figure 3a. The mean and standard deviation (error) for the peak voltages were calculated from the respective voltage output. At first, the peak values were obtained using the `find_peaks` function in the SciPy library³² in Python. For peak voltage calculation, all the peak values were recorded for 30 s period, from 70 to 100 s after the tapping began. This was to ensure the collection of the steady-state response of the system while avoiding any potential artifacts from the stopping process. Each measurement encompassed a total of 170 peak values, including both

the upper and the lower peaks of the voltage waveform. Following this, the mean value of the peak voltages was calculated to represent the average performance, while the standard deviation was computed to quantify the variability or error in the measurements. Each of the experiments was conducted at least twice to test the reproducibility of the result. In Appendix S1, we discuss in detail the calculation of the peak voltage. This cyclic test confirms that the addition of water is responsible for the observed enhancement in the electric output. It can also be argued that the jump in the output is due to the added weight of the liquid and not because of charging. To further strengthen our point that the observed increase in electric output was indeed because of the charging of the liquid, we tested the effect of weight on the output voltage. For this, three wooden blocks, each with a mass of 10–12 g and representing a mass of 10 mL of water, were placed in the beaker. Wood was chosen because of its antistatic nature. Since it does not get electrostatically charged,³³ it allows us to distinguish between the contributions of weight and electrostatic charging. We found that the addition of weight had only a minor effect, which was an order of magnitude smaller than that with water. As shown in Figure 3b, in the line plot of the output voltage for water and wood, the obtained voltage profile was almost flat, with only a slight increase with the addition of wooden weights. This further confirmed that weight alone has a very minimal effect on the output voltage, and the charging of liquids is important to account for the enhancement observed with water addition. In Figure S3, we show that a similar enhancement can be achieved with an electrode completely

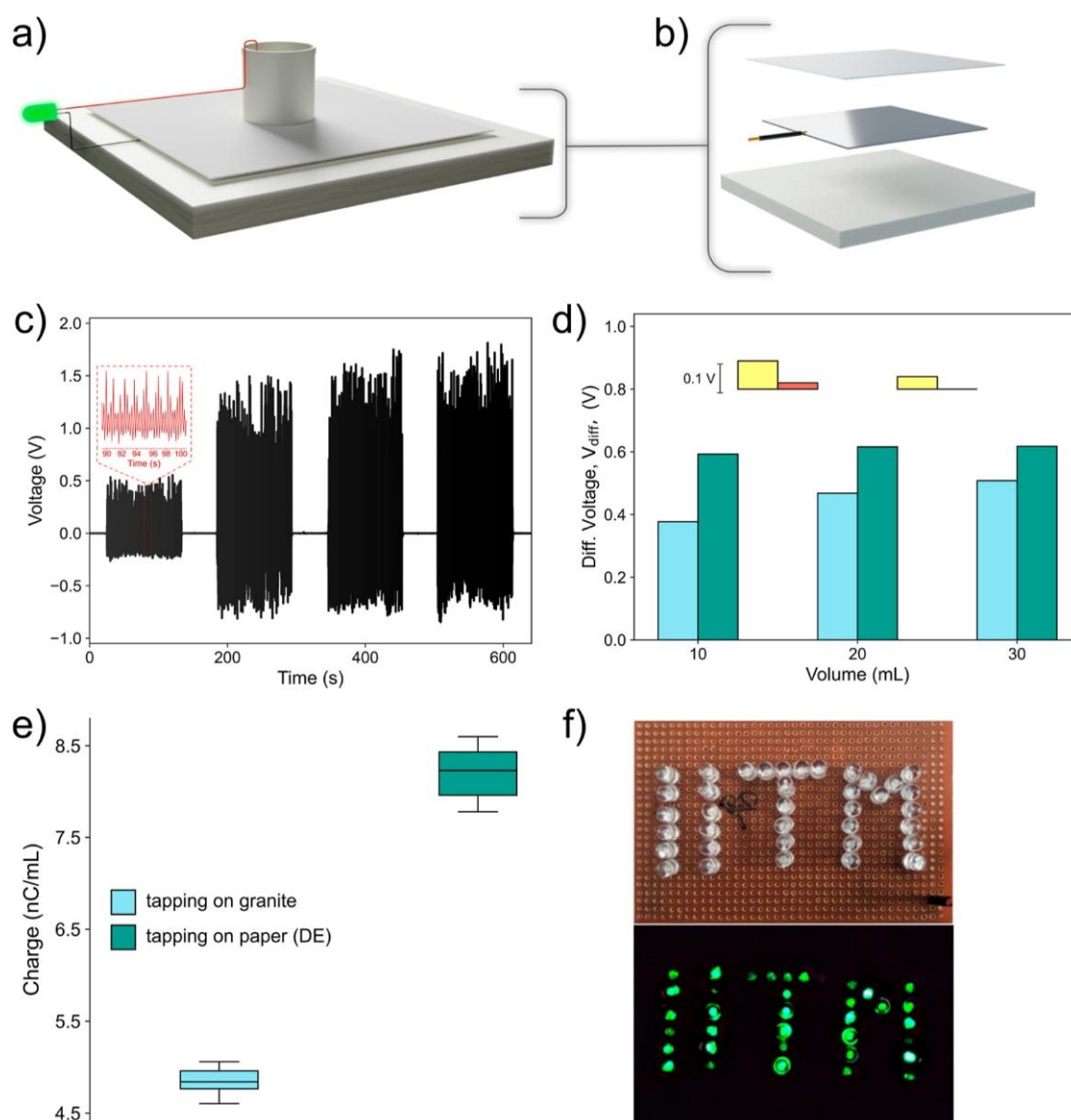


Figure 4. (a) Illustration of the DE-EG, (b) exploded view of the base, (c) output voltage of the DE-EG with subsequent addition of water, and the inset shows the zoomed-in view of the voltage profile at 0 mL, (d) bottom bar chart shows the differential voltage, V_{diff} , for SE-EG (light blue ■) and DE-EG (teal ■) and, the floating top bar chart shows the difference between consecutive voltages, $V_i - V_{i-1}$, for $i = 20$ and 30 mL for SE-EG (yellow ■) and DE-EG (coral ■), (e) charge of water when tapped on granite and paper, and (f) powering of multiple LEDs using the DE-EG.

covered with Teflon tape. This is significant because when exposed to a harsh environment, the electrode may get damaged, which will degrade the performance of the EG.

Effect of Electrode Wettability and pH. The effect of electrode wetting on the voltage output was investigated by fabricating electrodes with three distinct wetting patterns. To characterize the wetting properties of the prepared electrodes, contact angles were recorded. The measured values for philic-Al, untreated-Al, and phobic-Al electrodes were 37° , 74° , and 142° , respectively, as shown in Figure S4. The morphologies of the modified electrodes were captured by using FESEM at various magnifications. The FESEM images, Figure S5, showed a patchy-layered structure with grooves at deeper levels. Only one face of the electrode was modified, while the other side, which sticks to the Teflon beaker, was kept well protected by covering it with PTFE tape such that the conductivity was not lost. After the treatment, the electric continuity was checked on the back side to ensure that it was not lost in the process of

modification of the electrode surface. This was to ensure uninterrupted flow of the induced current during tapping. We compared the output voltage for each of these electrodes at pH 4, 7, and 10, as shown in Figure 3c. The pH 4 solution was prepared by the addition of HCl and the pH 10 by the addition of NaOH.

The differential voltage, V_{diff} , was compared for the three electrodes, i.e., philic-Al, untreated-Al, and phobic-Al, at three pH values. By differential voltage, we refer to a change in voltage with respect to the base voltage at 0 mL, i.e., $V_i - V_0$ where V_i represents voltage at i^{th} volume. From our experiments, we observed that this is a good way to negate small differences observed in the base value and allow an exclusive comparison of the effect of water addition. We observed a consistent increase in V_{diff} with increasing pH across all three electrodes, as shown in Figure 3c. This increase in voltage with pH corroborates well with higher charging with an increase in pH, as shown in Figure 3d. Previous studies have

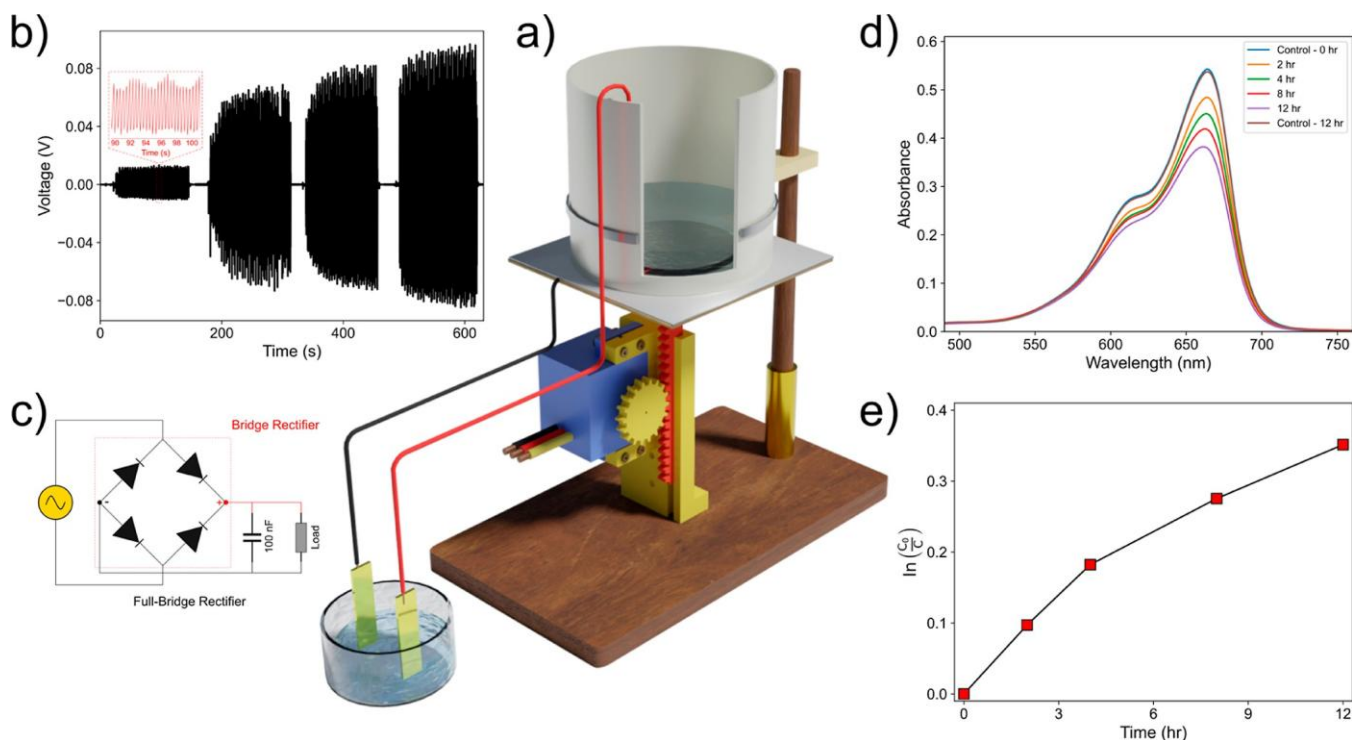


Figure 5. (a) Schematic of the LA, (b) output voltage of the LAB-EG at different volumes of water, and the inset shows the zoomed-in view of the voltage profile at 0 mL, (c) schematic of a full-bridge rectifier, (d) time-dependent UV-vis absorption spectra of MB solution, and (e) plot of $\ln(C_0/C)$ vs time for MB degradation.

shown positive charging of water on a water-polymer interface³⁴ and an observed increase in charge of water with pH.³⁵ Similarly, a decrease in ζ -potential was observed for the hydrophobic surface with pH at the water-hydrophobic interface.¹³ From Figure 3c, it appears that with an increase in electrode hydrophobicity, the output voltage increases. This may be because of better separation between the water and the hydrophobic electrode, which could result in better induction on the electrode surface.

Extension to a Double-Electrode System. In several electrochemical processes, two-electrode systems are required. With a simple modification, a single-electrode (SE) system was converted to a double-electrode (DE) system. A schematic of the modified DE system is illustrated in Figure 4a,b. To fabricate a DE-EG, a sheet of office paper was attached on top of aluminum foil. The paper was used as it is readily available, cheap, easy to work, and our prior experience of using it for the TG.²⁰ One output was taken from the foil, and the other was taken from the electrode inside the beaker. Figure 4c shows the voltage characteristic of the DE-EG. In Figure S6, we have shown the zoomed-in view of the voltage profile of the DE-EG for different volumes of water. In Figure 4d, the bottom bar chart depicts a differential voltage, V_{diff} , whereas the floating top bar chart shows the difference in the consecutive voltage readings, $V_i - V_{i-1}$, for $i = 20$ and 30 mL, for the SE-EG and DE-EG, respectively. For both the SE-EG and DE-EG, the jump in the voltage was highest for the first 10 mL added as it has a contribution from the bottom and side walls of the beaker. The subsequent additions only have contribution from the side wall, which leads to a smaller increase in voltage from 10 mL onward, as seen from Figure 4d (top). Furthermore, moving from 20 to 30 mL, we observed an even smaller increase compared to moving from 10 to 20 mL. This may be

due to the increase in separation between the top water surface and the bottom Al electrode. As most of the charge of water stays on the surface, this increase in separation causes a decrease in induced field experienced by the electrode, leading to a smaller rise in voltage.

We were expecting the change in the voltage from the base voltage with the addition of water (or the differential voltage, V_{diff}) to be similar for the two systems. The added water was solely in contact with the interior walls of the PTFE beaker, which was the same for both the SE-EG and DE-EG. Since the contacting areas were the same, the charging should be the same, and, hence, the V_{diff} should be the same. However, there was a significant increase in the differential voltage with the addition of water for the DE-EG compared to the SE-EG, as shown in Figure 4d. The higher base voltage (at 0 mL) for the DE-EG was expected because of the higher charging of the PTFE with paper than with granite, and this increase was reflected in their base voltage. The higher charging of the PTFE-paper interface for the DE-EG also meant that the water present in the beaker was exposed to higher electric field. We investigated whether the higher voltage jump from the base value for the DE-EG was the result of increased charging in the presence of stronger electric field. We have observed that when tapped on paper, the water in the PTFE beaker exhibited a significantly higher charge than on the granite, as shown in Figure 4e. This confirms that the charge of water scales (or increases) with the external electric field, which was reflected as the jump in output voltage. Previous studies^{17,36,37} have also shown such scaling of charge for water with the electric field. It is possible that this scaling of charge was due to the induced charging in the presence of an electric field.

The energy harvesting capability of the DE-EG was used to power multiple LEDs (37 in total), as shown in Figure 4f. This

demonstrates the utility of such systems in powering low-power electronics. We have tested the potential of such a power source for the treatment of wastewater containing dyes. A 3D-printed LA was used to do continuous tapping on the PTFE beaker fixed steadily to a buret stand. Much like the DE-EG, the LA-Beaker (LAB-EG) system is a two-electrode system. An Al-foil with paper attached on top was fixed on the rail of the actuator with the support of thick cardboard. A wire was attached to the foil as an output. The beaker, as before, had an electrode attached to the bottom, to which a wire was attached as another output. The two output wires were attached to two gold coated silica wafers acting as electrodes, which was inserted into a small beaker containing MB solution.²⁰ Figure 5a shows an illustration of the setup. As the rail of the actuator moves, the paper taps on the bottom of the beaker. This continuous tapping leads to the negative charging of the PTFE. The up-and-down movement of the rail produces an oscillating electric field between the two charged surfaces. This generates an electric current through induction at the electrodes. The tapping frequency of the LA was 2.5 Hz, as shown in Figure S7. The voltage output of the LAB-EG is shown in Figure 5b. The inset displays a zoomed-in base voltage (0 mL) profile. The Figure S8 shows a close-up view of the voltage profile for different volumes of water. The AC was converted to DC using a bridge rectifier and a filtering capacitor (100 nF) to smoothen the output DC voltage, as shown in Figure 5c. For the degradation, the electricity generated by the system was transferred to a small glass container filled with 6 mL of 2.5 ppm aqueous solution of MB with 100 ppm of NaCl. To enhance the output voltage, the tapping was performed with 20 mL of water in the beaker. It has been previously reported that the presence of salt increases the conductivity of the solution, which helps in the degradation process.³⁸ Furthermore, the presence of Cl⁻ produces various oxidants at the anode that promote the oxidation of the dye and hence faster degradation.³⁹ The degradation of MB was monitored periodically using a UV-vis spectrophotometer.

A decrease in MB peak intensity was recorded as the tapping progressed, confirming the degradation, as shown in Figure 5d. The degradation rate, k of the MB solution was calculated from the slope of the linear fit to the first-order equation, $\ln(C_0/C) = \ln(A_0/A) = k \cdot t$, where C_0 and A_0 and C and A are the concentration and absorption at time, $t = 0$ and t , respectively, at 664 nm, as shown in Figure 5e. The degradation rate, k obtained was 0.028 (h⁻¹) from the linear fit. The degree of degradation achieved was limited by the low power of the micro servo motor, which restricts the sloshing effect, resulting in a diminished electric output. The technique appears promising for harvesting energy from water currents.

Note on Sustainability. The methodology presented further improves electrostatic energy harvesting, a sustainable means of energy generation. The use of water in the process further improves the sustainability aspects as the only additional material needed for the enhanced energy generation is water, which is sustainable. Various types of mechanical energy may be used for the operation, including wind, water flow, etc. The utility of the process at multiple scales of operation may be visualized, at both micro- and macro scales.

CONCLUSIONS

In this study, we have shown enhancement in the electrical output of the EG by the addition of water. We demonstrated, through various measurements, that the charging of water was

responsible for the increased output. We further identified the sloshing of charged water in the beaker during tapping as the primary mechanism for the observed enhancement. Furthermore, the study explored the influence of pH on electrodes with different wettabilities and electric fields on the charging of water and resulting output voltage. Experiments on the effects of pH on output voltage have shown that increasing the pH led to a more pronounced charging of water and, consequently, an increase in the output voltage. Similarly, an increase in external electric field was observed to increase the charging of water, resulting in an increased output voltage. This means that both contact (streaming) electrification and induction charging could contribute to the electrification of water. The electricity generated could be used to power low-power electronics, as demonstrated by lighting multiple LEDs. We also showed that such systems could be useful in the treatment of wastewater containing a dye. Furthermore, the conclusions drawn in this work could be useful in diverse areas such as mass spectrometry, energy harvesting, electrospinning, electrowetting, electrohydrodynamic coatings, microfluidics, materials synthesis, electrophotography, and inkjet printing.

ASSOCIATED CONTENT

Supporting Information

The Supporting Information is available free of charge at <https://pubs.acs.org/doi/10.1021/acssuschemeng.4c01860>.

Tapping frequency distribution of the beaker using a hand, peak voltage calculation, illustration of peak-voltage calculation from a single pulse, output voltage of the SE-EG with the electrode covered, bar chart showing the contact angle of electrodes, FESEM images of electrodes, zoomed-in view of the voltage profile of DE-EG, tapping frequency distribution of the LA and its photograph, and zoomed-in view of the voltage profile of LAB-EG (PDF)

AUTHOR INFORMATION

Corresponding Authors

Ramamurthy Nagarajan – Department of Chemical Engineering, Indian Institute of Technology Madras, Chennai 600036, India; Email: nag@iitm.ac.in

Thalappil Pradeep – Department of Chemistry, DST Unit of Nanoscience (DST UNS) and Thematic Unit of Excellence (TUE), Indian Institute of Technology Madras, Chennai 600036, India; International Centre for Clean Water, IITM Research Park, Chennai 600113, India; orcid.org/0000-0003-3174-534X; Email: pradeep@iitm.ac.in

Authors

Vishal Kumar – Department of Chemistry, DST Unit of Nanoscience (DST UNS) and Thematic Unit of Excellence (TUE), Indian Institute of Technology Madras, Chennai 600036, India; Department of Chemical Engineering, Indian Institute of Technology Madras, Chennai 600036, India; orcid.org/0000-0002-2374-0568

Pillalamarri Srikrishnarka – Department of Chemistry, DST Unit of Nanoscience (DST UNS) and Thematic Unit of Excellence (TUE), Indian Institute of Technology Madras, Chennai 600036, India; Department of Chemical Engineering, Indian Institute of Technology Madras, Chennai 600036, India; orcid.org/0000-0001-5187-6879

Complete contact information is available at:

<https://pubs.acs.org/10.1021/acssuschemeng.4c01860>

Author Contributions

V.K., R.N., and T.P. conceptualized the project. V.K. performed the experiments. P.S. assisted in characterizing the samples. All the authors contributed to writing the manuscript.

Notes

The authors declare no competing financial interest.

ACKNOWLEDGMENTS

We thank the Department of Science and Technology, Government of India, for supporting our research program. V.K. and P.S. acknowledge IIT Madras for their research fellowships. T.P. acknowledges funding from the Centre of Excellence on Molecular Materials and Functions under the Institution of Eminence scheme of IIT Madras.

REFERENCES

- (1) Thomson, W. On a Self-Acting Apparatus for Multiplying and Maintaining Electric Charges, with Applications to Illustrate the Voltaic Theory. *Proc. R. Soc. London* 1868, 16, 67–72.
- (2) Treglohan, T. P. *Frictional Electricity*; Longmans, Green, and Company, 1886.
- (3) Harris, S. W. S.; Tomlinson, C. A. Treatise on Frictional Electricity. In *Theory and Practice*; Virtue, 1867.
- (4) Touchard, G. Flow Electrification of Liquids. *J. Electrostat.* 2001, 51–52, 440–447.
- (5) Creux, P.; Lachaise, J.; Graciaa, A.; Beattie, J. K.; Djerdjev, A. M. Strong Specific Hydroxide Ion Binding at the Pristine Oil/Water and Air/Water Interfaces. *J. Phys. Chem. B* 2009, 113 (43), 14146–14150.
- (6) Schoeler, A. M.; Josephides, D. N.; Sajjadi, S.; Lorenz, C. D.; Mesquida, P. Charge of Water Droplets in Non-Polar Oils. *J. Appl. Phys.* 2013, 114 (14), 144903.
- (7) Yatsuzuka, K.; Mizuno, Y.; Asano, K. Electrification Phenomena of Pure Water Droplets Dripping and Sliding on a Polymer Surface. *J. Electrostat.* 1994, 32 (2), 157–171.
- (8) Yatsuzuka, K.; Higashiyama, Y.; Asano, K. Electrification of Polymer Surface Caused by Sliding Ultrapure Water. *IEEE Trans. Ind. Appl.* 1996, 32 (4), 825–831.
- (9) Kudin, K. N.; Car, R. Why Are Water–Hydrophobic Interfaces Charged? *J. Am. Chem. Soc.* 2008, 130 (12), 3915–3919.
- (10) Burgo, T. A. L.; Galembeck, F.; Pollack, G. H. Where Is Water in the Triboelectric Series? *J. Electrostat.* 2016, 80, 30–33.
- (11) Wang, J.; Cao, L. J. The Study on Flow Electrification of Oil-Cellulose Insulating System in Large Power Transformer. *Proceedings 1995 International Conference on Energy Management and Power Delivery EMPD '95*, 1995; Vol. 1, p 422.
- (12) Nag, A.; Baksi, A.; Ghosh, J.; Kumar, V.; Bag, S.; Mondal, B.; Ahuja, T.; Pradeep, T. Tribochemical Degradation of Polytetrafluoroethylene in Water and Generation of Nanoplastics. *ACS Sustain. Chem. Eng.* 2019, 7 (21), 17554–17558.
- (13) Marinova, K. G.; Alargova, R. G.; Denkov, N. D.; Velev, O. D.; Petsev, D. N.; Ivanov, I. B.; Borwankar, R. P. Charging of Oil–Water Interfaces Due to Spontaneous Adsorption of Hydroxyl Ions. *Langmuir* 1996, 12 (8), 2045–2051.
- (14) Yan, X.; Delgado, M.; Aubry, J.; Gribelin, O.; Stocco, A.; Boisson-Da Cruz, F.; Bernard, J.; Ganachaud, F. Central Role of Bicarbonate Anions in Charging Water/Hydrophobic Interfaces. *J. Phys. Chem. Lett.* 2018, 9 (1), 96–103.
- (15) Manciu, M.; Ruckenstein, E. Ions near the Air/Water Interface: I. Compatibility of Zeta Potential and Surface Tension Experiments. *Colloids Surf., A* 2012, 400, 27–35.
- (16) Santos, L. P.; Ducati, T. R. D.; Balestrin, L. B. S.; Galembeck, F. Water with Excess Electric Charge. *J. Phys. Chem. C* 2011, 115 (22), 11226–11232.
- (17) Nauruzbayeva, J.; Sun, Z.; Gallo, A.; Ibrahim, M.; Santamarina, J. C.; Mishra, H. Electrification at Water–Hydrophobe Interfaces. *Nat. Commun.* 2020, 11 (1), 5285.
- (18) Fan, F.-R.; Tian, Z.-Q.; Lin Wang, Z. Flexible Triboelectric Generator. *Nano Energy* 2012, 1 (2), 328–334.
- (19) Nie, J.; Wang, Z.; Ren, Z.; Li, S.; Chen, X.; Lin Wang, Z. Power Generation from the Interaction of a Liquid Droplet and a Liquid Membrane. *Nat. Commun.* 2019, 10 (1), 2264.
- (20) Kumar, V.; Srikrishnarka, P.; Mohanty, J. S.; Kannan, M. P.; Nagarajan, R.; Pradeep, T. Triboelectric Generators for Sustainable Reduction Leading to Nanoparticles and Nanoclusters. *ACS Sustain. Chem. Eng.* 2021, 9 (22), 7431–7436.
- (21) Kim, T.; Chung, J.; Kim, D. Y.; Moon, J. H.; Lee, S.; Cho, M.; Lee, S. H.; Lee, S. Design and Optimization of Rotating Triboelectric Nanogenerator by Water Electrification and Inertia. *Nano Energy* 2016, 27, 340–351.
- (22) Zhang, Q.; Li, Y.; Cai, H.; Yao, M.; Zhang, H.; Guo, L.; Lv, Z.; Li, M.; Lu, X.; Ren, C.; Zhang, P.; Zhang, Y.; Shi, X.; Ding, G.; Yao, J.; Yang, Z.; Wang, Z. L. A Single-Droplet Electricity Generator Achieves an Ultrahigh Output Over 100 V Without Pre-Charging. *Adv. Mater.* 2021, 33 (51), 2105761.
- (23) Xu, W.; Zheng, H.; Liu, Y.; Zhou, X.; Zhang, C.; Song, Y.; Deng, X.; Leung, M.; Yang, Z.; Xu, R. X.; Wang, Z. L.; Zeng, X. C.; Wang, Z. A Droplet-Based Electricity Generator with High Instantaneous Power Density. *Nature* 2020, 578 (7795), 392–396.
- (24) Munirathinam, K.; Kim, D.-S.; Shanmugasundaram, A.; Park, J.; Jeong, Y.-J.; Lee, D.-W. Flowing Water-Based Tubular Triboelectric Nanogenerators for Sustainable Green Energy Harvesting. *Nano Energy* 2022, 102, 107675.
- (25) Zhu, X.; Zhang, Z.; Men, X.; Yang, J.; Xu, X. Rapid Formation of Superhydrophobic Surfaces with Fast Response Wettability Transition. *ACS Appl. Mater. Interfaces* 2010, 2 (12), 3636–3641.
- (26) McCarty, L. S.; Whitesides, G. M. Electrostatic Charging Due to Separation of Ions at Interfaces: Contact Electrification of Ionic Electrets. *Angew. Chem., Int. Ed.* 2008, 47 (12), 2188–2207.
- (27) Niu, S.; Wang, Z. L. Theoretical Systems of Triboelectric Nanogenerators. *Nano Energy* 2015, 14, 161–192.
- (28) Zhang, H.; Yao, L.; Quan, L.; Zheng, X. Theories for Triboelectric Nanogenerators: A Comprehensive Review. *Nanotechnol. Rev.* 2020, 9 (1), 610–625.
- (29) Bennet, A. Description of a New Electrometer. In a Letter from the Rev. Abraham Bennet, M. A. to the Rev. Joseph Priestley, LL.D. F. R. S. *Philos. Trans. R. Soc. London* 1787, 77, 26–31.
- (30) *Encyclopedia Britannica*, 11th ed.; Encyclopedia Britannica Inc., 1910; Vol. 9.
- (31) Constantin, L.; De Courcy, J. J.; Titurus, B.; Rendall, T. C. S.; Cooper, J. E. Sloshing Induced Damping across Froude Numbers in a Harmonically Vertically Excited System. *J. Sound Vib.* 2021, 510, 116302.
- (32) Virtanen, P.; Gommers, R.; Oliphant, T. E.; Haberland, M.; Reddy, T.; Cournapeau, D.; Burovski, E.; Peterson, P.; Weckesser, W.; Bright, J.; Van Der Walt, S. J.; Brett, M.; Wilson, J.; Millman, K. J.; Mayorov, N.; Nelson, A. R. J.; Jones, E.; Kern, R.; Larson, E.; Carey, C. J.; Polat, I.; Feng, Y.; Moore, E. W.; VanderPlas, J.; Laxalde, D.; Perktold, J.; Cimrman, R.; Henriksen, I.; Quintero, E. A.; Harris, C. R.; Archibald, A. M.; Ribeiro, A. H.; Pedregosa, F.; Van Mulbregt, P.; Vijaykumar, A.; Bardelli, A. P.; Rothberg, A.; Hilboll, A.; Kloeckner, A.; Scopatz, A.; Lee, A.; Rokem, A.; Woods, C. N.; Fulton, C.; Masson, C.; Häggström, C.; Fitzgerald, C.; Nicholson, D. A.; Hagen, D. R.; Pasechnik, D. V.; Olivetti, E.; Martin, E.; Wieser, G.; Silva, F.; Lenders, F.; Wilhelm, F.; Young, G.; Price, G. A.; Ingold, G. L.; Allen, G. E.; Lee, G. R.; Audren, H.; Probst, I.; Dietrich, J. P.; Silterra, J.; Webber, J. T.; Slavič, J.; Nothman, J.; Buchner, J.; Kulick, J.; Schönberger, J. L.; de Miranda Cardoso, J. V.; Reimer, J.; Harrington, J.; Rodríguez, J. L. C.; Nunez-Iglesias, J.; Kuczynski, J.; Tritz, K.; Thoma, M.; Newville, M.; Kümmerer, M.; Bolingbroke, M.; Tartre, M.; Pak, M.; Smith, N. J.; Nowaczyk, N.; Shebanov, N.; Pavlyk, O.; Brodtkorb, P. A.; Lee, P.; McGibbon, R. T.; Feldbauer, R.; Lewis, S.; Tygier, S.; Sievert, S.; Vigna, S.; Peterson, S.; More, S.; Pudlik, T.

Oshima, T.; Pingel, T. J.; Robitaille, T. P.; Spura, T.; Jones, T. R.; Cera, T.; Leslie, T.; Zito, T.; Krauss, T.; Upadhyay, U.; Halchenko, Y. O.; Vázquez-Baeza, Y.; Vázquez-Baeza, Y. SciPy 1.0: Fundamental Algorithms for Scientific Computing in Python. *Nat. Methods* 2020, *17* (3), 261–272.

(33) Özel, M.; Demir, F.; Aikebaier, A.; Kwiczak-Yiğitbaşı, J.; Baytekin, H. T.; Baytekin, B. Why Does Wood Not Get Contact Charged? Lignin as an Antistatic Additive for Common Polymers. *Chem. Mater.* 2020, *32* (17), 7438–7444.

(34) Roger, K.; Cabane, B. Why Are Hydrophobic/Water Interfaces Negatively Charged? *Angew. Chem., Int. Ed.* 2012, *51* (23), 5625–5628.

(35) Choi, D.; Lee, H.; Im, D. J.; Kang, I. S.; Lim, G.; Kim, D. S.; Kang, K. H. Spontaneous Electrical Charging of Droplets by Conventional Pipetting. *Sci. Rep.* 2013, *3* (1), 2037.

(36) Elton, E. S.; Tibrewala, Y. V.; Ristenpart, W. D. Statistical Analysis of Droplet Charge Acquired during Contact with Electrodes in Strong Electric Fields. *Langmuir* 2019, *35* (11), 3937–3948.

(37) Im, D. J.; Noh, J.; Moon, D.; Kang, I. S. Electrophoresis of a Charged Droplet in a Dielectric Liquid for Droplet Actuation. *Anal. Chem.* 2011, *83* (13), 5168–5174.

(38) Samarghandi, M. R.; Dargahi, A.; Shabanloo, A.; Nasab, H. Z.; Vaziri, Y.; Ansari, A. Electrochemical Degradation of Methylene Blue Dye Using a Graphite Doped PbO₂ Anode: Optimization of Operational Parameters, Degradation Pathway and Improving the Biodegradability of Textile Wastewater. *Arabian J. Chem.* 2020, *13* (8), 6847–6864.

(39) Baddouh, A.; Bessegato, G. G.; Rguiti, M. M.; El Ibrahimi, B.; Bazzi, L.; Hilali, M.; Zanoni, M. V. B. Electrochemical Decolorization of Rhodamine B Dye: Influence of Anode Material, Chloride Concentration and Current Density. *J. Environ. Chem. Eng.* 2018, *6* (2), 2041–2047.

Supporting Information

Enhanced Electrical Output in an Electrostatic Generator Using Charged Water

Vishal Kumar,^{†‡} Pillalamarri Srikrishnarka,^{†‡} Ramamurthy Nagarajan,^{‡*} Thalappil Pradeep^{†*}

[†]*Department of Chemistry, DST Unit of Nanoscience (DST UNS) and Thematic Unit of Excellence (TUE), Indian Institute of Technology Madras, Chennai 600036, India*

[◆]*International Centre for Clean Water, IITM Research Park, Chennai 600113, India*

[‡]*Department of chemical Engineering, Indian Institute of Technology Madras, Chennai 600036, India*

*E-mail: pradeep@iitm.ac.in

*E-mail: nag@iitm.ac.in

Number of pages : 10

Number of figures : 8

Table of Contents

S. No.	Description	Page No.
Figure S1	Tapping frequency distribution of the beaker using a hand	S3
Appendix – S1	Peak Voltage Calculation	S4
Figure S2	Illustration of peak-voltage calculation from a single pulse	S4
Figure S3	Output voltage of the SE-EG with electrode covered	S5
Figure S4	Bar chart showing the contact angle of electrodes	S6
Figure S5	FESEM images of electrodes	S7
Figure S6	The voltage output of DE-EG along with zoomed-in view of the voltage profile at various water volumes.	S8
Figure S7	Tapping frequency distribution of the LA and its photograph.	S9
Figure S8	The voltage output of LAB-EG along with zoomed-in view of the voltage profile at various water volumes.	S10

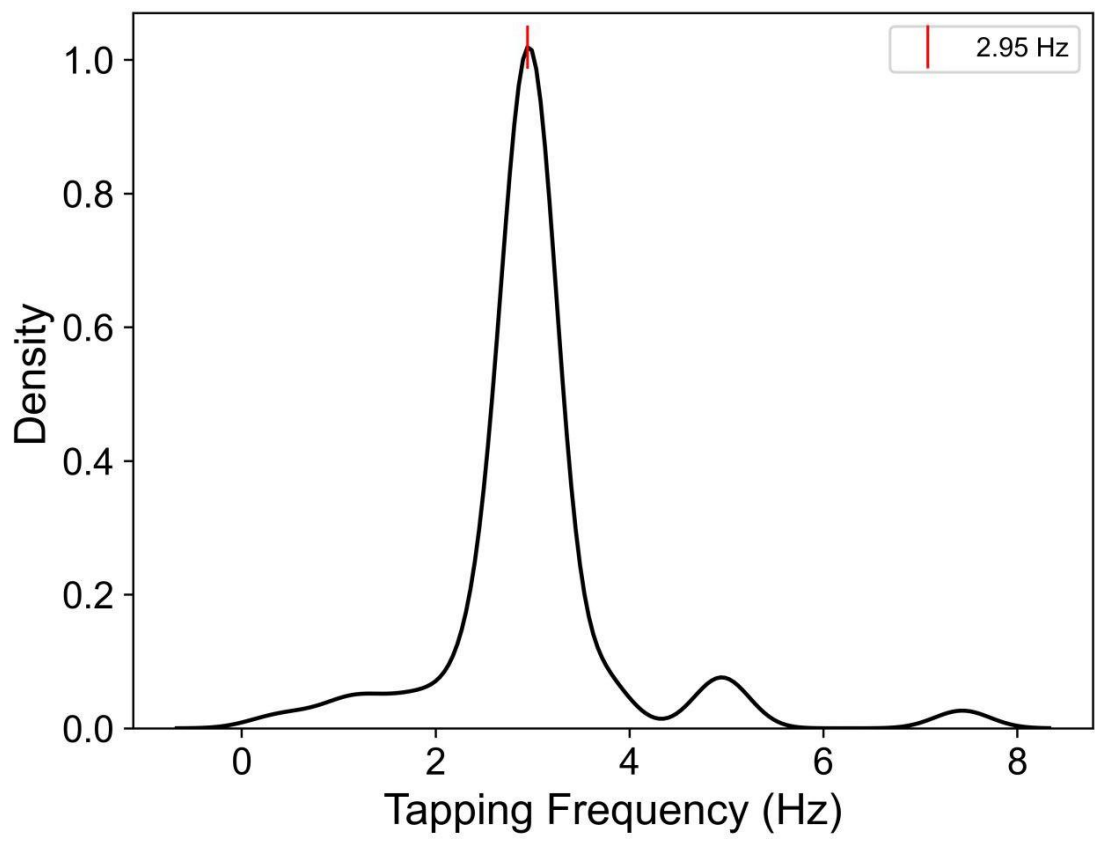


Figure S1. Tapping frequency distribution of the beaker using a hand.

Appendix – S1

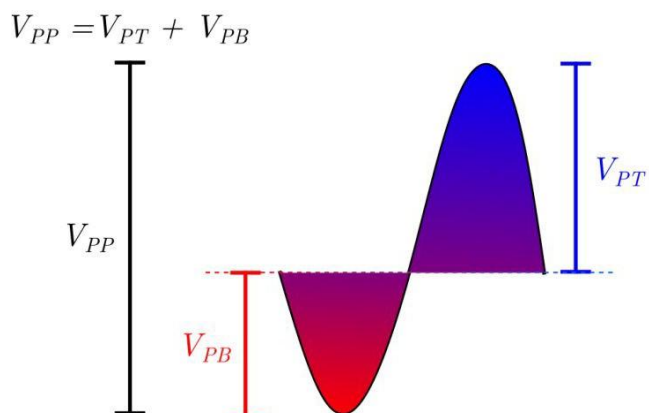


Figure S2. Illustration of peak-voltage calculation from a single pulse.

V_{PP} is the peak-to-peak voltage.

$$V_{PP} = V_{PB} + V_{PT} \quad (1)$$

where V_{PB} and V_{PT} are the bottom and top-peak voltage, respectively.

The peak-voltage, V_P is

$$V_P = \frac{V_{PP}}{2} \quad (2)$$

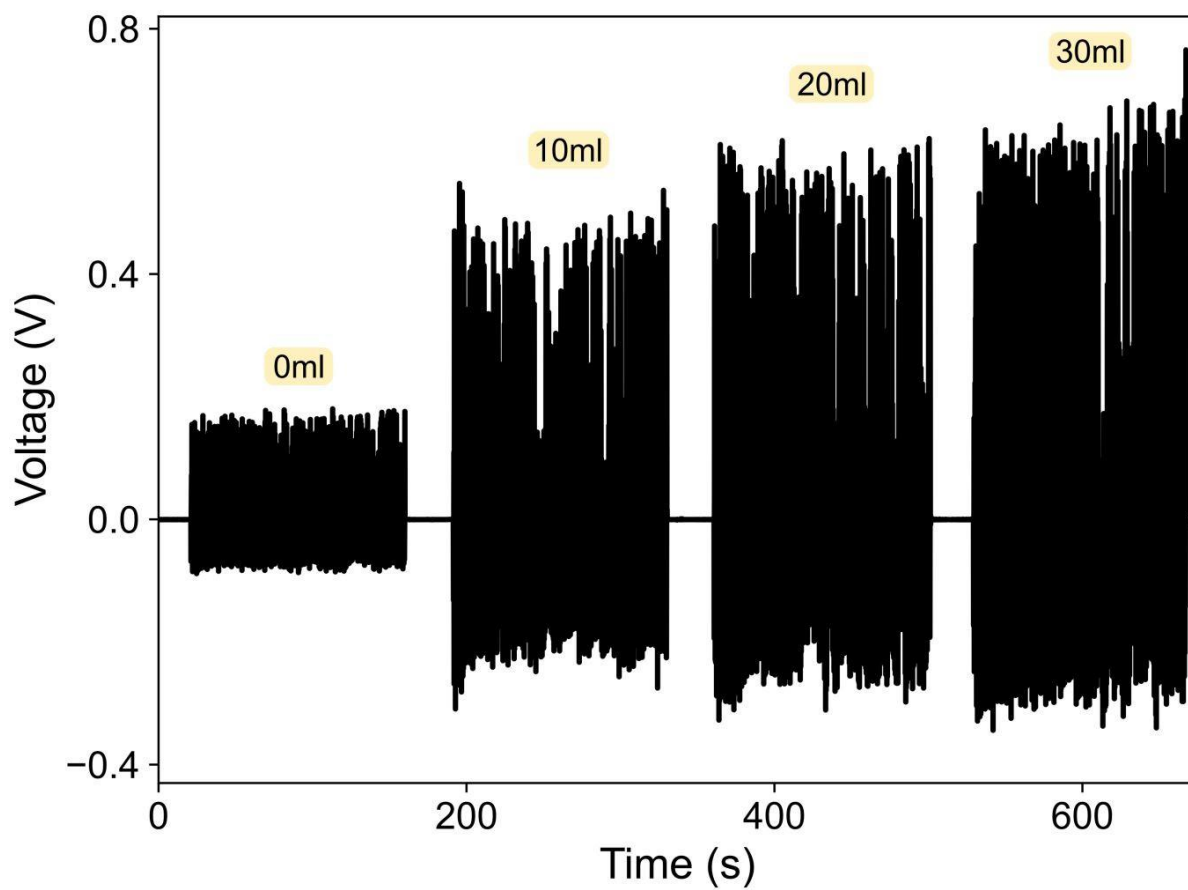


Figure S3. The output voltage of the SE-EG with electrode covered.

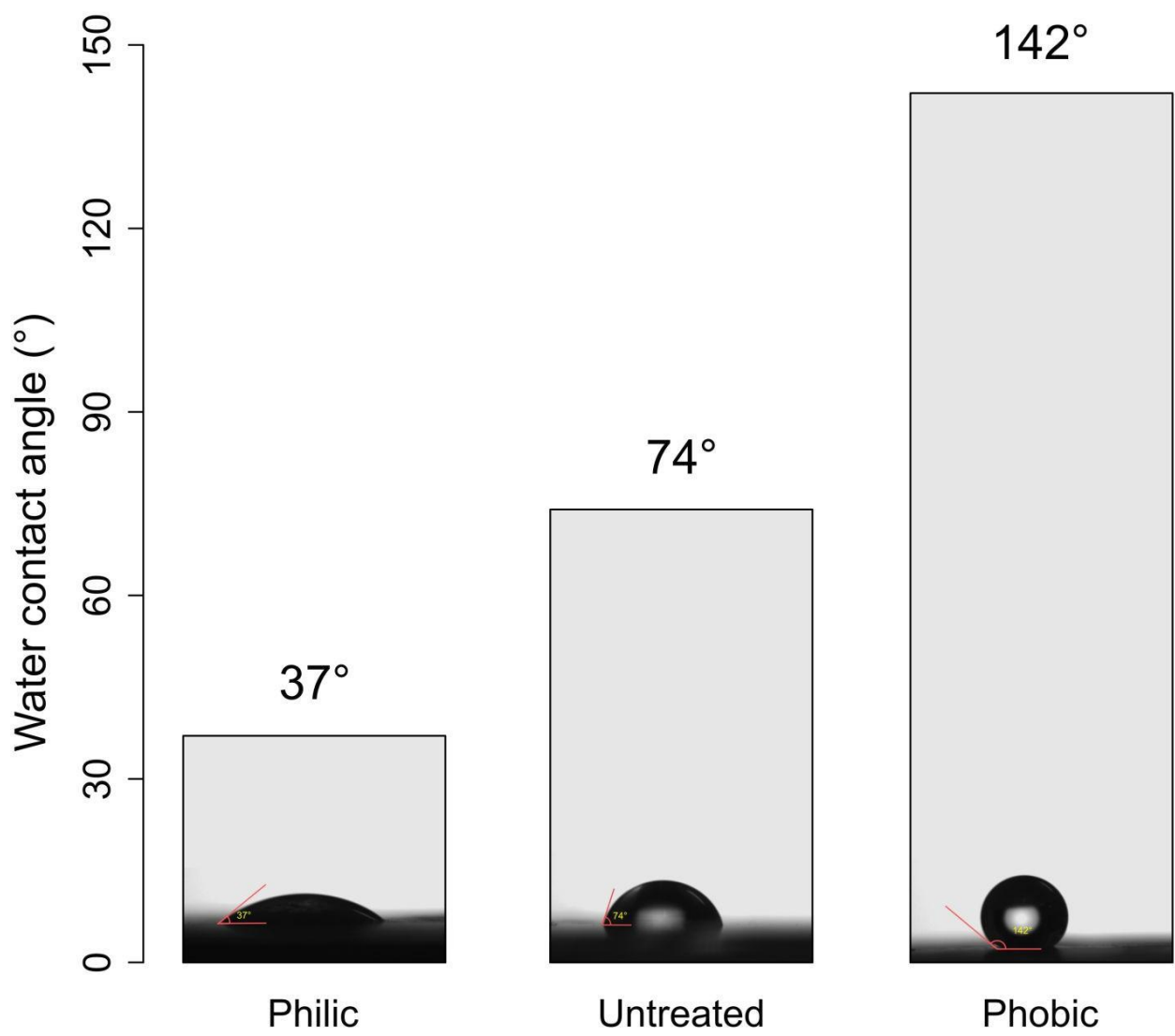


Figure S4. Bar chart showing contact angle of electrodes – Philic-Al, Untreated-Al, and Phobic-Al.

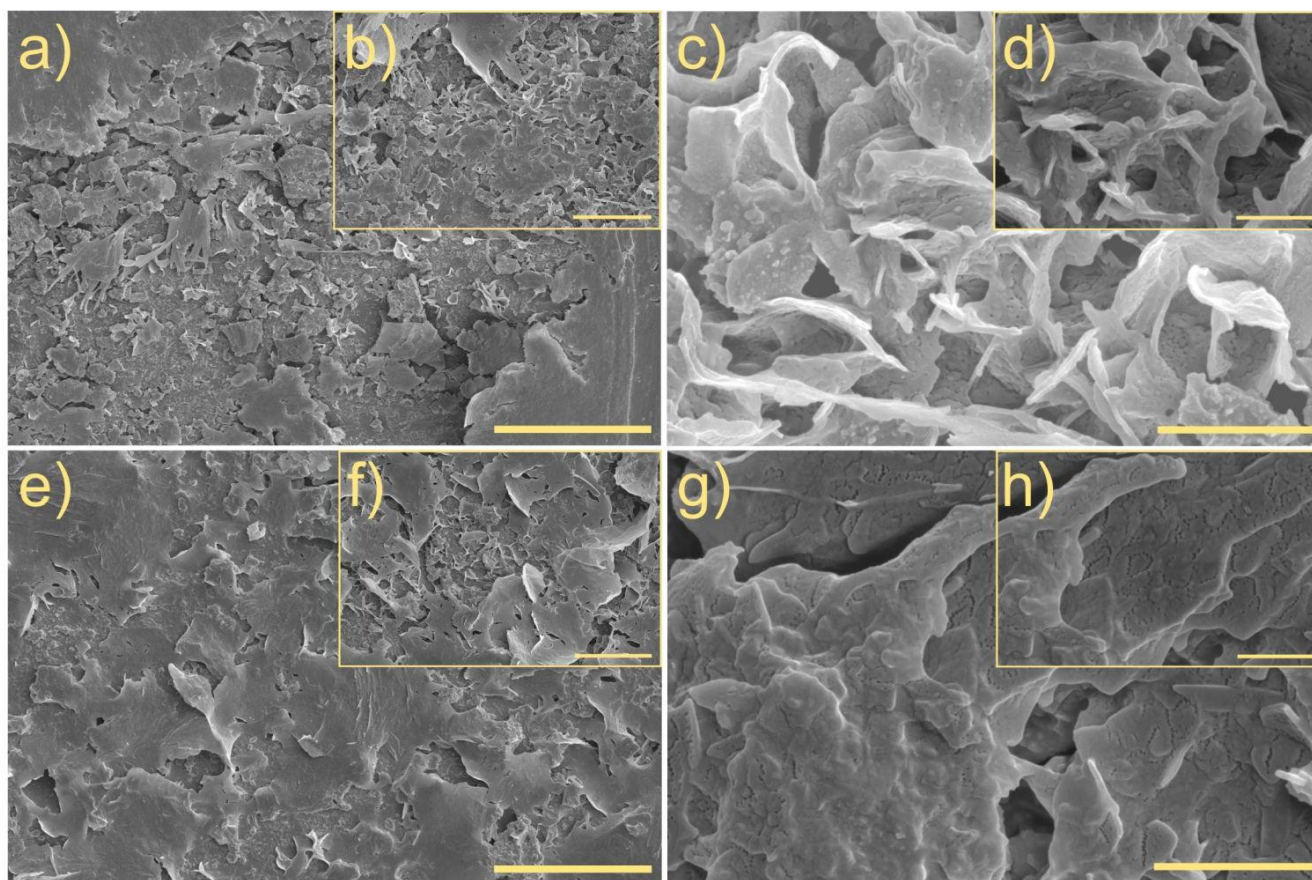


Figure S5. FESEM images of a) – d) Philic-Al scale bar 20 μm , b) 10 μm , c) 2 μm , and d) 1 μm and e) – h) Phobic-Al scale bar 20 μm , b) 10 μm , c) 2 μm , and d) 1 μm .

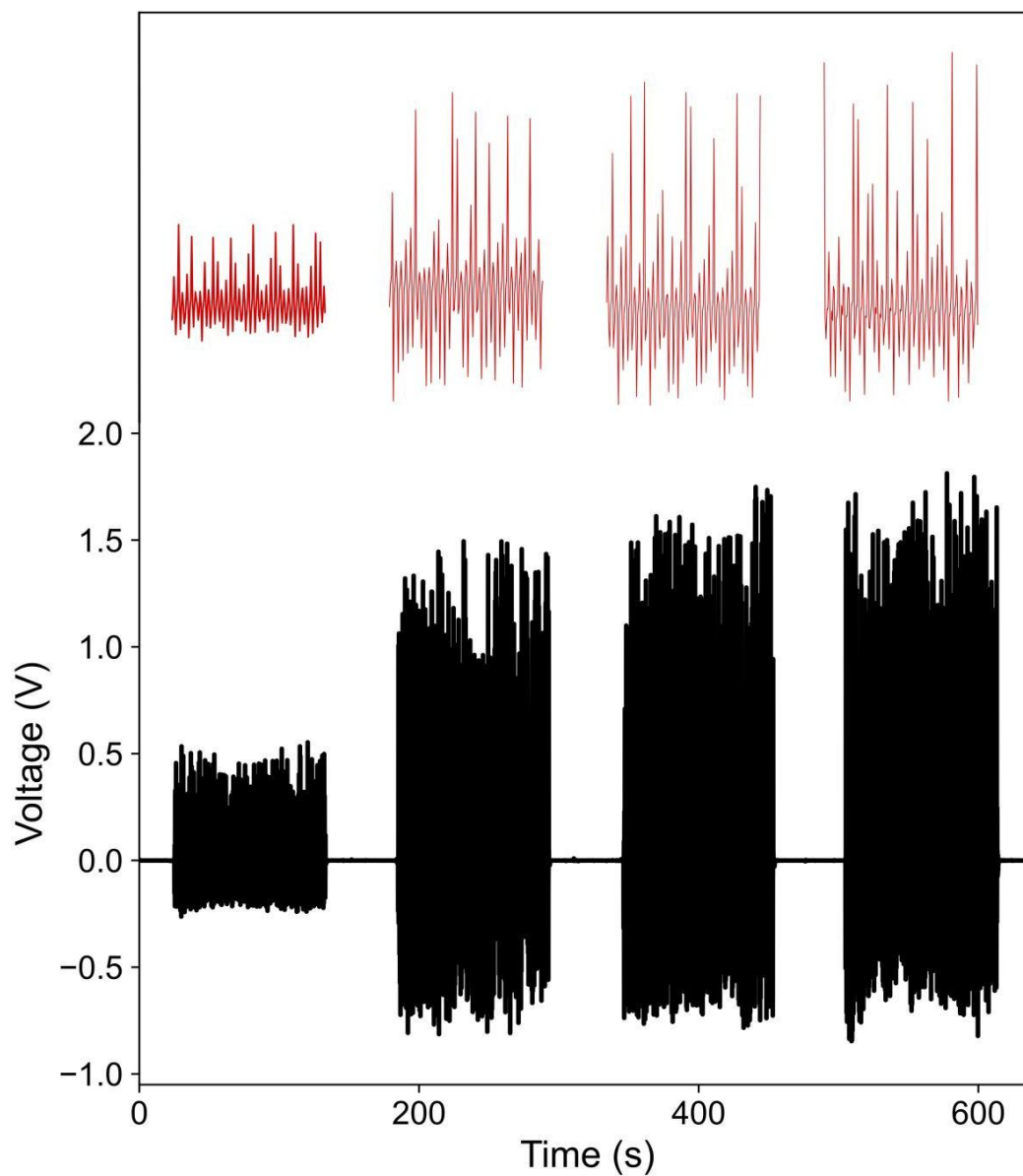


Figure S6. The voltage output of DE-EG along with zoomed-in view of the voltage profile at various water volumes.

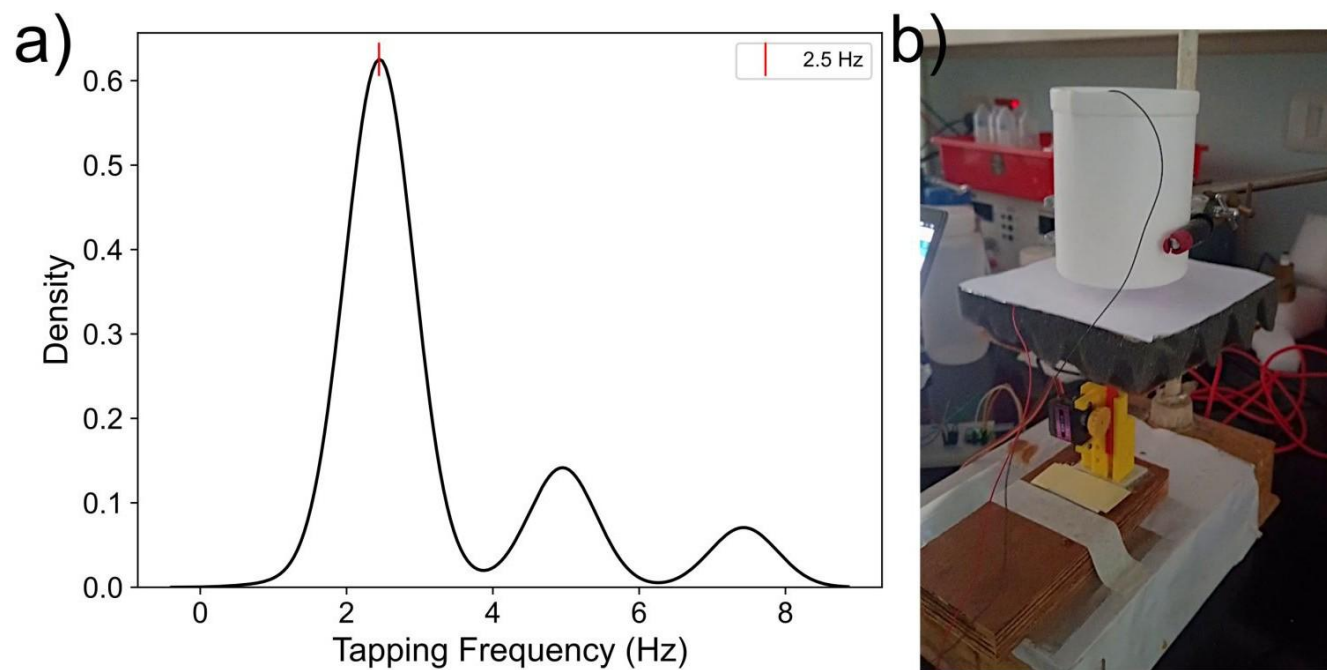


Figure S7. Tapping frequency distribution of LA, and b) Photograph of LA.

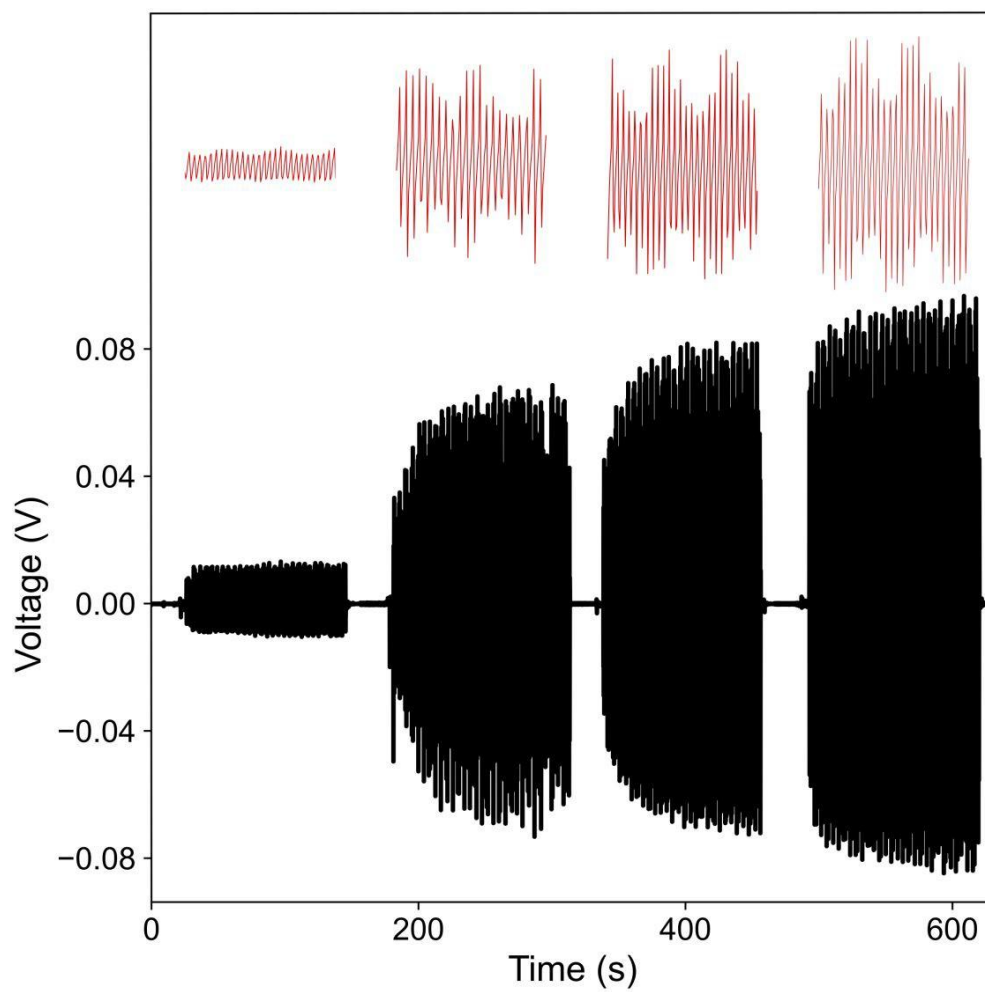


Figure S8. The voltage output of LAB-EG along with zoomed-in view of the voltage profile at various water volumes.



Cite this: DOI: 10.1039/d4nr02820a

Nanocluster reaction-driven *in situ* transformation of colloidal nanoparticles to mesostructures†‡

 Paulami Bose,^{id} §^a Pillalamarri Srikrishnarka,^{id} §^a Matias Paatelainen,^b Nonappa,^{id} ^b Amoghavarsha Ramachandra Kini,^a Anirban Som^{id} ^a and Thalappil Pradeep^{id} ^{*a}

Atomically precise noble metal nanoclusters (NCs) are molecular materials known for their precise composition, electronic structure, and unique optical properties, exhibiting chemical reactivity. Herein, we demonstrated a simple one-pot method for fabricating self-assembled Ag–Au bimetallic mesostructures using a reaction between 2-phenylethanethiol (PET)-protected atomically precise gold NCs and colloidal silver nanoparticles (Ag NPs) in a tunable reaction microenvironment. The reaction carried out in toluene at 45 °C with constant stirring at 250 revolutions per minute (RPM) yielded a thermally stable, micron-sized cuboidal mesocrystals of self-assembled AgAu@PET nanocrystals. However, the reaction in dichloromethane at room temperature with constant stirring at 250 RPM resulted in a self-assembled mesostructure of randomly close-packed AgAu@PET NPs. Using a host of experimental techniques, including optical and electron microscopy, optical absorption spectroscopy, and light scattering, we studied the nucleation and growth processes. Our findings highlight a strategy to utilize precision and plasmonic NP chemistry in tailored microenvironments, leading to customizable bimetallic hybrid three-dimensional nanomaterials with potential applications.

Received 8th July 2024,
Accepted 4th September 2024
DOI: 10.1039/d4nr02820a
rsc.li/nanoscale

1. Introduction

Atomically precise noble metal nanoclusters (NCs) are an emerging class of nanomaterials known for their precise composition and tuneable chemical, physical, and optical properties.^{1–8} The chemistry of noble metal NCs and its versatility to facilitate the formation of precise assemblies,^{9–12} nanocomposites,^{13,14} membranes,¹⁵ colloidal frameworks,¹⁶ and hybrid nanomaterials^{17–19} are currently gaining prominence.^{20–25} NC-assembled solids are well-known for their fascinating properties, such as photoluminescence, conductivity, magnetism, mechanical strength, and catalysis.^{12,26–29} NCs can be solidified using different approaches, such as solvent-induced crystallization,^{30–32} electro-crystallization,³³ and gelation.^{34,35} Ligand functionalization of the particle surface plays a prominent role in controlling interparticle

interactions and, eventually, the frameworks of assemblies.^{36–38} Such assemblies are mostly driven by supra-molecular forces, including H-bonding, electrostatic, dipolar, π -stacking, and van der Waals interactions.^{20,21,39,40} Tellurium nanowires (Te NWs) and Au₃₂SG₁₉ NCs (where SG refers to glutathione) react to form nanodumbbell-shaped Ag–Te hybrid NWS.¹⁸ Te NWs modified with Ag₄₄(*p*-MBA)₃₀ (where *p*-MBA refers to *para*-mercaptobenzoic acid) form a crossed bilayer assembly *via* ligand-mediated H-bonding.¹⁹ Similarly, Ag₄₄(*p*-MBA)₃₀ NCs encapsulate gold nanorods (Au GNRs) to form cage-like nanostructures.⁴¹ However, in most of the nanocluster–nanoparticle (NC–NP) assemblies, supramolecular interactions constitute the sole driving factor, resulting in superstructures where reacting particles preserve their intrinsic properties.^{9,15,20} Recent studies indicate that thiol (SR)-protected noble metal NCs can facilitate spontaneous interparticle (NC–NC and NP–NC) atom exchange in solution, leading to chemically modified particles.^{21,42–44} For instance, a galvanic exchange interparticle reaction between Ag@SR NPs and [Au₂₅(SR)₁₈][–] NCs results in self-assembled two-dimensional (2D) crystals of Ag–Au-bimetallic NPs (to be discussed in detail in the following section).⁴⁵ In our recent publication, we reported that an [Ag₂₅(SR)₁₈][–] NC-mediated unconventional anti-galvanic exchange reaction (AGR) in Au@SR NPs creates alloy NPs.⁴⁶ A reaction of [Au₂₅(SR)₁₈][–] NCs with CuO NPs induces the aggregation of Cu-doped Au NCs into a nanodisc-shaped superstructure.⁴⁷ [Ag₂₅(SR)₁₈][–] NCs can also enable

^aDST Unit of Nanoscience (DST UNS) and Thematic Unit of Excellence (TUE), Department of Chemistry, Indian Institute of Technology Madras, Chennai 600 036, India. E-mail: pradeep@iitm.ac.in

^bFaculty of Engineering and Natural Sciences, Tampere University, Korkeakoulunkatu 3, FI-33720 Tampere, Finland

†Dedicated to Parasuraman Selvam, a colleague and valued friend, to celebrate his 65th birthday.

‡Electronic supplementary information (ESI) available. See DOI: <https://doi.org/10.1039/d4nr02820a>

§Present address: Faculty of Engineering and Natural Sciences, Tampere University, Korkeakoulunkatu 3, FI-33720, Tampere, Finland

site-selective etching of anisotropic Au nanotriangles (Au NTs) to produce tuneable core-shell Ag@Au NT nanocomposites.⁴⁸ From the above examples, it is evident that the final hybrid nanostructures are the consequence of a careful selection of reacting/interacting interparticle systems in terms of particle shape, geometry, composition, and protecting ligands. However, the possibility of creating different nanoarchitectures from the same interparticle system, simply by tuning the reaction microenvironment (temperature and solvent, for instance), is relatively less explored. Additionally, there is a need to explore the feasibility of interparticle reactions further to create next generation three-dimensional (3D) materials.

The hierarchical assembly of colloidal NPs represents a transformative frontier in materials science for its ability to create next generation 3D materials with tailored functionalities.^{49–52} Typically, metal NPs are susceptible to polydispersity, lack of directional interactions, and non-specific aggregation.⁵³ However, size-selected metal NPs are known to self-assemble, leading to 3D crystals,⁵⁴ 2D arrays,^{55–60} supraparticles,^{61–65} and colloidal capsids.^{10,66,67} Mesocrystals are types of colloidal crystals formed by individual nanocrystals self-assembled into higher-order superstructures.^{68–74} This is an example of a non-classical crystallization technique.^{74–77} Classical crystallization involves layer-by-layer growth *via* nucleation and sequential addition of atomic, ionic, or molecular building blocks.^{78,79} In contrast, non-classical crystallization involves more complex pathways and intermediate structures, often involving larger building blocks such as NPs, complexes, oligomers, *etc.*, resulting in hybrid crystalline materials.^{77,79} Nanocrystal synthesis is a complex process of controlled precipitation in which the chemical environment,^{58,80} solvents,⁸¹ and ligands play a crucial role.^{81,82} Self-assembled mesocrystals find potential applications in electronics,^{83,84} plasmonics,⁸⁵ catalysis,^{86–88} energy storage,^{89,90} and many more.^{91,92} To engineer precise and configurable mesostructures, it is essential to have robust assembling protocols for their formation with a comprehensive understanding to fully harness their potential applications.

In our previous publication, we demonstrated that polydisperse 2-phenylethanethiol (PET)-protected plasmonic Ag NPs (also referred to as Ag@PET NPs) spontaneously react with atomically precise [Au₂₅(PET)₁₈][−] NCs to create a 2D superlattice of highly monodisperse bimetallic AgAu@PET NPs.⁴⁵ In the present study, we examined a strategy to utilize interparticle (NP–NC) reactions to create mesostructures of bimetallic NPs under adjustable reaction conditions (schematically illustrated in Fig. 1A). At a constant temperature and with mild agitation, the reaction resulted in the directed assembly of bimetallic nanocrystals with a platelet-like morphology into a cuboidal mesocrystal. The same reaction under ambient conditions produced a random close-packed (RCP) bimetallic NP mesostructure. *In situ* nucleation and growth of mesostructures are driven by interparticle reactions under given conditions. Interestingly, manipulating the reacting interparticle system along with the reaction microenvironment makes it

possible to create a variety of stable nanoarchitectures of self-assembled NPs. However, obtaining microscopic-level insight into such assembling events from experiments is incredibly challenging.

2. Results and discussion

Our previous publication was limited to the interparticle reaction between 2-phenylethanethiol (PET)-protected Ag NP–Au NCs, resulting in bimetallic NPs.⁴⁵ We observed that polydisperse Ag@PET NPs and [Au₂₅(PET)₁₈][−] NCs (*1a*) undergo a spontaneous interparticle atom-exchange reaction to form a self-assembled 2D superlattice of monodisperse alloy AgAu@PET NPs (*1b*), schematically illustrated in Fig. 1A (*1a* → *1b*). The present study explores the self-assembling properties of the reacted AgAu@PET NPs in different microenvironments in solution, schematically presented in Fig. 1A (*1b* → *1d*). To begin with, we utilized our previously reported protocol using atomically precise [Au₂₅(PET)₁₈][−] NCs and polydisperse plasmonic Ag@PET NPs to prepare bimetallic AgAu@PET NPs. The schematic representation and characterization details of the particles involved in the reaction, such as [Au₂₅(PET)₁₈][−] NCs (Fig. 1B a–c), AgAu@PET NPs (Fig. 1B d–f), and Ag@PET NPs (Fig. 1B g–i), are presented, as per their size as measured in transmission electron microscopy (TEM).^{30,93} The synthesized [Au₂₅(PET)₁₈][−] NCs exhibited a molecular ion peak centered at *m/z* 7391 in electrospray ionization mass spectrometry (ESI MS), an average diameter of ~1.8 nm in the TEM images, and characteristic optical absorption peaks at 675 and 450 nm in the UV-Vis spectrum (further characterization details are presented in ESI Fig. S1†). The parent Ag@PET NPs have an average diameter of 4.4 ± 2.3 nm (*d*-spacing 0.21 nm) and a characteristic localized surface plasmon resonance (LSPR) feature at ~450 nm (characterization details are presented in Fig. S2†). It should be noted that the particle size refers to the most probable metal core diameter measured using TEM.

We utilized a combination of scanning/transmission electron microscopy (S/TEM), field emission scanning electron microscopy (FESEM) imaging, optical absorption spectroscopy, and dynamic light scattering (DLS) techniques to capture the nucleation and growth of the NPs into mesostructures. Using our previously reported method, we prepared bimetallic AgAu@PET NPs by mixing known volumes of Ag@PET NP and [Au₂₅(PET)₁₈][−] NC solutions (refer to the Experimental section in ESI for details†).⁴⁵ NP–NC reactions are stoichiometric in nature.^{45,94} The reacted NPs are highly monodisperse in nature, with an average diameter of 3.5 ± 0.5 nm (TEM images in Fig. 1B e and f, and further characterization data are included in Fig. S3†). However, the parent monometallic Au@DMBT NPs were polydisperse in nature and exhibited no assembling tendency in solution (TEM image in Fig. 1B h). In a typical energy-dispersive X-ray spectroscopy (EDS) spectrum, the presence of Ag is detected using L-shell emissions (Ag L) at 2.98 keV, Au is detected using M-shell emissions (Au M) at

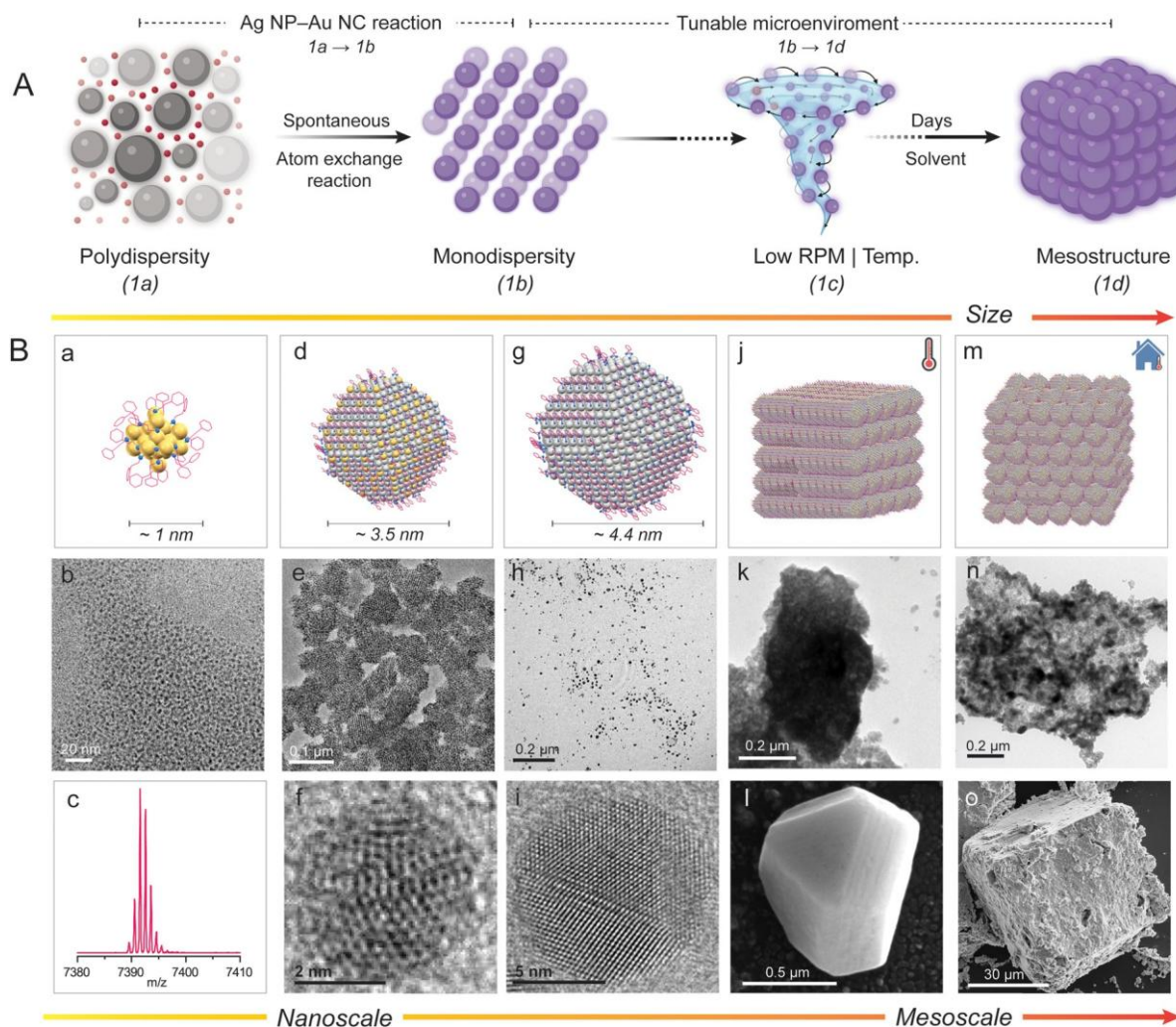


Fig. 1 (A) Schematic illustration of the interparticle, polydisperse Ag NPs (grey spheres) and Au NCs (magenta spheres), reaction driving the formation of the mesostructures of bimetallic NPs (purple spheres). (B) Schematic representation and characterization of (a–c) $[\text{Au}_{25}(\text{PET})_{18}]^{-}$ NCs, (d–f) AgAu@PET NPs, (g–i) Ag@PET NPs, and mesostructures obtained (j–l) with and (m–o) without heating conditions. PET refers to 2-phenylethanethiol. Color code: grey, Ag; yellow, Au; blue, S; magenta, C; H is omitted for clarity. Please note that the atomic dimensions and ligand attachments are not a true representation. Illustrations are created with a licensed version of BioRender.com.

2.12 keV, and both S and C are detected using K-shell emissions (S K and C K) at 2.30 and 0.28 keV, respectively. Dark-field STEM coupled with EDS estimated the atomic percentages of Ag, Au, and S in the reacted NPs to be 57, 27, and 16, respectively (Fig. S4†). Next, we stirred the reacted NP solution at a constant speed (250 revolutions per minute, RPM) and allowed the reaction to proceed for several days under different experimental conditions (see the Experimental section in ESI† for details†). Experimental conditions include reactions in (i) high boiling and less polar solvents, such as toluene with/without constant heating, and (ii) low boiling and polar solvents, such as DCM under ambient conditions. In order to prevent solvent loss over time, extra precautions were taken to ensure that the reaction vial was leakproof (Fig. S5†). We observed that the reacted NPs undergo *in situ* nucleation and growth to form cuboidal mesostructures with different orders of packing under various reaction conditions, as schematically

illustrated in Fig. 1B j (in toluene under heating conditions) and Fig. 1B m (in DCM under ambient conditions), respectively. Later sections will provide a detailed discussion on the morphology and composition of the as-obtained mesostructures.

The reacting particles dispersed well in toluene and remained stable. Under constant and gradual stirring at 45 °C, we observed that the reacted NP suspension required ~100 days to fully precipitate (schematically illustrated in Fig. 2A a, with further details provided in the Experimental section of the ESI†). We drop-cast about 10 μL from the reaction mixture onto a silicon wafer for FESEM, TEM, and optical microscopy imaging. Imaging revealed that the as-obtained precipitate was composed of multiple cuboidal mesostructures (schematically illustrated in Fig. 2A b). Each cuboid can be visualized as a collection of multiple platelet-shaped nanocrystals held together, presumably by a ligand–ligand interaction (schematically rep-

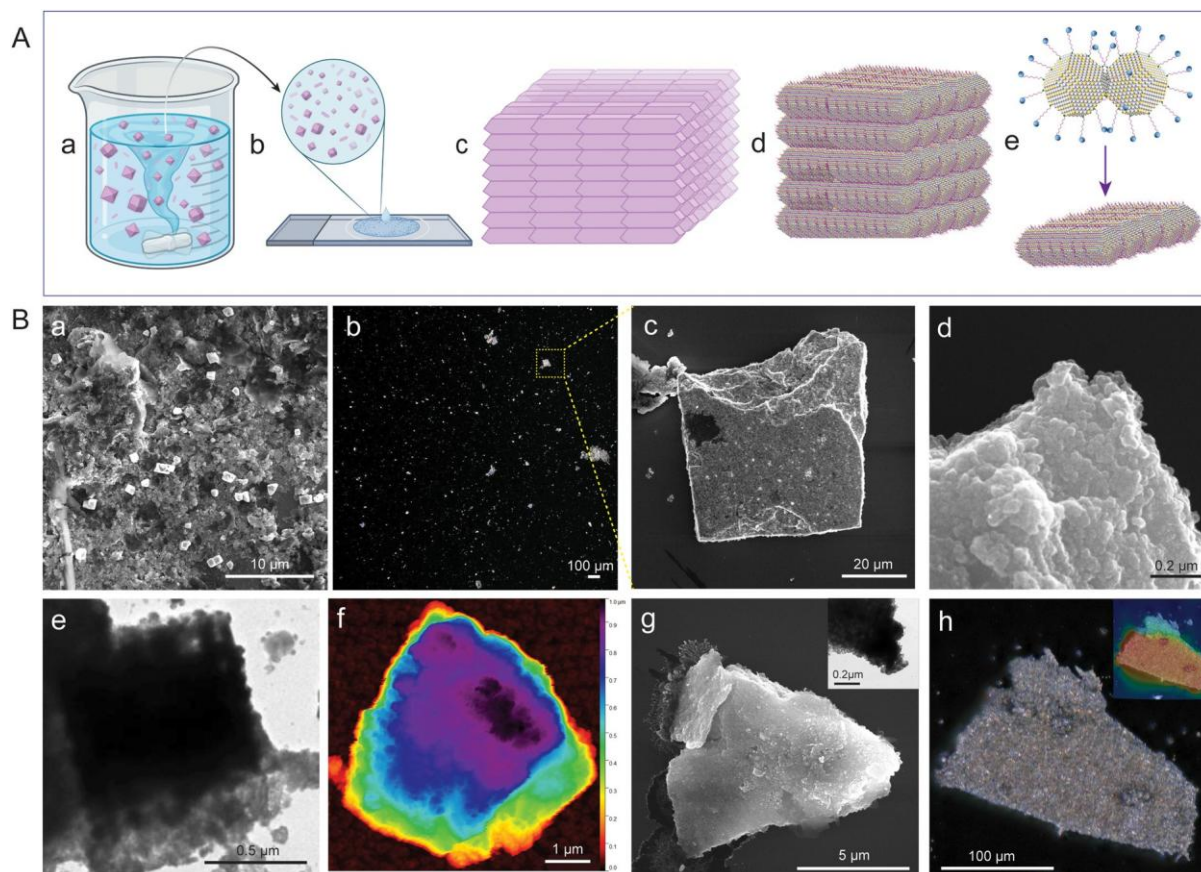


Fig. 2 (A) Schematic illustration of the experimental setup (a), sample preparation (b), and typical morphologies (c and d) and morphogenesis (e) of the mesocrystal obtained. (B) FESEM (a, c, and d), dark-field optical microscopy (b), TEM (e), and AFM (f) images of the mesocrystals obtained after ~ 100 days of reaction. Slanted cuboidal-shaped mesocrystals as imaged under FESEM (g) and TEM (in the inset), and an optical microscope in the dark field (h) and the corresponding depth-of-field (in the inset). Color code: grey, Ag; yellow, Au; green, S; pink-blue, ligand. Illustrations are created with a licensed version of BioRender.com.

resented in Fig. 2A c–e).^{67,95} FESEM, HRTEM, and the corresponding fast Fourier transform (FFT) images of the isolated nanocrystals with a platelet-like shape and a dimension of $0.3 \text{ nm} \times 0.3 \text{ nm}$ (length (l) \times breadth (b)) are presented in Fig. S6.† The FESEM image of the drop-cast sample captured at a magnification of $8000\times$ shows multiple mesocrystals with well-defined edges and flat facets (Fig. 2B a). The image was acquired using a beam energy of 10 keV and a secondary electron detector in field-free mode. We further centrifuged the reaction mixture to eliminate smaller structures, and the precipitate was imaged at $100\times$ magnification using an optical microscope (Fig. 2B b). We observed that the precipitate was composed of several micron-sized mesostructures using a dark-field optical microscope (Fig. 2B b). One of these mesostructures was further imaged using FESEM at a magnification of $2500\times$ (Fig. 2B c). The estimated dimensions of the cuboidal mesostructure are $\sim 48 \mu\text{m}$ (l) \times $\sim 50 \mu\text{m}$ (b); information on height is unavailable. The fissured edge of the cuboid indicates layer-by-layer growth of the platelet-shaped nanocrystals (Fig. 2B d). The FESEM image of one such edge viewed at a magnification of $250\,000\times$ further revealed that the cuboidal

mesostructure is composed of multiple layers of nanocrystals (dimensions of approximately $50 \text{ nm} \times 50 \text{ nm}$ in $l \times b$, respectively). TEM images further support the mesostructure formation involving a layer-by-layer arrangement of nanocrystal units (Fig. 2B e). We utilized atomic force microscopy (AFM) to analyze the height and surface topology of the mesocrystals (Fig. 2B f, and further details are provided in Fig. S7†). AFM analysis of the selected mesocrystal revealed a maximum height of $0.98 \mu\text{m}$ and a root mean square (RMS) roughness of 6.24 nm , indicating a highly ordered structure with minimal surface irregularities (Fig. S7†). The steep edges and lower roughness suggest a precise self-assembly of the nanocrystals into well-packed layer-by-layer mesocrystals.

We selected a mesocrystal with a slanted cuboidal shape for detailed investigation to obtain further insights into the morphology and composition of the constituent particles (Fig. 2B g and h). A slanted cuboid is one that has two of its opposing faces parallel to the line of sight, while the other four faces converge at a single point, giving the object a triangular appearance. The FESEM image of a selected mesostructure (face and edge length of $\sim 10 \mu\text{m}$ and $8 \mu\text{m}$, respectively)

acquired at 20 000 \times magnification revealed layered growth at the edges, and the TEM image revealed nanocrystals as building blocks (Fig. 2B g and inset, respectively). The optical image of the selected structure appears shiny, which can be attributed to the dense packing of the individual nanocrystals (Fig. 2B h). The depth-of-field optical image of the mesocrystals further confirms a layered crystal growth (inset, Fig. 2B h). We analyzed the mesocrystals using FESEM coupled with EDS to gain insight into the elemental composition and distribution. The composition of the slanted cuboid can be schematically represented as a collection of tightly packed AgAu@PET nanocrystals, as shown in Fig. 3A. The atomic percentages of the elements present in the mesostructure are as follows: 21% for Ag, 17% for Au, 20% for S, and 42% for C (Fig. S8†). EDS mappings of elemental gold (Au), silver (Ag), sulfur (S), and carbon (C) of the isolated mesostructure obtained using FESEM EDS are presented in Fig. 3B. Mapping data revealed a uniform distribution of Au, Ag, S, and C across the mesostructure, indicating the AgAu@PET NP crystallites as the building blocks of such mesostructures.

To comprehend the reaction-induced aggregation behavior of the particles in solution, we combined dynamic light scattering (DLS), the Tyndall effect, and optical absorption spectroscopy as a function of time (Fig. 4). DLS measures the scattered light intensity change caused by the motion of particles suspended in a solution. We conducted the study at a ten-fold dilution of the parent particle concentrations to maintain a lower polydispersity index (PDI). DLS measurements showed that the hydrodynamic radius (R_H) of the AgAu@PET NPs in solution gradually increased with reaction time (Fig. 4A). The continuous red-shift and the broadening in the DLS peak indi-

cate that the bimetallic NPs nucleated and grew in the solution, resulting in the formation of larger structures over time. Next, we used the Tyndall effect to probe the aggregation of colloidal dispersion by focusing a 630 nm laser beam (green laser) on the solution (Fig. 4B). As shown in Fig. 4B, on the 0th day, the suspension of the well-dispersed parent Ag@PET NPs appears homogeneous as the light passes through. The Tyndall effect was seen in the colloidal AgAu@PET NPs after 1 day of reaction, with further aggregation and eventual precipitation occurring over the next 10 days. The scattering of light becomes evident when the size of the particle aggregate exceeds the wavelength of incident light. Time-dependent optical absorption spectra of the particle mixture also showed a similar aggregation trend as observed in the light scattering experiment (Fig. 4C). Here, the optical absorption spectrum on the 0th day corresponds to the optical absorption spectrum of the parent Ag@PET NPs. The red-shift in the characteristic SPR peak of the Ag@PET NPs confirms the presence of bimetallic Au–Ag NPs in the reaction mixture. We also observed a progressive broadening in the SPR peak of the reaction mixture, indicating the onset of particle aggregation in the solution over time. Furthermore, the rise in the baseline as the reaction progresses can be attributed to particle aggregation. Under similar reaction conditions, FESEM and TEM images revealed the formation of comparably smaller-sized cuboidal-shaped mesocrystals in the solution (Fig. 4D). Only the dimensions of the as-obtained mesocrystals were impacted by diluting the reaction mixture; however, the overall morphology of the mesocrystals remained unchanged, as seen in the previous case.

Based on the above discussion, the interparticle reaction in a non-polar solvent and at elevated temperature results in the

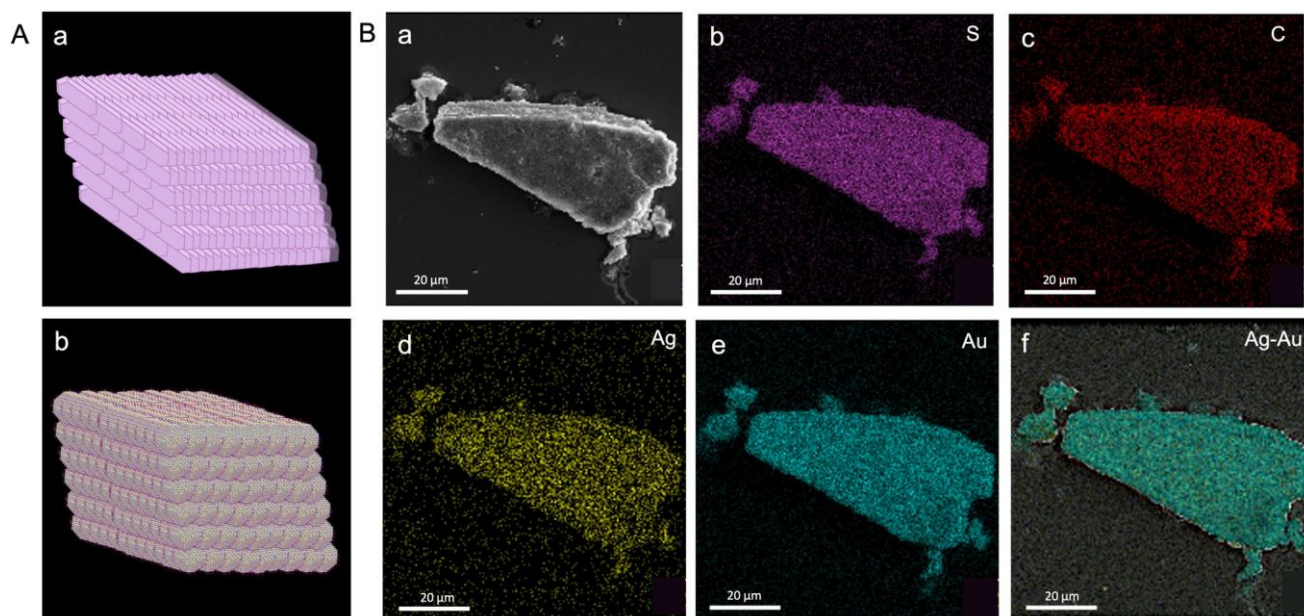


Fig. 3 (A) Schematic illustration of a slanted cuboidal-shaped mesocrystal (a) and its compositional representation (b). (B) FESEM image of such a crystalline entity (a) and the corresponding EDS maps of S (b), C (c), Ag (d), Au (e), and Ag–Au overlay (f). Illustrations are created with a licensed version of BioRender.com.

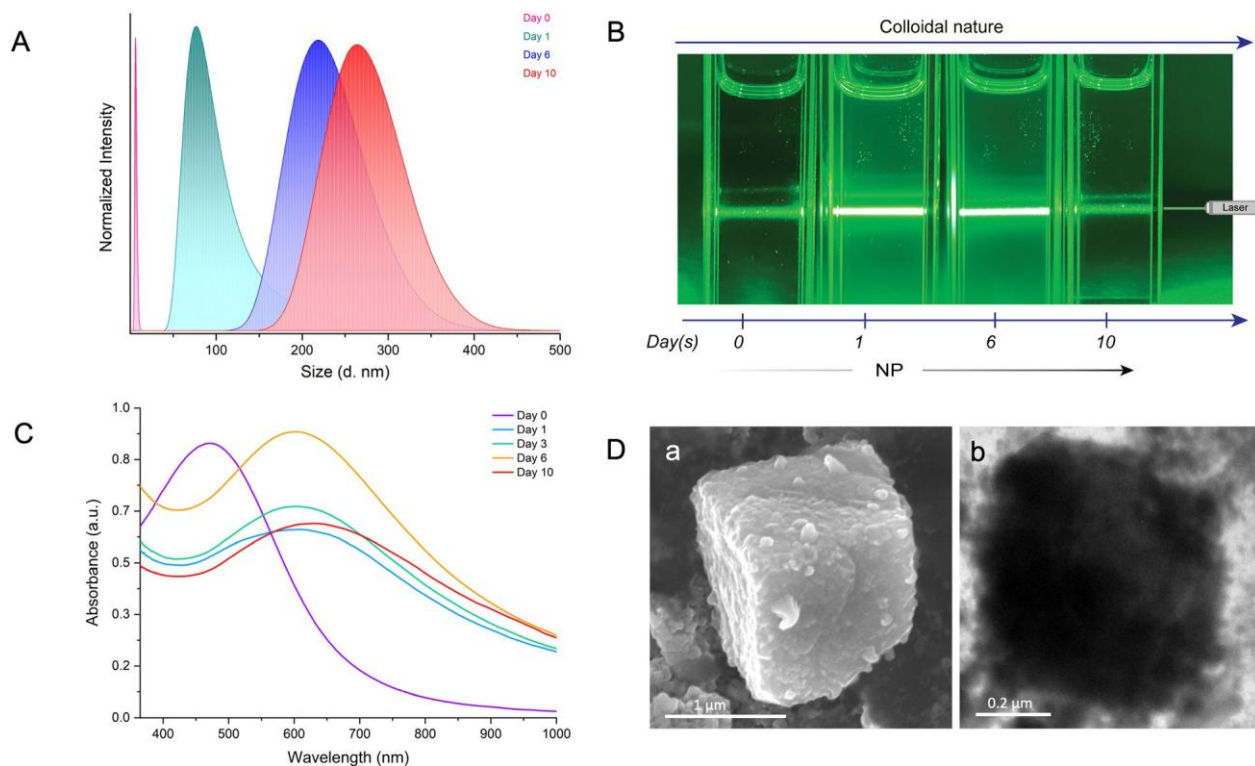


Fig. 4 Time-dependent evolution of colloidal particles into crystalline mesostructures as monitored using (A) dynamic light scattering, (B) the Tyndall effect under irradiation with a 630 nm green laser, and (C) optical absorption spectroscopy. (D) FESEM (a) and TEM (b) images of the final mesocrystals as-obtained after 10 days of reaction.

in situ formation of mesostructures with well-packed bimetallic AgAu@PET nanocrystals. The nucleation and growth rate, and thus the formation of the mesostructures, is known to be influenced by various reaction conditions such as temperature, pressure, pH, concentration, and solvent.⁹⁶ We carried out the same interparticle reaction at room temperature while keeping the other parameters, such as solvent, concentration, and RPM, constant (refer to the Experimental section in ESI for details[†]). Under the previous reaction conditions, the process of mesocrystallization took approximately 100 days when performed at 45 °C, and nearly no change was observed when the process was conducted at room temperature. Next, we studied the same interparticle reaction at room temperature in DCM while maintaining other parameters constant (schematic illustration in Fig. 5A). The particle mixture formed a stable dispersion in DCM, which was continuously stirred at 250 RPM under ambient conditions. The reaction took ~50 days for the complete precipitation to occur, and the product was analyzed using electron microscopy (Fig. 5B). In order to mitigate solvent loss over time, the reaction was conducted in the same leakproof container (as shown in Fig. S5[†]). The FESEM image shows the formation of much larger cuboidal mesostructures of 51 nm × 47 nm ($l \times b$; height information is unavailable) as a product (Fig. 5B a). The image was acquired at 3500× magnification using the same 10 keV accelerating voltage and a secondary electron detector in field-free mode. The mesostructure

exhibited visible signs of NP nucleation, resulting in layer-by-layer structural growth at intermediate phases, and, finally, densely packed structures were formed at the end of the process (Fig. S9[†]). The rough surface morphology of the as-obtained mesostructure can be attributed to the random packing of the NPs. The TEM image further confirmed the aggregation of the NPs within the precise boundaries of the mesostructures while retaining their original dimension (Fig. 5B b). To verify the retention of the NP characteristics in the final mesostructure, we degraded the sample by sonication in DCM. Post-sonication, the TEM image revealed the disintegration of the mesostructure into the NPs resembling the original AgAu@PET NPs (Fig. S10[†]). AFM analysis of the selected mesostructure revealed a maximum height of 3.19 μm and a root mean square (RMS) roughness of 22.05 nm, indicating a highly disordered structure with significant surface irregularities (Fig. 5B c, and further details are provided in Fig. S11[†]). Higher surface irregularity also suggests a random assembly of the NPs during the growth stage. A time-dependent optical absorption spectroscopic analysis of the interparticle reaction in DCM at ambient temperature is presented in Fig. 5C. Over time, we observed that the characteristic SPR peak corresponding to the parent Ag@PET NPs (corresponding spectrum on the 0th day) underwent a gradual red-shift and broadening upon reaction with [Au₂₅(PET)₁₈]⁻ NCs. According to the FESEM EDS study, the mesostructures are made up of about

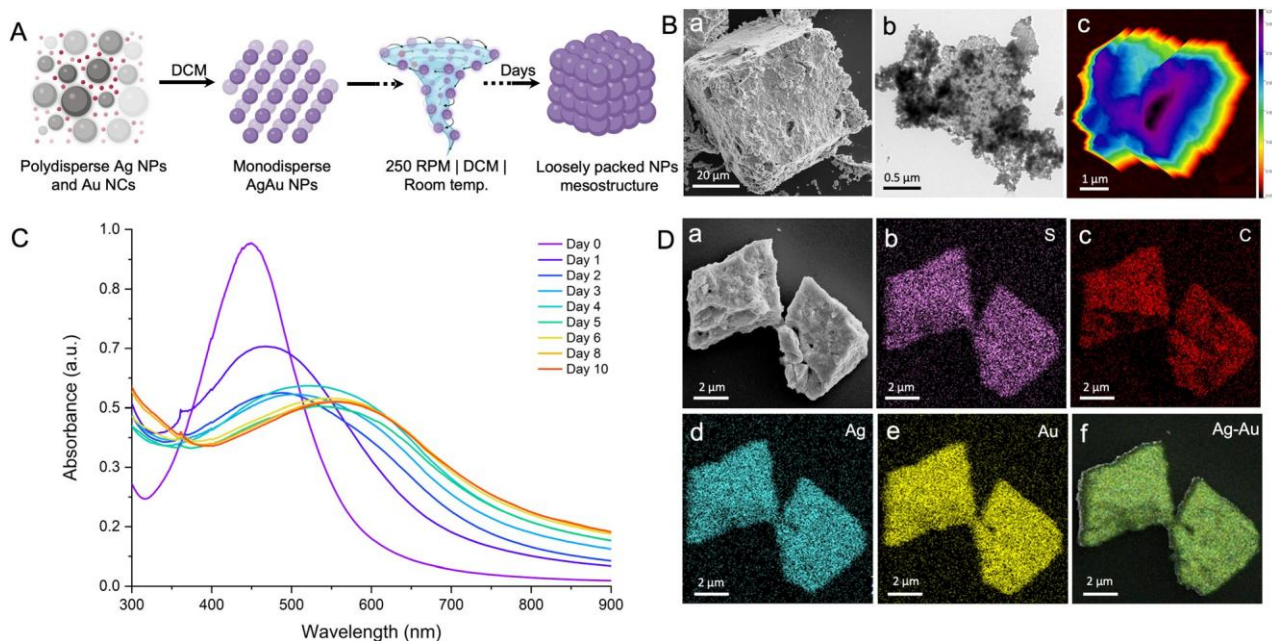


Fig. 5 (A) Schematic representation of a room temperature interparticle reaction carried out in DCM with constant stirring at 250 RPM, resulting in larger mesostructures with lower packing. (B) FESEM (a), TEM (b), and AFM (c) images of the mesostructures. (C) Time-dependent evolution of colloidal particles into mesostructures as monitored using optical absorption spectroscopy. (D) FESEM image of the mesostructures (a) and the corresponding EDS maps of S (b), C (c), Ag (d), Au (e), and Ag-Au overlay (f). Illustrations are created with a licensed version of BioRender.com.

25% gold (Au), 30% silver (Ag), 14% sulfur (S), and 31% carbon (C) (Fig. S12, † based on the intensities of the respective EDS features). Mapping data confirmed a uniform distribution of Au, Ag, S, and C across the mesostructure (Fig. 5D a), indicating the AgAu@PET NPs as the building blocks of such structures (Fig. 5D b–f). Thus, we can infer that the parent Ag@PET NPs react to form alloy AgAu@PET NPs and eventually aggregate into higher-order assemblies with time. The continuous rise in the baseline of the optical absorption spectrum with the progress of the reaction can be related to the gradual nucleation of particles to a larger structure in solution.

For control experiments, we checked the stability of the parent particles under identical reaction conditions. Over the course of ~05 days, a steady decline in the absorbance of the parent Ag@PET NPs was evident in the optical absorption spectra, indicating particle degradation (Fig. S13A †). The [Au₂₅(PET)₁₈]⁻ NCs showed an increased sensitivity to heat, and the NCs degraded rapidly (Fig. S13B †). To understand the *in situ* nucleation and growth process, we studied the evolution of the reacted NPs in solution with TEM at different intervals as the mesocrystallization process continued (Fig. S14 †). The time-dependent series of TEM images indicated a significant difference in the patterns of nucleation and growth of the AgAu@PET NPs under two reaction conditions. For instance, the AgAu@PET NPs in toluene nucleate under an elevated temperature to form platelet-like nanocrystals, which eventually assemble and grow layer-by-layer until the final mesocrystal is formed (Fig. S14A †). On the other hand, the AgAu@PET NPs in DCM randomize and then assemble under

ambient conditions, followed by a layered growth until the final mesostructure is formed (Fig. S14B †). From the above observation, we can understand that local chemical microenvironments involving temperature, solvent polarity, RPM, and interparticle forces play a crucial role in the morphogenesis of the mesocrystals.^{78,96} However, understanding such complex dynamics of nucleation and growth of the NPs requires *in situ* microscopic studies and advanced mesoscale modeling.

Inter-ligand interactions are known to play a prominent role in the self-assembly of metallic NPs.^{21,38,40,51} We performed reactions for various intermetallic (for example, Au NP–Ag NC) and intrametallic interparticle (Au NP–Au NC and Ag NP–Ag NC) systems to verify the role of ligands in such a reaction-driven *in situ* mesocrystallization process. Similar experimental conditions for the PET-capped particle system were used for the subsequent reactions (refer to the Experimental section in ESI †). We studied the same Ag–Au intermetallic system using the reaction between the 2,4-dimethylbenzenethiol (DMBT)-protected particles, such as ~4.5 nm Au@DMBT NPs and atomically precise [Ag₂₅(DMBT)₁₈]⁻ NCs (refer to the ESI for details, Fig. S15 †). We recently reported a detailed study on the interparticle chemistry of Au@DMBT NPs and [Ag₂₅(DMBT)₁₈]⁻ NCs, and showed that the Ag NCs mediate the alloying process *via* an interparticle metal–ligand exchange pathway.⁴⁶ As per the literature, the insertion of Ag atoms into an Au NP is known to strongly alter the SPR feature in terms of peak position and shape depending on the size and composition of the alloy NP.^{97–99} Within a day of reaction, we observed a strong

enhancement in the SPR feature, and a slight shift of ~ 9 nm in the peak position of the reacted NPs, indicating the insertion of Ag atoms in the parent Au@DMBT NPs. Subsequently, the reacted NPs steadily degraded with time. However, the reacted NPs underwent stable aggregation within a day in DCM at room temperature. In the following experiment, we utilized the 2-phenylethanethiol (PET)-protected Au@PET NPs and $[\text{Au}_{25}(\text{PET})_{18}]^-$ NCs (intrametallic particle system) to study the reaction (refer to the ESI for details, Fig. S16 \ddagger). The PET-protected particle mixture, however, displayed time-dependent optical absorption spectra that suggested a reaction over time. Over time, the reacted NPs in the solution self-assembled into a 2D capsid-like superstructure (Fig. S16A, \ddagger further details are provided in the ESI \ddagger). The optical absorption spectra of the parent Au@PET NP dispersion in toluene showed stability over a span of a few days at an elevated temperature (Fig. S17 \ddagger). Next, we carried out a similar intrametallic interparticle reaction with the Ag@PET NPs and $[\text{Ag}_{25}(\text{DMBT})_{18}]^-$ NCs (Fig. S18 \ddagger). However, in this case, the reaction product underwent rapid degradation (reaction at 45 °C in toluene). However, the product in solution showed a tendency to self-assemble into a 2D superlattice when the reaction was carried out at room temperature in DCM. A study of intrametallic systems is intriguing but goes beyond the scope of this paper.

3. Conclusions

In summary, we demonstrated a simple *in situ* reaction-driven technique for fabricating self-assembled bimetallic mesostructures. An interparticle reaction between PET-protected plasmonic Ag NPs and atomically precise Au NCs results in highly monodisperse bimetallic AgAu NPs with enhanced thermal stability and assembling properties. At an elevated temperature of 45 °C, the interparticle dispersion in toluene results in reaction-driven *in situ* nucleation and growth of AgAu@PET nanocrystals. These nanocrystals eventually self-assemble to create cuboidal mesocrystals. Under ambient conditions, however, the same interparticle reaction in DCM produces mesostructures of random close-packed AgAu@PET NPs. Electron microscopy coupled with EDS and light scattering experiments was used to examine the growth of NPs into mesostructures. An AFM study suggests that the reaction at 45 °C in toluene produces mesocrystals with reduced structural irregularity. Our studies also indicate that PET-capped intermetallic and intrametallic systems are capable of creating unique thermally stable NP-assembled nanoarchitectures. Tracing the origins of such an assembly event requires mesoscale modelling, which will be addressed in the future. This interparticle chemistry can be an alternative non-classical mesocrystallization method that offers flexibility to engineer bimetallic 3D nanomaterials. Using atomically precise noble metal NC reaction-driven phenomena with well-chosen NP–NC systems, it is now possible to achieve alloy particles with control over the size dispersity, leading to self-assembly, all in one pot.

Data availability

The data supporting the study are included in the main article and its ESI, \ddagger uploaded as separate files. Any additional and raw data that were used during the preparation of the manuscript and ESI \ddagger are available from the corresponding author upon request. Schematic illustrations are prepared using Mercury Cambridge Structural Database and [BioRender.com](https://www.biorender.com). The BioRender license files are compiled and uploaded separately with submission. The figure preparation includes professional tools like Adobe Illustrator and Microsoft PowerPoint 2021. Bibliographic references were prepared using the citing software Zotero.

For further inquiries or access to the data, please contact pradeep@iitm.ac.in.

Author contributions

P. B. performed the experiments and analyzed the results. P. S. carried out the FESEM imaging. M. P. carried out the AFM imaging. N. carried out the STEM imaging. A. R. K. contributed to the conceptualization of the experimental setup. A. S. carried out the TEM imaging. T. P. designed the project objective and supervised the progress. Every author contributed to the drafting of the manuscript.

Conflicts of interest

There are no conflicts to declare.

Acknowledgements

We thank the Department of Science and Technology (DST), Government of India, and the Centre of Excellence Program of the Indian Institute of Technology Madras on the theme of Molecular Materials and Functions, under the Institutes of Eminence of Ministry of Education, India, for supporting our research. We thank the Academy of Finland for project funding (No. 352900), the Photonics Research and Innovation (PREIN) flagship, and the Tampere Microscopy Centre for imaging facilities. We thank Bhanupriya S. for her technical assistance with the transmission electron microscopy imaging at the DST Unit of Nanoscience, Indian Institute of Technology Madras. T. P. thanks the Science and Engineering Research Board (SERB), India, for funding through the SPR/2021/000439 research grant and a JC Bose Fellowship.

References

- 1 Y. Du, H. Sheng, D. Astruc and M. Zhu, *Chem. Rev.*, 2020, 120, 526–622.
- 2 I. Chakraborty and T. Pradeep, *Chem. Rev.*, 2017, 117, 8208–8271.

- 3 A. Ghosh, O. F. Mohammed and O. M. Bakr, *Acc. Chem. Res.*, 2018, 51, 3094–3103.
- 4 K. Kwak and D. Lee, *Acc. Chem. Res.*, 2019, 52, 12–22.
- 5 X. Kang, Y. Li, M. Zhu and R. Jin, *Chem. Soc. Rev.*, 2020, 49, 6443.
- 6 Q. Yao, Z. Wu, Z. Liu, Y. Lin, X. Yuan and J. Xie, *Chem. Sci.*, 2021, 12, 99–127.
- 7 P. Bose, G. Natarajan and T. Pradeep, in *Atomically Precise Metal Nanoclusters*, Elsevier, 2023, pp. 313–343.
- 8 T. Pradeep, *Atomically precise metal clusters*, Elsevier, 1st edn, 2023.
- 9 Nonappa, T. Lahtinen, J. S. Haataja, T.-R. Tero, H. Häkkinen and O. Ikkala, *Angew. Chem., Int. Ed.*, 2016, 55, 16035–16038.
- 10 Nonappa, J. S. Haataja, J. V. I. Timonen, S. Malola, P. Engelhardt, N. Houbenov, M. Lahtinen, H. Häkkinen and O. Ikkala, *Angew. Chem., Int. Ed.*, 2017, 56, 6473–6477.
- 11 J. V. Rival, Nonappa and E. S. Shibu, *ACS Appl. Mater. Interfaces*, 2020, 12, 14569–14577.
- 12 M. Jash, A. Jana, A. K. Poonia, E. Khatun, P. Chakraborty, A. Nagar, T. Ahuja, K. V. Adarsh and T. Pradeep, *Chem. Mater.*, 2023, 35, 313–326.
- 13 A. Chakraborty, A. C. Fernandez, A. Som, B. Mondal, G. Natarajan, G. Paramasivam, T. Lahtinen, H. Häkkinen, Nonappa and T. Pradeep, *Angew. Chem., Int. Ed.*, 2018, 57, 6522–6526.
- 14 A. Chakraborty, H. Dave, B. Mondal, Nonappa, E. Khatun and T. Pradeep, *J. Phys. Chem. B*, 2022, 126, 1842–1851.
- 15 A. Som, A. Griffo, I. Chakraborty, H. Hähl, B. Mondal, A. Chakraborty, K. Jacobs, P. Laaksonen, O. Ikkala, T. Pradeep and Nonappa, *Small*, 2022, 18, 2201707.
- 16 S. Chandra, Nonappa, G. Beaune, A. Som, S. Zhou, J. Lahtinen, H. Jiang, J. V. I. Timonen, O. Ikkala and R. H. A. Ras, *Adv. Opt. Mater.*, 2019, 7, 1900620.
- 17 A. Ghosh, T. Pradeep and J. Chakrabarti, *J. Phys. Chem. C*, 2014, 118, 13959–13964.
- 18 A. Som, A. K. Samal, T. Udayabhaskararao, M. S. Bootharaju and T. Pradeep, *Chem. Mater.*, 2014, 26, 3049–3056.
- 19 A. Som, I. Chakraborty, T. A. Maark, S. Bhat and T. Pradeep, *Adv. Mater.*, 2016, 28, 2827–2833.
- 20 Nonappa and O. Ikkala, *Adv. Funct. Mater.*, 2018, 28, 1704328.
- 21 P. Chakraborty, A. Nag, A. Chakraborty and T. Pradeep, *Acc. Chem. Res.*, 2019, 52, 2–11.
- 22 J. V. Rival, P. Mymoona, K. M. Lakshmi, T. Pradeep and E. S. Shibu, *Small*, 2021, 17, 2005718.
- 23 A. Nag and T. Pradeep, in *Atomically Precise Metal Nanoclusters*, ed. T. Pradeep, Elsevier, 2023, pp. 101–111.
- 24 Nonappa, *Chem. Commun.*, 2023, 59, 13800–13819.
- 25 R. Nakatani, S. Das and Y. Negishi, *Nanoscale*, 2024, 16, 9642–9658.
- 26 X. Kang and M. Zhu, *Chem. Soc. Rev.*, 2019, 48, 2422–2457.
- 27 J. Liu, J. Huang, W. Niu, C. Tan and H. Zhang, *Chem. Rev.*, 2021, 121, 5830–5888.
- 28 A. Jana and T. Pradeep, in *Atomically Precise Metal Nanoclusters*, Elsevier, 2023, pp. 49–82.
- 29 N. Alam, A. Kumar Das, P. Chandrashekar, P. Baidya and S. Mandal, *Nanoscale*, 2024, 16, 10087–10107.
- 30 C. P. Joshi, M. S. Bootharaju, M. J. Alhilaly and O. M. Bakr, *J. Am. Chem. Soc.*, 2015, 137, 11578–11581.
- 31 A. Nag, P. Chakraborty, M. Bodiuzzaman, T. Ahuja, S. Antharjanam and T. Pradeep, *Nanoscale*, 2018, 10, 9851–9855.
- 32 C. Cerretani, H. Kanazawa, T. Vosch and J. Kondo, *Angew. Chem., Int. Ed.*, 2019, 58, 17153–17157.
- 33 S. Antonello, T. Dainese, F. Pan, K. Rissanen and F. Maran, *J. Am. Chem. Soc.*, 2017, 139, 4168–4174.
- 34 Z. Wu, C. Dong, Y. Li, H. Hao, H. Zhang, Z. Lu and B. Yang, *Angew. Chem., Int. Ed.*, 2013, 52, 9952–9955.
- 35 Z. Wu, J. Liu, Y. Li, Z. Cheng, T. Li, H. Zhang, Z. Lu and B. Yang, *ACS Nano*, 2015, 9, 6315–6323.
- 36 A. M. Smith, K. A. Johnston, S. E. Crawford, L. E. Marbella and J. E. Millstone, *Analyst*, 2016, 142, 11–29.
- 37 V. Jain, S. Roy, P. Roy and P. P. Pillai, *Chem. Mater.*, 2022, 34, 7579–7597.
- 38 A. Rao, S. Roy, V. Jain and P. P. Pillai, *ACS Appl. Mater. Interfaces*, 2023, 15, 25248–25274.
- 39 J. V. Rival, P. Mymoona, K. M. Lakshmi, Nonappa, T. Pradeep and E. S. Shibu, *Small*, 2021, 17, 2005718.
- 40 A. Nag and T. Pradeep, *ACS Nanosci. Au*, 2022, 2, 160–178.
- 41 A. Chakraborty, A. C. Fernandez, A. Som, B. Mondal, G. Natarajan, G. Paramasivam, T. Lahtinen, H. Häkkinen, Nonappa and T. Pradeep, *Angew. Chem., Int. Ed.*, 2018, 57, 6522–6526.
- 42 K. R. Krishnadas, A. Ghosh, A. Baksi, I. Chakraborty, G. Natarajan and T. Pradeep, *J. Am. Chem. Soc.*, 2016, 138, 140–148.
- 43 K. R. Krishnadas, A. Baksi, A. Ghosh, G. Natarajan, A. Som and T. Pradeep, *Acc. Chem. Res.*, 2017, 50, 1988–1996.
- 44 P. Bose, K. K. Ramankutty, P. Chakraborty, E. Khatun and T. Pradeep, *Nanoscale*, 2024, 16, 1446–1470.
- 45 P. Bose, P. Chakraborty, J. S. Mohanty, Nonappa, A. Ray Chowdhuri, E. Khatun, T. Ahuja, A. Mahendranath and T. Pradeep, *Nanoscale*, 2020, 12, 22116–22128.
- 46 P. Bose, J. Roy, V. Khokhar, B. Mondal, G. Natarajan, S. Manna, V. Yadav, A. Nyayban, S. S. R. K. C. Yamijala, Nonappa and T. Pradeep, *Chem. Mater.*, 2024, 36, 7581–7594.
- 47 J. Roy, B. Mondal, G. Vishwakarma, Nonappa, N. V. Sridharan, P. Krishnamurthi and T. Pradeep, *Nanoscale*, 2023, 15, 8225–8234.
- 48 A. Chakraborty, M. M. Stanley, B. Mondal, Nonappa, M. Bodiuzzaman, P. Chakraborty, M. P. Kannan and T. Pradeep, *Nanoscale*, 2023, 15, 2690–2699.
- 49 M. S. Lee, D. W. Yee, M. Ye and R. J. Macfarlane, *J. Am. Chem. Soc.*, 2022, 144, 3330–3346.
- 50 R. K. Cersonsky, G. van Anders, P. M. Dodd and S. C. Glotzer, *Proc. Natl. Acad. Sci. U. S. A.*, 2018, 115, 1439–1444.
- 51 V. Linko, H. Zhang, Nonappa, M. A. Kostianen and O. Ikkala, *Acc. Chem. Res.*, 2022, 55, 1785–1795.
- 52 C. L. Bassani, G. van Anders, U. Banin, D. Baranov, Q. Chen, M. Dijkstra, M. S. Dimitriyev, E. Efrati, J. Faraudo,

- O. Gang, N. Gaston, R. Golestanian, G. I. Guerrero-Garcia, M. Gruenwald, A. Haji-Akbari, M. Ibáñez, M. Karg, T. Kraus, B. Lee, R. C. Van Lehn, R. J. Macfarlane, B. M. Moggetti, A. Nikoubashman, S. Osat, O. V. Prezhdo, G. M. Rotskoff, L. Saiz, A.-C. Shi, S. Skrabalak, I. I. Smalyukh, M. Tagliacruzchi, D. V. Talapin, A. V. Tkachenko, S. Tretiak, D. Vaknin, A. Widmer-Cooper, G. C. L. Wong, X. Ye, S. Zhou, E. Rabani, M. Engel and A. Travesset, *ACS Nano*, 2024, 18, 14791–15328.
- 53 V. N. Manoharan, *Science*, 2015, 349, 1253751.
- 54 A. M. Kalsin, M. Fialkowski, M. Paszewski, S. K. Smoukov, K. J. M. Bishop and B. A. Grzybowski, *Science*, 2006, 312, 420–424.
- 55 T. P. Bigioni, X. M. Lin, T. T. Nguyen, E. I. Corwin, T. A. Witten and H. M. Jaeger, *Nat. Mater.*, 2006, 5, 265–270.
- 56 K. E. Mueggenburg, X. M. Lin, R. H. Goldsmith and H. M. Jaeger, *Nat. Mater.*, 2007, 6, 656–660.
- 57 W. Cheng, M. J. Campolongo, J. J. Cha, S. J. Tan, C. C. Umbach, D. A. Muller and D. Luo, *Nat. Mater.*, 2009, 8, 519–525.
- 58 A. Dong, J. Chen, P. M. Vora, J. M. Kikkawa and C. B. Murray, *Nature*, 2010, 466, 474–477.
- 59 T. Wen and S. A. Majetich, *ACS Nano*, 2011, 5, 8868–8876.
- 60 C. Yu, X. Guo, M. Muzzio, C. T. Seto and S. Sun, *ChemPhysChem*, 2019, 20, 23–30.
- 61 Y. Xia, T. D. Nguyen, M. Yang, B. Lee, A. Santos, P. Podsiadlo, Z. Tang, S. C. Glotzer and N. A. Kotov, *Nat. Nanotechnol.*, 2011, 6, 580–587.
- 62 D. Liu, F. Zhou, C. Li, T. Zhang, H. Zhang, W. Cai and Y. Li, *Angew. Chem., Int. Ed.*, 2015, 54, 9596–9600.
- 63 C. Pigliacelli, D. Maiolo, Nonappa, J. S. Haataja, H. Amenitsch, C. Michelet, P. Sánchez Moreno, I. Tirotta, P. Metrangolo and F. Baldelli Bombelli, *Angew. Chem., Int. Ed.*, 2017, 56, 16186–16190.
- 64 S. Li, J. Liu, N. S. Ramesar, H. Heinz, L. Xu, C. Xu and N. A. Kotov, *Nat. Commun.*, 2019, 10, 4826.
- 65 C. Pigliacelli, K. B. Sanjeeva, Nonappa, A. Pizzi, A. Gori, F. B. Bombelli and P. Metrangolo, *ACS Nano*, 2019, 13, 2158–2166.
- 66 K. Kimura and T. Pradeep, *Phys. Chem. Chem. Phys.*, 2011, 13, 19214.
- 67 M. A. Boles, M. Engel and D. V. Talapin, *Chem. Rev.*, 2016, 116, 11220–11289.
- 68 G. M. Whitesides and M. Boncheva, *Proc. Natl. Acad. Sci. U. S. A.*, 2002, 99, 4769–4774.
- 69 D. Frenkel, *Phys. A*, 2002, 313, 1–31.
- 70 C. Burda, X. Chen, R. Narayanan and M. A. El-Sayed, *Chem. Rev.*, 2005, 105, 1025–1102.
- 71 S. C. Glotzer and M. J. Solomon, *Nat. Mater.*, 2007, 6, 557–562.
- 72 J. Fang, B. Ding and H. Gleiter, *Chem. Soc. Rev.*, 2011, 40, 5347–5360.
- 73 P. Qiu, B. Ma, C. T. Hung, W. Li and D. Zhao, *Acc. Chem. Res.*, 2019, 52, 2928–2938.
- 74 H. Cölfen and M. Antonietti, *Angew. Chem., Int. Ed.*, 2005, 44, 5576–5591.
- 75 H. Cölfen and S. Mann, *Angew. Chem., Int. Ed.*, 2003, 42, 2350–2365.
- 76 D. Gebauer and S. E. Wolf, *J. Am. Chem. Soc.*, 2019, 141, 4490–4504.
- 77 M. Jehannin, A. Rao and H. Cölfen, *J. Am. Chem. Soc.*, 2019, 141, 10120–10136.
- 78 N. T. K. Thanh, N. Maclean and S. Mahiddine, *Chem. Rev.*, 2014, 114, 7610–7630.
- 79 S. Karthika, T. K. Radhakrishnan and P. Kalaichelvi, *Cryst. Growth Des.*, 2016, 16, 6663–6681.
- 80 J. De Roo, *Chem. Mater.*, 2022, 34, 5766–5779.
- 81 A. Sánchez-Iglesias, M. Grzelczak, T. Altantzis, B. Goris, J. Pérez-Juste, S. Bals, G. Van Tendeloo, S. H. Donaldson Jr., B. F. Chmelka, J. N. Israelachvili and L. M. Liz-Marzán, *ACS Nano*, 2012, 6, 11059–11065.
- 82 N. Vogel, S. Goerres, K. Landfester and C. K. Weiss, *Macromol. Chem. Phys.*, 2011, 212, 1719–1734.
- 83 D. V. Talapin, J.-S. Lee, M. V. Kovalenko and E. V. Shevchenko, *Chem. Rev.*, 2010, 110, 389–458.
- 84 C. Jenewein, S. M. Schupp, B. Ni, L. Schmidt-Mende and H. Cölfen, *Small Sci.*, 2022, 2, 2200014.
- 85 M. R. Jones, K. D. Osberg, R. J. Macfarlane, M. R. Langille and C. A. Mirkin, *Chem. Rev.*, 2011, 111, 3736–3827.
- 86 S. Sun, X. Yu, Q. Yang, Z. Yang and S. Liang, *Nanoscale Adv.*, 2019, 1, 34–63.
- 87 L. Zhang, M. Zhou, A. Wang and T. Zhang, *Chem. Rev.*, 2020, 120, 683–733.
- 88 Y. Shi, Z. Lyu, M. Zhao, R. Chen, Q. N. Nguyen and Y. Xia, *Chem. Rev.*, 2021, 121, 649–735.
- 89 T. Tachikawa and T. Majima, *NPG Asia Mater.*, 2014, 6, e100–e100.
- 90 E. Uchaker and G. Cao, *Nano Today*, 2014, 9, 499–524.
- 91 L. Zhou and P. O'Brien, *J. Phys. Chem. Lett.*, 2012, 3, 620–628.
- 92 B. Ni, G. Gonzalez-Rubio and H. Cölfen, *Acc. Chem. Res.*, 2022, 55, 1599–1608.
- 93 M. Brust, M. Walker, D. Bethell, D. J. Schiffrin and R. Whyman, *J. Chem. Soc., Chem. Commun.*, 1994, 801–802.
- 94 P. Chakraborty, P. Bose, J. Roy, A. Nag, B. Mondal, A. Chakraborty and T. Pradeep, *J. Phys. Chem. C*, 2021, 125, 16110–16117.
- 95 M. Grzelczak, J. Vermant, E. M. Furst and L. M. Liz-Marza, *ACS Nano*, 2010, 4, 3591–3605.
- 96 K.-J. Wu, E. C. M. Tse, C. Shang and Z. Guo, *Prog. Mater. Sci.*, 2022, 123, 100821.
- 97 M. P. Mallin and C. J. Murphy, *Nano Lett.*, 2002, 2, 1235–1237.
- 98 S. Tokonami, N. Morita, K. Takasaki and N. Toshima, *J. Phys. Chem. C*, 2010, 114, 10336–10341.
- 99 S. W. Verbruggen, M. Keulemans, J. A. Martens and S. Lenaerts, *J. Phys. Chem. C*, 2013, 117, 19142–19145.

Electronic Supplementary Information

Nanocluster reaction-driven *in situ* transformation of colloidal nanoparticles to mesostructures

Paulami Bose,^{a†} Pillalamarri Srikrishnarka,^{a†} Matias Paatelainen,^b Nonappa,^b Amoghavarsha Ramachandra Kini,^a Anirban Som,^a and Thalappil Pradeep^{a*}

^aDST Unit of Nanoscience (DST UNS) and Thematic Unit of Excellence (TUE), Department of Chemistry, Indian Institute of Technology Madras, Chennai 600 036, India.

^bFaculty of Natural Sciences and Engineering, Tampere University, Korkeakoulunkatu 3, FI-33720, Tampere, Finland

*E-mail: pradeep@iitm.ac.in

[†]Present address

Table of Contents

Name	Description	Page No.
SI 1	Instrumentation	2
SI 2	Experimental section	3
Fig. S1	Characterization of [Au ₂₅ (PET) ₁₈] ⁻ NC	7
Fig. S2	Characterization of Ag@PET NPs	7
Fig. S3	Characterization of reacted NPs	8
Fig. S4	Composition of reacted NP	8
Fig. S5	Demonstration of leak-proofing of the reaction bottle	8
Fig. S6	Electron microscopic images of individual nanocrystals	9
Fig. S7	AFM analysis of mesocrystals produced in toluene under heat	10
Fig. S8	EDS spectrum of mesocrystals produced in toluene under heat	10
Fig. S9	Electron microscopic images of mesostructure obtained in DCM at room temp.	11
Fig. S10	Degradation of mesostructure	11

Fig. S11	AFM analysis of mesostructure obtained at room temp.	12
Fig. S12	EDS spectrum of mesostructure obtained at room temp.	12
Fig. S13	Stability of PET-capped Ag NPs and Au NCs in reaction condition	13
Fig. S14	Time-dependent nucleation and growth of AgAu@PET NPs	14
Fig. S15	Au@DMBT NPs and $[\text{Ag}_{25}(\text{DMBT})_{18}]^{-}$ NC reaction	15
Fig. S16	Au@PET NPs and $[\text{Au}_{25}(\text{PET})_{18}]^{-}$ NC	16
Fig. S17	Stability of PET-capped Au NPs in reaction condition	17
Fig. S18	Au@PET NPs and $[\text{Ag}_{25}(\text{DMBT})_{18}]^{-}$ NC	17
SI 3	References	17

SI 1. Instrumentation

Instrumentation. *Optical Absorption Spectroscopy:* The optical absorption (UV-Vis) spectra were recorded using a Perkin Elmer Lambda 25 instrument with a range of 200 – 1100 nm and a bandpass filter of 1 nm.

High-resolution transmission electron microscopy: HRTEM imaging was carried out in JEOL 3010, JEOL JEM F200, and Thermo Scientific Talos 200i instruments. Gatan 794 multiscan CCD, Gatan OneView, and Ceta 16M CMOS cameras were used to capture the images. Samples were prepared by dropcasting the dispersion on carbon-coated copper grids (spi Supplies, 3530C-MB) and dried at ambient conditions.

High-resolution field emission scanning electron microscope: HR FESEM and energy-dispersive X-ray spectroscopy (EDS) imaging were carried out in a Thermo Scientific Verios G4 UC. The instrument was equipped with a Schottky FEG electron gun with an adjustable probe current ranging between 0.8 nA–100 nA. The surface was imaged using backscattered and secondary electrons, with an accelerating voltage of 10 kV and high vacuum conditions.

Optical microscope: Keyence VHX-6000 digital microscope with VH-Z100T field lens (100-1000x) magnification.

Dynamic light scattering: DLS measurements were performed in a glass cuvette (10 mm path length) using a Malvern Zetasizer Nano-ZS instrument.

Atomic Force microscopy: AFM images were collected using a Bruker Dimension Icon instrument. The ScanAsyst mode was utilized for the measurement, using RTESPA-150 and RTESPA-300 probes.

Scanning Transmission Electron Microscopy and EDS mapping: The STEM imaging was performed using a JEOL JEM F200 high throughput electron microscope equipped with a Schottky-type field emission gun operated at 200 kV with simultaneous bright field (BF) and dark field (DF) STEM imaging. EDS mapping and spectra were collected using dual silicon drift detectors.

SI 2. Experimental section

Materials. Silver nitrate (AgNO_3 , $\geq 99\%$), 2-phenylethanethiol (PET, 98%), tetraoctylammonium bromide (TOABr, 98%), 2,4-dimethylbenzenethiol (DMBT, 95%), sodium borohydride (NaBH_4 , $\geq 99\%$), and triphenylphosphine (TPP, 99%) were purchased from Sigma Aldrich. Tetrachloroauric acid ($\text{HAuCl}_4 \cdot 3\text{H}_2\text{O}$) was prepared from pure gold and aqua regia in the laboratory. All the solvents used were of HPLC grade without further purification. Millipore-produced deionized water ($\sim 18.2 \text{ M}\Omega$) was used throughout the experiments.

Synthesis of Ag@PET nanoparticles. 2-PET-capped Ag NPs were synthesized by modifying the traditional preparation method of silver NPs.^{1,2} 50 mg of AgNO_3 was dissolved in 0.5 mL of water and added to 58 μL of PET in 30 mL of methanol. Next, silver was reduced to the zero-valent state by slowly adding the freshly prepared aqueous NaBH_4 solution (75 mg in 8 mL ice-cold water) with vigorous stirring. The reaction mixture was further stirred for an hour, followed by overnight refluxing at 333 K. For purification, the precipitate was collected and repeatedly washed with methanol by centrifugal precipitation. Finally, the purified NPs were extracted in DCM, size-focussed using high-speed centrifugation, dried in a rotary evaporator, and stored in a refrigerator.

The synthesized Au@PET NPs were characterized using optical absorption spectroscopy and HRTEM; the characterization data are presented in Fig. 1B g-i and S2. From the particle size distribution, the NPs were found to have an average size of 4.4 ± 2.3 nm. The most probable diameter of the metallic core of the particle is considered for particle size calculation.

Synthesis of the $[Au_{25}(PET)_{18}]^-$ nanocluster. The NC was synthesized using a slightly modified reported protocol.³ Initially, a solution of 40 mg of $HAuCl_4 \cdot 3H_2O$ in 7.5 mL of THF was prepared. Next, 65 mg of TOABr was added to the reaction mixture and stirred for 15 min. Then, 68 μ L of PET was added, and the mixture was further stirred for an hour, followed by the slow addition of freshly prepared aqueous $NaBH_4$ solution (39 mg in 2.5 mL ice-cold water). The reaction mixture was stirred for another 5 h for a complete reduction and size focussing. For purification, the crude NC solution was centrifuged to remove free thiols and excess thiolates, and the collected supernatant was concentrated by rotary evaporation. The precipitate was washed multiple times with methanol. The NC was extracted in acetone and centrifuged, the supernatant was collected, and the precipitate containing larger NCs was discarded. The supernatant comprising the pure NC was vacuum-dried and finally collected in DCM.

The purified NC was characterized using optical absorption microscopy, HRTEM, and ESI MS (Fig. 1B a-c and S1).

Synthesis of the $[Ag_{25}(DMBT)_{18}]^-$ nanocluster. The NC was synthesized by slightly modifying a previously reported protocol.⁴ First, 38.0 mg of $AgNO_3$ was dissolved in 2 mL of methanol. To this mixture, 90 μ L of 2,4-DMBT was added, which produced an insoluble yellow Ag-thiolate, followed by 17 mL of DCM, and then it was stirred for 15 mins at 0 °C. Afterwards, 0.5 mL of methanolic solution of 6 mg PPh_4Br was added, followed by a dropwise addition of 15.0 mg of $NaBH_4$ in 0.5 mL of ice-cold water. The reaction mixture was further stirred for 7-8 h, followed by overnight ageing in the refrigerator. For purification, the crude NC solution was centrifuged to remove any insoluble impurities, and the collected supernatant was concentrated by rotary evaporation. The precipitate was washed multiple times with methanol. Then, the NC was extracted in DCM and centrifuged again to remove any remaining insoluble impurities. DCM was removed using rotavapor, and the purified NC was obtained in its powdered form.

Synthesis of Au@DMBT nanoparticles. The synthesis of 2,4-dimethylbenzenethiol-capped Au nanoparticles, referred to as Au@DMBT NPs, was carried out using a modified Brust-Schiffrin synthesis method.⁵ Initially, an aqueous H_{AuCl₄·3H₂O} (5.0 mg in 0.5 mL H₂O) was mixed with 13.4 mg of TOABr in 30 mL toluene. The aqueous-organic mixture was vigorously stirred for 15 min, and then 7 μL of 2,4-DMBT was added. Next, 2.0 mg of NaBH₄ in 10 mL of ice-cold water was added dropwise with vigorous stirring as the color of the reaction mixture turned purple. After stirring the reaction mixture for nearly an hour, the organic layer was separated, and the size focussing was done with overnight heating at 60 °C. After heating, the color of the organic layer changed from purple to wine-red. Further purification was performed by removing the solvent under reduced pressure using a rotary evaporator and washing it with ethanol. Finally, the purified NP was extracted in toluene, dried in a rotary evaporator, and stored in a refrigerator.

The synthesized Au@DMBT NPs were characterized using optical absorption spectroscopy and HRTEM, as presented in Fig. S15. From the particle size distribution, the NPs were found to have an average size of 4.5 ± 0.6 nm. Please note that for particle size calculation, we are referring to the most probable diameter of the metallic core of the particle.

Synthesis of Au@PET nanoparticles. The synthesis of 2-phenylethanethiol-capped Au nanoparticles, referred to as Au@PET NPs, was prepared using a modified Brust-Schiffrin synthesis method.⁵ Initially, an aqueous H_{AuCl₄·3H₂O} (5.0 mg in 0.5 mL H₂O) was mixed with 13.4 mg of TOABr in 30 mL toluene. The aqueous-organic mixture was vigorously stirred for 15 min, and then 7 μL of 2-PET was added. Next, a freshly prepared aqueous solution of NaBH₄ (6.0 mg in 10 mL of ice-cold water) was added dropwise with vigorous stirring as the color of the reaction mixture turned purple. After stirring the reaction mixture for nearly an hour, the organic layer was separated, and the size focussing was done with overnight heating at 60 °C. After heating, the color of the organic layer changed from purple to wine-red. Further purification was performed by removing the solvent under reduced pressure using a rotary evaporator and washing it with ethanol. Finally, the purified NP was extracted in toluene, dried in a rotary evaporator, and stored in a refrigerator.

The synthesized Au@PET NPs were characterized using optical absorption spectroscopy and HRTEM, as presented in Fig. S16.

Nucleation and assembly of mesostructures. For interparticle reaction, 7 mg of Ag@PET NPs were dissolved in 6 mL solvent, and about 0.9 mg of the Au₂₅(PET)₁₈ NC was dissolved in 600 μL of solvent, separately. The final reaction mixture was made by combining the NP and NC dispersions at room temperature in a leak-proof reaction bottle and allowing them to react under constant stirring and heating/no heating for an extended period of time (of the order of days); demonstration of the setup in Fig. S5. The reaction was monitored using microscopic (optical, TEM, and FESEM) and spectroscopic (UV-Vis and DLS) techniques.

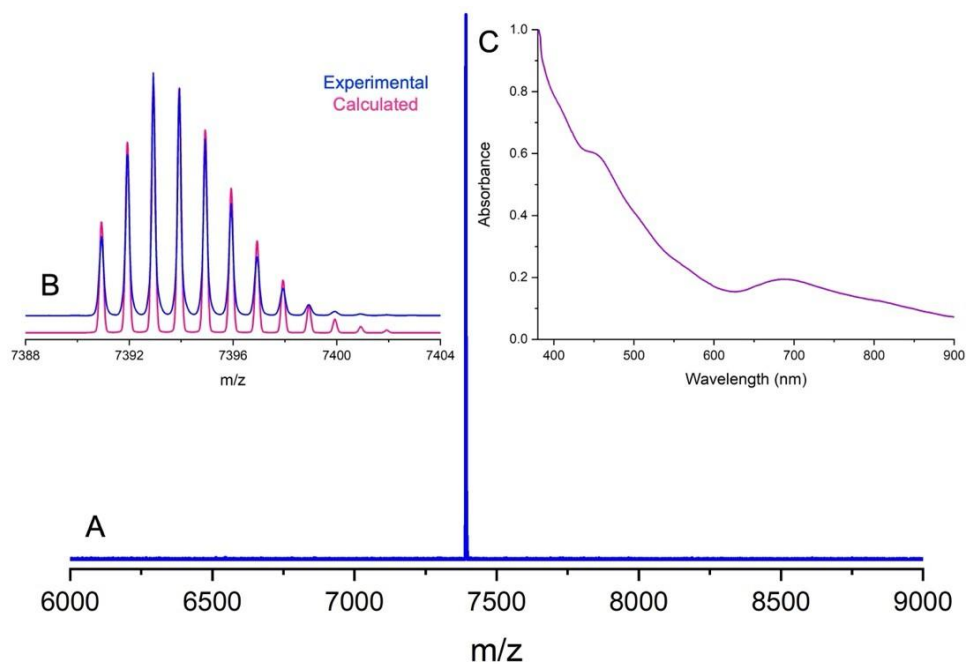


Fig. S1 Characterization of $[\text{Au}_{25}(\text{PET})_{18}]^{-}$ NC. (A) ESI MS of the molecular ion peak, (B) the corresponding experimental and theoretical comparison of the high-resolution isotopic distribution pattern, and (C) optical absorption spectrum.

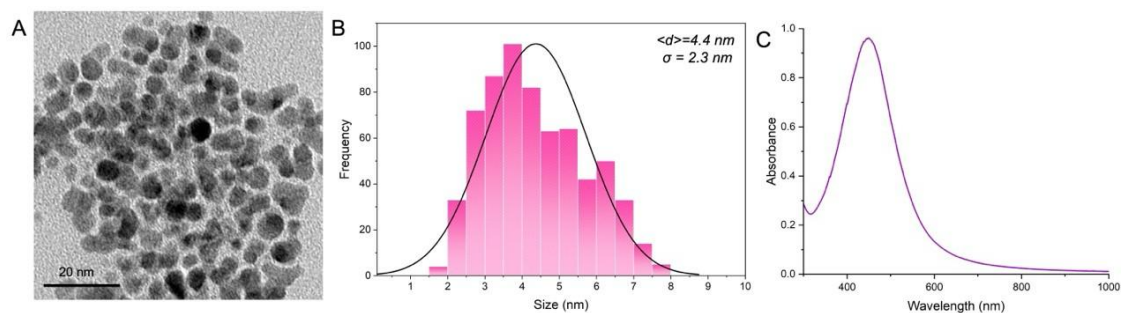


Fig. S2 Characterization of Ag@PET NPs. (A) TEM image, (B) the corresponding particle size distribution, and (C) the optical absorption spectrum of the polydispersed Ag@PET NPs. The terms $\langle d \rangle$ and σ refer to the mean diameter and standard deviation, respectively. Note that the most probable diameter of the metal core is considered for the estimation of particle size.

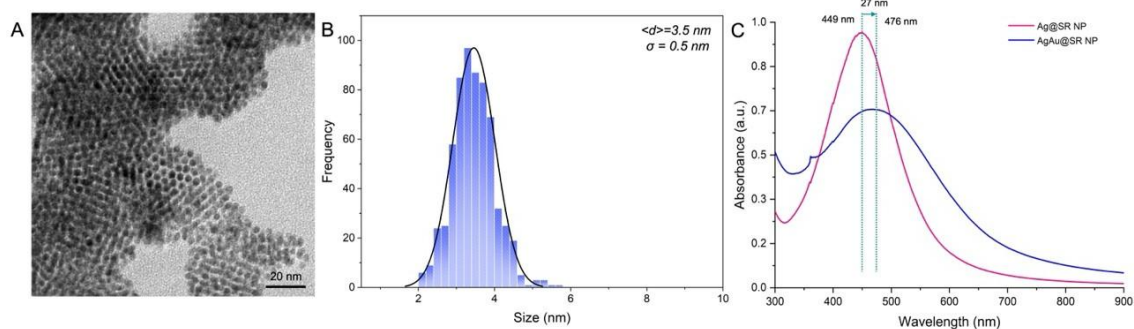


Fig. S3 Characterization of bimetallic AgAu@PET NPs. (A) TEM image, (B) particle size distribution, and (C) optical absorption spectrum (blue trace) of the reacted AgAu@PET NPs. The terms $\langle d \rangle$ and σ refer to the mean diameter and standard deviation, respectively.

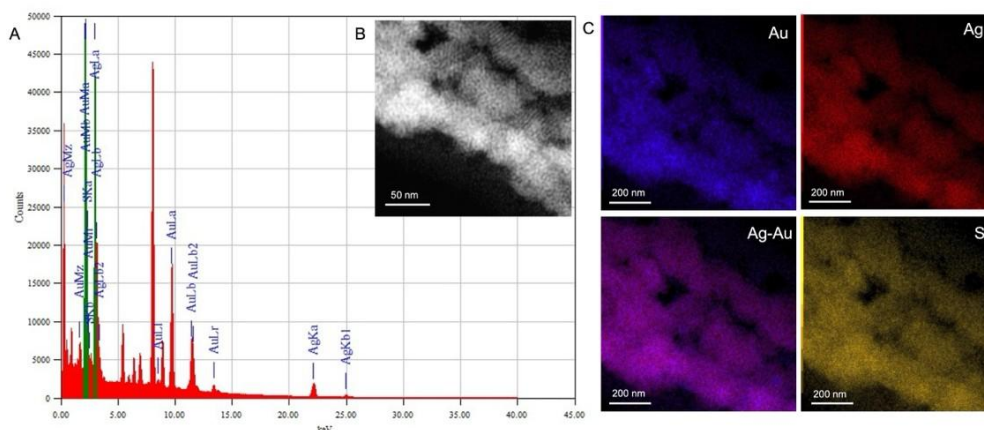


Fig. S4 Compositional analysis of reacted NPs. (A) EDS spectrum, (B) STEM image, and (C) the corresponding STEM-EDS elemental maps of the reacted NP.

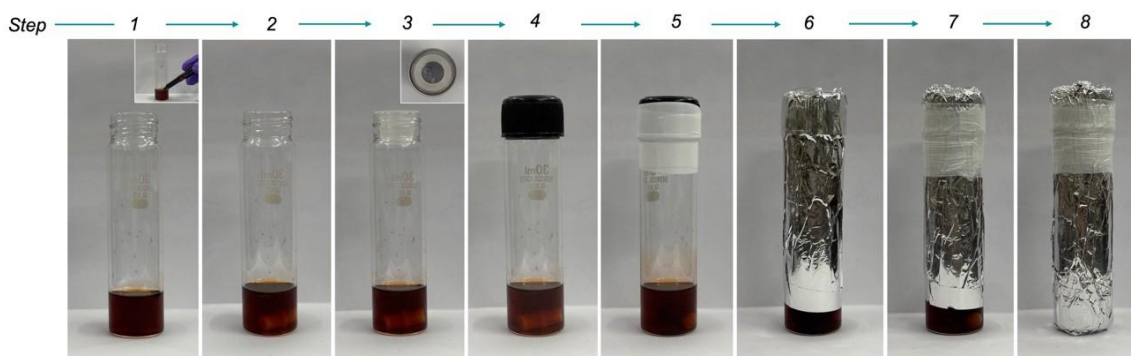


Fig. S5 Sequential of images demonstrating a step-by-step leak-proofing of the reaction setup so that it can handle the interparticle reaction for an extended period of time. In a glass vial, the reaction mixture was placed (step 1), and the total volume was marked for reference (inset of step 1). A magnetic pellet was then added, and the reaction was ready for further

processing (step 2). The vial was sealed with a stopper (step 3), a screw cap (step 4), and then secured with Teflon tape (step 5). An additional barrier against light and air was created by wrapping the vial with aluminium foil (step 6) and parafilm (step 7). The reaction bottles are now ready to be continuously stirred in the dark at 45 °C in an oil bath (step 7), and at room temperature (step 8).

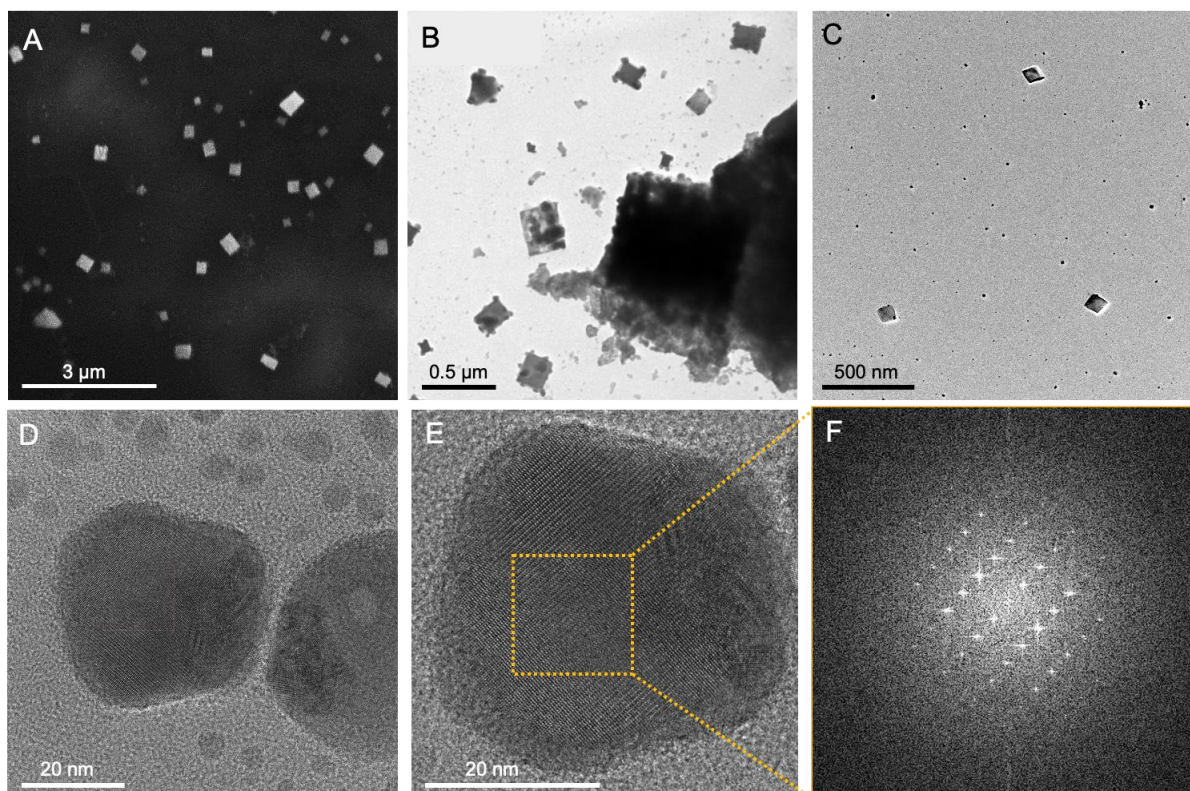


Fig. S6 FESEM (A), TEM (B, C), HRTEM (D, E), and the corresponding FFT (F) images of individual platelet-shaped nanocrystals, which are the building blocks of the cuboidal mesocrystals.

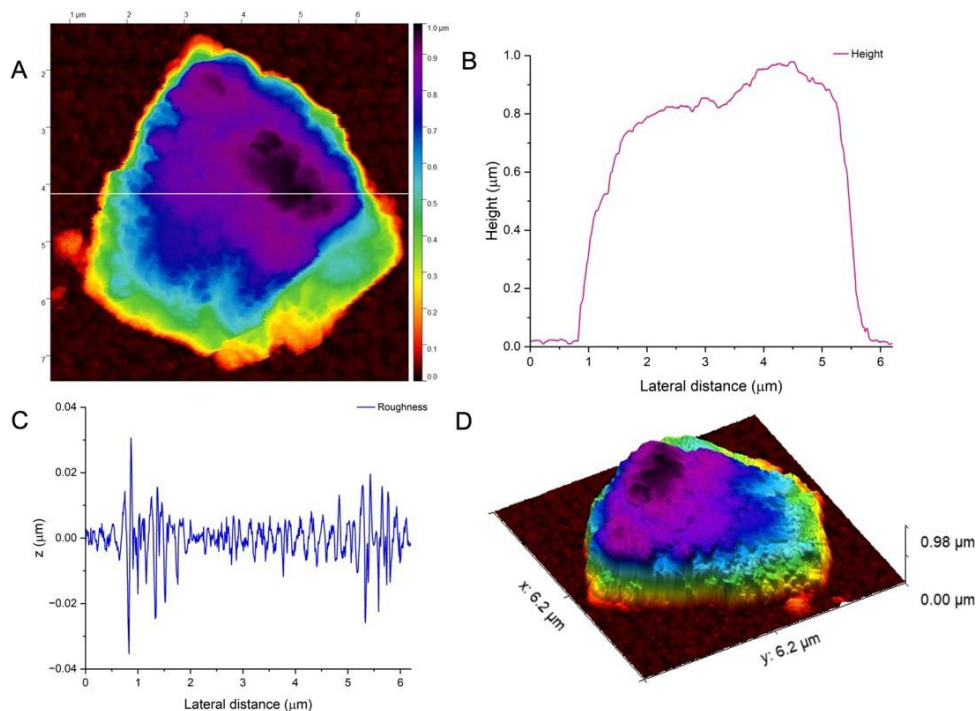


Fig. S7 AFM study of the mesocrystal obtained at the end of the interparticle reaction in toluene at 45 °C. AFM image of one of the mesocrystals (A), and its corresponding height profile (B), roughness (C), and the 3D representation of the surface topology (D).

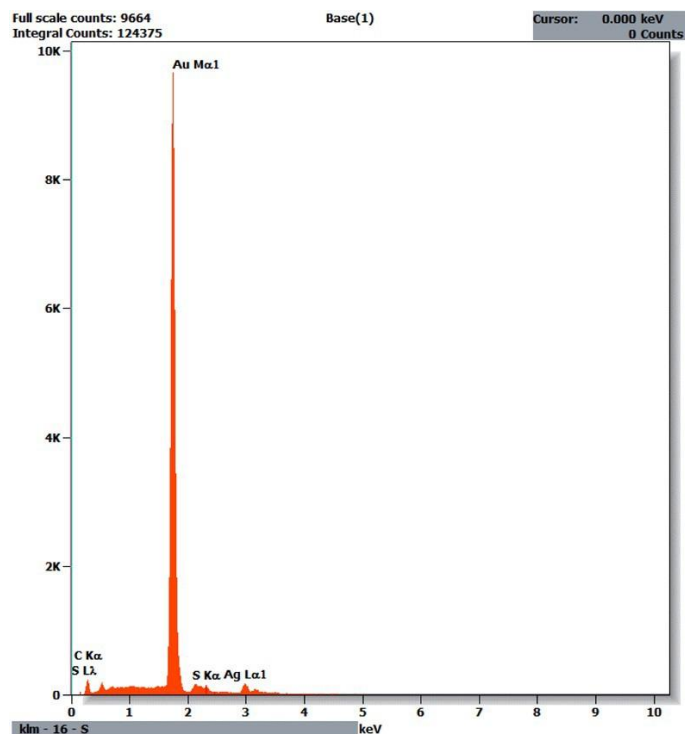


Fig. S8 EDS spectrum of the mesostructure produced by the interparticle reaction in toluene and under heating conditions.

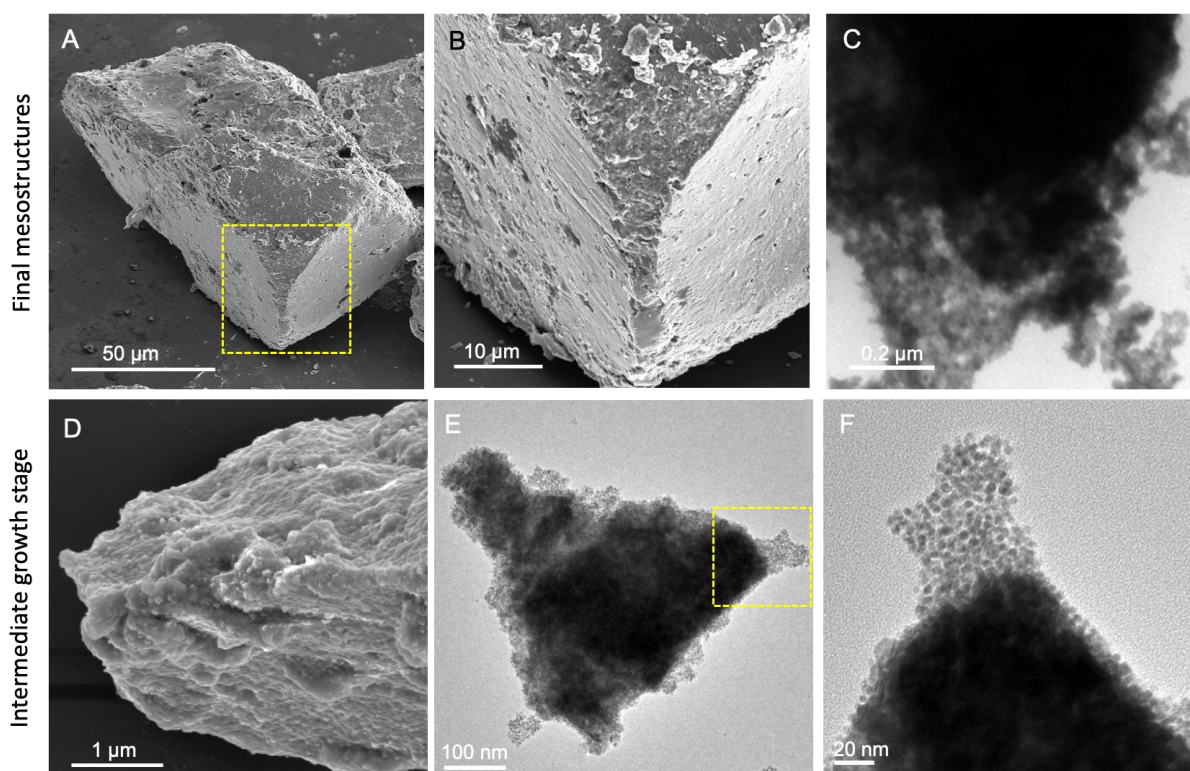


Fig. S9 Nucleation and growth of AgAu@PET NPs into random close-packed mesostructures. FESEM and TEM images of as-obtained mesostructure at the end of the reaction (A-C) and at the intermediate phase (D-F).

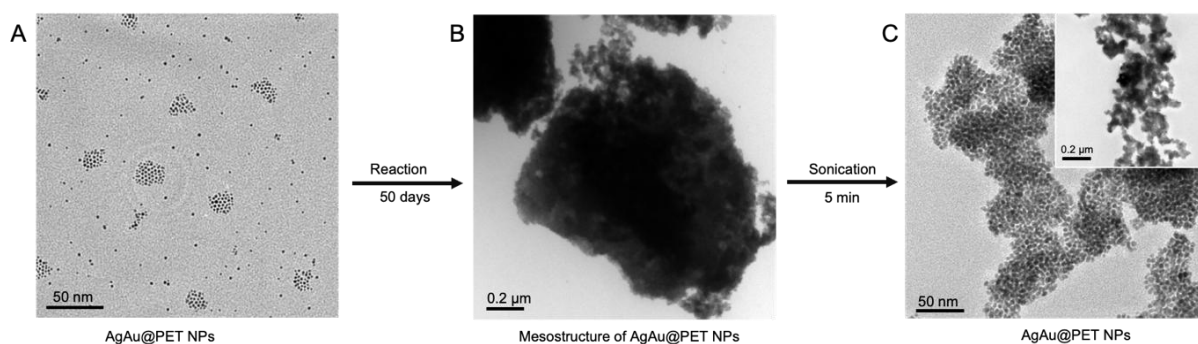


Fig. S10 TEM images of reacted AgAu@PET NPs before (A) and after assembly into a cuboidal mesostructure (B), and the recovered NPs after sonication (C). Inset (of C) shows the disintegration of larger mesostructure into original NP units.

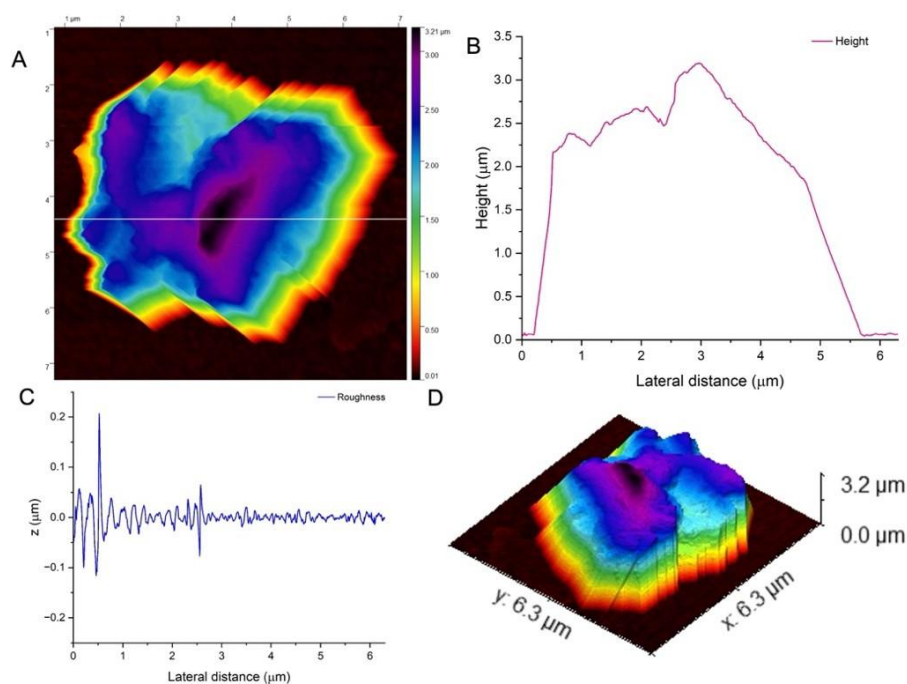


Fig. S11 AFM study of the mesostructure obtained at the end of the interparticle reaction in DCM at room temperature. AFM image of the mesostructure surface (A), and its corresponding height profile (B), roughness (C), and the 3D representation of the surface topology (D).

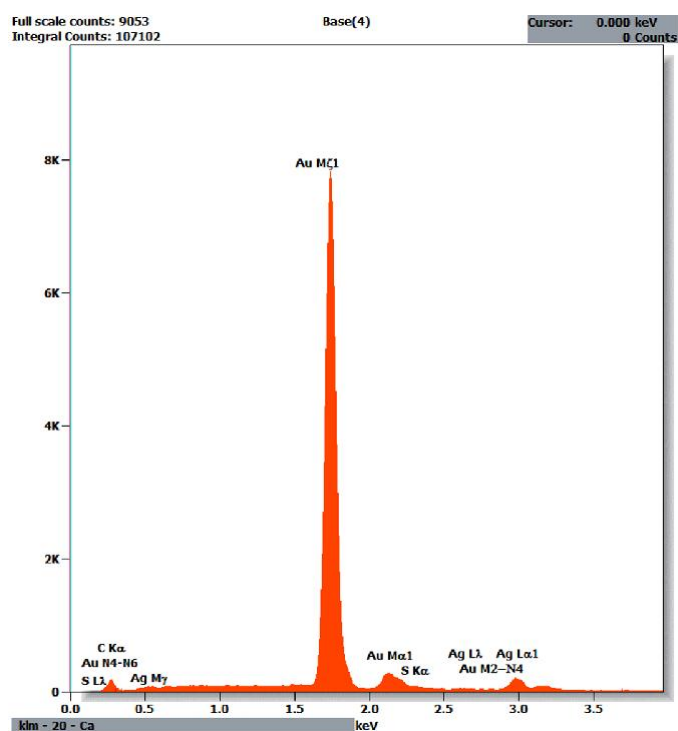


Fig. S12 EDS spectrum of the mesostructure produced by the interparticle reaction in DCM at room temperature.

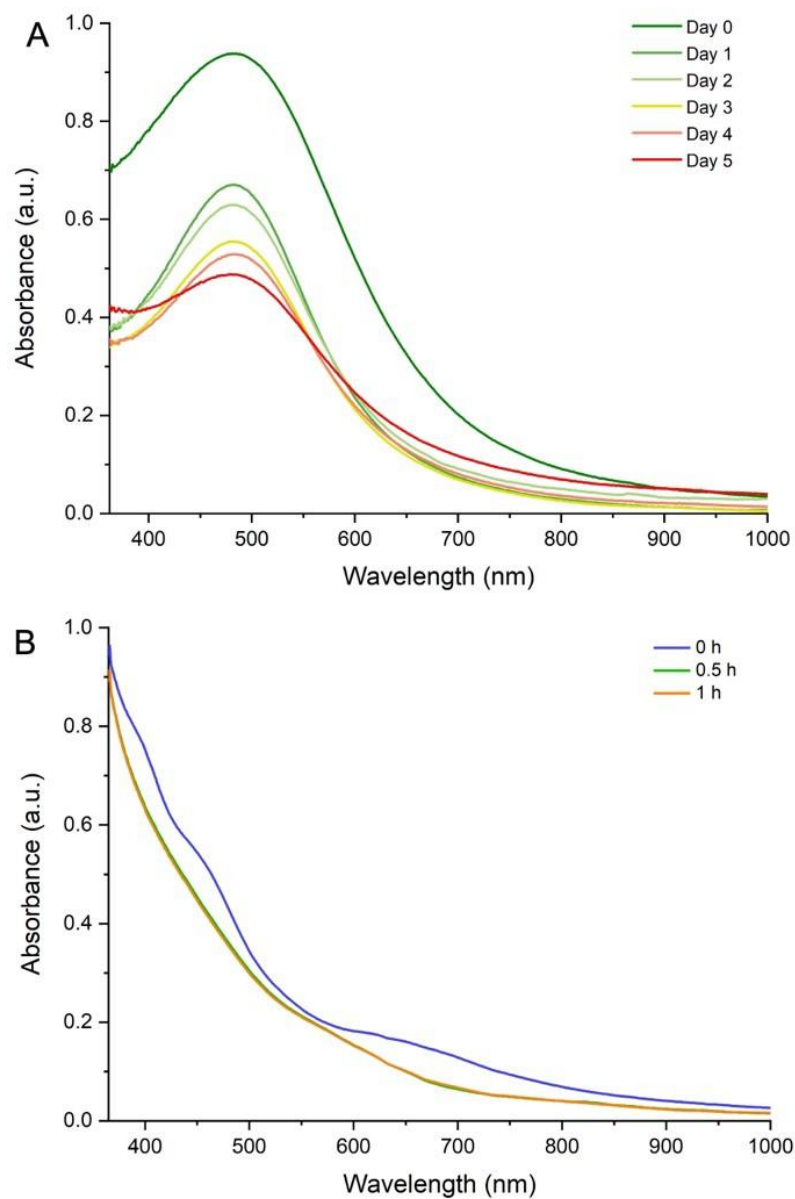


Fig. S13 Optical absorption spectra of the (A) parent polydispersed Ag@PET NPs, and (B) $[\text{Au}_{25}(\text{PET})_{18}]^{-}$ NC, showing degradation over time when heated to 45°C in toluene with a constant stirring at 250 RPM.

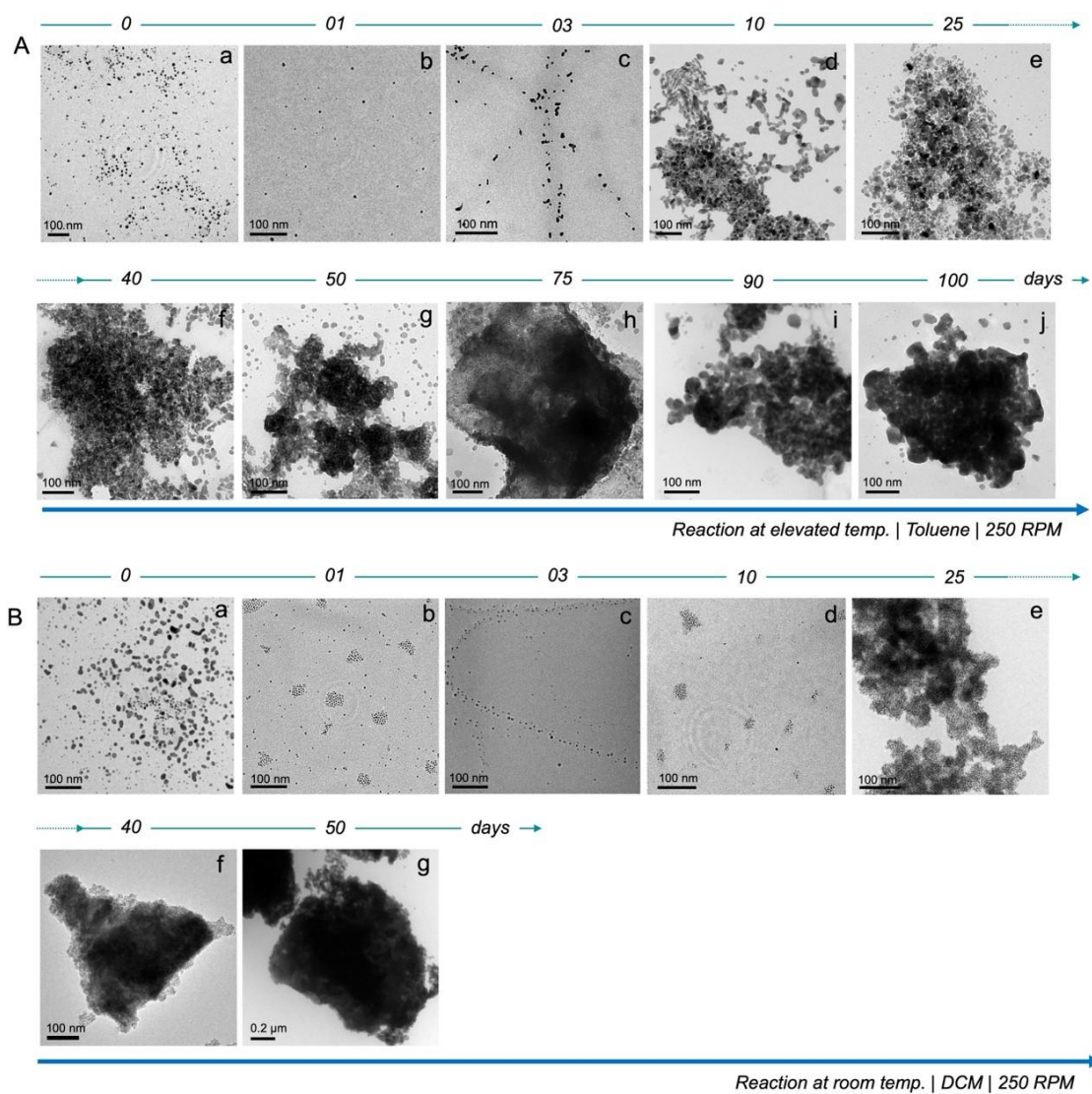


Fig. S14 TEM images showing time-dependent nucleation and growth of AgAu@PET NPs into the mesostructures when the interparticle reaction is carried out in toluene at 45°C (A) and in DCM at room temperature (B) with constant stirring at 250 RPM.

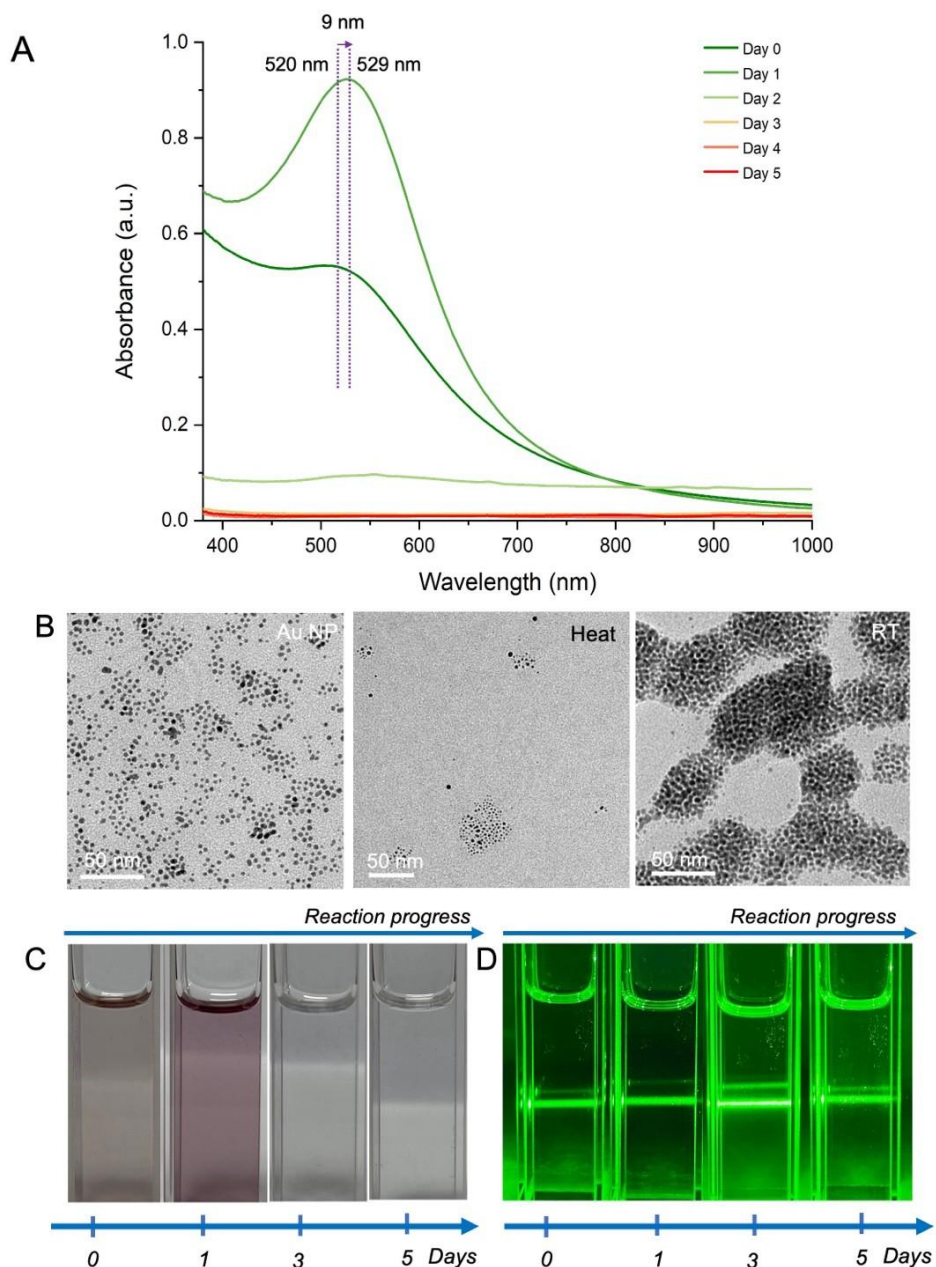


Fig. S15 (A) Time-dependent optical absorption spectra, (B) TEM images collected within a day, (C) photographic reaction progression, and (D) light scattering experiment with 630 nm laser light of interparticle reaction between Au@DMBT NPs and $[Ag_{25}(DMBT)_{18}]^-$ NC (Au NP–Ag NC). The particle mixture underwent degradation as the reaction was carried out at 45°C in toluene with constant stirring at 250 RPM (Heat in B). However, the particle mixture formed a stable assembly in DCM at room temperature (RT in B).

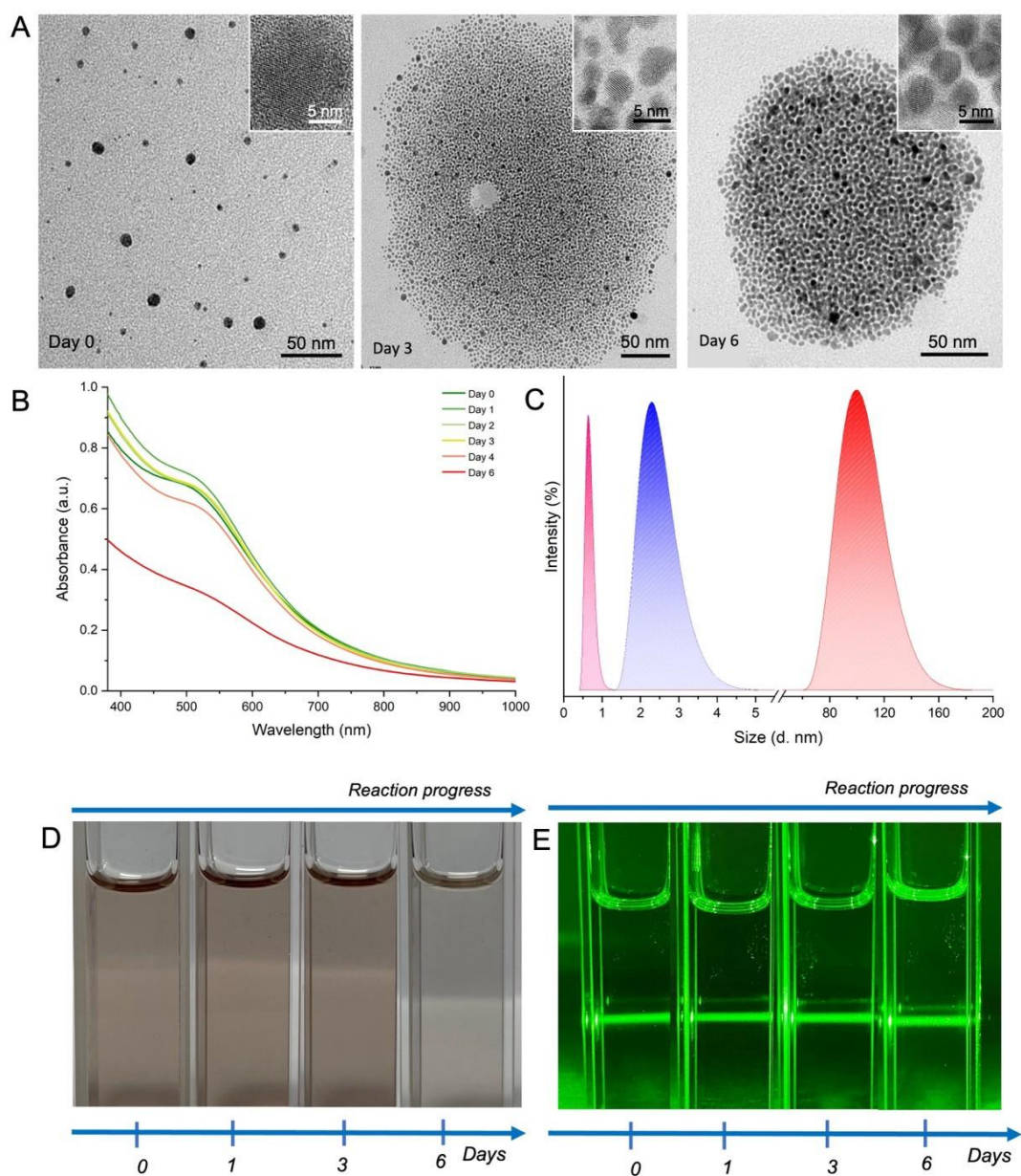


Fig. S16 Interparticle reaction between Au@PET NPs and [Au₂₅(PET)₁₈]⁻ NC (Au NP–Au NC) as a function of time (A) TEM and HRTEM images, (B) optical absorption spectra, (C) size distribution measured in dynamic light scattering spectra, (D) photographic reaction progression, and (E) light scattering experiment with 630 nm laser light. The reaction was carried out in toluene at 45 °C with constant stirring at 250 RPM.

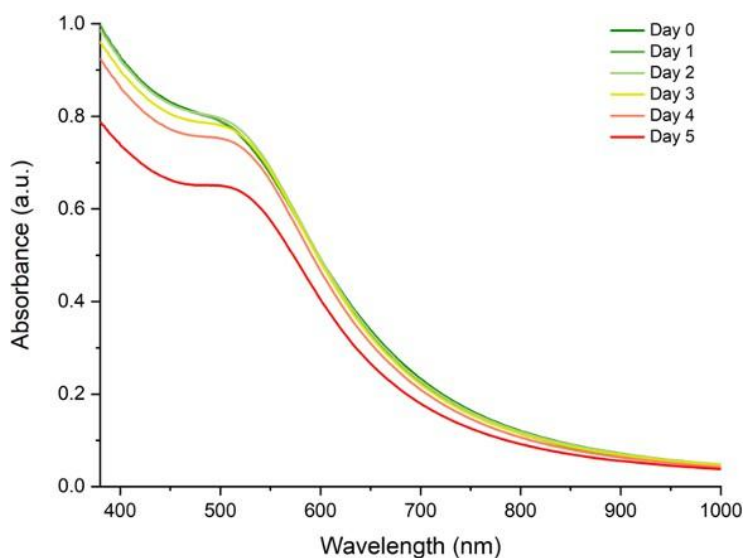


Fig. S17 Optical absorption spectra of the Au@PET NP dispersion in toluene with continual stirring at 250 RPM and heating at 45°C.

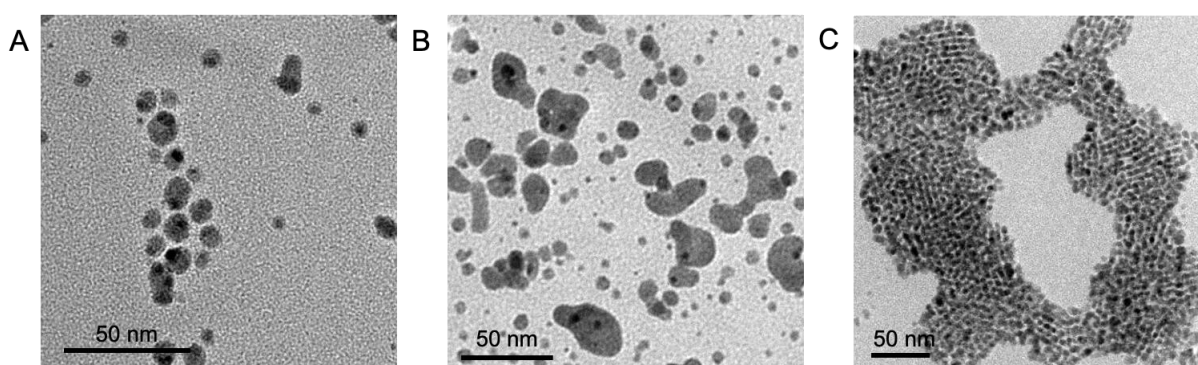


Fig. S18 TEM images show the parent Ag@PET NP (A) and its reaction with the $[\text{Ag}_{25}(\text{DMBT})_{18}]^{-}$ NC (Ag NP–Ag NC) carried out at 45°C in toluene (B) and room temperature in DCM (C) with a constant stirring at 250 RPM.

References

- 1 J. Kimling, M. Maier, B. Okenve, V. Kotaidis, H. Ballot and A. Plech, *J. Phys. Chem. B*, 2006, **110**, 15700–15707.
- 2 P. Bose, P. Chakraborty, J. S. Mohanty, Nonappa, A. Ray Chowdhuri, E. Khatun, T. Ahuja, A. Mahendranath and T. Pradeep, *Nanoscale*, 2020, **12**, 22116–22128.

- 3 Z. Wu, J. Suhan and R. Jin, *J. Mater. Chem.*, 2009, **19**, 622–626.
- 4 C. P. Joshi, M. S. Bootharaju, M. J. Alhilaly and O. M. Bakr, *J. Am. Chem. Soc.*, 2015, **137**, 11578–11581.
- 5 M. Brust, M. Walker, D. Bethell, D. J. Schiffrin and R. Whyman, *J. Chem. Soc. Chem. Commun.*, 1994, 801–802.

Milling-Induced “Turn-off” Luminescence in Copper Nanoclusters

Subrata Duary, Arijit Jana, Amitabha Das, Swetashree Acharya, Amoghavarsha Ramachandra Kini, Jayoti Roy, Ajay Kumar Poonia, Deepak Kumar Patel, Vivek Yadav, P. K. Sudhadevi Antharjanam, Biswarup Pathak,* Adarsh Kumaran Nair Valsala Devi,* and Thalappil Pradeep*



Cite This: *Inorg. Chem.* 2024, 63, 18727–18737



Read Online

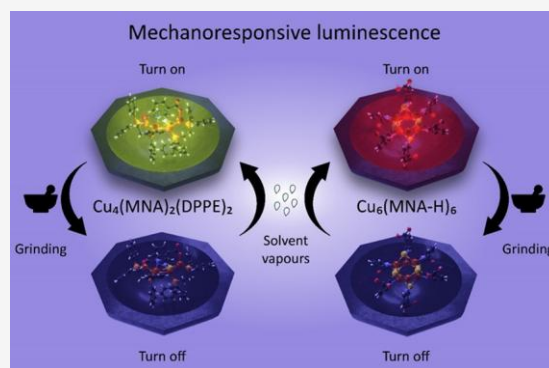
ACCESS

Metrics & More

Article Recommendations

Supporting Information

ABSTRACT: Atomically precise copper nanoclusters (NCs) attract research interest due to their intense photoluminescence, which enables their applications in photonics, optoelectronics, and sensing. Exploring these properties requires carefully designed clusters with atomic precision and a detailed understanding of their atom-specific luminescence properties. Here, we report two copper NCs, $[\text{Cu}_4(\text{MNA})_2(\text{DPPE})_2]$ and $[\text{Cu}_6(\text{MNA-H})_6]$, shortly Cu_4 and Cu_6 , protected by 2-mercaptonicotinic acid (MNA- H_2) and 1,2-bis(diphenylphosphino)ethane (DPPE), showing “turn-off” mechanoresponsive luminescence. Single-crystal X-ray diffraction reveals that in the Cu_4 cluster, two Cu_2 units are appended with two thiols, forming a flattened boat-shaped Cu_4S_2 kernel, while in the Cu_6 cluster, two Cu_3 units form an adamantane-like Cu_6S_6 kernel. High-resolution electrospray ionization mass spectrometry studies reveal the molecular nature of these clusters. Lifetime decay profiles of the two clusters show the average lifetimes of 0.84 and 1.64 μs , respectively. These thermally stable Cu NCs become nonluminescent upon mechanical milling but regain their emission upon exposure to solvent vapors. Spectroscopic data of the clusters match well with their computed electronic structures. This work expands the collection of thermally stable and mechanoresponsive luminescent coinage metal NCs, enriching the diversity and applications of such materials.



INTRODUCTION

Atomically precise nanoclusters (NCs) are a distinct category of nanomaterials with a core dimension below 3 nm, showing unique physicochemical properties.^{1–5} Such materials have intrinsic molecule-like discrete electronic energy levels with molecular luminescence.^{6–8} Noble metal NCs are protected by thiol, amine, carbene, alkyne, phosphine, and carboxylic acid ligands, which control their size, shape, stability, optoelectronic properties, and chemical reactivity.^{9–14} Extensive investigations of gold and silver NCs have yielded valuable insights into their synthesis, structure, properties, and structure–property relationships.^{15,16} However, complex synthetic procedures, expensive precursors, low synthetic yields, and poor chemical purity are prime drawbacks, limiting the practical utility of several clusters.¹⁷ Alternatively, Cu NCs are promising candidates because Cu is more earth-abundant and less expensive, and there are several nontoxic precursors. Besides, the methods provide high synthetic yields.^{18–22} Recently, many moderate-sized and large Cu clusters, such as Cu_{18} , Cu_{20} , Cu_{29} , Cu_{33} , Cu_{58} , Cu_{62} , Cu_{74} , Cu_{81} , Cu_{93} , Cu_{96} , and Cu_{136} were synthesized, and several single-crystal X-ray structures were determined.^{23–27} Noble metal NCs, composed of gold and silver with specific nuclearity, generally exhibit luminescence with relatively low quantum yields, and their emission lifetimes range from the picosecond to the nanosecond time scale. In

contrast, copper clusters show longer lifetimes of the microsecond time scale and higher quantum yields, which motivated us to investigate their structure–property relationships in greater detail.³⁵

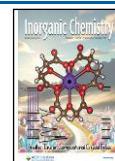
Generally, it has been observed that Cu NCs with low nuclearity exhibit strong, multicolor, and tunable luminescence due to their facile charge transfer between the ligand shell and metal.³⁶ Due to their intense luminescence in small Cu NCs, they may be used in various applications like light-emitting diodes, electroluminescence, anticounterfeiting, cell imaging, and optical sensing.^{28–34} Reports suggest that the involvement of Cu *d* orbitals and metal-to-ligand charge transfer or vice versa is likely to be responsible for their bright luminescence.^{37,38} For example, electron-donating ligands like amines and phosphines induce intense luminescence in ultrasmall Cu clusters.^{18,39} The intensity of emission originating in NCs depends on factors like chemical environment and restriction

Received: June 24, 2024

Revised: September 12, 2024

Accepted: September 17, 2024

Published: September 25, 2024



of intramolecular motion, controlled by surface ligands.^{40–42} Sometimes, a decrease in the molecular motions in the crystalline state enhances luminescence, popularly known as crystallization-induced emission.^{41,42} This type of intermolecular aggregation occurs due to CH– π and π – π interactions and hydrogen bonding, which together enhance the emission intensity.^{43,44} The bulky surface ligands, such as aromatic thiols, amines, and phosphines, stabilizing the metal–sulfur core in NCs, form a rigid framework, contributing to the chemical and thermal stability of the molecules or their packing in a stable crystalline state. The Cu–S core of a crystalline ordered structure in small Cu NCs is sensitive to external stimuli like temperature, pressure, and radiation.^{35,45–51} Cu NCs with such diverse properties motivated us to synthesize, crystallize, and explore the properties of new clusters for a rational understanding.

Reports of small Cu clusters and complexes with long Cu–Cu bond lengths protected by phosphines show mechanochromic luminescence.^{47–49} This is ascribed to the reversibility of molecular conformations and intermolecular interactions during transitions between thermodynamically stable crystalline and metastable amorphous states.⁵⁰ These transitions in Cu NCs are sometimes accompanied by changes in the excited states, which result in different types of luminescence upon mechanical stimuli.

In the present work, we have synthesized two luminescent Cu NCs, Cu₄ and Cu₆, primarily protected by 2-mercaptocotinic acid (MNA-H₂), following the strategy of ligand-exchange-induced structural transformation (LEIST). Single-crystal X-ray diffraction (SC-XRD) reveals their molecular structures and other spectroscopic studies were used to characterize them thoroughly. The Cu₄ cluster emits green luminescence, whereas Cu₆ emits red in its crystalline state under ambient conditions. Due to reversible phase transformations, these clusters manifest “turn-off” luminescence upon mechanical milling and partial luminescence recovery upon exposure to solvent vapor. Density functional theory (DFT) calculations provide a detailed understanding of their structures and properties. These mechanoresponsive Cu NCs with direct Cu–Cu bonds represent a burgeoning area of research with potential for applications.

EXPERIMENTAL SECTION

Materials and Chemicals. Copper iodide (CuI), 1,2-bis(diphenylphosphino)ethane (DPPE), sodium borohydride (NaBH₄, 98%), and 2-mercaptocotinic acid (MNA-H₂) were purchased from Sigma-Aldrich. Potassium bromide (KBr, IR grade) was obtained from Sigma-Aldrich. Milli-Q water was used for purification. HPLC-grade acetonitrile (ACN), methanol (MeOH), N,N-dimethylformamide (DMF), and dichloromethane (DCM) were purchased from Finar and Rankem Chemicals. All of the reagents and solvents were used as received, without further purification.

Characterization Techniques. Optical absorption spectral measurements were recorded using a PerkinElmer Lambda 365 UV–vis spectrometer with a bandpass filter of 1 nm. A Waters Synapt G2Si high-definition mass spectrometer was used to measure the mass of the NCs. The following conditions—flow rate of 20 μ L/min, capillary voltage of 3 kV, source temperature of 100 °C, desolvation temperature of 150 °C, and gas flow rate of 400 L/h—were optimized for ionization of the NCs in ACN. The photoluminescence spectra were collected using a Jobin Yvon NanoLog fluorescence spectrometer with a bandpass filter of 3 nm for emission and excitation. A HORIBA DeltaFlex time-correlated single-photon counting spectrometer equipped with a detector, HORIBA PPD-850 (HORIBA Delta Diode 405 nm laser), was used to measure the

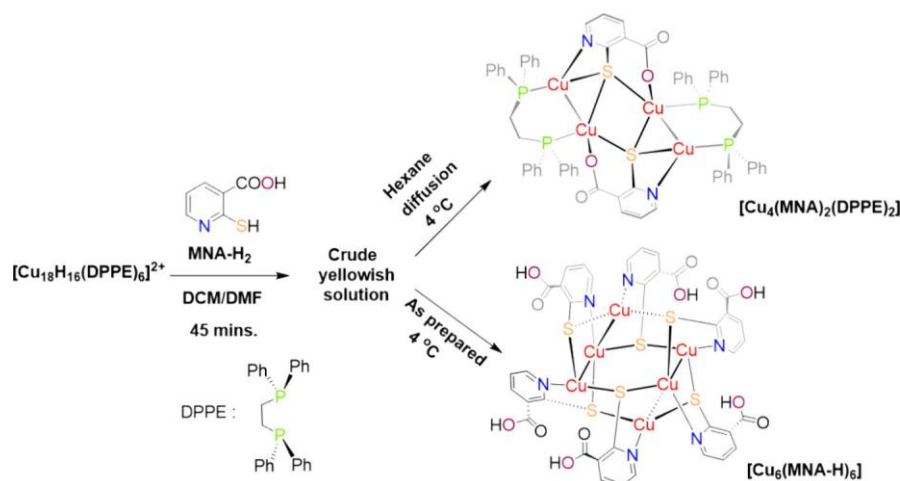
lifetime of the NCs. An FLS 1000 spectrometer with Fluoracore software equipped with a xenon arc lamp was used for photoluminescence quantum efficiency measurements. To calculate radiative and nonradiative decay rate constants (k_r and k_{nr}), the following formula was used, $k_r = \Phi / \tau_{avg}$, and $k_{nr} = 1 / \tau_{avg} - \Phi$ (where Φ is the quantum yield and τ_{avg} is the average lifetime). A PerkinElmer FT-IR JASCO-4100 spectrometer was also used (2 mg of sample in 20 mg of dry KBr). X-ray photoelectron spectroscopy (XPS) of NCs was recorded using an ESCA Probe TPD spectrometer of Omicron Nanotechnology, equipped with a polychromatic Mg K α X-ray source ($h\nu = 1253.6$ eV). The binding energy of different elements was calibrated for C 1s (285.0 eV). SCXRD data of single crystals were collected using a Bruker D8 VENTURE instrument, equipped with a Mo K α radiation source (0.71073 Å) and a PHOTON II detector. The structure was solved by SHELXT-2018 and refined by full-matrix least-squares techniques using the SHELXL-2018 software package incorporated in the WinGX system version v2018.3. For molecular-level DFT calculations, the Gaussian 09 D.01 program was used. Powder XRD data of microcrystalline solids were collected using a D8 Advance Bruker instrument with a Cu K α X-ray source of 1.54 Å. Thermogravimetric (TG) analysis, derivative thermogravimetry (DTG), and differential scanning calorimetry measurements of microcrystals were recorded (25–1000 °C, N₂ gas flow 20 mL/min.) using a NETZSCH STA 449 F3 Jupiter instrument equipped with Proteus-6.1.0 software. An optical microscope from LEICA equipped with LAS V4.8 software was used to see the single crystals of NCs at different magnifications and polarization angles. Field-emission scanning electron microscopy (FESEM) images of single crystals and their energy-dispersive X-ray spectroscopy analysis were performed with a Verios G4 UC FEI instrument. Crystals were drop-cast onto the substrate (TEM grid) and dried at room temperature. The sample was sputter-coated with gold (Au) to produce better-quality images.

Synthesis of [Cu₁₈H₁₆(DPPE)₆]²⁺. The Cu₁₈ NC was synthesized following the procedure available in the literature.⁵² In brief, 95 mg of CuI and 120 mg of DPPE were mixed in 13 mL of ACN. The metal ion was then reduced with 180 mg of dry NaBH₄. After 3 h of stirring, an orange precipitate was formed. The residue was washed multiple times with ACN and MeOH. After that, it was dissolved in DCM and used for characterization.

Synthesis of Cu₄ and Cu₆ NCs. The Cu₄ and Cu₆ NCs were synthesized by using a one-pot LEIST method starting from the Cu₁₈ precursor. The purified Cu₁₈ (~35 mg) dissolved in 4 mL of DCM was reacted with 15 mg of 2-mercaptocotinic acid in 1 mL of DMF. Initially, the reaction mixture was transparent and reddish. After 45 min, the solution became yellowish, and the reaction was stopped. Cu₄ was crystallized by hexane vapor diffusion to yield a crude yellowish solution at 4 °C, whereas Cu₆ was crystallized from the crude solution at 4 °C. The yields of Cu₄ and Cu₆ NCs were 75 and 60%, respectively, for the Cu precursor. UV/vis spectra of clusters were measured in acetonitrile.

Photoluminescence Measurement. Photoluminescence spectra of microcrystalline Cu₄ and Cu₆ NCs (around 70–80 mg) were measured. The Cu₄ NC shows green emission (around 560 nm), and the Cu₆ NC shows red emission (around 755 nm). The nature of the excited state of these clusters was verified through O₂ sensitivity PL experiments. Around 25 mg of the solid sample was taken in a glass vial and kept under a vacuum for 1 h. O₂ gas at atmospheric pressure was exposed for 2 h, and the corresponding emission spectrum was measured just after oxygen exposure. Temperature-dependent (ranging from ambient room temperature to 200 °C) photoluminescence spectra of microcrystalline NCs were measured.

Mechanosensitive Luminescence. Mechanical milling and solvent exposure studies were performed to evaluate the mechanoresponsive luminescence. The sample was ground in a mortar and pestle at room temperature. The luminescence of these materials (Cu₄ and Cu₆ NCs) was vanished upon milling, while the luminescence was regained after the diffusion of DCM and DMF vapors. This behavior of clusters was monitored through PL and PXRD measurements. The effect of other solvent vapors was also studied.

Scheme 1. Schematic Representation of the Synthesis of Cu₄ and Cu₆ Clusters Following the LEIST Method and Their Crystallization

RESULTS AND DISCUSSION

Synthesis and Characterization. The Cu₄(MNA)₂(DPPE)₂ and Cu₆(MNA-H)₆ clusters (Cu₄ and Cu₆ subsequently) were synthesized under ambient conditions, following the LEIST reaction in a DCM and DMF (4:1, v/v) mixture, starting from [Cu₁₈H₁₆(DPPE)₆]²⁺ as the precursor. Details of syntheses are described in the Experimental Section and in Scheme 1. Following the earlier report by Li et al., the precursor cluster was prepared by reducing the Cu-DPPE precursor.⁵² The essential characterization of the [Cu₁₈H₁₆(DPPE)₆]²⁺ cluster, including UV-vis and MS data, is summarized in Figure S1. After a one-pot synthesis, Cu₄ and Cu₆ clusters were separated efficiently through selective

crystallization. The Cu₄ NC was crystallized as transparent rhombus-shaped single crystals upon hexane vapor diffusion into a DCM/DMF mixture at 4 °C. In contrast, the Cu₆ NC was crystallized as yellow hexagonal crystals via slow evaporation of the reaction mixture at the same temperature. These crystals were soluble in DMF and ACN. The as-grown single crystals of Cu₄ exhibited intense green emission, while Cu₆ crystals exhibited bright red luminescence under a ~365 nm UV lamp.

Single-Crystal Structures. The molecular structures of the clusters were determined by SC-XRD. An optical microscopic image of the rhombus-shaped Cu₄ crystals is shown in Figure 1a. The FESEM micrograph further verified the morphology of the crystals, and the EDS elemental mapping shows the presence of Cu, S, N, O, and P in the atomic weight percentages of 26.03, 12.75, 9.56, 13.63, and 7.01, respectively (shown in Figure S3e). SC-XRD revealed that Cu₄ was crystallized in an orthorhombic crystal system with the space group of Pna2₁, having a cell volume of 5971.4 Å³ (Table S1). The structure of the cluster, including ligands, is presented in Figure 1c. This cluster comprises a Cu₄S₂ core protected by two mercaptionicotinic acid ligands and phosphines. Two dimeric (Cu₂) units are connected through bridging S atoms, with Cu–S distances ranging from 2.211 to 2.937 Å. For these Cu₂ units, one Cu center is tetra-coordinated (one μ₃-S, one P, one O, and one Cu), while the other Cu is penta-coordinated (two μ₃-S, one P, one N, and one Cu). The Cu–Cu distances are in the range of 2.75–2.81 Å, revealing intermetallic cuprophilic interactions. Each DPPE

ligand is connected with the Cu₂ unit through the P-end, covering Cu–P distances of 2.170–2.221 Å. The MNA ligand is connected to the Cu₄S₂ core through N and O atoms, where the C–N bond distances are 2.016 and 2.026 Å and the Cu–O bond distances are 1.917 and 1.981 Å, respectively. Four molecules of the Cu₄ cluster are presented in the unit cell (Figure S4a). Single crystals of the Cu₆ cluster were hexagonal (Figure 1b). The FESEM micrograph shows the surface morphology of the crystals, and the EDS elemental mapping confirms the presence of elements Cu, S, N, and O with atomic percentages of 34.58, 18.29, 5.29, and 10.26, respectively (shown in the inset of Figure S3f). SC-XRD reveals that Cu₆ was crystallized in a triclinic crystal system with the space group of P-1, having a cell volume of 1923.8 Å³ (Table S3). The asymmetric unit of the Cu₆ NC is Cu₃(MNA-H)₃·3.5 DMF, as one of the DMF molecules is disordered around the inversion center. This cluster is composed of a Cu₆S₆ core, where two Cu₃S₃ chair-like geometries are interconnected by Cu–Cu bonds, and it is protected by six 2-mercaptionicotinic acids (shown in Figure S4b). The Cu–Cu bond distances in each Cu₃ unit are 2.696 and 2.765 Å, respectively, while the Cu–S and Cu–N bond distances are 2.223–2.269 and 2.023–2.058 Å, respectively (Figure S4d). One molecule was present in each unit cell (Figure S4b). The extended structural packing of Cu₆ showed that the DMF molecules are entrapped in the lattice, forming H-bonds with mercaptionicotinic acid ligands (Figure S5b).

Other Characterizations. The molecular composition of the clusters was analyzed through high-resolution mass spectrometric studies using a Waters Synapt G2Si HDMS instrument. Instrumental details and ionization conditions are mentioned in the characterization part of the manuscript. The Cu₄ NC was ionized in positive ion mode with a characteristic peak at *m/z* 1357.95 (1+), which corresponds to [Cu₄(MNA)₂(DPPE)₂]⁺. The experimental and theoretical isotopic distributions agreed well (shown in Figure 2a, left inset). Other prominent mass peaks observed at *m/z* 1380.90 (1+), 1396.94 (1+), and 1434.92 (1+) (marked as i, ii, and iii, respectively) are attributed to sodium and potassium species attached to the molecular ion of the cluster (Figure S7a,b). Collision-energy (CE)-dependent fragmentation provides further structural insight into the molecular species. Upon increase in CE, another peak at *m/z* 960.28 was observed,

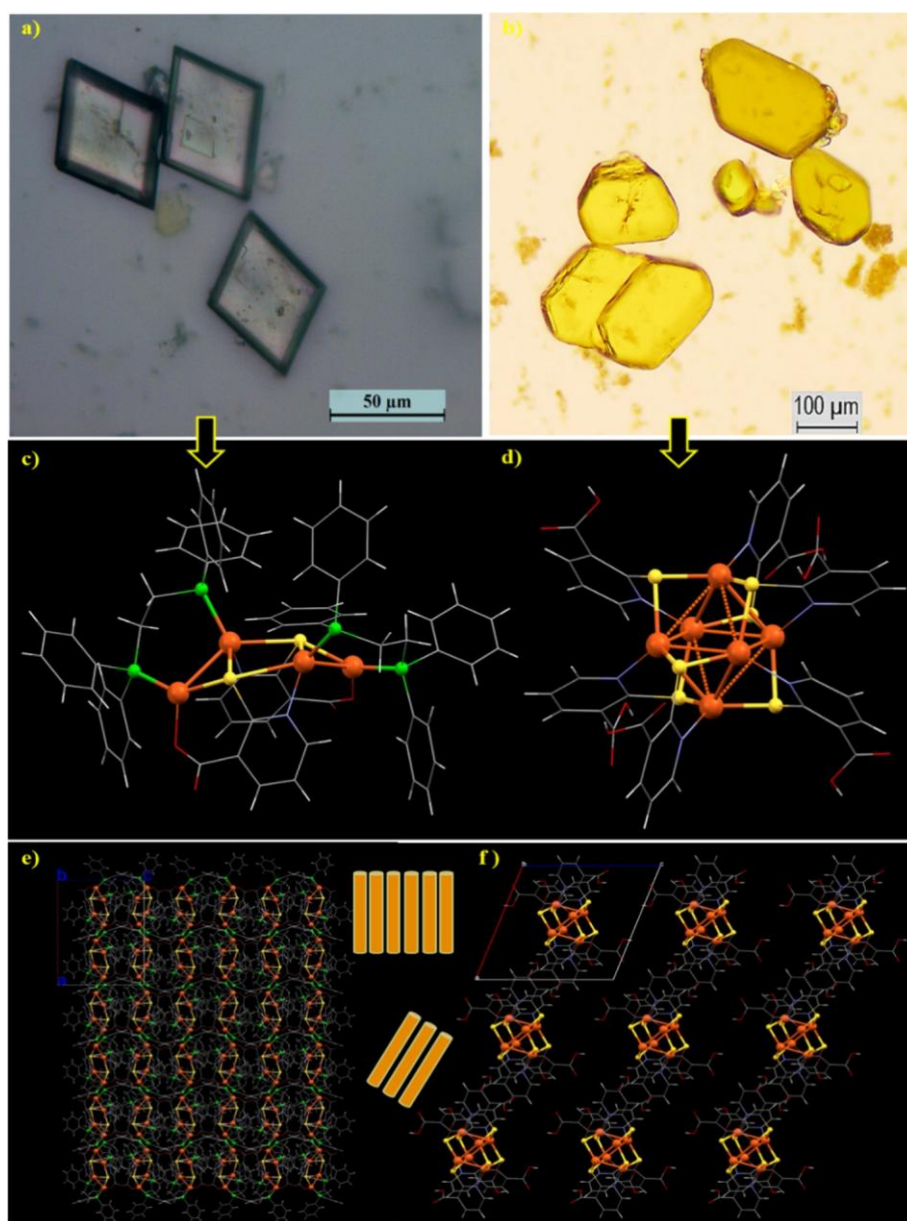


Figure 1. Optical microscopic images of the crystals of (a) Cu_4 and (b) Cu_6 NCs. Single-crystal structures of individual (c) Cu_4 and (d) Cu_6 (DMF molecules in the Cu_6 NC are removed for clarity). Structured packing ($3 \times 3 \times 3$ along the b -axis) of (e) Cu_4 and (f) Cu_6 NCs, respectively. Atomic color code: orange = Cu, yellow = S, green = P, gray = C, red = O, blue = N, and white = H.

which was assigned as $[\text{Cu}_4(\text{MNA})_2(\text{DPPE})]^+$. This species underwent a sequential loss of 44 mass units (due to CO_2 losses) upon increase in CE, resulting in species at m/z 916.14 and 872.38, respectively. Another species $[\text{Cu}_2(\text{MNA})-(\text{DPPE})]^+$ at $m/z = 678.95$ was observed as a product of symmetrical dissociation, where the parent molecule underwent a specific fragmentation that led to this new species. Loss of CO_2 yielded another species at $m/z = 635.16$. On the other hand, Cu_6 was ionized in negative ion mode. The molecular ion peak was observed at m/z 1305.25 (1^-), which corresponds to $[\text{Cu}_6(\text{MNA}-\text{H})_5(\text{MNA})]^-$. Experimental and theoretical mass spectra match well (shown in the right inset of Figure 3a). One MNA-H ligand loss yielded the peak at m/z 1151.12 (1^-), which corresponds to $[\text{Cu}_6(\text{MNA}-\text{H})_4(\text{MNA})]^-$ (Figure 3a). A further increase in CE to the molecular ion peak yielded a loss of two ligands, and the peaks at m/z 1151.12 (1^-) and m/z 996.12) were observed. The

peak at m/z 996.12 corresponds to $[\text{Cu}_6(\text{MNA}-\text{H})_3(\text{MNA})]^-$. Sequential loss of 44 mass units from this species was observed (shown in Figure 3b). The other fragmented species was at m/z 715.64, which corresponds to $[\text{Cu}_3(\text{MNA}-\text{H})_2(\text{MNA})]^-$. Sequential loss of three $-\text{CO}_2$ molecules yielded three other species (shown in Figure 3b). The other fragmented species was at m/z 715.64, which corresponds to $[\text{Cu}_3(\text{MNA}-\text{H})_2(\text{MNA})]^-$. Sequential loss of three $-\text{CO}_2$ molecules yielded other three species (shown in Figure 3b). The UV-vis absorption spectrum of the Cu_4 NC cluster in acetonitrile shows peaks at 296 and 385 nm, revealing a characteristic pattern indicating its molecular nature (Figure S2a). The Cu_6 NC in acetonitrile exhibits UV-vis absorption features at 207, 238, 300, and 382 nm (Figure S2b). Time-dependent UV-vis spectra indicate the structural stability of the cluster for up to 20 days (Figure S2). Comparative FT-IR studies were performed to understand the binding of ligands to the

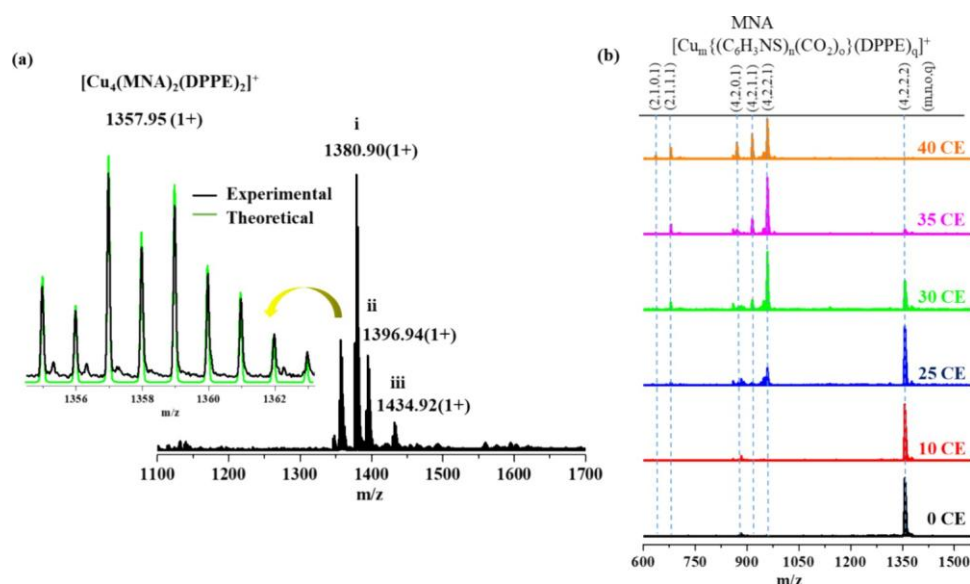


Figure 2. (a) Full-range high-resolution ESI MS spectrum of Cu_4 in positive ion mode; the left inset shows the isotopic mass distribution of theoretical and experimental spectra. (b) CE-dependent MS/MS fragmentation pattern of the molecular ion peak at m/z 1357.95 (1+).

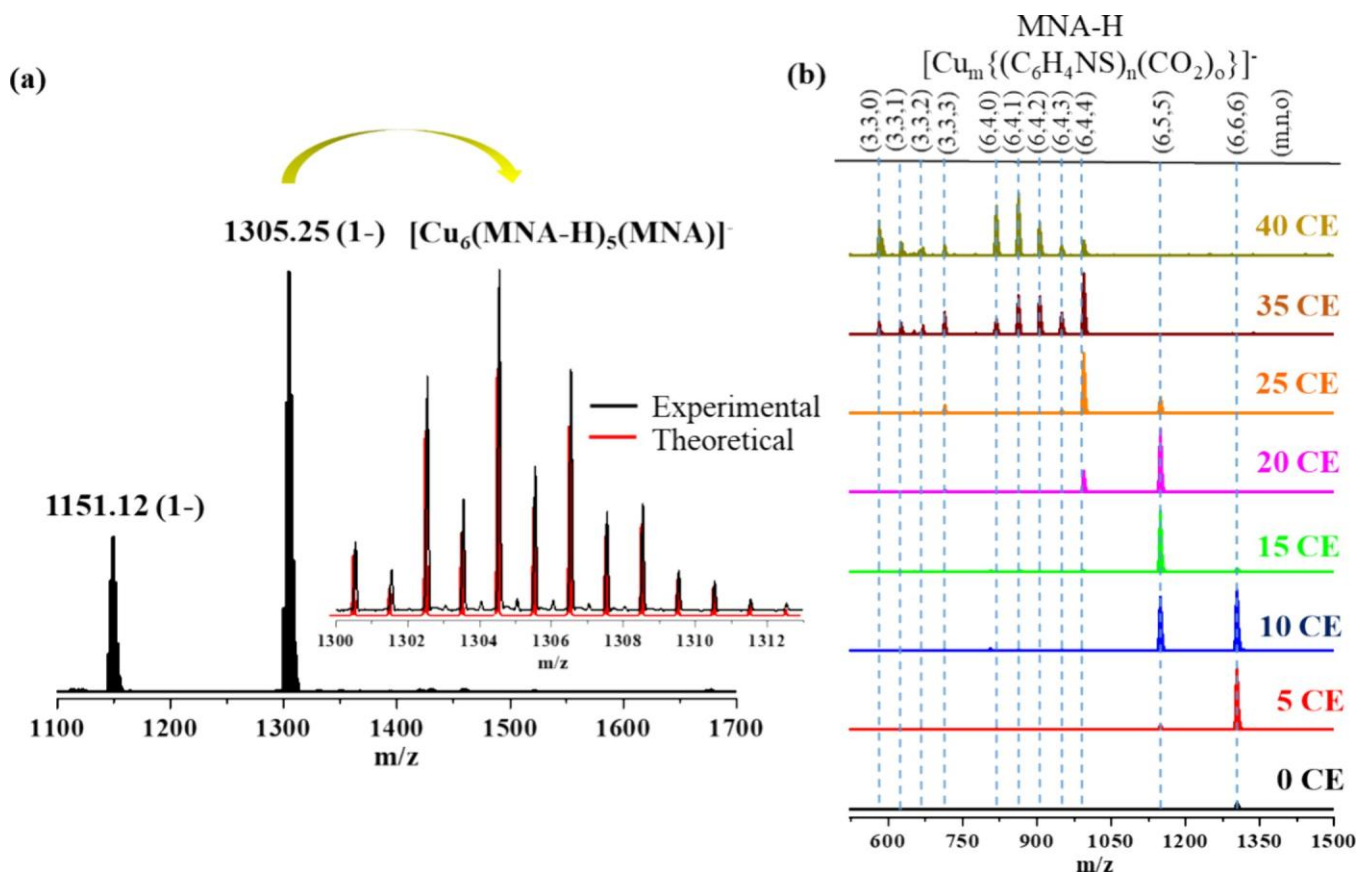


Figure 3. (a) Full range high-resolution ESI MS spectrum of the Cu_6 NC in negative ion mode; the right inset shows the isotopic mass distribution of theoretical and experimental spectra. (b) CE-dependent MS/MS fragmentation pattern of the molecular ion peak at m/z 1305.25 (1-).

molecular structure of Cu_4 and Cu_6 NCs. A strong vibrational peak at 1605 cm^{-1} corresponds to the $-\text{COO}$ vibration of the bound mercapto acid group in the Cu_4 NC. Another prominent peak at 577 cm^{-1} is due to the $\text{Cu}-\text{S}$ stretching mode (Figure S8). Besides, moderately intense peaks at 1093 , 1435 , and 1380 cm^{-1} were observed due to $\text{C}-\text{O}$, $\text{C}\equiv\text{C}$, and $\text{C}\equiv\text{N}$ stretching, respectively. The Cu_6 NC also shows a

similar type of spectrum except for two kinds of $-\text{COOH}$ stretching (Figure S9): one peak at 1696 cm^{-1} (uncoordinated $-\text{COOH}$) and the other peak at 1390 cm^{-1} ($-\text{COO}$ bonded to Cu). The XPS spectra of Cu_4 and Cu_6 show the oxidation state of the elements present in the cluster (Figures S10 and S11). In the Cu_4 NC, the Cu 2p region shows $2p_{3/2}$ and $2p_{1/2}$ features at 930.9 and 950.8 eV (Figure S10b), respectively, and

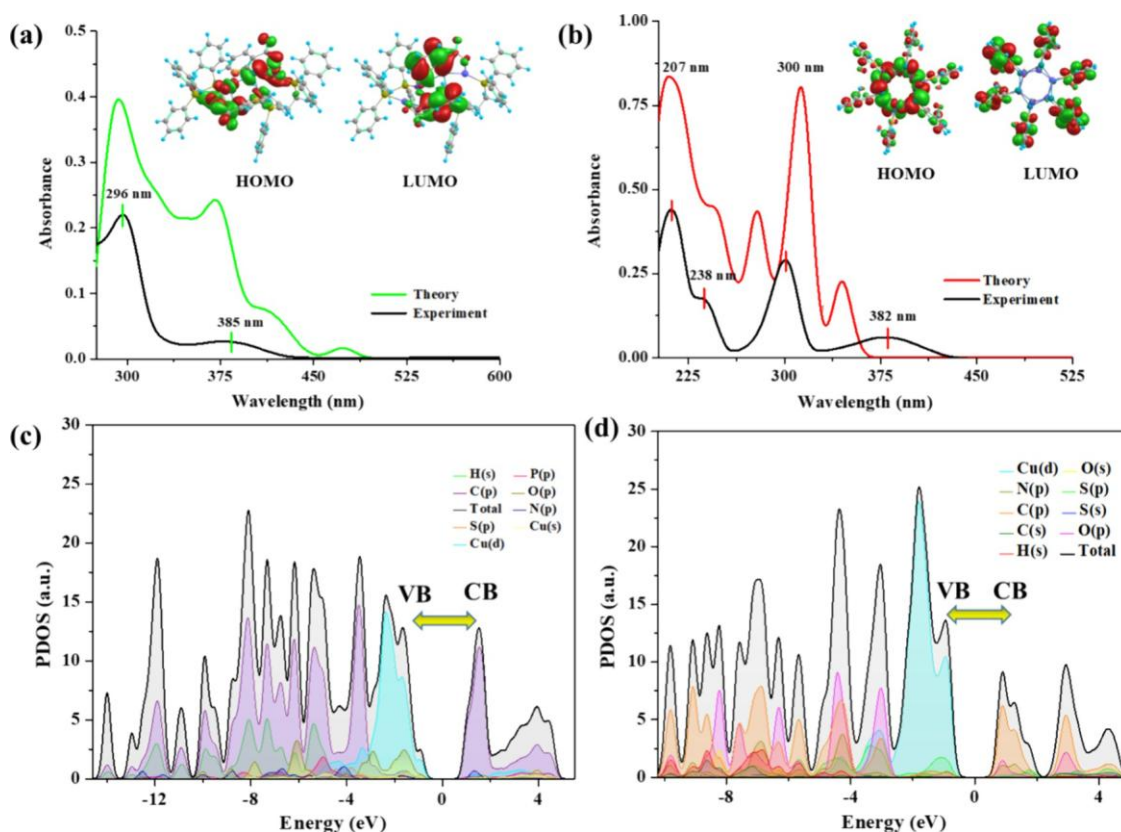


Figure 4. (a, b) Correlation between experimental absorption spectra (sample in acetonitrile solvent) and theoretical spectra (in solvent medium) of Cu_4 and Cu_6 NCs; the insets show the HOMO and LUMO of the respective clusters. (c, d) PDOS spectra of Cu_4 and Cu_6 NCs with respect to individual atomic orbitals (VB, valence band and CB, conduction band).

the absence of the satellite peak suggests the metal-like zero oxidation state for Cu. The XPS spectrum of Cu_6 follows a similar pattern (Figure S11). The presence of other elements is also verified in the XPS analysis (Figures S10 and S11). Thermogravimetric analysis (TGA) and DTG measurements showed thermal stability of Cu_4 and Cu_6 NCs up to 325 and 267 °C, respectively (Figures S22 and S23).

Theoretical Understanding of the Electronic Structure. Initially, both the clusters (Cu_4 and Cu_6) were optimized using the DFT method with the Gaussian 09 package,⁵³ and the optimized structures are shown in Figures S12a and S14a. Further computational details are provided in the Supporting Information. Using the optimized structures, electronic and optical spectra were analyzed. For the Cu_4 cluster, time-dependent DFT (TD-DFT) calculations in the presence of ACN solvent revealed two absorption peaks around 288 and 373 nm (Figure 4a), which closely resembled the experimentally observed bands. These peaks correspond to the transitions of HOMO−6 → LUMO + 20 (exp: 4.16 eV/296 nm) and HOMO−2 → LUMO + 7 (exp: 3.22 eV/385 nm), respectively. The theoretical calculations also showed two absorption bands in the low energy region around 408 and 468 nm, corresponding to the transitions of HOMO−2 → LUMO + 1 and HOMO → LUMO + 1, respectively. These transitions are shown in Figure S13a. Kohn–Sham (K–S) molecular orbital analysis indicated that the occupied MOs are composed of Cu(d), O(s-p), and S(s-p) orbitals (Figure S13b), while the unoccupied MOs are dominated by Cu(s-p), C(s-p), and N(s-p) orbitals. Electronic structures of the cluster were studied by conducting a projected density of states (PDOS) analysis using

the Vienna Ab initio Simulation Package and frontier molecular orbital analysis.^{54–56} The middle of the plots was set to zero to indicate the Fermi level. In this plot, orbitals with negative energy are considered to be HOMOs, and orbitals with positive energy are considered to be LUMOs. According to the PDOS analysis, the valence band of the Cu_4 NC consists predominantly of Cu(d), C(p), O(p), and H(s) states, and the conduction band is dominated by C(p) states (Figure 4c). The absorption peak of 385 nm is majorly due to metal-to-ligand transition (Figure S13). A TD-DFT calculation of the Cu_6 NC reveals four distinct optical absorption peaks (at 205, 240, 306, and 348 nm), which correspond to HOMO−25 → LUMO + 1 (5.99 eV/207 nm), HOMO−10 → LUMO + 11 (5.21 eV/238 nm), HOMO−8 → LUMO + 1 (4.13 eV, 300 nm), and HOMO−1 → LUMO + 4 (3.25 eV/382 nm) transitions, as shown in Figure S15a. The K–S analysis shows the dominance of core Cu(d) and S(s-p) orbitals in the occupied MOs, while unoccupied MOs are dominated by C(s-p) orbitals, as shown in Figure S15b. The PDOS analysis also agrees with the K–S analysis (Figure 4d). Therefore, the optical transitions take place mainly in the form of Cu-d (core) → C(s-p) (ligand) and S (s-p) (core) → C(s-p) (ligand).

Photoluminescence. The emission characteristics of Cu_4 and Cu_6 NCs were studied by photoluminescence spectroscopy. The NCs are nonemitting in solution (DMF and ACN), whereas bright luminescence appears in the solid crystalline state (Figures S16 and S17). The bulkiness of the ligands plays an essential role in decreasing the molecular motions, which helps to increase the radiative processes. Restriction of bond rotations and vibrations becomes more prominent in the solid

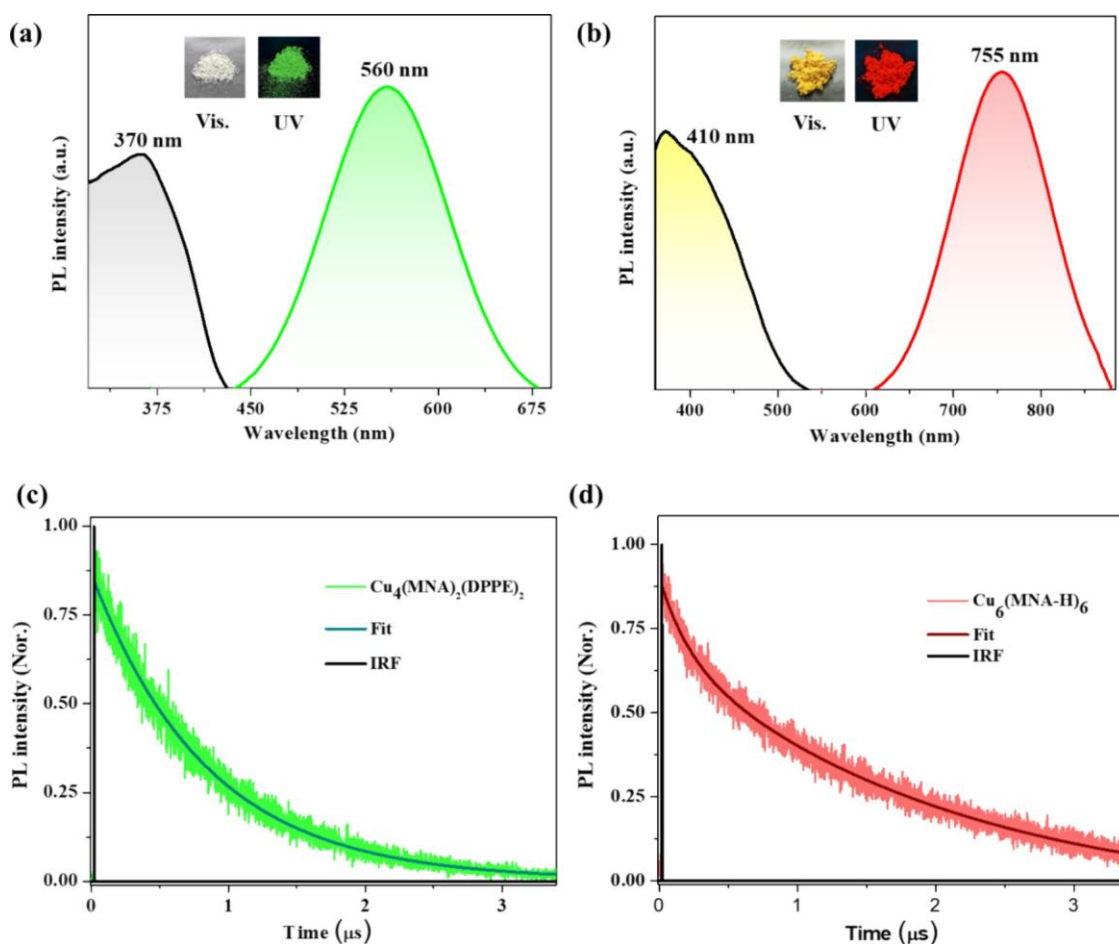


Figure 5. PL excitation and emission spectra of (a) Cu_4 and (b) Cu_6 NCs in the solid crystalline state. Insets show the photographs of respective clusters in microcrystalline powder form. Luminescence decay profiles of (c) Cu_4 and (d) Cu_6 NCs.

or well-ordered crystalline state due to strong intermolecular interactions ($\text{CH}-\pi$, $\text{CH}-\text{CH}$, and $\pi-\pi$), resulting in intense luminescence. A similar mechanism occurs for Cu_4 and Cu_6 NCs in their extended solid-state packing, which makes them emissive. In solution, molecules rotate freely and molecular vibrations dominate, which are responsible for quenching radiative paths. As a result, no luminescence was observed from the molecules in solution. Similarly, Cu clusters (Cu_4 and Cu_6) are nonluminescent in solution. Such an emission profile is reminiscent of several ultrasmall Cu NCs.^{45,46} The Cu_4 NC shows emission maxima around 560 nm upon excitation at 370 nm. In comparison, Cu_6 emits at 755 nm at an excitation of 410 nm. Ligands in such small clusters play a role in charge transfer (ligand to metal charge transfer or vice versa).^{18,37–39} Emission lifetimes were measured to understand the role of excited states in luminescence. The Cu_4 NC exhibits a monoexponential decay lifetime of 0.84 μs (Figure 5c). On the other hand, the Cu_6 NC exhibits biexponential decay lifetime components of 205 ns and 2.04 μs with relative amplitudes of 22 and 78% (Figure 5d). Thus, the average lifetime of the Cu_6 NC was 1.64 μs . Upon oxygen exposure, the PL intensity for both the clusters was quenched, which indicates phosphorescence (Figures S18 and S19). Temperature-dependent luminescence from room temperature to 200 °C shows a gradual decrease in emission intensity (Figures S20 and S21). Using the integrating sphere method, we estimated the photoluminescence quantum efficiencies of 9.56 and 1.59%

for microcrystalline Cu_4 and Cu_6 NCs, respectively. For the Cu_4 NC, the calculated radiative decay rate constant (k_r) was $1.1 \times 10^5 \text{ s}^{-1}$ and the nonradiative decay rate constant (k_{nr}) was $1.2 \times 10^6 \text{ s}^{-1}$. On the other hand, for the Cu_6 NC, the calculated radiative decay rate constant (k_r) was $9.7 \times 10^3 \text{ s}^{-1}$ and the nonradiative decay rate constant (k_{nr}) was $6.1 \times 10^5 \text{ s}^{-1}$.

Mechanosensitive Luminescence. External stimuli such as temperature and pressure sometimes have an effect on the photophysical properties of luminescent materials. In this context, Cu-based materials with structure-specific luminescence are interesting (Table S5). Phosphine-protected luminescent Cu clusters with small nuclearities are sensitive to stimuli. This is reportedly due to the shortening of the Cu–Cu bond length upon applied pressure.^{49,50} In our work, Cu_4 and Cu_6 NCs exhibit “turn-off” luminescence upon ambient mechanical milling. Green (560 nm) and red emission (755 nm) of Cu_4 and Cu_6 are lost in the process, but solvent diffusion brings them back to the emissive state (Figure 6a,b). The applied force provides pressing and shearing along different directions of the molecular structure and disrupts the extended solid-state packing. As a result, the crushed and ground samples lose their well-ordered structure, accompanied by quenching of luminescence originating from tight packing (Figure S5). This type of transition was monitored by powder XRD. It revealed the phase change of the NC materials during mechanical milling and solvent vapor exposure (Figure 6e,f).

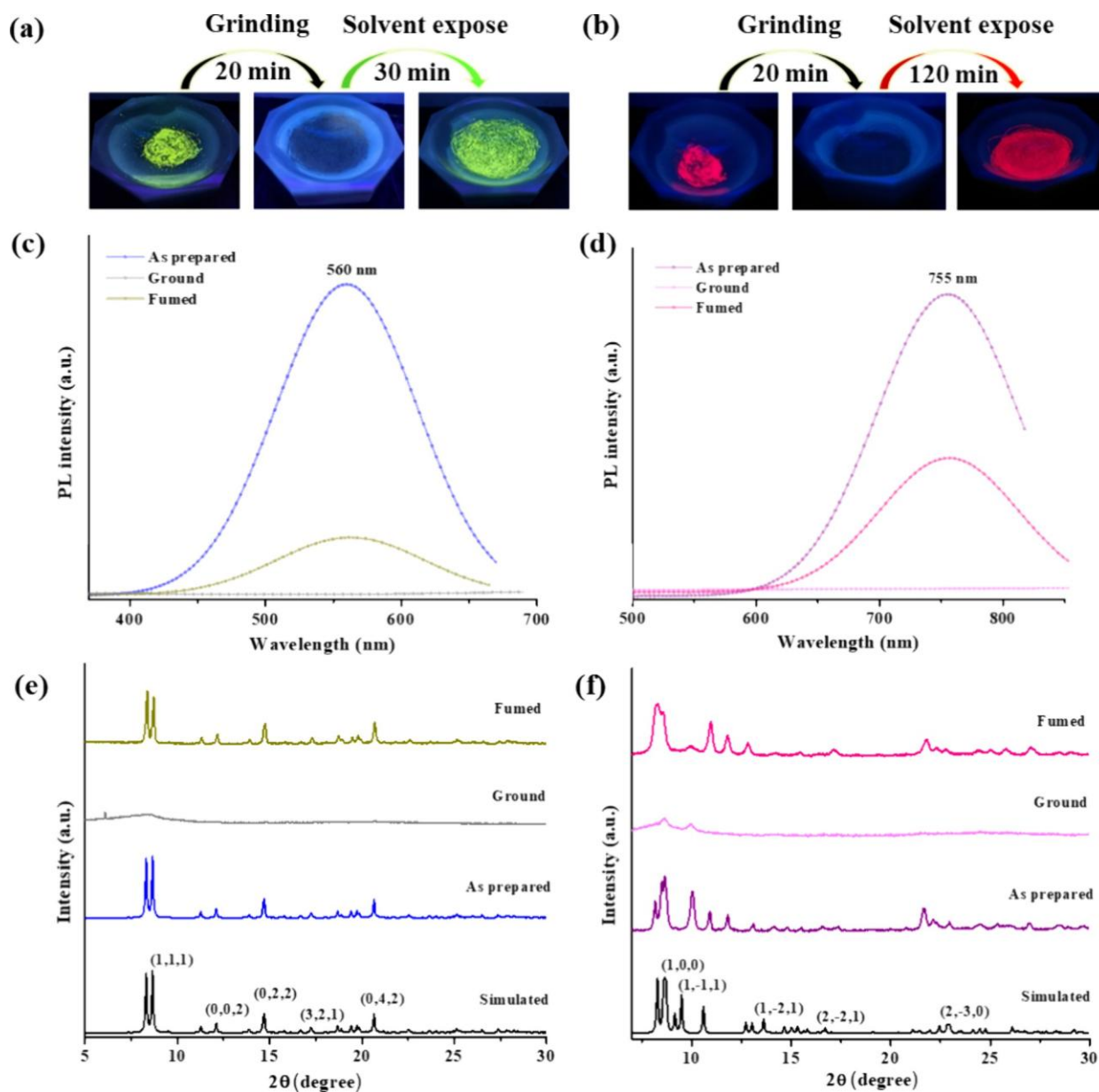


Figure 6. Mechanosensitive luminescence study. Photographic images of (a) Cu_4 and (b) Cu_6 NCs under 365 nm UV light. PL spectra of (c) Cu_4 and (d) Cu_6 NCs after ambient mechanical milling and vapor exposure. Comparative powder XRD patterns of microcrystalline (e) Cu_4 and (f) Cu_6 NCs.

Powder XRD peaks for both NCs match the theoretical data well, indicating the sample's crystalline purity. The ground NCs exhibit very few broad peaks in the powder XRD pattern, which reveals their nearly amorphous nature. PL was quenched for the ground sample. The reappearance of sharp diffraction peaks upon vapor diffusion shows reversible crystallinity induced by solvent molecules. The ground Cu_4 NC regains its emission within 30 min upon DCM vapor diffusion, whereas the Cu_6 NC takes around 120 min to regain emission by DMF vapor. The broadness of emission spectra is likely due to the materials' structural heterogeneity. Literature suggests that partial PL quenching is likely due to some permanent defects created when mechanical force is applied.⁵⁰ Roles of different solvents (volatile organic compounds and water) on luminescence recovery of the ground material were checked (Table S6). There were no significant changes in the emission wavelength in all of the cases. Polar solvents with H-bonding

ability play a crucial role in reverting the crystallinity and luminescence of the Cu_6 NC. It suggests the importance of noncovalent interactions between the ground NC and the solvent molecules.

CONCLUSIONS

This work presents the synthesis and characterization of a pair of luminescent mechanochromic Cu NCs. SC-XRD reveals flattened boat-like Cu_4S_2 and adamantane-like Cu_6S_6 kernel structures for Cu_4 and Cu_6 clusters, respectively. Both the nanomaterials show bright luminescence in their crystalline state, which relaxes in solution, making them nonemitting. The Cu_4 cluster shows green emission under exposure to UV light (365 nm), whereas Cu_6 shows red emission. The small cores of Cu_4S_2 and Cu_6S_6 are sensitive to mechanical milling, losing their luminescence but regaining it upon exposure to solvent vapors. The switchable mechanochromic luminescence ex-

hibited by these Cu NCs opens up possibilities for technologies such as strain sensing and chemical sensing. The ability to control luminescence through mechanical stimuli adds new attributes to such materials.

ASSOCIATED CONTENT

Supporting Information

The Supporting Information is available free of charge at <https://pubs.acs.org/doi/10.1021/acs.inorgchem.4c02617>.

Theoretical calculations, crystallographic information, UV–vis, FESEM, EDS, XPS, Fourier transform infrared, electronic transitions involving HOMO–LUMO, Kahn–Sham analysis, TG and DTG, and associated figures (PDF)

Accession Codes

CCDC numbers 2339995 and 2340002 contain the supplementary crystallographic data for this paper. These data can be obtained free of charge via www.ccdc.cam.ac.uk/data_request/cif, or by emailing data_request@ccdc.cam.ac.uk, or by contacting The Cambridge Crystallographic Data Centre, 12 Union Road, Cambridge CB2 1EZ, UK; fax: +44 1223 336033.

AUTHOR INFORMATION

Corresponding Authors

Biswarup Pathak – *Department of Chemistry, Indian Institute of Technology Indore, Indore 453552, India*; orcid.org/0000-0002-9972-9947; Email: biswarup@iiti.ac.in

Adarsh Kumar Nair Valsala Devi – *Department of Physics, Indian Institute of Science Education and Research Bhopal, Bhopal 462066, India*; orcid.org/0000-0002-6337-6545; Email: adarsh@iiserb.ac.in

Thalappil Pradeep – *DST Unit of Nanoscience (DST UNS) and Thematic Unit of Excellence (TUE), Department of Chemistry, Indian Institute of Technology, Madras, Chennai 600036, India*; orcid.org/0000-0003-3174-534X; Email: pradeep@iitm.ac.in

Authors

Subrata Duary – *DST Unit of Nanoscience (DST UNS) and Thematic Unit of Excellence (TUE), Department of Chemistry, Indian Institute of Technology, Madras, Chennai 600036, India*

Arijit Jana – *DST Unit of Nanoscience (DST UNS) and Thematic Unit of Excellence (TUE), Department of Chemistry, Indian Institute of Technology, Madras, Chennai 600036, India*

Amitabha Das – *Department of Chemistry, Indian Institute of Technology Indore, Indore 453552, India*; orcid.org/0000-0002-5000-4451

Swetashree Acharya – *DST Unit of Nanoscience (DST UNS) and Thematic Unit of Excellence (TUE), Department of Chemistry, Indian Institute of Technology, Madras, Chennai 600036, India*

Amoghavarsha Ramachandra Kini – *DST Unit of Nanoscience (DST UNS) and Thematic Unit of Excellence (TUE), Department of Chemistry, Indian Institute of Technology, Madras, Chennai 600036, India*

Jayoti Roy – *DST Unit of Nanoscience (DST UNS) and Thematic Unit of Excellence (TUE), Department of Chemistry, Indian Institute of Technology, Madras, Chennai 600036, India*

Ajay Kumar Poonia – *Department of Physics, Indian Institute of Science Education and Research Bhopal, Bhopal 462066, India*; orcid.org/0000-0002-5551-7299

Deepak Kumar Patel – *DST Unit of Nanoscience (DST UNS) and Thematic Unit of Excellence (TUE), Department of Chemistry, Indian Institute of Technology, Madras, Chennai 600036, India*; orcid.org/0000-0003-2509-4165

Vivek Yadav – *DST Unit of Nanoscience (DST UNS) and Thematic Unit of Excellence (TUE), Department of Chemistry, Indian Institute of Technology, Madras, Chennai 600036, India*

P. K. Sudhadevi Antharjanam – *Sophisticated Analytical Instrument Facility, Indian Institute of Technology Madras, Chennai 600036, India*; orcid.org/0000-0002-8801-7530

Complete contact information is available at:

<https://pubs.acs.org/doi/10.1021/acs.inorgchem.4c02617>

Author Contributions

S.D. performed the synthesis, crystallization, and most of the experimental studies. A.J. helped SD for single-crystal measurements and gave inputs while writing the manuscript. A.D. performed theoretical calculations. B.P. was involved in the discussion of theoretical data. S.A. and J.R. performed the mass spectrometric studies. A.K.P. measured the PL lifetime of clusters. K.N.V.D.A. was involved in the discussion of the PL data. S.A. collected and analyzed the single-crystal data. D.K.P. and V.Y. were involved in discussions. A.R.K. performed XPS of the clusters. S.D. prepared all manuscript drafts. T.P. supervised the work and finalized the manuscript.

Notes

The authors declare no competing financial interest.

ACKNOWLEDGMENTS

S.D. acknowledges the Prime Minister's Research Fellowship (PMRF) from the Government of India (GoI). S.D. is thankful to the Sophisticated Analytical Instrument Facility, Indian Institute of Technology Madras (SAIF-IITM), for the SC-XRD and TG measurements. A.J. and J.R. acknowledge financial support from the IIT Madras. A.D. and A.R.K. thank the GoI for the UGC fellowships. S.A., D.K.P., and V.Y. are thankful for the PMRF grant. A.K.P. acknowledges the GoI for a CSIR fellowship. T.P. acknowledges funding from the Centre of Excellence (CoE) on Molecular Materials and Functions from the Institute of Eminence scheme of IIT Madras. K.N.V.D.A. and T. P. thank the Science and Engineering Research Board (SERB) for funding through the CRG/2019/002808 and SPR/2021/000439 research grants, respectively. T.P. thanks the Science and Engineering Research Board (SERB) for a J.C. Bose Fellowship.

REFERENCES

- Chakraborty, I.; Pradeep, T. Atomically precise clusters of noble metals: emerging link between atoms and nanoparticles. *Chem. Rev.* 2017, *117* (12), 8208–8271.
- Jin, R.; Zeng, C.; Zhou, M.; Chen, Y. Atomically precise colloidal metal nanoclusters and nanoparticles: fundamentals and opportunities. *Chem. Rev.* 2016, *116* (18), 10346–10413.
- Jana, A.; Kini, A. R.; Pradeep, T. Atomically Precise Clusters: Chemical Evolution of Molecular Matter at the Nanoscale. *AsiaChemMag* 2023, *3*, 56–65.

- (4) Pradeep, T., Ed. *Atomically Precise Metal Nanocluster*; Elsevier: Amsterdam, 2023; pp. 1–643.
- (5) Chakraborty, P.; Nag, A.; Chakraborty, A.; Pradeep, T. Approaching materials with atomic precision using supramolecular cluster assemblies. *Acc. Chem. Res.* 2019, *52* (1), 2–11.
- (6) Kang, X.; Zhu, M. Tailoring the photoluminescence of atomically precise nanoclusters. *Chem. Soc. Rev.* 2019, *48* (8), 2422–2457.
- (7) Yang, S.; Zhu, M. Insight of the photoluminescence of atomically precise bimetallic nanoclusters with free electrons. *J. Chin. Chem. Soc.* 2020, *67* (12), 2171–2181.
- (8) Xie, Y. P.; Shen, Y. L.; Duan, G. X.; Han, J.; Zhang, L. P.; Lu, X. Silver nanoclusters: synthesis, structures and photoluminescence. *Mater. Chem. Front.* 2020, *4* (8), 2205–2222.
- (9) AbdulHalim, L. G.; Bootharaju, M. S.; Tang, Q.; Del Gobbo, S.; AbdulHalim, R. G.; Eddaoudi, M.; Jiang, D. E.; Bakr, O. M. Ag₂₉(BDT)₁₂(TPP)₄: a tetravalent nanocluster. *J. Am. Chem. Soc.* 2015, *137* (37), 11970–11975.
- (10) Jana, A.; Chakraborty, P.; Dar, W. A.; Chandra, S.; Khatun, E.; Kannan, M. P.; Ras, R. H.; Pradeep, T. Dual emitting Ag₃₅ nanocluster protected by 2-pyrene imine thiol. *Chem. Commun.* 2020, *56* (83), 12550–12553.
- (11) (a) Shen, H.; Wang, L.; López-Estrada, O.; Hu, C.; Wu, Q.; Cao, D.; Malola, S.; Teo, B. K.; Häkkinen, H.; Zheng, N. Copper-hydride nanoclusters with enhanced stability by N-heterocyclic carbenes. *Nano Res.* 2021, *14*, 3303–3308. (b) Shen, H.; Wu, Q.; Malola, S.; Han, Y. Z.; Xu, Z.; Qin, R.; Tang, X.; Chen, Y. B.; Teo, B. K.; Häkkinen, H.; Zheng, N. N-heterocyclic carbene-stabilized gold nanoclusters with organometallic motifs for promoting catalysis. *J. Am. Chem. Soc.* 2022, *144* (24), 10844–10853.
- (12) Maity, P.; Takano, S.; Yamazoe, S.; Wakabayashi, T.; Tsukuda, T. Binding motif of terminal alkynes on gold clusters. *J. Am. Chem. Soc.* 2013, *135* (25), 9450–9457.
- (13) McCandler, C. A.; Dahl, J. C.; Persson, K. A. Phosphine-Stabilized Hidden Ground States in Gold Clusters Investigated via a Au_n(PH₃)_m Database. *ACS Nano* 2023, *17* (2), 1012–1021.
- (14) Liu, K. G.; Gao, X. M.; Liu, T.; Hu, M. L.; Jiang, D. E. All-carboxylate-protected superatomic silver nanocluster with an unprecedented rhombohedral Ag₈ core. *J. Am. Chem. Soc.* 2020, *142* (40), 16905–16909.
- (15) (a) Yang, H.; Wang, Y.; Huang, H.; Gell, L.; Lehtovaara, L.; Malola, S.; Häkkinen, H.; Zheng, N. All-thiol-stabilized Ag₄₄ and Au₁₂Ag₃₂ nanoparticles with single-crystal structures. *Nat. Commun.* 2013, *4* (1), 2422. (b) Joshi, C. P.; Bootharaju, M. S.; Alhilaly, M. J.; Bakr, O. M. [Ag₂₅(SR)₁₈]⁻: The “golden” silver nanoparticle. *J. Am. Chem. Soc.* 2015, *137* (36), 11578–11581. (c) Jana, A.; Unnikrishnan, P. M.; Poonia, A. K.; Roy, J.; Jash, M.; Paramasivam, G.; Machacek, J.; Adarsh, K. N. V. D.; Base, T.; Pradeep, T. Carboranethiol-Protected Propeller-Shaped Photoresponsive Silver Nanomolecule. *Inorg. Chem.* 2022, *61* (23), 8593–8603.
- (16) (a) Heaven, M. W.; Dass, A.; White, P. S.; Holt, K. M.; Murray, R. W. Crystal structure of the gold nanoparticle [N(C₈H₁₇)₄][Au₂₅(SCH₂CH₂Ph)₁₈]. *J. Am. Chem. Soc.* 2008, *130* (12), 3754–3755. (b) Chen, T.; Lin, H.; Cao, Y.; Yao, Q.; Xie, J. Interactions of metal nanoclusters with light: fundamentals and applications. *Adv. Mater.* 2022, *34* (25), No. 2103918. (c) Jadzinsky, P. D.; Calero, G.; Ackerson, C. J.; Bushnell, D. A.; Kornberg, R. D. Structure of a thiol monolayer-protected gold nanoparticle at 1.1 Å resolution. *Science* 2007, *318* (5849), 430–433.
- (17) Häkkinen, H. Atomic and electronic structure of gold clusters: understanding flakes, cages and superatoms from simple concepts. *Chem. Soc. Rev.* 2008, *37* (9), 1847–1859.
- (18) Wang, J. J.; Chen, C.; Chen, W. G.; Yao, J. S.; Yang, J. N.; Wang, K. H.; Yin, Y. C.; Yao, M. M.; Feng, L. Z.; Ma, C.; Fan, F. J. Highly luminescent copper iodide cluster-based inks with photoluminescence quantum efficiency exceeding 98%. *J. Am. Chem. Soc.* 2020, *142* (8), 3686–3690.
- (19) Zhang, J.; Zhang, L.; Cai, P.; Xue, X.; Wang, M.; Zhang, J.; Tu, G. Enhancing stability of red perovskite nanocrystals through copper substitution for efficient light-emitting diodes. *Nano Energy* 2019, *62*, 434–441.
- (20) Wei, W.; Lu, Y.; Chen, W.; Chen, S. One-pot synthesis, photoluminescence, and electrocatalytic properties of subnanometer-sized copper clusters. *J. Am. Chem. Soc.* 2021, *133* (7), 2060–2063.
- (21) (a) Liu, L. J.; Wang, Z. Y.; Wang, Z. Y.; Wang, R.; Zang, S. Q.; Mak, T. C. Mediating CO₂ electroreduction activity and selectivity over atomically precise copper clusters. *Angew. Chem. Int. Ed.* 2022, *134* (35), No. e202205626. (b) Xu, H.; Rebollar, D.; He, H.; Chong, L.; Liu, Y.; Liu, C.; Sun, C. J.; Li, T.; Muntean, J. V.; Winans, R. E.; Liu, D. J. Highly selective electrocatalytic CO₂ reduction to ethanol by metallic clusters dynamically formed from atomically dispersed copper. *Nat. Energy* 2020, *5* (8), 623–632.
- (22) Wang, Y. M.; Lin, X. C.; Mo, K. M.; Xie, M.; Huang, Y. L.; Ning, G. H.; Li, D. An Atomically Precise Pyrazolate-Protected Copper Nanocluster Exhibiting Exceptional Stability and Catalytic Activity. *Angew. Chem., Int. Ed.* 2023, *62* (9), No. e202218369.
- (23) (a) Das, A. K.; Biswas, S.; Wani, V. S.; Nair, A. S.; Pathak, B.; Mandal, S. [Cu₁₈H₃(S-Adm)₁₂(PPh₃)₄Cl₂] of fusion of Platonic and Johnson solids through a Cu (0) center and its photophysical properties. *Chem. Sci.* 2022, *13* (25), 7616–7625. (b) Cook, A. W.; Jones, Z. R.; Wu, G.; Scott, S. L.; Hayton, T. W. An organometallic Cu₂₀ nanocluster: Synthesis, characterization, immobilization on silica, and “Click” chemistry. *J. Am. Chem. Soc.* 2018, *140* (1), 394–400.
- (24) (a) Das, A. K.; Biswas, S.; Pal, A.; Manna, S. S.; Sardar, A.; Mondal, P. K.; Sahoo, B.; Pathak, B.; Mandal, S. A thiolated copper-hydride nanocluster with chloride bridging as a catalyst for carbonylative C–N coupling of aryl amines under mild conditions: a combined experimental and theoretical study. *Nanoscale* 2024, *16* (7), 3583–3590. (b) Zhang, L. M.; Mak, T. C. Comproportionation synthesis of copper (I) alkynyl complexes encapsulating polyoxomolybdate templates: bowl-shaped Cu₃₃ and peanut-shaped Cu₆₂ nanoclusters. *J. Am. Chem. Soc.* 2016, *138* (9), 2909–2912.
- (25) (a) Biswas, S.; Hossain, S.; Kosaka, T.; Sakai, J.; Arima, D.; Niihori, Y.; Mitsui, M.; Jiang, D. E.; Das, S.; Wang, S.; Negishi, Y. Nested Keplerian architecture of [Cu₅₈H₂₀(SPR)₃₆(PPh₃)₈]²⁺ nanoclusters. *Chem. Commun.* 2023, *59* (61), 9336–9339. (b) Huang, R. W.; Yin, J.; Dong, C.; Ghosh, A.; Alhilaly, M. J.; Dong, X.; Hedhili, M. N.; Abou-Hamad, E.; Alamer, B.; Nematulloev, S.; Han, Y. [Cu₈₁(PhS)₄₆(tBuNH₂)₁₀(H)₃₂]³⁺ reveals the coexistence of large planar cores and hemispherical shells in high-nuclearity copper nanoclusters. *J. Am. Chem. Soc.* 2020, *142* (19), 8696–8705.
- (26) Fu, M. L.; Issac, I.; Fenske, D.; Fuhr, O. Metal-Rich Copper Chalcogenide Clusters at the Border Between Molecule and Bulk Phase: The Structures of [Cu₉₃Se₄₂(SeC₆H₄SMe)₉(PPh₃)₁₈], [Cu₉₆Se₄₅(SeC₆H₄SMe)₆(PPh₃)₁₈], and [Cu₁₃₆Se₅₆(SCH₂C₄H₃O)₂₄(dpppt)₁₀]. *Angew. Chem., Int. Ed.* 2010, *49* (38), 6899–6903.
- (27) Baghdasaryan, A.; Besnard, C.; Lawson Daku, L. M.; Delgado, T.; Burgi, T. Thiolate protected copper sulfide cluster with the tentative composition Cu₇₄S₁₅(2-PET)₄₅. *Inorg. Chem.* 2020, *59* (4), 2200–2208.
- (28) Huang, Q. Q.; Hu, M. Y.; Li, Y. L.; Chen, N. N.; Li, Y.; Wei, Q. H.; Fu, F. Novel ultrabright luminescent copper nanoclusters and application in light-emitting devices. *Chem. Commun.* 2021, *57* (77), 9890–9893.
- (29) Olaru, M.; Rychagova, E.; Ketkov, S.; Shynkarenko, Y.; Yakunin, S.; Kovalenko, M. V.; Yablonskiy, A.; Andreev, B.; Kleemiss, F.; Beckmann, J.; Vogt, M. A small cationic organo-copper cluster as thermally robust highly photo- and electroluminescent material. *J. Am. Chem. Soc.* 2020, *142* (1), 373–381.
- (30) (a) Huang, R. W.; Song, X.; Chen, S.; Yin, J.; Maity, P.; Wang, J.; Shao, B.; Zhu, H.; Dong, C.; Yuan, P.; Ahmad, T. Radio-luminescent Cu–Au Metal Nanoclusters: Synthesis and Self-Assembly for Efficient X-ray Scintillation and Imaging. *J. Am. Chem. Soc.* 2023, *145* (25), 13816–13827. (b) Kirakci, K.; Fejfarová, K.; Martincik, J.; Nikl, M.; Lang, K. Tetranuclear copper (I) iodide complexes: a new class of X-ray phosphors. *Inorg. Chem.* 2017, *56* (8), 4609–4614.

- (31) Das, N. K.; Ghosh, S.; Priya, A.; Datta, S.; Mukherjee, S. Luminescent copper nanoclusters as a specific cell-imaging probe and a selective metal ion sensor. *J. Phys. Chem. C* 2015, *119* (43), 24657–24664.
- (32) Jana, A.; Spoorthi, B. K.; Nair, A. S.; Nagar, A.; Pathak, B.; Base, T.; Pradeep, T. A luminescent Cu₄ cluster film grown by electrospray deposition: a nitroaromatic vapour sensor. *Nanoscale* 2023, *15* (18), 8141–8147.
- (33) Rival, J. V.; Mymoona, P.; Vinoth, R.; Mohan, A. V.; Shibu, E. S. Light-emitting atomically precise nanocluster-based flexible QR codes for anticounterfeiting. *ACS Appl. Mater. Interfaces* 2021, *13* (8), 10583–10593.
- (34) Nasrollahpour, H.; Sánchez, B. J.; Sillanpää, M.; Moradi, R. Metal nanoclusters in point-of-care sensing and biosensing applications. *ACS Appl. Nano Mater.* 2023, *6* (14), 12609–12672.
- (35) Jana, A.; Jash, M.; Dar, W. A.; Roy, J.; Chakraborty, P.; Paramasivam, G.; Lebedkin, S.; Kirakci, K.; Manna; Antharjanam, S.; Machacek, J.; Kucerakova, M.; Ghosh, S.; Lang, K.; Kappes, M. M.; Base, T.; Pradeep, T. Carborane-thiol protected copper nanoclusters: stimuli-responsive materials with tunable phosphorescence. *Chem. Sci.* 2023, *14* (6), 1613–1626.
- (36) Biswas, S.; Negishi, Y. A Comprehensive Analysis of Luminescent Crystallized Cu Nanoclusters. *J. Phys. Chem. Lett.* 2024, *15* (4), 947–958.
- (37) Yang, T. Q.; Peng, B.; Shan, B. Q.; Zong, Y. X.; Jiang, J. G.; Wu, P.; Zhang, K. Origin of the photoluminescence of metal nanoclusters: from metal-centered emission to ligand-centered emission. *Nanomater.* 2020, *10* (2), 261.
- (38) Zhu, C.; Xin, J.; Li, J.; Li, H.; Kang, X.; Pei, Y.; Zhu, M. Fluorescence or phosphorescence? The metallic composition of the nanocluster kernel does matter. *Angew. Chem. Int. Ed.* 2022, *134* (31), No. e202205947.
- (39) (a) Singh, N.; Raul, K. P.; Poulouse, A.; Mughesh, G.; Venkatesh, V. Highly stable pyrimidine based luminescent copper nanoclusters with superoxide dismutase mimetic and nitric oxide releasing activity. *ACS Appl. Bio Mater.* 2020, *3* (11), 7454–7461. (b) Wang, Z.; Zhang, S.; Xie, H.; Zhang, N.; Wang, W.; Li, S.; Xin, X. Dispersing hydrophobic copper nanoclusters in aqueous solutions triggered by polyoxometalate with aggregation-induced emission properties. *Colloids Surf. A Physicochem. Eng. Asp.* 2023, *664*, No. 131147. (c) Li, Y.; Feng, L.; Yan, W.; Hussain, I.; Su, L.; Tan, B. PVP-templated highly luminescent copper nanoclusters for sensing trinitrophenol and living cell imaging. *Nanoscale* 2019, *11* (3), 1286–1294. (c) Dong, G.; Pan, Z.; Han, B.; Tao, Y.; Chen, X.; Luo, G. G.; Sun, P.; Sun, D. Multi-layer 3D Chirality and Double-Helical Assembly in a Copper Nanocluster with a Triple-Helical Cu₁₅ Core. *Angew. Chem., Int. Ed.* 2023, *62* (24), No. e202302595.
- (40) Ai, Y.; Li, Y.; Chan, M. H. Y.; Xiao, G.; Zou, B.; Yam, V. W. W. Realization of distinct mechano- and piezochromic behaviors via alkoxy chain length-modulated phosphorescent properties and multidimensional self-assembly structures of dinuclear platinum (II) complexes. *J. Am. Chem. Soc.* 2021, *143* (28), 10659–10667.
- (41) Chen, T.; Yang, S.; Chai, J.; Song, Y.; Fan, J.; Rao, B.; Sheng, H.; Yu, H.; Zhu, M. Crystallization-induced-emission enhancement: A novel fluorescent Au-Ag bimetallic nanocluster with precise atomic structure. *Sci. Adv.* 2017, *3* (8), No. e1700956.
- (42) Crocker, R. D.; Pace, D. P.; Zhang, B.; Lyons, D. J.; Bhadbhade, M. M.; Wong, W. W.; Mai, B. K.; Nguyen, T. V. Unusual alternating crystallization-induced emission enhancement behavior in non-conjugated ω -phenylalkyltropylium salts. *J. Am. Chem. Soc.* 2021, *143* (48), 20384–20394.
- (43) Mei, J.; Leung, N. L.; Kwok, R. T.; Lam, J. W.; Tang, B. Z. Aggregation-induced emission: together we shine, united we soar! *Chem. Rev.* 2015, *115* (21), 11718–11940.
- (44) Shi, Y. E.; Ma, J.; Feng, A.; Wang, Z.; Rogach, A. L. Aggregation-induced emission of copper nanoclusters. *Aggregate* 2021, *2* (6), 112.
- (45) Kitagawa, H.; Ozawa, Y.; Toriumi, K. Flexibility of cubane-like Cu₄I₄ framework: temperature dependence of molecular structure and luminescence thermochromism of [Cu₄I₄(PPh₃)₄] in two polymorphic crystalline states. *Chem. Commun.* 2010, *46* (34), 6302–6304.
- (46) Yuan, J.; Wang, L.; Wang, Y.; Hao, J. Stimuli-Responsive Fluorescent Nanoswitches: Solvent-Induced Emission Enhancement of Copper Nanoclusters. *Chem. Eur. J.* 2020, *26* (16), 3545–3554.
- (47) Perruchas, S.; Le Goff, X. F.; Maron, S.; Maurin, L.; Guillen, F.; Garcia, A.; Gacoin, T.; Boilot, J. P. Mechanochromic and thermochromic luminescence of a copper iodide cluster. *J. Am. Chem. Soc.* 2010, *132* (32), 10967–10969.
- (48) Benito, Q.; Le Goff, X. F.; Maron, S.; Fargues, A.; Garcia, A.; Martineau, C.; Taulelle, F.; Kahlal, S.; Gacoin, T.; Boilot, J. P.; Perruchas, S. Polymorphic copper iodide clusters: insights into the mechanochromic luminescence properties. *J. Am. Chem. Soc.* 2014, *136* (32), 11311–11320.
- (49) Huitorel, B.; Utrera-Melero, R.; Massuyeau, F.; Mevelec, J. Y.; Baptiste, B.; Polian, A.; Gacoin, T.; Martineau-Corcus, C.; Perruchas, S. Luminescence mechanochromism of copper iodide clusters: a rational investigation. *Dalton Trans.* 2019, *48* (22), 7899–7909.
- (50) Utrera-Melero, R.; Huitorel, B.; Cordier, M.; Massuyeau, F.; Mevellec, J. Y.; Stephant, N.; Deniard, P.; Latouche, C.; Martineau-Corcus, C.; Perruchas, S. Mechanically responsive luminescent films based on copper iodide clusters. *J. Mater. Chem. C* 2021, *9* (25), 7991–8001.
- (51) Shi, P.; Deng, D.; He, C.; Ji, L.; Duan, Y.; Han, T.; Suo, B.; Zou, W. Mechanochromic luminescent materials with aggregation-induced emission: mechanism study and application for pressure measuring and mechanical printing. *Dyes and Pigment.* 2020, *173*, No. 107884.
- (52) Li, J.; Ma, H. Z.; Reid, G. E.; Edwards, A. J.; Hong, Y.; White, J. M.; Mulder, R. J.; O'Hair, R. A. Synthesis and X-Ray Crystallographic Characterization of Frustum-Shaped Ligated [Cu₁₈H₁₆(DPPE)₆]²⁺ and [Cu₁₆H₁₄(DPPA)₆]²⁺ Nanoclusters and Studies on Their H₂ Evolution Reactions. *Chem. Eur. J.* 2018, *24* (9), 2070–2074.
- (53) Frisch, M. J.; Trucks, G. W.; Schlegel, H. B.; Scuseria, G. E.; Robb, M. A.; Cheeseman, J. R.; Scalmani, G.; Barone, V.; Mennucci, B.; Petersson, G. A. et al. *Gaussian 09, Revision B.01*; Gaussian Inc.: Wallingford, CT, 2009.
- (54) Blöchl, P. E. Projector augmented-wave method. *Phys. Rev. B* 1994, *50* (24), 17953.
- (55) Kresse, G.; Joubert, D. From ultrasoft pseudopotentials to the projector augmented-wave method. *Phys. Rev. B* 1999, *59* (3), 1758.
- (56) Kresse, G.; Furthmüller, J. Efficient iterative schemes for ab initio total-energy calculation using a plane-wave basis set. *Phys. Rev. B* 1996, *54* (16), 11169.

Supporting Information

Milling-Induced ‘Turn-off’ Luminescence in Copper Nanoclusters

Subrata Duary,^a Arijit Jana,^a Amitabha Das,^b Swetashree Acharya,^a Amoghavarsha Ramachandra Kini,^a Jayoti Roy,^a Ajay Kumar Poonia,^c Deepak Kumar Patel,^a Vivek Yadav,^a P. K. Sudhadevi Antharjanam,^d Biswarup Pathak,^{*b} Adarsh Kumaran Nair Valsala Devi,^{*c} and Thalappil Pradeep^{*a}

^a DST Unit of Nanoscience (DST UNS) and Thematic Unit of Excellence (TUE), Department of Chemistry, Indian Institute of Technology, Madras, Chennai – 600036, India.

*Email: pradeep@iitm.ac.in

^b Department of Chemistry, Indian Institute of Technology Indore, Indore 453552, India.

*Email: biswarup@iiti.ac.in

^c Department of Physics, Indian Institute of Science Education and Research Bhopal, Bhopal 462066, India.

*E-mail: adarsh@iiserb.ac.in

^d Sophisticated Analytical Instrument Facility, Indian Institute of Technology Madras, Chennai 600036, India.

Table of contents

Items	Descriptions	Page No.
1	Computational details	S3
Table S1	Crystal data and structure refinement of $\text{Cu}_4(\text{MNA})_2(\text{DPPE})_2$	S4
Table S2	Atomic coordinates and equivalent isotropic displacement parameters for Cu_4 NC	S5-S7
Table S3	Crystal data and structure refinement of $\text{Cu}_6(\text{MNA-H})_6$	S8-S9
Table S4	Atomic coordinates and equivalent isotropic displacement parameters for Cu_6 NC	S9-S11
Table S5	List of mechanoresponsive copper clusters	S11

Table S6	List of solvents for recovery of luminescence	S12
Figure S1	Synthesis and characterization of the cluster $[\text{Cu}_{18}\text{H}_{16}(\text{DPPE})_6]^{2+}$ through UV-Vis absorption spectroscopic and mass spectrometric studies	S13
Figure S2	Stability check through UV-Vis absorption spectrum of Cu_4 and Cu_6 NCs in acetonitrile	S13
Figure S3	FESEM images and EDS elemental spectrum of Cu_4 and Cu_6 NCs	S14
Figure S4	Structures and molecular packing of Cu_4 and Cu_6 NCs along the b-axis	S 15
Figure S5	Non-covalent interactions involving crystal structures in the lattice	S16
Figure S6	ORTEP structure of Cu_4 and Cu_6 NCs	S17
Figure S7	ESI MS spectrum of sodium and potassium ions embedded to Cu_4 NC and tabulated MSMS fragments of Cu_4 and Cu_6 nanoclusters	S17
Figure S8	FTIR spectrum of Cu_4 NC	S18
Figure S9	FTIR spectrum of Cu_6 NC	S19
Figure S10	XPS spectrum of Cu_4 NC	S20
Figure S11	XPS spectrum of Cu_6 NC	S21
Figure S12	DFT optimized structural details of Cu_4 NC	S22
Figure S13	FMO and KS diagram of Cu_4	S22
Figure S14	DFT optimized structural details of Cu_6 NC	S23
Figure S15	FMO and KS diagram of Cu_6	S23
Figure S16	Photoluminescence (PL) spectrum of Cu_4 NC in solution and solid states	S24
Figure S17	PL spectrum of Cu_6 NC in solution and solid states	S24
Figure S18	PL upon oxygen exposure to solid Cu_4 NC	S25
Figure S19	PL upon oxygen exposure to solid Cu_6 NC	S25
Figure S20	Heating effect on the PL intensity of solid Cu_4 NC	S26
Figure S21	Heating effect on the PL intensity of solid Cu_6 NC	S26
Figure S22	Thermogravimetry (TG) and derivative thermogravimetry (DTG) plots of Cu_4 NC	S27

Figure S23	TG and DTG data of Cu ₆ NC	S27
2	References	

1. Computational details

Text S1:

For molecular-level DFT calculations, the Gaussian 09 D.01 program was used.⁵ The Becke's three-parameter hybrid exchange functional and Lee–Yang–Parr's (B3LYP), correlation functional with Pople's 6–31G* basis set was used for non-metal elements along with LANL2DZ-ECP (effective core potential) for Cu atoms, respectively.^{6–13}

In the TD-DFT calculations the PBEPBE and B3LYP functionals found to be accurately replicate the experimentally observed absorption bands for Cu₄ and Cu₆, respectively. All the calculations were performed implicit conductor-like polarizable continuum model (CPCM) with acetonitrile solvent (Comput. Chem., 2003, 24, 669–681; J. Phys. Chem. A, 1998, 102, 1995–2001). To identify the orbital contribution to molecular orbitals and corresponding energies, multi wave function 3.6 was employed to perform Kohn-Sham orbital analysis.¹⁴

Vienna Ab-Initio Simulation Package (VASP) was employed for periodic boundary condition-based calculations with Generalized gradient approximation of Perdew–Burke–Ernzerhof (PBE) functional.^{15–17} The Projector augmented wave (PAW) method was used to treat ion-electron interactions.^{18–19} The ionic relaxations were carried out using a Conjugate gradient algorithm with convergence criterion of 10⁻⁴ eV for minimum energy and 0.02 eV Å⁻¹ for Hellmann-Feynman forces on atoms. Due to the large size of the unit cells of the compounds, the Brillouin zone was sampled at the Gamma point (1×1×1). For the PDOS calculation, a higher (3×3×3) K-point was used.

Table S1. Crystal data and structure refinement for Cu₄ NC

Identification code	Cu ₄ SD
Empirical formula	C ₆₄ H ₅₄ Cu ₄ N ₂ O ₄ P ₄ S ₂
Formula weight	1357.25
Temperature	173(2) K
Wavelength	0.71073 Å
Crystal system	Orthorhombic
Space group	P n a 2 ₁
Unit cell dimensions	a = 19.2367(15) Å α = 90° b = 21.2522(17) Å β = 90°. c = 14.6063(11) Å γ = 90°.
Volume	5971.4(8) Å ³
Z	4
Density (calculated)	1.510 Mg/m ³
Absorption coefficient	1.632 mm ⁻¹
F(000)	2768
Crystal size	0.238 x 0.152 x 0.038 mm ³
Theta range for data collection	3.064 to 28.301°
Index ranges	-25 ≤ h ≤ 25, -28 ≤ k ≤ 28, -19 ≤ l ≤ 19
Reflections collected	283464
Independent reflections	14836 [R(int) = 0.0908]
Completeness to theta = 25.242°	99.7 %
Absorption correction	Semi-empirical from equivalents
Max. and min. transmission	0.7459 and 0.6417
Refinement method	Full-matrix least-squares on F ²
Data / restraints / parameters	14836 / 1 / 722
Goodness-of-fit on F ²	1.077
Final R indices [I > 2σ(I)]	R1 = 0.0345, wR2 = 0.0726
R indices (all data)	R1 = 0.0470, wR2 = 0.0783
Absolute structure parameter	0.033(10)
Extinction coefficient	n/a
Largest diff. peak and hole	0.770 and -0.391 e.Å ⁻³

Table S2. Atomic coordinates ($\times 10^4$) and equivalent isotropic displacement parameters ($\text{\AA}^2 \times 10^3$) for Cu₄-r1. U(eq) was defined as one third of the trace of the orthogonalized U^{ij} tensor.

	x	y	z	U(eq)
Cu(1)	1882(1)	4694(1)	5328(1)	37(1)
Cu(2)	769(1)	5292(1)	4426(1)	42(1)
Cu(3)	3254(1)	4846(1)	4217(1)	37(1)
Cu(4)	4279(1)	5312(1)	5351(1)	43(1)
C(1)	1053(3)	6251(2)	3059(3)	42(1)
C(2)	1820(2)	6213(2)	3285(3)	38(1)
C(3)	2218(3)	6745(2)	3153(4)	57(1)
C(4)	2919(3)	6749(2)	3355(5)	64(2)
C(5)	3217(3)	6206(2)	3680(4)	51(1)
C(6)	2165(2)	5673(2)	3621(3)	32(1)
C(7)	3866(2)	6260(2)	6683(3)	39(1)
C(8)	3098(2)	6106(2)	6540(3)	35(1)
C(9)	2821(2)	5562(2)	6149(3)	31(1)
C(10)	1700(2)	5952(2)	6291(4)	48(1)
C(11)	1927(3)	6490(2)	6698(4)	57(1)
C(12)	2632(3)	6564(2)	6818(4)	50(1)
C(13)	-793(2)	4784(2)	4921(3)	42(1)
C(14)	-943(3)	4985(3)	4043(4)	63(2)
C(15)	-1500(4)	4757(4)	3568(5)	86(2)
C(16)	-1915(3)	4300(3)	3969(5)	82(2)
C(17)	-1767(3)	4085(3)	4818(5)	74(2)
C(18)	-1210(2)	4327(2)	5310(4)	57(1)
C(19)	-264(2)	5799(2)	6116(3)	42(1)
C(20)	-515(4)	5770(3)	6995(5)	83(2)
C(21)	-629(5)	6315(4)	7504(6)	105(3)
C(22)	-524(4)	6890(3)	7114(6)	85(2)

C(23)	-290(3)	6929(3)	6229(5)	71(2)
C(24)	-152(3)	6381(2)	5736(4)	54(1)
C(25)	204(2)	4530(2)	6347(3)	38(1)
C(26)	460(2)	3909(2)	5926(3)	36(1)
C(27)	1625(2)	3685(2)	7132(3)	39(1)
C(28)	1122(3)	3547(3)	7793(3)	60(1)
C(29)	1331(5)	3431(3)	8684(4)	89(2)
C(30)	2021(6)	3439(4)	8909(5)	102(3)

C(31)	2514(4)	3560(3)	8269(5)	86(2)
C(32)	2315(3)	3692(3)	7376(4)	57(1)
C(33)	1530(2)	3084(2)	5387(3)	35(1)
C(34)	1707(3)	3077(3)	4479(3)	57(1)
C(35)	1736(4)	2513(3)	4003(4)	80(2)
C(36)	1614(3)	1961(3)	4437(5)	76(2)
C(37)	1466(4)	1963(2)	5337(6)	87(2)
C(38)	1422(4)	2523(2)	5823(4)	70(2)
C(39)	3495(2)	3716(2)	2486(3)	39(1)
C(40)	3902(3)	3422(3)	1822(4)	61(1)
C(41)	3586(4)	3091(3)	1119(4)	77(2)
C(42)	2882(4)	3038(3)	1071(4)	75(2)
C(43)	2479(4)	3340(3)	1691(5)	73(2)
C(44)	2783(3)	3676(3)	2399(4)	54(1)
C(45)	4026(2)	3425(2)	4211(3)	38(1)
C(46)	3553(3)	3284(2)	4897(4)	49(1)
C(47)	3621(3)	2762(2)	5436(4)	61(1)
C(48)	4176(3)	2359(3)	5292(5)	70(2)
C(49)	4661(3)	2499(3)	4614(5)	74(2)
C(50)	4584(3)	3023(2)	4062(4)	60(1)
C(51)	4717(2)	4360(2)	3064(3)	46(1)
C(52)	5271(2)	4488(2)	3768(3)	47(1)
C(53)	5964(2)	5093(2)	5195(3)	44(1)
C(54)	5901(4)	4750(3)	5992(4)	64(2)
C(55)	6469(5)	4642(4)	6541(5)	86(2)
C(56)	7105(4)	4897(4)	6305(6)	88(2)
C(57)	7166(3)	5236(3)	5547(6)	83(2)
C(58)	6597(3)	5338(3)	4965(5)	66(2)
C(59)	5336(2)	5858(2)	3747(3)	43(1)
C(60)	5558(3)	5817(3)	2846(4)	60(1)
C(61)	5629(4)	6349(3)	2327(5)	78(2)
C(62)	5485(4)	6935(3)	2682(5)	81(2)
C(63)	5277(4)	6982(3)	3572(5)	76(2)
C(64)	5198(3)	6451(2)	4110(4)	58(1)

N(1)	2854(2)	5673(2)	3795(2)	35(1)
N(2)	2132(2)	5487(2)	6024(2)	36(1)
S(1)	1763(1)	4935(1)	3804(1)	34(1)
S(2)	3294(1)	4882(1)	5815(1)	34(1)
O(1)	893(2)	6515(2)	2348(3)	60(1)
O(2)	621(2)	6035(2)	3631(3)	70(1)
O(3)	4298(2)	6089(2)	6089(3)	66(1)
O(4)	4015(2)	6570(2)	7362(3)	58(1)
P(1)	-16(1)	5101(1)	5466(1)	35(1)
P(2)	1410(1)	3844(1)	5939(1)	30(1)
P(3)	3856(1)	4106(1)	3492(1)	35(1)
P(4)	5187(1)	5184(1)	4489(1)	39(1)

Table S3. Crystal data and structure refinement for Cu₆NC

Identification code	Cu ₆ SD		
Empirical formula	C ₅₇ H ₇₃ Cu ₆ N ₁₃ O ₁₉ S ₆		
Formula weight	1817.88		
Temperature	296(2) K		
Wavelength	0.71073 Å		
Crystal system	Triclinic		
Space group	P -1		
Unit cell dimensions	a = 13.248(3) Å	α = 114.754(9)°.	
	b = 13.622(3) Å	β = 96.758(10)°.	
	c = 13.881(3) Å	γ = 115.050(8)°.	
Volume	1923.8(8) Å ³		
Z	1		
Density (calculated)	1.569 Mg/m ³		
Absorption coefficient	1.863 mm ⁻¹		
F(000)	928		
Crystal size	0.267 x 0.207 x 0.070 mm ³		
Theta range for data collection	3.300 to 26.000°		
Index ranges	-16 ≤ h ≤ 16, -16 ≤ k ≤ 16, -17 ≤ l ≤ 17		

Reflections collected	85081
Independent reflections	7547 [R(int) = 0.1101]
Completeness to theta = 25.242°	99.8 %
Absorption correction	Semi-empirical from equivalents
Max. and min. transmission	0.7457 and 0.6283
Refinement method	Full-matrix least-squares on F ²
Data / restraints / parameters	7547 / 67 / 478
Goodness-of-fit on F ²	1.064
Final R indices [I>2sigma(I)]	R1 = 0.0454, wR2 = 0.0981
R indices (all data)	R1 = 0.0822, wR2 = 0.1196
Extinction coefficient	n/a
Largest diff. peak and hole	1.082 and -0.502 e.Å ⁻³

Table S4. Atomic coordinates (x 10⁴) and equivalent isotropic displacement parameters (Å²x 10³) for Cu₆. U(eq) is defined as one third of the trace of the orthogonalized U^{ij} tensor.

	x	y	z	U(eq)
Cu(1)	5900(1)	4151(1)	4150(1)	42(1)
Cu(2)	4372(1)	3368(1)	5155(1)	44(1)
Cu(3)	3428(1)	4015(1)	3613(1)	41(1)
C(1)	3290(4)	1424(4)	2739(4)	34(1)
C(2)	2546(4)	217(4)	1752(4)	41(1)
C(3)	1784(5)	-774(5)	1862(5)	57(1)
C(4)	1795(5)	-584(5)	2920(6)	66(2)
C(5)	2580(5)	610(5)	3857(5)	51(1)
C(6)	2499(5)	-75(4)	571(4)	51(1)
C(7)	1842(3)	2956(4)	4678(3)	32(1)
C(8)	835(4)	2082(4)	4731(4)	37(1)
C(9)	-209(4)	1288(5)	3798(5)	55(1)
C(10)	-234(5)	1368(6)	2829(5)	65(2)

C(11)	797(4)	2221(5)	2830(4)	53(1)
C(12)	872(4)	2028(5)	5793(4)	46(1)
C(13)	7017(4)	3741(4)	5780(4)	36(1)
C(14)	7760(4)	3448(4)	6256(4)	44(1)
C(15)	8557(6)	3262(6)	5757(5)	68(2)
C(16)	8570(6)	3306(7)	4780(6)	81(2)
C(17)	7774(5)	3532(6)	4332(5)	65(2)
C(18)	7697(5)	3293(5)	7253(5)	54(1)
C(19)	2394(6)	6822(6)	86(6)	72(2)
C(20)	1375(8)	6073(11)	-1859(7)	158(5)
C(21)	3562(7)	7392(8)	-1013(8)	108(3)
C(22)	1521(6)	2522(6)	8642(5)	73(2)
C(23)	1300(8)	3585(8)	10437(6)	113(3)
C(24)	1826(12)	1974(11)	10040(8)	173(6)
C(25)	6294(10)	9816(11)	2086(8)	176(6)
C(26)	6224(8)	9261(10)	3443(10)	145(4)
C(27)	5191(8)	10291(8)	3246(10)	145(4)
N(1)	3324(3)	1594(3)	3774(3)	40(1)
N(2)	7014(3)	3749(4)	4809(3)	46(1)
N(3)	1820(3)	2998(4)	3723(3)	40(1)
N(4)	2432(5)	6752(5)	-878(4)	73(1)
N(5)	1575(5)	2717(5)	9666(4)	74(2)
N(6)	5896(5)	9810(5)	2902(4)	71(1)
O(1)	3534(4)	385(4)	487(3)	79(1)
O(2)	1571(4)	-740(5)	-213(4)	98(2)
O(3)	1474(4)	1560(4)	5999(3)	63(1)
O(4)	363(5)	2384(6)	6384(4)	97(2)
O(5)	6762(4)	2740(5)	7359(5)	99(2)
O(6)	8709(3)	3775(4)	7977(3)	72(1)
O(7)	1421(5)	6347(6)	227(5)	109(2)
O(8)	1761(5)	1776(5)	7959(4)	86(1)
O(9)	6382(6)	10060(7)	1502(5)	133(3)
S(1)	4149(1)	2804(1)	2699(1)	36(1)
S(2)	3181(1)	4039(1)	5873(1)	37(1)

S(3)	6123(1)	4227(1)	6450(1)	37(1)
N(7)	5070(40)	5080(40)	0(30)	150(6)
C(28)	5150(30)	5050(40)	1020(20)	213(14)
C(29)	5010(30)	4110(30)	-870(20)	179(9)
C(30)	4270(30)	5460(40)	-220(40)	276(16)
O(10)	5060(20)	3380(20)	-600(20)	255(11)

Table S5. List of mechanoresponsive copper nanoclusters

Molecular formula	λ_{max} . (emission)	Reference
[Cu ₄ I ₄ (PPh ₂ (CH ₂ CH=CH ₂)) ₄]	440 nm/530nm/580 nm	1
Cu ₄ I ₄ (PPh ₃) ₄	520 nm/560 nm	2
Cu ₄ (oCBT) ₄ /Cu ₄ (mCBT) ₄ /Cu ₄ (ICBT) ₄ (CBT=carborane thiol)	525nm/533nm/595nm	3
Au ₄ Cu ₂ (decz) ₂ (POP) ₂ (H ₃ decz= 3,6-di-tert-butyl-1,8-diethynyl-9H-carbazole, POP= bis(2-diphenylphosphinophenyl)ether)	576 nm	4
[Cu ₄ (MNA) ₂ (DPPE) ₂] ⁺ and [Cu ₆ (MNA-H) ₆] ⁺	560 nm and 755 nm	This work

Table S6. List of solvents used for the recovery of luminescence.

Solvent	Luminescence recovery	
	Cu ₄	Cu ₆
CH ₃ OH	√	√
H ₂ O	×	√
CH ₃ COCH ₃	√	√
CH ₂ Cl ₂	√	×
HCON(CH ₃) ₂	√	√
CH ₃ CN	√	√
(CH ₂) ₄ O	×	√
CH ₃ OCH ₃	×	×
SO(CH ₃) ₂	√	√
CHCl ₃	×	×

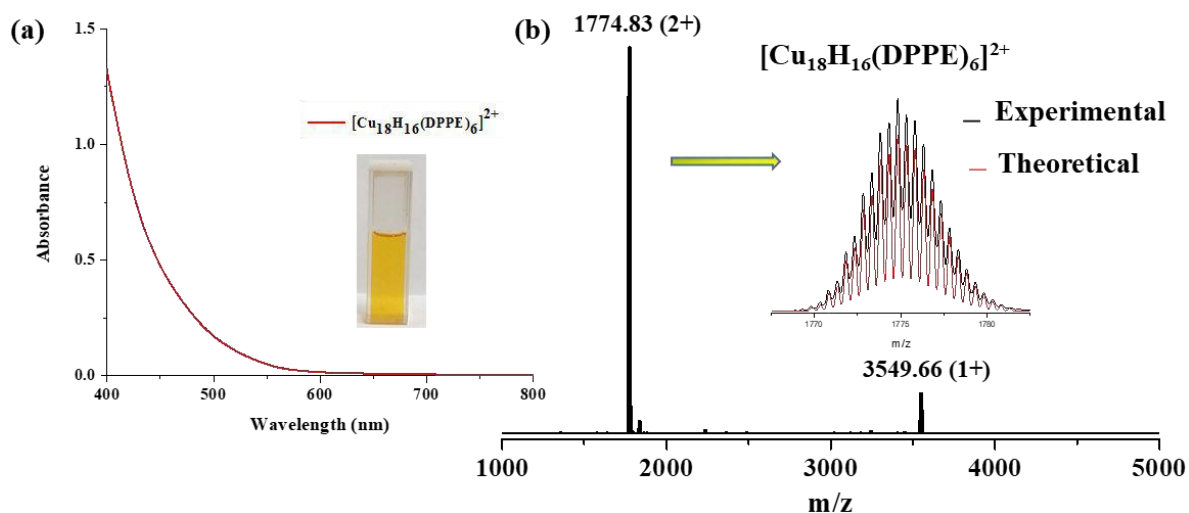


Figure S1. Characterization of $[\text{Cu}_{18}\text{H}_{16}(\text{DPPE})_6]^{2+}$ nanocluster. a) UV-vis spectrum (inset shows a photographic image of Cu_{18} NC in dichloromethane). b) ESI MS spectrum in the positive ion mode (inset shows good agreement between experimental and theoretical spectra).

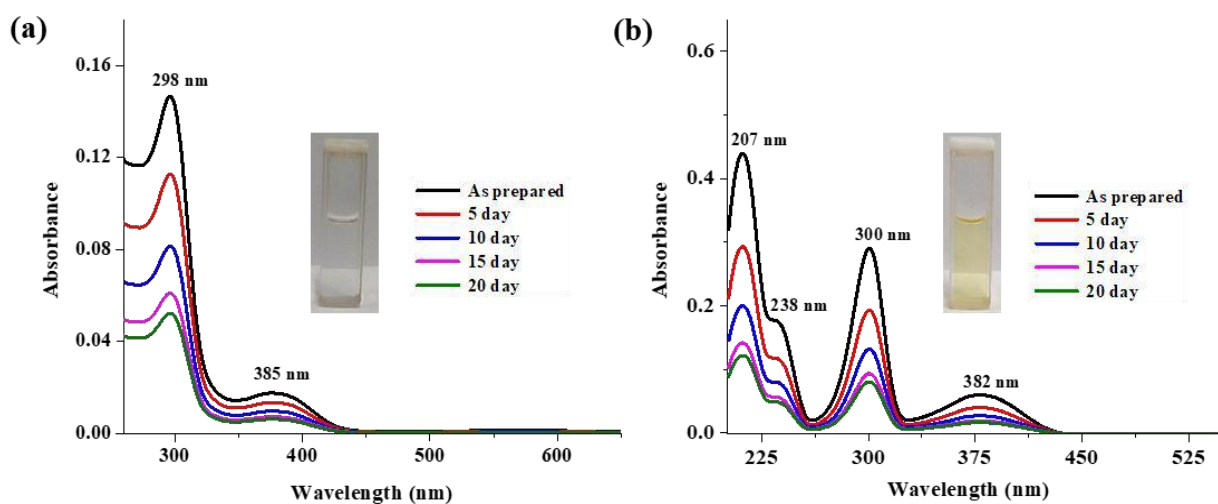


Figure S2. UV-vis. absorption spectra of (a) Cu_4 and (b) Cu_6 NCs in acetonitrile solvent. Insets show photographs of the solutions.

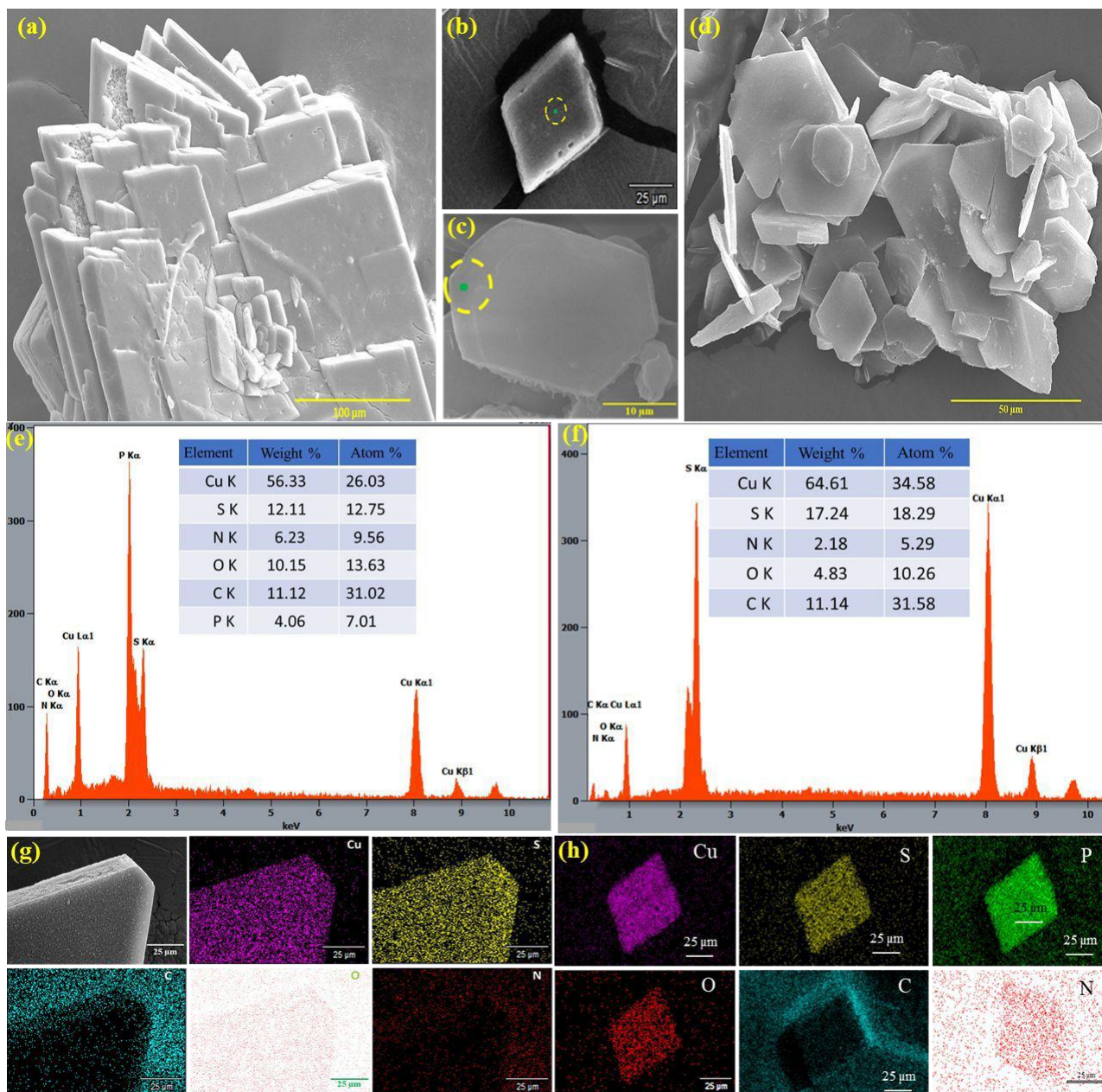


Figure S3. FESEM images of agglomerated single crystals of (a) Cu_4 and (d) Cu_6 NCs, (b, c) single crystals to determine EDS mapping, (e, f) EDS spectra of the same (inset shows weight and atomic percentages, respectively), (g, h) EDS mapping of each element present in Cu_4 and Cu_6 NCs.

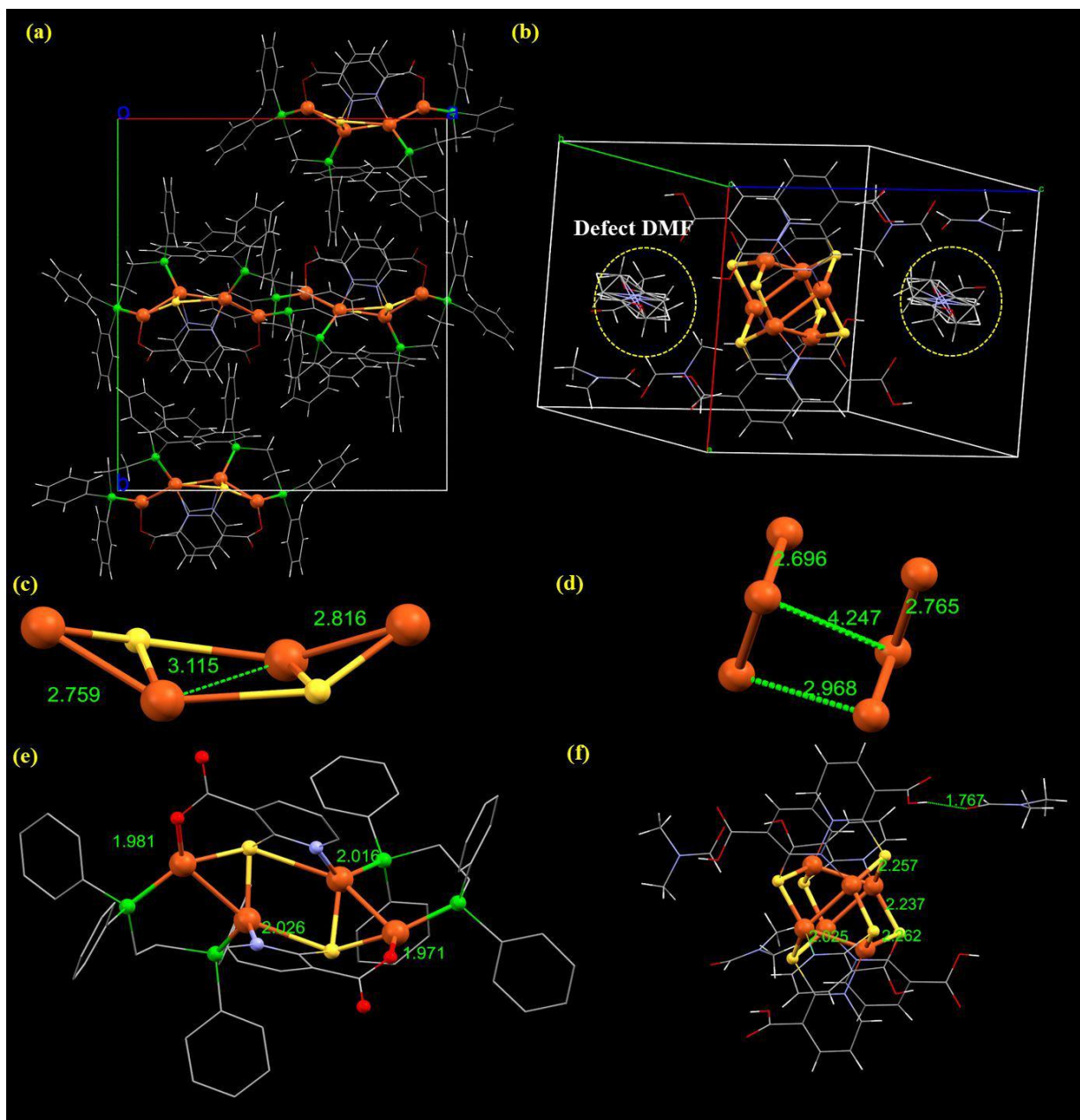


Figure S4. Structural packing per unit cell of (a) Cu₄ and (b) Cu₆ NCs. (c,e) Bond distances in Cu₄ and (d,f) Cu₆ NC along b-axis. Atomic color code: Orange=copper, yellow=S, Red=oxygen, blue=nitrogen, grey=carbon and white=hydrogen.

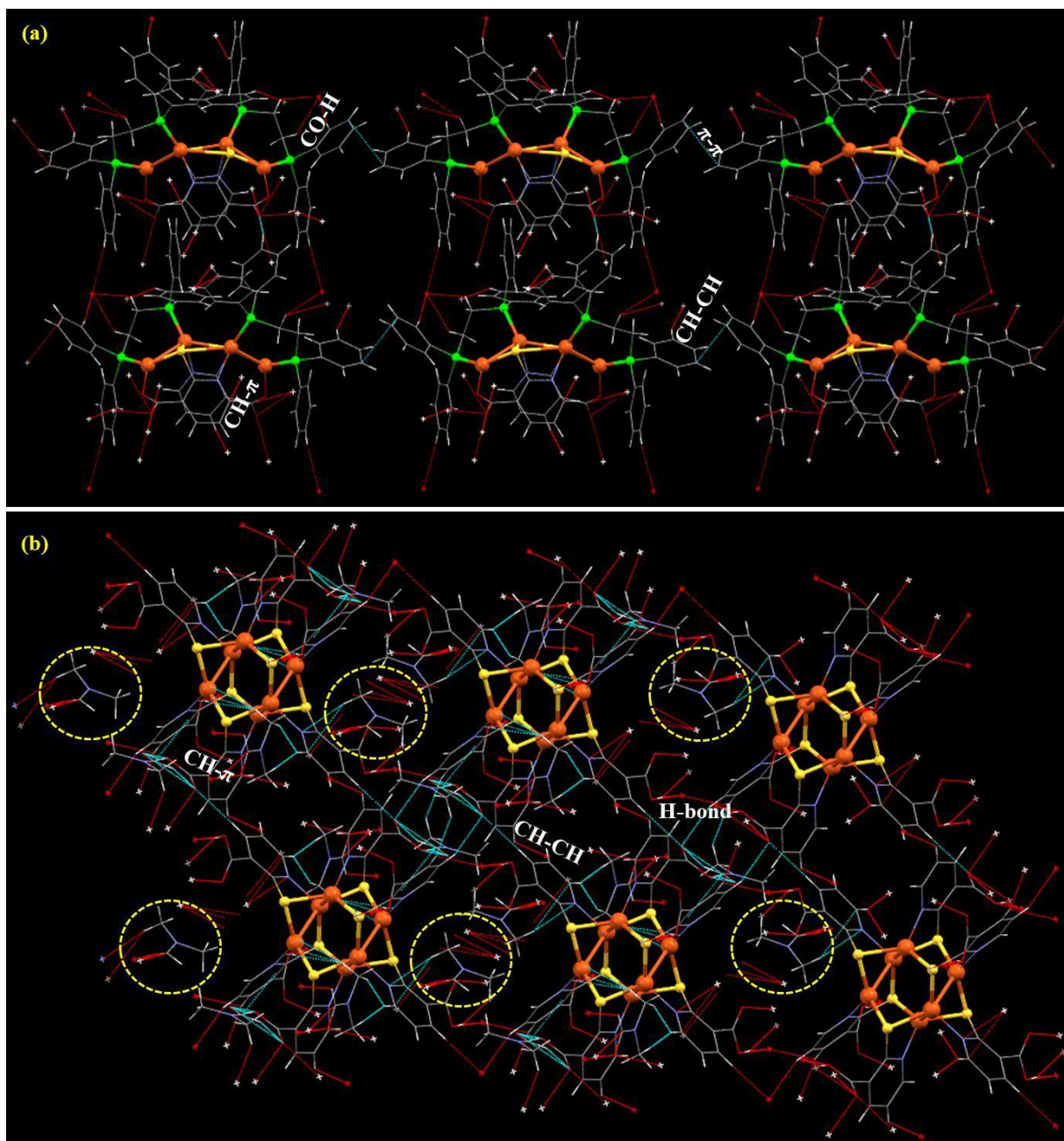


Figure S5. Ligand-centered non-covalent short contact interactions involve solid-state supramolecular packing of (a) Cu₄ and (b) Cu₆ NCs. Atomic color code: Orange=copper, yellow=S, Red=oxygen, blue=nitrogen, grey=carbon and white=hydrogen.

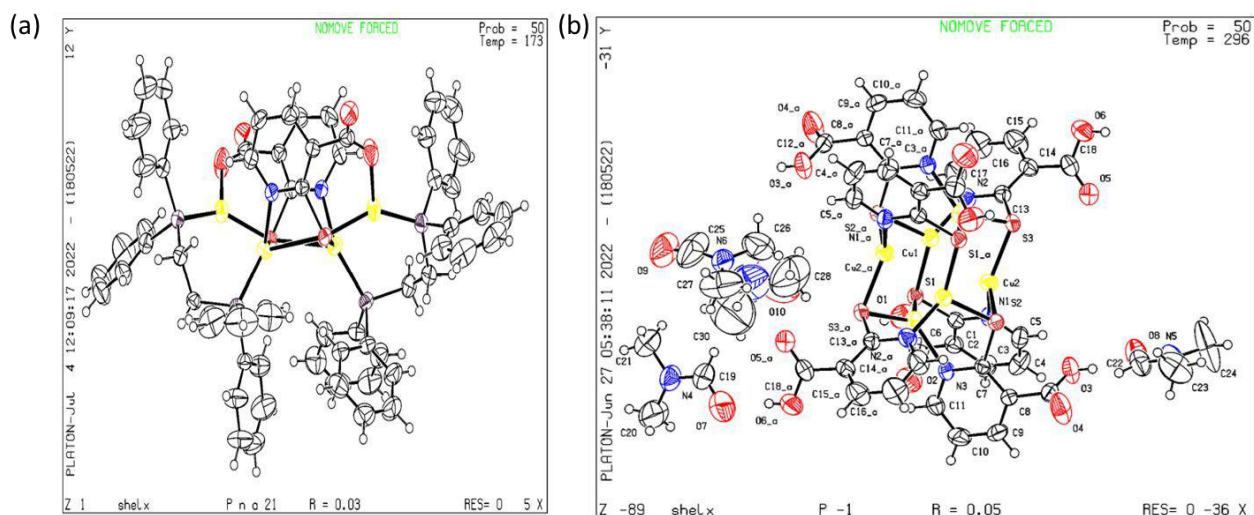


Figure S6. ORTEP structures of (a) Cu₄ and (b) Cu₆ NCs having 50% thermal ellipsoid parameters.

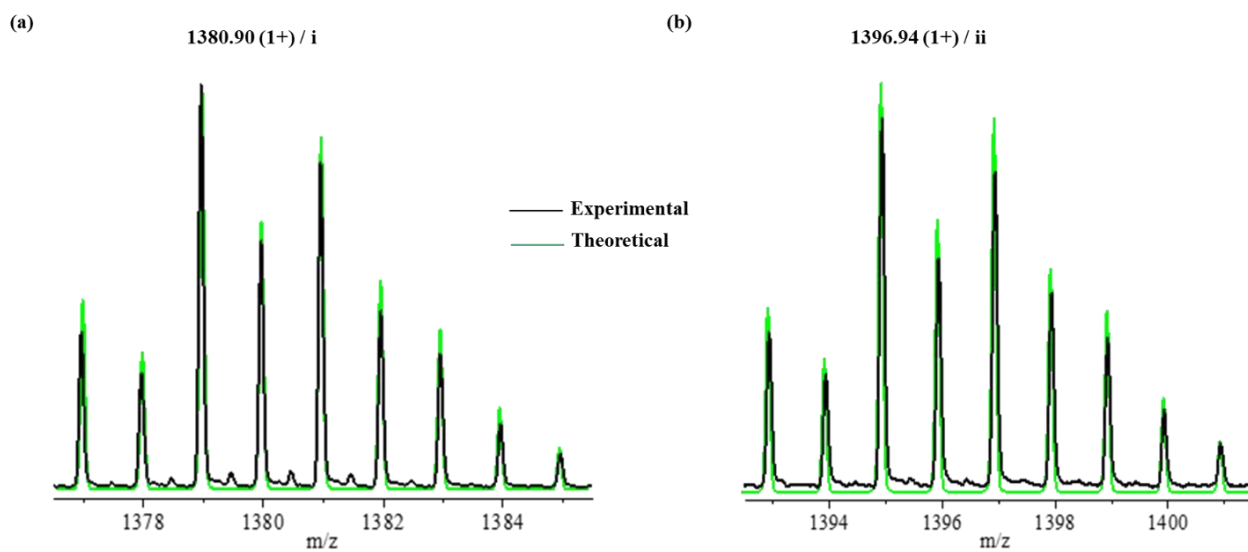


Figure S7. (a,b) Experimental and theoretical mass spectra of sodium and potassium attached to Cu₄ NC.

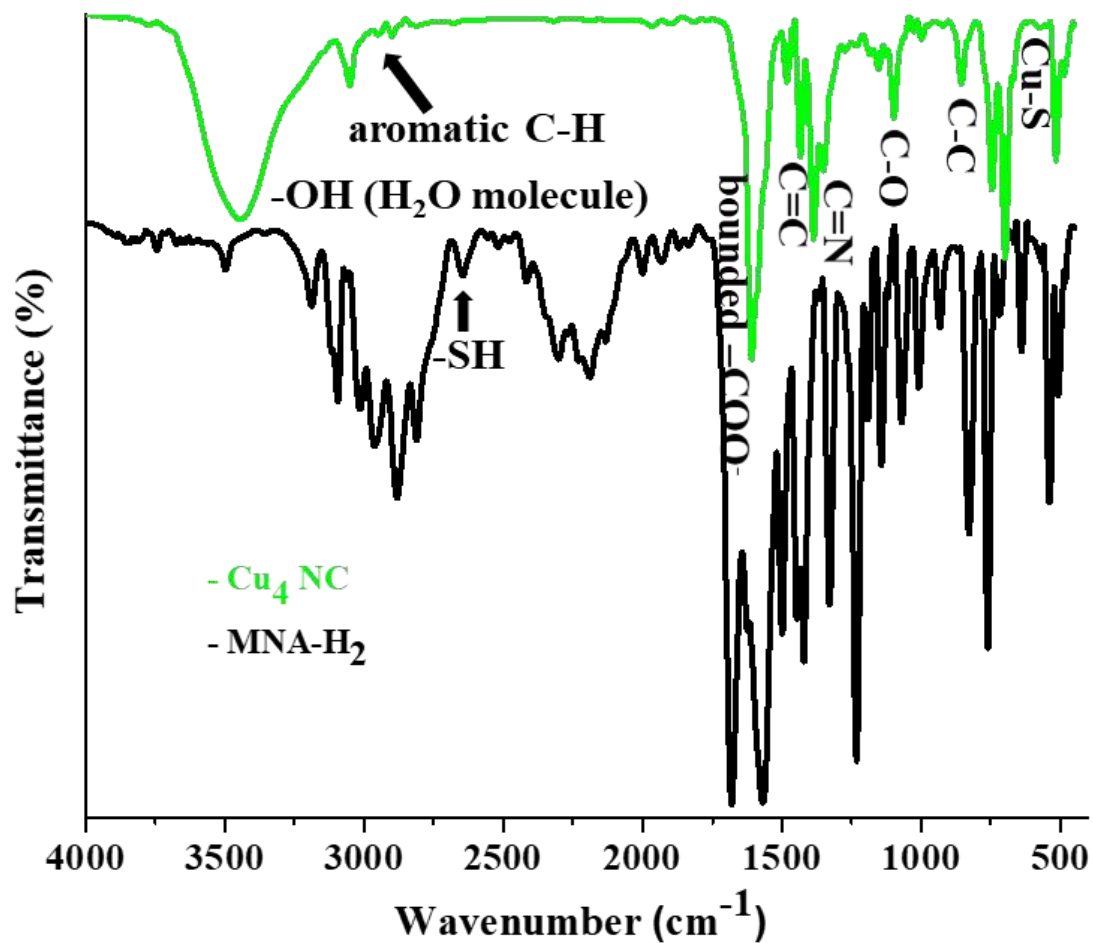


Figure S8. FTIR spectrum of Cu_4NC compared with that of the free ligand. Stretching vibrations are mentioned.

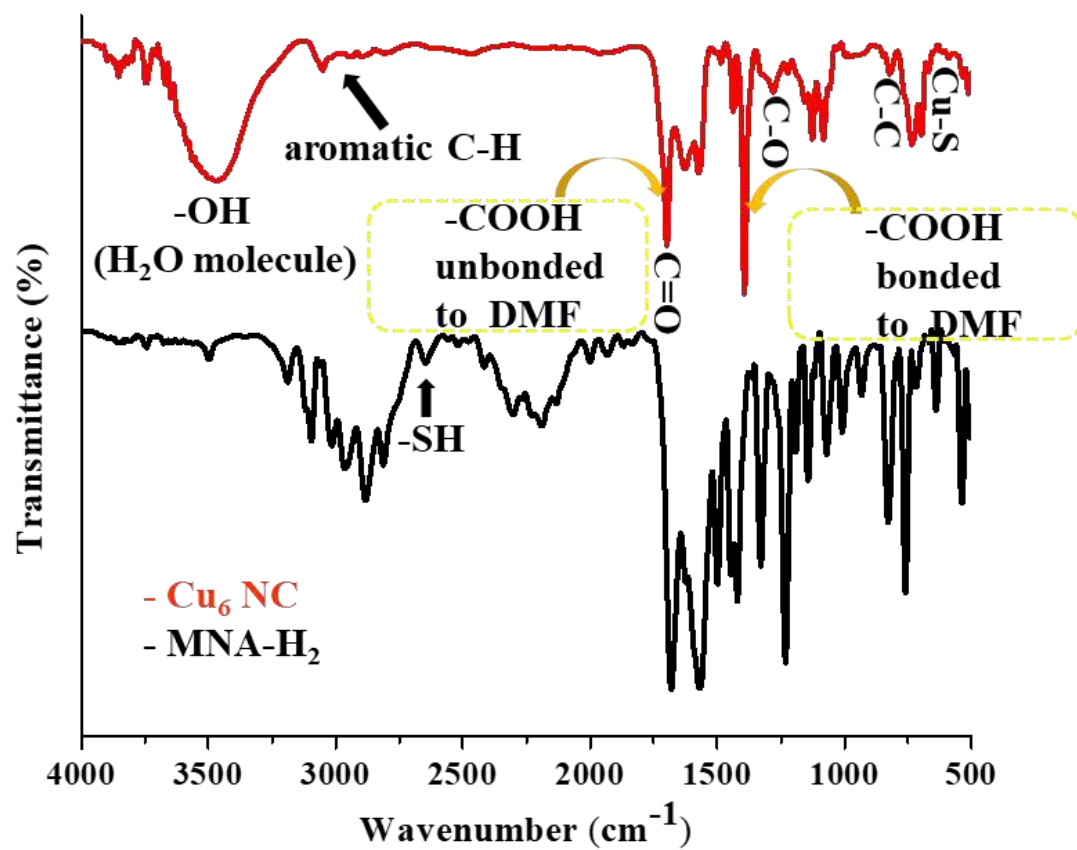


Figure S9. FTIR spectrum of Cu_6NC compared with that of the free ligand. Stretching vibrations are mentioned.

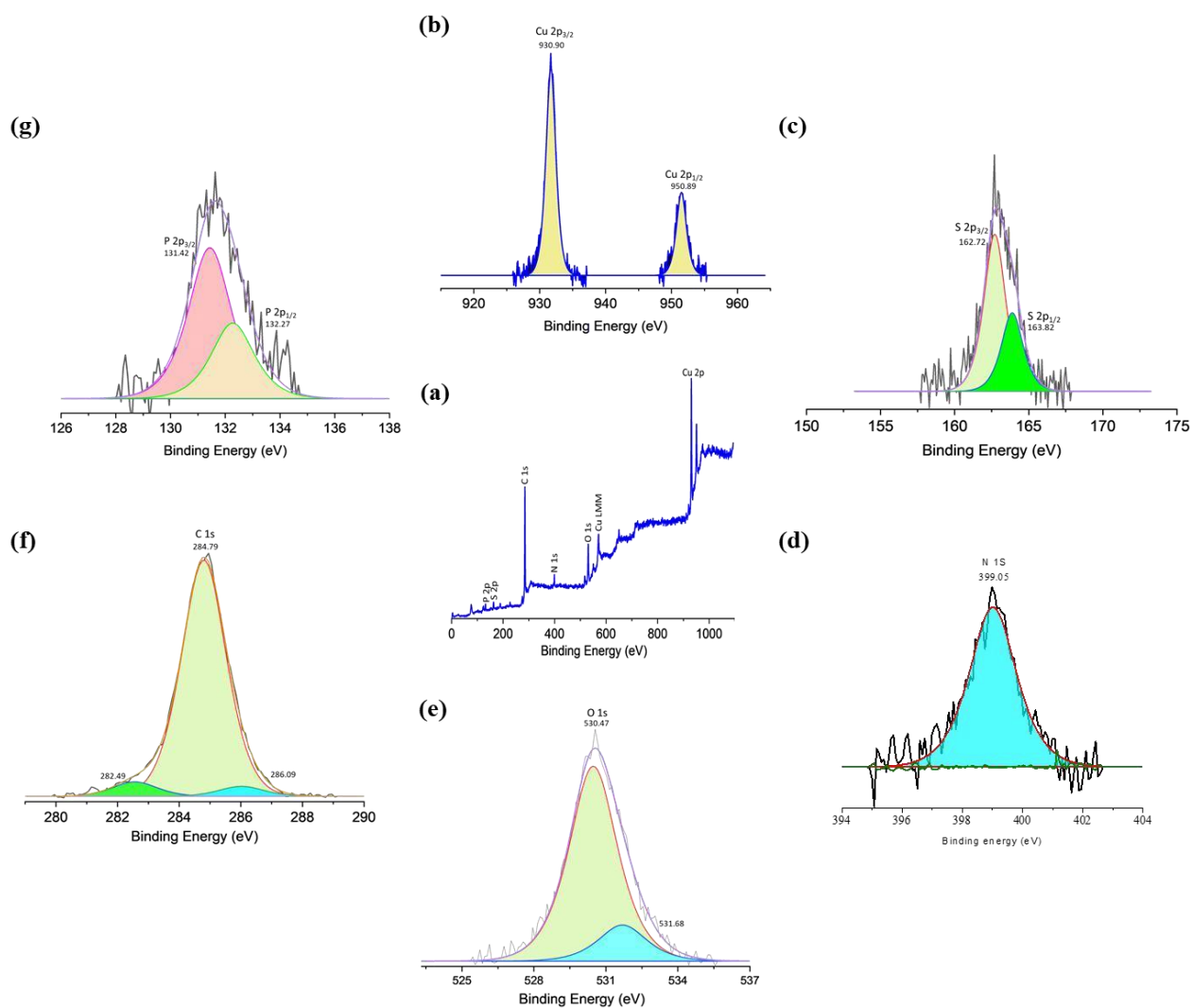


Figure S10. XPS spectrum of Cu_4NC . (a) Survey spectrum of the respective elements. Expanded peak fittings of (b) Cu 2p, (c) S 2p, (d) N 1s, (e) O 1s, (f) C 1s, and (g) P 2p spectral regions.

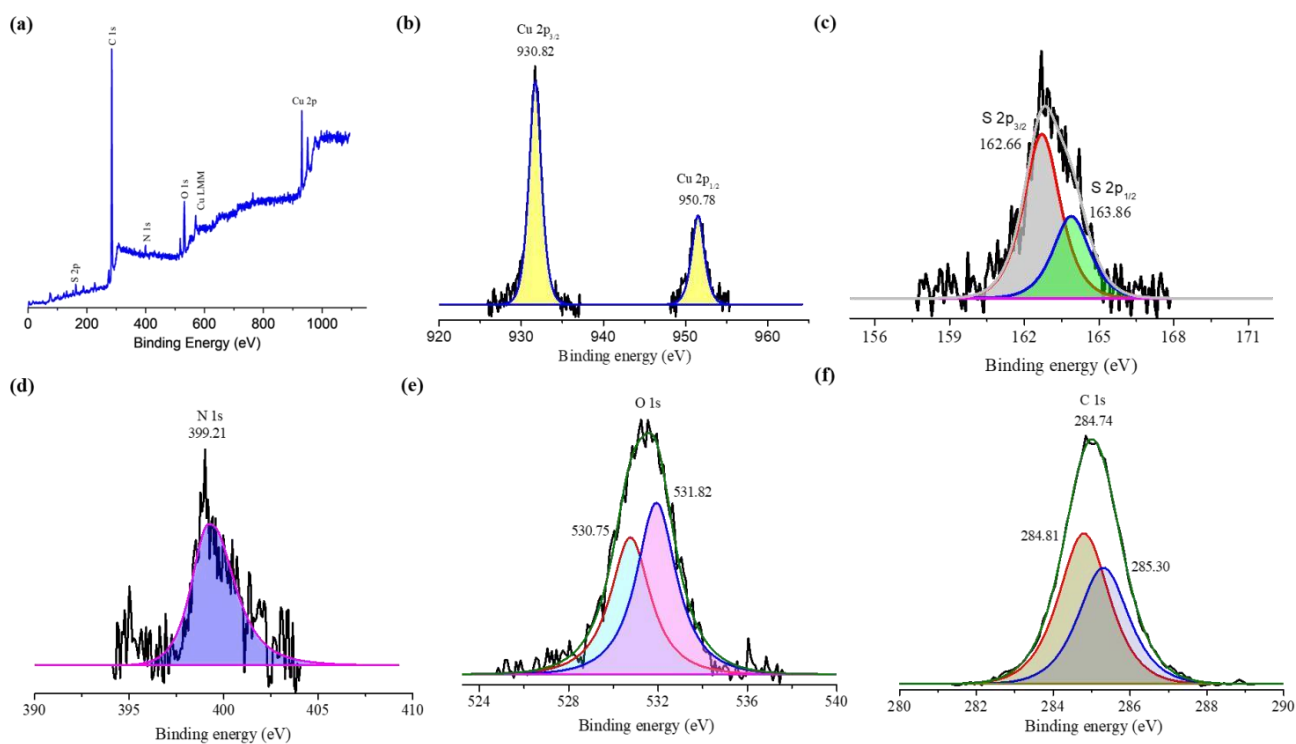


Figure S11. XPS spectrum of Cu_6NC . (a) Survey spectrum of respective elements. Expanded peak fitting of (b) Cu 2p, (c) S 2p, (d) N 1s, (e) O 1s, (f) C 1s spectral regions.

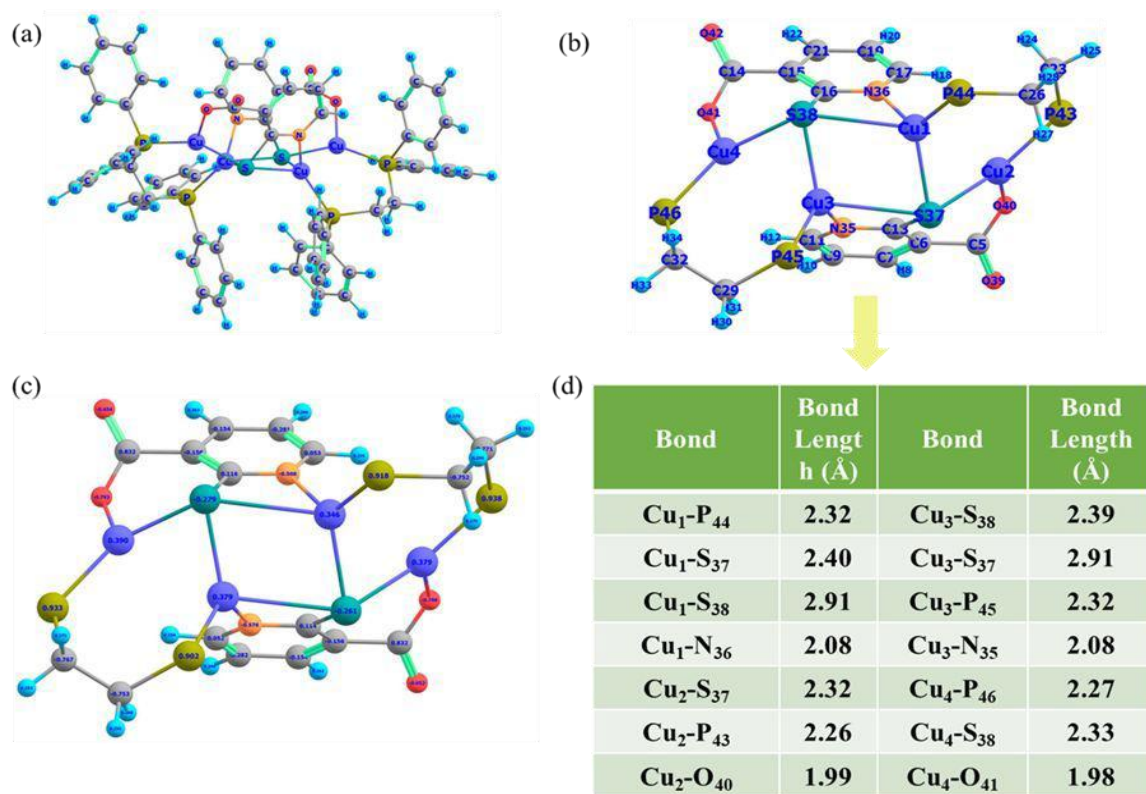


Figure S12. DFT optimized structural details of Cu₄ NC. (a) Full structure, (b) core cluster, (c) NBO charge distribution, and (d) bond distances in the optimized structure.

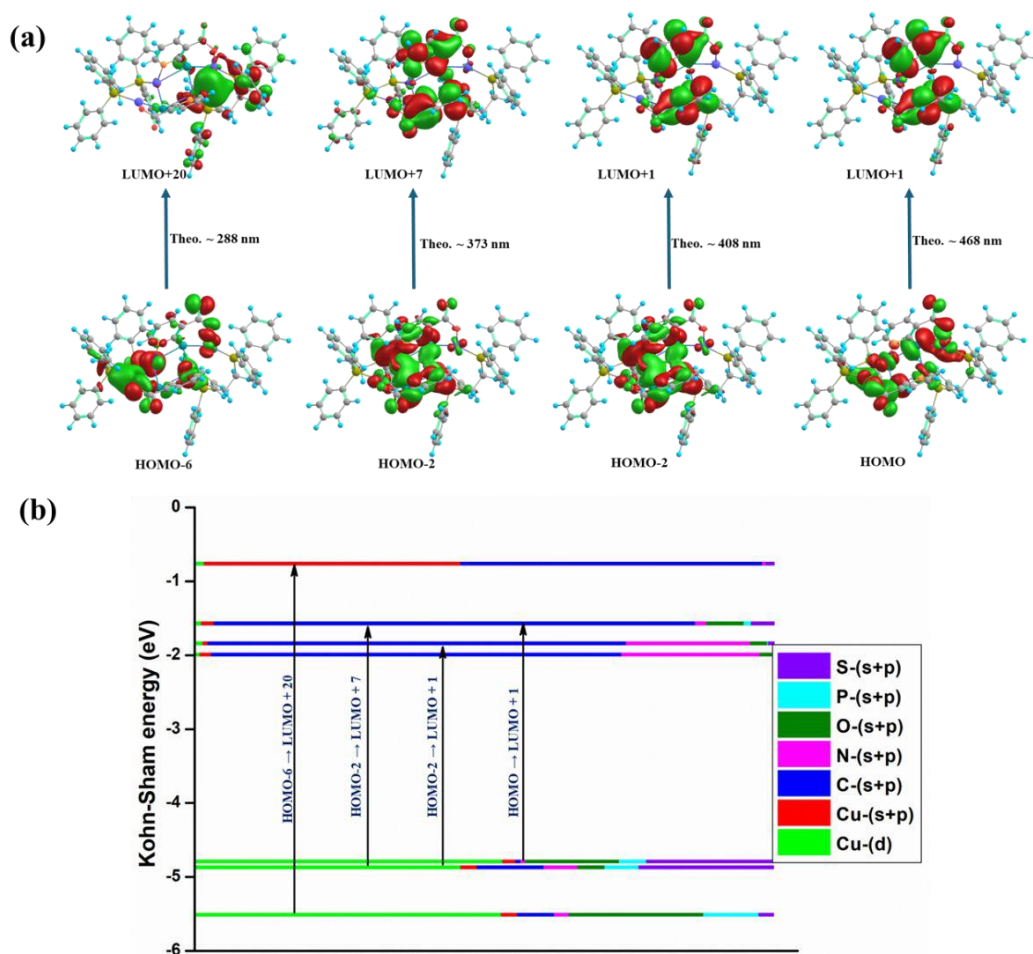


Figure S13. (a) Molecular orbitals involved in the electronic transitions of Cu₄ NC, calculated from TDDFT, (b) Kohn-Sham molecular orbital diagram of Cu₄ NC.

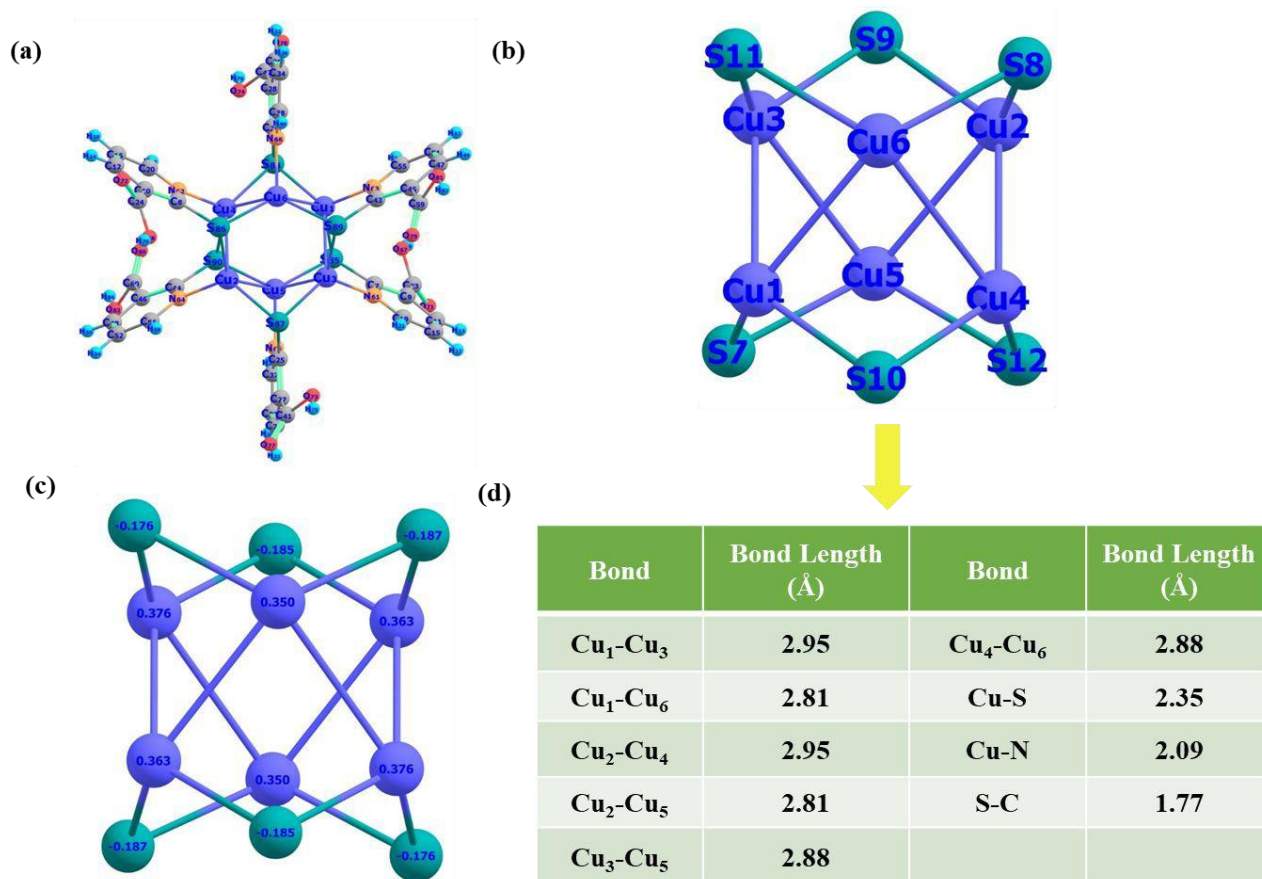


Figure S14. DFT optimized structural details of Cu₆ NC. (a) Full structure, (b) core cluster, (c) NBO charge distribution and (d) bond distances in the optimized structure.

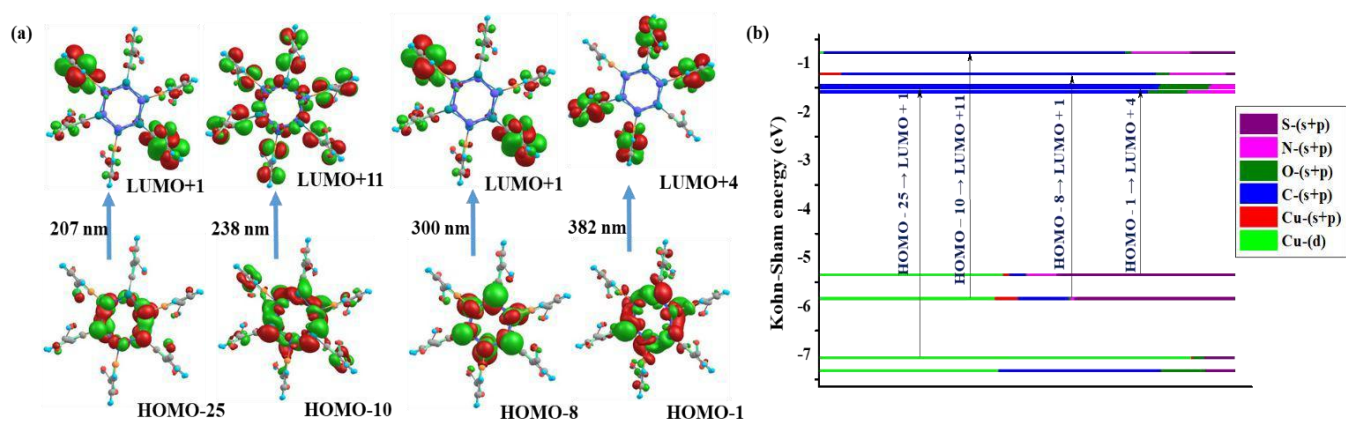


Figure S15. (a) Molecular orbitals involved in the electronic transition of Cu₆ NC, calculated from TDDFT, (b) Kohn-Sham molecular orbital diagram of Cu₆ NC.

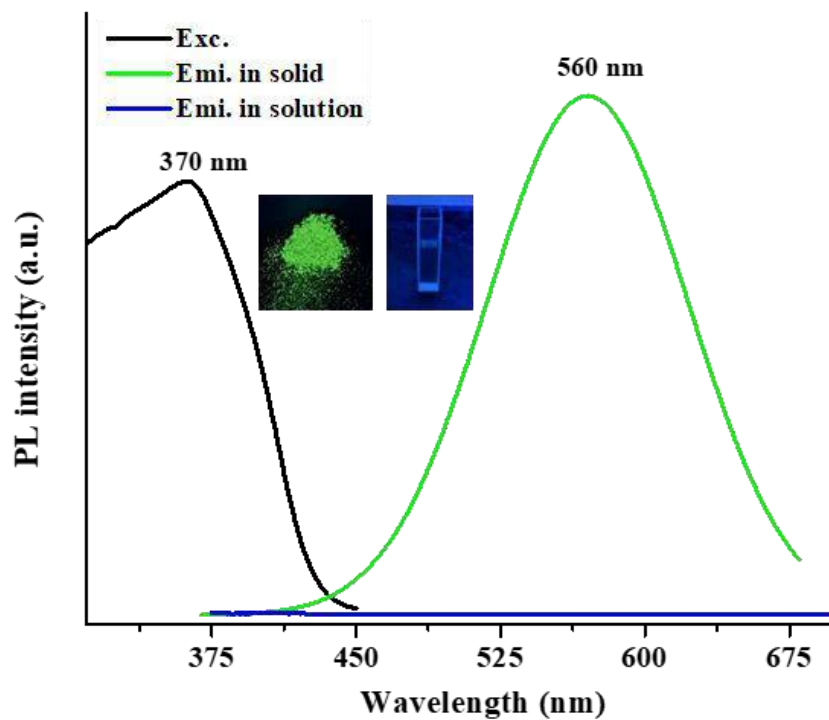


Figure S16. Photoluminescence emission spectrum of Cu_4NC in the solid and solution state. Inset shows the optical photographs of the cluster under UV light.

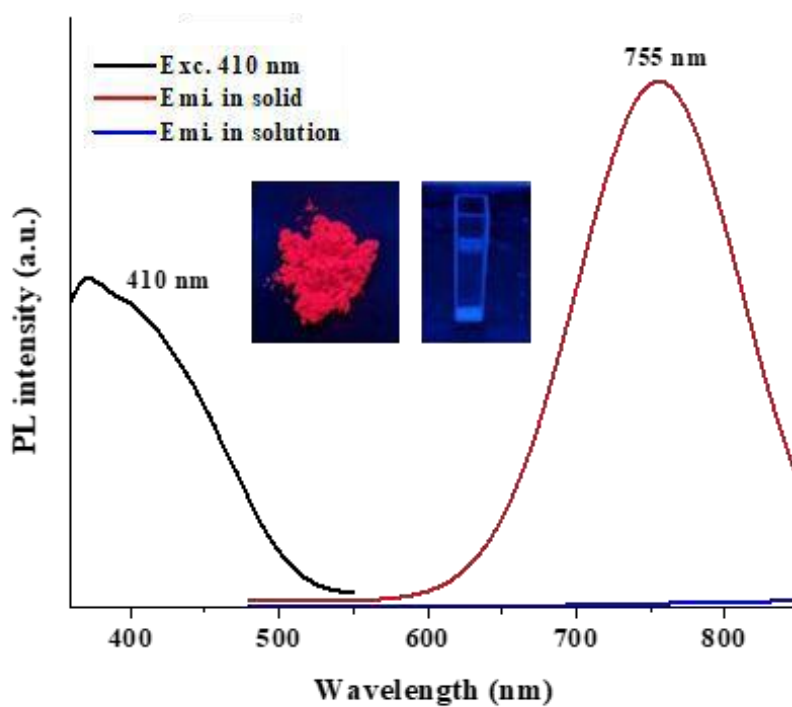


Figure S17. Photoluminescence emission spectrum of Cu_6NC in the solid and solution states. Inset shows the optical photographs of the cluster under UV light.

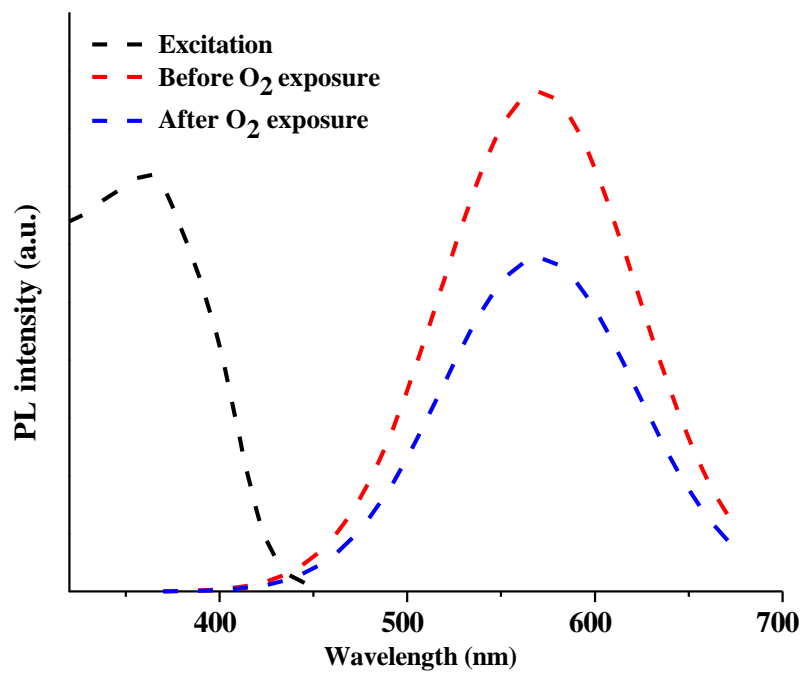


Figure S18. Photoluminescence (PL) emission spectra of Cu₄ NC in the solid state before and after O₂ exposure (Exc.370nm and Emi. 560 nm).

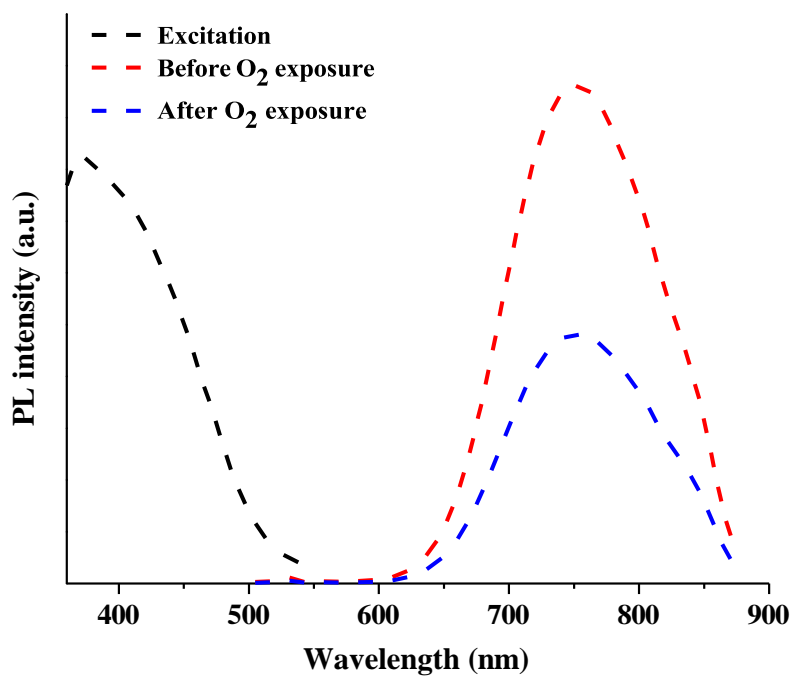


Figure S19. Photoluminescence (PL) emission spectra of Cu₆ NC in the solid state before and after O₂ exposure (Exc. 410 nm and Emi. 755 nm).

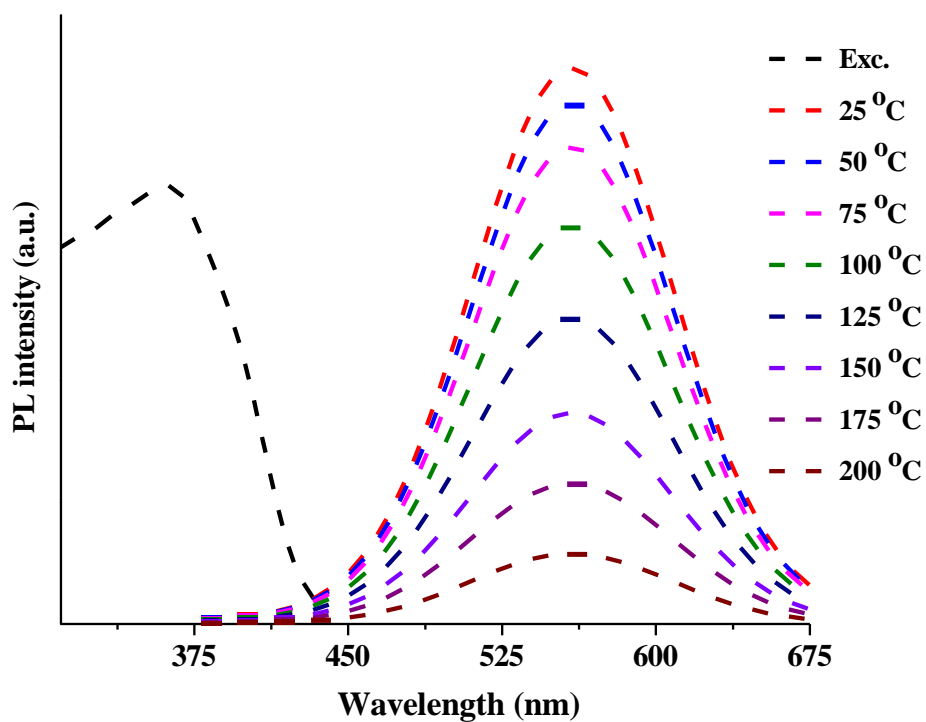


Figure S20. Photoluminescence emission spectra of Cu₄ NC crystals upon heating at different temperatures (Excitation at 370 nm and emission at 560 nm).

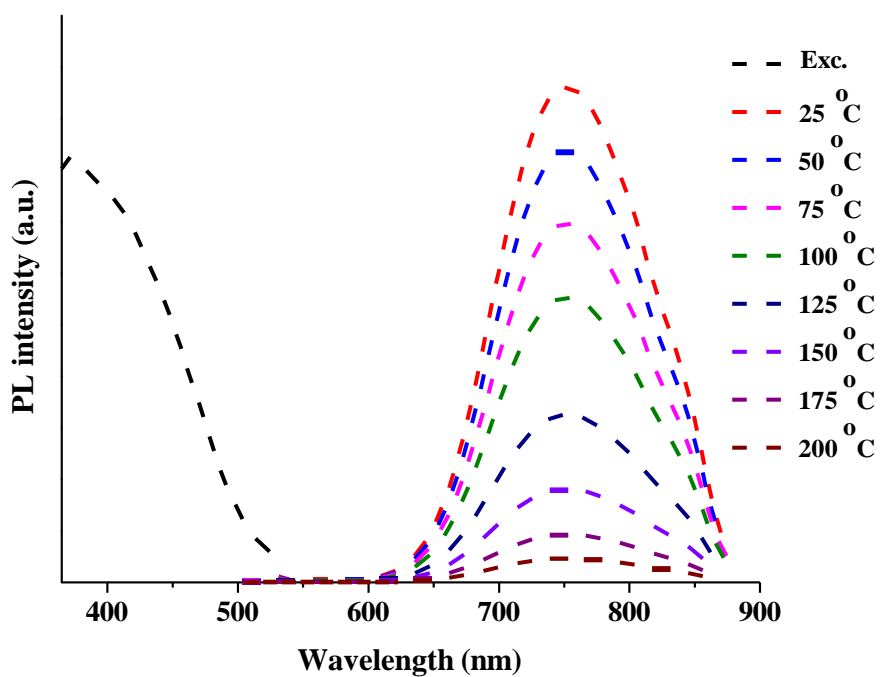


Figure S21. Photoluminescence emission spectra of Cu₆ NC crystals upon heating at different temperatures (Excitation at 410 nm and emission at 755 nm).

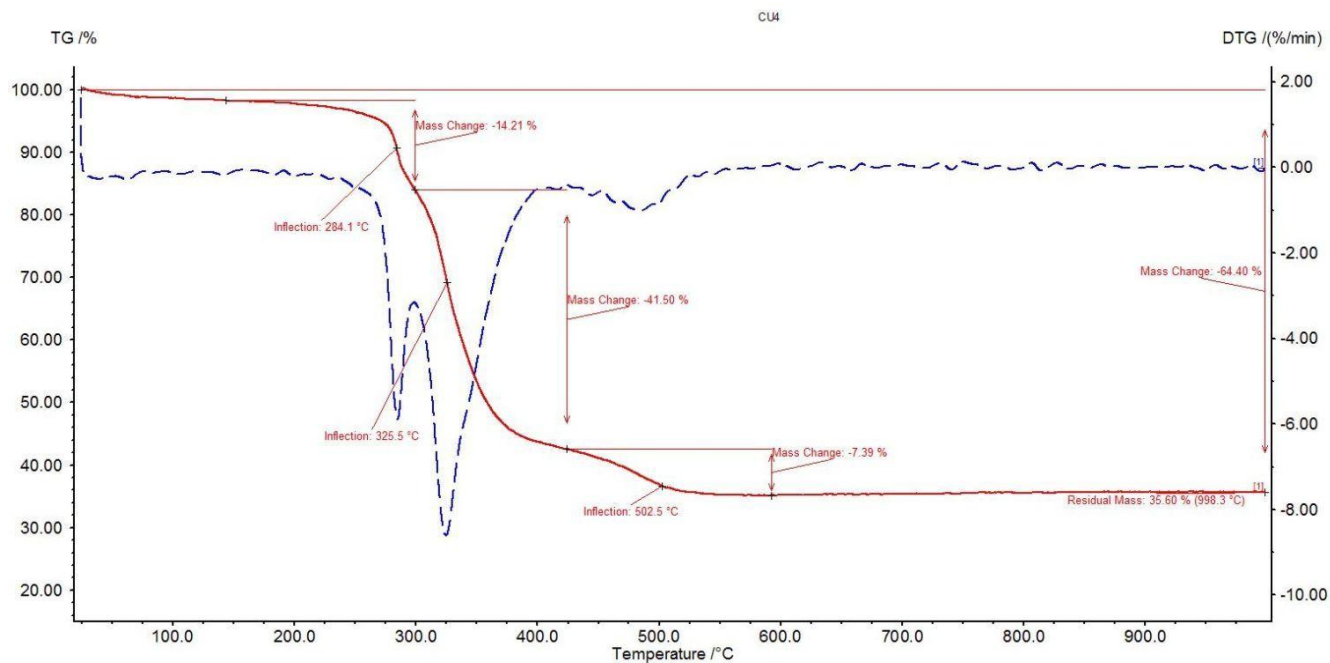


Figure S22. Thermogravimetry (TG) and derivative thermogravimetry (DTG) of Cu_4NC . Initial mass loss is likely to be due to the fragmentation of ligands.

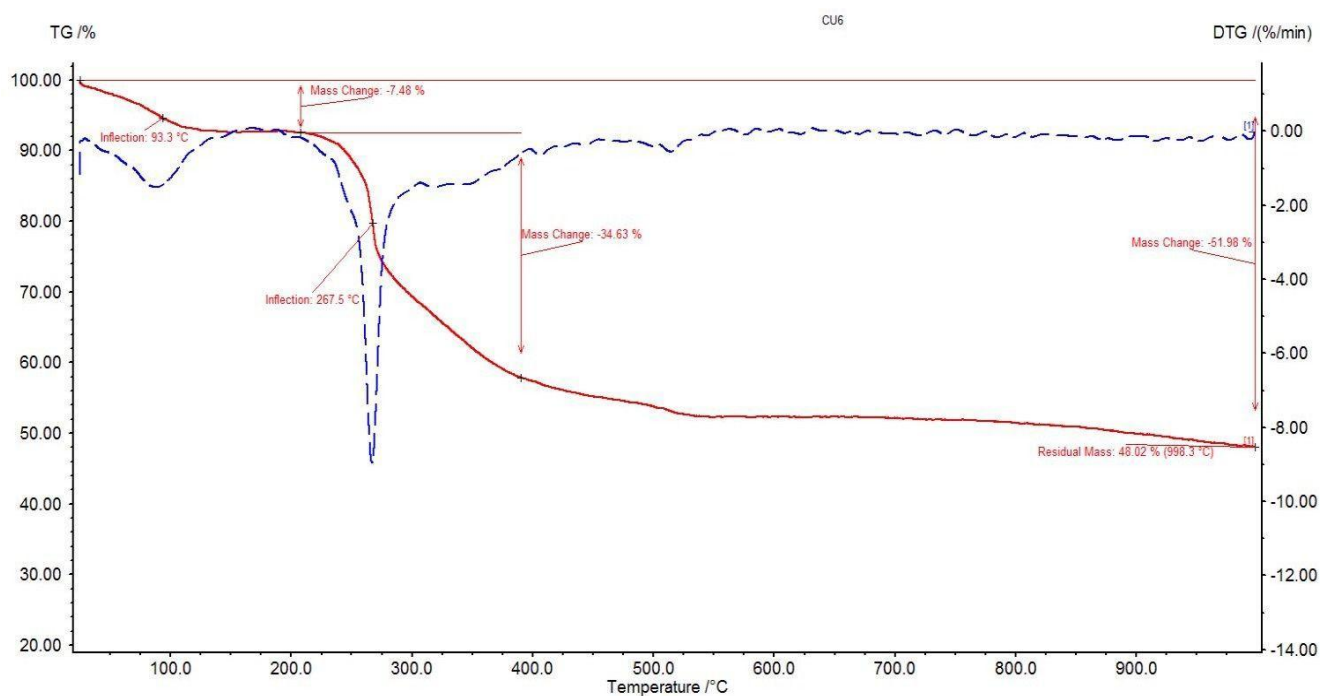


Figure S23. TG and DTG traces of Cu_6NC . Initial mass loss is likely to be due to the solvent molecules.

2. References

- (1) Perruchas, S.; Le Goff, X.F.; Maron, S.; Maurin, I.; Guillen, F.; Garcia, A.; Gacoin, T.; Boilot, J.P. Mechanochromic and thermochemic luminescence of a copper iodide cluster. *J. Am.Chem.Soc.* **2010**, 132(32), 10967-10969.
- (2) Kitagawa, H.; Ozawa, Y.; Toriumi, K. Flexibility of cubane-like Cu₄I₄ framework: temperature dependence of molecular structure and luminescence thermochemism of [Cu₄I₄(PPh₃)₄] in two polymorphic crystalline states. *Chem. Commun.* **2010**, 46(34), 6302-6304.
- (3) Jana, A.; Jash, M.; Jash, Dar, W.A. ; Roy, J.; Chakraborty, P.; Paramasivam, G.; Lebedkin, S.; Kirakci, K.; Manna; Antharjanam, S.; Machacek, J. ; Kucerakova, M. ; Ghosh, S.; Lang, K.; Kappes, M.M.; Base, T.; Pradeep, T. Carborane-thiol protected copper nanoclusters: stimuli-responsive materials with tunable phosphorescence. *Chem. Sci.* **2023**, 14, 1613-1626.
- (4) Wu, X.M.; Wang, J.Y.; Huang, Y.Z.; Chen, Z.N. Scissor-like Au₄Cu₂ Cluster with Phosphorescent Mechanochromism and Thermochemism. *Molecules* **2023**, 28(7), 3247.
- (5) Frisch, M. J.; Trucks, G. W.; Schlegel, H. B.; Scuseria, G. E.;Robb, M. A.; Cheeseman, J. R.; Scalmani, G.; Barone, V.; Mennucci,B.; Petersson, G. A. et al. *Gaussian 09*, Revision B.01; Gaussian Inc.:Wallingford, CT, **2009**.
- (6) Becke, A.D. Density-functional thermochemistry. I. The effect of the exchange-only gradient correction. *J. Chem. Phys.* **1992**, 96(3), 2155-2160.
- (7) Becke, A.D. Density-functional thermochemistry. IV. A new dynamical correlation functional and implications for exact-exchange mixing. *J. Chem. Phys.* **1996**, 104(3), 1040-1046.
- (8) Lee, C.; Yang, W.; Parr, R.G. Development of the Colle-Salvetti correlation-energy formula into a functional of the electron density. *Phys. Rev. B* **1988**, 37(2), 785.
- (9) Clark, T.; Chandrasekhar, J.; Spitznagel, G.W.; Schleyer, P.V.R. Efficient diffuse function-augmented basis sets for anion calculations. III. The 3-21+ G basis set for first-row elements, Li–F. *J. Comput. Chem.* **1983**, 4(3), 294-301.
- (10) Hariharan, P.C.; Pople, J.A. The influence of polarization functions on molecular orbital hydrogenation energies. *Theor. Chim. Acta* **1973**, 28, 213-222.

- (11) Hay, P.J.; Wadt, W.R. Ab initio effective core potentials for molecular calculations. Potentials for the transition metal atoms Sc to Hg. *J. Chem. Phys.* **1985**, 82(1), 270-283.
- (12) Grimme, S.; Antony, J.; Ehrlich, S.; Krieg, H. A consistent and accurate ab initio parametrization of density functional dispersion correction (DFT-D) for the 94 elements H-Pu. *J. Chem. Phys.* **2010**, 132(15).
- (13) Lu, T.; Chen, F. Multiwfn: A multifunctional wavefunction analyzer. *J. Comput. Chem.* **2012**, 33(5), 580-592.
- (14) Kresse, G.; Furthmüller, J. Efficiency of ab-initio total energy calculations for metals and semiconductors using a plane-wave basis set. *Comput. Mater. Sci.* **1996**, 6(1), 15-50.
- (15) Perdew, J.P.; Burke, K.; Ernzerhof, M. Generalized gradient approximation made simple. *Phys. Rev. Lett.* **1996**, 77(18), 3865.
- (16) Perdew, J.P.; Burke, K.; Ernzerhof, M. *Phys. Rev. Lett.* **1996**, 77, 3765.
- (17) Blöchl, P.E. Projector augmented-wave method. *Phys. Rev. B* **1994**, 50(24), 17953.
- (18) Kresse, G.; Joubert, D. From ultrasoft pseudopotentials to the projector augmented-wave method. *Phys. Rev. B* **1999**, 59(3), 1758.

Growth of Clathrate Hydrates in Nanoscale Ice Films Observed Using Electron Diffraction and Infrared Spectroscopy

Bijesh K. Malla, Ding-Shyue Yang,* and Thalappil Pradeep*



Cite This: *J. Phys. Chem. Lett.* 2025, 16, 365–371



Read Online

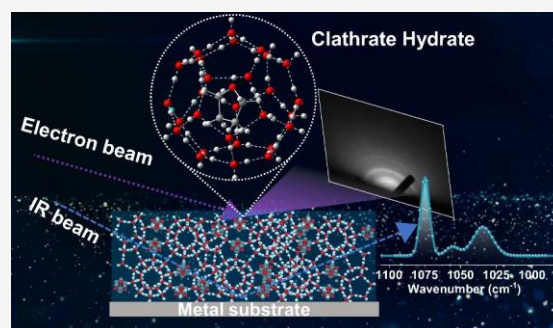
ACCESS

Metrics & More

Article Recommendations

Supporting Information

ABSTRACT: Clathrate hydrates (CHs) are believed to exist in cold regions of space, such as comets and icy moons. While spectroscopic studies have explored their formation under similar laboratory conditions, direct structural characterization using diffraction techniques has remained elusive. We present the first electron diffraction study of tetrahydrofuran (THF) and 1,3-dioxolane (DIOX) CHs in the form of nanometer-thin ice films under an ultrahigh vacuum at cryogenic temperatures. Using reflection high-energy electron diffraction, we show that THF CH grows readily on various substrates during thermal annealing of an amorphous ice mixture of THF and water, and the formation is independent of the nature of the substrate. The growth of DIOX CHs on a Au(111) substrate is similar. A comparison of electron diffraction patterns with calculated X-ray diffraction patterns indicates that THF and DIOX form structure II CH ($5^{12}6^4$) with a lattice constant of ~ 17.2 Å (cubic $Fd\bar{3}m$). Both CHs were also grown on Ru(0001) and were examined by reflection absorption infrared spectroscopy. A direct comparison of diffraction data to infrared spectra as a function of the temperature further demonstrates the strength of multiple probes in examining complex systems possessing diverse molecular interactions.



Existence of clathrate hydrates (CHs) in the simulated interstellar environment has been established by infrared spectroscopy.¹ CHs represent a unique class of compounds, where water molecules form cages to encapsulate guest molecules, creating crystalline solids. This molecular arrangement of water allows for the inclusion of a variety of molecules, such as CH₄, C₂H₆, C₃H₈, CO₂, N₂, O₂, and others, within the crystalline structures.² Typically, CHs exhibit three crystalline structures: structure I (sI, cubic $Pm\bar{3}n$), structure II (sII, cubic $Fd\bar{3}m$), and structure H (sH, hexagonal $P6/mmm$), and they generally occur under high-pressure conditions.^{3–5} Since the detection of methane CH in 2019 at 30 K under ultrahigh-vacuum (UHV) conditions⁶ principally using reflection absorption infrared spectroscopy (RAIRS), there have been several reports on the CHs of molecules. They include those of ethane (C₂H₆),⁷ formaldehyde (HCHO),⁸ acetone (CH₃COCH₃),⁹ acetaldehyde (CH₃COH),¹⁰ tetrahydrofuran [(CH₂)₄O],^{11,12} and dimethyl ether (CH₃OCH₃).¹³ The formation of CHs occurs typically starting from an amorphous ice mixture of the guest and host water molecules upon slow thermal annealing. It was noted in the original report that maintaining a methane/water mixture at 30 K for 25 h produces a characteristic methane CH peak at 3017 cm⁻¹, corresponding to the C–H stretch of CH₄ encaged in the 5¹² cage. Deconvolution of this feature showed that 13% of total methane exists as CH under this condition. Since then, it has been possible to encage different percentages of guest molecules in CHs under different temperature conditions in

UHV. CO₂, in particular, produces hydrate even at 10 K, for which the infrared spectrum was known in the literature.^{14,15} Additionally, studies of interactions of low-energy electrons and photons with various caged molecules have been conducted in UHV, although these have not been explicitly assigned to CHs.^{16–18}

A key question that comes up in such investigations is the independent confirmation of CHs by structural tools, especially using scattering techniques. As these experiments are conducted on thin films with thicknesses in the nanometer scale, a suitable option for structural characterization is electron diffraction.^{19–21} Electron diffraction in a transmission electron spectroscopy (of methanol CH) was reported in 1991, under 10⁻⁶ Torr.¹⁴ However, no report exists in UHV on any of the hydrates at temperatures below 160 K, which is typically the desorption temperature of water in UHV conditions.²² Considering the nature of RAIRS conducted on single-crystal surfaces, a natural choice for structural studies is reflection high-energy electron diffraction (RHEED). It is a well-suited technique for studying the structures and phase transitions of

Received: October 28, 2024

Revised: November 26, 2024

Accepted: December 6, 2024

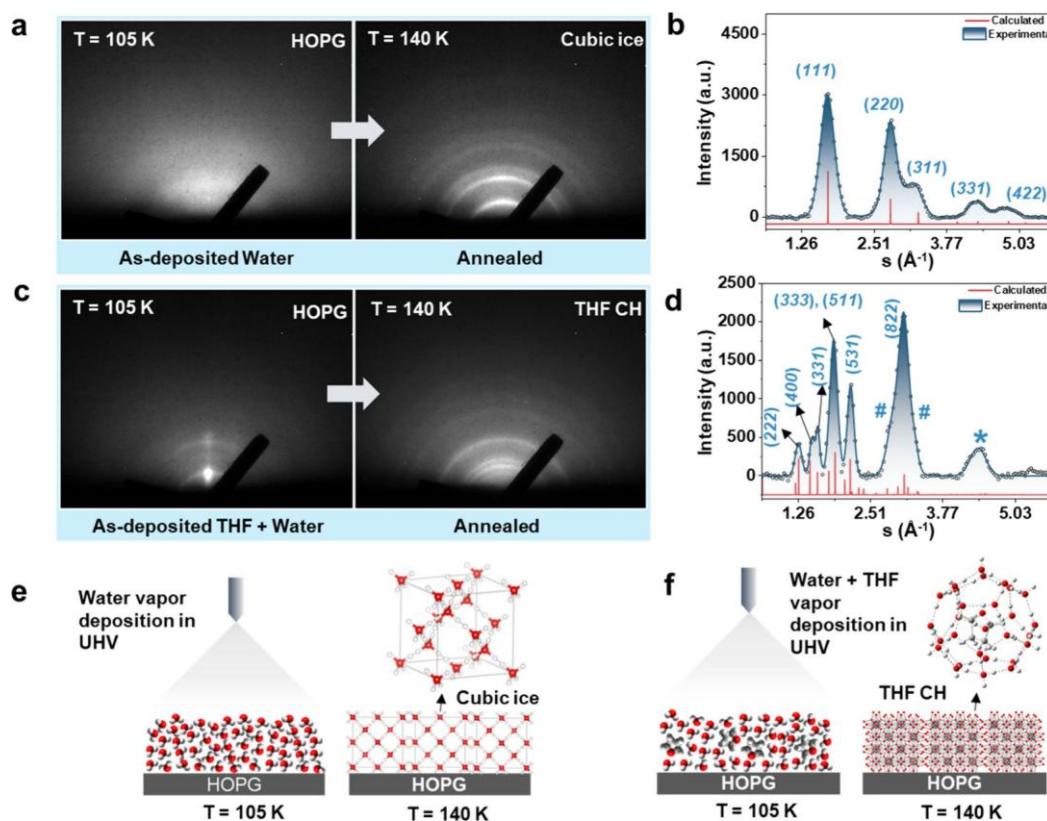


Figure 1. Evolution of ice Ic and THF CH explored with RHEED. (a) Electron diffraction images of as-deposited water on HOPG at 105 K and after annealing to 140 K. (b) Comparison of the experimental radially averaged electron diffractions of annealed water ice at 140 K with the calculated diffraction peaks (red lines) of ice Ic. (c) Electron diffraction images of the as-deposited THF–water ice mixture on HOPG at 105 K and after annealing to 140 K. (d) Comparison of the experimental radially averaged electron diffractions of annealed THF–water ice at 140 K with the calculated (red lines) diffraction peaks of sII THF CH. Peaks labeled with # are attributed to ice Ic, while that marked with * corresponds to the collection of low-intensity signals of THF CH, shown in the theoretical spectrum. (e) Schematic diagram of the formation of ice Ic on HOPG from vapor-deposited ice. (f) Schematic diagram of the formation of sII THF CH on HOPG from vapor-deposited ice.

solid-supported molecular thin films, and our lab has conducted several experiments in this regard.^{23–28} In the present work, we report the first RHEED experiment of tetrahydrofuran (THF, $\text{C}_4\text{H}_8\text{O}$) and 1,3-dioxolane (DIOX, $\text{C}_3\text{H}_6\text{O}_2$) CHs under UHV, and the results were compared to the simulated diffraction data. The emergence of CHs under the same temperature and pressure conditions was confirmed by RAIRS. Although THF and DIOX have not yet been detected in the interstellar medium (ISM), various similar molecules, such as dimethyl ether, propylene oxide, and ethylene oxide, have been identified.^{29–31} Given the ongoing advancements in astronomical observations, the detection of THF and DIOX in the ISM may be possible in the near future. We believe that these investigations further enrich our understanding of the formation of CHs in UHV and cryogenic conditions and present opportunities for their exploration using other UHV techniques, such as low-energy ion scattering.^{32,33} It is worth noting that, while the RHEED and RAIRS measurements were performed on separate instruments, both were conducted under identical temperature and pressure conditions to ensure consistency. For the RHEED experiments, ice films were grown on three distinct substrates: highly oriented pyrolytic graphite (HOPG, ZYA grade), single-crystalline Au(111) (Princeton Scientific), and a hydrophobic self-assembled monolayer (SAM) of 1-octadecanethiol on Au(111). Co-deposition methods were employed to create thin films of ice with an approximate thickness of 25 nm for

CH preparation. This process involved the simultaneous deposition of premixed vapors of THF or DIOX with water for 10 min. For the RAIRS experiments, the Ru(0001) substrate was used to prepare thin ice films. A mixed ice film with an approximate thickness of 60 nm, composed of THF/DIOX and water in a 1:3 ratio, was prepared on the Ru(0001) substrate at 105 K. This was achieved by backfilling the chamber with THF/DIOX and water vapor for a duration of 10 min at a total pressure of 5×10^{-7} mbar. The experimental procedures and ice thickness calculations for both RHEED and RAIRS are detailed in the Supporting Information. Calculated X-ray diffraction (XRD) patterns are shown in panels b and d of Figure 1 for cubic ice (ice Ic, $a = 6.35 \text{ \AA}$)³⁴ and THF CH ($a = 17.21 \text{ \AA}$)³⁵ along with Figure S4 of the Supporting Information for hexagonal ice (ice Ih, $a/b = 4.49 \text{ \AA}$ and $c = 7.33 \text{ \AA}$),³⁶ calculated using the VESTA software.³⁷ These patterns were compared to the experimental electron diffraction patterns to validate the phase identification.

In Figure 1, we present the evolution of ice Ic and CH of THF grown on HOPG in the temperature window of 105–140 K. Under high-vacuum ($\sim 10^{-6}$ – 10^{-8} mbar) conditions, amorphous ice typically crystallizes into ice Ic, ice Ih, or stacking-disordered ice.^{38–41} The crystal structure may be significantly influenced by the substrate and temperature.²⁰ Prior to investigating the formation of CH, we commenced our study with an examination of the structure of pure ice, as these are well-characterized by RHEED.^{21,23} Figure 1a shows the

Table 1. Electron Diffraction Results for Ice Ic, sII THF, and DIOX CH, with Calculated and Observed hkl (Crystallographic Indices) and d (Bragg Distance)^a

cubic ice calculated		cubic ice observed		sII THF CH calculated		sII THF CH observed		sII DIOX CH observed	
hkl	d	d		hkl	d	d		d	
				111(s)	9.94				
				311(w)	5.19	5.10 ^s			
				222(s)	4.97	4.98 ^{&}			
				400(s)	4.30	4.31 ^s			
				331(s)	3.94	3.93 ^s		3.92	
111(s)	3.67(s)	3.68		422(s)	3.51	3.50 ^s			
				333/511(s)	3.31	3.30 ^{&}		3.33 ^{&}	
				440(w)	3.04				
				531(s)	2.91	2.90		2.94	
				620(w)	2.72				
				533(w)	2.62				
220(s)	2.24(s)	2.24		731(w)	2.24	2.21 ^s		2.21 ^s	
				733(w)	2.02	2.02 ^s			
				822/660(s)	2.02	2.03 ^{&}		2.03 ^{&}	
				555/751(w)	1.98				
311(s)	1.91(s)	1.96				1.92 ^s		1.92 ^s	
331(s)	1.45(s)	1.47							
422(s)	1.29(s)	1.29							

^aCalculated d values (Å) are obtained using $a = 6.35$ Å for ice Ic and 17.21 Å for THF CH. The symbols & and \$ represent the composite broad peak having a peak center at the d value shown and the peak that combines with a broad peak; s represents strong peak intensity; and w represents weak peak intensity.

RHEED images of as-deposited water ice on HOPG and after its annealing to 140 K. Amorphous solid water (ASW) of approximately 120 nm thickness was accumulated on the HOPG surface by vapor deposition of water under UHV conditions, as shown in Figure 1e. Diffuse scattering with broad ring-like features at 105 K (Figure 1a) indicates low-density ASW with only a short-range order for the as-deposited ice. After annealing to 140 K, sharper Debye–Scherrer rings emerge in the electron diffraction pattern, which indicates the crystallization of ASW into a randomly oriented polycrystalline specimen around 140 K (Figure 1a). This ring pattern is unchanged until the desorption of ice. Figure 1b presents a comparison between the experimental radially averaged electron diffraction intensity curves as a function of momentum transfer, $s = (4\pi/\lambda)\sin(\theta/2)$, where θ is the total angle of scattering, and the calculated XRD spectrum for ice Ic. The observed positions of the (111), (220), (311), (331), and (442) electron diffraction peaks of ice Ic match well with the calculated values, indicating the formation of ice Ic with a lattice constant of $a = 6.35$ Å.^{23,34,42} The large diffraction width is the result of a finite crystallite size of a few nanometers on average, estimated according to the Scherrer formula.²³

To create THF CH, THF–water mixed vapor was co-deposited on the HOPG substrate at 105 K and then annealed to higher temperatures (panels c and f of Figure 1). At 105 K (Figure 1c), the observation of electron diffraction spots and diffuse ring patterns suggests the formation of crystalline THF in ASW. This may be understood because vapor deposition of pure THF on HOPG at 105 K results in a RHEED pattern of clear electron diffraction spots without rings, which signifies an ordered crystalline phase with respect to the supporting surface (Figure S1 of the Supporting Information). Additionally, the RAIRS study showed that THF undergoes a phase transition from an amorphous assembly to a crystalline phase near 90 K (Figure S2 of the Supporting Information). Upon thermal

annealing of the ice mixture to 140 K, the initial electron diffraction spots disappear and new Debye–Scherrer rings emerge, which are substantially different from those of ice Ic (panels b and d of Figure 1). Concurrently, during the thermal annealing process, an increase in the chamber pressure was noted, indicating the partial desorption of THF from the water ice matrix, as evidenced by the gradual disappearance of the electron diffraction spots (Figure S3 of the Supporting Information). The loss of THF from the ice matrix during annealing was again confirmed by the RAIRS study (Figure 4). This desorption as a result of increased mobility likely facilitates intermolecular motions of THF, leading to the formation of THF CH.

Radially averaged electron diffraction intensities were calculated from the RHEED image of Figure 1b at 140 K and were compared to the calculated diffraction peaks for sII THF CH.³¹ Agreement of the positions of high-intensity peaks is satisfactory, which signifies the presence of sII THF CH with a cubic lattice of $a = 17.2$ Å.^{35,43} The relatively smaller peaks corresponding to the (220) and (311) diffractions of ice Ic were noted (marked by # in Figure 1d), suggesting a minor fraction of ice Ic within the thin film. For clarity, a comparison of the observed and calculated interplanar distances of ice Ic and THF CH is provided in Table 1. The possible presence of ice Ih contributing to the stacking disorder was also considered, and a comparison of the calculated diffraction patterns of ice Ic, ice Ih, and THF CH against the experimental electron diffraction of THF CH is provided in Figure S4 of the Supporting Information. Although stacking faults are present, their occurrence is expected to be minimal in polycrystalline ice.

The formation of ice Ic and ice Ih significantly depends upon the substrate structure, as shown in the literature,^{19,20} but the emergence of CH is independent of the substrates used for deposition. This was established by conducting the same

experiments on two other substrates: Au(111) and a SAM of 1-octadecanethiol on Au(111), a hydrophobic surface. The electron diffraction streaks seen in the top row of Figure 2

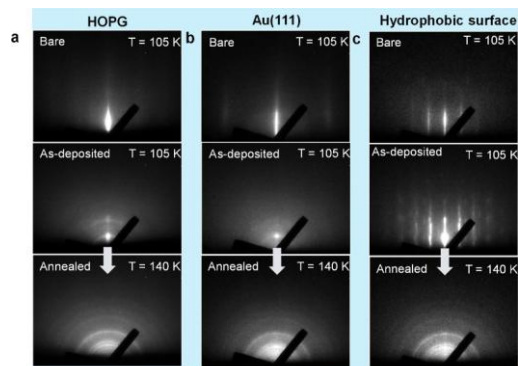


Figure 2. Evolution of THF CH on HOPG, Au(111), and the hydrophobic surface [SAM of 1-octadecanethiol on Au(111)]. The RHEED images, displayed vertically, show (a) bare HOPG, (b) Au(111), and (c) a hydrophobic surface at 105 K (top row), the as-deposited THF–water ice mixture on the respective substrate at 105 K (middle row), and the same ice mixture on the respective substrate after annealing at 140 K (bottom row).

correspond to the ordered ring structures of the bare surfaces.⁴⁴ Evidently, the same ring pattern was obtained at 140 K (bottom row of Figure 2), indicating CH formation on these substrates, even though the initial thin-film structures may exhibit differences (middle row of Figure 2). This confirmed that, regardless of the interface, THF and water formed CH around 140 K.

To examine the preference of CH formation under UHV conditions, we conducted experiments with DIOX, another guest for stable CHs. To create DIOX CH, a mixed vapor of DIOX–water was deposited on the Au(111) substrate at 105 K and annealed to 140 K. At 105 K, the diffused RHEED pattern seen from the as-deposited mixture of DIOX and water molecules indicates the largely amorphous nature of the ice mixture. The electron diffraction spots suggest the formation of DIOX crystallites, as noted in Figure 1c. After annealing to 140 K, the same Debye–Scherrer rings appeared as in the case of THF CH (Figure 3a). The experimental and calculated Bragg diffractions and their corresponding interplanar distances are compared in Table 1. Here, it is worth noting that the experimentally obtained electron diffraction pattern of DIOX CH is compared to the calculated XRD pattern of THF CH due to the unavailability of the crystallographic information file (CIF) for DIOX CH. DIOX is known to form sII CH under high-pressure conditions and has a lattice constant similar to that of THF,⁴³ with comparable van der Waals radii (THF, 2.95 Å; DIOX, 2.8 Å).⁴⁵ XRD patterns of CHs formed by different molecules are comparable if they adopt the same hydrate structure.³ This comparability has been utilized in selected area electron diffraction studies of methanol CH, with ethanol and THF, as they all form sII CH.¹⁴ In our study, we note that the positions of the (331), (333)/(511), (531), and (822) electron diffractions match well with the calculated peaks of sII THF CH. Additionally, the formation of a minor fraction of ice Ic was confirmed by the presence of the (220) and (311) intensities (Figure 3b). These electron diffraction results confirm the successful formation of sII CH of DIOX at 140 K in UHV.

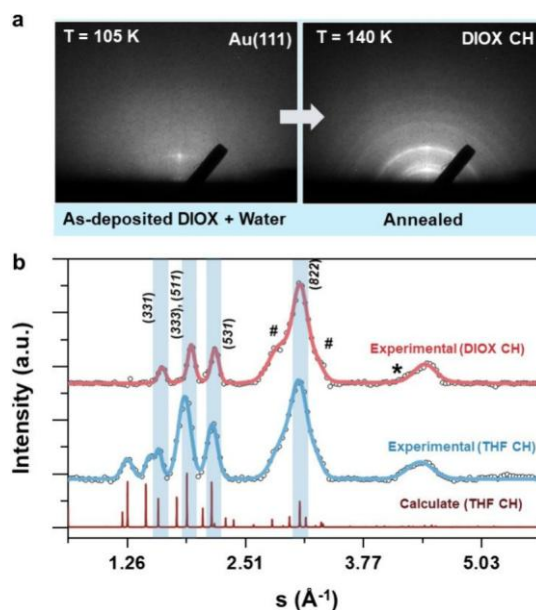


Figure 3. CH formation of DIOX was studied using RHEED. (a) Diffraction images of as-deposited water on the DIOX substrate at 105 K and after annealing to 140 K. (b) Experimental radially averaged diffraction pattern of annealed DIOX–water ice and that of annealed THF–water ice, both at 140 K, compared to the calculated diffraction pattern of sII THF CH. Peaks labeled with # are attributed to ice Ic, while that marked with * corresponds to the collection of low-intensity signals of DIOX CH, shown in theoretical THF CH.

The formation of CHs of THF and DIOX was further investigated using RAIRES. To form the CH, vapors of THF and water were co-deposited on a Ru(0001) substrate at 105 K and annealed to 140 K with a ramping rate of 2 K/min. Figure 4a shows the RAIRES spectra of the THF–water ice mixture at 105 and 140 K in the C–O antisymmetric stretching region of THF. The RAIRES spectrum at 105 K shows three peaks at 1053, 1032, and 1013 cm^{-1} and a weak broad peak around 1069 cm^{-1} , which are attributed to different fractions of THF trapped in ASW, with different hydrogen-bonding structures of the ice matrix. After annealing to 140 K, a new peak emerges at 1074 cm^{-1} , which is attributed to THF trapped in the large cage ($5^{12}6^4$) of sII CH. From the RAIRES spectrum, it is evident that there is some uncaged THF remaining in the matrix at 140 K. The decrease in the band area of the RAIRES spectra after annealing indicates the loss of THF due to its desorption. Analysis of the band areas revealed that only 17.4% of the total deposited THF forms CH, while 16.5% remains uncaged in the ice matrix, and 66.1% desorbs. In Figure 4c, the temperature-dependent evolution of the THF CH is shown. THF CH formation started around 130 K, and the fraction kept on increasing until 150 K.

For the formation of DIOX CH, DIOX and water vapors were co-deposited on the Ru(0001) substrate at 105 K and annealed to 140 K. Figure 4b shows the RAIRES spectra of the DIOX–water ice mixture at 105 and 140 K in the C–O ring stretching region. At 105 K, the peak at 1027 cm^{-1} indicates amorphous DIOX, trapped in ASW; the same peak was compared to pure amorphous DIOX (Figure S5 of the Supporting Information). Upon annealing to 140 K, a new peak emerged at 1036 cm^{-1} (Figure 4b), indicating the formation of DIOX CH, where DIOX molecules were trapped in the $5^{12}6^4$ cages of the sII hydrate structure. Simultaneously,

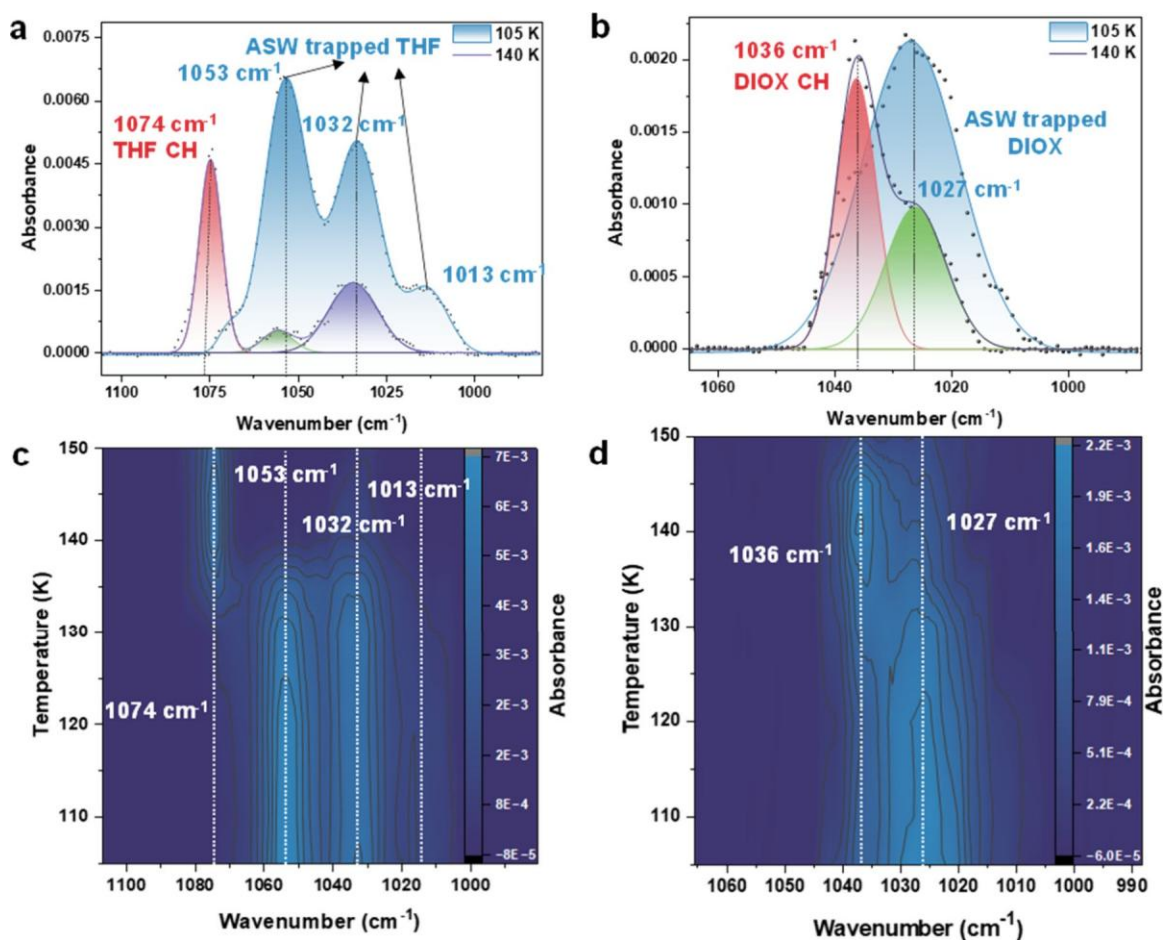


Figure 4. CH formation of THF and DIOX studied by RAIR spectroscopy. (a) RAIR spectra of the THF–water ice mixture in the C–O antisymmetric stretching region of THF at 105 and 140 K, respectively. At 140 K, the RAIR spectrum is deconvoluted into three components, highlighted in red (1074 cm^{-1}), green (1053 cm^{-1}), and violet (1032 cm^{-1}) colors. (b) RAIR spectra of the DIOX–water ice mixture in the C–O ring stretching region of DIOX at 105 and 140 K, respectively. At 140 K, the RAIR spectrum is deconvoluted into two components, highlighted in red (1036 cm^{-1}) and green (1027 cm^{-1}) colors. Temperature-dependent evolution of different peaks in the (c) C–O antisymmetric stretching region of THF in the THF–water ice mixture and (d) C–O ring stretch stretching region of DIOX in the DIOX–water ice mixture.

there was a notable decrease in the peak intensity at 1027 cm^{-1} , corresponding to trapped DIOX in the ice matrix. The observed blue shift in the peak position is attributed to the interaction between DIOX molecules and the host hydrate cages, reflecting a change in the molecular environment. Deconvolution of the RAIR spectrum at 140 K revealed that 35% of DIOX forms CH, while 28% remains uncaged within the ice matrix from the total deposited DIOX molecules. In Figure 4d, the temperature-dependent evolution of DIOX CH is shown, where DIOX CH started growing at 130 K. The electron diffraction data (Figures 1 and 3) showed the formation of sII CH of THF and DIOX. The infrared (IR) results provide evidence for the formation of 5¹²⁶⁴ cages of sII. We note that, while RHEED provides structural details of the topmost monolayers, RAIRS offers information about the entire thin film of ice. From the above results, it is evident that CH formation is facile in a nanometer-thin amorphous ice mixture in UHV conditions at a suitable temperature where the intermolecular mobility is high. The formation of CHs on different substrates proved that the structure of the interface did not significantly affect the nucleation of CHs.

The nucleation of CHs in amorphous solids can be classified as homogeneous nucleation due to the absence of any observable surface effects.⁵ Under high-pressure conditions,

two intermediate pathways are predicted for CH nucleation, theoretically.⁴⁶ One pathway follows the crystalline critical nucleus, while the other involves an amorphous critical nucleus as an intermediate step before transitioning into crystalline CH. Specifically, in the case of amorphous critical nucleation, a metastable amorphous CH is initially formed, which requires an additional activation barrier to convert into its crystalline form.^{5,46–48} In our system, starting with an amorphous mixture of water and guest molecules, the formation of a critical amorphous nucleus may be favored, which, with an increase in the temperature, results in the crystallization of CHs. Our previous study demonstrated that, at 120 K, the majority of THF forms CHs after a 110 h incubation period, which is significantly reduced to 6 h at 135 K; however, the current RHEED results indicate that, at 140 K, CH formation occurs rapidly, with a minimal time required for nucleation. The activation energy for this process was found to be 23.12 kJ mol^{-1} , lower than that required for the crystallization of ASW.⁸ On the basis of these findings, we propose that CH formation under UHV conditions likely follows the amorphous critical nucleation pathway. In this scenario, some molecules forming metastable amorphous CHs may fail to crystallize and will subsequently decompose into either ice Ic or ice Ih.^{9,10,13} To validate this suggestion, nucleation at the molecular level may

be examined using cryo-electron microscopy, and we will be pursuing this in the future.

The data presented in this study confirmed the formation of CHs under UHV conditions under cryogenic temperatures, as evidenced by RAIRS and RHEED data. Both THF and DIOX demonstrated the formation of CHs upon gradual thermal annealing around 140 K, where the intermolecular motion of water becomes possible. The RHEED data were compared to the available XRD data. This CH formation was shown to be substrate-independent, as similar results were obtained on HOPG, Au(111), and a hydrophobic SAM substrate. While this study specifically focuses on two guest molecules, a direct comparison of electron diffraction data with IR spectra of several CHs would expand the scope of this research, facilitating the study of diverse molecular interactions in cryogenic conditions. The confirmation of CH formation by electron diffraction and spectroscopy on different substrates may offer additional support for their existence in space.

ASSOCIATED CONTENT

Supporting Information

The Supporting Information is available free of charge at <https://pubs.acs.org/doi/10.1021/acs.jpcllett.4c03106>.

Experimental section, RHEED images of pure THF, electron diffraction spectra, and RAIRS of pure THF and DIOX (PDF)

AUTHOR INFORMATION

Corresponding Authors

Ding-Shyue Yang – Department of Chemistry, University of Houston, Houston, Texas 77204, United States; orcid.org/0000-0003-2713-9128; Email: yang@uh.edu
Thalappil Pradeep – DST Unit of Nanoscience (DST UNS) and Thematic Unit of Excellence (TUE), Department of Chemistry, Indian Institute of Technology Madras, Chennai 600036, India; International Centre for Clean Water, Chennai 600113, India; orcid.org/0000-0003-3174-534X; Email: pradeep@iitm.ac.in

Author

Bijesh K. Malla – DST Unit of Nanoscience (DST UNS) and Thematic Unit of Excellence (TUE), Department of Chemistry, Indian Institute of Technology Madras, Chennai 600036, India

Complete contact information is available at: <https://pubs.acs.org/10.1021/acs.jpcllett.4c03106>

Author Contributions

Thalappil Pradeep, Ding-Shyue Yang, and Bijesh K. Malla designed the research. Ding-Shyue Yang and Bijesh K. Malla have performed the experiments and analyzed the results. Thalappil Pradeep and Ding-Shyue Yang supervised the progress. The manuscript was prepared with contributions from all authors.

Notes

The authors declare no competing financial interest.

ACKNOWLEDGMENTS

The authors acknowledge the Science and Engineering Research Board (SERB), Department of Science and Technology (DST), and Government of India for research funding. Thalappil Pradeep acknowledges funding from the

Centre of Excellence on Molecular Materials and Functions under the Institution of Eminence Scheme of Indian Institute of Technology (IIT) Madras. Ding-Shyue Yang acknowledges the support of the National Science Foundation (CHE-2154363). Bijesh K. Malla thanks the Council of Scientific and Industrial Research (CSIR) for his research fellowship. Bijesh K. Malla was a recipient of the International Immersion Experience (IIE) travel fellowship of IIT Madras.

REFERENCES

- (1) Ghosh, J.; Vishwakarma, G.; Kumar, R.; Pradeep, T. Formation and Transformation of Clathrate Hydrates under Interstellar Conditions. *Acc. Chem. Res.* 2023, 56 (16), 2241–2252.
- (2) Sloan, E. D., Jr.; Koh, C. A. Introduction: Clathrate Hydrates of Natural Gases. *Clathrate Hydrates of Natural Gases*; CRC Press: Boca Raton, FL, 2008; pp I–XXV.
- (3) Sloan, E. D., Jr.; Koh, C. A. *Clathrate Hydrates of Natural Gases*; CRC Press: Boca Raton, FL, 2007; DOI: 10.1201/9781420008494.
- (4) Chong, Z. R.; Yang, S. H. B.; Babu, P.; Linga, P.; Li, X.-S. Review of Natural Gas Hydrates as an Energy Resource: Prospects and Challenges. *Appl. Energy* 2016, 162, 1633–1652.
- (5) Khurana, M.; Yin, Z.; Linga, P. A Review of Clathrate Hydrate Nucleation. *ACS Sustainable Chem. Eng.* 2017, 5 (12), 11176–11203.
- (6) Ghosh, J.; Methikkalam, R. R. J.; Bhuin, R. G.; Ragupathy, G.; Choudhary, N.; Kumar, R.; Pradeep, T. Clathrate Hydrates in Interstellar Environment. *Proc. Natl. Acad. Sci. U. S. A.* 2019, 116 (5), 1526–1531.
- (7) Malla, B. K.; Vishwakarma, G.; Chowdhury, S.; Selvarajan, P.; Pradeep, T. Formation of Ethane Clathrate Hydrate in Ultrahigh Vacuum by Thermal Annealing. *J. Phys. Chem. C* 2022, 126 (42), 17983–17989.
- (8) Ghosh, J.; Vishwakarma, G.; Das, S.; Pradeep, T. Facile Crystallization of Ice Ih via Formaldehyde Hydrate in Ultrahigh Vacuum under Cryogenic Conditions. *J. Phys. Chem. C* 2021, 125 (8), 4532–4539.
- (9) Ghosh, J.; Bhuin, R. G.; Vishwakarma, G.; Pradeep, T. Formation of Cubic Ice via Clathrate Hydrate, Prepared in Ultrahigh Vacuum under Cryogenic Conditions. *J. Phys. Chem. Lett.* 2020, 11 (1), 26–32.
- (10) Vishwakarma, G.; Malla, B. K.; Chowdhury, S.; Khandare, S. P.; Pradeep, T. Existence of Acetaldehyde Clathrate Hydrate and Its Dissociation Leading to Cubic Ice under Ultrahigh Vacuum and Cryogenic Conditions. *J. Phys. Chem. Lett.* 2023, 14, 5328–5334.
- (11) Ghosh, J.; Bhuin, R. G.; Ragupathy, G.; Pradeep, T. Spontaneous Formation of Tetrahydrofuran Hydrate in Ultrahigh Vacuum. *J. Phys. Chem. C* 2019, 123 (26), 16300–16307.
- (12) Vishwakarma, G.; Malla, B. K.; Reddy, K. S. S. V. P.; Ghosh, J.; Chowdhury, S.; Yamijala, S. S. R. K. C.; Reddy, S. K.; Kumar, R.; Pradeep, T. Induced Migration of CO₂ from Hydrate Cages to Amorphous Solid Water under Ultrahigh Vacuum and Cryogenic Conditions. *J. Phys. Chem. Lett.* 2023, 14, 2823–2829.
- (13) Malla, B. K.; Vishwakarma, G.; Chowdhury, S.; Nayak, S. K.; Yamijala, S. S. R. K. C.; Pradeep, T. Formation and Dissociation of Dimethyl Ether Clathrate Hydrate in Interstellar Ice Mimics. *J. Phys. Chem. C* 2024, 128 (6), 2463–2470.
- (14) Blake, D.; Allamandola, L.; Sandford, S.; Hudgins, D.; Freund, F. Clathrate Hydrate Formation in Amorphous Cometary Ice Analogs in Vacuo. *Science* 1991, 254 (5031), 548–551.
- (15) Fleyfel, F.; Devlin, J. P. Carbon Dioxide Clathrate Hydrate Epitaxial Growth: Spectroscopic Evidence for Formation of the Simple Type-II CO₂ Hydrate. *J. Phys. Chem.* 1991, 95 (9), 3811–3815.
- (16) Ramakrishnan, S.; Sagi, R.; Mahapatra, N.; Asscher, M. Effect of Coadsorbed Oxygen on the Photochemistry of Methane Embedded in Amorphous Solid Water. *J. Phys. Chem. C* 2018, 122 (27), 15287–15296.

- (17) Ayoub, Y.; Asscher, M. Interaction of Ethyl Chloride with Amorphous Solid Water Thin Film on Ru(001) and O/Ru(001) Surfaces. *J. Phys. Chem. A* 2009, *113* (26), 7514–7520.
- (18) Horowitz, Y.; Asscher, M. Electron-Induced Chemistry of Methyl Chloride Caged within Amorphous Solid Water. *J. Chem. Phys.* 2013, *139* (15), No. 154707.
- (19) Souda, R.; Aizawa, T. Reflection High Energy Electron Diffraction (RHEED) Study of Ice Nucleation and Growth on Ni(111): Influences of Adspecies and Electron Irradiation. *Phys. Chem. Chem. Phys.* 2019, *21* (35), 19585–19593.
- (20) Souda, R.; Aizawa, T.; Sugiyama, N.; Takeguchi, M. Structure Analysis of Water Ice Crystallites on NaCl(001), KCl(001), and CaF₂(111) by Reflection High-Energy Electron Diffraction. *J. Phys. Chem. C* 2020, *124* (28), 15180–15187.
- (21) Yang, D. S.; Zewail, A. H. Ordered Water Structure at Hydrophobic Graphite Interfaces Observed by 4D, Ultrafast Electron Crystallography. *Proc. Natl. Acad. Sci. U. S. A.* 2009, *106* (11), 4122–4126.
- (22) Minissale, M.; Aikawa, Y.; Bergin, E.; Bertin, M.; Brown, W. A.; Cazaux, S.; Charnley, S. B.; Coutens, A.; Cuppen, H. M.; Guzman, V.; Linnartz, H.; McCoustra, M. R. S.; Rimola, A.; Schrauwen, J. G. M.; Toubin, C.; Ugliengo, P.; Watanabe, N.; Wakelam, V.; Dulieu, F. Thermal Desorption of Interstellar Ices: A Review on the Controlling Parameters and Their Implications from Snowlines to Chemical Complexity. *ACS Earth Space Chem.* 2022, *6* (3), 597–630.
- (23) Yang, D.-S.; He, X. Structures and Ultrafast Dynamics of Interfacial Water Assemblies on Smooth Hydrophobic Surfaces. *Chem. Phys. Lett.* 2017, *683*, 625–632.
- (24) He, X.; Wu, C.; Rajagopal, K.; Punpongjareorn, N.; Yang, D. S. Ordered Ionic Liquid Structure Observed at Terraced Graphite Interfaces. *Phys. Chem. Chem. Phys.* 2016, *18* (5), 3392–3396.
- (25) Wu, C.; Yang, D. S. Ordered Structures and Morphology-Induced Phase Transitions at Graphite-Acetonitrile Interfaces. *J. Phys. Chem. C* 2019, *123* (36), 22390–22396.
- (26) He, X.; Wu, C.; Yang, D.-S. Communication: No Guidance Needed: Ordered Structures and Transformations of Thin Methanol Ice on Hydrophobic Surfaces. *J. Chem. Phys.* 2016, *145* (17), 171102.
- (27) He, X.; Yang, D. S. Order-Determined Structural and Energy Transport Dynamics in Solid-Supported Interfacial Methanol. *Nano Lett.* 2021, *21* (3), 1440–1445.
- (28) He, X.; Yang, D. S. Ethanol on Graphite: Ordered Structures and Delicate Balance of Interfacial and Intermolecular Forces. *J. Phys. Chem. C* 2021, *125* (43), 24145–24154.
- (29) Snyder, L. E.; Buhl, D.; Schwartz, P. R.; Clark, F. O.; Johnson, D. R.; Lovas, F. J.; Giguere, P. T. Radio Detection of Interstellar Dimethyl Ether. *Astrophys. J.* 1974, *191*, L79.
- (30) McGuire, B. A.; Carroll, P. B.; Loomis, R. A.; Finneran, I. A.; Jewell, P. R.; Remijan, A. J.; Blake, G. A. Detection of Interstellar Ethylene Oxide (c-C₂H₄O). *Science* 2016, *352* (6292), 1449–1452.
- (31) McGuire, B. A.; Carroll, P. B.; Loomis, R. A.; Finneran, I. A.; Jewell, P. R.; Remijan, A. J.; Blake, G. A. Discovery of the Interstellar Chiral Molecule Propylene Oxide (CH₃CHCH₂O). *Science* 2016, *352* (6292), 1449–1452.
- (32) Cyriac, J.; Pradeep, T.; Kang, H.; Souda, R.; Cooks, R. G. Low-Energy Ionic Collisions at Molecular Solids. *Chem. Rev.* 2012, *112* (10), 5356–5411.
- (33) Kang, H. Chemistry of Ice Surfaces. Elementary Reaction Steps on Ice Studied by Reactive Ion Scattering. *Acc. Chem. Res.* 2005, *38* (12), 893–900.
- (34) Jenniskens, P.; Blake, D. F. Structural Transitions in Amorphous Water Ice and Astrophysical Implications. *Science* 1994, *265* (5173), 753–756.
- (35) Dobrzycki, L.; Taraszewska, P.; Boese, R.; Cyrański, M. K. Pyrrolidine and Its Hydrates in the Solid State. *Cryst. Growth Des.* 2015, *15* (10), 4804–4812.
- (36) Dowell, L. G.; Rinfret, A. P. Low-Temperature Forms of Ice as Studied by X-Ray Diffraction. *Nature* 1960, *188* (4757), 1144–1148.
- (37) Momma, K.; Izumi, F. VESTA 3 for Three-Dimensional Visualization of Crystal, Volumetric and Morphology Data. *J. Appl. Crystallogr.* 2011, *44* (6), 1272–1276.
- (38) Huang, X.; Wang, L.; Liu, K.; Liao, L.; Sun, H.; Wang, J.; Tian, X.; Xu, Z.; Wang, W.; Liu, L.; Jiang, Y.; Chen, J.; Wang, E.; Bai, X. Tracking Cubic Ice at Molecular Resolution. *Nature* 2023, *617* (7959), 86–91.
- (39) Lee, M.; Lee, S. Y.; Kang, M.-H.; Won, T. K.; Kang, S.; Kim, J.; Park, J.; Ahn, D. J. Observing Growth and Interfacial Dynamics of Nanocrystalline Ice in Thin Amorphous Ice Films. *Nat. Commun.* 2024, *15* (1), 908.
- (40) Hong, J.; Tian, Y.; Liang, T.; Liu, X.; Song, Y.; Guan, D.; Yan, Z.; Guo, J.; Tang, B.; Cao, D.; Guo, J.; Chen, J.; Pan, D.; Xu, L. M.; Wang, E. G.; Jiang, Y. Imaging Surface Structure and Premelting of Ice Ih with Atomic Resolution. *Nature* 2024, *630* (8016), 375–380.
- (41) Park, J. S.; Noh, N.; Park, J.; Shim, Y.; Park, S.; Qureshi, Y.; Kang, S.; Huh, Y.; Lee, C.-W.; Yuk, J. M. Phase Transition of Cubic Ice to Hexagonal Ice during Growth and Decomposition. *Nano Lett.* 2024, *24* (37), 11504–11511.
- (42) Dowell, L. G.; Rinfret, A. P. Low-Temperature Forms of Ice as Studied by X-Ray Diffraction. *Nature* 1960, *188* (4757), 1144–1148.
- (43) Sargent, D. F.; Calvert, L. D. Crystallographic Data for Some New Type II Clathrate Hydrates. *J. Phys. Chem.* 1966, *70* (8), 2689–2691.
- (44) Ghosh, M.; Yang, D.-S. Structures of Self-Assembled n-Alkanethiols on Gold by Reflection High-Energy Electron Diffraction. *Phys. Chem. Chem. Phys.* 2020, *22* (30), 17325–17335.
- (45) Andersson, O.; Brant Carvalho, P. H.; Haussermann, U.; Hsu, Y.-J. Evidence Suggesting Kinetic Unfreezing of Water Mobility in Two Distinct Processes in Pressure-Amorphized Clathrate Hydrates. *Phys. Chem. Chem. Phys.* 2022, *24* (34), 20064–20072.
- (46) Guo, G.-J.; Zhang, Z. Open Questions on Methane Hydrate Nucleation. *Commun. Chem.* 2021, *4* (1), 1–3.
- (47) Li, L.; Zhong, J.; Yan, Y.; Zhang, J.; Xu, J.; Francisco, J. S.; Zeng, X. C. Unraveling Nucleation Pathway in Methane Clathrate Formation. *Proc. Natl. Acad. Sci. U. S. A.* 2020, *117* (40), 24701–24708.
- (48) Jacobson, L. C.; Hujo, W.; Molinero, V. Amorphous Precursors in the Nucleation of Clathrate Hydrates. *J. Am. Chem. Soc.* 2010, *132* (33), 11806–11811.

Supporting Information

Growth of Clathrate Hydrates in Nanoscale Ice Films Observed Using Electron Diffraction and Infrared Spectroscopy

Bijesh K. Malla¹, Ding-Shyue Yang^{2}, and Thalappil Pradeep^{1,3*}*

¹DST Unit of Nanoscience (DST UNS) and Thematic Unit of Excellence (TUE), Department of Chemistry, Indian Institute of Technology Madras, Chennai 600036, India.

² Department of Chemistry, University of Houston, Houston, Texas 77204, USA.

³International Centre for Clean Water, IIT Madras Research Park, Chennai 600113, India.

Corresponding authors

*Email: yang@uh.edu, pradeep@iitm.ac.in

This Pdf includes

Experimental Section-S2- S4

RHEED images – S5, S7

Diffraction pattern- S8

RAIR spectra – S6, S9

References – S10

Experimental Section

RHEED Setup

Details of the home-built UHV chamber system and the procedures for thin-film deposition and RHEED experiments have been described previously.¹⁻³ In this study, anhydrous THF ($\geq 99.9\%$, inhibitor-free) and anhydrous DIOX (99.8%) were purchased from Sigma Aldrich and used without further purification. The pure compounds were loaded separately into a stainless-steel reservoir and then quickly connected to the effusion-type doser assembly, followed by several freeze-pump-thaw cycles to ensure the purity of the molecular sources. The UHV chamber for molecular depositions, annealing, and RHEED measurements had a base pressure of $< 3 \times 10^{-10}$ mbar. The sample holder was coupled to a cryostat with an integrated heater. Using liquid nitrogen as the cryogen, the substrate reached ~ 100 K, whose temperature was directly measured by a K-type thermocouple at the surface. The deposition rate of immobilized molecules was a few nm/min at this low temperature. The deposited thin films then underwent thermal annealing with a typical ramp rate of ~ 1.3 K/min. The co-deposition method used premixed THF/DIOX and water vapors with a deposition time of 10 minutes. During the deposition, it was observed that a total of 134 seconds was required for the complete disappearance of the HOPG pattern. Considering the probe depth of RHEED (1-2 nm), it can be inferred that after 134 seconds, a homogeneous thin film of approximately 5 nm was formed. Given that the total deposition time was 600 seconds, this resulted in an estimated thin ice film thickness of approximately 25 nm. The substrate surfaces used for deposition and RHEED include highly oriented pyrolytic graphite (HOPG, ZYA grade), single-crystalline Au(111) (Princeton Scientific), and a hydrophobic self-assembled monolayer (SAM) of 1-octadecanethiol on Au(111). Methods of preparation of the substrate surfaces can be found in earlier reports.³ The use of different substrates helped examine the possible effects of surface structures and affinities on the formation of CHs.

For RHEED, the kinetic energy of electron source was 30 keV, corresponding to a de Broglie wavelength of 0.07 \AA . The electron diffraction patterns were recorded by an imaging assembly consisting of a phosphor screen fiber-coupled to an image intensifier and then a CMOS camera (Andor Zyla HF). The average flux of probe electrons was maintained at an extremely low level of $< 1 \text{ pA/mm}^2$ and confirmed to have no induced changes caused by electron impact or radiation damage within the measurement time. The typical image acquisition time was 1 second per frame

during thermal annealing of the deposited thin films. Given the large electron–matter scattering cross-section, the probe depth of RHEED was only up to a few nm at the typical angle of grazing incidence of $\sim 1^\circ$. The surface sensitivity of RHEED signifies the formation of CHs at the top of a film, not within the bulk.

RAIRS Setup

All the RAIRS experiments were carried out in a custom-built ultrahigh vacuum (UHV) instrument with a base pressure of $\sim 5 \times 10^{-10}$ mbar, discussed in detail in our previous reports.^{4,5} Millipore water (H_2O of 18.2 M Ω resistivity) and THF/DIOX (purity $\geq 99.9/99.8$ %, anhydrous, Sigma Aldrich) were taken in two separate vacuum-sealed test tubes (with a glass-to-metal seal) and were further purified by several freeze-pump-thaw cycles. Water and THF/DIOX are connected to the vacuum chamber through separate sample inlet lines. The deposition of two samples is controlled through all metal leak valves. A highly polished Ru(0001) single crystal was used as the substrate for creating thin ice films. The substrate was connected to a helium cryostat (ColdEdge Technologies), providing temperature cool down to 8 K. Temperatures ranging from 8 K to 400 K were achieved using a resistive heater (25 Ω), which was regulated by a temperature controller (Lakeshore 336). The vapor deposition coverage in the case of N_2 (ion gauge sensitivity factor - 1) was expressed in ML, assuming 1.33×10^{-6} mbar s = 1 ML, which was estimated to contain $\sim 1.1 \times 10^{15}$ molecules cm^{-2} , as outlined in other reports.^{1,2} A mixed ice was prepared on Ru(0001) substrate at 105 K by backfilling THF/DIOX-water vapor for 10 min at a total pressure of 5×10^{-7} mbar where THF/DIOX and water contributed equally.³ Taking into account the ion gauge sensitivity factors for water (0.97), THF (3.29), and DIOX (3.5), 150 ML of water and 45 ML of THF/DIOX were co-deposited with a THF/DIOX-to-water ratio of 1:3.² Based on the molecular diameters, this corresponds to approximately 37 nm of water and 23 nm of THF/DIOX, resulting in a total thin ice film thickness of about 60 nm. Considering potential inaccuracies in pressure readings and variations in the sticking coefficient at different temperatures, there may be an error of few nm in the calculated thickness values.

. During vapor deposition, mass spectra were recorded simultaneously to check the purity and the ratio of the deposited molecules. RAIR spectra were collected in the 4000–550 cm^{-1} range with a spectral resolution of 2 cm^{-1} using a Bruker Vertex 70 FT-IR spectrometer with a liquid-nitrogen-

cooled mercury cadmium telluride (MCT) detector. The IR beam path outside the UHV chamber was purged with dry nitrogen gas.

Supporting Information 1

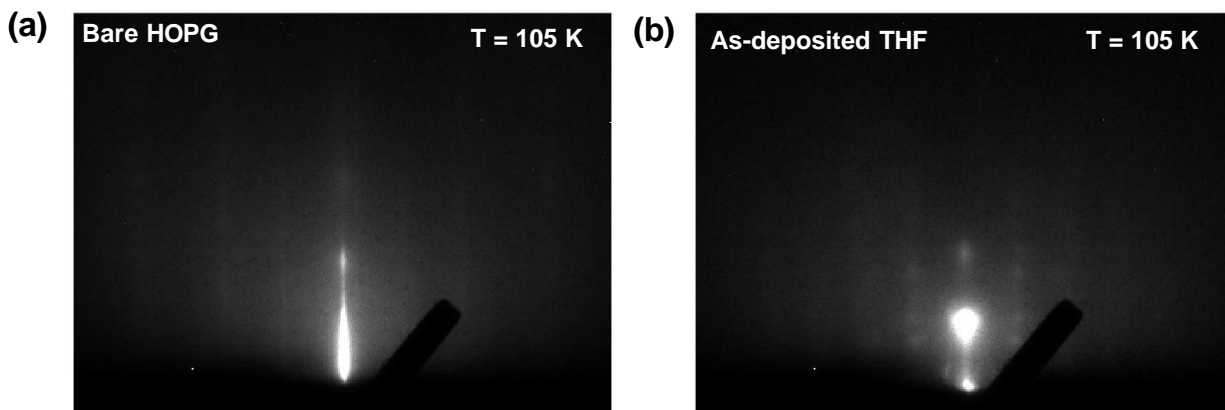


Figure S1. (a) RHEED image of bare HOPG substrate at 105 K. (b) RHEED image of as-deposited pure THF on HOPG substrate at 105 K.

Supporting Information 2

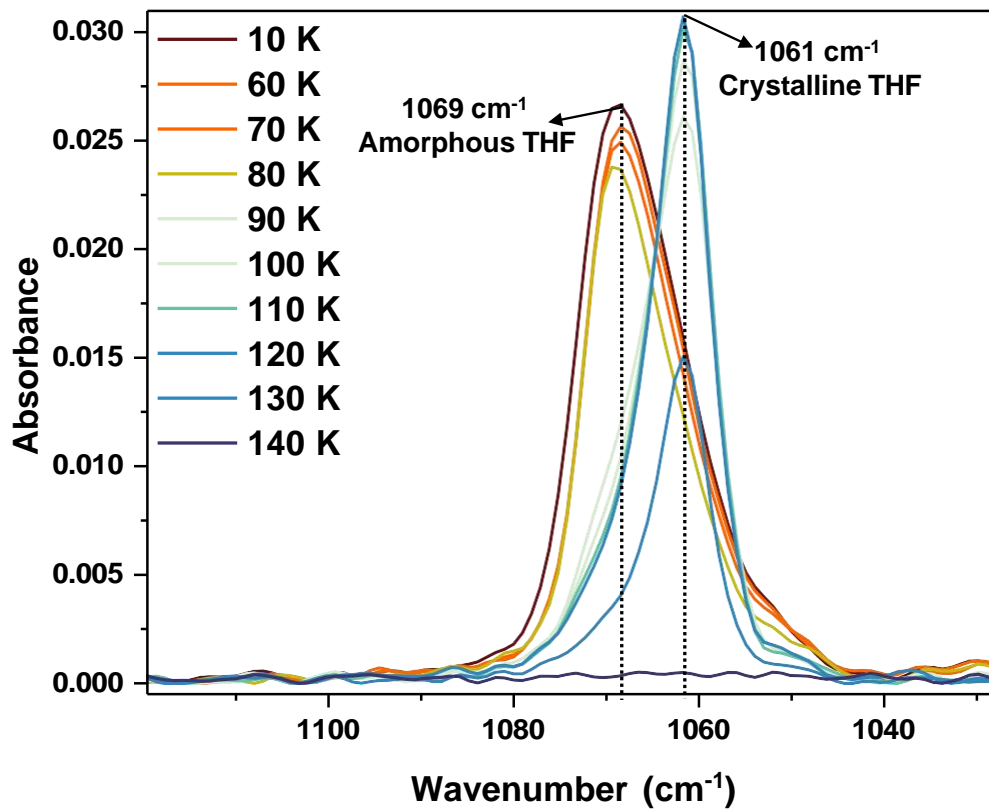


Figure S2. Temperature-dependent RAIR spectra of 150 ML of pure THF ice in C-O antisymmetric stretching region. Pure THF ice was prepared by vapor deposition on a Ru(0001) substrate at 10 K. The sample was then annealed to 140 K at a rate of 2 K/min.

Supporting Information 3

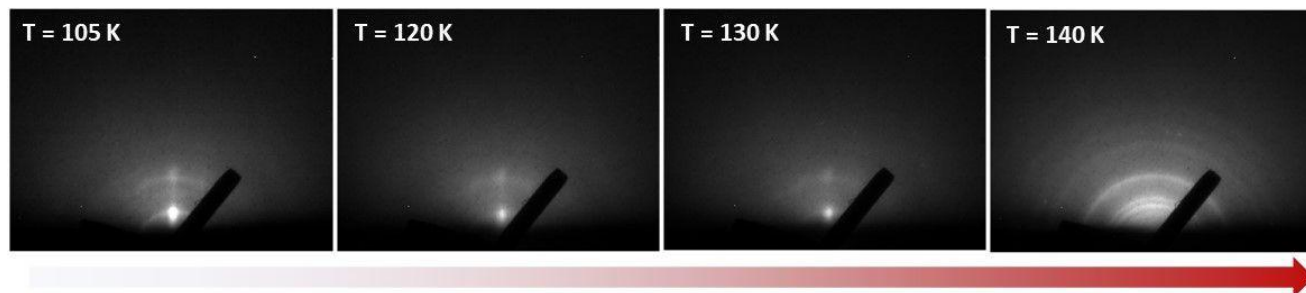


Figure S3. Temperature-dependent RHEED images of THF-water mixed vapor deposited on HOPG at 105 K, followed by thermal annealing.

Supporting Information 4

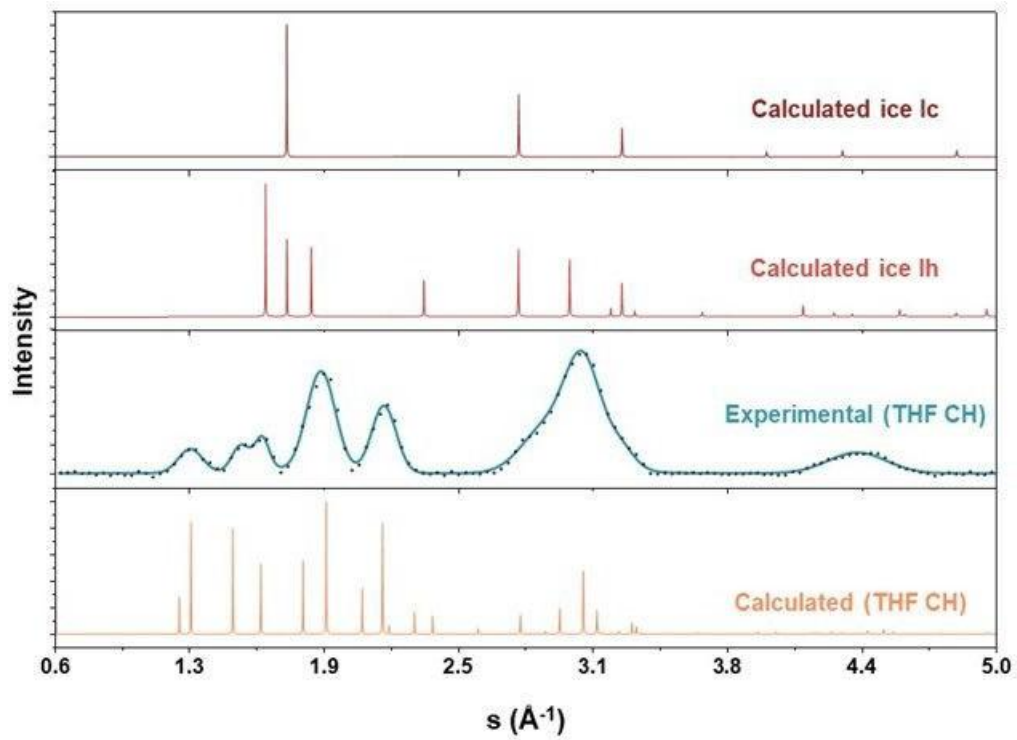


Figure S4. Comparison of the experimental radially-averaged electron diffractions of annealed THF-water ice at 140 K with the calculated diffraction peaks of sII THF CH, ice Ic, and ice Ih.

Supporting Information 5

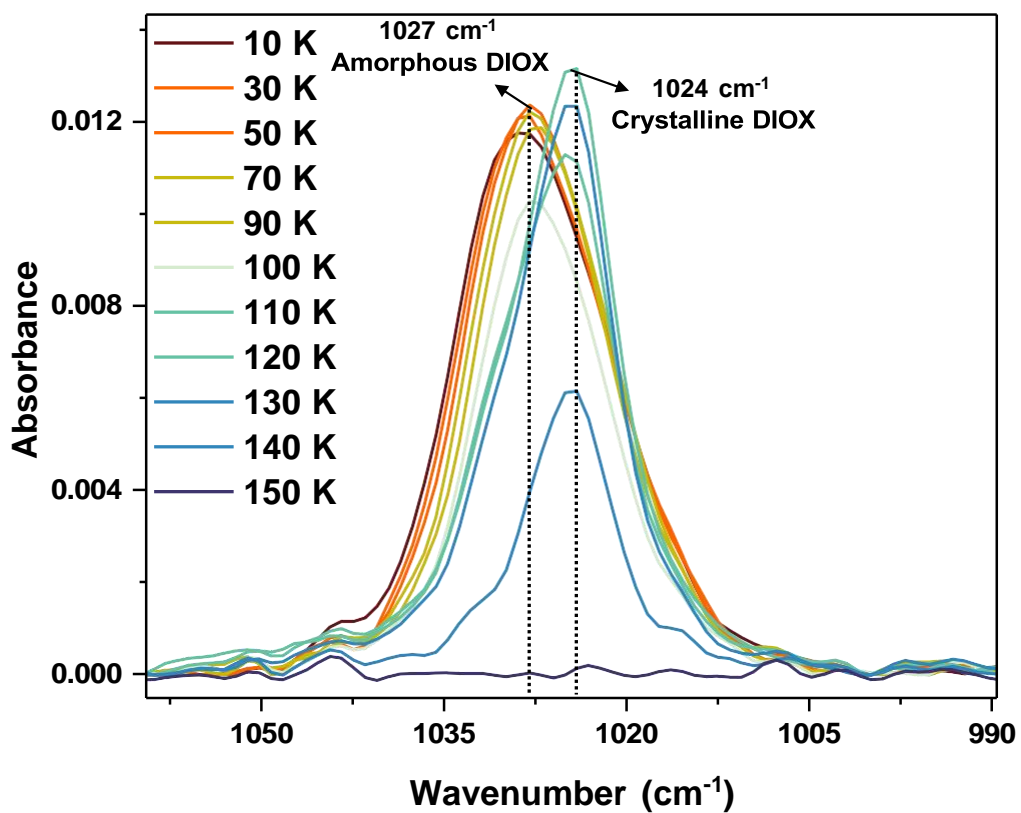


Figure S5. Temperature-dependent RAIR spectra of 150 ML of pure DIOX ice in C-O antisymmetric stretching region. Pure DIOX ice was prepared by vapor deposition on a Ru(0001) substrate at 10 K. The sample was then annealed to 140 K at a rate of 2 K/min.

References

- (1) He, X.; Wu, C.; Yang, D.-S. Communication: No Guidance Needed: Ordered Structures and Transformations of Thin Methanol Ice on Hydrophobic Surfaces. *J. Chem. Phys.* **2016**, *145* (17).
- (2) He, X.; Yang, D. S. Ethanol on Graphite: Ordered Structures and Delicate Balance of Interfacial and Intermolecular Forces. *J. Phys. Chem. C* **2021**, *125* (43), 24145–24154.
- (3) Wu, C.; Yang, D. S. Ordered Structures and Morphology-Induced Phase Transitions at Graphite-Acetonitrile Interfaces. *J. Phys. Chem. C* **2019**, *123* (36), 22390–22396.
- (4) Bag, S.; Bhuin, R. G.; Methikkalam, R. R. J.; Pradeep, T.; Kephart, L.; Walker, J.; Kuchta, K.; Martin, D.; Wei, J. Development of Ultralow Energy (1-10 eV) Ion Scattering Spectrometry Coupled with Reflection Absorption Infrared Spectroscopy and Temperature Programmed Desorption for the Investigation of Molecular Solids. *Rev. Sci. Instrum.* **2014**, *85* (1), 1–7.
- (5) Malla, B. K.; Vishwakarma, G.; Chowdhury, S.; Pradeep, T. Vacuum Ultraviolet Photolysis of Condensed Methyl Chloride in Interstellar Model Conditions and Trapping of Intermediates at Intergrain Interfaces. *J. Phys. Chem. C* **2023**, *127* (50), 24149–24157.
- (6) Lee, D. H.; Kang, H. Acid-Promoted Crystallization of Amorphous Solid Water. *J. Phys. Chem. C* **2018**, *122* (42), 24164–24170.
- (7) Bartmess, J. E.; Georgiadis, R. M. Empirical Methods for Determination of Ionization Gauge Relative Sensitivities for Different Gases. *Vacuum* **1983**, *33* (3), 149–153.
- (8) Opitz, A.; Scherge, M.; Ahmed, S. I. U.; Schaefer, J. A. A Comparative Investigation of Thickness Measurements of Ultra-Thin Water Films by Scanning Probe Techniques. *J. Appl. Phys.* **2007**, *101* (6), 64310.

Simulated Interstellar Photolysis of N₂O Ice: Selectivity in Photoproducts

Published as part of *The Journal of Physical Chemistry C special issue* “Heterogeneous Drivers of Ice Formation”.

Bijesh K. Malla, Soham Chowdhury, Devansh Paliwal, Hanoona K. M., Gaurav Vishwakarma, Rabin Rajan J. Methikkalam, and Thalappil Pradeep*



Cite This: <https://doi.org/10.1021/acs.jpcc.4c06624>



Read Online

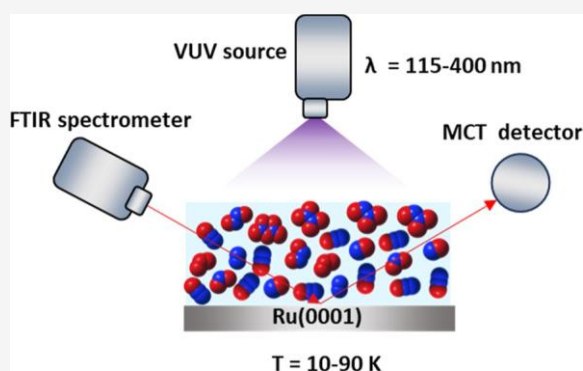
ACCESS

Metrics & More

Article Recommendations

Supporting Information

ABSTRACT: Thermal diffusion and recombination control the kinetics of photochemical reactions of reactive radicals formed by ultraviolet photon irradiation in interstellar ices. Here, we show that upon vacuum ultraviolet photolysis, N₂O ice produces O₃ and several oxides of nitrogen, such as NO, NO₂, N₂O₂, N₂O₃, N₂O₄, and N₂O₅ in interstellar ice mimics. Photoproducts within the bulk and on the surface were analyzed using reflection absorption infrared spectroscopy and Cs⁺ ion-based secondary ion mass spectrometry, while desorbed species were studied using temperature-programmed desorption mass spectrometry. Notably, thermal annealing of the photoirradiated ice to 90 K resulted in a significant increase in NO and N₂O₃. Photoirradiation at 10 K revealed the dominance of three atom photoproducts, such as NO₂ and O₃. In contrast, irradiation at 50 K significantly enhanced the production of four or higher atom photoproducts (N₂O₂, N₂O₃, N₂O₄, and N₂O₅). This behavior is attributed to the restricted diffusion of reactive radicals and unstable oxygen species (O and O₃) at 10 K, which confines radical–radical reactions to three or fewer atom photoproducts, whereas higher temperatures facilitate oxygen and other radical diffusion and recombination, yielding heavier photoproducts. These results throw light on the thermal diffusion effects on the kinetics of photoproducts in interstellar ice mimics.



INTRODUCTION

The photochemistry of the molecular ices present in the interstellar medium (ISM) plays a significant role in forming complex organic molecules.¹ More than 300 molecules, including neutrals, ions, and radicals, have been identified in

ISM.² Bigger molecules such as C₆₀, C₇₀, and polyaromatic hydrocarbons raise questions about their formation mechanisms in cold conditions.³ Molecules, dust grains, and atoms in the ISM are continuously exposed to ultraviolet (UV) photons from nearby stars and other sources, leading to photochemical reactions. These processes produce complex molecular species, including organic compounds essential to the emergence of life.⁴ Laboratory experiments involving the irradiation of molecular ices in simulated interstellar conditions with charged particles (ions and electrons) and UV photons have revealed the synthesis of amino acids and nucleobases, which is crucial for understanding the origins of biology.^{1,5,6} In such reactions, diffusion of reactive intermediates plays a critical role in determining reaction kinetics. When radicals are properly oriented, and the reaction is barrierless, it is expected to proceed efficiently. If the diffusion barriers are significantly higher than the reaction barriers, reactants are likely to remain adsorbed next to each other until the reaction occurs.^{7,8}

Although the photochemistry of various molecules has been reported in interstellar ice analogs, a crucial gap in our understanding is the diffusion behavior of different radicals within ice matrices.^{7,9–16} Specifically, how thermal and nonthermal diffusion occurs across various ices at different temperatures is not well understood.¹

N₂O was first detected in the gas phase within the molecular cloud Sgr B2(M) in 1994.¹⁷ Recently, the James Webb Space Telescope (JWST) has identified N₂O in the condensed phase within protostellar systems.¹⁸ N₂O plays a major role in the dissociation of ozone in our stratosphere.¹⁹ However, when N₂O was subjected to electron irradiation at very low temperatures (25 K), it produced ozone in the solid phase.²⁰ In the ISM, oxygen, and nitrogen are the major elements in molecular clouds and star-forming regions.^{21–23} Despite their ubiquity, only six molecules: nitrous oxide (N₂O),¹⁷ nitroxyl

Received: September 30, 2024

Revised: December 7, 2024

Accepted: December 12, 2024

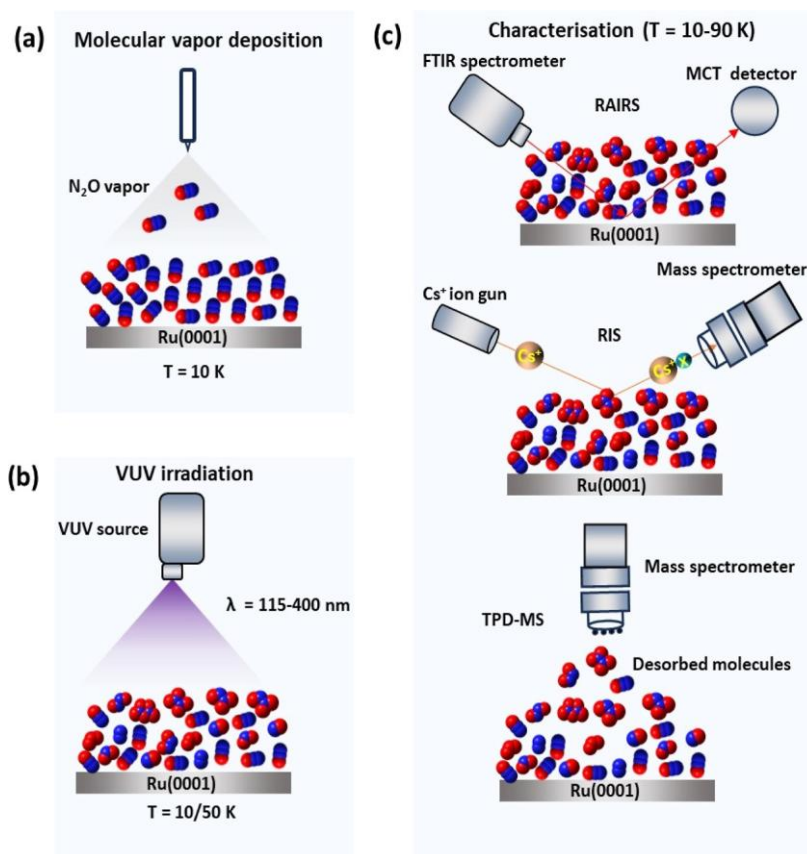


Figure 1. Schematic presentation of experimental protocols used in this study. (a) 150 ML of N_2O ice was created on Ru(0001) substrate by molecular vapor deposition at 10 K. (b) N_2O ice was irradiated with VUV photon by using deuterium lamp. (c) Photoirradiated ice was characterized by RAIRS, RIS, and TPD-MS.

(HNO),^{24,25} nitrous acid (HONO),²⁶ fulminic acid (HCNO),²⁷ nitric oxide (NO),²⁸ and hydroxylamine (NH_2OH)²⁹ containing N–O bond have been identified in the interstellar and circumstellar medium.

Under laboratory interstellar medium (ISM) conditions, Jamieson et al. investigated the formation of N_2O by irradiating N_2 and CO ice at 10 K with 5 keV electrons,³⁰ where Halfen et al. studied the gas phase formation mechanism of N_2O by radical–radical reaction.³¹ Sivaraman et al. demonstrated the formation of various N–O bond-bearing molecules by irradiating N_2O ice with 1 keV electron at 25 K.²⁰ Several studies also exist on the radiolysis of N_2O by bombarding fast ions ($^{14}N^+$),³² and ($^{136}Xe^{23+}$). No report exists on the vacuum ultraviolet (VUV) photolysis of N_2O ice in ISM-simulated conditions. Also, there is a lack of understanding of the diffusion and recombination of radicals in different thermal conditions. In our previous study,⁷ we demonstrated how nonthermal radical diffusion in highly and less ordered methyl chloride crystalline ice contributed to the formation of photoproducts. The present study focuses on the thermal diffusion of radicals in photoirradiated N_2O ice. In it, we have shown the VUV photolysis of pure N_2O ice under interstellar laboratory conditions, resulting in the formation of various N–O bearing molecules along with O_3 . Photoirradiation experiments conducted at both 10 and 50 K reveal distinct, temperature-dependent distributions of photoproducts. Higher temperatures play a crucial role in reducing the thermal diffusion barrier for oxygen allotropes and reactive radicals, facilitating further recombination with nitrous oxides to form

secondary photoproducts at higher temperatures. This suggests that varying temperature conditions could significantly influence the chemistry and composition of interstellar ices, providing valuable insights into the complex mechanisms underlying molecular evolution in space.

EXPERIMENTAL SECTION

Experimental Setup. The experiments were conducted within an ultrahigh vacuum (UHV) instrument, extensively described in our previous study.^{33–35} The instrument is equipped with various analytical techniques, including reflection absorption infrared spectroscopy (RAIRS), low energy ion scattering (LEIS), temperature-programmed desorption (TPD) mass spectrometry, Cs^+ ion-based secondary ion mass spectrometry (SIMS), and a VUV lamp. To maintain a base pressure of 5×10^{-10} mbar, six turbomolecular pumps are attached to the chambers backed by multiple oil-free diaphragm pumps. Chamber pressure is monitored using a Bayard–Alpert gauge, regulated by a Maxi Gauge vacuum gauge controller (Pfeiffer, Model TPG 256 A).

To create a thin film of ice, a finely polished Ru(0001) crystal was used as the substrate, which was attached to a copper holder. The assembly can be cooled to 8 K by connecting it to a helium cryostat (ColdEdge technology). The substrate assembly can be heated to 1000 K using a resistive heater (25 Ω), which was used to control the temperature. An accurate ± 0.5 K thermocouple sensor was used to detect the temperature of the substrate. Before each vapor deposition experiment, the substrate was repeatedly heated to a higher

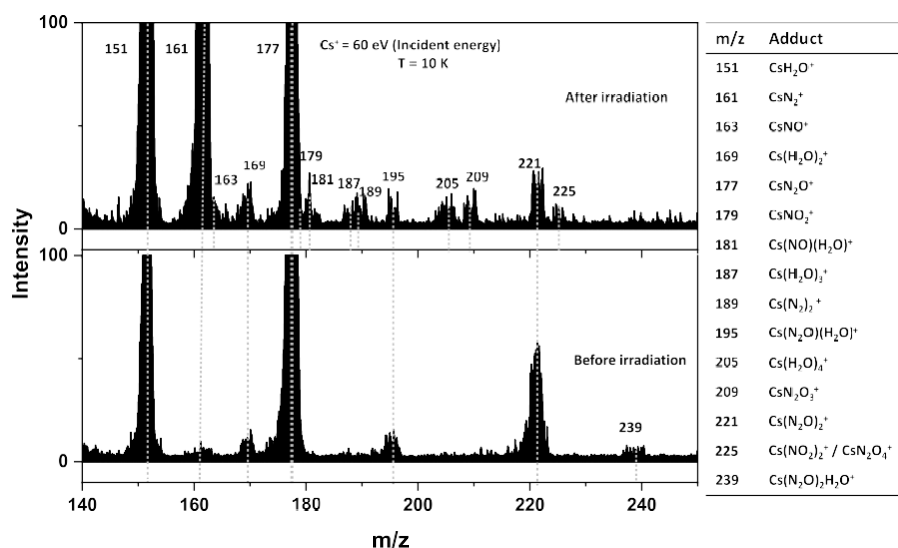
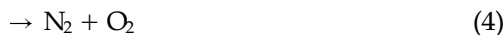


Figure 3. RIS mass spectra obtained after 60 min of VUV irradiation of amorphous N₂O ice. Mass spectrum of the irradiated ice was obtained by colliding the sample with 60 eV Cs⁺ ions at 10 K. All the RIS photoproducts have been assigned, as listed in the table on the right.

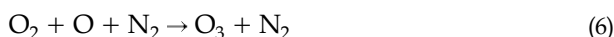
by IR spectroscopy. The dissociation of N₂O primarily follows two pathways: in the first pathway, N₂O dissociates to N₂ molecules and atomic oxygens (1), and in the second pathway, it produces NO and N radicals (2).⁴⁹ The dissociation energy of the bond N–N (4.93 eV) is higher than that of N–O (1.68 eV),⁵⁰ making the first dissociation pathway more favorable, resulting in a high concentration of N₂ and O radicals.



Another dissociation channel of N₂O is possible with the recombination of oxygen atoms, resulting in the formation of either two NO (3) or nitrogen and oxygen molecules (4).³² Among these four reaction channels, it can be understood that NO is the other most abundantly produced molecule.



Further, high reactive oxygen radicals combine to form oxygen molecules (5), which can then combine with another oxygen radical to form ozone molecules (6).^{20,32} During this process, N₂ absorbs an excess amount of energy.⁵¹ The second most abundant product is nitrogen dioxide, formed by the recombination of NO and oxygen radicals (7).⁵²



Higher nitrous oxide can be formed with the recombination of N₂O with the diffused O₂ (8, 9), O₃ (10) inside the ice matrix.³²



Further recombination of primarily produced radicals (NO and O) and reactive molecules (NO₂, O₃) generates heavier molecules through the reaction pathways outlined below.^{20,32,45,52}



From the above reaction mechanism, it is well understood that primary photodissociation and association lead to the formation of small molecules with 2 to 3 atoms, such as NO, O₃, NO₂, O₂, N₂, etc. Further recombination of these molecules and radicals produces larger molecules like N₂O₃, N₂O₂, N₂O₄, and N₂O₅. Here, O is the smallest reactive species and can diffuse much faster than O₂ and O₃, so the reaction path 3 can more sufficiently occur relative to paths 8, 9, and 10 at very low temperatures.

The evolution of RAIR spectra of N₂O and photoproducts with respect to irradiation time (from 0 to 4 h) are shown in Figure S3. We considered the major infrared band for each molecule, calculated the band area, and plotted it in Figure S4. It was observed that all the photoproducts exhibited a sigmoidal growth pattern. The formation of NO₂ and O₃ increased until 150 min and then began to saturate, as these are primary radical associations. In contrast, *c/t*-N₂O₂, N₂O₄, N₂O₃, and N₂O₅ concentrations were saturated only after 90 min. The reaction mechanism reveals that the earlier photoproducts, NO₂ and O₃, are formed by recombining NO with O, and O₂ species. Other photo products emerge from secondary photo processes, which require additional radical recombination reactions. These secondary processes may be hindered by the limited diffusion of oxygen within the ice matrix at 10 K. This reduced mobility could explain why the formation of secondary photoproducts saturates within 90 min. The concentration of three or fewer atom photoproducts keeps increasing until 150 min due to the availability of O and NO radicals in close proximity. It is worth noting that although

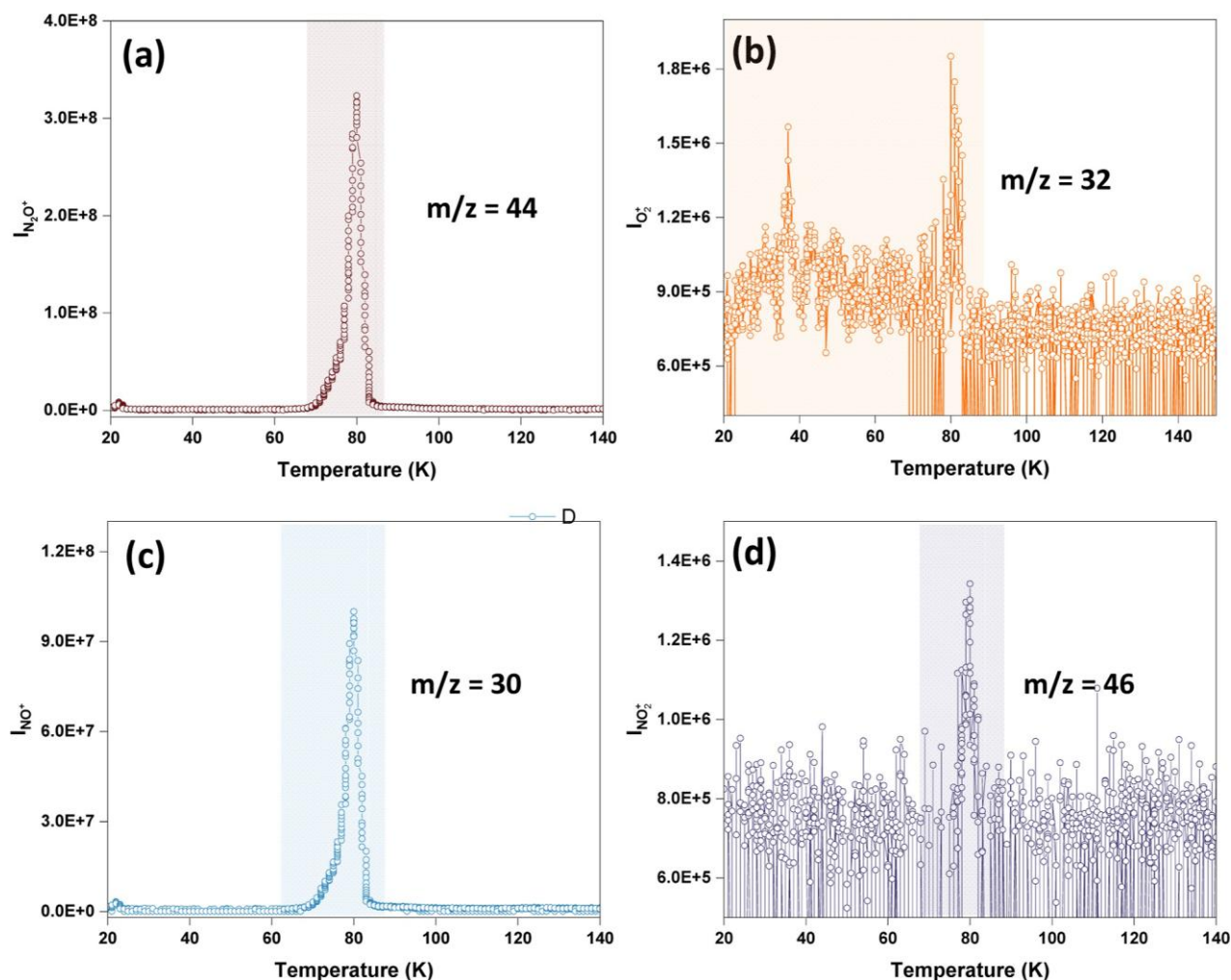


Figure 4. TPD-MS spectra of photo irradiated 150 ML of N_2O ice. Sublimation profiles using integrated ion counts at (a) $m/z = 44$, in (b) $m/z = 32$, in (c) $m/z = 30$ and (d) $m/z = 46$ are plotted.

photoinduced electrons may participate in this photochemistry, their impact is likely to be minimal due to multilayer ice, as electron penetration is confined to a depth of only 2 to 5 ML.^{53–56}

While RAIRS primarily analyses the bulk properties of the ice film, SIMS is capable of probing the topmost monolayer of the ice. To study the surface photochemistry, we irradiated N_2O ice for 1 h and subsequently used SIMS to analyze the photoirradiated surface, identifying the molecules present on the surface. RIS with Cs^+ was employed, wherein Cs^+ ions form ionic clusters with neutral molecules on the ice surface, which are subsequently accelerated to the quadrupole mass spectrometer. Figure 3 shows the RIS spectra before and after irradiation. Before photoirradiation, five molecular cluster ion peaks were observed: $m/z = 151$ [$\text{Cs}(\text{H}_2\text{O})^+$], $m/z = 169$ [$\text{Cs}(\text{H}_2\text{O})_2^+$], $m/z = 179$ [$\text{Cs}(\text{N}_2\text{O})^+$], $m/z = 195$ [$\text{Cs}(\text{H}_2\text{O})_2(\text{N}_2\text{O})^+$], $m/z = 221$ [$\text{Cs}(\text{N}_2\text{O})_2$], and $m/z = 239$ [$\text{Cs}(\text{N}_2\text{O})_2(\text{H}_2\text{O})^+$]. Here, we note that the mass peaks for water molecules are attributed to the background deposition of water at 10 K during the experiment. Although the residual water was present only in trace amounts and did not significantly affect the photochemistry, the high dipole moment of H_2O resulted in high peak intensity for water in the RIS analysis. The extreme surface sensitivity of Cs^+ scattering is another reason for its high intensity.

After 1 h of irradiation, five new peaks emerged, corresponding to the Cs^+ adducts of N_2 ($m/z = 161$ and 189), NO ($m/z = 163$), $\text{NO} + \text{H}_2\text{O}$ ($m/z = 181$), N_2O_3 ($m/z = 209$), and $(\text{N}_2\text{O})_2/\text{N}_2\text{O}_4$ ($m/z = 225$). We did not observe any peaks for N_2O_5 and N_2O_2 . Among the photoproducts, the intensity was generally low except for N_2 , which suggests that reaction pathway 1 is the major dissociation channel that was not observed by IR spectroscopy. Here, we note that only 1 h irradiation was carried out to avoid more residual deposition of water, which can potentially affect the experiment.

For further evaluation, we conducted a temperature-programmed desorption mass spectrometry (TPD-MS) study of photoirradiated N_2O . In this experiment, N_2O was irradiated for 2 h at 10 K, followed by annealing of the photoproducted ice mixture up to 200 K at a rate of 10 K/min, while monitoring the m/z values of 44, 32, 30, and 46 (Figure 4). This allows us to understand how molecules form in the

solid phase and transition to the gas phase during warming. We assigned $m/z 44$ to N_2O , which desorbs ~ 80 K, consistent with its typical desorption temperature (Figure S5). The $m/z 32$ signal was attributed to O_3 , with contributions from O_2 . The desorption of O_3/O_2 started at 20 K and was completed at 80 K. This extended desorption range can be explained by the dissociation of O_3 and the formation of O_2 during thermal annealing, which has a lower desorption temperature. The m/z

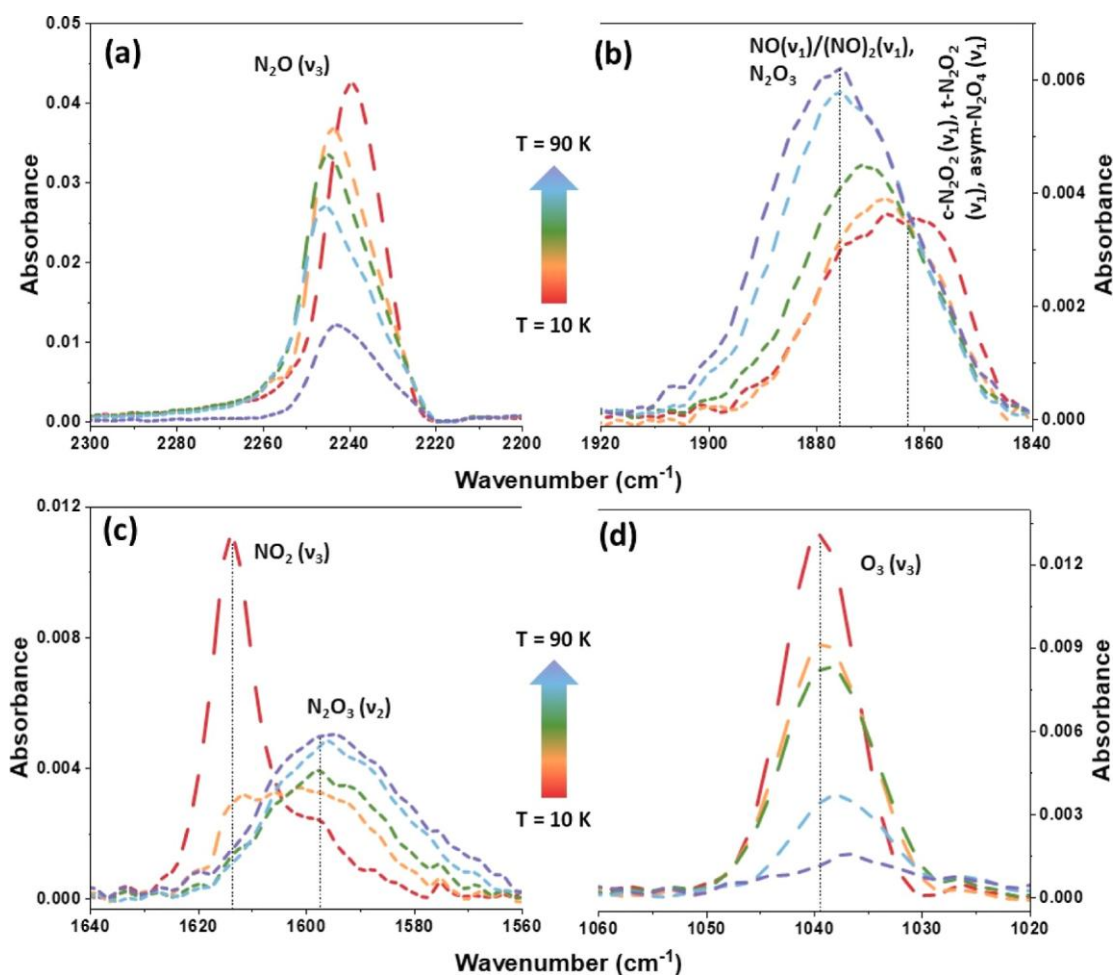


Figure 5. Temperature-dependent RAIR spectra of 4 h photoirradiated N_2O ice. Major IR bands are shown for N_2O , NO , NO_2 , N_2O_2 , N_2O_3 , N_2O_4 , O_3 . 150 ML of N_2O ice was photoirradiated for 4 h, then annealed to 90 K with a heating rate of 2 K min^{-1} .

30 signal can be attributed to various photoinduced products such as NO_2 , N_2O_5 , N_2O_3 , N_2O_2 , and N_2O_4 . This study provides valuable insights into the desorption behavior of photoproducts and their transition from solid to gaseous phase under cryogenic conditions.

Comparative Analysis of Radical Diffusion and Photoproduct Formation. At 10 K, the diffusion and mobility of the reactive intermediates are minimized, potentially arresting further reactions. To examine this theory, we annealed the 4 h photoirradiated sample to 90 K and collected temperature-dependent RAIR spectra (Figure 5). Interestingly, during thermal annealing of photoirradiated N_2O ice, we observed a significant increase in NO and N_2O_3 (Figure 5b,c) alongside a reduction in NO_2 and O_3 (Figure 5c,d). Additionally, a decrease in peak intensity in the ν_3 mode of N_2O was also observed (Figure 5a), which is attributed to the dissociation of N_2O by reacting with reactive diffused oxygen radicals (reaction paths 3, 4, 8, 9, and 14). Increase in the formation of more NO can be explained by the reaction path 3, where N_2O is combined with O to form two NO . Desorption of N_2O is unlikely here, as pure N_2O only starts desorbing after 80 K (Figure S5).

The increased formation of N_2O_3 molecules during thermal annealing of photoirradiated N_2O ice indicates a reaction pathway where NO_2 combines with O radicals. The availability of oxygen and NO radicals, which become mobile as the

temperature increases, leads to more reaction products. Notably, we did not calculate the column density of any molecules because of the significant band overlap among $\text{N}-\text{O}$ bond-bearing species. In the equation for calculating column density from band area, the band area and column density are directly proportional, assuming other factors remain constant. To gain a deeper understanding of the trapping of photoinduced intermediates at 10 K and the subsequent increase in molecular mobility of radicals at higher temperatures, we carried out photoirradiation at 50 K. We calculated the abundance of photoproducts and compared them with those produced at 10 K (Figure 6). Figure S6 shows the time-dependent formation of photoproducts at 50 K. At this temperature, the abundance of NO_2 and O_3 is very low compared to the larger photoproducts such as N_2O_3 , N_2O_5 , *c*/*t*- N_2O_2 , and N_2O_4 (Figure S6). The band area of photo-produced O_3 , and NO_2 start to decrease after 50 min, while $\text{N}_2\text{O}_2/\text{N}_2\text{O}_4$ and N_2O_5 begin to decrease after 150 min while N_2O_3 band area does not decrease until 240 min (Figure S7). In the case of O_3 , the reduced band area can be attributed to the desorption (Figure 4b) and dissociation followed by recombination with N_2O (reaction paths 9 and 14) in the ice matrix. A decrease in the band area of NO_2 after 50 min can be attributed to the dissociation of NO_2 and recombination with other molecules to produce secondary heavy molecules (reaction paths 12,13 and 14). Similarly, the decrease in the

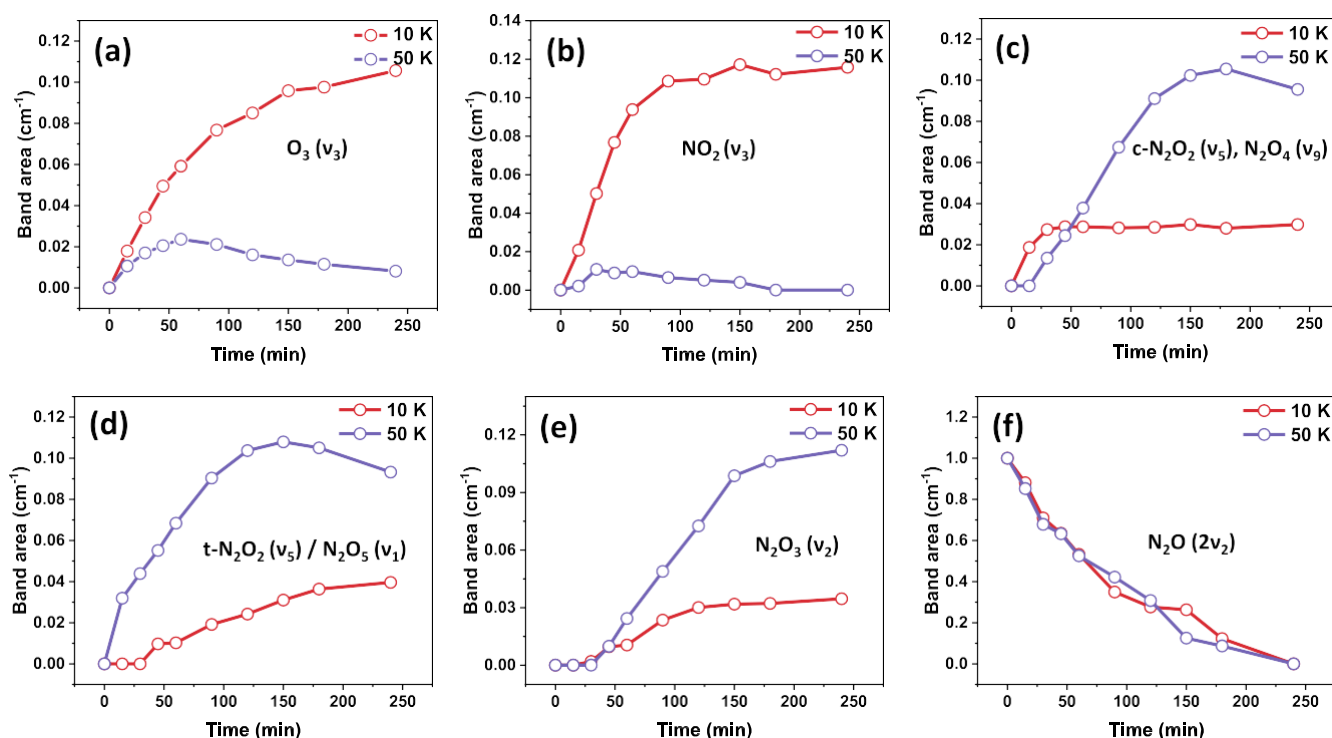


Figure 6. Integrated band areas versus VUV irradiation time for selected photoproducts at 10 and 50 K. The plots show: (a) O_3 (ν_3), (b) NO_2 (ν_3), (c) *cis(c)*- N_2O_2 (ν_5) and N_2O_4 (ν_9) and (d) *trans(t)*- N_2O_2 (ν_5), N_2O_5 (ν_1), (e) N_2O_3 (ν_2), and (f) N_2O ($2\nu_2$). For N_2O , the band areas are normalized for 10 and 50 K.

band area for N_2O_5 and $\text{N}_2\text{O}_2/\text{N}_2\text{O}_4$ can be attributed to dissociation due to intense VUV irradiation.

Figure 6 compares the abundance of photoproducts produced after 4 h of photoirradiation at 10 K, and 50 K. It shows that the earlier photoproducts, O_3 and NO_2 are relatively higher in abundance at 10 K, while the secondary photoproducts, N_2O_3 , $\text{N}_2\text{O}_2/\text{N}_2\text{O}_4$, and N_2O_5 are more abundant at 50 K. This comparison clearly shows a selective difference in the photoproduct concentration at two different temperatures. Importantly, the crystalline nature of N_2O ice at 50 K (Figure S8) does not contribute to this selective photoproduct formation. To substantiate this, we conducted a control experiment in which N_2O ice was first crystallized by annealing it to 50 K. Subsequently the sample was cooled to 10 K, and irradiated for 4 h. The resulting photoproducts were similar to those observed at 10 K (Figure S9), clearly indicating that the hindered diffusion of radicals at lower temperatures limits the formation of secondary photoproducts. Thus, we conclude that the diffusion of reactive radicals at higher temperatures plays a key role in selectively enhancing the concentration of secondary photoproducts.

CONCLUSIONS

This study demonstrated that VUV photolysis of N_2O generates a range of photoproducts, including O_3 , NO , NO_2 , N_2O_2 , N_2O_3 , N_2O_4 , and N_2O_5 , which were characterized using RAIRS, SIMS and TPD-MS. Thermal annealing of the photoirradiated N_2O ice showed an increase in NO and N_2O_3 and a decrease in NO_2 and O_3 , indicating that thermal diffusion of reactive intermediates, which are majorly reactive oxygen species (O and O_3) continue to drive the reactions. Experiments conducted at 10 and 50 K revealed that three atom photoproducts (O_3 and NO_2) dominate at 10 K, while

four or more atom photoproducts (N_2O_2 , N_2O_3 , N_2O_4 , and N_2O_5) are prevalent at 50 K. This behavior is attributed to the restricted diffusion of radicals at 10 K, which limits radical–radical reactions leading to primary products, whereas higher temperatures promote greater diffusion and recombination, leading to the formation of heavier photoproducts. These findings highlight the crucial role of diffusion restrictions and thermodynamic stability in the formation of photoproducts in icy matrices.

ASSOCIATED CONTENT

Supporting Information

The Supporting Information is available free of charge at <https://pubs.acs.org/doi/10.1021/acs.jpcc.4c06624>.

It includes temperature and time-dependent RAIR spectra and the emission spectrum of the model 634 Deuterium lamp (PDF)

AUTHOR INFORMATION

Corresponding Author

Thalappil Pradeep – DST Unit of Nanoscience (DST UNS) and Thematic Unit of Excellence (TUE), Department of Chemistry, Indian Institute of Technology Madras, Chennai 600036, India; International Centre for Clean Water, IIT Madras Research Park, Chennai 600113, India; orcid.org/0000-0003-3174-534X; Email: pradeep@iitm.ac.in

Authors

Bijesh K. Malla – DST Unit of Nanoscience (DST UNS) and Thematic Unit of Excellence (TUE), Department of Chemistry, Indian Institute of Technology Madras, Chennai 600036, India

Soham Chowdhury – DST Unit of Nanoscience (DST UNS) and Thematic Unit of Excellence (TUE), Department of Chemistry, Indian Institute of Technology Madras, Chennai 600036, India

Devansh Paliwal – DST Unit of Nanoscience (DST UNS) and Thematic Unit of Excellence (TUE), Department of Chemistry, Indian Institute of Technology Madras, Chennai 600036, India

Hanoona K. M. – Department of Chemistry, Mar Ivanios College, Thiruvananthapuram, Kerala 695015, India

Gaurav Vishwakarma – DST Unit of Nanoscience (DST UNS) and Thematic Unit of Excellence (TUE), Department of Chemistry, Indian Institute of Technology Madras, Chennai 600036, India; orcid.org/0009-0002-6076-3299

Rabin Rajan J. Methikkalam – Department of Chemistry, Mar Ivanios College, Thiruvananthapuram, Kerala 695015, India

Complete contact information is available at:
<https://pubs.acs.org/10.1021/acs.jpcc.4c06624>

Author Contributions

T.P. and B.K.M. designed the research. B.K.M., S.C., D.P., and H.K.M., have performed the experiments. T.P. supervised its progress. B.K.M. analyzed the results. The first draft of the manuscript was written by B.K.M. The final version of the manuscript was prepared, including the contributions of all authors.

Notes

The authors declare no competing financial interest.

ACKNOWLEDGMENTS

We acknowledge the Science and Engineering Research Board (SERB) for the Core Research grant (CRG/2018/003922), Department of Science and Technology (DST), and Government of India for research funding. T.P. acknowledges funding from the Centre of Excellence on Molecular Materials and Functions under the Institution of Eminence scheme of IIT Madras. B.K.M. thanks the Council of Scientific and Industrial Research (CSIR) for his research fellowship. S.C. thanks IITM for their research fellowship.

REFERENCES

- Oberg, K. I. Photochemistry and Astrochemistry: Photochemical Pathways to Interstellar Complex Organic Molecules. *Chem. Rev.* 2016, 116 (17), 9631–9663.
- McGuire, B. A. Census of Interstellar, Circumstellar, Extragalactic, Protoplanetary Disk, and Exoplanetary Molecules. *Astrophys. J. Suppl. Ser.* 2022, 259 (2), 30.
- Cami, J.; Bernard-Salas, J.; Peeters, E.; Malek, S. E. Detection of C_{60} and C_{70} in a Young Planetary Nebula. *Science* 2010, 329 (5996), 1180–1182.
- Arumainayagam, C. R.; Garrod, R. T.; Boyer, M. C.; Hay, A. K.; Bao, S. T.; Campbell, J. S.; Wang, J.; Nowak, C. M.; Arumainayagam, M. R.; Hodge, P. J. Extraterrestrial Prebiotic Molecules: Photochemistry vs. Radiation Chemistry of Interstellar Ices. *Chem. Soc. Rev.* 2019, 48 (8), 2293–2314.
- Singh, S. K.; Zhu, C.; La Jeunesse, J.; Fortenberry, R. C.; Kaiser, R. I. Experimental Identification of Aminomethanol (NH_2CH_2OH) as the Key Intermediate in the Strecker Synthesis. *Nat. Commun.* 2022, 13 (1), 375–377.
- Schutte, W. A.; Allamandola, L. J.; Sandford, S. A. Formaldehyde and Organic Molecule Production in Astrophysical Ices at Cryogenic Temperatures. *Science* 1993, 259 (5098), 1143–1145.
- Malla, B. K.; Vishwakarma, G.; Chowdhury, S.; Pradeep, T. Vacuum Ultraviolet Photolysis of Condensed Methyl Chloride in Interstellar Model Conditions and Trapping of Intermediates at Intergrain Interfaces. *J. Phys. Chem. C* 2023, 127 (50), 24149–24157.
- Cuppen, H. M.; Karssemeijer, L. J.; Lamberts, T. The Kinetic Monte Carlo Method as a Way to Solve the Master Equation for Interstellar Grain Chemistry. *Chem. Rev.* 2013, 113 (12), 8840–8871.
- Noble, J. A.; Michoulier, E.; Aupetit, C.; Mascetti, J. Influence of Ice Structure on the Soft UV Photochemistry of PAHs Embedded in Solid Water. *Astron. Astrophys.* 2020, 644, A22.
- Lilach, Y.; Asscher, M. Photochemistry of Caged Molecules: $CD_3Cl@Ice$. *J. Chem. Phys.* 2003, 119 (1), 407–412.
- Asscher, Y. A. and M. Water at Interfaces. *Phys. Chem. Chem. Phys.* 2008, 10 (32), 4676.
- Laffon, C.; Lasne, J.; Bournel, F.; Schulte, K.; Lacombe, S.; Parent, P. Photochemistry of Carbon Monoxide and Methanol in Water and Nitric Acid Hydrate Ices: A NEXAFS Study. *Phys. Chem. Chem. Phys.* 2010, 12 (36), 10865–10870.
- Ramakrishnan, S.; Sagi, R.; Mahapatra, N.; Asscher, M. Effect of Coadsorbed Oxygen on the Photochemistry of Methane Embedded in Amorphous Solid Water. *J. Phys. Chem. C* 2018, 122 (27), 15287–15296.
- Schrivier, A.; Coanga, J. M.; Schriver-Mazuoli, L.; Ehrenfreund, P. Vibrational Spectra and UV Photochemistry of $(CH_2)_2O$ Thin Films and $(CH_2)_2O$ in Amorphous Water Ice. *Chem. Phys.* 2004, 303 (1–2), 13–25.
- Yabushita, A.; Hama, T.; Kawasaki, M. Photochemical Reaction Processes during Vacuum-Ultraviolet Irradiation of Water Ice. *J. Photochem. Photobiol. C Photochem. Rev.* 2013, 16, 46–61.
- Kulikov, M. Y.; Feigin, A. M.; Schrems, O. H_2O_2 Photo-production inside H_2O and $H_2O:O_2$ Ices at 20–140 K. *Sci. Rep.* 2019, 9 (1), 11375–11379.
- Ziurys, L. M.; Apponi, A. J.; Hollis, J. M.; Snyder, L. E. Detection of Interstellar N_2O : A New Molecule Containing an N-O Bond. *Astrophys. J.* 1994, 436 (september 2016), L181.
- Nazari, P.; Rocha, W. R. M.; Rubinstein, A. E.; Slavicinska, K.; Rachid, M. G.; Van Dishoeck, E. F.; Megeath, S. T.; Gutermuth, R.; Tyagi, H.; Brunken, N.; et al. Hunting for Complex Cyanides in Protostellar Ices with the JWST - A Tentative Detection of CH_3CN and C_2H_5CN . *Astron. Astrophys.* 2024, 686, A71.
- Tsai, W.-T.; Fernando, J.; Gomes, P. Fate of Chloromethanes in the Atmospheric Environment: Implications for Human Health, Ozone Formation and Depletion, and Global Warming Impacts. *Toxics* 2017, 5 (4), 23.
- Sivaraman, B.; Ptasinska, S.; Jheeta, S.; Mason, N. J. Electron Irradiation of Solid Nitrous Oxide. *Chem. Phys. Lett.* 2008, 460 (1–3), 108–111.
- Knauth, D. C.; Andersson, B. G.; McCandliss, S. R.; Warren Moos, H. The Interstellar N_2 Abundance towards HD 124314 from Far-Ultraviolet Observations. *Nat.* 2004, 429 (6992), 636–638.
- Larsson, B.; Liseau, R.; Pagani, L.; Bergman, P.; Bernath, P.; Biver, N.; Black, J. H.; Booth, R. S.; Buat, V.; Crovisier, J.; et al. Molecular oxygen in the ρ Ophiuchi cloud. *Astron. Astrophys.* 2007, 466 (3), 999–1003.
- Goldsmith, P. F.; Liseau, R.; Bell, T. A.; Black, J. H.; Chen, J. H.; Hollenbach, D.; Kaufman, M. J.; Li, D.; Lis, D. C.; Melnick, G.; et al. Herschel measurements of molecular oxygen in Orion. *Astrophys. J.* 2011, 737 (2), 96.
- Snyder, L. E.; Kuan, Y.-J.; Ziurys, L. M.; Hollis, J. M.; Snyder, L. E.; Kuan, Y.-J.; Ziurys, L. M.; Hollis, J. M. New 3 Millimeter Observations of Interstellar HNO: Reinstating a Discredited Identification. *ApJL* 1993, 403, L17.
- Ziurys, L. M.; Apponi, A. J.; Hollis, J. M.; Snyder, L. E.; Ziurys, L. M.; Apponi, A. J.; Hollis, J. M.; Snyder, L. E. Detection of Interstellar N_2O : A New Molecule Containing an N-O Bond. *ApJL* 1994, 436, L181.
- Coutens, A.; Ligterink, N. F. W.; Loison, J. C.; Wakelam, V.; Calcutt, H.; Drozdovskaya, M. N.; Jørgensen, J. K.; Müller, H. S. P.; Van Dishoeck, E. F.; Wampfler, S. F. The ALMA-PILS Survey: First

Detection of Nitrous Acid (HONO) in the Interstellar Medium. *Astron. Astrophys.* 2019, 623, L13.

(27) Marcelino, N.; Cernicharo, J.; Tercero, B.; Roueff, E. Discovery of Fulminic Acid, HCNO, in Dark Clouds. *ApJL* 2009, 690 (1), L27–L30.

(28) Liszt, H. S.; Turner, B. E.; Liszt, H. S.; Turner, B. E. Microwave Detection of Interstellar NO. *ApJL* 1978, 224, L73–L76.

(29) Rivilla, V. M.; Martín-Pintado, J.; Jiménez-Serra, I.; Martín, S.; Rodríguez-Almeida, L. F.; Requena-Torres, M. A.; Rico-Villas, F.; Zeng, S.; Briones, C. Prebiotic Precursors of the Primordial RNA World in Space: Detection of NH₂OH. *Astrophys. J. Lett.* 2020, 899 (2), L28.

(30) Jamieson, C. S.; Bennett, C. J.; Mebel, A. M.; Kaiser, R. I. Investigating the Mechanism for the Formation of Nitrous Oxide [N₂O(X 1 Σ⁺)] in Extraterrestrial Ices. *Astrophys. J.* 2005, 624 (1), 436–447.

(31) Halfen, D. T.; Apponi, A. J.; Ziurys, L. M. Evaluating the N/O Chemical Network: The Distribution of N₂O and NO in the Sagittarius B2 Complex. *Astrophys. J.* 2001, 561 (1), 244–253.

(32) Almeida, G. C.; Pilling, S.; de Barros, A. L. F.; da Costa, C. A. P.; Pereira, R. C.; da Silveira, E. F. Processing of N₂O Ice by Fast Ions: Implications on Nitrogen Chemistry in Cold Astrophysical Environments. *Mon. Not. R. Astron. Soc.* 2017, 471 (2), 1330–1340.

(33) Bag, S.; Bhui, R. G.; Methikkalam, R. R. J.; Pradeep, T.; Kephart, L.; Walker, J.; Kuchta, K.; Martin, D.; Wei, J. Development of Ultralow Energy (1–10 eV) Ion Scattering Spectrometry Coupled with Reflection Absorption Infrared Spectroscopy and Temperature Programmed Desorption for the Investigation of Molecular Solids. *Rev. Sci. Instrum.* 2014, 85 (1), 1–7.

(34) Malla, B. K.; Vishwakarma, G.; Chowdhury, S.; Nayak, S. K.; Yamijala, S. S. R. K. C.; Pradeep, T. Formation and Dissociation of Dimethyl Ether Clathrate Hydrate in Interstellar Ice Mimics. *J. Phys. Chem. C* 2024, 128 (6), 2463–2470.

(35) Malla, B. K.; Vishwakarma, G.; Chowdhury, S.; Selvarajan, P.; Pradeep, T. Formation of Ethane Clathrate Hydrate in Ultrahigh Vacuum by Thermal Annealing. *J. Phys. Chem. C* 2022, 126 (42), 17983–17989.

(36) Vishwakarma, G.; Malla, B. K.; Kumar, R.; Pradeep, T. Partitioning Photochemically Formed CO₂ into Clathrate Hydrate under Interstellar Conditions. *Phys. Chem. Chem. Phys.* 2024, 26 (22), 16008–16016.

(37) Kang, H. Chemistry of Ice Surfaces. Elementary Reaction Steps on Ice Studied by Reactive Ion Scattering. *Acc. Chem. Res.* 2005, 38 (12), 893–900.

(38) Hahn, J. R.; Lee, C. W.; Han, S. J.; Lahaye, R. J. W. E.; Kang, H. Low-Energy Cs⁺ Scattering from Water on Pt(111): A Kinetic Energy Analysis of the Cs⁺-Water Clusters. *J. Phys. Chem. A* 2002, 106 (42), 9827–9831.

(39) Cyriac, J.; Pradeep, T.; Kang, H.; Souda, R.; Cooks, R. G. Low-Energy Ionic Collisions at Molecular Solids. *Chem. Soc. Rev.* 2012, 112, 5356–5411.

(40) Bartmess, J. E.; Georgiadis, R. M. Empirical Methods for Determination of Ionization Gauge Relative Sensitivities for Different Gases. *Vacuum* 1983, 33 (3), 149–153.

(41) Vishwakarma, G.; Malla, B. K.; Chowdhury, S.; Khandare, S. P.; Pradeep, T. Existence of Acetaldehyde Clathrate Hydrate and Its Dissociation Leading to Cubic Ice under Ultrahigh Vacuum and Cryogenic Conditions. *J. Phys. Chem. Lett.* 2023, 14, 5328–5334.

(42) Lee, D. H.; Kang, H. Acid-Promoted Crystallization of Amorphous Solid Water. *J. Phys. Chem. C* 2018, 122 (42), 24164–24170.

(43) Mokrane, H.; Chaabouni, H.; Accolla, M.; Congiu, E.; Dulieu, F.; Chehrouri, M.; Lemaire, J. L. Experimental Evidence for Water Formation via Ozone Hydrogenation on Dust Grains at 10 K. *Astrophys. J.* 2009, 705 (2), L195.

(44) Hisatsune, I. C.; Devlin, J. P.; Wada, Y. Infrared Spectra of Some Unstable Isomers of N₂O₄ and N₂O₃. *J. Chem. Phys.* 1960, 33 (3), 714–719.

(45) Fulvio, D.; Baratta, G. A.; Sivaraman, B.; Mason, N. J.; da Silveira, E. F.; de Barros, A. L. F.; Pandoli, O.; Strazzulla, G.; Palumbo, M. E. Ion Irradiation of N₂O Ices and NO₂:N₂O₄ Ice Mixtures: First Steps to Understand the Evolution of Molecules with the N–O Bond in Space. *Mon. Not. R. Astron. Soc.* 2018, 483 (1), 381–391.

(46) Hisatsune, I. C.; Devlin, J. P. Existence of N₂O₄ Isomers. *J. Chem. Phys.* 1959, 31 (4), 1130–1131.

(47) Hudson, R. L.; Loeffler, M. J.; Gerakines, P. A. Infrared Spectra and Band Strengths of Amorphous and Crystalline N₂O. *J. Chem. Phys.* 2017, 146 (2), 24304.

(48) Gimmler, G.; Havenith, M. High-Resolution IR Spectroscopy of the N₂O–H₂O and N₂O–D₂O van Der Waals Complexes. *J. Mol. Spectrosc.* 2002, 216 (2), 315–321.

(49) Zelikoff, M.; Aschenbrand, L. M. Vacuum Ultraviolet Photochemistry, Part I. Nitrous Oxide at 1470 Å. *J. Chem. Phys.* 1954, 22 (10), 1680–1684.

(50) Peyerimhoff, S. D.; Buenker, R. J. Theoretical Study of the Geometry and Spectrum of Nitrous Oxide. *J. Chem. Phys.* 1968, 49 (6), 2473–2487.

(51) Ellison, G. B. Chemistry of Atmospheres: An Introduction to the Chemistry of the Atmospheres of Earth, the Planets, and Their Satellites, 3rd Edition (Wayne, Richard P.). *J. Chem. Educ.* 2003, 80 (3), 264.

(52) Minissale, M.; Fedoseev, G.; Congiu, E.; Ioppolo, S.; Dulieu, F.; Linnartz, H. Solid State Chemistry of Nitrogen Oxides – Part I: Surface Consumption of NO. *Phys. Chem. Chem. Phys.* 2014, 16 (18), 8257–8269.

(53) Jo, S. K.; Kiss, J.; Castro, M. E.; White, J. M. Mass Effects in Photodissociation of Chloromethane. *J. Am. Chem. Soc.* 1992, 114 (11), 310–315.

(54) Gilton, T. L.; Dehnhostel, C. P.; Cowin, J. P. Electron Transmission through Layers of H₂O and Xe in the Ultrahigh Vacuum Photoreduction of CH₃Cl on Ni(111). *J. Chem. Phys.* 1989, 91 (3), 1937–1938.

(55) Jo, S. K.; White, J. M. Low Energy (<1 eV) Electron Transmission through Condensed Layers of Water. *J. Chem. Phys.* 1991, 94 (8), 5761–5764.

(56) Nagesha, K.; Fabrikant, I. I.; Sanche, L. Electron Attachment to CF₃Cl and CH₃Cl on the Surface and in the Bulk of Solid Kr. *J. Chem. Phys.* 2001, 114 (11), 4934–4944.

Simulated Interstellar Photolysis of N₂O Ice: Selectivity in Photoproducts

*Bijesh K. Malla¹, Soham Chowdhury¹, Devansh Paliwal¹, Hanoona KM², Gaurav Vishwakarma¹,
Rabin Rajan J. Methikkalam² and Thalappil Pradeep^{1,3*}*

¹DST Unit of Nanoscience (DST UNS) and Thematic Unit of Excellence (TUE), Department of Chemistry, Indian Institute of Technology Madras, Chennai 600036, India.

²Department of Chemistry, Mar Ivanios College, Thiruvananthapuram, Kerala 695015, India

³International Centre for Clean Water, IIT Madras Research Park, Chennai 600113, India.

Corresponding author

Email: pradeep@iitm.ac.in

This Pdf includes

Emission spectrum of Deuterium lamp – S2

RAIR spectra – S3, S4, S7, S9, S10

Band area vs time plot – S5, S8

TPD-MS plot – S6

Supporting information 1:

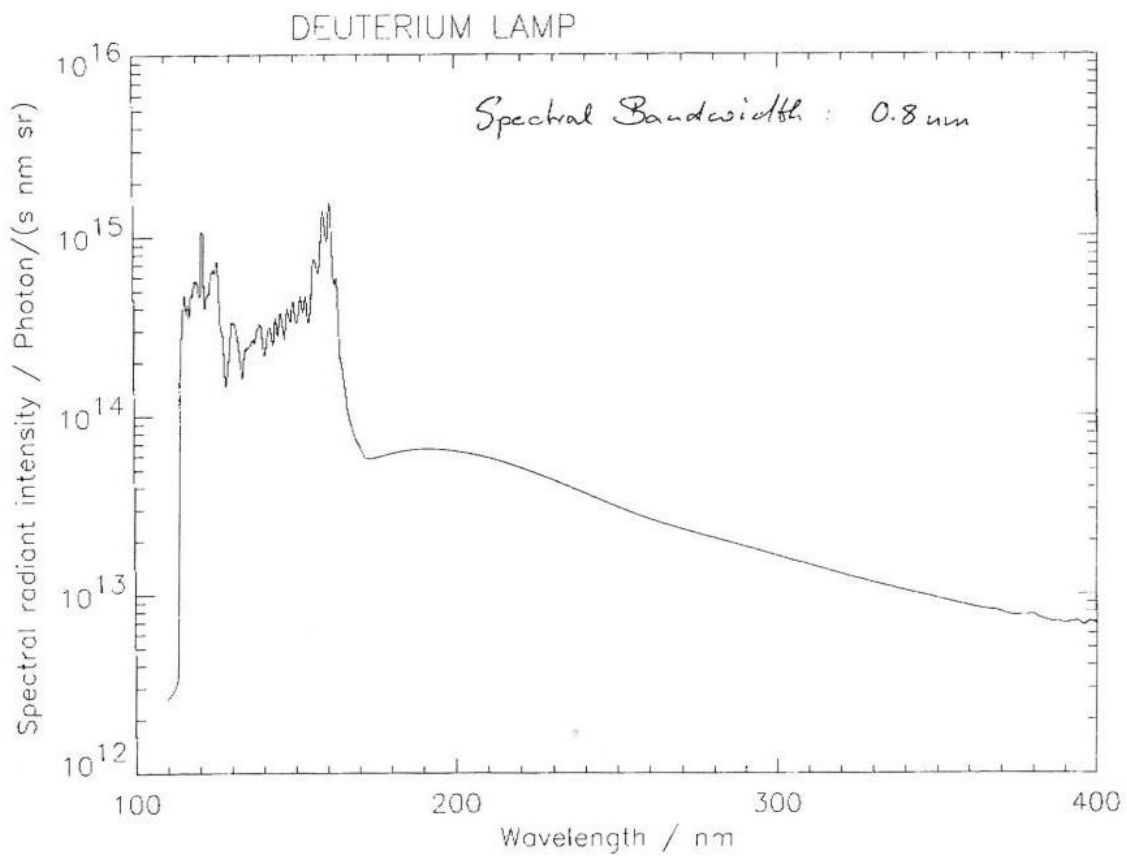


Figure S1. Emission spectrum of Model 634 Deuterium lamp, provided by the McPherson.

Supporting information 2:

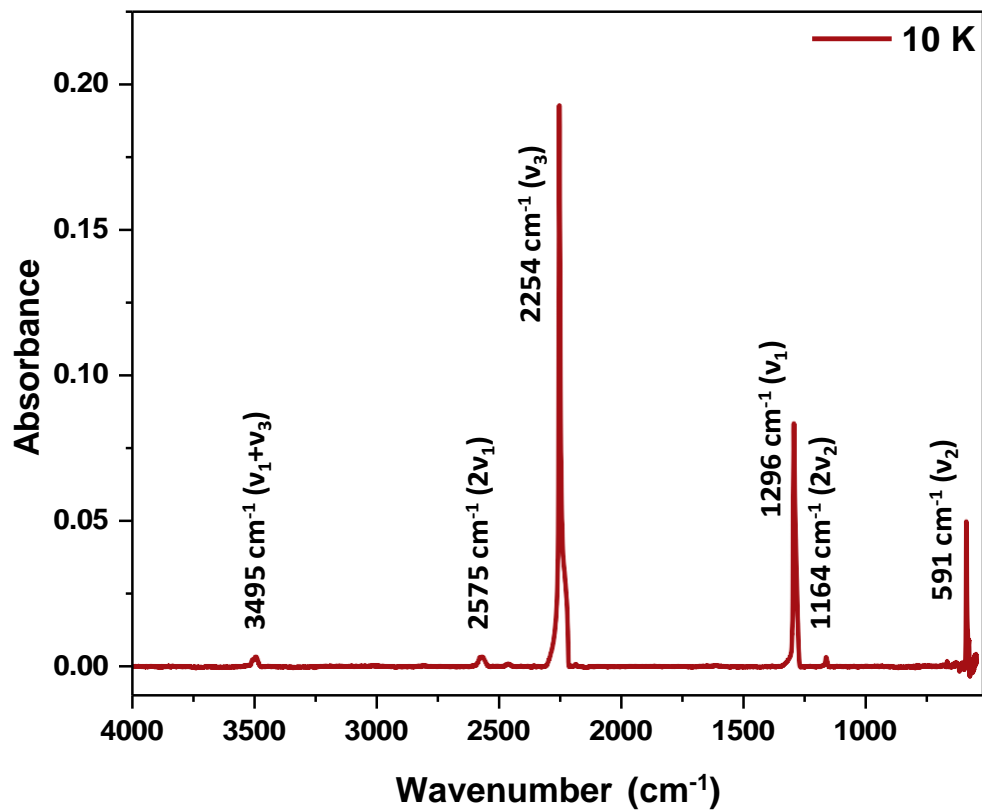


Figure S2. RAIR spectrum of 150 ML of N₂O ice at 10 K.

Supporting information 3:

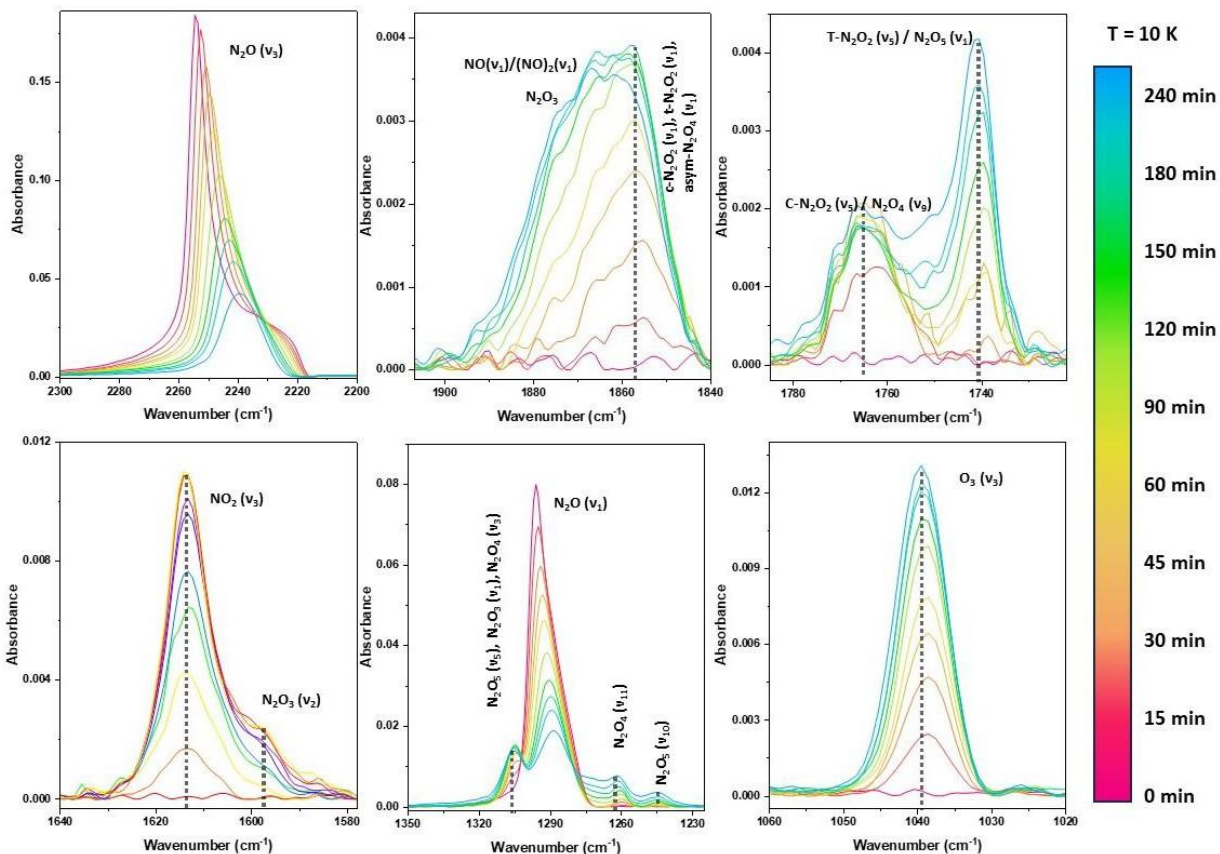


Figure S3. Time-dependent evolution of RAIR spectra of 150 ML of N_2O ice under VUV photon irradiation at 10 K. N_2O ice film was photo-irradiated for 4 h at 10 K, and the RAIR spectrum was taken at regular intervals of time.

Supporting information 4:

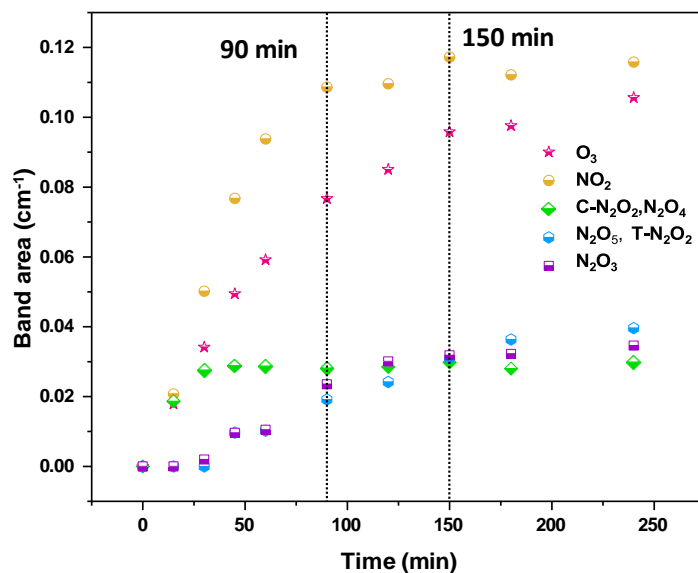


Figure S4. The evolution of the band area of photoproducts (O₃ (v₃), NO₂ (v₃), cis(c)-N₂O₂ (v₅), N₂O₄ (v₉), trans (t)-N₂O₂ (v₅), N₂O₅ (v₁), and N₂O₃ (v₂)) monitored as a function of irradiation time at 10 K.

Supporting information 5:

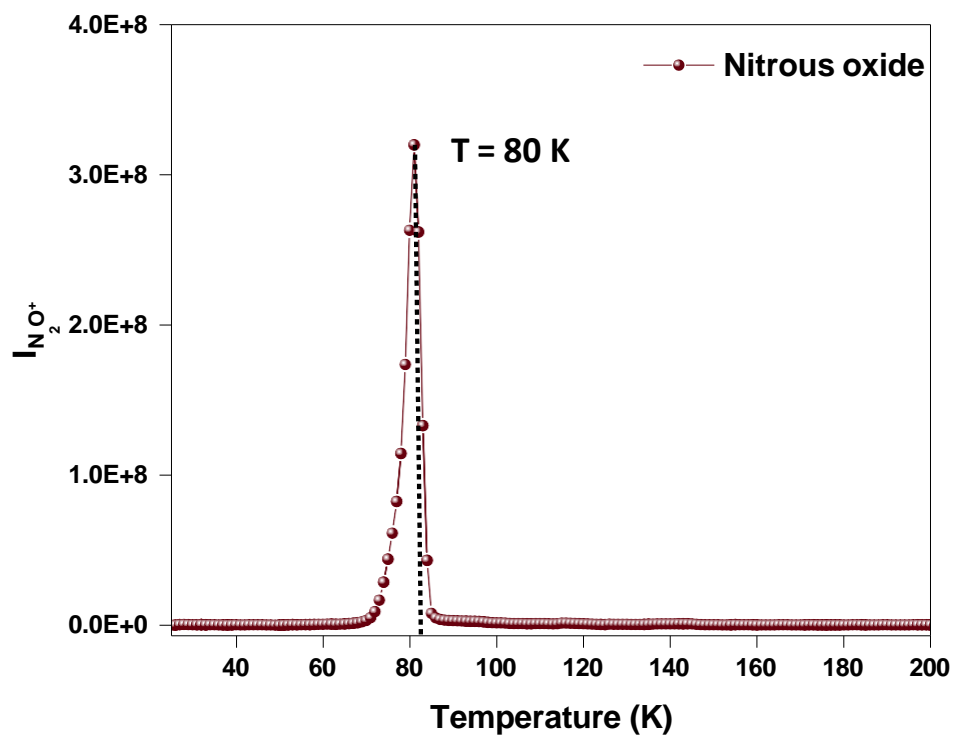


Figure S5. TPD-MS spectrum of 150 ML of N_2O ice. The sublimation profile was plotted using integrated ion counts at $m/z = 44$.

Supporting information 6:

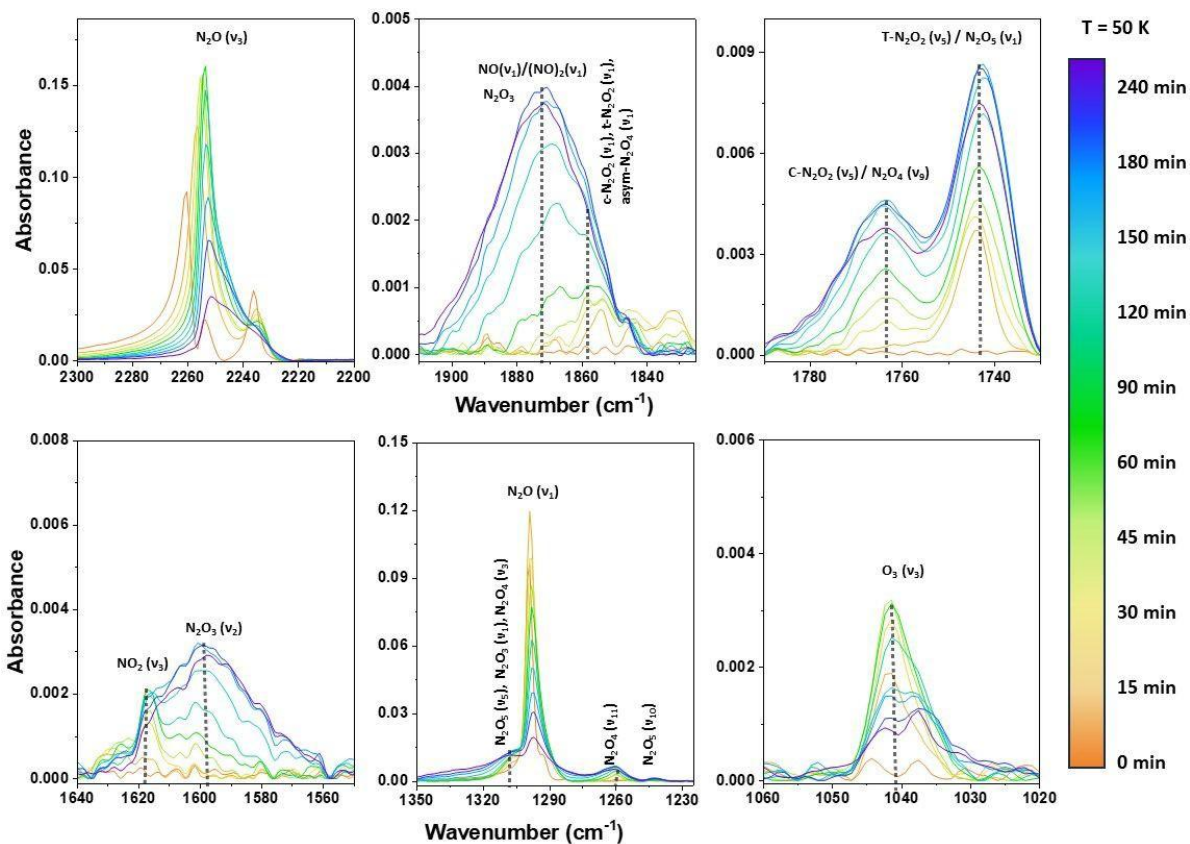


Figure S6. Time-dependent evolution of RAIR spectra of 150 ML of N_2O ice under VUV photon irradiation at 50 K. N_2O ice film was photo-irradiated for 4 h at 50 K, and the RAIR spectra were collected at a regular interval of time.

Supporting information 7:

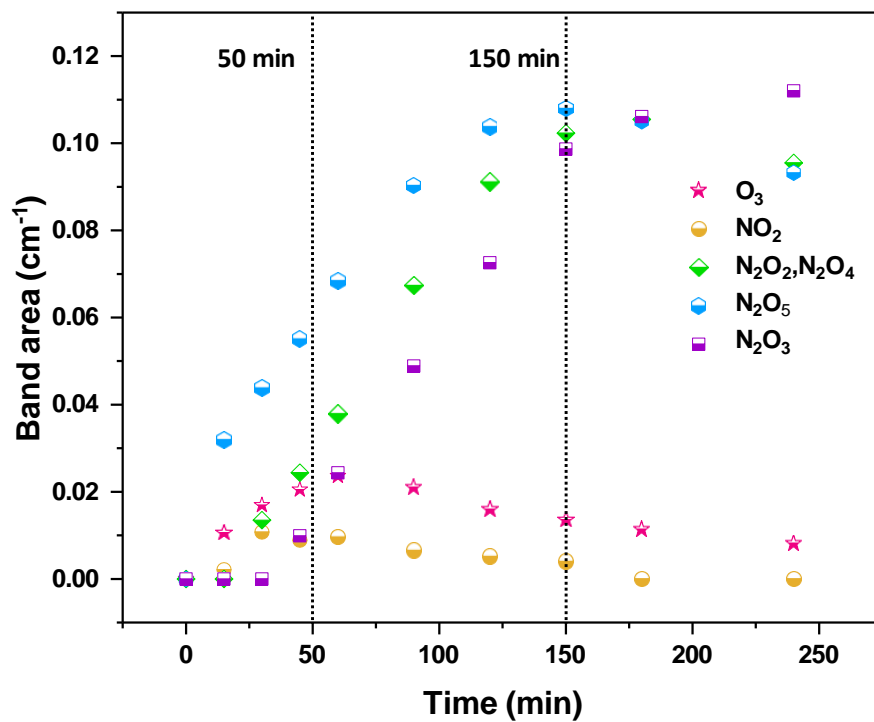


Figure S7. The evolution of the band area of photoproducts (O_3 (ν_3), NO_2 (ν_3), cis(c)- N_2O_2 (ν_5), N_2O_4 (ν_9), trans (t)- N_2O_2 (ν_5), N_2O_5 (ν_1), and N_2O_3 (ν_2)) monitored as a function of irradiation time at 50 K.

Supporting information 8:

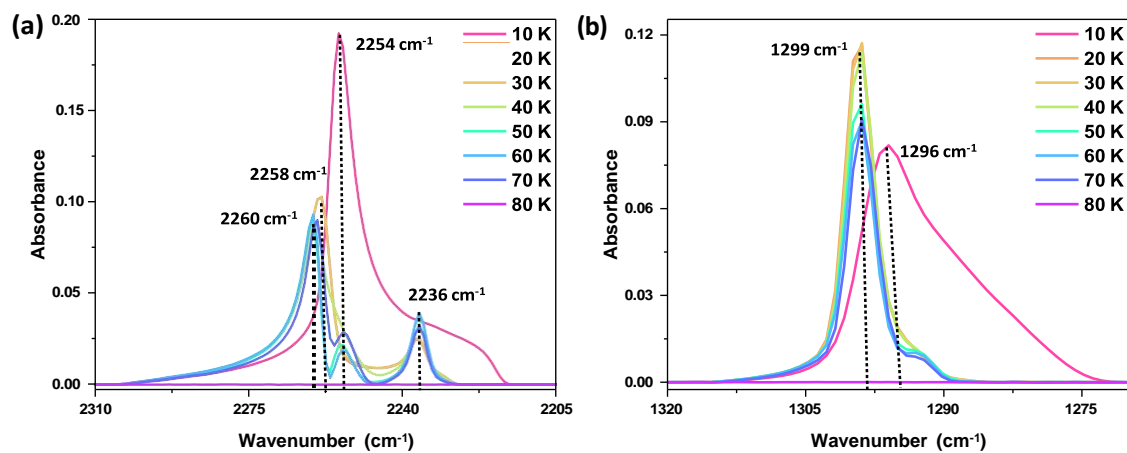


Figure S8. Temperature-dependent RAIR spectra of 150 ML of N_2O ice in N-O antisymmetric stretching region (a) and N-O symmetric stretching region (b).

Supporting information 9:

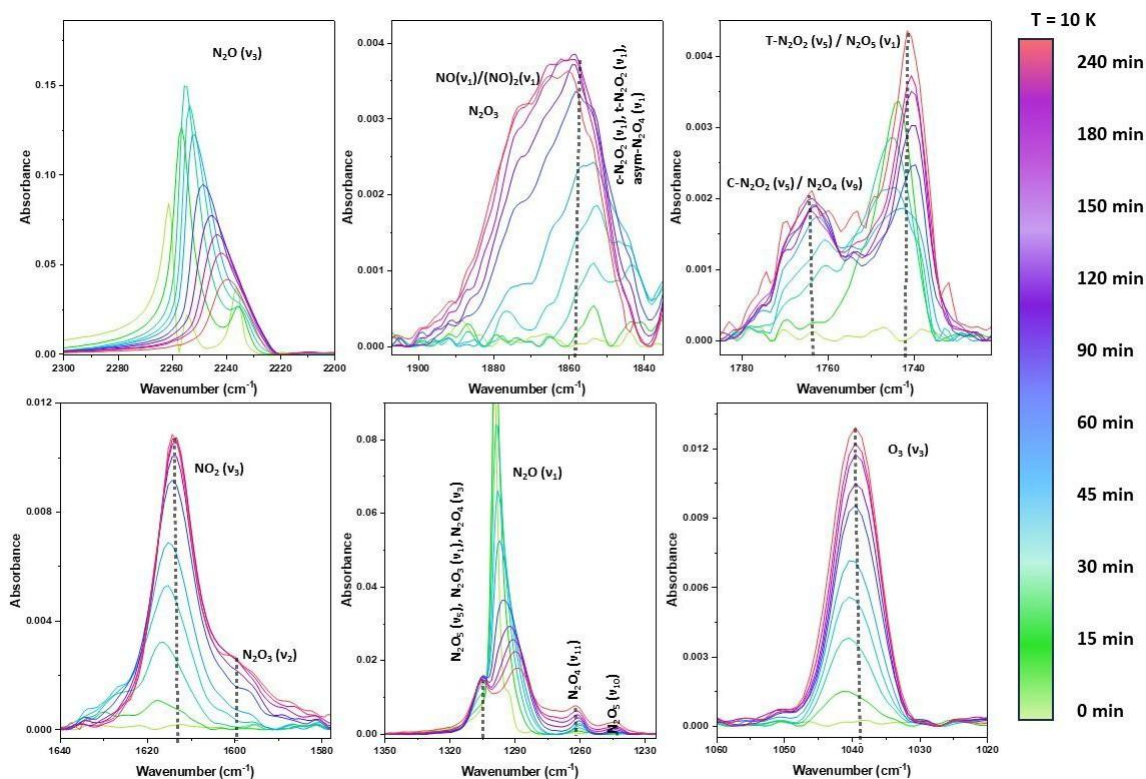


Figure S9. Time-dependent evolution of RAIR spectra of 150 ML of crystalline N_2O ice under VUV photon irradiation at 10 K. N_2O crystalline ice film was prepared by vapor deposition at 10 K, and then it was annealed to 50 K again cooled back to 10 K. N_2O ice film was photo-irradiated for 4 h at 10 K, and in a regular interval of time RAIR spectrum was taken.

Editorials


Publications from other groups

Managing Water, the Mother of Resources: Thoughts on World Water Day 2024

 Cite This: *ACS Sustainable Resour. Manage.* 2024, 1, 368–369

 Read Online

ACCESS

 Metrics & More

 Article Recommendations

While several nations of the world are going through wars to affirm their territorial boundaries, wars of another kind are being fought everyday by millions around their neighborhood: the war for access to water, a basic human right. This latter war is intensifying due to climate catastrophes and indiscriminate development, particularly evident in the developing world. The theme of World Water Day 2024 is *Water for Peace*.¹ We know that sharing water resources equitably can bring peace to any region, and the opposite can nucleate or propagate conflicts. Water can bring prosperity, food security, reduced mass migration, quality education, and all-around growth of the young, ultimately leading to harmony and stability of nations. Water can indeed bring joy in the long run!

Water is central to all aspects of life and development; thus, it is also a reason for conflicts at the local and national levels due to several factors. The factors may be broadly grouped as (a) 60% of global fresh water resources are trans-national involving 153 countries of which only 24 have cooperative agreements, (b) ~5 billion people experience water scarcity at least once a year, (c) over 2 billion people live without reliable and safe water supply and face major health consequences, such as over 500,000 diarrheal deaths per year due to microbial contamination,² and (d) rising inequality continues to exert pressure on the available water bodies that are shrinking in size and with reduced water quality. We realize that the central problem is associated with resource management, which is the theme of *ACS Sustainable Resource Management*.

Water resources of the planet are constant. We have just about 1.14×10^{45} molecules of water, with minor changes in the numbers over time due to anthropological activities. The sugar molecules which are components of cellulose which eventually made petroleum, and coal are derived from CO_2 and H_2O via photosynthesis through a quantitative reaction. Combustion then transforms these compounds back into the same starting molecules. Thus, from a planetary sense, “water for all” is a management problem.

We obtain water from rain and snow, and the availability of these resources has been constant over millennia, with local variations, particularly exacerbated due to climate change. The annual renewable water resource (ARWR) for the planet was ~5400 m³ per person in 2020.³ However, by 2050, the ARWR of 87 out of 180 countries will be less than 1700 m³ per person, and 45 of the 87 countries will face absolute water scarcity, i.e., 500 m³ per year.⁴ Water, being a dense molecule, poses another significant challenge in society: its transportation across and within nations to address this resource scarcity is

also an energy problem due to the large volumes required by humanity. Although technologies as exotic as transporting detached icebergs across the oceans has been considered,⁵ new science is essential to address and manage this important resource at the magnitude needed.

Sadly, water scarcity is a problem of the poor. Data suggest that the ratio of ARWR (per capita) for high-income to low income countries was 2.3 times (in 2015), and the disparity was expected to worsen to 5.8 times by 2050.⁴ New technological inputs are needed for water-efficient agriculture, energy production, and manufacturing, while water harvesting, recycling, and reuse must become standard practices to guarantee a safe planet.

What can be done by the scientific community? Sustainable water management must be practiced at the personal, institutional, and community levels. All good things must begin from the individual, each one of us. For this, our personal choices of food, clothing, personal care, transportation, housing, work, etc. must be evaluated, and sensible decisions must be taken, not necessarily on financial considerations alone. In the laboratory and workplace, sustainable water management practices need to be followed. For example, every liter of water used in the laboratory for various purposes goes through a series of purification processes, with losses at each step. A study⁶ showed that the loss can be as large as 75% when producing ultra-high purity water. Of course, water recovery and recycling may be practiced for wastewater. New science and technology are essential for efficient water management at the personal, institutional, and community levels.

Our research must find new ways to reduce water consumption in products, processes, and services. For instance, agricultural processes consume large amounts of water up to 70%–90% of the water resources on planet earth and new ways of efficient water management will be essential for humanity. Likewise, delivering fertilizers without runoff into bodies of water will reduce eutrophication. Precision pesticides and novel delivery mechanisms will reduce their load on water bodies and reduce their residues in agricultural produce.

Published: March 19, 2024



Efficient storage and transportation and reduced product loss at every stage will avoid excess cultivation, enhance profits, and make more quality time available with family and community. Much effort and advances are happening in each of the areas, and more are welcome.

For any ubiquitous substance, perceiving the importance of management is difficult—taps are kept open for longer periods than needed, and groundwater pumps run continuously causing paddy fields to flood. For the same reason, the use of solar pumps in the name of carbon credits poses a new risk for water resources.⁷ Therefore, the key to resource management is social awareness and responsibility. Coupled with it, technologies for rapid assessment of quality, quantity, and utilization along with strict enforcement are critical to ensure that water resources are not threatened. Creating credible, open access water data is necessary with advanced and affordable sensors and remote sensing, along with appropriate education and training. Academic institutions, through partnerships, can help build “People’s Water Data” by empowering human resources in any part of the world, taking advantage of digital education and access that was catapulted by the COVID-19 pandemic.⁸ Multi-institutional and transnational cooperations can build big data on water, and artificial intelligence can expand the scope that allows the prediction of the distribution of water resources and preventive measures necessary to ensure that the planetary boundaries are not breached.

ACS Sustainable Resource Management welcomes papers that are related to the management of this precious resource, our life-giving fluid. We look forward to receiving your manuscripts for publication and to serve you in advancing science for the benefit of humankind and disseminating your discoveries to our communities.

Thalappil Pradeep, Associate Editor, *ACS Sustainable Resource Management* orcid.org/0000-0003-3174-534X

Michael KC Tam, Deputy Editor, *ACS Sustainable Resource Management* orcid.org/0000-0002-7603-5635

Julio F. Serrano, Managing Editor, *ACS Sustainable Resource Management* orcid.org/0000-0002-7803-808X

AUTHOR INFORMATION

Complete contact information is available at:
<https://pubs.acs.org/10.1021/acssusresmgt.4c00096>

Notes

Views expressed in this editorial are those of the authors and not necessarily the views of the ACS.

REFERENCES

- (1) Water for Peace, 2024. *United Nations*. <https://www.un.org/en/observances/water-day> (accessed March 3, 2024).
- (2) Drinking-water, 2023. *World Health Organization*. <https://www.who.int/news-room/fact-sheets/detail/drinking-water> (accessed March 3, 2024).
- (3) Renewable internal freshwater resources, 2024. *The World Bank*. https://data.worldbank.org/indicator/ER.H2O.INTR.K3?most_recent_value_desc=true (accessed March 3, 2024).
- (4) Baggio, G.; Qadir, M.; Smakhtin, V. Freshwater availability status across countries for human and ecosystem needs. *Science of the Total Environment* 2021, 792, No. 148230.
- (5) Condron, A. Towing icebergs to arid regions to reduce water scarcity. *Sci. Rep.* 2023, 13, 356.

(6) Personal correspondence. Internal Report of the International Centre for Clean Water, Chennai, India, 2024.

(7) Balasubramanya, S.; Garrick, D.; Brozović, N.; Ringler, C.; Zaveri, E.; Rodella, A.-S.; Buisson, M.-C.; Schmitter, P.; Durga, N.; Kishore, A.; Minh, T. T.; Kafle, K.; Stifel, D.; Balasubramanya, S.; Chandra, A.; Hope, L. Risks from solar-powered groundwater irrigation. *Science* 2024, 383, 256–288.

(8) A course introduced by IIT Madras with Tel-Aviv University and KMCH Research Foundation. *NPTEL*. <https://elearn.nptel.ac.in/shop/iit-workshops/completed/water-quality-an-approach-to-peoples-water-data/>.

Reintroducing the INTRODUCTION: How to Write a Compelling Introduction for the ACS Sustainable Family of Journals

Cite This: *ACS Sustainable Chem. Eng.* 2024, 12, 8581–8583

Read Online

ACCESS

Metrics & More

Article Recommendations

In this editorial, we wish to share with the community some recommendations on the preparation of articles for submission to the ACS Sustainable family of journals. The ACS Sustainable family of journals, *ACS Sustainable Chemistry & Engineering (SCE)* and *ACS Sustainable Resource Management (SRM)*, are dedicated to publishing exciting, cutting-edge and high-quality research. As our readers and contributors will readily recognize, our journals provide a venue for sharing and discussing solutions to grand challenges of science and engineering while minimizing adverse impacts upon all planetary boundaries considered in the assessment of sustainability. Effective pursuit of this mission demands that our editorial teams periodically evaluate and refine the scope of our journals to embrace emerging topics, stimulate new ideas, and drive progress at the nexus of our core disciplinary strengths. This effort seeks to ensure that the ACS Sustainable family of journals remains a vibrant and leading forum to disseminate the latest discoveries and innovations in the constantly evolving fields of sustainable chemistry and engineering as well as resource management.

Our journals publish articles, letters, perspectives, and viewpoints on the discovery of novel molecules, materials, and/or processes. Published articles should clearly articulate how they significantly advance the state of the art in terms of understanding or insight and how they do so in a sustainable fashion. Simply claiming contribution or merit in the absence of substantiated benefits in sustainability must be avoided.

Toward this end, we offer guidance to prospective authors on a model that we feel promotes a well-crafted and scientifically balanced Introduction Section of a manuscript to be published in our ACS Sustainable journals. While we recognize that all parts of a manuscript must be meticulously prepared according to the respective journal guidelines, the introduction is an especially critical component to articulate the justification for publishing in our journal family. Readers, editors, and reviewers rely on the introduction to understand the context, novelty, significance, and scope of the work. The introduction also plays a key role in presenting the first impression and generating readers' interest in further exploring the article. Based on our collective experience as readers, editors, reviewers, and authors, we suggest a five-point structure for the introduction, presented in Figure 1, which effectively communicates the novelty and scope of the work and which is encountered in many of the most-cited articles

published in our journals. Fundamentally, this framework develops and reinforces a logical narrative able to highlight the presented research, while emphasizing its relevance to sustainability. It should be stressed that this framework is suggestive and shared here to provoke thought. As editors, we are open to alternative formats, as we fully recognize that each contribution is unique, and that diversity should be embraced and celebrated in every possible sense.

1. CONTEXT POSITIONING: WHERE ARE YOU?

Introductions typically start with a short preamble to provide broad context for the presented research. This is essential as our journals cover a vast space at the confluence of chemistry and engineering, exploring virtually all aspects of these disciplines through the sustainability lens. As such, our readership is broad in its interests and expertise. Authors must ensure that the research fits clearly within the published scope of the journal (*SCE* or *SRM*) to which the manuscript is being submitted. Authors are encouraged to set the scene for their research, anchoring it in contemporary societal, industrial, and/or scientific challenges. They should, however, be attentive to avoid elaborating on too many general concepts which are familiar to the readers. Instead, authors may cite key reviews in the field so that the interested readers can deepen their knowledge through accessing them.

2. STATE OF THE ART: WHAT WAS DONE?

Authors are expected to provide a succinct yet effective summary on the state of the art, which provides the necessary information for the readers to correctly understand *current* advances in the field. We expect authors to directly cite relevant literature, favoring original articles rather than reviews, being fair in pointing to relevant contributors in the field and refraining from excessive self-citation. Relevant literature includes seminal papers, especially for emerging fields, as well as appropriate examples of contemporary research. Published works using similar ideas or concepts must also be cited to

Published: May 31, 2024

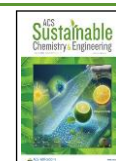




Figure 1. Proposed framework for introduction to articles published in the ACS Sustainable journals.

enable the knowledge gap discussion and proper novelty evaluation. Failure to cite important precedent literature could be interpreted as a breach of the ACS Ethical Guidelines to Publication of Chemical Research and is a reason for rejection without external review.

3. KNOWLEDGE GAP: WHAT IS MISSING?

Based on the state of the art, authors should articulate the limitations and challenges within existing literature. Of key importance is the requirement that the knowledge gap is framed in terms of significant advancements in sustainability. General qualitative characterizations such as “all past syntheses use large amounts of solvents, high temperatures, and extended reaction times” are not useful and should be replaced by more quantitative and precise assessments of the knowledge gap(s). To this end, we encourage the use of metrics, with relevant citations, as highlighted in the series of our prior editorials with guidance from our editorial team to our readers on this topic in diverse topical areas.^{1–6} Improvements should be clearly described, quantified, and compared to the most updated benchmark cases in the literature. For instance, if a certain synthesis always uses a toxic compound, the knowledge gap may be identification of a strategy to replace it with a more benign one. In another example, a specific process might have drawbacks because of the generation of waste, in which case the use of process mass intensity, the E-factor, or even just waste amounts could be useful to articulate the need for more research focusing on this. In this manner, authors should be able to identify knowledge gaps that their research addresses in a unique, clear, and concrete way.

4. ORIGINAL IDEA: WHAT DID YOU DO?

Usually, the original idea and implications (see point 5 below) of the work are summarized in the last paragraph of the introduction starting with a phrase such as “in this work”. As *SCE* and *SRM* are dedicated to publishing original ideas and new insights related to sustainable chemistry and engineering and resources management, articulating this point clearly assumes great importance. In this regard, an effective introduction to the state of the art and associated knowledge gaps (see points 2 and 3) should help authors make a strong case as to how their idea, approach, and solution are original, differ from past works, and represent a breakthrough in the field. It is important to remember that novelty here must be understood as being anchored in sustainability. Significant improvements in performance for any molecule, material, or process, where the sustainability aspect is not identified, do not meet the novelty threshold for *SCE* and *SRM*. It

must be noted that our journals are unable to publish either incremental advances, examples of which are noted in the cited previous editorials in our journals,⁷ or the mere juxtaposition of two already reported successful strategies.

5. IMPLICATIONS: WHY DOES IT MATTER?

Finally, it is good to end the introduction by stating the relevance and significance of the research. Based on the identified knowledge gap, authors can comment on how important their discovery or innovation is in the context of solving the identified problem.

In summary, points 1 through 5 describe the creation of an evidenced and logical argument that sets the scene for effective communication of new insight. The skeletal structure of the introduction can be augmented by the thoughtful addition of auxiliary content and comparative data sets that curate the discussion. As examples, authors are encouraged to consider summarizing past and present works in a concise table (that may be placed either in the main manuscript or in the Supporting Information). Tables should include topical performance data and whenever possible appropriate sustainability metrics which can be used to demonstrate progress or highlight opportunity. Similarly, the incorporation of a summary scheme that compares benchmark systems to newly proposed alternatives, while highlighting beneficial features, can be helpful to provide graphical support for discussion.

We would like to remind contributors to our journals that one of the tenets of Green Chemistry is the notion that a molecule, material, or process is never “green”, in the absolute sense of the term, but that it may be considered “greener”, when compared to what is already known. We suggest that, in the absence of comparative data, the inclusion of appropriate metrics or the presentation of an evidence-based narrative statement, the terms “clean”, “green”, or “sustainable” are avoided. In a similar sense, we also discourage the use of the terms “green” or “sustainable” in manuscript titles, as it is not a place conducive to the establishment of a comparative framework.

We hope that this suggested framework for constructing a compelling introduction is useful to the authors in articulating how their work incorporates the four foundational pillars of our journals, viz., *novelty*, *quality*, *scope*, and *metrics* (Figure 2).

In closing, we emphasize that a key differentiator associated with the ACS Sustainable family of journals (ACS Sustainable Chemistry & Engineering and ACS Sustainable Resource Management) remains our openly stated commitment to celebrate advances in sustainability



Figure 2. Four pillars of ACS Sustainable family of journals.

and highlight the realization of beneficial impacts which flow from papers that appear in our pages.

Audrey Moores, Executive Editor, *ACS Sustainable Chemistry & Engineering* orcid.org/0000-0003-1259-913X
 Jingwen Chen, Executive Editor, *ACS Sustainable Chemistry & Engineering* orcid.org/0000-0002-5756-3336
 Bala Subramaniam, Executive Editor, *ACS Sustainable Chemistry & Engineering* orcid.org/0000-0001-5361-1954
 Michael KC Tam, Deputy Editor, *ACS Sustainable Resource Management* orcid.org/0000-0002-7603-5635
 Elizabeth J. Biddinger, Associate Editor, *ACS Sustainable Chemistry & Engineering* orcid.org/0000-0003-3616-1108
 Dean Brady, Associate Editor, *ACS Sustainable Chemistry & Engineering* orcid.org/0000-0002-4815-1030
 Danielle Julie Carrier, Associate Editor, *ACS Sustainable Chemistry & Engineering* orcid.org/0000-0003-3322-4660
 Ivet Ferrer, Associate Editor, *ACS Sustainable Resource Management* orcid.org/0000-0002-4568-4843
 Nicholas Gathergood, Associate Editor, *ACS Sustainable Chemistry & Engineering* orcid.org/0000-0002-9398-9799
 Hongxian Han, Associate Editor, *ACS Sustainable Chemistry & Engineering* orcid.org/0000-0002-2522-1817
 Ive Hermans, Associate Editor, *ACS Sustainable Chemistry & Engineering* orcid.org/0000-0001-6228-9928
 King Kuok Mimi Hii, Associate Editor, *ACS Sustainable Chemistry & Engineering* orcid.org/0000-0002-1163-0505
 Bing Joe Hwang, Associate Editor, *ACS Sustainable Chemistry & Engineering* orcid.org/0000-0002-3873-2149
 Milad Kamkar, Topic Editor, *ACS Sustainable Resource Management* orcid.org/0000-0002-6822-7370
 Kevin Leonard, Associate Editor, *ACS Sustainable Chemistry & Engineering* orcid.org/0000-0002-0172-3150
 Watson Loh, Associate Editor, *ACS Sustainable Chemistry & Engineering* orcid.org/0000-0002-8049-3321
 Say Chye Joachim Loo, Associate Editor, *ACS Sustainable Resource Management* orcid.org/0000-0001-5300-1275
 Andrew C. Marr, Associate Editor, *ACS Sustainable Chemistry & Engineering* orcid.org/0000-0001-6798-0582
 Michael A.R. Meier, Associate Editor, *ACS Sustainable Chemistry & Engineering* orcid.org/0000-0002-4448-5279
 Ryuhei Nakamura, Associate Editor, *ACS Sustainable Chemistry & Engineering* orcid.org/0000-0003-0743-8534
 Graham N. Newton, Associate Editor, *ACS Sustainable Chemistry & Engineering* orcid.org/0000-0003-2246-4466
 Thalappil Pradeep, Associate Editor, *ACS Sustainable Resource Management* orcid.org/0000-0003-3174-534X
 Kotaro Satoh, Associate Editor, *ACS Sustainable Chemistry & Engineering* orcid.org/0000-0002-3105-4592
 Wil V. Srubar, III, Associate Editor, *ACS Sustainable Chemistry & Engineering* orcid.org/0000-0001-8226-2458
 Ning Yan, Associate Editor, *ACS Sustainable Chemistry & Engineering* orcid.org/0000-0003-3371-1709
 Asha James, Development Editor
 Mihir Jha, Development Editor
 Atal Shivhare, Development Editor

Julio F. Serrano, Managing Editor orcid.org/0000-0002-7803-808X

Peter Licence, Editor-in-Chief orcid.org/0000-0003-2992-0153

AUTHOR INFORMATION

Complete contact information is available at:
<https://pubs.acs.org/10.1021/acssuschemeng.4c04252>

Notes

Views expressed in this editorial are those of the authors and not necessarily the views of the ACS.

REFERENCES

- (1) Allen, D. T.; Carrier, D. J.; Gong, J.; Hwang, B.-J.; Licence, P.; Moores, A.; Pradeep, T.; Sels, B.; Subramaniam, B.; Tam, M. K. C.; Zhang, L.; Williams, R. M. Advancing the Use of Sustainability Metrics in ACS Sustainable Chemistry & Engineering. *ACS Sustainable Chem. Eng.* 2018, 6, 1.
- (2) Diorazio, L. J.; Richardson, P.; Sneddon, H. F.; Moores, A.; Briddell, C.; Martinez, I. Making Sustainability Assessment Accessible: Tools Developed by the ACS Green Chemistry Institute Pharmaceutical Roundtable. *ACS Sustainable Chem. Eng.* 2021, 9, 16862.
- (3) Vilaplana, F.; Ventura, S. P. M.; Sudarsanam, P.; Abdoulmoumine, N.; Carrier, D. J. Effective Assessment Practices for Using Sustainability Metrics: Biomass Processing. *ACS Sustainable Chem. Eng.* 2021, 9, 14654.
- (4) Meier, M. A. R.; Tam, M. K. C. Shaping Effective Practices for Incorporating Sustainability Assessment in Manuscripts Submitted to ACS Sustainable Chemistry & Engineering: Biomaterials. *ACS Sustainable Chem. Eng.* 2021, 9, 7400.
- (5) Debecker, D. P.; Kuok (Mimi) Hii, K.; Moores, A.; Rossi, L. M.; Sels, B.; Allen, D. T.; Subramaniam, B. Shaping Effective Practices for Incorporating Sustainability Assessment in Manuscripts Submitted to ACS Sustainable Chemistry & Engineering: Catalysis and Catalytic Processes. *ACS Sustainable Chem. Eng.* 2021, 9, 4936.
- (6) Subramaniam, B.; Licence, P.; Moores, A.; Allen, D. T. Shaping Effective Practices for Incorporating Sustainability Assessment in Manuscripts Submitted to ACS Sustainable Chemistry & Engineering: An Initiative by the Editors. *ACS Sustainable Chem. Eng.* 2021, 9, 3977.
- (7) Allen, D. T.; Carrier, D. J.; Gong, J.; Gathergood, N.; Han, H.; Hwang, B.-J.; Licence, P.; Meier, M.; Moores, A.; Pradeep, T.; Qiu, J.; Sels, B.; Subramaniam, B.; Tam, M. K. C.; Zhang, L.; Williams, R. M. Why Wasn't My ACS Sustainable Chemistry & Engineering Manuscript Sent Out for Review? *ACS Sustainable Chem. Eng.* 2019, 7, 1.

Fireside Chat with Man Mohan Sharma: Catalysis for Sustainability

Milad Kamkar,* Thalappil Pradeep, and Julio F. Serrano,

Cite This: *ACS Sustainable Resour. Manage.* 2024, 1, 2514–2517

Read Online

ACCESS

Metrics & More

Article Recommendations

KEYWORDS: Sustainability, Catalysis, Resource Management, Bioresource Valorization, Waste Management

Prof. Man Mohan Sharma, popularly known as M. M. Sharma, is a doyen of chemical engineering. He is one of the most successful chemical engineers of our time who elegantly balances multiple roles; a teacher of lasting influence, an impactful researcher, a much sought-after consultant, and someone who synthesizes encyclopedic data. He has influenced the path of resource management in chemical industry and therefore has a comprehensive view of the diverse issues facing the planet. We sat down to talk to him on his views of catalysis and its importance on sustainable chemical processes and resource management. M. M. Sharma shared his academic background and research contributions in chemical engineering, emphasizing his self-motivated pursuit of the field and his significant contributions to carbon dioxide (CO₂) absorption and reduction of energy consumption in chemical processes. He also discussed the importance of catalysis in achieving sustainability in various industries and potential solutions to the CO₂ crisis, including transitioning to nonfossil, renewable energy sources, and exploiting agro-waste. The conversation ended with a discussion on the extensive use of electricity in modern society and the need for sustainability and reducing demands for better living standards.

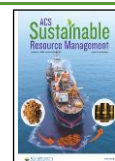
Editor: The first question focuses on your background. Could you provide a brief overview of your academic journey and research interests? In a recent article published in *I&ECR*,¹ you were described as a “knowledge and action seeker par excellence”. It is clear that your work has contributed significantly to advancing chemical technology. Could you also share your thoughts on the evolution of chemical engineering as a discipline and its critical role in nation building?

M. M. Sharma: Well, I was born in 1937 and grew up in the desert city of Jodhpur (Rajasthan), the city which created polo as a game. Although my town had an engineering college that offered different disciplines such as civil engineering, I was driven by a different passion. My interest in chemistry and mathematics naturally guided me towards chemical engineering, even though I had no formal guidance. It was a self-motivated decision, driven by a desire to apply these subjects in a practical way. At the time, in contrast to electrical, mechanical, and civil engineering, chemical engineering was an unknown or unfamiliar discipline to many in India. My

grandfather kept on asking me: What is this branch that you are studying?

Thus, in 1954, when I was 17, I came to Bombay to study chemical engineering. Interestingly, by the time I graduated with a bachelor's degree, jobs were available in chemical engineering, and one could have multiple job offers even before graduation. However, I was bent upon doing research, so I did not appear for a single interview to sway my decision. Although I could not pursue a Ph.D., I was lucky to get a full scholarship to go to Cambridge in England to work with Danckwerts. Afterwards, in 1961 to 1964, I did my Ph.D. in Cambridge. In the first year of my Ph.D. career, I had done enough work to earn my degree. I was the first one to show that the existing amines at that time were too slow in absorption processes, and there were much faster reacting amines, which can bring down the size of absorption columns. We also published a monograph² to show how we can complete a process design of a large absorption column for CO₂ removal from first principles. This was validated in practical industrial processes. At the same time, to reduce the energy consumption in desorption, we propounded the idea of using hindered amines which later, Exxon picked up. In line with these ideas, in recent years, innumerable papers have been published on the efficiency and performance of different amines. I also worked on carbonyl sulfide which had an excellent potential to be implemented in industry. My supervisor had strong industry connections, and through his support, Shell approached me with interest in my work. They took a preliminary patent on my idea, and I was paid handsomely for the rights to it. This marked a significant milestone, as it was the first time in the history of chemical engineering at Cambridge that something had been patented and sold for commercial use. It was a pivotal moment that not only validated my research but also demonstrated the practical, real-world impact of chemical engineering innovations. This is

Published: December 11, 2024



just before I left Cambridge to come back to teach in ICT Mumbai, although I knew there was no money in there for research in those days. Thus, I decided to conduct idea-oriented research. Our first breakthrough came when we devised a method of measuring interfacial area in any liquid–liquid system by chemical methods. Although, the Dutch people were doing lots of work on this, they could not succeed in it then. This indeed brought us international fame. And then we did the microphase work, in which we studied how particles smaller than diffusion film thickness can make a world of difference.³ We called them microphases. And one process studied had something to do with flue gas desulfurization. Here, we found that when the particle size becomes smaller than diffusion-film thickness, the rate of absorption goes up markedly.

That was some of our works in my early career, with no funding from any agency. We then created a *mantra* in our institution: that is, our priority is teaching, there is absolutely no compromise on it, ever. Then, we had to conduct high quality research and publish papers in renowned journals. At this point, I became an editor of the *Journal of Chemical Engineering Science*. And finally, we had to initiate interactions with industry to make a difference in applied science. Afterwards, our people became consultants to industry, which created a live pipeline for our graduate students to be employed. Before this, there was no culture of hiring Ph.D. graduates in chemical industry. Thus, we created that culture of how Ph.D. graduates can contribute to the growth of chemical industry in India. All in all, my journey has brought me various honors and awards, including the distinction of being the first engineer from India in history to be named a Fellow of the Royal Society in 1990.

Editor: Great! You have a very interesting background. I am sure you have more to say. Let's move to the next topic, which is about the relationship between catalysis and sustainability. Every large-scale chemical process is driven by catalysis. Examples include petroleum refining and polymerization reactions. In the era of sustainability, valorization of natural products is made possible, for example, by catalysis. In your view, what is the role of catalysis in sustainable resource management?

M. M. Sharma: Let me start by giving you a very classic example, that is, how to remove hydrogen sulfide (H₂S) from natural gas. If you remember in Middle Eastern countries such as Iran, they used to flare. Today all the sulfur used in industry is recovered sulfur and not mined sulfur. Today, mining sulfur is no longer a primary method of obtaining it, even though sulfur mines still exist in different parts of the world. If these mines were to be exhausted, we would still have a significant supply of sulfur through modern processes. Currently, by processing around 4 billion tons of crude oil annually and an additional 1.5 billion tons of natural gas, we can recover substantial amounts of sulfur. This sulfur comes from H₂S captured during natural gas processing and through hydrodesulfurization in oil refining.

I want to quote this as a classic example of sustainability. The entire sulfur today is from recovered sulfur, which was otherwise burned and created environmental problems. Now, hydrodesulfurization is a breakthrough in the history of catalysis because one could have a feed, for example, for diesel with sulfur content anywhere from 0.25 to 1%. But the exit had as low as 50 ppm, in a single reactor. This is both the wonder of catalysis and reaction engineering. Now, hasn't this

made processes sustainable because you now get gasoline as well as diesel almost completely free from sulfur? So, when you burn, there is no SO₂ emission from cars and from trucks.

With the help of catalysis, sustainability has been greatly advanced by reducing emissions from gasoline-powered vehicles. If you look at the impact of automobile exhaust catalysts, it is remarkable how effective these have been. Today, with the honeycomb catalyst technology made from noble metals, we see virtually no emissions of unburned hydrocarbons. All the exhaust gases are efficiently treated before being released, demonstrating how catalysis has played a crucial role in enhancing sustainability. But for catalysis, how could you have gotten H₂S conversion to sulfur almost at vanishing levels?

In Canada, there are several natural gas fields which have up to 20% H₂S, and even more in some other fields. These wells used to be sealed. But today they are utilized as it has been made possible to make sulfur from these resources, thanks to catalysis technology. These days, catalysis also plays a crucial role in removing and converting CO₂. Another example is hydrogenation. Currently, no hydrogenation process exists without a catalyst, as hydrogen must be activated. Another example is the conversion of ethylene to ethylene oxide which was only 65% efficient during its start in 1930. Science and practice of catalysis has made this an extraordinary process with 85% efficiency. Thus, the amount of CO₂ that is released in this process has come down drastically.

Editor: In your view, what catalysts have the greatest potential in addressing the carbon dioxide crisis? Should we be investing more into transformation or capture?

M. M. Sharma: Capture is a necessity. Let me give you my very strong view on this subject. Indeed, too much hype is being made for converting CO₂ to chemicals. If we are emitting ~40 billion tons of CO₂ by burning fossil fuels, coal, and hydrocarbons, there is no way this amount can be converted to chemicals—only a minute fraction of it can be. The maximum amount of chemicals being made is 350 million tons per year. Indeed, catalysis play a big role in converting CO₂ to ethylene, methanol, dimethyl ether, etc. However, the total amount of CO₂ that is needed to make chemicals is roughly 500 million tons per annum. Indeed, the most viable solution to address the environmental challenges caused by CO₂ is to use clean and renewable energies. However, due to the intermittency of renewable energy sources like wind and solar, maintaining a consistent power supply and backing up fossil fuel-based power stations remain a challenge. As a result, currently, the continued utilization of fossil fuels is indispensable. Therefore, avoiding the emission of ~40 billion tons of CO₂ annually is, unfortunately, inevitable. As I mentioned, CO₂ conversion is not the solution to the problem. However, one area that is very encouraging, and is about to be industrialized, thanks to the pilot plants in BASF, is dry reforming of methane. Instead of mixing methane and steam, it is reformed with CO₂ in this process. In this process, CH₄ plus CO₂ will produce CO and hydrogen. But still, the problem exists, that is, the production ~40 billion tons of CO₂. China alone burns about 2 billion tons of coal per annum, and there is still thermal power stations based on coal and hydrocarbons everywhere, including in the USA. Even if we replace coal with methane burning, production of CO₂ cannot be avoided. Indeed, like SO₂ and H₂S, there has been excellent advancement in the removal of CO₂. But, where are we going to use this huge amount of collected CO₂?

The other challenge is the cost of hydrogen. None of the CO₂ conversion process can become economically viable unless the cost of hydrogen decreases drastically. Indeed, production of chemicals from agro-waste is also possible. Even fuel production for automobiles from agro-waste is possible. But, at a heavy cost! Thus, CO₂ conversion with the aid of catalysis, much like many other processes, is possible, however, at a high price. Still, the maximum utilization of renewable and nuclear energies is the most viable solution to address the challenges caused by CO₂ emissions.

Editor: What do you see as the key focal themes that industries should prioritize to enhance sustainability and resource management?

M. M. Sharma: Valorization of agro-waste. No crop is possible without lignin, which is a phenolic substance. Millions of tons of lignin are potentially available from sources such as sugar cane and corn. Sucrose, another example, is available at a very low cost—around 40 cents per kilogram—and serves as a multifunctional feedstock. Therefore, the valorization of agricultural waste and its conversion to chemicals, such as ethanol, should be a priority for sustainable resource utilization. Cellulose can be also converted to fermentable sugars, and then, it is converted into different chemicals. Via fermentation technology, ethanol, acetone, isopropanol, etc. can be produced. However, still costs and agro-waste collection costs pose a significant challenge. For instance, millions of tons of polyethylene are needed each year. Production of this amount via utilization of hydrocarbons, as they exist in massive quantity in one single location, is drastically more cost effective compared to production of the same amount from agro-waste or other renewable resources in different locations.

Yet, there will be agro-waste as long as we need food. Agro-waste also exists naturally, such as leaves collected during autumn in countries such as Canada, that can be used as raw materials. For instance, Don Scot in Waterloo did a lot of work on the pyrolysis of agricultural waste collected during autumn, as one of the early persons.⁴ All in all, we need to focus more on valorization of raw materials, such as lignin and cellulose, derived from plants and agro-waste. Indeed, with today's knowledge, we can convert agro-waste into any desired materials.

Editor: Do you have any advice to young researchers in this area?

M. M. Sharma: As I mentioned, there are unlimited options in valorizing the agro-waste. In this regard, functionalization is not easy—similarly, defunctionalization is also a challenge. For instance, novel enzymes and directed evolution are needed. Indeed, more research is required to effectively valorize agro-waste and address challenges in this field. For instance, lignin features different chemical and physical properties based on the feedstocks; i.e., lignin from corn is different compared to lignin from sugar cane. If the petroleum industry can develop harmonious catalytic cracking processes for sophisticated advancements, there is no reason we wouldn't be able to apply catalytic cracking of lignin. This would require extensive research and the development of new catalysts, which should be done by our young scientists.

Editor: Lastly, the greed of humanity is the reason for the current climate crisis; in your view, do we have enough for everyone on the planet to enjoy the western way of life? And what can catalysis do to enable that life with sustainability?

M. M. Sharma: What is not in the hand of catalysis is extensive production of electrical power. Everybody wants air

conditioners, heaters, and a comfortable life. If we really want to sustainably manage our cities, we must find better ways of heating and cooling. In India, and other countries with a dry climate, such as Iran, there is a quantum jump in the consumption of power in summertime. The bulk of the supplied energy is based on fossil fuels. Thus, if we want to discipline ourselves, we must reduce our demands. Unfortunately, people are generally not willing to do so. Society consistently seeks a higher standard of living. We want to wash our garments very quickly. We want to use fashionable materials. We want to use more clothes than we need. Finally, they all get linked to the production of them. Then comes the question, what do you do with the utilization of all the waste we generate constantly? What do you do with the shirts and trousers made of polyester? I believe a circular economy aided with catalysis to enhance the chemical processes is crucial to keep the planet under control.

M. M. Sharma: In closing, I complement the journals *ACS Sustainable Resource Management* and *ACS Sustainable Chemistry & Engineering*, the latter I regularly follow. And now that you have this new journal, I have started following it. Thanks!

AUTHOR INFORMATION

Corresponding Author

Milad Kamkar, Topic Editor, *ACS Sustainable Resource Management*; orcid.org/0000-0002-6822-7370

Authors

Thalappil Pradeep, Associate Editor, *ACS Sustainable Resource Management*; orcid.org/0000-0003-3174-534X

Julio F. Serrano, Managing Editor; orcid.org/0000-0002-7803-808X

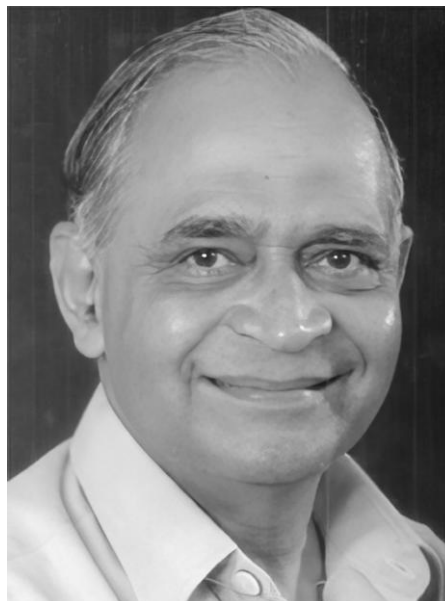
Complete contact information is available at:
<https://pubs.acs.org/10.1021/acssusresmgmt.4c00502>

Notes

Views expressed in this viewpoint are those of the authors and not necessarily the views of the ACS.

The authors declare no competing financial interest.

Biography



Man Mohan Sharma. I received my education in Jodhpur, Mumbai, and Cambridge, England. I was appointed as Professor of Chemical Engineering at the University Department of Chemical Technology, Mumbai University, just at the age of 27 years, in 1964. I got many honors and accolades which include the S. S. Bhatnagar prize in Engineering Sciences in 1973. I became a fellow of the INSA in 1976 and was President during 1989–1990. I have received from the President of India the second highest civilian award of Padma Vibhushan in 2001. I became the first engineer from India in 350 years of the Royal Society to become a Fellow, which I consider as my highest honor.

REFERENCES

- (1) Yadav, G. D. *Ind. Eng. Chem. Res.* 2007, *46*, 2911–2916.
- (2) Sharma, M. M.; Danckwerts, P. V. *Chem. Eng. Sci.* 1963, *18*, 729–735.
- (3) Ramachandran, P. A.; Sharma, M. M. *Chem. Eng. Sci.* 1969, *24*, 1681–1686.
- (4) Scott, D. S. *Fast pyrolysis of waste materials*. <https://publications.gc.ca/site/eng/9.611579/publication.html>.

Patents

Indian patents (Granted)

1. Synthesis of protein protected luminescent metal clusters and retaining the bioactivity of the protein, Pradeep, Debasmita Ghosh, Mohammad Bodiuzzaman, Anirban Som, Ananya Baksi, Atanu Ghosh, and Jyotirmoy Ghosh, application no. 201841049925, dated December 31, 2018, issued as patent no. 495343, issued on January 5, 2024.
2. A method of detection of low concentration of analytes by superhydrophobic pre-concentration paper spray ionization mass spectrometry (SHPPSI MS), T. Pradeep, Pallab Basuri, Avijit Baidya and Tripti Ahuja, application no. 201741047403, dated December 30, 2017, issued as patent no. 504588, issued on January 31, 2024.
3. A smartphone based fluoride-specific sensor for rapid and affordable colorimetric detection and precise quantification at sub-ppm levels for field applications, Thalappil Pradeep, Sritama Mukerjee, Manav Shaw and Kamalesh Choudhuri, application no. Pradeep Research Group 10 Annual Report 2024 202041026054, dated June 20, 2020, issued as patent no. 536268, issued on April 30, 2024.
4. A method to transform crystalline minerals to nanoparticles by microdroplets, T. Pradeep, B. K. Spoorthi and Pallab Basuri, application no. 202241038282, dated July 7, 2022, issued as patent no. 539562, issued on May 28, 2024.

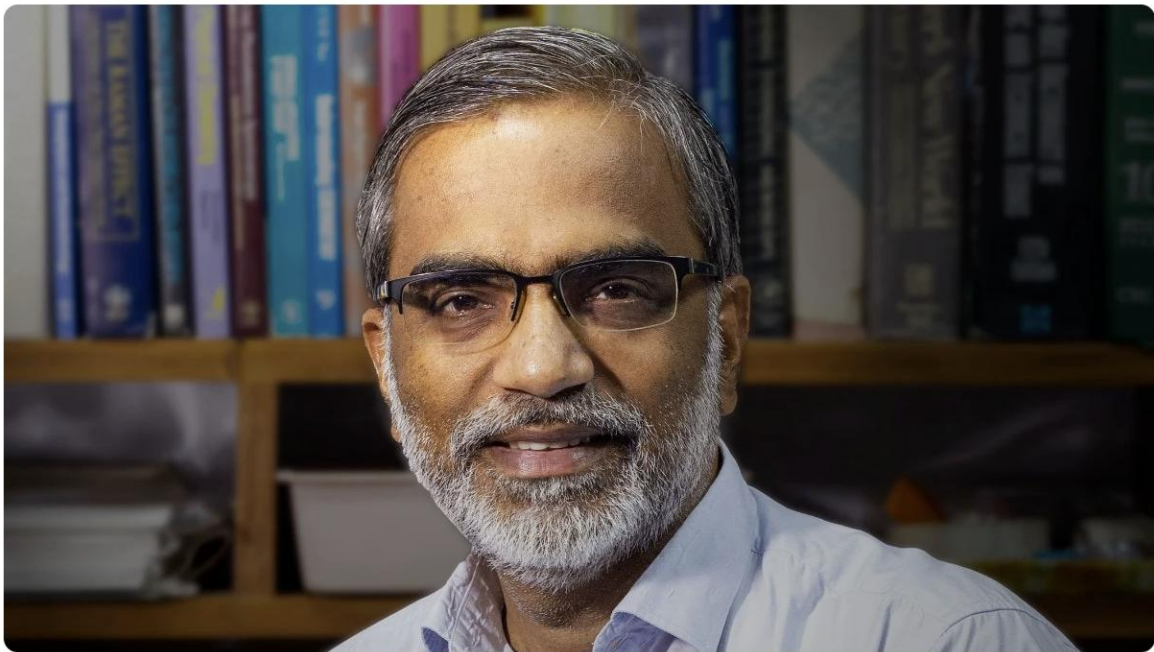
Patents Applied

1. Method of preparing assembled spheroids of copper nanoclusters for ultra-trace arsenic detection, Thalappil Pradeep, Tiju Thomas, Jenifer Shantha Kumar and Arijit Jana, application no. 202441041750, dated May 29, 2024.
2. Method of making nanoparticles from natural minerals in high-pressure water jets, T. Pradeep and B. K. Spoorthi, application no. 202441041814, dated May 29, 2024.
3. Electrospray deposited anisotropic alloy catalysis for efficient nitrate reduction in wastewater, Thalappil Pradeep, Aswathi K. S., Depanjan Sarkar, Keerthana Unni, Sourav Kanti Jana, Anirban Som, Soham Chowdhury, Sinchan Mukhopadhyay, application no. 202441104803, dated December 31, 2024.
4. A method of efficient transformation of crystalline minerals to nanoparticles by salt-containing microdroplets, Thalappil Pradeep, Jamshiyah Sulthana P, Anubhav Mahapatra, B. K. Spoorthi, Depanjan Sarkar, application no. 202441104922, dated December 31, 2024.

PCT Applied

1. Material and method for sustainable and affordable atmospheric water harvesting, Thalappil Pradeep; Ankit Nagar; Sonali Seth, application no. WO2024047666 A1, dated March 7, 2024.
2. Vertically aligned nanoplates of atomically precise Co₆S₈ cluster for practical arsenic sensing, T. Pradeep, Anagha Jose, Arijit Jana, Tanvi Gupte, Keerthana Unni, Ankit Nagar, Amoghavarsha R. Kini, B. K. Spoorthi, application no. WO2024142079 A1, dated April 7, 2024.

News reports (selected)



Indian professor at IIT Madras elected to National Academy of Engineering, US



India Today Education Desk

New Delhi, UPDATED: Feb 15, 2024 12:16 IST
Written By: Divya Chopra

Indian Institute of Technology Madras (IIT Madras) faculty Professor Thalappil Pradeep has become the 23rd foreign member from India to be elected to the United States National Academy of Engineering (NAE).

He was elected for his contributions to cluster chemistry and the discovery and implementation of affordable drinking water solutions. He will be formally inducted during the NAE's annual meeting on September 29, 2024.

NATIONAL ACADEMY OF ENGINEERING

Founded in 1964, the NAE is an independent institution that provides engineering leadership. It has more than 2,000 peer-elected members and international members, senior professionals in business, academia, and government who are among the world's most accomplished engineers. They provide the leadership and expertise for numerous projects focused on the relationships between engineering, technology, and the quality of life.

Election to the NAE is among the highest professional distinctions accorded to an engineer. Academy membership honours those who have made outstanding contributions to "engineering research, practice, or education, including, where appropriate, significant contributions to the engineering literature" and to "the pioneering of new and developing fields of technology, making major advancements in traditional fields of engineering, or developing/implementing innovative approaches to engineering education."

Accepting this honour, Professor T Pradeep, Institute Professor, Department of Chemistry, IIT Madras, said, "I am humbled by this recognition, which is a result of the hard work of my team. I could reach this far only because of the tremendous support my institution and my nation. This fellowship once again reaffirms my belief in the interdisciplinary nature of science."

Professor Pradeep works on diverse aspects of materials and has won many national recognitions including the Padma Shri and the Shanti Swarup Bhatnagar Prize. He has won coveted international recognitions such as the Eni Award, VinFuture Prize and Prince Sultan Bin Abdulaziz International Prize for Water. He has built advanced scientific instruments for his work. He has 550 papers and over 100 patents to his credit besides being a co-founder of half a dozen companies.

Professor Pradeep is a pioneer in nanotechnology applications for clear water. His work on pesticide removal has benefitted millions of people. Later, he and his team developed 'water-positive' materials to remove arsenic, uranium and several other toxic contaminants from water and the technology has been approved for national implementation. He is expanding the reach of these technologies to other countries now. ■

Published By: Divya Chopra

Published On: Feb 15, 2024

THE TIMES OF INDIA

Padmaja J / TNN / Updated: Jan 11, 2024, 08:03 IST

IIT-M unveils hybrid course to increase water literacy

Padmaja.J@timesgroup.com

Chennai: In order to create water-literate citizens, IIT Madras has unveiled a hybrid four-month certificate course — Water Quality — An Approach to People's Water Data.

Apart from teaching students, this course will help create a database of ground, surface and piped water quality, said T Pradeep, chemistry professor with IIT-M and one of the five instructors of the course. The institute has partnered with Tel Aviv University in Israel for the course.

As a pilot project, IIT Madras trained students of Stella Maris College, Madras Christian College and some students from Erode. It tested the water quality in 300 houses in Chennai and Erode and uploaded the data online. "Major findings from the previous exercise were that people were unaware about water quality and they believed that water from reverse osmosis is pure," said Prof Pradeep.

Now, IIT-M has launched



WATER QUALITY TESTED IN 300 HOUSEHOLDS

this course to expand the initiative. Theory classes will be conducted online and offline about water quality and its impact on human health. The offline practicals involve each student picking 10 houses and testing water quality, including measuring the pH, hardness, coliform, nitrate, chloride etc.

"This course is a deep-dive on water quality. Also, the course will generate water data. If we have 150 students, we will get 1,500 water sample data," said Pradeep.

T Swaminathan, former professor of chemical engineer-

ing professor at IIT-M, suggested that the course could involve how different organisms, apart from humans, are affected by water quality.

Students can have a certificate from IIT-M on water quality, which will add to their resumes, and they can apply to water or food testing centres, shared Pradeep.

The course will entail a fee of ₹1,500, which will be refunded after course completion. The fee will also include field test kits. For practicals, the students will be assigned the closest colleges or labs, said Prof Pradeep.

"The course can pick cities like Chennai, Trichy and Coimbatore for offline practicals," said Swaminathan.

Minimum eligibility for the course is final year of bachelors of science or engineering. The registration forms are on the NPTEL website and the last date to register is January 18. Classes will begin from January 22, on Mondays, Tuesdays and Wednesdays, between 5pm and 5.50pm.

IIT Chennai launches groundbreaking wastewater-based epidemiology project

Led by a team of distinguished researchers at IIT Chennai, this pioneering initiative seeks to revolutionize community health through a data-driven preventive healthcare approach using wastewater surveillance.

Written by [FE Science](#)

Updated: January 17, 2024 02:49 IST



'Blockchain for Impact' (BFI), a global social impact organization dedicated to utilizing technology for innovative solutions in healthcare, has joined forces with the Indian Institute of Technology, Chennai (IIT Chennai), to launch a groundbreaking Wastewater-Based Epidemiology (WBE) project. The collaboration, announced, involves a generous donation of USD 1 Million from BFI to IIT Chennai, aimed at acquiring advanced research technology and ensuring the efficient operation of the WBE study for the next two years.

Led by a team of distinguished researchers at IIT Chennai, this pioneering initiative seeks to revolutionize community health through a data-driven preventive healthcare approach using wastewater surveillance. The project's significance lies in its potential to identify health risk patterns and provide timely alerts, thereby contributing to a proactive healthcare system.

CEO Dr. Gaurav Singh's Perspective

Dr. Gaurav Singh, CEO of 'Blockchain For Impact,' expressed his enthusiasm for the collaboration, stating, "Under the banner of 'Blockchain for Impact,' we aim to act as catalysts, collaborating with partners to forge multi-sectoral alliances that deliver long-term, equitable medical preparedness mechanisms. Our collaboration with IIT Chennai for the wastewater epidemiology study is a step in the same direction. We are confident that this collaborative effort will foster innovation, drive positive change, and create a lasting impact on communities, aligning with our broader mission."

State-of-the-Art Technology for Research

The cornerstone of this endeavour is the installation of the Thermo Scientific Q Exactive™ Plus Hybrid Quadrupole-Orbitrap™ Mass Spectrometer at the IIT Chennai campus. This highly sensitive instrument will facilitate comprehensive surveys of wastewater samples, measuring chemical and biological molecules across the IIT Chennai campus and various locations in Chennai City.

Professor T. Pradeep's Research Initiative

Professor T. Pradeep, Professor of Chemistry at IIT Chennai, shared insights into the research initiative, emphasizing its objective to understand the prevalence of circulating viruses and Antimicrobial Resistance (AMR). The project initially focuses on universities, colleges, airports, hospitals, and targeted residential communities, gradually expanding to city and state-level wastewater sample collection.

Free-Access Online Dashboard for Data Sharing

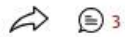
IIT Chennai plans to share health-related data with sampled communities through a free-access online dashboard. The preliminary version displays the prevalence of hazardous Viral and Bacterial presence in wastewater samples from across the IIT Chennai campus, including the capacity to identify the SARS-CoV-2 virus. Future enhancements will involve additional PIN CODES and public health-related parameters.

‘Outstanding work’: IIT-M team makes mineral nanoparticles with water PREMIUM

Infusing soil with silica nanoparticles made using the technique could transform agriculture

Updated - July 21, 2024 04:24 pm IST - Chennai

KARTHIK VINOD



 READ LATER  PRINT



B.K. Spoorthi, who just completed her PhD at IIT Madras, looking at an experiment in progress. | Photo Credit: IIT Madras

Updated - July 21, 2024 04:24 pm IST - Chennai

KARTHIK VINOD

‘Outstanding work’: IIT-M team makes mineral nanoparticles with water

In an important finding independent scientists called a ‘striking and non-intuitive result’, researchers used really small water droplets to blow up minerals suspended in them into nanoparticles. The underlying science has implications for many things from the origin of life to replenishing soils for farming

Karthik Vinod

Water drops are ubiquitous around us and come in different sizes. They can be as large as a raindrop or as small as aerosol particles released from a spray can.

They can be even smaller – invisible to the naked eye – when they come as microdroplets. The latter are just a thousandth the size of a typical raindrop.

“We think that droplets are very tiny, and they are not important enough,” Thalappil Pradeep, a chemist at IIT Madras, told *The Hindu*.

But they can pack a punch.

Dr. Pradeep led a study recently published in the journal *Science* that showed microdroplets of water can break minerals down into nanoparticles. The team involved researchers from IIT Madras and the Jawaharlal Nehru Centre for Advanced Studies, Bengaluru.

“This outstanding work adds significantly to the growing body of evidence that water droplets enable chemical transformations that bulk water does not make possible,” Richard Zare, a chemist at Stanford University who wasn’t involved in the study, told *The Hindu*.

Eccentricity of water microdroplets

In a bucket of water, water molecules at the surface can participate more easily in chemical reactions than those in the bulk. But even at the surface, they’ll need to be supplied with some energy before they can participate. The water molecules of microdroplets do one better: because they have so little room and are packed closely together, they’re more eager to participate in chemical reactions.

The water in microdroplets thus engages more readily in exotic chemical reactions that also proceed faster, up to a million-times in some cases. This isn’t possible with water molecules in bulk.

For the same reason, microdroplets are also good carriers of electric charge. Dr. Pradeep said they’re easy to encounter in this form. Go to the beach, and close to the shore, microdroplets from the spray of water could carry an excess of ions from the salt in the water and settle on your skin, he said.

A microdroplet can also become electrically charged in other ways. For example, when a larger droplet loses some water by evaporation and shrinks, the water molecules left behind are pushed closer together, and establish (weak) hydrogen bonds between themselves. This often results in a water molecule shedding one of its hydrogen atoms and becomes a negatively charged hydroxyl ion (OH⁻). The freed H⁺ is



B.K. Spoorthi, who just completed her PhD at IIT Madras, observing an experiment in progress. IIT MADRAS

essentially a proton.

This process happens in bulk water as well – but because each molecule is surrounded by other water molecules, the protons can’t move around much. In microdroplets, the protons easily reach the surface, rendering the surface more acidic and creating fertile ground for chemical reactions.

Researchers have shown that amino acids use free protons on their surfaces as an intermediary to form peptide linkages.

The new study reported microdroplets have yet another ability.

An explosive experiment

Dr. Pradeep & co. were interested in whether water microdroplets could break bonds in crystals like silica (SiO₂) and alumina (Al₂O₃) to create nanometre-sized pieces.

Spoorthi Bhat, then a PhD student under Dr. Pradeep and one of the paper’s coauthors, set up an experiment to confirm this hypothesis in crystals of quartz (silica), ruby, and fused alumina.

She pressed a battery terminal against the outside of a capillary tube. The terminal delivered a few thousand volts to mineral nanoparticles suspended in water inside the tube. The voltage elongated the suspension, squeezing it out of one end, and sending it flying through the air as a mist of microdroplets. They were still airborne when, in just 10 milliseconds, the mineral nanoparticles broke up into nanoparticles.

The researchers had a few ideas about



Water drops can be invisible to the naked eye when they come as microdroplets. The latter are just a thousandth the size of a typical raindrop

what could have caused this break up. The free protons could have squeezed themselves into crystal layers, which they scraped the mineral off from within if supplied some energy. The study suggests the electric fields produced by the charged surface could have provided this energy.

Surface tension – the force that keeps droplets spherical – could have been involved as well. In the experiment, a contest between surface tension, which is attractive, and like charges on the surface repelling each other could have set off shockwaves that blew up the microdroplets.

“This is a striking and non-intuitive result,” Shashi Thutupalli, a biophysicist at the National Centre for Biological Sciences, Bengaluru, who was not involved in the study, said to *The Hindu*. “It seems quite plausible that the high electric field within the droplets could cause the particle breakup.”

He added that the findings could be useful to the study of proto-cells, the precursors to cells as we know them today. Scientists are interested in

proto-cells because they could have played an important part in the processes that first created life on the earth. “For me personally, the relevance of these results to the context of the origins of life is very exciting.”

He said the microdroplets could mimic proto-cells by being little compartments in which biochemical reactions play out.

Making a green paradise

The formation of nanoparticles from microparticles, Dr. Pradeep said, is “related to the origin of life, the problem of agriculture, ... to issues as large as water itself. Another problem as big as water is food. It is in this context that soil is probably an interesting thing.”

Silica makes up half of sand. Plants absorb silica in the form of nanoparticles to help them become taller. The rice crop usually has high levels of silica.

Supplying soil with silica nanoparticles could thus have a positive impact on agriculture. “Here is a way to convert unproductive soil, unproductive fields or even desertified areas into productive areas,” Dr. Pradeep said.

He implored scientists to investigate whether water microdroplets react with minerals to form nanoparticles as part of atmospheric processes, in the form of ‘microdroplet showers’. Dr. Pradeep was optimistic they do.

(Karthik Vinod is a freelance science journalist and co-founder of Ed Publica. He has masters’ degrees in astrophysics and science, technology and society.)

THE GIST

Water molecules of microdroplets since they have so little room and are packed closely together are more eager to participate in chemical reactions. This isn’t possible with water molecules in bulk

The ability to create nanoparticles could be useful to the study of proto-cells, the precursors to cells as we know them today. Microdroplets could mimic proto-cells by being little compartments in which biochemical reactions play out

Plants absorb silica in the form of nanoparticles to help them become taller. Supplying soil with silica nanoparticles could have a positive impact on agriculture. This research provides ‘a way to convert unproductive soil, unproductive fields or even desertified areas into productive areas’

Home / Nanotechnology / Nanomaterials



- f** 32
- Twit
- Share
- Email

JUNE 11, 2024 REPORT

Editors' notes

Chemists discover spontaneous nanoparticle formation in charged microdroplets

by Bob Yirka , Phys.org

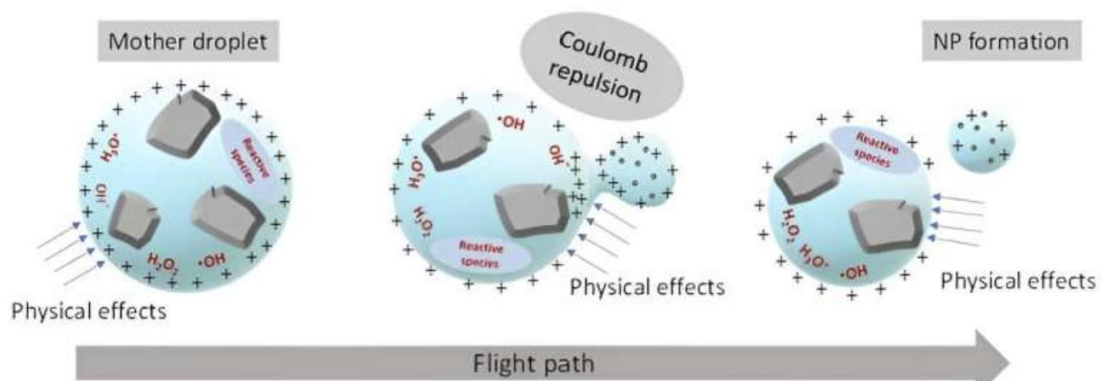
A team of chemists at the Indian Institute of Technology Madras, working with a pair of colleagues from the Jawaharlal Nehru Center for Advanced Scientific Research, both in India, has found that particles of minerals sometimes break down spontaneously when immersed in charged microdroplets, leading to the formation of nanoparticles.

JUNE 11, 2024 REPORT

Editors' notes

Chemists discover spontaneous nanoparticle formation in charged microdroplets

by Bob Yirka , Phys.org



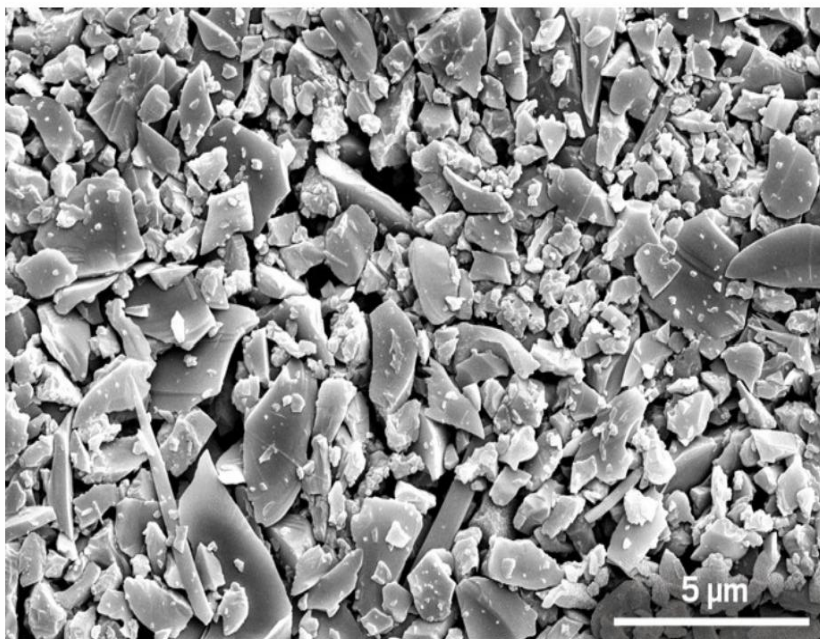
NANOMATERIALS

Charged microdroplets turn minerals into nanoparticles

Researchers show stable minerals easily breakdown in charged microdroplets

by *Fionna Samuels*

June 20, 2024 | A version of this story appeared in **Volume 102, Issue 19**



Credit: Courtesy of Thalappil Pradeep/IIT

A field emission scanning electron microscopy image of quartz sand after being finely ground

Microdroplets of water are capable of **incredible chemistry**; the tiny pools have vastly different properties different from those of bulk water. Now, researchers led by **Thalappil Pradeep** of the Indian Institute of Technology Madras have observed minerals spontaneously breaking down into nanoparticles when suspended in charged microdroplets (Science 2024, DOI: [10.1126/science.adl3364](https://doi.org/10.1126/science.adl3364)).

Silicon dioxide, or quartz, was chosen as the first mineral to investigate because of its high natural abundance, Pradeep says. For the experiment, graduate student **B. K. Spoorthi** ground a sample of river sand into a powder with grains fine enough to be suspended in microdroplets. The team loaded water and the sand into a home-built electrospray setup, which delivered charged microdroplets onto a piece of aluminum a few centimeters away.

Later, transmission electron microscopy revealed the metal was peppered with round silica nanoparticles: the bonds in the quartz had broken down in mere milliseconds. It's such a violent process that Pradeep thinks of the charged microdroplets as "wet fire."

"To see what they saw is astounding," says **Michael Hochella**, a geoscientist at Pacific Northwest National Laboratory who has studied the role of nanoparticles in nature for nearly 30 years. Despite both quartz and ruby taking millions of years to naturally dissolve, "here they are, breaking down dramatically and easily in very short amounts of time," Hochella says.

More research will reveal whether similar processes happen in naturally occurring microdroplets—a theory posited by the authors—but Hochella thinks "there's no question that they have hit on something that is going to be studied for a long time."

Water droplets accelerate formation of mineral nanoparticles essential for life



BY ANNA DEMMING | 10 JUNE 2024

Water microdroplets may play a role in the formation of soil. Experiments have revealed that microdroplets in electrospayed aerosols can cause the disintegration of minerals into the nanoparticles found in soils, some of which are essential for life.

Nanomaterials have been found to confer a number of beneficial properties to soil. Nanoclays can improve soil permeability, stability and plasticity, while nano-metal oxides and other materials can help by fertilising soils and enhancing the bioavailability of soil nutrients such as phosphorus. Previous work has suggested that nanomaterials are naturally present in soil due to weathering and mineral formation processes in the soil itself. This latest report suggests that aerosol microdroplets, which are naturally prevalent in the atmosphere, may play an important role in expediting these natural weathering processes.

Interest in microdroplet chemistry and its impact on a number of fields – though still controversial – has been attracting increasing interest over the past 10 years. ‘Aerosols are everywhere,’ says corresponding author Thalappil Pradeep at the Indian Institute of Technology Madras, India. ‘[I thought] there must be a connection between [aerosols and soil].’

As well as Pradeep’s own work a lot of the current interest in microdroplets was prompted by the work of Purdue University’s Graham Cooks, Stanford’s Richard Zare, Hong Gil Nam at South Korea’s Institute of Basic Science and their collaborators. They reported spontaneous reduction of gold ions and the formation of hydrogen peroxide evolution in water microdroplets in the late 2010s. Since then there have been reports of numerous intriguing chemical phenomena that take place in water droplets, suggesting explanations for various mysteries from the presence of hydrogen deposits where people dig for oil to the reactions that first initiated life itself.



Size matters

According to Zare, the unique chemistry found in water microdroplets is primarily brought about by two effects. One is the partial solvation of the hydrogen and hydroxide ions that all water at neutral pH contains. The other is the high electric field at the interface of the droplet and whatever medium it is in – in this case air. Crucially, these effects do not become significant unless the droplets are very small – microsized. ‘Normal water is, we consider, generally benign, a great solvent,’ he explains. ‘Water microdroplets – I’m telling you are highly reactive.’

In the new work, Pradeep and his collaborators ground up quartz into particles 5–10µm in size and suspended them in water. They then electrospayed the suspension through a capillary and then measured the deposit collected. Characterising the deposited minerals using transmission electron microscopy, x-ray diffraction and Raman spectroscopy revealed particles of quartz with an average diameter of 16nm. The results were similar using both ruby and fused alumina.

Pradeep emphasises the importance of multimodal characterisation for this kind of study, particularly as the phenomena that occur in microdroplets are controversial. ‘You may do some transmission electron microscopy, but that is not enough,’ he tells *Chemistry World*.

Pradeep and his collaborators also used density functional theory to calculate the cleavage and stacking fault energies. They also suggest that the presence of protons and an electric field plays a role in enhancing the fragmentation of the minerals into nanoparticles, which their mass spectrometry measurements corroborate.

In the experiment the microdroplets are generated by an electrospay but droplets of this size occur wherever water condenses. ‘This is the same thing, which goes on to cause all types of weathering and other types of chemical reactions,’ says Zare. ‘Am I surprised? No, no. No, no, not at all.’

Pradeep would now like to investigate how the fragmentation takes place in real time but in the longer term he has his sights on the potential benefits for agriculture. ‘I want to convert sand into soil,’ he says. This will require a better understanding of both experiment and theory but the key challenge, as he sees it, is scale. ‘It is not milligrams right, it is now mega tonnes,’ he says. ‘Extreme scale-up is required.’

A 'shock' discovery

MANUPRIYA
JUN 2024

from *Shastra* :: vol 03 issue 05 :: Jun 2024

PHOTO: BY SPECIAL ARRANGEMENT



Thalappil Pradeep with B.K. Spoorthi, lead author of the recent paper.

A new study establishes that charged microdroplets of water can break minerals and produce nanomaterials.

MCC introduces smart duck to track lake water quality

Ragu.Raman@timesofindia.com

Chennai: Madras Christian College has introduced a smart duck to track water quality of a lake inside its sprawling 300-acre campus in Tambaram.

The IoT-enabled, remote-controlled duck will move across the lake and gather real time data on seven key parameters, including water temperature, dissolved oxygen, turbidity and pH, among others.

The lake, one of the key water sources inside the campus, was desilted by Bilsleri International Limited as part of their CSR project. They also handed over

funds for developing a prototype for checking water quality.

A team from MCC-MRF Innovation Park developed the 3D-printed duck with sensors and created an app to receive and analyse data.

"We can make informed decisions on conserving the lake based on the data. It will help us to protect the ecology and wildlife inside the campus," says Paul Wilson, principal of Madras Christian College. The idea of deploying the smart duck was his.

He said any change in the water quality, including an increase in acidity levels,



HIGH ON TECH

could reveal contamination and help them take proactive measures to control the damage.

"The inbuilt solar panels can power the duck. It can be operated without sunlight for two days, and if needed, it can also be manually charged," said Kousik, founder of the startup KOLOZEN, which built the duck. The startup has now been fetching and transferring this data for the last two weeks.

Researchers say they could deploy similar ducks on other water bodies outside the campus to monitor water quality and collect data for local bodies.

"This data could tell us about what is happening to a water body during the rain, seasonal change, its environmental health, and diseases. We can also build a hydro informatics platform of a water body with this data. It has huge potential," said professor T Pradeep, department of chemistry, IIT Madras.

The scrub jungle inside the MCC campus is home to roughly about 90 spotted deer, porcupines, toddy cats, and bats. The duck has two cameras in its eyes to help the college track movements of wild animals within the campus.

Prof. M.V. Pylee Award for T. Pradeep

Published - March 12, 2024 08:12 pm IST - KOCHI

THE HINDU BUREAU



The award, instituted by the Cochin University of Science and Technology (Cusat), consists of a cash prize of ₹1 lakh, citation, and a memento. It is given to distinguished academicians in the country every year to honour their contributions as excellent educationalists, outstanding researchers, institution builders, and visionary scientists who bridge the gap between science and society. The award was instituted in the name of the late management expert and former Cusat Vice-Chancellor M.V. Pylee, according to a release.

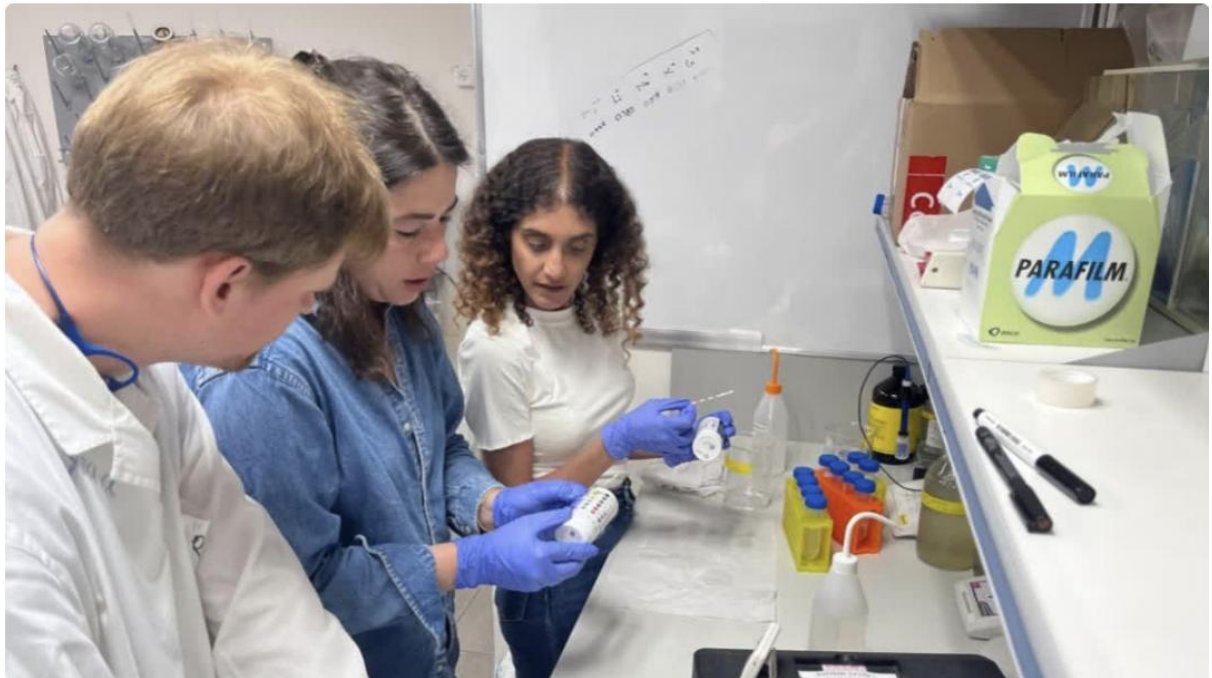
Dr. Pradeep had received the Padma Shri in 2020 for his contributions to science and technology and the Shanti Swarup Bhatnagar Prize in 2008. A native of Panthavoor in Malappuram district, he secured his PhD in Chemical Physics from the Indian Institute of Science, Bengaluru, under C.N.R. Rao. His research interests include molecular and nanoscale materials, clean water, surfaces, instrumentation, and business incubation, the release said.

Published - March 12, 2024 08:12 pm IST

ETV Bharat / Technology

IIT Madras Partners With Israel's Tel Aviv University, To Offer Water Quality Course: How To Apply, Last Date, Faculty | All Details Here

The last date for registration for this 4-month hybrid course is July 20. It aims to build a water quality map of India and the world by students, and in the process train them to become water quality professionals. Read on for more details.



Representational Image (IIT Madras)

Indian Institute of Technology, Madras (IIT Madras), in collaboration with Israel's Tel Aviv University and KMCH-Research Foundation (KMCH-RF), Coimbatore, is launching a four-month water quality course aimed at creating water-literate citizens.

The course will be delivered in hybrid mode through NPTEL's online platform, catering to final-year science and engineering students and individuals with a technical background interested in water quality.

The course organisers aim to create a comprehensive water map of India and globally with contributions from students, enhancing water literacy. Following an in-depth introduction to essential water quality concepts, students will conduct practical tests and surveys. Upon completion, they will receive a certificate that may count towards their degree programme.

The deadline for application submission is July 20. Interested and eligible candidates can apply through this link: bit.ly/3zgpkmY. The course duration is from July 29 to December.

Speaking about the course, professor Thalappil Pradeep, Department of Chemistry, IIT Madras, said, "Achieving Sustainable Development Goals of the United Nations is possible only when people understand the factors that hinder their realization. Water quality is crucial in this regard. This course aims to gather reliable water quality data and promote water literacy among participants. It is part of our initiative to train global water professionals."

Titled 'A Hybrid Course on Water Quality: An Approach to People's Water Data,' the course covers essential aspects of water quality, including parameter analysis and their health impacts. It aims to establish a comprehensive database from diverse sources such as households, rivers, borewells, groundwater, and pipelines.

Participants can attend lectures online or offline and access recorded sessions. Their understanding will be evaluated through online assignments and quizzes. Practical sessions involve field and lab measurements using handheld instruments and field test kits, focusing on parameters like chlorine levels, pH, conductivity, and bacterial presence.

The course design is based on a pilot study conducted last summer at various locations in Tamil Nadu, including Chennai and Erode, involving college students. Data collected during this initiative was compiled to create online records of water quality, including spatial coordinates and survey feedback.

Comments

Good News

Clean-water-for-all crusader Professor Thalappil Pradeep of IIT-Madras elected international member of US National Academy of Engineering

Professor Pradeep was bestowed the honour for his contributions to cluster chemistry and the discovery and implementation of affordable drinking water solutions.



Professor Thalappil Pradeep (Photo | chem.iitm.ac.in)

Professor Thalappil Pradeep, the Deepak Parekh Institute Chair Professor and professor of chemistry, from the Indian Institute of Technology, Madras, has become the latest Indian member of the prestigious United States National Academy of Engineering (NAE).

Professor Pradeep was bestowed the honour for his contributions to cluster chemistry and the discovery and implementation of affordable drinking water solutions.

A Padma Shri awardee, sixty-year-old Professor Pradeep is a recipient of the Shanti Swaroop Bhatnagar Prize and a student of Professors CNR Rao and MS Hegde, under whose tutelage he earned a Phd from the Indian Institute of Science, Bengaluru.

The National Academy of Engineering is organized into twelve engineering categories. It has 2310 active members from the US and 332 international members.

Reliance Chairman Mukesh Ambani is another notable member of the Academy.

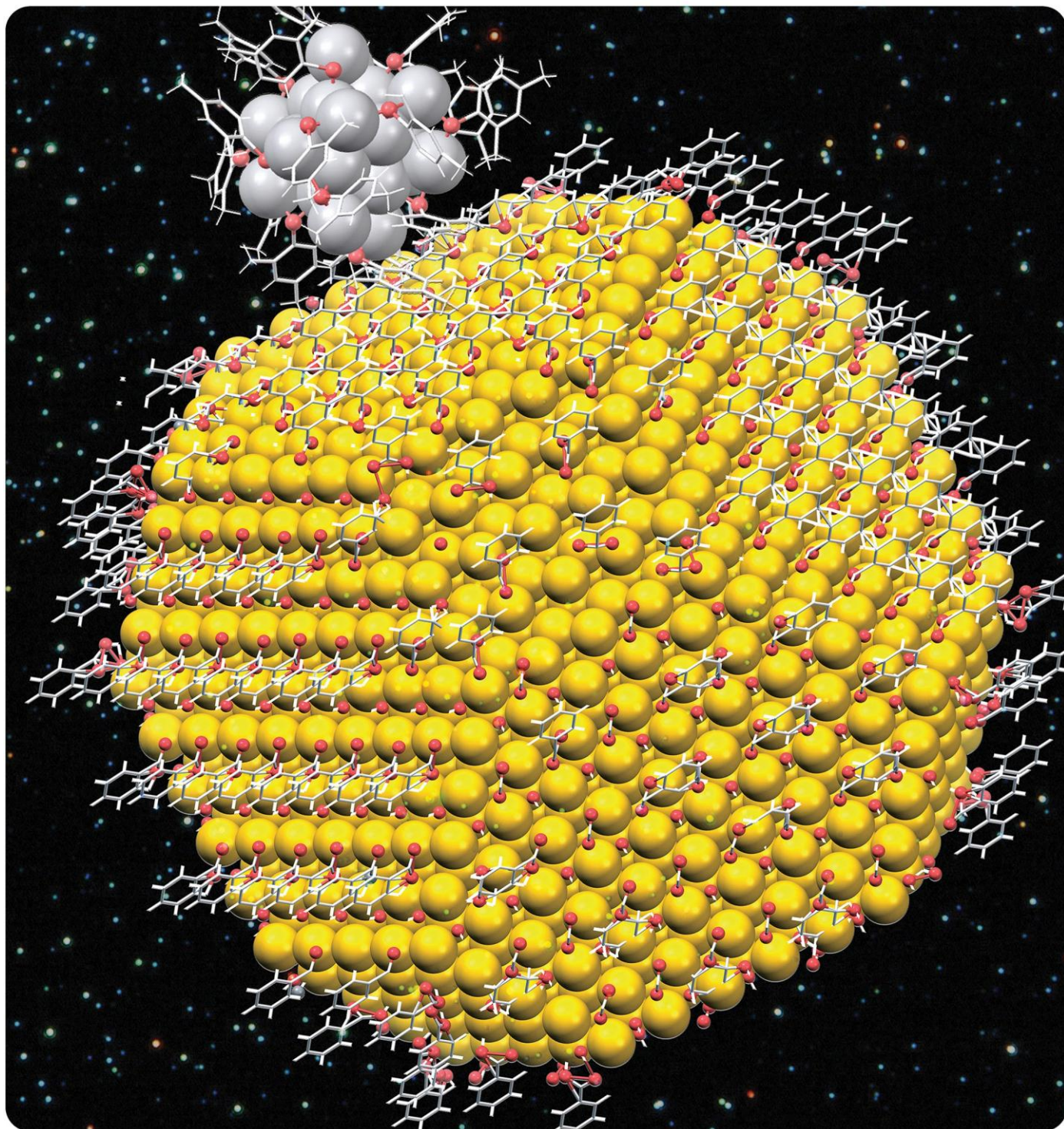
His election to the Academy comes a year after the induction of Professor Aniruddha Bhalachandra Pandit, vice chancellor and UGC Professor, Chemical Engineering, Institute of Chemical Technology, Mumbai and Professor Raman Sujith, Chair professor, Department of Aerospace Engineering, Indian Institute of Technology, Madras.

Like Professor Pradeep, sixty-six-year-old Professor Pandit was also inducted into the Chemical Engineering wing of the Academy.

Professor Sujith had earned the honour last year for his contributions to aerospace engineering and was the second Indian after Dr BN Suresh, ex-director of Vikram Sarabhai Space Centre, ISRO, to be elected to the wing.

Professor Ashok Jhunjhunwala was the first IIT-Madras professor to be elected to the National Academy of Engineering. He is currently President of IIT Madras Research Park and Incubation Cell.

Cover arts



July 23, 2024 Volume 40, Number 29

pubs.acs.org/Langmuir

LANGMUIR



CELEBRATING **40** YEARS



ACS Publications
Most Trusted. Most Cited. Most Read.

www.acs.org

Nanoscale

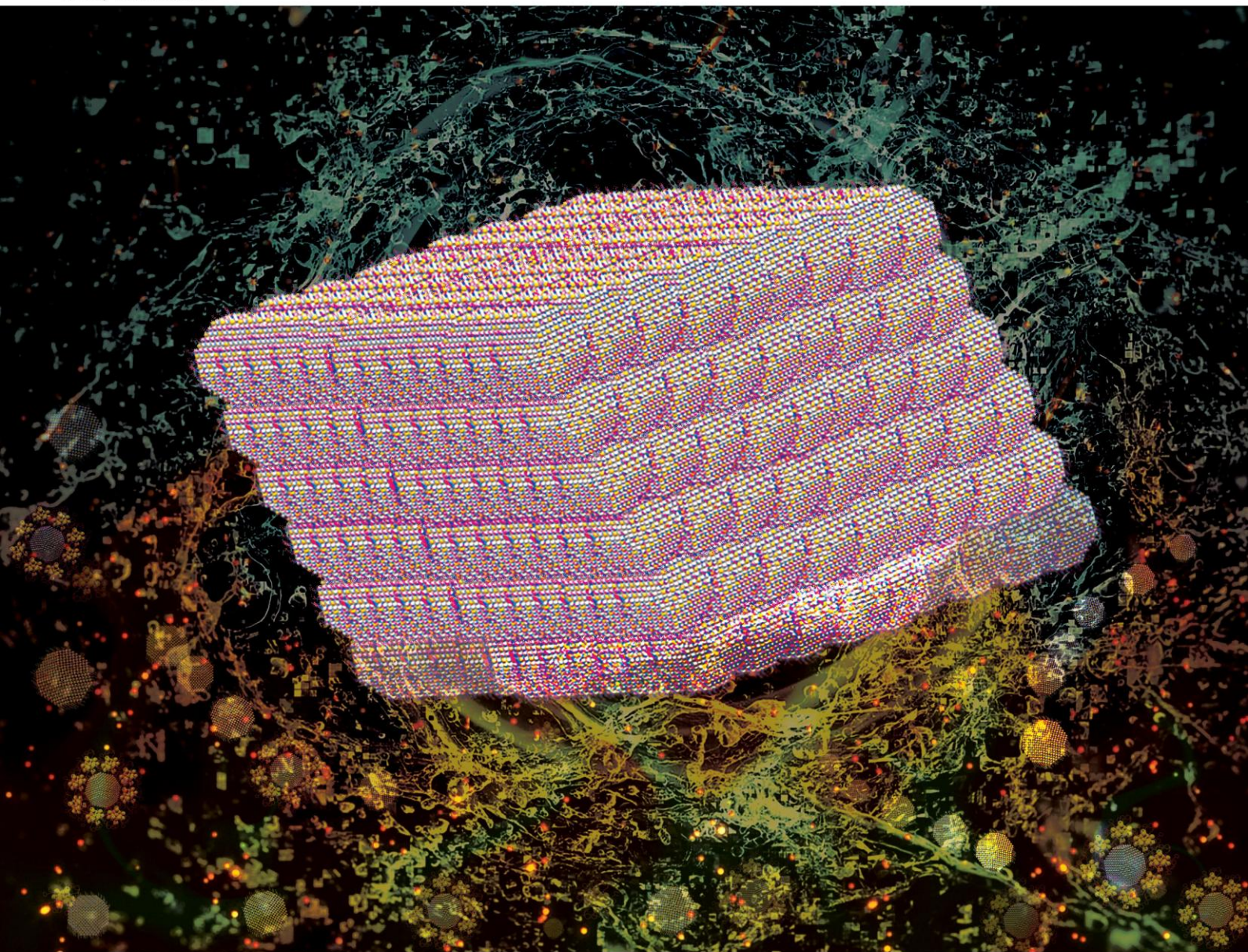
rsc.li/nanoscale



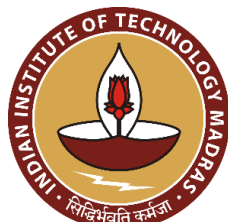
ISSN 2040-3372

Nanoscale

rsc.li/nanoscale



Pradeep Research Group



Acknowledgement

Students

And

Collaborators

Funding



खान मंत्रालय
MINISTRY OF
MINES

ANRF

CryptoRelief

